Transactions of the ASME

HEAT TRANSFER DIVISION
Chairman, R. GREIF
Secretary, G. P. PETERSON
Technical Editor, R. VISKANTA (1995)
Associate Technical Editors,
Y. BAYAZITOGLU (1995)
S. H. CHAN (1997)
V. K. DHIR (1996)
A. FAGHRI (1996)
W. L. GROSSHANDLER (1995)
C. E. HICKOX, JR. (1995)
Y. JALURIA (1996)
J. R. LLOYD (1995)
M. F. MODEST (1996)
R. A. NELSON, JR. (1996)
T. J. RABAS (1997)
T. W. SIMON (1995)
K. VAFAI (1997)
B. W. WEBB (1997)

BOARD ON COMMUNICATIONS
Chairman and Vice President
R. D. ROCKE

Members-at-Large
T. BARLOW, N. H. CHAO, A. ERDMAN,
G. JOHNSON, L. KEER, W. MORGAN,
E. M. PATTON, S. PATULSKI, R. E. REDER,
S. ROHDE, R. SHAH, F. WHITE,
J. WHITEHEAD

OFFICERS OF THE ASME
President, P. J. TORPEY
Executive Director,
D. L. BELDEN
Treasurer,
R. A. BENNETT

PUBLISHING STAFF
Mng. Dir., Publ.,
CHARLES W. BEARDSLEY
Managing Editor,
CORNELIA MONAHAN
Sr. Production Editor,
VALERIE WINTERS
Production Assistant,
MARISOL ANDINO

Transactions of the ASME, Journal of Heat Transfer (ISSN 0022-1481) is published quarterly (Feb., May, Aug., Nov.) for $185.00 per year by The American Society of Mechanical Engineers, 345 East 47th Street, New York, NY 10017. Second class postage paid at New York, NY and additional mailing offices. POSTMASTER: Send address changes to Transactions of the ASME, Journal of Heat Transfer, c/o THE AMERICAN SOCIETY OF MECHANICAL ENGINEERS, 22 Law Drive, Box 2300, Fairfield, NJ 07007-2300.
CHANGES OF ADDRESS must be received at Society headquarters seven weeks before they are to be effective. Please send old label and new address.
PRICES: To members, $40.00, annually; to nonmembers, $185.00.
Add $30.00 for postage to countries outside the United States and Canada.
STATEMENT from By-Laws. The Society shall not be responsible for statements or opinions advanced in papers or . . . printed in its publications (B7.1, para. 3).

INDEXED by Applied Mechanics Reviews and Engineering Information, Inc.
Canadian Goods & Services Tax Registration #126148048.

Journal of Heat Transfer

Published Quarterly by The American Society of Mechanical Engineers

VOLUME 116 • NUMBER 4 • NOVEMBER 1994

TECHNICAL PAPERS

(Contents continued on inside back cover)

(Contents continued)

Journal of Heat Transfer

Editorial

JOURNAL OF HEAT TRANSFER EDITORIAL POLICY STATEMENT ON NUMERICAL ACCURACY

The purpose of this statement is to establish and clarify acceptable standards for the publication of numerical results, and supplements the previously established JOURNAL OF HEAT TRANSFER Policy on Reporting Uncertainties in Experimental Measurements and Results.[1] In developing the current policy, the policy statement on control of numerical accuracy adopted by the ASME *Journal of Fluids Engineering*[2] was consulted, as well as similar policy statements currently under consideration by the AIAA journals and the *International Journal for Numerical Methods in Fluids.* We appreciate the willingness of those involved with the development of these latter policies to share their thinking with us and to allow our adoption of specific elements of their policy statements.

Succinctly stated, the editorial policy of the JOURNAL OF HEAT TRANSFER regarding the review and publication of numerical studies is as follows:

> *The JOURNAL OF HEAT TRANSFER will not accept for review or publication any manuscript reporting the numerical solution of a heat transfer problem that fails to establish adequately the accuracy of the computed results.*

The implementation of this policy will be at the discretion of the editor and associate editors in association with the reviewers, and will be guided, in essence, by the considerations set forth below and by the view attributed to Kline,[3] in the context of experimental uncertainty analysis, that "... any appropriate analysis is far better than none as long as the procedure is explained."

To be specific, all manuscripts submitted for review that include numerical simulations must contain the following essential elements:

- A problem statement that is of sufficient clarity and completeness to allow the reproduction of the results by informed readers. As a minimum, this should include a statement of the governing equations solved, all relevant boundary and initial conditions, and values of associated physical and numerical parameters. Values for any adjustable or arbitrary parameters employed to obtain the solution must be explicitly given.
- A description of the solution technique employed. If a standard method is used, the description can be via reference to appropriate prior publications. If a new method is introduced, the description must be sufficiently complete to allow implementation of the numerical scheme and replication of relevant results by informed readers.
- The numerical solution must be supplemented with acceptable accuracy estimates for both the method employed and the results presented. A single calculation using a fixed discretization will not be acceptable, since no error estimate can be inferred from such a calculation.

Authors may use any appropriate method for the estimation of errors. One, or more, of the following approaches may be useful in this regard:

- Comparison of numerical results with those from a sufficiently similar model problem available in the literature, possessing a known exact or highly accurate approximate analytical solution; or with an established, high-accuracy, fine-grid, numerical benchmark solution of the same, or closely similar, problem.
- A precisely defined and documented grid refinement or grid coarsening study. Marginal refinement showing a qualitative convergence trend is not acceptable. Other numerical and arbitrary parameters such as time step, convergence criterion, and boundaries of the computational domain should also be varied to ensure that the results are independent of these quantities.
- Comparison with reliable experimental results that possess an associated established uncertainty. Noting "reasonable agreement" with experimental data is not, in general, sufficient justification for acceptance of numerical results, especially when adjustable parameters are involved. Numerical and experimental results may be plotted or tabulated to indicate the level of agreement.

In the approaches described above, references to grid refinement are intended to be interpreted in a general sense to include numerical methods that are not explicitly dependent on a computational grid in the manner typically associated with, say, finite difference methods. For example, grid-free methods would require modification of the number, or size, of discrete elements in the computation to establish error estimates. An additional comment is in order regarding comparisons of numerical results with

[1] ASME JOURNAL OF HEAT TRANSFER, Vol. 115, February 1993, pp. 5–6.
[2] ASME *Journal of Fluids Engineering,* Vol. 115, September 1993, pp. 339–340.
[3] Kline, S. J., 1985, "The Purposes of Uncertainty Analysis," ASME *Journal of Fluids Engineering,* Vol. 107, pp. 153–164.

experimental data. It is recognized that, when the results of a numerical simulation are compared with experimental data, it may not be possible to separate errors in modeling from those associated with the numerical method. In these situations, a separate estimate of the numerical error should be established. In rare situations where none of the above approaches can be satisfactorily employed to establish the accuracy of the results, other methods of error estimation acceptable to the editor, associate editors, and reviewers may be appropriate. For an illustration of many of the elements involved in establishing the accuracy of a numerical solution, the study of natural convection reported by de Vahl Davis,[4] or the method discussed by Roache[5] for the uniform reporting of grid refinement studies, may be consulted.

By implementation of this policy, it is the intent of the editorial board to establish guideline requirements for the publication of numerical results and to enhance the quality of publications involving numerical simulations. It is not our intent to effect a significant increase in the length of papers published in the journal, or to impose excessive requirements on prospective authors. Rather, we hope to elicit a "good faith" effort from authors to establish the accuracy of their numerical simulations.

The Editorial Board

[4] de Vahl Davis, G., 1983, "Natural Convection of Air in a Square Cavity: A Bench Mark Numerical Solution," *Int. J. Numer. Methods Fluids*, Vol. 3, pp. 249–264.

[5] Roache, P. J., 1993, "A Method for Uniform Reporting of Grid Refinement Studies," *Quantification of Uncertainty in Computational Fluid Dynamics*, ASME FED-Vol. 158, pp. 109–120.

Invited Review Paper

Challenges in Microscale Conductive and Radiative Heat Transfer

C. L. Tien
A. Martin Berlin Professor,
Department of Mechanical Engineering,
University of California,
Berkeley, CA 94720
Honorary Mem. ASME

G. Chen
Assistant Professor,
Department of Mechanical Engineering
and Materials Science,
Duke University,
Durham, NC 27708
Assoc. Mem. ASME

This work addresses challenges in the emerging field of microlength scale radiative and conductive heat transfer in solids and recommends specific directions of future research. Microlength scale heat transfer involves thermal energy transport processes in which heat carrier characteristic lengths become comparable to each other or the characteristic device dimension. Identification of these characteristic lengths leads to the definition of different microscale heat transfer regimes. A review of the theoretical bases describing heat transfer in each regime is followed by a discussion of the obstacles confronted in current research. Engineering challenges are illustrated with the applications of microscale heat transfer in cryogenic systems, material processing, and electronic, optical, and optoelectronic devices. The experimental difficulties discussed have hampered the development of microscale heat transfer research and deserve great efforts to overcome them.

Introduction

Modern microfabrication technologies are shrinking devices into micro- and nanometer scales (Koshland, 1991). This trend of miniaturization has recently brought an unprecedented upsurge of research interests in microscale heat transfer (Garner and Udell, 1993; Tien et al., 1994). Actually, microscale heat transfer phenomena are replete in cryogenic systems and have been studied in the past, because the heat carrier mean free path (MFP) is long at low temperatures (Tien and Cunnington, 1973). Examples are cryogenic multilayer-insulation systems, spacecraft thermal control coatings, and superconducting thin films (Flik and Tien, 1990). Miniaturization of devices, however, has increased the importance of understanding microscale heat transfer processes over a wide temperature range encountered in the processing and operation of these devices. For example, in a vertical-cavity surface-emitting semiconductor laser, as illustrated in Fig. 1(a), excessive internal heating represents a major impediment to the increase of its output power and integration (Osinski, 1991; Chen et al., 1994a). Another example is sketched in Fig. 1(b) concerning a micromachined surface, often on silicon, which has thermal radiative properties drastically different from a smooth surface (Hesketh et al., 1986). Such microstructures offer the opportunity of maximizing the absorption of radiant energy detectors.

Microscale thermal phenomena may occur in either length or time scale or both. Microlength scale heat transfer involves heat transfer processes when the various characteristic lengths of heat carriers (electrons, phonons, and photons) become comparable to each other or to the characteristic device dimension. Microtime scale heat transfer involves heat transfer processes when the various characteristic times of heat carriers become comparable to the characteristic energy excitation time. For heat transfer in microlength scale, Kotake (1991) discussed molecular engineering problems in heat and mass transfer. Flik et al. (1992a) presented several regime maps to delineate the micro- and macroscale heat transfer regimes. Majumdar (1993) derived the equation of phonon radiative transfer from the Boltzmann transport equation. Chen (1993) clarified different microscale conduction and radiation heat transfer regimes. Kumar (1993) discussed various length scales in radiation transport. The main thrusts for the study of microtime scale heat transfer are the short-pulse laser applications and high speed electronics (Anisimov et al., 1974; Yajima et al., 1988; Fann et al., 1992; Qiu and Tien, 1993). More works in microscale heat transfer are scattered in various application domains.

This work addresses challenges in microlength scale radiative and conductive heat transfer in solids and recommends specific directions of future research. The next section identifies different microscale heat transfer regimes based on heat carrier characteristic lengths, describes principles governing the heat transfer process in each regime, and points out new theoretical challenges. The subsequent section discusses significant microscale heat transfer problems in engineering applications. Conducting experiments in microscale heat transfer regimes is extremely difficult because of the small dimensions generally involved. Challenges in experimental research are illustrated in a separate section.

Fundamentals of Microscale Heat Transfer

An understanding of the various heat carriers and their characteristic lengths is the first step toward solving a microlength scale heat transfer problem. The major heat carriers for conductive and radiative heat transfer in solids are electrons, phonons, and photons. Table 1 lists important features of the three different heat carriers, the motion of which governs heat transport. The traditional thermal science, or macroscale heat transfer, employs phenomenological laws, such as Fourier's law, without considering the detailed motion of the heat carriers. Decreasing device dimensions, however, has brought an increasing need of understanding the heat transfer processes from the microscopic picture of heat carriers.

Heat Conduction. Heat is conducted in solids through free electrons and phonons. In metals, free electrons dominate the heat conduction, while in insulators and semiconductors, phonons are the major heat carriers. Demarcation of the macro- and microscopic heat conduction regimes depends on the various characteristic lengths of the heat carriers (Table 2), which are illustrated in Fig. 2.

Contributed by the Heat Transfer Division and presented at the ASME Winter Annual Meeting, Anaheim, California, November 8–13, 1992. Manuscript received by the Heat Transfer Division November 1993; revision received April 1994. Keywords: Conduction, Radiation, Reviews. Associate Technical Editor: Y. Bayazitoglu.

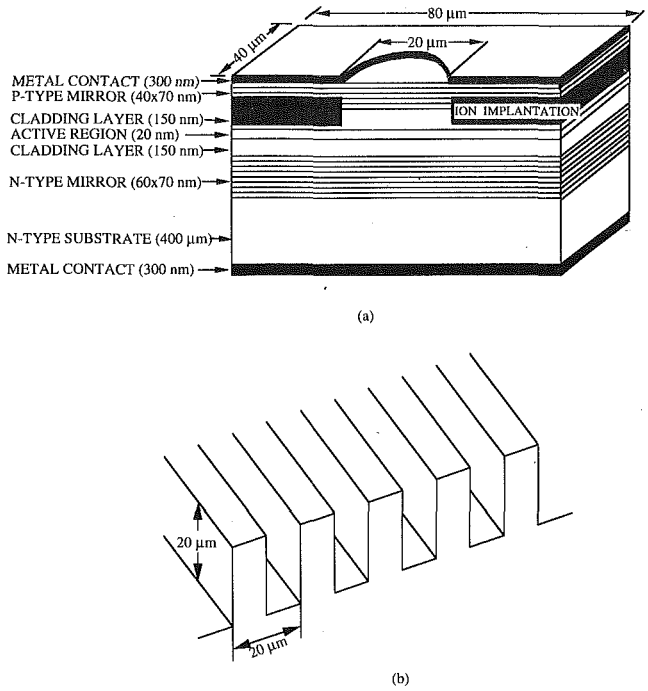

Fig. 1 Schematic illustration of (a) a vertical-cavity surface-emitting laser and (b) a micromachined surface

For thin-film devices, the film thickness is one of the characteristic device dimension. Since thin films often have complicated microstructures, the characteristic dimensions (such as grain size) associated with these microstructures can become very important for heat transfer.

The heat carrier mean free path Λ is the average distance a carrier travels in a bulk material before its excess energy is lost. It is determined by the various scattering mechanisms in the solid, including scattering by phonons, electrons, impurities, and imperfections. Since the strengths of various scattering mechanisms are strong functions of temperature, Λ also depends on temperature.

Due to the wave-particle duality, both electrons and phonons have a characteristic wavelength λ_c. The characteristic electron wavelength is its thermal de Broglie wavelength (Tien and Lienhard, 1979),

$$\lambda_c = \hbar/\sqrt{2\pi m\kappa T} \tag{1}$$

Table 1 General features of heat carriers

	Free Electron	Phonon	Photon
Generation	valence or excited electron	lattice vibration	atomic, molecule transition
Propagation media	in vacuum or media	in media	in vacuum or media
Statistics	Fermion	Boson	Boson
Frequency	0-infinte	Debye cut-off	0-infinte
Dispersion	$E=\hbar^2\mathbf{q}^2/(2m)$	$E=E(\mathbf{q})$	$\nu = c/\lambda$
Velocity (m/s)	$\sim 10^6$	$\sim 10^3$	$\sim 10^8$

where m is the effective electron mass. At high temperatures (above the Debye temperature), the dominant phonon wavelength is of the order of lattice constant a. At low temperatures, the characteristic phonon wavelength is of the order of $\theta_D a/T$ (Gurevich, 1986).

A length d_T characterizing the temperature gradient, called the temperature penetration depth in analogy to the radiation penetration depth, has not received much attention. Here, the temperature penetration depth is defined as the characteristic temperature divided by the maximum temperature gradient,

$$d_T = T/(dT/dx)_m \tag{2}$$

It is not an intrinsic length of the heat carrier but may depend on time, heat source distribution, and the thermal properties of the material. This characteristic length becomes important in fast heating processes.

Figure 3 shows the various characteristic lengths of gold as a function of temperature. The electron mean free path is estimated from the kinetic relation (Tien and Lienhard, 1979)

$$\Lambda \sim 3k/Cv_F \tag{3}$$

where the Fermi velocity v_F is taken as 1.39×10^6 m/s (Kittel, 1986). Tabulated values for the thermal conductivity, diffusivity, and specific heat are used (Touloukian et al., 1973). For laser heating of gold, the heat source is generally distributed within a surface layer of 20 nm. The temperature penetration depth can be taken as the characteristic thermal diffusion length $\sim(\alpha t_p)^{1/2}$ if it is much larger than 20 nm.

Depending on the relative magnitude of the various characteristic lengths described above, two microscale heat conduction regimes can be identified, as summarized in Table 3.

Nomenclature

a = lattice constant, m
$\mathbf{a}$ = heat carrier acceleration, m s^{-2}
c = speed of light
C = volumetric specific heat, J m^{-3} k^{-1}
d = radiation or temperature penetration depth, m
e = charge of an electron, C
E = energy, J
f = heat carrier distribution function
h = characteristic device dimension, m
$\hbar$ = Planck constant divided by 2π, J s
k = imaginary part of complex refractive index
K = thermal conductivity, W m^{-1} K^{-1}
L = coherence length, m
m = electron effective mass, kg
n = real part of complex refractive index
N = electron number density, m^{-3}
$\mathbf{q}$ = wavevector, m^{-1}
t = time, s
T = temperature, K
v_F = Fermi velocity, m s^{-1}
$\mathbf{v}$ = heat carrier group velocity, m s^{-1}
x = coordinate
α = thermal diffusivity, m s^{-2}
Δh = variation of film thickness, m
$\Delta\nu$ = half-bandwidth, Hz
θ_D = Debye temperature, K
κ = Boltzmann constant, J K^{-1}
λ = wavelength, m
Λ = heat carrier mean free path, m
ν = frequency, Hz
ρ = electrical resistivity, Ω m
τ = relaxation time, s

Subscripts

c = heat carrier
m = maximum
o = equilibrium distribution
p = heating pulse duration
$\mathbf{q}$ = wavevector
s = scattering
T = temperature

Table 2 Characteristic lengths in heat conduction and radiation

Conduction	Radiation
characteristic dimension, h	characteristic dimension, h
heat carrier MFP, Λ	photon-excited carrier MFP, Λ
temperature penetration depth, d_T	radiation penetration depth, d
heat carrier wavelength, λ_c	photon-excited carrier wavelength, λ_c
	photon wavelength, λ
	photon coherence length, L

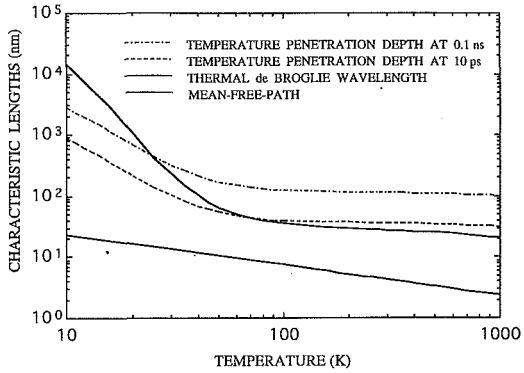

Fig. 3 Characteristic lengths for heat conduction in gold

The first microscale heat transfer regime is defined when

$$(i) \quad h/\Lambda < O(1) \quad \text{or} \quad d_T/\Lambda < O(1) \qquad (4a,b)$$

and

$$(ii) \quad h/\lambda_c > O(1) \qquad (5)$$

where an order of magnitude sign is used. Flik et al. (1992a) showed that the size effects on heat conduction become important when $h < 7\Lambda$. A quantitative demarcation of the various regimes requires more research.

The first microscale heat conduction regime is characterized by the classical size effects. When Eq. (4*a*) holds, the heat carrier Λ is limited by the boundary scattering in addition to the internal scattering mechanisms. When Eq. (4*b*) is true, heat carriers experience a large temperature difference within one Λ. In this case, the energy transfer becomes nonlocal and the effective thermal conductivity depends on the temperature gradient (Mahan and Claro, 1988). Such nonlocal transport effects are similar to the anomalous skin effects in radiation properties (Ziman, 1960). For both cases, the Boltzmann transport equation (BTE) can be used to describe the heat carrier distribution function, f (Kittel, 1986),

$$\frac{\partial f}{\partial t} + \mathbf{v}\cdot\nabla_x f + \mathbf{a}\cdot\nabla_q f = \left(\frac{\partial f}{\partial t}\right)_s \qquad (6)$$

where $\mathbf{v}$, $\mathbf{a}$ are the heat carrier group velocity and acceleration, respectively. Subscripts $\mathbf{x}$, $\mathbf{q}$, and s represent space, wavevector, and scattering terms, respectively. Solution of the BTE yields the heat flux, which in combination with the first law of thermodynamics gives the equation governing the temperature distribution.

The major difficulty lies in solving the BTE. Two approximations often used in solving the BTE are (1) neglect the deviation from equilibrium in the left-hand side of the equation: $f = f_o$, where f_o is the equilibrium distribution at the local temperature, and (2) the relaxation time approximation for the scattering term

$$\left(\frac{\partial f}{\partial t}\right)_s = -\frac{f - f_o}{\tau} \qquad (7)$$

where τ is the relaxation time. Under these two approximations, the Fourier law can be derived from the steady-state BTE, together with an expression for the thermal conductivity (Callaway, 1959). In the first microscale heat conduction regime, however, the first approximation is no longer valid and heat conduction becomes a nonlocal process. It is known that phonon transport is ballistic rather than diffusive when Λ is much longer than the characteristic dimension (Klitsner et al., 1988; Majumdar, 1993).

The relaxation time approximation has been applied in the first microscale regime in many works. A nontrivial question, however, is how to define the temperature in small structures because temperature is a concept at thermal equilibrium. In a bulk medium, the local thermal equilibrium is reached within a region of the order of heat carrier Λ, and the equilibrium heat carrier distributions are described by the Einstein distribution for phonons and Fermi–Dirac distribution for electrons. When Λ is greater than h or d_T, such a local equilibrium state is no longer reachable. Strictly speaking, the temperature concept is no longer applicable (Gurevich, 1986). Several equivalent temperatures have been defined (Ziman, 1960; Chen and Tien, 1993a; Goodson and Flik, 1992a). The validity of these temperature definitions requires further study and experimental proof.

Thermal conductivity is a very important property for bulk materials. In the first microscale regime, however, it is no longer an intrinsic property but depends on size, shape, boundary, and heating conditions. Consequently, there arises the question about whether the thermal conductivity or some more fundamental parameters such as the relaxation time or scattering rate should be used to describe heat conduction.

Microstructures are characterized by interfaces, boundaries, and grain boundaries. There are two ways to incorporate their effects on heat conduction into the BTE. One is to consider them as volumetric effects and combine them into the scattering term through either empirical rules, such as Matthiessen's rule, or through calculation from quantum mechanical principles (Ziman, 1960). The other is to treat them as boundary conditions for the

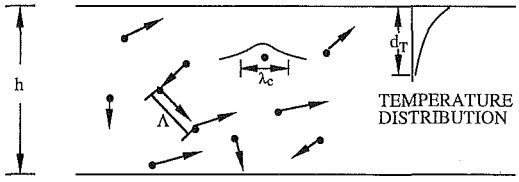

Fig. 2 Illustration of characteristic lengths in conduction

Table 3 Microscale conductive and radiative heat transfer regimes

Conduction	Radiation
	First microscale regime $h/L < O(1)$
First microscale regime i) $h/\Lambda < O(1)$ or $d_T/\Lambda < O(1)$ and ii) $h/\lambda_c > O(1)$	Second microscale regime i) $h/\Lambda < O(1)$ or $d/\Lambda < O(1)$ and ii) $h/\lambda_c > O(1)$
Second microscale regime $h/\lambda_c < O(1)$	Third microscale regime $h/\lambda_c < O(1)$

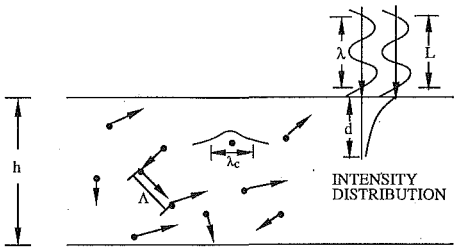

Fig. 4 Illustration of characteristic lengths in radiation

BTE. The first approach is simpler and more appropriate for grain boundaries because they spread in the volume of the structure. The second approach is more natural for boundaries, even though Matthiessen's rule is often applied to treat the boundary effects (Callaway, 1959). Interfaces lie between solid boundaries and grain boundaries. There is very little work on the effects of the interface on heat conduction except the traditional field of thermal boundary resistance (Swartz and Pohl, 1989). Chen and Tien (1993a) considered the phonon transmission and reflection effects on thermal conductivity at the interfaces of a GaAs quantum well by building appropriate boundary conditions. Because of the transmission of heat carriers at an interface, the thermal conductivity of an isolated film, either calculated or measured, may not be appropriate when the film becomes an inner layer of a multilayer system. Efforts should be directed to examine how interface conditions affect transmission and reflection of heat carriers, determine the conditions for specular and diffuse reflection, and quantify the interface effects on heat transport.

The second microscale regime is defined when the characteristic heat carrier wavelength of the material is of the same order as the characteristic dimension,

$$h/\lambda_c < O(1) \tag{8}$$

In this regime, the quantum size effects become important. The BTE has been used to describe the electron transport properties in quantum structures (QS) (Dharssi et al., 1991), though the quantum transport theory is available (Iafrate, 1983). Applicability of the BTE to the second microscale heat transfer regime has not been examined. Few papers on heat conduction in QS used the BTE (Ren and Dow, 1982; Chen and Tien, 1993a). The quantum effects are manifested in the change of phonon and electron spectra, which in turn affect their density of states, scattering mechanisms, and group velocity. In the BTE, these effects can be incorporated into the scattering and velocity terms.

Kotake (1991) and Wakuri and Kotake (1991) used the molecule dynamic equation based on the argument that the BTE is a statistical equation, and statistics is no longer valid when the film is very thin. This argument, however, does not hold for solids. For phonons, for example, a film of a few atomic layers only means that the phonon states are limited in the direction perpendicular to the film, but it is still possible to have enough phonons in each state to satisfy the statistics requirement, because the number of phonons is a measure of the amplitude of the lattice vibration. However, when the film is very thin, the generally used periodic boundary condition (Kittel, 1986) in the derivation of phonon spectrum may not be valid. The molecular approach is more advantageous in modeling the thin film growth (Fang et al., 1991). Work should be done to compare the results obtained from the BTE and from the molecule dynamics approach.

Radiation. Figure 4 illustrates the characteristic lengths for radiation (Table 2). Compared with heat conduction, there are two more characteristic lengths in thermal radiation. They are the photon wavelength and coherence length (Born and Wolf, 1980). The characteristic radiation wavelength depends on the radiation source. For a thermal source, it is given by Wien's displacement law,

$$\lambda T \sim 2898\ \mu\text{m K} \tag{9}$$

The photon coherence length is the maximum optical path difference between two wave trains from the same light source before their interference ability is lost. Metha (1963) gave the coherence length, L, of blackbody radiation in vacuum as

$$L = 0.3\pi c\hbar/\kappa T \tag{10}$$

The radiation penetration depth, d, characterizing the absorption in the medium, is the depth at which the intensity is attenuated to e^{-1} of its value at the boundary.

Figure 5 shows various radiative characteristic lengths in gold. For the radiative properties, the electron momentum Λ should be used (Ziman, 1960),

$$\Lambda = v_F m/(\rho n e^2) \tag{11}$$

where the electron number density n is taken as 5.9×10^{28} m^3 (Kittel, 1986). The electrical resistivity is obtained from the tabulated values (Hellwege, 1982). In Fig. 5, the radiation penetration depth is calculated from the Drude free electron model using the electron relaxation time derived from Eq. (11). The wavelength used for the penetration depth at each temperature corresponds to Wien's law. Comparing the two electron Λ curves in Figs. 3 and 5, it can be seen that the electron momentum Λ is longer than its energy Λ at low temperatures, while at high temperatures, the two are almost identical.

Three microscale radiation heat transfer regimes may be defined based on the relative magnitude of the various characteristic lengths. The first microscale radiation regime is defined when

$$h/L < O(1) \tag{12}$$

Again, order of magnitude is used. Exact demarcation of the first microscale radiation regime depends on the application. In this regime, the optical constants of the material are not affected by the size and boundary of the device; however, the derived radiative properties, such as the reflectance, transmittance, and scattering cross section have to include the wave nature of the radiation. They are obtained through the solution of the Maxwell electromagnetic wave equations (Born and Wolf, 1980). It is noted that it is not the radiation wavelength but the photon coherence length, that determines the first microscale regime. The latter is a function of the wavelength and the radiation frequency bandwidth, the radiation source shape and dimension, etc. (Born and Wolf, 1980).

Some specific criteria have been established to delineate the first microscale and the macroscale radiation regimes. Tien (1988) summarized radiation in particulate systems and regime maps for the dependent and independent scattering. Tuntomo et al. (1991) considered internal absorption inside a single particle and compared the wave optics and intensity superposition results. Chen and Tien (1992), and Richter et al. (1993) developed a

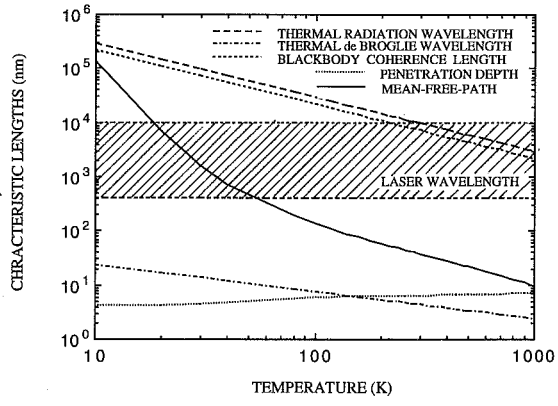

Fig. 5 Characteristic lengths for radiation absorption in gold

general formulation for the radiative properties of films based on the optical coherence theory of light and presented regime maps delineating the macro- and first microscale radiative transfer regime.

In addition to the interference effect, tunneling of evanescent waves near a solid surface to another object can also be included in the first microscale regime. Cravalho et al. (1967) considered tunneling effect on the radiative transfer between two dielectrics. The principle of photon tunneling has been used to construct optical microscopes which break the diffraction limit (Reddick et al., 1990).

Most of the studies of radiative transfer in the first microscale regime deal with nonparticipating media. For these cases, the solution of the electromagnetic wave equations will give the radiation intensity distribution inside the media. How to include thermal emission into the calculation of radiation heat transfer in the first microscale regime needs to be addressed. Rytov (1959) developed a semiphenomenological theory of electromagnetic fluctuation to account for thermal radiation in absorbing media. The applications of this theory, however, have been limited to a uniform temperature field (Kattawar and Eisner, 1970).

The second microscale radiation regime is defined when

$$(i) \quad h/\Lambda < O(1) \quad \text{and} \quad d/\Lambda < O(1) \qquad (13a,b)$$

and

$$(ii) \quad h/\lambda_c > O(1) \qquad (14)$$

The second microscale radiation regime is characterized by the classical size effects on the fundamental optical properties. When Eq. (13*a*) holds, the boundaries impose a limit on the carrier Λ. Classical models such as the Drude and Lorentz models can be used for the optical constants, but with the modified Λ. Similar to heat conduction, the boundary and interface conditions affect Λ in this regime and thus the optical constants (Monreal et al., 1982). Equation (13*b*) defines the anomalous skin effect region (Ziman, 1960). It can be seen from Fig. 5 that the anomalous skin effect will be important for gold, especially at low temperatures. Armaly and Tien (1970) considered the size and anomalous skin effects on the emissivity of gold films. It should be noted that the optical constants of a thin film may also depend on its adjacent medium when $h < d < \Lambda < L$, because the interference effects will change the electromagnetic field distribution in the film. While in most cases, the second and third microscale regimes are subsets of the first microscale regime, it is possible that the electron mean free path becomes longer than the coherence length. In this case, radiative transfer is in the second microscale regime but not in the first microscale regime.

The third microscale regime is defined when

$$h/\lambda_c < O(1) \qquad (15)$$

In this third microscale regime, the quantum size effects become important. These include the change of electronic band structures and phonon spectra, and discretization of the available quantum states. An example is the quantization of optical properties in a quantum well (Yariv, 1989). The optical constants can be calculated from principles of quantum mechanics and solid state physics.

A large amount of work has been done on the fundamental optical properties of thin films because of their applications in electronics, optics, and optoelectronics. Challenges from the heat transfer point of view are to delineate these microscale regimes clearly and obtain the thermal radiative properties and radiant heat source distributions in microstructures. For example, Phelan et al. (1992) considered maximizing the absorption in a superconducting thin film bolometer, and Hesketh et al. (1986) studied emissivity from a micromachined silicon surface. Chen et al. (1994a) examined spontaneous radiation transfer in a semiconductor laser cavity. More examples will be given in the discussion of the applications of microscale heat transfer.

Applications of Microscale Heat Transfer

There are many systems where microscale heat transfer plays an important role. Among them, cryogenic insulation systems have received more attention because the characteristic thermal radiation wavelength and the heat carrier Λ are long at low temperatures (Tien and Cunnington, 1973). The low-temperature operation of semiconductor and superconductor devices continues to be one of the major thrusts for understanding the microscale heat transfer phenomena (Goodson and Flik, 1992b). Modern microfabrication technologies and microelectronic device operation, however, have seen increasing importance of understanding the microscale heat transfer mechanisms in thin film devices over a wide temperature range.

Thin films are often fabricated at elevated temperatures. Temperature uniformity, both temporal and spatial, during the film growth is of paramount importance to the quality of the film. The temporal temperature uniformity requires that the temperature of the film surface be constant during the growth of the film. Both fundamental and derived optical properties vary during the film growth process because the change in the morphology and film thickness (Chu et al., 1991; Flik et al., 1992b). The variation of surface emissivity during rapid thermal processing of thin film devices is the major source of temperature measurement error (Ray, 1992). The spatial temperature uniformity demands a uniform temperature distribution over the film. It determines the uniformity of the film thickness because in many film growth processes, chemical reactions happen at the surface. The Arhenius type of reaction rate dictates that the area with higher temperature will have a faster growth rate (Sorrel et al., 1992). Detailed modeling, considering the thermophysical and optical property variation with the film growth process, will provide valuable information for the fabrication of high quality films.

Associated with film fabrication is the post annealing of thin films, including laser, electron beam, fast thermal, and conventional thermal annealing. During the annealing process, the structure of the film changes greatly, as do the optical and thermal physical properties. In the fast laser annealing processes, the temperature penetration depth may become shorter than the heat carrier (electron, phonon) Λ so that the nonlocal effects have to be included (Mahan and Claro, 1988). In the radiation models, controversy exists about whether the geometric optics or the wave optics should be used (Sorrel et al., 1992). The partial coherence formulation of the film radiative properties may clarify the confusion (Chen and Tien, 1992; Richter et al., 1993). Figure 6 shows a regime map built on the partial coherence approach, where $\Delta\nu_o$ is the effective bandwidth around the central frequency ν_o, and Δh is the film thickness variation. Patterning on a wafer significantly affects the local radiative properties and thus the temperature uniformity during rapid thermal annealing (Van-

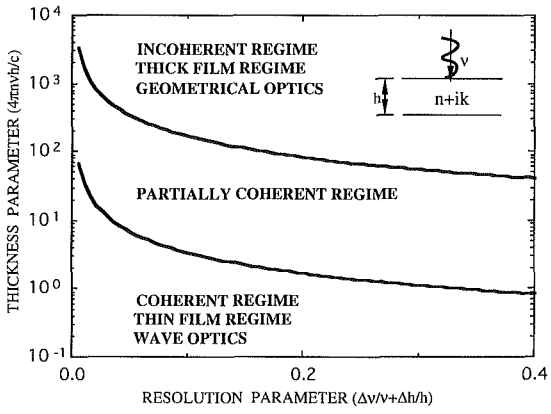

Fig. 6 Regime map for the radiation properties of films

denabeele et al., 1989). Effective methods of predicting the radiative properties of patterned structures should be developed.

Understanding microscale heat transfer is important for the operation of electronic, optical, and optoelectronic devices. Many electronic and optoelectronic devices now have a submicron active region. The reduction of the active region will impose a limitation on the electron Λ, thus altering the heat source distribution. For the phonon part, the effects of phonon scattering and transmission at the interfaces of various layers on heat conduction are very important but have not been examined in depth. In high current density devices, the injected carrier (electrons and holes) scattering of heat carriers can significantly affect the thermal conductivity and heat conduction processes. In high field devices, the electrons and phonons are not at an equilibrium temperature (Wang, 1989), and the energy deposition and transport processes need to be understood. Heating in semiconductor lasers represents a major impediment preventing the increase of their power output and integration (Osinski, 1991). Thermal modeling of these devices has shown that size effects significantly affect the device temperature rise (Chen and Tien, 1993b; Chen et al., 1994a; Norris et al., 1994; Chen, 1994). In optics, it was suggested that the severe reduction of thermal conductivity of optical coatings may be the cause of film damage, yet there is no commonly accepted way of predicting such reduction. Thin optical films are also widely used in many nonlinear optics experiments, such as the thermally induced optical bistability (Wherrett et al., 1990). Understanding the microscale heat transfer processes is important for predicting the optical behavior of these devices (Chen and Tien, 1994).

The heat dissipation problem in electronic, optical, and optoelectronic devices presents great challenges, but the opposite problem of the thermal insulation in small structures is also interesting. The problem arises because it is often desirable to prevent the thermal cross-talk between different components on the same chip, either in electronics or integrated optics. The two competing requirements, to dissipate the heat generated in each element and to prevent thermal cross-talk between different elements, call for ingenious thermal design and optimization.

A fundamental question is whether a thermal insulator as good as or close to an electronic insulator can be produced. To answer this question, it is instructive to see why there are almost perfect electrical insulators but no perfect thermal insulators. This can be explained by the energy band structures shown in Figs. 7(a–c). The electronic bandgap between the valence band and the conduction band of an insulator is very large, as shown in Fig. 7(a). A free electron in conductor A does not have enough energy to climb to the conduction band of the insulator and transfer to the right (except possible tunneling effects), so there is no current flow and no heat conduction by electrons. Heat, however, can still be transferred through phonons. Figure 7(b) illustrates phonon spectra of the three materials. It is clear that there are always phonons in the insulating layer having the same energy as those in both conducting layers. As a consequence, some phonons in conductor A can excite phonons in the insulating layer, which excite phonons in conductor B. The net effect is conduction of heat through the thermal insulator. The development in thin film fabrication technology, however, has shed some light on the possibility of super thermal insulation. The phonon spectra of a superlattice are shown in Fig. 7(c). There are some minibandgaps produced due to the long range coupling of phonons in a superlattice. If somehow, larger bandgaps can be produced, the situation will look more like an electrical insulator. Indeed, the experiments of Yao (1987) and Chen et al. (1994b) have shown that thermal diffusivity of superlattice structure is lower than its corresponding bulk value.

Microscale heat transfer in quantum structures (QS) provides many challenging problems. There are very little information on the thermophysical properties of two most commonly used QSs, quantum wells and superlattices (Esaki and Tsu, 1970). Even less is known about other QSs such as quantum wires and quantum dots. It was predicted that the phonon contribution to thermal conductivity in quantum wells and superlattices is severely reduced due to additional boundary scattering effects and the change of phonon spectra (Chen and Tien, 1993a; Ren and Dow, 1982). A few existing experimental data on superlattices have shown the reduction of thermophysical properties compared to their bulk values (Yao, 1987; Chen et al., 1994b). Narayanamurti et al. (1979) demonstrated interference effect of monochromatic phonons in a superlattice structure. One measurement of the thermal conductivity of GaAs fine wires suggests that the electron contribution to thermal conductivity is dominant at low temperatures (Potts et al., 1991). These few existing data are far from enough to test any theory. Challenges lie first in the real measurement of the thermal properties of QSs. Also, theoretical studies are needed to discriminate the quantum effects, such as the change of the electron and phonon spectra and density of states, and the classical effects, such as the reduction in Λ, on thermal conductivity. Further exploration of the quantum effects may also lead to "smart" thermal design. Imagine arranging quantum wires or dots into thicker layer, will it be possible to get super thermal insulating materials?

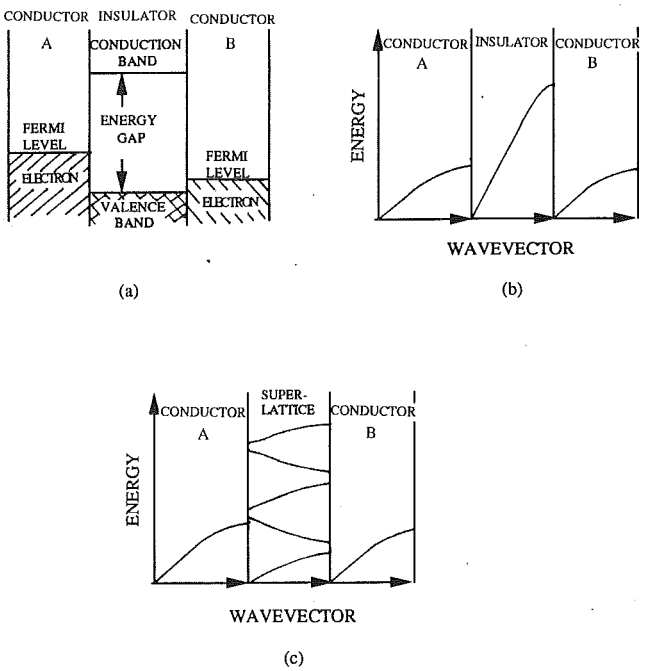

Fig. 7 Difference between electrical and thermal insulation: (*a*) electron energy; (*b*) phonon energy; (*c*) phonon energy in a superlattice.

Development of micro- to atomic scale probes demands an understanding of the microscale heat transfer processes. Phelan et al. (1993) demonstrated the feasibility of using thermoelectric voltage at a sharp metal-metal contact as a temperature probe. Marschall and Majumdar (1993) calculated the thermally induced tunneling current through a conductor-insulator-conductor junction. Understanding heat transfer mechanisms in small probes is necessary for the calibration and interpretation of experimental results.

Particulates are often involved in such diverse areas as combustion, material processing, climate, and laser diagnosis. Depending on its diameter, radiation in a particle can involve each of the three microscale regimes. Tuntomo et al. (1991) and Pluchino (1981) considered the wave effects on the heat transfer in small particles. When the particle gets smaller, the electron Λ is limited by its diameter and the optical constants will be modified correspondingly (Bohren and Huffman, 1983). Truong et al. (1987) discussed the quantum size effects of very fine aluminum particles. Most of the studies, however, are confined to simple

geometry. Study of the radiative properties and transfer in complex geometries, such as soot agglomerates, is important for understanding radiation in combustion process (Majumdar, 1992). In contrast to radiation, microscale heat conduction effects in particulates have received little attention. Besides the importance of heat conduction in a single particle, study of microscale heat conduction in particulate systems also benefits the understanding of the microscale heat conduction in thin film systems, because thin films are often composed of particulates.

Experimental Challenges

Experimental techniques for studying microscale heat transfer, especially microscale heat conduction, are not well developed. Great efforts should be directed to develop effective experimental techniques and conduct heat transfer experiments in microscale structures.

For heat conduction, there are increasing interests in the measurement of thermophysical properties of thin films, including thermal conductivity and thermal diffusivity. Both contact and noncontact methods have been devised. Lambropolous et al. (1991) gave a partial list of the current literature on the measurement of thermal conductivity and diffusivity. Besides the literature reviewed in that paper, Paddock and Eesley (1986) used the transient thermal reflectance to measure the thermal diffusivity of metallic thin films. Volklein and Kessler (1984) measured thermal conductivity of thin bismuth films. Most of these experiments have confirmed that the thermal conductivities of thin films are generally lower than their values in bulk materials. Exceptions are the experiments of Goodson and Flik (1993) on SiO_2 films and Graebner et al. (1992) on synthetic diamond films.

Since each experimentalist used his own sample films fabricated from different materials and by different methods and conditions, there is no consensus about what causes the reduction of thermal conductivity. It is suggested here that a comparative study be conducted: Each experimentalist would use similar samples provided by one supplier and measure their thermal conductivity or thermal diffusivity. Such a comparison will provide a basis for later experimental study. Most experiments give values of thermophysical properties without detailed characterization of the film structures. The values thus provided are hardly applicable to other films since film structures vary from film to film depending on the film growth processes. Because of the difficulty in making samples, most existing experiments are performed on polycrystalline thin films so that it is difficult to distinguish the boundary/interface and the grain size effects. Experiments on single-crystal thin films and polycrystalline films of the same material will increase the understanding of the relative importance of the boundary and the grain size effects. One choice is the molecular-beam-epitaxy grown GaAs thin film, which approaches a nearly perfect crystal (Chen et al., 1994b). Finally, a systematic measurement on the effects of the film thickness, interface condition, grain size, and microstructure on thermal conductivity should be performed.

Experimental techniques for measuring thermal conductivity of thin films await further development. Among the various methods for measuring thermophysical properties, some are suitable for the thermophysical properties perpendicular to the film and others applicable in the direction parallel to the film. Chen et al. (1994b) developed a technique that can determine thermal diffusivity of a thin-film sample in both parallel and perpendicular directions. The potential of using thermoelectric effects should be considered (Phelan et al., 1992; Marschall and Majumdar, 1993). Optothermal effects can be utilized for the measurement of both thermophysical and optical properties of thin films. However, care must be taken during the deduction of correct values of the desired properties (Chen and Tien, 1992, 1993c).

Direct measurement of the temperature field in microstructures has been a difficult task because of the small dimensions involved. Recent work in combining a scanning probe microscope with a thermocouple has shown great potential. Nonnenmacher and Wickramasinghe (1992) mapped local thermal conductivity of thin films to a nanometer resolution. Majumdar et al. (1993) combined a tiny thermocouple with atomic force microscope and reached submicron resolution. Optical methods have also been developed for local temperature measurement. Figure 8 shows the temperature distribution on the mirror of a GaAs/AlGaAs laser diode measured by Raman Spectroscopy (Brugger and Epperlein, 1990). The temperature rise is relative to the temperature of the mirror at threshold lasing current. Resolution less than one micron was reached. Combination of the Raman microprobe with a near-field optical microscope (Pohl, 1991) may break the diffraction barrier and reach high spatial resolution. One limitation of these methods is that it is difficult to measure local temperature inside the devices. Potential choices include the X-ray and electron beam. Larson and Tishler (1986) employed X-rays to detect the temperature distribution in silicon during pulsed-laser irradiation. Their experimental setup is sketched in Fig. 9(a), and the measured temperature distribution is plotted in Fig. 9(b).

Study of the radiative properties and radiative heat transfer in microscale regimes is relatively easier. The commonly used optical methods such as ellipsometry and spectrometry can be used to measure optical properties of thin films and other microstructures (Zhang et al., 1992; Chu et al., 1991). Experimental challenges for microscale radiative transfer are the radiative properties of microstructures at low and high temperatures and the deduction of the correct optical constants from the measured optical responses. Experimental techniques with high spatial resolution for measuring the local radiative properties should be developed. The optical properties, similar to the thermophysical properties, may vary from sample to sample because of their different structures. Systematic experimental studies, considering the film thickness, interface, grain boundary, porosity, and column structures, will be very helpful in distinguishing the contributions of each component.

Conclusions

Challenges in microscale radiative and conductive heat transfer exist in the theory, experiment, and engineering applications. This study addresses these challenges and recommends specific directions for future research.

Two microscale heat conduction and three microscale radiative heat transfer regimes are identified based on the relative magnitude of the various characteristic lengths involved in the heat transfer processes. The first and second microscale heat conduction regimes involve the classical and the quantum size effects, respectively. In the first radiative microscale regime, the wave nature of radiation should be considered and the derived radiative properties, such as emissivity and absorptivity, become size de-

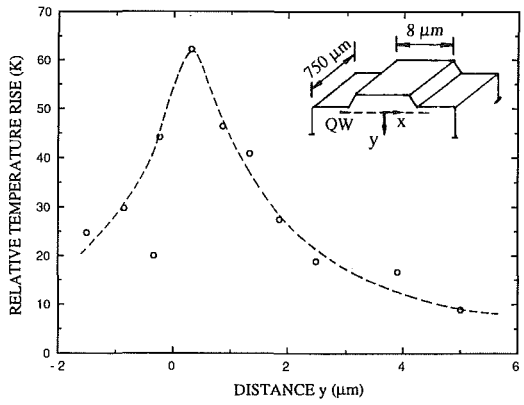

Fig. 8 Measured temperatures on the mirror of a GaAs quantum well laser, from Brugger and Epperlein (1990)

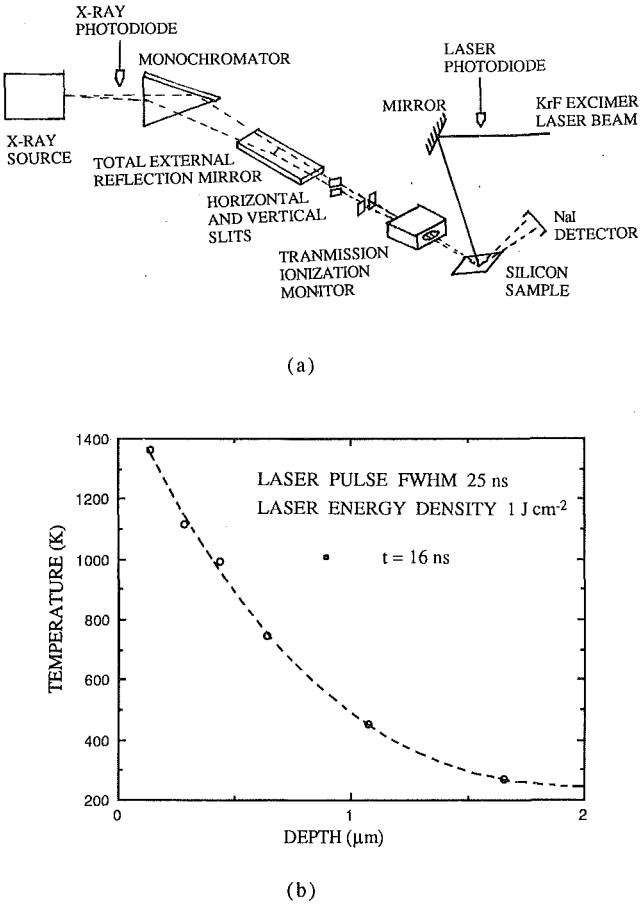

Fig. 9 X-ray time-resolved study of silicon during pulsed-laser irradiation: (*a*) experimental setup and (*b*) measured temperature distribution, from Larson and Tischler (1986)

pendent. In the second and third microscale radiation regimes the fundamental radiative properties, namely the optical constants and the dielectric function, are affected by the classical and quantum size effects, respectively. Governing principles and theoretical challenges for each regime microscale regime are discussed.

Challenging microscale heat transfer problems are illustrated with their applications in cryogenic systems, thin film processing, and the operation of electronic, optical, optoelectronic devices, and quantum structures. Experiments impose great challenges for microscale heat transfer study. Available and promising experimental techniques of conducting heat transfer experiments in microstructures are presented.

Acknowledgments

The authors gratefully acknowledge the financial support from the National Science Foundation, the Department of Energy, and the K. C. Wong Education Foundation in Hong Kong. G. Chen also acknowledges the financial support from the School of Engineering at Duke University.

References

Anisimov, S. I., Kapeliovich, B. L., and Perel'man, T. L., 1974, "Electron Emission From Metal Surface Exposed to Ultrashort Laser Pulses," *kSoviet Physics, JETP,* Vol. 39, pp. 375–377.

Armaly, B. F., and Tien, C. L., 1970, "Emissivities of Thin Metallic Films at Cryogenic Temperatures," *Proceedings of 4th International Heat Transfer Conference,* Paris, Vol. 3, R1.1.

Bohren, C. F., and Huffman, D. R., 1983, *Absorption and Scattering of Light by Small Particles,* Wiley, New York, pp. 336–338.

Born, M., and Wolf, E., 1980, *Principles of Optics,* 6th ed., Pergamon Press, Oxford, United Kingdom.

Brugger, H., and Epperlein, P. W., 1990, "Mapping of Local Temperatures on Mirrors of GaAs/AlGaAs Laser Diodes," *Applied Physics Letters,* Vol. 56, pp. 1049–1051.

Callaway, J., 1959, "Model for Lattice Thermal Conductivity at Low Temperatures," *Physical Review,* Vol. 113, pp. 1046–1051.

Chen, G., and Tien, C. L., 1992, "Partial Coherence Theory of Thin Film Radiative Properties," ASME JOURNAL OF HEAT TRANSFER, Vol. 114, pp. 636–643.

Chen, G., 1993, "Microscale Thermal Phenomena in Optical and Optoelectronic Thin-Film Devices," Ph.D. dissertation, University of California at Berkeley.

Chen, G., and Tien, C. L., 1993a, "Thermal Conductivity of Quantum Well Structures," AIAA *Journal of Thermophysics and Heat Transfer,* Vol. 7, pp. 311–318.

Chen, G., and Tien, C. L., 1993b, "Facet Heating of Quantum Well Lasers," *Journal of Applied Physics,* Vol. 74, pp. 2167–2174.

Chen, G., and Tien, C. L., 1993c, "Internal Reflection Effects on Transient Photothermal Reflectance," *Journal of Applied Physics,* Vol. 73, pp. 3461–3466.

Chen, G., 1994, "Comparison of Thermal Characteristics of Vertical-Cavity Surface-Emitting Lasers," presented at the 1994 ASME Winter Annual Meeting, Chicago, IL, Nov. 13–18.

Chen, G., and Tien, C. L., 1994, "Thermally-Induced Optical Nonlinearity During Transient Heating of Thin Films," ASME JOURNAL OF HEAT TRANSFER, Vol. 116, pp. 311–316.

Chen, G., Hadley, M. A., and Smith, J. S., 1994a, "Pulsed and Continuous-Wave Thermal Characteristics of External-Cavity Surface-Emitting Laser Diodes," *Journal of Applied Physics,* Vol. 76, pp. 3261–3271.

Chen, G., Tien, C. L., Wu, X., and Smith, J. S., 1994b, "Measurement of Thermal Diffusivity of GaAs/AlGaAs Thin-Film Structures," ASME JOURNAL OF HEAT TRANSFER, Vol. 116, pp. 325–331.

Chu, V., Fang, M., and Drevillon, B., 1991, "An In-Situ Ellipsometry Study of Amorphous Silicon/Amorphous Germanium Multilayer," *Journal of Applied Physics,* Vol. 69, pp. 13–18.

Cravalho, E. G., Tien, C. L., and Caren, R. P., 1967, "Effect of Small Spacing on Radiative Transfer Between Two Dielectrics," ASME JOURNAL OF HEAT TRANSFER, Vol. 89, pp. 351–358.

Dharssi, I., Butcher, P. N., and Warren, G., 1991, "Mobility and Hall Factor Calculations for a Superlattice," *Superlattices and Microstructures,* Vol. 9, pp. 335–339.

Esaki, L., and Tsu, R., 1970, "Superlattice and Negative Differential Conductivity in Semiconductors," *IBM Journal of Research and Development,* Vol. 14, pp. 61–65.

Fang, C. C., Jones, F., and Prasad, V., 1991, "Evaluation of Constant Temperature Control Algorithms in Modeling of Sputter-Deposited Thin Film Processes," ASME HTD-Vol. 184, pp. 63–71.

Fann, W. S., Storz, R., Tom, H. W. K., and Bokor, J., 1992, "Direct Measurement of Nonequilibrium Electron-Energy Distributions in Subpisecond Laser-Heated Gold Films," *Physical Review Letters,* Vol. 68, pp. 2834–2837.

Flik, M. I., and Tien, C. L., 1990, "Size Effects on the Thermal Conductivities of High-T_c Thin-Film Superconductors," ASME JOURNAL OF HEAT TRANSFER, Vol. 112, pp. 872–881.

Flik, M. I., Choi, B. I., and Goodson, K. E., 1992a, "Heat Transfer Regimes in Microstructures," ASME JOURNAL OF HEAT TRANSFER, Vol. 114, pp. 666–674.

Flik, M. I., Choi, B. I., Anderson, A. C., and Westerheim, A. C., 1992b, "Thermal Analysis and Control for Sputtering Deposition of High-T_c Superconducting Films," ASME JOURNAL OF HEAT TRANSFER, Vol. 114, pp. 255–263.

Garner, F. M., and Udell, K. S., eds., 1993, *Heat Transfer on Microscale,* ASME HTD-Vol. 253.

Goodson, K. E., and Flik, M. I., 1992a, "Microscale Phonon Transport in Dielectrics and Intrinsic Semiconductors," ASME HTD-Vol. 227, pp. 29–36.

Goodson, K. E., and Flik, M. I., 1992b, "Effects of Microscale Thermal Conduction on the Packing Limit of Silicon-on-Insulator Electronics," *IEEE Transactions on Components Hybrids and Manufacturing Technology,* Vol. 15, pp. 715–722.

Goodson, K. E., and Flik, M. I., 1993, "Annealing-Temperature Dependence of the Thermal Conductivity of LPCVD Silicon-Dioxide Layers," *IEEE Electron Device Letters,* Vol. 14, pp. 490–492.

Graebner, J. E., Jin, S., Kammlott, G. W., Herb, J. A., and Gardinier, C. F., 1992, "Large Anisotropic Thermal Conductivity in Synthetic Diamond Films," *Nature,* Vol. 359, pp. 401–403.

Gurevich, V. L., 1986, *Transport in Phonon Systems,* Elsevier, New York, pp. 110–152.

Hellwege, K. H., ed., 1982, *Landolt-Bornstein Numerical Data and Functional Relations in Science and Technology,* Vol. III/15a, Spring-Verlag, Berlin, pp. 17–18.

Hesketh, P. J., Zemel, J. N., and Gebhart, B., 1986, "Organ Pipe Radiant Modes of Periodic Micromachined Silicon Surfaces," *Nature,* Vol. 324, pp. 549–551.

Iafrate, G. J., 1983, "Quantum Transport and the Wigner Function," in: *The Physics of Submicron Semiconductor Devices,* H. L. Grubin, D. K. Ferry, and C. Jacoboni, eds., Plenum Press, New York, pp. 521–576.

Kattawar, G. W., and Eisner, M., 1970, "Radiation From a Homogeneous Isothermal Sphere," *Applied Optics,* Vol. 9, pp. 2685–2690.

Kittel, C., 1986, *Introduction to Solid State Physics,* 6th ed., Wiley, New York.

Klitsner, T., VanCleve, J. E., Fischer, H. E., and Pohl, R. O., 1988, "Phonon Radiative Heat Transfer and Surface Scattering," *Physical Review B,* Vol. 38, pp. 7576–7594.

Koshland, D. E., 1991, *Science, Special Section: Engineering a Small World, From Atomic Manipulation to Microfabrication,* Vol. 254, pp. 1300–1342.

Kotake, S., 1991, "Molecular Engineering Problems in Heat and Mass Transfer," *ASME/JSME Thermal Engineering Proceedings,* Vol. 4, pp. xxxiii–xl.

Kumar, S., 1993, "Thermal Radiation Transport in Micro-structures," *Thermal Science & Engineering,* Vol. 2, pp. 149–157.

Lambropolous, J. C., Jacobs, S. D., Burns, S. J., Shaw-Klein, L., and Hwang, S. S., 1991, "Thermal Conductivity of Thin Films: Measurement and Microstructural Effects," ASME HTD-Vol. 184, pp. 21–32.

Larson, B. C., and Tishler, J. Z., 1986, "Nanosecond Resolution Time-Resolved X-Ray Study of Silicon During Pulsed-Laser Irradiation," *Journal of Material Research,* Vol. 1, pp. 144–154.

Mahan, G. D., and Claro, F., 1988, "Nonlocal Theory of Thermal Conductivity," *Physical Review B,* Vol. 38, pp. 1963–1969.

Majumdar, A., 1992, "Role of Fractal Geometry in the Study of Thermal Phenomena," in: *Annual Review of Heat Transfer,* Vol. 4, pp. 51–110, Hemisphere, Washington, DC.

Majumdar, A., 1993, "Microscale Heat Conduction in Dielectric Thin Films," ASME JOURNAL OF HEAT TRANSFER, Vol. 115, pp. 7–16.

Majumdar, A., Carrejo, J. P., and Lai, J., 1993, "Thermal Imaging Using the Atomic Force Microscope," *Applied Physics Letters,* Vol. 62, pp. 2501–2503.

Marschall, J., and Majumdar, A., 1993, "Charge and Energy Transport by Tunneling Thermoelectric Effect," *Journal of Applied Physics,* Vol. 74, pp. 4000–4005.

Metha, C. L., 1963, "Coherence-Time and Effective Bandwidth of Blackbody Radiation," *Nuovo Cimento,* Vol. 21, pp. 401–408.

Monreal, R., Garcia-Moliner, F., and Flores, F., 1982, "Non Local Electrodynamics of Metal Film Systems," *Journal de Physique,* Vol. 43, pp. 901–913.

Narayanamurti, V., Stormer, H. L., Chin, M. A., Gossard, A. C., and Wiegmann, W., 1979, "Selective Transmission of High-Frequency Phonons by a Superlattice: The 'Dielectric' Phonon Filter," *Physical Review Letters,* Vol. 43, pp. 2012–2016.

Nonnenmacher, M., and Wickramasinghe, H. K., 1992, "Scanning Probe Microscopy of Thermal Conductivity and Subsurface Properties," *Applied Physics Letters,* Vol. 61, pp. 168–170.

Norris, P. M., Chen, G., and Tien, C. L., 1994, "Size-Effects on the Temperature Rise in Vertical-Cavity Surface-Emitting Lasers," *International Journal of Heat and Mass Transfer,* Vol. 37, Suppl. 1, pp. 9–17.

Osinski, M., 1991, "Vertical-Cavity Surface-Emitting Semiconductor Lasers: Present Status and Future Prospects," *SPIE,* Vol. 1418, pp. 1–24.

Paddock, C. A., and Eesley, G., 1986, "Transient Thermoreflectance From Thin Metal Films," *Journal of Applied Physics,* Vol. 60, pp. 285–290.

Phelan, P. E., Chen, G., and Tien, C. L., 1992, "Thickness-Dependent Radiative Properties of Y-Ba-Cu-O Thin Films," ASME JOURNAL OF HEAT TRANSFER, Vol. 114, pp. 227–233.

Phelan, P. E., Nakabeppu, O., Ito, K., Hijikata, K., Ohmori, T., and Torikoshi, 1993, "Heat Transfer and Thermoelectric Voltage at Metallic Point Contacts," ASME JOURNAL OF HEAT TRANSFER, Vol. 115, pp. 227–233.

Pluchino, A., 1981, "Emissivity Spectra of Composite Microscopic Particles," *Applied Optics,* Vol. 20, pp. 531–533.

Pohl, D. W., 1991, "Scanning Near-Field Optical Microscope (SNOM)," in: *Advances in Optical and Electron Microscope,* Vol. 12, pp. 243–312.

Potts, A., Kelly, M. J., Hasko, D. G., Smith, C. G., Cleaver, J. R. A., Ahmed, H., Peacock, D. C., Frost, J. E. F., Richie, D. A., and Jones, G. A., 1991, "Thermal Transport in Free-Standing Semiconductor Fine Wires," *Superlattice and Microstructures,* Vol. 9, pp. 315–318.

Qiu, T. Q., and Tien, C. L., 1993, "Heat Transfer Mechanisms During Short-Pulse Laser Heating of Metals," ASME JOURNAL OF HEAT TRANSFER, Vol. 115, pp. 835–841.

Ray, A., 1992, "RTP Temperature Control Requirement for Submicron Device Fabrication," *SPIE,* Vol. 1804, pp. 2–8.

Reddick, R. C., Warmack, R. J., Chilcott, D. W., Sharp, S. L., and Ferrell, T. L., 1990, "Photon Scanning Tunneling Microscopy," *Review of Scientific Instruments,* Vol. 61, pp. 3669–3677.

Ren, S. Y., and Dow, J. D., 1982, "Thermal Conductivity of Superlattice," *Physical Review B,* Vol. 25, pp. 3750–3755.

Richter, R., Chen, G., and Tien, C. L., 1993, "Partial Coherence Theory of Multilayer Thin-Film Optical Properties," *Optical Engineering,* Vol. 32, pp. 1897–1903.

Rytov, S. M., 1959, *Theory of Electric Fluctuations and Thermal Radiation,* AD226765, Defense Documentation Center, Arlington, VA.

Siegel, R., and Howell, J. R., 1981, *Thermal Radiation Heat Transfer,* McGraw-Hill, New York.

Sorrel, F. Y., Fordham, M. J., Ozturk, M. C., and Wortman, J. J., 1992, "Temperature Uniformity in PTR Furnaces," *IEEE Transactions on Electron Devices,* Vol. 39, pp. 75–80.

Swartz, E. T., and Pohl, R. O., 1989, "Thermal Boundary Resistance," *Review of Modern Physics,* Vol. 61, pp. 605–667.

Tien, C. L., and Cunnington, G. R., 1973, "Cryogenic Insulation Heat Transfer," in: *Advances in Heat Transfer,* Vol. 9, pp. 349–417.

Tien, C. L., and Lienhard, J. H., 1979, *Statistical Thermodynamics,* McGraw-Hill, New York.

Tien, C. L., 1988, "Thermal Radiation in Packed and Fluidized Bed," ASME JOURNAL OF HEAT TRANSFER, Vol. 110, pp. 1230–1242.

Tien, C. L., Majumdar, A., Flik, M. I., Kotake, S., Hijikata, K., and Hayashi, Y., 1994, "Molecular and Microscale Transport Phenomena: A Report on the Japan–US Joint Seminar," to appear in the *Annual Review of Heat Transfer,* Vol. VI.

Touloukian, Y. S., et al., 1973, *Thermal Physical Properties of Matter,* Vols. 1, 4, 10, IFI/Plenum, New York.

Truong, V., Courteau, P., and Singh, J., 1987, "Optical Properties of Very Fine Al Particles: Quantum Size Effects," *Journal of Applied Physics,* Vol. 62, pp. 4863–4866.

Tuntomo, A., Tien, C. L., and Park, S. H., 1991, "Internal Distribution of Radiation Absorption in a Spherical Particle," ASME JOURNAL OF HEAT TRANSFER, Vol. 113, pp. 407–412.

Vandenabeele, P., Maex, K., and Keersmaecker, D. R., 1989, "Impact of Patterned Layers on Temperature Non-uniformity During Rapid Thermal Processing for VLSI-Applications," *Materials Research Society Symposium Proceedings,* Vol. 146, pp. 149–160.

Volklein, F., and Kessler, E., 1984, "A Method for the Measurement of Thermal Conductivity, Thermal Diffusivity, and Other Transport Coefficients of Thin Films," *Physica Status Solidi (a),* Vol. 81, pp. 585–596.

Wakuri, S., and Kotake, S., 1991, "Molecular Dynamics Study of Heat Transfer in Very Thin Films," *ASME/JSME Thermal Engineering Proceedings,* Vol. 4, Reno, NV, pp. 111–116.

Wang, S., 1989, *Fundamentals of Semiconductor Theory and Device Physics,* Prentice Hall, Englewood Cliffs, NJ, pp. 462–470.

Wherrett, B. S., Darzi, A. K., Chow, Y. T., McGuckin, B. T., and Van Stryland, E. W., 1990, "Ultrafast Thermal Refractive Nonlinearity in Bistable Interference Filters," *Journal of Optical Society of America B,* Vol. 7, pp. 215–219.

Yajima, T., Yoshihara, K., Harris, C. B., and Shionoya, S., eds., 1988, *Ultrafast Phenomena VI,* Springer-Verlag, Berlin.

Yao, T., 1987, "Thermal Properties of AlAs/GaAs Superlattices," *Applied Physics Letters,* Vol. 51, pp. 1798–1800.

Yariv, A., 1989, *Quantum Electronics,* 3rd ed., Wiley, New York.

Zhang, Z. M., Choi, B. I., Le, T. A., Flik, M. I., Siegel, M. P., and Philips, J. M., 1992, "Infrared Refractive Index of Thin $YBa_2Cu_3O_7$ Superconducting Films," ASME JOURNAL OF HEAT TRANSFER, Vol. 114, pp. 644–652.

Ziman, J. M., 1960, *Electron and Phonons,* Oxford University Press, Oxford, United Kingdom.

Transient Effects of Uncertainties on the Sensitivities of Temperatures and Heat Fluxes Using Stochastic Finite Elements

T. D. Fadale
Department of Aeronautics and Astronautics.

A. F. Emery
Department of Mechanical Engineering.

University of Washington, Seattle, WA 98195

This paper addresses the question in the design of experiments of where to place sensors for optimal sensitivity and the post-experiment determination of which sensors yield relevant data. The authors in their previous works have described the spatial dependence of the response sensitivities and the importance of conducting a sensitivity analysis for a better understanding of the system response. This paper describes the formulation of the method for a transient analysis and its application to thermal problems. The results have been verified using the Monte Carlo sampling technique to simulate the variations in the parameters. The results show that there are not only optimal locations to maximize the sensitivities of the responses, but also optimal times of measurement. Sample test cases are used to demonstrate the effects of time of measurement and placement of sensors on the accuracy of the measured temperatures.

Introduction

One of the goals of engineering science is to model materials and engineering systems so that the responses can be predicted without expensive full-scale experiments. This is usually carried out by setting up a simple experiment in a controlled environment. The experimental responses are then compared to the responses predicted by the theory applied to the experiment. If the number of points at which an acceptable agreement is found between the measured and the predicted responses is large, then both the basic model and the model parameters are presumed to be correct. Based on these parameters, an engineering system is designed to satisfy certain objectives. But sometimes these systems fail to satisfy these objectives, sometimes leading to catastrophic failures. The search for the cause of such failures frequently points to deficiencies in the assumptions on which the design was based, factors such as material characterization, boundary conditions, operating conditions, etc. Even though the mathematical theories have been well developed, the predicted responses depend upon the accuracy of the model parameters, which, in the case of material systems, implies the accuracy of the material characterization or of the definition of boundary conditions. Imprecision in defining the boundary conditions or uncertainties involved in defining the material can lead to poor agreement between the predicted and the experimental results. Typically the input information is derived from experiments. For example, convective heat transfer coefficients (h) are determined by measuring temperatures and heat fluxes. Thermal diffusivities (α) are found from flash technique experiments in which the time at which the measured back face temperature equals half of its maximum can be used to estimate α. When such experimental results are reported in the literature, the overall uncertainty is also reported. For material systems the causes of uncertainties can be broadly classified into three categories: (1) Intrinsic uncertainty: uncertainty due to the natural heterogeneity of the material or boundary conditions. This leads to a spatial variability of properties, such as thermal conductivity or convective heat transfer coefficient. (2) Information uncertainty: uncertainty due to the limited availability of information about the properties. (3) Experimental uncertainty: uncertainty due to experimental errors. The experimental uncertainty itself can be said to consist of a fixed (bias) component and a random (precision) component (Abernethy et al., 1985; Moffat, 1988). Unfortunately it is not easy to incorporate these uncertainties into most thermal analysis programs. The general approach is to perform several computations using different values of h and α and to infer the sensitivities of the system by evaluating $\Delta_{\text{response}}(P)/\Delta h$ where P is a point chosen as representative of the system response. Also it is exceedingly time consuming to perform an adequate number of simulations and difficult to choose a representative point. In addition, quite often, even for linear problems, the predicted response is not a linear function of the model parameters exhibiting uncertainty. Thus a linear correlation between the model parameter and the response may not exist. Therefore a priori knowledge of the effect of these variable conditions on the responses and spatial maps of the responses will not only help in understanding any lack of agreement between the simulated and the measured response, but also will assist in the optimal design of experiments to characterize the parameters.

For an uncertainty analysis, the parameter under consideration is treated as a random variable, which is characterized by a probability distribution function. An analysis is then carried out by using either a statistical approach or a nonstatistical approach. The statistical analysis uses either experiments or Monte Carlo simulations. In both, repetitive tests are conducted in which one or more parameters are varied and the resulting response of interest is statistically analyzed. The nonstatistical approach, unlike sampling, is based upon an analytical treatment of the uncertainty. The nonstatistical approach is not only an elegant way to handle uncertainties in systems but also has an advantage over the statistical approach in terms of computer time and in ease of interpretation. The methods of solution in the nonstatistical approach range from functional integration (Lee, 1974), solution of the averaged equations for an equivalent solution, or perturbation methods (Lin, 1967). Some attempts have been made to obtain exact solutions to the effect of uncertainties using the

Contributed by the Heat Transfer Division for publication in the JOURNAL OF HEAT TRANSFER. Manuscript received by the Heat Transfer Division October 1992; revision received January 1994. Keywords: Numerical Methods, Thermophysical Properties, Transient and Unsteady Heat Transfer. Associate Technical Editor: C. E. Hickox, Jr.

method of functional integration, but the approach is applicable only to very specialized cases. The most widely used technique is the perturbation method. Although the perturbation method is based upon a *departure from a norm, its range of applicability is limited.* An extensive review of the various modeling methods of the uncertainties including a detailed description of the spectral representation of uncertainties and the solution techniques can be found in Ghanem and Spanos (1991).

Perturbation methods have been commonly used for nonlinear analysis, e.g., turbulence, nonlinear vibrations. One such perturbation method, which can be used for uncertainty modeling, is the First-order, second-order–second-moment analysis (Hafta and Kamat, 1985; Ditlevesen, 1981). This technique consists of expressing the response in terms of a Taylor series expanded about the mean value of the random parameter and truncating the series at the first or second-order terms. The system is then solved for the mean value and the standard deviation of the response. The first-order and the second-order derivatives of the responses with respect to the random parameters are, in effect, the sensitivities of the responses with respect to the random parameters. Thus, in the literature, this technique is commonly referred to as the first-order or second-order sensitivity analysis technique. The mathematical formulation of this technique can be found in the references listed above.

Applications of the first, second-order–second-moment analysis have been in the fields of reliability analysis of structures (Thoft-Christensen and Baker, 1982; Leporati, 1979), ground water flow or seepage problems through porous media (Dettinger and Wilson, 1981) and soil mechanics (Vanmarcke, 1977). The following discussion deals with the adaptation of the first/second-order–second-moment technique into the thermal finite element method, and is referred to as the Stochastic finite element method. Fadale and Emery (1991) have used Stochastic finite elements to produce contour maps of the first-order estimates of the standard deviation of temperature and heat fluxes for steady-state problems. Their results raised questions about the need for a second-order analysis and whether the conclusions were applicable to transient problems. This paper examines the use of the Stochastic finite element method to determine the transient effect of uncertainties in material properties and boundary conditions on temperatures and heat fluxes. The effect of the scatter in the random variable on the response is also investigated.

Stochastic Finite Elements

The mathematical formulation of the first/second-order, second-moment method in terms of matrices for incorporation into the finite element code is given in this section and in the appendix. The uncertainty parameters whose effects on the response are being studied are modeled as either random variables or as random fields defined in the interior or on the boundary of the system. For the finite element implementation, the continuous random field $\mathbf{B}(\vec{x})$, which represents any of the variable parameters (e.g., material properties, heat transfer coefficient), is discretized over the domain of application. Thus if we consider the discretized random field as an elemental quantity, then the average of the continuous random field over a finite element can be treated as an elemental quantity (Vanmarke, 1977). The local integral over a finite element of the random field is itself a random variable, referred to as B_i for the ith element:

$$B_i = \frac{1}{D_i}\int_{D_i} B(\vec{x})\,d\vec{x} \tag{2.1}$$

The discretization of the random field over the finite elements makes it possible to account for the autocorrelation between the discretized random variables and is also convenient to evaluate their stochastic properties. It also makes it easy to develop the matrices of the first and second-order equations. These advantages of using the finite element to define a localized random variable are lost for a finite difference method. Since a two-dimensional finite element code is being used, the random field, if present on the boundary (surface) of the system, will be defined in a one-dimensional space, i.e., $\vec{x} = (s)$ where s is a length parameter along the surface, and if present in the interior (volume) of the system, will be defined in a two-dimensional, space, i.e., $\vec{x} = (x_1, x_2)$. One stochastic property for a two-dimensional space localized random variable is given by Var $[\mathbf{B}] = \sigma_{\mathbf{B}}^2\gamma(D)$ where $\gamma(D)$ is a variance function of $\mathbf{B}$, which measures the reduction of the point variance $\sigma_{\mathbf{B}}^2$ under local averaging over the element D and can be precomputed for the mesh. The stochastic properties for the one-dimensional space localized random variables are analogous to those of two-dimensional space.

The finite element formulation of the first/second-order moment technique for a transient heat conduction problem is given in the appendix. A similar approach was used earlier by Liu et al. (1986) for structural analysis. The formulation in the appendix leads to the evaluation of derivatives of nodal temperature $\mathbf{\Phi}$ with respect to the elemental random variables B_i. These derivatives indicate the sensitivities of nodal temperature to the random variables $\mathbf{B}$. This large amount of data on derivatives can be concisely represented by the statistical properties, typically the means and the standard deviations. A better nondimensionalized indicator of the scatter in the temperature (and fluxes) due to the random parameters is the coefficient of variation (C.O.V.), which is defined as the ratio of the standard deviation of temperature to the mean of the temperature ($=\sigma_{\mathbf{\Phi}}/E[\mathbf{\Phi}]$).

Analogous to the derivation of the statistical properties, the data obtained by solving equations from the appendix can be

Nomenclature

B_i = specific outcome of $\mathbf{B}$
$B(\vec{x})$ = continuous random field
$\mathbf{B}$ = random variable vector
$\mathbf{C}$ = capacitance matrix
c_i = ith term of the transformed random variable
Cov [ ] = covariance operator
D_i = ith elemental domain
$E[\ ]$ = expected value operator
$f_{\mathbf{B}}$ = joint probability density function of $\mathbf{B}$
Fo = Fourier number
$\mathbf{G}$ = covariance matrix Cov $[B_i, B_j]$
h = heat transfer coefficient, W/m^2 K
k = thermal conductivity, W/m K
$\mathbf{K}$ = conductance matrix
m = mean of a random variable
P_1, p_1 = initial conditions
P_2, p_2 = boundary conditions
q = number of random variables
$\mathbf{q}$ = source matrix
Q_x, Q_y = heat flux in the x and y directions
s = length parameter, m
t = time, s
T_0 = prescribed temperature, °C
T_∞ = ambient temperature, °C
Var [ ] = variance operator
x = position, m
$\vec{x}$ = position vector, m
α = thermal diffusivity
γ = variance function
ϵ_b = boundary emissivity
ϵ_s = surface emissivity
Λ = variance matrix Var $[B_i, B_j]$
$\rho_{\mathbf{B}}$ = autocorrelation function
$\sigma_{\mathbf{B}}$ = standard deviation of $\mathbf{B}$
$\mathbf{\Phi}$ = temperature vector
$\mathbf{\Phi}_{B_i}$ = derivative of $\mathbf{\Phi}$ with respect to B_i
$\mathbf{\Phi}_{B_iB_j}$ = derivative of $\mathbf{\Phi}$ with respect to B_i and B_j
$\mathbf{\Psi}$ = fundamental matrix
ψ_{ij} = (i, j)th term of the fundamental matrix $\mathbf{\Psi}$

reduced to first and second-order estimates of mean and standard deviation of temperature and fluxes. The estimates of the mean temperature for the first and the second-order method are given respectively as

$$E[\Phi] = {}^{1}\,\overline{\Phi} \tag{2.2}$$

and

$$E[\Phi] = {}^{2}\,\overline{\Phi} + \overline{\Phi_2} \tag{2.3}$$

where $=^1$ and $=^2$ indicate the first and the second-order *estimates,* respectively, $\overline{\Phi}$ is the solution of the zeroth order equation, Eq. (A3), and $\overline{\Phi_2}$ is the solution of the second-order equation, Eq. (A5). It is important to note that while the expected response for the first-order method is the usual zeroth-order prediction, that for the second-order method may differ significantly. Unlike the mean temperatures and fluxes, which are second-order accurate, the truncation of the third and higher order moments of the random variable **B** in the above formulation leads to only a first-order estimate of the variance of temperatures.

$$\sigma_\Phi^2 = E[(\Phi - \bar{\Phi})^2] = \mathrm{Var}\,[\Phi]$$

$$= {}^{1}\,\mathrm{Diag}\,[\sum_{i=1}^{q}\sum_{j=1}^{q} \overline{\Phi_{B_i}}\,\overline{\Phi_{B_j}}^{T}\,\mathrm{Cov}\,[B_i, B_j]] \tag{2.4}$$

where B_i represents the random variable associated with the ith element. The second-order estimate of the variance of the nodal temperature requires retention of the third and the fourth-order moments of the random variable **B** and is given as,

$$\sigma_\Phi^2 = E[(\Phi - \bar{\Phi})^2] = \mathrm{Var}\,[\Phi]$$

$$= {}^{2}\,\mathrm{Diag}\,[\sum_{i=1}^{q}\sum_{j=1}^{q} \overline{\Phi_{B_i}}\,\overline{\Phi_{B_j}}^{T}\,\mathrm{Cov}\,[B_i, B_j]$$

$$+ \tfrac{1}{2}\sum_{i=1}^{q}\sum_{j=1}^{q}\sum_{k=1}^{q} \overline{\Phi_{B_i}}\,\overline{\Phi_{B_jB_k}}^{T}\,\mathrm{Cov}\,[B_i, B_j, B_k]$$

$$+ \tfrac{1}{2}\sum_{i=1}^{q}\sum_{j=1}^{q}\sum_{k=1}^{q} \overline{\Phi_{B_iB_j}}\,\overline{\Phi_{B_k}}^{T}\,\mathrm{Cov}\,[B_i, B_j, B_k]$$

$$+ \tfrac{1}{4}\sum_{i=1}^{q}\sum_{j=1}^{q}\sum_{k=1}^{q}\sum_{l=1}^{q} \overline{\Phi_{B_iB_j}}\,\overline{\Phi_{B_kB_l}}^{T}(\mathrm{Cov}\,[B_i, B_j, B_k, B_l]$$

$$- \mathrm{Cov}\,[B_i, B_j]\,\mathrm{Cov}\,[B_k, B_l])] \tag{2.5}$$

where Cov $[B_i, B_j, B_k]$ and Cov $[B_i, B_j, B_k, B_l]$ are the third and the fourth-order covariance functions of the multivariate random vector **B**. In practice, the mean and the standard deviation of random variables are the only statistical information made available through experiments. Hence it is almost impossible to evaluate the third and the higher order covariance functions of random variables based entirely on experimental results. Fortunately these higher order covariance functions can be expressed in terms of the second-order covariance functions when the multivariate random vector is characterized by a *normal distribution* (Anderson, 1958). In this case, the third-order covariance function reduces to

$$\mathrm{Cov}\,[B_i, B_j, B_k] = 0 \tag{2.6}$$

and the fourth-order covariance function reduces to

$$\mathrm{Cov}\,[B_i, B_j, B_k, B_l] = \mathrm{Cov}\,[B_i, B_j]\,\mathrm{Cov}\,[B_k, B_l]$$
$$+ \mathrm{Cov}\,[B_i, B_k]\,\mathrm{Cov}\,[B_j, B_l]$$
$$+ \mathrm{Cov}\,[B_i, B_l]\,\mathrm{Cov}\,[B_j, B_k] \tag{2.7}$$

In order to use Eq. (2.6) and Eq. (2.7) to evaluate the second-order estimate of the autocovariance of the nodal temperatures, the second-order equations need to be expressed in the most general form (Appendix A, Eq. (A6)). This general form leads to the assemblage and solution of $(q + 1)(q + 2)/2$ sets of simultaneous equations, namely one equation for Φ, q equations for Φ_{B_i} $(i = 1 \ldots q)$ and $q(q + 1)/2$ equations for $\Phi_{B_iB_j}$ $(i = 1 \ldots q, j = 1 \ldots q)$. For linear cases the problem is not too severe since the conductance and the capacitance matrix are assembled only once while solving the zeroth-order equation (Eq. (A3)). The rest of the q first-order equations (Eq. (A4)) and the $q(q + 1)/2$ second-order equations (Eq. (A6)) can be solved using the same capacitance and the conductance matrices. For nonlinear cases, e.g., when radiation is present, Eq. (A2) is nonlinear, i.e., $\bar{\mathbf{K}}$ is a function of the zeroth-order temperatures $\bar{\Phi}$. However, once the zeroth-order temperatures are evaluated, the nonlinearity in the conductance matrix does not exist, rendering the higher order equations (Eq. (A4) and Eq. (A6)) linear.

In these calculations a substantial computational effort is required for the double summation related to the covariance matrix Cov $[B_i, B_j]$. The number of matrix multiplications involved is proportional to $q(q + 1)/2$ for the first-order calculations while it is proportional to $q(q + 1)(q^2 + q + 1)/8$ for the second-order calculations and so it is important to reduce this computational effort when possible. The random vector **B** can be transformed to a random vector **c** such that

$$\mathrm{Cov}\,[c_i, c_j] = 0 \quad \text{for} \quad i \neq j; = \mathrm{Var}\,(c_i) \quad \text{for} \quad i = j \tag{2.8}$$

The number of matrix multiplications is then reduced to q. The transformation above is carried out by solving the eigenproblem

$$\mathbf{G}\Psi = \Psi\Lambda \tag{2.9}$$

where the **G** and Λ matrices are used to denote Cov $[B_i, B_j]$ and Cov $[c_i, c_j]$, respectively, and Ψ is a constant, orthogonal, $q \times q$ fundamental matrix, such that

$$B_i = \psi_{ij} c_j \quad \text{or} \quad c_i = \psi_{ji} B_j \tag{2.10}$$

Using the transformation above, Eqs. (2.4) – (2.7) are modified and the temperature derivatives are evaluated with respect to c_i instead of B_i. The expressions for the estimates of the mean and variances of the heat fluxes are not given here, but the procedure is similar to the one mentioned above. Finally Eqs. (2.4) and (2.5) can be reduced to

$$\sigma_\Phi^2 = {}^{1}\sum_{i=1}^{q} (\overline{\Phi_{c_i}})^2\,\mathrm{Var}\,(c_i) \tag{2.11}$$

as the first-order estimate of the variance of the temperature and,

$$\sigma_\Phi^2 = {}^{2}\sum_{i=1}^{q} (\overline{\Phi_{c_i}})^2\,\mathrm{Var}\,(c_i)$$
$$+ \tfrac{1}{2}\sum_{i=1}^{q}\sum_{j=1}^{q} (\overline{\Phi_{c_ic_j}})^2\,\mathrm{Var}\,(c_i)\,\mathrm{Var}\,(c_j) \tag{2.12}$$

as the second-order estimate of the variance of the temperature.

In general, varying parameters are considered as either global or local. For example, consider the convective heat transfer from a surface S which is formed of n elements. If a single heat transfer coefficient h is applied to the entire surface S, then a variation in h implies a variation in each element, with a correlation between the elements. In this case the covariance matrix **G** will be full. On the other hand, if the coefficient is assumed to vary randomly but independently on each element portion of S, then the **G** matrix will be diagonal. In the former case the transformation of the **G** matrix, Eq. (2.9), results in n descending eigenvalues, the diagonal elements of Λ, which drop quickly to zero. Thus only a few positive eigenvalues need be used to represent the **G** matrix, leading to a reduction of the number of first and second-order equations, Eq. (A4) and Eq. (A6). This advantage is lost in the latter case when the **G** matrix is a diagonal matrix, which essentially is the eigenvalue matrix Λ with most of eigenvalues

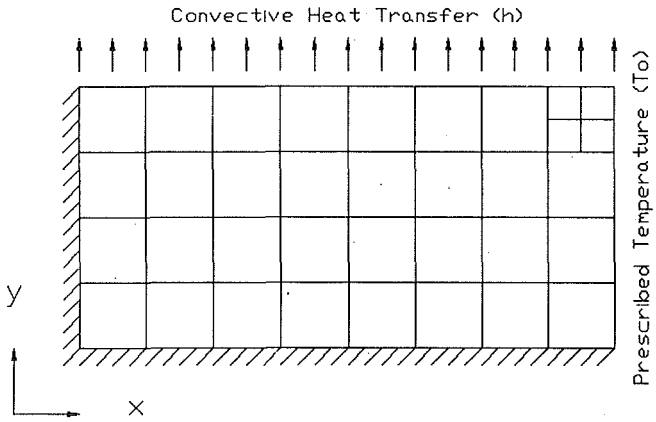

Fig. 1 Rectangular test case

being of the same magnitude. The physical significance of the transformation can be elucidated by considering a special case of the previous example of convective heat transfer coefficient h as a random variable. Let there be uniform correlation between the elemental heat transfer coefficient (B_i), i.e., variation in the heat transfer coefficient of one element indicates the same amount and same kind of variation in the heat transfer coefficient of other elements. Then the first-order derivative of temperature with respect to h is the sum of all the derivatives of temperature with respect to the elemental heat transfer coefficient, i.e., $\partial\Phi/\partial h = \sum_i (\partial\Phi/\partial B_i)$. By carrying out the transformation, we reduce the effect of all the elemental random variables B_i to just one transformed random variable c_1 with zero contributions from the rest of the transformed random variables c_i, i.e., $\partial\Phi/\partial h \sim \partial\Phi/\partial c_1$, thus reducing the computational effort.

The implementation of the procedure above deals with encoding Eqs. (A3), (A4), and (A6), into a conventional finite element code. Due to the computational advantage achieved through the transformation of Eq. (2.9), the equations above were modified and the temperature sensitivities were evaluated with respect to the transformed random variable c_i, instead of the random variable B_i. Presently, the following parameters can be chosen to exhibit uncertainty:

- Thermal conductivity: k_x, k_y, k (isotropic)
- Heat transfer coefficient: h
- Surface emissivity: ϵ_s
- Boundary emissivity: ϵ_b
- Prescribed heat flux: q_0

Test Cases and Discussion

A simple domain was considered to study the use of the stochastic finite element method in predicting the transient effect of the variation of material properties and boundary conditions on temperatures and heat fluxes. A rectangular slab ($x = 4$ m, $y = 2$ m) was maintained on one side at a constant temperature of T_0, exposed on the neighboring side to a convective boundary condition, and insulated on the remaining two sides (Fig. 1). The first part of the discussion deals with the transient effect of the uncertainties on the temperatures and heat fluxes when the uncertainties have a 20 percent standard deviation. The second part of the discussion deals with the extent to which stochastic finite elements can predict statistical properties of temperatures and fluxes when the uncertainties exhibit a large scatter (high standard deviations).

Transient Effects. The following are the characteristics of this test:

- Constant boundary temperature $T_0 = 100$°C
- Variation in conductivity with $k = 100$ W/m°C, $\sigma_k = 20.0$ W/m°C

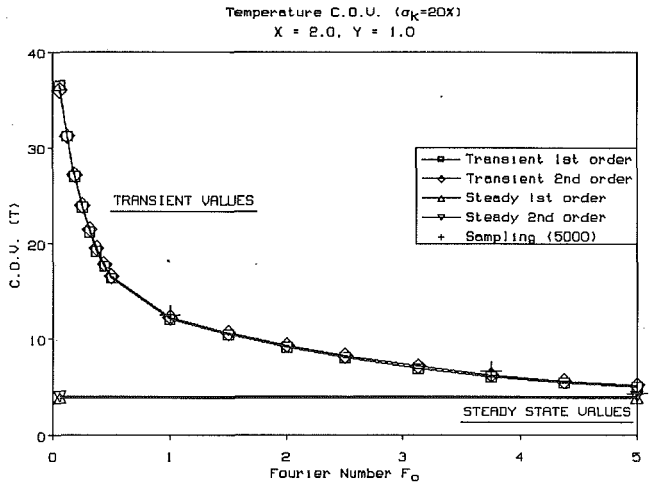

Fig. 2(a) C.O.V. of temperature for a 20 percent C.O.V. in conductivity

- Variation in convective heat transfer with $h = 10$ W/m^{2}C, $T_\infty = 0.C$, and $\sigma_h = 2.0$ W/m^2°C

The following observations are made at a specific point ($x = 2$ m, $y = 1$ m) on the slab. The spatial variations of the sensitivities were dealt with in a previous paper (Fadale and Emery, 1991).

Figures 2(a, b) show the transient behavior of the sensitivities of the temperature to variations in the conductivity k and convective heat transfer coefficient h, respectively. The sensitivity of temperatures (or fluxes) is given by the nondimensional coefficient of variation defined as (σ_Φ/Φ). The figures indicate that the temperature is very sensitive to conductivity at early times, showing nearly 40 percent variation at the initial time, but the effect decreases as steady state is approached (4 percent at steady state). In contrast, the temperature is only slightly affected by a variation in h. This effect is corroborated by the second-order estimate of the mean temperature for variation in h, which coincides with the first-order estimates. The figures also show the results of a Monte Carlo sampling of 5000 cases.

Figures 3(a, b, c) show the transient behavior of the mean heat flux in the x direction Q_x and its sensitivity to variations in k and h, respectively. The magnitude of the heat flux is seen to increase rapidly in the early stages, up to a Fourier number of approximately 0.5, and then gradually decreases to a lower steady-state value. It is interesting to note that the transient nature

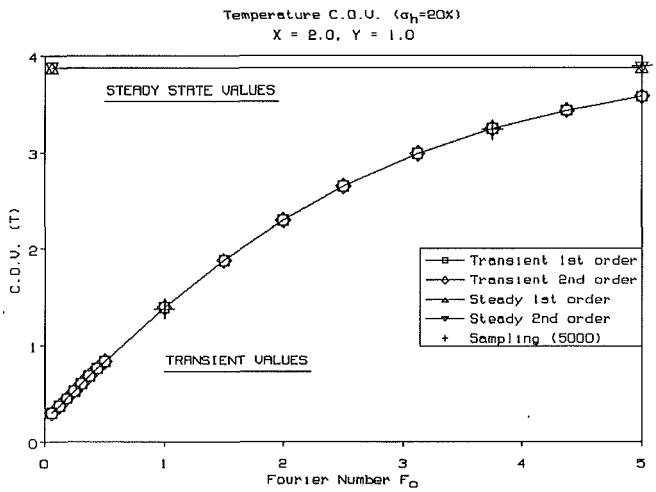

Fig. 2(b) C.O.V. of temperature for a 20 percent C.O.V. in the heat transfer coefficient

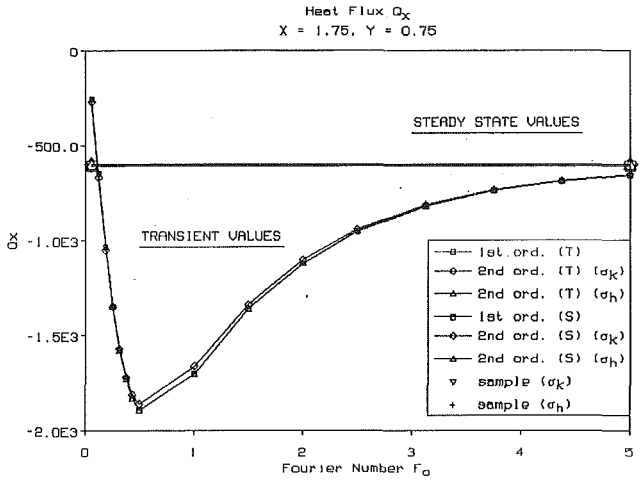

Fig. 3(*a*) Mean estimates of the heat flux in the *x* direction

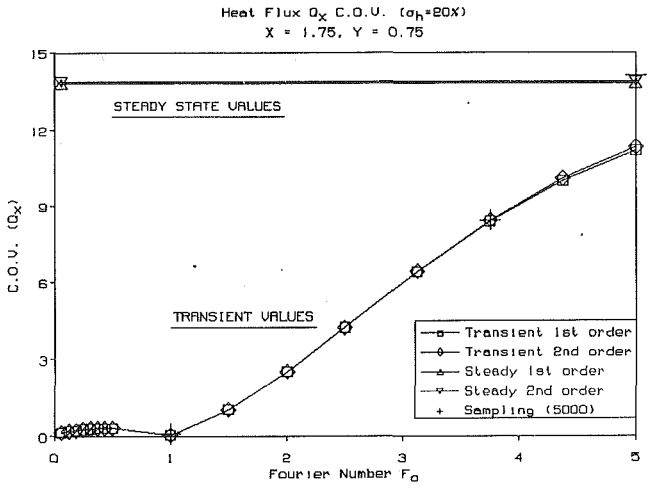

Fig. 3(*c*) C.O.V. of Q_x for a 20 percent C.O.V. in the heat transfer coefficient

of the sensitivity of heat flux for variations in k and h is not similar to the transient behavior of the mean flux. The heat flux sensitivity to variations in conductivity drops to its lowest at about Fourier number 3.4 before it increases again to steady state. In contrast, the heat flux is insensitive to a variation in h until about a Fourier number of 1.0, after which the sensitivity increases gradually until it reaches a maximum at steady state.

Figures 4(a, b, c) show the transient behavior of the mean heat flux in the y direction Q_y and its sensitivity to variations in k and h, respectively. The heat flux Q_y gradually increases until it reaches steady state, while the sensitivity of Q_y to variations in k gradually drops. The sensitivity of Q_y to variations in h, however, peaks and is a maximum at a Fourier number of 0.3.

Overall it is seen that the initial phase of this transient heat transfer problem is governed by the conductivity of the material while the latter phase is governed by the heat transfer coefficient. This effect is manifested as high sensitivities of temperature and fluxes to variations in k in the initial phases and to variations in h as steady state is approached. In terms of absolute magnitude, the temperatures and fluxes are twice as sensitive to the conductivity as to the heat transfer coefficient. All the data presented in this section have been verified using the Monte Carlo sampling technique and the data match very well for a 20 percent standard deviation of the uncertainties.

Effect of Standard Deviation. Table 1 compares the CPU time required to perform a steady-state analysis on the VAX 8820 system, for the deterministic case (zeroth order analysis), the stochastic cases of first-order and second-order analyses and the Monte Carlo simulation (5000 cases), with a 20 percent standard deviation in conductivity and heat transfer coefficient.

The second-order stochastic analysis does require more computer time compared to the first-order analysis, but the advantage of using the second-order stochastic analysis over the Monte Carlo simulation is clearly noticeable. This computational advantage achieved by the stochastic finite elements over statistical techniques, like the Monte Carlo simulation, is mainly due to the fact that it is based on a theory of small perturbations. This limits the application of stochastic finite elements to small variations in the uncertain parameters. In order to study the extent to which this method can be applied, the previous test case was analyzed for various coefficients of variation of the uncertain parameter, i.e., 20, 30, 40, and 50 percent. The estimates of the means and the coefficients of variation of the temperature and fluxes were compared with results obtained from the Monte Carlo simulation for 5000 samples. Figure 5 illustrates the relationship between the variation of temperature and conductivity. The second-order results agree with the Monte Carlo results for conductivity C.O.V. up to 40 percent. Because of the limited sample size, the Monte Carlo results may not be accurate at high values (50 percent) and further tests are required to confirm the exact relation-

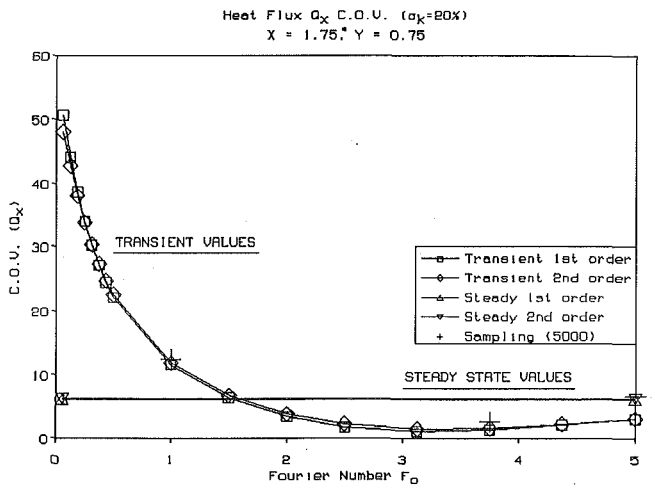

Fig. 3(*b*) C.O.V. of Q_x for a 20 percent C.O.V. in conductivity

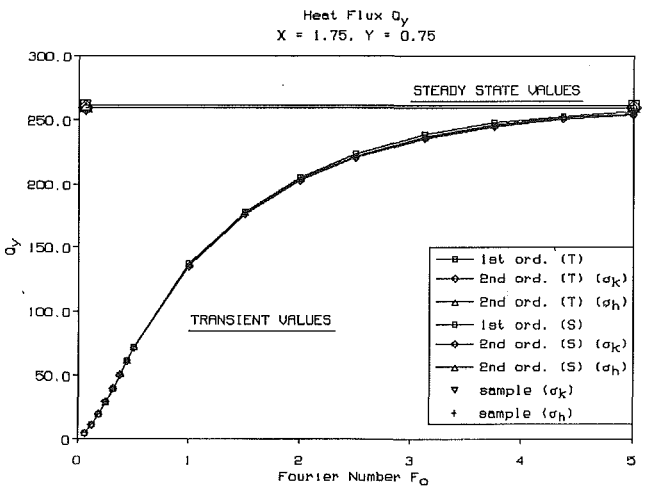

Fig. 4(*a*) Mean estimates of the heat flux in the *y* direction

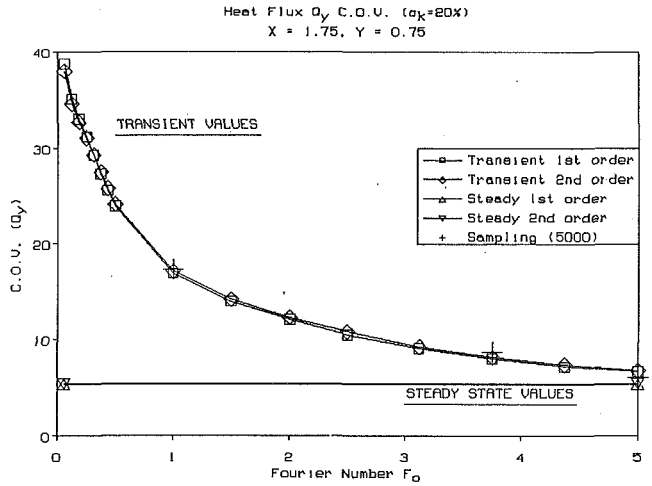

Fig. 4(*b*) C.O.V. of Q_y for a 20 percent C.O.V. in conductivity

ship. Following are the observations based on the study of the *relative* errors:

- Errors always increase with the increase in the coefficient of variation of the uncertain parameter, which is an intrinsic limitation of the perturbation method.
- The estimates of means of the temperatures and fluxes are better predicted than are the estimates of the coefficient of variations of temperatures and fluxes.
- For all the cases, the second-order estimates of the mean and the coefficient of variations predict the sampling properties better than do the first-order estimates.
- This improved prediction justifies the added computational load in calculating the second derivatives of temperatures required for the second-order estimates.
- The errors in the estimates also depend upon the kind of uncertain parameter under consideration. For example in the above-mentioned problem higher errors are noticed for the case with k (Fig. 3*b*) as the uncertain parameter than for the case with h (Fig. 3*c*) as the uncertain parameter.
- The maximum error (which occurs at 50 percent coefficient of variation of the uncertain parameter) in the estimates of the mean temperatures and fluxes is about 8 percent for the first-order and about 2 percent for the second-order estimates. The maximum error in the estimates of the coefficient of variation of temperatures and fluxes is about 35 percent for first-order and about 28 percent for the second-order estimates.

Table 1 Comparison of CPU time for steady-state analysis

	CPU time (minutes:seconds)	Variation in K	Variation in h
Zeroth-order analysis	00:01.19		
First-order analysis		00:06.98	00:03.34
Second-order analysis		00:07.38	00:03.47
Monte Carlo simulation		06:44.85	06:54.48

Conclusions

The development of stochastic finite elements has given us a new tool for analyzing engineering systems exhibiting uncertainties and for the development of better experiments. Compared to the previous statistical techniques used to analyze systems with uncertainties, such as the Monte Carlo simulation, this nonstatistical technique, which is based on perturbation theory, is more efficient and is easier to incorporate into major finite element programs. The effects of uncertainties in the material properties and the boundary conditions on the system response, which are also referred to as the response sensitivity to the uncertain parameters, can be studied by considering the mean and the standard deviation of the response. First and second-order estimates of mean and the standard deviation were developed based on the first/second-order, second-moment analysis.

As demonstrated in the test example, there is a transient nature to the response sensitivity which is markedly different from the transient nature of the response itself. This kind of information is very important for the development of an experiment and also addresses the question of an optimal time of measurement of a response with regards to its sensitivity. It is also important to note that different quantities, such as heat fluxes in the x and the y directions, behave much differently with respect to time. Similar differences were reported by Fadale and Emery (1991) in terms of the spatial map of the variation. In terms of Q_x and Q_y at the point chosen for this example, Fig. 3 (*c*) suggests that Q_y is a good measure of sensitivity at all times, but Q_x should only be used at later times ($>F_0 = 1$).

This technique was also studied for its accuracy in predicting the means and standard deviations of the responses. Observations indicate that the second order estimates are needed for high variations in the uncertain parameters, especially for estimates of

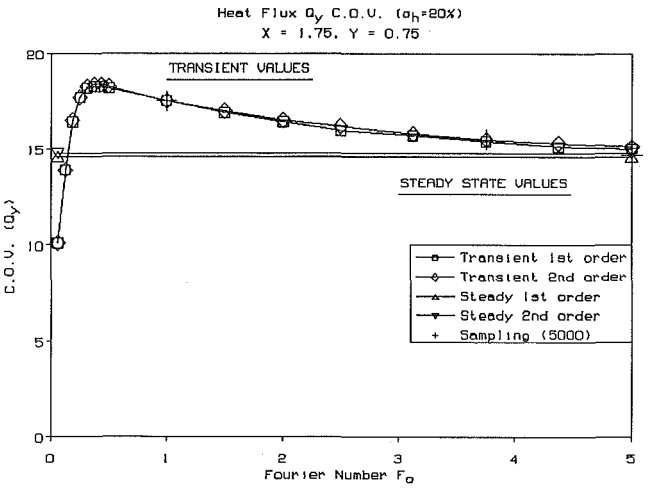

Fig. 4(*c*) C.O.V. of Q_y for a 20 percent C.O.V. in the heat transfer coefficient

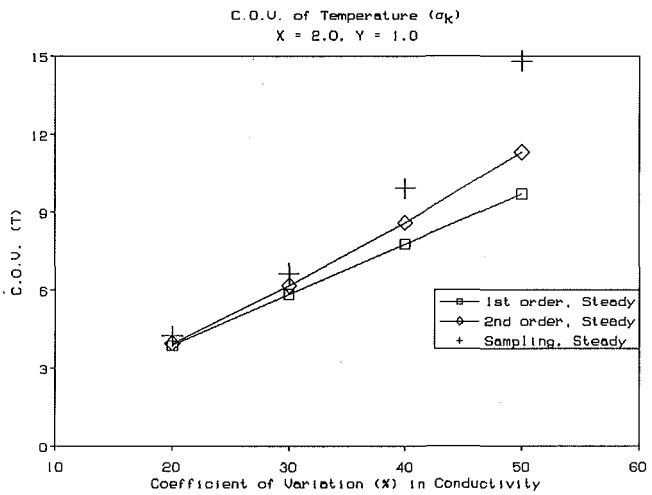

Fig. 5 C.O.V. of temperature for variation in conductivity

C.O.V. of fluxes for both the transient analysis and steady state analysis. In conclusion, Stochastic Finite Elements offer us a tool which can be used not only to analyze a system but also to study the effects of uncertainties on the system response. It can also be easily incorporated into an optimal design procedure.

Acknowledgments

The authors wish to acknowledge the support of NASA through grant No. NAG-1-41.

References

Abernethy, R. B., Benedict, R. P., and Dowell, R. B., 1985, "ASME Measurement Uncertainty," *ASME Journal of Fluids Engineering,* Vol. 107, pp. 161–164.

Anderson, T. W., 1958, *An Introduction to Multivariante Statistical Analysis,* Wiley, New York.

Dettinger, M. D., and Wilson, J. L., 1981, "First Order Analysis of Uncertainty in Numerical Models of Groundwater Flow. Part 1. Mathematical Development," *Water Resources Research,* Vol. 17, No. 1, pp. 149–161.

Ditlevsen, O., 1981, *Uncertainty Modeling—With Application to Multidimensional Civil Engineering Systems,* McGraw-Hill, New York.

Fadale, T. D., and Emery, A. F., 1991, "A Study of the Use of Stochastic Finite Element Analysis for Estimating the Effect of Uncertainties in Spatial and Boundary Parameters," presented at the 3rd ASME/JSME Thermal Engineering Joint Conference, Reno, NV, Mar. 17–22.

Ghanem, R. G., and Spanos, P. D., 1991, *Stochastic Finite Elements: A Spectral Approach,* Springer-Verlag, New York.

Hafta, R. T., and Kamat, M. P., 1985, *Elements of Structural Optimization,* Martinus Nijhoff Publishers.

Lee, L. C., 1974, "Wave Propagation in a Random Medium: A Complete Set of the Moment Equations With Different Wavenumbers," *Journal of Mathematical Physics,* Vol. 15, No. 9, pp. 1431–1435.

Leporati, E., 1979, *The Assessment of Structural Safety—A Comparative Statistical Study of the Evolution and Use of Level 3, Level 2, and Level 1,* Research Studies Press.

Lin, Y. K., 1967, *Probabilistic Theory of Structural Dynamics,* McGraw-Hill, New York.

Liu, W. K., Besterfield, G., and Belytschko, T., 1988, "Transient Probabilistic Systems," *Computer Methods in Applied Mechanics and Engineering,* Vol. 67, pp. 27–54.

Liu, W. K., Belytschko, T., and Mani, A., 1986, "Random Field Finite Elements," *International Journal for Numerical Methods in Engineering,* Vol. 23, pp. 1831–1845.

Moffat, R. J., 1988, "Describing the Uncertainties in Experimental Results," *Experimental Thermal and Fluid Science,* Vol. 1, pp. 3–17.

Tasaka, S., and Matsouka, O., 1982, "Finite Element Analysis of Non-stationary One-Dimensional Random Diffusion Problems," *International Journal for Numerical Methods in Engineering,* Vol. 18, pp. 1045–1054.

Thoft-Christensen, P., and Baker, M. J., 1982, *Structural Reliability Theory and Its Applications,* Springer-Verlag, Berlin.

Vanmarcke, E., 1977, "Probabilistic Modeling of Soil Profiles," *Journal of the Geotechnical Engineering Division,* Vol. 103, Paper No. GT11, pp. 1227–1246.

APPENDIX

Finite Element Formulation

Consider the semidiscrete transient heat conduction equation,

$$\mathbf{C}\frac{d\Phi}{dt} + \mathbf{K}\Phi = \mathbf{q}$$

$$\text{I.C. } P_1[\Phi] = p_1 \quad \text{B.C. } P_2[\Phi] = p_2 \tag{A1}$$

where Φ is the vector of temperatures, C, $\mathbf{K}$, and $\mathbf{q}$ are the capacitance, conductance, and source matrices, P_1 and P_2 are the initial conditions and boundary conditions expressed as functions of Φ, while p_1 and p_2 are known functions. Following the development of Liu et al. (1988) for the finite element formulation of the first/second-order, second-moment technique, the capacitance matrix $\mathbf{C}$, the conductance matrix $\mathbf{K}$, the source matrix $\mathbf{q}$, and the temperature vector Φ are expanded in a Taylor series about the mean values of the random variables. The third and higher order terms are neglected from each series. The temperature vector Taylor series is shown below in Eq. (A2). The Taylor series representations of the rest of the matrices have a similar form.

$$\Phi = \bar{\Phi} + \sum_{i=1}^{q} \overline{\Phi_{B_i}} dB_i + \tfrac{1}{2}\sum_{i=1}^{q}\sum_{j=1}^{q} \overline{\Phi_{B_iB_j}} dB_i\, dB_j \tag{A2}$$

Substituting the Taylor series expansion of the matrices in Eq. (A1), the equations corresponding to terms of equal order are given as:

Zeroth-Order Equation

$$\bar{\mathbf{C}}\frac{d\bar{\Phi}}{dt} + \bar{\mathbf{K}}\bar{\Phi} = \bar{\mathbf{q}}$$

$$\text{I.C. } P_1[\bar{\Phi}] = p_1 \quad \text{B.C. } P_2[\bar{\Phi}] = p_2 \tag{A3}$$

First-Order Equations

$$\bar{\mathbf{C}}\frac{d\overline{\Phi_{B_i}}}{dt} + \bar{\mathbf{K}}\overline{\Phi_{B_i}} = \mathbf{f}_{B_i} \quad i = 1, \ldots q$$

$$\text{I.C. } P_1[\overline{\Phi_{B_i}}] = 0 \quad \text{B.C. } P_2[\overline{\Phi_{B_i}}] = 0 \tag{A4}$$

where

$$\mathbf{f}_{B_i} = \overline{\mathbf{q}_{B_i}} - \overline{\mathbf{C}_{B_i}}\frac{d\bar{\Phi}}{dt} - \overline{\mathbf{K}_{B_i}}\,\bar{\Phi}$$

Second-Order Equations

$$\bar{\mathbf{C}}\frac{d\overline{\Phi_2}}{dt} + \bar{\mathbf{K}}\overline{\Phi_2} = \mathbf{f}_2$$

$$\text{I.C. } P_1[\overline{\Phi_2}] = 0 \quad \text{B.C. } P_2[\overline{\Phi_2}] = 0 \tag{A5}$$

where

$$\overline{\Phi_2} = \tfrac{1}{2}\sum_{i=1}^{q}\sum_{j=1}^{q} \Phi_{B_iB_j}\,\text{Cov}\,[B_i, B_j]$$

$$\mathbf{f}_2 = \tfrac{1}{2}\sum_{i=1}^{q}\sum_{j=1}^{q}\left\{\overline{\mathbf{q}_{B_iB_j}} - \overline{\mathbf{C}_{B_i}}\frac{d\overline{\Phi_{B_j}}}{dt} - \tfrac{1}{2}\overline{\mathbf{C}_{B_iB_j}}\frac{d\bar{\Phi}}{dt} - \overline{\mathbf{K}_{B_i}}\overline{\Phi_{B_j}} - \tfrac{1}{2}\overline{\mathbf{K}_{B_iB_j}}\bar{\Phi}\right\}\text{Cov}\,[B_i, B_j]$$

The second-order equation can also be written in the most general form as

$$\bar{\mathbf{C}}\frac{d\overline{\Phi_{B_iB_j}}}{dt} + \bar{\mathbf{K}}\overline{\Phi_{B_iB_j}} = \mathbf{f}_{B_iB_j} \quad i = 1, \ldots q \quad \text{and} \quad j = 1, \ldots q$$

$$\text{I.C. } P_1[\overline{\Phi_{B_iB_j}}] = 0 \quad \text{B.C. } P_2[\overline{\Phi_{B_iB_j}}] = 0 \tag{A6}$$

where

$$\mathbf{f}_{B_iB_j} = \left\{\overline{\mathbf{q}_{B_iB_j}} - \overline{\mathbf{C}_{B_i}}\frac{d\overline{\Phi_{B_j}}}{dt} - \tfrac{1}{2}\overline{\mathbf{C}_{B_iB_j}}\frac{d\bar{\Phi}}{dt} - \overline{\mathbf{K}_{B_i}}\overline{\Phi_{B_j}} - \tfrac{1}{2}\overline{\mathbf{K}_{B_iB_j}}\bar{\Phi}\right\}$$

Implementation of these equations using finite elements in the spatial domain and finite difference in the time domain leads to matrix equations. Therefore, the stochastic finite element method involves the solution of these matrix equations (Eqs. (A3), (A4), and (A6)). The Gauss elimination technique was used for the solution of the set of matrix equations. Due to finite differencing in the time domain, the zeroth-order solution $(\bar{\Phi})_{t_i}$ at time t_i is a function of the $(\bar{\Phi})_{t_{i-1}}$ at the previous time step t_{i-1} only, while the first-order solution $(\overline{\Phi_{B_i}})_{t_i}$ at time t_i is not only a function of $(\overline{\Phi_{B_i}})_{t_{i-1}}$ at the previous time step but is also a function of $(\bar{\Phi})_{t_i}$ at that time t_i. Therefore at any time step, it is necessary to solve the zeroth-order equation, Eq. (A3), before obtaining the solution of the first-order equations, Eq. (A4), at that time. A similar requirement exists for the solution of the second-order equations, Eq. (A6), i.e., the zeroth and first-order equations need to be solved before solving the second-order equation at any time step. For nonlinear cases, e.g., when radiation is present, Eq. (A2) is nonlinear, i.e., $\bar{\mathbf{K}}$ is a function of the zeroth-order temperatures $\bar{\Phi}$. However, once the zeroth-order temperatures are evaluated, the nonlinearity in the conductance matrix does not exist, rendering the higher order equations (Eqs. (A4) and (A6)) linear.

Direct Simulation of Phonon-Mediated Heat Transfer in a Debye Crystal

R. B. Peterson
Department of Mechanical Engineering,
Oregon State University,
Corvallis, OR 97331
Mem. ASME

A direct simulation of phonon-mediated heat transfer is described and preliminary results are reported. The method is derived from past work in simulating gas-dynamic flow and uses a linear array of cells for modeling a one-dimensional heat transfer problem. Central to the development of the technique is the Debye model for heat capacity of a crystal. The energy equation for this type of solid is presented and a phonon frequency distribution is obtained leading to a simulation technique that naturally takes into account changes in heat capacity. Using the linear array of cells, two fundamental problems are investigated. The first deals with the time evolution of the temperature profile in an array of 40 cells where the initial temperature distribution is 300 K, and at time zero the temperature of the first cell is raised to 500 K and maintained at this value. The second problem involves determining the steady-state heat transfer through an array of 20 cells where the two boundary cells are held at 500 K and 300 K. In this latter problem, the phonon mean free path is varied for each run and the results compared to both a continuum and radiation model for the heat transfer. Considering the simplistic approach used in modeling the phonon collisions, the results from both the time evolution problem and the steady energy transfer one are encouragingly close to predictions made with analytical solutions.

I Introduction

As electrical devices, sensors, and micromechanical components shrink into the submicron size regime, there is a fundamental shift in the description of conduction heat transfer from the common continuum approach to a heat carrier mediated one. This latter description relies on the premise that particles, whether electrons in metals or phonons in dielectrics, carry energy from one location to another. Research into this microscale regime has taken a number of paths and includes fundamental studies by Claro and Mahan (1989), Qiu and Tien (1992), Tien and Chen (1992), and Flik et al. (1992) as well as numerical simulation using molecular dynamics by Wakuri and Kotake (1991). For dielectric materials, a method based on the Boltzmann equation has been developed by a number of researchers that include Peierls (1955), Ziman (1960), and Goodson and Flik (1992). Recently, the connection between this approach and the equation of radiative heat transfer has been clarified by Majumdar (1991) for analysis of heat conduction within thin films. Further extension of these techniques to multidimensional problems remains questionable due to the complexity of the Boltzmann equation. Analytical solutions are only possible when the collision term is greatly simplified and then only a phonon distribution function is found. Monte Carlo techniques borrowed from radiative heat transfer can relieve some of the difficulty in solving practical problems involving phonon transfer (Klitsner et al., 1988). However, fundamental differences exist between phonon and photon behavior in the regime where scattering and collisional processes are important. With this in mind, a direct simulation method for phonons is presented. Its connection to the Boltzmann equation is through the application of a past similar method used for solving rarefied gas flow problems (Bird, 1976; Nambu, 1986). The ultimate goal of this work is to provide a numerical scheme for calculating energy transfer in complicated, microscale devices.

A comparison between rarefied gas dynamics and phonon-mediated heat transfer reveals many similarities. At length scales that are comparable to the mean free path of the particles, the continuum approach is no longer a valid description and reliance must be placed on a distribution function. For dilute gases, the Boltzmann equation provides a description of how the distribution function evolves in both space and time when molecular collisions are considered and when external forces are present. Analytical results exist for the Boltzmann equation in the form of the Chapman–Enskog solution (Vincenti and Kruger, 1965) where the collision term is highly simplified by introducing a relaxation time for departures from equilibrium. The reason the foregoing discussion is relevant to the present study is that intense research took place in this area during the 1960s because of the importance of rarefied gas flow around spacecraft. During this time, a direct simulation method was developed by G. A. Bird that has been shown in principle to capture all the features of a numerical solution to the Boltzmann equation (Bird, 1976; Nambu, 1986). Bird's method is not directly applicable to heat conduction in crystals due to fundamental differences between gas molecules and phonons. First among these differences is the lack of a simple collision model between phonons. For gas particles, all one needs to ensure is that energy and momentum are conserved in a binary collision. With this assumption, the Boltzmann distribution (Maxwellian speed distribution) is guaranteed and one can employ a cell time-counter as Bird does to keep track of molecular collisions in a simulation scheme. No such simplifying assumptions exist for phonons. Although energy will be conserved in phonon collisional processes, momentum is a property that may be conserved under one set of conditions and not conserved under others (Kittel, 1986). Even in perfect crystals, the so-called umklapp processes that are responsible for finite thermal conductivity do not obey momentum conservation. A second difference is the strict conservation of molecules during a nonreactive collision while phonons can be created or destroyed. Because of these considerations, phonon collisional behavior must be accounted for by using a statistical method based on known material properties of the solid.

One other important aspect of this work is that it contains the Debye (1912) description of a crystalline solid. Debye's model furnishes the distribution of energy quanta over the normal

Contributed by the Heat Transfer Division for publication in the JOURNAL OF HEAT TRANSFER. Manuscript received by the Heat Transfer Division June 1993; revision received December 1993. Keywords: Conduction, Numerical Methods. Associate Technical Editor: M. F. Modest.

modes within the crystal. As such, not only is it an accurate description of the crystalline energy content (and hence, specific heat), it also forms the basis of the phonon model. In the next section, results of the Debye theory are provided along with an explanation of how they are used in the direct simulation method. Although the concept of thermal resistance is not inherent in the equations used to determine specific heats, the distribution of quanta over the normal modes is an indispensable part of the energy transfer model developed here. With such an accurate accounting of energy within the crystal, specific heat changes become an implicit aspect of the simulation technique. The importance of this may not be immediately obvious; however, specific heat changes are large in devices operating under cryogenic conditions as well as for strongly bound crystals near room temperature (diamond and silicon).

II Theory

In the Debye theory, individual atoms of a crystal are assumed to move in a concerted fashion such that $3N - 6$ normal modes of vibration are established. Here, N represents the number of atoms or molecules comprising the crystal and the 6 involves the splitting out of the crystal rotational and translational degrees of freedom. Note that since N is almost always a very large number even for a crystal of small dimensions, the 6 is often ignored. Debye reasoned that the atomic spacing within the crystal is short when compared to the wavelengths of the normal modes so that a continuous elastic body could be assumed for the crystal. The theory treats all normal modes in this manner. The phonon connection with the Debye model comes into play as follows. The $3N$ normal coordinates have vibrational frequencies of $\nu_1, \nu_2, \ldots, \nu_{3N}$. The quantum of energy associated with each normal mode is $h\nu_1, h\nu_2, \ldots, h\nu_{3N}$, and each mode can have many quanta associated with it where a number $n_1, n_2, \ldots, n_{3N}$ identifies how many quanta are in each mode. The total energy for the crystal then becomes

$$E(n_j) = \sum_{j=1}^{3N} h\nu_j(n_j + \tfrac{1}{2}) \tag{1}$$

or the $\frac{1}{2}$ term in the expression can be summed independently to yield a constant giving

$$E(n_j) = \sum_{j=1}^{3N} h\nu_j n_j + E_0 \tag{2}$$

where E_0 is the zero point energy. This expression can be interpreted as the energy of a collection of particles whose total number is $n_1 + n_2 + \ldots n_{3N}$ and where the individual particle energy is identified as the quantum of the normal mode it is occupying. Since these particles are assumed to be indistinguishable, and there are no restrictions on their number in occupying a particular normal mode, the particles are bosons (Guinier and Jullien, 1989). These pseudoparticles have been given the name phonons.

Even though Eq. (2) is conceptually useful for giving the energy, a practical way of determining it is needed. In order to accomplish this, statistical thermodynamics can be used to develop a functional description of both the system energy and the phonon occupation numbers. This is done in detail elsewhere (McQuarrie, 1976) and will not be repeated here. The results of the derivation are

$$E = \int_0^\infty \left[\frac{h\nu}{e^{h\nu/kT} - 1} + \frac{h\nu}{2} \right] g(\nu) d\nu \tag{3}$$

where $g(\nu)$ is a function describing the density of states. Since only $3N$ normal modes exist, the restriction on $g(\nu)$ is,

$$\int_0^\infty g(\nu) d\nu = 3N \tag{4}$$

At this point in the development, the Debye model can be invoked for the purpose of yielding an expression for $g(\nu)$. The method used to find the functional form relies on the concept of elastic waves confined to a cubical element (McQuarrie, 1976; Waldram, 1985). With specified side lengths of L_x, L_y, and L_z for the element, it is rather straightforward to obtain the number of vibrational modes between the frequencies of ν and $\nu + d\nu$. Also, the elastic waves are assumed to be composed of one longitudinal and two transverse modes where an average velocity v_0 of propagation is used in the resulting expression, hence

$$g(\nu) d\nu = \frac{12\pi V}{v_0^3} \nu^2 d\nu \tag{5}$$

This relation combined with Eq. (4) gives an expression for the upper limit on the integration. This is needed because $g(\nu)$ is a monotonically increasing function of ν, yet only $3N$ normal modes exist in the elastic solid. By integrating Eq. (4) until an upper limiting frequency is reached that satisfies the relationship, the so-called Debye frequency can be found. Doing this yields

$$\nu_D = \left(\frac{3N}{4\pi V} \right)^{1/3} v_0 \tag{6}$$

and Eq. (5) becomes

$$g(\nu) d\nu = \frac{9N}{\nu_D^3} \nu^2 d\nu \tag{7}$$

Nomenclature

A = area of radiating surface
C_r = random cosine value
c_v = specific heat of crystal
D_0 = integral in Eq. (9*b*)
d = travel distance of phonon in one time step
E = system energy
E^* = system energy without zero point energy
E_0 = zero point energy of system
h = Planck's constant = 6.626×10^{-34} J s
K = thermal conductivity
k = Boltzmann's constant = 1.381×10^{-23} J/K
l = phonon mean free path
N = atoms in crystal
N^* = total number of phonons minus zero point number
n = atom number density
n_j = normal mode occupation number
Q = total power radiated from surface element
$\dot{q}$ = radiated power flux
S_r = random sine value
T = system temperature
$\tilde{T}$ = pseudo-temperature of system
T_D = Debye temperature
t = time
Δt = incremental time step
V = system volume
v_0 = phonon velocity
v_x = x-velocity component
v_y = y-velocity component
v_z = z-velocity component
W = phonon weighting value
x = spatial dimension or integrating variable
x_D = $h\nu_D/kT$
α = thermal diffusivity
ν = phonon frequency
ν_D = Debye frequency
ρ = material density
σ = Stefan–Boltzmann constant
σ_p = Stefan–Boltzmann constant for phonons
ϕ_r = random angle between 0 and 2π

for frequencies below ν_D and zero for frequencies above ν_D. This distribution function can then be substituted into Eq. (3) to give the energy of the crystal,

$$E = \int_0^\infty \left[\frac{h\nu}{e^{h\nu/kT} - 1} + \frac{h\nu}{2} \right] \frac{9nV}{\nu_D^3} \nu^2 d\nu \tag{8}$$

Two features of this expression are noteworthy. First, the integral is nominally taken from zero to infinity. However, the distribution function is zero after ν_D is exceeded, therefore the integral is functionally evaluated only from zero to the Debye frequency. Secondly, the last term in the brackets represents the zero point energy for each normal mode. The integration of this term is easily accomplished and yields a constant value representing E_0 in Eq. (2). To place the energy equation in a form useful for this work, the zero point energy will be evaluated and moved to the opposite side of the equation. Furthermore, the energy will be evaluated on a per unit volume basis. Finally, a new function will be defined that has the zero point energy removed from consideration, thus

$$\frac{E^*}{V} = \frac{E}{V} - \frac{E_0}{V} = \int_0^{\nu_D} \frac{9nh}{\nu_D^3} \frac{\nu^3}{e^{h\nu/kT} - 1} d\nu \tag{9a}$$

$$= \frac{9nkT}{(T_D/T)^3} \int_0^{x_D} \frac{x^3}{e^x - 1} dx \tag{9b}$$

where $x = h\nu/kT$, $T_D = h\nu_D/k$, and $x_D = T_D/T$. Now, in order to find an expression for the total number of quanta occupying all vibrational modes of the crystal, the differential form of the energy equation can be defined as $h\nu$ multiplied by the number of quanta residing in the frequency range between ν and $\nu + d\nu$, hence

$$\frac{dE^*}{V} = h\nu \frac{dN^*(\nu)}{V} \tag{10}$$

In this expression, the number of quanta is given by $N^*(\nu)$. Solving for the total number of energy quanta occupying all normal modes yields

$$\frac{N^*}{V} = \int_0^{\nu_D} \frac{9n}{\nu_D^3} \frac{\nu^2}{e^{h\nu/kT} - 1} d\nu \tag{11a}$$

$$= \frac{9n}{(T_D/T)^3} \int_0^{x_D} \frac{x^2}{e^x - 1} dx \tag{11b}$$

The starred quantity represents the number of energy quanta exclusive of the number residing in the zero point vibrational levels. The reason the zero point quantities are neglected in this development is that they contribute nothing to the energy transfer processes occurring in the crystal.

The expressions derived above for the total energy and number of quanta are central to the work described here. To study these equations further, consider the integrand of Eq. (9a),

$$\frac{9nh}{\nu_D^3} \frac{\nu^3}{e^{h\nu/kT} - 1} \tag{12}$$

A plot of this function is shown in Fig. 1 for a T_D of 115 K and a T of 40 K. The form is identical to that of Plank's distribution function for blackbody radiation. Also shown in the figure is the Debye cutoff frequency, which for this case is 2.4×10^{12} Hz. In contrast to problems involving blackbody radiation, the phonon energy spectrum is terminated abruptly due to the very real constraint of having no normal mode wavelengths shorter than the atomic spacing in the crystal (in the Debye model, the actual constraint comes out to be a few times the atomic spacing). This prevents a closed-form solution to Eq. (9). Also shown in the figure are two other curves with the same Debye cutoff frequency as before but crystal temperatures of 10 K and 300 K. Note that

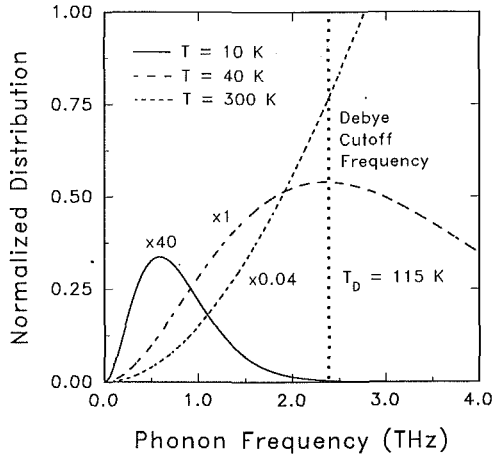

Fig. 1 Phonon frequency distribution for three different crystal temperatures. Note that each curve has a different scaling factor that permits an easy comparison of curve shapes.

the latter two curves have a scaling factor that permits an easy graphic comparison.

As the temperature is varied, the shape of the phonon distribution curve changes. In the low temperature limit where $T \ll T_D$, the curve approaches that of Planck's distribution for blackbody radiation. In this limit, the lower frequency phonons are the significant energy carriers and an analytical expression can be derived for the energy flux. This expression is found by first multiplying Eq. (9b) by $v_0/4$ and then rearranging to obtain

$$\dot{q} = \frac{3\pi k^4 D_0}{h^3 v_0^2} T^4 \tag{13}$$

The expression follows the familiar Stefan–Boltzmann relation, $q = \sigma T^4$, where σ for the phonon case is

$$\sigma_p = \frac{3\pi k^4 D_0}{h^3 v_0^2} \tag{14}$$

In this expression D_0 is the integral found in Eq. (9b). For the low temperature limit, D_0 can be evaluated as a definite integral and has the value of $\pi^4/15$. For higher temperatures, the integral must be evaluated numerically because the distribution curve is truncated at the Debye frequency. Using the blackbody radiation analogy further, the heat flow between two infinite parallel surfaces in the limit of no scattering is

$$\dot{Q} = A(\sigma_2 T_2^4 - \sigma_1 T_1^4) \tag{15}$$

where σ is determined by Eq. (14). This expression will be used later in a comparison of the numerical results from the simulation scheme.

There is one final point that must be addressed before leaving this section. All equations developed so far are fundamentally based on the premise that the crystal is in thermodynamic equilibrium. However, transport processes require nonequilibrium behavior, and thus the phonon distribution predicted by Eq. (11) cannot strictly apply. Practically, two arguments can be made for an acceptable compromise to this problem. First, if the departure from equilibrium is not great, then the thermodynamic property of temperature may still be an adequate quantity for determining the energy. This has been argued recently by Goodson and Flik (1992) as an acceptable practice in dealing with the Boltzmann equation for phonons. The second argument is concerned with rather large departures from equilibrium. In this case, a parameter with the units of temperature is assumed to be valid in both Eqs. (9) and (11). This parameter will be referred to as the pseudo-temperature and would be found by inverting Eq. (9) when a specific value of the energy density is known. With this pseu-

dotemperature, Eq. (11) would then give the phonon frequency distribution. This second case must be used in problems where a region of interest is bounded by surfaces in equilibrium and where the phonon mean free path is long compared to the physical dimensions of the region. For a location between the surfaces, the phonons passing through would come from different distributions, thus preventing the assumption of local thermodynamic equilibrium. The point, however, is often rendered moot by the simple argument that when the mean free path of phonons is large, collisions are rare and the need for a firmly established temperature disappears.

III Direct Simulation Method

The direct simulation method described here divides the spatial domain into a number of cells. Particles are allowed to drift collision free at a prescribed velocity during a short interval of time. Then, during a second phase, each particle has the opportunity to collide and thus change its momentum and energy. In the rarefied flow simulation developed by Bird (1963), collision partners are chosen among all particles existing within a cell, and a time counter is used so that only enough collisions take place to keep the counter close to the actual elapsed time. Since phonon processes do not lend themselves to this style of collision accounting, a mean free path technique is used for altering in a prescribed way the direction and frequency of the heat carriers. The details of the method are described in the following.

(A) Initialization of the Method. This work considers a one-dimensional spatial domain divided into a linear array of rectangular cells. Even though all three coordinates are used to describe a particle's position and velocity, only the z direction allows passage from one cell to another. If a particle arrives at an x or y face, it specularly reflects and continues on its way. The simulation method starts by filling each cell with a number of phonons. Since the actual number that exists is much larger than the number that can be simulated, a weighting factor is used to describe how many actual phonons are being simulated. For example, a cell with a side length of 10 nm, a number density of 6.02×10^{25} atoms per m^3, a Debye temperature of 115 K, and existing at a temperature of 300 K contains 6.22×10^5 phonons. A typical weighting factor may be on the order of 1000. Thus each cell contains 622 simulated phonons representing a larger actual number. As the cell temperature increases the number of phonons grow to take into account the increasing number of actual phonons. This method keeps the weighting factor constant.

The initial conditions of each cell are set by the properties of the phonons residing in that cell. The initial position of each phonon is chosen using a random number generator and a scaling factor so that a position between the cell walls is achieved. Initial phonon velocity is chosen with a random direction but with a magnitude that remains constant. This is a simplification of the true situation and ignores any variations in phonon velocity due to the dispersion curve. The velocity components are chosen (Bird, 1976) by first calculating a cosine value from a random number R_1 that varies between 0 and 1. Thus, $C_r = 2(R_1) - 1$ gives this cosine value, which is then used in determining a corresponding sine value from the equation

$$S_r^2 + C_r^2 = 1 \tag{16}$$

From another random number R_2 between 0 and 1, an angle $\phi_r = 2\pi R_2$ is calculated and the final velocity components are determined from

$$v_x = v_0 C_r \tag{17}$$

$$v_y = v_0 S_r \cos(\phi_r) \tag{18}$$

$$v_z = v_0 S_r \sin(\phi_r) \tag{19}$$

where v_0 is the acoustic velocity of the traveling phonons. This procedure is also used in determining a new phonon velocity after a scattering event (as described later).

The last parameter to define the phonon is its frequency. The total number of phonons (excluding the zero point number) per unit volume is given by Eq. (11). The integrand of this expression can be written as

$$\eta^*(\nu) = \frac{9n}{\nu_D^3} \frac{\nu^2}{e^{h\nu/kT} - 1} \tag{20}$$

It represents the distribution function describing the phonon frequencies. A technique referred to as the acceptance–rejection method (Bird, 1976) for sampling from a prescribed distribution is used in chosing the phonon frequency. The procedure is as follows. A random number between 0 and 1 is generated and then scaled to the range of the independent variable of the distribution function. In this case it would be a random frequency ν_r between 0 and ν_D. The value of the function at this random frequency is calculated and then normalized by the maximum value that the function can attain within the frequency interval. For the temperature range considered in this work (namely $T > T_D$), the value of the function is a maximum at ν_D so the normalization proceeds by way of $\eta^*(\nu_D)$. Next, a second random number between 0 and 1 is generated and compared to this normalized value. If the second random number is larger than the normalized value, ν_r is accepted as a sampled frequency from the distribution function. If the opposite is true, ν_r is rejected and the procedure is repeated until a frequency is found for the phonon. In this way a distribution of frequencies is built up that statistically follows the prescribed distribution of the generating function. Using this procedure, phonons are added to each cell until the sum of the phonon energies equals the initial energy of the cell.

(B) Particle Drift in Cells. As mentioned at the beginning of this section, the simulation scheme separates the movement of the phonons from scattering events. With this procedure all phonons "drift" a distance equal to $d = v_0 \Delta t$, where Δt is chosen as some incremental time element. If a wall is encountered during the drift phase, a specular reflection occurs and results in a change in velocity (direction only). The time interval Δt is chosen such that d is small compared to the cell dimension. In the results reported here, d is one fifth the cell dimension, or 2.0×10^{-9} m.

Energy transport occurs when a phonon passes from one cell to another. In doing so, an actual phonon would carry with it $h\nu$ amount of energy. In the simulation, each phonon represents a much larger number of real phonons, thus the actual amount of energy transferred from one cell to another is $h\nu W$, where W represents the weighting factor used in the phonon calculations. The numerical scheme performs the required bookkeeping so that energy is either added to or subtracted from the appropriate cell.

(C) Cell Temperature and Phonon Number. Under the nonequilibrium conditions that characterize energy transport, Eqs. (9) and (11) do not strictly apply since the temperature in each has little meaning. However, as argued earlier, a false or pseudotemperature may be postulated that to a close approximation would function in Eq. (9) to yield the energy. This pseudotemperature would be given the symbol $\tilde{T}$ and would replace the true temperature to give

$$\frac{E^*}{V} = \frac{9nk\tilde{T}}{(T_D/\tilde{T})^3} \int_0^{\tilde{x}_D} \frac{\tilde{x}^3}{e^{\tilde{x}} - 1} d\tilde{x} \tag{21}$$

Although this may involve an approximation to the true case of linking a temperature-like parameter to the cell energy, the real need for the pseudotemperature is in the sampling of the phonon frequency distribution. After a particular drift phase has been completed, a new cell energy generally results due to phonon exchange between cells. This new energy value determines a unique pseudotemperature through numerical inversion of Eq. (21). Based on this pseudotemperature, a new phonon frequency distribution for the cell is found from Eq. (20). Note, however,

that the frequencies of the individual phonons residing in the cell still conform to their original values and are not changed to the new distribution. At this point, the actual cell energy as determined by summing the energies of all phonons currently in the cell may be equal to the cell target energy. If this is the case, the next cell is considered. However, if the target energy is larger than the actual energy in the cell, the simulation scheme adds phonons until the energy is equal to that of the target energy. Each added phonon is placed in the cell with a randomly chosen position and velocity as indicated in the section describing the initialization routine. Also, frequencies are determined for each phonon through the sampling process described earlier. All temperature information needed for the sampled frequencies comes from using the new pseudotemperature. For the opposite case of too much cell energy, randomly chosen phonons are deleted until the actual cell energy equals the target cell energy. Typically, only a few phonons are added or deleted out of the approximately 600 to 1000 that are contained in each cell at any given time step.

(D) Collision Routine. The final task for the simulation scheme is to take into account phonon–phonon collisional processes and phonon scattering events by crystal imperfections. Unfortunately, the complexity of this aspect of the problem precludes the relatively simple solution used in simulating rarefied gas flows. Consider first the situation where two phonons collide to produce a third phonon; this gives rise to the so-called normal (N) process. Local thermodynamic equilibrium cannot be established since the total momentum of the phonon "gas" is not changed. At temperatures where the average phonon energy is of the order of kT or higher, umklapp (U) processes predominate. In this case two phonons interact with the reciprocal lattice vector so that a third phonon results, having a different momentum than the sum of the two collision partners. In all cases energy is conserved; however, momentum may or may not be depending on the type of collision. When phonon scattering from crystal imperfections is also considered, a very complicated picture emerges. The direct simulation scheme described here takes into account phonon collision and scattering by way of a mean free path model.

The simplest scheme possible is one where a single mean free path, l, is used to describe the probability of a collision regardless of the crystal temperature or the phonon frequency. This is in contrast to the known behavior of a phonon gas, that is, if the phonon number density increases in a particular cell, then the mean free path should go down due solely to the increased frequency of collisions (Kittel, 1987). In fact, the mean free path should vary as $l \propto 1/T$, which is borne out by experiments. Ignoring this argument in favor of both simplicity and the desire to have a constant thermal resistance, the simple model will be retained here. In order to implement this scheme, the distance traveled by a phonon during the drift period is first determined by multiplying the phonon velocity by the time interval Δt. A probability is then calculated based on the equation,

$$P(d) = 1 - e^{-d/l} \tag{22}$$

where $d = v_0 \Delta t$. This equation was originally derived for the mean free path of a molecule in a dilute gas (Tien and Lienhard, 1979), but its use here appears valid due to the fact that molecular parameters do not appear in the expression, and that similar statistics (Poisson) should apply to phonons as well. In the simulation scheme, each phonon in the cell is tested to determine whether it should undergo a collision. A random number between 0 and 1 is generated and compared to the magnitude of $P(d)$. If the random number is greater than $P(d)$, no collision takes place and the next particle is considered. If the random number is less than $P(d)$, a collision has taken place and the following procedure is performed. The phonon velocity is changed (direction, not magnitude) using the random procedure described earlier. In addition, the phonon frequency is changed by sampling the new frequency distribution using the new pseudotemperature for the cell. This, on average, thermalizes each phonon to local conditions in the time interval associated with one mean free path. However, since the cell dimension is chosen such that it is smaller than the mean free path, many phonons pass through cells without relaxing to the local cell conditions. This is especially true if the mean free path approaches the dimension of the entire cell array. In this case phonons may travel from one boundary cell to the other without thermalizing. This is a necessary condition for handling ballistic phonons that do not collide during transit through the cell array.

(E) Boundary Conditions. A constant-temperature boundary condition has been chosen as the most straightforward to implement. From the previous discussion, the cell energy is already monitored in two ways. First, the target energy of each cell is followed by accounting for the phonon movement across cell boundaries. Second, during each time step, the actual energy in each cell is found by summing each phonon energy in the cell. One possible way to impose the constant-temperature boundary condition is to set the target energy of the two end cells to the energy corresponding to the desired temperature. If this were done in isolation, then the cell energy could indeed be kept constant at the required level, but the possibility exists for a phonon entering the boundary cell to emerge again without thermalizing, especially if the mean free path is long compared with the cellular dimension. One important consideration in this respect is to have the emission characteristics of the boundary cell surface (the surface facing the interior array of cells) constant in time and independent of what is occurring in the interior of the array. Furthermore, the surface should emit energy in accordance with Eq. (13) in order to predict the energy exchange in the no-scattering limit correctly. The solution arrived at in this work involves changing all phonon characteristics within the two boundary cells during each time step. This is accomplished by first determining a new position within the cell and a new velocity for each phonon. these positions and velocities are chosen at random in a procedure that is similar to the initiation routine. Next, the phonon frequency is changed by sampling the frequency distribution using the temperature for the boundary cell. Finally, if the resulting cell energy differs from that which corresponds to the imposed temperature, phonons are either added or deleted until the energy is consistent with the temperature. With this procedure, conditions within the cell array cannot influence the boundary cell. For example, if a phonon leaves cell 2 and arrives in cell 1, then within the same time step a new random position within cell 1 is determined for the phonon along with a new velocity and sampled frequency. This procedure, in addition to yielding independent conditions in the boundary cells, also gives energy emission characteristics that are within 5 percent of those predicted by Eq. (8). Although a closer match may be desirable, the results of using this procedure are entirely adequate.

IV Results and Discussion

The first heat transfer problem chosen for study involves a linear array of 40 cells with a prescribed temperature at each boundary. In the first series of runs, the initial temperature for the cell array was 300 K. At time zero the first cell temperature was raised to 500 K and maintained at this value. Also, the last cell was held at the initial temperature of 300 K during the run. The evolution of the temperature distribution within the cell array was then monitored. In these first trials, the phonon mean free path was two cell lengths, or 20 nm. The second series of simulation runs involved steady-state energy transfer through an array of 20 cells. As in the first set of runs, the boundary cells were maintained at temperatures of 500 K and 300 K. Steady conditions were established by monitoring the energy transport over a large number of cycles. The physical parameters used in setting up the simulation runs are listed in Table 1. Of particular note is the Debye temperature chosen for the study. It is much lower than the temperature used in the runs; hence a regime was studied

Table 1 Various parameters used in the direct simulation method

Number of Cells	40	Mean Free Path	20 nm
Cell Length	10 nm	Time Interval	2 ps
Weighting Factor	1000	Phonon Speed	1000 m/s
Particles per Cell	622 @ 300 K	Debye Frequency	2.4×10^{12} Hz
Crystal Density	3000 kg/m^3	Debye Temperature	115 K
Molecular Weight	30	Debye Wavelength	0.4 nm
Initial Temperature	300 K	Atomic Number Density	6.02×10^{25} m^{-3}
Max Boundary Temp	500 K	Debye Heat Capacity[1]	824.7 J/kg-K
Thermal Diffusivity[1]	6.67×10^{-6} m^2/s	Thermal Conductivity[1]	16.5 W/m-K

[1]The temperature used in calculating heat capacity, thermal conductivity, and thermal diffusivity is 300 K.

where the thermal capacity of the material was relatively constant.

(A) Numerical Error Analysis. Assessing the numerical error of the simulation routine requires a knowledge of both the numerical noise associated with finite particle numbers and the overall accuracy of the technique. This latter aspect will be addressed in the following sections by using a comparison with known analytical solutions. The numerical noise and its effects on the accuracy of the technique will be addressed here.

A three-cell linear array was set up where the temperatures of the two boundary cells were held at 300 K. The properties of cell two were then monitored over a period of 500 time steps. The results of several simulation runs are presented in Fig. 2. Each run differs by the nominal number of particles occupying the cell. In the upper most curve $N = 62$ represents the average number of particles residing in cell number two. It is important to note that at any particular time step, the actual number of particles in cell 2 will vary from this average value, leading to the observed temperature fluctuations. Each vertical tick mark in Fig. 2 signifies a 10 K temperature difference, but each curve is plotted on its own vertical scale with a 300 K baseline. The standard deviation of the numerical noise is also shown in the figure as σ. It is shown to decrease from 29.8 K to 10.5 K as the average number of particles in the cell increases from 62 to 622. Important conclusions to draw from this exercise are that (1) the numerical scheme is relatively stable in that it fluctuates about the expected temperature value of 300 K, and (2) the numerical noise with an average of 622 particles in the cell is of the order of 10 K. This was observed to hold for a series of runs where the mean free path was varied from one cell length to 100 cell lengths (10 nm to 1000 nm).

(B) Continuum Model. The continuum model for the first series of experiments is the one-dimensional, time-dependent conduction equation,

$$\frac{\partial T}{\partial t} = \alpha \frac{\partial^2 T}{\partial x^2} \tag{23}$$

where the thermal diffusivity is $\alpha = K/c_v\rho$. Estimating the various quantities that yield the thermal diffusivity is accomplished as follows. The heat capacity can be determined from Eq. (9) by taking the partial derivative with respect to T at constant volume. This gives

$$c_v = \frac{9nk}{(T_D/T)^3} \int_0^{x_D} \frac{x^4 e^x}{(e^x - 1)^2}\, dx \tag{24}$$

Using the parameters in Table 1, Eq. (24) yields 824.7 J/kg-K for c_v at 300 K and 828.6 J/kg-K at 500 K. This shows that the heat transfer in the specified temperature range takes place in the high temperature limit where c_v undergoes little change. The other quantity needed for the continuum model is the thermal conductivity. From the kinetic theory of gases, the thermal conductivity can be expressed as

$$K = \tfrac{1}{3} c_v v_0 l \tag{25}$$

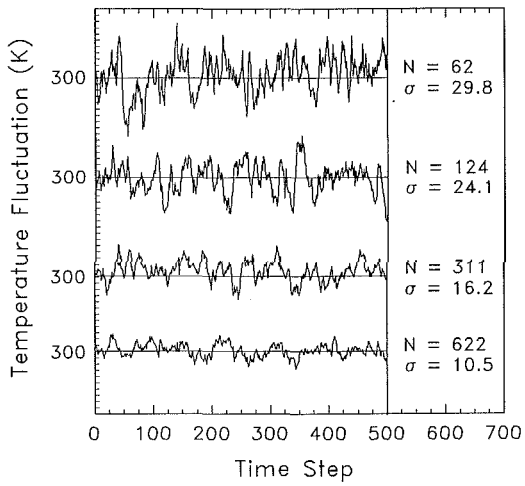

Fig. 2 Statistical fluctuation in cell temperature for various runs that differ by the number of particles in the cell. The number of particles in the cell (N) and the standard deviation of the fluctuations (σ) are provided for each data set.

where all terms have been previously described. This can also be applied to determining the thermal conductivity of dielectric crystals (Kittel, 1986) although the calculation should only be considered an estimate. Using the heat capacity at 300 K and a mean free path of 20 nm, Eq. (25) yields 16.5 W/m-K for the thermal conductivity. Applying these quantities to determining the thermal diffusivity gives 6.67×10^{-6} m^2/s. This is the value that will be used in the time-dependent, one-dimensional conduction equation.

(C) Results of the Simulation Runs. Figure 3 shows the results obtained for the one-dimensional heat transfer problem using the phonon simulation scheme. The numerical results are the open and filled symbols comprising the four curves. They represent times of 200 ps, 800 ps, 2 ns, and 6 ns. To reduce numerical noise, each point for a particular curve is the result of averaging five time steps. Furthermore, ten different simulation runs were averaged that differed only by the seed value used in the simulation's random number generator. This reduced the noise in the results by a factor of seven over what would have occurred if this averaging scheme had not been done. The solid

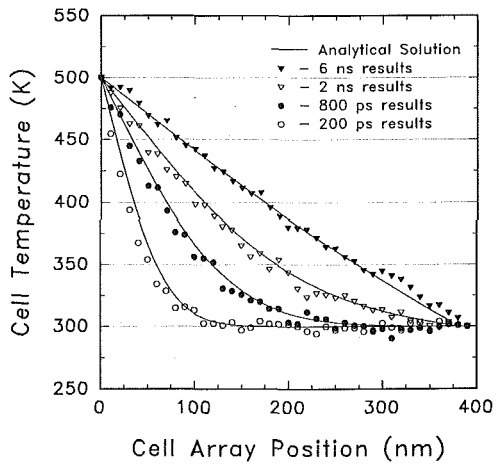

Fig. 3 Time evolution of the temperature distribution for a linear array of 40 cells. Phonon mean free path for the simulation was set at 2 cell lengths, or a phonon Knudsen number of 0.05.

lines associated with each of the four curves are the temperatures predicted by the continuum model. Equation (23) was used along with the previously determined value for the thermal diffusivity. Considering the simplistic approach taken in the simulation scheme for the phonon collision model, and recalling the rather elementary calculation for the thermal conductivity, the agreement between the numerical data and the analytical curves is encouraging. This supports the assertion that the phonon simulation scheme has captured essential features of the energy transfer process in the limit where the continuum model is valid. One note of interest is the possible beginnings of a divergence between the two approaches as shorter time intervals are considered. This is brought out in the data for the 200 ps case, and results from earlier times show similar differences. This effect may be caused by the nonlocal behavior of the energy transport process as described by Mahan and Claro (1988). Further study of this divergence is currently underway.

The utility of the phonon model is the ability to determine heat transfer rates when mean free paths approach the characteristic physical dimensions of the problem. To study this aspect, a steady-state system was set up that was comprised of a linear array of 20 cells where the first and last cells were maintained at temperatures of 500 K and 300 K, respectively. An initial temperature of 400 K was assigned to each interior cell. The simulation was then allowed to progress at least 1000 time steps while the energy transfer through the array of cells was monitored. When steady conditions were ensured, the rate of transfer was recorded by averaging at least 600 time steps of information. The parameter varied in this problem was the mean free path of the phonons. The initial value was one cell length, or 10 nm. For each subsequent run of the simulation, the mean free path was increased.

Figure 4 shows the rate of heat transfer from each simulation run as a function of the mean free path. Also plotted in the figure are the continuum model results and the "Radiation Limit" predicted by Eq. (15). The thermal conductivity used in the continuum model reflects the change in phonon mean free path. As is evident from the figure, at relatively short mean free paths, the continuum approach and the simulation method predict similar results. At a Knudsen number of 0.05 (based on mean free path divided by cell array length), each approach predict heat transfer rates that differ by only 2 percent. As the mean free path is increased, the continuum model predicts increasingly higher transfer rates while the simulation method approaches to within 3 percent the radiation limit of Eq. (15). Although not presented here, temperature profiles for the larger mean free path cases begin to show the temperature jump that should exist between the boundary cells and the interior ones as collisions become less frequent. These results suggest that the direct simulation method accurately takes into account the relevant mechanisms for phonon-mediated heat transfer.

V Conclusions

In this paper, a method has been presented that captures many of the processes that are important in modeling heat transfer by phonon transport. From elementary phonon frequency distributions derived from the Debye model, and assuming very simple phonon collision dynamics, the simulation code is able to predict accurately one-dimensional temperature profiles occurring in the continuum limit. Furthermore, when scattering ceases to become an important matter, the heat transfer rate between two parallel plates is also accurately determined. These conclusions are only for one-dimensional heat transfer, but extension to two or three dimensions and to complicated geometries appears straightforward. Also, the results are for the high temperature limit in the Debye model where the heat capacity is nearly constant. Of the various parts of the simulation method that may require further work, the collision routine and the lack of dispersion in the phonon velocity are the two that stand out. From the results encountered so far, a change in phonon velocity as a function of frequency is not warranted. However, assuming that a single mean free path is valid for all phonons regardless of their frequencies is too gross an approximation to use in all but the simplest of cases. A more sophisticated model based on different mean free paths for different phonon frequencies appears a more likely path to follow in future work. Furthermore, the mean free path could also be tied to two other quantities: (1) the number of phonons residing in a particular cell to model known variations in thermal conductivity as the temperature changes, and (2) the coordinate direction and the component of velocity in that direction. This latter consideration would permit material anisotropic behavior to be taken into account.

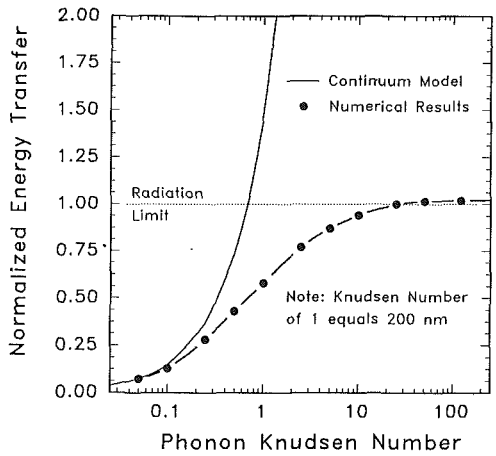

Fig. 4 Normalized energy transfer through an array of 20 cells as a function of phonon Knudsen number. The radiation limit for a square surface of dimension 10 nm × 10 nm is 1.18×10^{-5} W.

References

Bird, G. A., 1963, "Approach to Translational Equilibrium in a Rigid Sphere Gas," *Phys. Fluids,* Vol. 6, pp. 1518–1519.

Bird, G. A., 1976, *Molecular Gas Dynamics,* Clarendon Press, Oxford, United Kingdom, pp. 122–127, 131, 207–210.

Claro, F., and Mahan, G. D., 1989, "Transient Heat Transport in Solids," *J. Appl. Phys.*, Vol. 66, pp. 4213–4217.

Debye, P., 1912, "Zur Theorie der Spezifischen Warmen," *Ann. Physik,* Vol. 39, p. 789.

Flik, M. I., Choi, B. I., and Goodson, K. E., 1992, "Heat Transfer Regimes in Microstructures," ASME JOURNAL OF HEAT TRANSFER, Vol. 114, pp. 666–674.

Goodson, K. E., and Flik, M. I., 1992, "Microscale Phonon Transport in Dielectrics and Intrinsic Semiconductors," *Proceedings of the Winter Annual Meeting of the American Society of Mechanical Engineers,* Y. Bayazitoglu and G. P. Peterson, eds., ASME HTD-Vol. 227, pp. 29–36.

Guinier, A., and Jullien, R., 1989, *The Solid State From Superconductors to Superalloys,* Oxford University Press, Oxford, London, United Kingdom, pp. 23–55.

Kittel, C., 1986, *Introduction to Solid State Physics,* 6th ed., Wiley, New York, pp. 116–120.

Klitsner, T., VanCleve, J. E., Fischer, H. E., and Pohl, R. O., 1988, "Phonon Radiative Heat Transfer and Surface Scattering," *Phys. Rev. B,* Vol. 38, pp. 7576–7594.

Mahan, G. D., and Claro, F., 1988, "Nonlocal Theory of Thermal Conductivity," *Phys. Rev. B,* Vol. 38, pp. 1963–1969.

Majumdar, A., 1991, "Microscale Heat Transfer in Dielectric Thin Films," ASME HTD-Vol. 184, pp. 33–42.

McQuarrie, D. A., 1976, *Statistical Mechanics,* Harper and Row Publishers, New York, pp. 196–214.

Nambu, K., 1986, "Theoretical Basis of the Direct Simulation Monte Carlo Method," *Rarefied Gas Dynamics,* Vol. 15, pp. 369–383.

Peierls, R. E., 1955, *Quantum Theory of Solids,* Clarendon Press, Oxford, London, United Kingdom, pp. 27–52.

Qiu, T. Q., and Tien, C. L., 1992, "Size Effects on Nonequilibrium Laser Heating of metal Films," *Proceedings of the Winter Annual Meeting of the American Society of Mechanical Engineers,* D. Cho et al., eds., ASME DSC-Vol. 40, pp. 227–241.

Tien, C. L., and Lienhard, J. H., 1979, *Statistical Thermodynamics,* Hemisphere Publishing Corp., New York, p. 307.

Tien, C. L., and Chen, G., 1992, "Challenges in Microscale Radiative and Con-

ductive Heat Transfer," *Proceedings of the Winter Annual Meeting of the American Society of Mechanical Engineers,* Y. Bayazitoglu and G. P. Peterson, eds., ASME HTD-Vol. 227, pp. 1–13.

Vincenti, W. G., and Kruger, C. H., 1965, *Introduction to Physical Gas Dynamics,* Robert E. Krieger Publishing Co., Huntington, NY, pp. 328–390.

Wakuri, S., and Kotake, S., 1991, "Molecular Dynamics Study of Heat Transfer in Very Thin Films," *Proceedings of the ASME/JSME Thermal Engineering Conference,* Vol. 4, pp. 111–116.

Waldram, J. R., 1985, *The Theory of Thermodynamics,* Cambridge University Press, New York, pp. 102–111.

Ziman, J. M., 1960, *Electrons and Phonons,* Oxford University Press, London, United Kingdom.

ERRATA

To the paper "Rewetting Theory and the Dryout Heat Flux of Smooth and Grooved Plates With a Uniform Heating" by S. H. Chan and W. Zhang, published in the ASME JOURNAL OF HEAT TRANSFER, Vol. 116, February 1994, pp. 173–179.

In Eqs. (21), (30), and (31), the term $(1 + (A/B))$ should read as $(1 - (A/B))$. In Eq. (29), f_1 outside of the integral sign should be eliminated. In Eq. (50), the term $-\beta_n^2(\tau - \lambda)$ should read as

$$e^{-\beta_n^2(\tau-\lambda)}$$

while in Eq. (52), the term

$$e^{e^{-n^2\pi^2\tau/\eta_{L_1}^2}}$$

should be

$$e^{-n^2\pi^2\tau/\eta_{L_1}^2}$$

We regret the typographical error, which we failed to catch.

M. Mittelbach
Graduate Research Assistant.

C. Vogd
Graduate Research Assistant.

L. S. Fletcher
Thomas A. Dietz Professor.
Fellow ASME

G. P. Peterson
Tenneco Professor and Head.
Fellow ASME

Department of Mechanical Engineering,
Texas A&M University,
College Station, TX 77843-3123

The Interfacial Pressure Distribution and Thermal Conductance of Bolted Joints

Experimental interface pressure distributions and thermal conductance data are presented for a bolted joint. The variables considered included the bolt torque and associated axial load, the upper and lower plate thicknesses, and the mean interface temperature within the bolt radius. For 7.62-cm-dia Aluminum 6061-T6 plates, axial loads of 6.69 to 13.425 kN (1500 to 3000 lb), three heat fluxes, and mean junction temperatures of up to 310 K were considered. Pressure distribution data obtained with a pressure-sensitive film compared favorably with both theoretical predictions and published experimental data. Thermal conductance data obtained at three radial locations for the bare interface compared favorably with published data. These data also were compared with a previously published correlation for heat transfer in bolted joints. Thermal conductance data for high-conductivity elastomeric gasket materials were obtained to ascertain their suitability for thermal enhancement. The results of this investigation will be useful in the thermal analysis of bolted and riveted joints.

Introduction

Bolted or riveted joints, the most common types of mechanical connections, are found in numerous components, assemblies, and systems. These systems include engines, transformers, extrusion units, gas turbines, power generation equipment, and spacecraft thermal control systems, as well as microelectronic devices. The efficient transfer of heat through the bolted or riveted joints in these components and systems is essential for optimum thermal performance. As a consequence, an understanding of the thermal resistance associated with these joints is an important consideration in the overall thermal analysis.

Evaluation of the thermal resistance of these joints is complex because the contact pressure is not uniform over the entire interface of the joint. It is not possible, therefore, to use theoretical or analytical techniques for prediction of the thermal contact conductance (Fernlund, 1961). The contact pressure has been found to be highest near the bolt or rivet shank and decrease to zero a few bolt or rivet radii away from the centerline.

When an electronic component is attached to a base plate, or when two plates are bolted or riveted together, there will be contact in the immediate vicinity of the bolt or rivet. Such a joint may be modeled by two plates bolted together, as shown in Fig. 1. The actual contact area will be circular in shape, with the contact pressure decreasing with distance from the bolt centerline. The area of the actual contact zone is directly associated with the resistance to heat transfer. If there is a region of no contact and the temperature of the components is such that there is negligible radiative heat transfer, then the energy transfer will be constrained to flow parallel to the bolt axis through the contact zone at the interface. The area of the contact zone depends upon the pressure distribution between the surfaces caused by the tensile load in the bolt, and the thicknesses of the plates composing the joint. The heat transfer through a bolted joint, then, is dependent upon the pressure distribution at the joint as well as the macroscopic and microscopic contact resistance.

Contributed by the Heat Transfer Division for publication in the JOURNAL OF HEAT TRANSFER. Manuscript received by the Heat Transfer Division July 1992; revision received October 1993. Keywords: Conduction, Electronic Equipment, Thermal Packaging. Associate Technical Editor: R. Viskanta.

Pressure Distribution. Most of the theoretical and experimental studies of bolted joints have been conducted for an axisymmetric loading condition on two plates bolted together, as shown in Fig. 1. The pressure distribution is a function of several geometric variables such as the plate thicknesses, bolt diameter, load radius, and other variables including the axial force and interface surface characteristics.

Most theoretical studies have involved replacement of the interface pressure distribution between two bolted plates with the stress distribution at the midplane of an infinite plate with a hole, generally known as the single-plate model. In this case, the axial and radial replacements between the two plates within the contact zone are equal. Another assumption often made is that the loading pressure under the bolt head is constant.

Rötscher (1927) was probably the first investigator to calculate the contact zone radius. The stresses were considered to be dispersed within an angle of $\alpha = 45$ deg, with the assumption that the interface pressure was constant up to the distance of the contact radius. This assumption was a first approximation of the contact radius, but the pressure distribution was not characterized satisfactorily.

Fernlund (1961) assumed that the bolted plates could be represented by a single plate of the same total thickness. The interface pressure of the bolted joint could be approximated then as the midplane stress of the single plate. With the assumption of thick smooth plates of the same thickness $t_1 = t_2 = t$, with axisymmetric loading, Fernlund developed an exact solution for the pressure using Hankel transforms and the single-plate model. Fernlund also developed an approximate solution for the interface pressure distribution assuming that the pressure was a fourth-order polynomial of the ratio r/a:

$$\sigma_z = A\left(\frac{r}{a}\right)^4 + B\left(\frac{r}{a}\right)^3 + C\left(\frac{r}{a}\right)^2 + D\left(\frac{r}{a}\right) + E \qquad (1)$$

Assuming the boundary conditions:

$$\frac{r}{a} = 1 : \frac{\partial \sigma_z}{\partial\left(\frac{r}{a}\right)} = 0$$

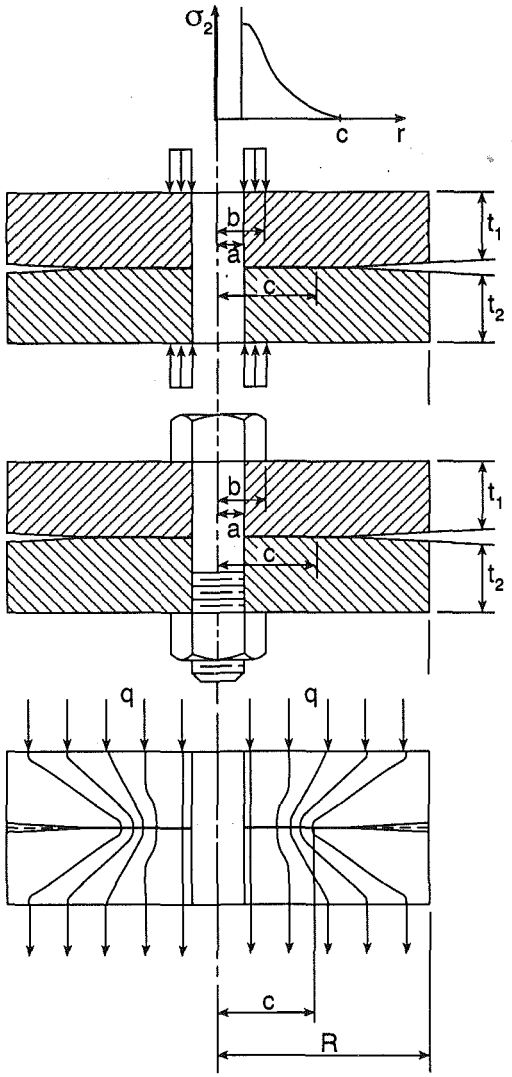

Fig. 1 Bolted joint under load with representative heat flux and pressure distributions

$$\frac{r}{a}=\frac{c}{a}:\frac{\sigma_z}{\left(\frac{r}{a}\right)}=0$$

$$\frac{r}{a}=\frac{c}{a}:\frac{\partial\sigma_z}{\partial\left(\frac{r}{a}\right)}=0$$

$$\frac{r}{a}=\frac{c}{a}:\frac{\partial^2\sigma_z}{\partial\left(\frac{r}{a}\right)^2}=0$$

the coefficients are of the form:

$$A=\frac{\frac{75}{4}P}{-\left(\frac{c}{a}\right)^6+2\left(\frac{c}{a}\right)^5+5\left(\frac{c}{a}\right)^4-20\left(\frac{c}{a}\right)^3+25\left(\frac{c}{a}\right)^2-14\left(\frac{c}{a}\right)+3}$$

$$B=-\frac{4}{3}\left(2\frac{c}{a}+1\right)A$$

$$C=2\frac{c}{a}\left(\frac{c}{a}+2\right)A$$

$$D=-4\left(\frac{c}{a}\right)^2A$$

$$E=-\frac{\left(\frac{c}{a}\right)^3}{3}\left(\frac{c}{a}-a\right)A$$

The contact radius, c, can then be calculated using Rötscher's assumption:

$$\frac{c}{a}=\frac{b}{a}+\frac{t}{a}\tan\alpha \tag{2}$$

$$P=\frac{F_{\text{axial}}}{\pi(b^2-a^2)} \tag{3}$$

Motosh (1975, 1976) used the same approach to analyze the pressure distribution at the bolted joint interface, and examined two different pressure distributions: a conical envelope and a spherical envelope.

Gould and Mikic (1971) investigated the pressure distribution and the contact zone radius using a finite element method. They used both a single-plate model and a two-plate model for several geometric configurations ($t/a=1$, 1.33, 2, and $b/a=1.3$, 1.6, 2.2, 3.1). In the two-plate model the radial displacements at the interface are not the same, and a shearing stress exists in the contact zone. A comparison of the results of these two models shows that the contact zone radii calculated with the two-plate model were less than for the single-plate model, which results in a significant reduction in the contact area. For example, in the case of $t/a=1$ and $b/a=2.2$ the contact area calculated with the two-plate model is 36.4 percent smaller than for the single-plate model. Gould and Mikic also calculated the radius of the contact area for bolted joints consisting of two plates of unequal thickness. A comparison of the contact radii between two bolted joints of the same total plate thickness, $t_1+t_2=0.986$ cm (0.381 in.), one bolted joint of two plates each 0.485 cm (0.191 in.) thick, the other bolted joint of a 0.315 cm (0.124 in.) and a 0.653 cm (0.257 in.) thick plate, showed that the contact radius of the unmatched pair is smaller than that of the pair of equal-thickness plates. A comparison of the calculated and experimentally measured

Nomenclature

a = bolt radius
b = load radius
c = contact zone radius
F_a = axial force
h_c = thermal contact resistance
k = thermal conductivity
p = applied pressure
P = interface pressure
q = heat flux
r = radial coordinate
R = plate outer radius
R_c^* = dimensionless thermal contact resistance
t = thickness of the plates
T = temperature
z = axial coordinate
α = half-angle of stress dispersing cone
ΔT = temperature drop at interface
ν = Poisson ratio
σ_z = axial stresses at interface

Subscripts

1 = upper plate
2 = lower plate
z = axial direction

contact radii showed good agreement with the calculations of the two-plate model.

Chandrashekhara and Muthama (1977, 1978, 1979) developed an exact theoretical solution in terms of Fourier–Bessel integrals for the stresses in a thick plate of infinite extent having a circular hole and axisymmetric loading. Several values for the ratios t/a and b/a were considered as well as several values of the Poisson ratio, ν. A graphic representation of the pressure distribution suggested the following conclusions:

- The interfacial pressure distribution tends to zero for $r/a > 5$;
- For elastic deformation, the only material property that may affect the pressure distribution is the Poisson ratio, but its effect can be neglected except when ν is very small (≤ 0.15); and,
- A single-plate model can be used if the plates are of the same thickness and the same material

Ziada and Abd El Latif (1980) investigated the effect of various plate thickness ratios of two plates, t_1/t_2, on the load and stress distribution in cylindrical bolted joints using a finite element technique. Computations were performed for four joints with the total joint thickness of 50 mm, with plate thicknesses of 5 mm/45 mm, 12.5 mm/37.5 mm, 20 mm/30 mm, and 25 mm/25 mm. A computation of the load distribution at the surface under the bolt head showed that the load is neither constant nor uniform, as assumed in previous studies. The contact radius at the interface is greatly affected by the thickness ratio of the two bolted plates. The maximum value of the contact radius, c, is reached at $c/a = 3.5$ for plates of equal thickness, and the minimum value of the contact radius approaches a constant value of $c/a = 2.5$ for thickness ratios of $t_1/t_2 \geq 10$.

Curti et al. (1985) computed the pressure distribution for different loadings using the boundary element for a single-plate model. The load shapes were constant load, a linearly increasing load from zero at $r = a$ to a maximum at $r = b$, and a linearly decreasing load from a maximum at $r = a$ to zero at $r = b$. Computation of the pressure distribution and the contact radius (end of interface pressure) for geometric ratios of $t/a = 1$, 1.36, 2 and $b/a = 1.6$, 2.2 showed that both depend on the shape of the load distribution under the bolt head. This influence decreased with the ratio $(b-a)/t$ and tended to disappear when this ratio was less than 0.3.

Bradley et al. (1971) employed a three-dimensional photoelastic analysis using a freezing technique to predict the interface pressure for nine different bolted joint geometries. The bolted plates were composed of smooth flat plates of photoelastic material, all of equal thickness. Nine bolted joint geometries ($t/a = 1, 4/3, 2$, and $b/a = 1.5, 2, 3$) were investigated. A comparison of the applied load with an integration of the interface pressure distribution over the contact area between the two plates was within 5–10 percent. The results were in good agreement with a finite element solution reported for one particular configuration ($t/a = 2$ and $b/a = 1.5$). For this configuration, a comparison with the results of Fernlund (1961) showed an overestimation of the contact zone radius by about 15 percent and an underestimation of the maximum pressure by about 20 percent.

Gould and Mikic (1971) measured the radii of separation (contact zone radii) by two different experimental methods. One method employed autoradiographic techniques, and the other measured the polished area around the bolt hole of the plate interface caused by sliding under load in the contact zone. Sixteen stainless steel plates, 10.16 cm (4 in.) in diameter, with thicknesses of $t = 0.159, 0.318, 0.476, 0.635$ cm (0.0625, 0.125, 0.188, 0.25 in.) (four plates of each thickness) were investigated. The computed and experimental results of the contact zone were in good agreement and showed that the contact zone was smaller than the contact radius measured in previous studies.

Plock (1971) investigated the effect of the connecting force using pressure-sensitive papers and found that the area of the interfacial pressure was wider than that determined by the Rötscher technique. Ito et al. (1979) measured the interfacial pressure distribution by means of ultrasonic waves. The results showed that the roughness of the plate surfaces, the material, and the plate thickness all influence the pressure distribution and the contact radius. The authors investigated plates made of semi-hard steel (S45C), brass (BsBM1), and an aluminum alloy (AlB1), with different surface roughnesses, $R_{max} = 0.8$ μm (for the steel plates) and three different contacting forces $F_a = 9.8$ kN, 14.7 kN, and 19.6 kN.

Madhusudana et al. (1990) presented a review of the literature of bolted joints addressing the interfacial pressure distribution and the size of the contact zone. They analyzed the contact pressure and determined that the exact form of the stress distribution within the contact zone does not affect the total pressure if the microscopic conductance is used. The total microscopic conductance will differ by 5 to 10 percent depending on the type of stress distribution chosen, if experimental correlations for local solid spot conductance are used.

Thermal Conductance. The macroscopic resistance in a bolted joint arises from the reduced area of the contact surrounding the bolt, and the microscopic resistance results from the actual contact spots occurring within the contact zone. A schematic of the heat flux lines through the bolted joint also is shown in Fig. 1.

Roca and Mikic (1972) noted the effect of surface roughness on the total resistance. If the surface roughness is increased, the total resistance may increase or decrease because the roughness asperities at the contact surfaces may affect the microscopic and the macroscopic resistance in different directions. Once the pressure distribution was known, it was possible to calculate the interfacial contact conductance and the total joint resistance. With the calculated example, it was possible to raise, lower, or maintain constant the total thermal resistance by varying the roughness.

Yip (1972) derived an expression for thermal contact resistance in vacuum for rough surfaces of normal height distribution. There was no significant difference in the microscopic contact resistance for three different pressure distributions (uniform, linear, and parabolic). The computed microscopic contact resistance for different applied loads showed the significant influence of the applied loads.

Madhusudana et al. (1990) evaluated the macroscopic contact conductance for a bolted joint using linear, parabolic, and polynomial pressure distributions. Results of the evaluation indicate that the radius of the contact zone is critical in the analysis of heat flow through bolted joints.

Fletcher et al. (1990) developed a nondimensional correlation for the thermal resistance of bolted and riveted joints using the geometric characteristics of the joint. Experimental verification was provided with results from an electrolytic analog. The correlation in dimensionless form was

$$R_c^* = 0.7524(t^* e^{2t^*})^{-0.5275} \tag{4}$$

where

$$R_c^* = \frac{R - R_o}{R_o} = \frac{R}{R_o} - 1$$

$$t^* = \frac{t_1 a^4 + t_2 c^4}{0.1 R^5}$$

or

$$R^* = 0.7524 \left[\frac{t_1 a^4 + t_2 c^4}{0.1 R^5}\right]^{-0.5275} e^{-1.055 \left[\frac{t_1 a^4 + t_2 c^4}{0.1 R^5}\right]} \tag{5}$$

Table 1 Test plate characteristics*

Plate	Diameter (cm)	Thickness (cm)	Roughness* (μm)
1	9.144	1.27	3.63
2	9.144	1.91	3.06
3	9.144	1.91	3.40
4	9.144	2.54	3.37

* Surface profilometer average values.

These are a few of the studies that deal with the effect of the interface pressure distribution on the thermal contact conductance. Most of these investigations provided a theoretical solution for the interface pressure distribution. Experimental investigations have been limited, so that results are not sufficiently conclusive. Because of the significant influence of the pressure on the thermal contact conductance, this dependence and the interface pressure distribution between two bolted plates warrants further investigation.

Experimental Program

The present study was directed toward an experimental investigation of the pressure distribution and thermal contact conductance at the interface of bolted joints. An experimental test facility was designed and built especially for this bolted joint investigation, and has been reported by Mittelbach (1989) and Vogd (1990).

Experimental Facility. The experimental test facility was constructed with plates machined from Aluminum 6061, with an outer radius of $R = 4.57$ cm (1.8 in.). Four plates, two of thickness 1.91 cm (0.75 in.), one of 1.27 cm (0.5 in.), and one of 2.54 cm (1.0 in.) were constructed so that experimental tests could be conducted with two plates of the same thickness, as well as with plates of different thickness. The plates were machined so that the surface roughness of each plate was less than 3.7 μm (over an average of 24 readings). Table 1 lists the surface roughness values. Each plate had a central hole for the bolt with a ratio of $b/a = 1.5$ and the two plates were bolted together using a hard steel bolt (grade 8).

In order to determine the range of axial force occurring when two plates are bolted together, a washer load cell was used to determine the axial force when the bolt was tightened. It was determined that a 34.5 MPa (5000 lb) washer load cell would provide the best signal for the range of tests to be conducted in this investigation. Further, the calibration of the washer load cell was marginal for axial loads below 3.45 MPa (500 lb).

The pressure distribution and contact radius were measured with a pressure-sensitive film manufactured by the Fuji Corporation. This film is available in a number of different pressure ranges and is composed of two special sheets (A-film and C-film, together 200 μm thick), which change color under pressure. The film used in this study included the ultra super low-pressure film (2 to 6 kg_f/cm^2) and the super low-pressure film (5 to 25 kg_f/cm^2). The precision of the pressure measurements using the Fuji film is reported to be ± 10 percent when the exposed film is measured with a calibrated Fuji densitometer. The pressure-sensitive film may be used over a temperature range of 5 to 35°C and humidity range of 20 to 90 percent relative humidity.

For the heat transfer measurements, each plate had 16 holes (#57 drill) for the thermocouples, which were located at four different axial coordinates and four different radii, $r = 0.89$, 1.93, 2.97, 4.01 cm (0.35, 0.76, 1.17, 1.58 in.). The K-type thermocouples used in this investigation were packed into the holes of the plates using a heat-sink compound and the thermocouples were externally attached to the plates using epoxy. A data-acquisition system was used to convert the incoming voltage into temperature data. The heat flux was produced by heating the upper side of the upper plate with a 45 W silicon heater and cooling the lower side of the bolted joint with a constant temperature bath. The heat sink had an inner diameter of 2.794 cm (1.1 in.) so that the washer load cell would fit inside and the measured axial force was the force acting on the washer. Figure 2 shows a schematic view of the test facility.

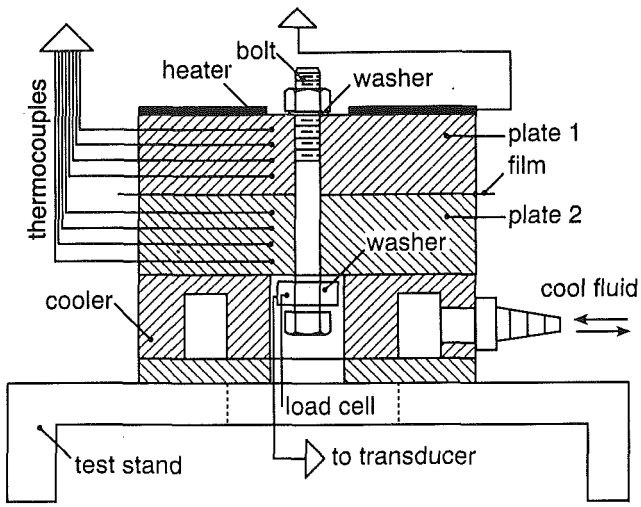

Fig. 2 Schematic of the experimental bolted-joint test facility

Experimental Procedure. The experimental investigation may be divided into two parts: measuring the pressure distribution with the pressure-sensitive film and measuring the temperatures at several points in the plates to calculate the thermal contact conductance. These tests were conducted for several different plate combinations and bolt torques. The torque on the bolt was applied and measured with a calibrated torque-wrench. The corresponding axial force was measured with the washer load cell.

The pressure-sensitive film was inserted between the two plates, and the pressure was applied by raising the torque gradually over a period of two minutes and maintaining the torque constant for another two minutes. The color pattern developed on the C-film and the color density were read with the densitometer, which averaged the intensity of the color in a circular area 2.0 mm in diameter. The intensity was measured four times at each location, and the pressure was calculated as the average of the two middle values of the readings. From the corresponding pressure-density characteristic curve for the Fuji film, the pressure at the measured point (area) could then be determined. For more accurate results the pressure was corrected for the humidity and the temperature. The humidity was measured using a psychometric chart after measuring the dry bulb and wet bulb temperatures. A stencil was used to analyze the same points at up to 10 different radii and in different locations on the film.

The temperature at four different radii, $r = 0.89/1.93/2.97/4.01$ cm (0.35/0.76/1.17/1.58 in.), and four different axial directions was measured. Using a linear regression, the temperature gradients in both plates were determined from the thermocouples and extrapolated to the plate surface to determine the interface temperatures. Knowing the thermal conductivity, k, of Aluminum 6061 from previous experiments:

$$k = 111.94 + 0.226\ T \tag{6}$$

where T is the average temperature of the plate in absolute temperature. The heat flux was then obtained by the relationship:

$$q = -k\left(\frac{dT}{dx}\right) \tag{7}$$

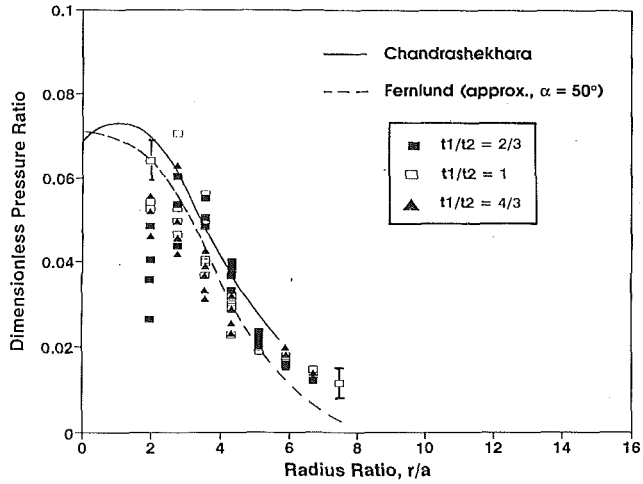

Fig. 3 Comparison of the experimental dimensionless pressure distributions as a function of dimensionless radius for plate thickness ratios of $t_1/t_2 = 2/3$, 1, and 4/3, with the analyses of Chandrashekhara and Muthanna (1978) and Fernlund (1961)

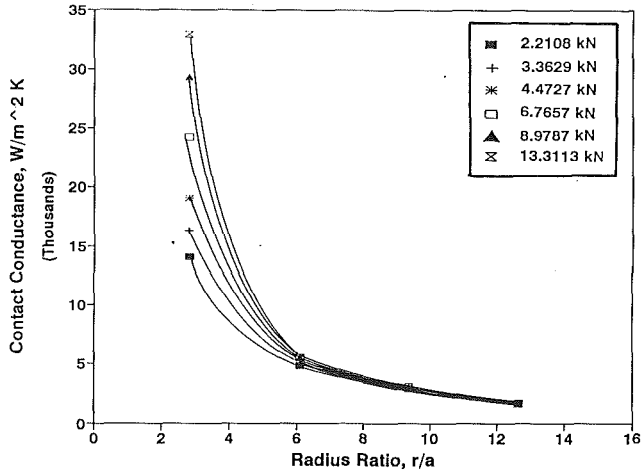

Fig. 4 Thermal contact conductance as a function of dimensionless radius and applied load for a plate thickness $t_1/t_2 = 2/3$

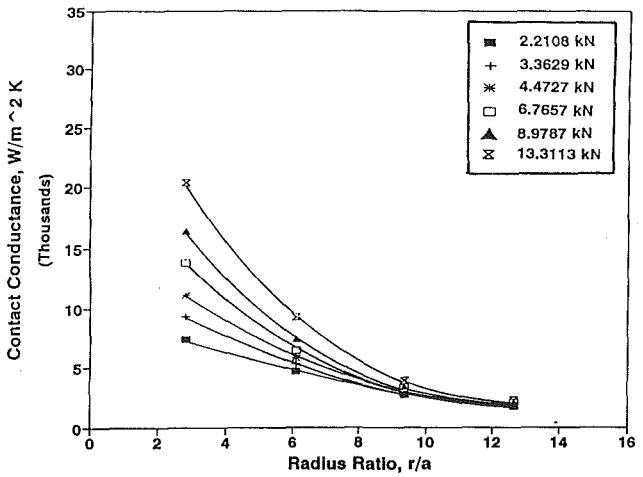

Fig. 5 Thermal contact conductance as a function of dimensionless radius and applied load for a plate thickness ratio $t_1/t_2 = 4/3$

The average of the heat flux in the upper and lower plates, divided by the temperature change at the interface, ΔT, is the thermal contact conductance, h_c, such that:

$$h_c = \left(\frac{q_{\text{upper}} + q_{\text{lower}}}{2\Delta T} \right) \tag{8}$$

The axial force was increased in five increments from the initial load. The system was allowed 1 to 2 hours to reach steady state for each load, before temperature measurements were obtained. Experimental tests were conducted using plates of different geometries bolted together with five different torques and three different heat fluxes.

Results and Discussion

Experimental tests were conducted to determine the contact pressure and thermal contact conductance for several different bolted joint geometries. The plate thickness ratio, t_1/t_2, ranged from 2/3 to 4/3, the load radius to bolt radius ratio, b/a, was 1.5, and the axial force loads ranged from 2.21 kN (548 lb) to 13.63 kN (3065 lb).

Pressure Distribution. The pressure distribution at the interface between the two different plates was determined for a number of different test conditions using the pressure sensitive film. The experimental pressure distribution results were reasonably similar for the different plate ratios and loads; therefore, the pressure distribution for all bolt geometries is shown in Fig. 3 for several different axial loads. These data are shown as dimensionless quantities: the interface pressure divided by the applied pressure as a function of the radial distance from the bolt hole divided by the bolt radius. The theoretical results of Fernlund (1961) and Chandrashekhara and Muthanna (1978) are also shown in Fig. 3 for comparison.

There appears to be some scatter at low values of r/a when compared to the theories of Fernlund (1961) and Chandrashekhara and Muthanna (1978); however, the trend is similar. At high values of r/a, the data were reasonably consistent for all axial force loads and bolt geometries. The scatter tends to diminish as the radius ratio approaches a value of 4 to 5. The resulting experimentally determined pressure distributions appear to be reasonable in terms of the theoretical analyses. There is, however, an experimental error associated with the use of Fuji film, and the resulting error is reflected through the use of error bars in Fig. 3.

All the data obtained show a variation in the pressure measurements for the different applied loads. This difference is greater near the bolt hole and appears to diminish with increasing distance from the bolt hole. This variation near the bolt hole was greater than the scatter associated with the errors in the measured pressure distribution.

The steady-state pressure distribution was reached approximately 3.5 minutes after applying the torque. This did not impact the heat transfer measurements because the load did not change after steady-state conditions were reached. But because most of the film development occurs in the first few seconds, increasing the force slowly and maintaining it constant for the particular value was very difficult. Thus, the uncertainty associated with the pressure-sensitive film contributes to the uncertainty in the overall measurements.

Thermal Conductance. The experimental results for the thermal contact conductance of the bolted joint configuration for two different plate thickness ratios as a function of radius ratio are illustrated in Figs. 4 and 5. The experimental data in Fig. 4 are for a plate thickness ratio of 2/3 with applied loads from 2.44 kN to 13.63 kN. It is interesting to note that the thermal contact conductance adjacent to the bolt hole is at a relatively high value, as might be expected, and decreases with increasing radial distance. Further, the data for the different applied loads coalesce in the radius ratio region between 6 and 7, and decrease as the radius increases.

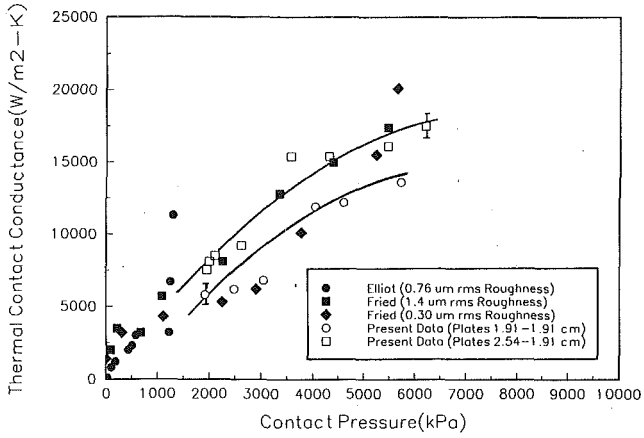

Fig. 6 Comparison of the experimental thermal contact conductance results as a function of pressure with published results

The experimental thermal contact conductance data presented in Fig. 5 are for a plate thickness ratio of 4/3, indicating thicker plates. For the same axial loads shown in the previous figure, the thermal contact conductance values are not as high, suggesting that the plates are much stiffer, with less deformation. The thermal contact conductance decreases steadily as the radius ratio increases, coalescing at a radius ratio of approximately 12. Clearly, the thicker plates reduce the overall thermal contact conductance of the bolted joint because there is less deformation and the plates stay in contact over a greater radius.

A comparison of Fig. 3, the pressure distribution as a function of radius ratio, with Figs. 4 and 5, the thermal contact conductance as a function of radius ratio, indicates that the thermal contact conductance is greatest near the edge of the bolt hole and decreases as the pressure decreases. While the effect of plate thickness ratio on the pressure distribution is rather limited, the effect on the thermal contact conductance is only significant in the region near the bolt and diminishes as the radius ratio increases.

The thermal contact conductance data for bolted joints as a function of interface pressure are illustrated in Fig. 6. Experimental results from Fried and Atkins (1965) and Elliott (1965) are also included in the figure. The thermal contact conductance of the bolted joint for plates of unequal thickness compared with the data for bolted joints of the same thickness are also shown. It is interesting to note that the thermal contact conductance was higher for the plates of unequal thickness, suggesting that the thinner plate deforms to the contours of the thicker plate. The experimental results for a contact pressure, $P \leq 3500$ kPa, show good agreement with those of Fried and Atkins (1965). For higher contact pressures, $P \geq 3500$ kPa, the improvement of the thermal contact conductance with increasing contact pressure is less than observed by Fried. The results of Elliott (1965) for contact pressures above 1000 kPa do not appear to be reasonable.

Conclusions and Recommendations

An experimental investigation of the pressure distribution at the interface of bolted joints, as well as the thermal contact conductance of these joints, was conducted. The results have been compared with those from previous studies. Based on the results of this investigation, the following conclusions may be drawn. First, the trend of the data for the interface pressure distribution shows good agreement with previously published analyses, even with the measurement scatter near the bolt hole. Second, there seems to be little influence of the plate thickness on the contact radius for plates with the geometric ratio of plate thickness divided by bolt radius equal to or greater than six. Even the influence of different plate thicknesses appears to be negligible. The thermal contact conductance is greatest near the bolt and decreases with increasing radius. The magnitude of the thermal contact conductance is a function of the plate thickness ratio, whereas the pressure distribution demonstrates little variation with plate thickness ratio.

It is recommended that this study be continued and experimental work on a broader range of bolted joints be conducted, especially the heat transfer measurements. Higher heat flux rates are recommended in order to assure the assumption of one-dimensional heat flow and to obtain higher temperature gradients and more accurate results.

References

Bradley, T. L., Lardner, T. J., and Mikic, B. B., 1971, "Bolted Joint Interface Pressure for Thermal Contact Resistance," ASME *Journal of Applied Mechanics*, Vol. 38, pp. 542–545.

Chandrashekhara, K., and Muthanna, S. K., 1977, "Stresses in a Thick Plate With a Circular Hole Under Axisymmetric Loading," *International Journal of Engineering Science*, Vol. 15, pp. 135–146.

Chandrashekhara, K., and Muthanna, S. K., 1978, "Pressure Distribution in Bolted Connections," *Report on Advances in Reliability and Stress Analysis*, ASME Winter Annual Meeting, San Francisco, CA, Dec., pp. 117–124.

Chandrashekhara, K., and Muthanna, S. K., 1979, "Analysis of a Thick Plate With a Circular Hole Resting on a Smooth Rigid Bed and Subjected to Axisymmetric Normal Load," *Acta Mechanica*, Vol. 33, pp. 33–44.

Curti, G., Raffa, F., and Strona, P., 1985, "Analysis of Contact Area and Pressure Distribution by Boundary Element Method," *Wire*, Vol. 35, No. 1, pp. 14–18.

Elliott, D. H., 1965, "Thermal Conduction Across Aluminum Bolted Joints," ASME Paper No. 65-HT-53.

Fernlund, I., 1961, "A Method to Calculate the Pressure Between Bolted or Riveted Plates," Report No. 17, Institute of Machine Elements, Chalmers University of Technology, Gothenburg, Sweden.

Fletcher, L. S., Peterson, G. P., Madhusudana, C. V., and Groll, E., 1990, "Constriction Resistance in Bolted and Riveted Joints," ASME JOURNAL OF HEAT TRANSFER, Vol. 112, pp. 857–863.

Fried, E., and Atkins, H. L., 1965, "Interface Thermal Conductance in a Vacuum," *Journal of Spacecraft and Rockets*, Vol. 2, No. 4, July–Aug., pp. 591–593.

Gould, H. H., and Mikic, B. B., 1971, "Areas of Contact and Pressure Distribution in Bolted Joints," Report No. DSR 71821-68, Department of Mechanical Engineering, Massachusetts Institute of Technology, Cambridge, MA, June.

Ito, Y., Toyoda, J., and Negata, S., 1979, "Interface Pressure Distribution in a Bolt-Flange Assembly," ASME *Journal of Mechanical Design*, Vol. 101, pp. 330–337.

Madhusudana, C. V., Peterson, G. P., and Fletcher, L. S., 1990, "The Effect of Non-uniform Interfacial Pressures on the Thermal Conductance in Bolted and Riveted Joints," ASME *Journal of Energy Resources Technology*, Vol. 112, pp. 174–182.

Mittelbach, M., 1989, "The Effect of Pressure Distribution on the Thermal Contact Conductance of Bolted Joints," Studienarbeit, Mechanical Engineering Department, Texas A&M University, College Station, TX.

Motosh, N., 1975, "Stress Distribution in Joints of Bolted or Riveted Connections," ASME *Journal of Engineering for Industry*, Vol. 97, pp. 157–161.

Motosh, N., 1976, "Determination of Joint Stiffness in Bolted Connections," ASME *Journal of Engineering for Industry*, Vol. 98, pp. 858–861.

Plock, R., 1971, "Die Ubergangssteifigkeit von Schraubenverbindungen," *Industrie Anzeiger J.*, Vol. 93, No. 27, March, pp. 571–575.

Roca, R. T., and Mikic, B. B., 1972, "Thermal Conductance in a Bolted Joint," AIAA Paper No. 72-282.

Rötscher, F., 1927, *Die Maschinenelemente*, Verlag von Julius Springer, Berlin, Federal Republic of Germany.

Vogd, C., 1990, "Thermal Contact Conductance of Bolted Joints," Studienarbeit, Mechanical Engineering Department, Texas A&M University, College Station, TX.

Yip, F. C., 1972, "Theory of Thermal Contact Resistance in Vacuum With an Application to Bolted Joints," AIAA Paper No. 72-281.

Ziada, H. H., and Abd El Latif, A. K., 1980, "Loading Conditions in Bolted and Riveted Joints Affected by Plate Thickness Ratio," ASME *Journal of Mechanical Design*, Vol. 102, pp. 851–857.

An Experimental Evaluation of the Effective Thermal Conductivities of Packed Beds at High Temperatures

K. Nasr

R. Viskanta

S. Ramadhyani

School of Mechanical Engineering,
Purdue University,
West Lafayette, IN 47907

Combined conduction and radiation heat transfer in packed beds of spherical particles was investigated. Three different packing materials (alumina, aluminum, and glass) of various particle diameters (2.5 to 13.5 mm) were tested. Internal bed temperature profiles and corresponding effective thermal conductivities were measured under steady-state conditions for a temperature range between 350 K and 1300 K. The effects of particle diameter and local bed temperature were examined. It was found that higher effective thermal conductivities were obtained with larger particles and higher thermal conductivity packing materials. The measured values for the effective thermal conductivity were compared against the predictions of two commonly used models, the Kunii–Smith and the Zehner–Bauer–Schlünder models. Both models performed well at high temperatures but were found to overpredict the effective thermal conductivity at low temperatures. An attempt was made to quantify the relative contributions of conduction and radiation. Applying the diffusion approximation, the radiative conductivity was formulated, normalized, and compared with the findings of other investigators.

Introduction—The Effective Thermal Conductivity

Packed beds are used in numerous industrial thermal systems such as chemical reactors, combustors, and thermal storage units. In the absence of convection, heat transfer in a packed bed occurs by a combination of conduction and radiation, the latter mode becoming dominant at high temperatures. As several previous investigators have suggested, if the particles comprising the packed bed are much smaller than the size of the bed, it is possible to model the radiative heat transfer component as a diffusion process with an associated radiative conductivity (e.g., Chen and Churchill, 1963; Vortmeyer, 1978; Tien, 1988). The effective conductivity of the bed may then be defined based on the total (combined conductive and radiative) heat flux and the temperature gradient in the bed.

The effective thermal conductivity of a bed of particles containing a stagnant fluid is a function of the solid and fluid thermal conductivities, the porosity of the bed, the local temperature, and the particle material, shape, and size. Several theoretical and experimental studies concerning the effective conductivity have been reported and many semi-empirical models describing the heat transfer mechanisms have been proposed (Beveridge and Haughey, 1971; Wakao and Kaguei, 1982; Churchill, 1986; Tsotsas and Martin, 1987; Tien, 1988; Kamiuto et al., 1989; Kamiuto, 1990; Kaviany, 1991).

Beveridge and Haughey (1971) experimentally studied heat transfer in stagnant beds at temperatures between 20 and 750°C. Their comparison of the experimental results with model predictions clearly shows the wide variation in predictions provided by the different models, both for the conductive and radiative components. Botterill et al. (1989) briefly reviewed various models, performed their own experiments on small particles of alumina (d_p = 0.376 mm) and silica (d_p = 0.59 and 0.41 mm), and found that none of the models correctly described the observed temperature dependence of the effective thermal conductivity. These studies along with other numerical investigations, showing discrepancies between heat transfer predictions and experimental data, serve as motivation for carrying out the present study.

The present experimental study was initiated to gain a better understanding of the physical phenomena, identify the relative contributions of the two transport processes, and create a data base for comparison with existing and future model predictions. This paper does not present an extensive comparison of the predictions from the various models, but instead presents new experimental data and compares the data against the predictions of two widely employed models, namely those of Kunii and Smith (1960) and of Schlünder and co-workers (Zehner and Schlünder, 1970; Bauer and Schlünder, 1978). A few comments concerning these models are offered in the following paragraphs.

Based on a one-dimensional heat diffusion model for a unit cell of packed spheres, Kunii and Smith (1960) developed an expression for the effective thermal conductivity by employing earlier theoretical and experimental findings, as well as their own experimental data. Their model accounted for void-to-void and surface-to-surface radiation in the packed bed. Their data reduction procedure involved temperature-dependent fluid thermal conductivity, but temperature-independent solid thermal conductivity and solid-surface emissivity. For the packed beds that they studied experimentally, they obtained linear temperature profiles and thus correlated their results in terms of a mean bed temperature. In addition, the values of the stagnant effective thermal conductivity were extrapolated to zero flow rates from those for a packed bed with fluid flow.

The efforts of Schlünder and co-workers, based on modeling a unit cell in the packed bed, have resulted in a comprehensive expression for the effective thermal conductivity. They accounted for various contributions through the use of factors (parameters) that must be determined experimentally. Specifically, the particle shape, radiation effects, contact conduction, and oxidation effects for metallic particles were accounted for using adjustable parameters. Here also, the thermal conductivity of the solid was taken as temperature-independent (except for steel, whose value was allowed to vary with temperature). The fluid thermal conductivity variation with temperature was accounted for, but the emissivity was taken to be temperature-independent. The stagnant effective thermal conductivity was extracted by

Contributed by the Heat Transfer Division for publication in the JOURNAL OF HEAT TRANSFER. Manuscript received by the Heat Transfer Division June 1993; revision received January 1994. Keywords: Packed and Fluidized Beds, Porous Media, Radiation. Associate Technical Editor: V. K. Dhir.

graphic extrapolation to zero flow conditions from measurements obtained at various flow rates.

We conclude this brief review by highlighting the work of Vortmeyer (1978) and the recent work by Kamiuto (1991) on the radiative conductivity. Vortmeyer (1978) summarized and compared the cell and pseudohomogeneous models in treating radiation in packed beds. The cell model approach is valid as long as the opacity of the packed bed is large and the particles are much larger than the wavelength of the radiation, while the pseudohomogeneous theory treats the dispersed phase as a continuum for radiation and renders the combined problem to that of modeling radiation in an absorbing, emitting, and scattering medium with heat conduction. A formulation for the effective thermal conductivity based on the pseudohomogeneous approach was given in terms of effective scattering and extinction coefficients, similar to that presented by Chen and Churchill (1963). Following the same approach as Vortmeyer, Kamiuto (1991) employed the optically thick limit to the spherical harmonics P_1-approximation and formulated an expression for the radiative conductivity.

The objectives of this experimental study are to measure the temperature-dependent effective thermal conductivity of packed beds of large particles, compare the results with the predictions of the Kunii–Smith (1960) and Zehner–Bauer–Schlünder (1978) models, and extract the radiative conductivity from the experimental data.

Experimental Apparatus and Procedures

The measurements for the effective thermal conductivity were performed using an apparatus similar in design to that used for measuring the thermal conductivity of refractories and insulation materials (ASTM, 1992). It involved measuring the bed temperature profile and the heat extraction rate from which the effective thermal conductivity was determined. The apparatus was constructed to provide one-dimensional heat transfer through the packed bed, withstand temperatures up to 1500 K, allow accurate measurement of internal bed temperatures, and provide total heat rate measurements. The major components of the apparatus consisted of an electric furnace, a test cell, a cooling system, and a data acquisition unit.

The electric furnace (Accutherm, Inc., Pataskala, OH) was used as a means of providing radiative heating. The furnace was loaded by placing the test cell on its base plate. The steel base plate could be raised and lowered using a winch mechanism. The furnace cavity, 380 mm square by 267 mm high, was bounded by insulative refractory bricks and equipped with six horizontal 32-mm-dia silicon carbide heating elements. These heating elements were controlled by a control unit based on the reading of a Pt/Pt-10 percent Rh (type *S*) thermocouple located at the cavity inner ceiling and shielded by a closed-end ceramic tube. The test cell, with inside dimensions of 305 × 305 × 127 mm, consisted of a stainless steel plate with four sides, two thermal guards, and a heat flux calorimeter. The calorimeter and thermal guards were designed in accordance with ASTM recommended practice (Anderson, 1985). The test cell was separated from the base plate of the furnace by a 25-mm-thick layer of insulation pads. Holes were drilled through both the stainless steel plate and the furnace base plate to provide the flux calorimeter and its thermal guards with cooling water. The test cell and its components are described below. Figure 1 is a cross section of the experimental setup showing relevant components.

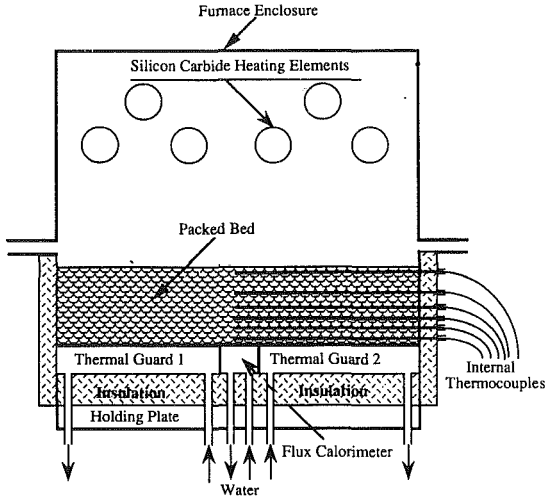

Fig. 1 Cross-sectional view of the conductive-radiative experimental apparatus

Test Cell Description. Special attention was directed toward the design of a test cell that would be able to survive a relatively high-temperature environment (1500 K), yield a uniform one-dimensional heat transfer through a bed of loose particles, provide temperature measurements inside the bed, give an accurate measurement of the heat transfer rate, and have flexibility in replacing the particles and positioning the thermocouples. Prior to fabricating the various component of the apparatus, heat transfer in a packed bed was simulated numerically. One of the purposes of the numerical simulation was to provide guidance on the

Nomenclature

A_c = area of the calorimeter
c_p = specific heat of the fluid circulating through the calorimeter
d_p = particle diameter
E = exchange factor used in the radiative thermal conductivity expression
k_{cond} = conductive component of the effective thermal conductivity
k_{eff} = effective thermal conductivity (combined conductive and radiative)
k_f = fluid thermal conductivity
$k_{K\text{-}S}$ = effective thermal conductivity obtained from Kunii–Smith model
k_r = radiative component of the effective thermal conductivity
k_s = solid thermal conductivity
$k_{Z\text{-}B\text{-}S}$ = effective thermal conductivity obtained from Zehner–Bauer–Schlünder model
m_c = mass flow rate of water through the calorimeter
q = heat flux
Q_c = heat rate picked up by water flowing through the calorimeter
T = local bed temperature
ϵ = solid surface emissivity
κ = ratio of the solid thermal conductivity to the fluid thermal conductivity
σ = Stefan–Boltzmann constant = 5.67×10^{-8} W/m^2 K^4
ϕ = bulk porosity of the packed bed

Subscripts

c = calorimeter
cond = conductive
eff = effective
f = fluid
K-S = Kunii and Smith
p = particle
r = radiative
s = solid
Z-B-S = Zehner, Bauer, and Schlünder

placement of the packed bed internal thermocouples. The numerical solutions predicted the existence of large temperature gradients near the calorimeter surface (Nasr, 1993), and, correspondingly, the thermocouples were positioned to capture these gradients.

The particles used in the experiments were solid spheres of aluminum, alumina, and glass covering a wide range of solid thermal conductivity and surface emissivity. Table 1 contains the physical characteristics and chemical composition of each material. It should be noted that for the experiments conducted on aluminum, polished spheres were used. Exposure of aluminum particles to high temperatures causes oxidation and results in an increase in the surface emissivity. In order to insure that oxidation effects were minimal, the particles were inspected upon completion of the test runs. This inspection revealed that oxidation effects were present but limited to the uppermost layer of particles, and no visible signs of oxidation were found in the vicinity of thermocouple junctions. The four sides of the test cell consisted of 6 mm insulated stainless steel plates. The welded steel plates were separated from a 12 mm bottom plate by a 25-mm-thick layer of insulation, and insulated on the inside and outside by 12 mm of insulation pads. The bottom plate ($300 \times 300 \times 12$ mm) was also separated from the furnace base plate by 25 mm of insulation. Sufficient insulation was employed to ensure the one dimensionality of heat transfer.

The heat sink plate, 25.4 mm in thickness, was essentially a heat exchanger designed to extract the heat imposed by the radiant heaters by circulating fluid through milled channels. The exchanger was made out of copper, water cooled, and consisted of a 100×100 mm central calorimeter surrounded by two thermal guards of the same material. The two thermal guards, which were insulated from both the calorimeter and the base plate of the furnace, served to minimize multidimensional effects and heat losses. Although no measurement of the lateral temperature profile was made to confirm one dimensionality, the coolant flow rates through the thermal guards were adjusted so as to render the difference between the calorimeter and surrounding guards small (<1°C). The packed bed, which was in direct contact with the water-cooled copper plate, had a height of approximately 100 mm. The heat flux calorimeter had a relatively small surface area (only 16 percent of the total area of both the calorimeter and the guards) and was placed at the center of the heat sink copper plate. Its sides were separated (thermally isolated) from the thermal guards by a 2 mm gap filled with Saffil alumina fiber insulation (Thermal Ceramics, Augusta, GA). The water flow rate to the flux calorimeter was measured using a calibrated rotameter. A schematic of the calorimeter-guards assembly can be found elsewhere (Anderson, 1985; Nasr, 1993).

Instrumentation and Data Acquisition. The test cell was instrumented with a number of thermocouples to monitor inside bed temperatures as well as the heat sink surface temperatures, furnace cavity temperature, and temperature difference across the flowing water. The calorimeter and thermal guards were instrumented with several copper-constantan (type T) thermocouples, which were welded to the top, bottom, and side surfaces. These temperatures were monitored throughout the experiment, and the flow rates through the guards were adjusted so as to minimize the temperature difference between the inside wall of the guard and the facing side of the flux calorimeter (<1°C).

Six chromel-alumel (type K) thermocouples were installed to measure internal bed temperatures. The thermocouples were carefully prepositioned inside the porous bed to measure the bed temperature at various vertical locations and at the surface of the heat sink. Temperatures inside the packed layer were measured at the midplane of the packed bed and directly above the flux calorimeter. The thermocouple probes were inserted through holes drilled through one side of the test cell. The wires of each thermocouple were supported inside 150-mm-long two-hole alumina ceramic tubing of 1.6 mm O.D. Due to the large temperature difference across the particulate layer, the thermocouples were positioned horizontally to minimize conduction losses along their wires. Since an accurate knowledge of the thermocouple bead location was extremely important to determine the effective thermal conductivity, a thin strip of stainless steel with precisely drilled holes was used as a template to guide the free ends of the thermocouple probes. The leads exiting the two-hole ceramic tubes were carefully insulated with a high-temperature ceramic fiber insulation (Nextel 312, OMEGA) and brought out of the test cell cavity through a hole in the base plate. In order to avoid stacking too many thermocouples next to each other, thereby disturbing both the bed structure and its temperature profile, only six thermocouples were installed to capture the temperature distribution inside the packed bed.

Table 1 Particle diameter, porosity, and description of the packing material

Material	d_p (mm)	ϕ (%)	Specification, Chemical Composition, and Description
Aluminum	3.24	0.37	Aluminum Alloy 1100, Al (99% min.), Si (0.95%) --- Shiny and perfectly spherical
	6.33	0.38	
Alumina	2.77	0.36	Al_2O_3 (86.4%), SiO_2 (8.32%), MgO (2.2%), BaO (1.5%), CaO (0.96%) -- White - squished spheres
	6.64	0.37	Al_2O_3 (90.4%), SiO_2 (5.63%), MgO (1.71%), BaO (1.04%), CaO (0.7%), Na2O (0.23%) ---White-
	9.61	0.38	Short cylinders with hemispherical caps
Glass	2.85	0.37	
	6.00	0.37	Soda-Lime Silica Glass ---spherical
	13.53	0.39	

The temperature difference between inlet and outlet of the flowing water through the flux calorimeter was measured several different ways to ensure an accurate reading. The inlet and outlet stainless steel tubes were instrumented with a differential thermocouple, two distinct Type T thermocouples, and a thermopile consisting of four junctions in each tube. All three readings were consistently within ± 5 percent of each other and the temperature difference in question was taken as the thermopile reading for added accuracy. All the thermocouple readings were monitored and recorded by a computerized data acquisition system.

Experimental Procedure. After positioning the thermocouples and measuring their vertical location inside the test cell, the particles were randomly poured into the test cell and the bed surface was leveled. The test cell was raised into the furnace cavity by the winch mechanism, the water flow through the flux calorimeter and the thermal guards was initiated, and the heating elements and the data acquisition system were activated. The transient response of all the thermocouples was monitored at preselected intervals of time. Due to the large thermal inertia of the furnace and the test cell, typically seven or eight hours were needed to establish steady-state conditions. During this period, the water flow rate was adjusted so as to obtain a small but measurable ($\sim 3-10$°C) temperature rise between inlet and outlet. Steady-state conditions were considered to be reached when both the furnace cavity wall temperature and inside bed temperatures changed no more than 1°C, over a period of one hour. After recording the water flow rate and the various temperatures, the furnace setpoint temperature was changed to initiate another run. After completing runs at several furnace temperatures, the furnace was allowed to cool slowly. The particles were removed from the test cell, the inside of the test cell was cleaned, and the entire process was repeated with a different packing material.

Data Reduction Procedure. For each run at a specified furnace temperature, the heat flow rate through the packed bed was

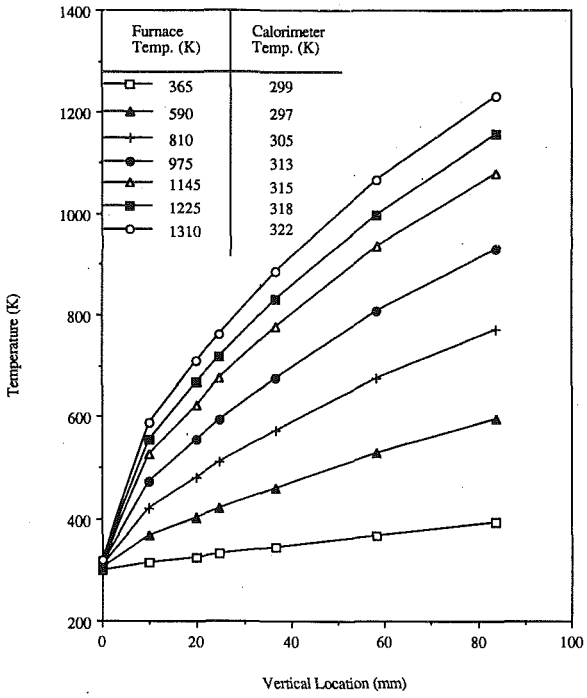

Fig. 2 A sample plot of internal bed temperatures for an alumina–air packed bed (d_p = 9.61 mm, ϕ = 0.38)

computed from measurements of the water flow rate through the flux calorimeter and the temperature difference between inlet and outlet at steady state. The heat transfer rate was expressed as

$$Q_c = m_c c_p \Delta T_c \tag{1}$$

The temperature gradient (dT/dx) at any location in the bed was obtained by differentiating a quadratic or cubic polynomial curve-fit to the measured bed temperatures. The combined conductive-radiative or effective thermal conductivity was computed from

$$k_{\text{eff}} = -(Q_c/A_c)/(dT/dx) \tag{2}$$

The experimental uncertainties resulting from errors in measuring the heat flux and the temperature gradients were estimated to be ±13 percent by following the experimental uncertainty analysis procedure described by Moffat (1988). The experimental uncertainty associated with the measured temperature was estimated to be ±5.8 percent. The particle diameters and bed porosities, needed for comparison with the model predictions, were measured for each packed bed. Bed porosities were determined from the ratio of the void volume to the total volume. The void volume was measured as the difference between the total volume and the volume of the particles.

Results and Discussion

Steady-State Temperatures Inside the Packed Bed. Figure 2 exhibits a sample plot of internal bed temperatures at six vertical locations for a bed of 9.61-mm-dia alumina particles. The calorimeter surface temperatures are also plotted. The different curves are for different furnace setpoint temperatures. Although only six discrete locations were monitored inside the bed, a smooth and continuous curve can be drawn through the interior points. This is also true for other packed beds, though the curvature depends on the constituents of the packed bed (packing material). The solid lines, connecting the points of Fig. 2, are drawn for clarity and are not to be interpreted as best fits. It is evident that the temperature level has a noticeable effect on the curvature of the temperature profile. At low furnace setpoints, the profiles are nearly linear, and the temperature difference across the packed bed is small. At high furnace setpoints, the temperature difference across the bed is large and the profile exhibits a curvature, which becomes more pronounced at higher temperatures. In addition, the profiles reveal the presence of sharp temperature gradients near the relatively cold surface of the calorimeter. The sharp gradients are a result of the negligible radiative contribution at low temperatures as well as the variation of the bed porosity near the bounding surface.

Measured Effective Thermal Conductivity. It was illustrated in Fig. 2 that the internal bed temperatures exhibited a continuous behavior. Second or third-order polynomial least-squares fits were applied to the temperature profiles, excluding the calorimeter surface temperature, and then differentiated with respect to position to obtain the local temperature gradients. The calorimeter surface temperatures were excluded from the least-squares fits since the diffusion approximation to radiative transfer becomes invalid very close to the bounding surface.

The effective thermal conductivities of an alumina–air system are depicted in Fig. 3. The lines drawn for each particle diameter are fitted equations, expressing k_{eff} in terms of the local bed temperature. The scatter in the experimental results should not be overlooked. It is a result of the nature of the experiment (packed beds) and the data reduction procedure in the temperature gradient evaluation. It is evident from this figure that the particulate bed with the largest particle diameter has the highest effective thermal conductivity. This outcome is consistent with the results of previous investigators (Kunii and Smith, 1960; Beveridge and Haughey, 1971). It is also found that at low temperatures (350 K), the effective thermal conductivity is approximately the same for all particle diameters of the same packing material. As expected, the radiation effects become more pronounced as both the particle diameter and the bed temperature increase.

Influence of the Temperature-Dependent Thermophysical Properties. Before providing comparisons between the measured effective thermal conductivities and the predictions of the

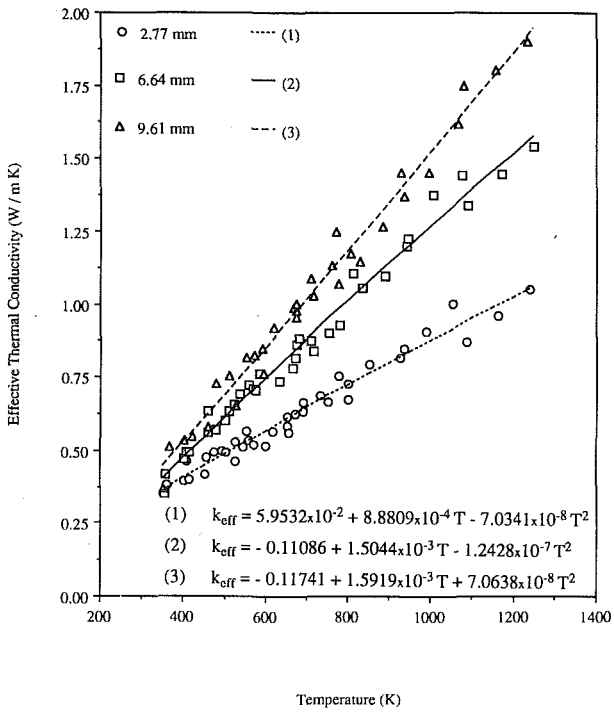

Fig. 3 Experimental effective thermal conductivity values of alumina–air packed beds

Table 2 Properties and their change over the temperature range for all packing materials: thermal conductivities are in W/m K and temperatures are in K (d_p = 6 mm, ϕ = 0.38)

Parameter	Glass	Alumina	Aluminum
T range	300 - 900	300 - 1250	300 - 800
k_s	1.16 - 1.53	36 - 6.3	220 - 202
k_f	0.026 - 0.062	0.026 - 0.079	0.026 - 0.057
k_s / k_f	44 - 24	1370 - 80	8415 - 3545
k_{cond}(K-S)	0.187 - 0.354	0.41 - 0.65	0.58 - 1.12
k_{cond} (Z-B-S)	0.189 - 0.358	0.47 - 0.70	0.63 - 1.2
k_{cond} / k_f	7.2 - 5.7	18 - 9	23 - 21
k_{eff} (K-S)	0.2 - 0.5	0.44 - 1.72	0.58 - 1.15
k_{eff} (Z-B-S)	0.2 - 0.5	0.49 - 1.43	0.50 - 0.96
ε	0.95 - 0.6	0.83 - 0.45	0.043 - 0.06

Kunii–Smith and Zehner–Bauer–Schlünder models, it is important to discuss the thermophysical properties that were supplied as inputs to the models. The thermophysical properties that are employed in evaluating the effective thermal conductivity were sought from various sources. The temperature dependence of the thermal conductivity of alumina was obtained from Touloukian et al. (1970). It is recognized that the alumina material tested is different from that whose properties are given in the aforementioned source. The authors performed an extensive search for the thermophysical properties of the tested alumina and were unable to find any. Nevertheless, the sensitivity of k_{eff} on the value of k_s was checked. According to the Kunii–Smith model, a 25 percent decrease in the value of k_s would cause the value of k_{eff} to decrease by 5 percent. Hust (1985) was used as a reference for the thermal conductivity of aluminum, and Mann et al. (1992) provided an expression for the thermal conductivity of glass. The thermal conductivities of air were obtained from ASHRAE (1976). Surface emissivities for all packing materials were obtained from Touloukian and DeWitt (1972). These properties have a considerable effect on the magnitude of the effective thermal conductivity, especially when they depend strongly on the temperature. Consider, for example, a packed bed made up of 6 mm alumina particles. The solid thermal conductivity decreases from a value of 36 W/m K at room temperature to approximately 6.3 W/m K at 1250 K. The fluid (air) thermal conductivity increases from 0.026 W/m K to 0.079 W/m K over the same temperature range. The variation of k_s and k_f with temperature causes the ratio (k_s/k_f) to decrease from 1370 to 80 and, as a consequence, the ratio of the conductive component of the effective thermal conductivity to the fluid thermal conductivity decreases by a factor of 2, while the conductive component itself increases from approximately 0.47 W/m K to 0.70 W/m K, a 50 percent increase. Since both the fluid and solid thermal conductivities vary with temperature, a dimensionless plot of k_{eff}/k_f versus k_s/k_f will not be presented, for it becomes difficult to deduce the effect of each property variation.

Another property that affects the radiative component and its relative contribution to heat transfer is the total surface emissivity of the solid and its functional dependence on temperature. Over the temperature range from 300 K to 1250 K, the emissivity of alumina decreases from a high value of 0.83 to a relatively low value of 0.42. Table 2 summarizes these properties, the corresponding ratios, and their change with temperature for three different packing materials of 6 mm nominal particle diameter. Thus, every effort should be made to utilize reliable values for the thermophysical and radiative properties and their dependence on temperature. Employing temperature-independent properties may lead to erroneous conclusions on the magnitude of the relative contributions to the heat transfer rate. In addition, extrapolation to higher temperature values should be scrutinized a priori. For instance, the thermal conductivity of alumina exhibits an increase above 1300 K. The actual expressions employed for the solid and fluid thermal conductivities and particle surface emissivity can be found from Nasr (1993).

Comparison With the Kunii–Smith and the Zehner–Bauer–Schlünder Models. Figures 4–6 feature the predictions from both the Kunii–Smith (1960) and the Zehner–Bauer–Schlünder (1978) models along with the experimentally determined effective thermal conductivities for alumina–air, aluminum–air, and glass–air packed beds, respectively. For convenience, the equations embodying the two models are presented in Table 3. It is noted that the predictions shown for the two models were obtained using temperature-dependent thermophysical and radiative properties. Variations in the air thermal conductivity, solid thermal conductivity, and solid surface emissivity with temperature were all taken into account. It is emphasized that variation of the thermophysical properties with temperature affects the magnitude of these predictions considerably. Both models are semi-empirical and involve parameters that were established based on extensive comparison with the available experimental data (Tsotsas and Martin, 1987). In addition, the previous experimental data were presented as a function of a mean bed temperature. The mean temperature is inappropriate for the present tests because of local effects and large temperature drop across the packed bed.

It is seen that for all three systems, both models seem to overpredict the values of k_{eff} at low temperatures, and the predictions based on the Zehner–Bauer–Schlünder model compare reasonably well with the experimental data at higher temperatures. The effect of particle diameter is quite obvious for both the alumina–

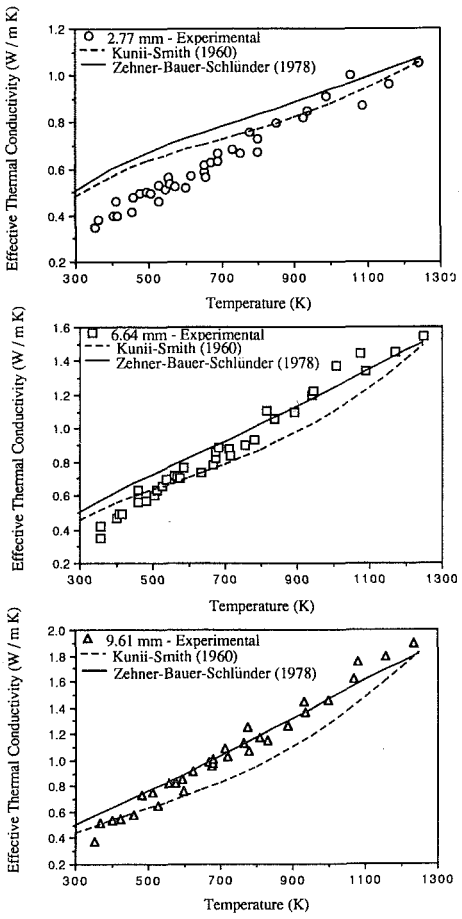

Fig. 4 Comparison of measurements with the predictions of Kunii–Smith and Zehner–Bauer–Schlünder models (alumina–air packed bed)

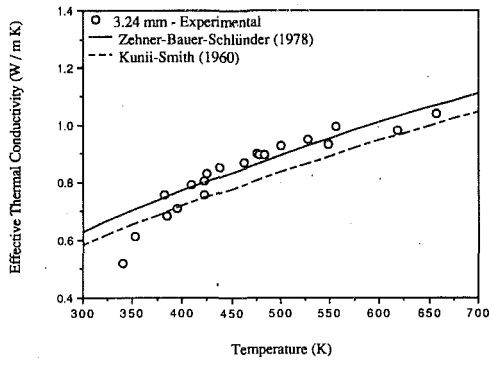

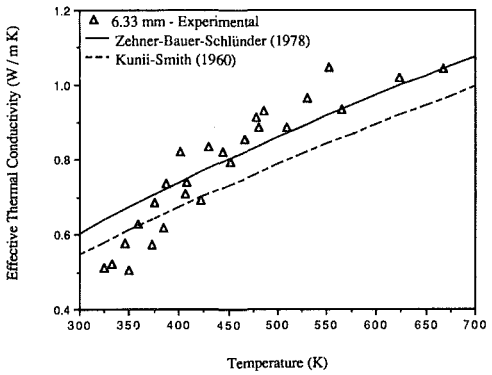

Fig. 5 Comparison of measurements with the predictions of Kunii–Smith and Zehner–Bauer–Schlünder models (aluminum–air packed bed)

air and glass–air systems, but not as distinct for the aluminum–air system due to the low emissivity of aluminum. It is important to note that the glass-air system is somewhat different from both the alumina–air and the aluminum–air systems due to the fact that glass is semitransparent to radiation. Thus, the comparisons with the predictions of the models were performed for the temperature range in which glass can be considered opaque ($\lambda > 5$ μm). Finally, it may be relevant to note that all the packed beds that were studied had approximately the same bulk porosity (0.38), and thus no attempt was made to examine the effect of porosity on the measured values of k_{eff}.

The Radiative Conductivity: Concept and Quantification. Due to the lack of knowledge of the radiative property data (extinction coefficient, absorption coefficient, single scattering albedo, etc.) needed for a more rigorous analysis of radiative transfer in a packed bed (Viskanta and Mengüc, 1989), radiative transfer in the bed is simplified using the diffusion approximation. The diffusion approximation reduces the integro-differential radiative transfer equation to a differential equation. In the case of optically thick media and regions far away from the boundaries, the radiative transfer can be treated as a diffusion process and the diffusion approximation is used to approximate the radiant heat flux (Vortmeyer and Kasparek, 1967; Kaviany, 1991; Kamiuto, 1991). Assuming negligible natural convection effects, energy may be transferred through the porous medium by conduction and radiation, and the one-dimensional steady-state heat diffusion equation becomes

$$\frac{dq}{dx} = \frac{d}{dx}\left(-k_{\text{cond}}\frac{dT}{dx} + q_r\right) = \frac{d}{dx}\left(-k_{\text{eff}}\frac{dT}{dx}\right) = 0 \qquad (3)$$

where $k_{\text{eff}}(T) = k_{\text{cond}}(T) + k_r(T)$. Many expressions for k_r have been formulated in the literature. In general, these formulations may be represented by a generic expression of the Damköhler type (Vortmeyer, 1978; Tien, 1988) for the radiative conductivity:

$$k_r = 4Ed_p\sigma T^3 \qquad (4)$$

The exchange factor E is a model-dependent parameter and is generally a function of the particle emissivity and possibly the particle shape and bed porosity. This formulation of the radiative conductivity was based on a temperature-independent emissivity. A summary of the exchange factor, E, based on the work of different investigators is presented in Table 4.

It was pointed out earlier that the predicted values for k_{eff} were found to be higher than the measured ones at low temperatures for all three systems, as shown in Figs. 4–6. In order to match the experimental data and quantify the contribution of radiation to heat transfer in the packed beds that were studied, an adjustment to the conductive contribution from the models was necessary. Various expressions from different models for the conductive component of k_{eff} were examined and found to differ greatly in their predictions (Nasr, 1993). The Zehner–Bauer–Schlünder model was chosen because it had been extensively compared to the available experimental data. Nevertheless, the discrepancies in the model predictions made the task of reliably calculating the conductive component very difficult. Tsotsas and Martin (1987), through their comparison of Zehner–Bauer–Schlünder model with experimental data, showed an interval of ±30 percent around the model predictions. Instead of adjusting the recommended values of the parameters in the Zehner–Bauer–Schlünder model, it was decided to leave them unaltered and to lower this model's conductive component by 20 percent

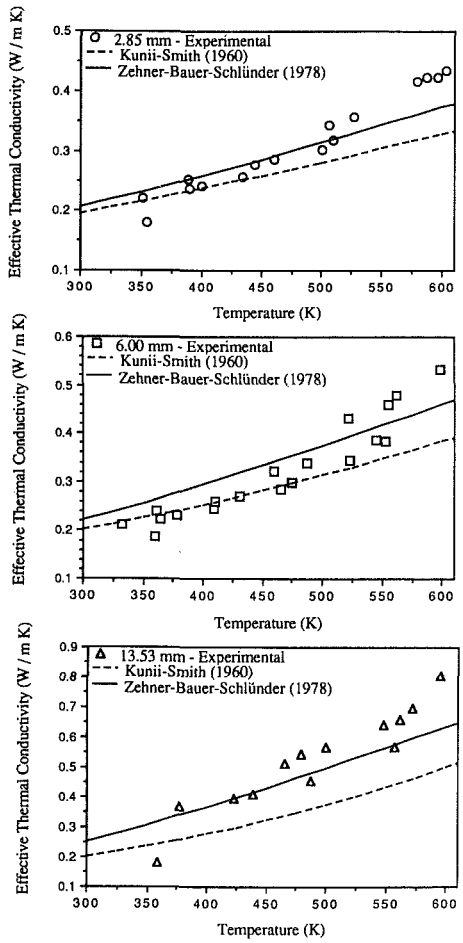

Fig. 6 Comparison of measurements with the predictions of Kunii–Smith and Zehner–Bauer–Schlünder models (glass–air packed bed)

Table 3 The Kunii–Smith and Zehner–Bauer–Schlünder models for the effective thermal conductivity

Kunii and Smith (1960)

$$\frac{k_{K\text{-}S}}{k_f} = \phi\left[1 + \frac{\beta\, h_{rv}\, d_p}{k_f}\right] + \beta(1-\phi) \Big/ \left[\frac{1}{\left(\frac{1}{\delta} + \frac{d_p\, h_{rs}}{k_f}\right)} + \frac{\gamma}{\kappa}\right]$$

$\gamma = 2/3$, and 0.9 (close packing) $< \beta < 1.0$ (loose packing)

$$\delta = \delta_2 + (\delta_1 - \delta_2)\frac{\phi - 0.26}{0.216}; \quad 0.26 < \phi < 0.476$$

$$\delta_1 = 0.352\left(\frac{\kappa - 1}{\kappa}\right)^2 \Big/ \{\ln[\kappa - 0.545(\kappa - 1)] - 0.455\left(\frac{\kappa - 1}{\kappa}\right)\} - \frac{2}{3\kappa}$$

$$\delta_2 = 0.072\left(\frac{\kappa - 1}{\kappa}\right)^2 \Big/ \{\ln[\kappa - 0.925(\kappa - 1)] - 0.075\left(\frac{\kappa - 1}{\kappa}\right)\} - \frac{2}{3\kappa}$$

$$h_{rv} = 4\sigma T^3 \Big/ \left[1 + \frac{\phi}{(1-\phi)}\frac{(1-\varepsilon)}{2\varepsilon}\right]$$

$$h_{rs} = 4\sigma T^3\left[\frac{\varepsilon}{2-\varepsilon}\right]$$

Zehner and Schlünder (1970); Bauer and Schlünder (1978)

$$\frac{k_{Z\text{-}B\text{-}S}}{k_f} = (1 - \sqrt{1-\phi})(1 + \phi\frac{k_r}{k_f}) + \sqrt{1-\phi}\left[\alpha\frac{k_s^*}{k_f} + (1-\alpha)\frac{k_{so}}{k_f}\right]$$

$$\frac{k_{so}}{k_f} = \frac{2}{N}\left[\frac{B\left(\frac{k_s^*}{k_f} + \frac{k_r}{k_f} - 1\right)\frac{k_f}{k_s^*}}{N^2}\ln\left(\left(\frac{k_s^*}{k_f} + \frac{k_r}{k_f}\right)/B\right) - \frac{B-1}{N} + \left(\frac{k_r}{k_f} - B\right)\frac{B+1}{2B}\right]$$

$$N = \left[1 + \left(\frac{k_r}{k_f} - B\right)\frac{k_f}{k_s^*}\right]$$

$$k_s^* = k_s\left(\frac{1}{1 + B_{iox}}\right); \quad B_{iox} = \left(\frac{S_{ox}}{k_{ox}}\right)\frac{k_s}{d_p}$$

$$k_r = 4\sigma\left(\frac{\varepsilon}{2-\varepsilon}\right)x_R T^3; \quad x_R = R_{form}\, d_p$$

$$B = C_{form}\left(\frac{1-\phi}{\phi}\right)^{\frac{10}{9}}$$

$$\alpha = \frac{23\,\rho_k^2}{1 + 22\,\rho_k^{4/3}}$$

C_{form} = particle shape factor, x_R = radiation effects factor

ρ_k^2 = contact conduction factor, and (S_{ox}/k_{ox}) = oxidation effects factor

for the whole temperature range. This approach was taken in order to obtain a better match between the predictions and the experimental data at low temperatures (350 K to 600 K). Therefore, the extracted values for the radiative conductivity are computed as the difference between the measured effective thermal conductivities, calculated from their least-squares fits, and 80 percent of the conductive component predicted by the Zehner–Bauer–Schlünder model. In Fig. 7, this difference, i.e., the radiative conductivity, is plotted against temperature for the range of temperatures studied and for all three particle diameters of the alumina–air particulate bed. As the temperature and the particle diameter increase, the radiative conductivity increases. At lower temperatures, the radiative conductivity practically vanishes.

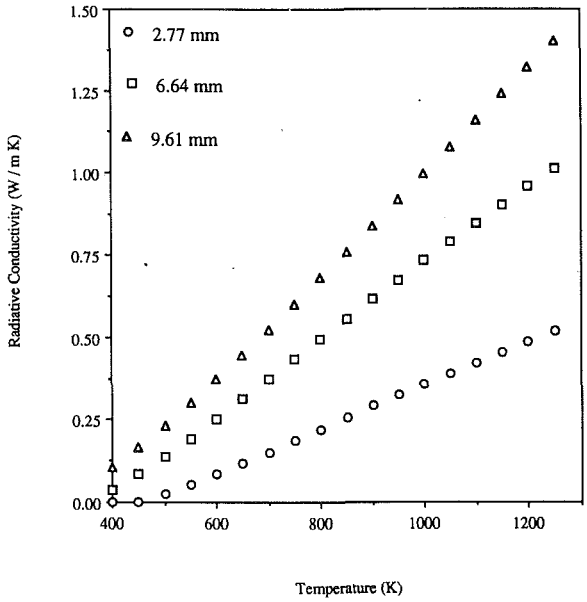

Fig. 7 Determined values for the radiative conductivity plotted against temperature for alumina–air packed beds

Figure 8 presents the ratio of the radiative conductivity to the conductive component vs. temperature. It illustrates practically the same points made in connection with those of Fig. 7 and points out their relative magnitudes. It may be more instructive, however, to express the relative contributions in terms of percentages as shown in Fig. 9. The relative contributions become equal to each other at different temperatures for different particle

Table 4 Various forma of the radiation exchange factor used in the Dämkohler type expression for the radiative conductivity

Investigator	Exchange Factor, E
Chen and Churchill (1963)	$\frac{2}{d_p(\kappa + 2\sigma)}$
Godbee and Ziegler (1966)	$\frac{\varepsilon\phi}{(1-\phi)}$
Kamiuto (1991)*	$\frac{(4/9)}{(1-\phi)[1 + 1.5(1-\phi) - 0.75(1-\phi)^2](1-\omega g)}$
Kasparek (1976)	$\frac{P + \varepsilon}{(1-P)}$
Kunii and Smith (1960)	$\frac{1}{\left(1 + \frac{\phi}{1-\phi}\frac{1-\varepsilon}{2\varepsilon}\right)}$
Laubitz (1959)	$\frac{\varepsilon[1 - (1-\phi)^{2/3} + (1-\phi)^{4/3}]}{(1-\phi)}$
Pavlyukevich (1990)	$\frac{8}{9}\frac{\phi^2}{(1-\phi)}$
Schotte (1960)	ε
Vortmeyer (1978)	$\frac{2P + \varepsilon(1-P)}{2(1-P) - \varepsilon(1-P)}$
Wakao and Kato (1969)	$\frac{2\varepsilon}{(2 - 0.264\varepsilon)}$
Zehner-Bauer-Schlünder (1970,1978)	$\frac{\varepsilon}{(2-\varepsilon)}$

* The single scattering albedo, ω, and the asymmetry factor, g, are given as functions of porosity and surface reflectivity in Kamiuto (1991).

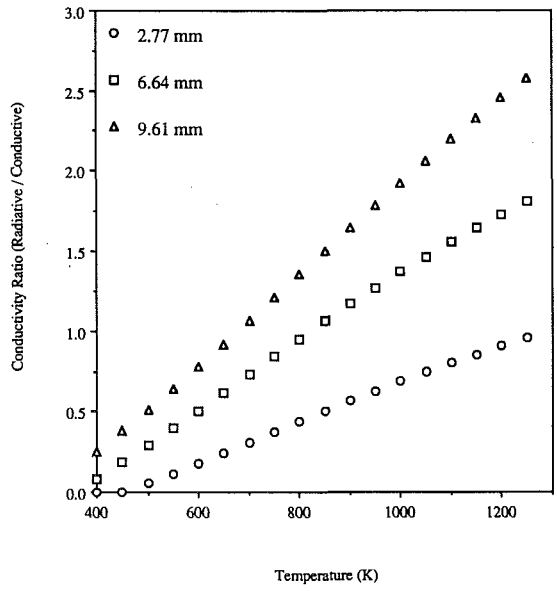

Fig. 8 Ratio of radiative to conductive thermal conductivities for alumina–air beds

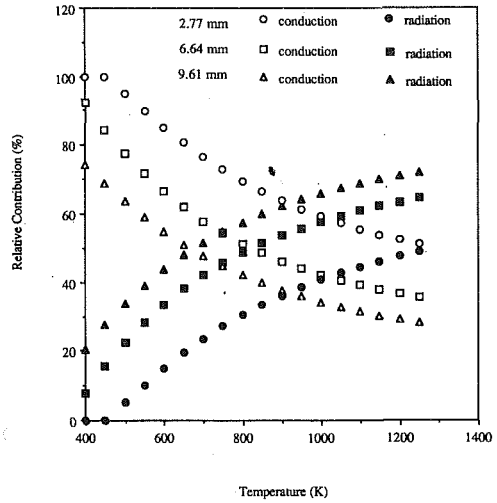

Fig. 9 Percent contributions of the radiation and conduction in alumina–air beds

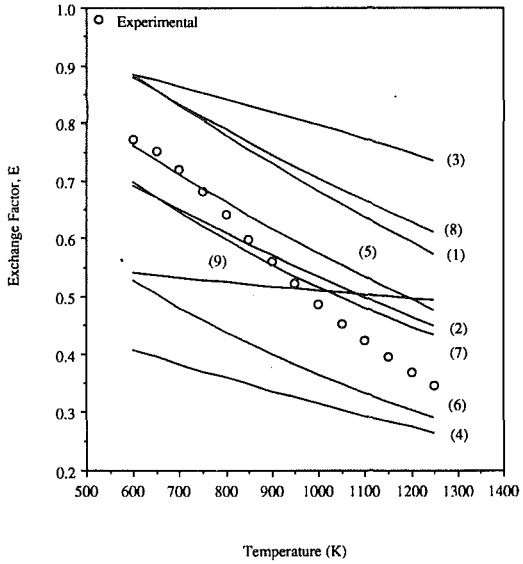

Fig. 10 Comparison of the exchange factor found experimentally with those of other investigators: (1) Laubitz, (2) Schotte, (3) Kunii–Smith, (4) Godbee–Ziegler, (5) Wakao–Kato, (6) Zehner–Bauer–Schlünder, (7) Vortmeyer, (8) Kasparek, and (9) Kamiuto

diameters. The temperature at which the conductive component is equal to the radiative component becomes smaller for larger particle diameters.

The Exchange Factor. Nondimensionalization of the determined radiative conductivity by the factor $(4d_p\sigma T^3)$ yields the exchange factor that may be compared to the models suggested in the literature and summarized in Table 4. Some of these expressions are formulated in terms of the surface emissivity of the solid alone, some in terms of the porosity alone, and some in terms of a combination of both. Figure 10 displays this comparison and shows the dependence of the exchange factor on temperature for an alumina bed of 6.64 mm particle diameter. The exchange factor was also found to be independent of particle diameter, i.e., the same for the 2.77 mm and the 9.61 mm size particles. All predictions follow the same pattern in decreasing with an increase of temperature as does the emissivity, except the recent work of Kamiuto (1991). It was found that the predictions based on the expressions by Schotte (1960), Wakao and Kato (1969), and Vortmeyer (1978) are the closest to the experimental values. Recall that Schotte (1960) simply used the emissivity for the exchange factor. The value of 0.1 was used for the transmission factor, P (see Table 4), as recommended by Vortmeyer (1978). It is important to note that the computed exchange factor based on the Vortmeyer expression is highly sensitive to the value used for the transmission factor. Had the value of 0.13 been used for P, the predictions from Vortmeyer's expression and that of Wako and Kato would become identical. Computations revealed that an increase in the value of P would cause an increase in the exchange factor based on Vortmeyer's expression. It was not possible to simply adjust the value of P to obtain a better match with the experimental data for the entire temperature range. Alternatively, the experimental values for the exchange factor may be least-squares fitted in terms of the emissivity or in terms of local temperature. However, such a fit would have no physical or fundamental justification and was therefore not carried out. Since the emissivity is reasonably close to the experimental data of the exchange factor, it was decided, for all practical purposes, to let the exchange factor be the emissivity of the solid material. The overall form for the effective thermal conductivity is then as follows:

$$k_{\text{eff}} = 0.8k_{\text{cond,Z-B-S}} + 4\epsilon d_p\sigma T^3 \qquad (5)$$

Such an approach is justifiable if Eq. (5), when employed in conjunction with Eq. (3), can reproduce the temperature profile inside the packed bed. For five different furnace setpoints, Fig. 11 displays discrete measured temperatures inside a packed bed made up of 6.64 mm alumina particles. The solid lines are the solution of the heat diffusion equation, employing Eq. (5) for the effective thermal conductivity. This figure shows good agreement between predictions and the measured temperatures for all furnace setpoints. Also (not shown here), the predictions of Eq. (5) were found to perform well for the other packed beds that were tested.

Conclusions

An experimental investigation of combined conduction and radiation in a randomly packed bed ($\phi \approx 0.38$) is reported. The

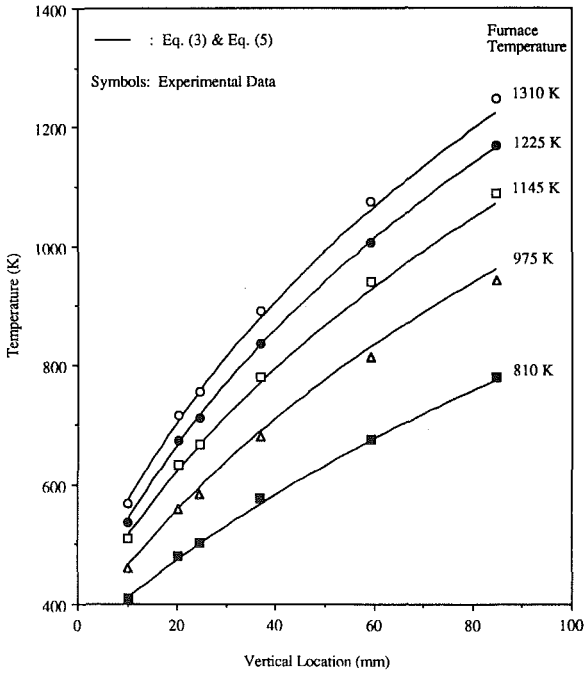

Fig. 11 Comparison of the measured temperatures inside an alumina–air packed bed with the predictions based on Eqs. (3) and (5)

local effective thermal conductivities of alumina–air, aluminum–air, and glass–air packed beds were determined and presented graphically as a function of the local bed temperature. The effects of particle diameter and local bed temperature were studied. The following conclusions can be drawn:

1 The effective thermal conductivity increases with an increase in the particle size and bed temperature.
2 Two models, the Kunii–Smith and the Zehner–Bauer–Schlünder models, were compared to the present experimental data and were found to overpredict the experimental values at low temperatures.
3 The radiative contribution was quantified and expressed in terms of the radiative conductivity using the diffusion approximation.
4 The radiative conductivity was cast as a function of particle diameter, local bed temperature, and an exchange factor made equal to the particle emissivity.
5 The exchange factor determined experimentally matches with good agreement those of Schotte (1960), Wakao and Kato (1969), and Vortmeyer (1978).
6 The diffusion approximation, with a modified expression of the effective thermal conductivity, reproduces the measured temperatures inside the packed bed.

Acknowledgments

This work was supported jointly by the Gas Research Institute, under Contract No. 5090-260-1927, and the Institute of Gas Technology's sustaining membership program.

References

American Society of Heating, Refrigerating, and Air-Conditioning Engineers, 1976, *ASHRAE Themophysical Properties of Refrigerants,* New York.

American Standard for Testing and Materials, Designation C201-86, 1992, "Standard Test Method for Thermal Conductivity of Refractories," *Annual Book of ASTM Standards,* Vol. 15.01, pp. 75–79.

Anderson, D. W., 1985, "Heat Transfer Through Coal Ash Deposits," Ph.D. Thesis, Purdue University, West Lafayette, IN.

Bauer, R., and Schlünder, E. U., 1978, "Effective Radial Thermal Conductivity of Packing in Gas Flow. Part II. Thermal Conductivity of the Packing Fraction Without Gas Flow," *International Chemical Engineering,* Vol. 18, No. 2, pp. 189–204.

Beveridge, G. S. G., and Haughey, D. P., 1971, "Axial Heat Transfer in Packed Beds. Stagnant Beds Between 20 and 750°C," *International Journal of Heat and Mass Transfer,* Vol. 14, pp. 1093–1113.

Botterill, J. S. M., Salway, A. G., and Teoman, Y., 1989, "The Effective Thermal Conductivity of High Temperature Particulate Beds—II. Model Predictions and the Implication of the Experimental Values," *International Journal of Heat and Mass Transfer,* Vol. 32, pp. 595–609.

Chen, J. C., and Churchill, S. W., 1963, "Radiant Heat Transfer in Packed Beds," *American Institute of Chemical Engineering Journal,* Vol. 39, pp. 35–41.

Churchill, S., 1986, "The Thermal Conductivity of Dispersions and Packed Beds—An Illustration of the Unexploited Potential of Limiting Solutions for Correlations," in: *Advances in Transport Processes,* Vol. IV, A. S. Mujumdar and R. A. Mashelkhar, eds., Wiley Eastern Ltd., New Delhi, pp. 394–418.

Godbee, H. W., and Ziegler, T. W., 1966, "Thermal Conductivities of MgO, Al_2O_3, and ZrO_2 Powders to 850°C. II. Theoretical," *Journal of Applied Physics,* Vol. 37, No. 1, pp. 56–65.

Hust, J. G., 1985, "Thermal Conductivity of Al, Cu, Fe, and W," *CODATA Bulletin,* Chap. 5, pp. 29–45.

Kamiuto, K., Nagumo, N., and Iwamoto, M., 1989, "Mean Effective Thermal Conductivities of Packed-Sphere Systems," *Applied Energy,* Vol. 32, No. 3, pp. 213–221.

Kamiuto, K., 1990, "Examination of Bruggeman's Theory of Effective Thermal Conductivities of Packed Beds," *Journal of Nuclear Science and Technology,* Vol. 27, No. 5, pp. 473–476.

Kamiuto, K., 1991, "Analytical Expression for Total Effective Thermal Conductivities of Packed Beds," *Journal of Nuclear Science and Technology,* Vol. 28, pp. 1153–1156.

Kasparek, G., 1976, "Warmestrahlung in Schuttungen Experiment und Theorie," Dissertation [in German], Technische Universität Munchen, Federal Republic of Germany.

Kaviany, M., 1991, *Principles of Heat Transfer in Porous Media,* Springer-Verlag, New York.

Kunii, D., and Smith, J., 1960, "Heat Transfer Characteristics of Porous Rocks," *American Institute of Chemical Engineering Journal,* Vol. 6, pp. 71–78.

Laubitz, M. J., 1959, "Thermal Conductivity of Powders," *Canadian Journal of Physics,* Vol. 37, pp. 798–809.

Mann, D., Field, R. E., and Viskanta, R., 1992, "Determination of Specific Heat and True Thermal Conductivity of Glass From Dynamic Temperature Data," *Wärme und Stoffübertragung,* Vol. 27, pp. 225–231.

Moffat, R. J., 1988, "Describing Uncertainties in Experimental Results," *Experimental Thermal and Fluid Science,* Vol. 1, pp. 3–17.

Nasr, K. J., 1993, "Experimental and Numerical Studies of Forced Convection and Radiation Heat Transfer in Packed Beds," Ph.D. Thesis, Purdue University, West Lafayette, IN.

Pavlyukevich, N. V., 1990, "Radiation Slip in a Highly Porous Material Layer," *Journal of Engineering Physics,* Vol. 59, No. 4, pp. 1284–1286.

Schotte, W., 1960, "Thermal Conductivity of Packed Beds," *American Institute of Chemical Engineering Journal,* Vol. 6, pp. 63–67.

Tien, C. L., 1988, "Thermal Radiation in Packed and Fluidized Beds," ASME JOURNAL OF HEAT TRANSFER, Vol. 110, pp. 1230–1242.

Touloukian, Y. S., Powell, R. W., Ho, C. Y., and Klemens, P. G., 1970, *Thermal Conductivity—Nonmetallic Solids,* Vol. 2, IFI/Plenum, New York.

Touloukian, Y. S., and DeWitt, D. P., 1972, *Thermal Radiative Properties of Nonmetallic Solids,* Vol. 8, IFI/Plenum, New York.

Tsotsas, E., and Martin, H., 1987, "Thermal Conductivity in Packed Beds: A Review," *Chemical Engineering Process,* Vol. 22, pp. 19–38.

Viskanta, R., and Mengüc, M., 1989, "Radiative Transfer in Dispersed Media," *Applied Mechanics Reviews,* Vol. 42, No. 9, pp. 241–259.

Vortmeyer, D., and Kasparek, G., 1967, "Radiative Heat Transfer in Packed Beds," *JSME Semi-international Symposium,* Tokyo, pp. 27–32.

Vortmeyer, D., 1978, "Radiation in Packed Solids," in: *Heat Transfer,* Hemisphere, Washington, DC, Vol. 6, pp. 525–539.

Wakao, N., and Kato, K., 1969, "Effective Thermal Conductivity of Packed Beds," *Journal of Chemical Engineering of Japan,* Vol. 2, pp. 24–33.

Wakao, N., and Kaguei, S., 1982, *Heat and Mass Transfer in Packed Beds,* Gordon & Breach, New York.

Zehner, P., and Schlünder, E. U., 1970, "Thermal Conductivity of Granular Materials at Moderate Temperatures," *Chemie Ingenieur Technik,* Vol. 42, pp. 933–941 [in German].

Approximate Analytical Solution of Forced Convection Heat Transfer From Isothermal Spheres for All Prandtl Numbers

G. Refai Ahmed
Graduate Research Assistant.
Mem. ASME

M. M. Yovanovich
Professor and Director.
Fellow ASME

Microelectronics Heat Transfer Laboratory,
Department of Mechanical Engineering,
University of Waterloo,
Waterloo, Ontario, Canada N2L 3G1

A new, simple and approximate analytical method based on linearization of the energy equation is proposed to develop solutions for forced convection heat transfer from isothermal spheres. Furthermore, heat transfer correlations from spheres are proposed in the range of Reynolds number, $0 \leq Re_D \leq 2 \times 10^4$, and all Prandtl numbers. This technique is performed as follows. The first step is to approximate the energy equation to the form of a transient heat conduction equation that has an existing solution. The second step is to evaluate the effective velocity through scaling analysis in the limit of $Pr \to \infty$ and $Pr \to 0$ and then resubstitute the effective velocity into the solution of the energy equation. Finally, a "blending method" is used to provide a general model for all Prandtl numbers. Comparison of the heat transfer correlations for Nu_D versus Re_D from the present study with the available correlations in the literature reveals very good agreement.

1 Introduction

Forced convection heat transfer from isothermal or isoflux external convex surfaces is an important problem for engineers. There are many engineering systems that are modeled using forced convection, such as electronic components on printed circuit boards placed in cabinets, hot-wire anemometers, and heat exchanger design. Steady laminar forced convection heat transfer from an isothermal sphere into a substantial amount of air or water has been investigated experimentally, theoretically, and numerically by many researchers for over 90 years. These researchers presented their area-averaged heat transfer results in the following general form:

$$\mathrm{Nu}_D = C_1 + C_D\,\mathrm{Re}_D^m\,\mathrm{Pr}^b \tag{1}$$

where C_1, C_D, m, and b are constants. The diffusive term, C_1, has been reported to lie in the range 1 to 3.2. Other investigators have reported values of zero or $1.2\,\mathrm{Pr}^{0.3}$ (Vliet and Leppert, 1961; Lochiel and Calderbank, 1964). The constant C_D depends on the range of Re_D. From the literature, it is seen that for $0.1 \leq \mathrm{Re}_D \leq 2 \times 10^5$, C_D is reported between 0.921 and 0.175, respectively. The exponents of Re_D and Pr varied from 0.47 to 0.62, and 0 to 0.42, respectively. The previous correlations, $\mathrm{Nu}_D = \mathrm{Nu}_D(\mathrm{Re}_D, \mathrm{Pr})$, are summarized in Table 1.

Most of the previous investigators agreed on the following:

1 In the diffusive limit, $\mathrm{Re}_D \to 0$, Nu_D is 2.0.
2 Exponent of Pr, b, is $\frac{1}{3}$.

However, the previous investigators disagreed on the value of C_D and the exponent of Reynolds number. On the other hand, Churchill (1977) proposed another function for Pr, $\mathrm{Pr}^{1/3}/[1 + (0.45/\mathrm{Pr})^{2/3}]^{1/4}$, instead of $\mathrm{Pr}^{1/3}$, which provides two limits: as $\mathrm{Pr} \to \infty$, $F(\mathrm{Pr}) \to \mathrm{Pr}^{1/3}$ and as $\mathrm{Pr} \to 0$, $F(\mathrm{Pr}) \to \mathrm{Pr}^{1/2}$. From the theoretical view, it has been proven by Lochiel and Calderbank (1964) using an analytical approach that $\mathrm{Sh} = \mathrm{Sh}(\mathrm{Re}^{1/2}\mathrm{Sc}^{1/3})$ for $\mathrm{Re} \gg 1$. Therefore, the analytical solution agrees with the experimental results, as seen in Table 1, for $\mathrm{Pr} \geq 1$. In addition, as $\mathrm{Pr} \to 0$, Sideman (1966) and Hsu (1963) (see Witte, 1968) have demonstrated through their analytical solutions that $F(\mathrm{Pr}) \to \mathrm{Pr}^{1/2}$. This also agrees with the experimental heat transfer correlations of Witte (1968) and Churchill (1977).

One of the objectives of this study is to develop a simple approximate analytical method based on linearization of the energy equation in order to develop an approximate analytical solution of the forced convection heat transfer from isothermal spheres. Another objective of the present study is to propose heat transfer correlations from spheres for the range of Reynolds number, $0 \leq \mathrm{Re}_D \leq 2 \times 10^4$, and all Prandtl numbers. One of the main goals of the present investigation is to explain why the previous studies appear to be in disagreement in regard to the exponent of Re_D and the constant C_D.

This paper is organized as follows: In the following section, the theoretical analysis is developed with appropriate assumptions; in the third section, results and discussions are presented; and conclusions are given in Section 4.

2 Theoretical Analysis

Figure 1 shows an isothermal sphere of temperature T_S and diameter D, which is immersed in a steady, laminar, incompressible flow of a constant property fluid ($0 < \mathrm{Pr} < \infty$) at constant temperature T_∞ and uniform velocity V_∞. The energy equation inside the boundary layer is

$$v_r \frac{\partial T}{\partial r} + \frac{v_\theta}{r}\frac{\partial T}{\partial \theta} = \alpha\left[\frac{1}{r^2}\frac{\partial}{\partial r}\left(r^2\frac{\partial T}{\partial r}\right)\right] \tag{2}$$

The terms on the left side of Eq. (2) will be approximated by a single equivalent term, i.e., $(\bar{v}_e/r)(\partial T/\partial\theta)$, where $\bar{v}_e$ is the average effective velocity, which will be determined later. This idea has been proposed by Oseen in order to linearize the inertia term for creeping flow, where Oseen assumed the convective term to be $V_\infty \nabla \cdot \mathbf{v}$, (for more details see Happel and Brenner, 1973). In addition, the effective velocity has been introduced by Yovanovich et al. (1992) and Jafarpur (1992); therefore, Eq. (2) becomes

$$\frac{\bar{v}_e}{r}\frac{\partial T}{\partial \theta} = \alpha\left[\frac{1}{r^2}\frac{\partial}{\partial r}\left(r^2\frac{\partial T}{\partial r}\right)\right] \tag{3}$$

This equation is limited to the range $r \geq D/2$ and $0 \leq \theta \leq \pi$. Equation (3) will be transformed to transient heat conduction in

Contributed by the Heat Transfer Division for publication in the JOURNAL OF HEAT TRANSFER. Manuscript received by the Heat Transfer Division April 1993; revision received November 1993. Keywords: Forced Convection, Modeling and Scaling. Associate Technical Editor: Y. Bayazitoglu.

order to find a suitable solution. Let us assume that the flow particles are moving with a constant velocity, $\bar{v}_e$, around the body. Therefore, the particles will take time, Δt, to travel a distant $r\Delta\theta$. Furthermore, for $\Delta\theta \to 0$ and $\Delta t \to 0$, one can obtain

$$\bar{v}_e = r\frac{\partial\theta}{\partial t} \quad \text{where} \quad D/2 \le r \le \delta + D/2 \tag{4}$$

This concept was also used by Sideman (1966) and Yovanovich et al. (1992). Therefore, the energy equation will also be reduced to the form of the transient heat conduction equation. Thus, by substituting Eq. (4) into Eq. (3) the energy equation can be written as follows:

$$\frac{\partial T^*}{\partial t} = \alpha\left[\frac{1}{r^2}\frac{\partial}{\partial r}\left(r^2\frac{\partial T^*}{\partial r}\right)\right] \tag{5}$$

where $r \ge D/2$, $0 \le t \le \pi D/2\bar{v}_e$, and

$$T^* = (T - T_\infty)/(T_S - T_\infty).$$

The solution of Eq. (5) from Carslaw and Jaeger (1959) is

$$T^* = \frac{D}{2}\frac{1}{r}\,\text{erfc}\left(\frac{r - D/2}{2\sqrt{\alpha t}}\right)\Bigg|_{t=(\theta D)/(2\bar{v}_e)}$$

$$= \frac{D}{2}\frac{1}{r}\,\text{erfc}\left(\frac{r - D/2}{2\sqrt{(\alpha\theta D)/(2\bar{v}_e)}}\right) \tag{6}$$

The local Nusselt number

$$\text{Nu}_D(\theta) = \frac{q_S(\theta)D}{(T_S - T_\infty)k} \tag{7}$$

where $q_S(\theta) = -k(T_S - T_\infty)(\partial T^*/\partial r)|_{r=D/2}$.

Taking the derivative of Eq. (6) and substituting it into Eq. (7) gives

$$\text{Nu}_D(\theta) = 2 + \frac{1}{\sqrt{\pi}}\frac{\sqrt{D}}{\sqrt{(\alpha\theta)/(2\bar{v}_e)}} \quad \theta > 0 \tag{8}$$

The transient conduction solution provides an analytic solution for the local Nusselt number, which consists of the linear sum of the local boundary layer term and the constant term corresponding to the diffusive limit ($\text{Re}_D \to 0$). The area-averaged Nusselt number, $\text{Nu}_D = 1/A\int\int_A \text{Nu}_D(\theta)dA$, is given by

Table 1 Correlation coefficients and parameters for heat and mass transfer from spheres

Author	C_1	C_D	m	b	$Pr(Sc)$	Re_D
Frössling (1938)†	2.0	0.55	1/2	1/3	0.6 - 2.7	2 - 1,000
Kramers (1946)	3.2	0.59	1/2	1/3	0.71	540 - 1,460
Kudryashev (1949)†	2.0	0.33	1/2	0.0	0.71	
Drake-Backer (1952)	2.0	0.459	0.55	0.333	0.71	0.1 - 200,000
Radusich (1956)†	2.83	0.6	1/2	1/3	0.71	
Griffth (1960)	2.0	0.6	1/2	1/3	0.7	
Yuge (1960)	2	0.551	1/2	1/3	0.715	10 - 1,800
	2	0.335	0.5664	1/3	0.715	1,800 - 150,000
Pasternak-Gauvin (1960)	0.0	0.692	0.514	1/3	0.71	500 - 5,000
Vliet-Leppert (1961)	$1.2Pr^{0.2}$	0.53	0.54	0.3	2-380	1 -300,000
Hsu (1964)*	0.0	0.921	0.5	0.5	$Pr \to 0$	
Rowe et al. (1965)	2	0.69	1/2	1/3	0.73	65 - 1,750
Lochiel-Calderbank (1964)	0.0	0.7	1/2	1/3		>> 1
Sideman (1966)	0.0	1.13	0.5	0.5	$Pr \to 0$	
Hughmark (1967)	2.0	0.6	1/2	1/3	< 250	26 - 450
	2.0	0.5	1/2	1/3	> 250	1 - 17
	2.0	0.4	1/2	1/3	> 250	17 - 450
	2.0	0.27	0.62	1/3	< 250	450-10,000
	2.0	0.175	0.62	0.42	> 250	450-10,000
Witte (1968)	2.0	0.386	0.5	0.5	Sodium	35,000 - 153,000
Raithby-Eckert (1968)	2.0	0.235	0.606	1/3	0.71	3,600 - 52,000
Churchill (1977)	2.0	0.5505	1/2	$F(Pr)$‡		
Clift et al. (1978)	1.0	0.757	0.47	1/3	0.7 - 0.73	100 - 4,000
	1.0	0.304	0.58	1/3	0.7 - 0.73	4,000 - 100,000
	1.0	0.724	0.48	1/3	$Pr > 188$	100 - 200
	1.0	0.425	0.55	1/3	$Sc > 1,100$	2,000 - 100,000
Yovanovich (1988)**	2.0	0.15	0.5	1/3	0.71	10 - 150,000

† From Yovanovich (1988)
* From Witte (1968)
‡ $\frac{Pr^{1/3}}{[1+(0.45/Pr)^{2/3}]^{1/4}}$
** $2.0 + (0.15\,Re_D^{0.5} + 0.273\,Re_D^{0.568})\,Pr^{1/3}$

$$\text{Nu}_D = 2 + 0.714\sqrt{\frac{D\bar{v}_e}{\alpha}} \tag{9}$$

The average effective velocity, $\bar{v}_e$, will be defined for the limiting cases of Pr $\gg$ 1 and Pr $\ll$ 1, then an interpolation function will be obtained to provide a relationship for all Prandtl numbers.

The present analysis has been based on the assumption that the flow does not separate at any point on the surface of the sphere. In fact, flow separation occurs in this type of problem at high Reynolds numbers. However, we will proceed with our analysis and compare it with the available experimental results which already have the separation effect in order to determine the capabilities of the present model.

2.1 $\bar{v}_e^\infty$ at Pr $\to \infty$. We will consider the high Prandtl number fluids first. Scaling analysis will be applied to the continuity,

Nomenclature

A = surface area, m^2
b = exponent in Eq. (1)
C_1, C_D = constants in Eq. (1)
D = sphere diameter, m
D_{AB} = binary mass diffusion coefficient, m^2/s
h = coefficient of convection heat transfer, W/m^{2}K
h_m = coefficient of convection mass transfer, m/s
k = thermal conductivity, W/m K
m = exponent in Eq. (1)
n = exponent in Eqs. (33)–(38)
Nu_D = area-averaged Nusselt number $= Dh/k$
Pr = Prandtl number $= \nu/\alpha$
Q = total heat flow rate, W
q = heat flux, W/m^2
Re_D = Reynolds number $= DV_\infty/\nu$
$\text{Re}_D(\theta)$ = local Reynolds number $= DV(\theta)/\nu$
T = temperature, K
T^* = nondimensional temperature $= (T - T_\infty)/(T_S - T_\infty)$
t = time, s
Sc = Schmidt number $= \nu/D_{AB}$
Sh_D = Sherwood number $= h_m D/D_{AB}$
V = local velocity at edge of thermal boundary layer, m/s
$V(\theta)$ = local velocity at edge of hydrodynamic boundary layer, m/s
V_∞ = free-stream velocity, m/s
$\bar{v}_e$ = area-averaged effective velocity, m/s
$v_e(\theta)$ = local effective velocity, m/s
α = thermal diffusivity $= k/C_p\rho$, m^2/s
γ = constant in Eq. (26)
δ = local thickness of HBL, m
δ_T = local thickness of TBL, m
δ_D^T = displacement thickness of TBL, m
δ_M^T = momentum thickness of TBL, m
η = nondimensional quantity $= y/\delta$
ν = kinematic viscosity, m^2/s
ρ = density, kg/m^3

Subscripts

D = displacement
e = effective
M = momentum
S = surface

Abbreviations

CE = continuity equation
EE = energy equation
GEs = governing equations
HBL = hydrodynamic boundary layer
ME = momentum equation
TBL = thermal boundary layer

Coordinates

r, θ, ϕ = spherical coordinates
x, y = local coordinates
X, Y, Z = Cartesian coordinates

momentum, and energy equations to determine the area-averaged effective velocity. Consider that the hydrodynamic boundary layer, HBL, δ, is very thin, i.e., $D/2 + \delta \simeq D/2$ (see Fig. 1) where $\mathrm{Re}_D \gg 1$ and also consider that the flow outside of the hydrodynamic boundary layer, HBL, is effectively inviscid. Thus, the local velocity at the edge of the HBL is equal to $v_\theta(D/2 + \delta) = V(\theta)$, where $V(\theta)$ is the solution to the inviscid flow problem, as shown in Fig. 1. The continuity equation inside the HBL is

$$\frac{2}{r}v_r + \frac{\partial v_r}{\partial r} + \frac{1}{r}\frac{\partial v_\theta}{\partial \theta} + \frac{\cot\theta}{r}v_\theta = 0 \tag{10}$$

Using scaling analysis (the scaling analysis rules are stated by Bejan, 1985) on the continuity equation within the HBL gives the relationship:

$$\frac{4v_r|_{D/2}}{D} + \frac{v_r|_{\delta+D/2} - v_r|_{D/2}}{\delta} + \frac{2}{D}\frac{v_\theta}{\theta} + \frac{2}{D}\frac{v_\theta}{\theta} \sim 0$$

with $v_\theta|_{\delta+D/2} = V(\theta)$, the inviscid flow solution and $v_r|_{D/2} = 0$, we obtain

$$v_r|_{\delta+D/2} \sim 2\frac{\delta}{D}\cdot\frac{V(\theta)}{\theta} \tag{11}$$

Applying scaling analysis on the continuity equation inside the thermal boundary layer, TBL, gives the relationship

$$v_r|_{\delta_T+D/2} \sim 2\frac{\delta_T^2}{D\delta}\cdot\frac{V(\theta)}{\theta} \tag{12}$$

where it is assumed that the ratio $V/V(\theta)$ is approximately equal to δ_T/δ, i.e., the flow has a linear velocity distribution as shown in Fig. 1.

The momentum equation in an axisymmetric flow along the body using the boundary layer theory has been discussed by White (1991). This equation can be converted to spherical coordinates (note that $x = r\theta$, i.e., $\partial x \simeq r\partial\theta$, and $y = r - D/2$, i.e., $\partial y = \partial r$), in steady-state form as follows:

$$v_r\frac{\partial v_\theta}{\partial r} + \frac{v_\theta}{r}\frac{\partial v_\theta}{\partial \theta} \simeq \frac{V(\theta)}{r}\frac{\partial V(\theta)}{\partial\theta} + \nu\frac{\partial^2 v_\theta}{\partial r^2} \tag{13}$$

Using scaling analysis on the momentum equation inside the HBL with Eq. (11) gives the following relationship:

$$\frac{2\delta V^2(\theta)}{D\delta\theta} + \frac{2V^2(\theta)}{D\theta} \simeq \frac{2V^2(\theta)}{D\theta} + \nu\frac{V(\theta)}{\delta^2} \tag{14}$$

Therefore, the local hydrodynamic boundary layer thickness is given by

$$\frac{\delta}{D} \sim \sqrt{\frac{\theta}{2\,\mathrm{Re}_D(\theta)}} \tag{15}$$

where $\mathrm{Re}_D(\theta) = DV(\theta)/\nu$. Applying scaling analysis on the energy equation, Eq. (2), and keeping in mind that $D/2 \gg \delta_T$ and $v_\theta|_{\delta_T} = V = [(\delta T/\delta)\cdot V(\theta)]$ we find that

$$\frac{2\delta_T^2}{D\delta}\cdot\frac{V(\theta)}{\theta}\cdot\frac{\Delta T}{\delta_T} + \frac{\delta_T V(\theta)\Delta T}{\delta\theta D/2} \sim \frac{\alpha\Delta T}{\delta_T^2} \tag{16}$$

The two convective terms on the left-hand side of Eq. (16) have the same magnitude, therefore we equate one of the convective terms to the diffusion term as follows:

$$\frac{\delta_T V(\theta)\Delta T}{\delta\theta D/2} \sim \frac{\alpha\Delta T}{\delta_T^2} \tag{17}$$

Therefore, the local dimensionless thermal boundary layer thickness is given by

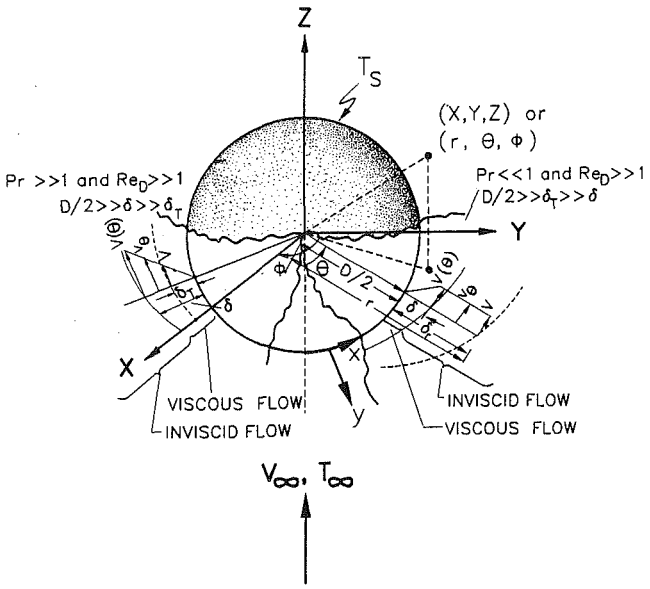

Fig. 1 Schematic diagram of the boundary layers over the sphere for $\mathrm{Pr} \to \infty$ and $\mathrm{Pr} \to 0$

$$\frac{\delta_T}{D} \sim \mathrm{Pr}^{-1/3}\sqrt{\frac{\theta}{2\,\mathrm{Re}_D(\theta)}} \tag{18}$$

Comparing Eq. (18) against Eq. (15) we find that

$$\frac{\delta_T}{\delta} \sim \frac{V}{V(\theta)} \sim \frac{1}{\mathrm{Pr}^{1/3}} \tag{19}$$

This result will be used later to define $\overline{v}_e^\infty$.

The local effective velocity, $v_e^\infty(\theta)$, for large Prandtl numbers fluids will be obtained from momentum flux balances through the thermal boundary layer. The momentum flux inside the thermal boundary layer is

$$\frac{\rho}{\delta_T}\int_0^{\delta_T} v_\theta(V - v_\theta)dy \tag{20}$$

On the other hand, if we determine the momentum flux by assuming that the flow has a uniform local effective velocity, $v_e^\infty(\theta)$ is constant in the y direction and variable in the x direction, we have

$$\frac{\rho}{\delta_T}\int_0^{\delta_T} v_e^\infty(\theta)(V - v_\theta)dy \tag{21}$$

Equating Eqs. (20) and (21) and solving for the local effective velocity, we obtain

$$v_e^\infty(\theta) = V\frac{\displaystyle\int_0^{\delta_T}\frac{v_\theta}{V}(V - v_\theta)dy}{\displaystyle\int_0^{\delta_T}(V - v_\theta)dy} \tag{22}$$

which can be expressed in terms of the momentum and displacement thicknesses as follows:

$$v_e^\infty(\theta) \sim V(\theta)\cdot\frac{\delta_T}{\delta}\cdot\frac{\delta_M^T}{\delta_D^T} \sim V(\theta)\cdot\frac{1}{\mathrm{Pr}^{1/3}}\cdot\frac{\delta_M^T}{\delta_D^T} \tag{23}$$

For convenience of the subsequent analysis, we introduce the similarity parameter, $\eta = y/\delta_T$. This allows one to express the momentum and displacement thicknesses in the following forms:

$$\delta_M^T = \delta_T \int_0^1 \frac{v_\theta}{V}\left(1 - \frac{v_\theta}{V}\right) d\eta \tag{24}$$

$$\delta_D^T = \delta_T \int_0^1 \left(1 - \frac{v_\theta}{V}\right) d\eta \tag{25}$$

Clearly these important hydrodynamic thicknesses depend on the velocity distribution within the TBL. We may assume that v_θ is a power-law function of y in order to have a general form for the velocity profiles at different Reynolds numbers, i.e., $v_\theta/V = (y/\delta_T)^\gamma$ or $v_\theta/V = \eta^\gamma$ where $0 \le \gamma \le 1$. This form is chosen for the following reasons: It has been proposed by Kays and Crawford (1980) for the flat plate at high Re where $\gamma = \frac{1}{7}$ and it also agrees with the analytical solution where the velocity is linear at $\gamma = 1$. We introduce the power-law velocity distribution into Eq. (24) and Eq. (25) and integrate. One can obtain the relationship between the momentum and displacement thicknesses in terms of the power-law exponent:

$$\frac{\delta_M^T}{\delta_D^T} = \frac{1}{2\gamma + 1} \tag{26}$$

Therefore, the local effective velocity from Eq. (23) with Eq. (26) is

$$v_e^\infty(\theta) \sim \frac{V(\theta)}{(2\gamma + 1)\,\mathrm{Pr}^{1/3}} \tag{27}$$

The area-averaged effective velocity is defined as

$$\overline{v}_e^\infty \sim \frac{1}{(2\gamma + 1)\,\mathrm{Pr}^{1/3}} \cdot \frac{1}{A} \iint_A V(\theta) dA \tag{28}$$

Furthermore, the ideal flow solution can be used to represent the flow in the region outside of the boundary layer; therefore,

$$v_\theta|_{\delta + D/2} = V(\theta) = 1.5 V_\infty \sin\theta \tag{29}$$

After substitution of Eq. (29) into Eq. (28) we find that the area-averaged effective velocity as $\mathrm{Pr} \to \infty$ is given by

$$\overline{v}_e^\infty \sim \frac{1.178 V_\infty}{(2\gamma + 1)\,\mathrm{Pr}^{1/3}} \tag{30}$$

2.2 $\overline{v}_e^0$ at Pr → 0. Let us consider that the flow is inviscid, i.e., $\mathrm{Pr} \ll 1$, and $\mathrm{Re}_D \gg 1$. Therefore the HBL, δ, is very small; however, the TBL, δ_T, is very large relative to δ. Therefore at the edge of the TBL we have

$$v_\theta|_{(\delta + D/2)} = \frac{V_\infty}{2} \cdot \left[2 + \left(\frac{D}{2(\delta + D/2)}\right)^3\right] \sin\theta \tag{31}$$

However, Fig. 1 shows that $\delta \ll D/2$. So, $v_\theta|_{(\delta + D/2)} = V = 1.5 V_\infty \sin\theta$.

Therefore, the local velocity at arbitrary θ will be considered uniform across the TBL. As a result of that $v_e^0(\theta) = V$ as shown in Fig. 1 (V is the local maximum velocity at the edge of the TBL and $v_e^0(\theta)$ is the local effective velocity at $\mathrm{Pr} \ll 1$). The area-mean effective velocity is

$$\overline{v}_e^0 = \frac{1}{A} \iint_A V dA = 1.178 V_\infty \tag{32}$$

2.3 $\overline{v}_e$ for all Pr. At this point the effective velocity has been found for the two limiting cases where $\mathrm{Pr} \gg 1$ and $\mathrm{Pr} \ll 1$. In order to develop an expression for $\overline{v}_e$ valid for any Prandtl number, the Churchill and Usagi (1972) blending technique will be used. The effective velocity can be determined in different ways such as:

$$(\overline{v}_e)^n = (\overline{v}_e^0)^n + (\overline{v}_e^\infty)^n \quad n \ge 1 \tag{33}$$

or

$$\overline{v}_e = \sqrt{\overline{v}_e^0 \cdot \overline{v}_e^\infty} \tag{34}$$

or

$$\frac{1}{(\overline{v}_e)^n} = \frac{1}{(\overline{v}_e^0)^n} + \frac{1}{(\overline{v}_e^\infty)^n} \quad n \ge 1 \tag{35}$$

The first two forms are not applicable at $\mathrm{Pr} \ll 1$ because $\overline{v}_e \to \infty$. However, the last form is consistent at both limits; at $\mathrm{Pr} \ll 1$, $\overline{v}_e \to \overline{v}_e^0$ and at $\mathrm{Pr} \gg 1$, $\overline{v}_e \to \overline{v}_e^\infty$. The area-averaged effective velocity can now be expressed in the following form:

$$\overline{v}_e = \frac{\overline{v}_e^\infty}{\left[1 + \left(\frac{\overline{v}_e^\infty}{\overline{v}_e^0}\right)^n\right]^{1/n}} \tag{36}$$

Substituting $\overline{v}_e^0$ and $\overline{v}_e^\infty$ into Eq. (36) gives the effective velocity valid for all Prandtl numbers in terms of the power-law parameter γ and the blending parameter n,

$$\frac{\overline{v}_e}{V_\infty} = \frac{1.178/[(2\gamma + 1)\,\mathrm{Pr}^{1/3}]}{(1 + [1/(2\gamma + 1)\,\mathrm{Pr}^{1/3}]^n)^{1/n}} \quad 0 < \mathrm{Pr} < \infty \tag{37}$$

where $0 \le \gamma \le 1$. The constant n will be determined in the following section.

3 Results and Discussion

In order to determine the equation of Nu_D, one must substitute Eq. (37) into Eq. (9). The area-averaged Nusselt number, Nu_D, becomes

$$\mathrm{Nu}_D = 2 + \frac{0.775}{\sqrt{2\gamma + 1}} \mathrm{Re}_D^{1/2} \frac{\mathrm{Pr}^{1/3}}{\left[1 + \left(\frac{1.0}{(2\gamma + 1)^3\,\mathrm{Pr}}\right)^{n/3}\right]^{1/(2n)}} \tag{38}$$

By examining the two asymptotic values of the area-averaged Nusselt number for $\mathrm{Pr} \ll 1$ and $\mathrm{Pr} \gg 1$, from Eq. (38), we obtain

$$\text{for } \mathrm{Pr} \ll 1, \quad \mathrm{Nu}_D = 2 + 0.775\,\mathrm{Re}_D^{1/2}\,\mathrm{Pr}^{1/2} \tag{39}$$

and

$$\text{for } \mathrm{Pr} \gg 1, \quad \mathrm{Nu}_D = 2 + \frac{0.775}{\sqrt{2\gamma + 1}} \mathrm{Re}_D^{1/2}\,\mathrm{Pr}^{1/3} \tag{40}$$

independent of the value of the blending parameter n. The constant C_D as defined in Eq. (1) is $0.775/\sqrt{2\gamma + 1}$ in Eq. (38). It is equal to 0.447 at $\gamma = 1.0$, 0.633 at $\gamma = \frac{1}{4}$, and 0.683 at $\gamma = \frac{1}{7}$. In addition, it has been found that $n = 3$ gives the best fit by matching Eq. (38) with the available air data correlation equations in the literature (Yuge, 1960; Churchill, 1977; Yovanovich, 1988). Therefore, Eq. (38) can be written in the following forms for $\gamma = 1$ and $\frac{1}{7}$, respectively:

$$\mathrm{Nu}_D = 2 + 0.447\,\mathrm{Re}_D^{1/2} \frac{\mathrm{Pr}^{1/3}}{\left[1 + \left(\frac{0.037}{\mathrm{Pr}}\right)\right]^{1/6}} \quad (\gamma = 1) \tag{41}$$

$$\mathrm{Nu}_D = 2 + 0.683\,\mathrm{Re}_D^{1/2} \frac{\mathrm{Pr}^{1/3}}{\left[1 + \left(\frac{0.471}{\mathrm{Pr}}\right)\right]^{1/6}} \quad (\gamma = \tfrac{1}{7}) \tag{42}$$

Figure 2(a) shows the comparison between the present results (Eqs. (41) and (42)) and the correlations of Frössling (1938), Drake and Backer (1952), and Yuge (1960) for air ($\mathrm{Pr} = 0.71$). It can be seen that at the low range of Re_D, $10^{-1} \le \mathrm{Re}_D \le 10$, the values of the Nusselt number correlations are in very good agreement with Eq. (41). However, at the high range of Re_D, 10

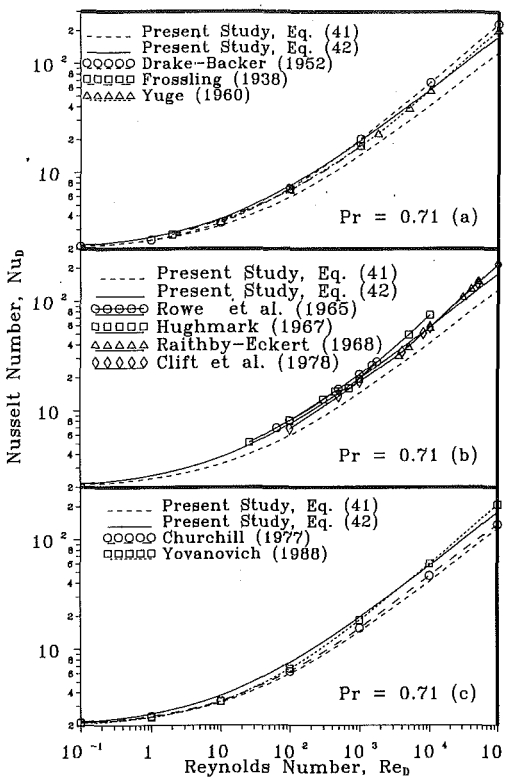

Fig. 2 Comparison between the present analytical model and the previous studies for air

$\leq \mathrm{Re}_D \leq 10^4$, the experimental correlations of Frössling (1938), Drake and Backer (1952), and Yuge (1960) approach Eq. (42), where the velocity profile has the power $\frac{1}{7}$.

In addition, Fig. 2(b) shows the same comparison between Rowe et al. (1965), Hughmark (1967), Raithby and Eckert (1968), and Clift et al. (1978) with the present study. The correlations of Raithby and Eckert (1968) and Clift et al. (1978) behave similarly to the correlations of Drake and Backer (1952) and Yuge (1960). On the other hand, the results of Rowe et al. (1965) are higher than the present study. Furthermore, Yovanovich and Vanoverbeke (1988) examined carefully the work of Rowe et al. (1965) and they concluded that Rowe et al. (1968) had not removed the effect of free convection from their data. In addition, the correlations of Hughmark (1967) were higher than the present study. However, from Table 1, it is seen that Hughmark (1967) presented two correlations for $\mathrm{Pr} < 250$. These two correlations cover the range of Re_D from 26 to 450 and 450 to 10^4, respectively. However, his correlation for the high range of Re_D predicted lower values of Nu_D at $\mathrm{Re}_D < 700$, if it is compared with his low range correlation. In addition, Eq. (42) is compared with the general equation of Pasternak and Gauvin (1960), which was developed for several body shapes and it was found that the maximum difference is 15 percent, which occurs at $\mathrm{Re}_D = 5000$. In addition, the turbulent intensity in the measurements of Pasternak and Gauvin (1960) was around 9–10 percent. Also, Eq. (42) is compared with the correlation of Kramers (1946) and it is found that the maximum difference of 2 percent occurs at $\mathrm{Re}_D = 540$.

Figure 2(c) shows the comparison between the present study and the models of Churchill (1977) and Yovanovich (1988) for air. It is observed that the Yovanovich (1988) and Churchill (1977) models are in very good agreement with Eq. (41) up to $\mathrm{Re}_D = 100$. After that the Yovanovich (1988) model approaches Eq. (42) and finally crosses it at $\mathrm{Re}_D = 10^4$. However, the Churchill model (1977) lies between Eqs. (41) and (42). We observe that the Churchill model behavior is similar to the present model

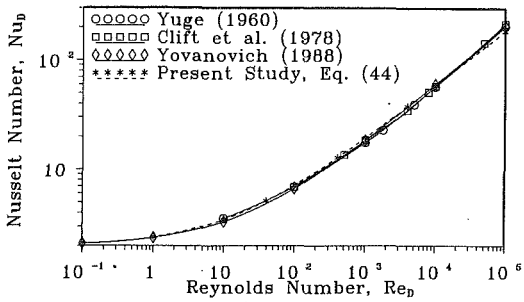

Fig. 3 Comparison between the present general analytical model and the previous studies for air

if $\gamma = \frac{2}{3}$. On the other hand, if $\gamma \to 0$, Eq. (42) will be higher than the Yovanovich model up to $\mathrm{Re}_D = 10^5$, i.e., Yovanovich was able to model different velocity profiles in one equation.

3.1 General Model. Figure 2 shows that the correlations of Yuge (1960), Drake and Backer (1952), Clift et al. (1978), and Yovanovich (1988) are in very good agreement with Eq. (41) up to $\mathrm{Re}_D = 100$ and after that their correlations approach Eq. (42) and finally, cross it at $\mathrm{Re}_D = 10^4$. This leads us to conclude that the previous studies fitted their data in various ranges of Re_D, which could have different velocity profiles because Eq. (41) was developed for a linear velocity profile and Eq. (42) was developed for the power-low velocity profile, $\gamma = \frac{1}{7}$. Therefore, if we correlate γ as a function of Re_D based on the trend of the previous studies between Eq. (41) and Eq. (42), a general model can be developed for the forced convection heat transfer from spheres. It is found that a simple form for γ as $f(\mathrm{Re}_D)$ based on the previous work is given by:

$$\gamma = 1.0/\mathrm{Re}_D^{0.25} \quad (\text{if } \gamma > 1 \text{ put } \gamma = 1) \tag{43}$$

From Eq. (38) with $n = 3$ we obtain the general equation:

$$\mathrm{Nu}_D = 2 + 0.775\,\mathrm{Re}_D^{1/2}\,\frac{\mathrm{Pr}^{1/3}/[\sqrt{2\gamma+1}]}{\left[1+\left(\dfrac{1.0}{(2\gamma+1)^3\,\mathrm{Pr}}\right)\right]^{1/6}} \tag{44}$$

$\mathrm{Re}_D < 10^5$ and $0 < \mathrm{Pr} < \infty$ with Eq. (43).

The right-hand side of Eq. (44) can be written as follows: $\mathrm{Nu}_D^0 + C_D\,\mathrm{Re}_D^{0.5} F(\mathrm{Pr}, \gamma)$, where Nu_D^0 is 2 and C_D is 0.775 and $F(\mathrm{Pr}, \gamma)$ is $\mathrm{Pr}^{1/3}/[\sqrt{2\gamma+1}]/[1 + (1.0/(2\gamma+1)^3\,\mathrm{Pr})]^{1/6}$.

Figure 3 shows the comparison between the general model, Eq. (44), and the previous studies of Yuge (1960), Clift et al. (1978), and Yovanovich (1988) for air. In addition, very good agreement between the previous studies and Eq. (44) up to $\mathrm{Re}_D = 2 \times 10^4$ is shown in Fig. 3. After that the Yuge (1960), Clift et al. (1978), and Yovanovich (1988) correlations cross the pres-

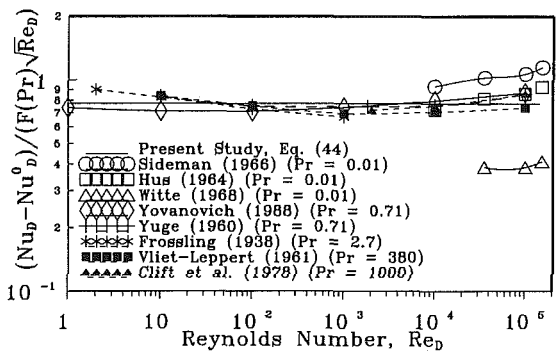

Fig. 4 Comparison between the present general analytical model and the previous studies for different Prandtl numbers

ent model, Eq. (44). The maximum differences between Yuge (1960), Clift et al. (1978), and Yovanovich (1988) correlations and Eq. (44), which occur at $Re_D = 10^5$, are 9.7, 13.9, and 10.8 percent, respectively.

Figure 4 shows the relationship between $[(Nu_D - Nu_D^0)/(F(Pr)\,Re_D^{0.5})]$ (which is C_D) and Re_D. Also, Fig. 4 presents the comparison between the present model and the previous studies for various Prandtl numbers. One observes that the maximum difference between the previous studies and the present model in the range $1 < Re_D < 10^5$ is approximately 11 percent, which generally occurs at $Re_D = 10^5$. On the other hand, there is almost a 33 percent difference between the present model and that of Sideman (1966). The main reason for this is that Sideman approximated the convective term of the energy equation by assuming $(V_\infty/r)/(\partial T/\partial\theta)$. Therefore, Sideman's model overpredicted the Nusselt number because the velocity in this model is very high. Figure 4 also shows that there is 50 percent difference between the present model and the experimental correlation (for sodium) of Witte (1968). Finally, it can be concluded from Fig. 4 that the constant C_D for the sphere is approximately 0.775. In addition, $F(Pr, \gamma)$ is quite acceptable over the range of $0 < Re_D < 10^5$.

4 Summary and Conclusions

An approximate analytical solution is developed for the area mean Nusselt number for forced convection from isothermal spheres valid for the range of Reynolds number, $0 \le Re_D \le 10^4$ and all Prandtl numbers. In addition, the present solution is found to be in very good agreement with many previous studies such as Frössling (1938), Kramers (1946), Yuge (1960), Raithby and Eckert (1968), Churchill (1977), and Yovanovich (1988). Furthermore, in the present study, it is concluded that the main reason for the differences in the exponent of Re_D and the constant C_D in the previous studies is due to their fitting data in various ranges of Re_D, which have different velocity profiles. This was observed very clearly from the trends of the previous studies, which are between the bounds of Eqs. (41) and (42), where the velocity profile in Eq. (41) is assumed linear and in Eq. (42) it is a power law with $\gamma = \frac{1}{7}$. Finally, this study has led to a design correlation, Eq. (44), which is very accurate for the range of Reynolds number $0 \le Re_D < 10^5$ and all Prandtl numbers $0 < Pr < \infty$.

Acknowledgments

The authors wish to acknowledge the financial support of the Natural Sciences and Engineering Research Council of Canada under grant No. A7455. The authors also thank Professor G. Davidson for his valuable discussion. The authors appreciate the comments and suggests of the reviewers.

References

Bejan, A., 1985, "The Method of Scale Analysis: Natural Convection in Fluids," *Natural Convection Fundamentals and Applications,* S. Kakac, W. Aung, and R. Viskanta, eds., Hemisphere Publishing Corporation, pp. 75–94.

Carslaw, H. S., and Jaeger, J. C., 1959, *Conduction of Heat in Solids,* 2nd ed., Clarendon Press, London, United Kingdom.

Churchill, S. W., and Usagi, R., 1972, "A General Expression for the Correlation of Rates of Transfer and Other Phenomena," *AIChE J.,* Vol. 18, pp. 1121–1132.

Churchill, S. W., 1977, "A Comprehensive Correlating Equation for Laminar, Assisting, Forced and Free Convection," *AIChE J.,* Vol. 23, No. 1, pp. 10–16.

Clift, R., Grace, J. R., and Weber, M. E., 1978, *Bubbles, Drops, and Particles,* Academic Press, New York.

Drake, R. M., and Backer, G. H., 1952, "Heat Transfer From Spheres to a Rarefied Gas in Supersonic Flow," *Trans. ASME,* Vol. 74, pp. 1241–1249.

Frössling, N. M., 1938, "The Evaporation of Falling Drops," *Gerlands Beitr. Geophys.,* Vol. 52, pp. 170–216.

Griffith, R. M., 1960, "Mass Transfer From Drops and Bubbles," *Chemical Engineering Science,* Vol. 12, pp. 198–213.

Happel, J., and Brenner, H., 1973, *Low Reynolds Number Hydrodynamics,* 2nd ed., Noordhoff, Leyden, The Netherlands.

Hsu, S. T., 1963, *Engineering Heat Transfer,* D. Van Nostrand, New York.

Hughmark, G. A., 1967, "Mass and Heat Transfer From Rigid Spheres," *AIChE J.,* Vol. 13, No. 6, pp. 1219–1221.

Jafarpur, K., 1992, "Analytical and Experimental Study of Laminar Free Convection Heat Transfer From Isothermal Convex Bodies of Arbitrary Shapes," Ph.D. thesis, Department of Mechanical Engineering, University of Waterloo, Waterloo, Ontario, Canada.

Kays, W. M., and Crawford, M. E., 1980, *Convection Heat and Mass Transfer,* 2nd ed., McGraw-Hill, New York.

Kramers, H., 1946, "Heat Transfer From Spheres to Flowing Media," *Physica,* Vol. 12, No. 2–3, pp. 61–81.

Lochiel, A. C., and Calderbank, P. H., 1964, "Mass Transfer in the Continuous Phase Around Axisymmetric Bodies of Revolution," *Chemical Engineering Science,* Vol. 19, pp. 471–484.

Pasternak, I. S., and Gauvin, W. H., 1960, "Turbulent Heat and Mass Transfer From Stationary Particles," *Can. J. Chem. Engr.,* Vol. 38, pp. 35–42.

Raithby, G. D., and Eckert, E. R. G., 1968, "The Effect of Turbulence Parameters and Support Position on the Heat Transfer From Spheres," *Int. J. Heat Mass Transfer,* Vol. 11, pp. 1233–1252.

Rowe, P. N., Claxton, K. T., and Lewis, J. B., 1965, "Heat and Mass Transfer From a Single Sphere in an Extensive Fluid," *Trans. Inst. Chem. Engrs.,* Vol. 43, pp. T14–T31.

Sideman, S., 1966, "The Equivalence of the Penetration Theory and Potential Flow Theories," *Industrial and Engineering Chemistry,* Vol. 58, No. 2, pp. 54–58.

Vliet, G. C., and Leppert, G., 1961, "Forced Convection Heat Transfer From an Isothermal Sphere to Water," ASME JOURNAL OF HEAT TRANSFER, Vol. 83, pp. 163–75.

White, F. M., 1991, *Viscous Fluid Flow,* 2nd ed., McGraw-Hill, New York.

Witte, L. C., 1968, "An Experimental Study of Forced Convection Heat Transfer From a Sphere to Liquid Sodium," ASME JOURNAL OF HEAT TRANSFER, Vol. 90, pp. 9–12.

Yovanovich, M. M., 1988, "General Expression for Forced Convection Heat and Mass Transfer From Isopotential Spheroids," Paper No. AIAA-88-0743.

Yovanovich, M. M., and Vanoverbeke, C. A., 1988, "Combined Natural and Forced Convection Heat Transfer From Isothermal Spheres," Paper No. AIAA-88-2618.

Yovanovich, M. M., Lee, S., and Gayowsky, T. J., 1992, "Approximate Analytical Solution of Laminar Forced Convection Heat From an Isothermal Plate," Paper No. AIAA-92-0248.

Yuge, T., 1960, "Experiments on Heat Transfer From Spheres Including Combined Natural Convection," ASME JOURNAL OF HEAT TRANSFER, Vol. 82, pp. 214–220.

A Near-Wall Eddy Conductivity Model for Fluids With Different Prandtl Numbers

R. M. C. So

T. P. Sommer

Mechanical and Aerospace Engineering,
Arizona State University,
Tempe, AZ 85287-6106

Near-wall turbulence models for the velocity and temperature fields based on the transport equations for the Reynolds stresses, the dissipation rate of turbulent kinetic energy, and the temperature variance and its dissipation rate are formulated for flows with widely different Prandtl numbers. Conventional high-Reynolds-number models are used to close these equations and modifications are proposed to render them asymptotically correct near a wall compared to the behavior of the corresponding exact equations. Thus formulated, two additional constants are introduced into the definition of the eddy conductivity. These constants are found to be parametric in the Prandtl number. The near-wall models are used to calculate flows with different wall thermal boundary conditions covering a wide range of Reynolds numbers and Prandtl numbers. The calculated Nusselt number variations with Prandtl number are in good agreement with established formulae at two different Reynolds numbers. Furthermore, the mean profiles, turbulence statistics, heat flux, temperature variance, and the dissipation rates of turbulent kinetic energy and temperature variance are compared with measurements and direct numerical simulation data. These comparisons show that correct near-wall asymptotic behavior is recovered for the calculated turbulence statistics and the calculations are in good agreement with measurements over the range of Prandtl numbers investigated.

Introduction

In spite of recent advances made in the turbulence modeling of incompressible and compressible flows with heat transfer (Nagano and Kim, 1988; Lai and So, 1990a; Nagano et al., 1991; Sommer et al., 1992, 1993a), most computational and theoretical investigations are still based on the hypothesis of an eddy viscosity and the assumption of a constant turbulent Prandtl number, Pr_t (Myong et al., 1989; Antonia and Kim, 1991a; Sommer et al., 1992, 1993a). Strictly speaking, the physical arguments for these assumptions are applicable only for fluids whose Prandtl numbers, Pr, are approximately 1. In practice, these assumptions are invoked for fluids with Pr that ranges from 10^{-2} to 10^4. However, according to Jischa and Rieke (1979), Pr_t is weakly dependent on Pr for $Pr > 1$, but Pr_t increases rapidly as Pr decreases. The increase is particularly steep for $Pr < 0.1$. Furthermore, Reynolds number also affects the dependence of Pr_t on Pr for values of $Pr < 0.1$. Therefore, this suggests that a constant Pr_t assumption may be valid for fluids with $Pr > 1$; however, it is not suitable for fluids with $Pr < 1$.

Recently, Myong et al. (1989) argued that the constant Pr_t assumption is still applicable for heat transfer problems with widely different Pr provided that the eddy viscosity is estimated correctly near a wall. They proposed to use an improved near-wall two-equation turbulence model (Myong and Kasagi, 1990) to calculate the eddy viscosity. Different Pr_t assumptions are investigated; these include the use of empirical correlations proposed by Quarmby and Quirk (1974) and Kays and Crawford (1980) and constant Pr_t to evaluate the eddy conductivity. Their study shows that, in the range of Prandtl numbers investigated, 10^{-2} to 5×10^4, the constant Pr_t assumption gives the best results. However, three different Pr_t values have to be assumed. A value of 1.5 is found to be suitable for $Pr < 0.1$, but this value differs greatly from those reviewed by Jischa and Rieke (1979). Consistent with other researchers' work, a $Pr_t = 0.86$ is found to give the best result for the range $1 < Pr < 10$ and a value of about 1 is appropriate for $Pr > 10^2$. Their calculations of Nusselt number, Nu, versus Pr in these three different regimes correlate well with empirical relations proposed by previous investigators (Skupinski et al., 1965; Petukhov, 1970; Notter and Sleicher, 1971, 1972; Sleicher and Rouse, 1975; Gnielinski, 1976; Chen and Chiou, 1981). Based on their analysis, they proposed an empirical relation for Pr_t applicable in the range $10^{-2} < Pr < 5 \times 10^4$. This proposal is empirical at best and may not be applicable to flow geometries other than the pipe flow considered.

The success of the approach of Myong et al. (1989) to the prediction of Nu is partly due to the fact that the integral parameters are relatively insensitive to the local variation of Pr_t in the flow field. However, other flow properties, such as temperature variance, heat fluxes, and turbulence statistics, are greatly influenced by the behavior of the local Pr_t (Hishida et al., 1986; Krishnamoorthy and Antonia, 1987; Antonia and Kim, 1991b). Besides, the appropriate Pr_t values to use in the wide range of Pr encountered in practical flows have not been established yet. Furthermore, evidence that Pr_t varies across the wall layer even in simple shear flows is provided by the recent direct numerical simulation (DNS) data of Kim and Moin (1989), Lyons et al. (1991), Kasagi et al. (1992), and Kasagi and Ohtsubo (1992). These studies show that the variations of Pr_t are greater for lower values of Pr. Therefore, it is desirable to formulate a turbulent heat transfer model that does not assume constant Pr_t, especially if a wide range of flows with vastly different Pr is to be predicted.

From the discussion above, it is apparent that there is a need for a turbulent heat transfer model that is capable of calculating flows with widely different Pr and Re. The importance of correctly modeling the turbulent shear stress in near-wall flows with heat transfer has already been pointed out by Myong et al. (1989). If the near-wall region is to be calculated properly, as is necessary for complex flows even without heat transfer, it is important to achieve proper near-wall balance of the model terms, thus emphasizing the need for asymptotically consistent turbulence models. Therefore, the proposed model should incorporate an asymptotically consistent near-wall turbulence model for the

Contributed by the Heat Transfer Division for publication in the JOURNAL OF HEAT TRANSFER. Manuscript received by the Heat Transfer Division November 1992; revision received November 1993. Keywords: Forced Convection, Nonequilibrium Flows, Turbulence. Associate Technical Editor: R. J. Simoneau.

calculation of the velocity field. Numerous near-wall turbulence models are available; they include two-equation models (Myong and Kasagi, 1990; Patel et al., 1985; So et al., 1991a; Zhang et al., 1993a) and second-order models (So et al., 1991b; Zhang et al., 1993a). However, according to Zhang et al. (1993a, b), only asymptotically consistent second-order models are capable of correctly predicting existing DNS data over a wide range of Re and at the same time also give good results for high supersonic flows and near-separating flows. Therefore, the near-wall second-order model and its corresponding $k-\epsilon$ model formulated by Zhang et al. (1993a) are adopted for the calculation of the velocity field.

As for the calculation of the temperature field, one alternative is to use a model that is of the same order as the velocity field, such as the second-order heat transfer model of Lai and So (1990a). Another alternative is to adopt the suggestion of Cebeci and Bradshaw (1984); namely, a heat transfer model that is one order lower than the velocity field model could be used to obtain reliable results in the calculations of turbulent flows with heat transfer. This suggestion is based on the argument that, for incompressible flows, the uncoupled-flow approximation (Cebeci and Bradshaw, 1984) applies. Thus the velocity field results are not affected by the temperature field, while the velocity field plays an important role in the calculation of turbulent heat transfer. Besides, the velocity field itself is often of primary interest. In view of this, modeling the turbulent heat fluxes at a lower level than the Reynolds stresses does not degrade the quality of the results for the velocity field. Therefore, a point can be made to use a closure at a lower level for the temperature field. This suggestion has recently been verified by So et al. (1992), who compared the performance of heat transfer models that are of the same order or one order lower than the velocity field models in the calculations of channel flows with heat transfer. Their calculations cover the DNS cases analyzed by Kim et al. (1987), Kim and Moin (1989), and Kasagi et al. (1992), where detailed near-wall profiles are available for both the mean field and the turbulence statistics. The results show that, in all cases examined, there is no deteriation in the predictions of mean temperature, temperature variance, and normal heat flux when the heat transfer model is one order lower than the velocity field model. In view of this, a two-equation model is proposed for the calculation of the temperature field irrespective of whether the velocity field is calculated by a $k-\epsilon$ model or a second-order model. The two-equation heat transfer model is based on the solution of the equations governing the transport of temperature variance and its dissipation rate. Gradient transport is assumed. Therefore, the turbulent heat flux is calculated from the product of an eddy conductivity and the mean temperature gradient. Thus formulated, the model is used to calculate pipe and channel flows with different thermal boundary conditions and widely different Pr. The calculated results are compared with the DNS data of Kim et al. (1987), Kim and Moin (1989), and Kasagi et al. (1992), the empirical correlations of Skupinski et al. (1965), Notter and Sleicher (1972), Gnielinski (1976), and Kader (1981) and the high-Reynolds-number measurements of Johnk and Hanratty (1962) and Hishida et al. (1986).

Near-Wall Turbulence Models

A near-wall second-order turbulence model formulated for incompressible flows is used to evaluate the turbulent stresses, $-\overline{u_i u_j}$. The model is based on the solution of the equations that govern the transport of these stresses and the dissipation rate, ϵ, of the turbulent kinetic energy, k. In their modeled

Nomenclature

A^+ = model constant taken to be parametric in Pr
a_k = coefficients in the expansion for k^+ in the near-wall region
a_u, b_u = coefficients in the expansion for $u_{\rm rms}$ in the near-wall region
a_v = coefficients in the expansion for $v_{\rm rms}$ in the near-wall region
a_w, b_w = coefficients in the expansion for $w_{\rm rms}$ in the near-wall region
a_{uv}, b_{uv} = coefficients in the expansion for $-\overline{uv}^+$ in the near-wall region
a_θ, b_θ = coefficients in the expansion for $\theta_{\rm rms}$ in the near-wall region
$a_{v\theta}$, $b_{v\theta}$ = coefficients in the expansion for $-\overline{v\theta}^+$ in the near-wall region
$a_{\epsilon\theta}$, $b_{\epsilon\theta}$ = coefficients in the expansion for ϵ_θ^+ in the near-wall region
C_1 = model constant = 1.50
C_2 = model constant = 0.40
C_s = model constant = 0.11
C_ϵ = model constant = 0.10
$C_{\epsilon 1}$ = model constant = 1.50
$C_{\epsilon 2}$ = model constant = 1.83
C_p = specific heat at constant pressure
$C_{\lambda 1}$ = model constant taken to be parametric in Pr
C_{d1} = model constant = 1.8
C_{d2} = model constant = 0
C_{d3} = model constant = 0.72
C_{d4} = model constant = 2.2
C_{d5} = model constant = 0.8
C_w = model coefficient that is a function of Re
C_λ = model constant = 0.095
C_μ = model constant = 0.096
C_{θ^2} = model constant = 0.11
$C_{\epsilon\theta}$ = model constant = 0.11
D = pipe diameter or channel height
D_{ij} = production tensor = $-[\overline{u_i u_k}(\partial U_k/\partial x_j) + \overline{u_j u_k}(\partial U_k/\partial x_i)]$
D_{ij}^T = turbulent diffusion tensor
f_{w1} = near-wall damping function for Reynolds-stress equation = $\exp[-(\mathrm{Re}_t/150)^2]$
f_{w2} = near-wall damping function for ϵ equation = $\exp[-(\mathrm{Re}_t/40)^2]$
$f_{w,\epsilon\theta}$ = near-wall damping function for ϵ_θ equation = $\exp[-(\mathrm{Re}_t/80)^2]$
f_λ = near-wall damping function for turbulent heat diffusivity
$f_{\lambda 1}$ = near-wall damping function = $[1 - \exp(-y^+/A^+)]^2$
f_μ = damping function = $[1 + 3.45/\sqrt{\mathrm{Re}_t}\tanh[y^+/115]$
k = turbulent kinetic energy
k^+ = normalized turbulent kinetic energy = k/u_τ^2
n_i = unit normal vector measured positive outward from wall
Nu = Nusselt number
P = mean pressure
$\tilde{P}$ = production of k due to mean shear = $-\overline{u_i u_j}(\partial U_i/\partial x_j)$
P_{ij} = production of the Reynolds stresses = $-[\overline{u_i u_k}(\partial U_j/\partial x_k) + \overline{u_j u_k}(\partial U_i/\partial x_k)]$
P_θ = production due to mean temperature = $-\overline{u_k\theta}[\partial\Theta/\partial x_k]$
P_θ^* = production term due to mean temperature gradient in the x direction
Pr = Prandtl number
Pr_t = turbulent Prandtl number
q'' = heat source per unit volume
q_w = wall heat flux
Re = Reynolds number based on mean bulk velocity = $U_m D/\nu$
Re_t = turbulent Reynolds number = $k^2/\nu\epsilon$
S = source term in Eq. (15)
S_{ij} = strain rate tensor = $(1/2)[\partial U_i/\partial x_j + \partial U_j/\partial x_i]$
t = time
U_m = mean bulk velocity
U = mean velocity along x direction

form, the transport equations are given by Zhang et al. (1993a) as:

$$\frac{\partial \overline{u_i u_j}}{\partial t} + U_k \frac{\partial \overline{u_i u_j}}{\partial x_k} = \frac{\partial}{\partial x_k}\left(\nu \frac{\partial \overline{u_i u_j}}{\partial x_k}\right) + D_{ij}^T + \left[-\overline{u_i u_k}\frac{\partial U_j}{\partial x_k} - \overline{u_j u_k}\frac{\partial U_i}{\partial x_k}\right] + \Pi_{ij} - \epsilon_{ij}, \quad (1)$$

$$\frac{\partial \epsilon}{\partial t} + U_j \frac{\partial \epsilon}{\partial x_j} = \frac{\partial}{\partial x_j}\left(\nu \frac{\partial \epsilon}{\partial x_j}\right) + \frac{\partial}{\partial x_j}\left(C_\epsilon \frac{k}{\epsilon}\overline{u_i u_j}\frac{\partial \epsilon}{\partial x_i}\right) + C_{\epsilon 1}\frac{\epsilon}{k}\tilde{P} - C_{\epsilon 2}\frac{\epsilon\tilde{\epsilon}}{k} + \xi. \quad (2)$$

In these equations, D_{ij}^T, Π_{ij}, and ϵ_{ij} represent the turbulent diffusion of $-\overline{u_i u_j}$, the velocity–pressure gradient correlation, and the viscous dissipation of turbulent stresses, and the model constants in Eq. (2) are given by Zhang et al. (1993a). These equations are not closed and the terms D_{ij}^T, Π_{ij}, ϵ_{ij}, and ξ need modeling if they are to be applicable for near-wall flow calculations.

If D_{ij}^T, Π_{ij}, and ϵ_{ij} are modeled by their conventional high-Reynolds-number models (Launder et al., 1975), Eq. (1) is identical to the modeled equation proposed by Launder et al. (1975). The equation is not in balance as a wall is approached. Therefore, the high-Reynolds-number models have to be modified to render them asymptotically consistent compared to the exact second-moment equation. Since the exact turbulent diffusion term is of higher order and is not important near a wall, the model for this term does not need modification. Asymptotic analysis along the line suggested by Lai and So (1990a, b) can be applied to treat the exact and modeled equations. This will lead to correcting functions for the high-Reynolds-number models adopted for Π_{ij} and ϵ_{ij}. Thus modified, the respective models are valid near a wall. Therefore, according to Zhang et al. (1993a), the proposed near-wall models are:

$$D_{ij}^T = \frac{\partial}{\partial x_k}\left[C_s \frac{k}{\epsilon}\left(\overline{u_i u_l}\frac{\partial \overline{u_j u_k}}{\partial x_l} + \overline{u_j u_l}\frac{\partial \overline{u_k u_i}}{\partial x_l} + \overline{u_k u_l}\frac{\partial \overline{u_i u_j}}{\partial x_l}\right)\right], \quad (3)$$

$$\Pi_{ij} = -C_1\frac{\epsilon}{k}\left(\overline{u_i u_j} - \tfrac{2}{3}k\delta_{ij}\right) - \alpha_1\left(P_{ij} - \tfrac{2}{3}\tilde{P}\delta_{ij}\right) - \beta_1\left(D_{ij} - \tfrac{2}{3}\tilde{P}\delta_{ij}\right) - 2\left(\gamma_1 + C_w\frac{k^{3/2}}{\epsilon x_2}\right)kS_{ij} + f_{w1}\left[C_1\frac{\epsilon}{k}\left(\overline{u_i u_j} - \tfrac{2}{3}k\delta_{ij}\right) - \frac{\epsilon}{k}\left(\overline{u_i u_k}n_k n_j + \overline{u_j u_k}n_k n_i\right) + \alpha^*\left(P_{ij} - \tfrac{2}{3}\tilde{P}\delta_{ij}\right)\right], \quad (4)$$

$$\epsilon_{ij} = \tfrac{2}{3}\epsilon\delta_{ij} + f_{w1}\frac{\epsilon}{k}\left[-\frac{2}{3}k\delta_{ij} + \frac{\overline{u_i u_j} + \overline{u_i u_k}n_k n_j + \overline{u_j u_k}n_k n_i + n_i n_j\overline{u_k u_l}n_k n_l}{1 + 3\overline{u_k u_l}n_k n_l/2k}\right]. \quad (5)$$

The damping function f_{w1} is introduced to insure that the near-wall corrections to the high-Reynolds-number models will become negligible outside of the near-wall region. In this formulation, the "pressure echo" model is given by the term having C_w as a coefficient. Zhang et al. (1993a) found that C_w is a function of Re when Re < 5500 and an appropriate expression is given by $C_w = 0.00414 + 0.003(\log \mathrm{Re})$. For Re > 5500, C_w is essentially constant and its value is 0.0153. Again, the model constants used by Zhang et al. (1993a) are adopted in the present study. The values of all model constants are listed in the Nomenclature section.

Since Eq. (2) with ξ set equal to zero is also not in balance as a wall is approached, modification is required to render the equation asymptotically correct compared to the behavior of the exact ϵ equation. An asymptotic analysis similar to the one proposed by Lai and So (1990a, b) has been carried out to order y by Zhang et al. (1993a) and the result is a new correcting function ξ, which can be written as:

$$\xi = f_{w2}\left(-2\frac{\epsilon\tilde{\epsilon}}{k} + 1.5\frac{\bar{\epsilon}^2}{k} - 1.5C_{\epsilon 1}\frac{\epsilon}{k}\tilde{P}\right), \quad (6)$$

Nomenclature (cont.)

U_i = ith component of the mean velocity
U^+ = normalized mean U velocity = U/u_τ
u_i = ith component of the fluctuating velocity
u, v, w = fluctuating velocity components along x, y, and z, respectively
u_{rms} = root mean square of $\overline{u^2}$ normalized by u_τ
v_{rms} = root mean square of $\overline{v^2}$ normalized by u_τ
w_{rms} = root mean square of $\overline{w^2}$ normalized by u_τ
u_τ = friction velocity = $(\tau_w/\rho)^{1/2}$
$-\overline{uv}^+$ = normalized turbulent shear stress = $-\overline{uv}/u_\tau^2$
$-\overline{v\theta}^+$ = normalized turbulent heat flux = $-\overline{v\theta}/u_\tau\Theta_\tau$
x_i = ith component of the coordinate
x, y, z = coordinates along stream, normal, and transverse directions
y^+ = normalized y coordinate = yu_τ/ν
α = thermal diffusivity = $\kappa/\rho C_p$
α_1 = model constant = $[8 + C_2]/11$
α_t = turbulent heat diffusivity
α^* = model constant = 0.45
β_1 = model constant = $[8C_2 - 2]/11$
γ_1 = model constant = $[30C_2 - 2]/55$
ϵ = dissipation rate of k
ϵ_w = dissipation rate of k evaluated at the wall = $2\nu[\partial\sqrt{k}/\partial y]^2$
ϵ_θ = dissipation rate of temperature variance
$(\epsilon_\theta)_w$ = dissipation rate of temperature variance evaluated at the wall = $\alpha[\partial\sqrt{\overline{\theta^2}}/\partial y]^2$
$\tilde{\epsilon}$ = modified dissipation rate = $\epsilon - 2\nu(\partial\sqrt{k}/\partial y)^2$
$\tilde{\epsilon}_\theta$ = modified dissipation rate of temperature variance = $\epsilon_\theta - \alpha[\partial\sqrt{\overline{\theta^2}}/\partial y]^2$
$\bar{\epsilon}$ = modified dissipation rate = $\epsilon - 2\nu k/y^2$
ϵ_θ^* = modified dissipation rate of temperature variance = $\epsilon_\theta - \alpha\overline{\theta^2}/y^2$
ϵ^+ = normalized dissipation rate = $\epsilon\nu/u_\tau^4$
ϵ_θ^+ = normalized dissipation rate of the temperature variance = $\epsilon_\theta\nu/u_\tau^2\Theta_\tau^2$
ϵ_{ij} = dissipation rate tensor
θ = fluctuating temperature
θ_{rms} = root mean square of the temperature variance normalized by Θ_τ
$\overline{\theta^2}$ = temperature variance
Θ = mean temperature
Θ_τ = friction temperature = $q_w/\rho C_p u_\tau$
Θ^+ = normalized mean temperature = Θ/Θ_τ
κ = thermal conductivity
ν = fluid kinematic viscosity
ξ = near-wall correction to ϵ equation
$\xi_{\epsilon\theta}$ = near-wall correction to ϵ_θ equation
Π_{ij} = velocity pressure gradient correlation tensor
ρ = fluid density
σ_k = model constant = 1.0
σ_ϵ = model constant = 1.45
σ_θ = model constant = 0.75
$\sigma_{\epsilon\theta}$ = model constant = 1.0
τ_w = wall shear stress

where the damping function f_{w2} is introduced to insure that ξ would approach zero away from a wall. Thus modified, Eqs. (1) and (2) are valid as a wall is approached and can be used to calculate wall-bounded flows where the correct boundary conditions on $-\overline{u_i u_j}$ and ϵ are specified as: $-\overline{u_i u_j} = 0$ and $\epsilon = \epsilon_w$, the dissipation rate evaluated at the wall.

The equations for the $k-\epsilon$ model are given by Eq. (2) and the trace of Eq. (1) simplified by assuming Π_{ii} to be zero and ϵ_{ii} to be isotropic. Consistent with the isotropic assumption, the turbulent diffusion terms in the k and ϵ equations also have to be modeled. According to Zhang et al. (1993a), the k equation obtained from the trace of Eq. (1) is given by

$$\frac{\partial k}{\partial t} + U_j \frac{\partial k}{\partial x_j} = \frac{\partial}{\partial x_j}\left(\nu \frac{\partial k}{\partial x_j}\right) + \frac{\partial}{\partial x_j}\left(\frac{\nu_t}{\sigma_k}\frac{\partial k}{\partial x_j}\right) + \tilde{P} - \epsilon, \quad (7)$$

and the diffusion term in Eq. (2) is replaced by the isotropic diffusion term $\partial[(\nu_t/\sigma_\epsilon)(\partial\epsilon/\partial x_j)]/\partial x_j$. Therefore, the eddy viscosity is given by $\nu_t = C_\mu f_\mu k^2/\epsilon$ and the Reynolds stresses are defined by $-\overline{u_i u_j} = \nu_t S_{ij} - (2/3)k\delta_{ij}$. The damping function and the model constant specified by Zhang et al. (1993a) are adopted without change.

Near-Wall Model for Eddy Conditivity

As pointed out by Cebeci and Bradshaw (1984) and verified by So et al. (1992), reliable results can be obtained for the calculations of turbulent flows with heat transfer even when the heat flux model is one order lower than the velocity field model. Since the proposed model for the velocity field is either a second-order model or a $k-\epsilon$ model, a two-equation model for the temperature field would be most appropriate. Therefore, gradient transport is assumed so that the ith component of the turbulent heat flux is given by $-\overline{u_i\theta} = \alpha_t(\partial\Theta/\partial x_i)$. This choice of heat transfer model has several advantages. The first is that the two-equation model is the lowest order variable Pr_t model available that is reliable (Nagano et al., 1991; Sommer et al., 1992). The second advantage is more practical and has to do with the number of equations involved in the modeling effort. Up to three equations have to be solved for the heat fluxes when a second-order model is used. If flows at Prandtl numbers much larger than one are to be calculated, these equations would have to include a thermal time scale (Launder, 1976), thus making it necessary to solve additional equations for the temperature variance and its dissipation rate. Therefore, the total number of equations to be solved become five rather than three. This is in addition to the equations required for the Reynolds stresses. It is difficult to justify this many equations for most engineering applications, especially if there are no significant differences between second-order and two-equation model results (So et al., 1992). Finally, it is not immediately obvious how to improve second-order heat transfer models, such as that proposed by Lai and So (1990a), to account for Prandtl number effects.

Several near-wall two-equation models have been proposed for the turbulent heat flux vector (Nagano and Kim, 1988; Nagano et al., 1991; Sommer et al., 1992). Nagano and Kim's model (1988) is asymptotically incorrect and gives a zero ϵ_θ at the wall; therefore, it is not consistent with the behavior of the near-wall turbulence model described in the previous section. The other two models give asymptotically correct results near a wall and are appropriate for the present application. However, the model proposed by Nagano et al. (1991) has not yet been tested for flows that span a wide range of Reynolds numbers and Mach numbers, while the model developed by Sommer et al. (1992, 1993a) has. Therefore, the present approach adopts the model of Sommer et al. (1992) as a base and proceeds to generalize it for applications to turbulent heat transfer where Pr varies from 10^{-2} to 10^4.

The exact and modeled incompressible equations for $\overline{\theta^2}$ and ϵ_θ are given by Launder (1976). Sommer et al. (1992) use the high-Reynolds-number modeled equations of Launder (1976) as a starting point and proceed to modify them for near-wall flows using the methodology proposed by Lai and So (1990a). The equations thus modified can be written as:

$$\frac{\partial\overline{\theta^2}}{\partial t} + U_k\frac{\partial\overline{\theta^2}}{\partial x_k} = \frac{\partial}{\partial x_k}\left(\alpha\frac{\partial\overline{\theta^2}}{\partial x_k}\right) + \frac{\partial}{\partial x_k}\left(C_{\theta^2}\overline{u_k u_j}\frac{k}{\epsilon}\frac{\partial\overline{\theta^2}}{\partial x_j}\right) - 2\overline{u_k\theta}\frac{\partial\Theta}{\partial x_k} - 2\epsilon_\theta, \quad (8)$$

$$\frac{\partial\epsilon_\theta}{\partial t} + U_k\frac{\partial\epsilon_\theta}{\partial x_k} = \frac{\partial}{\partial x_k}\left(\alpha\frac{\partial\epsilon_\theta}{\partial x_k}\right) + \frac{\partial}{\partial x_k}\left(C_{\epsilon\theta}\overline{u_k u_j}\frac{k}{\epsilon}\frac{\partial\epsilon_\theta}{\partial x_j}\right) + C_{d1}\frac{\epsilon_\theta}{\overline{\theta^2}}P_\theta + C_{d2}\frac{\epsilon}{k}P_\theta + C_{d3}\frac{\epsilon_\theta}{k}\tilde{P} - C_{d4}\frac{\tilde{\epsilon}_\theta}{\overline{\theta^2}}\epsilon_\theta - C_{d5}\frac{\tilde{\epsilon}_\theta}{k}\epsilon_\theta + \xi_{\epsilon\theta}, \quad (9)$$

where the effects of both thermal ($\overline{\theta^2}/\epsilon_\theta$) and velocity ($k/\epsilon$) time scale on the dissipation of $\overline{\theta^2}$ are modeled into the ϵ_θ equation. The eddy conductivity can be defined by the product of a turbulent velocity scale and a turbulent length scale. For incompressible flows with heat transfer, the appropriate turbulent velocity scale is $k^{1/2}$, while an appropriate length scale could be determined from the product of $k^{1/2}$ and a time scale. If both thermal and velocity time scales are of importance in the transport of heat, then a reasonable proposal for α_t would be:

$$\alpha_t = C_\lambda f_\lambda k[k\overline{\theta^2}/\epsilon\epsilon_\theta]^{1/2}, \quad (10)$$

where f_λ is a damping function to be defined subject to certain near-wall constraints. A constant value of $C_\lambda = 0.11$ has been put forward by Nagano and Kim (1988) and adopted by Sommer et al. (1992, 1993a). Furthermore, $C_\lambda = 0.10$ also has been assumed by Nagano et al. (1991). In all these calculations, the value 0.1 is found to give good results for the flow cases tested. Therefore, it is prudent to assume a value not too different from 0.1. For the present calculations, $C_\lambda = 0.095$ is found to give the best results. If Eqs. (8) and (9) are to be used with the $k-\epsilon$ model for the velocity field, the turbulent diffusion terms have to be modeled because the Reynolds stresses are not calculated separately. Sommer et al. (1993a) suggested replacing the turbulent diffusion of $\overline{\theta^2}$ in Eq. (8) by the isotropic diffusion term $\partial[(\alpha_t/\sigma_\theta)(\partial\overline{\theta^2}/\partial x_k)]/\partial x_k$ and the turbulent diffusion of ϵ_θ in Eq. (9) by the isotropic diffusion term $\partial[(\alpha_t/\sigma_{\epsilon\theta})(\partial\epsilon_\theta/\partial x_k)]/\partial x_k$.

In order to analyze the near-wall behavior of Eqs. (8) and (9), the asymptotic behavior of the mean and fluctuating properties has to be known. If the assumption of analyticity is invoked, Taylor expansions of the fluctuating quantities can be made in terms of y near a wall. Since the fluctuating velocities have to satisfy the no-slip condition at the wall, the leading term in the fluctuating velocity expansions, u and w, is of order y, while the leading term in the expansion of v is of order y^2 as a result of incompressibility. On the other hand, the expansion of θ depends on the wall thermal boundary conditions. It should be of order y for constant wall temperature and of order y^0 for constant wall heat flux (Nagano et al., 1991). When θ is assumed to be finite at the wall, a different wall boundary condition, other than vanishing temperature variance, has to be specified for θ^2 because the leading coefficient in the θ expansion is unknown. The boundary condition adopted by Nagano et al. (1991) in their boundary-layer calculations is the vanishing of the normal gradient of θ^2 at the wall for the constant wall heat flux case. This boundary condition creates a problem for internal flow calculations where the normal gradient of θ^2 also vanishes at a symmetry line. Therefore, the temperature variance equation and associated boundary conditions constitute an ill-posed problem. In view of this, the assumption of nonvanishing θ for the constant wall heat flux case may not be very appropriate. On the other hand, according to Polyakov (1974), under certain conditions, θ

can be assumed to be of order y near the wall even when the wall heat flux is specified. This assumption has been thoroughly examined by Sommer et al. (1993b) for both constant temperature and constant heat flux wall boundary conditions in channel and pipe flows. Their calculations were carried out over a range of Re, but most were at Re = 40,000. Since the value of θ^2 at the wall depends very much on the thermal conductivities of the fluid and the wall, different combinations of fluid and wall material have also been studied by Sommer et al. (1993b). In all the cases examined, the effects of finite θ^2 at the wall on the calculations of mean temperature are found to be essentially negligible. The differences come in the predictions of θ^2, and even then significant discrepancies only occur in the viscous region, i.e., in a region whose thickness is no greater than $y^+ = 20$, except for the case where Pr = 0.025. For this case, the viscous region becomes very large and occupies a substantial portion of the channel height or pipe diameter. In other words, the zero wall fluctuating temperature assumption is quite appropriate for most engineering applications where Pr > 0.1.

The present model is developed by invoking this assumption and its asymptotic consistency can be verified by comparing the model calculations with DNS data. Based on these expansions, the following dimensionless near-wall asymptotes can be deduced:

$$u_{\rm rms} = a_u y^+ + b_u y^{+2} + \ldots, \tag{11a}$$

$$v_{\rm rms} = a_v y^{+2} + \ldots, \tag{11b}$$

$$w_{\rm rms} = a_w y^+ + b_w y^{+2} + \ldots, \tag{11c}$$

$$-\overline{uv}^+ = a_{uv} y^{+3} + b_{uv} y^{+4} + \ldots, \tag{11d}$$

$$k^+ = a_k y^{+2} + b_k y^{+3} + \ldots, \tag{11e}$$

$$\epsilon^+ = 2a_k + 4b_k y^+ + \ldots, \tag{11f}$$

$$-\overline{v\theta}^+ = a_{v\theta} y^{+3} + b_{v\theta} y^{+4} + \ldots, \tag{11g}$$

$$\theta_{\rm rms} = a_\theta y^+ + b_\theta y^{+2} + \ldots, \tag{11h}$$

$$\epsilon_\theta^+ = a_{\epsilon\theta} + b_{\epsilon\theta} y^+ + \ldots, \tag{11i}$$

$$k^+/\epsilon^+ y^{+2} = 0.5, \tag{11j}$$

$$\theta_{\rm rms}^2/\epsilon_\theta^+ y^{+2} = (a_\theta)^2/a_{\epsilon\theta} = \Pr. \tag{11k}$$

With these expansions, an appropriate damping function can be proposed for f_λ. According to these expansions, the asymptotic behavior of the normal heat flux is y^3 as a wall is approached. This implies that α_t should also behave like y^3 near a wall. The damping functions proposed by Nagano et al. (1991) and Sommer et al. (1992) satisfy this requirement; however, the damping function of Nagano and Kim (1988) does not. If, in addition, the model is to work well with flows having different Pr, then α_t also has to be parametric in Pr. The effects of Pr can be accounted for in a manner similar to that proposed by van Driest (1956) in his attempt to include viscous effects in the evaluation of the incompressible, isothermal Reynolds shear stress near a wall. van Driest (1956) proposed a simple oscillator model to explain the damping effects of viscosity in the near-wall region and suggested a damping function that dies off exponentially away from the wall as a modifier to the eddy viscosity. If the flow is nonisothermal, fluid conductivity is also important in the near-wall region. It would influence the turbulent heat flux in a manner similar to the role played by viscosity in the determination of the Reynolds shear stress. Therefore, this suggests that the effects of viscosity and thermal conductivity could be accounted for by making the damping function f_λ to be parametric in y^+ and Pr. When these requirements are used to deduce a f_λ, the following expression is obtained:

$$f_\lambda = C_{\lambda 1}(1 - f_{\lambda 1})/{\rm Re}_t^{1/4} + f_{\lambda 1}, \tag{12}$$

where $C_{\lambda 1}$ is a model constant parametric in Pr, the damping function $f_{\lambda 1}$ is defined as $f_{\lambda 1} = [1 - \exp(-y^+/A^+)]^2$, and the model constant A^+ is also parametric in Pr. This expression is by no means unique. Other expressions that satisfy the asymptotic behavior outlined above could also be found. Typically, for flows with Pr $\approx$ 1, the values for $C_{\lambda 1}$ and A^+ are 0.1 and 40, respectively. Their variations with Pr will be determined in this investigation.

If the proposed model is to approach the high-Reynolds-number limit correctly, the model constants in Eqs. (8) and (9) cannot differ from conventional values adopted by other researchers. A generally acceptable set of values for these constants is given in the Nomenclature section. In other words, the near-wall correcting function $\xi_{\epsilon\theta}$ has to be determined so that Eqs. (8) and (9) would approach their high-Reynolds-number counterparts correctly, i.e., $\xi_{\epsilon\theta}$ would asymptote rapidly to zero away from a wall. When these constraints are used to derive $\xi_{\epsilon\theta}$ correct to order y near a wall, the following expression is obtained:

$$\xi_{\epsilon\theta} = f_{w,\epsilon\theta}\left[(C_{d4} - 4)\frac{\epsilon_\theta}{\overline{\theta^2}}\tilde{\epsilon}_\theta + C_{d5}\frac{\tilde{\epsilon}}{k}\epsilon_\theta - \frac{\epsilon_\theta^{*2}}{\overline{\theta^2}} + (2 - C_{d1} - C_{d2}\,\Pr)\frac{\epsilon_\theta}{\overline{\theta^2}}P_\theta^* \right]. \tag{13}$$

The presence of P_θ^* is a consequence of the constant wall heat flux boundary condition, where $\partial\Theta/\partial x$ is finite. Therefore, the near-wall correcting function is valid for all thermal wall boundary conditions. The damping function $f_{w,\epsilon\theta} = \exp[-({\rm Re}_t/80)^2]$ is introduced to ensure that the contribution of $\xi_{\epsilon\theta}$ would vanish rapidly away from the wall. Thus formulated, the model has no new constants compared to its high-Reynolds-number counterpart, except for the fact that $C_{\lambda 1}$ and A^+ are taken to be parametric in Pr. The functional dependence of $C_{\lambda 1}$ and A^+ on Pr will be determined in this study. With the equations so modified and consistent with the assumptions made in the derivation of Eqs. (11) and (13), the wall boundary conditions for $\overline{\theta^2}$ and ϵ_θ can now be stated as: $\overline{\theta^2} = 0$ and $\epsilon_\theta = (\epsilon_\theta)_w = \alpha(\partial\sqrt{\overline{\theta^2}}/\partial y)^2$.

Method of Solution

The second-order/eddy conductivity and k–ϵ/eddy conductivity models outlined in the previous two sections are used to calculate fully developed turbulent channel and pipe flows with constant wall temperature and constant wall heat flux boundary conditions. Under the assumption of fully developed flows in channels or pipes, the governing mean flow equations for constant-density fluids can be reduced to ordinary differential equations, or

$$\frac{1}{y^j}\frac{d}{dy}\left[y^j\left(\nu\frac{dU}{dy} - \overline{uv} \right)\right] - \frac{1}{\rho}\frac{dP}{dx} = 0, \tag{14}$$

$$\frac{1}{y^j}\frac{d}{dy}\left[y^j\left(\alpha\frac{d\Theta}{dy} - \overline{v\theta} \right)\right] - S = 0, \tag{15}$$

where $S = 2(2^j)Uq_w/(\rho C_p U_m D)$ is the source term with constant wall heat flux specified, $S = -q''/(\rho C_p)$ is the source term with constant wall temperature specified, $j = 0$ denotes channel flows, $j = 1$ denotes pipe flows, and dP/dx is related to the wall shear. Similarly, the modeled turbulence equations are also reducible to ordinary differential equations. Therefore, the governing equations can be solved by standard numerical techniques and the numerical errors are essentially the same for all calculated cases. The models are tested against flows with widely different Pr and Re. DNS data at low Re with Pr varying from 0.1 to 2 (Kim et al., 1987; Kim and Moin, 1989; Kasagi et al., 1992) are used to validate the models for their performance in the low Re and Pr range. The empirical formulae proposed by Skupinski et al. (1965), Notter and Sleicher (1972), Gnielinski (1976), and

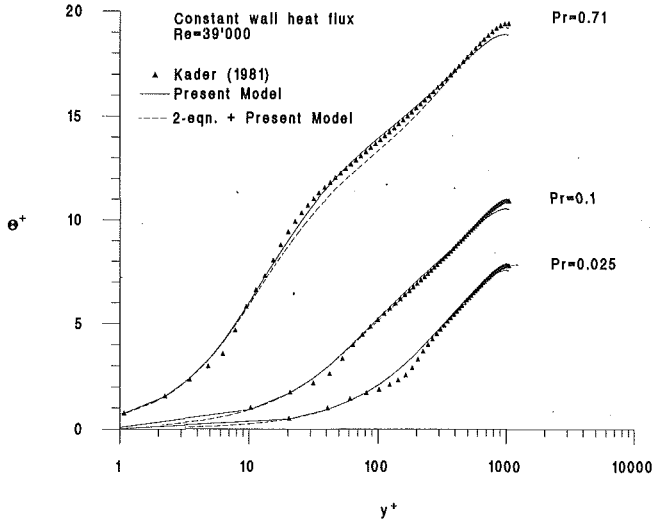

Fig. 1 Comparisons of Θ^+ with Kader's correlation for Pr < 1

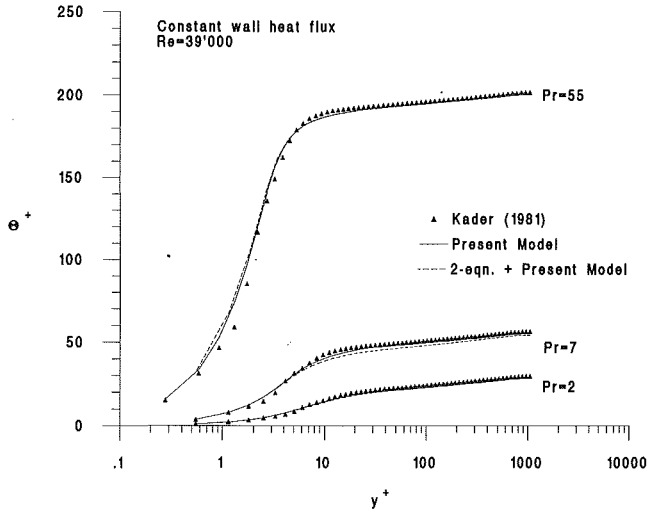

Fig. 2 Comparisons of Θ^+ with Kader's correlation for Pr < 10^2

Kader (1981) and the experimental measurements of Johnk and Hanratty (1962) and Hishida et al. (1986) are used to verify the models in the high Re and Pr range. These empirical formulae have been shown to correlate well with experimental measurements over a range of Re up to 10^6 and Pr varying from 0.01 to 10^4; therefore, they are most suitable for validating the present models.

Besides the wall boundary conditions stated above for $-\overline{u_i u_j}$, ϵ, θ^2, and ϵ_θ, no-slip condition is assumed for the velocity field at the wall, symmetry conditions are invoked for all variables at the pipe or channel centerline, and the appropriate thermal boundary condition is used to evaluate the temperature at the wall. The governing equations are solved by a relaxation scheme. With slight modifications, the numerical scheme and grid distribution proposed by Lai and So (1990b) and So et al. (1991b) are used to solve the modeled equations. The modifications involved refining the grid as Pr increases. Since the solutions have been shown to be grid independent (Lai and So, 1990b; So et al., 1991b), there is no need for such calculations to be repeated.

Results and Discussion

Calculations are first carried out to compare with the empirical temperature log-law deduced by Kader (1981). The empirical log-law is formulated based on numerous sets of pipe and channel flow data that encompass a wide range of Pr obtained with constant wall heat flux thermal boundary condition. The resultant formula is found to correlate well with all data sets examined. Therefore, this formula will be most suitable for use to evaluate the parametric dependence of $C_{\lambda 1}$ and A^+ on Pr. A series of calculations on fully developed pipe flow with heat transfer using the second-order/eddy conductivity model are carried out assuming constant wall heat flux thermal boundary condition. These calculations are made with Re = 40,000 over a wide range of Pr, varying from Pr = 0.025 to Pr = 10^3. The results are optimized by adjusting the values of $C_{\lambda 1}$ and A^+ and compared with the empirical formula of Kader (1981). Thus, the parametric dependence of $C_{\lambda 1}$ and A^+ on Pr can be determined and their values can be used to calculate other experiments for comparison. Some sample plots of the calculated temperature log-law are compared with Kader's (1981) empirical formula. In these plots are also shown the results obtained by using the $k-\epsilon$/eddy conductivity model with the same expressions for $C_{\lambda 1}$ and A^+. From this point on, the term "present model" is used to denote the second-order/eddy conductivity model, while "2-eqn + present model" is used to denote the $k-\epsilon$/eddy conductivity model. All plots are made nondimensional with Θ^+ versus log y^+. In Fig. 1, the plots for Pr < 1 are shown, while the results for 1 < Pr < 100 are given in Fig. 2. The calculations for Pr > 100 are compared in Fig. 3. It can be seen that, with proper choice of $C_{\lambda 1}$ and A^+, the calculated profiles correlate well with Kader's empirical formula in the range of Pr investigated. The agreement is not just limited to the log region. It also extends to the viscous region, and most important of all, the buffer region. Furthermore, about the same agreement is obtained irrespective of whether the second-order/eddy conductivity model or the $k-\epsilon$/eddy conductivity model is used to perform the calculations. This shows that basically the formulation is sound, the proposal for f_λ as given in Eq. (12) is applicable, and the postulate that $C_{\lambda 1}$ and A^+ are parametric in Pr is correct. The variations of $C_{\lambda 1}$ and A^+ with Pr are shown in Fig. 4 and the following relations for $C_{\lambda 1}$ and A^+ can be deduced: $A^+ = 10/\text{Pr}$ for Pr < 0.25 and $A^+ = 39/\text{Pr}^{1/16}$ for Pr ≥ 0.25; $C_{\lambda 1} = 0.4/\text{Pr}^{1/4}$ for Pr < 0.1 and $C_{\lambda 1} = 0.07/\text{Pr}$ for Pr ≥ 0.1. These results reveal that, for a wide range of Pr, $C_{\lambda 1}$ and A^+ vary as $(\text{Pr})^{-1}$ and A^+ is essentially constant for Pr > 0.25, while $C_{\lambda 1}$ remains approximately unchanged for Pr < 0.1.

Having deduced the parametric dependence of $C_{\lambda 1}$ and A^+ on Pr, the next step is to use them in conjunction with the second-order/eddy conductivity model to calculate the variations of Nu with Pr. Various empirical expressions for Nu covering the range

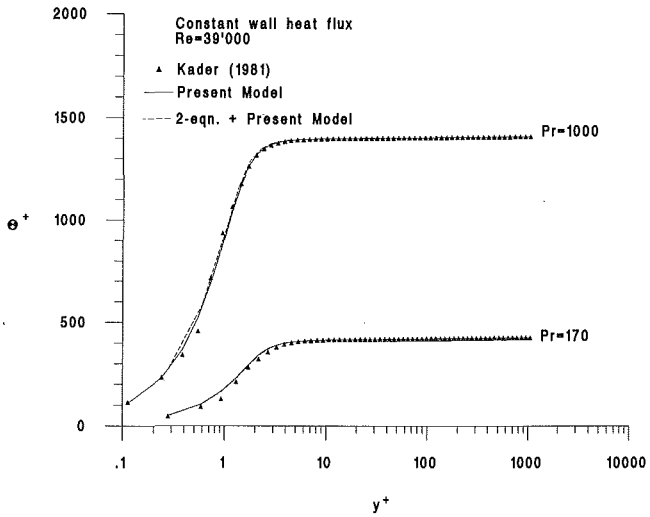

Fig. 3 Comparisons of Θ^+ with Kader's correlation for Pr < 10^4

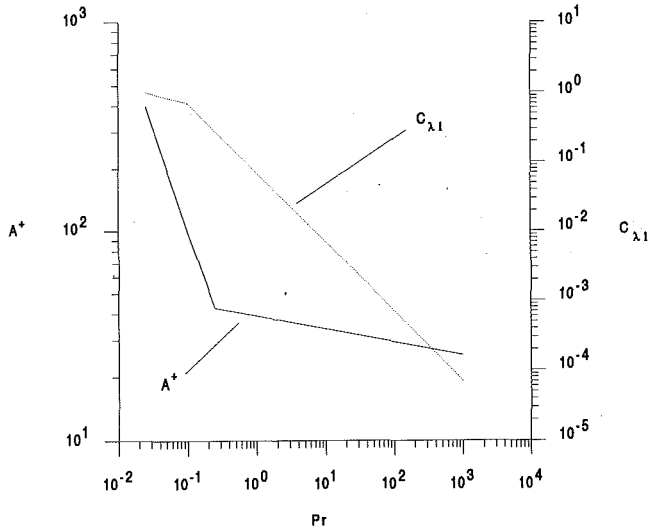

Fig. 4 Variations of $C_{\lambda 1}$ and A^+ with Pr

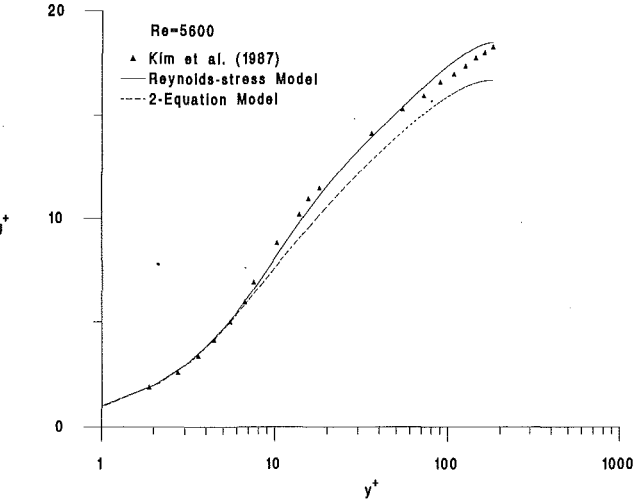

Fig. 6 Comparisons of U^+ with DNS data

of Pr from 0.025 to 10^4 and Re from 10^3 to 10^7 can be found in the literature. Among the more acceptable ones are those proposed by Skupinski et al. (1965), Notter and Sleicher (1972), and Gnielinski (1976). A comparison of the present calculations with these empirical formulae at two different Reynolds numbers is shown in Fig. 5. The two Reynolds numbers chosen are about one order of magnitude apart, therefore, the ability of the present formulation to predict low- as well as high-Reynolds-number flows is tested in this comparison. Good agreement with these formulae over the range of Pr and Re examined is obtained.

A third validation is carried out with the channel flow DNS velocity field data of Kim et al. (1987) and the mean temperature and temperature variance data of Kim and Moin (1989). The channel flow simulation is obtained assuming the wall temperature to be constant and uses the velocity field results of Kim et al. (1987). Three different Prandtl numbers have been investigated; these are Pr = 0.1, 0.71 and 2. Since these are incompressible flow calculations, only one set of velocity field results is required. The simulation is carried out at Re = 5600; therefore, $C_w = 0.0153$ is adopted. Both the second-order/eddy conductivity and $k-\epsilon$/eddy conductivity models are used to perform the calculations and their results are compared with the DNS data. Comparisons are made with both the velocity and temperature field data. The velocity properties compared are U^+, k^+, $-\overline{uv}^+$, u_{rms}, v_{rms}, and w_{rms}. The second-order model results are shown in Figs. 6, 7, and 8, while the $k-\epsilon$ model results are plotted in Figs. 6 and 7 only. It can be seen that the $k-\epsilon$ predictions of U^+ and k^+ are, in general, inferior to those given by the second-order model (Figs. 6 and 7). In particular, the prediction of the log law at low Reynolds number is very much in error (Fig. 6). The predictions of the normal stresses (Fig. 8) are in fair agreement with data; however, the discrepancies are probably due to the performance of the high-Reynolds-number models used to close the Reynold-stress equation. The temperature properties compared are Θ^+ and θ_{rms} and they are plotted in Figs. 9 and 10. In general, the calculated mean temperature profiles using the second-order/eddy conductivity and the $k-\epsilon$/eddy conductivity model correlate well with data. However, the same cannot be said of the Pr =2 model results. The reason can be attributed to the rather poor prediction of the mean velocity field. Overall, the comparison shown in Fig. 10 for θ_{rms} is fairly good. There is one exception though, and that is the underprediction of the maximum θ_{rms} for the Pr = 2 case (Fig. 10). The underprediction is significant and the reason for this is not clear. However, in all three cases compared, the near-wall behavior is predicted correctly, including the buffer region. On the other hand, the predictions of the $k-\epsilon$/eddy conductivity model are comparable to

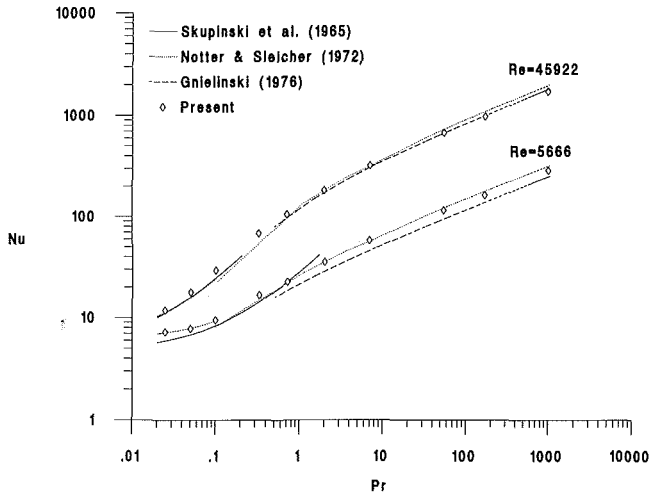

Fig. 5 Comparison of calculated Nu versus Pr with other established formulae

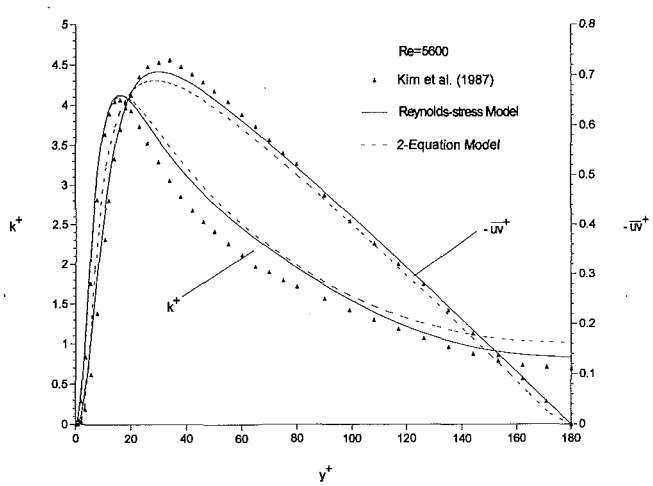

Fig. 7 Comparisons of k^+ and $-\overline{uv}^+$ with DNS data

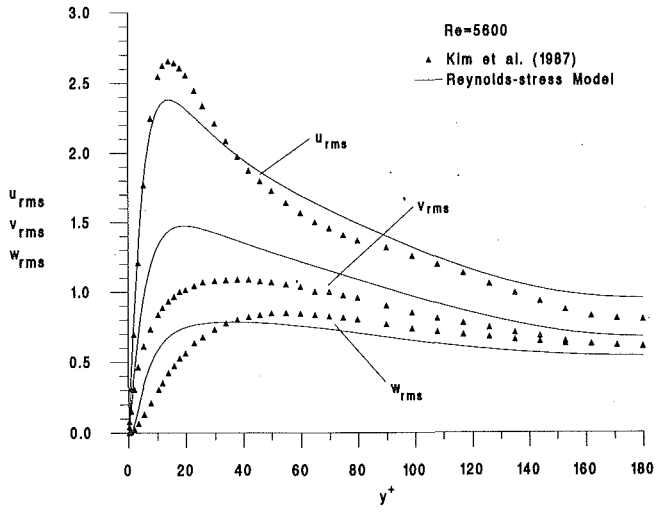

Fig. 8 Comparisons of u_{rms}, v_{rms}, w_{rms} with DNS data

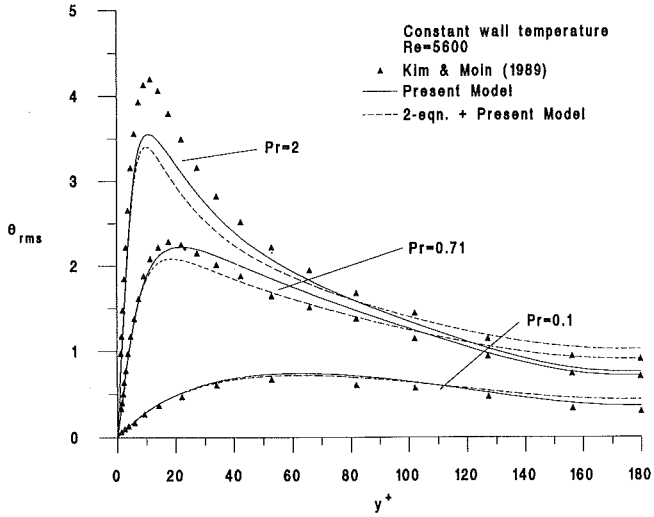

Fig. 10 Comparisons of θ_{rms} with DNS data

those of the second-order/eddy conductivity model for Θ^+ and are decidedly worst for θ_{rms}; it underpredicts the maximum θ_{rms} by an even wider margin and overpredicts the value of θ_{rms} near the center of the channel. Finally, the normalized dissipation rate of k is compared with DNS data (Fig. 11). The behavior of ϵ near a wall is reproduced correctly, i.e., the maximum of ϵ^+ is calculated at the wall and a local maximum away from the wall is also predicted.

A fourth comparison is carried out with the constant wall heat flux data of Kasagi et al. (1992). These data are obtained from direct numerical simulation of a fully developed channel flow at Re = 4560 and Pr = 0.71. In making this calculation, C_w = 0.00414 + 0.003(log Re) is used to determined the value of C_w. Furthermore, the values of $C_{\lambda 1}$ and A^+ are determined from Fig. 4. Results from both the second-order/eddy conductivity and $k-\epsilon$/eddy conductivity models are presented in Figs. 12 and 13. Only the comparisons of Θ^+, θ_{rms}, and $-\overline{v\theta}^+$ are shown in these figures. Near-wall asymptotic behavior of all properties shown is estimated correctly and the good correlation extends to the pipe center for θ_{rms} and $-\overline{v\theta}^+$ (Fig. 13). In general, the overall agreement between the predictions of the second-order/eddy conductivity model and data is good. Just as before, the $k-\epsilon$/eddy conductivity model results are in poorer agreement with data. For example, the model underpredicts the maximum θ_{rms} and overpredicts its value at the channel center (Fig. 13). As for the velocity field, according to Kasagi et al. (1992), it is very similar to that given by Kim et al. (1987). Therefore, it is not necessary to compare the velocity field results again. Finally, the comparison of the dissipation rate ϵ_θ is shown in Fig. 11. In this comparison, both the DNS data (Kasagi et al., 1992) and the experimental measurements (Krishnamoorthy and Antonia, 1987) are shown. The agreement in the near-wall region is poor; however, this does not seem to have too much of an effect on the predictions of other properties.

The ability of the second-order/eddy conductivity model to predict pipe flow heat transfer with constant wall heat flux thermal boundary condition at different Reynolds numbers is tested against the measurements of Johnk and Hanratty (1962) and Hishida et al. (1986). Comparisons are made with the mean temperature measurements of Johnk and Hanratty (1962) at four different Reynolds numbers that range from 17,700 to 77,200 (Fig. 14) and with the near-wall heat flux measurements of Hishida et al. (1986) at Re = 40,000 (Fig. 15). In these calculations, Pr = 0.71 is specified because the working fluid is air. In addition to presenting the calculations and the measurements, the empirical distributions given by Kader (1981) are also shown in Fig. 14 for comparison. It can be seen that the predictions are in very good agreement with the empirical relation proposed by Kader (1981). At high Reynolds numbers, the calculations are

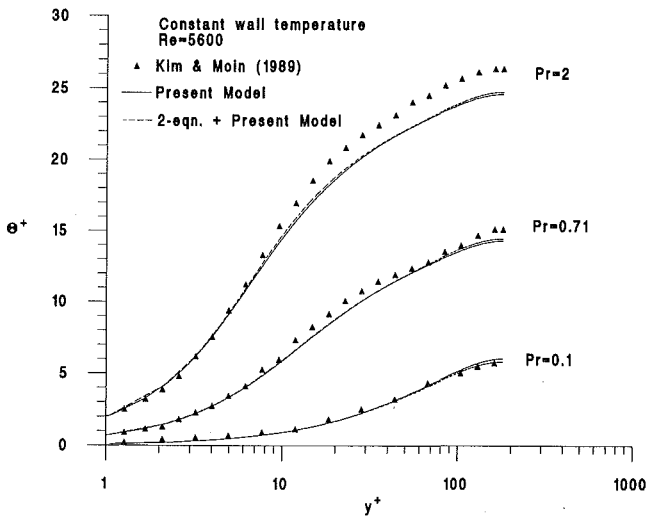

Fig. 9 Comparisons of Θ^+ with DNS data

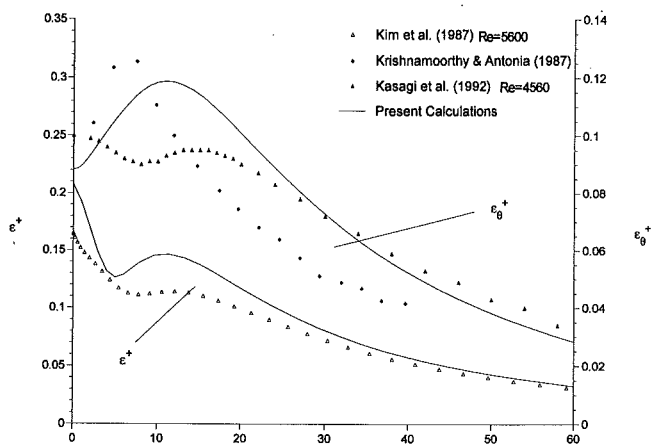

Fig. 11 Comparisons of ϵ^+ and ϵ_θ^+ with DNS data

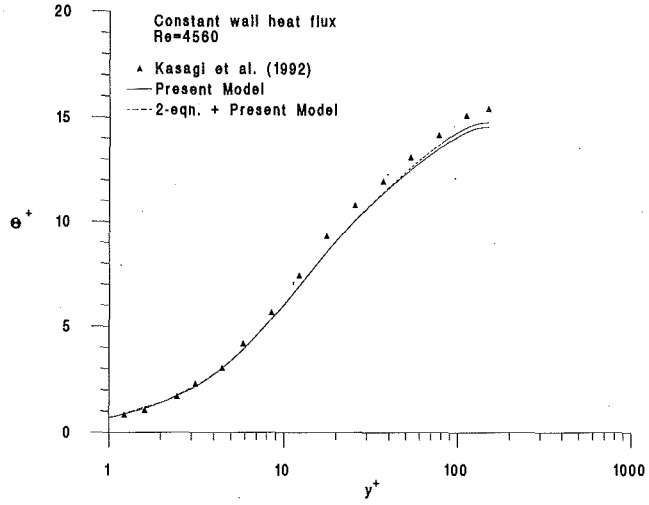

Fig. 12 Comparisons of Θ^+ with DNS data

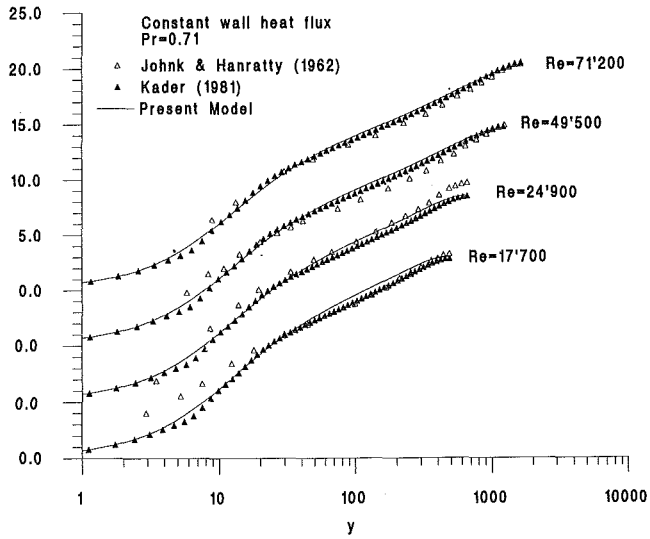

Fig. 14 Comparisons of Θ^+ with pipe flow measurements at high Reynolds numbers

also in good agreement with measurements. As the Reynolds number decreases, discrepancies begin to appear in the buffer region. Kader (1981) attributes these discrepancies to measurement errors in the near-wall region, which after all need to be corrected for wall proximity effects. In general, the calculated near-wall heat flux also compares well with measurements (Fig. 15).

A comparison of the leading coefficients in the expansions, Eqs. (11), with DNS data could validate the asymptotic consistency of the second-order/eddy conductivity model and would further lend credence to the suitability of the assumption $\overline{\theta^2} = 0$ at the wall for both constant heat flux and constant temperature wall boundary conditions. It should be pointed out that the asymptotes are determined from the plots given in the various DNS papers. Therefore, errors as much as 10 percent could occur. The near-wall asymptotes can be determined from the papers of Kim et al. (1987) and Kim and Moin (1989). However, only a_θ and $a_{\epsilon\theta}$ can be evaluated with some degree of accuracy from the paper of Kasagi et al. (1992). Consequently, these are the only values reported in Table 1. From the DNS data of Kim et al. (1987), the following values are obtained: $a_u = 0.36$, $a_v = 0.9 \times 10^{-2}$, $a_w = 0.19$, $a_{uv} = 0.72 \times 10^{-3}$, $a_k = 0.083$, and $k^+/\epsilon^+ y^{+2} = 0.5$. The model calculations are 0.41, 0.24×10^{-2}, 0.21, 1.55×10^{-3}, 0.109, and 0.5, respectively. These values are in good agreement with DNS data and $k^+/\epsilon^+ y^{+2} = 0.5$ is reproduced exactly. This comparison lends credence to the second-order model for the velocity field. The calculated coefficients for the temperature field are compared with DNS data in Table 1. Good correlation with data is obtained and the behavior $(a_\theta)^2/a_{\epsilon\theta} = \mathrm{Pr}$ is recovered correctly. In general, the best agreement with data is given by a_θ and the worst by $a_{v\theta}$. The discrepancy could be partially attributed to the not so correct prediction of the near-wall behavior of the normal stress in the y direction (Fig. 8).

Overall, it can be seen that the eddy conductivity model for the temperature field is asymptotically consistent and the assumption $\overline{\theta^2} = 0$ at the wall appears to be applicable for both constant heat flux and constant temperature wall boundary conditions for the test cases examined.

Conclusions

A turbulent heat transfer model for flows with widely different Prandtl numbers has been formulated. The model is based on a near-wall second-order model for the velocity field and a near-wall two-equation model for the temperature field. These models

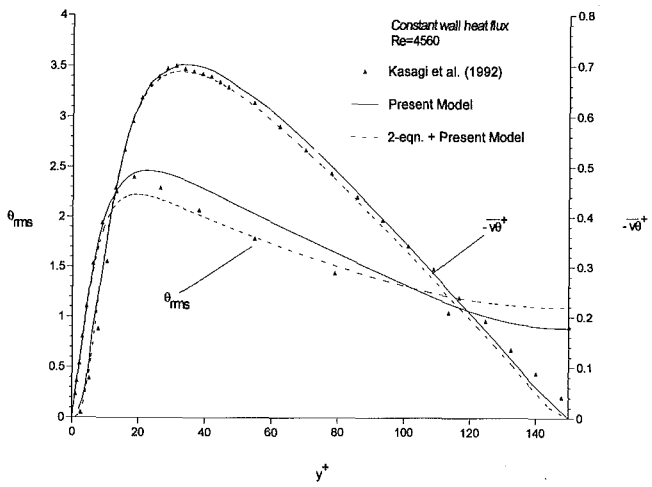

Fig. 13 Comparisons of θ_{rms} and $-\overline{v\theta}^+$ with DNS data

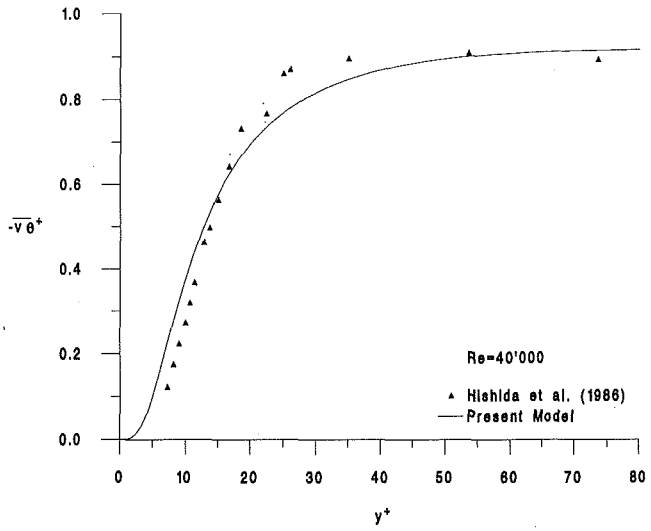

Fig. 15 Comparison of $-\overline{v\theta}^+$ with measurements in the near-wall region

Table 1 Comparison of the calculated near-wall coefficients for the temperature field with data

	Pr of fluid	$a_{v\theta} \times 10^3$	a_θ	$a_{\varepsilon\theta} \times 10^2$	$\theta_{rms}^2 / \varepsilon_\delta^* y^{+2}$
DNS data (Kasagi et al. 1992)	0.71		0.253	9.01	0.71
Model calculations	---	0.784	0.252	8.94	0.71
DNS data (Kim and Moin 1989)	0.1	0.674	0.0265	0.7023	0.1
Model calculations	---	0.292	0.033	1.088	0.1
DNS data (Kim and Moin 1989)	0.71	0.479	0.255	9.159	0.71
Model calculations	---	0.861	0.247	8.581	0.71
DNS data (Kim and Moin 1989)	2.0	1.358	0.746	27.83	2.0
Model Calculations	---	1.507	0.603	18.17	2.0

are formulated to satisfy the exact wall boundary conditions as well as the near-wall asymptotics of the turbulence statistics of both the velocity and temperature fields. As a result, the modeled equations are asymptotically consistent with the exact equations near a wall, at least to the first order of the wall normal coordinate. Gradient transport is assumed for the normal heat flux and the eddy conductivity is evaluated from the calculated temperature variance and its dissipation rate. Both velocity and thermal time scales are used to determine the eddy conductivity. All constants derived from the high-Reynolds-number models are adopted without change for the present calculations. Two additional constants, $C_{\lambda 1}$ and A^+, are introduced in the eddy conductivity model and they are postulated to be parametric in Pr. The damping function containing these two constants has to satisfy certain near-wall constraints and the conditions are used to determine the variations of $C_{\lambda 1}$ and A^+ with Pr.

This analysis yields two simple parametric relations for $C_{\lambda 1}$ and A^+. For $Pr > 0.1$, $C_{\lambda 1}$ varies as Pr^{-1}. However, for $Pr < 0.1$, $C_{\lambda 1}$ is essentially constant. On the other hand, A^+ varies as Pr^{-1} for $Pr < 0.25$ and remains relatively constant for values of Pr greater than 0.25. Thus determined, these expressions are used to calculate the variations of Nu with Pr and the results are compared with established formulae covering a wide range of Pr and Re. Good agreement is obtained for the range of Pr and Re examined. The second-order/eddy conductivity model is further applied to calculate fully developed pipe flow heat transfer with constant wall heat flux and constant wall temperature boundary conditions. The calculations over a range of Pr are compared with DNS data and good correlation with data is obtained. In particular, the near-wall asymptotics are predicted correctly and the limiting behavior at the wall for the dissipation rates of the turbulent kinetic energy and the temperature variance is recovered. The good agreement extends to the pipe center for mean flow properties, but they are not as good for some turbulence statistics far away from the wall. In spite of the slight discrepancy noted in the outer region, the calculated mean flow and turbulence properties are in good agreement with DNS data in the buffer region.

Acknowledgments

Funding support under Grant No. NAG-1-1080 from NASA Langley Research Center, Hampton, Virginia 23665, is gratefully acknowledged. The grant is monitored by Dr. T. B. Gatski.

References

Antonia, R. A., and Kim, J., 1991a, "Reynolds Shear Stress and Heat Flux Calculations in a Fully Developed Turbulent Duct Flow," *International Journal of Heat and Mass Transfer,* Vol. 34, pp. 2013–2018.

Antonia, R. A., and Kim, J., 1991b, "Turbulent Prandtl Number in the Near-Wall Region of a Turbulent Channel Flow," *International Journal of Heat and Mass Transfer,* Vol. 34, pp. 1905–1908.

Cebeci, T., and Bradshaw, P., 1984, *Physical and Computational Aspects of Convective Heat Transfer,* Springer-Verlag, Berlin, Germany, pp. 13 and 150–151.

Chen, C. J., and Chiou, J. S., 1981, "Laminar and Turbulent Heat Transfer in the Pipe Entrance Region for Liquid Metals," *International Journal of Heat and Mass Transfer,* Vol. 24, pp. 1179–1189.

Gnielinski, V., 1976, cited in: F. P. Incropera and D. P. deWitt, *Fundamentals of Heat and Mass Transfer,* 3rd ed., Wiley, New York, 1990, p. 497.

Hishida, M., Nagano, Y., and Tagawa, M., 1986, "Transport Processes of Heat and Momentum in the Wall Region of Turbulent Pipe Flow," *Proceedings of the 8th International Heat Transfer Conference,* Vol. 3, pp. 925–930.

Jischa, M., and Rieke, H. B., 1979, "About the Prediction of Turbulent Prandtl and Schmidt Numbers From Modeled Transport Equations," *International Journal of Heat and Mass Transfer,* Vol. 22, pp. 1547–1555.

Johnk, R. E., and Hanratty, T. J., 1962, "Temperature Profiles for Turbulent Flow of Air in a Pipe—I. The Fully Developed Heat Transfer Region," *Chemical Engineering Sciences,* Vol. 17, pp. 867–879.

Kader, B. A., 1981, "Temperature and Concentration Profiles in Fully Turbulent Boundary Layers," *International Journal of Heat and Mass Transfer,* Vol. 24, pp. 1541–1544.

Kasagi, N., and Ohtsubo, Y., 1992, "Direct Numerical Simulation of Low Prandtl Number Thermal Field in a Turbulent Channel Flow," *Turbulent Shear Flows 8,* Springer-Verlag, Berlin, Germany, pp. 97–119.

Kasagi, N., Tomita, Y., and Kuroda, A., 1992, "Direct Numerical Simulation of the Passive Scalar Field in a Turbulent Channel Flow," ASME JOURNAL OF HEAT TRANSFER, Vol. 114, pp. 598–606.

Kays, W. M., and Crawford, M. E., 1980, *Convective Heat and Mass Transfer,* 2nd ed., McGraw-Hill, New York, pp. 227–229.

Kim, J., Moin, P., and Moser, R. D., 1987, "Turbulence Statistics in Fully Developed Channel Flow at Low Reynolds Number," *Journal of Fluid Mechanics,* Vol. 177, pp. 133–186.

Kim, J., and Moin, P., 1989, "Transport of Passive Scalars in a Turbulent Channel Flow," *Turbulent Shear Flows 6,* Springer-Verlag, Berlin, Germany, pp. 85–96.

Krishnamoorthy, L. V., and Antonia, R. A., 1987, "Temperature Dissipation Measurements in a Turbulent Boundary Layer," *Journal of Fluid Mechanics,* Vol. 176, pp. 265–281.

Lai, Y. G., and So, R. M. C., 1990a, "Near-Wall Modeling of Turbulent Heat Fluxes," *International Journal of Heat and Mass Transfer,* Vol. 33, pp. 1429–1440.

Lai, Y. G., and So, R. M. C., 1990b, "On Near-Wall Turbulent Flow Modeling," *Journal of Fluid Mechanics,* Vol. 221, pp. 641–673.

Launder, B. E., Reece, G. J., and Rodi, W., 1975, "Progress in the Development of a Reynolds Stress Turbulence Closure," *Journal of Fluid Mechanics,* Vol. 68, pp. 537–566.

Launder, B. E., 1976, "Heat and Mass Transport," *Topics in Applied Physics—Turbulence,* P. Bradshaw, ed., Vol. 12, pp. 232–287.

Lyons, S. L., Hanratty, T. J., and McLaughlin, J. B., 1991, "Direct Numerical Simulation of Passive Heat Transfer in a Turbulent Channel Flow," *International Journal of Heat and Mass Transfer,* Vol. 34, pp. 1149–1161.

Myong, H. K., Kasagi, N., and Hirata, M., 1989, "Numerical Prediction of Turbulent Pipe Flow Heat Transfer for Various Prandtl Number Fluids With Improved k–ϵ Turbulence Model," *JSME International Journal,* Series II, Vol. 32, pp. 613–623.

Myong, H. K., and Kasagi, N., 1990, "A New Approach to the Improvement of the k–ϵ Turbulence Model for Wall Bounded Shear Flows," *JSME International Journal,* Series II, Vol. 33, pp. 63–72.

Nagano, Y., and Kim, C., 1988, "A Two-Equation Model for Heat Transport in Wall Turbulent Shear Flows," ASME JOURNAL OF HEAT TRANSFER, Vol. 110, pp. 583–589.

Nagano, Y., Tagawa, M., and Tsuji, T., 1991, "An Improved Two-Equation Heat Transfer Model for Wall Turbulent Shear Flows," *Proceedings of the 3rd ASME–JSME Thermal Engineering Joint Conference,* Vol. 3, pp. 223–240.

Notter, R. H., and Sleicher, C. A., 1971, "The Eddy Diffusivity in the Turbulent Boundary Layer Near a Wall," *Chemical Engineering Science,* Vol. 26, pp. 161–171.

Notter, R. H., and Sleicher, C. A., 1972, "A Solution to the Turbulent Graetz Problem—III. Fully Developed and Entry Region Heat Transfer Rates," *Chemical Engineering Science,* Vol. 27, pp. 2073–2093.

Patel, V. C., Rodi, W., and Scheuerer, G., 1985, "Turbulence Models for Near-Wall and Low-Reynolds-Number Flows: A Review," *AIAA Journal,* Vol. 23, pp. 1308–1319.

Petukhov, B. S., 1970, "Heat Transfer and Friction in Turbulent Pipe Flow With Variable Physical Properties," *Advances in Heat Transfer,* Vol. 6, pp. 503–564.

Polyakov, A. F., 1974, "Wall Effect on Temperature Fluctuations in the Viscous Sublayer," *Teplofizika Vysokikh Temperatur,* Vol. 20, pp. 328–337.

Quarmby, A., and Quirk, R., 1974, "Axisymmetric and Non-axisymmetric Turbulent Diffusion in a Plain Circular Tube at High Schmidt Number," *International Journal of Heat and Mass Transfer,* Vol. 17, pp. 143–147.

Skupinski, E., Tortel, J., and Vautrey, L., 1965, "Determination des Coefficients de Convection d'un Alliage Sodium–Potassium Dans un Tube Circulaire," *International Journal of Heat and Mass Transfer,* Vol. 8, pp. 937–951.

Sleicher, C. A., and Rouse, M. W., 1975, "A Convenient Correlation for Heat Transfer to Constant and Variable Property Fluids in Turbulent Pipe Flow," *International Journal of Heat and Mass Transfer,* Vol. 18, pp. 677–683.

So, R. M. C., Zhang, H. S., and Speziale, C. G., 1991a, "Near-Wall Modeling of the Dissipation-Rate Equation," *AIAA Journal,* Vol. 29, pp. 2069–2076.

So, R. M. C., Lai, Y. G., Zhang, H. S., and Hwang, B. C., 1991b, "Second-Order Near-Wall Turbulence Closures: A Review," *AIAA Journal,* Vol. 29, pp. 1819–1835.

So, R. M. C., Yuan, S. P., and Sommer, T. P., 1992, "A Hierarchy of Near-Wall Closures for Turbulent Heat Transfer," *Research Trends,* Vol. 2, pp. 203–221.

Sommer, T. P., So, R. M. C., and Lai, Y. G., 1992, "A Near-Wall Two-Equation Model for Turbulent Heat Fluxes," *International Journal of Heat and Mass Transfer,* Vol. 35, pp. 3375–3387.

Sommer, T. P., So, R. M. C., and Zhang, H. S., 1993a, "A Near-Wall Variable-Prandtl-Number Turbulence Model for Compressible Flows," *AIAA Journal,* Vol. 31, pp. 27–35.

Sommer, T. P., So, R. M. C., and Zhang, H. S., 1993b, "On the Assumption of Vanishing Temperature Fluctuations at the Wall for Heat Transfer Modeling," AIAA Paper No. 93-0088.

van Driest, E. R., 1956, "On Turbulent Flow Near a Wall," *Journal of Aeronautical Sciences,* Vol. 23, pp. 1007–1011, 1036.

Zhang, H. S., So, R. M. C., and Zhu, M. L., 1993a, "A Near-Wall Second-Order Turbulence Model and Its Application to Wall-Bounded Flows," *Proceedings of the 9th Symposium on Turbulent Shear Flows,* Kyoto, Japan, Aug. 16–18, 1993.

Zhang, H. S., So, R. M. C., Gatski, T. B., and Speziale, C. G., 1993b, "A Near-Wall Second-Order Closure for Compressible Turbulent Flows," *Near-Wall Turbulent Flows,* R. M. C. So, C. G. Speziale, and B. E. Launder, eds., Elsevier, Amsterdam, pp. 209–218.

ERRATA

To the paper "Solidification of Liquid Metal Droplets Impacting Sequentially on a Solid Substrate." by B. Kang, Z. Zhao, and D. Poulikakos, published in the ASME JOURNAL OF HEAT TRANSFER, Vol. 116, May 1994, pp. 436–445.

The following corrections need to be made in the appendix of the above paper. The right-hand side of Eq. (A1) should be multiplied by the factor $(6/d)$. The thermophysical properties in this equation are obviously those of the droplet material. The second term in the left-hand side of Eq. (A4) should be multiplied by the factor $(6/d)(k/k_{\text{drop}})$. The symbol α in this equation denotes the thermal diffusivity of the droplet material. The expression inside the curly bracket of Eq. (A6) should read as follows:

$$-(2 + 0.4\,\mathrm{Re}^{1/2}\mathrm{Pr}^{1/3})\,\frac{6}{d}\,\frac{k}{k_{\text{drop}}}\,\frac{\alpha_{\text{drop}}t}{d}\,.$$

These corrections have absolutely no effect on any of the results or formulations in the paper since the appendix was only used to obtain an estimate of the droplet temperature at impact, which was not utilized in any of the calculations.

Heat Transfer Modeling and the Assumption of Zero Wall Temperature Fluctuations

T. P. Sommer

R. M. C. So

H. S. Zhang

Mechanical and Aerospace Engineering,
Arizona State University,
Tempe, AZ 85287

At present, it is not clear how the fluctuating temperature at the wall can be properly specified for near-wall turbulent heat-flux models. The conventional approach is to assume zero fluctuating temperature or zero gradient for the temperature variance at the wall. These are idealized specifications and the latter condition could lead to an ill-posed problem for fully developed pipe and channel flows. In this paper, the validity and extent of the zero fluctuating wall temperature condition for heat transfer calculations are examined. The approach taken is to assume Taylor series expansions in the wall normal coordinate for the fluctuating quantities that are general enough to account for both zero and nonzero temperature fluctuations at the wall and to develop a near-wall turbulence model allowing finite values of the wall temperature variance. As for the wall temperature variance boundary condition, it is estimated by solving the coupled heat transfer problem between the fluid and the solid wall. The eddy thermal conductivity is calculated from the temperature variance and its dissipation rate. Heat transfer calculations assuming both zero and nonzero fluctuating wall temperature reveal that the zero fluctuating wall temperature assumption is quite valid for the mean field and the associated integral heat transfer properties. The effects of nonzero fluctuating wall temperature on the fluctuating field are limited only to a small region near the wall for most fluid/solid combinations considered.

Introduction

When solving the Reynolds-averaged momentum and energy equations for turbulent flows, the use of an asymptotically consistent near-wall model has been shown to be crucial for the success of the calculations (So et al., 1991; Zhang et al., 1993). Proper wall boundary conditions for the turbulence statistics are required for a near-wall model. This is straightforward for the velocity field. From the no-slip condition, it follows that the instantaneous velocities have to be the same as the wall velocity. Therefore, the fluctuating velocities and the Reynolds stresses vanish at the wall. Consequently, the near-wall behavior of the Reynolds stresses can be analyzed using Taylor series expansions in the wall normal coordinate and the leading coefficients of these expansions are identically zero.

The appropriate boundary conditions for the temperature field, on the other hand, cannot be easily specified. Due to unsteady heat conduction in the wall, the temperature fluctuations at the wall are not necessarily zero. The boundary conditions for the fluctuating temperature are also not known in the case of heat transfer experiments. Quite often, isothermal and isoflux wall boundary conditions are specified. In the most ideal situation, isothermal wall boundary condition implies that the fluctuating wall temperature is zero, i.e., $\theta_w = 0$. On the other hand, isoflux wall boundary condition gives rise to a zero first derivative of the temperature variance at the wall. In practical applications, however, these ideal conditions are not likely to occur. Rather, it is normally assumed that the mean temperature or the mean heat flux is constant, but not their instantaneous counterparts. These specifications leave the wall fluctuations undetermined. In spite of these realities, most current calculations assume $\theta_w = 0$.

Direct numerical simulations (DNS) of heat transfer in a two-dimensional channel have been attempted by Kim and Moin (1989). They tackled the case of an ideal isothermal wall with an internal heat source, i.e., $\Theta_w = 0$ and $\theta_w = 0$. Kasagi et al. (1992), on the other hand, assumed a constant wall heat flux boundary condition. This could be achieved by holding the wall temperature constant in time, but varying it with a constant gradient along the channel walls. Such a treatment is essentially equivalent to assuming $\theta_w = 0$. Therefore, it is obvious that, even for DNS calculations, approximations concerning temperature fluctuations at the wall cannot be avoided as long as the calculations are performed for the fluid side only.

The simplest turbulent heat transfer model is obtained by assuming gradient transport and a constant turbulent Prandtl number across the flow. Turbulent normal heat flux can then be related to the Reynolds shear stress. Since no boundary condition needs to be specified for the temperature variance or the turbulent heat flux, the problem with the fluctuating thermal boundary conditions is avoided. However, closer examination reveals that since the heat flux is related to the Reynolds shear stress, and since the shear stress is zero at the wall, this model tacitly assumes $\theta_w = 0$.

The two-equation heat-flux models of Nagano and Kim (1988), Sommer et al. (1992), and So and Sommer (1994), as well as the second-order heat-flux model of Lai and So (1990), specify $\theta_w = 0$ as boundary condition for the calculations of heat fluxes, temperature variance, and its dissipation rate. Even then, the models give good predictions of the mean temperature profiles when compared with DNS data. Furthermore, the latter three models also yield good agreement in their predictions of the asymptotic behavior of the turbulence statistics near the wall (Sommer et al., 1992; So and Sommer, 1994). This can be attributed to the use of the same thermal boundary conditions as the DNS calculations. Comparisons with heat transfer measurements are also quite good, although the boundary conditions assumed for the temperature fluctuations may not be identical to those specified for the experiments (So and Sommer, 1994).

Nagano et al. (1991) modified Nagano and Kim's (1988) model to allow for nonzero temperature fluctuations at the wall. Nagano et al. (1991) then performed calculations of a flat plate boundary layer with an ideal isoflux wall boundary condition, i.e., $\bar{q}_w$ = constant and $q'_w = 0$, and obtained good agreement

Contributed by the Heat Transfer Division for publication in the JOURNAL OF HEAT TRANSFER. Manuscript received by the Heat Transfer Division March 1993; revision received November 1993. Keywords: Forced Convection, Modeling and Scaling, Turbulence. Associate Technical Editor: R. J. Simoneau.

with measurements. This is an idealized thermal boundary condition and would lead to an ill-posed problem for the temperature variance equation in the case of a fully developed channel flow. In view of this, the ideal isoflux wall boundary condition is not a viable alternative to the zero fluctuating wall temperature specified by such researchers as Nagano and Kim (1988), Sommer et al. (1992), So and Sommer (1994), and Lai and So (1990). Therefore, the question of a correct thermal boundary condition for near-wall heat transfer modeling still remains.

Some work has been carried out to estimate temperature fluctuations at the wall. For example, Polyakov (1974) presented an analytic solution for the coupled problem of temperature fluctuations in the viscous sublayer of a turbulent flow adjacent to a semi-infinite solid. His results lead to a spectrum for the temperature fluctuations at the wall. The spectrum can be integrated to give the temperature variance at the wall. Thus calculated, the temperature variance depends on the heat transfer interaction between the fluid and the solid. Two parameters characterizing this interaction are K, the thermal activity ratio, and Pr, the Prandtl number of the fluid. For small values of K, heat conduction in the wall is much more efficient than that in the fluid and fluctuations are transported away from the wall quickly. Therefore, the temperature variance at the wall is small for low values of K. In general, θ_{rms} increases with increasing K. Kasagi et al. (1989) investigated this conjugate heat transfer problem numerically. They used a structural turbulence model to determine the velocity field for the region close to the wall and solved the time-dependent heat conduction problem in the solid as well as in the fluid region very near the wall. For a very thick wall, the results are in good agreement with Polyakov's (1974) analysis for a semi-infinite wall. When K becomes large, their results show that θ_{rms} asymptotes to a constant value for a given Pr. The limiting value is identical to that obtained for an ideal isoflux wall. Their calculations give important information about the conjugate heat transfer problem. However, this procedure is not very convenient and cannot be directly applied to engineering heat transfer calculations. Likewise, Polyakov's (1974) analytical results are very useful in estimating the temperature fluctuations at the wall; however, due to the assumed geometry, they cannot be easily extended to calculate general heat transfer problems. These results are nevertheless very important because, for the first time, they allow reasonable estimates of the temperature fluctuations that can be expected for various fluid/solid combinations.

From this discussion, it is clear that most methods used to solve the conjugate heat transfer problem are not very practical. The more practical near-wall modeling approaches (Nagano and Kim, 1988; Sommer et al., 1992; So and Sommer, 1993; Lai and So, 1990) yield solutions on the fluid side only and essentially decouple the heat transfer problem on the fluid side from that on the solid side. Consequently, there is a need to invoke an assumption for the wall temperature fluctuations. Clearly, the assumption of vanishing temperature fluctuations at the wall is the most convenient one. It is for this reason that the assumption has been adopted by most researchers to date. The validity and extent of this assumption can be assessed by comparing the calculated results with other estimates that are not based on this assumption. Furthermore, the calculations can be compared to experimental measurements, even though most data available do not report on the temperature fluctuations at the wall.

The present objective is to attempt a validation of the zero fluctuating wall temperature assumption for heat transfer modeling and the approach taken is to use the results of Polyakov (1974) and Kasagi et al. (1989) to estimate those wall temperature fluctuations that could be realistically expected. These estimates, therefore, provide the boundary conditions for a near-wall turbulence model that is formulated to handle zero as well as nonzero wall temperature fluctuations. Since the model of So and Sommer (1994) has been shown to be valid for a wide range

Nomenclature

A^+ = model constant taken to be parametric in Pr
a_k = coefficients in the expansion for k^+ in the near-wall region
a_u, b_u = coefficients in the expansion for u_{rms} in the near-wall region
a_v = coefficients in the expansion for v_{rms} in the near-wall region
a_w, b_w = coefficients in the expansion for w_{rms} in the near-wall region
a_{uv}, b_{uv} = coefficients in the expansion for $-\overline{uv}^+$ in the near-wall region
a_θ, b_θ = coefficients in the expansion for θ_{rms} in the near-wall region
$a_{v\theta}$, $b_{v\theta}$ = coefficients in the expansion for $-\overline{v\theta}^+$ in the near-wall region
$a_{\epsilon\theta}$, $b_{\epsilon\theta}$ = coefficients in the expansion for ϵ_θ^+ in the near-wall region
C_1 = model constant = 1.50
C_2 = model constant = 0.40
C_s = model constant = 0.11
C_ϵ = model constant = 0.10
$C_{\epsilon 1}$ = model constant = 1.50
$C_{\epsilon 2}$ = model constant = 1.83
C_p = specific heat at constant pressure
$C_{\lambda 1}$ = model constant taken to be parametric in Pr
C_{d1} = model constant = 1.8
C_{d2} = model constant = 0
C_{d3} = model constant = 0.72
C_{d4} = model constant = 2.2
C_{d5} = model constant = 0.8
C_w = model coefficient that is a function of Re
C_λ = model constant = 0.095
C_μ = model constant = 0.096
C_{θ^2} = model constant = 0.11
$C_{\epsilon\theta}$ = model constant = 0.11
D = pipe diameter or channel height
D_{ij} = production tensor = $-[\overline{u_iu_k}(\partial U_k/\partial x_j) + \overline{u_ju_k}(\partial U_k/\partial x_i)]$
D_{ij}^T = turbulent diffusion tensor
f_{w1} = near-wall damping function for Reynolds-stress equation = $\exp[-(\text{Re}_t/150)^2]$
f_{w2} = near-wall damping function for ϵ equation = $\exp[-(\text{Re}_t/40)^2]$
$f_{w,\epsilon\theta}$ = near-wall damping function for ϵ_θ equation = $\exp[-(\text{Re}_t/80)^2]$
$f_{w\epsilon\theta,1}$ = near-wall damping function for ϵ_θ equation = $\exp(-\text{Re}_T/10)$
f_λ = near-wall damping function for turbulent heat diffusivity
$f_{\lambda 1}$ = near-wall damping function = $[1 - \exp(-y^+/A^+)]^2$
f_μ = damping function = $[1 + 3.45/\sqrt{\text{Re}_t}]\tanh[y^+/115]$
K = thermal activity ratio = $\sqrt{(\rho C_P\kappa)_{\text{fluid}}/(\rho C_P\kappa)_{\text{solid}}}$
k = turbulent kinetic energy
k^+ = normalized turbulent kinetic energy = k/u_τ^2
L = model constant = 2
M = model constant = 2
N = model constant = 1.5
n_i = unit normal vector measured positive outward from wall
Nu = Nusselt number
P = mean pressure
$\tilde{P}$ = production of k due to mean shear = $-\overline{u_iu_j}(\partial U_i/\partial x_j)$
P_{ij} = production of the Reynolds stresses = $-[\overline{u_iu_k}(\partial U_j/\partial x_k) + \overline{u_ju_k}(\partial U_i/\partial x_k)$
P_θ = production due to mean temperature = $-\overline{u_k\theta}[\partial\Theta/\partial x_k]$
P_θ^* = production term due to mean temperature gradient in the x direction
Pr = Prandtl number
Pr_t = turbulent Prandtl number
$\bar{q}_w$ = mean wall heat flux
q_w' = fluctuating wall heat flux
Re = Reynolds number based on mean bulk velocity = U_mD/ν

of Pr, it serves as a convenient starting point for the present analysis. The model needs to be modified in order to account for the change in the wall thermal boundary conditions. This is accomplished through asymptotic analysis in a manner similar to that outlined by Sommer et al. (1992). The modified model is used to calculate fully developed turbulent channel flows. Estimated values of the temperature variance from the analysis of Polyakov (1974) and Kasagi et al. (1989) are used to calculate the near-wall asymptotes for a wide range of Pr and for different combinations of fluid and solid. Since the results of Polyakov (1974) and Kasagi et al. (1989) are only valid for incompressible flows, the present analysis is also limited by this assumption.

The results obtained with the earlier models (Nagano and Kim, 1989; Sommer et al., 1992; So and Sommer, 1994; Lai and So, 1990) agree well with measurements (Hishida et al., 1986; Johnk and Hanratty, 1962) that are likely to have nonzero temperature fluctuations at the wall. Therefore, it is expected that, outside the viscous sublayer, the calculated temperature variance and its dissipation rate obtained with the new formulation should not differ significantly from previous calculations. If this is true, it would lend credence to the use of the assumption of vanishing temperature fluctuations at the wall, thus greatly simplifying heat transfer modeling and calculations.

Near-Wall Model for Reynolds Stresses

In turbulent incompressible flow modeling, the uncoupled-flow approximation (Cebeci and Bradshaw, 1984) can be applied. As a result, velocity field models affect the temperature field calculations but not vice versa. This means that a velocity field model can be chosen independent of the near-wall model for turbulent heat transfer. It is commonly assumed (Cebeci and Bradshaw, 1984; So and Sommer, 1994) that turbulence models for the velocity field should be of equal or higher order than those invoked for the temperature field. The present approach proposes the use of a two-equation model for turbulent heat transfer. Therefore, a second-order near-wall turbulence model would be most appropriate for the Reynolds stresses. Since the focus of this investigation is on the temperature field, the relative merits of the different near-wall models for the velocity field are not discussed in detail here. Rather, a recent near-wall model proposed by Zhang et al. (1993) that has been validated against different flows is adopted in the present study. The model derivation and validation have previously been described in detail by Zhang et al. (1993). Therefore, they will not be repeated here. Instead, for the sake of completeness, the model equations are quoted below as:

$$\frac{D\overline{u_i u_j}}{Dt} = \frac{\partial}{\partial x_k}\left(\nu \frac{\partial \overline{u_i u_j}}{\partial x_k}\right) + D_{ij}^T + \left[-\overline{u_i u_k}\frac{\partial U_j}{\partial x_k} - \overline{u_j u_k}\frac{\partial U_i}{\partial x_k}\right] + \Pi_{ij} - \epsilon_{ij}, \quad (1)$$

$$\frac{D\epsilon}{Dt} = \frac{\partial}{\partial x_j}\left(\nu \frac{\partial \epsilon}{\partial x_j}\right) + \frac{\partial}{\partial x_j}\left(C_\epsilon \frac{k}{\epsilon}\overline{u_i u_j}\frac{\partial \epsilon}{\partial x_i}\right) + C_{\epsilon 1}\frac{\epsilon}{k}\tilde{P} - C_{\epsilon 2}\frac{\epsilon\tilde{\epsilon}}{k} + \xi, \quad (2)$$

where D/Dt is the material derivative. Only D_{ij}^T, Π_{ij}, ϵ_{ij}, and ξ need modeling. Near-wall models proposed by Zhang et al. (1993) for D_{ij}^T, Π_{ij}, ϵ_{ij}, and ξ can be quoted as:

Nomenclature (cont.)

Re_t = turbulent Reynolds number = $k^2/\nu\epsilon$
S = source term in Eq. (15)
S_{ij} = strain rate tensor = $(1/2)[\partial U_i/\partial x_j + \partial U_j/\partial x_i]$
t = time
U_m = mean bulk velocity
U = mean velocity along x direction
U_i = ith component of the mean velocity
U^+ = normalized mean U velocity = U/u_τ
u_i = ith component of the fluctuating velocity
u, v, w = fluctuating velocity components along x, y, and z, respectively
u_{rms} = root mean square of $\overline{u^2}$ normalized by u_τ
v_{rms} = root mean square of $\overline{v^2}$ normalized by u_τ
w_{rms} = root mean square of $\overline{w^2}$ normalized by u_τ
u_τ = friction velocity = $(\tau_w/\rho)^{1/2}$
$-\overline{uv}^+$ = normalized turbulent shear stress = $-\overline{uv}/u_\tau^2$
$-\overline{v\theta}^+$ = normalized turbulent heat flux = $-\overline{v\theta}/u_\tau\Theta_\tau$
x_i = ith component of the Cartesian coordinates, x, y, z
x, y, z = coordinates along stream, normal, and transverse directions
y^+ = normalized y coordinate = yu_τ/υ
α = thermal diffusivity = $\kappa/\rho C_p$
α_1 = model constant = $[8 + C_2]/11$
α_t = turbulent heat diffusivity
α^* = model constant = 0.45
β_1 = model constant = $[8C_2 - 2]/11$
γ_1 = model constant = $[30C_2 - 2]/55$
ϵ = dissipation rate of k
ϵ_w = dissipation rate of k evaluated at the wall = $2\nu[\partial\sqrt{k}/\partial y]^2$
ϵ_θ = dissipation rate of temperature variance
$(\epsilon_\theta)_w$ = dissipation rate of temperature variance evaluated at the wall = $\alpha[\partial\sqrt{\overline{\theta^2}}/\partial y]^2$
$\hat{\epsilon}$ = modified dissipation rate = $\epsilon - 2\nu(\partial\sqrt{k}/\partial y)^2$
$\tilde{\epsilon}_\theta$ = modified dissipation rate of temperature variance = $\epsilon_\theta - \alpha[\partial\sqrt{\overline{\theta^2}}/\partial y]^2$
$\overline{\epsilon}$ = modified dissipation rate = $\epsilon - 2\nu k/y^2$
ϵ_θ^* = modified dissipation rate of temperature variance = $\epsilon_\theta - \alpha(\overline{\theta^2} - \overline{\theta_w^2})/y^2$
$\hat{\epsilon}_\theta$ = modified dissipation rate of temperature variance = $\epsilon_\theta - (\alpha/2)(\partial^2\overline{\theta^2}/\partial y^2)$
ϵ^+ = normalized dissipation rate = $\epsilon\nu/u_\tau^4$
ϵ_θ^+ = normalized dissipation rate of the temperature variance = $\epsilon_\theta\nu/u_\tau^2\Theta_\tau^2$
ϵ_{ij} = dissipation rate tensor
θ = fluctuating temperature
θ_w = wall fluctuating temperature
θ_{rms} = root mean square of the temperature variance normalized by Θ_τ
$\overline{\theta^2}$ = temperature variance
Θ = mean temperature
Θ_τ = friction temperature = $q_w/\rho C_p u_\tau$
Θ^+ = normalized mean temperature = Θ/Θ_τ
κ = thermal conductivity
ν = fluid kinematic viscosity
ξ = near-wall correction to ϵ equation
$\xi_{\epsilon\theta}$ = near-wall correction to ϵ_θ equation
Π_{ij} = velocity pressure gradient correlation tensor
ρ = fluid density
τ_w = wall shear stress

$$D_{ij}^T = \frac{\partial}{\partial x_k}\left[C_s \frac{k}{\epsilon}\left(\overline{u_i u_l}\frac{\partial \overline{u_j u_k}}{\partial x_l} + \overline{u_j u_l}\frac{\partial \overline{u_k u_i}}{\partial x_l} + \overline{u_k u_l}\frac{\partial \overline{u_i u_j}}{\partial x_l}\right)\right], \tag{3}$$

$$\Pi_{ij} = -C_1 \frac{\epsilon}{k}(\overline{u_i u_j} - \tfrac{2}{3}k\delta_{ij}) - \alpha_1(P_{ij} - \tfrac{2}{3}\tilde{P}\delta_{ij}) - \beta_1(D_{ij} - \tfrac{2}{3}\tilde{P}\delta_{ij}) - 2\left(\gamma_1 - C_w\frac{k^{3/2}}{\epsilon x_2}\right)kS_{ij} + f_{w1}\left[C_1\frac{\epsilon}{k}(\overline{u_i u_j} - \tfrac{2}{3}k\delta_{ij}) - \frac{\epsilon}{k}(\overline{u_i u_k}n_k n_j + \overline{u_j u_k}n_k n_i) + \alpha^*(P_{ij} - \tfrac{2}{3}\tilde{P}\delta_{ij})\right], \tag{4}$$

$$\epsilon_{ij} = \tfrac{2}{3}\epsilon\delta_{ij} + f_{w1}\frac{\epsilon}{k}\left[-\tfrac{2}{3}k\delta_{ij} + \frac{\overline{u_i u_j} + \overline{u_i u_k}n_k n_j + \overline{u_j u_k}n_k n_i + n_i n_j \overline{u_k u_l}n_k n_l}{1 + 3\overline{u_k u_l}n_k n_l/2k}\right], \tag{5}$$

$$\xi = f_{w2}\left(-2\frac{\epsilon\tilde{\epsilon}}{k} + 1.5\frac{\overline{\epsilon}^2}{k} - 1.5C_{\epsilon 1}\frac{\epsilon}{k}\tilde{P}\right). \tag{6}$$

The unknown second-order tensors in Eq. (4) are given by:

$$S_{ij} = (1/2)(\partial U_i/\partial x_j + \partial U_j/\partial x_i), \tag{7a}$$

$$P_{ij} = -[\overline{u_i u_k}\partial U_j/\partial x_k + \overline{u_j u_k}\partial U_i/\partial x_k], \tag{7b}$$

$$D_{ij} = -[\overline{u_i u_k}\partial U_k/\partial x_j + \overline{u_j u_k}\partial U_k/\partial x_i]. \tag{7c}$$

The damping functions f_{w1} and f_{w2} are introduced to insure that the near-wall corrections would approach zero away from a wall. The modified ϵ, $\tilde{\epsilon} = \epsilon - 2\nu(\partial\sqrt{k}/\partial y)^2$ and $\overline{\epsilon} = \epsilon - 2\nu k/y^2$, are introduced to ensure proper behavior of ϵ near a wall. Finally, $C_w = -0.00805 + 0.00519$ (log Re). Thus modeled, Eqs. (1) and (2) are valid as a wall is approached and can be used to calculate wall bounded flows where the boundary conditions on $-\overline{u_i u_j}$ and ϵ are given by: $-\overline{u_i u_j} = 0$ and $\epsilon_w = 2\nu(\partial\sqrt{k}/\partial y)^2$.

Near-Wall Model for Eddy Thermal Conductivity

In order to investigate heat transfer modeling with nonzero temperature fluctuations at the wall, an asymptotically correct near-wall model that can handle finite wall temperature fluctuations has to be formulated. This means that the expansion assumed for θ near a wall should be general enough to handle both types of boundary conditions. The model of So and Sommer (1994) assumes an expansion for θ that vanishes at the wall; therefore, the model becomes singular when finite temperature fluctuations at the wall are specified. Nagano et al. (1991) proposed a near-wall model that is regular, even for nonzero wall temperature fluctuations. However, the results shown in their paper are only for air and do not span a wide range of Prandtl numbers. Their model, therefore, will also need modifications if adopted for the present investigation. In view of this, the model of So and Sommer (1994) is modified to incorporate the proper asymptotic behavior at the wall for both zero and nonzero wall temperature fluctuations. This can be achieved by examining the modeled $\overline{\theta^2}$ and ϵ_θ equations (So and Sommer, 1994), which are given as:

$$\frac{D\overline{\theta^2}}{Dt} = \frac{\partial}{\partial x_k}\left(\alpha\frac{\partial\overline{\theta^2}}{\partial x_k}\right) + \frac{\partial}{\partial x_k}\left(C_{\theta^2}\overline{u_k u_j}\frac{k}{\epsilon}\frac{\partial\overline{\theta^2}}{\partial x_j}\right) - 2\overline{u_k\theta}\frac{\partial\Theta}{\partial x_k} - 2\epsilon_\theta, \tag{8}$$

$$\frac{D\epsilon_\theta}{Dt} = \frac{\partial}{\partial x_k}\left(\alpha\frac{\partial\epsilon_\theta}{\partial x_k}\right) + \frac{\partial}{\partial x_k}\left(C_{\epsilon\theta}\overline{u_k u_j}\frac{k}{\epsilon}\frac{\partial\epsilon_\theta}{\partial x_j}\right) + C_{d1}\frac{\epsilon_\theta}{\overline{\theta^2}}P_\theta + C_{d2}\frac{\epsilon}{k}P_\theta + C_{d3}\frac{\epsilon_\theta}{k}\tilde{P} - C_{d4}\frac{\tilde{\epsilon}_\theta}{\overline{\theta^2}}\epsilon_\theta - C_{d5}\frac{\tilde{\epsilon}}{k}\epsilon_\theta + \xi_{\epsilon\theta}, \tag{9}$$

where $\xi_{\epsilon\theta}$ is a near-wall correcting function for the ϵ_θ equation.

The function, $\xi_{\epsilon\theta}$, is derived by So and Sommer (1994) using the expansions:

$$u = a_u y + b_u y^2 + \ldots, \tag{10a}$$

$$v = b_v y^2 + \ldots, \tag{10b}$$

$$w = a_w y + b_w y^2 + \ldots, \tag{10c}$$

$$\theta = a_\theta y^p + b_\theta y^{p+1} + \ldots, \tag{10d}$$

and the coincidence condition:

$$\frac{\partial\epsilon_\theta}{\partial t} = \frac{\alpha^2}{2}\frac{\partial^2}{\partial x_m\partial x_m}\left(\frac{\partial^2\overline{\theta^2}}{\partial x_k\partial x_k}\right) - \alpha\frac{\partial^2}{\partial x_m\partial x_m}\left(\overline{u_i\theta}\frac{\partial\Theta}{\partial x_i}\right) - \alpha\frac{\partial^2\epsilon_\theta}{\partial x_k\partial x_k}, \tag{11}$$

where $p = 1$ has been assumed. The coincidence condition (11) is derived by following the procedure outlined by Shima (1988) for the treatment of the dissipation-rate equation. Thus derived, the correcting function is given by:

$$\xi_{\epsilon\theta} = f_{w,\epsilon\theta}\left[(C_{d4} - 4)\frac{\epsilon_\theta}{\overline{\theta^2}}\tilde{\epsilon}_\theta + C_{d5}\frac{\tilde{\epsilon}}{k}\epsilon_\theta - \frac{\epsilon_\theta^{*2}}{\overline{\theta^2}} + (2 - C_{d1} - C_{d2}\,\mathrm{Pr})\frac{\epsilon_\theta}{\overline{\theta^2}}P_\theta^*\right]. \tag{12}$$

The presence of P_θ^* is a consequence of the constant mean heat flux thermal boundary condition, where $\partial\Theta/\partial x$ is finite. Therefore, the near-wall correcting function is valid for all thermal boundary conditions where $\theta_w = 0$. A damping function $f_{w,\epsilon\theta}$ is introduced to ensure that the contribution of $\xi_{\epsilon\theta}$ would vanish away from the wall. In deriving Eq. (12), thin shear layer approximations have been invoked with only one exception. That is, $\partial\Theta/\partial x$ is allowed to exist so that the constant mean heat flux thermal boundary condition can be accounted for properly.

The term ϵ_θ^* in this correcting function becomes singular when $p = 0$ is specified in Eq. (10d). In other words, the near-wall correcting function fails for flows with nonzero temperature fluctuations specified at the wall. Therefore, a correction to Eq. (12) has to be formulated in order to render the near-wall heat transfer model valid for both zero and nonzero fluctuating wall temperature boundary conditions. This can be achieved by analyzing the near-wall behavior of Eqs. (8), (9), and (11) using the Taylor series expansions given in Eq. (10) with $p = 0$ specified in Eq. (10d). Substitution of Eq. (10) into Eq. (8) shows that there is no need to modify the temperature variance equation. However, substitution of Eq. (10) into Eq. (9) results in several terms that need modifications. A near-wall correcting function can again be deduced through the use of Eq. (11) and the requirements that, near a wall, the terms in the equation are correctly balanced to the first order of the wall normal coordinate. Two points should be noted in this derivation. The first is the expression for ϵ_θ^*, which is given by $\epsilon_\theta^* = \epsilon_\theta - \alpha\theta^2/y^2$ consistent with the assumption of $p = 1$. This expression becomes singular when $p = 0$ is specified in Eq. (10d). In order to make it regular again, a more general expression would be to redefine ϵ_θ^* by including the wall temperature variance, θ_w^2, in the definition. A simple yet straightforward extension is to define ϵ_θ^* as:

$$\epsilon_\theta^* = \epsilon_\theta - \alpha(\overline{\theta^2} - \overline{\theta_w^2})/y^2. \tag{13}$$

The second consideration is to deduce a correcting function so that it would reduce to Eq. (12) exactly when $p = 1$ is specified. This suggests a new correcting function, $\xi^N_{\epsilon\theta}$, defined as:

$$\xi^N_{\epsilon\theta} = \xi_{\epsilon\theta} + \xi^c_{\epsilon\theta}, \tag{14}$$

where Eq. (13) is used to replace ϵ^*_θ in Eq. (12). The same asymptotic analysis is carried out and, after much algebra, the expression for $\xi^c_{\epsilon\theta}$ is derived to be:

$$\xi^c_{\epsilon\theta} = (1-p) f_{w\epsilon\theta,1}\left[-L\frac{\alpha\hat{\epsilon}_\theta}{y^2} - M\frac{\alpha}{y}\frac{\partial\overline{u_1\theta}}{\partial y}\frac{\partial\Theta}{\partial x} - N\frac{\alpha}{y}\frac{\partial\overline{u_2\theta}}{\partial y}\frac{\partial\Theta}{\partial y} - 4\frac{\hat{\epsilon}_\theta\epsilon_\theta}{\overline{\theta^2}} + 4\frac{\tilde{\epsilon}_\theta\epsilon_\theta}{\overline{\theta^2}} - (2 - C_{d1} - C_{d2}\,\mathrm{Pr})\frac{\epsilon_\theta}{\overline{\theta^2}}P^*_\theta\right], \tag{15}$$

where $f_{w\epsilon\theta,1}$ is a damping function and L, M, and N are model constants. As before, Eq. (15) is deduced by invoking the thin shear layer approximations, which are valid in the near-wall region. Consequently, Eq. (15) is written with all other gradients neglected compared to the normal gradient. The only exception is the mean temperature gradient along the flow direction. It should be noted that when Eq. (10) is substituted into the L and M terms in Eq. (15), the leading term in each is singular. However, their sum is zero. This can be shown to be the case by first taking the derivative of Eq. (8) with respect to the normal coordinate, y. The stationarity assumption and the thin shear layer approximations are invoked to simplify the equation. Substituting Eq. (10) into this resultant expression and then evaluating the result as y goes to zero gives:

$$\frac{\partial\epsilon_\theta}{\partial y} = \frac{\alpha}{2}\frac{\partial}{\partial y}\left(\frac{\partial^2\overline{\theta^2}}{\partial x_k\partial x_k}\right) - \frac{\partial\overline{u_1\theta}}{\partial y}\frac{\partial\Theta}{\partial x}, \tag{16}$$

which on further expansion can be shown to yield two terms whose sum is zero and is identical to the sum of the leading terms in L and M in Eq. (15).

In the process of deriving Eq. (15), an estimate of the order of magnitude of L, M and N could be made. Based on this estimate, the values of L, M, and N are found to be of order 1. Later calculations show that they should take on values given by: $L = M = 2$ and $N = 1.5$. It can be seen that Eq. (15) vanishes identically when $p = 1$ and $\theta^2_w = 0$. Under these conditions, Eq. (14) reduces exactly to Eq. (12).

Once $\overline{\theta^2}$ and ϵ_θ are known, the eddy conductivity α_t, can be expressed in terms of a turbulent length scale and a turbulent velocity scale. Both turbulent thermal and velocity field time scales are used to define an appropriate length scale for α_t, while the turbulent velocity scale is taken to be $\sqrt{k}$. The two different time scales are given by $\overline{\theta^2}/\epsilon_\theta$ and k/ϵ. According to So and Sommer (1994), an appropriate definition for α_t can be obtained through a combination of these scales as:

$$\alpha_t = C_\lambda f_\lambda k[k\overline{\theta^2}/\epsilon\epsilon_\theta]^{1/2}, \tag{17}$$

where C_λ is a model constant and f_λ is a damping function. The heat flux vector can now be defined in terms of the mean temperature gradient as:

$$-\overline{u_i\theta} = \alpha_t\frac{\partial\Theta}{\partial x_i}. \tag{18}$$

If α_t is to be general enough for fluids with vastly different Pr, f_λ has to be parametric in Pr. The expression deduced by So and Sommer (1994) can be written as:

$$f_\lambda = C_{\lambda 1}(1 - f_{\lambda 1})/\mathrm{Re}_t^{1/4} + f_{\lambda 1}, \tag{19}$$

where $C_{\lambda 1}$ and A^+ are model constants parametric in Pr and $f_{\lambda 1}$ is a damping function. The expressions deduced for $C_{\lambda 1}$ and A^+ are: $A^+ = 10/\mathrm{Pr}$ for $\mathrm{Pr} < 0.25$ and $A^+ = 39/\mathrm{Pr}^{1/16}$ for $\mathrm{Pr} \geq 0.25$; $C_{\lambda 1} = 0.4/\mathrm{Pr}^{1/4}$ for $\mathrm{Pr} < 0.1$ and $C_{\lambda 1} = 0.07/\mathrm{Pr}$ for $\mathrm{Pr} \geq 0.1$. Thus formulated, the model gives good temperature field results over a Pr range from 0.025 to 10^4.

Boundary Conditions

If $p = 0$ is assumed in Eq. (10d), a boundary condition for the temperature variance has to be specified in addition to that for ϵ_θ. A detailed discussion of the boundary condition for $\overline{\theta^2}$ is given below. As for ϵ_θ, its boundary condition at the wall can be determined from Eq. (8) in the limit of $y \to 0$. It can be written as:

$$\epsilon_{\theta,w} = \frac{\alpha}{2}\frac{\partial^2\overline{\theta^2}}{\partial x_k\partial x_k}. \tag{20}$$

If Eq. (10d) is used to evaluate Eq. (20) at the wall, the value obtained for the zero fluctuating wall temperature case is $\epsilon_{\theta,w} = \alpha\overline{a^2_\theta}$, while for the nonzero fluctuating wall temperature case, $\epsilon_{\theta,w} = \alpha[(\partial^2\overline{a^2_\theta}/\partial x^2 + \partial^2\overline{a^2_\theta}/\partial z^2)/2 + (\overline{b^2_\theta} + 2\overline{a_\theta c_\theta})]$ is deduced. The wall dissipation rate does not vanish for both types of fluctuating wall temperature boundary condition. As for the mean heat flux, it is assumed to be constant along the pipe or channel walls for all test cases calculated. Furthermore, no-slip conditions are invoked for the mean and fluctuating velocity field.

Two different wall boundary conditions for the temperature variance are investigated. The first is derived from the ideal isoflux wall, or $\overline{q}_w = \text{const}$ and $q'_w = 0$. Therefore, it follows that the first derivative of the temperature variance with respect to y is zero at the wall. Invoking this boundary condition leads to an ill-posed problem for the case of pipe/channel flows, because the temperature variance gradient is also zero at the symmetry plane. In view of this, an alternative boundary condition for the temperature variance is required. The case of an ideal isoflux wall is one of the cases investigated by Kasagi et al. (1989); therefore, the temperature variance at the wall could be determined. It is this value, rather than the zero derivative condition, that is prescribed for the temperature variance at the wall. The results of Kasagi et al. (1989) show that the wall temperature variance increases with increasing Pr, until it approaches a constant value at high Prandtl numbers.

The ideal isoflux case represents a limiting condition, because the wall temperature fluctuations for other thermal boundary conditions could not achieve values higher than those given by the ideal isoflux case. In practice, the temperature fluctuations will probably be much lower. It is for this reason that the case of finite fluctuations at the wall with $\overline{q}_w = \text{const}$ and $q'_w \neq 0$ is investigated also. From the work of Polyakov (1974), the spectrum for the wall temperature fluctuations can be written as:

$$E_0 = \frac{0.072\,\mathrm{Pr}^4\sqrt{f}\,\exp(-9\sqrt{f})}{\beta^6[f\,\mathrm{Pr}\Lambda^2 + \beta^2 + 1.4f\beta(t+s)\sqrt{f\,\mathrm{Pr}}]}, \tag{21}$$

$$\beta = [0.014 + (f + 0.05)^2\,\mathrm{Pr}^2]^{1/4}, \tag{22a}$$

$$t = \cos\{\tfrac{1}{2}\,\mathrm{arctg}\,[10\,\mathrm{Pr}(f + 0.05)]\}, \tag{22b}$$

$$s = \sin\{\tfrac{1}{2}\,\mathrm{arctg}\,[10\,\mathrm{Pr}(f + 0.05)]\}, \tag{22c}$$

where $\Lambda = 1/K$ and f is the frequency. The temperature variance for a given Pr and K can be obtained by integrating E_0 from $f = 0$ to $f = \infty$, or

$$\overline{\theta^2_w} = \int_0^\infty E_0(f;\,\mathrm{Pr},\,K)\,df. \tag{23}$$

Thus defined, the wall temperature variance varies not only with Pr, but also with K. Wall temperature variance for various fluid/solid combinations, or different K values, can be deduced from Eq. (23) as well as from the study of Kasagi et al. (1989). These results, therefore, give a more realistic representation of the actual thermal boundary conditions for practical heat transfer problems.

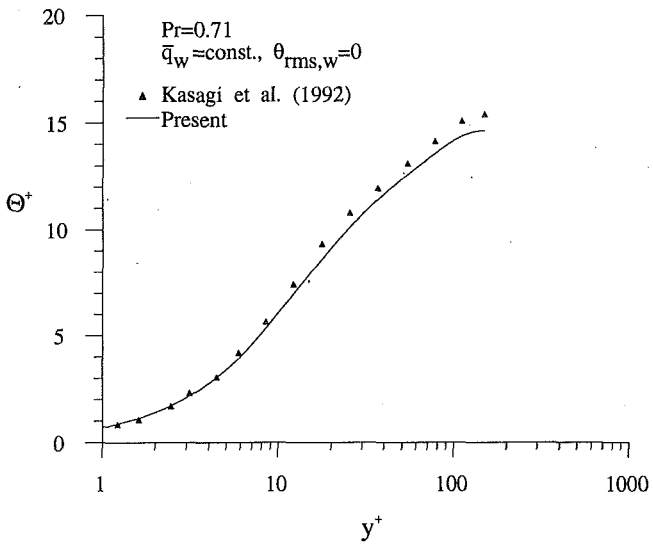

Fig. 1 Comparison of calculated mean temperature with data with zero wall temperature variance specified

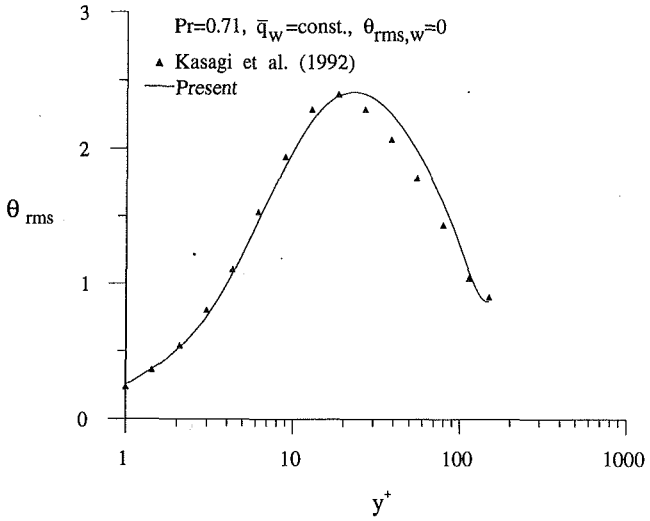

Fig. 2 Comparison of calculated temperature variance with data with zero wall temperature variance specified

Model Validation

Before proceeding to investigate the effects of nonzero fluctuating wall temperature on heat transfer modeling and calculations, the ability of the present model to predict the case of zero fluctuating wall temperature correctly has to be firmly established. This is carried out by comparing the calculated results with the DNS data of Kasagi et al. (1992) and Kim and Moin (1989) at different values of Pr. The numerical method used to solve the governing equations is the same as that described by So and Sommer (1994). These cases represent two different thermal wall boundary conditions; however, the authors of both studies assume the fluctuating wall temperature to be zero. Only the calculations of the constant heat flux case at Pr = 0.71 are shown in this paper. Results for Prandtl numbers other than Pr = 0.71 are reported by So and Sommer (1994). Figures 1 and 2 give the comparisons of Θ^+ and θ_{rms}, respectively, at a Reynolds number based on u_τ of Re_τ = 150 or a bulk Re of 4560. Here, the friction temperature, Θ_τ, is used to normalize the mean and fluctuating temperatures and the results are presented with the dependent variables plotted versus y^+. The model predictions correlate well with DNS data across the entire width of the channel. Similar results are also obtained when the calculations of the isothermal case are compared with the DNS data of Kim and Moin (1989). Further details of this comparison can be found in So and Sommer (1994).

Effect of Nonzero Wall Temperature Fluctuations

The case where $\bar{q}_w$ = const and $q'_w = 0$ is examined first. For this case, the wall temperature variance is determined from the results of Kasagi et al. (1989). These calculations are compared with those obtained assuming constant mean heat flux with zero temperature fluctuations at the wall, or $\theta_{rms,w} = 0$. All calculations are carried out at Re_τ = 1052 or Re = 50,000. Figures 3(*a*) and 3(*b*) show the mean temperature profiles for two different Prandtl numbers: Pr = 0.025 and Pr = 7, respectively. Again, the normalized mean temperature Θ^+ is plotted against y^+. There is no discernible difference between the results for the two different wall thermal boundary conditions. It should be noted that, here and in figures appearing later, all the calculated results indicated in the legend are shown. Since some of these results are essentially identical, the different curves tend to overlap each other and cannot be distinguished in the plots. The plot of θ_{rms} versus y^+ for the Pr = 0.025 case is given in Fig. 4. It can be seen that, due to high molecular conductivity, the region where molecular diffusion of heat dominates over turbulent heat flux extends to about $y^+ = 300$. Beyond this point, the difference between the calculated θ_{rms} is insignificant. However, for Pr = 7, the extent of the sublayer dominated by molecular diffusion is limited to only $y^+ = 20$, which is obvious from the Θ^+ plots

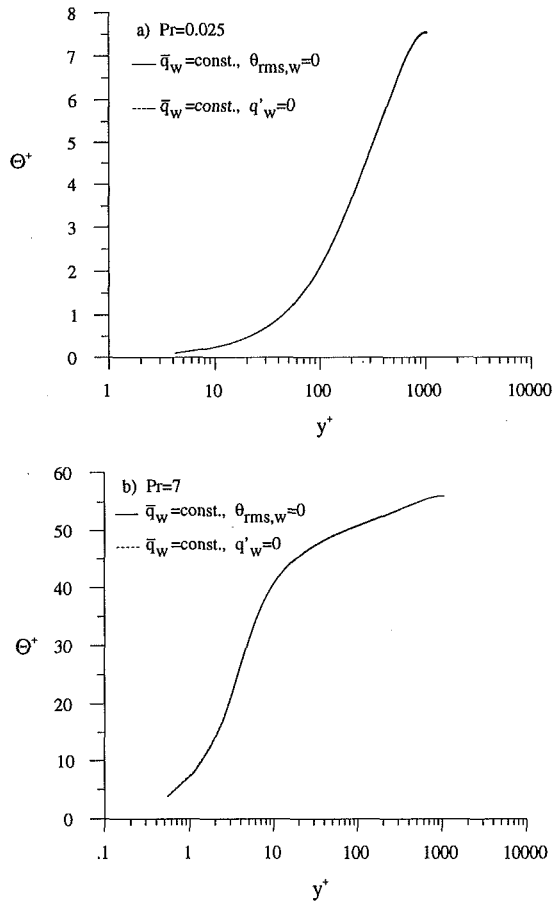

Fig. 3 Comparison of calculated mean temperature profiles with different thermal wall boundary conditions: (*a*) Pr = 0.025, (*b*) Pr = 7

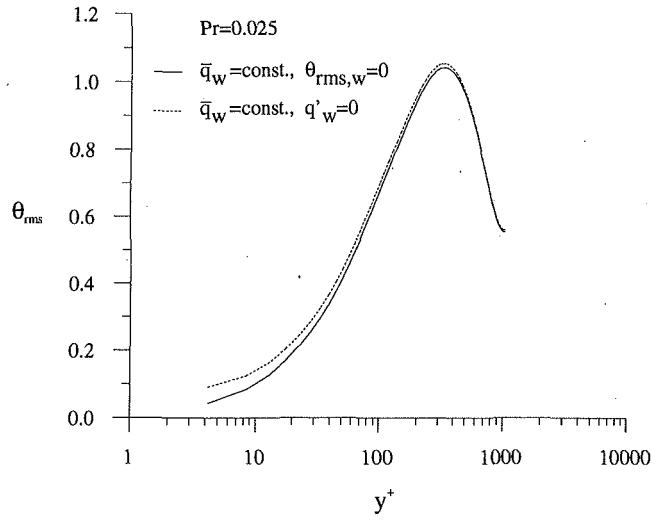

Fig. 4 Comparison of calculated root mean square temperature variance for different thermal wall boundary conditions at Pr = 0.025

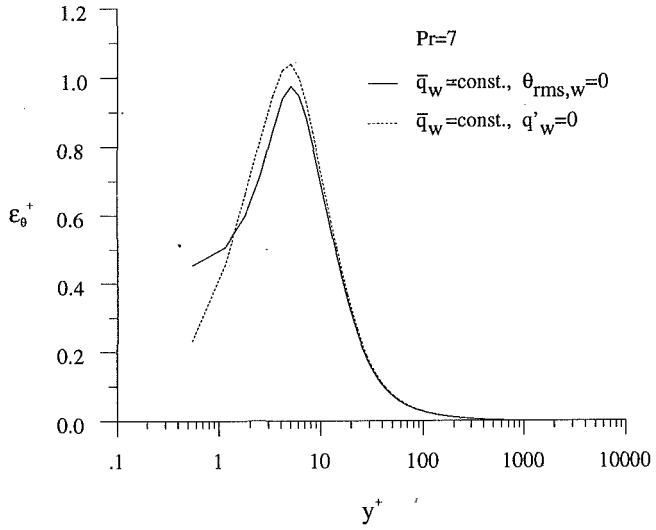

Fig. 6 Comparison of calculated dissipation rate of temperature variance for different thermal wall boundary conditions at Pr = 7

shown in Fig. 3(b). An examination of the dissipation rate of the temperature variance lends credence to this conclusion. Only the results for Pr = 7 are shown in Fig. 6 for comparison. Consistent with the boundary conditions invoked, ϵ_θ^+ tends to zero at the wall for the ideal isoflux case, while it approaches a finite, nonzero value at the wall for all other cases. Again, the difference between the two results is insignificant beyond $y^+ = 20$.

As mentioned above, the ideal isoflux case is a limiting case not likely to occur in practice. In actual heat transfer problems and/or experiments, smaller wall temperature fluctuations will occur compared to the ideal isoflux case. Therefore, the effects of different thermal boundary conditions represented by various combinations of fluid and solid are investigated. Each of these combinations yields a different value for θ_{rms} at the wall. Representative calculations are performed for the following combinations: water (Pr = 7), air (Pr = 0.71), and mercury (Pr = 0.025) flowing over aluminum, lead, glass, and plexiglass. Wall temperature variances for these different fluid/solid combinations are determined in the following manner. For water and air, their values are deduced from the study of Kasagi et al. (1989). For mercury, the wall temperature variance is determined from Eq. (23) because Kasagi et al. (1989) have not attempted a simulation for mercury. This result is further verified by using Eq. (23) to calculate the wall temperature variances for air and water flowing over copper and compared to those deduced from Kasagi et al. (1989). Good agreement is obtained. The highest temperature fluctuations at the wall are expected for the case of plexiglass, which has poor thermal conductivity and therefore does

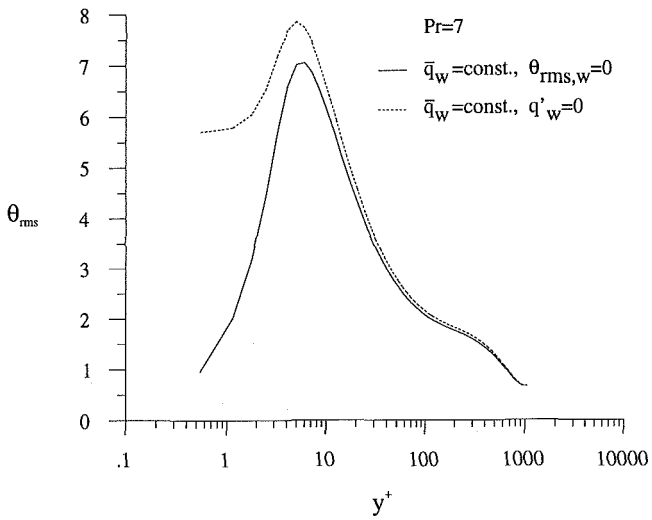

Fig. 5 Comparison of calculated root mean square temperature variance for different thermal wall boundary conditions at Pr = 7

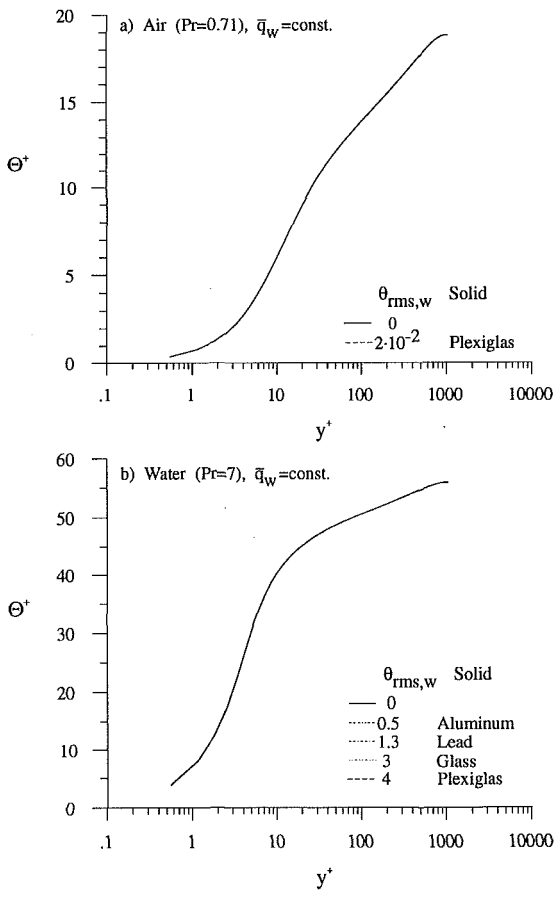

Fig. 7 Comparison of calculated mean temperature profiles for different fluid/solid combinations: (a) Pr = 0.71 (air), (b) Pr = 7 (water)

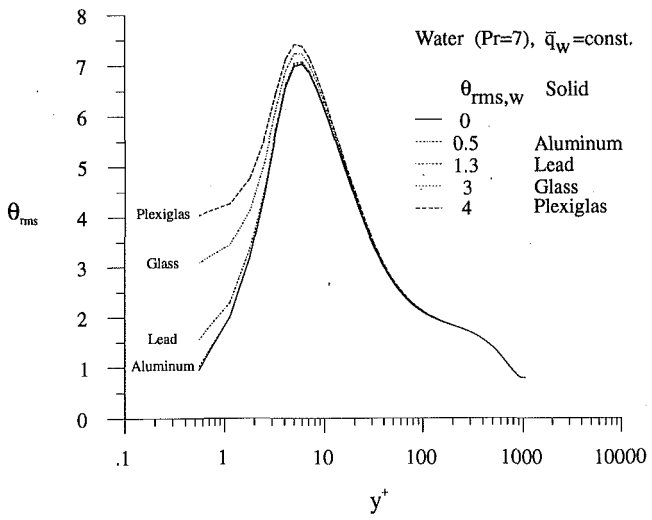

Fig. 8 Comparison of calculated root mean square temperature variance for water (Pr = 7) flowing over different solids

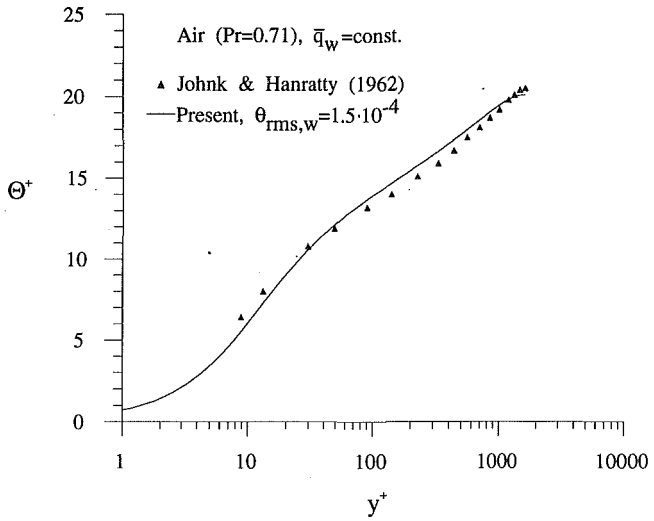

Fig. 10 Comparison of calculated mean temperature with measurements

not transport temperature fluctuations away from the wall as efficiently as aluminum. Again, calculations are carried out at Re_τ = 1052 or Re = 50,000. Plots of Θ^+ and θ_{rms} versus y^+ are shown in Figs. 7–9. It can be seen that the mean temperature profiles are not affected by the different levels of θ_{rms} specified at the wall (Fig. 7). The θ_{rms} plots for water are given in Fig. 8. Here, the effects of the different levels of wall θ_{rms} are limited to a region very close to the wall. For all the cases calculated, the effects are not felt beyond $y^+ = 20$. Similar plots for mercury and air are shown in Figs. 9(*a*) and 9(*b*), respectively. The different boundary conditions have little or no effects on the calculated θ_{rms} as evidenced by the extreme case represented by a plexiglass wall.

Finally, comparisons are made with the measurements of Hishida et al. (1986) at a Re_τ = 1042 or Re = 40,000, and Johnk and Hanratty (1962) at Re_τ = 1644 or Re = 71,200. Since the temperature fluctuations at the wall were not measured, they have to be estimated for the present calculations. Both experiments were carried out with air as the working fluid; therefore, Pr = 0.71. If the wall is assumed to be steel, θ_{rms} at the wall can be estimated from the studies of Polyakov (1974) and Kasagi et al. (1989). Another calculation with zero fluctuating wall temperature boundary condition has also been carried out for these two experiments. The results are plotted in Figs. 10 and 11 for comparison with measurements. The Θ^+ results for a fully developed pipe flow are plotted in Fig. 10, while the normal turbulent heat flux, $-\overline{v\theta}^+$, results in the near-wall region are shown in Fig. 11. The heat flux is normalized by Θ_τ and u_τ. In both cases, the calculations with two different boundary conditions yield essen-

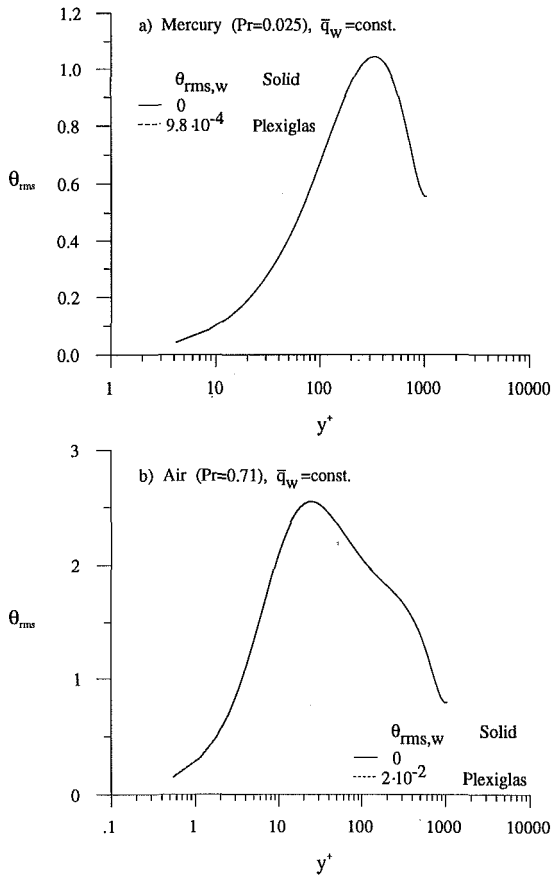

Fig. 9 Comparison of calculated root mean square temperature variance for different fluid/solid combinations: (*a*) Pr = 0.025 (mercury), (*b*) Pr = 0.71 (air)

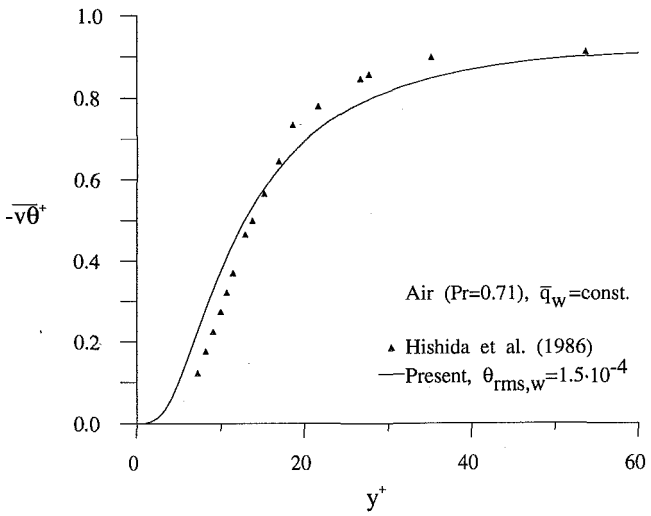

Fig. 11 Comparison of calculated turbulent normal heat flux with measurements

tially identical results. Since the purpose of these two figures is to verify that good agreement with data is also achieved with the calculations obtained assuming nonzero wall temperature fluctuations, results with zero wall temperature fluctuations are not shown here. The agreement with experiments is good, thus further verifying the validity of the zero fluctuating wall temperature assumption.

Conclusions

A near-wall two-equation turbulence model is used to investigate the validity and extent of the assumption of zero fluctuating wall temperature boundary condition for heat transfer modeling and calculations. The model is based on the transport equations for the temperature variance and its dissipation rate. Near-wall correcting functions are sought so that the resultant equations are equally valid for zero and nonzero fluctuating wall temperature boundary conditions. The near-wall analysis of the equations is carried out by assuming Taylor series expansions for the fluctuating velocities that vanish as the wall is approached, and the fluctuating temperature that remains finite at the wall. Correct boundary conditions for the fluctuating velocity field are no-slip at the wall. As for the fluctuating temperature field, the wall temperature variance is specified. This boundary condition depends on fluid properties as well as the conductive characteristics of the solid. The coupled heat transfer problem has been investigated by Polyakov (1974) who proposed a spectrum for the wall temperature fluctuations. This spectrum is parametric in Pr and K and can be integrated to give the wall temperature variance. Therefore, for a given fluid/solid combination, the wall temperature variance can be determined and used as boundary condition for heat transfer calculations.

Heat transfer calculations are carried out with different fluid/solid combinations and the results are compared with other calculations assuming the wall temperature variance to be zero. Estimates of the wall temperature variance for different fluid/solid combinations are obtained from Eq. (23) and/or the DNS results of Kasagi et al. (1989). These comparisons show that the calculated mean temperature and the associated integral heat transfer properties are essentially independent of the boundary conditions for the fluctuating wall temperature. In other words, both zero and nonzero fluctuating wall temperature boundary conditions yield the same mean temperature distributions. On the other hand, nonzero fluctuating wall temperature boundary condition has a limited effect on the turbulence statistics in a small region near the wall. Beyond this region, the calculated temperature variance and its dissipation rate using both zero and nonzero fluctuating wall temperature boundary conditions are essentially identical. This observation is true for the highest wall temperature fluctuations that can be expected from the different fluid/solid combinations examined as well as for the extreme case of an ideal iso-flux wall boundary condition. Since the zero fluctuating wall temperature boundary condition is valid for the mean field and is the simplest available, it should be recommended for adoption in practical turbulent heat transfer calculations.

Acknowledgments

Funding support under Grant No. NAG-1-1080 from NASA Langley Research Center, Hampton, VA 23665, monitored by Dr. T. B. Gatski, is gratefully acknowledged.

References

Cebeci, T., and Bradshaw, P., 1984, *Physical and Computational Aspects of Convective Heat Transfer,* Springer-Verlag, New York Inc., p. 13.

Hishida, M., Nagano, Y., and Tagawa, M., 1986, "Transport Processes of Heat and Momentum in the Wall Region of Turbulent Pipe Flow," *Proceedings of the 8th International Heat Transfer Conference,* Vol. 3, pp. 925–930.

Johnk, R. E., and Hanratty, T. J., 1962, "Temperature Profiles for Turbulent Flow of Air in a Pipe—I. The Fully Developed Heat Transfer Region," *Chemical Engineering Sciences,* Vol. 17, pp. 867–879.

Kasagi, N., Kuroda, A., and Hirata, M., 1989, "Numerical Investigation of Near-Wall Turbulent Heat Transfer Taking Into Account the Unsteady Heat Conduction in the Solid Wall," ASME JOURNAL OF HEAT TRANSFER, Vol. 111, pp. 385–392.

Kasagi, N., Tomita, Y., and Kuroda, A., 1992, "Direct Numerical Simulation of the Passive Scalar Field in a Turbulent Channel Flow," ASME JOURNAL OF HEAT TRANSFER, Vol. 114, pp. 598–606.

Kim, J., and Moin, P., 1989, "Transport of Passive Scalars in a Turbulent Channel Flow," *Turbulent Shear Flows 6,* Springer-Verlag, Berlin, pp. 85–96.

Lai, Y. G., and So, R. M. C., 1990, "Near-Wall Modeling of Turbulent Heat Fluxes," *International Journal of Heat and Mass Transfer,* Vol. 33, pp. 1429–1440.

Nagano, Y., and Kim, C., 1988, "A Two-Equation Model for Heat Transport in Wall Turbulent Shear Flows," ASME JOURNAL OF HEAT TRANSFER, Vol. 110, pp. 583–589.

Nagano, Y., Tagawa, M., and Tsuji, T., 1991, "An Improved Two-Equation Heat Transfer Model for Wall Turbulent Shear Flows," *ASME–JSME Thermal Engineering Proceedings,* Vol. 3, pp. 233–240.

Polyakov, A. F., 1974, "Wall Effect on Temperature Fluctuations in the Viscous Sublayer," *Teplofizika Vysokikh Temperatur,* Vol. 12, pp. 328–337.

Shima, N., 1988, "A Reynolds Stress Model for Near-Wall and Low-Reynolds-Number Regions," ASME *Journal of Fluids Engineering,* Vol. 110, pp. 38–44.

So, R. M. C., Zhang, H. S., and Speziale, C. G., 1991, "Near-Wall Modeling of the Dissipation Rate Equation," *AIAA Journal,* Vol. 29, pp. 2069–2076.

So, R. M. C., and Sommer, T. P., 1994, "A Near-Wall Eddy Conductivity Model for Fluids With Different Prandtl Numbers," ASME JOURNAL OF HEAT TRANSFER, Vol. 116, this issue, pp. 844–854.

Sommer, T. P., So, R. M. C., and Lai, Y. G., 1992, "A Near-Wall Two-Equation Model for Turbulent Heat Fluxes," *International Journal of Heat and Mass Transfer,* Vol. 35, pp. 3375–3387.

Zhang, H. S., So, R. M. C., and Zhu, M. L., 1993, "An Asymptotically Correct Near-Wall Reynolds-Stress Turbulence Model," *Proceedings of the 9th Symposium on Turbulent Shear Flows,* Kyoto, Japan, Aug. 16–18.

P. A. Dellenback
Assistant Professor.
Mem. ASME

J. L. Sanger
Graduate Student.
Student Mem. ASME

Department of Mechanical Engineering,
University of Wyoming,
Laramie, WY 82071-3295

D. E. Metzger[1]
Regent's Professor,
Department of Mechanical and Aerospace Engineering,
Arizona State University,
Tempe, AZ 85287
Fellow ASME

Heat Transfer in Coaxial Jet Mixing With Swirled Inner Jet

Convective heat transfer data are presented for coaxial jet mixing in a constant-diameter tube. The inner jet diameter was approximately twice the annular gap dimension. Water, with a nominal inlet Prandtl number of 6, was used as the working fluid. For the inner jet, Reynolds numbers of 30,000 and 100,000 were examined and the swirl number was varied from zero to one. Annular flow rates were characterized by a ratio of annular-to-inner jet axial momentum, which was varied from 0 to 8.3. In all cases the annular jet was unswirled. Plots of local Nusselt numbers show minima and maxima corresponding to the separation and reattachment associated with wall-bounded recirculation. As inner jet swirl strength increased from zero to its maximum value, the location of peak Nusselt number shifted upstream. Local Nusselt numbers achieved magnitudes as high as 9.7 times fully developed values for cases with high swirl and low annular flow rate. As the annular jet's flow rate was increased, the heat transfer enhancement decreased while the near-wall recirculation zones were stretched and shifted downstream, until at sufficiently high values of the momentum flux ratio, the zones were no longer in evidence from the heat transfer data.

Introduction

The shearing between two confined coaxial jets results in mixing rates, and subsequently, heat transfer coefficients that are substantially higher than those obtained at the same Reynolds number in fully developed pipe flow. This enhancement in diffusion rates occurs in spite of an annular recirculation region that may exist near the confining wall when the inner jet velocity exceeds the annular jet velocity. In the recirculation region, mean velocities are typically much lower than those found in the core flow, yet very high heat transfer coefficients are usually found at the wall that bounds the recirculation region. The high heat transfer coefficients are mostly attributable to the high levels of turbulent kinetic energy generated by shearing as the inner and annular jets interact. Because length scales are large in the shear layer, the turbulent kinetic energy generated there dissipates relatively slowly, thereby maintaining higher levels than would be found in ordinary pipe flow.

As the annular jet's velocity is increased, there may be some flow conditions for which the wall-bounded recirculation will not be in evidence. For sufficiently high annular flow rates, one might intuitively expect a recirculation region to occur near the tube centerline as shearing induced by the annular jet tends to draw the outer edge of the inner jet downstream at a rate faster than it had upon initial entrance into the mixing region. To the authors' knowledge, this type of on-axis recirculation has not been documented, probably because most investigations of coaxial jet mixing have focused on high-speed inner jets with relatively slower annular jets.

Several interesting features may appear in the flowfield with the introduction of swirl into the inner jet. First among these is an on-axis recirculation region, provided the initial swirl is of sufficient strength (see Fig. 1). The on-axis recirculation arises when the circumferential velocity component decays in the streamwise direction, resulting in a corresponding increase in pressure that provides the adverse pressure gradient necessary to drive the recirculation. If a wall-bounded recirculation region of the type discussed above is present, it tends to be shortened as inner jet swirl strength is increased because centrifugal forces encourage rapid spreading of the inner jet. Swirl is also responsible for increased shear rates and greater turbulence production, so that when it is coupled with the shearing from coaxial jet mixing, the convective heat transfer is augmented even further.

The objective of the present investigation was experimentally to examine local convective heat transfer characteristics associated with the mixing of two confined coaxial jets, with the inner jet swirled. The existence and influence of wall-bounded recirculation regions were of particular interest. Parameters varied in the present study included the inner jet Reynolds number and swirl strength, and the annular flow rate, which was characterized by a ratio of annular-to-inner jet momentum fluxes.

Review of Related Investigations

A substantial number of experiments that have examined the flow features in coaxial jet mixing have been reported, but relatively little is available concerning the associated heat transfer problem. Past investigations have examined free jets issuing into ambient surroundings, confined jets issuing into a sudden or gradually expanding mixing region, and coaxial jet mixing in a tube whose diameter is the same as the annular jet diameter. Here, discussion of related investigations will be limited to those concerned with mixing in a constant diameter tube, as this was also the geometry examined in the present study.

Investigations of coaxial jet mixing incorporating unswirled jets have been reported by Barchilon and Curtet (1964), Durao and Whitelaw (1973), Kang et al. (1979), Suzuki et al. (1983), Choi et al. (1986), and Khodadadi and Vlachos (1989). One commonly employed parameter in confined jet mixing that has been used in most of these investigations is the Craya–Curtet number (C_t). For constant jet diameter ratio, the Craya–Curtet number becomes larger with increasing annular-to-inner jet velocity ratio, but the C_t number is undefined for velocity ratios (U_a/U_i) greater than one.

In an early investigation by Barchilon and Curtet (1964) at very small jet diameter ratio (d/D) of 0.075, flow visualization and hot-wire measurements were used to document and focus attention upon wall-bounded recirculation. It was observed that as the Craya–Curtet number increased from zero to one, the reattachment point remained fixed at $X/D = 3$, but the separation point moved from approximately $X/D = -0.5$ to $X/D = 3$. That is, the recirculation region was shortened considerably until it disappeared altogether for $C_t = 1$.

Durao and Whitelaw (1973) reported a series of hot-wire measurements, with emphasis on normal and Reynolds shear stresses,

[1] Deceased.

Contributed by the Heat Transfer Division for publication in the JOURNAL OF HEAT TRANSFER. Manuscript received by the Heat Transfer Division December 1992; revision received November 1993. Keywords: Forced Convection, Furnaces and Combustors, Rotating Flows. Associate Technical Editor: Y. Jaluria.

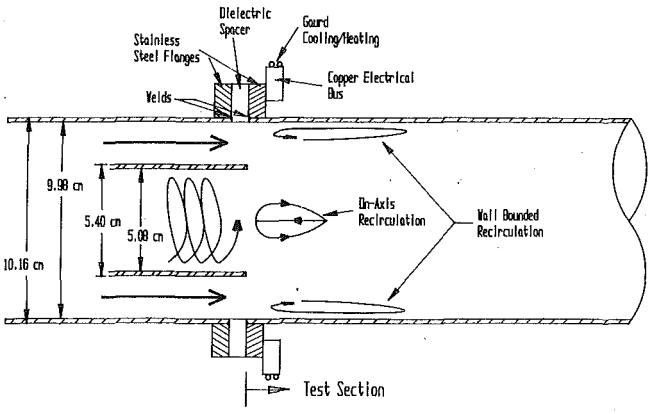

Fig. 1 Relationship between coaxial jets and principal flow features

for three different jet velocity ratios at a jet diameter ratio of 0.36. There was no evidence of wall-bounded recirculation in the data, presumably because the annular-to-inner jet bulk velocity ratios were moderate to large in their experiments.

Kang et al. (1979) presented data from an experimental investigation of heat transfer in unswirled jet mixing with inner jet velocity and velocity ratios as parameters. For many flow conditions, and especially at high annular-to-inner jet velocity ratios, two peaks in the local Nusselt number were observed. The first peak was attributed to a laminar/turbulent boundary layer transition. The maximum heat transfer usually occurred at the second peak, the location of which was found to be independent of inner jet velocity when U_a/U_i was held constant. In fact, the location of peak heat transfer was determined to be a function only of the Craya–Curtet number. A follow-on investigation by Suzuki et al. (1983) examined axial mean and fluctuating velocities, with emphasis in and around the wall-bounded recirculation zone in order to test the Kang et al. premise that peak Nusselt numbers occurred upstream of the reattachment point, coincident with the highest fluctuating velocities that were also believed to lie upstream of the reattachment point. The premise did seem to be verified except at large annular-to-inner jet velocity ratios for which the measurements revealed no wall-bounded recirculation, but there were still clear maxima in fluctuating velocities adjacent to locations of peak Nusselt number. At lower velocity ratios, the peaks in Nusselt number and axial rms velocity were found to be as much as one diameter upstream of reattachment while the length of the entire recirculation region was on the order of three diameters.

Khodadadi and Vlachos (1989) examined wall-bounded recirculation regions both numerically and with laser-Doppler anemometry (LDA) measurements, again at very small jet diameter ratios (d/D) between 0.04 and 0.08 for weak annular jets having $U_a/U_i = 0.08$ and 0.22. The locations of separation points were generally consistent with those reported by Barchilon and Curtet (1964), but there was considerably more variation in the location of computed reattachment points, which were observed to shift from about $X/D = 5.2$ to 2.8 as the jet velocity ratio approached one.

In contrast to those investigations cited above, others have considered the influence of swirled jets on the mixing process. For example, Hendricks and Brighton (1975) computationally modeled a swirled inner jet ($0 < S_i < 0.3$) mixing with an unswirled annular jet. The results given in the paper are limited to centerline velocities and wall pressure distributions.

Vu and Gouldin (1982) conducted a comprehensive investigation examining the effect of a coswirled and counterswirled annular jet, with one case having no swirl in the annular jet. For an inner jet swirl number of 0.68, on-axis recirculation extending from $X/D = 0.12$ to $X/D = 1.0$ was documented. The recirculation region had a maximum diameter corresponding to 11 percent of the mixing tube diameter (D). Maximum reverse velocities in the recirculation zone were 15 percent of the inner jet bulk axial velocity. No recirculation near the tube wall occurred because the annular jet velocities were comparatively high (yielding Craya–Curtet numbers of between 5 and 6; Khodadadi and Vlachos (1989) reported that wall-bounded recirculation is generally not expected for Craya–Curtet numbers in excess of 0.85).

Experimental Apparatus

A water flow loop comprised the main element of the test facility. The swirl number of the 5.08-cm-dia inner jet was continuously variable via tangential slot generation. Details of the inner jet swirl generator construction are available in Dellenback et al. (1988). Termination of the inner tube (that point at which mixing of the two jets began) was 16 inner jet diameters (d) downstream of the tangential slots, providing a substantial length for flow development of the inner jet. The unswirled annular jet was introduced 22 annular gap spacings (i.e., $(D - d_o)/2$) upstream of the mixing region by a large annular plenum. Two sets

Nomenclature

C_t = Craya–Curtet number = $U_m/((U_i^2 - U_a^2)(d/D)^2 + 0.5(U_a^2 - U_m^2))^{1/2}$, where $U_m = (U_i - U_a)(d/D)^2 + U_a$
d = diameter of inner jet
d_o = outside diameter of inner tube
D = diameter of annular jet and mixing region
f = friction factor for fully developed turbulent flow
h = local heat transfer coefficient
k = thermal conductivity of water
$\dot{m}$ = mass flow rate
MFR = annular-to-inner jet momentum flux ratio
Nu = local Nusselt number
Nu_G = fully developed Nusselt number for turbulent tube flow computed from the Gnielinski correlation
Pr = Prandtl number
q = local heat flux
r = radial position in tube confining inner jet
R = radius of the test section
Re = Reynolds number of the inner jet based on U_i and d
Re_D = local Reynolds number in mixing region based on total bulk velocity, D, and local bulk temperature
S = swirl number of inner jet upstream of mixing region, defined by:

$$S = \frac{2\int_0^{d/2} r^2 uv\,dr}{d\int_0^{d/2} ru^2\,dr}$$

T_b = bulk fluid temperature
T_w = inside tube wall temperature
u = local axial velocity
U = bulk axial velocity
v = local circumferential velocity
X = axial distance from location where jets begin mixing

Subscripts

a = annular jet
i = inner jet

of screens were installed just downstream of the plenum. The outer diameter of the annular jet was 9.98 cm, while the inside diameter was 5.40 cm. The jet diameter ratio of 0.51 was selected so that data could be directly compared to sudden expansion data previously generated by two of the present authors (Dellenback et al., 1987).

Heat transfer measurements were made in a horizontal stainless steel tube by passing alternating current in the tube wall, thus producing a nearly uniform heat flux boundary condition. Heating began at the same streamwise location where the two jets began mixing. The heated test section had an inside diameter of 9.98 cm, a wall thickness of 0.89 mm, and a length of 1.04 m. Stainless steel flanges were carefully attached to each end of the tube by very shallow welds at the extreme ends of the tube. Further details of the test section construction are available in Dellenback et al. (1987).

Conduction losses from the test section to the upstream tube were minimized by inserting a low thermal conductivity spacer (Melamine) between the two connecting flanges. The flanges and spacer were held together with nylon bolts to minimize further heat conduction to or from the test section. A plenum was installed downstream of the test section, also using a dielectric spacer and nylon bolts, to allow measurement of a bulk fluid temperature.

Electrical busses, machined from copper plate 1.27 cm thick, joined current carrying cables to the stainless steel flanges of the test section. Two water-carrying copper tubes were soldered around the periphery of the busses' outer rim for the purpose of guard heating or cooling. Each test section flange had a pair of thermocouples imbedded at different radial locations so that radial temperature gradients could be monitored and minimized through appropriate adjustment of the guard heaters/coolers.

Temperatures on the outside surface of the test section were measured with thermocouples mounted on the outside of the tube. Nineteen thermocouples were employed, spaced at smaller intervals near the upstream end of the test section to provide high-temperature resolution in the region of rapidly changing heat transfer coefficients. Reference to the free/forced convection regimes identified by Metais and Eckert (1964) suggests that free convection effects are negligible in flows that exhibit even less rigorous mixing than those examined in the present study. Thus, the circumferential position of the thermocouples was not felt to be important and they were placed on the side of the test section as a matter of convenience. Finally, 5 in. of fiberglass insulation surrounded the test section, flanges, and the outer rim of the electrical busses.

Power input levels to the working fluid of approximately 15 kW were determined in two ways. In the first, power was taken as the product of the test section resistance and the square of the current through the test section. Current through the test section was measured with a current transformer. Resistance of the type 321 stainless steel test section was computed during the data reduction process by taking account of the local temperature-dependent resistivities (Touloukian, 1967) along the test section.

Input power was also determined from the measured fluid enthalpy rise through the test section. To this end, bulk fluid temperatures were measured at the inlet and outlet of the test section with immersion thermocouples. For the data presented herein, the absolute discrepancy between the electrical power dissipated and the fluid enthalpy rise averaged 1.9 percent and was never more than 4.1 percent for any one run. The power dissipation was neither consistently larger nor smaller than the enthalpy rise; rather the discrepancies in power input appeared to be randomly related.

The time required for the test loop to reach steady state after application of the electrical power was about 60 minutes, as determined through continuous monitoring of fluid and wall temperatures.

Procedures and Data Reduction

Local heat transfer results are presented in terms of Nusselt numbers normalized with those for fully developed nonswirling flow, where

$$\mathrm{Nu} = hD/k. \tag{1}$$

The thermal conductivity of water (k) was evaluated at the local bulk temperature, and the local heat transfer coefficient was defined as

$$h = q/(T_w - T_b). \tag{2}$$

The local heat flux is designated by q, the local wall temperature by T_w, and the local bulk temperature by T_b. Bulk fluid temperatures ranged from 23 to 31°C, while typical temperature differences between T_w and T_b ranged from 8°C near flow reattachment to 20°C in the downstream region.

Although the present experiments had a nominally uniform heat flux boundary condition (with a heat flux of about 4.5 W/cm^2), the local heat fluxes were not strictly uniform due to both the temperature dependence of tube material properties, and axial heat conduction in the tube wall. The procedure used for finding the local heat fluxes began by dividing the wall into 19 hypothetical control volumes centered on the locations of the 19 wall-temperature thermocouples. The magnitude of Joule heating in each volume was determined as the product of the control volume's temperature-dependent resistance and the square of the current. Heat loss from the outside of the tube wall through the fiberglass insulation that surrounded the test section was assumed negligible. This loss was calculated to be no more than 0.1 percent of the total power input in a worst case analysis of the data. The axial variation in heat transfer coefficients gave rise to axial temperature gradients and conduction in the tube wall. The heat conducted from one control volume to its neighbors was computed as a part of the data reduction process and used to correct the local heat flux for each control volume (at most, the axial heat conducted from one control volume to another represented 0.3 percent of the total heat generated in that element).

The wall temperature (T_w) in Eq. (2) is the temperature of the inside surface of the test section wall. Because exterior surface temperatures were actually measured, the interior surface temperatures were determined from solution of the one-dimensional heat conduction equation for a cylindrical shell (Carslaw and Jaeger, 1959).

Since the local heat flux and inside tube wall temperature were functions of each other, their determination was inherently an iterative process, but one which converged in one or two iterations because the temperature differences across the thickness of the tube wall were small (typically on the order of 1°C). For the worst case in the present experiments, the maximum variation in local heat flux between any two locations on the tube was calculated during the data reduction process to be less than 2.3 percent. However, the extreme variations in heat flux for other cases were typically less than 0.5 percent, and the difference in heat flux between any two adjacent control volumes was less than 0.5 percent for all cases. Finally, to be consistent in methodology, local bulk temperatures were computed adjacent to each of the 19 control volumes from an energy balance that considered the local, slightly nonuniform, heat input for each control volume.

Nusselt numbers for fully developed turbulent flow were determined from the Gnielinski (1976) correlation, which Kakac et al. (1987) recommend as probably the best available general purpose correlation:

$$\mathrm{Nu}_G = (f/2)(\mathrm{Re}_D - 1000)\mathrm{Pr}/(1 + 12.7(f/2)^{0.5}(\mathrm{Pr}^{0.667} - 1)). \tag{3}$$

The friction factor that appears in Eq. (3) was evaluated from the Techo et al. (1965) correlation, again recommended by Kakac et al.:

$$f = (1.7372 \ln (Re_D/(1.964 \ln (Re_D) - 3.8215)))^{-2}. \quad (4)$$

All fluid properties used in Eqs. (3) and (4) were evaluated at the local bulk temperature.

The methods of Kline and McClintock (1953) were employed to determine that the largest uncertainties were about 2 percent in inner jet Reynolds number and momentum flux ratio, and 8 percent in swirl number. The largest uncertainties in Nusselt number were computed to be about 9 percent, with these occurring near the location of peak Nusselt number where wall-to-bulk temperature differences were smallest.

Results and Discussion

Prandtl numbers of the fluid entering the heated test section varied from 5.0 to 6.5 over the course of the experiments. This variation in Prandtl number is probably insignificant when examining the present results, as suggested by the near congruence of Krall and Sparrow's (1966) sudden expansion data for Prandtl numbers of 3 and 6.

Inner jet swirl numbers were interpolated from the results of Dellenback et al. (1988), which were obtained by the direct measurement of velocity profiles with an LDA for the same swirl generator and inlet sections. The measurements were made at a location two inner jet diameters (d) upstream of the expansion. Inner jet Reynolds numbers were based on inlet bulk fluid properties and the bulk axial velocities in the upstream tube. Reynolds numbers were maintained at nominal values of 30,000 to within ±1.3 percent and at 100,000 to within ±1.1 percent.

A ratio of axial momentum fluxes was used to characterize the annular flow rate. While the Craya–Curtet number has proven suitable for correlating data in many past investigations of coaxial jet mixing, it is undefined at the larger annular-to-inner jet velocity ratios examined in the present study (i.e., for $U_a/U_i > 1$). The ratio of annular-to-inner jet streamwise momentum flux ($\dot{m}_a U_a/\dot{m}_i U_i$) is denoted by the acronym for "momentum flux ratio," or MFR. In the present experiments, the MFR was related to velocity ratios, Reynolds number ratios, and to the Craya–Curtet number through the geometry of the jets as shown in Table 1.

Summary of the Flowfield. Axial and circumferential mean velocity profiles and distributions of turbulence intensity are available for the inner jet, upstream of the mixing region, in Dellenback et al. (1988). While no detailed velocity data were measured for the annular jet, because it had 22 gap spacings to develop prior to reaching the mixing region, it is probably reasonable to assume that the velocity profiles and turbulence levels possessed classical turbulent distributions just upstream of the mixing region (velocity profiles at $X/D = 0$ were probably altered somewhat due to downstream effects feeding back upstream via recirculation in these flows; see Dellenback et al. for documentation and further discussion of this feature).

There have been many measurements reported of coaxial jet flow fields and it was not the authors' intent to duplicate those studies. However, to obtain a preliminary understanding of the flow processes involved in the mixing region, profiles of the axial mean and fluctuating velocities were measured with an LDA for two cases having different MFRs, but both with inner jet Reynolds numbers of 30,000 and swirl number of 1. The LDA measurements were made in a clear acrylic test section having the same dimensions as the stainless steel heat transfer test section. The instrument and techniques were the same as described by Dellenback et al. (1988).

Figures 2 and 3 show the interaction and redevelopment of the jets for MFRs of 0.37 and 2.74. Both the mean and rms velocities have been normalized with the maximum axial velocity occurring in the inner jet, which was 0.56 m/s just upstream of the mixing region. The axial velocity reaches a maximum in the shear layer (Fig. 2) because the largest axial velocities in the highly swirled inner jet occur near its outer diameter. In fact, the flow actually accelerated slightly near $r/R = 0.5$ as evidenced by normalized velocities in excess of one at the $X/D = 0.032$ location. The acceleration is due to the flow blockage associated with the large on-axis recirculation region. For both momentum flux ratios, the recirculation region is of finite length, with the rear stagnation point between $X/D = 0.5$ and 1.0. In contrast, the sudden expansion data of Dellenback et al. (1988) for Re = 30,000 and $S = 1$ showed that the on-axis recirculation persisted to beyond $X/D = 4$. In the present data, redevelopment of the velocity profiles appeared to be nearing completion by $X/D = 4.6$.

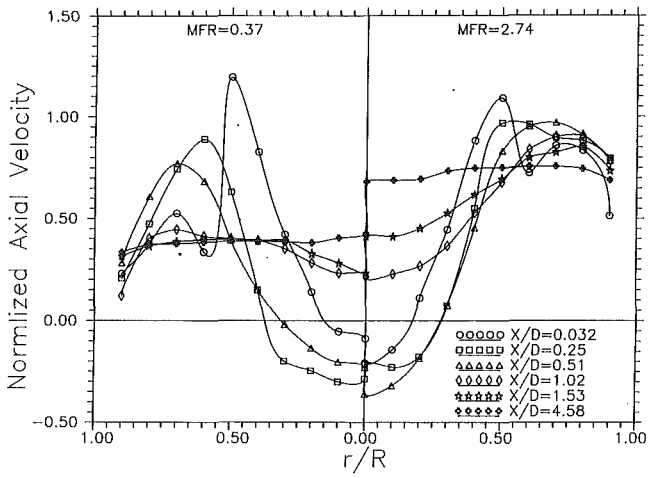

Fig. 2 Axial mean velocity distributions in the mixing region

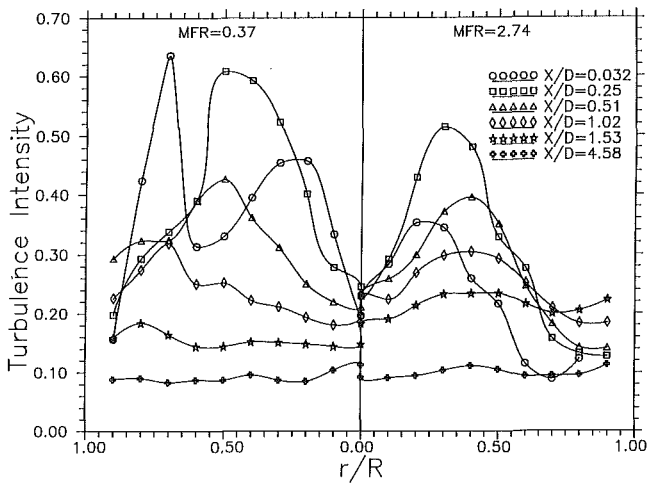

Fig. 3 Axial turbulence intensities in the mixing region

Table 1 Relationship between various parameters for characterizing the annular flow

MFR	0	0.15	0.37	0.90	1.46	2.77	8.30
U_a/U_i	0	0.23	0.37	0.57	0.73	1.00	1.74
C_t	0.55	0.84	1.38	2.12	3.08	N/A	N/A
Re_a/Re_i*	0	0.21	0.33	0.52	0.66	0.90	1.57

* Re_a is based on the hydraulic diameter of the annular jet (D_H=D-d_o)

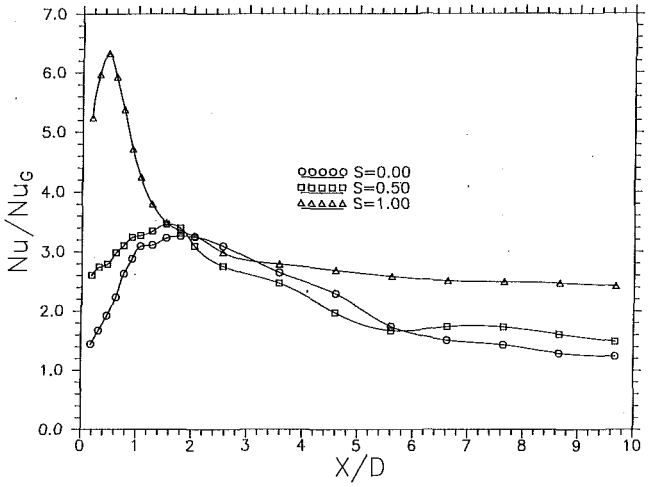

Fig. 4 The effect of inner jet swirl for Re = 100,000, MFR = 0

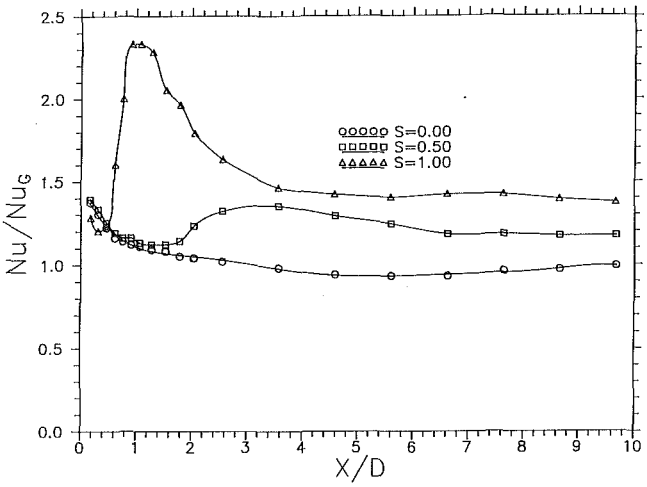

Fig. 5 The effect of inner jet swirl for Re = 100,000, MFR = 0.90

Figure 3 shows that the distributions of axial turbulence intensities have somewhat different shapes for the two momentum flux ratios, with less turbulence generation apparent for MFR = 2.7. This is expected since an MFR of 2.7 corresponds to the inner and annular jets having the same bulk axial velocities. In contrast, for MFR = 0.37, the inner jet has much higher velocity than the annular jet, resulting in more severe shearing at small X/D and average turbulence intensities higher than those associated with the MFR = 2.7 case. In spite of the large difference between inner and outer jet velocities, the MFR = 0.37 case is at least as quick as the MFR = 2.7 case to redevelop, apparently due to the higher mixing rates. The magnitudes of turbulence intensity associated with the Dellenback et al. (1988) sudden expansion data are similar to the present MFR = 0.37 data, but the peak intensities in the sudden expansion data are located closer to the tube centerline.

The Effect of Re, *S*, and MFR on the Present Data. Figure 4 shows the influence of inner jet swirl number for a Reynolds number of 100,000 and an MFR of zero. The peak Nusselt numbers are larger for the higher swirl number, while fully developed flow and heat transfer are being approached somewhat more quickly at lower swirl numbers. Figure 4 shows that the peak Nusselt number moved dramatically upstream with the addition of swirl to the inner jet. This observation implies an upstream movement of the reattachment point. The reattachment zone moves upstream with increasing swirl of the inner jet since the accompanying increase in centrifugal force on a fluid element encourages the element to move toward the wall more quickly as it moves downstream. This tendency of the inner jet to rapidly fill the larger tube into which it issues promotes a rapid redistribution of the flow so that beyond $X/D = 2.5$ in Fig. 6, the Nusselt number declines very slowly as the swirl decays. While the redistribution of momentum and internal energy occurs very quickly in the swirled flows, the turbulent kinetic energy levels and the associated Nusselt numbers remain higher than for unswirled flows due to the turbulence generation that results from increased shearing in the swirled flows.

Throughout the present results, peaks in the local Nusselt number correspond approximately to reattachment points where the inner jet impinges on the test section wall. Similarly, minima in Nusselt number correspond to separation points where flow in the vicinity of the wall moves away from the wall. If temperature instrumentation had been located upstream of $X/D = 0.2$ (which was not possible due to interference from test section flanges), then it is probable that each of the curves in Fig. 4 would also have shown a minimum in local Nusselt number (note that Barchilon and Curtet (1964) documented separation points as far upstream as $X/D = -0.5$).

With the introduction of annular flow (Fig. 5), the wall-bounded recirculation region is stretched in length and swept downstream. With the downstream shift, Fig. 5 clearly shows Nusselt number minima that correspond to flow separation points. When contrasting Figs. 4 and 5, we see that the degree of "downstream flushing" and streamwise stretching is a function of inner jet swirl strength. Downstream displacement and stretching of the wall-bounded recirculation region are most apparent at weaker swirl strengths where centrifugal forces are lower and the inner jet slower to cut through the annular jet.

With no swirl in the inner jet, Fig. 5 shows the minimum in Nusselt number to be at about $X/D = 5$ and the peak value apparently lies beyond the end of the test section at $X/D > 10$. With swirl number of zero, there is relatively little shearing between inner and annular jets, and consequently little enhancement in heat transfer, so that the normalized Nusselt number ratio falls below one in the region of separation. At higher swirl numbers, the Nusselt number ratio never falls below one because there is sufficient shearing and turbulent transport to provide some nominal heat transfer enhancement, even at the locations where separation is occurring.

Figure 6 exhibits the effect of varying the MFR on heat transfer with an unswirled inner jet. At an MFR of 0.15, a minimum and

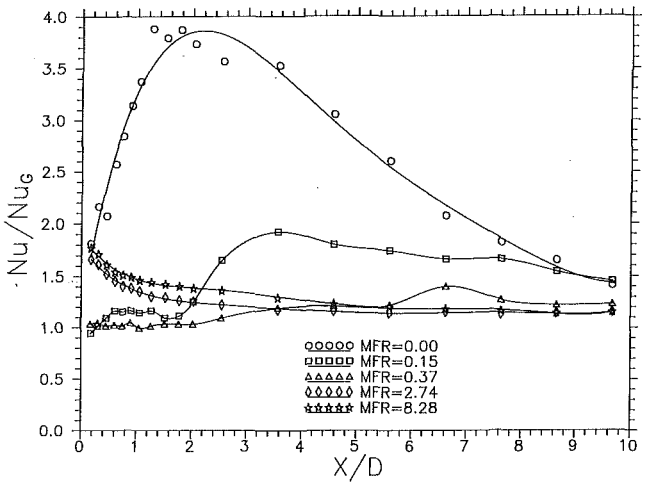

Fig. 6 The effect of MFR for Re = 30,000, S = 0

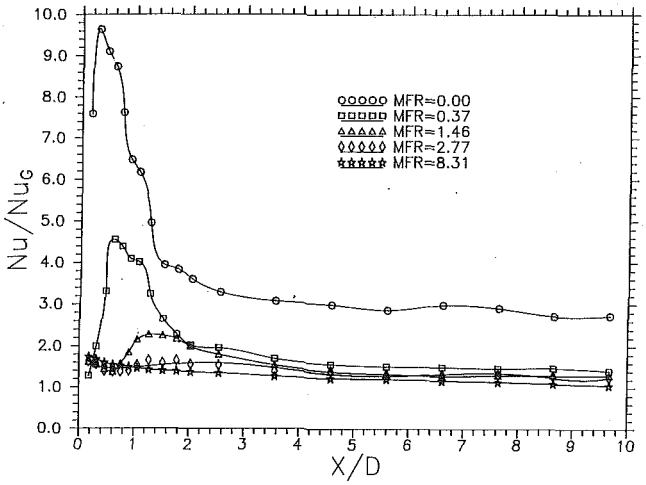

Fig. 7 The effect of MFR for Re = 30,000, S = 1

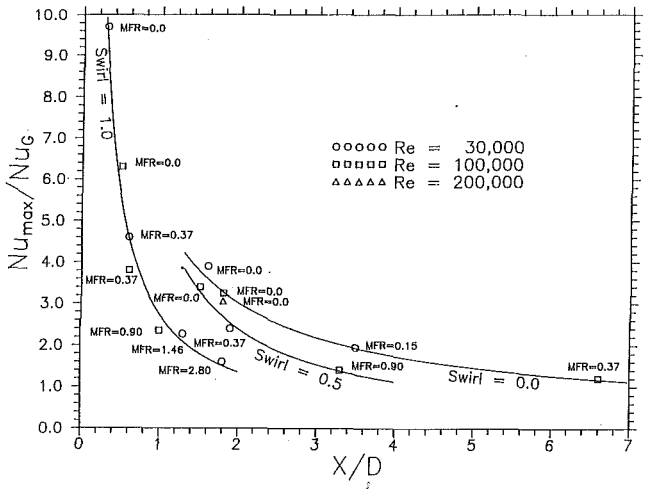

Fig. 8 Peak Nusselt numbers and their locations

maximum in Nusselt number can be discerned. At MFR = 0.37 (C_r = 1.38), we fail to see definitive evidence of wall-bounded recirculation, which is consistent with the Khodadadi and Vlachos (1989) suggestion that there should be no recirculation for values of the Craya–Curtet number larger than 0.85. At values of MFR higher than 0.37, the annular jet dominates the flow structure and heat transfer. This is suggested by the near congruence of results for MFRs of 2.7 and 8.3 for which we observe more shearing and consequently, slightly higher heat transfer rates at the larger MFR, as we might expect since an MFR of 2.7 corresponds to the inner and annular jets having the same bulk axial velocity, and consequently relatively little shearing. At the two higher MFRs in Fig. 6, we see no evidence of a near-wall recirculation region. In fact, at an MFR of 8.3 we should probably expect any recirculation to lie between radius ratios (r/R) of zero and 0.5, since the bulk annular velocity exceeds the inner jet velocity for this case.

The influence of the MFR is even more pronounced when the inner jet is swirled, as shown in Fig. 7. From Fig. 7, we see that increasing the annular flow rate from an MFR of zero to 0.37 (with inner jet Reynolds and swirl numbers held constant) has only a small impact on the position and length of the wall-bounded recirculation region. However, the film cooling effect of the annular jet is readily apparent when comparing these two cases as the normalized Nusselt numbers decrease by a factor of about two at all streamwise locations. Further increasing the MFR to 1.5 and 2.8 shifts the separation and reattachment locations downstream more noticeably and greatly compromises the peak heat transfer coefficients. This feature is in sharp contrast with the case of unswirled inner jet where there was no evidence of a recirculation region adjacent to the wall for an MFR of 2.7. Apparently then, the centrifugal forces associated with the swirling flow are sufficiently strong to allow the inner jet to penetrate the annular flow. The average heat transfer enhancement over the length of the test section due to swirling of the inner jet is noticeable, but small for an MFR of 2.7. Finally, at an MFR of 8.3, Fig. 7 shows that the Nusselt number decreases monotonically and has about the same magnitude as it did for an unswirled inner jet. Thus, swirling of the inner jet is inconsequential at sufficiently high MFR because the annular flow dominates heat transfer rates.

Figure 7 suggests the presence of wall-bounded recirculation for MFRs of 0.37 and 2.7, while the cold-flow velocity measurements presented in Fig. 2 show little evidence of same, or alternatively suggest that any such region would have to be very thin. The heat transfer measurements were performed by heating the fluid at the tube wall, thereby decreasing its density, so that centrifugal forces act to encourage recirculation near the wall. Thus, conditions for flow field and heat transfer measurements were subtly different. Similarly, a hot flow issuing into a cool test section can be expected to exhibit somewhat different flow field and heat transfer behavior, as the centrifugal forces result in a stable flow.

Figure 8 is a composite of maximum Nusselt numbers and their locations. The location of peak Nusselt numbers, and hence the reattachment points, is nearly independent of Reynolds number, but a strong function of swirl number and MFR. However, the magnitude of the peak Nusselt number depends in a complicated way on the Reynolds number. By normalizing the local Nusselt number with a fully developed value, essentially a $Re^{0.8}$ dependence has been applied to the data of Fig. 8. The peak Nusselt numbers have some further dependence on Reynolds number, and a simple modification of the Reynolds number exponent is insufficient to eliminate the dependence.

Comparison With Sudden Expansion Data. In the limiting case of no annular flow, the heat transfer should be similar to that for flow through a sudden expansion. Figure 9 shows a comparison of the present data with an unswirled inner jet to the sudden expansion data of Dellenback et al. (1987). At a Reynolds number of 30,000, the behavior of the normalized Nusselt num-

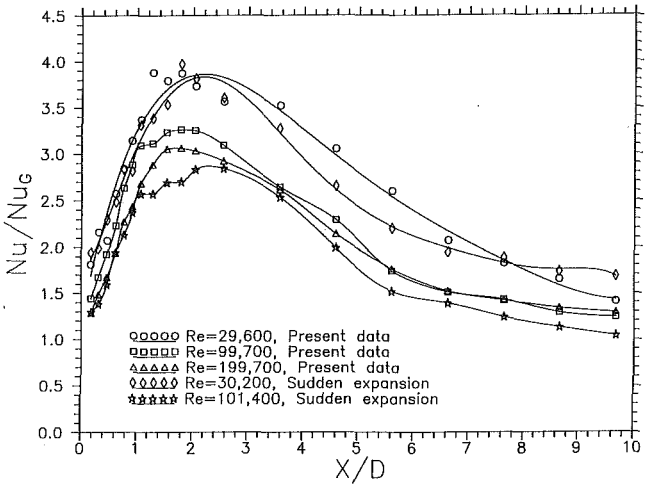

Fig. 9 Comparison of the present S = 0, MFR = 0 data with those for unswirled flow through a sudden expansion (Dellenback et al., 1987)

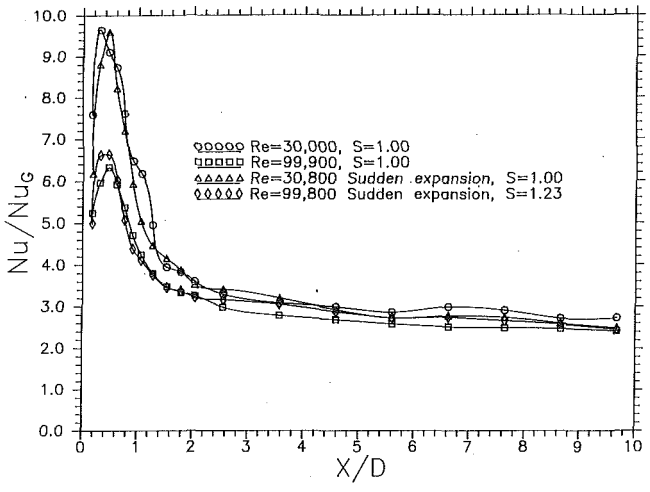

Fig. 10 Comparison of the present $S = 1$, MFR = 0 data with those for unswirled flow through a sudden expansion (Dellenback et al., 1987)

ber for the present experiments is nearly identical to the sudden expansion data. At Re = 100,000, the qualitative similarity is again apparent but there is a discrepancy between magnitudes of peak Nusselt number that will be addressed in a following paragraph. For both data sets, the normalized Nusselt numbers are larger for lower values of Reynolds number because Nusselt numbers for separated flow depend approximately on $Re^{2/3}$, whereas the fully developed flow Nusselt numbers used to form the Nusselt number ratio depend approximately on $Re^{0.8}$; thus their ratio depends on $Re^{-0.13}$ so that heat transfer enhancements are larger for smaller Reynolds numbers. Figure 9 also includes one case with an inner jet Reynolds number of 200,000. Once again, the normalized Nusselt number is lowered with increasing Reynolds number and the streamwise location of the peak Nusselt number does not appear to possess a significant Reynolds number dependence. This last conclusion is also consistent with heat transfer data for sudden expansion flow.

Figure 10 shows a second comparison of the sudden expansion data with the present data for MFR = 0, but with the inner jet highly swirled. The peak Nusselt numbers are nearly coincident, but this is somewhat misleading at Re = 100,000 because the swirl number is higher for the sudden expansion data. This observation is consistent with results in Fig. 9 where the coaxial jet experiment produced slightly higher Nusselt numbers, at least for Re = 100,000. The authors hypothesize that in the absence of an expansion face, there is less wall area at which turbulence dissipation occurs, resulting in slightly larger values of turbulent kinetic energy and higher heat transfer coefficients for the coaxial jet data. This cannot be completely confirmed by examining the velocity data because none were available for MFR = 0 in the coaxial jet work, but the turbulence intensity data of Fig. 3 did show that turbulence intensities near the beginning of the mixing region were higher than in the sudden expansion data of Dellenback et al. (1988) at the same inner jet Reynolds number. Furthermore, because the swirled inner jet causes the wall-bounded recirculation region to be shortened and displaced upstream, we would probably expect this effect to be more dramatic in the swirled flows than in the unswirled flows.

For the purely axial inner jet of Fig. 9, the small length scales at which turbulence dissipation occurs are lower valued for larger Reynolds numbers, so that the larger Reynolds number flows approach a fully developed heat transfer condition more quickly than do flows with lower Reynolds numbers. However, this argument needs to be reconsidered when the inner jet is swirled (Fig. 10) because the turbulence kinetic energy produced through the additional shearing dominates the heat transfer. The swirl is slow to decay as evidenced by the persistence of the normalized Nusselt numbers in maintaining values near 2.5 at the end of the test section. These can be contrasted to the values between 1.0 and 1.5 at the same far-downstream location when the inner jet is unswirled (Fig. 9).

Conclusions

Local heat transfer rates have been shown to be a strong function of the three parameters examined herein; namely the Reynolds and swirl numbers of the inner jet, and the annular-to-inner jet momentum flux ratios. Locations of the peak Nusselt numbers, and thus of flow reattachment points, are strongly swirl number and MFR dependent, but depend minimally on Reynolds number. For no annular flow, the heat transfer data resemble those for flow through a sudden axisymmetric expansion. For weak annular jets, a wall-bounded recirculation region is still in evidence in the heat transfer data, but it is elongated and located farther downstream. As the annular jet flow rates are increased, there is some point at which there does not appear to be any wall-bounded recirculation region and the annular jet dominates the heat transfer so that the magnitude of inner jet swirl strength is inconsequential.

References

Barchilon, W. D., and Curtet, R., 1964, "Some Details of the Structure of an Axisymmetric Confined Jet With Backflow," ASME *Journal of Basic Engineering*, Vol. 86, pp. 777–787.

Carslaw, H. S., and Jaeger, J. C., 1959, *Conduction of Heat in Solids*, Oxford Press, Oxford, United Kingdom.

Choi, D. W., Gessner, F. B., and Oates, G. C., 1986, "Measurements of Confined, Coaxial Jet Mixing With Pressure Gradient," ASME *Journal of Fluids Engineering*, Vol. 108, pp. 39–46.

Dellenback, P. A., Metzger, D. E., and Neitzel, G. P., 1987, "Heat Transfer to Turbulent Swirling Flow Through a Sudden Axisymmetric Expansion," ASME JOURNAL OF HEAT TRANSFER, Vol. 109, pp. 613–620.

Dellenback, P. A., Metzger, D. E., and Neitzel, G. P., 1988, "Measurements in Turbulent Swirling Flow Through an Abrupt Axisymmetric Expansion," *AIAA Journal*, Vol. 26, pp. 669–681.

Durao, D., and Whitelaw, J. H., 1973, "Turbulent Mixing in the Developing Region of Coaxial Jets," ASME *Journal of Fluids Engineering*, Vol. 95, pp. 467–473.

Gnielinski, V., 1976, "New Equations for Heat and Mass Transfer in Turbulent Pipe and Channel Flow," *Int. Chem. Eng.*, Vol. 16, pp. 359–368.

Hendricks, C. J., and Brighton, J. A., 1975, "The Prediction of Swirl and Inlet Turbulence Kinetic Energy Effects on Confined Jet Mixing," ASME *Journal of Fluids Engineering*, Vol. 97, pp. 51–59.

Kakac, S., Shah, R. K., and Aung, W., 1987, *Handbook of Single-Phase Convective Heat Transfer*, Wiley, New York.

Kang, Y., Suzuki, K., and Sato, T., 1979, "Heat Transfer in an Axisymmetric Confined Jet," *Studies in Heat Transfer*, J. P. Hartnett et al., eds., Hemisphere, New York, pp. 103–125.

Khodadadi, J. M., and Vlachos, N. S., 1989, "Experimental and Numerical Study of Confined Coaxial Turbulent Jets," *AIAA Journal*, Vol. 27, pp. 532–541.

Kline, S. J., and McClintock, F. A., 1953, "Describing Uncertainties in Single-Sample Experiments," *Mechanical Engineering*, Vol. 75, Jan., pp. 3–8.

Krall, K. M., and Sparrow, E. M., 1966, "Turbulent Heat Transfer in the Separated, Reattached, and Redevelopment Regions of a Circular Tube," ASME JOURNAL OF HEAT TRANSFER, Vol. 88, pp. 131–136.

Metais, B., and Eckert, E. R. G., 1964, "Forced, Mixed and Free Convection Regimes," ASME JOURNAL OF HEAT TRANSFER, Vol. 86, pp. 295–297.

Suzuki, K., Ida, S., and Sato, T., 1983, "Turbulence Measurements Related to Heat Transfer in an Axisymmetric Confined Jet With Laser Doppler Anemometer," *Proc. 4th Int. Symp. on Turbulent Shear Flows*, Univ. Karlsruhe, Federal Republic of Germany, pp. 18.1–18.6.

Techo, R., Tickner, R. R., and James, R. E., 1965, "An Accurate Equation for the Computation of the Friction Factor for Smooth Pipes From the Reynolds Number," ASME *Journal of Applied Mechanics*, Vol. 32, p. 443.

Touloukian, Y. S., ed., 1967, *Thermophysical Properties of High Temperature Solid Materials, Vol. 3: Ferrous Alloys*, Thermophysical Properties Research Center, Purdue Univ., McMillan.

Vu, B. T., and Gouldin, F. C., 1982, "Flow Measurements in a Model Swirl Combustor," *AIAA Journal*, Vol. 20, pp. 642–651.

The Effect of Embedded Longitudinal Vortex Arrays on Turbulent Boundary Layer Heat Transfer

W. R. Pauley
Assistant Professor,
Department of Aerospace Engineering,
The Pennsylvania State University,
University Park, PA 16802

J. K. Eaton
Professor,
Department of Mechanical Engineering,
Stanford University,
Stanford, CA 94305

Heat transfer and fluid mechanics data were obtained for a turbulent boundary layer with arrays of embedded streamwise vortices containing both counterrotating and corotating vortex pairs. The data show that these arrays can cause both large local variations in the heat transfer rate and significant net heat transfer augmentation over large areas. Close proximity of other vortices strongly affects the development of the vortex arrays by modifying the trajectory that they follow. The vortices in turn produce strong distortion of the normal two-dimensional boundary layer structure, which is due to their secondary flow. When one vortex convects another toward the wall, a strong boundary layer distortion occurs. The heat transfer is elevated where the secondary flow is directed toward the wall and reduced where the secondary flow is directed away from the wall. When adjacent vortices lift their neighbor away from the wall, minimal modification of the heat transfer results. The primary influence of grouping multiple vortex pairs into arrays is the development of stable patterns of vortices. These stable vortex patterns produce vortices that interact with the boundary layer and strongly modify the heat transfer far downstream, even where the vortices have decayed in strength.

Introduction

Regular arrays of longitudinal vortices embedded in a turbulent boundary layer occur frequently behind evenly spaced protuberances, as Taylor–Gortler vortices on concave surfaces, and behind vortex generator rows installed to increase mixing. Vortex arrays embedded in boundary layers cause periodic variations in the skin friction with a net average increase. Roughly corresponding increases also occur in the heat transfer.

Early research in this area examined the effects of vortex generator arrays on the mean flow with particular emphasis on skin friction modifications and boundary layer separation control. Important early work included Schubauer and Spangenberg (1960), Pearcey (1961), and Spangler and Wells (1964). More recently, researchers including Rao and Mehrotra (1983) and Brown (1983) have addressed the specific application of vortex arrays to aircraft. All this research has led to extensive use of vortex generator arrays on modern aircraft (cf. Stein, 1985). Similarly, Brown (1968) and Senoo and Nishi (1973) found dramatically improved conical diffuser performance using vortex generator arrays. More detailed fluid dynamics research on vortex/boundary layer interactions has been devoted to developing adequate turbulence models to represent these complex flows. This research includes the work of Bradshaw and co-workers (Mehta et al., 1983; Shabaka et al., 1985; Mehta and Bradshaw, 1988; Cutler and Bradshaw, 1987; Westphal et al., 1987a, b; and Takagi and Sato, 1983).

There have also been a few studies on the heat transfer effects of vortex arrays. The bulk of this has been for laminar flows where vortex generators have produced large increases in the heat transfer rate (cf. Russell et al., 1982; Turk and Junkhan, 1986). Fiebig and co-workers (cf. Fiebig et al., 1986) have explored improvements in heat exchanger performance by punching arrays of vortex generators into the fins. They have reported considerable success with a variety of configurations all in the laminar regime. In the turbulent regime, McEwan (1961) measured the spanwise-averaged heat transfer coefficient with and without vortex generators finding no significant change. However, later work by Edwards and Alker (1974) showed large increases in heat transfer using arrays of cubes or vortex generators. Hsi and Meroney (1975) examined the effects of arrays of vortex generators on the mass transport in a developing channel flow finding increases ranging from 29 to 88 percent. However, their measurement technique based on naphthalene sublimation was highly uncertain and the results showed variations in excess of ±50 percent. More recently Eibeck and Eaton (1985, 1986, 1987) examined the heat transfer effects of a single longitudinal vortex interacting with a turbulent boundary layer. They found large local variations in the heat transfer coefficient and a significant average increase. Detailed velocity and temperature measurements showed that the boundary layer structure near the wall was not much different than an ordinary turbulent boundary layer. Both the velocity and temperature profiles collapsed onto the standard laws of the wall when normalized using the local skin friction measurements. Wroblewski and Eibeck (1991) explored the details of the turbulent heat flux in the vicinity of an embedded vortex and found that it was well represented by an eddy diffusivity model. They found that the turbulent heat flux was augmented more than the shear stress. Ligrani and co-workers (Ligrani et al., 1988, 1991; Ligrani and Schwartz, 1990) examined the interaction of an embedded vortex with film cooling jets, motivated by turbomachinery applications. They found that the vortices significantly modified the distribution of the cooling flow and observed complex interactions between jets and vortices.

This paper addresses the augmentation of turbulent boundary layer heat transfer by arrays of embedded vortices. The paper builds upon the parametric investigation of the mean flow and vorticity development presented by Pauley and Eaton (1988b) for vortex pairs and vortex arrays. That work and previous work, notably that of Pearcey (1961), has shown that the strength of the vortex interaction with the wall is strongly dependent on the arrangement of vortices in the array. For example, considering only vortex pairs, three arrangements are possible: corotating

Contributed by the Heat Transfer Division for publication in the JOURNAL OF HEAT TRANSFER. Manuscript received by the Heat Transfer Division November 1992; revision received November 1993. Keywords: Augmentation and Enhancement, Forced Convection, Turbulence. Associate Technical Editor: T. W. Simon.

pairs and counterrotating pairs with the flow between the vortices directed either toward or away from the wall. In a corotating pair one vortex is lifted away from the wall while the other is pushed toward the wall by mutual induction. Eventually, if the vortices are strong enough, they will coalesce into a single large vortex. Vortices in a counterrotating pair with the common flow directed away from the wall are driven toward one another by the image vortices. As they approach each other they are lifted rapidly out of the boundary layer. Based on previous skin friction measurements (cf. Mehta et al., 1983; Pauley and Eaton, 1988b), it seems like such a pair would have a relatively minor effect on the heat transfer rate. On the other hand, the vortices of the counterrotating pair with the opposite sense are driven toward the wall and away from each other. The strength of the interaction is dependent on the initial vortex spacing.

The goal of this research was to relate the behavior of flow patterns observed for streamwise vortex arrays to the resulting heat transfer performance both locally and globally. By observing the heat transfer behavior side by side with the flow measurements it is possible to generalize much of the previous literature. Details of several vortex pairs and two representative vortex arrays are presented in order to understand the heat transfer effects of these interactions on the integrated behavior of counter- and corotating vortex arrays.

Experimental Apparatus

The experiments were carried out in the two-dimensional boundary-layer wind tunnel described by Eibeck and Eaton (1987). This is a blower-driven wind tunnel that includes in order a large air filter, a 5 hp blower, a diffuser and set of grids to remove flow nonuniformity, a honeycomb consisting of uniformly packed plastic soda straws, three 24 mesh wire screens, and a 4.8:1 two-dimensional contraction designed with a symmetric fifth order polynomial profile. The flow conditioning produced mean flow uniformity at the contraction exit of better than 1 percent and a free-stream turbulence intensity of approximately 0.2 percent. The test section (shown in Fig. 1) is a constant area duct, which is 13 cm high by 61 cm in span and 210 cm in length. The experiments were conducted at a nominal free-stream velocity of 16 m/s although there was a weak favorable pressure gradient due to boundary layer growth. From the contraction inlet to the final measurement station at $x = 188$ cm the free-stream velocity increased by approximately 4 percent. The boundary layers on all four test section walls were tripped using a 0.16 by 1.27 cm phenolic strip glued to the walls 4 cm downstream of the contraction exit. Integral parameters of the two-dimensional boundary layer are reported in Table 1. Pauley and Eaton (1988a) reported detailed comparisons of the turbulence quantities including the three normal stress components, the Reynolds shear stress, and the turbulence spectra, to the data of Klebanoff (1954), Purtell et al. (1981), and Murlis et al. (1982). The excellent agreement demonstrated that the undisturbed boundary layer behaves as a canonical two-dimensional boundary layer.

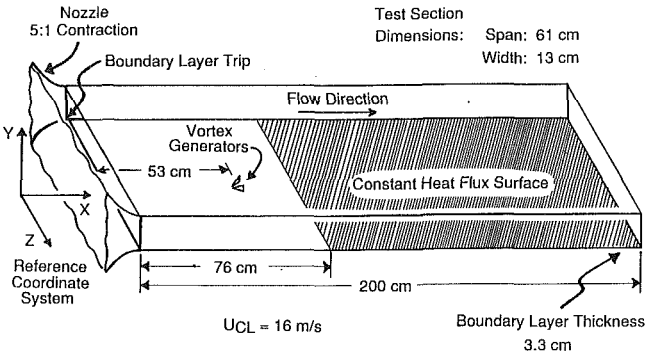

Fig. 1 The turbulent boundary layer test facility

The boundary layer on the opposite wall developed identically because unused probe access slots were filled with flush-fitting plugs and the slot in use was closed with a flexible rubber seal.

The heat transfer coefficient was measured using the constant heat flux plate described by Eibeck and Eaton (1987). The plate contains 160 thermocouples arranged in dense spanwise rows to provide a spatial resolution of 0.6 cm. The thermocouples are positioned over only one half of the heat transfer surface, which can then be used in two orientations, effectively doubling the number of thermocouple positions available. Eibeck and Eaton (1985) estimated the uncertainty in the heat transfer coefficient to be ±5 percent with the main contributors being uncertainties in the individual thermocouple calibrations, in the actual power delivered to the surface, and in the back loss corrections. These uncertainties were combined using the method of Kline and McClintock. Statistical uncertainties were eliminated by acquiring large numbers of samples under computer control. The uncertainty estimate was shown to be conservative by comparison of the two-dimensional data to well-established correlations. The measurements were repeatable within ±2 percent allowing detailed comparison among different cases.

All three mean velocity components were measured using a miniature five-hole pressure probe positioned using a two-axis computer-controlled traverse. The probe was calibrated using the scheme outlined by Westphal et al. (1987a, b), which decouples the yaw and pitch response. The five-hole tip was 2.7 mm in diameter with 0.4 mm diameter pressure ports on 45 deg facets. The six pressures (five ports plus reference dynamic pressure) were measured using a single Celesco P7D pressure transducer (±0.7 kPa range) multiplexed through a custom-built manifold and computer-controlled solenoid valves. Using a single-pressure transducer eliminates any potential uncertainty due to transducer drift. One thousand samples were acquired for each pressure measurement making statistical errors in the pressure measurement negligible. The linear velocity gradient correction developed by Westphal et al. (1987) was used to correct for flow angle bias, which occurred when the relatively large probe operated in

Nomenclature

C = specific heat at constant pressure
h = heat transfer coefficient $= \dot{q}_0''/(T_0 - T_\infty)$
d = vortex generator spacing
h = vortex generator height
l = vortex generator length
$\dot{q}_0''$ = wall heat flux
St = Stanton number $= h/\rho C U_\infty$
T = temperature
T_0 = wall temperature
U, V, W = mean velocity components in x, y, and z directions, respectively
U_∞ = free-stream velocity
x, y, z = streamwise, wall normal, and spanwise components of Cartesian coordinate system
Γ = positive circulation (only positive regions included, see text)
δ_{99} = location where $U = 0.99U_\infty$ (boundary layer thickness)
ρ = fluid density
ϕ = vortex generator angle of attack
Ω_x = streamwise vorticity

Subscripts

e = evaluated at outer edge of boundary layer ($y = \delta_{99}$)
cl = evaluated at the wind tunnel centerline

Table 1 Two-dimensional hydrodynamic and thermal boundary layer parameters

X (cm)	U_∞ ($\frac{m}{s}$)	δ_{99} (cm)	δ^* (cm)	Θ (cm)	H	Re_Θ	u_τ ($\frac{m}{s}$)	$\frac{C_f}{2}$	Δ_{99} (cm)	Δ_2 (cm)	Re_Δ	St
66	15.62	1.59	.249	.176	1.415	1790	.669	.00186	–	–	–	–
97	15.86	1.88	.307	.215	1.427	2220	.659	.00175	.904	.118	1223	.00259
142	15.74	2.29	.377	.268	1.408	2770	.640	.00166	1.20	.155	1557	.00245
188	16.37	2.67	.423	.308	1.373	3322	.662	.00165	2.57	.220	2244	.00203

a steep velocity gradient. Westphal et al. estimated the uncertainty to be 1.5 percent of the velocity magnitude and 0.3 percent of the flow angle using an identical probe in a similar flow. The dominant contributor was the uncertainty in the calibration data and the deviation of the data from the calibration functions used. Further evidence of the low uncertainty was provided by comparison to multicomponent hot-wire measurements at over 1000 positions in the present experiments. The agreement was within the uncertainty limit at all but one measurement point.

The arrays of longitudinal vortex pairs were generated using half-delta-wing vortex generators mounted on the test wall. The vortex generators were located 53 cm downstream of the boundary layer trip at a point where the undisturbed boundary layer thickness was 1.3 cm and the momentum thickness Reynolds number was 1700. Various vortex orientations were obtained by varying the spacing and angle of attack of the generators. The vortex generators used were half-delta-wings with a height of 2 cm and a length of 5 cm. The spacing between the generators was measured at their midlength and their angles of attack were measured between the vortex generators and the test wall centerline.

Results and Discussion

The results are described in two parts, the first of which describes measurements with pairs of counterrotating vortices. This section illuminates the physical mechanisms and the degree to which vortices can modify the heat transfer rate. The second section describes measurements on two representative vortex arrays, which allows assessment of the integrated effect of a periodic set of vortex generators. In all cases, the vortices must be considered fairly weak with maximum secondary flow angles less than 25 deg.

Vortex Pairs. Previous research on vortex pairs has shown that common-flow-down vortex pairs cause the strongest boundary layer distortion over the greatest streamwise extent (cf. Pauley and Eaton, 1988b). A vortex pair with common flow down moves apart as it develops in the streamwise direction because of the image flow due to the wall, producing an ever-widening region of boundary layer thinning between the vortices. Convection of each vortex by the flow field of the other holds the vortices close to the wall. Two parameters were varied independently in studying these pairs, the spacing between the vortices and the vortex generator angle of attack. The spacing between the vortex generators was varied from 2 cm to 14 cm while holding the angle of attack of the generators at 18 deg. Holding the spacing between the generators fixed at 4 cm, the angle of attack of the generators was varied from 6 deg to 24 deg. It was found that over this range the circulation of the vortices increased almost linearly with the angle of attack of the vortex generators and was nearly independent of generator spacing (see Table 2). For each of these cases Stanton number measurements were performed and one plane of mean flow data was obtained near the leading edge of the heat transfer surface. The case with generator spacing of 4 cm (two generator heights) and an 18 deg angle of attack was chosen as the "base case" for purposes of comparison.

The secondary velocity data for one-half of a plane 97 cm downstream of the boundary layer trip for the base case are shown in a $Y-Z$ plane looking downstream in Fig. 2(a). At this streamwise location, 44 cm downstream of the vortex generators (22 generator heights), the maximum secondary flow angle is 15 deg. The secondary flow vectors show the character of the embedded vortices, which appear similar to Rankine vortices with images to account for the effects of the solid wall. The vortices, while only moderate in strength, have a dramatic effect on the boundary layer. The streamwise velocity contours for the same location are shown in Fig. 2(b). Here the outer contour indicates the location of the edge of the boundary layer, δ_{99}. The interval between successive contours is 5 percent of the free-stream velocity. The boundary layer is thinned in the regions where the secondary flow is directed toward the wall and thickened where the secondary flow is directed away from the wall. Because the

Table 2 Vortex strength and heat transfer parameters

Common Flow	Angle (degrees)	Spacing (cm)	Positive Circulation Γ/Ue (cm)	Maximum Vorticity Ω_X/Ue 1/cm	Maximum St (x1000)	Minimum St (x1000)	Centerline St (x1000)
Down	18	2	1.06	0.61	3.26	2.41	3.01
Down	18	3	1.15	0.83	3.36	2.43	3.00
Down	18	4	1.19	0.85	3.34	2.39	3.01
Down	18	6	1.20	0.85	3.30	2.41	2.92
Down	18	10	1.16	0.79	3.29	2.37	2.78
Down	18	14	1.19	0.80	3.31	2.44	2.77
Down	6	4	0.47	0.25	3.17	2.51	3.11
Down	12	4	0.83	0.57	3.35	2.41	3.12
Down	24	4	1.37	0.85	3.34	2.46	2.96
Up	18	4	1.10	.625	2.97	2.72	2.72
Up	18	6	--	--	3.15	2.60	2.60
Up	18	10	--	--	3.34	2.30	2.30
Up	18	14	--	--	3.38	2.40	2.48

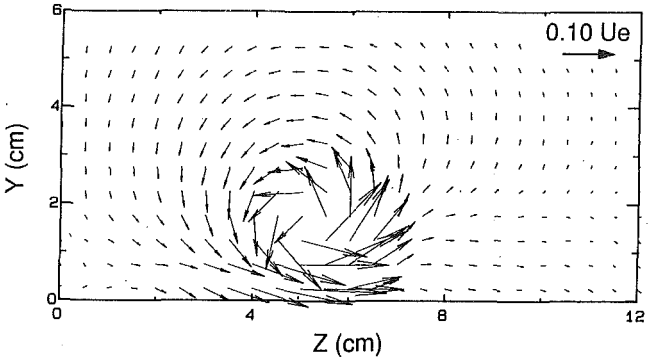

Fig. 2(*a*) Common-flow-down (BASE CASE) with $h = 2$ cm, $d = 4$ cm, and $\phi = 18$ deg at $X = 97$ cm; secondary velocity vectors

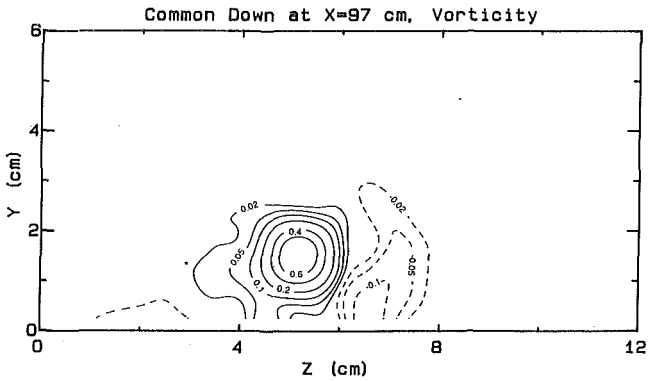

Fig. 2(*c*) Common-flow-down (BASE CASE) with $h = 2$ cm, $d = 4$ cm, and $\phi = 18$ deg at $X = 97$ cm; streamwise vorticity contours; contour values: $\Omega_x/U_e = \pm 0.02, 0.05, 0.1, 0.2, 0.4, 0.6, 0.9, 1.2$ (1/cm) (dotted lines are negative values)

vortex is formed by rolling up the boundary layer, a velocity deficit forms in the central "core" region of the vortex as indicated by the streamwise velocity contours.

The secondary velocity measurements were used to determine the streamwise vorticity at each data point by computing cubic splines through the data points and analytically differentiating these splines to form the terms of the streamwise vorticity:

$$\Omega_x = \left(\frac{\partial W}{\partial y} - \frac{\partial V}{\partial z} \right).$$

The uncertainty in this is affected by the uncertainty in the secondary velocity measurements and the inability of the spline functions to represent the velocity profile precisely. Positioning uncertainty is insignificant (<0.0003 cm). Combining the uncertainty contributions following Kline and McClintock yields an overall uncertainty of 8 percent for normalized vorticity values above 0.1 1/cm and 10–15 percent for smaller values. The vorticity field for the base case is shown in Fig. 2(*c*). Normalized contours (Ω_x/U_e) out to the 0.2 1/cm contour are quite circular. The interaction of the secondary flow and the no-slip condition at the wall produces negative vorticity, which is convected by the primary vortex and accumulates on the upwash side of the vortex. As the vortex develops downstream, the accumulation of negative vorticity grows, but a clear rollup of a secondary vortex is never observed.

The circulation of the vortices was calculated at the $X = 97$ cm station to compare the strength of the vortices formed by different arrangements of generators. Circulation was calculated by integrating all positive vorticity values in a half-plane ($Z > 0$), which reduces to calculating secondary velocity differences at the edge of the positive vorticity domain. The computer code used introduced less than a 1 percent error in circulation given an analytical velocity field and the data spacing used in the experiment. Therefore, the only significant contributor to the uncertainty is that in the relative secondary velocity between points on opposite sides of the domain. Combining all of these small contributions at constant confidence level produces an uncertainty estimate of 0.06 1/cm or about 5 percent of the base case circulation. The measurements were repeatable to within 0.03 1/cm, lending some credence to this estimate. Additional bias is introduced if significant positive vorticity is present below the bottom row of measurements. The error is difficult to evaluate but may produce up to a 5 percent additional error.

Pauley and Eaton (1988b) have discussed the development of the vorticity and vortex strength of these vortices. While common-flow-down vortices never interact strongly, the peak longitudinal vorticity decays rapidly as the vortex grows in size. The strength of the vortices generated was found to be independent of delta wing spacing for separations greater than two generator heights. Closer spacing of the vortex generators slightly inhibits

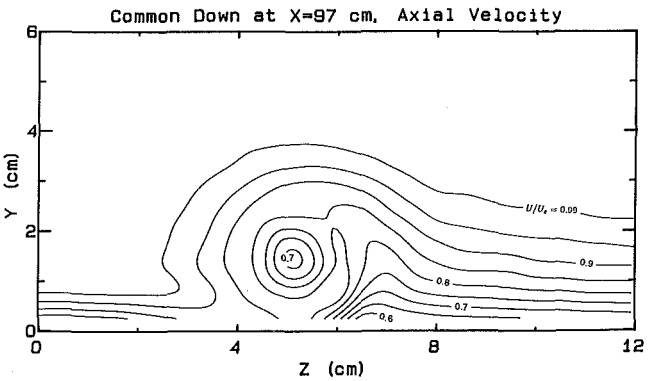

Fig. 2(*b*) Common-flow-down (BASE CASE) with $h = 2$ cm, $d = 4$ cm, and $\phi = 18$ deg at $X = 97$ cm; streamwise velocity contours; contour values: $U/U_e = 0.99, 0.95, 0.90, 0.85, 0.80, 0.75, 0.70, 0.65, 0.60, 0.55, 0.50$

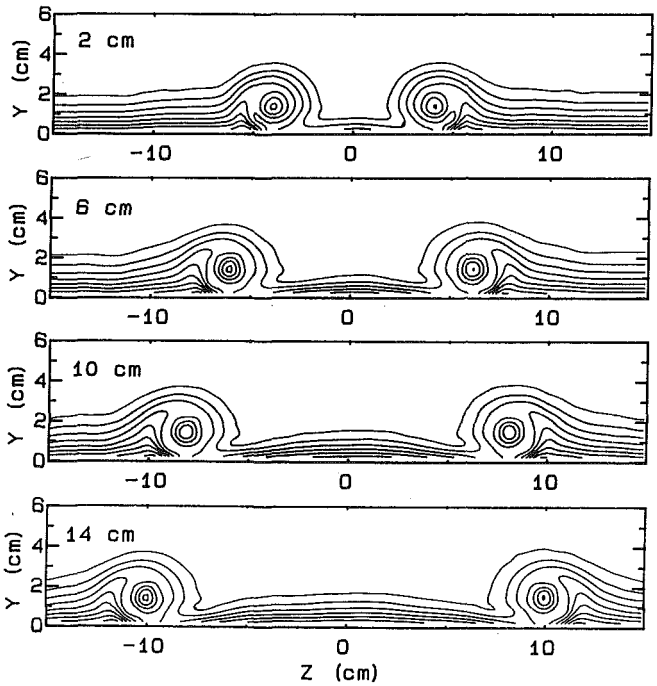

Fig. 3 Streamwise velocity contours for common-flow-down pairs with $h = 2$ cm, $\phi = 18$ deg, and $d = 2, 6, 10, 14$ cm at $X = 97$ cm

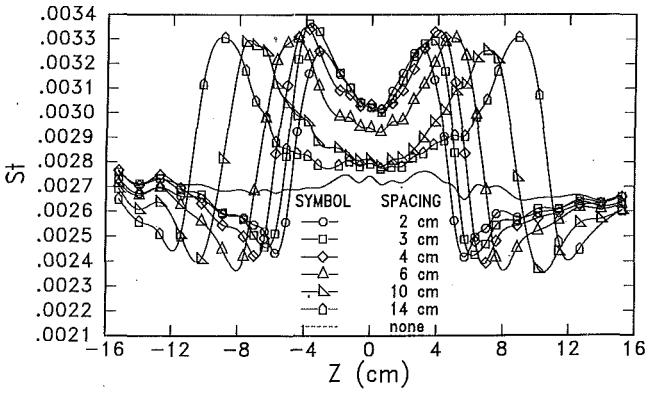

Fig. 4(*a*) Spanwise profiles of Stanton number for common-flow-down pairs with h = 2 cm, ϕ = 18 deg, and d = 2, 3, 4, 6, 10, 14 cm at X = 97 cm

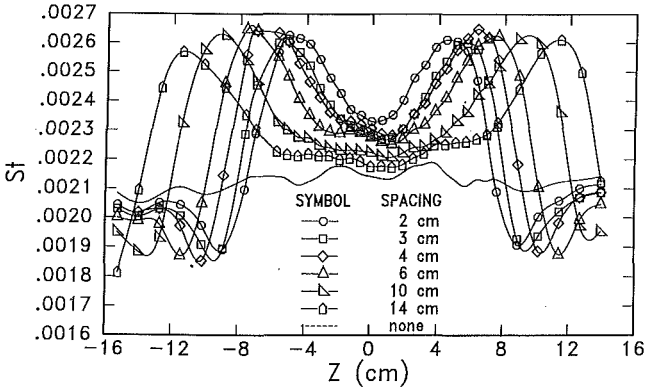

Fig. 4(*b*) Spanwise profiles of Stanton number for common-flow-down pairs with h = 2 cm, ϕ = 18 deg, and d = 2, 3, 4, 6, 10, 14 cm at X = 188 cm

their ability to generate a vortex. It was found, however, that once generated, the rate of circulation decrease in the streamwise direction was the same for all vortex generator spacings.

Full planes of three-component velocity data and spans of Stanton number were collected for each common-flow-down configuration at X = 97 cm. The effect of varying the vortex spacing on the degree of boundary layer thinning between the vortices is shown in Fig. 3. The level of boundary layer thinning between the vortices decreases with increased vortex spacing but is still significant even at the largest vortex spacing.

The impact of varying the vortex spacing on the heat transfer at X = 97 and 188 cm is shown in Figs. 4(a, b) and summarized in Table 2. Each case shows a very similar profile; there is a peak in the Stanton number beneath the downwash side of each vortex, a dip on the upwash side, and a central region of augmented heat transfer between the vortices. The peak augmentation is approximately 30 percent and the minimum value is 8 percent below the undisturbed level for all cases. The strong gradients in the Stanton number near each vortex are caused by changes in the lateral divergence. The peak Stanton number corresponds to the point where the flow toward the wall is strongest, producing strong lateral divergence and a very thin boundary layer. There is lateral convergence on the other side of each vortex, producing an upward flow and thickening of the boundary layer. The decrease in heat transfer there is less than the increase on the opposite side because of the strongly nonlinear relationship between boundary layer thickness and Stanton number. The main difference between the cases is in the centerline region. The closely spaced case with 2 cm spacing produced a 12 percent heat transfer increase on the centerline. For larger spacings, the boundary layer thinning on the centerline was not so pronounced but even at the widest spacing the centerline heat transfer is still enhanced by 5 percent. The difference between the minimum and maximum values of the Stanton number remains nearly constant over the length of the test surface while the difference between the centerplane Stanton number and the undisturbed boundary layer decreases slightly. In general the level of heat transfer distortion increases on a percentage basis moving downstream with the ratio of maximum to minimum Stanton number increasing from 38 percent at X = 97 cm to 41 percent at X = 188 cm. This increase on a percentage basis is because the magnitude of the heat transfer coefficient is decreasing as the boundary layer develops.

These data indicate that the highest performance heat transfer will be obtained by placing the vortices as close as possible to allow more generators to be placed in a given area. Practical spacing limits exist for counterrotating arrays because vortices with flow between them directed away from the wall convect each other out of the boundary layer when they get sufficiently close (see common-flow-up pairs below). Both boundary layer thinning and heat transfer enhancement in the region between the vortices were surprisingly persistent, extending to the largest vortex spacing studied (14 cm or seven generator heights).

For angles of attack less than 18 deg the strength of the vortex pair increases linearly with angle of attack. Beyond 18 deg the rate of increase declines as expected for a delta wing generator (see Pauley and Eaton, 1988b). Contours of streamwise velocity for several different angles of attack but with a fixed generator spacing are shown in Fig. 5. The level of boundary layer thinning is not affected by increasing the generator angle. Instead, the width of the thinned region is increased. The insensitivity of the boundary layer thickness between the vortices to vortex strength is apparently due to offsetting effects; the stronger image flow of the stronger vortices carries them farther apart and as a result, the secondary velocities directed toward the wall and the corresponding lateral divergence in the centerplane region are approximately the same for all cases. This results in a boundary layer between the vortices with the same boundary layer thickness but with increased width.

The Stanton number distribution for several angles of attack at X = 97 cm and X = 188 cm is shown in Figs. 6(a) and 6(b).

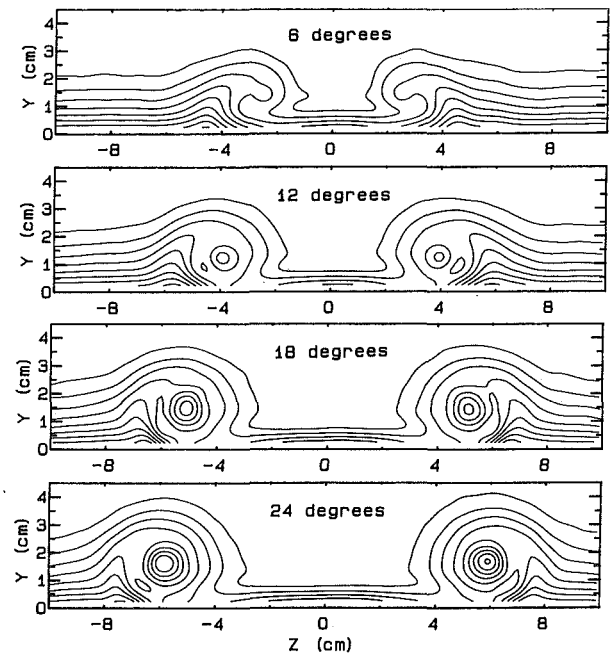

Fig. 5 Streamwise velocity contours for common-flow-down pairs with h = 2 cm, d = 4 cm, and ϕ = 6, 12, 18, 24 deg at X = 97 cm

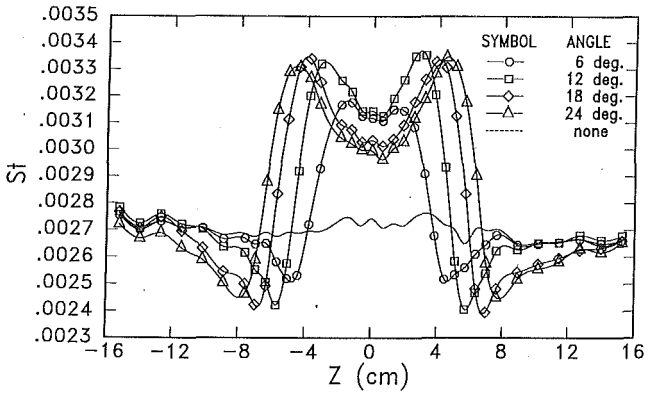

Fig. 6(*a*) Spanwise profiles of Stanton number for common-flow-down pairs with h = 2 cm, d = 4 cm, and ϕ = 6, 12, 18, 24 deg at X = 97 cm

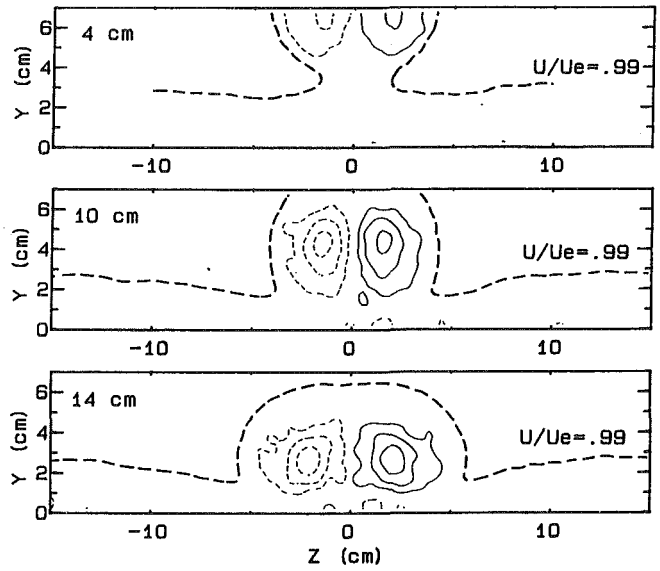

Fig. 7 Axial velocity and vorticity contours for common-flow-up pairs with h = 2 cm, ϕ = 18 deg, and d = 4, 10, 14 cm at X = 188 cm

The minimum and maximum values of Stanton number are nearly independent of the generator angle with only slightly lower peaks present for the 6 deg case. The level of heat transfer augmentation between the vortices is high for all angles and is also relatively independent of angle of attack at X = 97 cm. The spanwise extent of heat transfer augmentation increases with angle of attack as expected from the streamwise velocity contours. At X = 188 cm the behavior was qualitatively similar except on the centerline. At this downstream location the vortices due to the smallest angle of attack generators, 6 deg, actually produced the maximum heat transfer enhancement. Both the angle-of-attack independence of the Stanton number peaks and the large centerline enhancement found for the smallest angle of attack are surprising results. These results suggest a complex interaction between the vortices in addition to the modification produced by the vortices on the boundary layer.

Four different cases of equal strength, counterrotating vortices with the common flow up were investigated. The parameter varied in this study was the vortex generator spacing. The image flow causes the vortices to move toward the centerline until they get close enough together that the effects of the images nearly cancel each other. As they move close to each other at the centerline the vortices convect each other away from the wall. The common-flow-up vortices thus interact strongly with each other, but only weakly with the viscous flow near the wall and their image vortices. This is the opposite of the common-flow-down pair.

The common-flow-up pair with the closest spacing (4 cm) displayed strong vortex interaction. The pair produced a strong vertical flow directed away from the wall between the two vortices. The secondary flow due to one vortex was significant in the vicinity of the other vortex and served to lift its neighbor away from the wall. For this case the vortices modified the boundary layer only over a relatively limited axial distance. Vorticity contours measured at X = 188 cm for three different initial vortex spacings are shown in Fig. 7. The edge of the boundary layer is also indicated as a heavy dotted line. The vortices with the smallest initial spacing lift completely out of the boundary layer (and the measurement domain) before reaching the farthest downstream location. The vorticity contours are elongated in the vertical direction indicating a significant interaction between the two vortices. The vortices, which started with an intermediate initial spacing (10 cm), lift somewhat but are still low enough to cause significant boundary layer perturbation. The vortex pair with the greatest initial spacing (14 cm) is still well embedded in the boundary layer, causing a significant perturbation to the boundary layer thickness. The vorticity contours remain round with no evidence of either vertical or horizontal elongation, which is typical of strong interaction with a neighboring or image vortex, respectively. At large initial spacing, the secondary velocities decay before the vortices approach close enough to convect each other out of the boundary layer. By the downstream measurement location (X = 188 cm) the secondary velocities are too weak to distort the vortex significantly.

Increasing the spacing of the vortices produces a dramatic increase in the heat transfer augmentation because vortices with

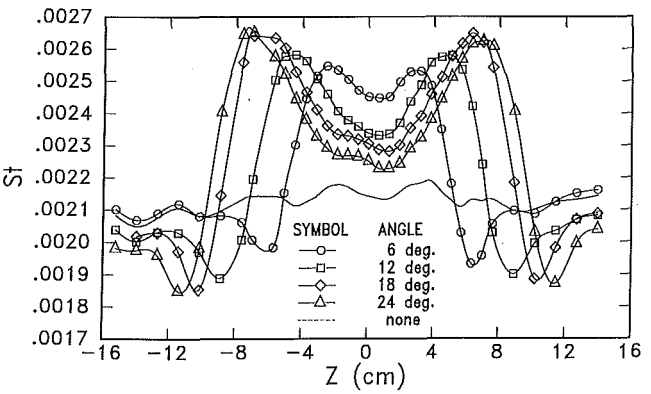

Fig. 6(*b*) Spanwise profiles of Stanton number for common-flow-down pairs with h = 2 cm, d = 4 cm, and ϕ = 6, 12, 18, 24 deg at X = 188 cm

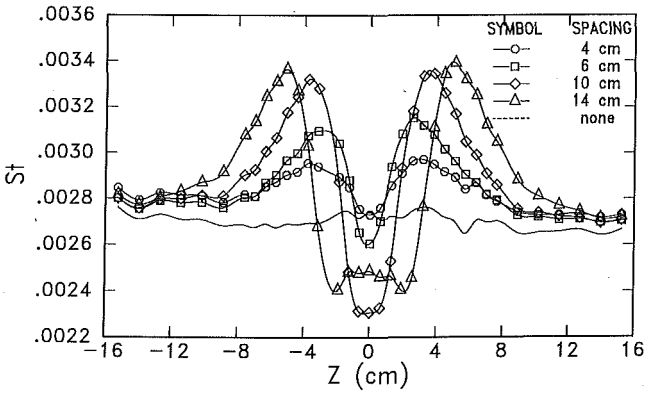

Fig. 8(*a*) Spanwise profiles of Stanton number for common-flow-up pairs with h = 2 cm, ϕ = 18 deg, and d = 4, 10, 14 cm at X = 97 cm

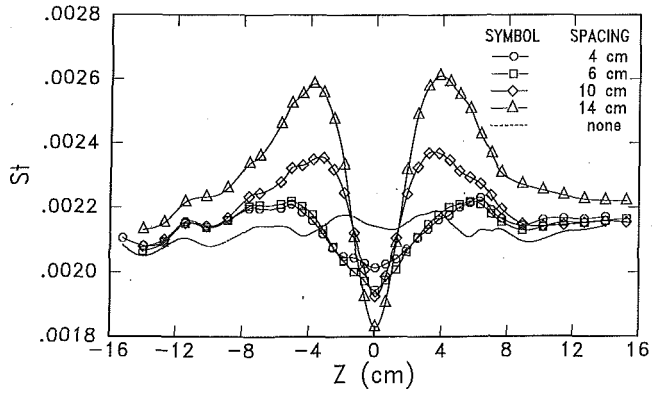

Fig. 8(*b*) Spanwise profiles of Stanton number for common-flow-up pairs with h = 2 cm, ϕ = 18 deg, and d = 4, 10, 14 cm at X = 188 cm

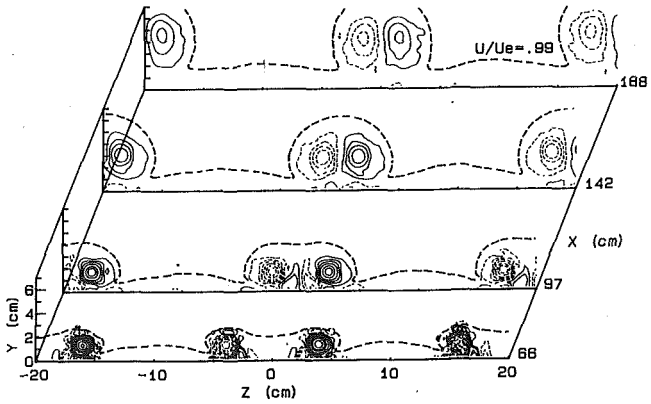

Fig. 9 Alternating array with h = 2 cm, d = 10 cm, D = 10 cm, and ϕ = 18 deg; axial velocity and vorticity contours at X = 66, 97, 142, 188 cm

larger initial spacing are less able to lift their neighbor away from the wall. The heat transfer augmentation for four spacings of the generators is shown at two streamwise locations in Figs. 8(*a*) and 8(*b*). The closely spaced common-flow-up pair (4 cm) does not strongly affect the heat transfer. There is some heat transfer augmentation in the region just outboard of the pair (about 6 percent) where there is moderately strong downwash due to the vortices. The heat transfer augmentation decreases to nearly zero in the streamwise direction as the vortices lift out of the boundary layer. The vortex with the greatest spacing, 14 cm, produces about the same peak and minimum heat transfer coefficient as observed for the common-flow-down pairs. Here there is only a weak interaction between the vortices of the pair. At X = 97 cm the peak Stanton number rises with increasing spacing up to 10 cm. Beyond this spacing the peak remains nearly the same. Spanwise integration over the profile indicates that the 10 cm spacing would provide the maximum net heat transfer augmentation at this upstream location. Looking at the downstream profiles it is observed that the pairs with less than 14 cm original spacing have a significantly reduced heat transfer augmentation. If the maximum heat transfer augmentation is desired for a greater streamwise extent, then this larger initial spacing between the common-flow-up vortices would be desirable.

Vortex Arrays. In applications of counterrotating vortices the vortex generators are usually arranged to produce pairs alternating between common flow up and common flow down. To determine if regular arrays produce different vortex development than produced by pairs, a counterrotating array was used. This array was chosen using design guidelines reported by Pearcey (1961) to produce the maximum degree of boundary layer thinning over the available length of test section. The vortex generators were spaced 10 cm (five generator heights) apart with an angle of attack of 18 deg and the sign of the angle of attack was alternated. Three pairs of generators were used with the six vortex generators placed at $z = \pm 5$ cm, ± 15 cm, and ± 25 cm.

The streamwise development of the vorticity and the corresponding edge of the boundary layer are shown in Fig. 9. Pauley and Eaton (1988b) observed that the magnitudes of the vortex strengths and the streamwise rate of decay of the vortices observed for this array closely matched that of the common-flow-up pair with the same initial spacing (10 cm). Comparing Figs. 9 and 7 we see that the positions of the vortices and shapes of the vorticity contours at X = 188 cm were the same as well. The common-flow-up interaction is dominant in determining the shape of the vorticity contours in this array because the image flow rapidly drives the array into a set of common-flow-up pairs. The extent of the common-flow-down region is limited in the array configuration because the vortices encounter an adjacent pair. At X = 188 cm the spacing between the vortices is 17 cm instead of 22 cm as seen for the common-flow-down pair with 10 cm generator spacing.

The heat transfer coefficient downstream of this array is shown in Fig. 10. The distribution of the heat transfer coefficient in the central region of the array is similar to that produced by a common-flow-up pair with 10 cm spacing. There is a 6 percent increase between the common-flow-down pairs. This is similar to the behavior seen for the common-flow-down pair with a slightly smaller initial spacing. Downstream where the vortices have lifted themselves out of the boundary layer, the peaks in heat transfer augmentation become less pronounced and a 7 to 18 percent level of heat transfer augmentation is seen across the channel. This array produces roughly a 10 percent integrated heat transfer augmentation over the heat transfer measurement region (-15 cm $\leq z \leq$ 15 cm).

In order to study the development of corotating vortices in a stable configuration and to measure their decay rate in the absence of the merging process, a regular array was constructed with a spacing of three generator heights. A total of six generators was used, located at $z = \pm 3$ cm, ± 9 cm, and ± 15 cm. The streamwise development of the vorticity contours and of the outer axial velocity contour for this regular array are shown in Fig. 11. The vortices move laterally across the tunnel at a rate approximately 1.5 times larger than an isolated vortex due to the combined effects of all of the image vortices and a spanwise flow along the wall that is set up around the wind tunnel by this array of generators. The vortices on the ends were convected out of position somewhat by their neighbors, but vortices in the middle of the array remained in a stable position. It should be noted that

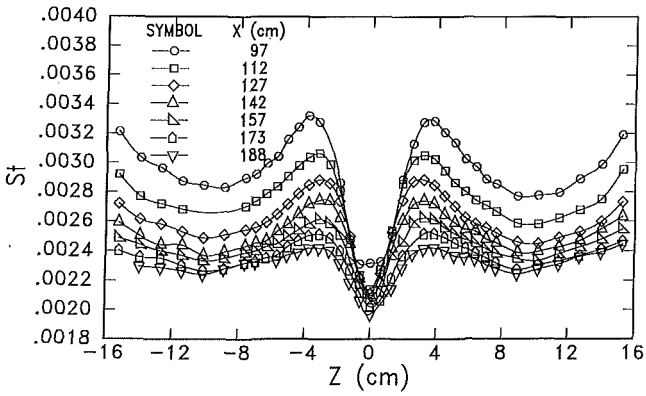

Fig. 10 Alternating array with h = 2 cm, d = 10 cm, D = 10 cm, and ϕ = 18 deg; spans of Stanton number at X = 97, 112, 127, 148, 157, 173, 188 cm

the wind tunnel was 60 cm wide so the vortices were not constrained by the sidewalls as might be suggested by the figure.

The rate of vorticity spreading is quite similar to that observed for a common-flow-down vortex pair with the same initial spacing. This indicates that the vortices in the array are essentially independent. An isolated vortex has a region of negative (secondary) vorticity on the upwash side. However, in the corotating array the primary vortex is surrounded by two regions of negative vorticity. This apparently has little effect on the diffusion of vorticity away from the primary vortex.

The heat transfer distribution shown in Fig. 12 for this array indicates that the array exhibits a heat transfer performance similar in character to that seen for the corotating pairs that were sufficiently far apart to avoid merging. The corotating array produces a heat transfer augmentation that oscillates between about a 20 percent augmentation in the strong downwash region of a vortex to negligible heat transfer enhancement in the strong upwash region of a vortex. This array produces roughly a 13 percent augmentation of the heat transfer over the entire surface, which is somewhat higher than observed for the alternating array.

Conclusions

Summarizing these results, we have examined the interactions of several vortex pairs embedded in an otherwise two-dimensional turbulent boundary layer. Qualitatively the vortices move about the flow field as would be expected from potential flow theory with some allowance for the presence of induced vortices. The major mean effects of the pairs are the thickening of the boundary layer in regions where the secondary flow is away from the wall and thinning where this flow is toward the wall.

Close proximity of other vortices strongly affects the spreading of the vorticity. This is seen as a more rapid drop in peak vorticity and a growth of the vortex. The heat transfer modification produced by the vortex was strongly dependent on vortex interaction. The situation where one vortex convects another toward the wall produced a very strong boundary layer modification and high heat transfer coefficient in the vicinity of the vortex close to the wall. A designer wishing to avoid the damaging effects of high heat transfer due to embedded vortices would wish to avoid this type of interaction. Common-flow-up vortices lift their neighbor away from the wall, decreasing the heat transfer augmentation provided by the vortices. A designer wishing to obtain the maximum heat transfer augmentation will avoid common-flow-up vortices that are in close proximity. Either the corotating or the counterrotating array can be designed to produce a significant net heat transfer augmentation. Because the design of the corotating pairs is less critical, they may provide the more practical choice in many applications.

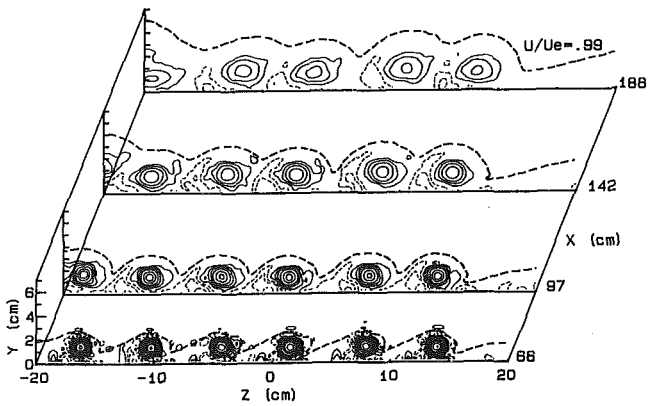

Fig. 11 Axial velocity and vorticity contours for corotating array with h = 2 cm, D = 6 cm, and ϕ = 18 deg at X = 66, 97, 142, 188 cm

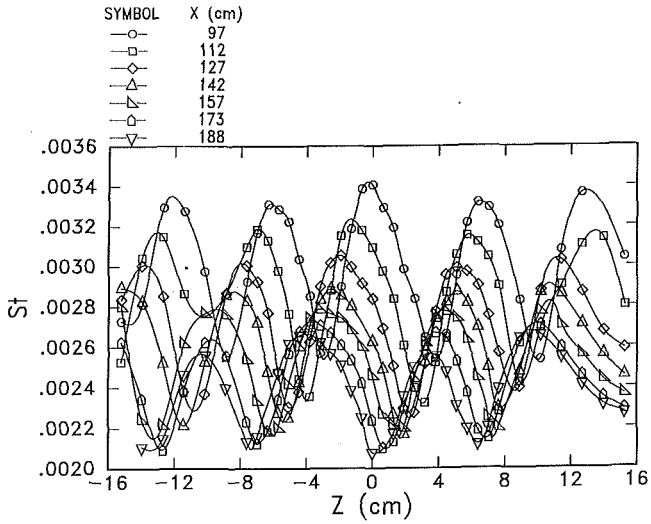

Fig. 12 Spanwise profiles of Stanton number for corotating array with h = 2 cm, D = 6 cm, and ϕ = 18 deg at X = 97, 112, 127, 148, 157, 173, 188 cm

Acknowledgments

We gratefully acknowledge the financial support of the Department of Energy Basic Energy Sciences Program (Contract No. DEFG0386ER-13608).

References

Bradshaw, P., and Cutler, A. D., 1987, "Three-Dimensional Flows With Imbedded Longitudinal Vortices," *Perspectives in Turbulence Studies,* H. U. Meier and P. Bradshaw, eds., Springer-Verlag, New York, p. 382.

Brown, A. C., 1968, "Subsonic Diffusers Designed Integrally With Vortex Generators," *J. Aircraft,* Vol. 5, pp. 221–229.

Brown, A. P., 1983, "An Investigation of the Aerodynamic Effects of Forward Facing Wedges on the Upper and Leading Edge of an Aerofoil, With Emphasis at High Angles of Attack," Defense Science and Technology Organisation Aeronautical Research Laboratories, Melbourne, Victoria, Australia.

Cutler, A. D., and Bradshaw, P., 1986, "The Interaction Between a Strong Longitudinal Vortex and a Turbulent Boundary Layer," Paper No. AIAA-86-1071.

Cutler, A. D., and Bradshaw, P., 1989, "Vortex/Boundary-Layer Interactions," Paper No. AIAA-89-0083.

Edwards, F. J., and Alker, C. J. R., 1974, "The Improvement of Forced Convection Surface Heat Transfer Using Surface Protrusions in the Form of (A) Cubes and (B) Vortex Generators," presented at the 5th International Heat Transfer Conference, Tokyo.

Eibeck, P. A., and Eaton, J. K., 1985, "An Experimental Investigation of the Heat-Transfer Effects of a Longitudinal Vortex Embedded in a Turbulent Boundary Layer," Rept. MD-48, Thermosciences Div., Dept. Mech. Engr., Stanford Univ., Stanford, CA.

Eibeck, P. A., and Eaton, J. K., 1986, "The Effects of Longitudinal Vortices Embedded in a Turbulent Boundary Layer on Momentum and Thermal Transport," *Proc. Eighth International Heat Transfer Conference,* Vol. 3, San Francisco, CA.

Eibeck, P. A., and Eaton, J. K., 1987, "Heat Transfer Effects of a Longitudinal Vortex Embedded in a Turbulent Boundary Layer," ASME JOURNAL OF HEAT TRANSFER, Vol. 109, pp. 16–24.

Fiebig, M., Kallweit, P., and Mitra, N. K., 1986, "Wing Type Vortex Generators for Heat Transfer Enhancement," *Proc. Eighth International Heat Transfer Conference,* Vol. 6, San Francisco, CA.

Hsi, G., and Meroney, R. N., 1975, "Vortex Enhancement of Parallel Plate Heat and Mass Transport," *Wood Science,* Vol. 4, No. 4, pp. 328–335.

Klebanoff, P. S., 1954, "Characteristics of Turbulence in a Boundary Layer With Zero Pressure Gradient," NACA TN-3178.

Ligrani, P. M., Joseph, S. L., Ortiz, A., and Evans, D. L., 1988, "Heat Transfer in Film-Cooled Turbulent Boundary Layers at Different Blowing Ratios as Affected by Longitudinal Vortices," *Experimental Thermal and Fluid Science,* Vol. 1, pp. 347–362.

Ligrani, P. M., and Schwartz, G. E., 1990, "Control of Embedded Longitudinal Vortices Using a Wall Jet," *Int. J. Heat Fluid Flow,* Vol. 11, No. 4, pp. 274–283.

Ligrani, P. M., Subramanian, C. S., Craig, D. W., and Kaisuwan, P., 1991, "Effects of Vortices With Different Circulations on Heat Transfer and Injectant Downstream of a Row of Film-Cooling Holes in a Turbulent Boundary Layer," ASME JOURNAL OF HEAT TRANSFER, Vol. 113, pp. 79–90.

McEwan, A. D., 1961, "Turbulent Convective Heat Transfer From a Flat Plate and its Improvement Using Vortex Generators," Masters Thesis, Dept. Mech. Engr., Univ. of Melbourne, Australia.

Mehta, R. D., Shabaka, I. M. M. A., Shibl, A., and Bradshaw, P., 1983, "Longitudinal Vortices Imbedded in Turbulent Boundary Layers," Paper No. AIAA-83-0378.

Mehta, R. D., and Bradshaw, P., 1988, "Longitudinal Vortices Imbedded in Turbulent Boundary Layers. Part 2. Vortex Pair With 'Common Flow' Upwards," *J. Fluid Mech.,* Vol. 188, pp. 529–546.

Murlis, J., Tsai, H. M., and Bradshaw, P., 1982, "The Structure of Turbulent Boundary Layers at Low Reynolds Number," *J. Fluid Mech.,* Vol. 122, pp. 13–56.

Nishi, M., and Senoo, Y., 1974, "Investigation of Strength and Paths of Vortices Shed From Vortex Generators in a Pipe and Application to Conical Diffusers," *Bulletin JSME,* Vol. 17, No. 105, pp. 326–334.

Pauley, W. R., and Eaton, J. K., 1988a, "The Fluid Dynamics and Heat Transfer Effects of Streamwise Vortices Embedded in a Turbulent Boundary Layer," Stanford University, Thermo. Div. Rept. MD-51.

Pauley, W. R., and Eaton, J. K., 1988b, "Experiments on the Development of Longitudinal Vortex Pairs Embedded in a Turbulent Boundary Layer," *AIAA Journal,* Vol. 26, No. 7, pp. 816–823.

Pearcey, H. H., 1961, "Shock-Induced Separation and Its Prevention by Design and Boundary Layer Control," Part IV, *Boundary Layer and Flow Control,* G. V. Lachmann, ed.

Purtell, L. P., Klebanoff, P. S., and Buckley, T. T., 1981, "Turbulent Boundary Layer at Low Reynolds Number," *Phys. Fluids,* Vol. 24, pp. 802–811.

Rao, D. M., and Mehrotra, S. C., 1983, "Flat-Plate Drag Measurements With Vortex Generators in Turbulent Boundary Layer," NASA-CR-172125.

Russell, C. M. B., Jones, T. V., and Lee, G. H., 1982, "Heat Transfer Enhancement Using Vortex Generators," *Proc. 7th Intl. Conf. on Heat Transfer,* Munich, W. Germany, Vol. 3, pp. 283–288.

Senoo, Y., and Nishi, M., 1973, "Improvement of the Performance of Conical Diffusers by Vortex Generators," ASME Paper No. 73-WA/FE-1.

Schubauer, G. B., and Spangenberg, W. G., 1960, "Forced Mixing in Boundary Layers," *J. Fluid Mech.,* Vol. 8, pp. 10–31.

Shabaka, I. M. M. A., Mehta, R. D., and Bradshaw, P., 1985, "Longitudinal Vortices Imbedded in Turbulent Boundary Layers. Part 1. Single Vortex," *J. Fluid Mech.,* Vol. 155, pp. 37–57.

Spangler, J. G., and Wells, C. S., Jr., 1964, "Effects of Spiral Longitudinal Vortices on Turbulent Boundary Layer Skin Friction," NASA CR-145.

Stein, D. E., 1985, "Vortex Generators," *Boeing Airliner,* Oct.–Dec., pp. 5–10.

Takagi, S., and Sato, H., 1983, "An Experiment on the Interaction of a Turbulent Boundary Layer and a Row of Longitudinal Vortices," *J. Jpn. Soc. Fluid Mech.,* Vol. 2, pp. 288–300.

Turk, A. Y., and Junkhan, G. H., 1986, "Heat Transfer Enhancement Downstream of Vortex Generators on a Flat Plate," *Proc. Eighth International Heat Transfer Conference,* Vol. 6, pp. 2903–2908, San Francisco, CA.

Westphal, R. V., Eaton, J. K., and Pauley, W. R., 1987a, "Interaction Between a Vortex and a Turbulent Boundary Layer in a Streamwise Pressure Gradient," *Turbulent Shear Flows 5,* Springer-Verlag, New York, pp. 266–277.

Westphal, R. V., Pauley, W. R., and Eaton, J. K., 1987b, "Interaction Between a Vortex and a Turbulent Boundary Layer. Part I: Mean Flow and Turbulence Properties," NASA TM 88361.

Wroblewski, D. E., and Eibeck, P. A., 1991, "Measurements of Turbulent Heat Transport in a Boundary Layer With an Embedded Streamwise Vortex," *Int. J. Heat Mass Transfer,* Vol. 34, No. 7, pp. 1617–1631.

St. Tiggelbeck[1]
Scientist.

N. K. Mitra
Professor.
Mem. ASME

M. Fiebig
Professor.
Mem. ASME

Institut für Thermo- und Fluiddynamik,
Ruhr-Universität Bochum,
Postfach 10 21 48,
4630 Bochum, Federal Republic of Germany

Comparison of Wing-Type Vortex Generators for Heat Transfer Enhancement in Channel Flows

Longitudinal vortices can be generated in a channel flow by punching or mounting small triangular or rectangular pieces on the channel wall. Depending on their forms, these vortex generators (VG) are called delta wing, rectangular wing, pair of delta winglets, and pair of rectangular winglets. The heat transfer enhancement and the flow losses incurred by these four basic forms of VGs have been measured and compared in the Reynolds number range of 2000 to 9000 and for angles of attack between 30 and 90 deg. Local heat transfer coefficients on the wall have been measured by liquid crystal thermography. Results show that winglets perform better than wings and a pair of delta winglets can enhance heat transfer by 46 percent at Re = 2000 to 120 percent at Re = 8000 over the heat transfer on a plate.

Introduction

In plate-fin or fin-tube heat exchangers the flow between the plates can be considered as a channel flow. For reduction of the thermal resistance, the heat transfer coefficient needs to be augmented. The heat transfer coefficient can be increased by wing-type vortex generators (*VG*), which can be punched from the plates or attached to them, Fig. 1. Depending on their form these vortex generators can be called delta wing, rectangular wing, and corresponding winglets. The vortex generators, while remaining attached to the plate at the base, stick out in the flow with an angle of attack with the main flow direction. They generate longitudinal vortices along their leading edges. These vortices turn the flow field perpendicular to the main flow direction and enhance mixing between the fluid close to the fin and the fluid in the middle of the channel.

The influence of longitudinal vortices on heat transfer and on flat plates was experimentally investigated by Edwards and Alker (1974), Russel et al. (1982), Turk and Junkhan (1986), and Eibeck and Eaton (1986).

Russel et al. (1982) found that the rectangular winglets with punching on the pressure side give higher heat transfer than the triangular vortex generators. Fiebig et al. (1991) found that the delta wings are most effective per unit *VG* area for heat transfer enhancement, closely followed by the delta winglet pairs. Rectangular wings and rectangular winglets are much less effective. The experiments of Fiebig et al. (1993) have been performed over a Reynolds number range of 1200 to 2100 and for angle of attack of 10 to 50 deg. The Reynolds number, Re, has been defined with average velocity and the channel height (i.e., the spacing between the fins). Numerical simulations of channel flows with *VG* have shown that the difference in performance between mounted delta wings and delta winglet pairs is negligible; see Brockmeier (1987). However, punched winglets give much better heat transfer than punched wings.

Systematic experimental investigations on the influence of wing-type vortex generators on heat transfer and flow losses have been performed by the last author and his group; see Kallweit (1986), Fiebig et al. (1991), and Zhang et al. (1991). Kallweit (1986) and Fiebig et al. (1991) considered single *VGs* in the Reynolds number range of 2400 and 4200 and at angles of attack between 10 and 50 deg. The Reynolds number Re was defined with U the average velocity and $2H$ (H: channel height). Locally the heat transfer can be increased by several hundred percent, the average increase for an area 50 times the *VG* area can be as high as 60 percent; see Kallweit (1986). Zhang et al. (1991) investigated one row of delta wings in the Reynolds number range of 4000 to 16,000 and at angles of attack between 20 and 70 deg. He found that vortex breakdown occurred at angles of attack around 27 deg. But it had little effect (≈ 4 percent) on the average heat transfer enhancement. While breakdown of vortices has disastrous effects on generated lift, its effects on channel flow are negligible.

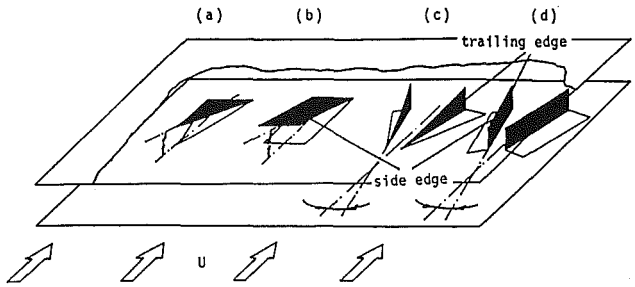

Fig. 1 Schematic of longitudinal vortex generators punched out of a fin: (*a*) delta wing, (*b*) rectangular wing, (*c*) delta winglet pair, (*d*) rectangular winglet pair

Essential findings in these publications can be summarized as follows:

- Wing-type vortex generators at angles of attack generate strong and stable vortices.
- The heat transfer is increased considerably over an area up to 100 times the vortex generator area.
- The heat transfer increases up to angles of attack of 60 deg.

Although some experimental studies have been presented on the performance comparison of some of the four basic forms of vortex generators, they are not yet conclusive; see Kallweit (1986) and Fiebig et al. (1991). The purpose of present work is to compare the performances regarding heat transfer and flow losses of the four basic forms of longitudinal vortex generator (see Fig. 1*a*). The present investigations are performed experimentally. To this purpose, local heat transfer coefficients on the channel wall with punched *VG* are determined. The detailed structure of the heat transfer coefficients elucidates the areas of enhanced and reduced heat transfer and can suggest the optimum locations of the *VGs*.

[1]Current address: Berufschule Essen, Federal Republic of Germany.

Contributed by the Heat Transfer Division for publication in the JOURNAL OF HEAT TRANSFER. Manuscript received by the Heat Transfer Division December 1992; revision received October 1993. Keywords: Finned Surfaces, Forced Convection, Heat Exchangers. Associate Technical Editor: T. W. Simon.

Experimental Methods and Facilities

The experimental investigations are carried out with test models consisting of parallel plate channels, representing the test fins, with punched vortex generators in a small wind tunnel. Local convective heat transfer coefficients are measured on the model surface by liquid crystal thermography. Flow losses are estimated from the measured drag of the test fin.

Wind Tunnel. Figure 2(*a*) shows the schematic of the wind tunnel. It has twin interchangeable vertical test sections (numbered 8*a* and 8*b*) each of dimensions 160 mm × 320 mm × 800 mm (width × breadth × length). One of the test sections is empty, the other contains the test model (Fig. 2*b*). The empty test section stays in the wind tunnel until the measurements with the test model are performed; see next section. The average axial velocity U in the test section can be varied from 0.4 to 7 m/s. At the entrance of the test section the axial velocity distribution in the 120 mm × 240 mm core is uniform to within ±3 percent. The air before the test section can be heated electrically from room temperature (20°C) to 50°C. At the entrance of the test section local, temperature deviations of 0.15°C occur for an air temperature of 50°C in the core. The measured degree of turbulence of the axial velocity

$$Tu_x = (\overline{u'^2})^{1/2}/U$$

lies between 0.7 and 0.9 percent for the whole velocity range.

Test Model. The test model consists of three parallel plates each with a row of three vortex generators; see Fig. 2(*c*). Heat transfer has been measured only on the middle of the central plate. Other plates and vortex generators ensure symmetry conditions. All the plates are punched for vortex generators. However, because of the outer boundary walls flow through the punched holes is negligible. The plates are made of transparent plastic (polycarbonate, trade name: Lexan) sheets of (0.8 ± 0.02) mm thickness. The thermal conductivity of the material is 0.2 W/mK. The density and specific heat are 1220 kg/m^3 and 1170 J/kgK, respectively.

Local Heat Transfer Measurements. Thermochromic liquid crystals (TLC) reflect incident monochromatic light only at a specified temperature. This enables one to record the temporal development of a specified isotherm during transient heating of a test surface. In the experiments, the test surface is first blackened for better contrast and then a thin layer of encapsulated TLC is sprayed on it by an air brush. The total thickness of the blackened test plate with liquid crystal film is 0.84 ± 0.02 mm. The thermal conductivity of the liquid crystals is also 0.2 W/mK. The density and specific heat are 1020 kg/m^3 and 1600 J/kgK, respectively.

The test section with the model stays outside the wind tunnel at room temperature T_{fo} until steady flow conditions with constant temperature T_a (normally 42°C) are established. Then, the empty test section is pushed out and the test section with the model is pushed into the wind tunnel. The time required for this change is less than 1 s. Once in the tunnel, the transient heating of the model begins. The test surface is illuminated by an argon-ion laser with a wavelength of 514 nm. For the specific TLC the reflection of the 514 nm wavelength from the test surface corresponds to a local surface temperature of 30.8°C. The temporal development of this 30.8°C isotherm on the test surface is recorded by an automated camera (1 photo per second).

For the determination of the local heat transfer coefficient, h, the investigated plate area is divided into small elements. With the assumptions of (1) steady incompressible flow, (2) negligible heat conduction on the fin surface, and (3) negligible temperature gradient over the fin thickness, the local heat transfer coefficient, h, can be derived from the energy balance on an element as:

$$h = \frac{\rho_f c_f \delta}{2t(T_f)} \ln \frac{T_a - T_{fo}}{T_a - T_f} \tag{1}$$

Here h is the average of the local heat transfer coefficient for the upper and lower sides of the fin, and t (T_f) stands for the time interval needed to heat the element from the initial temperature T_{fo} to T_f, i.e., to 30.8°C. Only t (T_f) has to be measured to determine h. T_a is the air temperature at the inlet, δ is the fin thickness, ρ_f is the density, and c_f is the specific heat of the fin material. The thermal boundary condition represented by this method is the constant wall temperature under steady conditions; see Russel et al. (1982). The heat transfer coefficient is defined with respect to the air and wall temperature difference $(T_a - T_f)$ and not with the bulk temperature. With this h, one can define the local Nusselt number $\mathrm{Nu} = hD_h/k$ where $D_h = 2h$ is the hydraulic diameter of the channel and k is the thermal conductivity of the flow medium.

The assumption of negligible temperature gradient across the plate is acceptable since the Biot number based on the measured h and the plate thickness (0.8 mm) is of the order of 0.12. The validity of the assumption of negligible heat conduction along the wall has been investigated numerically. The computations show that for a thin wall of low thermal conductivity, significant heat conduction occurs only in front of the vortex generators where the distribution of heat transfer coefficients has local extrema. There the experimental error due to the heat conduction can reach 10 percent. These areas with significant error in h are, however, very small compared to the investigated model surface area (of the order of 2–3 percent). So, even with the error in h due to conduction, the

Nomenclature

A_F = fin area
A_{VG} = area of the vortex generator
b = base length of winglet
B = breadth of the channel
c_F = friction coefficient
c_f = specific heat of the fin material
c_p = pressure coefficient
D_h = hydraulic diameter of the channel
h = winglet height
h = heat transfer coefficient
H = channel height
k = thermal conductivity of the flow medium
l = span of the vortex generator
L = length of the channel
Nu = Nusselt number
p = pressure
Pr = Prandtl number
Re = Reynolds number
s = distance between the tips of winglets
t = time
T_f = local fin temperature
T_{fo} = fin temperature at time $t = 0$
T_a = air temperature
Tu_x = degree of turbulence of the axial velocity
u = axial velocity
u' = turbulent fluctuation in u
U = average velocity in the channel
w = drag force
x = axial distance from the test section entrance
x_v = axial distance of the wing tip from the test section entrance
x^* = $x/(D_h \cdot \mathrm{Re} \cdot \mathrm{Pr})$
x' = axial distance from the base of the vortex generator
β = angle of attack
δ = fin thickness
Λ = b^2/A_{VG} = aspect ratio of wing or winglet
ρ_f = density of the fin material

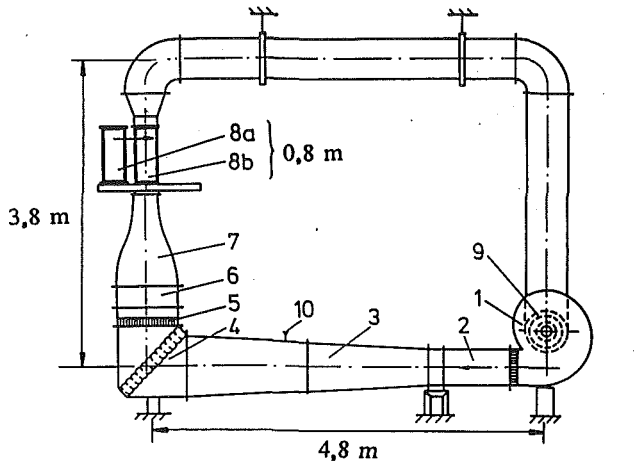

wind tunnel components

1. blower
2. expansions
3. wide angle diffuser
4. 90° turn around
5. straightener chamber
6. mixing chamber
7. nozzle
8a. test section with model (160x320x800 mm^3) (not shown here, see fig. 7)
8b. test section without model
9. heater
10. ref. temp. sensor

Fig. 2(*a*) Schematic of the wind tunnel setup

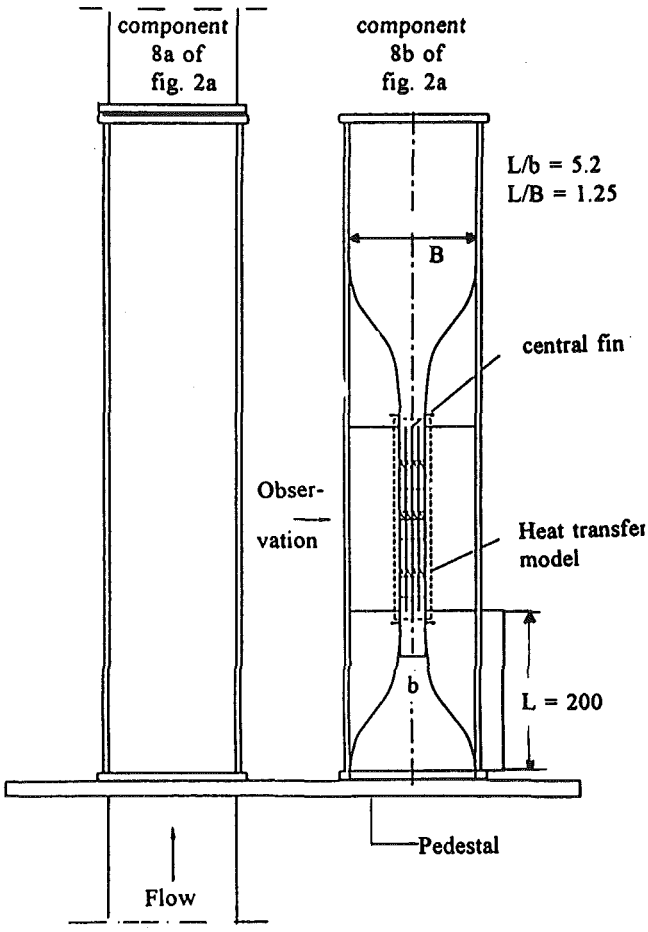

Fig. 2(*b*) Schematic of the wind tunnel test section; measurement are performed only on the central fin

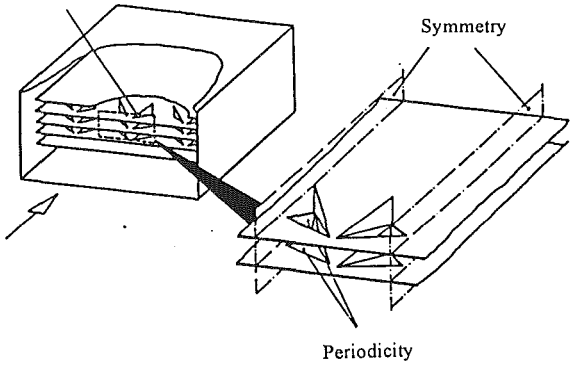

Fig. 2(*c*) Test model with vortex generator; local heat transfer is measured only on the middle section of the central fin

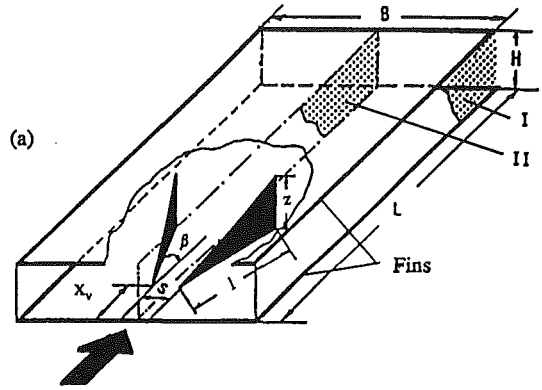

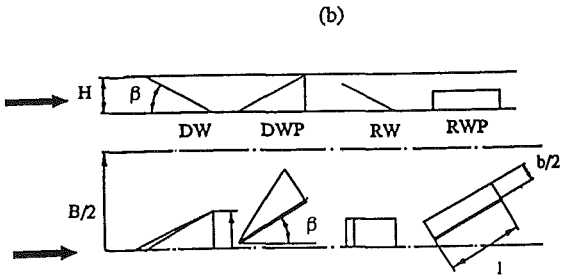

Fig. 3 Vortex generator geometry and notations; Fig. 3(*a*) shows a pair of delta winglets. I and II are symmetry planes; Fig. 3(*b*) shows elevation and plan view of different *VG*s

error in the average heat transfer coefficient over the total area will be negligible.

Drag Measurement. Because of very low pressure drops in the test configurations (of the order of 10^{-2} Pa) the additional flow losses due to the vortex generator within the test configuration have been determined by measuring the drag.

We define the drag coefficient, c_F:

$$c_F = \frac{2w}{\rho u^2 A_F} \tag{2}$$

where w is the drag, and A_F is the fin or plate area. The relation between c_F and the pressure coefficient, c_p, can be derived from the integration of the Navier-Stokes and the mechanical energy equations; see Gersten (1987). The difference between c_F and c_P can amount to 10 percent of c_F for the chosen channel geometry with a delta wing for Re of 2000 because of the

Table 1 Tolerances of experimental variables

air temperature	Ta	0.2 K
fin temperature	T_{fo}	0.2 K
indication temperature of TLC coating	TLC	0.1 K
plate thickness	δ	0.02 mm
heating time	t	0.1 s
velocity of air flow	U	3 %

Table 2 Test model geometry; see also Figs. 1 and 3

Channel:				
Height H	20 [mm]			
Breadth B	5 H			
Length L	15 H			
Fin Area A_F	30,000 mm^2			
Vortex Generator:	DW	DWP	RW	RWP
Angle of attack β	30°	30°	30°	30°
Base length b	2 H	H	1.5 H	H/4
Span l	2 H	2 H	1.3 H	2 H
Area A_{VG} [mm^2]	800	800	800	800
A_F/A_{VG}	37.5	37.5	37.5	37.5
Distance of the wingtip from the channel entrance x_v	H	H	H	H
Distance between tips of winglet pairs s		0.2 H		0.2 H

DW: Delta wing; DWP: Delta winglet pair; RW: Rectangular wing, RWP: Rectangular winglet pair

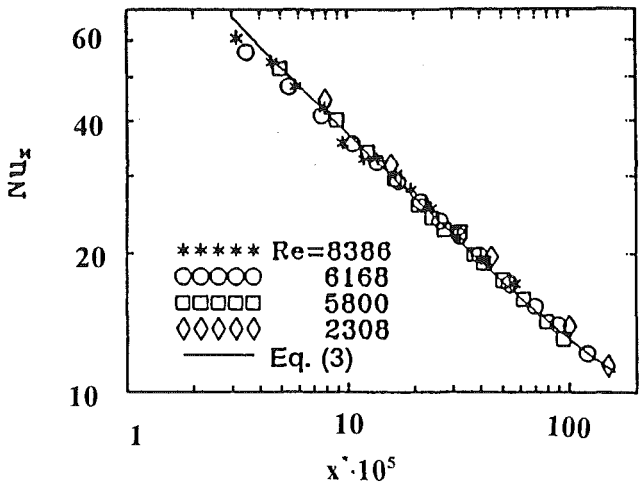

Fig. 4 Comparison of local Nusselt number, Nu_x, of thermally developing flow in a channel

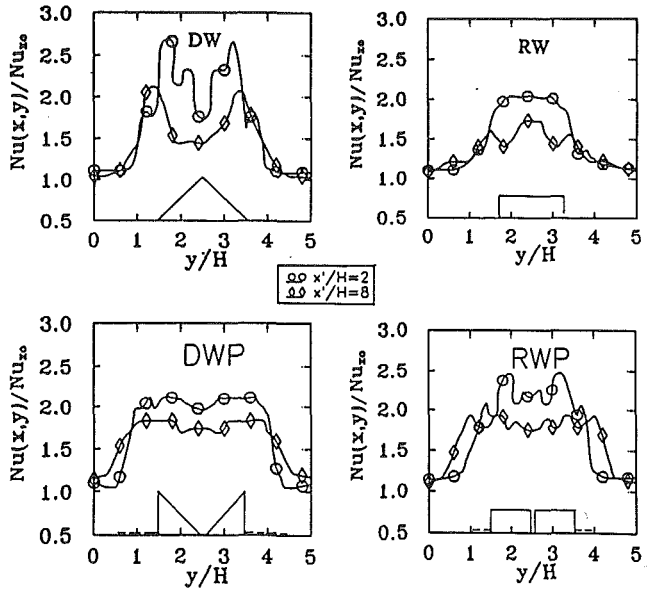

Fig. 5 Spanwise distribution of the Nusselt numbers normalized with the corresponding Nusselt number, Nu_{xo}, of channel flow without *VG*. $x' = 0$ corresponds to the rear end of the *VG*; Re = 4600, geometry: Table 2

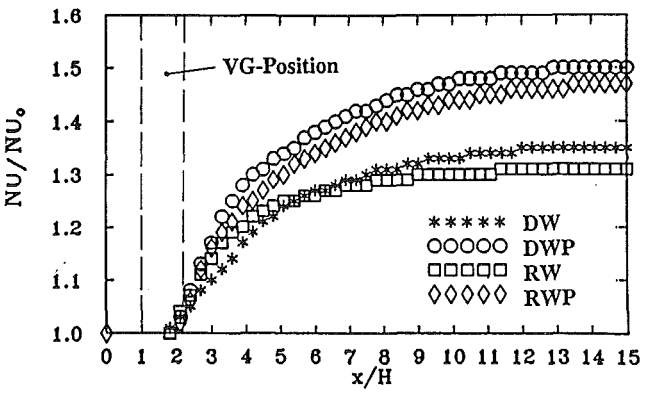

Fig. 6 Area-averaged Nusselt number, Nu, normalized with corresponding Nusselt number, Nu_o, for channel flow without *VG*, Re = 4600, geometry: Table 2

different velocity profiles at the inlet and exit; see Brockmeier (1987).

In the vertical test section, the drag can be determined by measuring the change of weight of a test configuration with and without vortex generators and with and without flow. The change represents the additional drag induced by the vortex generators. The test fin is hung from a weight measuring balance by means of thin wires. The influence of the wire on the measurement is taken into account by separate experiments for each configuration; see Tiggelbeck (1991).

The tolerances of the experimental variables are given in Table 1. The RSS uncertainty as given by Moffat (1988) is 6.3 and 2.65 percent for heating times of 10 s and 30 s, respectively. The Reynolds number of the flow can be adjusted with an accuracy of 3 percent.

Results and Discussion

For the comparison of the performance of four basic forms of vortex generators (delta and rectangular wings and winglets, see Fig. 1) in rectangular channels, four test models, each with a particular form of *VG*, are built. The *VG*s are punched with holes on the pressure side. For the comparison of the different configurations, the following conditions are satisfied:

(*i*) the area of the vortex generator A_{VG} is the same for all cases;
(*ii*) the area of the test fin A_F is the same for all cases;
(*iii*) the blockage of the channel cross section caused by the *VG* is the same for all cases;
(*iv*) the angle of attack β is the same for all cases;
(*v*) the channel geometry is the same for all cases.

Table 2 gives the details of the geometry.

In order to be able to judge the performance of *VG*s, a reference case of heat transfer in the plane channel flow is selected.

Figure 4 compares the measured span averaged Nusselt numbers on the wall of the test channel without vortex generator with the Nu obtained from the following formula given by Kakac et al. (1987):

$$x^* = \frac{x}{D_h \mathrm{Re} \mathrm{Pr}}$$

$$\mathrm{Nu} = 7.55 + \frac{0.024 x^{*-1.14} [0.0179 \mathrm{Pr}^{0.17} x^{*-0.64} - 0.14]}{[1 + 0.0358 \mathrm{Pr}^{0.17} x^{*-0.64}]^2} \quad (3)$$

Table 3 Global Nusselt number Nu and drag coefficient c_F; Re = 4600

	DW	DWP	RW	RWP
Nu	22.54	24.76	21.48	24.26
Nu/Nu_o	1.36	1.49	1.29	1.46
$c_F.(10^{-2})$	2.26	2.89	2.30	2.79
c_F/c_{Fo}	1.50	1.91	1.52	1.85

DW: delta wing, DWP: delta winglet pair, RW: rectangular wing, RWP: rectangular winglet pair; $Nu_o = 16.62$, $c_{Fo} = 1.51.10^{-2}$

Here Re is the Reynolds number based on the average velocity U and D_h. The experiments have been performed in the Re range of 2300 to 8400. The experimental results agree extremely well with Eq. (3). Hence Eq. (3) has been used for the computation of the reference values of Nu.

Figure 5 compares the normalized Nusselt number distributions for delta rectangular wings and winglets at $x/H = 2$ and 8 for Re = 4600. The reference Nusselt number, Nu_{xo}, has been calculated with Eq. (3) for a channel without VG.

From $x = 2H$ downward, delta wings have the highest peaks on the traces of the vortex cores and the lowest trough in between. A rectangular winglet pair gives a structurally similar Nu distribution as given by the delta winglet. A rectangular wing gives the narrowest influence zone with the smallest enhancement (≤ 100 percent). A delta winglet pair gives the broadest influence zone. Figure 5 shows that the worst performance is given by the rectangular wing.

Spanwise-averaged Nusselt numbers have been integrated in the flow direction to obtain the area-averaged Nu. Figure 6 compares these normalized Nusselt numbers. Here Nu_o is obtained from the integration of Eq. (3). Best performance is given by the delta winglet, closely followed (within 50 percent) by the rectangular winglets. An enhancement of heat transfer by 5 percent is given by delta winglets at $x/H \geq 12$. The corresponding enhancement for wings lies within 30 percent.

From the measured drag, the drag coefficient, c_F, has been computed. Table 3 presents the area-averaged Nusselt number for the complete fin and c_F for the four configurations. The reference values for a channel without VG, Nu_o, has been computed from Eq. (3) but c_{Fo} has been obtained from the measurements.

The winglets give higher heat transfer along with higher c_F than given by the wings. In spite of the same projected area (blockage) of all four configurations, the values of c_F are not the same. This is in contrast to Kallweit (1986) who found that c_F values depend mainly on the projected area of the VG. However, Kallweit (1986) investigated only at low Reynolds numbers (~ 1700).

Because of relatively poor performance of wings, further experiments are carried out only with winglets in order to investigate the effect of the angle of attack and the Reynolds number.

Figure 7 compares the normalized area-averaged Nusselt numbers and c_F for delta and rectangular winglets at different angles of attack, β, for Re = 4600. Results show that the maximum heat transfer occurs at a β between 50 and 70 deg. At $\beta = 90$ deg, a sharp decrease in Nu is observed. Flow visualizations did not indicate the formation of longitudinal vortices at $\beta = 90$ deg but indicate unsteady flow with separation; see Tiggelbeck (1991). Apparently, some amount of swirl must have been generated at $\beta = 90$ deg, causing 60 percent enhancement of the Nusselt number.

Measurements with rectangular winglets show that the maximum Nu lies somewhere between $\beta = 45$ and 65 deg and this maximum is smaller than that of a delta winglet pair. The measured c_F for both configurations increases monotonically with β. However, Fig. 7 hints that the rate of increase at higher angles of attack ($\beta > 60$ deg) becomes smaller.

Table 4 compares the effect of Reynolds number on Nu and c_F for plane channel flows and channel flows with delta and

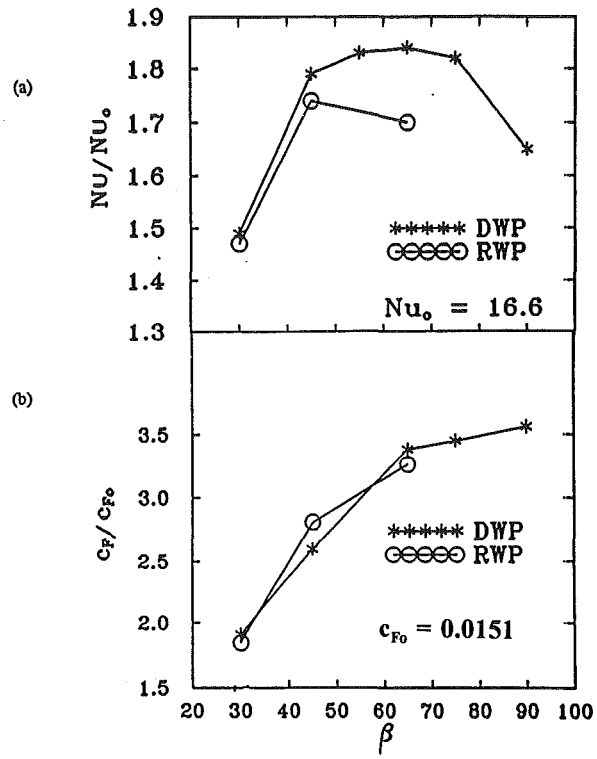

Fig. 7 Complete fin area-averaged Nusselt number, Nu, normalized with Nu_o and the friction coefficient normalized with c_{Fo} as function of the angle of attack β, c_{Fo} has been measured, Nu_o has been calculated from the integration of Eq. (3); Re = 4600, geometry: Table 2

Table 4 Global Nusselt number, Nu, and drag coefficient c_F, for different Re

Re	Nu/Nu_o		c_F/c_{Fo}		$(Nu/Nu_o)/c_F c_{Fo}$	
	DWP	RWP	DWP	RPW	DWP	RWP
2000	1.46	1.39	2.77	2.53	0.53	0.53
4000	1.72	1.66	3.29	3.19	0.52	0.52
6000	2.00	1.83	3.69	3.53	0.54	0.52
8000	2.20	2.00	4.17	3.88	0.53	0.52

rectangular winglets at $\beta = 65$ deg. Nusselt number increases almost linearly with Re. However, the rate of increase is the highest for DWP. In contrast, the c_F for the channel without VG decreases faster with Re than with VG for Re ≤ 3000. At higher Re, c_F for channels with VGs start slowly increasing whereas c_F for a channel without a VG still decreases.

The effect of the aspect ratio, Λ, has been investigated only for DWP for $\Lambda = 1$, 1.5, and 2. Results show that the average Nu values on the plate for all the three cases lie within 5 percent of one another. The variation of the positioning of DWP shows that for $x_v/H = 1$, 2, and 3, the change in the average Nu lies within the experimental accuracy; see Tiggelbeck (1991).

Conclusions

Local transfer and drag of plate fins with four basic forms of longitudinal vortex generators have been measured and compared in the Reynolds number range of 2000 and 8000 and the angle angle of attack range of 30 to 90 deg. The vortex generators are punched out of the fin and they generate swirling motion in the flows in the channel formed by the fin and thereby increase the heat transfer and also the flow losses in the channel. For all the vortex generator geometries there exists an optimum angle of attack for the maximum heat transfer. However, the flow losses increase monotonically with the angle of attack. With increasing Reynolds number the average Nusselt number increases monotonically at a higher rate than the

channel without a vortex generator. The corresponding drag coefficient becomes nearly constant at higher Re in contrast to the drag coefficient for the channel without a *VG*, which continuously decreases in the Re range of the experiments.

Results show that the winglets give better performance than the wings and a pair of delta winglets performs slightly better than a pair of rectangular winglets at higher (>30 deg) angles of attack and at higher (>3000) Reynolds numbers.

The present results can be easily implemented in practice by using rows of delta or rectangular winglet pairs as fins for plate-fin heat exchangers. The performance of such heat exchangers has already been numerically investigated; see Fiebig et al. (1993). A comparison of the performance of wing-type vortex generators (obtained from numerical simulation) and the traditional offset-strip or louvered as given by Kays and London (1984) can be found in Güntermann (1992) and Brockmeier et al. (1993). The results indicate that for the same mass flow, heat duty and pumping power, fins in the form of rectangular winglets may need less heat transfer surface that needed by offset-strip fins.

References

Brockmeier, U., 1987, "Numerisches Verfahren zur Berechnung dreidimensionaler Strömungs- und Temperaturfelder in Kanälen mit Längswirbelerzeugern und Untersuchung von Wärmeübergang und Strömungsverlust," Dissertation, Institut für Thermo- und Fluiddynamik, Ruhr-Universtät Bochum, Federal Republic of Germany.

Brockmeier, U., Güntermann, Th., and Fiebig, M., 1993, "Performance Evaluation of a Vortex Generator Heat Transfer Surface and Comparison With Different High Performance Surfaces," *International Journal of Heat and Mass Transfer*, Vol. 36, No. 10, pp. 2575–2587.

Edwards, F. J., and Alker, C. J. R., 1974, "The Improvement of Forced Surface Heat Transfer Using Surface Protrusions in the Form of Cubes and Vortex Generators," *Fifth Int. Heat Transfer Conf.*, Tokyo, pp. 244–248.

Eibeck, P. A., and Eaton, J. K., 1986, "The Effects of Longitudinal Vortices Embedded in a Turbulent Boundary Layer on Momentum and Thermal Transport," *Eighth Int. Heat Transfer Conf.*, San Francisco, CA, pp. 1115–1120.

Fiebig, M., Kallweit, P., Mitra, N. K., and Tiggelbeck, S., 1991, "Heat Transfer Enhancement and Drag by Longitudinal Vortex Generators in Channel Flow," *ETF Science*, Vol. 4, pp. 103–114.

Fiebig, M., Güntermann, Th., and Mitra, N. K., 1993, "Numerical Analysis of Heat Transfer and Flow Loss in a Compact Plate Heat Exchanger Element With Longitudinal Vortex Generators as Fins," presented at the ASME Winter Annual Meeting, New Orleans, LA, Nov. 28–Dec. 3.

Gersten, K., 1987, *Single Phase Fluid Flow, Introduction and Fundamentals, Heat Exchanger Design Handbook 2: Fluid Mechanics and Heat Transfer*, E. U. Schlünder, ed., Hemisphere.

Güntermann, T., 1992, "Dreidimensionale stationäre und selbsterregtschwingende Strömungs- und Temperaturfelder in Hochleistungswärmeübertragern mit Wirbelerzeugern," Dr.-Ing-Dissertation, Ruhr-Universität Bochum, Federal Republic of Germany.

Kakac, S., Shah, R. K., and Aung, W., eds., 1987, *Handbook of Single Phase Convective Heat Transfer*, Wiley, New York.

Kallweit, P., 1986, "Längswirbelerzeuger für der Einsatz in Lamellenwärmetauschern," Dissertation, Institut für Thermo- und Fluiddynamik, Ruhr-Universität Bochum, Federal Republic of Germany.

Kays, W. M., and London, A. L., 1984, *Compact Heat Exchangers*, 3rd ed., McGraw-Hill, London, United Kingdom.

Moffat, R. J., 1988, "Describing the Uncertainties in Experimental Results," *ETF Science*, Vol. 1, pp. 3–17.

Russel, C. M. B., Jones, T. V., and Lee, G. H., 1982, "Heat Transfer Enhancement Using Vortex Generators," *Seventh Int. Heat Transfer Conf.*, Munich, Federal Republic of Germany, pp. 283–288.

Tiggelbeck, S., 1991, "Experimentelle Untersuchungen an Kanalströmungen mit Einzel- und Doppelwirbelerzeugereihen für den Einsatz in kompakten Wärmetauschern," *Fortschritt-Berichte VDI*, Vol. 19, No. 49, VDI-Verlag GmbH, Düsseldorf, Federal Republic of Germany.

Turk, A. J., and Junkhan, G. H., 1986, "Heat Transfer Enhancement Downstream of Vortex Generators on a Flat Plate," *Eighth Int. Heat Transfer Conf.*, San Francisco, CA, pp. 2903–2908.

Zhang, Z., Fiebig, M., and Mitra, N. K., 1991, "Vortex Breakdown and Its Effect on Heat Transfer in Flows Between Parallel Plates," *ENTROPIE*, Creteil, France, pp. 29–32.

Effect of Flow Pulsations on the Cooling Effectiveness of an Impinging Jet

H. S. Sheriff
Research Assistant.
Student Mem. ASME

D. A. Zumbrunnen
Associate Professor.
Mem. ASME

Thermal Sciences Research Laboratory,
Department of Mechanical Engineering,
Clemson University,
Clemson, SC 29634-0921

An experimental investigation has been performed to study the effect of flow pulsations on local, time-averaged convective heat transfer to an impinging water jet. Sinusoidal and square-pulse waveforms were considered. For the square waveform, the flow was completely halted for a portion of the pulsation cycle. Hot-film anemometry was used to characterize both the steady and the pulsating flows with regard to turbulence level and the spatial uniformity in the velocity profile across the nozzle width in order to assess separately the influence of flow pulsation on convective heat transfer. Pulse magnitude, which was defined as the ratio of the mean-to-peak velocity change to the mean flow velocity, was varied from 0.5 to 100 percent. Pulse frequencies ranged from 5 to 280 Hz, which corresponded to Strouhal numbers based on jet width and velocity of 0.014 to 0.964. Observed effects on convective heat transfer are explained in terms of nonlinear dynamic responses of the hydrodynamic and thermal boundary layers, boundary layer renewal, and bulges in the jet free surface.

Introduction

Heat transfer to pulsating flows has been studied chiefly in efforts to improve heat exchanger performance and has therefore been largely related to flows in or past tubes. However, little work regarding pulsating impinging jet flows has been performed, even though jet flows are used extensively in cooling, heating, and drying processes. Perhaps since high convective heat transfer rates are readily attainable in the vicinity of a turbulent impinging jet, motivation to study the effect of flow pulsations may have been diminished. However, independent means to alter the transport characteristics of an impinging flow can be of practical interest. For example, in microelectronic and micromechanical applications, enhancement due to turbulence may not be possible or effective when jet Reynolds numbers are necessarily low or moderate because of small characteristic dimensions. Moreover, enhancements derived from turbulence effects remain small at low Reynolds numbers even when high turbulence intensities are induced (Smith and Kuethe, 1966). Since impinging jets are related fundamentally to stagnation flows in general, insights gained from studies of pulsating jet flows can find further application to flows past cylinders, spheres, and other bluff bodies, such as gas turbine blades.

Although convective heat transfer is very effective near the stagnation region of impinging flows, very little of the incident fluid is directly involved in removing heat. Most of the fluid presides in a relatively thick overriding layer that establishes the favorable pressure gradient needed to induce thin boundary layers characteristic of accelerating flows. A well-established streamline pattern for a steady impinging jet flow is shown in Fig. 1(*a*). For an impinging planar jet, the flow bifurcates along a line of symmetry known as the *stagnation line* where the fluid velocity is zero and the static pressure is highest. For a particular incident velocity and geometry, the velocity gradient C (see Nomenclature) at the stagnation line is a constant and is calculable from potential flow theory or static pressure measurements (Zumbrunnen et al., 1992). In this study, it was deemed appropriate to investigate whether time-averaged heat transfer characteristics of an *impinging*, nonsubmerged jet flow can be altered by inducing pulsations in the incident jet velocity. Three phenomena that may lead to convective heat transfer enhancements in pulsating jet flows are depicted in Figs. 1 (*b–d*): (*i*) Pulsations may lead to instabilities in the jet free surface, higher turbulence levels, and a more complex streamline pattern (Fig. 1*b*). Kimura and Bejan (1983) showed experimentally that a vertical liquid column impinging onto a horizontal surface was buckled into a planar sinuous shape. Related theoretical work (Bejan, 1981) indicated that inviscid jets have a natural frequency. A type of resonance in jets with free surfaces might be achieved by pulsing them at this natural frequency and thereby inducing instabilities. (*ii*) Chaotic mixing describes the condition in which fluid particles no longer follow well-defined streamlines but move erratically and unpredictably through the stagnation region (Fig. 1*c*). Such large-scale chaotic fluid motion, which may occur at *low* Reynolds numbers, is generally not regarded as turbulence but arises due to a periodic flow disturbance (e.g., a flow pulsation). Chaotic mixing within enclosures has been documented in simple, laminar flows subjected to periodic forcing (Aref, 1984; Khakhar et al., 1986; Ottino, 1989). Such chaotic fluid motion, if instilled in an unconfined flow to an extent that fluid mixing near the surface is improved, would mimic the beneficial effects of turbulence and may promote heat transfer. (*iii*) Periodic restart of boundary layer growth on an impingement surface can be induced to obtain enhanced convective heat transfer (Zumbrunnen and Aziz, 1993). In addition, the nonlinear dynamic responses of the hydrodynamic and thermal boundary layers to flow pulsations have been investigated recently (Zumbrunnen, 1992; Mladin and Zumbrunnen, 1994a) and might be exploited to induce thinner boundary layers by careful selection of pulse waveforms (Fig. 1*d*). In any *particular* pulsating jet flow, one or more of the mechanisms depicted in Figs. 1(*b–d*) might occur to enhance heat transfer. However, as will be seen, pulsations can also alter the geometry of an impinging jet and lead to reduced convective heat transfer.

Several investigators have studied the flow field of pulsating, *nonimpinging* air jets. For an axisymmetric (d_n = 25 mm) jet, Binder and Favre-Marinet (1973) found that the turbulence intensities along the jet axis downstream of the nozzle increased at a much faster rate in pulsating jets than in steady jets. Moreover, the final turbulence levels in the pulsating jets were appreciably higher and mixing was improved at distant points downstream where the pulsation was completely abated. Curtet and Girard

Contributed by the Heat Transfer Division and presented at the National Heat Transfer Conference, Atlanta, Georgia, August 8–11, 1993. Manuscript received by the Heat Transfer Division July 1993; revision received January 1994. Keywords: Augmentation and Enhancement, Jets, Transient and Unsteady Heat Transfer. Associate Technical Editor: A. Faghri.

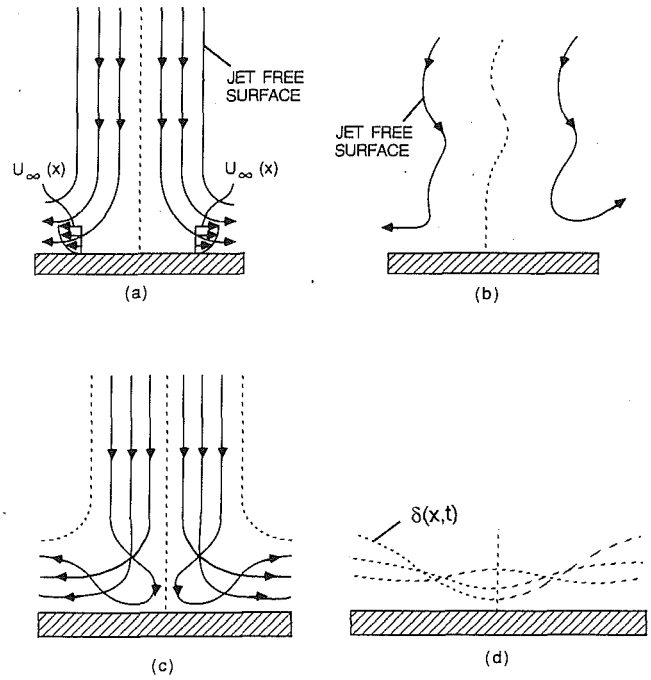

Fig. 1 Phenomena in pulsating jet flows that may affect convective heat transfer to an impinging jet: (a) steady jet; (b) induced instability in jet; (c) chaotic fluid motion in stagnation region; (d) periodic boundary layer renewal or destabilization

(1973) photographed an axisymmetric (d_n = 24 mm) jet and observed that the steady jet spread progressively downstream of the nozzle, whereas the pulsating jet expanded sharply very near the nozzle exit. High-speed photographs revealed a cyclic generation of vortex rings at the nozzle exit for the pulsating jets, which subsequently traveled downstream. Increased entrainment and spreading of air jets under flow pulsation were also observed by Bremhorst (1979) and Bremhorst and Hollis (1990). Vortex ring generation and spreading in these submerged jets were due to interaction with a stagnant ambient fluid. The jet used in the present investigation is a free (i.e., unsubmerged) jet and similar vortex generation and spreading effects are not expected. Unlike a submerged jet, a free jet has a comparatively larger density than the medium into which it discharges and momentum exchange from the jet is negligible.

Nevins and Ball (1961) measured temporally and spatially averaged Nusselt numbers for heat transfer between a flat copper plate and a pulsating, impinging, axisymmetric (d_n = 6.35 mm) air jet. Results indicated no effect of pulse magnitude and pulse frequency on Nusselt number for the pulsation frequencies investigated, which corresponded to Strouhal numbers S_d ($=fd/u_j$) from 0.0001 to about 0.01. However, in conjunction with a related experimental study, Zumbrunnen and Aziz (1993) utilized a theoretical model of the boundary layer dynamics and showed that the boundary layer response was sufficiently fast to maintain boundary layer thicknesses effectively for steady-state conditions over this pulsation frequency range. They referred to pulsating jet flows with pulse magnitudes of 100 percent as *intermittent jet flows*, since a complete flow stoppage occurred during each pulsation cycle. Enhancements in convective heat transfer to a planar, intermittent water jet were achieved by briefly and repetitively interrupting the incident jet flow and thereby halting the development of the hydrodynamic and thermal boundary layers. Although little or no cooling was available during a brief interval when the flow was interrupted, the thermal resistance due to the newly forming thermal boundary layer was extremely small each time the flow was resumed and a net enhancement thereby arose. The time needed for boundary layer development was estimated from a theoretical boundary layer dynamics model and was used to determine a dimensionless frequency above which enhancements can be expected. For moderate Prandtl numbers, the theoretical model revealed that the free-stream velocity gradient C in the stagnation region principally governs the *dimensional* boundary layer time response and the boundary layer dynamics scale temporally with C^{-1}. With the time for thermal boundary layer development given in terms of this time scale, the threshold frequency was determined to be $S_w > 0.26$, where $S_w = fw/u_j$. This expression was in good agreement with experimental results.

The stagnation region for a cylinder in a crossflow is similar geometrically to the stagnation region arising beneath an impinging planar jet. Thus, research with cylinders can provide important insights with regard to impinging planar jets. Gundappa and Diller (1991) studied coupling between the effects of free-stream turbulence and flow pulsation on heat transfer from a cylinder in a crossflow of air. With incident velocity and cylinder diameter as reference values, the Reynolds number was held at 50,000 while the Strouhal number was changed from 0.016 to

Nomenclature

C = free-stream velocity gradient at stagnation line and near impingement surface for steady jet $= U_\infty/x_j$, 1/s
d = diameter of a circular jet or of a cylinder, m
d_n = diameter of a circular nozzle, m
f = pulsation frequency, Hz
f_* = dimensionless frequency $= f/C$
$g(x)$ = function given by Eq. (3)
h = convective heat transfer coefficient, W/m² °C
H = ratio of distance between nozzle opening and hot-film sensor to nozzle width or ratio of distance between nozzle opening and test strip to nozzle width
H_s = thickness of test strip, m
I = electrical current passing through test strip, amp
J = nozzle width, m
k = thermal conductivity of fluid, W/m °C
k_s = thermal conductivity of test strip, W/m °C
L = length of test strip, m
Nu_w = time-averaged Nusselt number based on jet width $= hw/k$
Nu_{ss} = Nusselt number based on jet width under steady flow conditions $= hw/k$
Nu_* = time-averaged Nusselt number normalized by steady-state value $= Nu_w/Nu_{ss}$
Pr = Prandtl number evaluated at local film temperature
Pr_0 = Prandtl number at stagnation line ($x = 0$)
R = electrical resistance of exposed length of test strip, Ω
Re_j = Reynolds number evaluated at jet temperature $= u_j w/\nu$
Re_w = Reynolds number evaluated at local film temperature $= u_j w/\nu$
Re_{w0} = Reynolds number at stagnation line ($x = 0$) $= u_j w/\nu$
S_w = Strouhal number $= fw/u_j$
t = time, s
t_{bl} = time period for boundary layer growth in jets with square pulse waveform (equals time for continuous flow in pulse cycle), s
T = temperature in strip, °C
T_{bs} = local temperature at bottom side of test strip (Fig. 2), °C
T_f = local film temperature $= [T_s(x_j) + T_\infty]/2$, °C
T_s = temperature of the impingement surface, °C

0.218. Turbulence intensities from 0.4 to 7.5 percent were considered and the amplitude of the pulsating flow velocity ranged from 4.0 to 15.5 percent of the mean flow velocity. Heat transfer in the stagnation region for the steady and pulsating flows did not differ measurably for identical turbulence intensities. Thus, no interaction between flow pulsation and turbulence was indicated. In a related earlier study (Andraka and Diller, 1985), time-averaged convective heat transfer was found to be unaffected by sinusoidal variations in the incident flow. Rosiczkowski and Hollworth (1991) measured the local and instantaneous heat transfer from an isothermal cylinder oscillating in an air cross-flow. Strong in-line motion produced periodic fluctuations in the heat transfer coefficient with a frequency equal to the driving frequency while strong transverse motion produced fluctuations equal to twice the driving frequency. Maximum instantaneous heat transfer coefficients were up to 10 percent higher than the corresponding heat transfer coefficients for steady state, but time-averaged values were unaffected.

In consideration of the potential enhancement mechanisms that may result (Fig. 1) and in view of the small amount of prior related work, an experimental investigation was carried out to determine the effect of flow pulsation on convective heat transfer to an impinging, nonsubmerged, water jet flow.

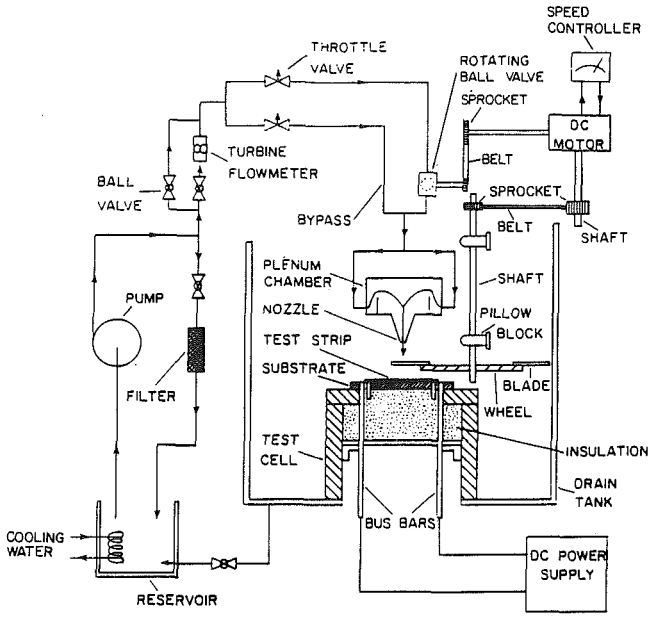

Fig. 2 Schematic representation of the experimental apparatus (not to scale)

Experimental Apparatus and Methods

A schematic representation of the apparatus is shown in Fig. 2. Details of its construction and instrumentation as well as those related to data reduction are available in an earlier paper (Zumbrunnen and Aziz, 1993). In summary, filtered water was supplied by a centrifugal pump to a convergent nozzle, which generated a low-turbulence planar water jet with a width of 5.08 mm. The jet plane was vertically oriented and discharged downward onto the upper face of a thin (0.084 mm), electrically heated test strip. The lower face of the thin test strip was thermally insulated. Water temperature was maintained by circulating cooling water through a heat exchanger submerged in the reservoir of the filtered water system.

Two separate devices were used to generate pulsations in the impinging jet flows. Sinusoidal pulse waveforms with $\epsilon < 85$ percent were produced with a rotating ball valve installed in a fluid flow line upstream of the nozzle (Fig. 2). Isolation valves to a turbine flow meter were shut to protect it from flow pulsations and a bypass valve was opened. A branch network with precision throttle valves was used to partition the flow between the rotating ball valve and a bypass line in order to maintain a prescribed mean flow velocity. The ball valve was rotated by a gear-belt arrangement driven by a variable speed, direct current motor. Rotational speed was maintained by a speed controller and was determined with a digital stroboscope. Instantaneous flow velocities from the nozzle were measured by hot-film anemometry. However, the hot-film probe was retracted during heat transfer measurements to eliminate any disturbances caused by the sensor body. For the square-pulse waveforms ($\epsilon = 100$ percent), the variable speed direct current motor was disconnected from the ball valve and reconnected to a rotating wheel through a separate shaft and gear-belt assembly. The wheel was rotated such that six stainless-steel blades penetrated the free surface of the water jet, causing a periodic blockage of the flow impinging on the test strip. The blade width was larger than the nozzle width to deflect the jet completely from the test strip and thereby induce an on/off *incident* jet flow. Since hot-film probes in anemometry systems must be immersed in a continuous flow to avoid burnout, turbulence measurements of the on/off flow were not made and the velocity of the steady jet upstream of the rotating blades was determined with the turbine flow meter. Further details of the

Nomenclature (cont.)

T_{s0} = initial surface temperature, °C
T_t = time period for flow pulsation, s
T_{ts} = local surface temperature along test strip, °C
T_∞ = fluid free-stream temperature, °C
Tu = turbulence intensity = $\sqrt{u'^2}/u_{avg}$
u = flow velocity, m/s
u_{amp} = pulse amplitude [Eq. (1)], m/s
u_{avg} = mean flow velocity [Eq. (1)], m/s
u_d = disturbance velocity = $u^* + u'$, m/s
u_H = time-averaged jet velocity at specified location beneath nozzle opening, m/s
$u_{H,c}$ = time-averaged jet velocity along jet centerline at specified location beneath nozzle opening, m/s
u^* = periodic component of flow velocity, m/s
u' = turbulence component of flow velocity, m/s
u_j = time-averaged incident jet velocity, m/s
U_∞ = local free-stream velocity component parallel to surface at stagnation line for steady jet, m/s
w = incident jet width, m
w_H = jet width at hot-film sensor location, m
W = spanwise dimension of test strip, m
x = dimensionless distance = x_j/w
x_H = distance across jet width from jet plane of symmetry, m
x_j = distance along impingement surface from stagnation line, m
y = vertical position within test strip, m
Γ = dimensionless time for boundary layer growth = Ct_{bl}
δ = hydrodynamic boundary layer thickness, m
δ_t = thermal boundary layer thickness, m
ϵ = pulse magnitude = u_{amp}/u_{avg}
θ = $(T_s - T_\infty)/(T_{s0} - T_\infty)$
Λ = dimensionless hydrodynamic boundary layer thickness = $C\delta^2/\nu$
ν = kinematic viscosity, m²/s
ξ = dimensionless thermal boundary layer thickness = $C\delta_t^2/\nu$
τ = dimensionless time = Ct

ensuing flow and of the wheel-blade assembly have been described by Zumbrunnen and Aziz (1993).

Thermocouples of ANSI Type T (copper-constantan) for test cell instrumentation were fabricated and inlaid in spanwise grooves machined on the substrate plate (Fig. 2). An intrinsic frequency response for the thermocouples of 250 Hz was calculated by idealizing a thermocouple bead as a one-dimensional slab subjected to a step change in temperature. The time response of the test strip itself was also evaluated with a transient numerical heat conduction model. Convective cooling, with a rapidly varying periodic heat transfer coefficient anticipated for a pulsating flow, was imposed at the upper surface to generate simulated temperature data at the bottom surface of the test strip. Results indicated that time-averaged temperatures at the bottom surface and a steady-state thermal analysis can be used to determine the time-averaged convective heat transfer coefficients at the surface to within 0.2 percent for the pulsation frequencies investigated in this study. Thus, in a steady-state heat conduction analysis, the bottom side of the test strip was modeled as an adiabatic surface ($dT/dy = 0$) and the heat flux to the jet was calculated from the strip resistance, electrical current, and exposed strip surface area. Surface temperatures corresponding to the measured, time-averaged temperatures at the bottom side of the thin test strip at each thermocouple location were calculated from the solution to the one-dimensional heat conduction equation with uniform volumetric heat generation due to ohmic heating (McMurray et al., 1966). The resulting expression [$T_{ts} = T_{bs} - QH_s^2/2k_s$, where $Q = I^2R/LWH_s$] and the measured jet temperature were used with Newton's law of cooling to determine local convective heat transfer coefficients. The jet temperature was measured with a copper-constantan thermocouple probe placed in the nozzle plenum chamber. All thermophysical properties were evaluated at the local film temperature T_f [$=(T_s(x_j) + T_\infty)/2$]. Corrections to time-averaged jet discharge velocity and width were made to account for thinning due to gravitational acceleration (Zumbrunnen et al., 1989). Jet Reynolds numbers (Re_w) and Nusselt numbers (Nu_w) were calculated from the corrected jet velocity and jet width for both the steady and pulsating jet flows. Distances between the nozzle and test strip ranged from 3.5 to 7 jet widths ($w = 0.508$ cm), with all experiments done for a distance of 3.5 except for those done to assess the influence of nozzle height. Corrections to jet velocity due to gravitational acceleration were less than 1 percent for Re $\approx$ 20,000 and 10 percent for Re $\approx$ 6000. Detailed information about the instrumentation, time responses, and data acquisition procedures has been previously reported (Zumbrunnen and Aziz, 1993).

The flow fields for the steady jets and the pulsating jets with the sinusoidal pulse waveform were characterized using a hot-film anemometer and a cylindrical hot-film probe. A probe extension was mounted to a linear traversing mechanism with two axes of freedom to position the hot-film probe accurately in a selected horizontal plane. Vertical positioning was accomplished by mounting the traversing mechanism on a scissors-truss support table. The active cylindrical probe element was supported by two fine support needles with a right angle bend to position the element upstream of the probe body and reduce flow disruption. The sensor was mounted in a crossflow configuration with the cylindrical sensor body parallel to the jet plane. This arrangement preserved the two dimensionality of the planar jet and allowed measurements of the pulsating flow velocity, as well as the component of the turbulent velocity in the direction of the mean flow. The velocity information from the anemometer control circuit was interrogated at 1190 samples per second. This sampling rate was deemed to be adequate since power spectra indicated that more than 99 percent of the turbulence energy pertained to low frequencies (Brereton and Kodal, 1992). The raw data were then transferred to a microcomputer where they were stored for processing.

It was desired to estimate turbulence levels in both the steady and pulsating jet flows in order to ascribe properly any differences in convective heat transfer to appropriate phenomena. The pulsating jet flow-field data contained superimposed steady, periodic, and turbulent velocity components and can be effectively represented by $u = u_{avg} + u^* + u'$. An optimal digital filter, known as a Wiener filter (Peebles, 1980), was used to separate the periodic and turbulent components. This separation method (Brereton and Kodal, 1992) is less sensitive to cycle-to-cycle variations in the pulse characteristics as compared to the phase-averaging technique of Hussain and Reynolds (1970). Insensitivity yielded improved turbulence estimates since small variations ($\cong$2 percent) in the pulsation frequency occurred. To implement this method, the raw flow-field data were time-averaged to obtain the mean free-stream velocity u_{avg}, which was then subtracted from the raw velocity data to obtain the disturbance velocity u_d ($=u^* + u'$). As suggested by Brereton and Kodal (1992), the Fourier transform was taken of the resulting time series of u_d values over about ten pulsation cycles. A specified filter function was applied to the Fourier transform of the disturbance velocity u_d to remove the periodic component and obtain $u'(t)$ upon executing an inverse Fourier transformation. The corresponding values of Tu were then calculated directly from the resolved $u'(t)$.

So as to acquire representative pulse magnitudes for the velocity waveforms containing turbulence fluctuations, the resulting values of $u'(t)$ were also useful in obtaining correct magnitudes for the periodic velocity components. A sinusoidal function [Eq. (1)] was found to represent the pulse reasonably well with u_{amp} equal to the root-mean square of $u^*(t)$ determined with Eq. (2) (Evans, 1975). With representative values for u_{amp} and u_{avg} determined, the pulse magnitude ϵ was given by u_{amp}/u_{avg}. As determined from the power spectra for the pulsating jets, more than 95 percent of the pulse energy was at the fundamental frequency of the pulse. Thus, a near-sinusoidal velocity pulse was produced in the experiments, which utilized the rotating ball valve.

$$u = u_{avg} + u_{amp} \sin(2\pi ft) \tag{1}$$

$$\overline{[u^*(t)]^2} = \overline{[u_d(t)]^2} - \overline{[u'(t)]^2} \tag{2}$$

High-speed photographs were taken to characterize further the pulsating jets generated with the ball valve assembly. In order to relate the flow conditions to the photographs, the rotation of the wheel shown in Fig. 2 was synchronized with the pulsation frequency by simultaneously driving the wheel and the rotating ball valve with the direct current motor. Graduations were placed on the rim of the wheel, which corresponded to specific phases of the pulse cycle. Photographs were taken with the wheel visible in the background and information regarding the nature of the pulse and the phase in the pulsation cycle were thereby conveniently recorded. A digital stroboscope was used to view the jets in a darkened laboratory and resolve any ambiguities in the photographs.

A detailed uncertainty analysis was performed to account for all possible error sources using the method outlined by Kline and McClintock (1953). The experimental uncertainties in time-averaged Nusselt numbers for the steady and pulsating jets differed by less than 0.1 percent since nearly identical data acquisition and reduction procedures were used. Small disparities were due to different errors associated with jet velocity measurements determined from the turbine flow meter and anemometer. Relative uncertainties in stagnation line Nusselt numbers (Nu_{w0}) with 20 to 1 odds were found to vary from 7 to 11 percent for jet Reynolds numbers (Re_{w0}) ranging from 3000 to 20,000, respectively. Uncertainties at positions beyond about four jet widths from the stagnation line ranged from about 4 to 6 percent over the same Reynolds number range. Slightly higher uncertainties occurred at the larger Reynolds numbers and at the stagnation line since temperature differences between the strip surface and jet were smaller.

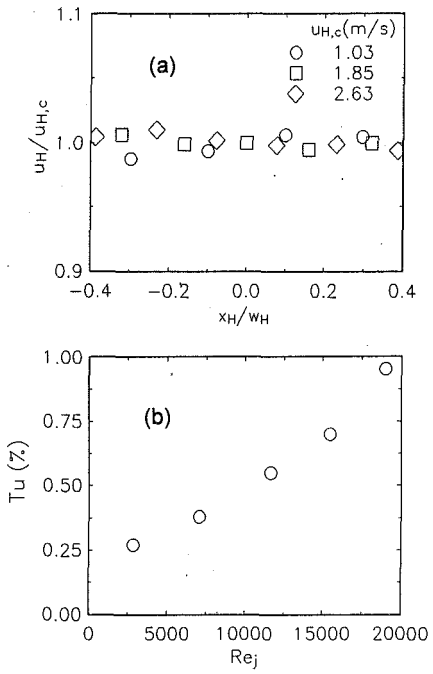

Fig. 3 Steady jet flow field characteristics with $H = 4.5$; (a) time-averaged velocity profile across jet width; (b) turbulence intensity

Results and Discussion

Flow Field Characteristics. The jet flow field was characterized with respect to the time-averaged velocity profile across the jet width, the intrinsic turbulence intensity, and the pulse profile (i.e., jet velocity versus time) in the case of the pulsating jet. The motivation was to verify that changes in the velocity profile and turbulence level were sufficiently small so as not to affect convective heat transfer significantly in the pulsating jets in comparison to the steady jets. Any observed changes in convective heat transfer could then be ascribed possibly to one or more of the phenomena depicted in Fig. 1.

Time-averaged velocity profiles across the steady jet width are shown in Fig. 3(a) for three representative jet velocities. These corresponded to the low, medium, and high Reynolds numbers in this study. Close to the free surface of the jet ($x_j/w_H \cong \pm 0.4$), the hot-film sensor could not be completely immersed in the jet flow and velocity measurements are not reported. It can be seen that the time-averaged velocity profile was essentially flat with a variation of less than 3 percent across the jet width. The profile was similar at other transverse locations along the jet length and was also similar at other jet heights. The plot of turbulence intensity versus jet Reynolds number for the steady jet is shown in Fig. 3(b). The turbulence intensities increase from about 0.25 to 0.95 percent. Actual turbulence intensities at the smaller Reynolds numbers were somewhat lower, since for Re$_j$ < 8000, ripples originated around the hot-film sensor and were presented as false turbulence. However, all measured turbulence intensities were small and will be shown below to give enhancements in convective heat transfer of less than about 2.8 percent. Thus, turbulence did not affect convective heat transfer measurements appreciably in the steady jets. Time-averaged velocity profiles for the pulsating jets were also essentially flat with a variation of less than 3 percent. Typical values of turbulence intensities for the pulsating jets, within the range of parameters investigated, were similar to those for the steady jets and increased with jet Reynolds number as in Fig. 3(b). Thus, if the influence of turbulence is similar to the steady flow case, it is expected that changes in turbulence levels did not affect convective heat transfer measurements appreciably in the pulsating jets of this study. Any differences in heat transfer between the pulsating and steady jets must be attributed to other causes, such as those depicted in Fig. 1.

Normalized pulse profiles at the jet centerline are shown in Fig. 4(a). The abscissa denotes time, normalized by the pulse period T_t. Sinusoidal pulses developed using Eq. (1) are superimposed for comparison. The profiles are essentially sinusoidal; however, small deviations from a sinusoidal profile are evident. Such deviations, although small, depended on the pulse amplitude and pulse frequency and were principally due to fluid inertia and occasional galling of the valve stem by loosened packing in the rotating ball valve (Fig. 2). A typical power spectrum for a pulsating jet is shown in Fig. 4(b). The spectrum, although obscured by the log scale, indicates that more than 95 percent of the pulse energy is at the pulsation frequency.

The free surfaces of the flows emanating from the nozzle are shown in Fig. 5 for one cycle of the steady periodic pulsating jet produced with the rotating ball valve assembly. [Similar results for jets produced with the wheel/blade assembly have been presented previously (Zumbrunnen and Aziz, 1993).] When the rotating ball valve was closed, the flow emanating from the nozzle was due only to flow passing through the bypass valve (Fig. 2) and the jet appeared much like a steady jet (Fig. 5a). When the ball valve opened, a surge of flow was produced and a bulge appeared in the jet free surface that was *wider* than the nozzle opening (Fig. 5b). The bulge moved downstream and depressed the thin liquid film existing on the impingement surface (Fig. 5c). Subsequently, the bulge of fluid displaced fluid to form disturbances on the free surface (Figs. 5d and 5e), which moved away from the jet centerline (Fig. 5f). The appearance of a bulge that *extends beyond the nozzle opening* is an important phenomenon and will be shown to measurably influence convective heat transfer. The bulge occurs, since when the flow velocity is increasing during the pulsation cycle, higher velocity fluid is impeded momentarily by the fluid in the jet stream ahead of it with

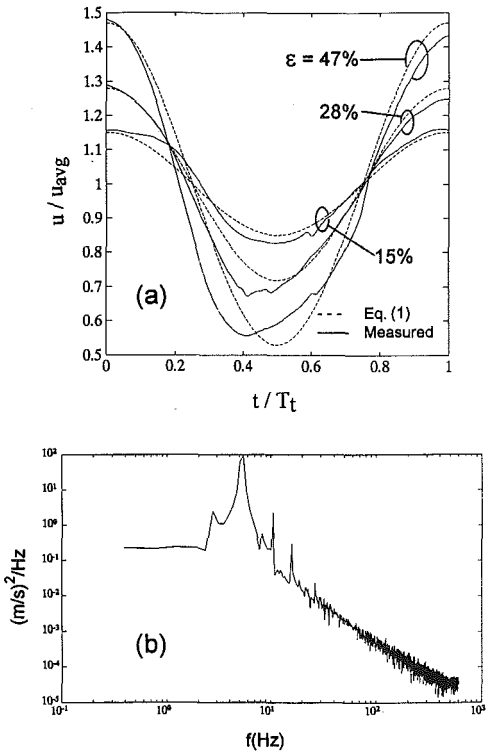

Fig. 4 (a) Representative comparison of normalized velocity profiles for various pulse magnitudes to sinusoidal pulse variation with Re$_j$ = 4300 ± 250, f = 4.7 Hz, and $S_w \cong 0.024$ and (b) power spectrum for a pulsating jet with Re$_j$ = 6500, f = 5.1 Hz ± 0.2 Hz, ϵ = 41.5 percent

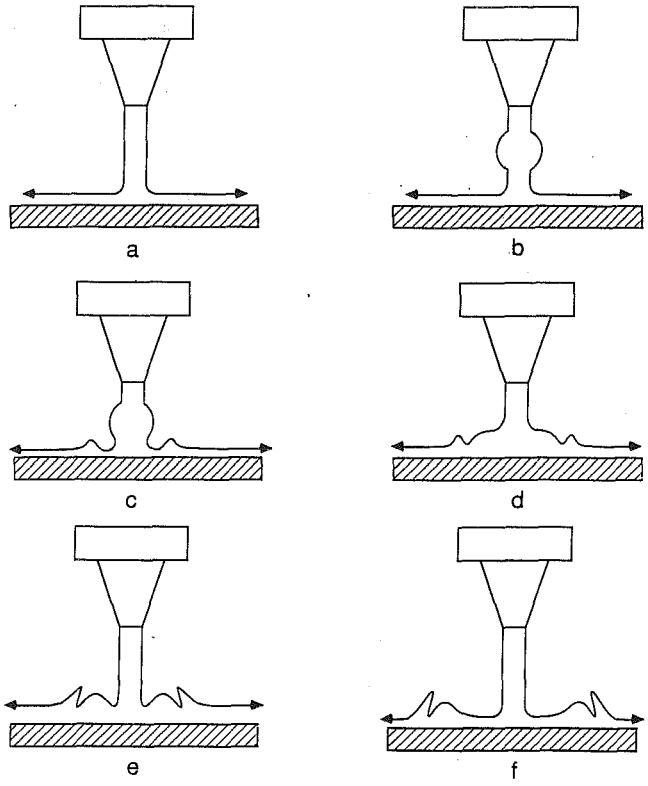

Fig. 5 Summary of photographic and stroboscopic observations of the jet free surface during pulsation

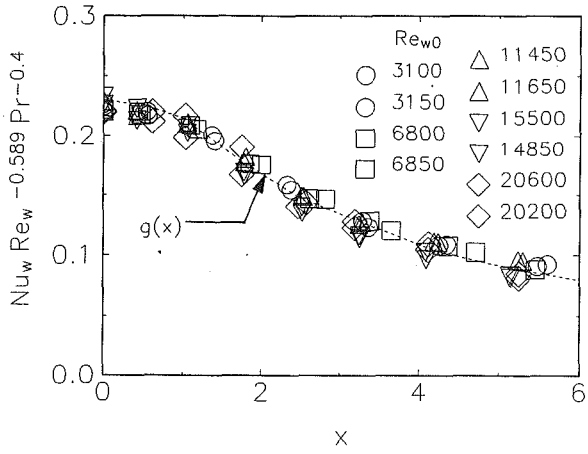

Fig. 6 Convective heat transfer distributions for the steady jets with $Pr_0 \cong 5.1$

lower velocity. To maintain mass continuity, the jet must broaden and a bulge in the jet free surface is formed. It is interesting to note by contrast that jets that accelerate due to gravity become thinner. Since turbulence levels in the pulsating jets with the rotating ball valve were determined to be less than about 1 percent and since the interaction between the jet and the rotating, thin blade in the on/off incident jet was very brief, bulges and ripples for the pulsating jets did not lead to splattering from the spreading liquid film as reported for fully turbulent steady jets by Lienhard et al. (1992). Instead, at very high frequencies with the on/off incident jets, the jet flow was transformed to a spray with essentially single packets of water striking the surface in rapid succession.

Baseline Experiments With Steady Jets. Convective heat transfer distributions were determined for steady-flow conditions in order to establish a baseline against which to compare the pulsating jet results. Experiments were performed for $3100 < Re_{w0} < 20{,}600$ and $4.7 < Pr_0 < 5.5$. An existing correlation [Eq. (3)] for steady jets (Zumbrunnen and Aziz, 1993), which was produced earlier with the experimental apparatus, is given below:

$$Nu_w(x)\ Re_w^{-0.589}\ Pr^{-0.4} = g(x) \tag{3a}$$

where for $0 < x < 1.6$,

$$g(x) = 0.230 - 0.01547x^2 \tag{3b}$$

and for $1.6 < x < 6.0$,

$$g(x) = 0.293 - x(0.08058 - 0.01124x + 0.0006x^2) \tag{3c}$$

In Eq. (3), all thermophysical properties are evaluated at the *local* film temperature T_f. Local Nusselt numbers that were acquired in this study for the steady jets ($\epsilon = 0$) are shown in Fig. 6 at the thermocouple locations beneath the test strip (Fig. 2). Results agreed with the correlation to within 5 percent. Nusselt numbers predicted by Eq. (3) were compared with the Falkner–Skan solution for two-dimensional, laminar stagnation flow (Evans, 1962). The correlation yielded values 4.2 percent lower at $Re_{w0} = 6000$ and 2.3 percent higher at $Re_{w0} = 20{,}600$. The correlation has been shown elsewhere (Zumbrunnen and Aziz, 1993) to be in good agreement with correlations developed in experimental studies with similar planar water jets. Over the Reynolds number range $6000 < Re_{w0} < 20{,}600$, the turbulence intensity varied from 0.25 to 0.95 percent (Fig. 3*b*). The observed agreement with laminar flow theory is supported by the correlation presented by Sikmanovic et al. (1974) for heat transfer along the stagnation line of cylinders in a crossflow [$Nu/Re^{0.5} = 0.945 + 1.94(0.01Tu\ Re^{0.5}) - 2.41(0.01Tu\ Re^{0.5})^2$], which predicts an enhancement of 2.8 percent for $Tu = 1$ percent at a Reynolds number of about 20,000. It also agrees with the observations of Mehendale et al. (1991) on the influence of mainstream turbulence on leading edge heat transfer with air. The spanwise-averaged heat transfer at a Reynolds number based on leading edge diameter of 25,000 and local streamwise turbulence intensity of 1.37 percent was found to agree with the laminar stagnation solution.

Experiments With Sinusoidal Pulse Waveforms. Experiments were performed with the sinusoidal pulse waveform for the ranges in parametric values indicated in Table 1. Smaller amplitude, lower frequency pulsations ($S_w = fw/u_j$) were attained at the higher jet Reynolds numbers as a natural consequence of increased fluid inertia. (High-magnitude/high-frequency pulsations generated with the wheel/blade assembly are described later.) In Fig. 7(*a*), local time-averaged Nusselt numbers remain essentially unchanged from those predicted by the steady jet correlation [Eq. (3)] until the pulse magnitude ϵ exceeded 40 percent. Above this pulse magnitude, decreases become measurable, are most pronounced in the vicinity of the stagnation line ($x = 0$), and become smaller farther from the jet. For $\epsilon = 85$ percent, the deviation from the correlation is about -17 percent. Reductions are ascribed principally to nonlinear dynamic responses of the hydrodynamic and thermal boundary layers and also to the bulges in the jet free surface (Fig. 5). These

Table 1 Parametric ranges for experiments with sinusoidal pulse waveforms

Re_{w0}	ϵ (percent)	S_w
3150	0.5–85	0.020–0.144
4500	0.5–85	0.019–0.063
7000	0.5–85	0.014–0.040
10,700–15,800	3.0	0.012–0.049

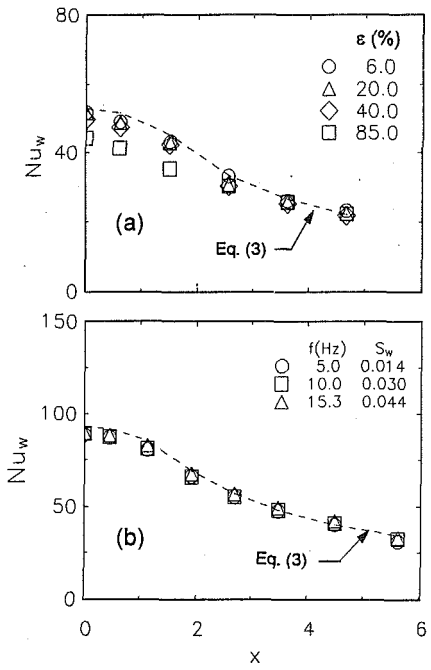

Fig. 7 Local Nusselt numbers due to sinusoidal flow pulsations with (a) $Re_{w0} = 3150 \pm 100$, $Pr_0 = 6.3 \pm 0.4$, $H = 3.5$, $f = 4.7 \pm 0.2$ Hz, $S_w \cong 0.020$, and (b) $Re_{w0} = 7050 \pm 250$, $Pr_0 = 6.3 \pm 0.4$, $H = 5.0$, $\epsilon = 6.2 \pm 0.3$ percent

effects are discussed further below. For $\epsilon < 40$ percent, the heat transfer distributions agreed with the steady-state correlation [Eq. (3)]. This agreement is further illustrated in Fig. 7(*b*). (Other results with smaller pulse magnitudes in Table 1 also closely resembled Fig. 6 for the steady jets and are therefore not presented separately.) Little sensitivity to small magnitude flow pulsations in the stagnation region is consistent with results for pulsating air flows past cylinders. Rosiczkowski and Hollworth (1991) measured local and instantaneous heat transfer from a cylinder oscillating in an air crossflow. They showed that the oscillations resulted in a cyclic variation in the convective heat transfer in the stagnation region with no change in time-averaged heat transfer. The results of Andraka and Diller (1985) for a cylinder in a pulsating air crossflow indicated no effect of flow pulsation on convective heat transfer for pulse magnitudes as high as 25 percent.

In Fig. 8(*a*), time-averaged Nusselt numbers Nu_w are normalized to the Nusselt number Nu_{ss} for a steady jet of the same jet Reynolds number in order to assess generally the influence of pulse magnitude at the stagnation line ($x = 0$). Values of Nu_* ($=Nu_w/Nu_{ss}$) are relatively insensitive to the jet Reynolds number and decrease with increasing pulse magnitude. Since decreases and the bulge sizes were more pronounced at lower jet Reynolds numbers, a portion of the reductions is attributed to bulges in the incident jet flow (Fig. 5). In order to disclose principal physical mechanisms accurately, the nonlinear dynamics of the hydrodynamic and thermal boundary layers to a sinusoidally varying incident flow impinging on a constant heat flux surface was recently considered in a companion theoretical study (Mladin and Zumbrunnen, 1994a, b). Results indicated that, due to nonlinear dynamic effects, a sinusoidal flow pulsation [Eq. (1)] causes *nonsinusoidal* oscillations in the thermal and hydrodynamic boundary layer thicknesses [Fig. 8(*b*)]. Calculated time-averaged thicknesses are greater than the corresponding steady values, which correspond to those for $f_*\tau = 0$ in Fig. 8(*b*). Theoretically predicted time-averaged Nusselt numbers in Fig. 8(*a*) decrease as a consequence and are in good agreement with the experimental results. Predicted reductions are independent of jet Reynolds number, depend chiefly on pulse magnitude, but also are greater at lower pulsation frequencies. This phenomenon is systematically reported in a recent paper (Mladin and Zumbrunnen, 1994b). Thus, for large pulse magnitudes, both nonlinear dynamic effects and free surface bulges induced decreases in stagnation region Nusselt numbers with nonlinear dynamic effects generally more prevalent as suggested by theoretical predictions. Since it is well known that Nusselt numbers at $x = 0$ are larger for higher velocity gradients (White, 1974), the bulge may have broadened the distance for lateral fluid acceleration. However, it is important to note that the bulge signified a departure from a planar jet geometry, so such bulge effects may be specific to the aspect ratio of the nozzle opening and may reflect complex distortions in the jet flow.

Convective heat transfer was found to be insensitive to the nozzle height above the impingement surface for nozzle heights ranging from 3.5 to 7.5 nozzle widths. This insensitivity is consistent with the spatial uniformity of the jet velocity profile shown in Fig. 3(*a*). For example, if gravity accelerates a jet with a parabolic velocity profile, the velocity profile becomes progressively more uniform at larger distances from the nozzle opening, since the velocity of each fluid element is increased by the same amount. The jet *incident* at the surface is thereby transformed and the resulting pressure and velocity distributions adjacent to the impingement surface are altered, affecting convective heat transfer directly. Increased entrainment and more rapid spreading of submerged, *nonimpinging,* pulsating jets discussed earlier (Binder and Favre-Marinet, 1973; Curtet and Girard, 1973; Bremhorst, 1979; Bremhorst and Hollis, 1990) suggest that submerged, *impinging,* pulsating jets would exhibit a strong dependence on nozzle height. Whereas bulges in the free surface of a free pulsating jet develop due to slower moving fluid impeding the motion of faster moving fluid downstream (Fig. 5), the more slowly moving fluid in the pulsation cycle of a submerged jet culminates in more rapid entrainment and spreading. *Thus, containment of the flow by a free surface can lead to a markedly different response to flow pulsations.*

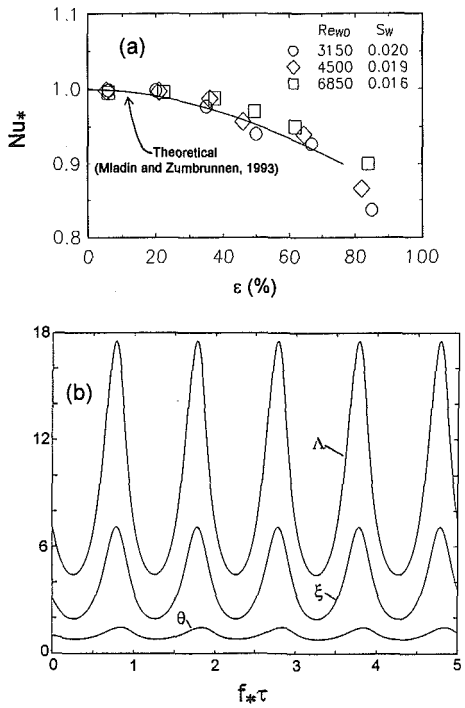

Fig. 8 (a) Effect of pulse magnitude on Nusselt number with $f = 4.7 \pm 0.2$ Hz, $H = 3.5$, $Pr \approx 6$, and $x = 0$ and comparison to theoretical predictions (Mladin and Zumbrunnen, 1994a) for $S_w = 0.016$ and $Pr = 6$; (b) calculated responses (Mladin and Zumbrunnen, 1994b) of the hydrodynamic and thermal boundary layers and surface temperature to sinusoidal flow pulsations for $S_w = 0.016$ and $Pr = 6$

It is noteworthy that reductions in Nusselt numbers for a pulsating flow may also be attributable simply to quasi-steady behavior. Under quasi-steady conditions, correlations for steady state can be applied to predict heat transfer coefficients for transient flows by using the instantaneous flow velocity in lieu of the steady flow velocity. This procedure is only applicable when the pulsations are sufficiently slow to permit the boundary layer to assume essentially steady-state values during the pulsation cycle. The aforementioned nonlinear dynamics aspects make it difficult to assess generally when quasi-steady conditions apply since responses depend in a complex manner on both the pulse frequency and pulse magnitude, in addition to Prandtl number and pulse waveform (Mladin and Zumbrunnen, 1994a). However, the nonlinear dynamics model, which was applied in Fig. 8, accurately represents quasi-steady behavior when it arises and provides results, which may include *both* nonlinear dynamic responses and quasi-steady effects. In order to distinguish quasi-steady behavior from nonlinear dynamics effects in Figs. 7(*a*) and 8(*a*), the time-averaged Nusselt number for a pulsating jet with flow velocity given by Eq. (1) was calculated from a general expression for a stagnation region heat transfer correlation. The time-averaged Nusselt number decreased with increasing pulse magnitude ϵ, since the Reynolds number exponent in the correlation was smaller than unity and time-averaging over a pulse cycle thereby yielded more pronounced decreases in Nu_w. For $\epsilon = 85$ percent in Fig. 7(*a*), calculated reductions for laminar flow were less than 6 percent. (Calculated reductions for quasi-steady behavior are smaller for a turbulent flow.) Since reductions of about 17 percent were measured with $\epsilon = 85$ percent in Figs. 7(*a*) and 8, nonlinear dynamic effects and bulges in the jet free surface (Fig. 5) are likely responsible for most of the measured reductions as previously described.

Results indicate that nonlinear dynamic effects, bulges in the jet free surface, and quasi-steady behavior all tend to decrease convective heat transfer in pulsating jet flows with sinusoidal flow variations over the parametric range in Table 1. However, as will be demonstrated, enhancements can be obtained with square-pulse waveforms and an on/off incident jet flow ($\epsilon = 100$ percent) due to periodic boundary layer renewal.

Experiments With Square Pulse Waveform. Because of the large inertial forces associated with the relatively dense pulsating water jets at high pulsation frequencies, square-pulse waveforms were approximated with the wheel/blade assembly shown in Fig. 2. It was desired to generate high-frequency, high-amplitude pulsations owing to the theoretically estimated rapid response of the thermal boundary layer (Zumbrunnen, 1992; Mladin and Zumbrunnen, 1994a). These nonlinear dynamics models suggest that $S_w > 0.26$ if the hydrodynamic and thermal boundary layers are to remain only partially developed over the pulsation cycle. For consistency with the definition of the pulse magnitude ϵ for the sinusoidal pulse waveforms, the pulse magnitude for the square-pulse waveform was also based on the arithmetic-averaged jet velocity and the peak variation of the jet velocity from the average. Thus, $\epsilon = 100$ percent for the square-pulse waveform in all cases. Time-averaged local heat transfer measurements were made for $6600 \leq Re_{w0} \leq 19{,}300$ and $60 \text{ Hz} \leq f \leq 280$ Hz. The experiments complement those reported by Zumbrunnen and Aziz (1993), which covered the range of pulsation frequencies from 30 Hz to 142 Hz. Only representative new cases will be shown for brevity. These new cases demonstrate that maximum enhancements are attained as pulsation frequency is raised. During the course of the experiments, the Strouhal number S_w and a dimensionless time Γ ($=Ct_{bl}$) were calculated in addition to the Nusselt number Nu_w, Reynolds number Re_w, and Prandtl number Pr. The dimensionless time Γ is a measure of the period available for thermal boundary layer growth upon rewetting of the impingement surface during *each* pulsation cycle for the square pulse waveform. Values of Γ were therefore determined from the time for continuous flow during each pulsation cycle, which was readily calculated from the speed of the blades mounted on the rotating wheel. Its use is based on a theoretical model (Zumbrunnen, 1992) of the boundary layer dynamics in planar stagnation flows. Since the velocity gradient C depends on the flow geometry and scale, Γ permits adaption of results to other planar stagnation flows. For $\Gamma > 3$ or equivalently $S_w < 0.26$, sufficient time is available for the thermal boundary layer essentially to reach its steady-state thickness when $0.7 < Pr < 15$. To obtain enhancements, it is desired to truncate this time so that the thermal boundary layer remains thinner than its steady-state value.

Local time-averaged Nusselt numbers for the square-pulse waveform ($\epsilon = 100$ percent) with $Re_{w0} \cong 12{,}500$ are shown in Fig. 9(*a*) at the positions corresponding to the locations of the thermocouples beneath the test strip. Results are given both to the left and to the right of the planar jets, since symmetry is no longer assured due to the action of the moving blade. In its motion through the jet, the blade traversed the length of the test strip starting at negative values of the dimensionless distance x and moved towards the positive values. (The negative dimensionless distances will be described as the *blade entry side* of the test strip while the positive values will be described as the *blade exit side* of the test strip.) For $f = 100$ Hz in Fig. 9(*a*), local Nusselt numbers are lower than the steady jet Nusselt numbers given by Eq. (3). This reduction occurs since the enhanced cooling during boundary layer development is insufficient to offset the reduced cooling during the brief period when the jet flow ceases during each pulsation cycle. As the frequency is raised, Nusselt numbers increase along the entire length of the test strip as the period for decreased heat transfer is reduced and the time for boundary layer development given by Γ becomes shorter. However, increases are not monotonic and local Nusselt numbers eventually decrease at higher frequencies. Stroboscopic observations revealed that the coherence of the impinging jet flow eventually became degraded as the pulsation frequency was raised. *The high frequency, pulsating jet with $\epsilon = 100$ percent was essentially transformed into a collimated spray with individual packets of water striking the test strip in succession.* The jet structure was thereby degraded to such an extent that the favorable characteristics of the stagnation flow were lost and heat transfer was reduced. It should be noted that the actual pulsation frequencies at which peak enhancements are attained is dependent on the method employed to induce the pulsations. For example, pulsations in miniature jets can be produced by rapidly varying the flow supplied to the nozzle and degradation to the impinging flow would likely occur at higher frequencies than those in this study in which a moving blade induced pulsations by directly contacting a relatively large jet. Alternately, air injection into the nozzle might yield periodic boundary layer renewal as air bubbles strike the surface. Higher enhancements than shown in Fig. 9(*a*) might therefore be achieved with alternate pulsation techniques.

The maximum Strouhal number ($S_w = fw/u_j$) in Fig. 9(*b*) was restricted due to the comparatively high jet Reynolds number ($Re_{w0} \cong 19{,}300$). This Strouhal number is below the values at which peak enhancements occur in Fig. 9(a). Consequently, local Nusselt numbers increase monotonically with pulsation frequency. Enhancements arose above 181 Hz ($S_w = 0.279$) and were more prominent on the blade entry side of the jet ($x < 0$) since a portion of the jet was deflected by the moving blade and generated a backwash (Zumbrunnen and Aziz, 1993).

In Fig. 9, heat transfer enhancements as high as 33 percent were measured as the pulsation frequency was raised. Enhancements occurred for Strouhal numbers above about 0.27, which agrees with a threshold Strouhal number proposed in the related study by Zumbrunnen and Aziz (1993) based on boundary layer dynamics. A portion of the measured enhancements may have been due to increased turbulence intensity generated as the on/off flow initially impinged on the surface. However, the agreement between the experimentally determined and theoretically predicted Strouhal numbers suggests that boundary layer renewal is the principal mechanism for heat transfer enhancement in the

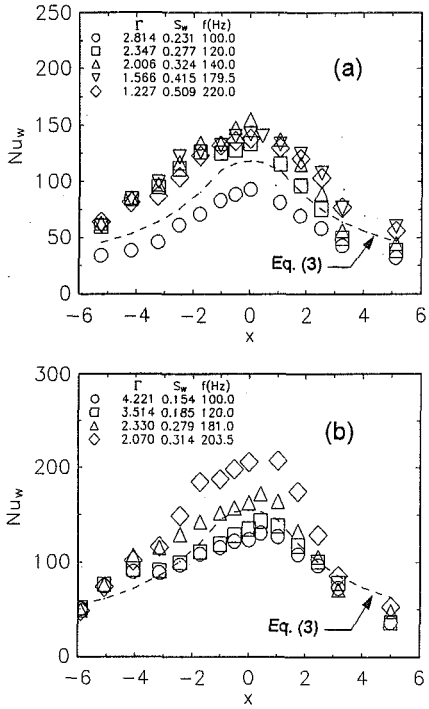

Fig. 9 Effect of pulsation frequency on Nusselt number with the square-pulse waveform (ϵ = 100 percent) for (a) Re_{w0} = 12,500 ± 300, Pr_0 = 4.6 ± 0.8; (b) Re_{w0} = 19,300 ± 300, Pr_0 = 4.7 ± 0.6

on/off pulsating jet flows of this study. Elementary calculations, which utilize the steady correlation result [Eq. (3*a*)] and assume turbulent flow conditions in the fluid supply system, show that comparable improvements to heat transfer can be obtained by raising the flow rate supplied to the nozzle by a factor of about 1.62 and increasing the supply pressure by a factor of 2.63. Although such modifications are often a more feasible or desirable means to achieve improved cooling, enhancements due to the on/off jet flow were obtained without an increase in supply pressure and may be of practical benefit where an increase in system flow rate is not desirable or attainable.

Although measured enhancements were generally in good agreement with those reported in the related study by Zumbrunnen and Aziz (1993), the maximum enhancements were less. This discrepancy is attributed to a slightly premature degradation in the on/off jet flow at high pulsation frequencies due to minor reductions made to the thickness of the rotating hydrofoil-like blades on the wheel depicted in Fig. 2. Such degradation in a purely on/off incident jet flow, although slight, can have a pronounced effect on enhancement since heat transfer coefficients increase theoretically in an exponential fashion with pulsation frequency. Thus, larger enhancements might be attainable by carefully developing a system that preserves the impinging jet flow structure at high pulsation frequencies. However, the extended range in pulsation frequency of this study demonstrates that maximum enhancements eventually arise in an on/off jet flow as frequency is raised since the jet is eventually transformed to a spray.

Conclusions

The flow field characteristics and convective heat transfer distributions of pulsating, impinging planar water jets were investigated. For a sinusoidal pulse profile, time-averaged, stagnation region Nusselt numbers were reduced by as much as 17 percent when the pulse magnitude was large. Reductions decreased markedly away from the stagnation line and were attributed chiefly to the nonlinear dynamic responses of the hydrodynamic and thermal boundary layers and to a lesser degree to bulges in the jet free surface. For pulsating jets with a square-pulse profile and an on/off incident flow, Nusselt numbers at the stagnation line were enhanced by as much as 33 percent for $S_w > 0.26$ due to periodic boundary layer renewal. However, enhancements eventually decreased with increasing frequency as the coherence of the impinging jet flow became degraded by the intermittency and the on/off jet flow was effectively transformed to a spray. Enhancements obtained with the on/off pulsating jet (ϵ = 100 percent) suggest that enhancements might also be obtained at high pulsation frequencies as $\epsilon \rightarrow 100$ percent with the sinusoidal pulse waveform.

Acknowledgments

Support for this work was provided by the National Science Foundation of the United States under Grant No. CTS-8918154 and is gratefully acknowledged. We appreciate the assistance of Ms. Shari Keller and Mr. Patrick Sullivan for preparing the anemometry equipment and photographically documenting the pulsating jet flows as part of the NSF Research Experience for Undergraduates Program.

References

Andraka, C. E., and Diller, T. E., 1985, "Heat-Transfer Distribution Around a Cylinder in Pulsating Crossflow," *ASME Journal of Engineering for Gas Turbines and Power,* Vol. 107, pp. 976–982.

Aref, H., 1984, "Stirring by Chaotic Advection," *Journal of Fluid Mechanics,* Vol. 143, pp. 1–21.

Aref, H., and Balachandar, S., 1986, "Chaotic Advection in a Stokes Flow," *Physics of Fluids,* Vol. 29, pp. 3515–3521.

Bejan, A., 1981, "On the Buckling Properties of Inviscid Jets and the Origin of Turbulence," *Letters of Heat and Mass Transfer,* Vol. 8, pp. 187–194.

Bendat, J. S., and Piersol, A. G., 1986, *Random Data: Analysis and Measurement Procedures,* Wiley-Interscience, New York.

Binder, G., and Favre-Marinet, M., 1973, "Mixing Improvement in Pulsating Turbulent Jets," *Proceedings of the Symposium on Fluid Mechanics of Mixing,* ASME, New York, pp. 167–172.

Bremhorst, K., 1979, "Unsteady Subsonic Turbulent Jets," in: *Recent Developments in Theoretical and Experimental Fluid Mechanics,* Springer-Verlag, Berlin, pp. 480–500.

Bremhorst, K., and Hollis, P. G., 1990, "Velocity Field of an Axisymmetric Pulsed, Subsonic Air Jet," *AIAA Journal,* Vol. 28, pp. 2043–2049.

Brereton, G. J., and Kodal, A., 1992, "A Frequency-Domain Filtering Technique for Triple Decomposition of Unsteady Turbulent Flow," *ASME Journal of Fluids Engineering,* Vol. 114, pp. 45–51.

Ching, C. Y., and O'Brien, J. E., 1991, "Unsteady Heat Flux in a Cylinder Stagnation Region With High Freestream Turbulence," *Fundamental Experimental Measurements in Heat Transfer,* ASME HTD-Vol. 179, pp. 57–66.

Curtet, R. M., and Girard, J. P., 1973, "Visualization of a Pulsating Jet," *Proceedings of the Symposium on Fluid Mechanics of Mixing,* ASME, New York.

Evans, H. L., 1962, "Mass Transfer Through Laminar Boundary Layers—7. Further Similar Solutions to the *b*-Equation for the Case $B = 0$," *International Journal of Heat and Mass Transfer,* Vol. 5, pp. 35–57.

Evans, R. L., 1975, "Turbulence and Unsteadiness Measurements Downstream of a Moving Blade Row," *ASME Journal of Engineering for Power,* Vol. 97, pp. 131–139.

Gundappa, M., and Diller, T. E., 1991, "The Effects of Free-Stream Turbulence and Flow Pulsation on Heat Transfer From a Cylinder in Crossflow," ASME JOURNAL OF HEAT TRANSFER, Vol. 113, pp. 766–769.

Hussain, A. K. M. F., and Reynolds, W. C., 1970, "The Mechanics of an Organized Wave in Turbulent Shear Flow," *Journal of Fluid Mechanics,* Vol. 41, pp. 241–258.

Khakhar, D. V., Rising, H., and Ottino, J. M., 1986, "Analysis of Chaotic Mixing in the Two Model Systems," *Journal of Fluid Mechanics,* Vol. 172, pp. 419–451.

Kimura, S., and Bejan, A., 1983, "The Buckling of a Vertical Liquid Column," *ASME Journal of Fluids Engineering,* Vol. 105, pp. 469–473.

Kline, S. J., and McClintock, F. A., 1953, "Describing Uncertainties in Single Sample Experiments," *Mechanical Engineering,* Jan., pp. 3–8.

Lienhard, J. H., V, Liu, X., and Gabour, L. A., 1992, "Splattering and Heat Transfer During Impingement of a Turbulent Jet," ASME JOURNAL OF HEAT TRANSFER, Vol. 114, pp. 362–372.

McMurray, D. C., Myers, P. S., and Uyehara, O. A., 1966, "Influence of Impinging Jet Variables on Local Heat Transfer Coefficients Along a Flat Surface With Constant Heat Flux," *Proceedings of the Third International Heat Transfer Conference,* Vol. II, pp. 292–299.

Mehendale, A. B., Han, J. C., and Ou, S., 1991, "Influence of High Mainstream Turbulence on Leading Edge Heat Transfer," ASME JOURNAL OF HEAT TRANSFER, Vol. 113, pp. 843–850.

Mladin, E. C., and Zumbrunnen, D. A., 1994a, "Nonlinear Dynamics of Laminar Boundary Layers in Pulsatile Stagnation Flows," *Journal of Thermophysics and Heat Transfer,* Vol. 8, pp. 514–523.

Mladin, E. C., and Zumbrunnen, D. A. 1994b, "Dependence of Convective Heat Transfer to a Pulsating Stagnation Flow on Incident Velocity Pulse Characteristics," *1994 AIAA/ASME Thermophysics and Heat Transfer Conference,* Colorado Springs, CO, ASME HTD-Vol. 271, pp. 11–21, General Papers Session; also: *Journal of Thermophysics and Heat Transfer,* in press.

Nevins, R. G., and Ball, H. D., 1961, "Heat Transfer Between a Flat Plate and a Pulsating Impinging Jet," *Proceedings of the National Heat Transfer Conference,* Boulder, CO, Vol. 60, pp. 510–516.

Ottino, J. M., 1989, *The Kinematics of Mixing: Stretching, Chaos, and Transport,* Cambridge University Press, Cambridge, United Kingdom.

Peebles, P. Z., 1980, *Probability, Random Variables and Random Signal Principles,* McGraw-Hill, New York.

Rosiczkowski, J., and Hollworth, B., 1991, "Local and Instantaneous Heat Transfer From an Isothermal Cylinder Oscillating in a Cross-flow," *Fundamental Experimental Measurements in Heat Transfer,* ASME HTD-Vol. 179, pp. 49–56.

Scholtz, M. T., and Trass, O., 1970, "Mass Transfer in a Nonuniform Impinging Jet," *American Institute of Chemical Engineering Journal,* Vol. 16, pp. 82–96.

Sikmanovic, S., Oka, S., and Komar, S., 1974, "Influence of the Structure of Turbulent Flow on Heat Transfer From a Single Cylinder in a Cross-Flow," *Proceedings of the 5th International Heat Transfer Conference,* Vol. II, pp. 320–324, AIChE, New York.

Smith, M. C., and Kuethe, A. M., 1966, "Effects of Turbulence on Laminar Skin Friction and Heat Transfer," *The Physics of Fluids,* Vol. 9, pp. 2337–2344.

White, F. M., 1974, *Viscous Fluid Flow,* McGraw-Hill, New York, pp. 273–284.

Zumbrunnen, D. A., Incropera, F. P., and Viskanta, R., 1989, "Convective Heat Transfer Distributions on a Plate Cooled by Planar Water Jets," ASME JOURNAL OF HEAT TRANSFER, Vol. 111, pp. 889–896.

Zumbrunnen, D. A., 1992, "Transient Convective Heat Transfer in Planar Stagnation Flows With Time-Varying Surface Heat Flux and Temperature," ASME JOURNAL OF HEAT TRANSFER, Vol. 114, pp. 85–93.

Zumbrunnen, D. A., Incropera, F. P., and Viskanta, R., 1992, "A Laminar Boundary Layer Model of Heat Transfer Due to Nonuniform Planar Jet Impinging on a Moving Plate," *Wärme- und Stoffübertragung,* Vol. 27, pp. 311–319.

Zumbrunnen, D. A., and Aziz, M., 1993, "Convective Heat Transfer Enhancement Due to Intermittency in an Impinging Jet," ASME JOURNAL OF HEAT TRANSFER, Vol. 115, pp. 91–98.

Influence of Mainstream Turbulence on Heat Transfer Coefficients From a Gas Turbine Blade

L. Zhang[1]
Research Assistant.

J.-C. Han
HTRI Professor.
Fellow ASME

Turbine Heat Transfer Laboratory,
Department of Mechanical Engineering,
Texas A&M University,
College Station, TX 77843-3123

The influence of mainstream turbulence on surface heat transfer coefficients of a gas turbine blade was studied. A five-blade linear cascade in a low-speed wind tunnel facility was used in the experiments. The mainstream Reynolds numbers were 100,000, 200,000, and 300,000 based on the cascade inlet velocity and blade chord length. The grid-generated turbulence intensities at the cascade inlet were varied between 2.8 and 17 percent. A hot-wire anemometer system measured turbulence intensities, mean and time-dependent velocities at the cascade inlet, outlet, and several locations in the middle of the flow passage. A thin-foil thermocouple instrumented blade determined the surface heat transfer coefficients. The results show that the mainstream turbulence promotes earlier and broader boundary layer transition, causes higher heat transfer coefficients on the suction surface, and significantly enhances the heat transfer coefficient on the pressure surface. The onset of transition on the suction surface boundary layer moves forward with increased mainstream turbulence intensity and Reynolds number. The heat transfer coefficient augmentations and peak values on the suction and pressure surfaces are affected by the mainstream turbulence and Reynolds number.

Introduction

In recent years, the trend for higher inlet gas temperatures in turbine engine designs has caused an increase of the heat load to the turbine components. Highly sophisticated cooling techniques such as film cooling and augmented internal cooling maintain acceptable safety requirements in turbine airfoils under extreme operating conditions. The effect of mainstream turbulence generated by the combuster and/or the upstream blade row on the airfoil heat transfer is a crucial problem in advanced gas turbine engine design. To provide a better cooling design, it is important to understand where the heat is transferred in the turbine airfoils. This study focuses on the influence of high mainstream turbulence on the surface heat transfer coefficient distributions on a turbine airfoil model.

Consider convective heat transfer for turbulent flow over a flat plate. Blair (1983a, 1983b) studied the effect of grid-generated turbulence on flat plate heat transfer and reported that the turbulent heat transfer coefficient for a turbulence intensity of 6 percent increases by 18 percent as compared to that without a grid. Simonich and Bradshaw (1978) and Hancock and Bradshaw (1983) reported similar results. Young et al. (1992) investigated the influence of jet-grid-generated turbulence on flat plate heat transfer. They reported that the turbulent heat transfer coefficient for a turbulence intensity of 15 percent increases by 50 percent when compared to the zero turbulence correlation in the fully turbulent region. O'Brien and VanFossen (1985) studied the effect of jet-grid-generated turbulence on heat transfer from the leading edge of a circular cylinder in crossflow. They found that for cylinder Reynolds numbers 48,000–180,000 the heat transfer coefficient for a turbulence intensity of 10–12 percent increases by 37–53 percent over the zero turbulence intensity case. Bellows and Mayle (1986) examined heat transfer downstream of a leading edge separation bubble on a blunt body. They reported that heat transfer through a separation region and for a turbulence intensity of 0.4 percent increases almost an order of magnitude and is about 50 percent higher near reattachment than that predicted by the turbulent flat plate correlation. Mehendale et al. (1991) investigated the effect of jet-grid-generated turbulence on leading edge heat transfer and reported an increase of up to 50 percent, which can be correlated by the Lowery and Vachon (1975) equation. They also reported that the mainstream turbulence intensity (up to 15 percent) does not shift the location of the separation–reattachment region. The reattachment heat transfer coefficients are about the same despite mainstream turbulence levels and are much higher than the turbulent flat plate correlation. Brown and Martin (1979, 1982) studied the effects of mainstream turbulence on turbine blade heat transfer coefficients. They showed that under gas turbine engine conditions, the scale and frequency of mainstream turbulence may be as important as its intensity in determining local heat transfer coefficients around the blades.

Many studies have investigated the effect of upstream unsteady wake and mainstream turbulence on the surface heat transfer coefficient distributions from a turbine blade. Dunn (1986), Dunn et al. (1986, 1989, 1994), Blair et al. (1989a, 1989b), Abhari et al. (1992), and Blair (1994) conducted experiments in rotor–stator blade rows. Two techniques produced unsteady wakes in laboratory simulations. Pfeil et al. (1983), Liu and Rodi (1989, 1992), and Priddy and Bayley (1988) used a squirrel cage type wake generator. Doorly and Oldfield (1985), Ashworth et al. (1985), Doorly (1988), Wittig et al. (1987, 1988), Dullenkopf et al. (1991), Dullenkopf and Mayle (1994), O'Brien and Capp (1989), O'Brien (1990), and Han et al. (1993) used a spoked wheel type wake generator. All results show that an unsteady passing wake promotes earlier and broader boundary layer transition and causes a higher heat transfer coefficient on the suction surface (up to 3.4 times). It also enhances the heat transfer coefficient on the pressure surface (up to 1.8 times). Mayle and Dullenkopf (1990) and Mayle (1991) introduced a time-averaged intermittence factor to develop a theory to incorporate the unsteady effect into a steady flow analysis. They found the theory to predict very well the experimental heat transfer coef-

[1] Current address: Solar Turbines, San Diego, CA 92186-5376.

Contributed by the Heat Transfer Division and presented at the National Heat Transfer Conference, Atlanta, Georgia, August 8–11, 1993. Manuscript received by the Heat Transfer Division March 1993; revision received March 1994. Keywords: Flow Transition, Forced Convection, Turbines. Associate Technical Editor: R. J. Simoneau.

ficients on the suction surface of a turbine blade in a spoked wheel generated wake flow condition (Dullenkopf et al., 1991).

This study is a continuation of Han et al. (1993) and focuses on the effects of grid-generated turbulence (instead of unsteady, wake-generated) on turbine blade heat transfer. A five-blade linear cascade was installed in a low-speed wind tunnel for the flow and heat transfer coefficient measurements. Two different sizes of grid, similar to those used by Mehendale et al. (1991), produced upstream turbulence. The first, a coarse grid, could produce a turbulence intensity of up to 17.0 percent and the second, a fine grid, could generate a turbulence intensity of up to 8.1 percent at the cascade inlet. Both pressure and suction surface local heat transfer coefficients were obtained for mainstream flow Reynolds numbers of 100,000, 200,000, and 300,000, based on the cascade inlet velocity and blade chord length. The main objectives of this study were: (1) to determine the effect of grid-generated turbulence on the blade heat transfer coefficients at a given mainstream flow Reynolds number, (2) to determine the effect of mainstream flow Reynolds number on the blade heat transfer coefficients at a given upstream grid-generated turbulence level, (3) to identify the peak heat transfer coefficient augmentation and the boundary layer transition location induced by the grid-generated turbulence, and (4) to identify the peak heat transfer coefficient augmentation and the onset of boundary layer transition induced by the mainstream Reynolds number.

Test Apparatus and Instrumentation

Low-Speed Wind Tunnel. Figure 1 is a schematic of the low-speed, open-loop wind tunnel. It was designed as a suction-type wind tunnel to avoid uncontrolled turbulence of the discharge side of the blower. Two separate pieces of stainless steel screen assure the uniform and parallel flow going into the nozzle. The two-dimensional, 4.5:1 contraction nozzle produced a uniform flow entering the test channel. The test channel was 25.4 cm high, 75.0 cm wide in cross section, and had a 107.49 deg turn to fit the turning of a five-airfoil cascade. The test channel width was reduced to 35 cm at the cascade outlet to guide the trailing edge parallel flow. The cascade inlet velocity (mainstream Reynolds number) was varied by controlling a sliding gate at the discharge end of the 15 hp (11.2 kW) blower and was continuously monitored by a pitot probe located inside the wind tunnel. A central air-conditioning system maintained the cascade inlet temperature at 25°C.

Linear Cascade Design and Analysis. Figure 2 shows the linear cascade designed to fit the low-speed wind tunnel facility with an inlet velocity between 7 and 21 m/s. The airfoil configuration was scaled up by a factor of 5 to produce a velocity ratio distribution similar to that inside a typical advanced high-pressure turbine-blade row. The airfoil design and analysis were done by the computer software BLADES. The cascade, made of high-quality model wood (RAN SHAPE), had a chord length of 22.68 cm, a radial span of 25.4 cm, and a blade spacing of 17.01 cm. The middle blade could be instrumented as a pressure tap blade or a heat transfer blade. Figures 4 and 5 show the blade's orientation and coordinates. Four slots were located on either side of the middle blade at the cascade inlet and outlet plane while three additional slots were located in the middle path between the middle blade and the blade on the pressure side. These slots measured flow velocities, turbulence intensities, turbulence fluctuations at the cascade inlet and outlet, and along the middle flow path. They also checked flow periodicity in either side of the middle blade at the inlet and outlet plane.

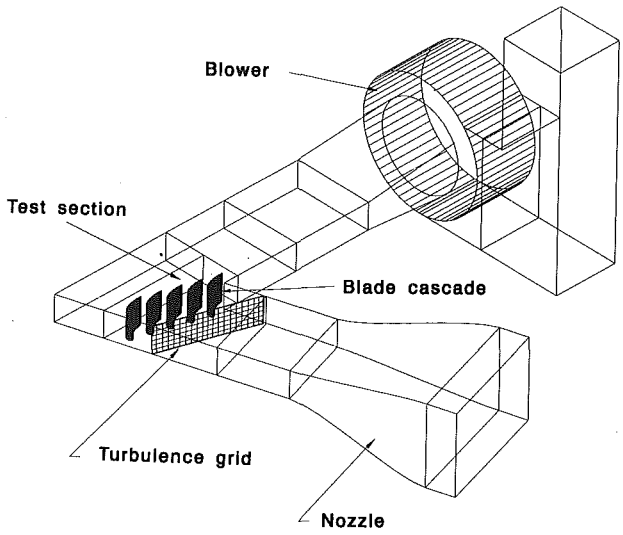

Fig. 1 Schematic of test apparatus

Grid-Generated Turbulence. Figure 3 shows two different grids used to generate different levels of turbulence intensity. Both grid #1 and grid #2 were made of square bars and located upstream from the cascade as shown in Fig. 2. Grid #1 (coarse) had 1.3 cm bar width and 4.8 cm bar pitch, and was designed to generate higher turbulence intensities. Grid #2 (fine) had 0.5 cm bar width and 1.9 cm bar pitch, and was designed to generate lower turbulence intensities. The horizontal bars were placed in front of the vertical bars in each grid. Fifty-four percent (54%) of each grid was an open space for air flow. The grids were located 21 cm, 30 cm, and 60 cm, respectively, upstream from the leading plane of the cascade. Table 1 shows the grid locations and corresponding turbulence intensities measured at the cascade inlet for each of the three Reynolds numbers. Grid #1 upstream location turbulence intensities at the cascade inlet are 17 percent for the 21 cm ($s/d = 16$), 13.4 percent for the 30 cm ($s/d = 23$), 5 percent for the 60 cm ($s/d = 46$). The corresponding dissipation length scales are about 1.3 cm, 1.4 cm, and 1.5 cm, respectively. The grid #2 upstream location turbulence intensities at the cascade inlet are 8 percent for the 21 cm ($s/d = 42$), 5.7 percent for the 30 cm ($s/d = 60$), and 2.8 percent for the 60 cm ($s/d = 120$). The corresponding length scales are about 0.8 cm,

Nomenclature

C = airfoil chord length
d = bar width of turbulence grid
h = local heat transfer coefficient
H = blade radial (spanwise) length
k = thermal conductivity of air
Nu = local Nusselt number based on blade chord length = hC/k
q'' = net surface convective heat flux
q''_{gen} = foil-generated surface heat flux
q''_{loss} = surface heat flux loss
Re = Reynolds number based on chord length and cascade inlet velocity = V_1C/ν
s = distance from turbulence grid to cascade inlet
T_w = blade surface temperature
T_∞ = mainstream air temperature at the inlet of the cascade
Tu = local turbulence intensity
U = local instantaneous velocity
$\bar{U}$ = local time-mean velocity
V = mean velocity in flow path
V_1 = mean velocity at cascade inlet
V_2 = mean velocity at cascade outlet
X = blade surface coordinate in streamwise direction
Y = blade radial (spanwise) coordinate
ν = kinematic viscosity of air

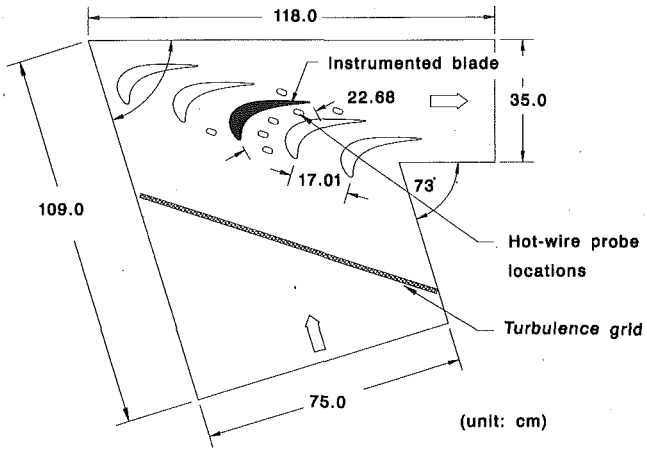

Fig. 2 Schematic of the linear turbine blade cascade

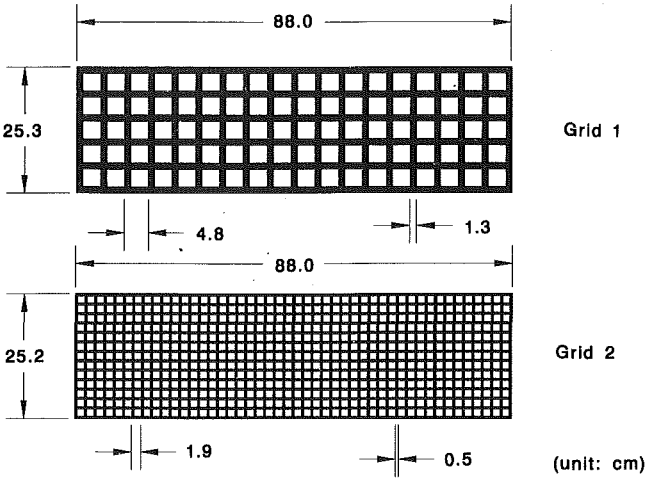

Fig. 3 Sketch of the two turbulence grids

1.1 cm, and 1.7 cm, respectively. These dissipation length scales are estimated from the method proposed by Hancock and Bradshaw (1983).

Hot-Wire Instrumentation. A calibrated single hot-wire probe was located in one of seven slots around the middle blade shown in Fig. 2. The probe was connected to the TSI IFA100 anemometer, the TSI IFA200 digitizer, and the DATA TRANSLATION A/D convertor, which has a sample frequency up to 100 kHz. The sample frequency was 50 kHz and the sample size was 30,000. Both the digitizer and A/D convertor were interfaced to an IBM PC. The data can be analyzed further on a Micro VAX to get the turbulence intensity, the turbulence fluctuation, and the mean velocity. The local time-mean velocity $\bar{U}$ and local turbulence intensity Tu can be calculated by Eqs. (1) and (2), respectively:

$$\bar{U} = \frac{1}{N}\sum_{i=1}^{N} U(i) \tag{1}$$

$$Tu = \frac{\sqrt{\sum_{i=1}^{N} (U(i) - \bar{U})^2/(N-1)}}{\bar{U}} \tag{2}$$

where N is the number of samples.

Heat Transfer Blade Instrumentation. Twenty-six stainless steel foil strips are cemented vertically on the outer surface of the instrumented blade (see Fig. 4). Each strip of foil is 25.4 cm long, 1.75 cm wide, and 0.038 mm thick. The foils are connected in series by copper bus bars. This surface, when heated, serves as a constant heat flux surface for the heat transfer tests. Seventy-eight calibrated thermocouples of 36 gage copper-constantan are soldered on the underside of the foils (three for each strip around the middle portion of the radial span). A Fluke 2285b data logger, interfaced with an IBM PC, and the Micro VAX analyzed the output data of all thermocouples. An autotransformer provides heat generation in the foils by controlling current and voltage in the circuit. Circuit current and voltage (and resistance) are measured by a Fluke digital multimeter and a Fluke AC current clamp, respectively. The local heat transfer coefficient can be calculated as

$$h = \frac{q''}{T_w - T_\infty} \simeq \frac{q''_{\text{gen}} - q''_{\text{loss}}}{T_w - T_{aw}} \tag{3}$$

where q'' is a net local convective heat flux from the foil surface, q''_{gen} is the surface-generated heat flux from voltage-current measurements, and q''_{loss} is local heat loss and is a function of the local wall temperature. T_w is local steady-state foil surface temperature (or local wall temperature), which was about 40–50°C, and T_{aw} was about 25°C and is the local adiabatic wall temperature measured when the air flow was on but the foil heat was off. In this study, $T_{aw} \simeq T_\infty$ since Mach number is much less than 1. Loss tests found total heat loss from the test blade for a no-flow condition. The loss calibration was done by supplying power to the test blade for steady state. This was done for several different power inputs to get the relation between the total heat loss and the individual foil temperature. Local radiation loss was estimated using a foil emissivity of 0.22 at 45°C. By knowing the two, conduction loss was estimated. The total heat loss for the entire blade surface is about 10 percent of the heat input (4 percent due to conduction and 6 percent due to radiation). The local heat losses vary from 6 to 11 percent depending on location and surface temperature. The local heat transfer coefficient was then converted into the local Nusselt number, $\text{Nu} = h\,C/k$, based on the blade chord length and the air thermal conductivity. The uncertainty analysis was carried out based on Kline and McClintock (1953). The uncertainties due to q''_{gen}, q''_{loss}, and $(T_w - T_{aw})$ are 2, 4, and 4 percent, respectively. The maximum uncertainty in Nu is less than 7 percent for all three Reynolds number cases.

Pressure Tap Blade Instrumentation. Twenty-six pressure taps were located in the midspan of the pressure tap instrumented blade: 1 at the leading edge (stagnation point), 11 on the pressure side, and 14 on the suction side. The pressure taps were connected to an inclined manometer for the blade surface static pressure measurements. A pitot probe also measured mainstream

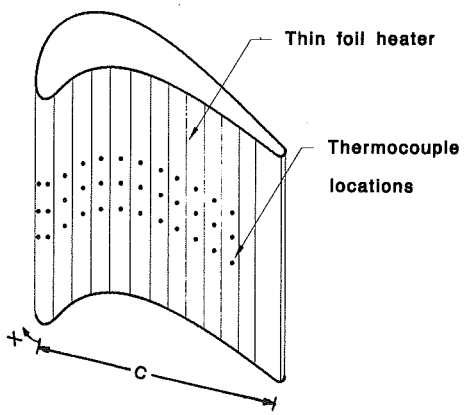

Fig. 4 Heat transfer instrumented blade

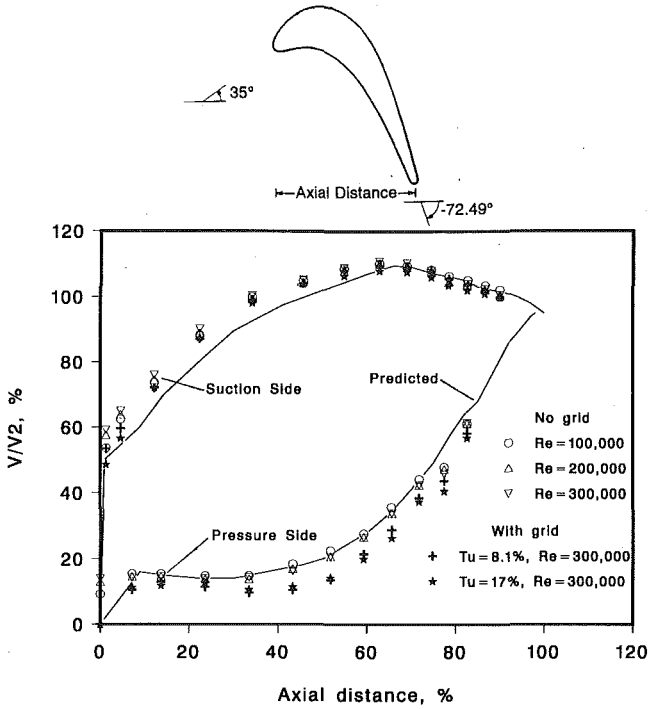

Fig. 5 Velocity distribution on the pressure-tap blade under mainstream turbulence conditions

flow velocity at the inlet and exit of the cascade and to check the results from the hot-wire anemometer.

Test Conditions and Flow Measurement

Before conducting the heat transfer test, a measurement was made to confirm the periodicity of velocity profiles between adjacent flow paths on either side of the middle blade (instrumented blade). Velocity profiles in the radial (spanwise) direction for three Reynolds numbers at flow paths on either side of the middle blade at inlet and outlet planes have been measured to make sure the flow in the middle part of the span is two dimensional. The results show that the inlet and outlet velocity profiles for no inserted turbulence grid are uniform between a 25 and 75 percent span (Han et al., 1993). Thus, the Nusselt numbers are free from the top and bottom wall boundary layer effects. Surface static pressure distribution was measured using the pressure tap instrumented blade (see Fig. 5 for the blade's orientation and coordinates). This can calculate the velocity distribution on both the pressure and suction sides of the airfoil. The uncertainty of the velocity calculated by using the static pressure distributions along the blade is about 5 percent. Figure 5 shows the distribution of velocity ratio (V/V_2) between local (V) and cascade exit (V_2) velocity for flow with no turbulence grid (for Re = 100,000, 200,000, 300,000), and for grid #1 and grid #2 flow at the upstream location 21 cm from the cascade leading plane (for Re = 300,000). Note that the horizontal coordinate is the percentage of the axial distance on both the pressure and suction sides of the blade. The solid line in Fig. 5 is the pretest prediction based on Re = 200,000. The velocity distributions for the flow with and without turbulence grids are similar, except that velocity distributions for the flow with a grid are lower than that without a grid.

Table 1 Mainstream velocity and turbulence conditions

Grid	Location cm (s/d)	V_0, m/s	Re	Tu, %
Grid #1	21(16), 30(23), 60(46)	21 14 7	300,000 200,000 100,000	17, 13.4, 5 17, 13, 5 14.2, 11, 5
Grid #2	21(42), 30(60), 60(120)	21 14 7	300,000 200,000 100,000	8, 5.7, 2.8 8.2, 6, 3.1 7, 5, 3
No Grid	None	21 14 7	300,000 200,000 100,000	0.75 0.72 0.70

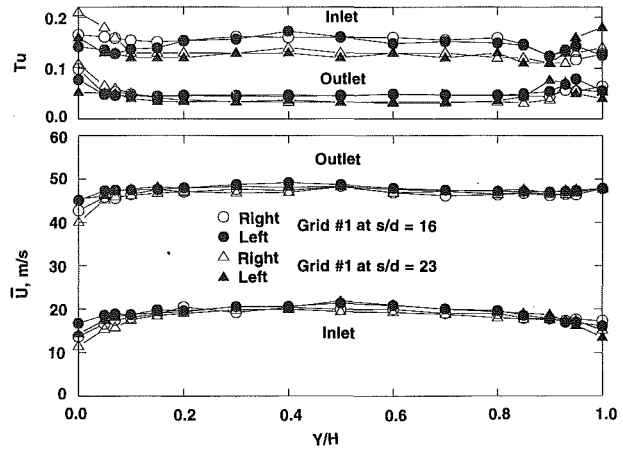

Fig. 6 Inlet and outlet velocity and turbulence intensity profiles for Re = 300,000

Mainstream turbulence intensity at the cascade inlet without the insertion of any turbulence grid is about 0.7 percent. Higher turbulence intensities are obtained by inserting one of two turbulence grids at one of the three upstream locations listed in Table 1. The turbulence grids are located parallel to the leading surface of the blade cascade instead of perpendicular to the flow direction as noted in Fig. 2. Table 1 shows that the same grid at the same location creates slightly different turbulence intensities for the three tested Reynolds numbers. A single-wire hot-wire probe (4 μm diameter, tungsten wire) measured time-dependent velocities and turbulence intensities in the inlet, outlet, and three locations in the middle of the flow path (see Fig. 2, hot-wire probe holes). The hot-wire probe was frequently calibrated using a fourth-order polynomial approximation to ensure true velocity. The uncertainties of the velocity and turbulence intensity calculated by using the hot-wire anemometer are 5 and 10 percent, respectively. Figure 6 shows velocity and turbulence intensity profiles in the radial direction at the inlet and outlet of the left

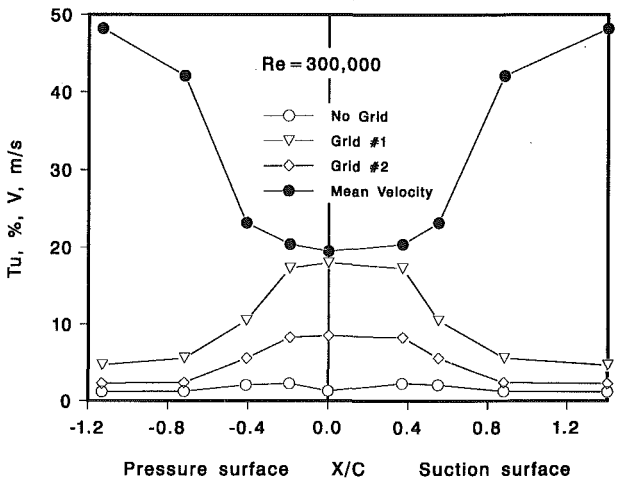

Fig. 7 Turbulence intensity and mean velocity along the flow path

and right flow paths with grid #1 at the upstream location 21 cm ($s/d = 16$, $Tu = 17$ percent at the cascade inlet) and 30 cm ($s/d = 23$, $Tu = 13.4$ percent at the cascade inlet), respectively, from the cascade leading plane. The results suggest that the inlet and outlet velocity and turbulent intensity profiles in both flow paths are uniform in the 60 percent midspan region. The periodicity of velocity and turbulence profiles between adjacent flow paths is acceptable. Also, the flow directions at the inlet and outlet of both flow paths were uniform. Thus, the uniformity of the flow and the homogeneity of the turbulence was established. Figure 7 shows the measured turbulence intensity distributions for the flow with no grid, flow with grid #1 and flow with grid #2 at the 21 cm upstream location, respectively. Note that the turbulent fluctuations decay slightly from the inlet to the outlet of the cascade but the turbulent intensities decay significantly along the flow path for both grid #1 and grid #2. This is because the mainstream mean velocity increases along the flow path (pressure side $X/C < -0.2$, suction side $X/C > 0.4$) as shown on the same plot. The outlet mean velocity is about 2.4 times the inlet mean velocity. Therefore, the local turbulence intensity (based on the local mean velocity) at the cascade exit is lower due to a higher mean velocity. The turbulent intensity for the flow without a grid at the second location (pressure side $X/C = -0.2$; suction side $X/C = 0.4$) is slightly higher than that of the inlet because the flow is disturbed by the cascade's leading edge. This study was not intended to find the detailed velocity and turbulence distributions in the entire boundary layer flow. The present measurements do not provide a detailed picture of the flow field around the airfoil. Nevertheless, it may be helpful to understand the heat transfer data.

Heat Transfer Results

Heat transfer coefficient distributions under no-grid conditions for Reynolds numbers of 100,000, 200,000, and 300,000 were measured to serve as a comparison basis. Those measurements were repeated to make sure the data were repeatable. The results showed that the variation for different test runs was no more than 3 percent.

Figure 8 shows the effect of mainstream turbulence on local Nusselt number distributions on the pressure and suction surfaces of the airfoil for a Reynolds number of 300,000. Grid #1 is at 21 cm, 30 cm, and 60 cm upstream from the cascade and produces the cascade inlet turbulence intensities of 17.0, 13.4, and 5.0 percent, respectively. Grid #2, at the same three locations as grid #1, produces the cascade inlet turbulence intensities of 8.1, 5.7, and 2.8 percent. The Nusselt number distributions for the flow without a grid ($Tu = 0.7$ percent) were also included for comparison. Results for $Tu = 0.7$ percent show that the Nusselt number on the suction surface decreased monotonically with increasing streamwise distance from stagnation due to boundary layer growth. However, the Nusselt number increases sharply past $X/C = 0.85$ due to boundary layer transition. The low turbulence data of this study follow the predicted results from the modified version of the STAN5 program (Gaugler, 1981). The Nusselt number on the pressure surface decreases sharply with increasing X/C for the same 0.7 percent turbulence condition, but gradually starts to increase from $X/C = -0.2$ due to strong acceleration. The high turbulence results show that the local Nusselt number increases with increasing mainstream turbulence intensity over the entire blade surface. The Nusselt number near the suction side leading edge for a 17 percent cascade inlet turbulent intensity is 25–30 percent higher than the 0.7 percent turbulent intensity case. Since the Nusselt number near the suction side leading edge for the flow without a grid ($Tu = 0.7$ percent) is already very high (Nu = 1600), this 25 percent is a big increase in the absolute value of the heat transfer rate. The local Nusselt number increment due to higher mainstream turbulence intensity is significant for the blade suction surface. The corresponding turbulent intensity at the cascade inlet is as high as 17 percent for grid #1 at 21 cm upstream from the cascade. The maximum local Nusselt number near the suction side transition region ($X/C = 0.8$, Nu = 1200) is about 3.5 times that of the no-grid 0.7 percent turbulence intensity case ($X/C = 0.8$, Nu = 350). Figure 8 shows that the higher mainstream turbulent intensity produces the higher suction side surface heat transfer coefficient. This is because the higher turbulent intensity induces an early boundary layer transition from laminar to turbulent flow. The onset of transition on the suction surface boundary layer moves forward with increased mainstream turbulence intensity. For example, the transition point moves from $X/C = 0.8$ to $X/C < 0.4$ when the mainstream turbulent intensity increases from 0.7 to 17 percent. The results also show that the higher turbulence creates a broader transition length than the lower turbulence. This is because transition begins earlier (i.e., smaller X/C) at the higher turbulence intensities. However, the flow acceleration (see Fig. 5) reduces the production of turbulence spots and delays the completion of the transition process. Thus, the higher turbulence causes an earlier transition and the flow acceleration produces a broader transition length on the suction surface when compared to the lower turbulence. The present results of the mainstream turbulence-induced transition phenomena support Mayle's (1991) intermittency transition theory. Mayle found that the boundary layer transition from laminar to turbulent flow on the blade suction surface is composed of two parts: bypass (or natural) transition and unsteady wake-induced transition. The increase in mainstream turbulence intensity causes an earlier turbulence-induced transition that results in a higher heat transfer coefficient over the blade surface. He showed that the time-averaged heat transfer distribution on the suction surface can be obtained from the predicted time-averaged intermittency factor, and the laminar and turbulent heat transfer distributions calculated from steady-flow low turbulence conditions. Zhang (1993) applied Mayle's theory to this study and obtained the time-averaged intermittency factor at elevated turbulence conditions. He then combined the time-averaged intermittency factor with the steady-flow laminar and turbulent heat transfer data at 0.7 percent low turbulence conditions for heat transfer predictions. Figure 8 shows that Mayle's theory (1991) predicts the present data well but the theory underpredicts the data before transition for the high turbulence levels. Note that when the turbulent intensity is greater than 10 percent, the suction surface Nusselt number increases greatly even in the laminar boundary layer region $X/C < 0.4$. This may be because the laminar boundary layer in this region is highly disturbed by the high mainstream turbulence and, therefore, the heat transfer is enhanced.

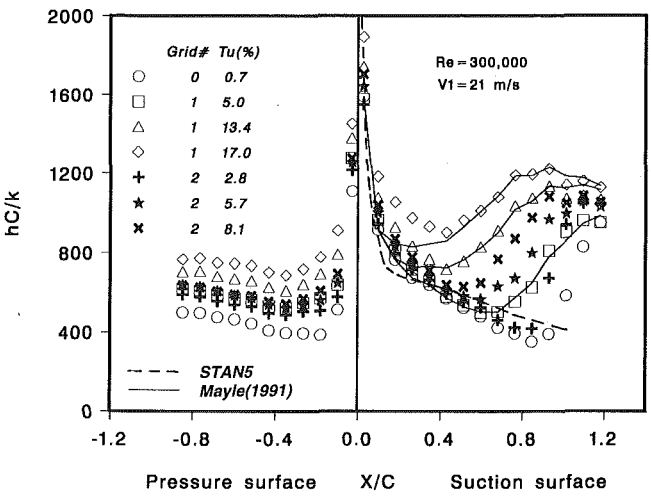

Fig. 8 Effect of mainstream turbulence on local Nusselt number distribution for Re = 300,000

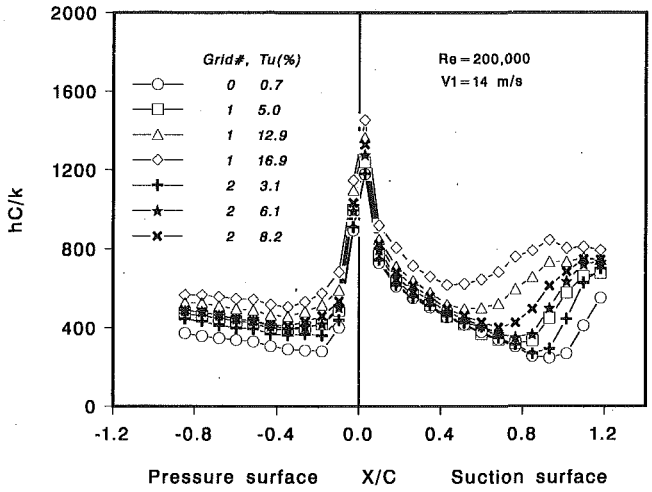

Fig. 9 Effect of mainstream turbulence on local Nusselt number distribution for Re = 200,000

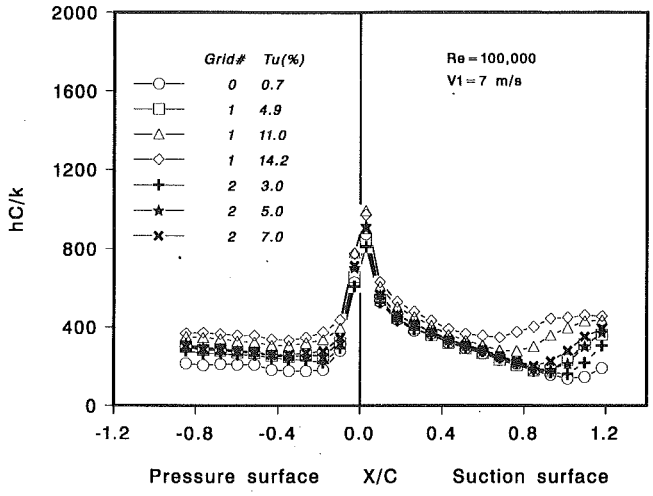

Fig. 10 Effect of mainstream turbulence on local Nusselt number distribution for Re = 100,000

Consider the Nusselt number distributions on the pressure surface. Figure 8 shows that the pressure surface Nusselt number increases incrementally with increasing mainstream turbulence intensity. The Nusselt number remains uniform over the main portion of pressure surface at each level of turbulence. This is because the laminar boundary layer is highly disturbed with no transition occurring on the pressure surface. For a 17 percent turbulence intensity, the maximum local Nusselt number increment on the pressure surface (at $X/C = -0.2$) is about 2 times that of the no-grid 0.7 percent turbulence intensity case.

Consider the effect of mainstream turbulence on the Nusselt number distributions for other Reynolds numbers. Figure 9 shows the effect of mainstream turbulence on local Nusselt number distributions for Re = 200,000 and Fig. 10 is for Re = 100,000. The results show that the turbulence intensity effect on the local Nusselt number distributions is similar to those for Re = 300,000 as discussed above. However, the local Nusselt numbers over the entire blade surface are lower for the smaller Reynolds number and the transition locations are closer to the trailing edge for the smaller Reynolds number despite mainstream turbulence levels.

Grid-Induced Transition and Heat Transfer Augmentation

The local heat transfer coefficients are replotted to examine further the relation between the heat transfer coefficient distribution and the mainstream turbulence level for a given Reynolds number flow. Figure 11 shows the effect of mainstream turbulence on the local Nusselt number augmentation over the blade surface for Reynolds numbers 300,000, 200,000, and 100,000, respectively. The local Nusselt number augmentation is the ratio of local heat transfer coefficient with grid-generated turbulence to that with no grid. The results show that the higher the mainstream turbulence intensity the greater the heat transfer coefficient augmentation on both pressure and suction surfaces. The mainstream turbulence effect on the local heat transfer increments on both the pressure and suction surfaces show a similar trend for the three Reynolds numbers studied. There exists a peak value of the heat transfer coefficient ratio (augmentation) on the respective suction and pressure surface for each inlet turbulence intensity level at a given Reynolds number. For the given Reynolds number, the suction side heat transfer augmentation and its peak ratio increase and shift forward with increasing turbulence level. This is due to the turbulence-induced earlier transition as discussed above. The highest peak ratios are about the same (3.2–3.5) for the three Reynolds numbers. There is a sharp increase and decrease before and after each peak heat transfer ratio and the heat transfer ratio near the leading is larger than that near the trailing. This is because the mainstream turbulence has more impact on the laminar boundary layer than that on the turbulent boundary layer. Figure 11 also shows that the pressure side heat transfer augmentation and its peak ratio increase with increasing turbulence level for a given Reynolds number. The highest peak ratios are about 2.0 for all three Reynolds numbers. Each peak ratio is at $X/C = -0.2$ no matter the turbulence level and the Reynolds number. The peak heat transfer ratio near $X/C = -0.2$ may be due to the interactions between the pressure side Görtler vortices and high mainstream turbulence.

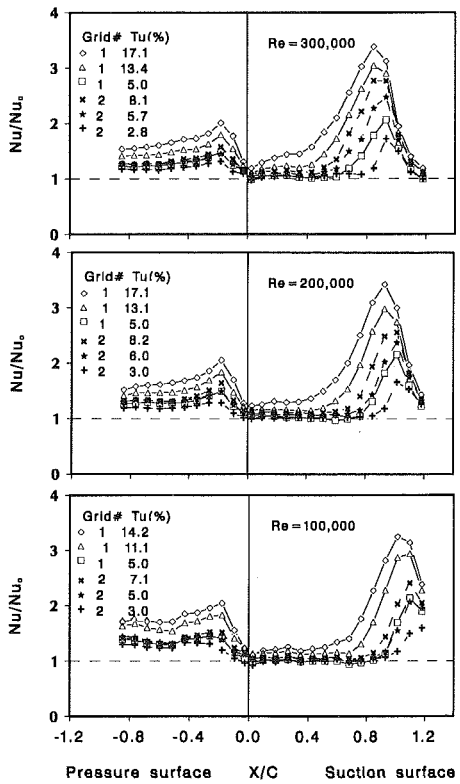

Fig. 11 Effect of mainstream turbulence on local Nusselt number ratio distribution for studied Reynolds numbers

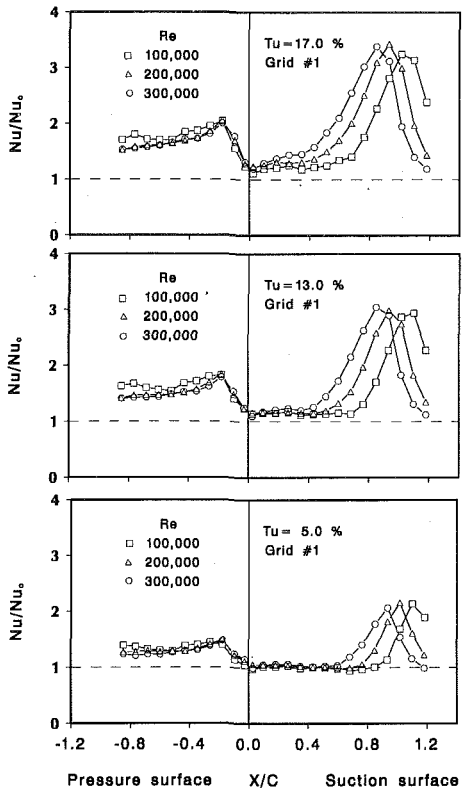

Fig. 12 Effect of Reynolds number on local Nusselt number ratio distribution for studied mainstream turbulence levels

Figure 12 shows the effect of the Reynolds numbers on blade surface heat transfer augmentation at several mainstream turbulence levels generated by grid #1. The results show that the peak heat transfer ratio is about the same for a given turbulence level. However, the peak ratio on the suction surface shifts forward because the higher Reynolds number causes an earlier boundary layer transition. The heat transfer augmentation on the pressure surface ($X/C < -0.2$) decreases with increasing Reynolds number. However, the peak ratios are still at $X/C = -0.2$ for all Reynolds numbers and turbulence levels studied. Figure 12 also shows that the Reynolds number effect on the heat transfer ratios for lower turbulence level is similar to the higher turbulence levels, except that the corresponding heat transfer ratios and their peak values are lower.

Concluding Remarks

The influence of high mainstream turbulence on surface heat transfer coefficients of a gas turbine blade has been investigated. Local Nusselt number distributions on the blade surface were obtained under six, grid-generated turbulence levels for three mainstream Reynolds numbers. The main conclusions are:

1 The grid-generated turbulence promotes a much earlier and broader boundary layer transition on the suction surface and greatly augments its surface heat transfer coefficients. The mainstream turbulence also significantly augments the pressure surface heat transfer coefficients.
2 The leading edge, the suction surface, and the pressure surface heat transfer coefficients for a 17 percent cascade inlet turbulence intensity can be 25–30, 200–250, and 100 percent higher than that of the no-grid 0.7 percent turbulence intensity case.
3 For a given Reynolds number flow, the heat transfer coefficient augmentation on the suction surface increases and its peak ratio moves forward with increased mainstream turbulence level. The heat transfer coefficient augmentation on the pressure surface also increases but its peak ratio location is always at $X/C = -0.2$ regardless of turbulence level. The peak Nusselt number augmentations on the suction surface are greater than that on the pressure surface regardless of Reynolds number and turbulence level.
4 For a given mainstream turbulence level, the peak heat transfer augmentation on the suction surface remains constant but shifts forward with increased Reynolds number. There are sharp increases and decreases in heat transfer ratios before and after these peak ratios. The locations of those peak ratios are associated with the suction surface boundary layer transition induced by the mainstream Reynolds number and the strength of the mainstream turbulence level. Those peak ratios are lower for the lower mainstream turbulence level despite the Reynolds number.
5 It should be noted that the present results are based on grid-generated turbulence levels for Reynolds numbers between 100,000 and 300,000. Although the present Reynolds numbers are lower than in most gas turbine applications, transition is still important at full scale and the present data should be useful for testing laminar-transition-turbulent prediction methods.

Acknowledgments

The project was supported by the Texas Higher Education Coordinating Board Advanced Technology Program under grant number 999903-104 (TEES 7090). Special thanks are due to Ms. H. Wanda Jiang of Texas A&M University for preparing Fig. 6 and the STAN5 prediction shown in Fig. 8.

References

Abhari, R. S., Guenette, G. R., Epstein, A. H., and Giles, M. B., 1992, "Comparison of Time-Resolved Measurements and Numerical Calculations," ASME *Journal of Turbomachinery,* Vol. 114, pp. 818–827.

Ashworth, D. A., LaGraff, J. E., Schultz, D. L., and Grindrod, K. J., 1985, "Unsteady Aerodynamic and Heat Transfer Processes in a Transonic Turbine Stage," ASME *Journal of Engineering for Gas Turbines and Power,* Vol. 107, pp. 1022–1030.

Bellows, W. J., and Mayle, R. E., 1986, "Heat Transfer Downstream of a Leading Edge Separation Bubble," ASME *Journal of Turbomachinery,* Vol. 108, pp. 131–136.

Blair, M. F., 1983a, "Influence of Free-Stream Turbulence on Turbulent Boundary Layer Heat Transfer and Mean Profile Development, Part I—Experimental Data," ASME JOURNAL OF HEAT TRANSFER, Vol. 105, pp. 33–40.

Blair, M. F., 1983b, "Influence of Free-Stream Turbulence on Turbulent Boundary Layer Heat Transfer and Mean Profile Development, Part II—Analysis of Results," ASME JOURNAL OF HEAT TRANSFER, Vol. 105, pp. 41–47.

Blair, M. F., Dring, R. P., and Joslyn, H. D., 1989a, "The Effects of Turbulence and Stator/Rotor Interactions on Turbine Heat Transfer: Part I—Design Operating Conditions," ASME *Journal of Turbomachinery,* Vol. 111, pp. 87–96.

Blair, M. F., Dring, R. P., and Joslyn, H. D., 1989b, "The Effects of Turbulence and Stator/Rotor Interactions on Turbine Heat Transfer: Part II—Effects of Reynolds Number and Incidence," ASME *Journal of Turbomachinery,* Vol. 111, pp. 97–103.

Blair, M. F., 1994, "An Experimental Study of Heat Transfer in a Large-Scale Turbine Rotor Passage," ASME *Journal of Turbomachinery,* Vol. 116, pp. 1–13.

Brown, A., and Martin, B. W., 1979, "Heat Transfer to Turbine Blades, With Special Reference to the Effects of Mainstream Turbulence," ASME Paper No. 79-GT-26.

Brown, A., and Martin, B. W., 1982, "Flow Transition Phenomena and Heat Transfer Over the Pressure Surfaces of Gas Turbine Blades," ASME *Journal of Engineering for Power,* Vol. 104, pp. 360–367.

Doorly, D. J., and Oldfield, M. L. G., 1985, "Simulation of the Effects of Shock-Waves Passing on a Turbine Rotor Blade," ASME *Journal of Engineering for Gas Turbines and Power,* Vol. 107, pp. 998–1006.

Doorly, D. J., 1988, "Modeling the Unsteady Flow in a Turbine Rotor Passage," ASME *Journal of Turbomachinery,* Vol. 110, pp. 27–37.

Dullenkopf, K., Schulz, A., and Wittig, S., 1991, "The Effect of Incident Wake Conditions on the Mean Heat Transfer of an Airfoil," ASME *Journal of Turbomachinery,* Vol. 113, pp. 412–418.

Dullenkopf, K., and Mayle, R. E., 1994, "The Effect of Incident Turbulence and Moving Wakes on Laminar Heat Transfer in Gas Turbines," ASME *Journal of Turbomachinery,* Vol. 116, pp. 23–28.

Dunn, M. G., 1986, "Heat Flux Measurements for the Rotor of a Full-Stage Turbine: Part I—Time-Averaged Results," ASME *Journal of Turbomachinery,* Vol. 108, pp. 90–97.

Dunn, M. G., George, W. K., Rae, W. J., Woodward, S. H., Moller, J. C., and Seymour, J. P., 1986, "Heat Flux Measurements for the Rotor of a Full-Stage Tur-

bine: Part II—Description of Analysis Technique and Typical Time-Resolved Measurements," ASME *Journal of Turbomachinery,* Vol. 108, pp. 98–107.

Dunn, M. G., Seymour, J. P., Woodward, S. H., George, W. K., and Chupp, R. E., 1989, "Phase-Resolved Heat Flux Measurements on the Blade of a Full-Scale Rotating Turbine," ASME *Journal of Turbomachinery,* Vol. 111, pp. 8–19.

Dunn, M. G., Kim, J., Civinskas, K. C., and Boyle, R. J., 1994, "Time Averaged Heat Transfer and Pressure Measurements and Comparison With Prediction for a Two-Stage Turbine," ASME *Journal of Turbomachinery,* Vol. 116, pp. 14–22.

Gaugler, R. E., 1981, "Some Modifications to, and Operational Experiments With, the Two-Dimensional, Finite-Difference Boundary-Layer Code, STAN5," NASA TM-81631.

Han, J. C., Zhang, L., and Ou, S., 1993, "Influence of Unsteady Wake on Heat Transfer Coefficients From a Gas Turbine Blade," ASME JOURNAL OF HEAT TRANSFER, Vol. 115, pp. 904–911.

Hancock, P. E., and Bradshaw, P., 1983, "The Effect of Free-Stream Turbulence on Turbulent Boundary Layers," ASME *Journal of Fluids Engineering,* Vol. 105, pp. 284–289.

Kline, S. J., and McClintock, F. A., 1953, "Describing Uncertainties in Single Sample Experiments," *Mechanical Engineering,* Vol. 75, Jan., pp. 3–8.

Liu, X., and Rodi, W., 1989, "Measurements of Unsteady Flow Over and Heat Transfer From a Flat Plate," ASME Paper No. 89-GT-2.

Liu, X., and Rodi, W., 1992, "Measurement of Unsteady Flow and Heat Transfer in a Linear Cascade," ASME Paper No. 92-GT-323.

Lowery, G. W., and Vachon, R. I., 1975, "The Effect of Turbulence on Heat Transfer From Heated Cylinders," *International Journal of Heat and Mass Transfer,* Vol. 18, pp. 1229–1242.

Mayle, R. E., and Dullenkopf, K., 1990, "A Theory of Wake-Induced Transition," ASME *Journal of Turbomachinery,* Vol. 112, pp. 188–195.

Mayle, R. E., 1991, "The Role of Laminar–Turbulent Transition in Gas Turbine Engines," ASME *Journal of Turbomachinery,* Vol. 113, pp. 509–537.

Mehendale, A. B., Han, J. C., and Ou, S., 1991, "Influence of High Mainstream Turbulence on Leading Edge Heat Transfer," ASME JOURNAL OF HEAT TRANSFER, Vol. 113, pp. 843–850.

O'Brien, J. E., and VanFossen, G. J., 1985, "The Influence of Jet-Grid Turbulence on Heat Transfer From the Stagnation Region of a Cylinder in Crossflow," ASME Paper No. 85-HT-58.

O'Brien, J. E., and Capps, S. P., 1989, "Two-Component Phase-Averaged Turbulence Statistics Downstream of a Rotating Spoked-Wheel Wake Generator," ASME *Journal of Turbomachinery,* Vol. 111, pp. 475–482.

O'Brien, J. E., 1990, "Effects of Wake Passing on Stagnation Region Heat Transfer," ASME *Journal of Turbomachinery,* Vol. 112, pp. 522–530.

Pfeil, H., Herbst, R., and Schroeder, T., 1983, "Investigation of the Laminar–Turbulent Transition of Boundary Layers Disturbed by Wakes," ASME *Journal of Engineering for Power,* Vol. 105, pp. 130–137.

Priddy, W. J., and Bayley, F. J., 1988, "Turbulence Measurements in Turbine Blade Passages and Implications for Heat Transfer," ASME *Journal of Turbomachinery,* Vol. 110, pp. 73–79.

Simonich, J. C., and Bradshaw, P., 1978, "Effect of Free-Stream Turbulence on Heat Transfer Through a Turbulent Boundary Layer," ASME JOURNAL OF HEAT TRANSFER, Vol. 100, pp. 671–677.

Wittig, S., Dullenkopf, K., Schulz, A., and Hestermann, R., 1987, "Laser-Doppler Studies of the Wake-Effected Flow Field in a Turbine Cascade," ASME *Journal of Turbomachinery,* Vol. 109, pp. 170–176.

Wittig, S., Schulz, A., Dullenkopf, K., and Fairbanks, J., 1988, "Effects of Free-Stream Turbulence and Wake Characteristics on the Heat Transfer Along a Cooled Gas Turbine Blade," ASME Paper No. 88-GT-179.

Young, C. D., Han, J. C., Huang, Y., and Rivir, R. B., 1992, "Influence of Jet-Grid Turbulence on Flat Plate Turbulent Boundary Layer Flow and Heat Transfer," ASME JOURNAL OF HEAT TRANSFER, Vol. 114, pp. 65–72.

Zhang, L., 1993, "Influence of Mainstream Turbulence and Unsteady Wake on Turbine Blade Heat Transfer," Ph.D. Dissertation, Texas A&M University, College Station, TX.

Mass Transfer With Flow Through an Array of Rectangular Cylinders

H. H. Cho

M. Y. Jabbari

R. J. Goldstein

Heat Transfer Laboratory,
Department of Mechanical Engineering,
University of Minnesota,
Minneapolis, MN 55455

The mass transfer from an array of naphthalene-coated parallel rectangular cylinders, through which air passes in a slitlike flow, has been measured. The local Sherwood numbers indicate that the flow pattern is asymmetric in spite of using an array of two-dimensional, equally spaced identical cylinders. Smoke-wire flow visualization verifies this asymmetry, showing alternate short and long wakes around the cylinders, due probably to the instability of vortex shedding. On the side surfaces of the cylinders with the short wakes, the air flow deflects and reattaches, resulting in a high mass transfer. Also, a strong impinging effect is observed on the leeward (back) surface of these cylinders at high Reynolds numbers. Reattachment is not observed on the side surface for cylinders with the long wakes. On these, however, the mass transfer on the leeward surface is higher than on the short wake cylinders. This may be due to the relatively low naphthalene vapor concentration in the long wakes. The distribution of the short wakes (and the long wakes) is periodic and relatively stable. However, their position can be changed from one cylinder to the adjacent one by a disturbance. Measurements were taken over a moderate Reynolds number range of 300 to 3000 (based on the cylinder-to-cylinder pitch and approaching velocity). The laminar, transition, and turbulent nature in the wake flows can be inferred from the results.

Introduction

Two-dimensional flow through an array of rectangular cylinders is of fundamental importance. Limiting cases occur when the spacing between cylinders is very large or very small. In the former case, the flow is similar to flow around a single cylinder (no interaction with neighboring cylinders). With very small spacing, a two-dimensional jetlike flow occurs. However, flows with moderate spacing occur in many engineering applications, such as heat exchangers, electronic chips, and turbine blades.

Two-dimensional flow patterns around bluff bodies have been investigated experimentally and numerically over a long period. Researchers have usually used an array of flat plates with large spacing in which individual symmetric flows occurred. Arie and Rouse (1956) observed symmetric flow behind a series of normal plates with tail plates for large spacing, but found asymmetric and unstable flow with nonreproducible results at a small spacing ($S/W = 2.0$). Milos et al. (1987) found numerically that the wake length for the flow past a cascade expansion increased linearly with Re_s and decreased with increasing spacing at a given Re_s for $S/W \leq 3.5$. Two-dimensional steady symmetric flow through a uniform cascade of normal flat plates was studied by Ingham et al. (1990). Their numerical results were in good agreement with flow visualization at very low Reynolds numbers (up to $Re_s = 22.2$).

All of these studies considered steady symmetric flow behind bluff bodies for large spacing and low Reynolds number. However, the flow becomes asymmetric and two dimensional (jetlike) when the spacing between the bluff bodies is small enough and as Reynolds number increases. Asymmetric separation in a plane duct with symmetric sudden expansion is well understood. Similar flow can occur behind an array of cylinders, with the side walls replaced by symmetry lines. Numerous investigators have studied the asymmetric flow separation, but only a few have studied the heat transfer for a two-dimensional duct with sudden expansion.

Abbott and Kline (1962), Durst et al. (1974) and Cherdron et al. (1978) investigated the asymmetric flow, vortex pattern, shedding frequency, and size of wakes in symmetric, two-dimensional, sudden expansion ducts for low Reynolds numbers. They found that with increasing Reynolds number, the flows become asymmetric with separation regions of unequal size on opposite sides of the duct, but exist in a stable manner on either side.

Filetti and Kays (1967) measured the local heat transfer on duct walls for a sudden expansion in flow cross section. They observed stable asymmetric flow. The sizes of the long and the short recirculating zones were independent of Reynolds number ($7 \times 10^4 \leq Re \leq 2.05 \times 10^5$, Re based on the hydraulic diameter of the duct cross section and an average velocity in the duct).

Asymmetric flows have also been observed behind a pair of bluff bodies placed side by side in a free stream. Spivack (1946), Quadflieg (1977), and Williamson (1985) studied the critical gap size between a pair of bluff bodies at which the flows become asymmetric.

The asymmetric pressure distributions for side-by-side circular cylinders and flat plates (two, three, or four cylinders) with small spacing were investigated by Gerhardt and Kramer (1981) and Hayashi et al. (1986), respectively. They observed asymmetric gap flow in a stable manner as in the previous cases. Most flows around several bluff bodies placed side by side are affected by the outside free stream, so that the wake flow patterns are irregular. Both these studies concentrated on the wake flow, drag coefficients, vortex shedding frequency, and wake sizes, rather than the heat transfer.

The present study deals with a spacing of $S/W = 0.5$, where S is the slit width and W is the width of the cylinders. Under such spacing, the flows around neighboring cylinders interact and become asymmetric (Fig. 1). The objective of the present investigation is to determine the flow patterns around the cylinders and obtain local mass transfer coefficients on the cylinder surfaces, which can also be used in heat transfer analysis.

The heat transfer as well as the vortex flow and drag from an array of rectangular cylinders or nozzle surfaces of slit-jet flows are important in many applications. Asymmetric heat (mass) transfer influenced by the flow instability has not generally been considered with flow around an array of rectangular cylinders or through slits. The present study reports on such mass transfer at

Contributed by the Heat Transfer Division for publication in the JOURNAL OF HEAT TRANSFER. Manuscript received by the Heat Transfer Division February 1993; revision received January 1994. Keywords: Flow Instability, Flow Separation, Mass Transfer. Associate Technical Editor: R. J. Simoneau.

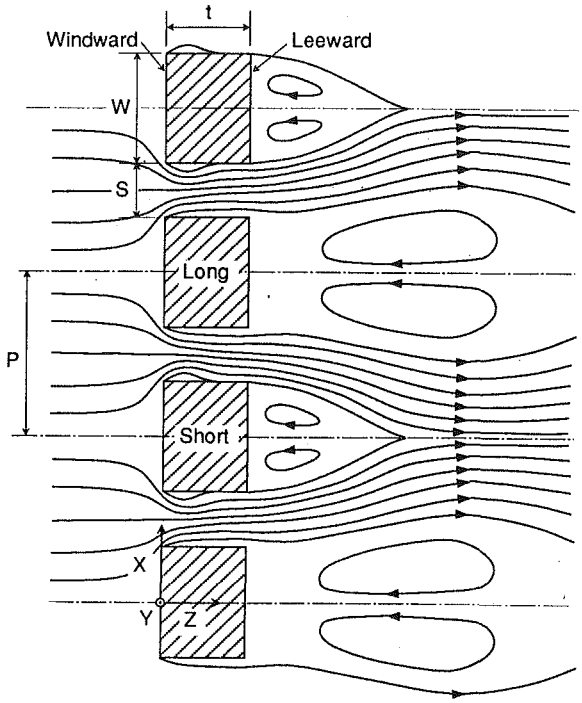

Fig. 1 Schematic diagram of asymmetric flow ($W = 2S$, $P = 3S$, and $t = 1.43S$)

a moderate Reynolds number ($300 \leq \mathrm{Re}_s \leq 3{,}000$). It reports on mass transfer for laminar, transition, and turbulent wake flows. In support of the mass transfer measurement, a smoke-wire visualization of the flow is carried out (Fig. 2). The results clearly show asymmetric flow patterns.

Experimental Apparatus and Procedure

1 Experimental Apparatus. A sketch of the experimental apparatus is shown in Fig. 3. The test plate is positioned at the center of the plenum's top wall. The plenum chamber is 572 by 572 by 1400 mm. The test plate has eight identical rectangular cylinders (with seven slits between them).

There are a number of factors to be considered in selecting the three geometric parameters of the array of slits; the slit width S, the pitch P, and the thickness (depth) t. Each slit has $S = 4.76$ mm, $L/S = 16.8$ ($L = 80$ mm), and $t/S = 1.43$ ($t = 6.81$ mm). The pitch P is selected as $3S$, hence the width of the cylinder W is $2S$ (Fig. 4). The experiments are intended to model two-dimensional flow through a row of rectangular cylinders. It is necessary to have sufficient aspect ratio so that end effects are minimal. The aspect ratio is 16.8 to achieve two-dimensional fluid flow in the middle region, and a two-dimensional mass transfer field from the cast naphthalene of the middle region. The thickness of the cylinder, $1.43S$, is chosen so that the reattachment occurs at the side surface of the cylinder because the reattachment point for a thick circular orifice is about 1.2 times hole diameter downstream from the hole inlet (Lichtarowicz et al., 1965).

Provisions are made to cover the peripheral surfaces of the middle cylinders by naphthalene. All surfaces of the cylinders were polished except the surfaces holding the cast naphthalene, which are roughened to aid in casting.

Without the guide duct (Fig. 3), three dimensionality of the Sherwood number was observed particularly on the leeward side in spite of the large aspect ratio (Cho, 1992). This might occur from strong entrainment of the fluid from the sides of jets (spanwise-directional flow). To increase the two dimensionality of the air flow and mass transfer over the test cylinders, a guide duct surrounding the test plate is fitted on the upstream and downstream of the cylinders. The guide duct is attached to the centers of both end cylinders as symmetric lines to simulate an infinite numbers of cylinders on the plate (Fig. 4). The guide duct extends for 10 cm in the upstream direction (nozzle type) and 20

Nomenclature

C = constant in the correlation Eq. (6)
d = effective cylinder diameter = $2Wt/(W + t)$
D_{naph} = mass diffusion coefficient for naphthalene vapor in air (Eq. (3))
h_m = local mass transfer coefficient
$\overline{h}_m$ = mass transfer coefficient averaged over a surface
L = length of the cylinder in lateral direction (Fig. 4)
L_n = length coated by naphthalene on the rectangular cylinder (Fig. 4)
$\dot{m}$ = local naphthalene mass transfer rate per unit area from the rectangular cylinder surface
n = exponent in the correlation Eq. (6)
P = slit-to-slit pitch (Fig. 4)
P_{atm} = atmospheric pressure in mm Hg
S = slit width (space between cylinders, Fig. 4)
T = temperature of naphthalene surface in degrees Kelvin
t = thickness of the rectangular cylinder (Fig. 4)
U_∞ = approaching velocity (0.33 m/s to 3.3 m/s in present tests)
W = width of the rectangular cylinder (Fig. 4)
X = distance across the slits (Fig. 4)
X_p = position along the periphery of the cylinder (Fig. 6)
Y = distance along the slit in lateral direction (Fig. 4)
Z = distance through the slit in streamwise direction; $Z = 0$ at the inlet of the slit (Fig. 4)
Δz = local sublimation depth of naphthalene
$\Delta\tau$ = exposure time in air flow
ν = kinematic viscosity of air
σ = standard deviation
ρ_s = density of solid naphthalene
$\rho_{v,w}$ = naphthalene vapor density on the cylinder surface
ρ_∞ = naphthalene vapor density in approaching flow = 0

Dimensionless parameters

Nu = Nusselt number
Nu_w = Nusselt number based on cylinder width = hW/k
Pr = Prandtl number = ν/α
Re_d = Reynolds number based on the effective cylinder diameter and the approaching velocity = $U_\infty d/\nu$
Re_s = Reynolds number based on the slit width and a mean velocity in slit (equivalent to the pitch and an approaching velocity) = $U_\infty P/\nu$ = 300 to 3000 in present tests
Re_w = Reynolds number based on the width of cylinder and the approaching velocity = $U_\infty W/\nu$
Sc = Schmidt number for naphthalene in air = ν/D (Eq. (4))
Sh = Sherwood number based on the pitch = $h_m P/D_{\mathrm{naph}}$
Sh_0 = Sherwood number at the stagnation point ($X = 0$)
$\overline{\mathrm{Sh}}$ = average Sherwood number on each side of rectangular cylinder = $\overline{h}_m P/D_{\mathrm{naph}}$
$\overline{\overline{\mathrm{Sh}}}$ = overall average (around all four sides) Sherwood number
$\overline{\overline{\mathrm{Sh}}}_d$ = overall average Sherwood number based on the effective cylinder diameter (Eqs. (9) and (10))

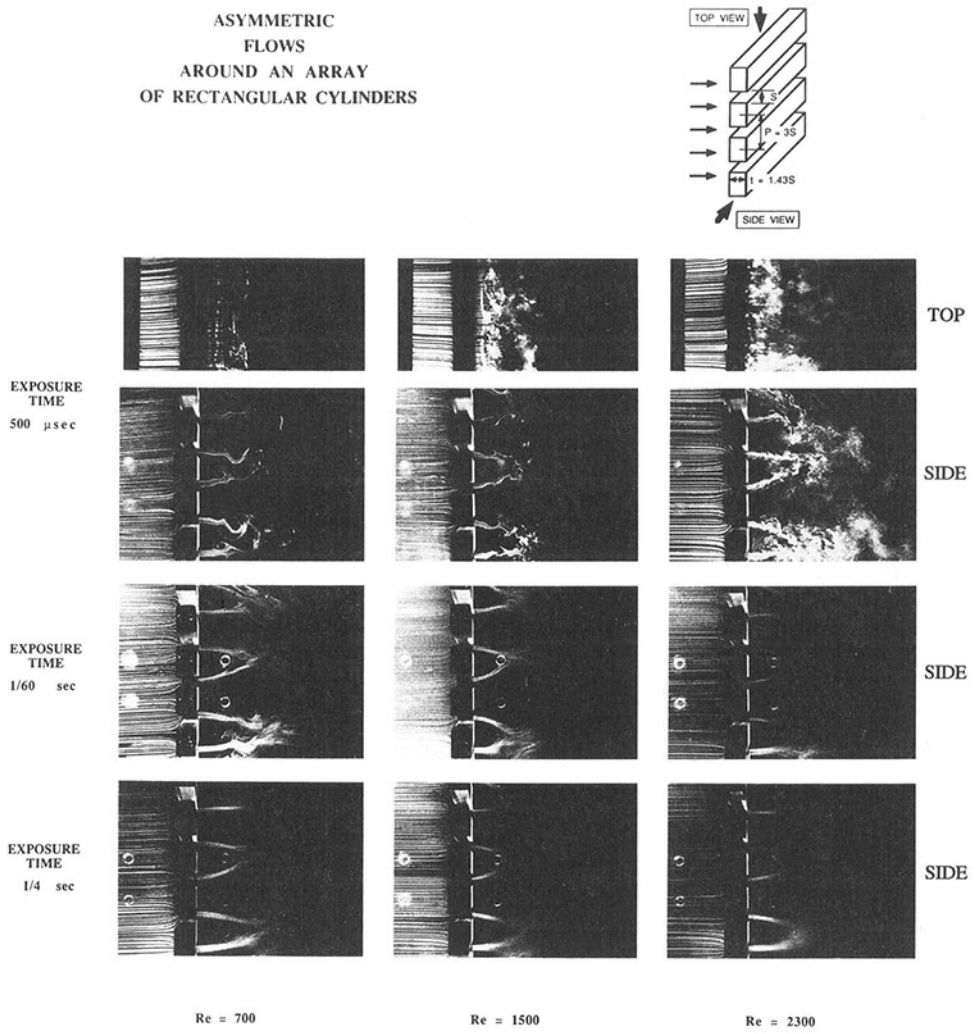

Fig. 2 Flow visualization using smoke wire

cm in the downstream direction. The resulting uniformity of the Sherwood number in the spanwise direction (Y direction) is shown in Fig. 5.

Room air drawn into a settling baffle passes through the perforated test plate into the plenum chamber, and is discharged outside through the blower. The settling baffle greatly reduces the effect of random motion of room air. It has openings at the top and around the plenum chamber at its bottom. The openings of the settling baffle are covered with screen and cloth to break down eddies in the incoming air (Fig. 3).

2 Data Acquisition System. A computer-controlled measurement system (Goldstein et al., 1985) is used to obtain measurements of local sublimation depth with precise positioning, accurate surface elevation measurement, and rapid data acquisition. The system consists of a depth gage, a linear signal conditioner, a digital multimeter, two stepper motors, a motor controller, an HP-85 microcomputer, and a personal computer. The local sublimation depths are obtained using a linear variation differential transformer (hereafter LVDT) gage, which is a Schaevitz model PCA-200-010 LVDT having 0.5 mm linear range and 25.4 nm (1.0 μin.) resolution. The linearity of the LVDT is within 0.1 percent over the measuring range (depth (mil) = 1.001 * voltage output (mV)). The random error of the LVDT due to electrical noise is determined by mock measurements performed on the nonsubliming metal surface. The mean value of the errors is less than 12.7 nm (0.5 μin.). The standard deviation (σ) of rms values is 76.2 nm (3 μin.). Therefore the random error is about 150 nm (6 μin.; 2σ) at a 95 percent confidence interval. For precise positioning, two single-axis tables are able to move 25.4 μm (0.001 in.) with a noncumulative 3 percent error for step increment. A digital multimeter, Keithley model 196, acquires the signals from the signal conditioner and integrates several signals (usually seven) to produce a more accurate reading at a given position. Finally, an HP-85 microcomputer controls the movements of the XY table and reads the depth levels from LVDT. The data are then transferred to a personal computer for storage and subsequent reduction.

3 Procedure

(a) Casting. The naphthalene surfaces employed in the experiments are made by casting. The naphthalene remaining on the cylinders from a previous run is first removed by melting. Each rectangular cylinder is then mounted within a four-piece highly polished aluminum mold (polished using aluminum powder grade #3). The inside dimension of the mold matches the size of the required rectangular cylinder. Molten naphthalene (near boiling point) is poured into the molds. Each mold has two vent holes for the air displaced by the molten naphthalene. To improve adhesion of the naphthalene, the surface of the test piece is roughened with grooves. After the molds are filled and the naphthalene solidifies and cools to room temperature, the molds are separated from the test piece by applying a shear force. The smoothness of the exposed naphthalene surface is comparable to that of the polished aluminum adjacent to it.

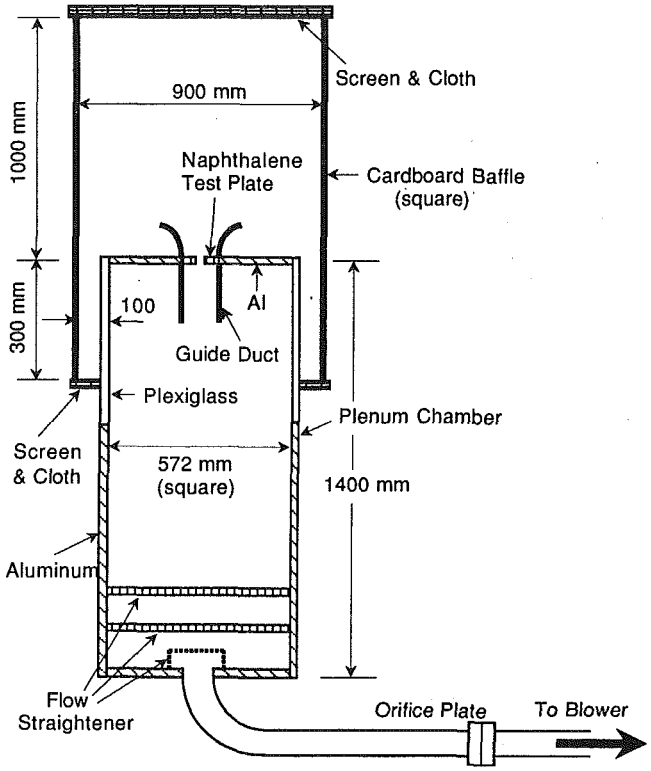

Fig. 3 Schematic front view diagram of the experimental apparatus

(b) Local Measurements. To determine the mass transfer rate, the profile of the naphthalene surface elevation is measured on the XY table before and after each data run. The difference between the two sets of surface elevations (with respect to a reference level on the nonsubliming metal surface) is a measure of the sublimation depth. Each run time is selected so that the average sublimation depth of the naphthalene surface would be about 0.05 mm (0.002 in.). At a typical room temperature (24°C), the run time ranged from 30 to 120 minutes depending on the Reynolds numbers. Because the vapor pressure of naphthalene is quite sensitive to temperature (about 10 percent change per °C), the naphthalene surface temperature is measured precisely using T-type (copper-constantan) thermocouples installed inside the naphthalene (as close as possible to the surface) during a test run. The airflow temperature and the room temperature are also measured. The local mass transfer coefficient is defined as

$$h_m = \frac{\dot{m}}{\rho_{v,w} - \rho_\infty} = \frac{\rho_s(\Delta z/\Delta\tau)}{\rho_{v,w}} \tag{1}$$

The naphthalene vapor pressure is obtained from a correlation (vapor pressure–temperature relation) of Ambrose et al. (1975). The naphthalene vapor density, $\rho_{v,w}$, is calculated from the perfect gas law. During the depth measurement on the XY table, sublimation by natural convection is not negligible, possibly up to 10 percent of a measurement at 24°C (normally less than 5 percent). A natural convection rate determined by experiment is about 92.2 nm/min (3.63 μin./min) at 24°C. For data correction, an amount based on this rate and the measuring time is subtracted from the total sublimation depth. The Sherwood number can be expressed as

$$\mathrm{Sh} = \frac{h_m P}{D_{\mathrm{naph}}} \tag{2}$$

There are no well-accepted experimental data for diffusion coefficient (Goldstein and Cho, 1993). D_{naph} is determined from average values of Cho's experiment (1989) and Chen and Wung's experiment (1990) at 298.16 K, which have about a 6 percent difference. Also, an exponent of temperature correlation is taken from average values of their results for a temperature range of 288 K to 310 K. The correlation equations for D_{naph} and resulting Sc are

$$D_{\mathrm{naph}} = 0.0681\left(\frac{T}{298.16}\right)^{1.93}\left(\frac{760}{P_{\mathrm{atm}}}\right) \quad [\mathrm{cm}^2/\mathrm{s}] \tag{3}$$

$$\cdot\ \mathrm{Sc} = 2.28\left(\frac{T}{298.16}\right)^{-0.1526} \tag{4}$$

Uncertainty of the Sherwood numbers using Kline and McClintock's (1953) method for single sample experiments, considering the measured temperature, depth, position, and correlation equations, is within 6.9 percent in the entire operating range of the measurement based on a 95 percent confidence interval ($\pm 2\sigma$) (detailed in Table 1).

(c) Weighing Method. The overall mass transfer rate for each cylinder is determined using a precision balance. This method has a small measuring error and little natural convection loss during the measurement because it takes little time. The balance is a Sartorius analytical balance with a resolution of 0.1 mg and a capacity of 200 g. A run time is selected so that 70 to 100 mg of naphthalene sublime during the run, which results in an average sublimation depth of 38 to 50 μm (1.5 to 2.0 mil). Some overall Sherwood numbers from the weighing measurements are compared with the numerically integrated values from local measurements. The overall Sh number (from weighing) is approximately 6 percent higher than the numerical integrated Sherwood

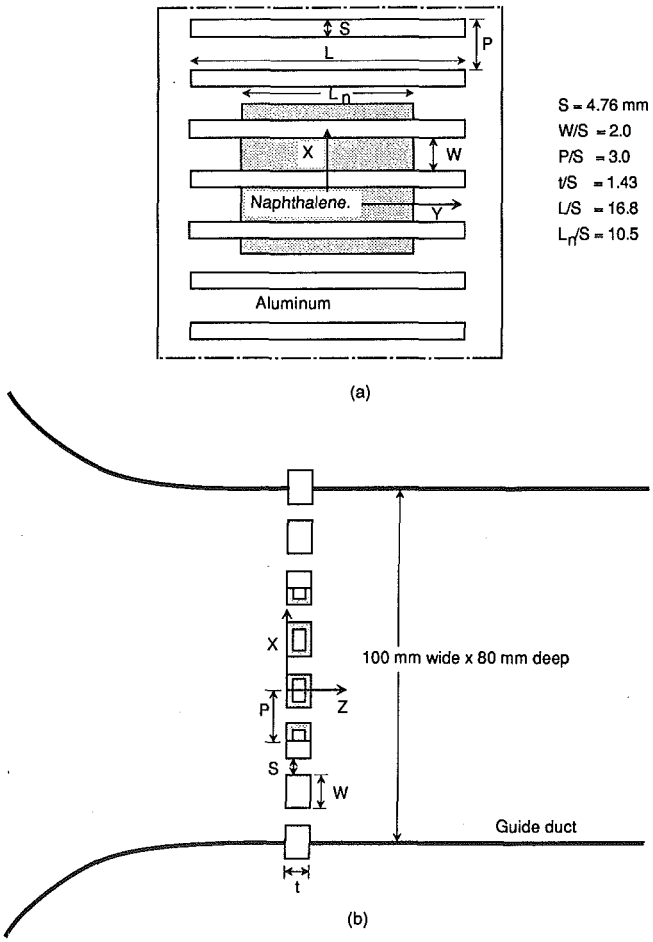

Fig. 4 Test plate with cast naphthalene: (a) front view; (b) sectional side view

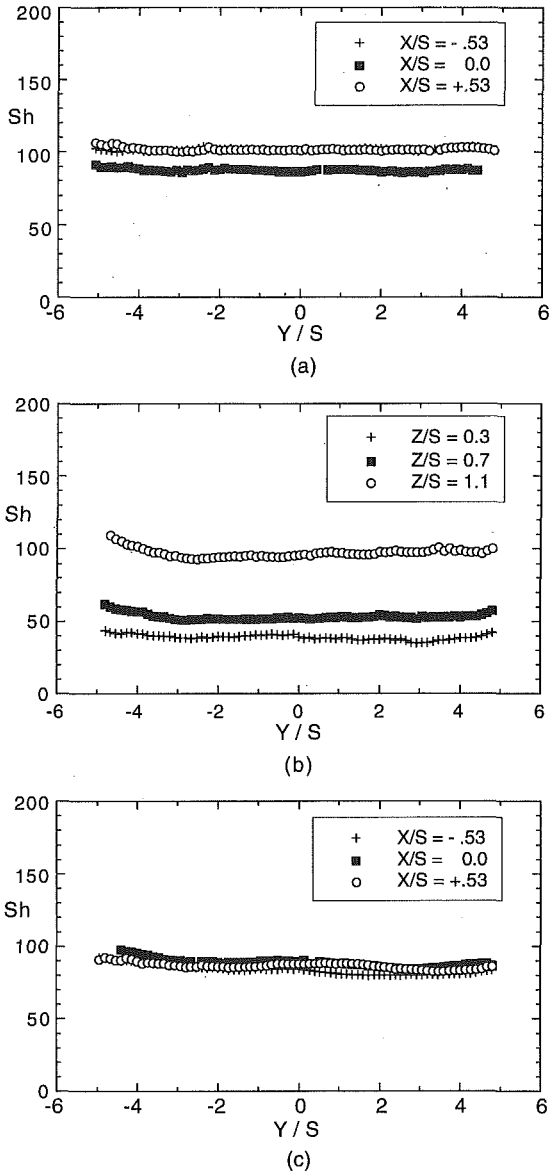

Fig. 5 Local Sh along the rectangular cylinder with guide duct at Re_s = 2970 (uncertainty estimate: Sh ± 6.9 percent): (a) windward; (b) side; (c) leeward surfaces

number (from local data). This might be caused by the corner edges of the cylinder (5 percent of size, i.e., 2.5 percent from each corner), which are not counted in the local measurement and are regions of high mass transfer.

(d) Flow Visualization. A smoke wire is employed to produce discrete smoke streaklines around the array of cylinders. The visualization is performed with a nichrome wire of about 0.15 mm diameter, which is manually coated with oil: "Smoke Fluid" or "Life-like Model train smoke oil." The wire is prestressed to prevent sagging due to thermal expansion during heating. This technique can be safely used for Reynolds number (based on wire diameter) less than 40. In the present tests this Reynolds number is less than 15. For a slow approach velocity, the smoke lines appear to lift up around the wire during the heating due to natural convection. The smoke, actually small liquid particles produced by vaporizing oil, remains visible for about 1 second. Two 600 watt halogen lamps provide illumination; the exposure times of the photographs are $\frac{1}{2000}$, $\frac{1}{60}$, and $\frac{1}{4}$ second in order to get instantaneous and average flow patterns (0.38 m/s $\leq U_\infty \leq$ 1.26 m/s in present visualization tests).

Table 1 Estimated uncertainties for each variable and parameter used

Variable or parameter	Estimated uncertainty
Δz	±0.80 percent
T	±0.084 percent
ρ_s	±1.1 percent
$\rho_{v,w}$	±4.5 percent
D_{naph}	±5.1 percent
h_m	±4.7 percent
Sh	±6.9 percent

Results and Discussion

Figure 1 shows an asymmetric flow pattern through an array of rectangular cylinders (two-dimensional multiple-slit jet flow). The pattern is inferred from local measurements of mass transfer from the cylinders and visualization of the flow through the array. Measurements indicate that the flows behind the cylinders consist of long and short wakes. The wakes may alternate between the cylinders from one run to the next due to instability of the flow. Williamson (1985) found an asymmetric flow pattern for gaps below about $S/W = 1.5$ using two flat plates. In the present geometry, the value of $S/W = 0.5$ meets Williamson's criterion.

The mass transfer rates, expressed in terms of Sherwood number, are measured around the periphery of the two middle cylinders (Fig. 4). For a fixed Reynolds number, the mass transfer distributions on the side and leeward surfaces of the neighboring cylinders are not the same (Fig. 6). This is despite an excellent match of the Sherwood numbers on the upstream surfaces and the symmetric distribution around each of the individual cylin-

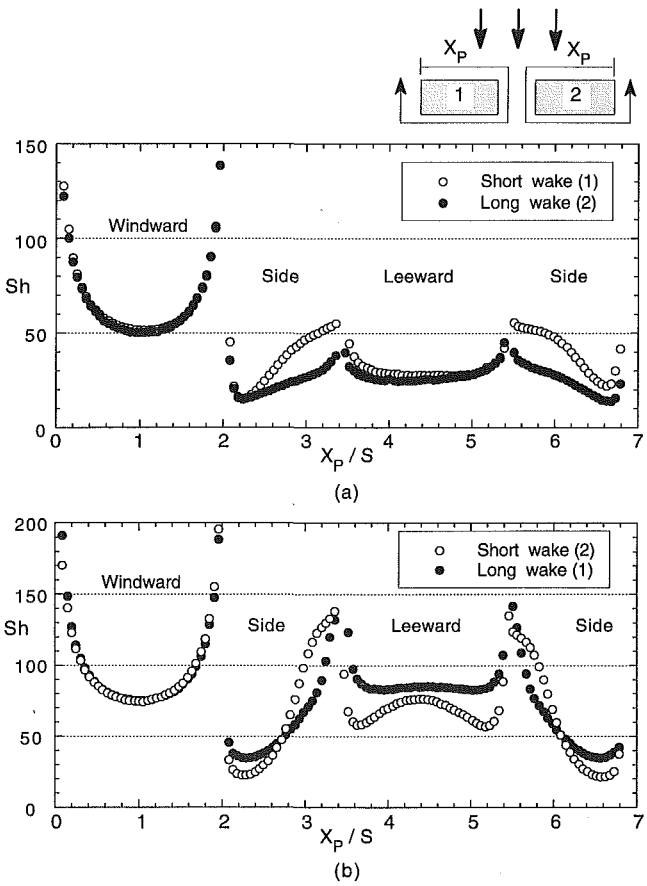

Fig. 6 Local Sh on adjacent cylinders showing asymmetric flow (uncertainty estimate: Sh ± 6.9 percent): (a) Re_s = 1105; (b) Re_s = 2605

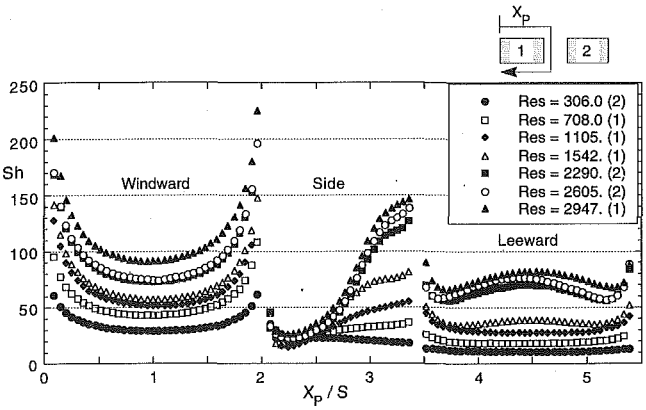

Fig. 7 Local Sh on each surface for a short wake cylinder (uncertainty estimate: Sh ± 6.9 percent)

ders. The dissimilar mass transfer process is attributed to different flow patterns around each of the cylinders. The approaching flow appears to be symmetric on the upstream side of the array rendering symmetric and similar distributions of mass transfer on the windward surface.

Within the slits, separated flow from the front edges of the cylinders tends to shift toward one of the cylinders and reattach on the side surface, while it remains detached from the other. This pattern of flow is evidenced by flow visualization and the slope change in Sh on the side surface (Figs. 6 and 7). The wake behind the present cylinders appears to be affected by the deflected flow and reattachment, but the key influence may be that of the dissimilar wakes, which trigger the deflected flow leaving the slits and change the reattachment inside the slit.

Uniform inlet flow conditions and identical test cylinder pieces can be verified from identical local mass transfer rates on the upstream surfaces of adjacent cylinders (Fig. 6) and straight streaklines in the approach flow (Fig. 2). Hence, it can be assumed that the asymmetric flow downstream is not due to disturbed upstream flow or cylinder nonuniformity.

A jetlike flow coming out from a slit entrains fluid from outside the jet, but the entrainment of the fluid is restricted by the presence of the neighboring jets. Therefore, the jetlike flow tends to bend toward a side of low pressure as a "Coanda" effect. In a tunnel flow start-up, some difference in roundness of edges, or instability of vortex shedding could give a slightly perturbed jetlike flow or pressure difference. Then, the jetlike flow may deflect to the lower pressure side and merge with a similarly deflected neighboring jet, making a short wake with a lower base pressure distribution. A long wake with slightly higher pressure occurs between these two jets. These phenomena produce different size wakes with every other cylinder having a short wake and the adjacent one a long wake. These asymmetric flows with curved streamlines of the slit-jetlike flows, once established, are preserved by the different pressures within the two adjacent wakes.

The smoke-wire flow visualization shows the instantaneous ($\frac{1}{2000}$ second) and time-averaged ($\frac{1}{4}$ second) flow patterns for a range of Reynolds number of Re_s = 700 to 2300 (0.38 m/s $\leq$ $U_\infty \leq$ 1.26 m/s) (Fig. 2). The jetlike flows behave as mentioned above and the asymmetric wake flows stay in a stable manner shown in the time-averaged visualization. The length of the asymmetric wakes behind the cylinders varies with position in the array. The short wake decreases in length from Re_s = 700 to 1100 and then doesn't change up to Re_s = 2300. Its length is 1.2 to 2.0 times the cylinder width, and the long wake is three to five times the cylinder width. Observation of various runs, from flow visualization and mass transfer measurements, indicates that the long and the short wakes can be readily interchanged with a small disturbance. The interchange can occur when air is sucked from the long wake and air is blown into the short wake (which has a lower base pressure), or by temporarily inserting a vane in the upstream flow, but the flow stays stable once it is changed.

Mass transfer from the leeward face of the short wake cylinder is generally lower than on the adjacent, long wake cylinders. This may be due to the short wake with less circulating air essentially trapping a higher concentration of naphthalene vapor within it than does the long wake. At high Reynolds number a peak in the mass transfer appears in the middle on the leeward side of the short wake cylinder (Fig. 6*b*). The peak of mass transfer in the middle of the leeward face on the short wake cylinder can be explained by stronger recirculation flows with a lower base pressure because of higher mass transfer at impingement (middle) and lower mass transfer at detachments (near the edges). The Sherwood number profile on the cylinder with the long wake is flat, but the Sh is higher than on the cylinder with the short wake apparently due to lower naphthalene vapor concentration caused by larger recirculation.

In Figs. 7 and 8, mass transfer from cylinders with short wake and with long wake, respectively, are presented for different Reynolds numbers. The general trend is an increase in mass transfer with increasing Reynolds number. Closer examination indicates that at low Reynolds numbers (less than about 700), there is no appreciable difference in mass transfer from the two cylinders in spite of the asymmetric wake flows shown in the flow visualization, and the flow appears to reattach to both of the cylinders after a short separation. At about Re_s = 1100, a shift in the flow to one side of the slit and its reattachment to one of the cylinders begins to appear. This continues up to Re_s = 3000, the highest Reynolds number used in the present study.

Mass transfer rates on the side surface with reattachment (on the cylinder with short wake) increase quickly near the reattachment point with Reynolds numbers, while the rates inside of the separation eddy (near the inlet region) change only slightly. The separation length (from the separation point, i.e., the corner edge, to the reattachment point, i.e., the Sh slope change point) on the side surface of this short wake cylinder has a constant value of about 1.2*S* above Re_s = 2300 (up to 3000, the highest Reynolds number in the present study) after increasing continuously from Re_s = 300. For $Re_s \geq$ 1100, the Sherwood numbers on the long wake cylinder increase continuously with Re_s along the whole side surface affected by reverse flow from the downstream wake; whereas, for Re_s = 708 to 1105, they decrease slightly since the flow starts to detach from the side wall.

The average Sherwood number on the leeward surface of a long wake cylinder is higher than on its side surface, except at low Reynolds number, due to high turbulent intensity caused by vortex shedding. Cherdron et al. (1978) showed that the intensity of fluctuation energy in wake flows behind a sudden expansion duct, even at low Reynolds number, is higher than in corresponding boundary layer-type turbulent flows. A separated flow is

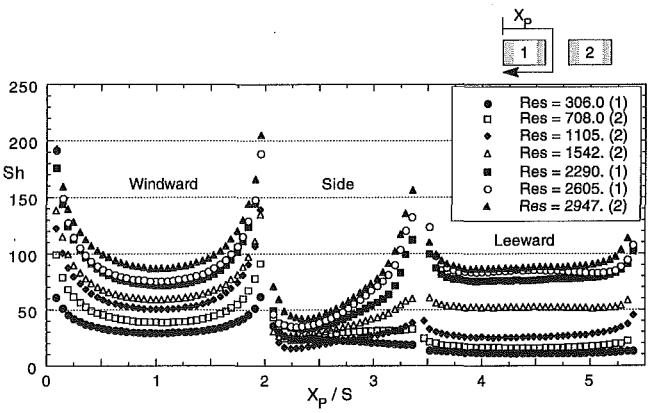

Fig. 8 Local Sh on each surface for a long wake cylinder (uncertainty estimate: Sh ± 6.9 percent)

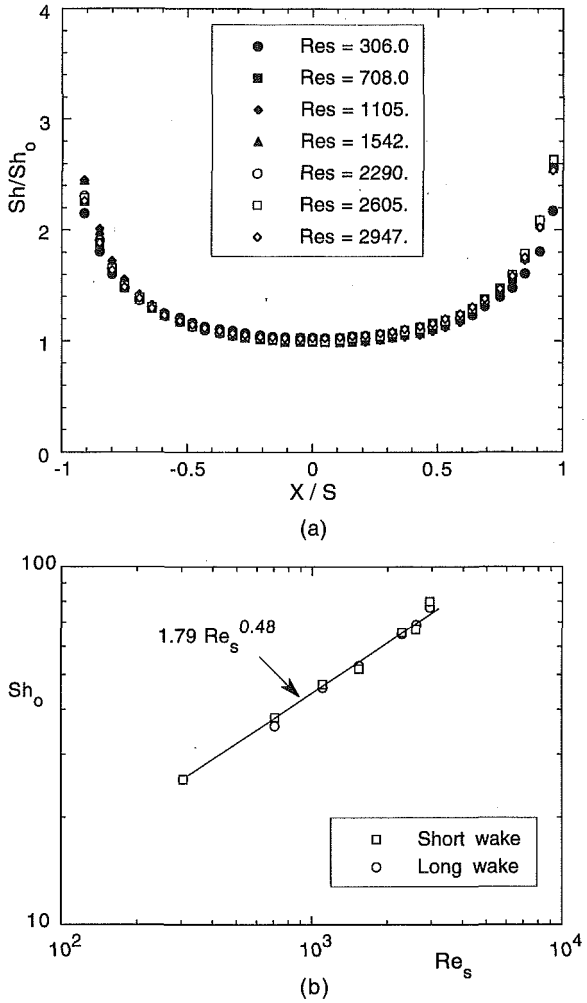

Fig. 9 (a) Normalized Sh on the approaching surface; (b) Sh at stagnation points for both cylinders

much more unstable than a boundary layer flow, so the separated flow could undergo transition quickly to a turbulent flow. It is usually found that the vortex street past a circular cylinder is turbulent above a Reynolds number of 400 based on approaching velocity and diameter (Tritton, 1979). This criterion may hold for flows past other bluff bodies. The streaklines of smoke at a comparable $Re_d \cong 390$, corresponding to $Re_s = 700$, do not disperse, indicating that the flow is laminar (Fig. 2). The vortices for $Re_d \geq 830$ ($Re_s \geq 1500$) appear as turbulent wake flows (Fig. 2).

For any Reynolds number flow, the windward side Sherwood numbers are essentially the same on the short and long wake cylinders. Even though the cylinder centerline on the windward surface is the stagnation line, Sherwood numbers increase from the stagnation line to the sides due to acceleration of the flow and thinning of the boundary layer.

Figure 9(a) shows that the normalized Sherwood number (Sh/Sh_0) is fairly independent of the Reynolds number and is only a function of X/S:

$$\frac{Sh}{Sh_0} = f(X/S) \tag{5a}$$

As shown in Fig. 9(b), the stagnation point Sherwood number (Sh_0) can be correlated with Reynolds number (Re_s) as

$$Sh_0 = 1.79\ Re_s^{0.48} \quad (\text{or } 1.54\ Re_s^{0.5}) \tag{5b}$$

for both long and short wake cylinders. The power of 0.48 in the correlation is similar to a laminar stagnation mass (heat) transfer.

Average Sherwood numbers for each surface are shown in Fig. 10. The correlation curves of the average Sherwood numbers are given by

$$\overline{Sh} = C\ Re_s^n \tag{6}$$

	Short wake		Long wake	
	C	n	C	n
Windward	2.05 (2.00)	0.496 (0.5)	2.04 (1.98)	0.496 (0.5)
Side	1.09	0.521	1.36*	0.474*
Leeward	0.068*	0.873*	0.048	0.949

(* The coefficients do not represent the data very well due to the slope change at $Re_s \cong 1500$.)

The correlations for the windward and side surfaces have the power of about 0.5, which often occurs with laminar flow. The visualization indicates laminar flow patterns for the approaching and inside flows. The local Sherwood numbers on the leeward surface indicate that the transition point is near $Re_s = 1100$ where the Sherwood numbers start increasing quickly and fuzzy streaklines appear in the wakes.

On the windward surface, the average Sherwood number is almost the same for the short and the long wakes, as mentioned in the comparison of local Sherwood numbers. On the side surface, the average Sherwood number with a short wake is higher than that with a long wake, especially in the transition region (for $Re_s \sim 1500$, about 30 percent higher), because the stream reat-

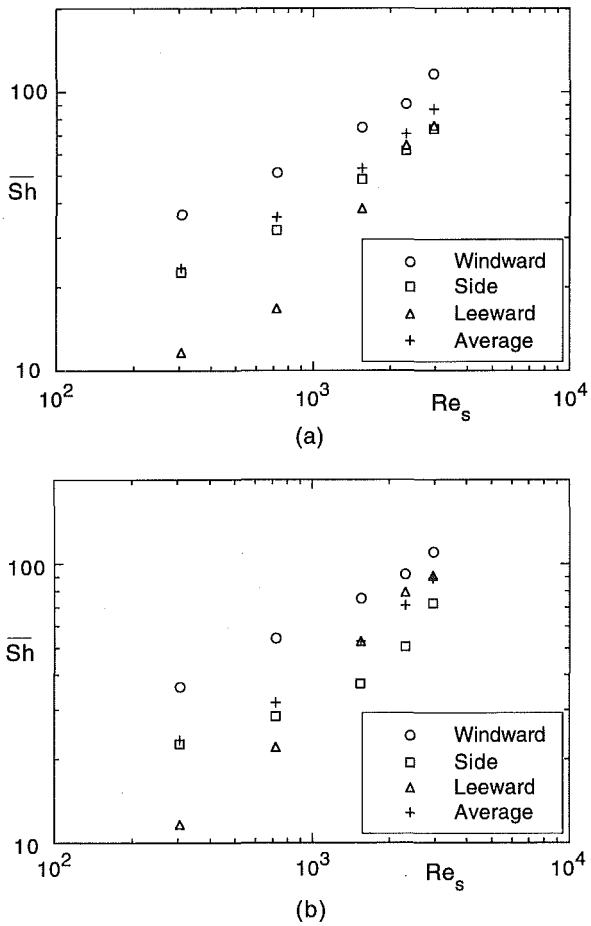

Fig. 10 Average Sherwood number on each surface (uncertainty estimate: $\overline{Sh} \pm 6.9$ percent): (a) short; (b) long wake cylinders

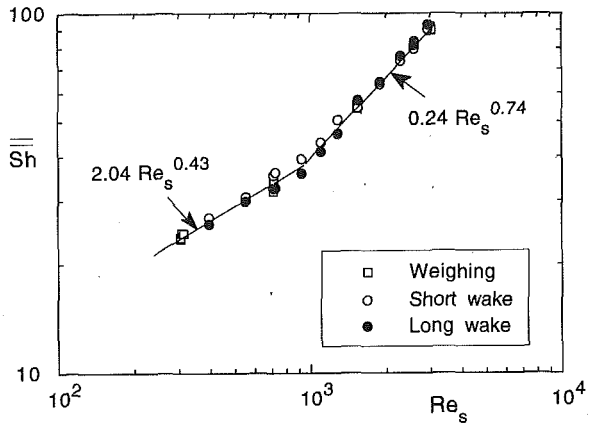

Fig. 11 Overall average Sherwood numbers on both cylinders (uncertainty estimate: $\overline{\overline{Sh}}$ ± 6.9 percent)

taches only on the side wall of the short wake cylinder and reattachment results in high Sh. However, the average Sherwood number with the long wake is about 30 percent higher than that with the short wake on the leeward surface over the whole Reynolds number range.

For the short wake cylinder, the upstream-facing (windward) surface has higher mass transfer than the other two surfaces for all Reynolds numbers (Fig. 10*a*). The average Sherwood number on the leeward surface is very low at the lower Reynolds numbers, but increases rapidly with Reynolds number due to the vortex shedding, high turbulence, and impingement. The trend of the average Sherwood numbers is similar on the long wake cylinder; a difference is a change in slope on the side surface, which may be caused by a different size separation region inside the slit and different turbulent intensity, due to reverse flow from the downstream wake, at different Reynolds numbers.

Figure 11 shows overall average Sherwood numbers, which are obtained from numerical integration (data extrapolated to the corner edges of the cylinder) of local Sherwood number measurements and the overall average values obtained from the weighing measurements (results are within a ±3 percent deviation on repeated trials). The overall average values of Sh for the short wake and long wake cylinders have a break in slope at around $Re_s = 1000$. A transition seems to occur, but the values on the two cylinders are almost the same at lower and higher Reynolds numbers. The overall average Sherwood numbers of the cylinders are not very different. A correlation curve is $\overline{\overline{Sh}} = 0.67\ Re_s^{0.6}$ in the whole domain, but it is better to correlate the results by dividing the domain into two regions of Reynolds number:

$$\overline{\overline{Sh}} = 2.04\ Re_s^{0.43} \quad \text{for} \quad 300 \le Re_s < 1000 \tag{7}$$

$$\overline{\overline{Sh}} = 0.24\ Re_s^{0.74} \quad \text{for} \quad 1000 \le Re_s \le 3000 \tag{8}$$

The present results are compared with the heat transfer results, $\overline{\overline{Nu}}_w = 0.14\ Re_w^{0.66}$, of Igarashi (1985), which were obtained from local measurement on a single square cylinder in a free stream with a constant heat flux boundary condition in the Reynolds number range of 5.6×10^3 to 5.6×10^4. The present correlation curve at the higher Reynolds number is steeper than that of Igarashi. If the two equations are compared via the heat and mass transfer analogy, $Sh/Nu \sim (Sc/Pr)^{0.4}$, and at the same dimension (effective diameter), the converted equations are given by

$$\overline{\overline{Sh}}_d = 0.206\ Re_d^{0.74} \quad \text{(present)} \tag{9}$$

$$\overline{\overline{Sh}}_d = 0.225\ Re_d^{0.66} \quad \text{(Igarashi)} \tag{10}$$

The transfer rates at the present geometry are higher by approximately 70 percent than for the single square cylinder around $Re_d = 2000$.

Concluding Remarks

Asymmetry occurs in the flow through an array of symmetric rectangular cylinders for a spacing of $S/W = 0.5$ used in the present study. This is observable from flow visualization and from local measurements of mass transfer on the cylinder surfaces using a naphthalene sublimation technique.

The local mass transfer rates from the neighboring cylinders are different due to the asymmetric flows around the cylinders. However, the overall mass transfer around the whole periphery of the two (long wake and short wake) cylinders are similar because the cylinder with short wake has higher mass transfer on the side surfaces due to reattachment (while the other cylinder with larger wake has no reattachment on the side wall), but lower on the leeward surface.

Acknowledgments

Support from the Air Force Office of Scientific Research and through the Engineering Research Program of the Department of Energy aided greatly in the conduct of this study.

References

Abbott, D. E., and Kline, S. J., 1962, "Experimental Investigation of Subsonic Turbulent Flow Over Single and Double Backward Facing Steps," *ASME Journal of Basic Engineering*, Vol. 84, pp. 317–325.

Ambrose, D., Lawrenson, I. J., and Sparke, C. H. S., 1975, "The Vapor Pressure of Naphthalene," *J. Chem. Thermodynam.*, Vol. 7, pp. 1173–1176.

Arie, M., and Rouse, H., 1956, "Experiments on Two-Dimensional Flow Over a Normal Wall," *J. Fluid Mech.*, Vol. 1, pp. 129–141.

Chen, P. H., and Wung, P. H., 1990, "Diffusion Coefficient of Naphthalene in Air at Room Temperature," private communication.

Cherdron, F., Durst, F., and Whitelaw, J. H., 1978, "Asymmetric Flows and Instabilities in Symmetric Ducts With Sudden Expansions," *J. Fluid Mech.*, Vol. 84, pp. 13–31.

Cho, H. H., 1992, "Heat/Mass Transfer Flow Through an Array of Holes and Slits," Ph.D. thesis, University of Minnesota, Minneapolis.

Cho, K., 1989, "Measurement of the Diffusion Coefficient of Naphthalene Into Air," Ph.D. thesis, State University of New York at Stony Brook.

Durst, F., Melling, A., and Whitelaw, J. H., 1974, "Low Reynolds Number Flow Over a Plane Symmetric Sudden Expansion," *J. Fluid Mech.*, Vol. 64, pp. 111–128.

Filetti, E. G., and Kays, W. M., 1967, "Heat Transfer in Separated, Reattached, and Redevelopment Regions Behind a Double Step at Entrance to a Flat Duct," ASME JOURNAL OF HEAT TRANSFER, Vol. 89, pp. 163–168.

Gerhardt, H. J., and Kramer, C., 1981, "Interference Effects for Groups of Stacks," *J. Wind Eng. Ind. Aero.*, Vol. 8, pp. 195–202.

Goldstein, R. J., Chyu, M. K., and Hain, R. C., 1985, "Measurement of Local Mass Transfer on a Surface in the Region of the Base of a Protruding Cylinder With a Computer Controlled Data Acquisition System," *Int. J. Heat Mass Transfer*, Vol. 28, pp. 977–985.

Goldstein, R. J., and Cho, H. H., 1993, "A Review of Mass (Heat) Transfer Measurements Using Naphthalene Sublimation," *Proceedings, 3rd World Conference on Experimental Heat Transfer, Fluid Mechanics and Thermodynamics*, Honolulu, HI, Vol. 1, pp. 21–40.

Hayashi, M., Sakurai, A., and Ohya, Y., 1986, "Wake Interference of a Row of Normal Flat Plates Arranged Side by Side in a Uniform Flow," *J. Fluid Mech.*, Vol. 164, pp. 1–25.

Igarashi, T., 1985, "Heat Transfer From a Square Prism to an Air Stream," *Int. J. Heat Mass Transfer*, Vol. 28, pp. 175–181.

Ingham, D. B., Tang, T., and Morton, B. R., 1990, "Steady Two-Dimensional Flow Through a Row of Normal Flat Plates," *J. Fluid Mech.*, Vol. 210, pp. 281–302.

Kline, S. J., and McClintock, F. A., 1953, "Describing Uncertainty in Single-Sample Experiments," *Mechanical Engineering*, Vol. 75, Jan., pp. 3–8.

Lichtarowicz, A., Duggins, R. K., and Markland, E., 1965, "Discharge Coefficients for Incompressible Non-cavitating Flow Through Long Orifices," *J. Mech. Eng. Science*, Vol. 7, pp. 210–219.

Milos, F. S., Acrivos, A., and Kim, J., 1987, "Steady Flow Past Sudden Expansions at Large Reynolds Number. II. Navier–Stokes Solutions for the Cascade Expansion," *Phys. Fluids*, Vol. 30, pp. 7–18.

Quadflieg, H., 1977, "Wirbelinduzierte belastungen eines zylinderpaares in inkompressibler stromung bei grosen Reynoldszahlen," *Forsch. Ing.-Wes.*, Vol. 43, pp. 9–18.

Spivack, H. M., 1946, "Vortex Frequency and Flow Pattern in the Wake of Two Parallel Cylinders at Varied Spacing Normal to an Air Stream," *J. Aero. Sci.*, Vol. 13, pp. 289–301.

Tritton, D. J., 1979, *Physical Fluid Dynamics*, Van Nostrand Reinhold Co. Ltd., London, United Kingdom, p. 26.

Williamson, C. H. K., 1985, "Evolution of a Single Wake Behind a Pair of Bluff Bodies," *J. Fluid Mech.*, Vol. 159, pp. 1–18.

Augmented Heat Transfer in a Rectangular Channel With Permeable Ribs Mounted on the Wall

Jenn-Jiang Hwang
Associate Professor.
Department of Mechanical Engineering,
Chung-Hua Polytechnic Institute,
Hsinchu, Taiwan 30067

Tong-Miin Liou
Professor.
Department of Power Mechanical Engineering,
National Tsing-Hua University,
Hsinchu, Taiwan 30043

Turbulent heat transfer and friction in a rectangular channel with perforated ribs arranged on one of the principal walls are investigated experimentally. The effects of rib open-area ratio, rib pitch-to-height ratio, rib height-to-channel hydraulic diameter ratio, and flow Reynolds number are examined. To facilitate comparison, measurements for conventional solid-type ribs are also conducted. Laser holographic interferometry is employed to determine the rib permeability and measure the heat transfer coefficients of the ribbed wall. Results show that ribs with appropriately high open-area ratio at high Reynolds number range are permeable, and the critical Reynolds number of initiation of flow permeability decreases with increasing rib open-area ratio. By examining the local heat transfer coefficient distributions, it is found that permeable ribbed geometry has an advantage of obviating the possibility of hot spots. In addition, the permeable ribbed geometry provides a higher thermal performance than the solid-type ribbed one, and the best thermal performance occurs when the rib open-area ratio is 0.44. Compact heat transfer and friction correlations are also developed for channels with permeable ribs.

Introduction

Forced convection from surfaces with large-scale roughness is encountered in many technological applications such as heat exchangers, advanced gas-cooled reactor fuel elements, and electric cooling devices. The flow passages or surfaces of these devices are usually roughened by solid-type ribs in a periodic manner along the flow direction. Generally, the increased heat transfer coefficient is accompanied by an increase in friction factor. Thus, engineers or designers have been trying to optimize the rib geometry to yield a best heat transfer coefficient for either a given coolant flow rate or an available pressure drop. The present investigation is concerned with an improved rib geometry, i.e., permeable ribs, for application to the turbulent flow in a rectangular duct.

There are numerous publications in which the effectiveness of the aforementioned augmentation was investigated. The relevant works about turbulent duct flows with solid-type ribs are briefly reviewed below. Burggraf (1970) reported the results of turbulent airflow in a square duct ($A/B = 1$) with transverse solid-type ribs ($\alpha = 90$ deg, $\beta = 0$) on two opposite walls for Reynolds numbers ranging from 13,000 to 130,000. The wall temperature distributions were measured by thermocouples. With a hydrodynamically fully developed condition at the heated duct entrance, the average Nusselt number of the ribbed side wall and the friction factor were approximately 2.38 times and 8.6 times the corresponding values for fully developed smooth duct flows, respectively. The average Nusselt number of the smooth side wall was 19 percent greater than for the duct with four smooth walls. Similar trends were obtained for three channel entrance geometries (long duct, short duct, and bent entrance). Han (1988) investigated the effect of the channel aspect ratios ($A/B = 1/4, 1/2, 1, 2, 4$) on the distributions of local heat transfer coefficients in channels with two opposite ribbed walls. Both the local and average Nusselt numbers were measured by the thermocouple technique and resistance (stainless steel foil) heating method. The results were obtained for the solid-type rib with an angle-of-attack of 90 deg. It was found that the increased ribbed-side-wall heat transfer in a smaller aspect ratio channel was higher than that in a large aspect ratio channel for a constant pumping power; however, the increased average heat transfer was slightly lower. Lockett and Collins (1990) conducted the double-exposure holographic interferometry measurement in a fully developed channel flow with square and rounded rib roughness on one wall. The ribs were solid. One rib spacing ($PR = 7.2$) and one rib height ($H/2B = 0.106$) were tested in their work. It was found that the heat transfer distribution was dependent on Reynolds number for the rounded rib, but independent for the square rib. Lau et al. (1991) performed an experimental work to study the effects of replacing the aligned 90 deg full ribs on two opposite walls of a square channel with angled discrete ribs (five equal segments of the angled full ribs staggered in alternate rows of three and two ribs) on turbulent heat transfer and friction for fully developed airflow. The temperature distributions were measured by thermocouples. Results showed that parallel 60 deg discrete ribs had the highest ribbed wall heat transfer, parallel 30 deg discrete ribs caused the lowest pressure drop, and crossed arrays of angled ribs had poor thermal performance and were not recommended. Liou and Hwang (1993) experimentally studied the effect of the rib shapes on the heat transfer and friction characteristics in periodic fully developed duct flows. Three rib shapes (square, triangular, and semicircular) with the same rib height ($H/De = 0.081$) were investigated in their work. The local as well as the average Nusselt numbers were determined by a real-time laser holographic interferometry (LHI). It was found that the three shaped ribs had comparable thermal performances under constant pumping power constraint. Note that in both Liou and Hwang (1993) and Lockett and Collins (1990), hot spots were found to exist behind the solid-type ribs for periodic fully developed conditions.

All the above-mentioned studies were performed in channels

Contributed by the Heat Transfer Division for publication in the JOURNAL OF HEAT TRANSFER. Manuscript received by the Heat Transfer Division March 1993; revision received August 1993. Keywords: Augmentation and Enhancement, Forced Convection, Heat Exchangers. Associate Technical Editor: W. A. Fiveland.

with solid-type ribs. For works of turbulent flows around perforated baffles in a straight plate/channel, Tanasawa et al. (1983) employed the resistance heating method and thermocouple technique to determine the heat transfer coefficients in a channel with turbulence promoters mounted on two opposite walls. Three types of turbulence promoter, namely, fence-type, perforated plate-type, and slitted plate-type, were tested in their work. Results showed that surfaces with perforated plate-type turbulence promoters gave excellent performance under constant pumping power conditions. Ichimiya et al. (1991) experimentally investigated the effect of a single porous-type roughness on the heat transfer and friction characteristics in a parallel plate duct. The porous-type roughness was applied to the insulated wall facing the heated smooth surface. Results showed that the thermal performance under the constant pumping power constraint is better in the laminar region than in the turbulent region. Recently, Yamada and Osaka (1992) conducted experiments to study the effects of the aspect ratio and the open-area ratio of the plate on the heat transfer characteristics of the flow over a perforated plate standing on the wall. Only one flow velocity (U = 5 m/s) was tested in their work. An important finding they made was that the critical open-area ratio in which there was a circulation region behind the plate was between 0.325 and 0.485.

The present work focuses on the heat transfer enhancement in a channel containing perforated ribs. The perforated ribs are mounted on one of the principal walls of the channel and are placed periodically and transversely to the streamwise direction. The experimental techniques employed in this work are laser holographic interferometry and Pitot tube probing. As for laser holographic interferometry, two categories of results are presented, namely, finite-fringe interference for qualitative determination of the rib permeability and infinite-fringe interference for quantitative measurements of the local heat transfer coefficients. Although prior studies have proposed that perforated ribs will provide superior heat transfer per unit pumping power, no data have been reported systematically concerning the combined effects of rib open-area ratio, rib height, rib spacing, and flow Reynolds number on the heat transfer and friction characteristics for channels with periodic perforated ribs mounted on one wall. Moreover, information about local heat transfer coefficient distributions along the perforated ribbed wall is important but relatively sparse in the open literature. The parameters investigated in this work are rib open-area ratio, β = 0, 10, 22, 38, 44, and 50 percent; rib pitch-to-height ratio, PR = 5 and 10; rib height-to-channel hydraulic diameter ratio, H/De = 0.081 and 0.162; and Reynolds number, 10,000 < Re < 50,000. The research reported here is carried out to fulfill four objectives:

1 *Determine the permeability of perforated ribs.* By using finite-fringe interferometry, the permeability of the perforated rib is examined and a permeability limit is proposed. Permeability limit is a criterion for the change of flow patterns, which strongly affect friction and heat transfer characteristics of the ribbed channel. Such a study has not been done in the past.

2 *Assess the possibility of hot spots on the perforated ribbed wall.* According to previous measurements of the detailed local heat transfer coefficient distributions (Lockett and Collins, 1990; Liou and Hwang, 1992a, 1992b, 1993), a serious disadvantage is accompanied by the duct with solid-type ribs: Hot spots ($\mathrm{Nu}/\overline{\mathrm{Nu}}_s < 1$) exist in the recirculating region behind the solid-type rib because the flow in this region is nearly stagnant relative to the main stream. It is important to search for a more efficient rib configuration for improving heat transfer in the recirculating region. Since the airflow passes partly through the perforated rib and directly impinges the recirculating cell behind the rib, it is interesting whether the channel with perforated ribs has the advantage of obviating the possibility of hot spots.

3 *Quantify thermal performances of perforated ribbed ducts.* In a ribbed duct, the increase in heat transfer rate is always accompanied by an increase in pressure loss. The practical advantage of using such a ribbed surface would be reduced if the increase in pumping power exceeds the gain in enhanced heat transfer. Thus, it is necessary and appropriate to analyze the thermal performance of the perforated ribbed ducts with respect to corresponding smooth-walled ducts under constant pumping constraint, this can provide conclusions about the effectiveness of the perforated ribs as an enhancement technique. First, experiments are undertaken to examine the effects of rib and flow parameters on average heat transfer coefficients and friction factors. Then, analyses of thermal performance are conducted by employing the average heat transfer and friction data. Finally, the optimal rib and flow parameters that yield the best performance are identified.

Nomenclature

A = half-width of channel
A_{rib} = heat transfer area of the rib
A_t = total heat transfer area in one rib pitch
B = half-height of channel
c_p = specific heat at constant pressure
De = hydraulic diameter
H = rib height
h = heat transfer coefficient
k_f = air thermal conductivity
L_h = wetted length in one pitch
m = mass flow rate
Nu = local Nusselt number
$\overline{\mathrm{Nu}}_p$ = periodic fully developed (average) Nusselt number for the ribbed duct
$\overline{\mathrm{Nu}}_s$ = average Nusselt number for the smooth duct (at the same mass flow rate)
$\overline{\mathrm{Nu}}_s^*$ = average Nusselt number for the smooth duct (at the same pumping power)
Pi = rib pitch
PR = rib pitch-to-height ratio = Pi/H
Pr = Prandtl number
Q_{rib} = rib heat transfer
Q_t = total heat transfer in one rib pitch
q_{conv} = convective heat transfer flux from the wall = Q_t/A_t
Re = Reynolds number = $U \cdot De/\nu$
Re_δ = Reynolds number based on the boundary layer thickness = $U \cdot \delta/\nu$
T = temperature of air
T_b = local bulk mean temperature of air
T_{in} = air temperature at duct inlet (i.e., room temperature)
T_w = local wall temperature
$\overline{T}_b$ = average bulk mean temperature of air = $\left(\int_0^{Lh} T_b dX\right)/L_h$
$\overline{T}_w$ = average wall temperature
U = mean velocity
W = rib width
X_h = axial coordinate (X_h = 0 at inlet reference, Fig. 2)
X_N = axial coordinate (X_N = 0 at rib real edge, Fig. 2)
Y = transverse coordinate, Fig. 2
Z = spanwise coordinate, Fig. 2
α = rib angle-of-attack
β = open-area ratio of the perforated rib
δ = boundary layer thickness
ρ = air density
ϕ = radius of the hole distributed over the perforated rib

Subscripts

b = bulk mean
N = rib index
s = smooth
w = wall

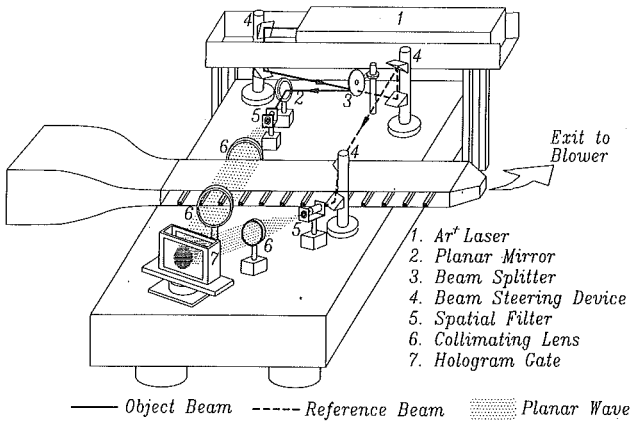

Fig. 1 Schematic drawing of flow system and experimental apparatus

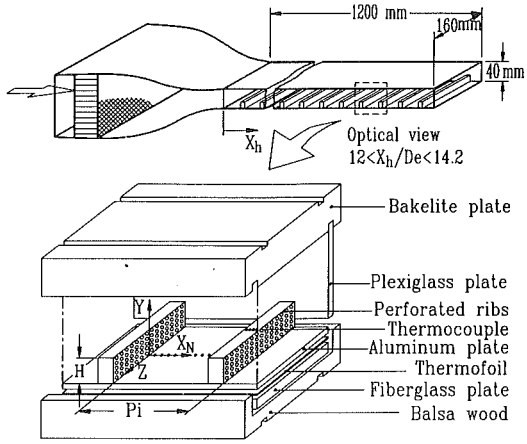

Fig. 2 Sketch of configuration, coordinate system, and dimensions of the test section

4 *Develop heat transfer and friction correlations.* Semi-empirical correlations of fully developed heat transfer and friction are developed for channels with perforated ribs. Such correlations have not been proposed in the past, and may be helpful for the design of related devices such as compact heat exchangers and electronic cooling systems.

Experimental Program and Conditions

Instrumentation. In this work, a real-time holographic interferometer is employed to measure the temperature distribution of airflow in the ribbed duct. The overall arrangement of the holographic interferometer is illustrated in detail in Fig. 1. The laser used is a high-power, argon-ion laser (1), Spectra-Physic Model 2000. After passing through a shutter, the laser beam is divided into two equal components by a variable-silvered mirror (i.e., a beam splitter, 3). One beam, the reference beam, bypasses the test section and is expanded and filtered by a spatial filter (5). The expanded wave is subsequently collimated to a planar wave by a collimating lens (6). The other beam, the object beam, is also expanded, filtered, and collimated to a planar wave by a spatial filter and a collimating lens. Both the planar waves fall onto the holographic plate (7) with an angle of 30 deg. Before the ribbed walls are heated, the hologram is exposed so that the comparison wave is recorded. When the planar object wave passes through the heated test section, it is distorted as a result of the refractive index field generated by local temperature variation in the test section. The distorted object wave passes through the hologram where it interferes continuously with the comparison beam reconstructed by the reference wave. Thus, an instantaneous interference field forms behind the hologram plate. A combination of the holographic film plate holder and a liquid gate is used to provide in-place development of the film plate as required for subsequent real-time work. The photographic emulsion 8E56 made by Agfa-Gevaert Ltd. is found to be a suitable recording material for a good compromise between light sensitivity and resolution. To adjust the unwanted interference fringes caused by a shrinkage of the photographic emulsion in the developed and fixed processes, the liquid gate associated with the film plate holder is mounted on multi-axis micropositioning base. This arrangement is designed to provide constriction-free submicron positioning of the hologram in linear (three orthogonal axes) and rotational (θ) directions. The instantaneous interference field is digitized by a CCD camera (COHU, Model 6400), which allows 512 by 512 pixel resolution with 256 grey levels per pixel and recorded on a VHS videocassette recorder for storage and further image processing.

While the flow field temperature is measured by LHI, the wall temperature of the test section is measured by copper-constantan thermocouples (i.e., T-type). The junction bead of the thermocouple is about 0.15 mm in diameter. The temperature signals are transferred to a hybrid recorder (Yokogawa, DA-2500) with 30 channels. All the data are then sent to a PC-AT via GPIB interface. The preprocessing of the raw data can be carried out by use of a built-in BASIC program by which the nondimensional parameter can be calculated. The static pressure at the test section is measured by a microdifferential transducer (Kyowa) connected to pressure taps. The measured pressure signals are subsequently amplified by an amplifier (Kyowa WGA-200A) and read from a digital readout.

Test Section. The open-loop air flow circuit, as shown in Fig. 1, is operated in the suction mode and oriented horizontally. The air flow is drawn into the test section from a temperature-controlled laboratory by a centrifugal blower, which is located in a service corridor outside the laboratory to minimize vibration. The test duct, as shown in Fig. 2, is 1200 mm long and has a rectangular cross section of 160 mm by 40 mm (YZ plane). The coordinate system, construction, and dimension of the test duct are also sketched in Fig. 2. The perforated ribs are attached to the bottom wall (aluminum plates, 3 mm in thickness) of the test duct by a thin layer of thermal glue. The rib angle-of-attack is 90 deg. Aluminum plates and ribs are adopted in this work for their high conductivity and machinability. Thermofoils of thickness 0.18 mm are attached uniformly between the aluminum plate and a 6-mm-thick fiberglass board to insure good contact. In addition, a piece of balsa wood (20 mm in thickness) is used to minimize the heat loss from the back side of the heated plate. The thermal resistance of the glue (0.13 mm thick or less) used at each of the above-mentioned interfaces is negligible (less than 2 percent). For wall temperature measurements, as shown in Fig. 2, the region of optical view is instrumented with 28 thermocouples distributed along the spanwise centerline ($Z = 0$) of the heated plate and ribs. Two pressure taps situated at $X_h/De = 9$ and 16 are used to measure the static pressure drop for the fully developed duct flows. The pressure drop of the present work is based on adiabatic conditions (without heating).

The perforated ribs investigated are 160 mm in length and 5.2 mm in width (or thickness, i.e., W), and have two different heights of 5.2 mm and 10.4 mm, respectively, for $H/De = 0.081$ and 0.162. A photograph of the typical perforated ribs for different rib open-area ratios with a fixed rib height ($H/De = 0.081$) is shown in Fig. 3. The rib open-area ratio (β) is defined as

$$\beta = (n\pi\phi^2)/(2A\ H) \quad (1)$$

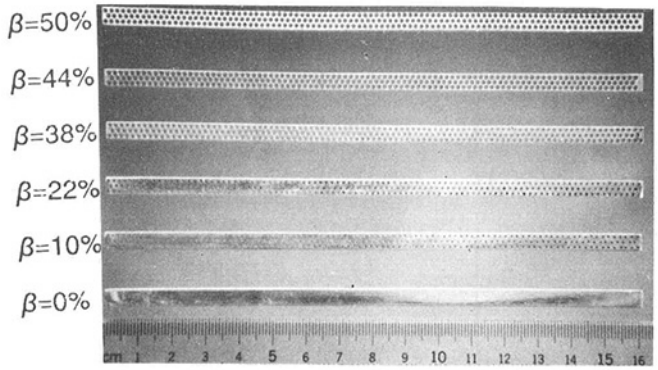

Fig. 3 Photograph of various perforated ribs (H/De = 0.081)

where n is the number of perforations drilled through the rib, ϕ, the perforation radius, A, the half-width of the channel (i.e., half-length of the perforated rib), and H, the rib height. In this work, the rib open area ratios investigated are 0, 10, 22, 38, 44, and 50 percent. Besides the rib open-area ratio, the parameters investigated include the rib pitch-to-height ratios, 5 and 10; the Reynolds number (based on the duct hydraulic diameter and bulk mean velocity), from 10,000 to 50,000; and the rib-to-channel height ratio (or the ratio of the rib height-to-channel hydraulic diameter), 0.13 and 0.26 (0.081 and 0.162).

Experimental Conditions. The two dimensionality of the actual temperature field, and the thermal boundary conditions of the test section have been described in detail by Liou and Hwang (1992b), and will not be elaborated on in this paper.

Data Analysis. In this study, the entire temperature field is revealed by the infinite-fringe interferometry, and subsequently enables the calculations of local and average heat transfer coefficients of the heated surface (Hauf and Grigull, 1970). The significant errors of the interferometry usually encountered are the end effect and the refraction effect errors. By using the interferometry error analysis suggested by Goldstein (1976), it is found that the resulting errors in the fringe shift due to the end and refraction effects are about 8 percent and 4.2 percent, respectively. The convection heat transfer coefficient of the heated wall can be presented in terms of the local Nusselt number Nu, which is defined as

$$\mathrm{Nu} = h\ De/k_f = -(dT/dY)_w De/(T_w - T_b) \tag{2}$$

where $(dT/dY)_w$ is determined by a second-order curve fitting, based on a least-squares method through the near-wall values for temperature and fringe shift (Liou and Hwang, 1993); T_w is read from the thermocouple output; and T_b is calculated from an energy balance, $T_b = T_{in} + Q/(m \cdot c_p)$, where Q is the quantity of heat given to air from entrance to the considered cross section of the duct and can be obtained by the integrated form of $\int_0^X [k_f \cdot (dT/dY)_w \cdot 2A] \cdot dX$. The maximum uncertainties of the local temperature gradient and Nusselt number are estimated to be less than 5.2 and 6.5 percent, respectively, by the uncertainty estimation method of Kline and McClintock (1953). The average Nusselt number for the periodically fully developed region is evaluated by the following equation (Liou and Hwang, 1992a):

$$\overline{\mathrm{Nu}}_p = q_{\mathrm{conv}} De/[k_f(\overline{T}_w - \overline{T}_b)] = (q - q_{\mathrm{loss}}) De/[k_f(\overline{T}_w - \overline{T}_b)] \tag{3}$$

where q_{conv} is the convective heat flux from the wall and is estimated by subtracting the heat loss (q_{loss}) from the supplied electrical input (q), $\overline{T}_w$ is the average wall temperature in one rib pitch, and $\overline{T}_b$ is the average bulk mean temperature of air. The maximum uncertainty of $\overline{\mathrm{Nu}}_p$ is estimated to be less than 9.8 percent. The local and average Nusselt numbers of the present study are normalized by the Nusselt number for fully developed turbulent flow in smooth circular tubes correlated by Dittus-Boelter as:

$$\mathrm{Nu}/\overline{\mathrm{Nu}}_s = \mathrm{Nu}/(0.023\ \mathrm{Re}^{0.8}\mathrm{Pr}^{0.4}) \tag{4}$$

The following equation is used to calculate the friction factor of the periodically fully developed flow:

$$f = [(-\Delta P/\Delta X) De]/(\rho U^2/2) \tag{5}$$

In this expression, $\Delta P/\Delta X$ is an axial pressure gradient, which is evaluated by taking the ratio of the pressure difference and the distance of two successive pressure taps. The maximum uncertainty of f is estimated to be less than 7.3 percent.

Results and Discussion

Interference Patterns. Typical examples of the interferograms taken from the temperature fields of the solid-type and perforated ribbed geometries are shown in Figs. 4(a)-(d). The mean flow direction is from left to right. The comparison of the disturbed finite-fringe interferograms for the solid-type and perforated ribs is made in Figs. 4(a) and 4(b) at Re = 20,000. As for the characteristics of finite-fringe interference, if there are no disturbances in the flow field, parallel, equally spaced, and alternately bright and dark fringes will appear on the interferogram. When a disturbance occurs in the test section, the optical path will no longer be uniform, and consequently the fringes will no longer be straight, but curved. For the solid-type rib (β = 0) in Fig. 4(a), there is no fluid passing through the rib, and the flow has to turn from the duct wall into the contraction between the rib and the opposite duct wall. It can be observed that the fringes are highly distorted in the regions of the flow over and behind the rib top. This indicates that the flow introduces a strong shear layer from the rib top, which drives the recirculating flow behind the rib. For β = 44 percent, as shown in Fig. 4(b), the rib is permeable. The saw-shaped fringes are found behind the rib, which reveals that a part of the fluid passes through the rib and the separation bubble behind the rib is thus broken up. In addition, the distorted region on the top of the permeable rib becomes thinner than that on the solid-type rib, which indicates that the low convective heat transfer from the rib-top surface is accompanied with the permeable rib. The reason is that for the permeable rib a large amount of the heat conducted from the rib base has been convected by the fluid that passes through the rib, hence a reduction of heat transfer rate on the rib top. This is reflected by the lower local Nusselt number distribution, and will be shown later. Figures 4(c) and 4(d) are the typical isotherm-pattern interferograms (infinite-fringe set) for the rib geometry. From the information of the whole-field air temperature distributions given by the interferograms (infinite fringe set), the local heat transfer coefficient of the perforated-ribbed walls can be calculated.

Rib Permeability. According to the flow visualization results observed from finite-fringe interferences, the permeability limit of the perforated rib may be plotted as a function of Reynolds number and rib open-area ratio, as shown in Fig. 5. The half-solid symbols are the actual values obtained from the experiment, and the bounds represent the experimental errors caused by the unsteady or intermittent appearance of the separation bubble (or saw-shaped fringes). The curve passing through these symbols is a curve-fitting result. The permeability limit is a criterion for the change of flow patterns. When ribs are permeable (above the curve), the flow pattern of the multi-mixing-layers appears behind the rib and is caused by the multi-jets emitting from the rear face of the rib. For data lying below the curve, the ribs are impermeable with typical flow patterns of separation, recirculation, and reattachment. This figure shows that the impermeable zone is found to be

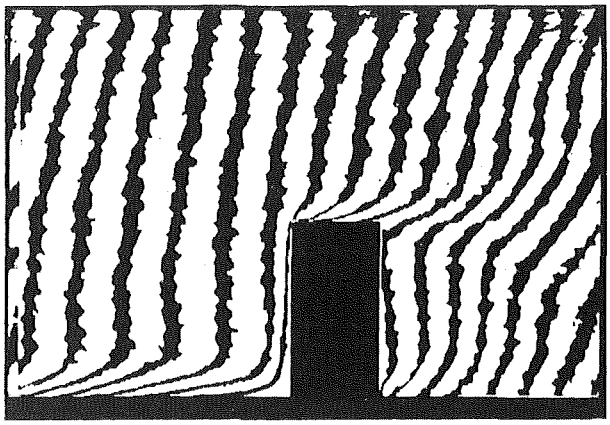

(a)

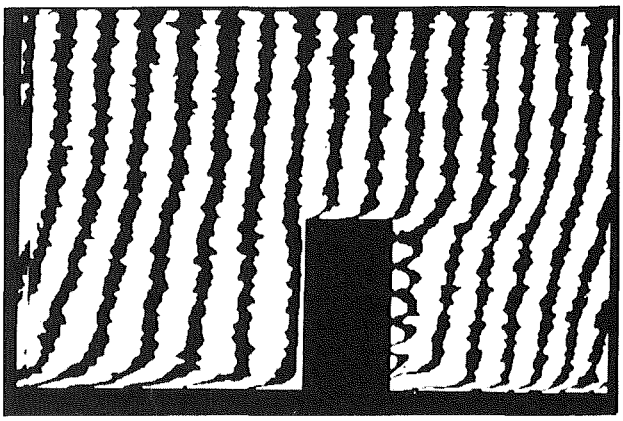

(b)

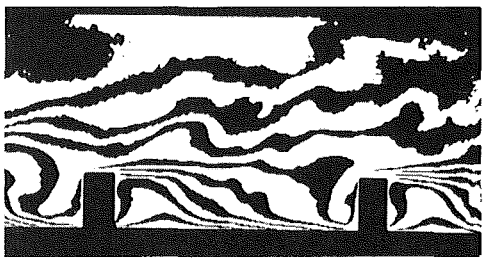

(c)

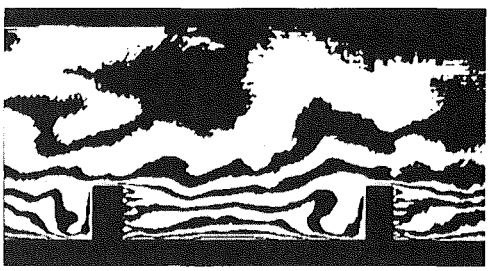

(d)

Fig. 4 Examples of the holographic interferograms for perforated-ribbed duct flows: (*a*) Re = 20,000, *PR* = 5, *H/De* = 0.162, and β = 0 percent (finite fringe, five fold magnification); (*b*) Re = 20,000, *PR* = 5, *H/De* = 0.162, and β = 44 percent (finite fringe, five fold magnification); (*c*) Re = 20,000, *PR* = 5, *H/De* = 0.162, and β = 0 percent (infinite fringe, full-field); (*d*) Re = 20,000, *PR* = 5, *H/De* = 0.162, and β = 44 percent (infinite fringe, full-field)

in the region where the values of the Reynolds number and the rib open-area ratio are lower. The critical Reynolds number for evidence of flow permeability decreases with increasing rib open-area ratio. Note that for the range of the Reynolds number investigated, ribs with β = 10 percent are impermeable. A critical value of β exists between 10 and 22 percent that makes the rib permeable for the range of Reynolds number investigated. The solid and open circular points in Fig. 5 are the results obtained by using the smoke-wire flow visualization technique (Yamada and Osaka, 1992). In the work of Yamada and Osaka (1992), a single perforated rectangular plate was used to stand against a flat wall where the turbulent boundary layer was developing. The Reynolds number (Re_δ) based on the boundary layer thickness was 3150. It was concluded that the critical value of β was between 32.5 and 48.5 percent. Below these values there was a recirculation cell behind the plate. As can be seen in Fig. 5, the results obtained in the previous work are very satisfactory for the solid curve obtained in this work. Note that the permeability limit of the perforated rib is a function of only the rib open-area ratio and flow Reynolds number, but independent of the rib spacing and rib height.

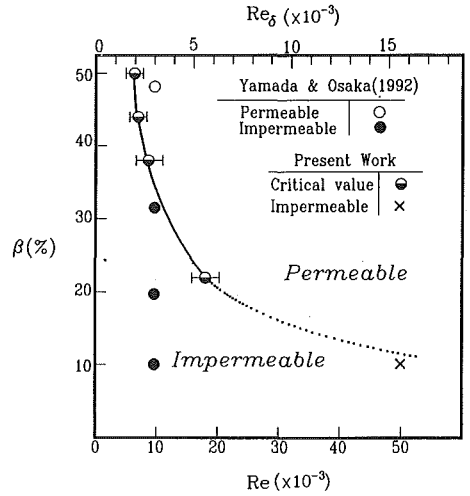

Fig. 5 Dependence of permeability limit as a function of Reynolds number and rib open-area ratio

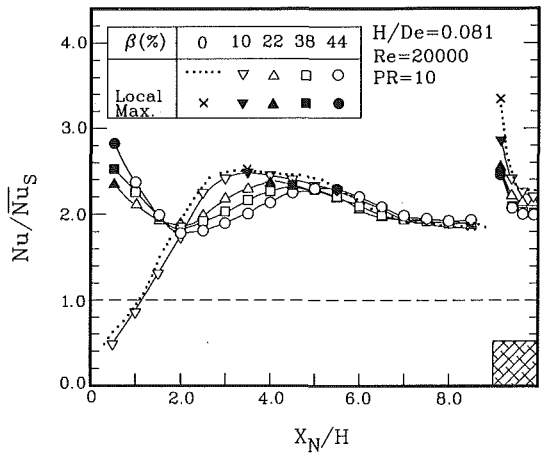

Fig. 6 Local Nusselt number distributions along the perforated ribbed surface

Local Nusselt Number Distribution. The distributions of the local Nusselt number ratio along the ribbed wall for various β (0, 10, 22, 38, and 44 percent) are shown in Fig. 6. The Reynolds number, rib pitch-to-height ratio, and rib height-to-channel hydraulic diameter are fixed at values of 20,000, 10, and 0.081, respectively. As can be observed from this figure, the $Nu/\overline{Nu}_s$ distributions along the duct walls (X_N/H = 0–9) are evidently different between the permeable and solid-

type rib geometries. The results of the duct with solid-type ribs have been described in detail by Liou and Hwang (1992a). For the duct with permeable ribs ($\beta > 22$ percent), there are two peak values of $Nu/\overline{Nu}_s$ within the streamwise distance of two successive ribs. The first local peak value occurs at the duct wall just downstream of the rib and increases with increasing β. Although the level of turbulence intensity is not measured quantitatively in this work, it is believed to be caused by the effect of the intense jet turbulence generated from the rear of the rib as judged by the qualitative observation of the highly fluctuating fringes in this region. The second peak appearing in the middle of the successive ribs is considered to be caused by an approach of the shear layer from the rib top to the duct wall. As β increases, the second peak of $Nu/\overline{Nu}_s$ moves downward because the flow rate through the perforated walls increases with an increase of β. Note that the hot spots ($Nu/\overline{Nu}_s < 1$) around the concave corner behind the solid-type rib do not occur with the permeable-ribbed wall. Concerning the results of the $Nu/\overline{Nu}_s$ distributions along the rib-top walls, similar trends are found for both permeable and impermeable ribbed geometries. However, the values of $Nu/\overline{Nu}_s$ for the permeable ribs are slightly lower than those for the solid-type rib and decrease with increasing β. This is reasonable because with the ribbed wall and a large value of β, a large amount of heat conducted from the rib base has been convected by the airflow through the rib; therefore, the conductive heat to the rib top (or convective heat from the rib-top surface to the test section) is reduced. In addition, the flow acceleration (increased forced convection) between the rib top and the opposite duct wall decreases as β increases due to the reduction of the channel blockage. Both of these facts may be supported by observation of the fringe patterns given in Fig. 4, which shows that the more highly distorted fringes are found on the rib top for the solid-type rib as compared with those for the permeable ribs.

Rib Effectiveness. The total heat transfer from the perforated rib is not obtained by integrating the local heat transfer along the periphery of the rib as that done for the solid-type rib (Liou and Hwang, 1993), but by the energy balance (Liou and Hwang, 1992b), i.e., subtracting the duct wall heat transfer from the total convective heat transfer.

Figure 7 shows the rib heat transfer ratio of the perforated rib as a function of the rib open-area ratio for $PR = 10$, $H/De = 0.081$, and $Re = 20{,}000$. The open symbols in this figure are the measured data and the solid curve passing through these symbols is a curve-fitting result. Note that two limiting cases $\beta = 0$ and 100 percent yield the results of the solid-type ribbed and ribless walls, respectively. The dotted line is an extrapolation from the present experiment to the upper limiting case $\beta = 1$. From the results obtained by Liou and Hwang (1993), it is known that for the solid-type rib, the ratio of Q_{rib}/Q_t is comparable to the fraction that the rib occupies in the one-rib-pitch wetted area (typically, $A_{rib}/A_t = 25$ percent for the solid-type rib). When ribs are perforated but are not yet permeable, i.e., $\beta = 10$ percent in this work, the rib heat transfer ratio becomes slightly lower than that of the solid-type rib because of the reduction in effective rib conductivity due to the stagnant air, which fills up the perforations of the rib. When permeable ribs with $\beta = 22$ percent are applied to the duct wall, Q_{rib}/Q_t becomes larger than that of the solid-type rib. This can be considered as the effect of the enhancement of the forced convection due to the increase of the convective heat transfer surface within the permeable rib. As β increases further, the effect of the enhancement of the forced convection becomes more evident. However, such a trend does not hold continuously when β increases from $\beta = 44$ to 50 percent. As shown in Fig. 7, the value of Q_{rib}/Q_t for $\beta = 50$ percent is slightly lower than that for $\beta = 44$ percent. The reason can be explained as follows: Although the convective

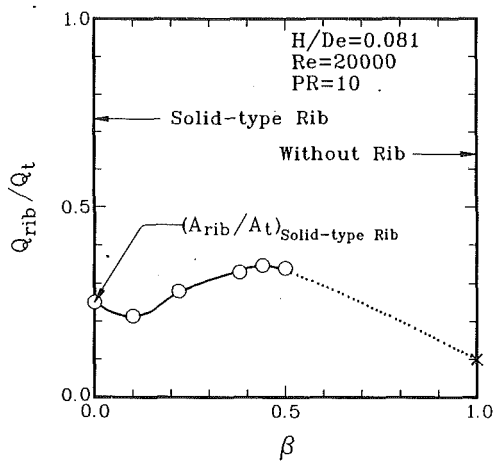

Fig. 7 Rib effectiveness as a function of rib open-area ratio

heat transfer within the perforated ribs increases with an increase in the value of β, the conductive heat transferred from the rib base to the rib top decreases due to the reduction in the conductive area caused by the presence of the perforated holes. Thus, the total heat transfer from the rib may be restricted to the capacity of the conductive heat transfer from the rib base (duct wall). For $\beta = 44$ percent, the conductive heat transfer and the convective heat transfer are more similar than those for $\beta = 50$ percent. From the point of view of rib effectiveness, the rib with $\beta = 44$ percent is recommended because it can transfer the most heat on a unit of total heat transfer.

Note should also be taken in this figure that there is about 20–30 percent of the total heat transfer from the rib, yet only 10 percent of the total flat plate area (the corresponding ribless surface area) is occupied by the rib for $PR = 10$. This can be reflected by the effect of the extended surfaces provided by the rib on the magnitude of the average Nusselt number, which is based on the projective area of the corresponding ribless wall. The results of the average Nusselt number will be shown later.

Average Nusselt Number. Ribs with a relatively high open-area ratio are accompanied with a higher heat transfer area as compared with the solid-type ribs. To place the results on a common basis, the averaged Nusselt number is based on the projected area of the corresponding ribless wall. Thus the magnitude of the averaged Nusselt number can reflect the combined effects of the extended surfaces provided by the ribs and the enhanced turbulence by distorting the velocity and temperature fields caused by the presence of the ribs (Liou et al., 1992). The Reynolds number dependence of the average Nusselt number ratio for the perforated-ribbed walls with different rib open-area ratios, pitches, and heights is plotted in Fig. 8, where the Nusselt number is normalized by the Dittus-Boelter correlation, which provides an excellent representation of the present data for a smooth duct (Liou and Hwang, 1992a).

Figure 8 has been prepared to facilitate a comparison between the results for the perforated ribs and those for the conventional solid-type ribs. The open and half-open symbols in Fig. 8 pertain to the two investigated rib heights, i.e., $H/De = 0.081$ and 0.162, respectively, at $PR = 10$. For clarity, the results for the solid-type ribbed geometries are presented as different types of lines, which are curve fit from the present experimental data. It can be seen from this figure that both the permeable and impermeable ribs give rise to substantial enhancement relative to the smooth duct, ranging from 70 to 200 percent. The extent of the enhancement is larger at low Reynolds numbers. The average Nusselt number ratios for the

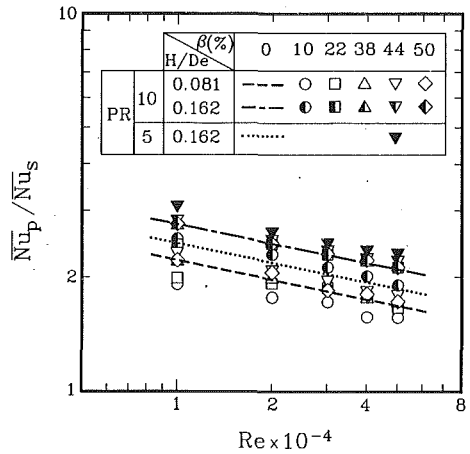

Fig. 8 Average Nusselt number ratio versus Reynolds number

Table 1 Constants for Eqs. (6) and (7)

H/De	c_1	c_2	c_3	c_4	d_1	d_2	d_3
0.081	0.181	0.624	1.474	-1.698	0.062	-0.07	-0.245
0.162	0.251	0.624	0.672	-0.817	0.153	-0.02	-0.284

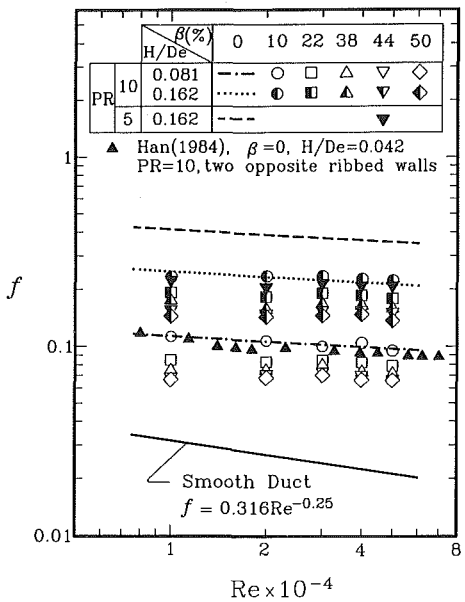

Fig. 9 Friction factor versus Reynolds number

permeable ribbed geometry are slightly higher than those for the solid-type ribbed geometry, typically up to 20 percent. However, for the impermeable perforated-ribbed geometry, i.e., $\beta = 10$ percent for all Reynolds numbers investigated and $\beta = 22$ percent at Re = 10,000, the Nusselt number ratios are slightly lower than those of the solid-type ribbed geometry. The explanation of this fact is as follows: As shown in Fig. 6, although the solid-type and impermeable perforated-ribbed geometries have comparable heat transfer enhancements in the interrib region (X_N/H = 0-9), the heat transfer rate for the top wall of the impermeable perforated rib is slightly lower than that of the solid-type rib. The lower heat transfer rate for the impermeable perforated ribs may be due to a reduction of the effective rib conductivity caused by the presence of the stagnant air in the perforations. Thus, the averaged rib and duct-wall heat transfer coefficient for the impermeable perforated-ribbed geometry is lower as compared to that for the solid-type ribbed configuration. Actually, channels with solid-type and impermeable perforated ribs may be simply considered as those with relatively high and low-conductivity ribs, respectively. The higher heat transfer enhancement accompanied by the channel with higher conductivity ribs is reasonable (Liou and Hwang, 1993). Note should be taken in this figure that the preferred rib open-area ratio in this work is also about 44 percent, which provides the highest heat transfer enhancement at a fixed rib height and spacing.

Concerning the effect of rib height, the Nusselt number ratio increases as expected with increasing rib height because of the augmented flow acceleration caused by the increase in the cross-sectional blockage of the channel. A similar trend is also found for the solid-type ribbed geometry.

A comparison of the effect of the rib spacing on the average Nusselt number ratio between the permeable and solid-type ribbed geometries is also shown in Fig. 8. In this regard, the rib pitch-to-height ratio is varied from 5 to 10, and rib height-to-channel hydraulic diameter ratio is kept at a value of 0.162. As expected, for the solid-type ribbed geometry, the value of the Nusselt number ratio for $PR = 5$ is smaller than that for $PR = 10$. This is because the flow patterns of these two cases are different. Cavity flow is present in the former case, whereas flow reattachment is present in the latter case. Generally, the reattachment flow is associated with a high turbulence intensity, and hence a high heat transfer (Liou et al., 1992). In contrast to the results of the solid-type ribbed geometry, as shown in Fig. 8, the Nusselt number ratio for the permeable ribbed geometry ($\beta = 44$ percent) decreases with increasing rib pitch-to-height ratio from $PR = 5$ to 10. This is physically reasonable because the flow patterns around the permeable ribs are the same for $PR = 5$ and 10. Thus, the heat transfer enhancement is affected by the frequency of flow acceleration, which decreases with increasing PR.

With the values illustrated in the above figures, the average Nusselt numbers for the permeable rib geometry can be further correlated in terms of the rib and flow parameters as follows:

$$\overline{Nu}_p = c_1 Re^{C2}(1 + c_3\beta + c_4\beta^2) \quad (6)$$

(22 percent $< \beta <$ 50 percent, 10,000 $<$ Re $<$ 50,000)

where c_1, c_2, c_3, and c_4 are constants and are listed in Table 1 for various rib heights. The deviation of the equation above is 7 percent for 90 percent of the experimental data shown in Fig. 8.

Friction Factor. The dependence of friction factor on Reynolds number for various rib open-area ratios, rib height-to-channel hydraulic diameter ratios, and rib pitch-to-height ratios is shown in Fig. 9. The pressure drops across the test channel are measured under unheated flow conditions. The open and half-solid symbols in this plot represent the results of the perforated ribbed geometries for H/De = 0.081 and 0.162, respectively, at $PR = 10$. The results of the solid-type rib geometries are described by different types of lines for different combinations of the parameters. In this plot the smooth duct results (solid-line, Blasius correlation) are also displayed for comparison.

As shown in Fig. 9, the friction factor for the permeable rib geometry is considerably smaller than that for the solid-type rib geometry with the same rib height and pitch, but higher than that for the smooth channel (solid-line). At the same rib height, the values of friction factor for the perforated rib geometry with $\beta = 10$ percent are found to be almost the same as those for the solid-type rib geometry. This reflects the fact of impermeability for $\beta = 10$ percent concluded before. As

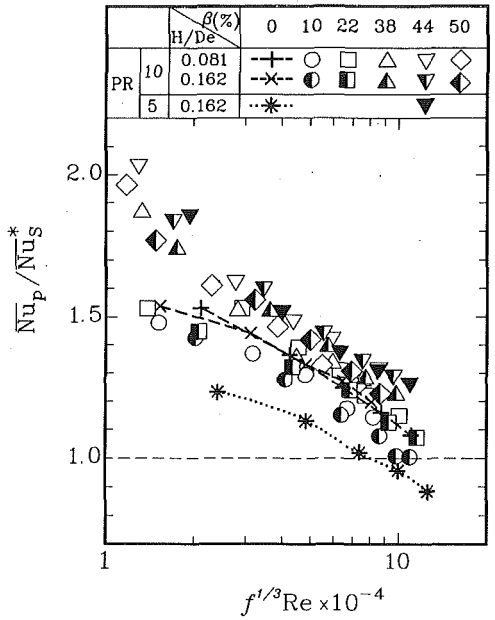

Fig. 10 Performances of the perforated ribbed ducts under a constant pumping power constraint

expected, for a given Reynolds number the friction factor decreases with increasing β because of less cross-sectional blockage for ribs with larger β. Considering the effects of the rib height and rib spacing, respectively, as shown in Fig. 9, the friction factor increases with increasing *H/De* for a given *PR*, β, and Re, while it decreases with increasing *PR* for a fixed *H/De*, β, and Re. Both tendencies are similar to those of the solid-type geometry.

It is worthwhile to make a comparison of the friction factor between the permeable and impermeable ribbed channels with the same cross-sectional blockage ratio. As shown in Fig. 9, although the ribbed channel with β = 50 percent and *H/De* = 0.162 has the same channel blockage ratio as that with β = 0 percent and *H/De* = 0.081 (centerline), the permeable ribbed geometry has a higher friction factor due to the increased surface drag. A comparison of the effect on the friction factor between the geometry of the symmetric ribs arranged on two opposite walls (Han, 1988) and that of asymmetric ribs arranged on one wall (present work) is also interesting. In Han's work, solid-type ribs with *H/De* = 0.042 are arranged on the two opposite walls of the channel. Thus, the channel blockage ratio adopted in Han's work (triangular solid symbols) and that adopted in the present work for *H/De* = 0.081 and β = 0 (centerline) are nearly identical. The comparison shows satisfactory agreement between these two works.

The effects of Reynolds number and rib open-area ratio on the friction factor can be correlated for the different rib heights as follows:

$$f = d_1 \mathrm{Re}^{d_2} \beta^{d_3} \tag{7}$$

$$(22 \text{ percent} < \beta < 50 \text{ percent},\ 10{,}000 < \mathrm{Re} < 50{,}000)$$

where the coefficients d_1, d_2, and d_3 are listed in Table 1. Comparing the equation above with the experimental data, the maximum deviation is 6 percent. Note that the correlation above is valid only for the permeable ribbed geometry.

Thermal Performance Analysis. The selection of performance evaluations depends on the purpose and application (Bergles et al., 1974). In the present study, the thermal performance is evaluated by comparing the average heat transfer coefficient for a channel with ribs with that for a smooth channel without ribs per unit pumping (or blowing) power for a constant heat transfer surface. With ribs applied on the wall, the pressure loss is increased. To keep the fluid pumping power constant, the flow velocity must be reduced. This leads to a reduction in the average Nusselt number, but this reduction can sometimes be overcome by heat transfer enhancement given by rib turbulators. The general result found in the previous discussion of the solid-type rib is that the value of f is large when $\overline{Nu}_p$ is large. From the results of the moderate heat transfer enhancement and lower pressure drop penalty followed by the permeable ribbed geometry, a high thermal performance under the constant pumping power constraint may be expected to be accompanied by the permeable ribbed geometry. The pumping power required to feed the fluid through the duct is proportional to $f \cdot \mathrm{Re}^3$. Thus in Fig. 10 the performance shown by the ratio of $\overline{Nu}_p/\overline{Nu}_s^*$ is plotted against $f^{1/3} \cdot \mathrm{Re}$, where $\overline{Nu}_s^*$ is the average Nusselt number for a smooth duct with the flow rate at which the pumping power is the same as that obtained in the ribbed duct. The calculation of the $\overline{Nu}_s^*$ was described in detail by Liou and Hwang (1992b). It is obvious in this figure that the improvement in Nusselt number ratio of the permeable ribbed duct is more pronounced than that of the solid-type ribbed duct (three different lines). Figure 10 further shows that at the lower Reynolds number range both the perforated and solid-type ribbed geometries give higher thermal performance than those at the higher Reynolds number range. Therefore, the usage of the permeable ribs, especially for β = 44 percent (triangular symbols), at the low Reynolds number range is recommended.

Concluding Remarks

Turbulent heat transfer and friction characteristics in a channel with perforated ribs mounted on one of the principal walls have been studied experimentally. The effects of variations in the Reynolds number, rib spacing, rib height, and rib open-area ratio have been examined.The main findings are:

1 A criterion of permeability of perforated ribs has been obtained from the finite-fringe LHI interferograms. The critical Reynolds number for evidence of flow permeability decreases with increasing rib open-area ratio. Appropriately high rib open-area ratio together with high Reynolds number allow the ribs to be permeable.

2 Since part of the air flow passes through the permeable rib and directly impinges on the recirculating bubble behind the rib, the hot spots occurring in the region around the concave corner behind the solid-type rib do not result in a corresponding hot-spot region of the permeable ribbed geometry.

3 Compact correlations of the friction and heat transfer for permeable ribbed duct flows are obtained for the first time. The friction factor decreases monotonously with increasing rib open-area ratio from 22 to 50 percent, whereas a maximum in the value of average Nusselt number occurs when the rib open-area ratio is about 44 percent.

4 As compared with the conventional solid-type ribs, the moderate heat transfer coefficient and lower pressure drop are accompanied with the permeable ribbed geometry, which reflects a higher thermal performance. The ribs with β = 44 percent give the best thermal performance among the rib open-area ratios investigated.

Acknowledgments

Support for this work was provided by the National Science Council of the Republic of China under contract No. NSC 82-0113-E-216-31-T.

References

Bergles, A. E., Blumenkrantz, A. E., and Taborek, J., 1974, "Performance Evaluation Criteria for Enhanced Heat Transfer Surface," *Proc. 5th Int. Heat Transfer Conference*, Vol. 2, pp. 239–243.

Burggraf, F., 1970, "Experimental Heat Transfer and Pressure Drop With

Two-Dimensional Discrete Turbulence Promoters Applied to Two Opposite Walls of a Square Tube," *Augmentation of Convective Heat and Mass Transfer*, A. E. Bergles and R. L. Webb, eds., ASME, New York, pp. 70–79.

Goldstein, R. J., 1976, "Optical Measurement of Temperature," *Measurements in Heat Transfer*, 2nd ed., E. R. G. Eckert and R. J. Goldstein, eds., Hemisphere, Washington, DC, pp. 241–294.

Han, J. C., 1988, "Heat Transfer and Friction Characteristics in Rectangular Channels With Rib Turbulators," ASME JOURNAL OF HEAT TRANSFER, Vol. 110, pp. 321–328.

Hauf, W., and Grigull, U., 1970, "Optical Method in Heat Transfer," *Advances in Heat Transfer*, Vol. 6, J. P. Hartnett and T. F. Irvine, Jr., eds., Academic, New York, pp. 133–136.

Ichimiya, K., Katayama, M., Miyazawa, T., and Kondoh, H., 1991, "Experimental Study on Effects of a Single Porous-Type Roughness Element in a Parallel Plate Duct," *Experimental Heat Transfer*, Vol. 4, pp. 319–330.

Kline, S. J., and McClintock, F. A., 1953, "Describing Uncertainties in a Single-Sample Experiment," *Mechanical Engineering*, Jan., pp. 3–8.

Lau, S. C., McMillin, R. D., and Han, J. C., 1991, "Turbulent Heat Transfer and Friction in a Square Channel With Discrete Rib Turbulators," ASME *Journal of Turbomachinery*, Vol. 113, pp. 360–366.

Liou, T. M., and Hwang, J. J., 1992a, "Turbulent Heat Transfer and Friction in Periodic Fully Developed Channel Flows," ASME JOURNAL OF HEAT TRANSFER, Vol. 114, pp. 56–64.

Liou, T. M., and Hwang, J. J., 1992b, "Developing Heat Transfer and Friction in a Rectangular Ribbed Duct With Flow Separation at Inlet," ASME JOURNAL OF HEAT TRANSFER, Vol. 114, pp. 565–573.

Liou, T. M., Hwang, J. J., and Chen, S. H., 1992, "Turbulent Transport Phenomena in a Channel With Periodic Rib Turbulators," *AIAA J. Thermophysics*, Vol. 6, pp. 513–521.

Liou, T. M., and Hwang, J. J., 1993, "Effects of Ridge Shapes on Turbulent Heat Transfer and Friction in a Rectangular Channel," *Int. J. Heat Mass Transfer*, Vol. 36, pp. 931–940.

Lious, T. M., Hwang, J. J., and Chen, S. H., 1993, "Simulation and Measurement of Enhanced Turbulent Heat Transfer in a Channel With Periodic Rib on One Principal Wall," *Int. J. Heat Mass Transfer*, Vol. 36, pp. 507–517.

Lockett, J. F., and Collins, M. W., 1990, "Holographic Interferometry Applied to Rib-Roughness Heat Transfer in Turbulent Flow," *Int. J. Heat Mass Transfer*, Vol. 33, No. 11, pp. 2439–2449.

Tanasawa,I., Nishio, S., Takano, K., and Tado, M., 1983, "Enhancement of Forced Convection Heat Transfer in Rectangular Channel Using Turbulence Promoters," *Proc. ASME-JSME Thermal Engineering Joint Conference*, pp. 395–402.

Yamada, H., and Osaka, H., 1992,"Flow Around a Permeable Rectangular Plate Standing Vertically on the Flat Wall, 2nd Report, Effects of the Aspect and the Open Area Ratios," *Trans. JSME*, Vol. 56, No. 546, pp. 120–128.

Unsteady Wake Effect on Film Effectiveness and Heat Transfer Coefficient From a Turbine Blade With One Row of Air and CO_2 Film Injection

S. Ou
Mechanical Engineer,
Aeropropulsion and Power Laboratory,
Wright Patterson Air Force Base, OH
45433

J. C. Han
HTRI Professor,
Turbine Heat Transfer Laboratory,
Department of Mechanical Engineering,
Texas A&M University,
College Station, TX 77843
Fellow ASME

The effect of unsteady wake and film injection on heat transfer coefficients and film effectiveness from a gas turbine blade was found experimentally. A spoked wheel type wake generator produced the unsteady flow. Experiments were done with a five airfoil linear cascades in a low-speed wind tunnel at a chord Reynolds number of 3×10^5, two wake Strouhal numbers of 0.1 and 0.3, and a no-wake case. A model turbine blade injected air or CO_2 through one row of film holes each on the pressure and suction surfaces. The results show that the large-density injectant (CO_2) causes higher heat transfer coefficients on the suction surface and lower heat transfer coefficients on the pressure surface. At the higher blowing ratios of 1.0 and 1.5, the film effectiveness increases with increasing injectant-to-mainstream density ratio at a given Strouhal number. However, the density ratio effect on film effectiveness is reversed at the lowest blowing ratio of 0.5. Higher wake Strouhal numbers enhance the heat transfer coefficients but reduce film effectiveness for both density ratio injectants at all three blowing ratios. The effect of the wake Strouhal number on the heat transfer coefficients on the suction surface is greater than that on the pressure surface.

Introduction

The thermal efficiency of a gas turbine engine can be improved by increasing the turbine inlet temperature. A continuing trend toward higher gas turbine inlet temperatures has resulted in an increase in heat loads on turbine components. Therefore, it is necessary to employ internal and film cooling techniques in a turbine blade for performance requirements.

Many efforts have been made in studying the effect of density ratio on heat transfer and film cooling under the steady flow condition. Teekaram et al. (1989) studied the effect of different injectants on heat transfer coefficients over a flat plate with an injection angle of 30 deg. Air and CO_2 at the same density were used for film cooling and both injectants were made of equal density by controlling their temperatures. They found that the heat transfer coefficients were independent of the gas used for injection (air or CO_2) as long as the densities were kept the same. Ammari et al. (1990) investigated the effect of density ratio on heat transfer coefficients over a flat plate using air ($DR = 1.0$) and CO_2 ($DR = 1.52$) as injectants. They showed that heat transfer coefficients for 90 deg injection are insensitive to density for all blowing ratios (0.5–2.0). However, heat transfer coefficients for inclined 35 deg injection decrease with increasing density ratio for all blowing ratios.

Ito et al. (1978) studied the effect of density ratio (mass transfer method) on the film effectiveness of a gas turbine blade model. They showed that an increase in density ratio at the 0.5 blowing ratio causes a decrease in film effectiveness on the suction surface. The trend is reversed on the pressure surface. It was also found that an increase in density ratio at the 1.0 blowing ratio causes an increase in film effectiveness on both pressure and suction surfaces. Haas et al. (1991) studied the density ratio effect (CO_2 as injectant) on suction surface film cooling of a model turbine blade under a mainstream turbulence intensity of 6.2 percent. They found that an increase in density ratio at the low blowing ratio of 0.5 causes a decrease in suction surface film effectiveness. However, an increase in density ratio at higher blowing ratios of 1.0 and 1.5 causes an increase in suction surface film effectiveness.

Abhari and Epstein (1994) studied local heat transfer on a rotor blade with or without film injection using a blowdown facility with a full turbine stage. They pointed out that time-averaged heat transfer on the suction surface is reduced 60 percent by film cooling; however, the reduction on the pressure surface is small. Takeishi et al. (1992) compared film effectiveness values between a stationary cascade and a rotor blade using the heat–mass transfer analogy. The first-stage blades of a high-temperature gas turbine were used for the two-dimensional stationary cascade test and the three-dimensional rotating test. They reported that film effectiveness values in the leading edge region and on the suction surface of the stationary cascade match those of the rotating blade. The film effectiveness values on the pressure surface of the stationary cascade are higher than those of the rotating blade.

The relative motion between the stationary upstream nozzle guide vanes and the downstream rotor blades invokes the unsteady flow in turbine operations. The interaction between the rotor and stator blades can generate unsteadiness in two ways: potential and wake interactions. Gallus et al. (1982) showed that, except for a very small axial gap (on the order of 5 percent axial chord, where the contributions of the wakes and potential flow interaction are of equal amplitude), unsteadiness due to the wakes is dominant. Dunn (1985) reported that unsteadiness generated by the downstream rotor can significantly affect the heat transfer rate to the upstream stator (15–25 percent). Doorly and Oldfield (1985) showed that unsteadiness due to potential flow interaction is greater on the upstream blade than on the downstream blade and decays rapidly with increasing axial gap. The

Contributed by the Heat Transfer Division and presented at the ASME Winter Annual Meeting, New Orleans, Louisiana, November 28–December 3, 1993. Manuscript received by the Heat Transfer Division May 1993; revision received December 1993. Keywords: Jets, Turbines, Wakes. Associate Technical Editor: R. J. Simoneau.

axial gap between rotor and stator blades for high-pressure turbine engines may be sufficiently large to reduce potential flow interaction. Wake passing may dominate the unsteadiness. The effect of unsteady wake on the downstream blade heat transfer coefficients has been studied. Some investigators have conducted experiments in actual gas turbine engines while others have done laboratory simulations of upstream unsteady wake conditions. Two techniques have produced unsteady wake in laboratory simulations. Pfeil et al. (1983), Priddy and Bayley (1988), and Liu and Rodi (1992) used a squirrel-type wake generator. Doorly and Oldfield (1985), Wittig et al. (1988), O'Brien and Capp (1989), Dullenkopf et al. (1991), and Han et al. (1993) used a spoked wheel type wake generator. These investigators found that unsteady wake promotes earlier and longer boundary layer transition on the blade suction surface for a given Reynolds number. The surface heat transfer coefficients also increase with the wake passing frequency or Strouhal number.

Ou et al. (1994) and Mehendale et al. (1994) studied the unsteady wake effect and the effect of air ($DR = 1.0$) or CO_2 ($DR = 1.5$) film injection on blade film effectiveness and heat transfer distributions. A spoked wheel type wake generator produced unsteady flow. The axial gap between the wake generator and downstream blade leading edge was about 39 percent of the blade axial chord length. The unsteady wake interaction, instead of the potential flow interaction, was considered to dominate the impact on the downstream blade boundary layer flow and heat transfer. The turbine blade had three rows of film holes in the leading edge region and two additional rows each on the pressure and suction surfaces. They found that an increase in the unsteady wake passing frequency causes a decrease in film effectiveness. However, it causes an increase in the heat transfer coefficients over most of the blade surface for both density ratio injectants and all blowing ratios ($M = 0.4–1.2$).

This study focuses on the effects of unsteady wake and injectant-to-mainstream density ratio on the heat transfer coefficient and film effectiveness distributions of a turbine blade model. Air or CO_2 film is injected through one row of film holes each on the pressure and suction surfaces. The major difference between this and the previous studies (Ou et al., 1994; Mehendale et al., 1994) is that the present blade has only one row of film holes each on the pressure and suction surfaces. The previous blade has three rows of film holes in the leading edge region and two additional rows each on the pressure and suction surfaces. This was done by plugging and covering all film hole rows except the last row on the suction ($X/C \cong 0.4$) and pressure ($X/C \cong -0.2$) surfaces. The previous multirow design results in film interaction between jets and film accumulation from the upstream jets on both pressure and suction surfaces. The present single-row design allows the study of the sole interaction between the unsteady wake and the film jet as well as the consequent effect on the blade film effectiveness and heat transfer coefficients. Higher density ratio is achieved by injecting CO_2 gas. The main objectives are to find: (*a*) the effect from one row of film injection for the no wake flow condition, (*b*) the effect of density ratio from one row of air ($DR = 1.0$) or CO_2 ($DR = 1.5$) film injection, and (*c*) the combined effect of unsteady wake and one row of air or CO_2 injection on the blade heat transfer coefficients and film effectiveness.

The following sections describe the test apparatus and instrumentation, test conditions, and data analysis. The measurement results are then presented. Conclusions are made that include the effects of blowing ratio, density ratio, and wake Strouhal number on heat transfer coefficients and film effectiveness.

Test Apparatus and Instrumentation

The test apparatus consists of a low-speed wind tunnel with an inlet nozzle, a spoked wheel type wake generator, a linear five-blade cascade with an instrumented blade in the center, and a suction blower (Han et al., 1993). Figure 1 shows the top view of the cascade, wake generator, wind tunnel, and hot-wire measurement locations. The blade shape is designed to produce velocity distributions similar to those in a typical advanced high-pressure turbine blade row. The selected blade has a 107.49 deg turning with relative flow angles of 35 deg and −72.51 deg at the blade inlet and exit, respectively. A model scaled up five times simulates the engine blade. The cascade has five blades spaced 17.01 cm apart and each has a chord length of 22.86 cm and a radial span of 25.4 cm. The leading edge of the cascade is 8.82 cm downstream from the wake generator (Fig. 1). All cascade blades are of model wood with only the center one instrumented with foils and thermocouples. The wake generator has 32 rods, each 0.63 cm in diameter, to simulate the trailing edge of the upstream blade. Its shaft is located 20 cm below the bottom

Nomenclature

C = blade chord length
d = wake generator rod diameter
D = film hole diameter
DR = density ratio = ρ_s/ρ_∞
FH = film holes
h = local heat transfer coefficient
I = momentum flux ratio = $(\rho V^2)_s/(\rho V^2)_\infty$
k = local thermal conductivity
M = blowing ratio (secondary to mainstream mass flux ratio) = $(\rho V)_s/(\rho V)_\infty$
n = number of rods in the wake generator
N = wake generator rotation speed, rpm
Nu = local Nusselt number based on blade chord length = hC/k
$\overline{\text{Nu}}$ = spanwise-averaged Nusselt number
P = film hole pitch
q'' = net forced convection heat flux
q''_{cond} = local conduction heat loss flux
$q''_{\text{cond,g}}$ = local conduction heat gain flux from within the model blade
q''_{gen} = foil-generated heat flux
q''_{loss} = local total heat loss flux
q''_{rad} = local radiation heat loss flux
r_m = distance between the wake generator shaft center and the cascade midspan
Re = Reynolds number based on blade chord = V_1C/ν
S = wake Strouhal number = $2\pi Ndn/(60V_1)$
T_{aw} = local adiabatic wall temperature
T_s = injectant temperature within the injection cavity
T_f = local film temperature
T_w = local wall temperature
T_∞ = mainstream temperature at the cascade inlet
U_r = rotational speed at cascade midspan
V = local mainstream velocity
V_1 = mean mainstream velocity at the cascade inlet
V_2 = mean mainstream velocity at the cascade exit
X = blade surface coordinate from stagnation in the streamwise direction, $X > 0$ along the suction surface and $X < 0$ along the pressure surface
η = local film effectiveness
$\overline{\eta}$ = spanwise-averaged film effectiveness
ν = kinematic viscosity
ρ_s = density of secondary flow
ρ_∞ = density of mainstream flow
$(\rho V)_s$ = local secondary mass flux
$(\rho V)_\infty$ = local mainstream mass flux
$(\rho V^2)_s$ = local secondary momentum flux
$(\rho V^2)_\infty$ = local mainstream momentum flux

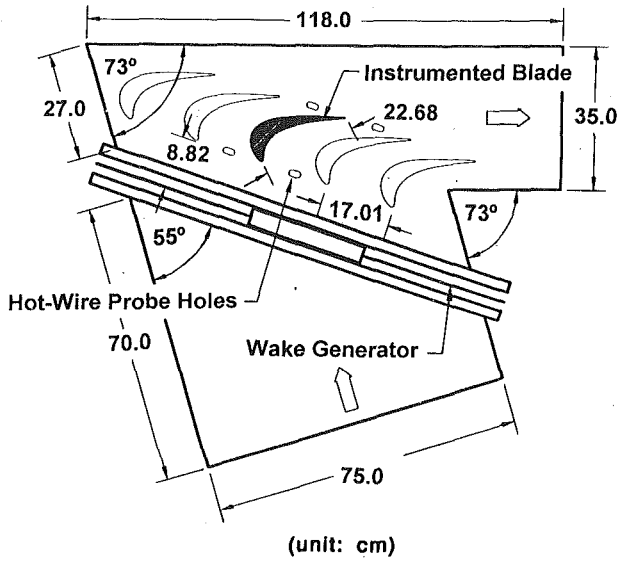

Fig. 1 Test apparatus and instrumentation location layout

wall of the wind tunnel. A casing covers the wake generator to avoid flow leakage. The wake Strouhal number is varied by controlling the motor speed. The rotation speed of the wake generator is measured by a Pioneer DT-36M digital photo tachometer.

Four slots were machined in the top wall of the wind tunnel, two near the leading edge and two near the trailing edge. The slots were midway between the instrumented blade and the two blades next to it (see Fig. 1). A hot-wire probe measured the inlet flow velocities and exit flow velocities of two adjacent channels. The hot-wire probe also measured the rod-induced wake profiles and turbulence fluctuations between the two adjacent flow passages.

The wakes produced by the wake generator rotating rods are deflected and interacted with the mainstream. They undergo severe distortion and are not parallel to the blade stagnation line as shown in the conceptual view of unsteady wake effect in Fig. 2. This figure also shows a schematic diagram of the instrumented blade used for the film effectiveness and heat transfer coefficient tests with film injection. Two separate cavities within the blade supply coolant for injection through a row of film holes. One cavity is for the holes on the pressure surface and the other is for the holes on the suction surface. Each cavity is individually controlled for injectant (air or CO_2) flow rate. Details of the film (round) hole pattern shown in Fig. 2 are typical of a gas turbine blade. The film holes on both surfaces are distributed between 32 and 68 percent of the radial blade span and have a compound angle (radial and tangential) to the blade surface. The pressure side row ($X/C \cong -0.2$) and suction side row ($X/C \cong 0.4$) have 10 holes with a hole pitch-to-diameter ratio of 5.00 and 5.71, respectively.

Thirty-five stainless steel foil strips are cemented vertically on the outer surface of the instrumented blade. Each strip of foil is 25.4 cm long, 1.2 cm wide, and 0.00378 cm thick. A gap of 0.8 mm separates any two foils. All foils are connected in series by copper bus bars. A gap is left for the row of film holes on both the pressure and suction surfaces. The gaps between any two foils and the gaps for the film row are carefully filled with wood putty and made flush with the foil to provide a smooth surface. The heated foils, when electrically heated for the heat transfer coefficient tests, produce a nearly constant wall heat flux boundary condition due to the same resistance and same surface area. Thirty-six gage copper constantan thermocouples are soldered on the underside of the foils. There are nine rows of thermocouples on the pressure surface and 13 rows on the suction surface. Each row has four thermocouples placed in the 4.06-cm-wide midspan region (or 16 percent of radial midspan), two placed in-line with the film hole exits and two placed halfway between hole exits on both surfaces. Since the thermocouples are far (10.6 cm) from the top and bottom walls of the wind tunnel, the temperature measurements are free from endwall effects, and a two-dimensional measurement is ensured. A thermocouple mounted in each injection cavity measures the injectant temperature. All thermocouples are connected to a Fluke 2280A datalogger interfaced with an IBM 386SX 20 MHz personal computer. Fluke multimeters are used to measure the input voltage and current for the heat transfer tests.

A blade without film holes is also instrumented with thin foils and thermocouples for the heat transfer measurements with and without upstream unsteady wake flow (Han et al., 1993).

Test Conditions and Data Analysis

The chord Reynolds number is $\mathrm{Re} = V_1 C/\nu$, where V_1 is the mainstream mean velocity at the cascade inlet, C the blade chord length, and ν the kinematic viscosity based on the cascade inlet temperature. The Reynolds number is set at $\mathrm{Re} = 3 \times 10^5$ for all tests, which corresponds to an inlet velocity of 21 m/s and an exit velocity of 50 m/s.

The wake Strouhal number, defined by O'Brien and Capp (1989) as $S = 2\pi Ndn/(60V_1)$, simulates the unsteady wake flow characteristics of turbine operation. The Strouhal number can be varied by changing N, d, n, or V_1. It has been shown that the blade heat transfer coefficients are functions of a wake Strouhal number for a given Reynolds number (Han et al., 1993). In this study, the variables of n, d, and V_1 are maintained the same for all tests ($n = 32$, $d = 0.63$ cm, $V_1 = 21$ m/s). Three upstream conditions were studied: (1) no wake condition where all rods from the wake generator were removed, (2) medium wake Strouhal number of 0.1, which corresponds to $N = 96$ rpm, and (3) high wake Strouhal number of 0.3, which corresponds to $N = 287$ rpm. The maximum wake passing frequency for the present

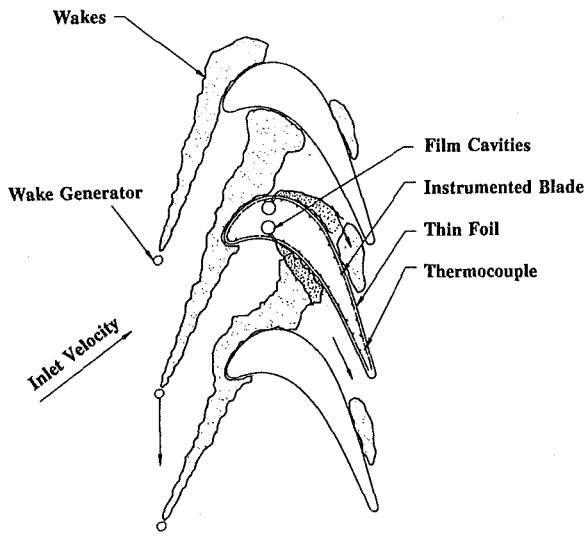

Film Hole Row Location	X/C	P/D	Radial Angle	Tangential Angle
Pressure Side Cavity	-0.2	5.00	35°	50°
Suction Side Cavity	0.4	5.71	90°	30°

Fig. 2 Schematic of the test blade with film hole configuration and the conceptual view of unsteady wake effect

study is 153 Hz. However, it can be as high as 6000 Hz for a typical blade. The flow coefficients at the Strouhal numbers of 0.1 and 0.3, defined by O'Brien and Capp (1989) as $V_1/U_r = dn/r_m S$, are 5.7 and 1.9, respectively. Note that using nonlinear rotating rods with a linear blade cascade causes the wakes at the top of the cascade to pass by the blade faster than the wakes at the bottom of the cascade. However, heat transfer tests (with no film holes) show that the spanwise four thermocouple readings in the midspan region were off about only ±0.5 percent. Therefore, the error was small.

The hot-wire measurements show that the inlet (and exit) velocity profile is essentially uniform between a 25 and 75 percent span. The periodicity of velocity profile between adjacent flow paths is excellent. The hot-wire measurements also show the phase-averaged turbulence intensity can reach as high as 20 percent inside the wake. Time-averaged turbulence intensities are about 8, 13, and 0.75 percent for the wake Strouhal numbers of 0.1, 0.3, and the no-wake case, respectively. The mean mainstream velocity increases from 21 m/s at the cascade inlet (V_1) to 50 m/s at the cascade exit (V_2). A pressure tap instrumented blade measures the cascade inlet total pressure and the surface static pressure distribution converted to local mainstream velocity distribution around the blade (Han et al., 1993). Figure 3 shows the distribution of local to exit velocity ratio (V/V_2) around the blade. The solid line represents a pretest prediction based on $\mathrm{Re} = 2 \times 10^5$. The measured and predicted values match on the pressure surface, whereas the measured local mainstream velocities are higher than the predicted values on the upstream portion on the suction surface.

The injectant mass flux for the film injection tests at a given row of film holes was determined by the local mainstream velocity at that location and the desired blowing ratio, M. Tests were conducted at three blowing ratios of 0.5, 1.0, and 1.5.

Heat Transfer Coefficient Tests. The following heat transfer data analysis method for the thin foil instrumented blade is the same as Ou et al. (1994). The injectant (air or CO_2) and ambient mainstream temperatures are kept the same during the tests, which results in a constant density ratio of 1.00 for air and 1.52 for CO_2. The local heat transfer coefficient with film injection, h, is

$$h = \frac{q''}{T_w - T_f} \tag{1}$$

Equation (1) can be modified as follows since both mainstream and injection flows are at the same ambient temperature ($T_f = T_\infty$) and Mach number $\ll 1$ ($T_\infty \approx T_{aw}$):

$$h = \frac{q''}{T_w - T_\infty} = \frac{q''}{T_w - T_{aw}} \tag{2}$$

The local heat transfer coefficient shown below is calculated for heat loss during the tests:

$$h = \frac{q''_{\mathrm{gen}} - q''_{\mathrm{loss}}}{T_w - T_\infty} = \frac{q''_{\mathrm{gen}} - (q''_{\mathrm{cond}} + q''_{\mathrm{rad}})}{T_w - T_{aw}} \tag{3}$$

where T_w is the measured local wall temperature with foil heat, T_∞ the mainstream temperature at the cascade inlet, and T_{aw} the measured local adiabatic wall temperature without foil heat. The local heat transfer coefficient for the blade without film holes is also calculated using Eq. (3). Heat loss tests estimate the conduction and radiation heat losses in Eq. (3). During the tests, T_w is in the 40°–50°C range and T_{aw} is about 25°C. The measured total heat loss is about 10 percent of the foil generated heat. The conduction and radiation heat losses are 4 and 6 percent, respectively. Quasi-steady-state data are taken through the computer after three hours. Five continuous sets of wall temperature readings are used to obtain the averaged local temperatures and all relevant data are also recorded for the calculation of heat transfer coefficients. Similar procedures are also used in the film effectiveness tests.

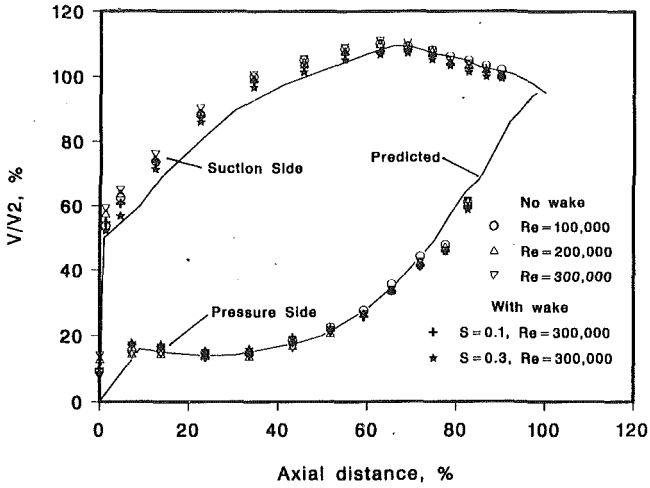

Fig. 3 Velocity distribution around the model blade with and without wake conditions

An uncertainty analysis is carried out using Kline and McClintock's method (1953) for propagation of uncertainties. The uncertainty in the heat transfer coefficient is contributed mainly by the net heat flux and wall-to-mainstream temperature difference. The generated heat for all tests is usually operated at the same level of power input (voltage × current). The uncertainty in the net heat flux primarily comes from the estimation of heat loss from the foil. The uncertainty for decreasing X/C in the heat transfer coefficient increases because the wall-to-mainstream temperature difference decreases. The maximum uncertainty of the net heat flux is about 4 percent and the maximum uncertainty of the wall-to-mainstream temperature difference is about 3 percent. Therefore, the maximum uncertainty in Nusselt number is estimated to be 5.2 percent at the location immediately downstream of film injection. The uncertainty in wake Strouhal number is estimated to be 1.58 percent for the worst case of S = 0.1.

Film Effectiveness Tests. The following film effectiveness data analysis method for the thin-foil instrumented blade is the same as used by Mehendale et al. (1994). The injectant temperature (air or CO_2) within the injection cavity is kept at 45°C. The local film effectiveness, η, is

$$\eta = \frac{T_f - T_\infty}{T_s - T_\infty} \tag{4}$$

where T_f is the local film temperature due to mixing between the injection and mainstream flows, T_s the injectant temperature in the injection cavity, and T_∞ the mainstream temperature.

The model blade surface is initially assumed to be adiabatic. There is no heat transfer at the surface under this assumption and, therefore, the local film temperature must be equal to the local adiabatic wall temperature. Thus, for an adiabatic wall, Eq. (4) is equivalent to

$$\eta = \frac{T_{aw} - T_\infty}{T_s - T_\infty} \tag{5}$$

where T_{aw} is the local adiabatic wall temperature.

Heat losses and gains must be considered because the blade surface is not perfectly adiabatic. Because the injectant is hotter than the mainstream, however, there is a conduction gain from within the model blade that results in higher wall temperatures at locations near injection cavities. Heat loss from the surface due to conduction and radiation results in lower wall temperatures. These gains and losses in wall temperature measurements

are accounted for by dividing their local heat fluxes by the local heat transfer coefficient to yield an "equivalent corrective wall to mainstream temperature difference." The corrective temperature difference is positive or negative depending on the relative strengths of these fluxes. The film effectiveness is finally calculated as

$$\eta = \frac{T_w - T_\infty}{T_s - T_\infty} + \frac{(q''_{\text{cond}} + q''_{\text{rad}}) - q''_{\text{cond},g}}{h(T_s - T_\infty)} \tag{6}$$

where T_w is the measured local wall temperature from mixing of the hotter injectant with the ambient mainstream (a local temperature measured at wall for the local film temperature T_f), q''_{cond} the local conduction heat loss flux, q''_{rad} the local radiation heat loss flux, $q''_{\text{cond},g}$ the local conduction heat gain flux, and h the local heat transfer coefficient for the corresponding test conditions from the heat transfer coefficient tests. The local conduction heat gain flux is estimated based on the thermal conductivity of model wood, the shortest distance between the injectant cavity and the corresponding thermocouple position, the measured local wall temperature, and the injectant temperature measured in the injectant cavity. Depending on the location, the maximum heat losses and heat gain are estimated to be 53.5 W/m^2 and 95.2 W/m^2, respectively.

The uncertainty in the film effectiveness is influenced mainly by the wall-to-mainstream temperature difference and the estimation of heat loss and gain from the foil. The uncertainty for increasing X/C increases because the wall-to-mainstream temperature difference decreases. The maximum uncertainty of the heat loss and gain is about 4 percent and the maximum uncertainty of the wall-to-mainstream temperature difference is about 6 percent. Therefore, the maximum uncertainty in the film effectiveness is estimated to be 7.4 percent at the maximum value of X/C.

Results and Discussion

The results of the heat transfer measurements from the blade without film holes (Ou et al., 1994) for the no-wake case and S = 0.1 and 0.3 show that as the wake Strouhal number increases, the increased flow unsteadiness disturbs the boundary layer and causes an increase in the heat transfer coefficients on both surfaces. This effect is more severe on the suction surface than on the pressure surface. The upstream unsteady flow causes an earlier laminar layer transition on the suction surface ($X/C \cong 0.4$ compared with $X/C \cong 0.8$ for the no-wake case) and the transition length increases with increasing wake Strouhal number.

Heat Transfer Coefficients

Blowing Ratio Effect. Figure 4 shows the effect of film injection on the spanwise-averaged Nusselt number distribution for the no-wake condition. The heat transfer coefficients upstream of the film injection on both sides ($-0.2 \leq X/C \leq 0.4$) are the same as those of no film holes and no wake. The sharp increases in heat transfer coefficients immediately downstream of the film injection on both sides (at $X/C \cong 0.4$ and -0.2) are caused by the highly disturbed boundary layer caused by interaction between the injectant and mainstream. Following these peaks, the boundary layer growth and stabilization cause the heat transfer coefficients to decrease except the lower blowing ratios on the suction surface. In these cases, early boundary layer transitions start and result in increases in heat transfer coefficients. The boundary layer on the pressure surface is thicker (due to lower velocity) than that on the suction surface; therefore, the film injection effect on the pressure surface heat transfer coefficients is reduced. Heat transfer coefficients on the pressure surface increase with increasing blowing ratio for both air and CO_2 injectants because higher blowing ratios cause more interaction between the injectant and mainstream. On the suction surface, however, the heat transfer coefficients increase with decreasing

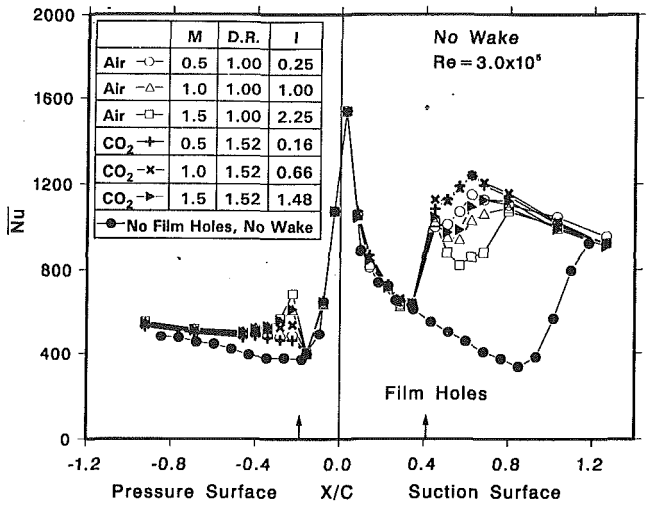

Fig. 4 Effect of air or CO_2 injection on spanwise-averaged Nusselt number for no-wake flow condition

blowing ratio for both injectants. This behavior may result because the lower blowing ratio ($M = 0.5$) with lower momentum flux ratio causes less injectant penetration and promotes an earlier and shorter boundary layer transition to a turbulent boundary layer ($0.4 \leq X/C \leq 0.6$). This earlier and shorter boundary layer transition leads to higher heat transfer coefficients. However, a higher blowing ratio ($M = 1.5$) with higher momentum flux ratio causes more injectant penetration and less effect on the boundary layer. This leads to a delayed boundary layer transition into a turbulent boundary layer ($0.5 \leq X/C \leq 0.8$) and results in lower heat transfer coefficients. The blowing ratio effect on the variations of the heat transfer coefficients due to different momentum flux ratios is more evident for air than for CO_2. Note that the effect of blowing ratio diminishes toward the trailing edge on both surfaces due to film dilution.

Density Ratio Effect. The momentum flux ratio decreases as the density ratio increases for a given blowing ratio. The injectant with lower density penetrates farther for a given blowing ratio on the pressure surface due to higher momentum flux ratio than that with higher density. This leads to more jet–mainstream interaction for lower density injectant and results in higher heat transfer coefficients. However, for a given blowing ratio on the suction surface, the CO_2 injection (with lower momentum flux ratio) causes less injectant penetration and makes the injectant stay closer to the blade suction surface than the air injection. More disturbance by CO_2 injection causes an earlier boundary layer transition to turbulent boundary layer due to a thinner boundary layer on the suction surface. Therefore, the higher density ratio injectant (with lower momentum flux ratio) promotes earlier boundary layer transition and produces higher heat transfer coefficients on the suction surface than the lower density ratio injectant.

Unsteady Wake Effect. Figures 5–7 show the effect of wake Strouhal number on the spanwise-averaged Nusselt number distribution at the blowing ratios of 0.5, 1.0, and 1.5, respectively. The effects of unsteady wake and film injection are displayed in these figures. The effects of blowing ratio and density ratio as described in Fig. 4 can be seen again in these figures. The heat transfer coefficients upstream of the film injection on both surfaces ($-0.2 \leq X/C \leq 0.4$) increase with an increase in the unsteady wake Strouhal number. The heat transfer coefficients downstream of film injection on both sides ($X/C < -0.2$ or $X/C > 0.4$) increase due to the interaction between the injectant and unsteady mainstream. As discussed earlier, the film injection can promote boundary layer transition on the suction surface and

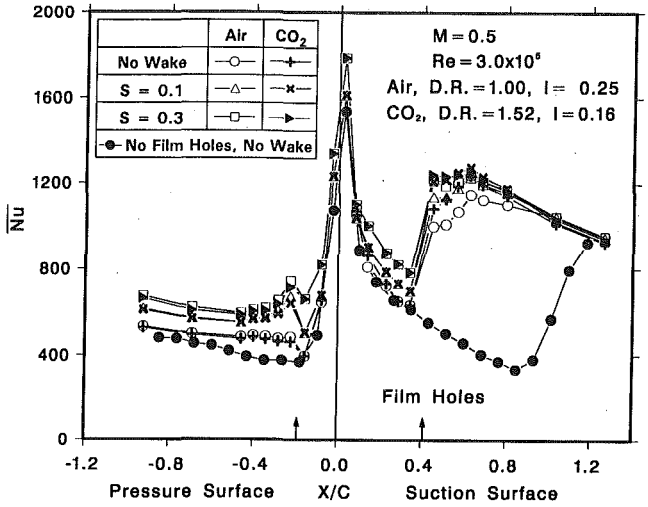

Fig. 5 Effects of unsteady wake and air or CO_2 injection on spanwise-averaged Nusselt number for $M = 0.5$

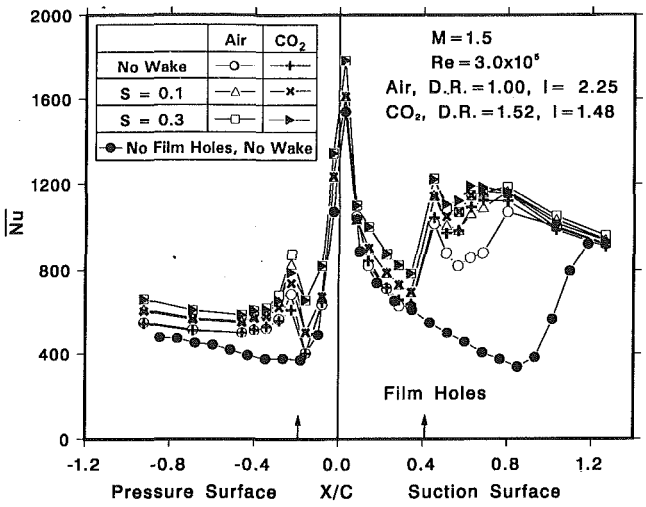

Fig. 7 Effects of unsteady wake and air or CO_2 injection on spanwise-averaged Nusselt number for $M = 1.5$

cause higher heat transfer coefficients on both surfaces for the no-wake condition. As the wake Strouhal number increases, the increases in unsteady flow fluctuations further disturb the boundary layers and further augment the heat transfer coefficients on both surfaces for both injectants at all blowing ratios. Boundary layer disturbances increase as the blowing ratio increases on the pressure surface and, therefore, reduce the increases in the heat transfer coefficients due to the unsteady wake (from the no-wake case to S = 0.3). The increases in the heat transfer coefficients due to the unsteady wake show the same level for both injectants. On the suction surface downstream of the film holes, however, the increases in the heat transfer coefficients due to the unsteady wake are more significant at the highest blowing ratio of 1.5 (the lowest heat transfer coefficients). This is because the transition is delayed at higher blowing ratios (lower heat transfer coefficients) and becomes a turbulent boundary layer because the transitional boundary layer is easily affected by the unsteady wake disturbance. Increases in the heat transfer coefficients due to unsteady wake are greater for the lower density ratio injectant (air) than for the higher density ratio injectant (CO_2) for all blowing ratios.

Film Effectiveness

Blowing Ratio and Density Ratio Effect. Figure 8 presents the effect of film injection on spanwise-averaged film effectiveness under a no-wake flow condition. This figure shows the effect of film injection for different density ratio injectants. The film effectiveness upstream of the film injection on both sides ($-0.2 \leq X/C \leq 0.4$) is nearly zero because there are no film holes in these regions. As expected, the film effectiveness is highest immediately downstream of the film injection due to better film protection. Far downstream, past the peaks, it decreases due to film dilution. The film effectiveness on both sides ($X/C \leq -0.2$ or $X/C \geq 0.4$) decreases with increasing blowing ratio for both injectants. This is because the higher blowing ratio causes more severe lift-off of film jets and reduces the film coverage. However, this trend is not consistent for CO_2 injection on the suction surface where the blowing ratio of 1.0 produces the highest film effectiveness. This is probably because an insufficient amount of CO_2 (due to large density) is injected at $M = 0.5$ and, therefore, the film effectiveness drops quickly. It is expected that there is an optimum blowing ratio for each injectant. Thus, the optimum blowing ratio for air is $M \leq 0.5$ and the optimum blowing ratio for CO_2 is $M \cong 1.0$. The blowing ratio effect is more evident for

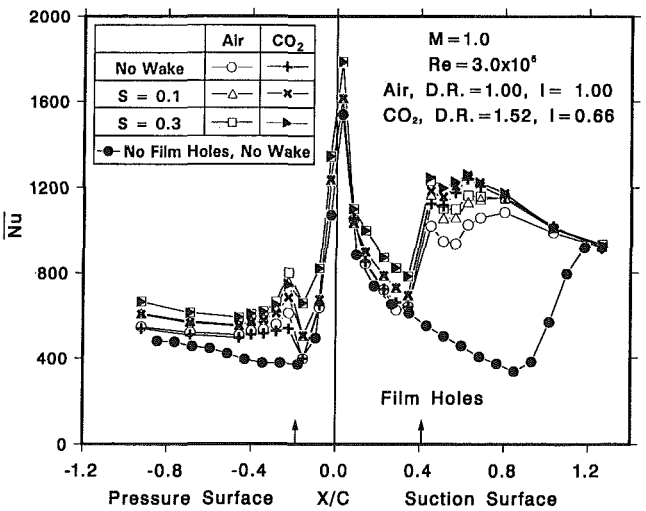

Fig. 6 Effects of unsteady wake and air or CO_2 injection on spanwise-averaged Nusselt number for $M = 1.0$

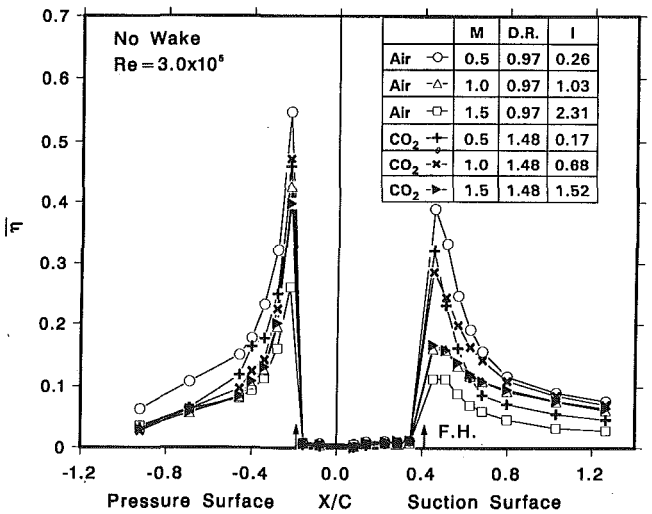

Fig. 8 Effect of air or CO_2 injection on spanwise-averaged film effectiveness for no wake flow condition

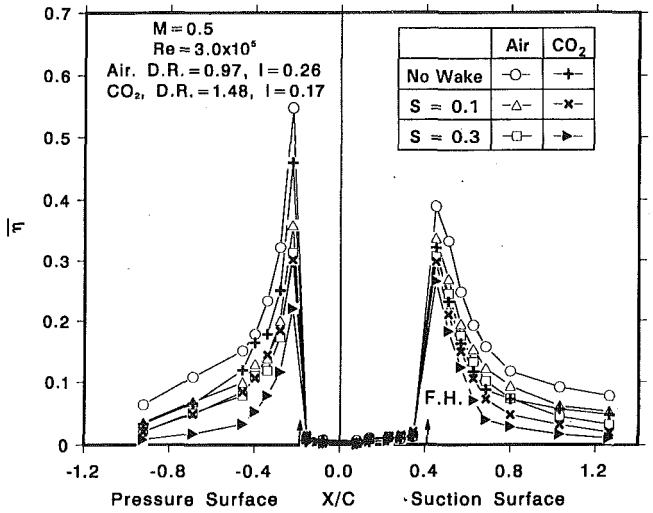

Fig. 9 Effects of unsteady wake and air or CO_2 injection on spanwise-averaged film effectiveness for $M = 0.5$

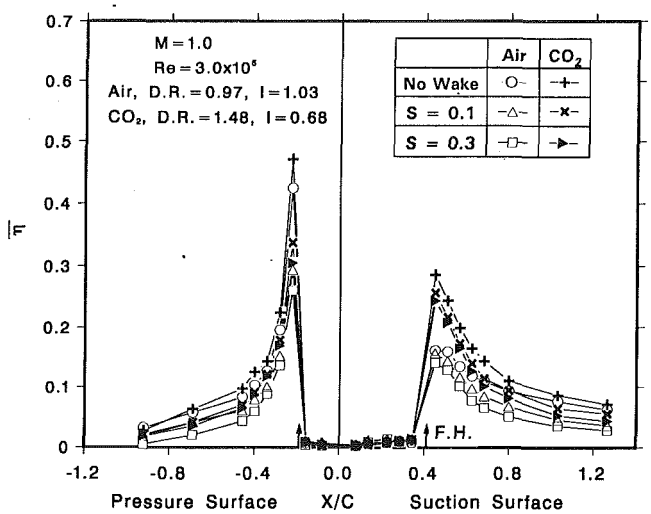

Fig. 10 Effects of unsteady wake and air or CO_2 injection on spanwise-averaged film effectiveness for $M = 1.0$

the lower density ratio injectant of air than for the higher density ratio injectant of CO_2. At the higher blowing ratio of 1.0 or 1.5, the air injection (higher momentum flux ratio) has more jet lift-off than the CO_2 injection (lower momentum flux ratio). Therefore, higher density ratio injectant (CO_2) gives higher film effectiveness than lower density ratio injectant (air) when compared at the same blowing ratio. However, the reverse is true at the lowest blowing ratio of 0.5. The injectants at the small blowing ratio may stay closer to the blade surfaces and a velocity deficit is formed. A larger density injectant may cause a larger velocity deficit and result in larger velocity gradients, which produces higher turbulence and therefore reduces the film effectiveness. The effect of density ratio on the suction side film effectiveness agrees with the previous study by Haas et al. (1992).

Unsteady Wake Effect. Figures 9–11 show the effect of wake Strouhal number on spanwise-averaged film effectiveness distribution for the blowing ratios of 0.5, 1.0, and 1.5, respectively. These figures show the combined effects of unsteady wake and film injection. The effects of blowing ratio and density ratio described in Fig. 8 can be observed in these figures. The film effectiveness on both surfaces downstream of the film injection decreases with increasing wake Strouhal number at the studied three blowing ratios. This is because the higher turbulence intensity level created by the upstream unsteady wake flow disrupts the boundary layer and reduces the film coverage. However, the film effectiveness distributions retain a similar trend when compared to those for the no-wake flow condition. The decrease in film effectiveness due to unsteady wake is most significant at $M = 0.5$ for both injectants. These reductions are about 43 and 21 percent for air and 52 and 17 percent for CO_2 immediately downstream of film holes on the pressure and suction surfaces, respectively. The film effectiveness with air injection ($DR = 0.97$) for the lower blowing ratio ($M = 0.5$) is higher than that with CO_2 injection ($DR = 1.48$) on both surfaces. The film effectiveness with air injection for the higher blowing ratio ($M = 1.0$ or 1.5) is much lower than that with CO_2 injection.

Concluding Remarks

The effect of unsteady wake on the heat transfer coefficient and film effectiveness of a model turbine blade with one row of film holes on the pressure and suction surfaces was investigated using a spoked wheel type wake generator. Two wake Strouhal numbers of 0.1 and 0.3 and a no-wake case were studied at a chord Reynolds number of 3×10^5. Air ($DR \approx 1$) and CO_2 ($DR \approx 1.5$) were used as injectants at three blowing ratios of 0.5, 1.0, and 1.5. Several conclusions can be drawn from this study.

1 A higher blowing ratio on the pressure surface results in higher heat transfer coefficients and lower film effectiveness. An increase in density ratio is seen to cause a decrease in heat transfer coefficients. A higher blowing ratio on the suction surface results in lower heat transfer coefficients and lower film effectiveness, except that CO_2 has the highest effectiveness at the blowing ratio of 1.0. A higher density ratio causes higher heat transfer coefficients.
2 The film effectiveness increases with increasing density ratio on both surfaces for the higher blowing ratios of 1.0 and 1.5. The reverse is true for the lowest blowing ratio of 0.5.
3 Both unsteady wake and film injection can promote boundary layer transition on the suction surface and cause higher heat transfer coefficients. The interactions between the injectant and mainstream disturb the boundary layer immediately downstream of the film holes on both surfaces and cause sharp increases in the heat transfer coefficients. Higher wake Strouhal numbers enhance the heat transfer coefficients and reduce the film effectiveness on both sur-

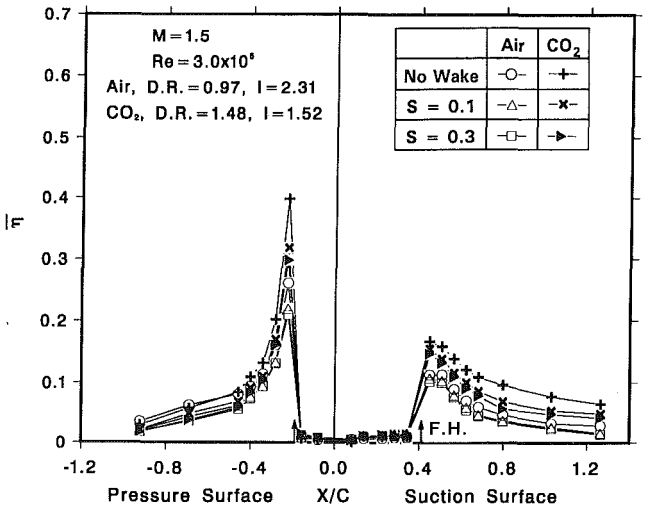

Fig. 11 Effects of unsteady wake and air or CO_2 injection on spanwise-averaged film effectiveness for $M = 1.5$

faces for all three blowing ratios. The effect of unsteady wake on the suction surface heat transfer coefficients is more pronounced than on the pressure surface heat transfer coefficients. On the suction surface, the increases in the heat transfer coefficients due to the unsteady wake are greater for the lower density ratio injectant (air) than for higher density ratio injectant (CO_2). The unsteady wake effect on the pressure surface heat transfer coefficients for both injectants is about the same.

4 The conclusions for one row injection are consistent with previous multirow injection studies (Ou et al., 1994; Mehendale et al., 1994), which have film interaction between jets and film accumulation from the upstream jets on both pressure and suction surfaces. It should be noted that these results are based on a low-speed flow at the blade cascade entrance. The readers should be careful in extrapolating the results from the current work to actual gas turbine conditions.

Acknowledgments

This project was sponsored by the Texas Higher Education Coordinating Board—Advanced Technology Program under grant number 999903-104.

References

Abhari, R. S., and Epstein, A. H., 1994, "An Experimental Study of Film Cooling in a Rotating Transonic Turbine," ASME *Journal of Turbomachinery,* Vol. 116, pp. 63–70.

Ammari, H. D., Hay, N., and Lampard, D., 1990, "The Effect of Density Ratio on the Heat Transfer Coefficient From a Film Cooled Flat Plate," ASME *Journal of Turbomachinery,* Vol. 112, pp. 444–450.

Doorly, D. J., and Oldfield, M. L. G., 1985, "Simulation of the Effects of Shock-Waves Passing on a Turbine Rotor Blade," ASME *Journal of Engineering for Gas Turbines and Power,* Vol. 107, pp. 998–1006.

Dullenkopf, K., Schulz, A., and Wittig, S., 1991, "The Effect of Incident Wake Conditions on the Mean Heat Transfer of an Airfoil," ASME *Journal of Turbomachinery,* Vol. 113, pp. 412–418.

Dunn, M. G., 1985, "Turbine Heat Flux Measurements: Influence of Slot Injection on Vane Trailing Edge Heat Transfer and Influence of Rotor on Vane Heat Transfer," ASME *Journal of Engineering for Gas Turbines and Power,* Vol. 107, pp. 76–83.

Gallus, H. E., Grollius, H., and Lambertz, J., 1982, "The Influence of Blade Number Ratio and Blade Row Spacing on Axial-Flow Compressor Stator Blade Dynamic Load and Stage Sound Pressure Level," ASME *Journal of Engineering for Power,* Vol. 104, pp. 633–641.

Haas, W., Rodi, W., and Schönung, B., 1992, "The Influence of Density Difference Between Hot and Coolant Gas on Film Cooling by a Row of Holes: Predictions and Experiments," ASME *Journal of Turbomachinery,* Vol. 114, pp. 747–755.

Han, J. C., Zhang, L., and Ou, S., 1993, "Influence of Unsteady Wake on Heat Transfer Coefficient From a Gas Turbine Blade," ASME JOURNAL OF HEAT TRANSFER, Vol. 115, pp. 904–911.

Ito, S., Goldstein, R. J., and Eckert, E. R. G., 1978, "Film Cooling of a Gas Turbine Blade," ASME *Journal of Engineering for Power,* Vol. 100, pp. 476–481.

Kline, S. J., and McClintock, F. A., 1953, "Describing Uncertainties in Single-Sample Experiments," *Mechanical Engineering,* Vol. 75, Jan., pp. 3–8.

Liu, X., and Rodi, W., 1992, "Measurements of Unsteady Flow and Heat Transfer in a Linear Turbine Cascade," ASME Paper No. 92-GT-323.

Mehendale, A. B., Han, J. C., Ou, S., and Lee, C. P., 1994, "Unsteady Wake Over a Linear Turbine Blade Cascade With Air and CO_2 Film Injection: Part II—Effect on Film Effectiveness and Heat Transfer Distributions," ASME *Journal of Turbomachinery,* Vol. 116, pp. 730–737.

O'Brien, J. E., and Capp, S. P., 1989, "Two-Component Phase-Averaged Turbulence Statistics Downstream of a Rotating Spoked-Wheel Wake Generator," ASME *Journal of Turbomachinery,* Vol. 111, pp. 475–482.

Ou, S., Han, J. C., Mehendale, A. B., and Lee, C. P., 1994, "Unsteady Wake Over a Linear Turbine Blade Cascade With Air and CO_2 Film Injection: Part I—Effect on Heat Transfer Coefficients," ASME *Journal of Turbomachinery,* Vol. 116, pp. 721–729.

Pfeil, H., Herbst, R., and Schroeder, T., 1983, "Investigation of the Laminar-Turbulent Transition of Boundary Layers Disturbed by Wakes," ASME *Journal of Engineering for Power,* Vol. 105, pp. 130–137.

Priddy, W. J., and Bayley, F. J., 1988, "Turbulence Measurements in Turbine Blade Passages and Implications for Heat Transfer," ASME *Journal of Turbomachinery,* Vol. 110, pp. 73–79.

Takeishi, K., Aoki, S., Sato, T., and Tsukagoshi, K., 1992, "Film Cooling on a Gas Turbine Rotor Blade," ASME *Journal of Turbomachinery,* Vol. 114, pp. 828–834.

Teekaram, A. J. H., Forth, C. J. P., and Jones, T. V., 1989, "The Use of Foreign Gas to Simulate the Effect of Density Ratios in Film Cooling," ASME *Journal of Turbomachinery,* Vol. 111, pp. 57–62.

Wittig, S., Schulz, A., Dullenkopf, K., and Fairbank, J., 1988, "Effects of Free-Stream Turbulence and Wake Characteristics on the Heat Transfer Along a Cooled Gas Turbine Blade," ASME Paper No. 88-GT-179.

Heat Transfer and Surface Renewal Dynamics in Gas-Fluidized Beds

D. V. Pence

D. E. Beasley

R. S. Figliola

Thermal-Fluid Sciences Research Laboratory,
Department of Mechanical Engineering,
Clemson University,
Clemson, SC 29634

Local instantaneous heat transfer between a submerged horizontal cylinder and a gas-fluidized bed operating in the bubble-flow regime was measured and the resulting signals analyzed. Unique to this investigation is the division of particle convective heat transfer into transient and steady-state contact dynamics through analysis of instantaneous heat transfer signals. Transient particle convection results from stationary particles in contact with the heat transfer surface and yields a heat transfer rate that decays exponentially in time. Steady-state particle convection results from active particle mixing at the heat transfer surface and results in a relatively constant heat transfer rate during emulsion phase contact. The average time of contact for each phase is assessed in this study. Signals were acquired using a constant-temperature platinum film heat flux sensor. Instantaneous heat transfer signals were obtained for various particle sizes by varying the angular position of the heat transfer probe and the fluidization velocity. Individual occurrences of emulsion phase heat transfer that are steady-state in nature are characterized by contact times significantly higher than both the mean transient and mean emulsion phase contact times under the same operating conditions. Transient and steady-state contact times are found to vary with angular position, particle size, and fluidizing velocity. Due to the extremely short transient contact times observed under these fluidization conditions, mean transient heat transfer coefficients are approximately equal to the mean steady-state heat transfer coefficients.

Introduction

Transport phenomena in bubbling, gas-fluidized beds are dominated by surface renewal mechanisms associated with the local hydrodynamics at submerged surfaces. In the case of heat transfer, the fundamental physics of the process are reasonably modeled using the concept of two phases comprising the bed: bubble and emulsion. The term emulsion phase implies a volume in the bed having a fairly uniform void fraction near 0.5, while the term bubble phase is used to describe small volumes in the bed composed primarily of the fluidizing gas. Employing such an approach to model the physics of local heat transfer assumes that a point on a submerged surface will alternately be in contact with emulsion phase and bubble phase as a result of local hydrodynamics. Surface renewal is a concept that implies recurrent replacement of the emulsion phase in contact with the surface with emulsion phase at the bulk bed temperature. Bubble contact with the surface, or the passage of a bubble near the surface, creates the hydrodynamics that promote surface renewal. This study has focused primarily on submerged horizontal cylinders.

Local emulsion phase and bubble phase contact at a submerged surface can be characterized using several parameters that serve to describe the essential physics and that also allow quantitative prediction of the local heat transfer rate. Emulsion phase and bubble phase contact times and emulsion and bubble contact time fractions are useful in describing the contact dynamics, and can be used as input to predictive models. Experimentally quantifying these parameters may yield correlating equations. These characterizations are based on physical models that assume that distinct phases constitute the bed; in actuality, there is a range of void fractions in areas of the bed that might be classified as bubble or emulsion.

Contributed by the Heat Transfer Division for publication in the JOURNAL OF HEAT TRANSFER. Manuscript received by the Heat Transfer Division March 1993; revision received November 1993. Keywords: Measurement Techniques, Packed and Fluidized Beds, Transient and Unsteady Heat Transfer. Associate Technical Editor: W. A. Fiveland.

Observations in this laboratory using high-speed film techniques and time accurate local heat flux and void fraction measurements have led to the conclusion that several types of emulsion phase contact routinely occur at submerged surfaces in bubbling gas-fluidized beds. However, the concept of a "packet" of stationary particles has been employed in the majority of previous studies for developing models or describing the underlying physics of heat transfer during emulsion phase contact. This assumed physical behavior implies a heat transfer coefficient that decays rapidly and monotonically in time during emulsion phase contact, until the packet is replaced by bubble interaction. However, the observed physics also reveals emulsion phase contact periods in which the heat transfer coefficient does not decay, but rather fluctuates about an average value. Some emulsion phase contacts have decaying heat transfer rates, but decay rates are often significantly less than those predicted by a packet model approach. Therefore, the present study was undertaken to examine contact dynamics and surface renewal through the analysis of local, time accurate heat transfer measurements from a submerged horizontal cylinder to a bubbling gas-fluidized bed. Modeling efforts will be furthered by investigating quantitatively the nature of heat transfer rates during emulsion phase contact and associated contact dynamics.

Background

Measurements that describe surface renewal and emulsion and bubble phase contact dynamics are essential to understanding and modeling heat transfer physically in fluidized beds. Mickley and Fairbanks (1955) proposed a model of local heat transfer based on transient conduction into the emulsion phase, which was modeled as having uniform effective thermophysical properties. This model has served as the basis for essentially all of the subsequent descriptions of emulsion phase heat transfer. During emulsion phase contact with the heat transfer surface, the heat transfer rate predicted in such models decreases in time as a result of thermal penetration depth effects, as in a semi-infinite solid. The model predicts that the average emulsion phase heat transfer rate is dependent upon emulsion phase contact times. In a subsequent pa-

per, Mickley et al. (1961) examined experimentally the heat transfer between a bubbling gas-fluidized bed and a vertical tube. Continuous records of the local heat transfer were obtained, and statistical aspects of the emulsion phase residence time examined. By assuming a model of the emulsion phase heat transfer coefficient that can be expressed as

$$h = \frac{1}{\sqrt{\pi}} \sqrt{k_p \rho_p c_p} \frac{1}{\tau^{1/2}}, \quad (1)$$

the authors were able to derive an appropriate average value of contact time to describe the mean emulsion phase heat transfer rate. The assumption that all emulsion phase contact is described by a "packet" model approach, which predicts a sharply decaying heat transfer coefficient, yields an expression for the mean heat transfer coefficient over all contacts as

$$\bar{h} = \frac{2}{\sqrt{\pi}} \sqrt{k_p \rho_p c_p} \frac{\sum_i \tau_i^{1/2}}{\sum_i \tau_i} \quad (2)$$

Mickley et al. (1961) then chose to define an average packet residence time as

$$\bar{\tau}_{\text{rsa}} = \left[\frac{\sum_i \tau_i}{\sum_i \tau_i^{1/2}} \right]^2 \quad (3)$$

In order for this average to appropriately describe the heat transfer, the underlying assumption of transient decay in the heat transfer rate during emulsion phase contact must correctly describe the actual physics. In addition, it should be noted that Eq. (2) results from integrating the model equation, Eq. (1), over a contact time, and then averaging this result for the number of contact periods.

Both transient and mixing characteristics are evident in Fig. 8(*a*) of Mickley et al. (1961) although the authors did not discuss this aspect of the signal. Other investigators have also examined the emulsion phase contact dynamics for vertical surfaces and horizontal tubes in fluidized beds. Ozkaynak and Chen (1980) and Chandran and Chen (1982) examined the contact dynamics for vertical and horizontal tubes in fluidized beds by measuring the local void fraction using capacitance probes and, for a vertical tube, local heat transfer coefficients. Average residence times for the emulsion phase were reported based on Eq. (3), called the root-square average emulsion residence time. Residence times for the vertical tube were seen to follow a log-normal distribution. Local time averaged heat transfer rates were measured for the vertical tube, and compared with the packet model and existing correlations.

Saxena and Rao (1991) and Saxena et al. (1990) presented temperature traces from a heat transfer probe, and determined renewal frequencies. Chandran and Chen (1982) measured local void fraction using a capacitance probe. In each of these cases the data are not presented in a manner that would allow comparison with the present signals.

Kurosaki et al. (1988) measured pressures and local heat transfer coefficients at the surface of a horizontal heated cylinder. In addition, visual observation was made of the behavior of particles at the surface of the horizontal cylinder. Fiber optics were used to convey a laser beam to the surface of the cylinder, where transmission or interruption of the light signal to a photomultiplier tube indicated the absence or presence of emulsion phase. Three fundamental particle behaviors were identified at the cylinder surface:

1 stationary behavior with no particle motion,
2 sliding of the particles along the surface, and
3 mixing behavior where emulsion and void phases interact.

The maximum values of the heat transfer coefficient were observed at the boundary between sliding and mixing behaviors. In a previous study in this laboratory, still photography and high-speed motion films showed distinct particle motion at the surface of a submerged cylinder in a two-dimensional fluidized bed (Suarez, 1983). These observations are in qualitative agreement with those of Kurosaki et al. (1988).

Particle motion adjacent to a submerged cylinder may result in local fluctuations in void fraction, which have been measured by several investigators using capacitance probes. Chockalingam (1985), using the same experimental facility as Suarez (1983), recorded local, instantaneous void fraction at the surface of a horizontal cylinder in a gas-fluidized bed of particles having mean diameters from 256 to 509 μm. In this range of particle sizes, he concluded that void fraction fluctuations contributed to time variations in heat transfer, but that void fraction fluctuations alone did not account for the variations in heat transfer rate found by Suarez (1983). Decker (1983) measured the spacing between the surface and adjacent particles in large particle beds. This spacing was observed to fluctuate significantly during emulsion phase contact for large particles. Ginoux et al. (1973) used a two-dimensional bed to examine local hydrodynamics around a horizontal cylinder. The authors discuss clearly the basis for the independence of the heat transfer coefficient from the contact time for vigorous agitation, or very short contact times.

Beasley et al. (1987) and Figliola et al. (1993) developed a model for the particle convection heat transfer component of the emulsion phase heat transfer in a bubbling bed. The model employs a convective boundary condition at the interface between the surface and the emulsion phase, and allows variations in local

Nomenclature

A = constant in correlation (Eqs. (5) and (6))
B = constant in correlation (Eqs. (5) and (6))
C = constant in correlation (Eqs. (5) and (6))
c = specific heat
D = diameter of the horizontal cylinder
$E(t)$ = voltage
d_p = mean particle diameter
f = contact time fraction, typically bubble phase
g = acceleration due to gravity
h = instantaneous local heat transfer coefficient
$\bar{h}$ = mean heat transfer coefficient
k = thermal conductivity
r = resistance
R = ratio
t = time
U = gas velocity
Δ = peak-to-peak value for a heat transfer signal
θ = angular position from stagnation point
ρ = density
τ = emulsion phase contact time
$\bar{\tau}$ = mean contact time

Subscripts

avg = average (emulsion)
b = bubble
crit = critical
gc = gas convection
i = individual contact condition
mean = mean value
m = mixing
mf = minimum fluidization
min = minimum
p = packet
rsa = root square average
s = steady-state heat transfer or mixing particle behavior
t = transient heat transfer or stationary particle behavior
θ = local average

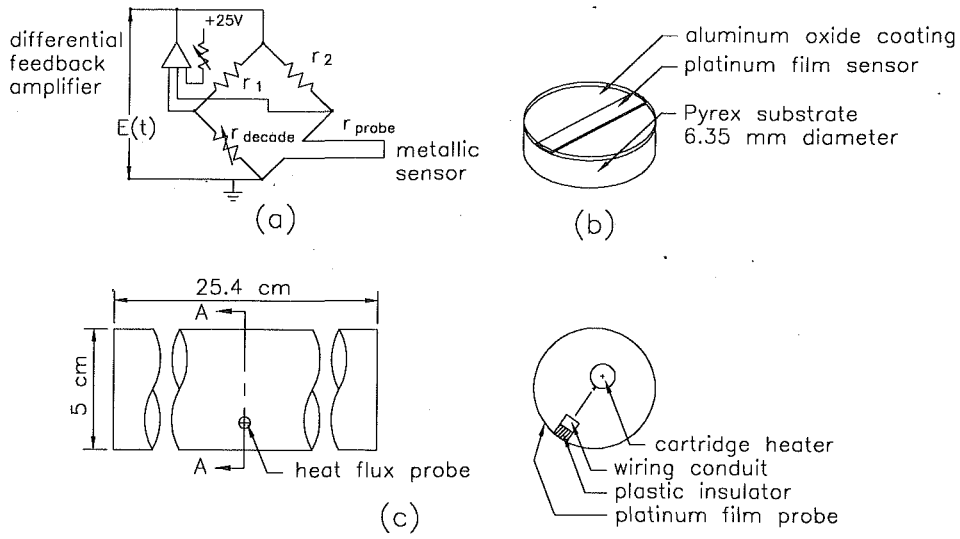

Fig. 1 *(a)* **Constant-temperature bridge circuit,** *(b)* **heat flux probe, and (c) heated cylinder configuration**

void fraction in the region adjacent to the surface. The concept of surface coverage is introduced to account for particle contact and void fraction variations at a heat transfer surface. As far as is known, all published models for predicting emulsion phase or particle convection heat transfer require contact time information, either for single particles or the emulsion phase.

Experimental Facilities and Measurements

Time-accurate measurements of local heat transfer rates were performed in a 92 cm high, 30 cm by 30 cm cross-sectional bed with air as the fluidizing medium. The distributor plate was porous polyethylene, with a typical pressure drop of 3 kPa. Three particle sizes were studied: two base mixtures having narrow size distributions with weight mean averages of 256 and 568 μm, and a binary mixture of these two sizes having a weight mean of 340 μm. The measurements were made in the bubbling flow regime, with fluidization velocity ratios ranging from 1.0 to 3.1. Heat transfer rates were recorded for a single cylinder having a uniform surface temperature approximately 35°C above the bulk bed temperature. Overall (time and spatial) averaged values, local time averaged values, and instantaneous local values of the heat transfer were measured. The horizontal cylinder was 5 cm in diameter, internally heated, and located 30 cm above the distributor plate. Instantaneous heat transfer rates were measured with a platinum film probe, as shown in Fig. 1; the probe was flush-mounted on the cylinder surface, and the platinum film temperature controlled by a constant-temperature bridge circuit. The probe was maintained within 0.25°C of the cylinder temperature. The power supplied to maintain the probe temperature is a direct measure of the heat transfer coefficient. Raw bridge voltage data and the probe electrical resistance were used to calculate the heat transfer rate to the fluidized bed by using the calibrated effective area of the probe, and after correcting for probe conduction losses. These calculations and benchmark tests have been described previously (Suarez, 1983; Suarez et al., 1983). The probe response time was determined experimentally to be less than 1 ms, which is much faster than the measured dynamic frequencies occurring within the bed. Further descriptions of the characteristics of film probes employed for heat flux measurement are found in Beasley and Figliola (1988) and Figliola et al. (1993).

Heat transfer measurements were made at angular positions of 0, 45, 90, 135, and 180 deg, with zero corresponding to the bottom of the cylinder, or the upstream side. The bridge output signal was recorded by a data acquisition system at 5 ms intervals. In benchmark tests, the spatially and temporally integrated average values of the instantaneous signals agreed with the overall cylinder heat transfer rates to within the 7 percent uncertainty of the system. This overall heat transfer rate was determined from the power input to maintain the temperature of the copper cylinder above the bed temperature. Other baseline tests with single-phase gas flow normal to the cylinder showed agreement with existing experimental data and correlations for the stagnation point on a cylinder in crossflow (Giedt, 1949) to within ±10 percent. These tests confirm the accuracy of the probe calibration, operation, and stability of the bridge circuit. Uncertainty analysis of experimental data from the present fluidized bed resulted in uncertainty levels of ±10 percent for the maximum emulsion phase heat transfer rate, and this value increased to ±30 percent for the bubble phase minimum.

Surface Renewal Characteristics

The physical mechanisms of heat transfer in gas-fluidized beds where radiation effects are negligible include bubble phase and emulsion phase heat transfer. As shown in Fig. 2, the onset of emulsion phase contact is characterized by a dramatic increase in the value of the heat transfer coefficient, whereas an abrupt decrease in the heat transfer coefficient is recognized as initiation of bubble phase contact. Traditionally, the emulsion phase heat transfer has been further divided into two additional components: gas and particle convection. The gas convection component can be predicted or measured (see, for example, Baskakov et al.,

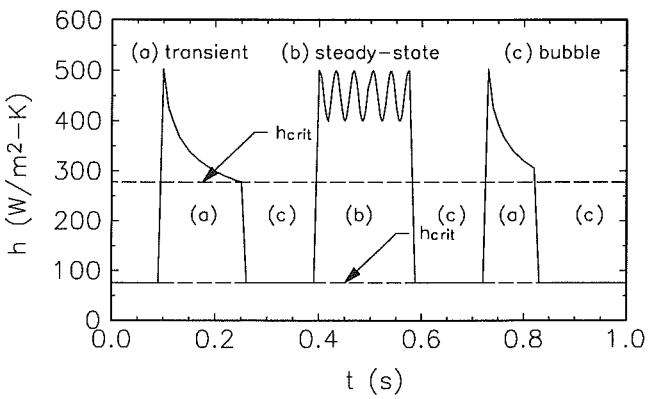

Fig. 2 Range of appropriate h_{crit} for an ideal signal

1973). There exist several models for predicting the rate of particle convection heat transfer based on transient conduction to the particles and stagnant gas within the emulsion phase. However, experimental observations indicate that such transient conduction behavior does not completely characterize particle convection heat transfer.

In one scenario, the resulting transient decay of the instantaneuos heat transfer coefficient suggests that particles remain stationary during contact with the heat transfer surface, such as depicted by (*a*) in Fig. 2. However, visual inspection of the instantaneous heat transfer coefficient signals obtained by Suarez (1983) suggests that transient heat transfer is not the sole means of heat transfer when emulsion phase is in contact with the heat transfer surface. There also clearly exist periods of emulsion phase contact where the heat transfer coefficient fluctuates about a constant value, such as depicted by the ideal signal in (*b*), Fig. 2. This steady-state behavior is assumed to be attributed to the mixing of particles and/or variations in local void fraction while the emulsion is in contact with the heat transfer surface. Occasionally, a combination of the two signals appears.

Original to this work is the division of the particle convection heat transfer into stationary and mixing particle behavior, which corresponds to transient and steady-state emulsion phase contacts, respectively. Mean heat transfer coefficients, which include bubble phase, gas convection, transient particle convection and steady-state particle convection heat transfer, can be predicted according to the following equation:

$$\bar{h} = f_b\bar{h}_b + f_t(\bar{h}_t + \bar{h}_{gc}) + f_s(\bar{h}_s + \bar{h}_{gc}) \qquad (4)$$

Both the bubble phase heat transfer coefficient, $\bar{h}_b$, and steady-state particle convection heat transfer coefficient, $\bar{h}_s$, are independent of time and do not require knowledge of contact time. However, in order to predict the average heat transfer coefficient during a transient contact, $\bar{h}_t$, information regarding contact time for this condition is essential. As for the fractional contribution of the bubble phase, f_b, a correlation for predicting such values for vertical cylinders in gas-fluidized beds does exist. With knowledge of f_b and mean transient contact time information, the fractional contribution due to transient emulsion phase, f_t, can also be determined. Finally, the fraction of steady-state emulsion phase, f_s, can be determined from the bubble fraction and transient emulsion fraction.

To predict $\bar{h}_t$ accurately, a transient contact time incorporating the probability density distribution of average individual transient contact times should be used; however, Koppel et al. (1966) showed that for typical transport models, the shape of the probability density function for residence times at a surface have an insignificant effect on the predicted average transport coefficient. Thus, mean transient contact times, $\bar{\tau}_t$, are expected to provide reasonable results. In either case, mean values are required. As a source of comparison, mean values of steady-state contact time, $\bar{\tau}_s$, and emulsion phase contact time, $\bar{\tau}_{avg}$, are also investigated. The procedure followed for determining these values is described in the following paragraphs.

Signal Analysis

Under ideal circumstances such as those displayed in Fig. 2, when a group of particles comes in contact with a heat transfer surface, one of two conditions exist. If the particles are in a state of mixing, the heat transfer coefficient increases immediately upon contact and fluctuates about a constant value, whereas if the particles remain motionless at the surface, the immediate increase in heat transfer is followed by a tendency of the heat transfer coefficient to decay exponentially. Either condition persists until a bubble, free of particles, displaces the emulsion phase. Such bubble phase contact results in an immediate drop in the heat transfer coefficient to some minimum value. Again, in the present idealized model, each time the emulsion phase or bubble phase comes in contact with the heat transfer surface, a consistent maximum or minimum value of heat transfer coefficient results. Individual emulsion phase contact times can be determined by analyzing the signal at an appropriate value of the heat transfer coefficient, h_{crit}, which accurately represents the duration of contact for each phase. The emulsion phase contact time is evaluated as the time between consecutive crossings of the h_{crit} value, with a crossing having an increasing heat transfer coefficient indicating onset of emulsion phase contact. A range of possible values for h_{crit} lies between the two dashed lines in Fig. 2. However, low-frequency and high-frequency noise present in essentially all of the experimental signals in the present study interfered with the accurate determination of these mean values of contact time from this raw data. For this reason, appropriate band-pass filtering techniques were developed to provide signals free of unwanted noise without altering the original widths of contact of the signal.

In order to determine the threshold for the band pass filter, power spectral density functions of several signals were analyzed. A band-pass filter was created in the frequency domain with threshold frequencies of 0.2 Hz and 15 Hz. After filtering, the signals were free of unwanted noise, yet the contact times were essentially unaltered. Visual confirmation of unaltered contact times as well as noise elimination is available in Fig. 3. Provided in the figure is the original signal prior to filtering and the filtered signal, which is offset for clarity.

After removal of the noise from the signal, the most appropriate location for the critical heat transfer coefficient, h_{crit}, can be determined. It is desired to develop a data reduction method that allows h_{crit} to be specified from statistical parameters of each signal. Two candidate methods for specifying a value of h_{crit} were judged promising from preliminary evaluation of representative signals. The first of these is located at the mean heat transfer coefficient, $\bar{h}_{avg}$, less some fraction of Δ, the difference between the maximum and minimum (or peak-to-peak) heat transfer coefficient values of each signal. The second involves evaluation of the contact times with h_{crit} located at the minimum heat transfer coefficient, h_{min}, plus some fraction of the peak-to-peak value. Inspection of Fig. 4 shows that of the four candidate locations identified for h_{crit}, all could provide plausible results for the mean contact times. These four candidate locations for h_{crit} were plotted on each of the 148 signals that formed the database for this study. The contact times that resulted from data reduction were compared to contact times determined directly from the signals through visual analysis. For the signals identified in Figs. 3 and 5 the average emulsion phase contact time determined through the signal analysis algorithm proposed in this study varied by 3 and 1 percent, respectively, from those derived manually. Actual bed contact dynamics present a range of void fraction during emulsion phase contact, creating challenges in interpreting individual contacts. Figure 4 contains an example of this complexity.

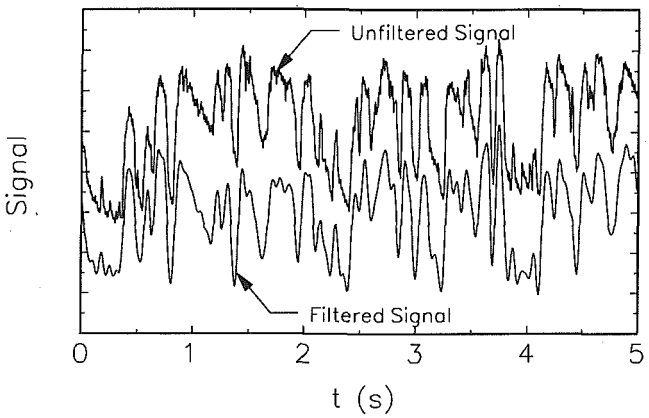

Fig. 3 Comparison of filtered to unfiltered signal (offset for clarity)

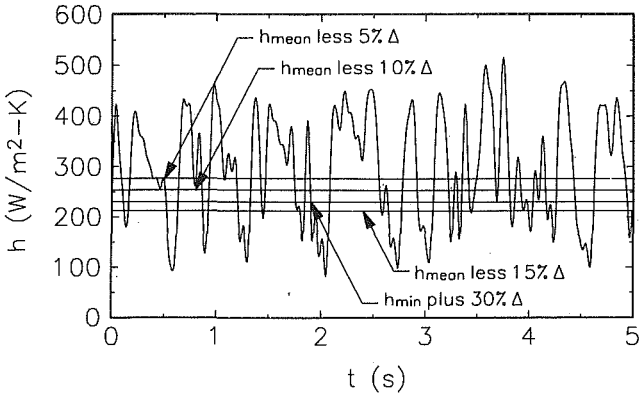

Fig. 4 Candidate values of h_{crit} for a representative signal

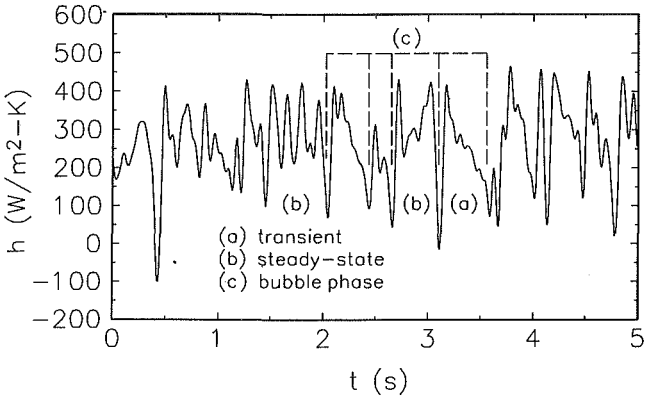

Fig. 5(*a*) Signal containing both steady-state and transient emulsion phase contacts

Between 3.85 and 4.25 seconds a degree of subjectivity exists in evaluating the emulsion phase contact. The signal analysis algorithm recognizes three distinct emulsion phase contacts. Manual estimates of the average emulsion phase contact time for this signal could be as much as 12 percent higher than the signal analysis algorithm if this portion of the signal was considered as a single contact. Despite the complexities of emulsion phase dynamics, the present signal analysis algorithm effectively characterizes the contact dynamics associated with heat transfer. These observations were conclusive concerning the gross ability of the data analysis scheme to identify bubble and emulsion phase contact. Additional quantitative comparisons were made with a predictive model of heat transfer rate as a function of emulsion phase contact time for each signal. Together these assessment measures provided the following conclusions. The minimum heat transfer coefficient plus 30 percent of the peak-to-peak difference yielded reasonable results for only 80 percent of the instantaneous signals. Other fractional values of the peak-to-peak difference added to the minimum value yielded reasonable results for even fewer signals. On the other hand, the mean heat transfer coefficient value less 10 percent of the peak-to-peak value was found to be most representative of each signal. The sensitivity of the mean contact time to changes in h_{crit} can be illustrated by considering a representative case. For the signal in Fig. 4, values of average emulsion phase contact time varied from 132.2 to 169.7 ms for h_{crit} ranging from the mean less 5 percent to the mean less 15 percent of the peak-to-peak value.

In summary, a small degree of variation exists in identifying the onset of emulsion or bubble phase contact in the heat transfer signals. The method developed here yields results that agree intuitively and quantitatively with examination of the individual signals, and will be shown to represent accurately both magnitude and trends in the heat transfer coefficient. Only results for one out of 148 signals were found to be unjustifiable, and upon further evaluation the data from this signal were determined to be spurious and excluded from further analyses.

After selecting h_{crit}, the task of evaluating the mean emulsion phase contact time is conceptually quite simple. However, determining the mean transient and steady-state contact times separately requires a method by which to distinguish between the two types of contact. This can be accomplished by employing the first derivative of the signal in the following manner. Figures 5(a) and 5(b) show the filtered signal and the derivative of the filtered signal, respectively. Consider idealized heat transfer signals (Fig. 2). In this case, transient emulsion phase contacts are characterized by a negative value of the first time derivative of the signal, whereas steady-state conditions are represented by alternating positive and negative values. No positive values of the time derivative would occur during transient emulsion phase contact in the ideal case, since the heat transfer monotonically decays until surface renewal occurs. In examining actual heat transfer signals, transient contacts routinely contain increases in the heat transfer rate. Thus, an effective data reduction technique must be able to distinguish those occurrences of a positive slope that indicate true particle mixing from small variations during transient decay of the heat transfer rate.

Close investigation of individual transient and steady-state contacts and their corresponding derivatives show that a significant positive slope of the derivative of the signal is indicative of the initial onset of emulsion phase contact, and is the case whether the period of contact is characterized by stationary or mixing conditions. A signal that is truly transient in nature displays either negative or only slightly positive slopes, as seen by condition (a) in Fig. 5(b). Individual emulsion phase contacts exhibiting steady-state heat transfer characteristics display several peaks, which have first derivative values significantly larger than for transient contacts as is evident from contacts denoted by (b) in Fig. 5(b).

From the preceding discussion, it is evident that two major requirements need to be addressed when identifying criteria for emulsion phase characterization. These are the number of occurrences and the magnitude of the positive slopes, or peaks, in the derivative of the signal. After visual comparisons between emulsion phase conditions and their respective derivatives were made for numerous signals, the following criterion for emulsion phase classification was developed. In order for an emulsion phase condition to be considered steady-state, its corresponding derivative signal must yield two or more positive slopes with magnitudes greater than or equal to 1200 W/m^2-K-s. As a result, all other emulsion phase conditions are assumed to be transient. This method of characterizing emulsion phase contacts was found to

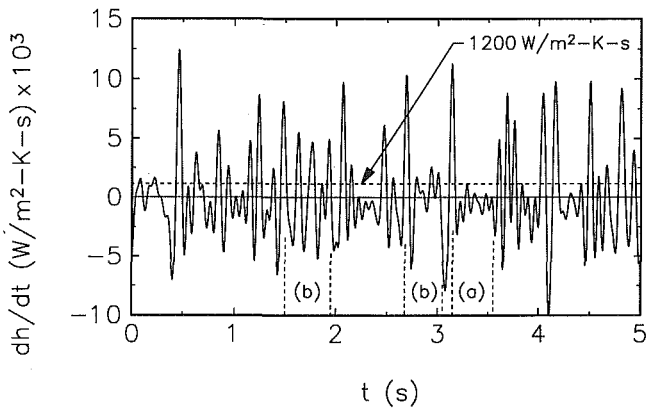

Fig. 5(*b*) Representative derivative of the heat transfer signal (from Fig. 5*a*) illustrating the criterion for evaluating steady-state contact

identify mixing and stationary contacts that were verifiable through direct comparison with individual signals. These signals were representative of the complete range of signals in the data. The sensitivity of the classification procedure to the threshold value for the derivative was investigated for values ranging from 600 W/m^2-K-s to 1800 W/m^2-K-s for each of the locations where surface renewal was observed to occur. Surface renewal occurred at 0, 45, and 90 deg locations. The fraction of time classified as mixing contact was calculated for each threshold value, and averaged for all the signals. The average change in mixing fraction for all signals was 11.5 percent for a change in the threshold value of 300 W/m^2-K-s. Further, this relationship was linear over the range investigated with an average slope (indicative of the sensitivity) of -1.38×10^{-2} (W/m^2-K-s)$^{-1}$. Also, a significantly larger standard deviation of the changes in mixing fraction resulted for a threshold of 900 W/m^2-K-s, as compared to a threshold of 1500 W/m^2-K-s. This result implies that individual contacts are more sensitive to decreases in threshold values below 1200 W/m^2-K-s. In summary, examination of signals and their derivatives clearly yields a candidate range of threshold values. The signal analysis algorithm has thus been shown to classify emulsion phase contacts accurately, without detrimental sensitivity to selection of the threshold value for the derivative.

Methods have been established for evaluating contact times from instantaneous signals and for classifying these contacts as steady-state or transient. Two parameters are required in these methods: h_{crit} and a threshold value of the derivative. Values of these parameters were established in the present study; however, further evaluation of these parameters is needed to confirm the general applicability of these values. In addition, average emulsion phase contact times were used as input to existing models and were found to yield predicted values that agree with the measured data to the extent generally expected for fluidized beds. As such, it is reasonable to conclude that the wide range of contact times observed in this study and by Ozkaynak and Chen (1980) may in fact include stationary and mixing particle behavior, and yet be characterized with typical accuracy by existing models. Further discussion of model comparisons will be made in the following section.

Results and Discussion

As previously discussed, transient contact times are required for determining both the transient emulsion phase fraction, f_t, and the mean heat transfer coefficient for the emulsion phase contacts exhibiting transient decay, $\bar{h}_t$. Results comparing the mean transient contact time, $\bar{\tau}_t$, to the mean steady-state contact time, $\bar{\tau}_s$, are shown in Fig. 6. In Fig. 7, results for the mean transient contact time, $\bar{\tau}_t$, are compared to the mean emulsion phase contact time, $\bar{\tau}_{avg}$. All contact times reported, including those in Figs. 6 and 7, are averaged for those angular positions experiencing surface renewal. For all three particle distributions, surface renewal did not occur at 135 and 180 deg from the stagnation point, resulting in infinite values of emulsion phase contact time at these angular positions. For this reason, only values for those azimuthal positions around the axis of the horizontal cylinder where bubble phase contact was found to exist, which include 0, 45, and 90 deg from the stagnation point, are presented and analyzed for contact dynamics. All contact time data are appropriately weighted average values for 0, 45, and 90 deg. Comprehensive uncertainty analyses were performed for values of emulsion, stationary and mixing contact times (Pence, 1992). The average uncertainty in these values is approximately 12 percent with a standard deviation of 8 percent. The 95 percent uncertainty intervals are provided on Figs. 6, 7, and 9.

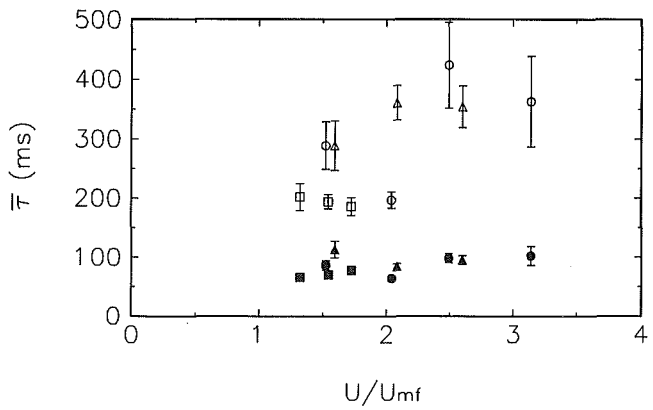

Fig. 6 Average transient and steady-state contact times as a function of fluidization velocity ratio; transient conditions: ● d_p = 256 μm, ▲ d_p = 340 μm, ■ d_p = 568 μm; steady-state conditions: ○ d_p = 256 μm, △ d_p = 340 μm, □ d_p = 568 μm

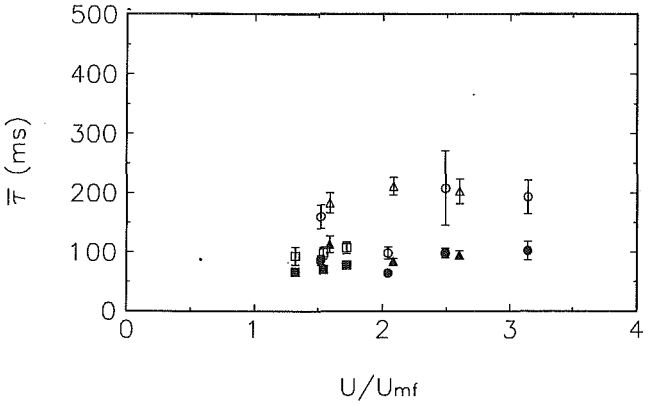

Fig. 7 Average transient and emulsion phase contact times as a function of fluidization velocity ratio; transient conditions: ● d_p = 256 μm, ▲ d_p = 340 μm, ■ d_p = 568 μm; emulsion phase: ○ d_p = 256 μm, △ d_p = 340 μm, □ d_p = 568 μm

Figure 6 shows that the mean contact times for the steady-state condition are far greater than those for the transient contacts. Figure 7 compares mean transient and emulsion phase contact times. The signals represented in these figures typically contained more transient emulsion phase contacts than steady state; the percentage of emulsion phase contacts exhibiting steady-state characteristics ranged from 10 to 50 percent with 20 to 30 percent as typical. However, because the steady-state contact times were very much longer than the transient, steady-state contacts significantly influence the average emulsion phase contact time. As previously discussed, the root-square average values of emulsion phase contact time are required in packet type models to yield appropriate predictions of mean values of heat transfer. Values of $\bar{\tau}_{avg}$ and $\bar{\tau}_{rsa}$ were calculated for the present data; mean emulsion phase contact times, $\bar{\tau}_{avg}$, or root-square average emulsion resident times, $\bar{\tau}_{rsa}$, as defined by Eq. (3) (Mickley et al., 1961), yield contact times in most instances that are much greater than the mean contact times for transient contact. Since significant percentages of the heat transfer signals are steady state in nature, and that portion of the signals for which the heat transfer decays in time has very short contact times, it is not clear that the root-square average value of contact time provides for more physically meaningful predictions of heat transfer. It is therefore desirable to develop a correlation to predict $\bar{\tau}_t$.

A correlation developed by Baskakov (1964), which provides a means for predicting emulsion phase contact times for vertical cylinders, was employed as the basis for correlating the present data. The general form of this correlation is

$$\tau = B\left[\frac{d_p g}{U_{mf}^2 (U/U_{mf} - A)^2}\right]^C \left(\frac{d_p}{D}\right)^{0.225} \quad (5)$$

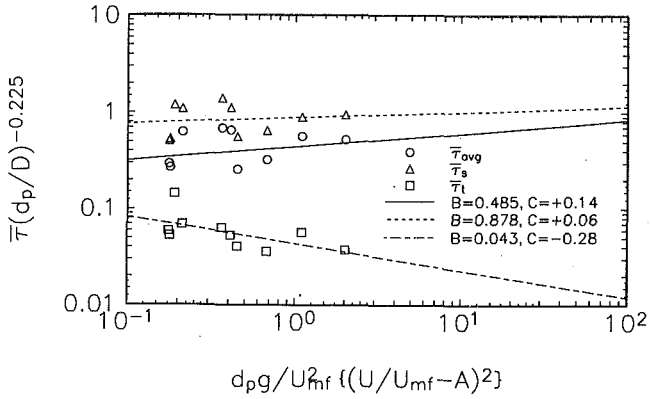

Fig. 8 Comparison of contact times with correlating equation (A = 0.8)

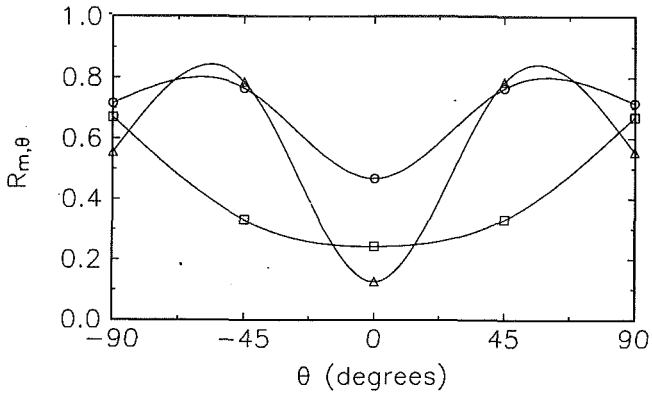

Fig. 10 Locally averaged mixing ratio variations with azimuthal angle for fluidization ratios of approximately 1.5; ○ d_p = 256 μm, △ d_p = 340 μm, □ d_p = 568 μm

where the values of A, B, and C are determined by performing a curve fit using experimental data. From the present experimental data for a horizontal cylinder, the values of the parameter A, coefficient B, and exponent C were determined to be 0.8, 0.485, and 0.143, respectively. These values were found to be remarkably similar to those obtained by Baskakov (1964) for a vertical cylinder, where the values of A, B, and C were found to be 0.8, 0.44 and 0.14, respectively. The resulting correlation proves to yield representative contact times for the emulsion phase. This same correlation was modified for predicting transient and steady-state contact times as well. Results of each curve fit along with experimental data are shown in Fig. 8. For the average value, $\bar{\tau}_{avg}$, the standard error of the fit is 0.18 seconds, with a resulting confidence interval of ±0.41 seconds.

Although potentially quite different, the mean transient and steady-state heat transfer coefficients, $\bar{h}_t$ and $\bar{h}_s$, respectively, were found to be within 10 percent of each other for the cases investigated. It is the large difference between the transient and steady-state contact times that accounts for this condition. Longer transient contact times than were observed in the present data would yield much lower values of the mean heat transfer coefficient. For the present experimental conditions, it would appear that dividing the particle phase heat transfer into two components, as in Eq. (4), would not be necessary. Still, accurate values of transient contact time would yield improved predictions from existing models of particle convection heat transfer. If there exist cases in which the transient contact is of the same order of magnitude as the steady-state, $\bar{h}_t$ and $\bar{h}_s$ would no longer be of the same value and the need for correlations or models for predicting their magnitudes, as well as fractional contributions, would be necessary. Therefore, further investigation is needed.

As for the other contributions in Eq. (4), it is evident that a correlation for predicting bubble fraction is also necessary for predicting the rate of heat transfer between an immersed object and a gas-fluidized bed. Baskakov (1964) developed the following correlation:

$$f_b = B\left[\frac{d_p g}{U_{mf}^2(U/U_{mf}-A)^2}\right]^C \tag{6}$$

for vertical cylinders. From the experimental data for a horizontal cylinder, the values of A, B, and C were determined to be 0.8, 0.323, and −0.05, respectively. Baskakov (1964) determined, for a vertical cylinder, values of these constants to be 0.8, 0.33, and −0.14. Both the correlations for vertical and horizontal cylinders, along with experimental data for a horizontal cylinder, are shown in Fig. 9. Values of U/U_{mf} for the data in this figure range from 1.0 to 3.1. Bubbles do not form at the surface of vertical cylinders below minimum fluidization velocity, although local bubble formation can occur at velocities below U_{mf} for a horizontal cylinder. Upon initial consideration, it appears that the form of the correlation is appropriate for horizontal as well as vertical cylinders, and upon verification with additional data points, could prove to be a reliable predictor for bubble fraction for horizontal submerged cylinders. Such data could be extended to examine local bubble fractions below minimum fluidization for horizontal cylinders.

The extensive nature of the present data allows variations in the local contact dynamics to be examined. Figure 10 shows the variation with angular position of the mixing ratio for a value of U/U_{mf} of approximately 1.5. This ratio is defined as

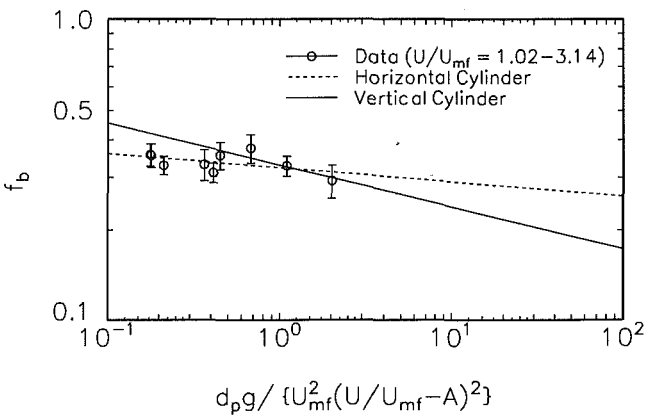

Fig. 9 Comparison of experimental bubble fraction with correlations

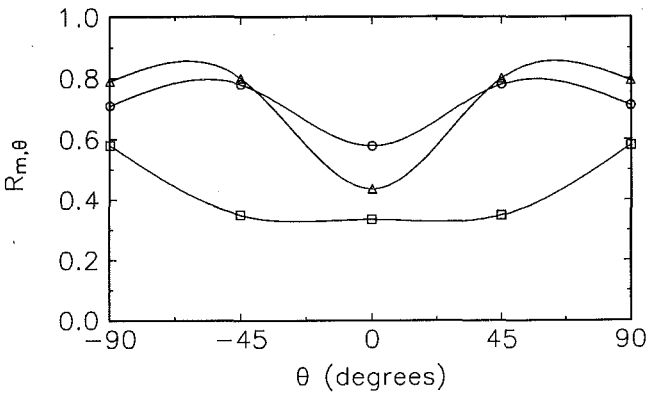

Fig. 11 Locally averaged mixing ratio variations with azimuthal angle for various fluidization ratios; ○ d_p = 256 μm (U/U_{mf} = 2.49), △ d_p = 340 μm (U/U_{mf} = 2.08), □ d_p = 568 μm (U/U_{mf} = 1.72)

$$R_m = \frac{\Sigma\, \bar{\tau}_m}{\Sigma\, \bar{\tau}_{\text{avg}}} \qquad (7)$$

Examining the two uniform particle sizes, 256 and 568 μm, shows drastically different fractions of the emulsion phase contact that are steady-state. The effect of the binary particle size distribution (340 μm) appears to magnify variations with angular position, especially at zero degrees (Fig. 10). A complete explanation of this behavior must await further understanding of the bed hydrodynamics. Figure 11 examines the mixing ratio for the maximum value of fluidization velocity tested for each particle size. The data presented in this figure and Fig. 10, and additional data examined by Pence (1992), seem to imply an increasing or constant mixing ratio with fluidization velocity, and less variation with angular position. The largest effect of fluidization velocity on mixing appears to occur at the stagnation point, zero degrees, while little effect of fluidization velocity is seen at the 45 deg location.

Variations in the locally averaged heat transfer coefficients with angular position are presented in Fig. 12. Data for each mean particle size, 256, 340, and 568 μm, acquired at an approximate fluidization ratio of 1.5, are shown. In the region of the cylinder experiencing surface renewal for the small, uniformly distributed particles and the binary mixture of particles, locally averaged steady-state heat transfer coefficients are slightly higher than their corresponding locally averaged transient heat transfer coefficients. This is also the case at 90 deg for the 568 μm uniform particles. However, at an angular position of 45 deg, the heat transfer coefficients for transient conditions are higher than those for mixing conditions, but the difference is close to the experimental uncertainty.

In addition to providing insight into the fundamental physics underlying emulsion phase contact, the present study also provides contact time data, which may be employed in modeling efforts. Figliola and Beasley (1993) propose a model for particle convection heat transfer that contains parameters that attempt to describe local contact variations and mixed particle size effects. The model predictions are a function of contact time, and predict a transient decay of the heat transfer coefficient similar to previous models based on the packet concept. A comparison between the model predictions and measured values from the present data is presented in Fig. 13 for 256 μm particles. Although the predicted values are reasonable, it is clear that opportunities to include more of the underlying physics in models exist. Angular variations in contact dynamics may not be appropriately represented by averaging contact times.

Conclusions

A method has been developed for distinguishing, from time accurate heat transfer data, transient and steady-state contacts in a bubbling gas-fluidized bed. These two types of emulsion phase contact dynamics can be successfully identified employing the first derivative of the heat transfer signal, and evaluating the number and magnitude of positive values of the derivative. Criteria for assigning a particular emulsion phase contact as steady-state were established for the present fluidization conditions. Two or more positive values of the first derivative having a magnitude greater than 1200 W/m^2-K-s were found to identify a steady-state contact; emulsion phase contacts that did not meet these criteria were characterized as transient.

Transient contacts, which result in transient decay of the local heat transfer coefficient, were found to be characterized by significantly shorter mean contact times than for steady-state conditions. This has significant implications for heat transfer models.

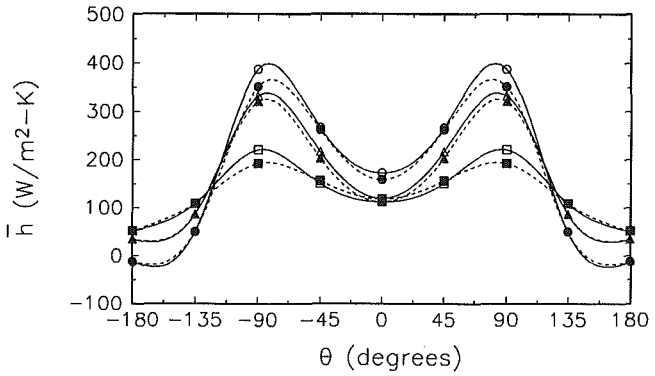

Fig. 12 Comparison of local time-averaged mixing and transient heat transfer coefficients as a function of azimuthal position (U/U_{mf} = 1.5); transient conditions: ● d_p = 256 μm, ▲ d_p = 340 μm, ■ d_p = 568 μm; steady-state conditions: ○ d_p = 256 μm, △ d_p = 340 μm, □ d_p = 568 μm

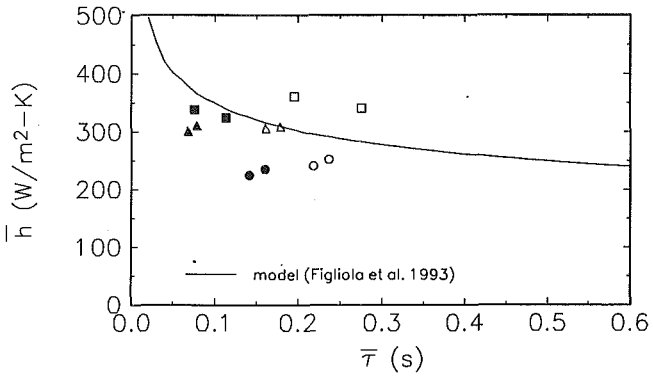

Fig. 13 Local time-averaged heat transfer coefficient variations with contact time for both particle convection and transient heat transfer (d_p = 256 μm and U/U_{mf} = 2.49); transient conditions: ● 0 deg, ▲ 45 deg, ■ 90 deg; particle convection: ○ 0 deg, △ 45 deg, □ 90 deg

References

Baskakov, A. P., 1964, "The Mechanism of Heat Transfer Between a Fluidized Bed and a Surface," *International Chemical Engineering,* Vol. 4, p. 320.

Baskakov, A. P., Berg, B. V., Vitt, O. K., Fillippovsky, N. F., Kirakosyan, V. A., Goldobin, J. M., and Maskaev, V. K., 1973, "Heat Transfer to Objects Immersed in Fluidized Beds," *Powder Technology,* Vol. 8, pp. 273–282.

Beasley, D. E., and Figliola, R. S., 1988, "A Generalized Analysis of a Local Heat Flux Probe," *J. Physics E: Sci. Instrum.,* Vol. 21, pp. 316–322.

Beasley, D. E., Figliola, R. S., Khan, J., and Chakravorty, M., 1987, "A Model for Particle Convection Heat Transfer in a Bubbling Fluidized Bed of Mixed Particle Sizes," ASME Paper No. 87-HT-40.

Chandran, R., and Chen, J. C., 1982, "Bed-Surface Contact Dynamics for Horizontal Tubes in Fluidized Beds," *AIChE Journal,* Vol. 28, pp. 907–914.

Chockalingam, S., 1985, "An Instrumented Cylinder to Measure Instantaneous Void Fraction in a Three-Dimensional, Gas Fluidized Bed," M.S. Thesis, Clemson University, Clemson, SC.

Decker, N. A., 1983, "Heat Transfer to Horizontal Tubes in Large Particle Gas-Fluidized Beds," Ph.D. Dissertation, MIT, Cambridge, MA.

Figliola, R. S., and Beasley, D. E., 1993, "A Study of the Particle Convection Contribution to Heat Transfer in Gas Fluidized Beds," *Chemical Engineering Science,* Vol. 48, No. 16, pp. 2901–2911.

Figliola, R. S., Swaminathan, M., and Beasley, D. E., 1993, "A Study of the Dynamic Response of a Local Heat Flux Probe," *Measurement Science and Technology,* Vol. 4, pp. 1052–1053.

Giedt, W. H., 1949, "Investigation of Variation of Point Unit Heat-Transfer Coefficient Around a Cylinder Normal to an Air Stream," *Trans. ASME,* Vol. 71, pp. 375–381.

Ginoux, J. J., De Geyter, F. M., and Kilkis, B., 1973, "Hydrodynamics of a Two-Dimensional Fluidized Bed in the Vicinity of a Cylinder With Horizontal Axis," *Congr. Int. Sur. La. Fluid,* pp. 274–282.

Koppel, L. B., Patel, R. D., and Holmes, J. T., 1966, "Statistical Models for Surface Renewal in Heat and Mass Transfer: Part I. Dependence of Average Transport Coefficients on Age Distribution," *AIChE Journal,* Vol. 12, pp. 941–946.

Kurosaki, Y., Ishiguro, H., and Takahashi, K., 1988, "Fluidization and Heat-Transfer Characteristics Around a Horizontal Heated Circular Cylinder Immersed in a Gas Fluidized Bed," *Int. J. Heat Mass Transfer,* Vol. 31, pp. 349–358.

Mickley, H. S., and Fairbanks, D. F., 1955, "Mechanism of Heat Transfer to Fluidized Beds," *AIChE Journal,* Vol. 1, pp. 374–384.

Mickley, H. S., Fairbanks, D. F., and Hawthorn, R. D., 1961, "The Relation Between the Transfer Coefficient and Thermal Fluctuations in Fluidized-Bed Heat Transfer," *Chem. Engng. Progress Symp. Series,* pp. 51–60.

Ozkaynak, T. F., and Chen, J. C., 1980, "Emulsion Phase Residence Time and Its Use in Heat Transfer Models in Fluidized Beds," *AIChE Journal*, Vol. 26, pp. 544–550.

Pence, D. V., 1992, "Heat Transfer and Surface Renewal Dynamics in Gas-Fluidized Beds," M.S. Thesis, Clemson University, Clemson, SC.

Saxena, S. C., Rao, N. S., and Zhou, S. J., 1990, "Fluidization Regime Delineation in Gas-Fluidized Beds," *AIChE Symposium Series Advances in Fluidization*, Vol. 86, No. 276, pp. 95–103.

Saxena, S. C., and Rao, N. S., 1991, "Determination of Fluidization Quality of Beds of Spherical Particles," *Energy*, Vol. 16, pp. 1199–1206.

Suarez, E. G., 1983, "Instantaneous, Azimuthal and Average Heat Transfer for a Horizontal Cylinder in a Mixed Particle Size Fluidized Bed," Ph.D. Dissertation, Clemson University, Clemson, SC.

Suarez, E. G., Figliola, R. S., and Pitts, D. R., 1983, "Instantaneous Heat Transfer Coefficients From a Horizontal Cylinder in a Mixed Particle Size Fluidized Bed," ASME Paper No. 83-HT-93.

Thermal and Mechanical Effects in the Spreading of a Liquid Film Due to a Change in the Apparent Finite Contact Angle

P. C. Wayner, Jr.
The Isermann Department of Chemical Engineering,
Rensselaer Polytechnic Institute,
Troy, NY 12180-3590

A new physical model for the spreading dynamics of fluids with an apparent finite contact angle on solid substrates is presented. The model is based on the premise that both interfacial intermolecular forces and temperature control change-of-phase heat transfer and (therefore) motion in the moving contact line region. Classical change-of-phase kinetics and interfacial concepts like the Kelvin–Clapeyron, Young–Dupre, and augmented Young–Laplace equations are used to compare the effects of stress (change in apparent dynamic contact angle) and temperature (superheat). Explicit equations are obtained for the velocity, heat flux, and superheat in the contact line region as a function of the change in the apparent contact angle. Comparisons with experimental data demonstrate that the resulting interfacial model of evaporation/condensation not only describes the "apparently isothermal" contact line movement in these systems at 20°C but also describes the substrate superheat at the critical heat flux.

Introduction

The spreading dynamics of fluids on solid substrates is important in such diverse processes as wetting, coating, soldering, lubrication, drying, and thin film change-of-phase heat transfer. Therefore, a simple physical model for contact line motion based on intermolecular forces would not only be useful in correlating heat transfer data but also lead to improvements in the understanding of the generic wetting process. Herein, we focus on interfacial physics and develop a change-of-phase heat transfer model for contact line motion where the vapor and liquid meet on a solid substrate. As discussed in the initial paper on the model by Wayner (1993), the proposed process obviates the infinite stress at this junction. Of more importance to heat transfer, both thermal and mechanical effects are included. The contact line velocity (which is directly related to the heat flux at the contact line) and the superheat are obtained as a function of an observable change in the dynamic apparent contact angle. A predictive equation for the substrate superheat at the critical heat flux is also obtained. Comparisons of theoretical predictions with experimental data from the literature for significantly different systems demonstrate the efficacy of the model.

The equilibrium vapor pressure of a liquid is a function of the temperature and pressure (negative of the stress) field at the liquid–vapor interface. This concept has been used to describe the change in vapor pressure of curved interfaces relative to that of a bulk fluid with a planar interface: For example, the increased vapor pressure at the surface of a small drop and the decreased vapor pressure associated with a meniscus have been discussed extensively in the literature (see, e.g., Wayner et al., 1976; Wayner, 1991). Swanson and Peterson (1993) and Khrustalev and Faghri (1993) have used these concepts to discuss a micro heat pipe. Holm and Goplen (1979), Xu and Carey (1990), and Stephan and Busse (1992) used them to analyze evaporation from a groove. Herein, we address the model of the contact line region presented in Fig. 1, which is composed of a curved film formed on a solid substrate. The model represents (initially) a partially wetting fluid–solid system, which has an apparent finite equilibrium contact angle in the range $0 < \theta_e < 90$ deg. However, in the detailed description of the *isothermal* contact line region given by Broeckhoff and deBoer (1968) and Wayner (1982), the real contact angle vanishes on the molecular scale at the contact line, i.e., $\theta \to 0$ where $\delta \to \delta_0$ and $K \to K_0$. Conceptually, this can be represented by the curved patches of average thickness δ_0 presented in Fig. 1. Therefore, both curvature (K) and thickness (δ) can affect the vapor pressure in the contact line region. This model of the profile is based on the Kelvin equation, which describes the effect of the pressure (stress) field on the equilibrium vapor pressure: In a partially wetting system at equilibrium, the vapor pressure increase due to a change in the stress field resulting from the close proximity of the solid substrate (thickness effect) is offset by a vapor pressure decrease due to capillarity (curvature effect). In essence, curvature and thickness describe the change in the stress field at the liquid–vapor interface relative to that at the surface of a pool of bulk liquid. It was used successfully to predict the effect of a forced change in the apparent contact angle on the spreading velocity in an "*isothermal*" system (Wayner, 1993). Briefly, a forced change in the apparent contact angle, $\theta_e \to \theta_d$, leads to condensation because of a curvature change near the contact line and, therefore, contact line motion. As a result, the change in apparent contact angle, which can be measured at a location away from the contact line, is related to the phase-change process near the contact line, which cannot be directly measured because of the small size of the region. A schematic drawing of this model is presented in Fig. 2. Although the partially wetting system is emphasized in the development, the results also apply to the completely wetting case, $\theta_e = 0$.

Herein, the isothermal model is extended to also include the effect of a nonisothermal temperature field on contact line dynamics case. A previous evaporation/condensation model based on the extended Kelvin equation addressed the steady state completely wetting case with evaporation (Wayner and Schonberg, 1992). We find that using a simple model based on kinetic theory and classical interfacial concepts like the Kelvin–Clapeyron, Young–Dupre, and augmented Young–Laplace equations, the velocity, superheat, and heat flux in the contact line region can be related to the change in the dynamic apparent contact angle. The effects of temperature and pressure can be directly compared.

Contributed by the Heat Transfer Division for publication in the JOURNAL OF HEAT TRANSFER. Manuscript received by the Heat Transfer Division June 1993; revision received January 1994. Keywords: Boiling, Condensation, Phase-Change Phenomena. Associate Technical Editor: V. K. Dhir.

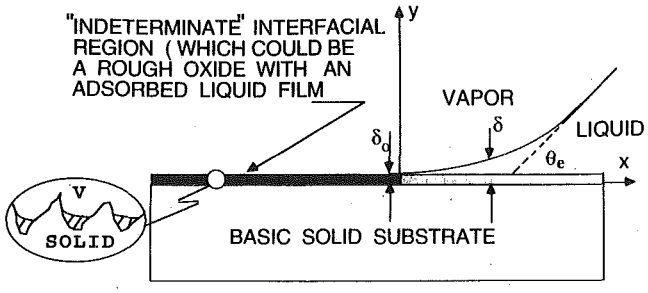

Fig. 1 Conceptual view of equilibrium contact line region with $\theta = 0$, $\delta = \delta_0$, and $K = K_0$ at the leading edge and $\theta \to \theta_e$ as δ increases and $K \to 0$. Additional details are given in Figs. 3 and 4 presented and discussed in the next section.

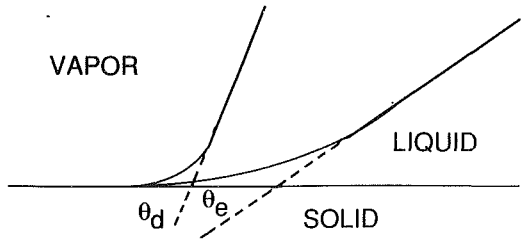

Fig. 2 Forced change in profile for nonequilibrium system represented by $\theta_e \to \theta_d$ with increase in curvature causing condensation. The resulting phase change, movement, and δ_0 are not shown.

Theoretical Development

The thermodynamic equation for the differential change in fugacity, f_l, with the temperature, T_l, and the pressure field, P_l, in the liquid at the liquid–vapor interface is (Wayner et al., 1976; Wayner, 1991)

$$d \ln f_l = \frac{dP_l}{\rho_{lM} R T_l} + \frac{H_{lv}^{id}}{R T_l^2} dT_l \tag{1}$$

in which ρ_{lM} is the molar density, H_{lv}^{id} is the "ideal" molar heat of evaporation, and R is the gas constant. For convenience, the fugacity, f_l, will be approximated subsequently by the equilibrium vapor pressure of the film, P_v.

For the pressure field, which is a function of the film profile, we assume that the following augmented Young–Laplace equation gives the change in the effective pressure in the liquid relative to the vapor pressure of a bulk liquid:

$$P_l = P_r - (\Pi + \sigma_{lv} K) \tag{2}$$

where P_r is the reference vapor pressure at the liquid–vapor interface at the reference temperature when $(\Pi + \sigma_{lv} K) = 0$, which represents a bulk liquid. P_l is the pressure in the liquid at the interface, Π is the disjoining pressure, which is a function of the film thickness, σ_{lv} is the liquid–vapor interfacial free energy, and K is the curvature of the liquid–vapor interface. Therefore, the vapor pressure is a function of both the thickness and temperature profiles.

Combining Eqs. (1) and (2) and integrating at constant liquid molar density between a reference state ($f = P_v$, $\Pi = 0$, $K = 0$, T_v) and a final state (P_{lv}, Π, K and T_{lv}) gives

$$\rho_{lM} R T_{lv} \ln \frac{P_{lv}}{P_v} = -(\Pi + \sigma_{lv} K) + \frac{\rho_{lM} H_{lv}^{id}}{T_v} (T_{lv} - T_v) \tag{3}$$

For the horizontal isothermal equilibrium case presented in Fig. 1, the equilibrium vapor pressure is constant for the contact line region in which the film thickness changes by a small amount. Therefore, with $P_{lv} = P_v$ and $T_{lv} = T_v$

$$\Pi + \sigma_{lv} K = 0, \quad P_{lv} = P_v \tag{4}$$

It is important to note that, in this equilibrium case, the reference vapor pressure is fixed by the closest liquid interface where both K and Π vanish. The disjoining pressure, Π, decreases rapidly as the film thickness increases. At this location, the thicker liquid with $K = 0$ has bulk liquid properties and its normal vapor pressure. Equation (4) is the augmented Young–Laplace equation for the equilibrium contact line region. It can also be viewed as an extended Kelvin equation for the isothermal equilibrium case and it fixes the relative value of the reference stress field in the liquid at 0.

Using Eqs. (5) and (6), Eq. (4) is expanded and nondimensionalized to obtain Eq. (7) for the dimensionless curvature, ψ, and Eq. (8) for the equilibrium case, ψ_e.

$$K = \frac{d^2\delta}{dx^2}\left(1 + \left(\frac{d\delta}{dx}\right)^2\right)^{-1.5}$$

$$\Pi = -\frac{\bar{A}}{\delta^3}, \quad \bar{A} = \frac{A_{ll} - A_{ls}}{6\pi} \tag{5}$$

Nomenclature

A = Hamaker constant
$\bar{A}$ = $A/(6\pi)$
a_1 = defined by Eq. (14)
a_2 = defined by Eq. (22)
a_3 = defined by Eq. (31)
b = defined by Eq. (6)
c = change in effective curvature, defined in Eq. (24)
C_1 = constant (evaporation coefficient)
f = fugacity
H = heat of vaporization
K = curvature
k = thermal conductivity
M = molecular weight
$\dot{M}$ = dimensionless mass flux, defined in Eq. (17)
$\dot{m}$ = interfacial mass flux
P = pressure
q = dimensionless slope
q'' = heat flux
R = gas constant
r = radius
T = temperature
t = time
U = velocity
x = parallel to flow direction
γ = dimensionless velocity, Eq. (21)
Δ = difference
$\Delta\tau$ = dimensionless temperature difference, Eq. (15)
δ = liquid film thickness
η = dimensionless film thickness
θ = contact angle
ξ = dimensionless position
Π = disjoining pressure
ρ = fluid density
σ = surface free energy per unit area
Φ = dimensionless chemical potential difference, Eq. (14)
Ψ = dimensionless curvature, Eq. (7)

Subscripts and Superscripts

d = dynamic value (evaluated at $\eta = 3$ herein)
$d\eta$ = local dynamic value at η
e = equilibrium
$e\eta$ = local equilibrium value at η
eff = effective
id = ideal
l = liquid
M = molar
m = unit mass
o = contact line
r = reference
s = solid
v = vapor
$'$ = derivative
η = at thickness η

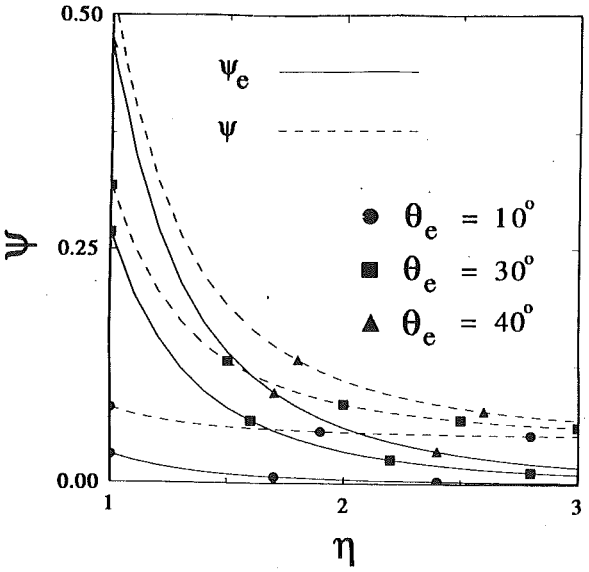

Fig. 3 Theoretical dimensionless curvature profile for equilibrium case, ψ_e, obtained using Eq. (8) with $b^{-1} = 2(1 - \cos\theta_e)$ and for the nonequilibrium case, ψ, obtained using Eq. (24) with $c = 0.05$. Symbols do not represent data.

where δ is the film thickness, $A_{ls} < A_{ll}$ are the Hamaker constants for the liquid–solid and liquid–liquid systems, respectively (the partial wetting case with a finite apparent contact angle is emphasized herein). Restrictions on the use of this simple model are discussed by Truong and Wayner (1987) for a completely wetting case.

$$x = \delta_0\xi, \quad \delta(x) = \delta_0\eta(\xi), \quad b = \sigma_{lv}\delta_0^2/\bar{A},$$

$$\frac{d\delta}{dx} = \frac{d\eta}{d\xi}, \quad \frac{d^2\delta}{dx^2} = \frac{d^2\eta}{\delta_0 d\xi^2} \tag{6}$$

$$\psi \equiv \left(1 + \left(\frac{d\eta}{d\xi}\right)^2\right)^{-1.5}\frac{d^2\eta}{d\xi^2} \tag{7}$$

in which the constant, δ_0, is a characteristic length of molecular size that is used as the thickness at the contact line. For simple systems, we find that it is equal to a "universal constant" for a "cut-off" distance used to calculate surface energies (see, e.g., Israelachvili, 1992).

$$\Psi_e = (b\eta^3)^{-1} \tag{8}$$

Ψ_e is the dimensionless isothermal equilibrium curvature, which is a function of dimensionless film thickness.

Using the substitution $q = d\eta/d\xi$ in Eq. (8) and the boundary conditions $\eta(0) = 1$ for the dimensionless thickness at the contact line and $q = \eta'(0) = 0$ for a zero slope at the contact line gives

$$\int_0^q \frac{qdq}{(1+q^2)^{1.5}} = \int_1^\eta \frac{d\eta}{b\eta^3} \tag{9}$$

Equation (9) has been integrated and discussed (Wayner, 1982, 1993) for constant "b" to obtain Eq. (10) for the cos $\theta_{e\eta}$ where $\theta_{e\eta}(\eta) = \arctan\delta'$ is the local angle at η.

$$\cos\theta_{e\eta} = 1 - \frac{1}{2b} + \frac{1}{2b\eta^2} \tag{10}$$

In the limit of "large" η, the last term on the right-hand side of Eq. (10) can be neglected and the Young–Dupre equation is obtained:

$$\sigma_{lv}\cos\theta_e = \sigma_{sv} - \sigma_{ls} \tag{11}$$

where the approximation $\sigma_{lv} = 2b(\sigma_{lv} - \sigma_{sv} + \sigma_{ls})$ has been used. It is important to note that the "transition region," where $1/2b\eta^2$ is important, is very small since the characteristic length is of molecular size. Although the effect of the assumption of a constant value for "b" on the details of the film profile has not been completely resolved, the final result agrees with the Young–Dupre equation and the observable apparent contact angle on the macroscopic scale. We find that the apparent contact angle is a measure of the stress field due to thickness and curvature in the contact line region. Equations (8) and (10) are presented in Figs. (3) and (4). The value of the constant, b, can be obtained using $b^{-1} = 2(1 - \cos\theta_e)$, which is Eq. (10) for large η.

From Eq. (8), the following equation can be obtained for the equilibrium curvature at the contact line, K_{e0}, where $\delta = \delta_0$:

$$K_{e0} = -\frac{\Pi_0}{\sigma_{lv}} = \frac{1}{b\delta_0} \tag{12}$$

Within the context of the extended Kelvin model, Eq. (12) suggests that the film of average thickness δ_0 in the region ahead of the contact line can be described as numerous small "curved patches" (which could be of molecular size): The reduction in vapor pressure due to "curvature" offsets the vapor pressure increase due to thickness (disjoining pressure). Since real surfaces are not perfectly flat at least at the molecular scale, these patches (or individual molecules in the limit of very small concentration) could fit in the "surface depressions." Conceivably, the contact line connects a series of depressions. Typical nanoscale pictures of molecularly smooth surfaces also suggest that, in the limit, adsorbed molecules can fit into the "spaces" in the surface plane. However, we note that the previous description might be only a consistent but extremely useful schematic view.

Using Eq. (7) and the definition of $b = \sigma_{lv}\delta_0^2/\bar{A}$, Eq. (3) can be rewritten for the nonisothermal case in dimensionless form as

$$\Phi = (b\eta^3)^{-1} - \Psi + \Delta\tau \tag{13}$$

in which

$$\Phi = a_1 \ln\frac{P_{lv}}{P_v}, \quad a_1 = \frac{\rho_{lM}RT_{lv}\delta_0}{\sigma_{lv}} \tag{14}$$

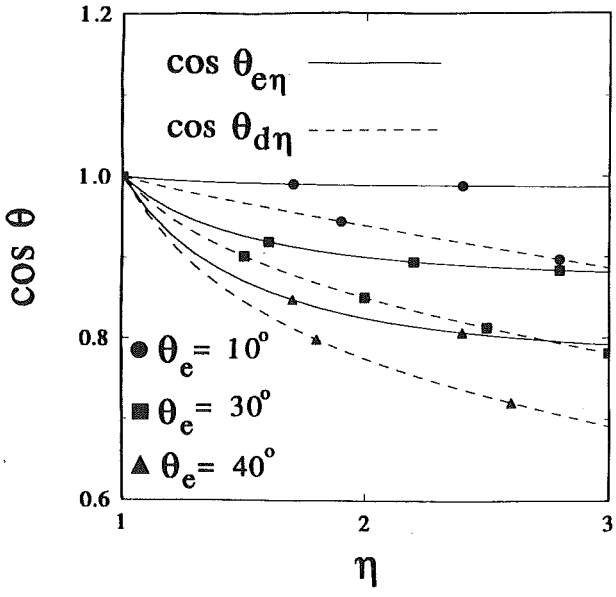

Fig. 4 Theoretical variation of cos (arc tan δ') for the equilibrium case, $\theta_{e\eta}$, obtained using Eq. (10) with $b^{-1} = 2(1 - \cos\theta_e)$ and for the nonequilibrium case, $\theta_{d\eta}$, obtained using Eq. (26) with $c = 0.05$. Symbols do not represent data.

and

$$\Delta\tau = \frac{H_{lv}^{id}\delta_0\rho_{lM}}{\sigma_{lv}T_v}(T_{lv} - T_v) \tag{15}$$

Therefore, the dimensionless chemical potential, Φ, is a function of the film shape (thickness and curvature) and temperature difference. For the partially wetting case, the vapor pressure is increased by a decrease in the thickness and an increase in the temperature. The thickness effect results from solid molecules, which have a lower force of attraction in the partial wetting case, replacing liquid molecules. To offset the temperature and thickness effects for equilibrium, $P_v = P_{lv}$, a positive curvature decreases the vapor pressure.

Using interfacial kinetic theory in the form of Eq. (16) to relate the net mass flux of matter crossing a liquid–vapor interface (Schrage, 1953) to the vapor pressure change from equilibrium in Eq. (14), $P_{lv} - P_v$, Eq. (17) is obtained for the nonequilibrium case:

$$\dot{m} = C_1\left(\frac{M}{2\pi RT_{lv}}\right)^{0.5}(P_{lv} - P_v) \tag{16}$$

where $\dot{m} < 0$ is the condensation flux, $\dot{M}$ is the dimensionless mass flux, and M is the molecular weight.

$$\Phi = a_1 \ln(1 + \dot{M}), \quad \dot{M} = \frac{\dot{m}}{P_v C_1}\left(\frac{2\pi RT_{lv}}{M}\right)^{0.5} \tag{17}$$

The velocity of the liquid–vapor interface due to phase change can be obtained from the condensation rate using the following procedure. Since the film profile is a function of time and position, $\delta(x, t)$, the interfacial velocity, U, at a particular film thickness ($d\delta = 0$) is

$$U = \left(\frac{\partial x}{\partial t}\right)_\delta = \frac{-\left(\frac{\partial \delta}{\partial t}\right)_x}{\left(\frac{\partial \delta}{\partial x}\right)_t} \tag{18}$$

Using Eqs. (18) and (19) for a condensation process, which is perpendicular to the interface, gives Eq. (20):

$$\frac{\left(\frac{\partial \delta}{\partial t}\right)_x}{\left(\frac{\partial \delta}{\partial x}\right)_t} = \frac{-\frac{\dot{m}}{\rho_l}\cos\theta_{d\eta}}{\tan\theta_{d\eta}} \tag{19}$$

$$U = \frac{\dot{m}}{\rho_l}(\cos\theta_{d\eta})(\cot\theta_{d\eta}) \tag{20}$$

The local horizontal velocity, U, can be a function of film thickness (because of $\theta_{d\eta}$) and $\dot{m}$. The local dynamic angle at η is $\theta_{d\eta} = \arctan\delta'$. Two cases will be discussed below: (I) the isothermal case with $\dot{m} = \text{const}$; and (II) the nonisothermal case (varying $\dot{m}$) with $U = \text{const}$. The comparison demonstrates the importance of heat transfer because Case (I) leads to an infinite velocity at $\delta = \delta_0$ whereas Case (II) has a finite velocity at $\delta = \delta_0$. In the isothermal Case (I) previously discussed by Wayner (1993), the infinite velocity at $\delta = \delta_0$ is a result of the isothermal assumption which gives $\dot{m} = \text{const}$ where $\theta_{d\eta} = 0$. For the nonisothermal case, U can be a constant because $\dot{m}$ is a function of both P and T. Therefore, due to a variation in the local temperature with position, $\dot{m}/\sin\theta_{d\eta}$ can have a finite value as $\theta_{d\eta} \to 0$ because $\dot{m} \to 0$. Combining Eqs. (17) and (20) gives the change in the dimensionless chemical potential in terms of the velocity:

$$\Phi = a_1 \ln(1 + \gamma), \quad \gamma = \frac{a_2 U}{C_1 \cos\theta_{d\eta}\cot\theta_{d\eta}} \tag{21}$$

with

$$a_2 = \frac{\rho_l}{P_v}\left(\frac{2\pi RT}{M}\right)^{0.5} \tag{22}$$

It is useful to rewrite Eq. (13) as Eq. (23) with the dimensionless shape (stress field) on the left-hand side:

$$\Psi - (b\eta^3)^{-1} = \Delta\tau - \Phi \tag{23}$$

In order to integrate Eq. (23) easily, we assume that the stress field over an extremely short distance at the contact line is a parameter with a constant value, c, relative to the reference value given by Eq. (4) and Eq. (8):

$$\Psi - (b\eta^3)^{-1} = c \tag{24}$$

We will find that this assumption leads to extremely useful results because, even though the stress field is a constant, both $\Delta\tau$ and ϕ can vary as $\Delta\tau = \phi + c$. The constant c in Eq. (24) is the value of the change in dimensionless curvature at η relative to the equilibrium curvature, which causes a change in the local vapor pressure at the liquid–vapor interface. As demonstrated by Eq. (8), the equilibrium curvature at η, Ψ_e, is equal to $(b\eta^3)^{-1}$. Therefore, we are assuming that condensation dominates and that viscous liquid flow can be neglected in this very small region. In essence, this is a two-region model: a "Kelvin–Clapeyron" region and a viscous flow region. A schematic of the model is presented in Fig. 5. The change-of-phase process in the Kelvin–Clapeyron region is assumed critical and dominates the process.

Using the same techniques outlined above [for Eqs. (8)–(10)] for integrating Eq. (24) gives Eq. (25) for the local dynamic angle, $\theta_{d\eta}$:

$$\cos\theta_{d\eta} = 1 - \frac{1}{2b} + \frac{1}{2b\eta^2} + c(1 - \eta) \tag{25}$$

Subtracting Eq. (25) from Eq. (10) for the same value of η gives

$$\cos\theta_{e\eta} - \cos\theta_{d\eta} = c(\eta - 1) \tag{26}$$

Therefore, the change in contact angle over $(\eta - 1)$ is a measure of the change in effective dimensionless curvature, $c = \Psi - \Psi_e$. Using Eq. (23), we find that

$$\cos\theta_{e\eta} - \cos\theta_{d\eta} = (\Delta\tau - \Phi)(\eta - 1) \tag{27}$$

This constant also represents the difference between the superheat and the change in the chemical potential, $c = \Delta\tau - \Phi$. Therefore, for a given constant, the local value of the change-of-phase mass flux is a function of the local superheat. For example, for $\dot{m} = 0$ ($\Phi = 0$), $\Delta\tau = c$.

For $\Delta\tau = 0$, $c > 0$ results in condensation ($U < 0$), and $c < 0$ results in evaporation ($U > 0$). If $\Delta\tau > c$, evaporation

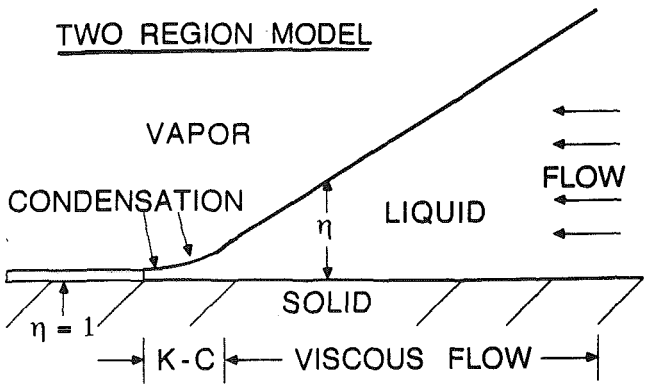

Fig. 5 Two-region model of contact line motion. Since viscous stresses increase rapidly as $\eta \to 1$, we focus only on the critical Kelvin–Clapeyron region, K–C, defined as $1 \le \eta \le 3$ with $\eta_d = 3$.

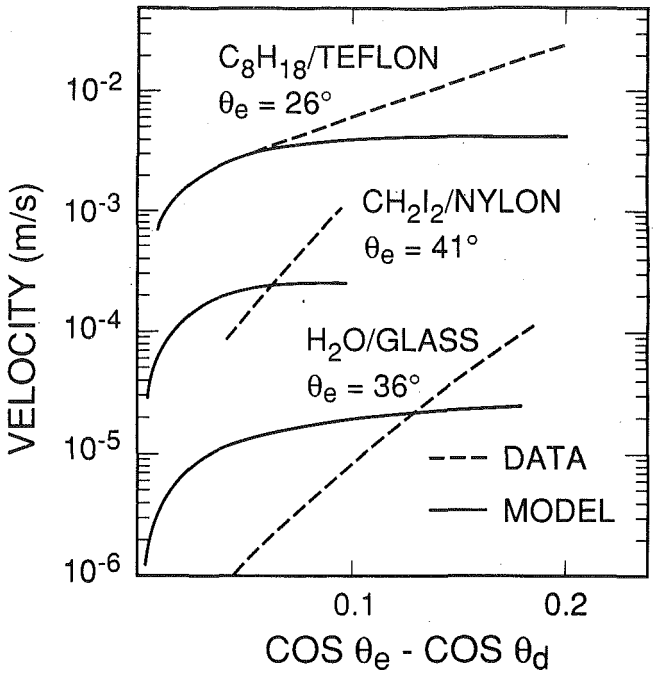

Fig. 6 Comparison of the absolute value of the velocity obtained using Eq. (28) with experimental data: octane on teflon and methylene–iodide on nylon obtained on flat surfaces by Schwartz and Tejada (1972); and the capillary rise of water in a dehydroxylated glass capillary obtained by Gribanova (1992).

occurs, and if $\Delta\tau < c$, condensation occurs. Using Eq. (26), values of the local dynamic angle, $\theta_{d\eta}$, for $c = 0.05$ are also presented in Fig. (4). Values for the local dynamic curvature, Ψ, obtained using Eq. (24) for $c = 0.05$ are presented in Fig. 3.

Equation (27) has many potential uses because it relates the observable change in apparent contact angle (which represents changes in the stress field) with the change-of-phase process, Φ, and the temperature difference, $\Delta\tau$, in the contact line region. However, because of some of the simplifying assumptions, the equation has to be applied carefully. For example, although we would expect the dynamic contact angle to be a function of position and therefore film thickness, the result presented in Eq. (27) is partially artificial because of the assumed constant stress field change in Eq. (24). This gives a constant curvature where $\Pi \to 0$, $K_{d\delta} = K_d$, which can be obtained using Eq. (24) and, if η is too large in Eq. (27), the change in θ is too large. However, we would expect that, in at least some real cases, both K and Π would vanish as the thickness increases where the value of the stress field decreases. Therefore, we assume a step change to $K_d = 0$ at the unknown position η_d where the contact angle reaches the apparent dynamic value θ_d. No additional change in slope occurs beyond this location in the current application of the model. This two-region model is presented in Fig. 5. The junction of the Kelvin–Clapeyron region, K–C, discussed herein and the viscous region is represented by the dimensionless thickness η_d. In addition, we note that, since viscous effects have not been included, these equations only evaluate the effect of phase change on contact line movement, thereby making it the controlling resistance to movement. Nevertheless, if we restrict the value of η to η_d and assume that the change $\Delta \cos\theta$ occurs over the dimensionless thickness change $(\eta - 1) = (\eta_d - 1)$, this result is found to be extremely useful below. In essence, viscous phenomena dominate fluid flow and interfacial velocity in the region $\eta > \eta_d$ and phase-change phenomena dominate interfacial velocity in the region $\eta < \eta_d$. Since for laminar flow, the pressure gradient is inversely proportional to η^3, we focus only on the more critical region $\eta < \eta_d$ where phase change precludes the large stress associated with the no-slip boundary condition in viscous liquid flow. Although the value of η_d is small but arbitrary, a value of $\eta_d = 3$ works well with experimental data.

Case I: Comparison of Isothermal Model With Velocity Data

Wayner (1993) compared the following isothermal form of Eqs. (21 and 27) with experimental data:

$$\cos\theta_e - \cos\theta_d = a_1(1 - \eta_d) \times \ln\left(1 + \frac{a_2 U}{C_1 \cos\theta_{d\eta} \cot\theta_d \eta}\right) \quad (28)$$

These results are re-presented in Fig. 6 because they evaluate the modeling and represent the critical isothermal foundation for the subsequent nonisothermal results. Experimentally, the contact line velocity is measured as a function of the change in the apparent contact angle for systems with known properties a_1 and a_2. Although the value of δ_0 could be difficult to estimate in some systems, values are readily available for simple systems like alkanes on teflon. The ratio $C_1/(1 - \eta_d)$ is an unknown. Since the evaporation coefficient, C_1, has a maximum ideal value of 2 and η_d, the distance over which the dynamic contact angle varies in Eq. (25), probably has an estimated value of approximately 3, we presume that this ratio has a constant value of approximately −1. This arbitrary choice is based on the assumption that the large decrease in resistance to liquid flow in the thicker region would not allow significant curvature in the relatively thick region $\eta > 3$. These values, and the assumption $\theta_{d\eta} = \theta_d$ at $\eta = 3$, were used with the following experimental data to evaluate the model: low-velocity spreading data for octane on teflon ($\theta_e = 26$ deg) and methylene–iodide on nylon ($\theta_e = 41$ deg) obtained on flat surfaces by Schwartz and Tejada (1972); and low-velocity data for the capillary rise of water in a cylindrical dehydroxylated glass capillary, which was initially equilibrated with water vapor for 6 hours ($\theta_e = 36$ deg) obtained by Gribanova (1992). As demonstrated by the large velocity range for the same values of $\Delta \cos\theta = \cos\theta_e - \cos\theta_d$, these data represent significantly different systems. The values for the important physical properties used in the comparison are given in Table 1. As demonstrated by the results in Table 1 and Fig. 6, the important product a_1a_2 organizes the data. Considering the large number of assumptions associated with the development of the model and the calculations, we believe that the results presented in Fig. 6 demonstrate the general validity of the model. The hard to find vapor pressure for CH_2I_2 was obtained from Kudchadker et al. (1979). The value of $\delta_0 = 0.16$ nm for octane–teflon was selected based on previous results in the literature on interfacial physics (Wayner, 1982; Israelachvili, 1992). The same value was used for methylene–iodide because of the presumed similarity of adsorption on the plastic substrate. The value of $\delta_0 = 5$ nm for water was selected based on the comments concerning experimental data on adsorption at 293 K by Gribanova (1992) and by Ershova et al. (1975). We note that these additional experimental data for the adsorption of water were necessary because a value of $\delta_0 = 0.16$ nm gave theoretical results that did not agree with the experimental data on velocity. We feel that this result confirms the importance of the details of the adsorption isotherm on con-

Table 1 Physical properties for Eqs. (31)–(33) evaluated at 293 K

System	P_v N/m^2	σ_{lv} x 10^3 N/m	δ_0 nm	a_2 s/m	a_1a_2 s/m	a_3 W/m^2
C_8H_{18}/Teflon	1,391	21.8	0.16	185	19	1.39 x 10^6
CH_2I_2/Nylon	97	51	0.16	3,241	115	
H_2O/Glass	2,327	73	5	395	3,665	6.95 x 10^6

tact line motion and adds insight. It is also important to note that highly polar water is not a "simple" fluid (as demonstrated by its adsorption isotherm) and we would not expect it to behave like a "simple" fluid (e.g., an alkane). No additional effort was necessary to obtain the correct velocity range in the comparison. However, since the values of C_1 and η_d are currently unknown functions of the spreading velocity, a more accurate tracking of the data is not possible with this simple method. Nevertheless, important microscopic modeling of the details of phase-change phenomena in the contact line region has been obtained. We note that the need for a constant $\dot{m}$ in the isothermal model is removed by $c = \Delta\tau - \Phi$ in the next section where numerical estimates of nonisothermal effects are addressed.

We find that the velocity is a function of $(a_1a_2)^{-1}$ and that Ua_1a_2 is a dimensionless velocity. This agrees qualitatively with additional data for water obtained at higher temperature by Gribanova (1992). However, the predicted velocity is found to be too large. Therefore, it appears that additional resistances to condensation at the liquid–vapor interface, vapor diffusion, and/or viscous flow in the liquid film are present at these higher fluxes. This is not surprising because of previously reported difficulties in measuring the ideal condensation coefficient at high fluxes and with water generally (Maa, 1983). To fit the data, nonconstant values of C_1 and η_d could be used. On the other hand, these results do demonstrate that sufficiently large velocities are theoretically justified with the model. The terms in brackets in Eq. (29) below give the percent change in vapor pressure: for the "isothermal" octane/teflon system, this is 23 percent for $\Delta \cos\theta = 0.054$; and 0.6 percent for water for $\Delta \cos\theta = 0.107$. Although the heat fluxes are large, the temperature differences are found to be small in the next section because the conduction path is of the order $10^{-8} - 10^{-9}$ m. Therefore, in hindsight, these results based on the "isothermal" model would agree with nonisothermal results obtained using this complete model because of the small value of $\Delta\tau$.

Case II: Comparison of Effects Due to Changes in Curvature and Superheat

The effects due to changes in both interfacial shape (change in apparent contact angle) and interfacial superheat (needed for the conduction of the heat of condensation-evaporation) on velocity and phase change heat transfer can be estimated using Eqs. (29) and (30), which were obtained using Eq. (21):

$$U = \frac{C_1 \cos\theta_{d\eta} \cot\theta_{d\eta}}{a_2}\left(\exp\frac{1}{a_1}(\Delta\tau - c) - 1\right) \quad (29)$$

$$q'' = C_1 a_3\left(\exp\frac{1}{a_1}(\Delta\tau - c) - 1\right) \quad (30)$$

in which,

$$a_3 = P_v H_{lvm}\left(\frac{M}{2\pi RT}\right)^{0.5} \quad \text{and} \quad c = \frac{\cos\theta_{e\eta} - \cos\theta_{d\eta}}{\eta - 1} \quad (31)$$

Since $\Delta\tau$ is the dimensionless superheat and c is the dimensionless curvature difference, Eqs. (29) and (30) have many uses. It is important to note that for constant c and a constant value of the velocity U, $\Delta\tau$ is a function of η because the product $\cos\theta_{d\eta} \cot\theta_{d\eta}$ varies with η. Therefore, the heat flux is also a function of η.

An estimate of the size of the thermal resistance can be obtained using the approximate model presented in Fig. 7. First, the velocity and equivalent heat flux, q'', are estimated using Eqs. (29) and (30) for a given value of $\Delta \cos\theta$ with $\Delta\tau = 0$. Then the approximate value for the dimensionless temperature difference, $\Delta\tau_{slv}$, is determined using Eq. (15) with $(T_{lv} - T_v)$ obtained from the following one-dimensional circumferential solution to the conduction equation in the liquid and the solid substrate:

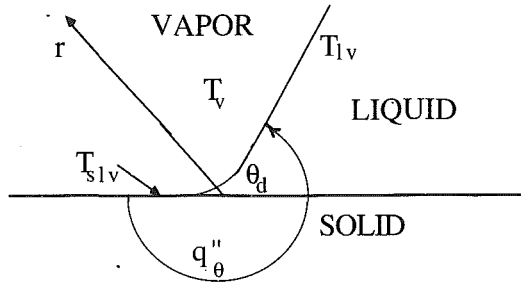

Fig. 7 Schematic of one-dimensional approximation of conduction

$$T_{slv} - T_v = q''_\theta r\left(\frac{\theta_d}{k_f} + \frac{\pi}{k_s}\right), \quad q''_\theta = -q'' \quad (32)$$

This is based on the premise that, in a pure system, the major thermal resistances are in the solid and liquid. We find that, for the "isothermal model" results presented previously, the additional temperature difference associated with local conduction is very small because the conduction path is very short in the immediate vicinity of the contact line. For water on glass with $r = 1$ nm, use of Eq. (32) gives $T_{slv} - T_v = 3.51 \times 10^{-9} q''_\theta$ for a heat flux in W/m^2. For the octane–teflon system, $T_{slv} - T_v = 1.37 \times 10^{-8} q''_\theta$. For example, using Eq. (30) for octane–teflon with $\Delta \cos\theta = 0.1$, $\eta = 3$, $C_1 = 2$, $a_3 = 1.39 \times 10^6$ W/m^2, $a_1 = 0.103$, and $\Delta\tau = 0$, gives $q'' = -1.07 \times 10^6$ w/m^2. Using Eq. (15) with $T_{slv} - T_v = 1.37 \times 10^{-8} q''_\theta$, gives $T_{slv} - T_v = 1.47 \times 10^{-2}$ K and $\Delta\tau_{slv} = 9.45 \times 10^{-5}$. Therefore, thermal (superheat) and mechanical (curvature change) effects can be compared using $\Delta\tau_{slv} = 9.45 \times 10^{-5}$ versus $\Delta \cos\theta/(\eta - 1) = 0.05$ in Eq. (30). These results demonstrate how a forced increase in the apparent contact angle causes condensation in the region $\eta < 3$, which results in a temperature increase at the solid–vapor interface, $T_{slv} - T_v$. Although the heat flux is of the order 10^6 W/m^2, we find that the additional temperature increase in the contact line region due to condensation is relatively small, approximately $T_{slv} - T_v = 1.47 \times 10^{-2}$ K. Therefore, the dimensionless temperature difference is relatively small compared to the dimensionless stress and the isothermal approximation for the velocity, Eq. (28), is accurate under ideal conditions for the velocities discussed above. In the next section, we look at the case where the thermal and stress effects are equal.

Discussion of $U = 0$ (Superheat at CHF)

Using Eq. (29) for a stationary contact line, $U = 0$, with Eq. (15) and $H^{id} = H$ gives

$$T_{lv} - T_v = \frac{\sigma_{lv} T_v c}{H_{lvm}\rho_l \delta_0} \quad (33)$$

Defining an average change in effective curvature as

$$\Delta K_{\text{eff}} = \frac{c}{\delta_0} \quad (34)$$

in Eq. (33) gives the following familiar looking equation:

$$T_{lv} - T_v = \frac{\sigma_{lv} T_v}{H_{lvm}\rho_l}\Delta K_{\text{eff}} \quad (35)$$

It differs from the classical equation for superheat in nucleate boiling since the liquid density appears instead of the vapor density: It is based on the Kelvin–Clapeyron equation instead of just the Clapeyron equation. This results from the use of a flat interface for the reference vapor pressure, which is also the constant vapor pressure in the vapor space for $U = 0$ (we note that ΔK_{eff} at the contact line is extremely large compared to the average value in the vapor bubble). In Eq. (35), the increase in vapor

pressure due to superheat is equal and opposite in sign to the decrease in vapor pressure due to interfacial forces resulting from the shape change. This can be related to the superheat at the critical heat flux, CHF, if we assume that CHF is caused by the inability of liquid to move across the substrate and rewet the surface, $U = 0$. Recently Unal et al. (1992) presented a discussion of the critical heat flux and quenching. They estimated that the critical liquid–solid contact temperature for water at the CHF was in the range 157–180°C. However, they also demonstrated that the surface temperature is nonuniform and estimated that the numerical value of the superheat at the junction of the dry patch and microlayer to be in the range 138–144°C.

Using Eq. (33) with the approximations ($\cos \theta_{e\eta} - \cos \theta_{d\eta}$) = 1, $\delta_0 = 1.6 \times 10^{-10}$ m, and $\eta = 3$ results in the predictions presented in Table 2 for the superheat at the critical heat flux (CHF). These results are found to be good estimates of experimental values in the literature, which are also presented and referenced in Table 2. Since there are (possibly) large additional effects due to cleanliness, roughness, and substrate preparation and shape, we feel that these initial comparisons also demonstrate the efficacy of this initial form of the proposed model. In addition, this description of superheat at CHF represents a consistent extension of past phenomenological ideas in interfacial physics. The values of σ_{lv}, H_{lvm} and ρ_l in Eq. (33) were evaluated at T_s. The values of δ_0 and η were chosen to be consistent with the values used and discussed in the calculations presented above. The values $\theta_d = 90$ deg and $\theta_e = 0$ were selected because a cylinder appears to approximate vapor columns near the CHF and, as discussed next, $\theta_e = 0$.

Since fluids with low surface tensions spread readily on oxide surfaces, we would expect that the fluids (except water) presented in Table 2 would have an "equilibrium contact angle," $\theta_e = 0$ as a reference for the superheats discussed in Table 2. Even though $\theta_e = 0$, the equations derived for $\theta_e > 0$ would apply to this case as presented. Water is potentially a more complicated situation. However, at the CHF, on a clean oxide surface, we would expect the value of the "equilibrium contact angle" to have a reference value sufficiently close to $\theta_e = 0$ so that the same approximate value of ΔK_{eff} is useful.

The exact solid–liquid temperature field could be obtained by a two-dimensional solution of the conduction problem, which is beyond the scope of this paper. Recently, Stephan and Busse (1992) used an initial simpler model presented by Wayner et al. (1976) and Holm and Goplen (1979) for a completely wetting system to add important two-dimensional details to the description of evaporation from a microgroove. Using this procedure, a further iteration on the solution presented herein could be obtained. This would also lead to a preliminary estimation of the effect of large temperature gradients on more complex flow fields like Marangoni flow. However, in summary, we feel that these additional concerns would not affect the basic conclusion: a model has been developed that directly relates contact line motion and heat flux to both changes in the stress field (due to a change in the apparent dynamic contact angle) and temperature (due to superheat).

Table 2 Comparison of theoretical superheat at CHF obtained using Eq. (33) with experimental data at approximately 1 atm from various references

Reference	Experimental	Eq. (33)
	K°	K°
H_2/copper Drayer and Timmerhaus (1962)	2	3.4
N_2/copper tube Flynn, Draper and Roos (1962)	10	10
N_2/copper flat (quenching) Peyayopanakul and Westwater (1978)	7	10
H_2O/aluminum flat CH_3OH/aluminum flat (quenching) Dhuga and Winterton (1986)	28 30	28 23
H_2O/copper flat, P = $9x10^4$ N/m^2 CH_3OH/copper flat, P = $9x10^4$ N/m^2 Wu, Ma, and Li (1982)	30 27	28 23
H_2O/copper Gaertner (1965)	44	28
C_5H_{12}/copper, lap E finish C_5H_{12}/copper, mirror finish Berenson (1962)	44 85	52 52
F113/nickle flat (horizontal) Auracher (1992)	47	45
F113/copper flat (vertical) Liaw and Dhir (1986)	35	45

Conclusions

1 A Kelvin–Clapeyron, change-of-phase, heat transfer model can be used to model contact line motion.
2 The spreading velocity of a fluid with an apparent finite contact angle is a function of both the temperature and the intermolecular stress fields in the contact line region.
3 The change in the apparent contact angle is a measure of the change in the intermolecular stress field.
4 The change-of-phase heat flux in the contact line region is a function of both the change in the apparent contact angle, which is a measure of the change in the intermolecular stress field, and the temperature field.
5 A Kelvin–Clapeyran, change-of-phase heat transfer model can be used to obtain an estimate of the substrate superheat at CHF.

Acknowledgment

This material is based on work supported by the National Science Foundation under grant # CTS-9123006. Any opinions, findings, and conclusions or recommendations expressed in this publication are those of the author and do not necessarily reflect the view of the NSF.

References

Auracher, H., 1992, "Transition Boiling in Natural Convection Systems," *Pool and External Flow Boiling*, V. K. Dhir and A. E. Bergles, eds., ASME, New York, pp. 219–236.

Berenson, P. J., 1962, "Experiments on Pool-Boiling Heat Transfer," *Int. J. Heat Mass Transfer*, Vol. 5, pp. 985–999.

Broekhoff, J. C. P., and de Boer, J. H., 1968, "Studies of Pore Systems in Catalysts XIV," *J. Catalysis*, Vol. 10, pp. 391–400.

Broekhoff, J. C. P., 1969, "Adsorption and Capillarity," Ph. D. Thesis, University of Technology, Delft, pp. 92–101.

Dhuga, D. S., and Winterton, R. H. S., 1986, "The Pool Boiling Curve and Liquid-Solid Contact," *Proceedings of the 1986 International Heat Transfer Conference*, Vol. 4, Hemisphere Publishing Corp., pp. 2055–2059.

Drayer, D. E., and Timmerhaus, K. D., 1962, "An Experimental Investigation of the Individual Boiling and Condensing Heat-Transfer Coefficients for Hydrogen," *Advances in Cryogenic Engineering*, K. D. Timmerhaus, ed., Plenum Press, Inc., New York, Vol. 7, pp. 401–412.

Ershova, I. F., Zorin, Z. M., and Churaev, N. V., 1975, *Kolloid Zh.*, Vol. 37, 190–192 [English translation].

Flynn, T. M., Draper, J. W., and Roos, J. J., 1962, "The Nucleate and Film Boiling Curve of Liquid Nitrogen at One Atmosphere," *Adv. Cryogenic Engineering*, K. D. Timmerhaus, ed., Plenum Press, Inc., New York, Vol. 7, pp. 539–545.

Gaertner, R. F., 1965, "Photographic Study of Nucleate Pool Boiling on a Horizontal Surface," ASME JOURNAL OF HEAT TRANSFER, Vol. 87, pp. 17–29.

Gribanova, E. V., 1992, "Dynamic Contact Angles: Temperature Dependence and the Influence of the State of the Adsorption Film," *Advances in Colloid and Interface Science*, Vol. 39, pp. 235–255.

Holm, F. W., and Goplen, S. P., 1979, "Heat Transfer in the Meniscus Thin-Film Region," ASME JOURNAL OF HEAT TRANSFER, Vol. 101, pp. 543–547.

Israelachvili, J., 1992, *Intermolecular and Surface Forces,* Academic Press Limited, London, pp. 201–209.

Khrustalev, D., and Faghri, A., 1993, "Thermal Analysis of a Micro Heat Pipe," personal communication concerning paper to be presented at 1993 National Heat Transfer Conference.

Kudchadker, A. P., Kudchadker, S. A., Shukla, R. P., and Patnaik, P. R., 1979, "Vapor Pressures and Boiling Points of Selected Halomethanes," *J. Phys. Chem. Ref. Data,* Vol. 8, pp. 499–517.

Liaw, S.-P., and Dhir, V. K., 1986, "Effect of Surface Wettability on Transition Boiling Heat Transfer From a Vertical Surface," *Proceedings of the Eighth International Heat Transfer Conference,* Hemisphere Publishing Corp., pp. 2031–2036.

Maa, J. R., 1983, "The Role of Interfaces in Heat Transfer Processes," *Advances in Colloid and Interface Science,* Vol. 18, pp. 227–280.

Peyayopanakul, W., and Westwater, J. W., 1978, "Evaluation of the Unsteady-State Quenching Method for Determining Boiling Curves," *Int. J. Heat Mass Transfer,* Vol. 21, pp. 1437–1445.

Schwartz, A. M., and Tejada, S. B., 1972, "Studies of Dynamic Contact Angles on Solids," *J. Colloid Interface Sci.,* Vol. 38, pp. 359–375.

Schrage, R. W., 1953, *A Theoretical Study of Interphase Mass Transfer,* Columbia University Press, New York.

Stephan, P. C., and Busse, C. A., 1992, "Analysis of the Heat Transfer Coefficient of Grooved Heat Pipe Evaporator Walls," *Int. J. Heat Mass Transfer,* Vol. 35, pp. 383–391.

Swanson, L. W., and Peterson, G. P., 1993, "The Interfacial Thermodynamics of the Capillary Structures in Micro Heat Pipes," personal communication concerning paper to be presented at 1993 National Heat Transfer Conference.

Truong, J. G., and Wayner, P. C., Jr., 1987, "Effects of Capillary and van der Waals Dispersion Forces on the Equilibrium Profile of a Wetting Liquid: Theory and Experiment," *J. Chem. Phys.,* Vol. 87, pp. 4180–4188.

Unal, C., Daw, V., and Nelson, R. A., 1992, "Unifying the Controlling Mechanisms for the Critical Heat Flux and Quenching: The Ability of Liquid to Contact the Hot Surface," ASME JOURNAL OF HEAT TRANSFER, Vol. 114, 972–982.

Wayner, P. C., Jr., Kao, Y. K., and LaCroix, L. V., 1976, "The Interline Heat Transfer Coefficients of an Evaporating Film," *Int. J. Heat Mass Transfer,* Vol. 19, pp. 487–492.

Wayner, P. C., Jr., 1982, "The Interfacial Profile in the Contact Line Region and the Young–Dupre Equation," *J. Colloid Interface Sci.,* Vol. 88, pp. 294–295.

Wayner, P. C., Jr., 1991, "The Effect of Interfacial Mass Transport on Flow in Thin Liquid Films," *Colloids and Surfaces,* Vol. 52, pp. 71–84.

Wayner, P. C., Jr., and Schonberg, J., 1992, "Spreading of a Liquid Film on a Substrate by the Evaporation-Adsorption Process," *J. Colloid Interface Sci.,* Vol. 152, pp. 507–520.

Wayner, P. C., Jr., 1993, "Spreading of a Liquid Film With a Finite Apparent Contact Angle by the Evaporation/Condensation Process," *Langmuir,* Vol. 9, pp. 294–299.

Wu, W.-G., Ma, T.-Z., and Li, H.-Q., 1982, "Experimental Study of Critical Heat Flux in Pool Boiling at Low Pressure," *Proceedings of the 1982 International Heat Transfer Conference,* Hemisphere Publishing Corp., Vol. 4, pp. 119–123.

Xu, X., and Carey, V. P., 1990, "Film Evaporation From a Micro-grooved Surface—An Approximate Heat Transfer Model and Its Comparison With Experimental Data," *J. Thermophysics,* Vol. 4, pp. 512–520.

Transient Heat and Moisture Transfer in Thin Silica Gel Beds

K. D. Kafui
Aston University,
Birmingham, United Kingdom

A numerical model has been developed to simulate the transport of heat and moisture in thin beds of microporous silica gel, assuming surface and pore volume diffusion of moisture and conduction of heat as the dominant intraparticle transport mechanisms in the desiccant. Predictions from the model have been compared with the results of single-blow tests for packed beds of silica gel from the literature and for a matrix of silica gel-coated parallel passages from this study. The model has been used to explore the significance of intraparticle diffusion resistance to heat and moisture transport in packed beds and parallel passage matrices of silica gel for different desiccant sizes and air velocities.

1 Introduction

A silica gel regenerative dehumidifier is a key component of Open-Cycle Desiccant Cooling Systems using solar and/or waste heat. Pressure drop constraints require the use of thin-bed dehumidifiers (<0.15 m thick) whose operation is transient and therefore cannot be designed using quasi-steady breakthrough methods. Research aimed at developing high-efficiency dehumidifiers also requires an understanding of the effects of heat and mass diffusion within the desiccant particles.

Current numerical models for the regenerative dehumidifier such as those of Maclaine-cross (1974), Holmberg (1979), and Mathiprakasam and Lavan (1980) either neglect intraparticle diffusion resistances or approximate them by using an overall convective transfer coefficient. There is, however, no reliable method of estimating an overall transfer coefficient that adequately models the complex intraparticle diffusion processes in microporous silica gel. The mechanism of surface diffusion plays a significant part in the transport of adsorbate within microporous silica gel. Pesaran's (1983) study of intraparticle transport of moisture in silica gel took into account both surface and pore volume diffusion but assumed uniform temperatures in the desiccant at any time. Large radial variations in water content were obtained across the desiccant particle and volume-averaged water contents were therefore employed in evaluating the heat of adsorption for energy conservation in the desiccant. In systems where the heat of adsorption is strongly dependent on the water content, this treatment can lead to significant errors.

The basic objective of this study is to develop and validate a numerical model to simulate the dynamic performance of thin packed beds and parallel passage matrices of silica gel for the general case where the desiccant temperature ($T_r(r, t)$) and water content ($W(r, t)$) vary both spatially and with time. The packed bed model is validated by comparing its predictions with the single-blow experimental results of Pesaran (1983), while the results of similar tests carried out in this study on the parallel passage matrix are compared with the equivalent model predictions. Using the validated models for various air flow rates, the study then seeks to establish desiccant particle size limits above which the resistance to moisture diffusion and heat conduction is significant.

2 Model

2.1 Assumptions. The following assumptions were made in formulating mathematical descriptions of the physical processes taking place in the bed or matrix:

(*i*) The bulk air stream contains only one adsorbable component, water vapor.
(*ii*) The time-variant bulk air state (temperature and humidity ratio) is uniform at any axial cross section of the bed.
(*iii*) Axial conduction and diffusion in the air stream are negligible compared to the bulk flow of heat and mass.
(*iv*) Direct particle-to-particle transfer of heat and mass is negligible compared to convective transfer.
(*v*) The desiccant particles are porous spheres of uniform diameter d_p with radially symmetric distributions of temperature, water content, and humidity ratio.
(*vi*) The adsorption process in the desiccant is adiabatic, reversible, and infinitely fast in comparison with the diffusion processes.
(*vii*) The mechanisms of pore volume diffusion and surface diffusion are not coupled.
(*viii*) The pressure drop across the bed is small compared with ambient pressure.

2.2 Packed Bed Equations. The transport of moisture from the bulk air stream into the particle takes place in four stages. A sectional view of a porous silica gel particle is illustrated with its network of pores and the steps involved in the transport of moisture into the interior of the particle in Fig. 1(*a*). In the first step, water vapor is transferred by convection from the bulk stream at humidity ratio w to the surface of the particle where the humidity ratio is w_{rs}. Unadsorbed water vapor is transferred in the pore volume by Knudsen diffusion into the interior of the particle, a process that is in series with the first step. Diffusion by Knudsen's molecular flow dominates in the pore volume since the mean free path of water molecules (~100 nm at atmospheric pressure) is considerably greater than the mean pore diameter of microporous silica gels (generally ≪ 10 nm). The water vapor is adsorbed on the surface of the pore walls in the third step with very fast and reversible kinetics. Finally, surface diffusion of the adsorbed water along the pore walls takes place in parallel with pore volume diffusion.

The total diffusive mass flux N_r at a radial location r in the desiccant particle can thus be written as

$$N_r = -D_{pe\rho} \frac{\partial w_r}{\partial r} - D_{se\rho_d} \frac{\partial W}{\partial r} \quad (1)$$

Note that adsorption can occur on the external surface of the desiccant and the adsorbed layer is subsequently transported by surface diffusion into the interior of the particle. For an element of thickness dr in which convective or bulk flow in the desiccant pore volume is assumed to be negligible, mass conservation requires that

Contributed by the Heat Transfer Division for publication in the JOURNAL OF HEAT TRANSFER. Manuscript received by the Heat Transfer Division August 1993; revision received January 1994. Keywords: Mass Transfer, Packed and Fluidized Beds, Transient and Unsteady Heat Transfer. Associate Technical Editor: R. Viskanta.

$$\epsilon_p \rho \frac{\partial w_r}{\partial t} + \rho_d \frac{\partial W}{\partial t} = \frac{\rho D_{pe}}{r^2} \frac{\partial}{\partial r}\left(r^2 \frac{\partial w_r}{\partial r}\right) + \frac{\rho_d D_{se}}{r^2} \frac{\partial}{\partial r}\left(r^2 \frac{\partial W}{\partial r}\right) \quad (2)$$

The corresponding energy conservation equation is

$$-H_s \rho_d \frac{\partial W}{\partial t} + \rho_d c_d \frac{\partial T_r}{\partial t} = k_d \frac{\partial^2 T_r}{\partial r^2} + \frac{2k_d}{r} \frac{\partial T_r}{\partial r} \quad (3)$$

Equations (2) and (3) are subject to the boundary conditions

$$k_d \frac{\partial T_r}{\partial r} = \begin{cases} 0 & \text{at } r = 0 \\ h_c(T - T_{rs}) & \text{at } r = r_p \end{cases} \quad (4)$$

$$D_{pe}\rho \frac{\partial w_r}{\partial r} + D_{se}\rho_d \frac{\partial W}{\partial r} = \begin{cases} 0 & \text{at } r = 0 \\ h_m \rho (w - w_{rs}) & \text{at } r = r_p \end{cases} \quad (5)$$

and the initial conditions

$$[T_r, W, w_r](r)(t = 0) = [T_{r0}, W_0, w_{r0}] \quad (6)$$

If the resistances to heat conduction and adsorbate diffusion in the desiccant particles are neglected, the mass and energy conservation equations result in

$$\rho_d \frac{\partial W}{\partial t} = \rho h_m a_s (w - w_{rs}) \quad (7)$$

$$\rho_d c_d \frac{\partial T_r}{\partial t} = h_c a_s (T - T_{rs}) + \rho_d H_s \frac{\partial W}{\partial t} \quad (8)$$

Equations (7) and (8) are of the same form as the "lumped capacitance" models in the literature, which modify the transport coefficients h_c and h_m to account for the resistances in the desiccant. In this study, air-side coefficients are used in these equations in order to assess the significance of the intraparticle resistances.

For an element dz of the bed at axial distance z from the entrance, mass and energy conservation in the fluid stream leads to

$$\frac{dw}{dz} = -\frac{a_v h_m}{\epsilon_b v}(w - w_{rs}) \quad (9)$$

$$\frac{dT}{dz} = \left(-\frac{a_v h_c}{\epsilon_b \rho v c_p} + \frac{c_{pv} a_v h_m}{\epsilon_b v c_p}(w - w_{rs})\right)(T - T_{rs}) \quad (10)$$

with an inlet fluid state of (T_i, w_i) at $z = 0$.

2.3 Parallel Passage Matrix Equations. The geometry of the parallel passage matrix used in the experimental program is shown in Fig. 1(b). A typical passage in such a matrix is approximated as shown in Fig. 1(c), where the desiccant coating is treated as a slab of thickness equal to the mean desiccant particle diameter. The mass and energy conservation equations in the desiccant for this case reduce to

$$\epsilon_p \rho \frac{\partial w_r}{\partial t} + \rho_d \frac{\partial W}{\partial t} = \rho D_{pe} \frac{\partial^2 w_r}{\partial r^2} + \rho_d D_{se} \frac{\partial^2 W}{\partial r^2} \quad (11)$$

$$-H_s \rho_d \frac{\partial W}{\partial t} + \rho_d c_d \frac{\partial T_r}{\partial t} = k_d \frac{\partial^2 T_r}{\partial r^2} \quad (12)$$

For this geometry, the distance r is taken from the carrier/desiccant interface and the boundary conditions, which are the same as for the packed bed (Eqs. (4) and (5)), apply at the carrier/desiccant ($r = 0$) and air/desiccant ($r = d_p$) interfaces. The initial condition in Eq. (6) is used here as well.

When the resistances to heat conduction and moisture diffusion in the desiccant are neglected, the mass and energy conservation equations are the same as given in Eqs. (7) and (8). The fluid stream conservation equations are also the same as derived for the packed bed (Eqs. (9) and (10)). The external surface area per unit volume with this approximation ($a_s \simeq 1/d_p$) is within 5 percent of the values derived from adsorption experiments (Van den Bulck, 1987).

2.4 Simplification and Numerical Solution of Equations. Assumption (*vi*) implies adsorption equilibrium exists in the pores and thus T_r, W, and w_r are related by the sorption equilibrium relation for silica gel. Equations (2) and (11) can therefore be written in terms of T_r and W and on substituting the independent dimensionless variables $\theta = t/T$ and $x = r/r_p$ ($= r/d_p$ for parallel passage matrix), the two sets of conservation equations (Eqs. (2), (3) and (11), (12)) in the desiccant become

$$\mathscr{A}_1 \frac{\partial W}{\partial \theta} + \mathscr{A}_2 \frac{\partial T_r}{\partial \theta} = \begin{cases} \dfrac{\mathscr{A}_3}{x^2} \dfrac{\partial}{\partial x}\left(x^2 \dfrac{\partial W}{\partial x}\right) & \text{(packed bed)} \\ \dfrac{\mathscr{A}_3}{4} \dfrac{\partial^2 W}{\partial x^2} & \text{(parallel passage matrix)} \end{cases} \quad (13)$$

Nomenclature

a_s = surface area per unit volume of desiccant particle, m^{-1}
a_v = external transfer area of desiccant per unit volume of packed bed or matrix, m^{-1}
Bi = Biot number = $h_c r_p/k_d$
c_d = specific heat capacity of desiccant, J/kg-K
c_{mi} = specific heat capacity of matrix i = 1, 2, 3; J/kg-K
c_p = specific heat capacity of moist air, J/kg-K (c_{pa}: dry air; c_{pv}: water vapor)
D_{pe} = effective pore volume diffusion coefficient, m^2/s
D_{se} = effective surface diffusion coefficient, m^2/s
D_w = molecular diffusion coefficient of water in air, m^2/s
d_p = mean desiccant particle diameter, m
H_s = heat of adsorption, J/kg
H_v = enthalpy of vaporisation of water, J/kg
h_c = convective heat transfer coefficient, W/m^2-K
h_m = convective mass transfer coefficient, m/s
k = thermal conductivity of moist air, W/m-K
k_d = thermal conductivity of desiccant, W/m-K
L = length of packed bed or matrix, m
M = molecular weight of water, kg/kmol
$\dot{m}$ = mass flow rate of air in packed bed or matrix, g/s
m_g = mass of silica gel in packed bed or matrix, kg
m_w = defined by Eq. (22), g/kg-m·s^{-1}
N_r = mass flux at radial distance r in the desiccant, kg/m^2-s
Nu = Nusselt number = $h_c d_p/k$
R = gas constant, J/kmol-K
r = radial distance in desiccant or distance from carrier in matrix, m
r_e = mean pore radius in desiccant, m
r_p = mean desiccant particle radius, m
Sh = Sherwood number = $h_m d_p/D_w$
ssr = intraparticle modeling indicator
T = air temperature at z, °C
T_K = absolute air temperature in desiccant pore, K
T_r = desiccant temperature at radius r, °C
t = time, s

$$\mathscr{B}_1 \frac{\partial W}{\partial \theta} + \mathscr{B}_2 \frac{\partial T_r}{\partial \theta} = \begin{cases} \dfrac{\mathscr{B}_3}{x^2} \dfrac{\partial}{\partial x}\left(x^2 \dfrac{\partial T_r}{\partial x}\right) & \text{(packed bed)} \\ \dfrac{\mathscr{B}_3}{4} \dfrac{\partial^2 T_r}{\partial x^2} & \text{(parallel passage matrix)} \end{cases} \quad (14)$$

with the initial conditions

$$[T_r, W](x)(\theta = 0) = [T_{r0}, W_0] \quad (15)$$

The boundary condition Eqs. (4) and (5) are reduced to

$$\frac{\partial T_r}{\partial x} = \begin{cases} 0 & \text{at } x = 0 \\ \text{Bi}(T - T_{rs}) & \text{at } x = 1 \end{cases} \quad (16)$$

$$\frac{\partial W}{\partial x} = \begin{cases} 0 & \text{at } x = 0 \\ -\gamma_1 \text{ Bi}(T - T_{rs}) + \gamma_2(w - w_{rs}) & \text{at } x = 1 \end{cases} \quad (17)$$

Equations (7) and (8), written in terms of θ, become

$$\frac{\partial W}{\partial \theta} = \beta_1(w - w_{rs}) \quad (18)$$

$$\frac{\partial T_r}{\partial \theta} = \beta_2(T - T_{rs}) + \beta_3(w - w_{rs}) \quad (19)$$

The fluid stream conservation Eqs. (9) and (10), with $y = z/L$, take the forms

$$\frac{\partial w}{\partial y} = -K_m(w - w_{rs}) \quad (20)$$

$$\frac{\partial T}{\partial y} = (-K_h + K_m\chi(w - w_{rs}))(T - T_{rs}) \quad (21)$$

In the numerical solution of the equations above, a predictor-corrector variant of the Crank–Nicolson finite difference scheme (Douglas and Jones, 1963) was used to discretize Eqs. (13) and (14). Equations (18) and (19) were discretized using first-order finite differences while the fluid stream Eqs. (20) and (21) were solved with a fourth-order Runge–Kutta scheme. In order to handle adequately the extremely steep initial temperature gradients, which require very small time steps, a nonuniform time grid was adopted following Holmberg (1979). The iterative solution technique, detailed by Kafui (1989), uses as a convergence criterion the condition that the results of consecutive iterations are within 0.01 percent of each other.

2.5 Properties. The thermophysical and sorption properties used in the models for regular density and microbead silica gel are summarized in Table 1. The heat of adsorption correlation for the microbead was obtained using the Clausius–Clapeyron equation and the Dubinin–Polanyi theory. The expression for the pore volume diffusion coefficient D_{pe} is based on Knudsen diffusion (Villet and Wilhem, 1961) while that for the surface diffusion coefficient D_{pe} is from Sladek et al. (1974). For both types of silica gel, a specific heat capacity (c_d) of 921.12 J/kg-K, a mean pore radius (r_e) of 1.1 nm, and a pore tortuosity factor (τ_p) of 3.35 were used. Correlations for h_c from Wakao et al. (1979) and h_m from Wakao and Funazkri (1978) were employed for the packed bed simulations. Using established parameters for fully developed laminar flow in an infinitely long parallel passage and pressure drops measured for the test matrices used here, the average Nusselt number Nu was found to be 8.141 and 8.294 for matrix A and B, respectively. Van den Bulck (1987) used the experimental outlet air state response as input to solve for Nu and Sh in a parallel passage and found values within 5 percent of the constant heat flux value of 8.235. The maximum deviations occurred in the entrance region where flow development and entrance effects are most severe. Thus for the parallel passage matrix, constant Nu and Sh values of 8.235 can justifiably be used to obtain the heat and mass transfer coefficients.

3 Experimental Method

Single-blow adsorption and desorption tests were carried out on the parallel passage matrices shown in Fig. 1(*b*) to provide data for comparison with the numerical models described earlier. The test matrices were obtained by winding 52-μm-thick double-sided adhesive polyester tape on an aluminum frame. The tape was then coated with 100 μm diameter microbead silica gel (Fuji-Davison grade 3A) by filling the passages with the desiccant. The results reported here are for two matrices with passage widths of 0.9 mm (A) and 2.0 mm (B).

The single-blow test rig, shown schematically in Fig. 2, consists of an air state generation section, a mixing loop, the test section, and the outlet section. The process air temperature and humidity were controlled with single-acting temperature and humidity controllers to within 0.1°C and ±2 percent, respectively, of the set values. The maximum estimated uncertainty in the humidity ratio measurements is less than 4 percent and that for the dry bulb temperature is less than 0.2°C. Error estimates for air

Nomenclature (cont.)

v = superficial air velocity in packed bed or matrix, m/s
W = water content of desiccant, kg of water/kg of dry desiccant
w = air humidity ratio in bulk stream, kg of vapor/kg of air
w_r = equilibrium air humidity ratio at T_r, W, kg of vapor/kg of air
x = r/r_p or r/d_p
y = z/L
z = axial distance in packed bed or matrix measured from inlet, m
ϵ_b = porosity of packed bed or matrix
ϵ_p = porosity of desiccant
θ = t/τ_0
ρ = density of moist air, kg/m^3
ρ_d = density of desiccant, kg/m^3
τ_0 = duration of single-blow test, s
τ_p = pore tortuosity factor
ϕ_r = relative humidity

$$\mathscr{A}_1 = \frac{\rho}{\tau_0}\left(\frac{\rho_d}{\rho} + \epsilon_p \frac{\partial w_r}{\partial W} + \frac{D_{pe}\rho_d H_s}{k_d}\frac{\partial w_r}{\partial T_r}\right)$$

$$\mathscr{A}_2 = \frac{\epsilon_p \rho}{\tau_0}\left(1 - \frac{D_{pe}\rho_d c_d}{\epsilon_p k_d}\right)\frac{\partial w_r}{\partial T_r}$$

$$\mathscr{A}_3 = \frac{1}{r_p^2}\left(D_{se}\rho_d + D_{pe}\rho \frac{\partial w_r}{\partial W}\right)$$

$$\mathscr{B}_1 = -\frac{\rho_d H_s}{\tau_0}$$

$$\mathscr{B}_2 = \frac{\rho_d c_d}{\tau_0}$$

$$\mathscr{B}_3 = \frac{k_d}{r_p^2}$$

$$K_h = \frac{La_v h_c}{\epsilon_b \rho v c_p}$$

$$K_m = \frac{La_v h_m}{\epsilon_b v}$$

$$\beta_1 = \frac{\tau_0 \rho h_m a_s}{\rho_d}$$

$$\beta_2 = \frac{\tau_0 h_c a_s}{\rho_d c_d}$$

$$\beta_3 = \frac{\tau_0 H_s \rho h_m a_s}{\rho_d c_d}$$

$$\gamma_1 = \frac{D_{pe}\rho}{r_p^2 \mathscr{A}_3}\frac{\partial w_r}{\partial T_r}$$

$$\gamma_2 = \frac{\rho h_m}{r_p \mathscr{A}_3}$$

$$\chi = \frac{c_{pv}}{c_{pa}}$$

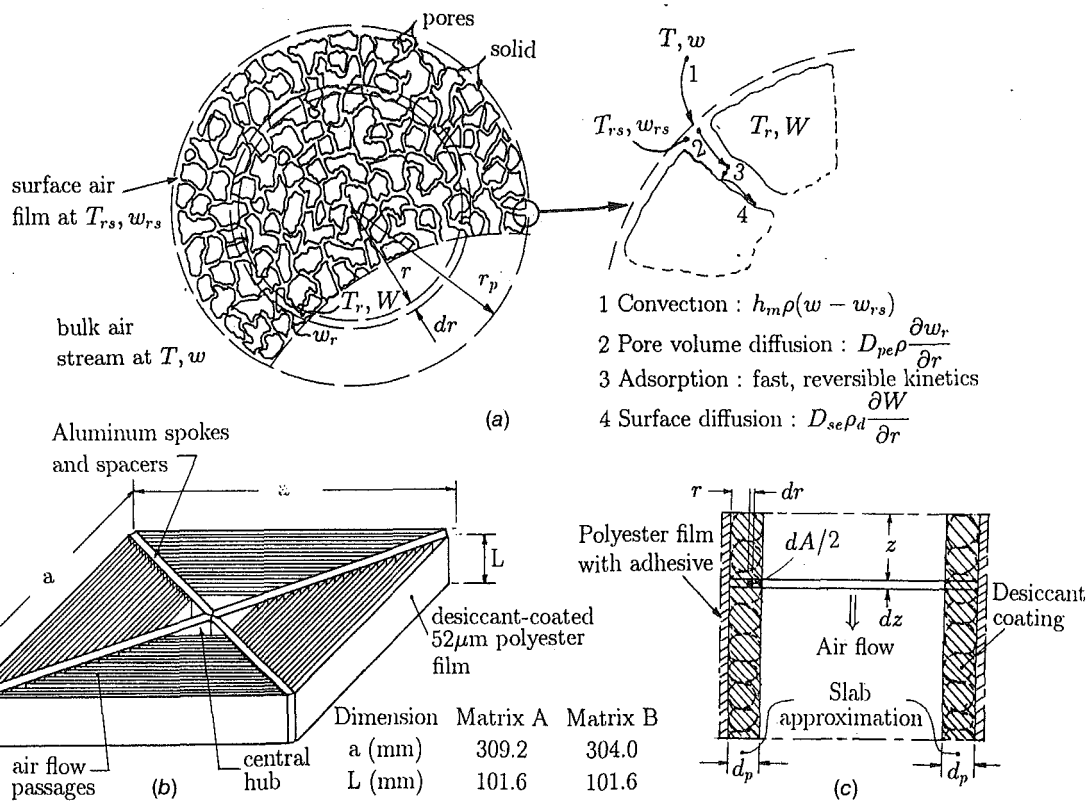

Fig. 1 Intraparticle mass transport, test matrix, and flow passage discretization

flow rate and pressure drop are within ±2 and ±4 percent, respectively.

In the tests, process air was prepared to the temperature and humidity controller settings during which stage the flow diverting valve was used to isolate the test chamber. The initial matrix state preparation was done in a forced convection oven maintained at a temperature close to the process air temperature in the test rig. The introduction of the matrix into the test chamber followed by the direction of the process air into the matrix marked the step change in inlet conditions and the commencement of each test. Inlet and outlet air temperatures and humidity ratios were recorded as a function of time.

Table 1 Thermophysical and sorption properties of silica gel

Property	Regular Density Silica Gel	Microbead Grade 3A Silica Gel
Particle porosity ε_p	0.453	0.301
Bulk density ρ_d	1200	1156.7
Adsorption Equilibrium Relation	$\phi_r = c_0 + c_1W + c_2W^2 + c_3W^3 + c_4W^4$	
c_i (i=0..4)	0.0078, -0.05759, 24.166, -124.78, 204.226	0.0, 0.534, 18.302, -82.877, 116.295
Heat of Adsorption H_s	$a - bW$	$H_v(1 + 0.3097e^{-8.8052W})$
$W < 0.05$	a=3500,b=-12400	-
$W \geq 0.05$	a=2950,b=-1400	-
Pore volume diffusion coefficient D_{pe}	$\frac{2}{3}\frac{\varepsilon_p}{\tau_p}r_e\left[\frac{8RT_K}{\pi M}\right]^{\frac{1}{2}}$	
Surface diffusion coefficient D_{se}	$1.6 \times 10^{-6}e^{-(0.0009742H_s/T_K)}$	
*Thermal conductivity k_d	$0.37 + 0.97W + 0.0014T_r$	

* (Bjurstroem et al. (1984))

4 Results and Discussion

Table 2 shows the conditions for two packed bed tests (1A, 25D) and two parallel passage matrix tests (P1A, P3B) to which the model predictions are compared in this section. In test 1A, the desiccant size d_p and bed length L were 3.88 mm and 0.0775 m and for test 25D, these were 5.20 mm and 0.050 m, respectively. In the simulations, ssr = 1 models diffusion and conduction resistances in the desiccant and uses Eqs. (13), (14), (20), (21) while ssr = 0 neglects these resistances and uses Eqs. (18)–(21).

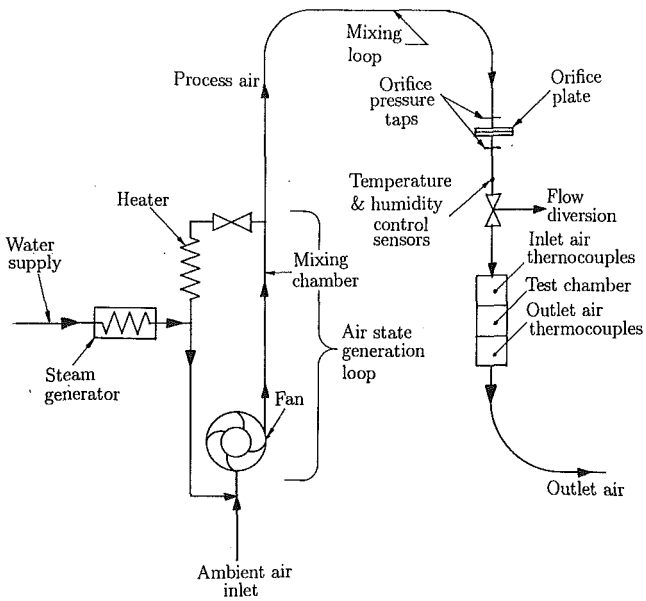

Fig. 2 Schematic diagram of single-blow test rig

Table 2 Single-blow test conditions

Test	Initial Matrix State		Inlet Air State		Air velocity	Duration
	T_{ro}	W_o	T_i	w_i	v	τ_o
1A	23.30	0.0417	23.30	0.01010	0.21	1800
25D	25.44	0.2600	25.44	0.00070	0.67	1200
P1A	35.32	0.07486	35.62	0.01603	1.304	631
P3B	38.02	0.13505	35.83	0.01899	1.443	421

4.1 Packed Bed Tests. The general trend in the predicted outlet air state is consistent with the measured values for both the packed bed and parallel passage matrix tests (Figs. 3*a*, *b*, 5, 6). For the adsorption tests, there is an initially sharp rise in both temperature and humidity ratio, the temperature curve reaching a maximum generally within $0.2\tau_0$ and then decreasing subsequently at a more gradual rate depending on the air flow rate. The initially high slope of the $w - \theta$ curve falls sharply just prior to the temperature peak, although the humidity ratio continues to rise slowly. The temperature rise in the outlet air results from the initially high rate of moisture extraction, which is accompanied by a high rate of heat of adsorption release into the air stream and the consequent heating up of the bed. As the adsorptive capacity of the desiccant bed falls, the rate of release of heat of adsorption falls leading to the peak in the temperature response curve. In the desorption tests, the trend is the inverse of what happens in the adsorption tests.

The outlet air state at or near $\theta = 0$ is strongly influenced by the state of the air in the bed at the start of the test and, as Fig. 3(*a*) for $\theta < 0.08$ suggests, the duration of this state may be prolonged by a low air velocity and a thicker desiccant bed. Beyond this region, the initially high adsorption on the external desiccant surface appears to control the adsorption response curves leading to the temperature peak. A region in the bed where the water content of the outermost parts of the desiccant is relatively high thus develops. This region expands from the inlet of the bed with time and its arrival at the bed outlet precipitates the sharp change in the slopes of the response curves. Figure 4, which illustrates the variation in these slopes ($dT/d\theta$, $dw/d\theta$) over the test duration for test 1A using $ssr = 1$, shows a drop in the $w - \theta$ response slope from 0.04 to 0.005 between $\theta = 0.10$ and $\theta = 0.15$. After the region of rapid change, a combination of intraparticle diffusion of adsorbed moisture and convection transfer at the desiccant surface controls the response curves. As Fig. 4 shows for $\theta > 0.2$, the slopes of the curves remain fairly constant in this region.

The good agreement between all three models in Figs. 3(*a*) and 3(*b*) prior to the sharp changes in the response curve slopes confirms that the controlling influence in this region is adsorption

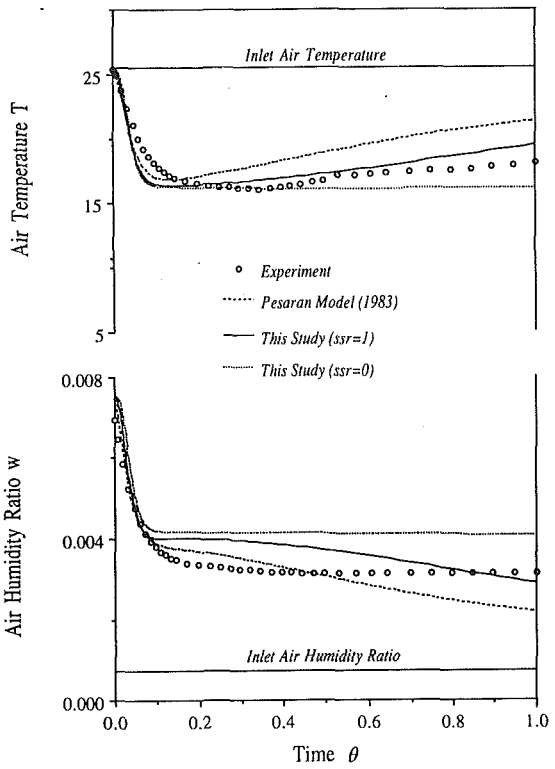

Fig. 3(*b*) Model predictions compared with experiment (Test 25D)

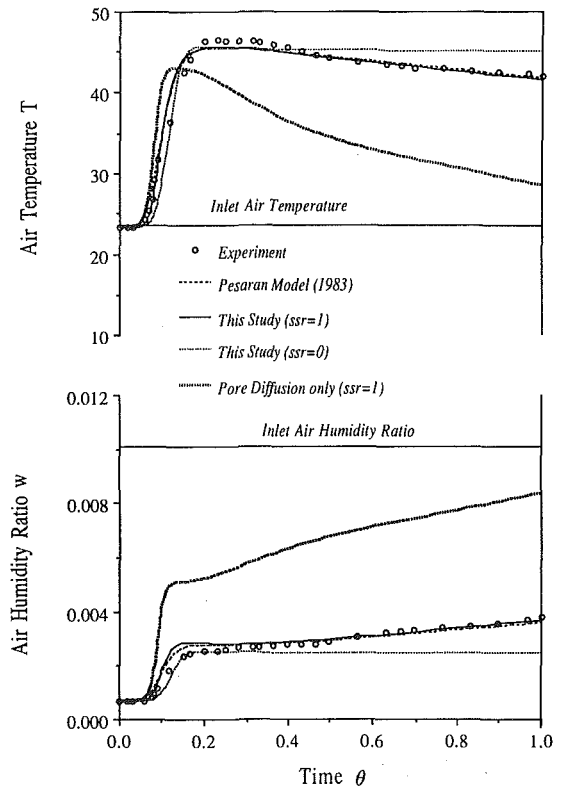

Fig. 3(*a*) Model predictions compared with experiment (Test 1A)

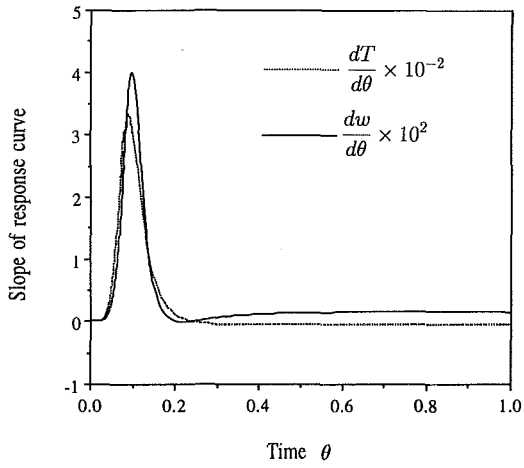

Fig. 4 Variation of response curve slope (Test 1A, *ssr* = 1)

on the external surface of the desiccant and not intraparticle diffusion. Beyond this region, the $ssr = 0$ simulation consistently overpredicts the amount of moisture extracted from (or added to) the air stream and consequently the air temperature. The model predictions, which account for intraparticle diffusion ($ssr = 1$ and Pesaran, 1983) agree better with the experimental results than the $ssr = 0$ model outside the rapid change zone, indicating the controlling influence of intraparticle diffusion here. In general, the $ssr = 1$ and Pesaran models were found to give comparable agreement with experiment for desiccant particle size $d_p \leq 3.88$ mm. For tests with $d_p = 5.20$ mm, the $ssr = 1$ model predictions were found to agree better with the experimental results. Convergence was achieved in fewer iterations with the $ssr = 1$ model than for the Pesaran model in all the simulations. The improved predictions given by the $ssr = 1$ model over the Pesaran model, especially for the larger desiccant particle size, is quite clearly attributable to the way the energy conservation equations are formulated in the two models.

An additional response curve is shown in Fig. 3(a), which illustrates the effect of neglecting surface diffusion. When pore diffusion is neglected, the effect on the $ssr = 1$ response curve is negligible. Similar results were obtained for simulations with $d_p = 5.20$ mm. Thus for microporous regular density silica gel of diameter d_p between 3.88 mm and 5.20 mm, surface diffusion is the dominant intraparticle moisture transport mechanism and pore volume diffusion may be neglected.

4.2 Parallel Passage Matrix Tests. In Figs. 5 and 6, predicted adsorption test response curves for matrices B and A, respectively, are compared with experimental results. Little or no difference was observed between the predicted curves for $ssr = 0$ and $ssr = 1$ as shown in Fig. 5, as well as for Fig. 6 in which only the $ssr = 1$ predictions are shown. This indicates that intraparticle diffusion resistances are insignificant for 100-μm-dia microbead silica gel under the parallel passage flow conditions employed in the tests. A reasonably good agreement is obtained between the predicted and measured response curves. The same trends were observed for the desorption tests for both matrices and the general shape of the response curves are the same as in the packed bed tests.

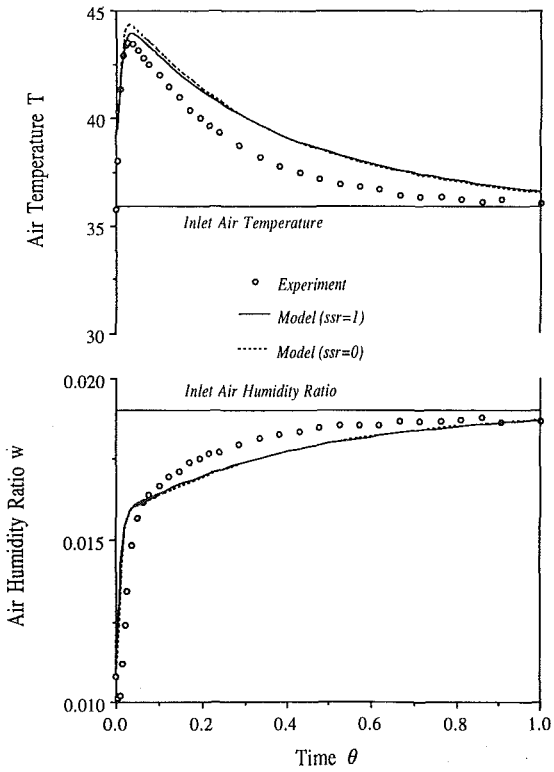

Fig. 5 Model predictions compared with experiment (Test P3B)

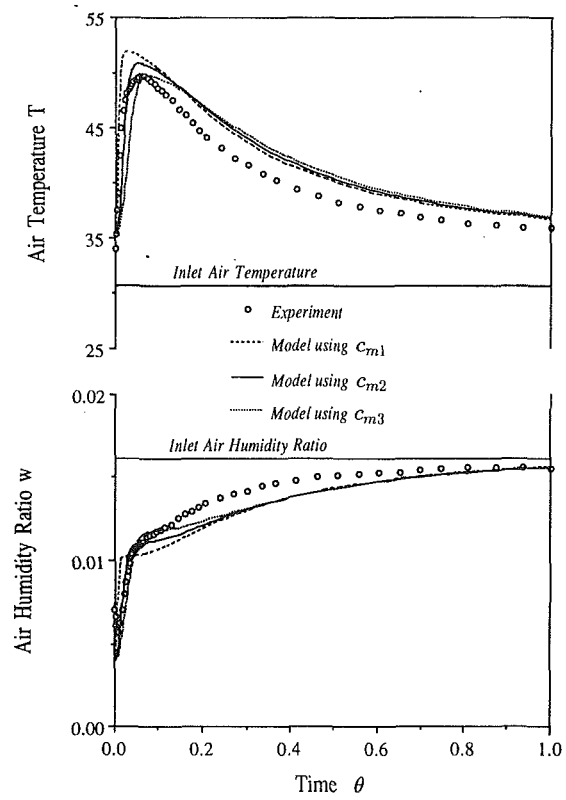

Fig. 6 Effect of matrix component thermal capacities on outlet air state predictions (Test P1A)

Although the test matrices consisted of three components (desiccant, carrier, and frame), the outlet air thermocouple sensors were located so as to minimize the effect of the frame on the outlet air state. The specific heat capacity used for matrix B in Fig. 5 is thus a weighted mean based on the masses of desiccant and carrier. The predicted response curves when the specific heat capacity of matrix A is based on the desiccant (c_{m1}) or desiccant and carrier (c_{m2}) or desiccant, carrier, and frame (c_{m3}) are compared with the measured response in Fig. 6 for test P1A. The significant difference between the three cases is in the slope of

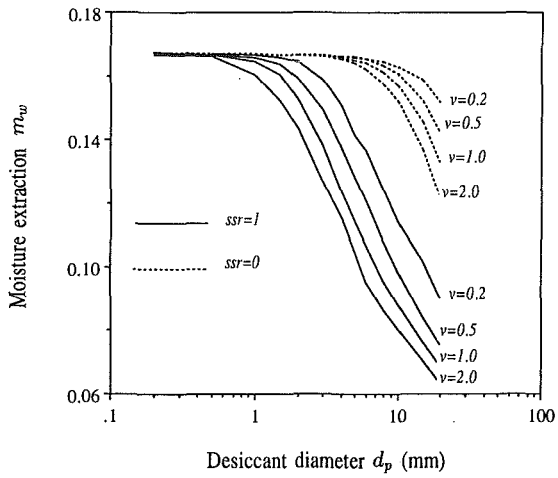

Fig. 7 Variation of packed bed moisture extraction with d_p for different air velocities v

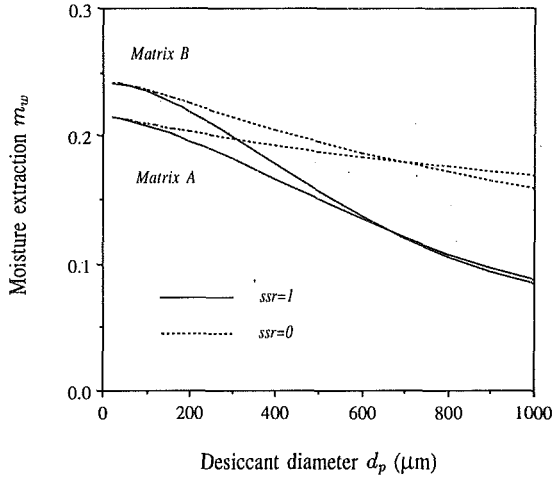

Fig. 8 Moisture extraction variation with d_p for matrices A and B at v = 1.304 m/s

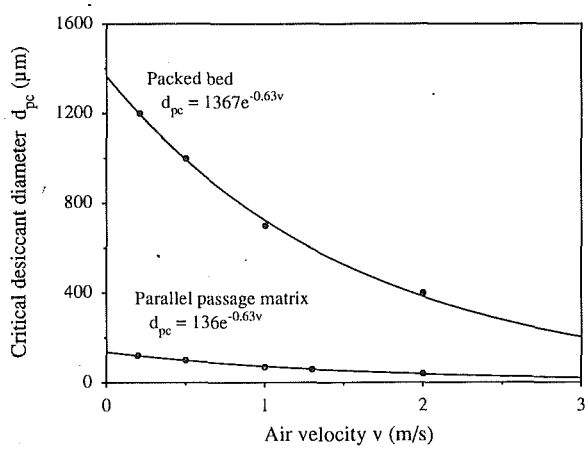

Fig. 10 Critical desiccant diameters d_{pc} for packed and parallel passage desiccant beds

the predicted curves in the adsorption controlled region, the higher specific heat capacity resulting in a lower slope. From $\theta \sim 0.25$, the three cases predict approximately the same outlet air state. In the adsorption-controlled region where the curves differ, the predictions that use c_{m2} give the best agreement with the measured response. This may be a direct result of the location of the thermocouples in the experiments. In a rotary desiccant dehumidifier where all the components are equally exposed to the outlet air state sensors, the use of c_{m3} may be more appropriate.

4.3 Effect of Varying Desiccant Size. Using test 1A conditions, several packed bed adsorption tests were simulated for desiccant particle diameters varying from 0.5 mm to 20.0 mm. The superficial air velocity affects moisture extraction directly through the residence time in the bed and indirectly through the dependence on v of the convective transfer coefficients h_c and h_m. The effect of intraparticle diffusion on moisture removal from (or addition to) the air stream for different desiccant sizes is thus expected to depend on the prevailing air flow conditions. The total moisture removed from the air stream in time τ_0, expressed as a ratio of the mass of desiccant in the bed m_g and the superficial air velocity v, is given by

$$m_w = \frac{1}{m_g v} \int_0^{\tau_0} \dot{m}(w_i - w)dt \qquad (22)$$

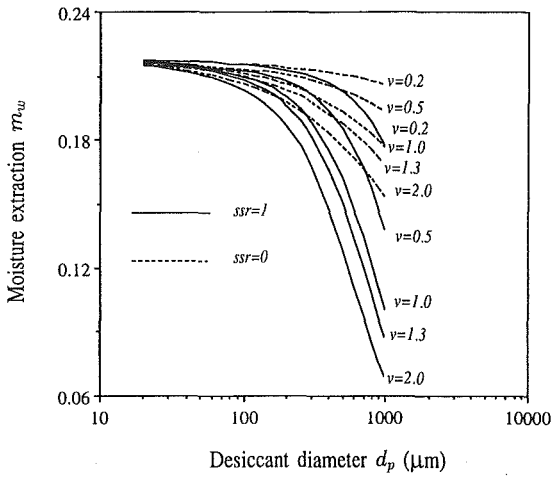

Fig. 9 Variation of matrix A moisture extraction with d_p for different air velocities v

The quantity m_w provides an indication of the sorption effectiveness of the bed. In order to compare this quantity at different air velocities as the desiccant diameter is varied, the value of τ_0 is varied such that the total quantity of air which flows through the bed in any simulation is the same as in test 1A. Figure 7 shows m_w (g/kg-m·s^{-1}) plotted against desiccant diameter d_p for air velocities of 0.2, 0.5, 1.0, and 2.0 m/s. The convergence of the $ssr = 1$ and $ssr = 0$ predictions at different d_p values as air velocity varies confirms the dependence of the effect of intraparticle diffusion on the bulk air flow conditions. As the air velocity increases, the critical desiccant diameter d_{pc} above which intraparticle diffusion resistance becomes significant is reduced.

A comparison of m_w for matrices A and B as d_p varies is shown in Fig. 8 for test P1A conditions. Matrix B quite clearly performs better than matrix A for $d_p \leq 650$ μm. The other significant feature of Fig. 8 is that the $ssr = 0$ and $ssr = 1$ predictions converge at the same d_p value for both matrices. Thus d_{pc} appears to be independent of the width of the parallel passages. Predictions of m_w for matrix A using test P1A conditions are shown in Fig. 9 for air velocities of 0.2, 0.5, 1.0, 1.3, 2.0 m/s as d_p varies from 20 to 1000 μm. The critical desiccant diameter d_{pc} varies with air velocity in a manner similar to that observed for the packed bed.

Figure 10 shows the critical desiccant diameter d_{pc} extracted from Figs. 7 and 9 plotted against air velocity v. The figure illustrates the dependence of d_{pc} on the air velocity v for both the packed bed and the parallel-passage matrix, which dependence, for the simulations of this study, has been found to fit a correlation of the form

$$d_{pc} = Ae^{-0.63v} \qquad (23)$$

The constant A is 1367.0 for the packed bed and 136.0 for the parallel passage matrices. For desiccant diameters $d_p > 1.37$ mm (packed bed) and $d_p > 136$ μm (parallel passage matrix), intraparticle diffusion resistances are significant irrespective of air flow rate.

5 Conclusions

A general numerical model for simulating transient heat and moisture transfer in thin silica gel beds has been presented and validated by comparing its predictions with single-blow sorption test results. Surface diffusion has been found to be the dominant intraparticle moisture transport mechanism in microporous silica gel. The critical desiccant diameter d_{pc} above which intraparticle resistances to heat and moisture transport become significant depends on the air velocity and differs for packed bed and parallel passage matrix configurations. In general, these resistances have to be taken into account for moisture sorption in microporous

silica gel diameters $d_p > 1.37$ mm in thin packed beds and for $d_p > 136$ μm in thin parallel passage matrices.

Acknowledgments

The author wishes to acknowledge the contributions of the late Mr. C. W. Ambrose, to whose memory this paper is dedicated, Mr. R. Gani of Monash University, Dr. J. G. van Leersum formerly of CSIRO, and Dr. I. L. Maclaine-cross of the University of New South Wales. Computing time was provided by the Monash University Computer Center and the Particle Technology Research Group at Aston University.

References

Bjurstroem, H., Karawacki, E., and Carlsson, B., 1984, "Thermal Conductivity of a Microporous Particulate Medium: Moist Silica Gel," *Int. J. Heat Mass Transfer,* Vol. 27, pp. 2025–2036.

Douglas, J., Jr., and Jones, B. F., Jr., 1963, "On Predictor-Corrector Methods for Nonlinear Parabolic Differential Equations," *J. SIAM,* Vol. 11, pp. 195–204.

Holmberg, R. B., 1979, "Combined Heat and Mass Transfer in Regenerators With Hygroscopic Materials," ASME JOURNAL OF HEAT TRANSFER, Vol. 101, pp. 205–210.

Kafui, K. D., 1989, "Heat and Mass Transfer in Regenerative Dehumidifiers—The Effects of Finite Intraparticle Diffusion Rates in Silica Gel," Ph.D. Thesis, Monash University, Melbourne, Australia.

Maclaine-cross, I. L., 1974, "Heat and Mass Transfer in Regenerators," Ph.D. Thesis, Monash University, Melbourne, Australia.

Mathiprakasam, B., and Lavan, Z., 1980, "Performance Predictions for Adiabatic Desiccant Dehumidifiers Using Linear Solutions," ASME JOURNAL OF HEAT TRANSFER, Vol. 102, pp. 72–79.

Pesaran, A. A., 1983, "Moisture Transport in Silica Gel Particle Beds," Ph.D. Thesis, School of Engineering and Applied Sciences, University of California, Los Angeles, CA.

Sladek, K. J., Gilliland, E. R., and Baddour, R. F., 1974, "Diffusion on Surfaces II: Correlation of Physically and Chemically Adsorbed Species," *Ind. Eng. Chem. Fundam.,* Vol. 13, pp. 100–105.

Van den Bulck, E., 1987, "Convective Heat and Mass Transfer in Compact Regenerative Dehumidifiers," Ph.D. Thesis, University of Wisconsin—Madison, Madison, WI.

Villet, R. H., and Wilhem, R. H., 1961, "Knudsen Flow—Diffusion in Porous Pellets," *Ind. Eng. Chem.,* Vol. 53, pp. 837–840.

Wakao, N., and Funazkri, T., 1978, "Effect of Fluid Dispersion Coefficients on Particle-to-Fluid Mass Transfer Coefficients in Packed Beds," *Chem. Eng. Sci.,* Vol. 33, pp. 1375–1384.

Wakao, N., Kaguei, S., and Funazkri, T., 1979, "Effect of Fluid Dispersion Coefficients on Particle-to-Fluid Heat Transfer Coefficients in Packed Beds," *Chem. Eng. Sci.,* Vol. 34, pp. 325–336.

H. Ban
Graduate Student.

S. Venkatesh[1]

K. Saito
Professor.

Combustion and Fire Research Laboratory,
Department of Mechanical Engineering,
University of Kentucky,
Lexington, KY 40506

Convection–Diffusion Controlled Laminar Micro Flames

Small laminar diffusion flames (flame height ≃2–3 mm) established by a fuel jet issuing into a quiescent medium are investigated. It was found that for these flames buoyancy effects disappeared as the flame size decreased ($Fr \gg 1$), and diffusive transport of the fuel was comparable to the convective transport of the fuel. The effect of buoyancy on these flames was studied by examining the flame shape for horizontally oriented burners. A phenomenological model was developed (based on experimentally determined flame shapes) to compare diffusion and convection transport effects. Finally, the flame shapes were theoretically determined by solving the conservation equations using similarity methods. It was seen that when the axial diffusion (in momentum and species equations) terms are included in the conservation equations, the calculated flame shape is in better agreement (as compared to without the axial diffusion term) with the experimentally measured flame shape.

Introduction

Studies on laminar hydrocarbon diffusion flames are always of interest because of their fundamental nature. Beginning with Faraday's pioneering work, "Chemical History of a Candle," in 1861, many studies have been conducted on this subject, and that there is still a need to study them was further established through recent observations by Ban et al. (1992), where small laminar diffusion flames (with flame heights of a few millimeters) were studied, by issuing a hydrocarbon fuel jet into a quiescent atmosphere. They found that the flame shape of these small flames is spherical and different from the more commonly observed candlelike laminar diffusion flames, and for sufficiently small flame sizes there were no buoyancy effects. These observations led to the current investigations on the physical characteristics of the small flames, since we were unable to find published literature on this class of flames. Experiments were conducted to collect data on the flame height and flame shape as a function of flow rate for three different fuels. It was found that the small flames have interesting characteristics that allow phenomenological evaluation of the effects of molecular diffusion, momentum, and buoyancy. In order to understand the physical characteristics better, we attempted to model the flame height and shape theoretically using similarity methods.

Based on past studies, laminar jet diffusion flames can be classified into two main types: the Burke-Schumann (1928) flame controlled by diffusion, and the Roper flame (1977) controlled by buoyancy. The small flames studied here have the following characteristics: $Fr \gg 1$ and $u_e \simeq u_D$, where u_e is the fuel exit velocity at the burner port, u_D is the characteristic molecular diffusion velocity, $Fr = u_e^2/gd$, and d is the burner port diameter. A scale analysis reveals that for $Fr \geq 1$, $u_e \simeq 0.1$ m/s, and $d \simeq 1$ mm, the buoyancy effects can be neglected (Williams, 1985). In addition, for small flames $u_e \simeq u_D$, implying they are convection–diffusion controlled.

In this paper we investigate: (1) the magnitude of diffusive transport in small laminar diffusion flames and its effect on the flame structure, and (2) the relative importance of buoyancy, molecular diffusion, and convection in small flames.

Experimental Methods

The flames were established on circular-port stainless-steel burners with inner diameters 0.15, 0.25, and 0.40 mm; the outer diameters were twice the inner diameters. Research grade ethane, ethylene, and acetylene were used as fuels. The flow rates of the fuels were calibrated using a specially designed soap-bubble flow meter capable of measuring low flow rates of the order 0.01 cc/s. The fuel was injected into the quiescent ambient at atmospheric conditions. The flame shape was recorded by a 35 mm still camera in a color slide film, which was projected in a large screen. From the magnified image, dimensions of the flame were measured using the technique developed by Saito et al. (1986).

Experimental Results and Discussion

The diffusion flames observed were laminar (Re = 1–10). The visible flame shapes for ethane, ethylene, and acetylene are shown by tracing them from the recorded photographs (Figs. 1–3). It can be seen from the figure that the flame height increases with increasing fuel exit velocity; as the flame becomes larger, it becomes spherical and part of it goes below the burner port. On further increasing the fuel exit velocity, however, the spherical shape disappears, and results in a flame shape typical of a momentum-controlled (high Re number) jet diffusion flame. The spherical flame occurs when the ratio of the mean exit velocity, u_e (flow rate/burner port area), to the diffusion velocity, $u_D = D/l_D$ (D is the mass-diffusion coefficient, and l_D is a characteristic diffusion length in the flame), is less than 5 ($Pe = u_e/u_D = u_e l_D/D$). This implies that the molecular-diffusion velocity is comparable to the convective velocity of the fuel, and analogous to point-source diffusion, a spherical concentration distribution of the fuel is attained. For very low exit velocities, however, a spherical flame was not established due to larger burner-wall heat loss effects. Our recent burner port heat-up tests proved that l_D remains the same regardless of the heating up to 500 K.

The effect of buoyancy may be estimated by rotating the burner to a horizontal position and observing the flame shape; the flame shapes for ethylene and acetylene are shown in Fig. 4. As the flame size increases (u_e increases), buoyancy effects increase, and therefore, the flame tends to tilt upward. For flames with $Fr = 10–10^3$, however, the buoyancy effect is minor.

A schematic of a low Peclet number (Pe) flame is shown in Fig. 5. The height of the flame, a, and the width of the flame, b, can be described as:

$$a = (u_e + u_D)t_1 \quad (1)$$

$$b = 2u_D t_1 + d \quad (2)$$

[1] Present address: Acurex Environmental Corp., Jefferson, AR 72079.

Contributed by the Heat Transfer Division for publication in the JOURNAL OF HEAT TRANSFER. Manuscript received by the Heat Transfer Division April 1993; revision received November 1993. Keywords: Combustion, Fire/Flames, Reacting Flows. Associate Technical Editor: W. L. Grosshandler.

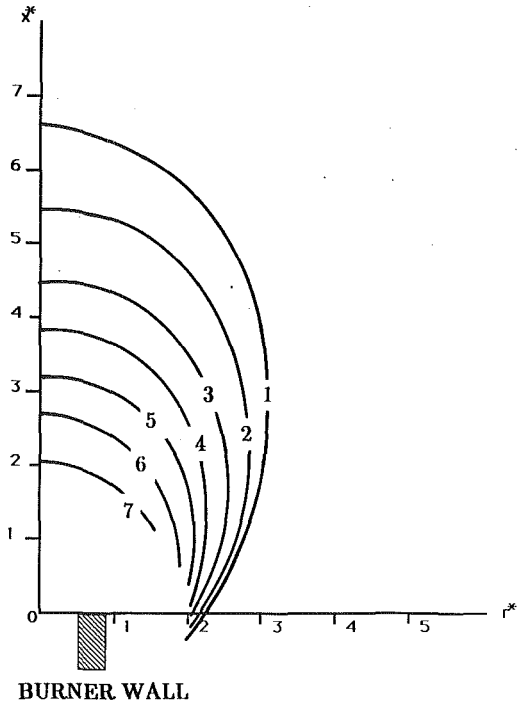

Fig. 1 Photographically measured visible flame sheet with C_2H_6 as fuel: (1) u_e = 1.1 m/s; (2) u_e = 0.926 m/s; (3) u_e = 0.726 m/s; (4) u_e = 0.601 m/s; (5) u_e = 0.486 m/s; (6) u_e = 0.387 m/s; (7) u_e = 0.246 m/s; burner port diameter d = 0.406 mm

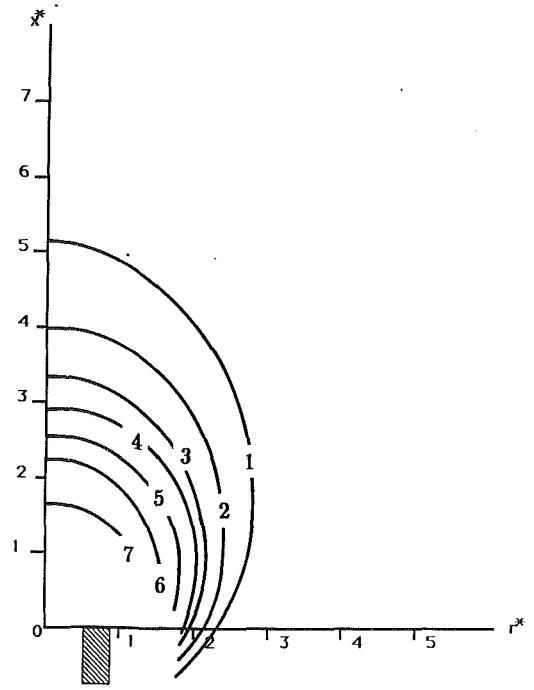

Fig. 2 Photographically measured visible flame sheet with C_2H_4 as fuel: (1) u_e = 0.923 m/s; (2) u_e = 0.726 m/s; (3) u_e = 0.582 m/s; (4) u_e = 0.477 m/s; (5) u_e = 0.396 m/s; (6) u_e = 0.332 m/s; (7) u_e = 0.195 m/s; burner port diameter d = 0.406 mm

where t_1 = the characteristic time of travel from the burner exit to the flame sheet. Combining Eqs. (1) and (2) and using $u_D = D/l_D$, we can eliminate t_1 and obtain the expression

$$a = \frac{(b-d)}{2}[1 + u_e l_D/D] \tag{3}$$

The characteristic diffusion length, l_D, is also shown in Fig. 5. Based on Figs. 1–3, the values of a and b were determined for the various fuels and flow conditions, from which the Pe number, hence the diffusion velocity, u_D, was evaluated. The characteristic features and properties calculated using Eq. (3) and Figs. 1–3 are presented in Table 1.

For a given flow rate and burner diameter, the flame height increases in the following order: $C_2H_6 > C_2H_4 > C_2H_2$. This is consistent with the order of measured characteristic diffusion lengths, $l_{D,C_2H_6} > l_{D,C_2H_4} > l_{D,C_2H_2}$ (Table 1). The values of the average diffusion coefficient calculated from Eq. (3) give the same order as shown in Table 1, i.e., $D_{C_2H_6} > D_{C_2H_4} > D_{C_2H_2}$.

This is inconsistent with the fact that as the temperature increases (T_{ad} in Table 1) and the molecular weight decreases, the diffusion coefficient should increase, while consistent with the fact that the pyrolysis rates and the chemical kinetics of the three fuels are different. This indicates that the effects of temperature and molecular weight on molecular diffusion are minor, while fuel pyrolysis is important. The pyrolysis rates are in the order $C_2H_2 > C_2H_4 > C_2H_6$. Acetylene is likely to produce heavier molecules earlier than ethylene or ethane; hence, the diffusion coefficients calculated from Eq. (3) and presented in Table 1 reflect a global average value of all the species.

The fuel residence times ($t_1 = l_D/u_D$) and the stoichiometric ratios, φ, are consistent with the flame size observations; as φ increases the flame size increases and hence t_1 increases.

Theoretical Description of Flame Shape

The case of a combustible laminar jet issuing into a quiescent medium was theoretically described by Spalding (1979). Spalding's analysis uses the similarity procedure described by Schlichting to develop closed-form expressions for the flame height and flame shape for circular jet laminar diffusion flames. Temperature effect was studied by Klajn and Oppenheim (1982). Here we describe the flame height and flame shape of the small laminar convection–diffusion controlled flames using

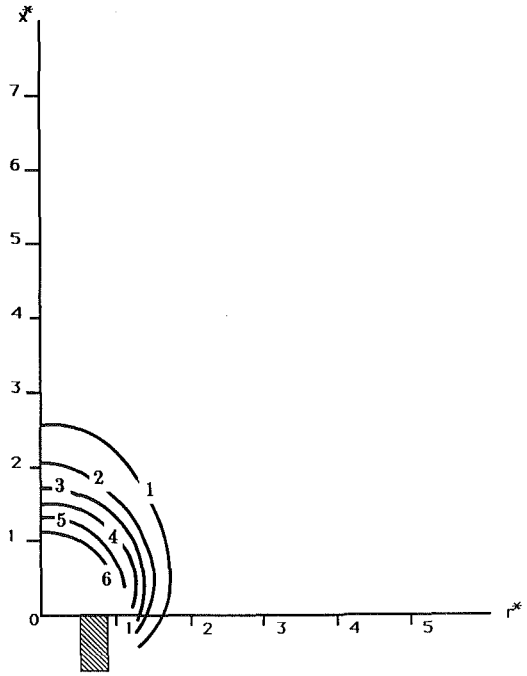

Fig. 3 Photographically measured visible flame sheet with C_2H_2 as fuel: (1) u_e = 0.547 m/s; (2) u_e = 0.436 m/s; (3) u_e = 0.348 m/s; (4) u_e = 0.290 m/s; (5) u_e = 0.214 m/s; (6) u_e = 0.161 m/s; burner port diameter d = 0.406 mm

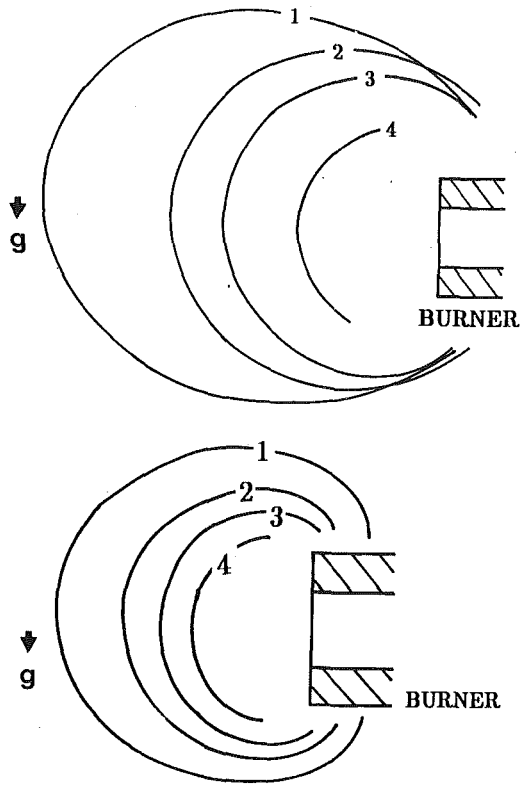

Fig. 4 Diffusion flames established on horizontally oriented burners: (A) fuel—C_2H_4; (1) u_e = 2.05 m/s; (2) u_e = 1.53 m/s; (3) u_e = 1.17 m/s; (4) u_e = 0.566 m/s; burner port diameter d = 0.25 mm; (B) fuel—C_2H_2; (1) u_e = 1.32 m/s; (2) u_e = 0.892 m/s; (3) u_e = 0.639 m/s; (4) u_e = 0.426 m/s; burner port diameter d = 0.25 mm

similarity analysis. The fundamental difference between this study and the two studies mentioned above is that transport by axial diffusion is comparable to the convective transport and cannot be neglected when determining the flame height/shape.

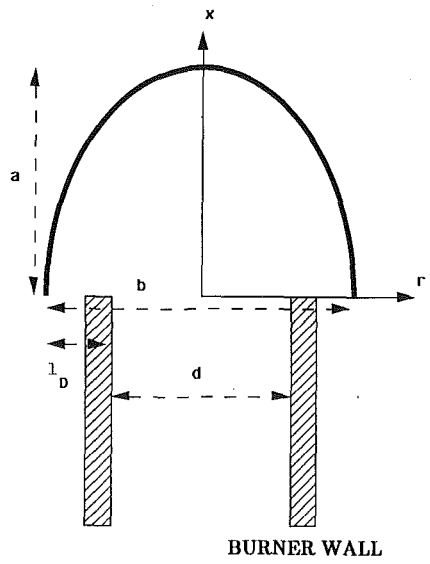

Fig. 5 Schematic of a laminar momentum–diffusion controlled diffusion flame established due to a circular fuel jet issuing into a quiescent medium: a = height of the flame; b = width of the flame at the base; l_D = characteristic diffusion length; x = axial coordinate; r = radial coordinate

Table 1 Summary of calculated flame characteristics and properties

	C_2H_6	C_2H_4	C_2H_2
φ	3.5	3	2.5
T_{ad} [K]	2364	2549	2918
l_D [m]	7.1×10^{-4}	4.6×10^{-4}	3.5×10^{-4}
t_1 [s]	1.7×10^{-3}	1.3×10^{-3}	1.0×10^{-3}
u_D [m/s]	0.43	0.35	0.35
D [m^2/s]	2.9×10^{-4}	1.5×10^{-4}	1.2×10^{-4}

Here T_{ad} is Adiabatic Flame Temperature, and φ is defined as number of moles of oxygen needed to completely oxidize one mole of fuel.

With the assumptions of negligible buoyancy and constant pressure, the governing equations for the small flames for axisymmetric geometry are:

For mass conservation:

$$\frac{\partial}{\partial x}(\rho u r) + \frac{\partial}{\partial r}(\rho v r) = 0 \tag{4}$$

For axial momentum conservation:

$$\frac{\partial}{\partial x}(\rho u r u) + \frac{\partial}{\partial r}(\rho u r v) = \frac{\partial}{\partial r}\left(\mu r \frac{\partial u}{\partial r}\right) + \frac{\partial}{\partial x}\left(\mu r \frac{\partial u}{\partial x}\right) \tag{5}$$

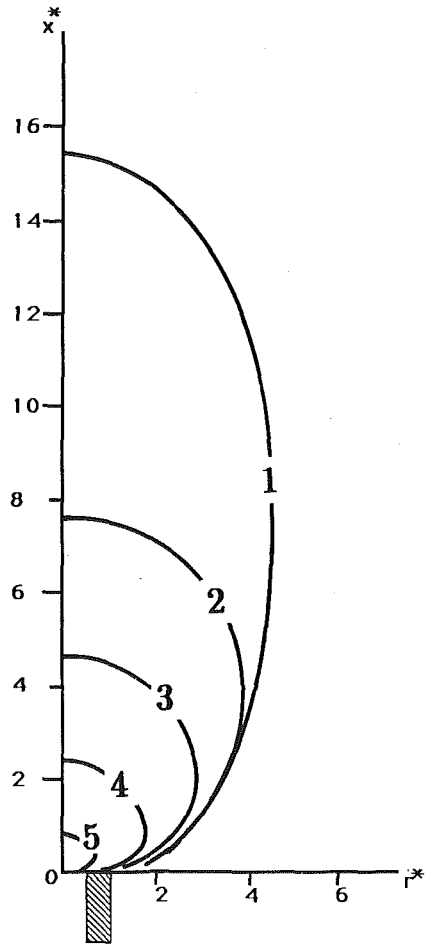

Fig. 6 Calculated (with axial diffusion) flame shape for C_2H_4: (1) Re = 10, γ = 2.17; (2) Re = 5, γ = 1.085; (3) Re = 3, γ = 0.65; (4) Re = 1.5, γ = 0.325; (5) Re = 0.5, γ = 0.108

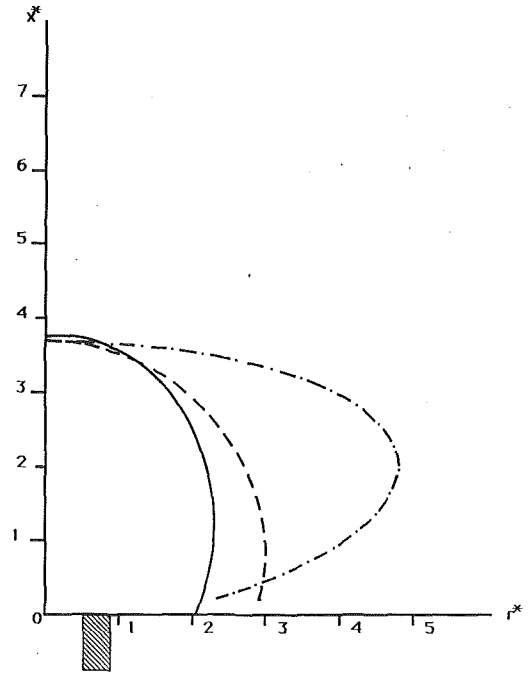

Fig. 7 Calculated and measured flame shapes for C_2H_6 (Re = 2.44, γ = 0.53): —— experimental; – – – calculated (with axial diffusion); and –·–·–· calculated (without axial diffusion)

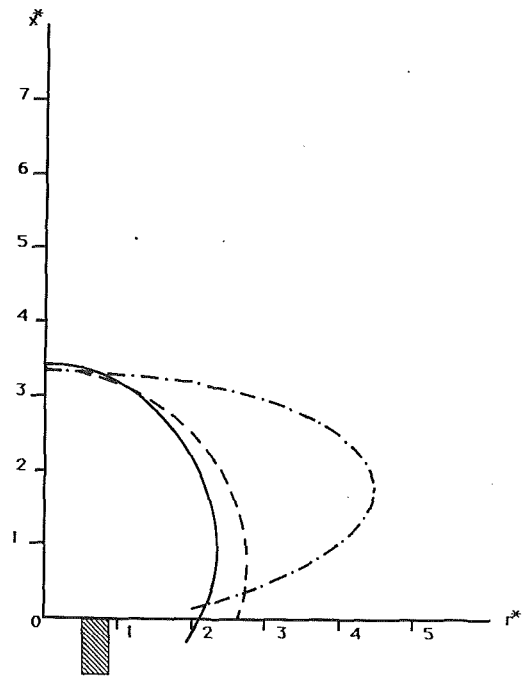

Fig. 9 Calculated and measured flame shapes for C_2H_4 (Re = 2.37, γ = 0.51); for symbols, see Fig. 7

For fuel species conservation:

$$\frac{\partial}{\partial x}(\rho u r Y_F) + \frac{\partial}{\partial r}(\rho v r Y_F) = \frac{\partial}{\partial r}\left(\rho D_F r \frac{\partial Y_F}{\partial r}\right) + \frac{\partial}{\partial x}\left(\rho D_F r \frac{\partial Y_F}{\partial x}\right) + r\omega_F \quad (6)$$

For oxidant species conservation:

$$\frac{\partial}{\partial x}(\rho u r Y_o) + \frac{\partial}{\partial r}(\rho v r Y_o) = \frac{\partial}{\partial r}\left(\rho D_o r \frac{\partial Y_o}{\partial r}\right) + \frac{\partial}{\partial x}\left(\rho D_o r \frac{\partial Y_o}{\partial x}\right) + r\omega_o \quad (7)$$

where x = axial coordinate; r = radial coordinate; u = axial velocity; v = radial velocity; ρ = fluid density; μ = fluid viscos-

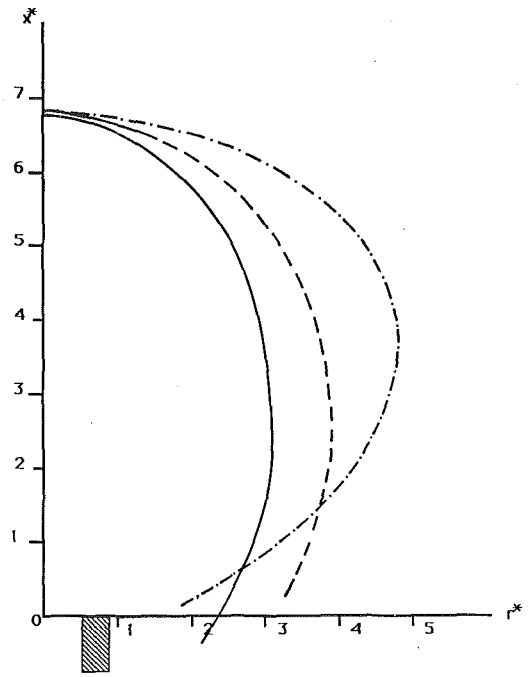

Fig. 8 Calculated and measured flame shapes for C_2H_6 (Re = 4.47, γ = 0.97); for symbols, see Fig. 7

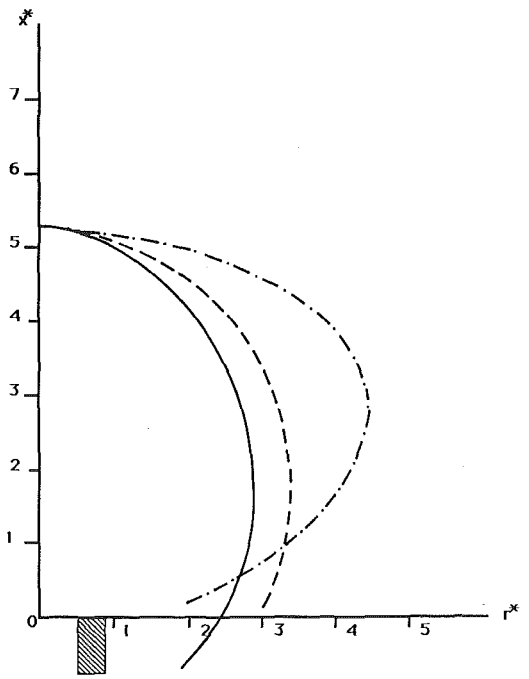

Fig. 10 Calculated and measured flame-shapes for C_2H_4 (Re = 3.75, γ = 0.81); for the symbols, see Fig. 7

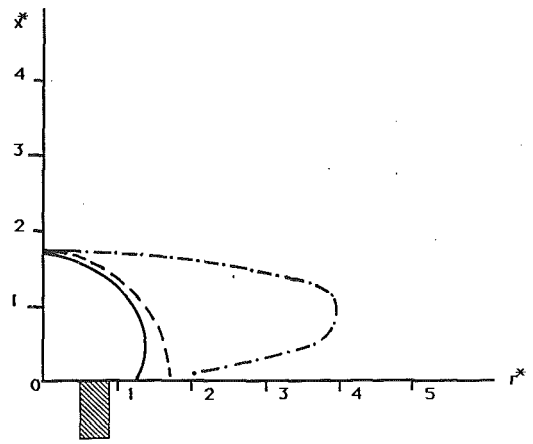

Fig. 11 Calculated and measured flame shapes for C_2H_2 (Re = 1.18, γ = 0.26); for the symbols, see Fig. 7

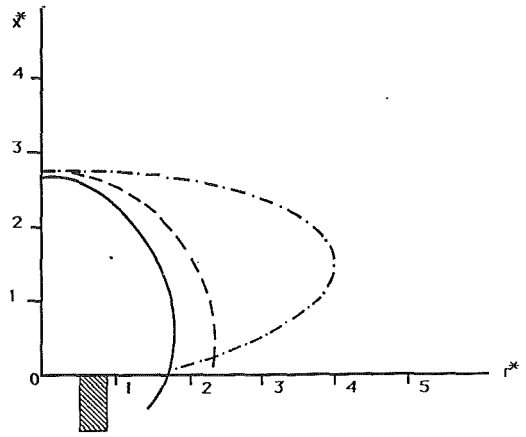

Fig. 12 Calculated and measured flame shapes for C_2H_2 (Re = 2.22, γ = 0.48); for the symbols, see Fig. 7

ity; D_F = fuel mass diffusivity; D_o = oxidizer mass diffusivity; ω_F = fuel consumption rate; ω_o = oxidizer consumption rate; Y_F = fuel mass fraction; and Y_o = oxidizer mass fraction.

Without distorting the physics, the theoretical analysis may be greatly simplified by assuming that the transport properties are constant, and the mass diffusivity of the various species are same. If the fuel and oxidizer react in stoichiometric ratios at the flame sheet, then

$$\omega_F = (F/O)_{st}\omega_o \tag{8}$$

where $(F/O)_{st}$ = the fuel to oxidizer stoichiometric mass ratio and Sc = Pr = Le = 1, where Sc = ν/D; Pr = ν/α; Le = Sc/Pr; ν = momentum diffusivity; and α = thermal diffusivity.

We define a mixture fraction

$$f = (\xi - \xi_o)/(\xi_F - \xi_o) \tag{9}$$

where $\xi = Y_F - (F/O)_{st}Y_o$. The governing Eqs. (4)–(7) can be rewritten as

$$u\frac{\partial u}{\partial x} + v\frac{\partial u}{\partial r} = \frac{\nu\partial}{r\partial r}\frac{(r\partial u)}{\partial r} + \nu\frac{\partial^2 u}{\partial x^2} \tag{10}$$

$$u\frac{\partial f}{\partial x} + v\frac{\partial f}{\partial r} = \frac{D\partial}{r\partial r}\frac{(r\partial f)}{\partial r} + D\frac{\partial^2 f}{\partial x^2} \tag{11}$$

with the far-field boundary conditions, as $r \to \infty$, $u = 0$, and $f = 0$. Comparing Eqs. (10) and (11) it can be seen that the solutions for u and f will be alike. Equations (7) and (8) are nondimensionalized using $u^* = u/u_e$, $v^* = v/u_e$, $r^* = r/d$, and $x^* = x/d$, and defining Re = $u_e d/\nu$. It can be seen that Re = Pe = $u_e d/D$. Equation (10) can be reduced to an ordinary differential equation by using the following stream function and similarity variables (Schlichting, 1987):

$$\psi = \nu \times G(\eta) \quad \text{and} \quad \eta = r/x$$

Therefore,

$$u^* = f = (1/x^* \text{ Re})\frac{G'(\eta)}{\eta} \tag{12}$$

Equation (10) then takes the form

$$(\eta^3 + \eta)G'' + G'(G - 1) = 0 \tag{13}$$

with the far-field boundary conditions $\eta \to \infty$, $G = 0$, and $G' = 0$. As $\eta \to 0$, i.e., at the centerline, the solution to Eq. (13) approaches the solution to the following equation:

$$\eta G'' + G'(G - 1) = 0 \tag{14}$$

Equation (14) is the same as Spalding's equation (1979); it is derived from Eqs. (10) and (11) eliminating the first terms of right-hand side. To obtain a particular solution with the far-field boundary conditions, it is necessary to introduce the constant of integration γ, where $\zeta = \gamma\eta$ (if $G(\gamma\eta)$ is a solution of Eq. (13) or (14), then $G(\zeta)$ is also a solution). Hence, Eqs. (14) and (13), respectively, become

$$\zeta G'' + G'(G - 1) = 0 \tag{15}$$

$$\left(\frac{\zeta^3}{\gamma^2} + \zeta\right)G'' + G'(G - 1) = 0 \tag{16}$$

with the far-field conditions still as $\zeta \to \infty$, $G = 0$, and $G' = 0$. A closed-form solution for G exists for Eq. (15), where the constant γ is estimated from the invariance of the momentum jet (Spalding, 1979):

$$G = \frac{\zeta^2}{(1 + 0.25\zeta^2)}$$

and

$$\gamma = \frac{\sqrt{3}}{8}\text{Re}$$

Substitution of $\zeta = \gamma\eta$ yields for the velocity

$$u^* = f = (\gamma^2/x^* \text{ Re})\frac{G'(\zeta)}{\zeta} \tag{17}$$

If the flame is assumed to exist at the stoichiometric value of f, then the expression for the flame height is:

$$x^*_{fh} = \frac{\gamma^2}{\text{Re} f_{st}}G''(0) \tag{18}$$

where x^*_{fh} is the dimensionless flame height and f_{st} is the stoichiometric value of the mixture fraction (Table 2).

Table 2 Stoichiometric values of the mixture fraction based on the general combustion reaction at the flame sheet: $C_xH_y + (x + y/4)(O_2 + 3.76N_2) \rightarrow xCO_2 + (y/2)H_2O + 3.76(x + y/4)N_2$

FUEL	F	O	F/O	f_{st}
C_2H_6	30	112	0.268	0.058
C_2H_4	28	96	0.292	0.063
C_2H_2	26	80	0.325	0.069

Here F/O = mass of fuel/mass of oxidizer,
$Y_o = [M_{O_2}/(M_{O_2} + M_{N_2})] = 0.23$, and
$f_{st} = [(F/O)_{st}Y_o]/[1 + (F/O)_{st}Y_o]$.

The invariance of the momentum (J) for the jet is defined as:

$$J = \nu^2\gamma^2 \int_0^\infty (G'^2/\zeta)d\zeta = \text{const} \tag{19}$$

and is the same for both with and without axial diffusion. J depends only on the inlet velocity, u_e. Therefore, γ, which is a constant (dependent only on u_e) is same for both with and without axial diffusion.

Equations (15) (without axial diffusion) and (16) (with axial diffusion) were both solved numerically. The flame height was determined from Eq. (18) and the flame shape was determined from

$$x^* = \frac{\gamma^2}{\text{Re}f_{st}} \frac{G'(\zeta)}{\zeta} \tag{20}$$

for both with and without axial diffusion.

The flame height and flame shapes were determined for three fuels (C_2H_6, C_2H_4, and C_2H_2) for the cases of with and without axial diffusion. In Fig. 6 the flame shapes calculated using Eq. (16) (with axial diffusion) are presented for a C_2H_4 flame for various Re numbers. The calculated flame shapes for both with and without axial diffusion are plotted in comparison with the photographically measured visible flame sheet in Figs. 7–12. It can be seen that the flame shapes calculated with the axial diffusion term are in much better agreement with the measured flame shape. The far-field solution is not valid near the entrance of the jet (Spalding, 1979) and hence the experimental and calculated flame locations cannot be compared near the burner rim.

Summary and Conclusions

1 Small convection–diffusion controlled laminar micro flames with Pe numbers ($u_e l_D/D$) less than 5 were investigated. It was observed that these flames tend to achieve a spherical shape due to the comparable effects of convection and convection–diffusion.
2 It was found that the effect of buoyancy in these flames is negligible, by rotating the burner. The Froude numbers of these flames were in the range $10–10^3$.
3 A phenomenological model was developed (Eq. (3)) to understand the flame shape and estimate the convection/diffusion effects.
4 The flame height/shape was theoretically determined starting with the governing equations and applying similarity methods. It was seen that when axial diffusion terms are used in the governing equations, the calculated flame shape is in better agreement (as compared without the axial diffusion terms) with the experimentally determined flame shape.

Acknowledgments

We wish to acknowledge Professor F. A. Williams for his instructions on the early development of the model. This work was supported in part from USEPA under grant 1D1155NAEX.

References

Ban, H., Venkatesh, S., and Saito, K., 1992, "Small Laminar Hydrocarbon–Air Jet Diffusion Flames," *Proceedings of the Spring Technical Meeting,* Central States Section/The Combustion Institute, Columbus, OH pp. 90–96.

Burke, S. P., and Schumann, T. E. W., 1928, "Diffusion Flames," *Ind. Eng. Chem.,* Vol. 20, pp. 998–1004.

Faraday, M., 1861, *Chemical History of a Candle,* Harper & Brothers, Publishers, New York.

Klajn, M., and Oppenheim, A. K., 1982, "Influence of Exothermisity on the Shape of a Diffusion Flame," *Nineteenth Symposium (International) on Combustion,* The Combustion Institute, pp. 223–235.

Roper, F. G., 1977, "Prediction of Laminar Jet Diffusion Flames: Part I. Theoretical Model," *Combustion and Flame,* Vol. 29, pp. 219–226.

Saito, K., Gordon, A. S., and Williams, F. A., 1986, "Effects of Oxygen on Soot Formation in Methane Diffusion Flames," *Combustion Science and Technology,* Vol. 47, pp. 117–138.

Schlichting, H., 1987, *Boundary-Layer Theory,* 7th ed., McGraw-Hill, New York.

Spalding, D. B., 1979, *Combustion and Mass Transfer,* 1st ed., Pergamon Press, New York.

Williams, F. A., 1985, *Combustion Theory,* 2nd ed., Benjamin Cummings, New York.

Mixed Convection From Simulated Electronic Components at Varying Relative Positions in a Cavity

E. Papanicolaou[1]
IBM Corporation;
Advanced Thermal Engineering Laboratory,
Endicott, NY 13760
Assoc. Mem. ASME

Y. Jaluria
Department of Mechanical and
Aerospace Engineering,
Rutgers,
The State University of New Jersey,
New Brunswick, NJ 08903
Fellow ASME

A numerical study of the combined-forced and natural convective cooling of heat-dissipating electronic components, located in a rectangular enclosure, and cooled by an external throughflow of air is carried out. A conjugate problem is solved, describing the flow and thermal fields in air, as well as the thermal field within the walls of the enclosure and the electronic components themselves. The interaction between the components is of interest here, depending on their relative placement in the enclosure, and different configurations are considered. For $Re = 100$ laminar, steady flow is predicted for up to $Gr/Re^2 = 10$, but a single-frequency oscillatory behavior is observed for most of the configurations studied, at $Gr/Re^2 = 50$. Heat transfer results are presented for both the laminar and the oscillatory domains. The mixed convection regime, where the buoyancy effects are comparable to the forced flow, occurs at values of Gr/Re^2 between 0.01 and 10. The results are of value in the search for a suitable placement of electronic components in an enclosed region for an effective heat removal.

Introduction

Air cooling is still the most attractive method for computer systems and other electronic equipment, due to its simplicity and low cost. Thermal engineers in the electronics industry are always trying to achieve the best possible performance out of air cooling. In this effort, the need for understanding the variety of flow phenomena and convective heat transfer mechanisms that are present in air-cooled electronic systems is obvious. A large number of relevant configurations have been studied in detail to the present date, both analytically and experimentally, by researchers in industry and universities. However, for an equally large number of such configurations results are still not well documented, and the associated physical phenomena not well understood. Extensive surveys of the various modes of convective heat transfer and relevant configurations, along with the associated heat transfer and other correlations have been presented by Incropera (1988) and more recently by Schmidt (1991). These two recent studies made it obvious that there is still a lack of adequate data for a very common situation in electronic equipment cooling, i.e., the heat transfer from discrete heat sources in enclosures. This is particularly true for cases where the induced natural convective flow interacts with the fan or blower-driven forced flow.

In a recent numerical study, Papanicolaou and Jaluria (1990) obtained results for a heat source located on and flush with one of the vertical walls of an enclosure with adiabatic walls. The source was cooled by an external flow, which flowed through openings in the vertical walls. Numerical results on the thermal and flow fields and on the corresponding Nusselt numbers from the source were presented for various Grashof and Reynolds numbers. Later, in another study by Papanicolaou and Jaluria (1993), the walls of the enclosure were taken as conducting (conjugate problem), while the heat source was still flush with one of the vertical walls or the bottom of the enclosure. Numerical results were presented on the resulting laminar flow and the associated heat transfer. In the present study, the enclosure walls are again taken as conducting, but the heat sources are taken as protruding. Also, rather than studying the behavior of a single source, the interaction between two heat sources at different relative positions, as well as three sources is studied. The effect of varying the extent of protrusion of the source has been studied for a single source on the left side-wall by Papanicolaou (1991).

At the present time, a fair amount of work dealing with protruding heat sources (or blocks) is available in the literature. Almost all of these studies considered the problem as related to the cooling of electronic equipment. Different modes of convective heat transfer have been considered. Forced convection has been studied by Zebib and Wo (1985), Davalath and Bayazitoglu (1987), and Rizk and Kleinstreuer (1989), all of them dealing with steady flows in a horizontal channel. Natural convection cooling of blocks was studied by Afrid and Zebib (1989), Said and Muhanna (1990), and Sathe and Joshi (1990). In the work of Afrid and Zebib (1989), single and multiple electronic components were treated as protruding heat sources, mounted on a vertical plate and a steady, laminar, conjugate problem was solved numerically for different heat inputs, spacings between the components, and component thicknesses. A similar configuration was considered by Said and Muhanna (1990), but the component was taken as protruding from one of the two vertical plates forming a channel. Sathe and Joshi (1990) studied numerically the natural convection transport from a heat-generating protrusion, mounted on a substrate inside a square enclosure. Various heat inputs, dimensions of the protrusion, and of the substrate and solid/fluid thermal conductivity ratios were considered.

There is also some work in the literature dealing with mixed convection effects in the cooling of protruding heat sources or electronic components. Braaten and Patankar (1984) considered the mixed convection from an array of blocks in a horizontal channel. Both conducting and nonconducting components were treated in the numerical solutions. In the work of Habchi and Archarya (1986), the cooling of a single elec-

[1]This work was conducted while the author was with the Department of Mechanical and Aerospace Engineering, Rutgers University, New Brunswick, NJ. Presently at the Institute of Hydromechanics, University of Karlsruhe, Germany.

Contributed by the Heat Transfer Division and presented at the ASME Winter Annual Meeting, New Orleans, Louisiana, November 28–December 3, 1993. Manuscript received by the Heat Transfer Division March 1993; revision received August 1993. Keywords: Conjugate Heat Transfer, Electronic Equipment, Mixed Convection. Associate Technical Editor: R. Viskanta.

tronic module, treated as an isothermal protruding heat source mounted on the right wall of a vertical channel, was studied. An array of blocks in a vertical channel cooled by an upward flow was the configuration in the study of Kim and Boehm (1990). They obtained numerical results for the steady, non-conjugate case using a control-volume scheme, for various Reynolds and Rayleigh numbers. More recently, in an experimental study, Kang et al. (1990) obtained experimental results for the cooling of a protruding heat generating module on a horizontal plate. Correlations between the Nusselt number from the module and the parameter $Gr/Re^{5/2}$, over a range of Grashof and Reynolds numbers, were derived.

As can be concluded from the preceding, the cooling of protruding heat sources in the various modes of convective heat transfer has so far been considered with respect to external or channel flows. The blocks in all the studies mentioned here were located on the same surface, which was either horizontally or vertically oriented. The case of blocks mounted on different surfaces, forming an angle of 90 deg with respect to each other, has not been considered before, to the authors' knowledge. Besides, in all cases where numerical solutions were obtained, the steady equations were solved. The only studies that report time-dependent solutions of the full equations for a similar problem of mixed convection from discrete heat sources are those by Khalilollahi and Sammakia (1989) and Elpidorou et al. (1991) considering only embedded sources.

In the present work, therefore, where a cavity configuration is considered, with protruding heat sources at various locations, the following circumstances are considered simultaneously for the first time:

- Convective heat transfer in the cavity with conduction through the walls (conjugate effects).
- Protruding heat sources (blocks) in the cavity, mounted on surfaces that are either parallel or perpendicular to each other.
- Interaction between a buoyancy-induced flow and a forced flow whose direction is perpendicular to the gravity vector.
- Solution of the time-dependent equations, allowing for the detection of potential oscillatory phenomena (which were indeed observed here, under certain conditions).

The geometry of the cavity and the relevant parameters considered here are shown in Fig. 1. For the study of the conjugate problem, the walls are assumed to be of finite thickness. The total dimensions H_{tot}, W_{tot} include the corresponding dimensions of the air-filled cavity plus the thicknesses of the walls. The configuration shown in Fig. 1 is a generic case, including three locations of the sources, corresponding to the **L**eft and **R**ight side walls and the **B**ottom. This case will be referred to as **LBR** for brevity from now on. However, most of the results presented here will consider only two sources at different locations and the corresponding configurations will be, respectively, named as **LR** (for sources on the left and right walls), **LB** (left wall and bottom), and **BR** (bottom and right wall) configurations. The heat sources will be referred to as **L**, **B**, and **R**, depending on their respective location. The two-dimensional problem is studied here, where each heat source actually represents a row of electronic components, sufficiently long in the third dimension. Also, the focus here is in the laminar regime, although results in the turbulent regime have also been obtained for a similar configuration (Papanicolaou, 1991).

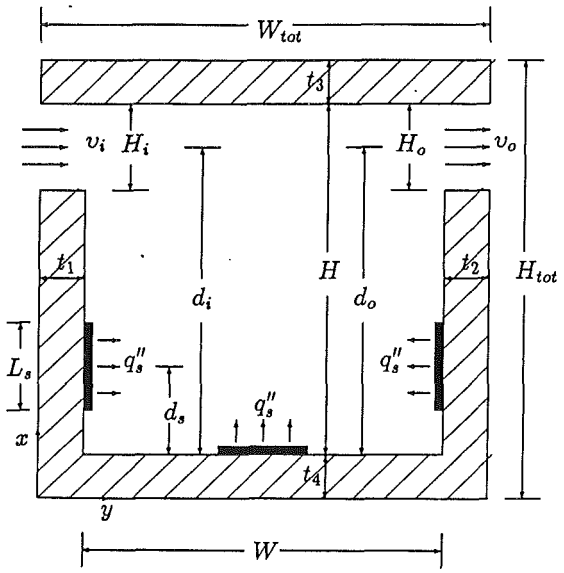

Fig. 1 The geometry of the cavity under consideration, showing three heat source locations. This case and the cavity with two sources, taking all possible pairs, are studied in this work.

Mathematical Formulation

Model Equations. The equations describing the problem

Nomenclature

d = vertical distance from the bottom of the enclosure
Gr = Grashof number = $g\beta\Delta TH_i^3/\nu^2$
h = local heat transfer coefficient, varying along a surface s
$\bar{h}$ = average heat transfer coefficient over the surface of the heat source, based on the total flux from the source q_s''
H = height of the air-filled cavity
H_i, H_o = height of the inflow and outflow channels, respectively
J = total convection-diffusion flux vector, defined in Eq. (8)
k = thermal conductivity
L_s = length of the heat sources
Nu = local Nusselt number, $\mathrm{Nu}(s) \equiv hs/k_f$
$\overline{\mathrm{Nu}}_s$ = average Nusselt number over the surface of the heat source, based on the total heat flux q_s'' from the source (Eq. (12))
P = dimensionless local pressure = $p/\rho v_i^2$
Pr = Prandtl number of air = ν/α_f
q_s'' = heat input per unit surface area of the source
Q_s = total heat generation from each source (per unit width)
r_k = thermal conductivity ratio = k_s/k_f
r_c = thermal capacity ratio = $(\rho C_P)_s/(\rho C_P)_f$
r_α = thermal diffusivity ratio = α_s/α_f
Re = Reynolds number = $v_i H_i/\nu$
s = coordinate along the perimeter of the source
t = thickness of solid walls
T = physical temperature
$\bar{T}$ = mean temperature over a surface
U, V = dimensionless vertical and horizontal velocity component, respectively, $U = u/v_i$, $V = v/v_i$

for the configuration of Fig. 1 are the Navier–Stokes equations for the fluid, with buoyancy effects taken into account and using the Boussinesq approximations, as well as the energy equation, which describes the temperature variation through both the fluid and the solid walls. With the introduction of the stream function and the vorticity as the independent variables, the nondimensional equations can be written as:

Vorticity equation (fluid region):

$$\frac{\partial \Omega}{\partial \tau} + \nabla \cdot (\mathbf{V}\Omega) = -\frac{\mathrm{Gr}}{\mathrm{Re}^2}\frac{\partial \theta}{\partial Y} + \frac{1}{\mathrm{Re}}\nabla^2 \Omega \tag{1}$$

Stream function equation (fluid region):

$$\nabla^2 \Psi = -\Omega \tag{2}$$

Energy equation (both regions):

$$\rho C_P \left[\frac{\partial \theta}{\partial \tau} + \nabla \cdot (\mathbf{V}\theta)\right] = \nabla \cdot \left(\frac{k}{\alpha_f}\frac{1}{\mathrm{RePr}}\nabla \theta\right) \tag{3}$$

In the nondimensionalization, the height of the inflow opening H_i is taken as the characteristic length scale. The velocity scale is the inlet velocity of air v_i and the temperature scale is $\Delta T = Q_s/k_f$, where Q_s is the total input by the source per unit width (W/m) and k_f is the thermal conductivity of the fluid. The dimensionless parameters are the Reynolds number Re, the modified Grashof number Gr, and the Prandtl number $\mathrm{Pr} = \nu/\alpha_f$ (=0.71 for air at normal room temperature). The total heat input can be written as:

$$Q_s = q_s'' \Pi_s = q_s'' (L_s + 2t_s) \tag{4}$$

where Π_s is the perimeter and t_s the thickness of the heat source.

Boundary Conditions. The boundary conditions at the inflow and the outflow are, respectively:

$$U_i = 0,\ V_i = 1,\ \Psi_o = 1 - \left[X - \left(d_i^* - \frac{1}{2}\right)\right],\quad \Omega_i = 0,\ \theta_i = 0 \tag{5}$$

$$U_o = 0,\ \left(\frac{\partial V}{\partial Y}\right)_o = \left(\frac{\partial \Psi}{\partial Y}\right)_o = \left(\frac{\partial \Omega}{\partial Y}\right)_o = \left(\frac{\partial \theta}{\partial Y}\right)_o = 0 \tag{6}$$

The sensitivity of the solution to the outflow boundary conditions was tested by Papanicolaou and Jaluria (1993). In that work the zero gradient condition was compared against specifying the same flow conditions at the outflow as at the inflow. Slight discrepancies were felt only in the flow field near the outflow boundary, while the effect on the flow and heat transfer results over the rest of the computational domain were insignificant (less than 0.03 percent). The boundary conditions for the temperature are: $\partial\theta/\partial n = 0$ at the outer walls, where n is the direction normal to the wall. At the solid–fluid interfaces, the condition is:

$$\left(\frac{\partial \theta}{\partial n}\right)_{\text{fluid}} = r_k \left(\frac{\partial \theta}{\partial n}\right)_{\text{solid}} + \begin{cases} -1/\Pi_s^* & \text{at the heat sources} \\ 0 & \text{on other walls} \end{cases} \tag{7}$$

which expresses the continuity of the fluxes, where the stars denote dimensionless quantities. If the source is flush, $\Pi_s^* = L_s^*$ and for $L_s^* = 1$, $1/\Pi_s^* = 1$, which leads to the same condition derived by Papanicolaou and Jaluria (1993).

Numerical Procedure

Discretization. A 45×49 grid was chosen for most of the numerical results presented here. The grid was nonuniform, with the grid points placed at geometrically decreasing distances in the regions next to the walls, where, especially near heat sources, large velocity and thermal gradients are expected. Inside the solid, where the conduction equations had to be solved, the grid was uniform. Other grid dimensions were also tested for comparison, such as 23×25 and 67×73. The comparison was based on several typical results such as the maximum values of the stream function and the temperature and the average Nusselt numbers from the sources (to be defined later). These were compared against the corresponding results obtained with the finest of the three grids (67×73) and showed an 18 percent maximum difference for the 23×25 grid and a 2.5 percent maximum difference for the 45×49 grid. Since the latter grid requires approximately 9 times less computational effort than the 67×73 grid, it was chosen for the solutions presented here, as a trade-off between accuracy and efficiency.

Numerical Method. The numerical scheme is similar to the one described by Papanicolaou and Jaluria (1990), but it has now been enhanced to incorporate protruding heat sources and conjugate conditions, which will be described below. The time-dependent equations, Eqs. (1) and (3), were advanced in time using a transient scheme. The Alternating Direction Implicit (ADI) method was used for the temperature and vorticity equations, with the power-law approximation for the convective terms (Patankar, 1980). The second upwind and central differencing scheme were also used for comparison and no sig-

Nomenclature (cont.)

$\mathbf{V}$ = dimensionless velocity vector = (U, V)
W = width of the air-filled cavity
X, Y = dimensionless vertical and horizontal coordinate distance, respectively, $X = x/H_i$, $Y = y/H_i$
α = thermal diffusivity
β = coefficient of thermal expansion of air $\equiv -(1/\rho)(\partial\rho/\partial T)_p$
Γ = diffusion coefficient in Eq. (8)
ΔT = temperature scale $= Q_s/k_f$
$\Delta\tau$ = dimensionless time step
$\Delta X, \Delta Y$ = dimensionless area of the control volume face in the X and Y direction, respectively
ϵ = convergence criteria for the SOR method and the time iteration scheme
θ = dimensionless temperature = $(T - T_i)/\Delta T$
ν = kinematic viscosity of air
Π_s = perimeter of the heat sources
τ = dimensionless time $= \tau' v_i/H_i$
v_i = mean value of the horizontal velocity component at the inflow
Ψ = dimensionless stream function $U = \partial\Psi/\partial Y$, $V = -\partial\Psi/\partial X$
Ω = dimensionless vorticity $\Omega = \partial V/\partial X - \partial U/\partial Y$

Subscripts

e, w, n, s = right, left, top, and bottom control volume face, respectively
E, W, N, S = neighbor grid point to the right, left, top, and bottom of the control volume, respectively
f = fluid
i = inflow
o = outflow
P = grid point at the center of the control volume
s = solid region; also, source

Superscripts

$*$ = dimensionless quantities

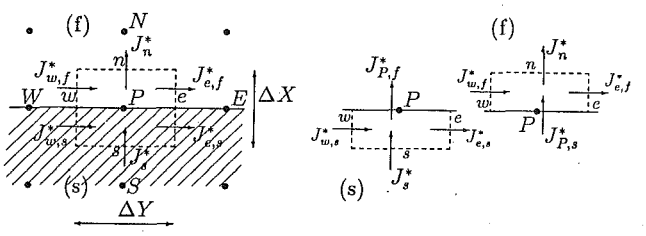

Fig. 2 Derivation of the interface temperature from the two partial control volumes in the solid (*s*) and the fluid (*f*) regions. Imposing $J^*_{P,s} = J^*_{P,f}$ at the surface *P* gives the interface temperature θ_P.

nificant differences were found. Since the ADI method requires rectangular domains, the inflow channel, the interior of the cavity, and the outflow channel were solved separately at each time step. The Successive-Over-Relaxation (SOR) (Jaluria and Torrance, 1986) method is used for the Poisson stream function equation, where the optimum relaxation factor was found to be: $\omega_{opt} = 1.85$. The wall vorticity is updated at each time step using a second-order finite-difference formula (Papanicolaou and Jaluria, 1990).

The Solid-Fluid Interface Condition. The boundary condition at the interface is taken such that the grid points lying there can be treated as interior points in the computational domain. If the nondimensional convective-diffusive flux vector $\mathbf{J}^*$ in the energy equation is defined as:

$$\mathbf{J} = \mathbf{V}(\rho C_P \theta) - \Gamma \nabla (\rho C_P \theta) \tag{8}$$

with $\Gamma = r_\alpha(1/\mathrm{RePr})$ in the solid and $\Gamma = 1/(\mathrm{RePr})$ in the fluid region, and if J^*_s is the flux on the solid side and $\mathbf{J}^*_f$ is the flux on the fluid side, the continuity of flux condition requires that: $\mathbf{J}^*_s = \mathbf{J}^*_f$. The procedure employed to derive the equation for the temperature of the interface grid point *P* is illustrated in Fig. 2, where the notation of Patankar (1980) is used for the central node and the neighboring nodes, as well as the control volume faces. Every interface control volume can be considered as composed of two partial control volumes (half volumes if the grid is uniform), one on the fluid side and one on the solid side. For each of these, an expression for the total fluxes $\mathbf{J}^*_{P,s}$ and $\mathbf{J}^*_{P,f}$, respectively, at the interface *P* can be derived, by writing the integrated energy balance equations over each partial control volume. Then imposing the condition $\mathbf{J}^*_s = \mathbf{J}^*_f$ at surface *P* yields an expression for the temperature θ of the interface grid point, similar to those of the interior points, except that the ratios of the thermal capacities and diffusivities are now included in the equation. This procedure was chosen here, rather than the harmonic mean approach (Patankar, 1980), because it allows for heat generation at the solid-fluid interface, as is the case here and because it yields directly the interface temperature without interpolation. The exact form that the equation for the interface grid points assumes was shown in the previous study for a single, flush-mounted source (Papanicolaou and Jaluria, 1993). The same method is followed for the protruding surfaces of the heat sources without any additional difficulties.

Numerical Stability and Convergence. The stability of the numerical scheme depends on the values of Gr and Re, but also on the value of the thermal conductivity ratio (Papanicolaou and Jaluria, 1993). For $r_k \leq 1$ as is the case here, and for the 45×49 grid used, the value of the time step that guarantees the numerical stability is $\Delta\tau = 0.1$, but if higher values of r_k are used, $\Delta\tau$ has to be reduced accordingly. The value $\Delta\tau = 0.1$ is adequate for steady solutions, but for periodic solutions that occur at high values of $\mathrm{Gr/Re}^2$, the time step has to be reduced further, for the capturing of the oscillations. The time step has to be reduced for a 67×73 grid as well, to a value of 0.025 and this increases the computational effort significantly.

The convergence to steady-state conditions is attained when the relative error between two successive time steps for the variables Ψ, Ω, or θ is less than $\epsilon = 10^{-5}$, which was found to be adequate for the determination of the final steady solution, without unnecessary additional computational effort. In addition, if Q_{tot} denotes the total heat generation at the sources:

$$Q_{tot} = \sum_{k=1}^{N} Q_{s,k} \tag{9}$$

where *N* is the number of the heat sources (either 2 or 3) and $Q_{s,k}$ is the total heat input from source *k*, the following, more reliable heat balance convergence criterion is checked:

$$\frac{|Q_{tot}| - (|Q_i| + |Q_o|)}{|Q_{tot}|} \leq 10^{-2} \tag{10}$$

When starting from rest, this was found to require approximately 12,000 time steps to be satisfied. When starting from the converged solution at a lower Grashof number as the initial condition, 6000–8000 time steps were found to be sufficient.

As no benchmark problem have been established yet with respect to conjugate heat transfer in cavities, the code validation was done on its nonconjugate version. The benchmark problem with the most relevance to our particular configuration was that of natural convection in a square cavity. Our results were compared against the results by the various contributors in the comparative study by de Vahl Davis and Jones (1982) and very good agreement was found in the selected values presented, such as the maximum stream function and the Nusselt numbers along the vertical walls (within 2.5 percent).

Results and Discussion

Definition of Physical and Geometric Parameters. The results to be presented here will focus on the effect of certain parameters, while keeping the others fixed. More specifically, the parameters listed below in dimensionless form, chosen to represent a cavity that would most likely appear in an electronic system, although not exclusively so, are kept fixed at the following values (see Fig. 1): thermal diffusivity ratio $r_\alpha = 0.8$, thermal capacity ratio $r_c = 1$ (therefore $r_\alpha = r_k$), aspect ratio of the air-filled cavity $A = H^*/W^* = 1$, $H^*_i = H^*_o = 1$, $d^*_i/H^* = d^*_o/H^* = 0.875$, $t^*_1 = t^*_2 = t^*_3 = t^*_4 = t^* = H^*/8$, $L^*_s = H^*_i = 1.0$, $t^*_s = 0.0886$ (two grid spacings). A study of the effect of the source thickness and the thermal conductivity ratio can be found in Papanicolaou (1991). The distance of the center of the sources from the bottom of the cavity is taken such that $d^*_s/H^* = 0.25$, while on the bottom wall the corresponding distance is $d^*_s/W^* = 0.5$, measured from the left vertical wall.

The value $r_k = 0.8$ was chosen as a representative value from the range covered in the study by Papanicolaou and Jaluria (1993), which was $r_k = 0$–10. The numerical procedure developed here, however, is valid for any value of r_k, provided that the value of the time step is adjusted accordingly to ensure numerical stability, as explained earlier. Defining the actual thermal properties of the materials encountered in electronic systems is, by itself, not a trivial matter. Many of these materials are composites and anisotropic in nature, printed circuit boards being a very good such example. Therefore, using a single value for the thermal conductivity of the solid and, thus, for r_k here is understood to be only an approximation. Since the objective in this study is to demonstrate how conjugate boundary conditions can be incorporated into the numerical solution of a convective heat transfer problem and how this can affect the results, some simplifications were considered justified. The same reasoning can be given to the fact that the heat sources are assigned the same physical properties as the

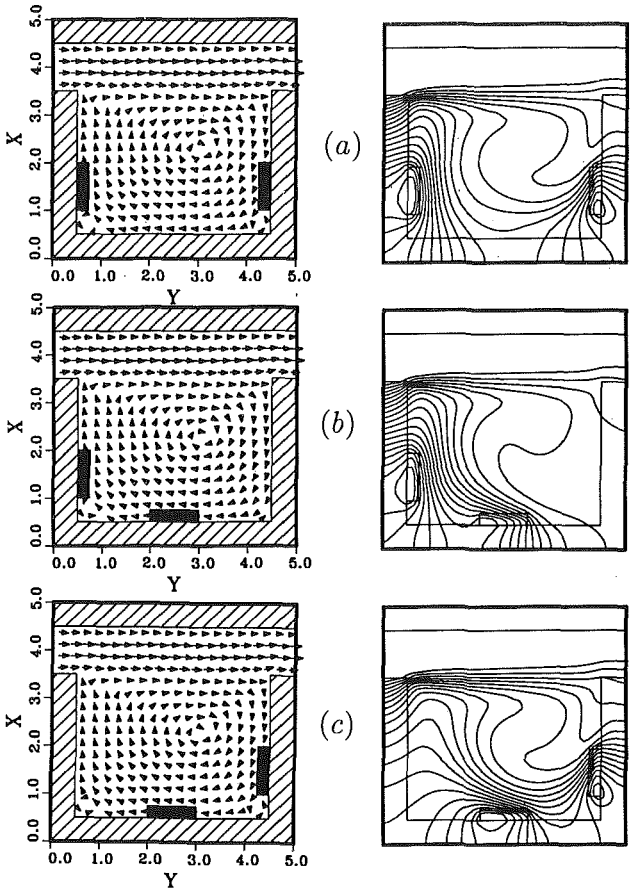

Fig. 3 Velocity vectors and isotherms obtained in the various configurations for Re = 100 and Gr = 0 (forced convection): (*a*) LR, $\Psi_{max} = 1.243$, $\theta_{max} = 0.636$; (*b*) LB, $\Psi_{max} = 1.243$, $\theta_{max} = 0.714$; (*c*) BR, $\Psi_{max} = 1.241$, $\theta_{max} = 0.589$.

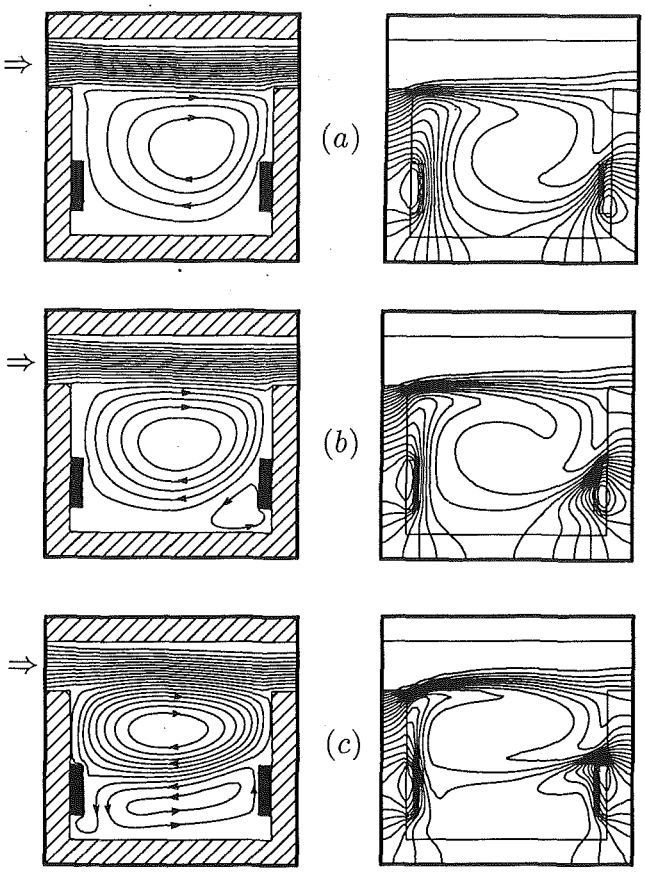

Fig. 4 Calculated streamlines and isotherms for the steady solutions obtained in the LR configuration, for Re = 100 and: (*a*) $Gr/Re^2 = 0.1$, $\Psi_{max} = 1.282$, $\theta_{max} = 0.542$; (*b*) $Gr/Re^2 = 1.0$, $\Psi_{max} = 1.422$, $\theta_{max} = 0.448$; (*c*) $Gr/Re^2 = 10.0$, $\Psi_{max} = 1.691$, $\theta_{max} = 0.337$

walls of the cavity. In reality, one would have to examine the internal structure of the electronic module that the heat source represents and derive effective values for the properties needed. Since the same physical properties are used throughout the solid domain, no special boundary conditions need to be employed at the heat source-solid wall interfaces. Had this not been the case, Eq. (7) would have been employed again, with a suitable value of r_k.

The parameters to be varied here are the Grashof number, the number of the sources, and the relative locations of the sources. All the alternative cases will be compared to each other. The Reynolds number is being kept fixed in this work at Re = 100, a value representative of the laminar regime, characterizing an incoming flow of a relatively low velocity. For instance, an air flow of about 0.1 m/s entering through an opening 2 cm high at 20°C would yield a Reynolds number of the above-mentioned order of magnitude. Higher values of Re have been considered before (Papanicolaou and Jaluria, 1990) and the basic flow patterns in the cavity were not affected significantly as long as $Re < 1000$. The Grashof number is varied in the range $Gr = 10^3 - 5 \times 10^5$ and this effect will be presented, in what follows, as a variation in the Richardson number Gr/Re^2 over the corresponding range. Gr/Re^2 is a more suitable parameter in mixed convection problems and since the Reynolds number is kept fixed, varying the value of Gr/Re^2 will be equivalent to varying the heat input from the sources. Generally, the Grashof numbers encountered in electronic cooling are of the order of 10^5 or higher, but in this case, in order to get a more complete picture of the effect of Gr/Re^2 on the heat transfer, the range of Gr has been extended to lower values.

It should also be pointed out that radiation effects were not included in this study, since this would overly complicate the problem, especially when no previous investigations were available for a similar configuration involving convection alone. In practical terms, the results obtained here would apply to surfaces of sufficiently low emissivity, so that the radiation effects relative to those of buoyancy and forced convection can be neglected.

Flow and the Thermal Fields for Forced Convection (Two Sources). Results are first presented for forced convection heat transfer. For this case, the buoyancy term is dropped from the vorticity equation, Eq. (1). The computed velocity vectors and isotherms at Re = 100 are shown in Fig. 3. The flow field is basically unicellular, with small cells near the protruding sources due to flow separation. The thermal field shows a relatively uniform temperature distribution inside the cavity, with no regions of steep thermal gradients that normally appear when natural convection boundary layers develop along heat sources (Papanicolaou and Jaluria, 1990, 1993).

Flow and Thermal Fields for Steady Mixed Convection. Figure 4 shows the streamlines and isotherms for two sources in the **LR** configuration, for Reynolds number Re = 100 and three different Richardson numbers, $Gr/Re^2 = 0.1$, 1, and 10. All these cases lead to steady laminar solutions. The flow field shows a unicellular pattern at $Gr/Re^2 = 0.1$, but at $Gr/Re^2 = 1.0$, a secondary flow develops due to the buoyancy effects from source **R**, at the base of the right sidewall. At $Gr/Re^2 = 10$, the secondary cell becomes bigger and occupies more of the space originally belonging to the primary cell. The temperature field in the fluid adjacent to source **L** exhibits the

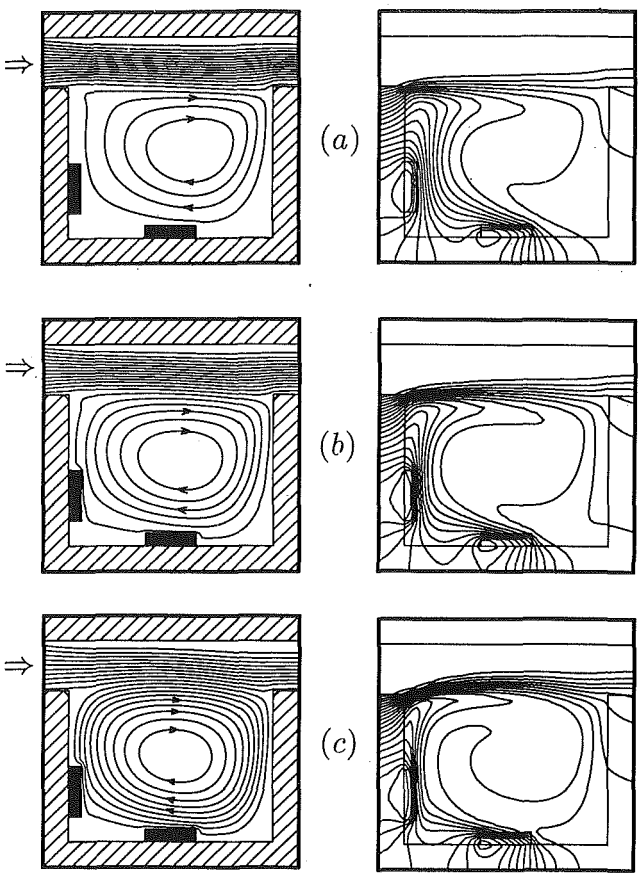

Fig. 5 Calculated streamlines and isotherms for the steady solutions obtained in the LB configuration, for Re = 100 and: (*a*) $Gr/Re^2 = 0.1$, $\Psi_{max} = 1.291$, $\theta_{max} = 0.582$; (*b*) $Gr/Re^2 = 1.0$, $\Psi_{max} = 1.461$, $\theta_{max} = 0.427$; (*c*) $Gr/Re^2 = 10.0$, $\Psi_{max} = 1.937$, $\theta_{max} = 0.292$

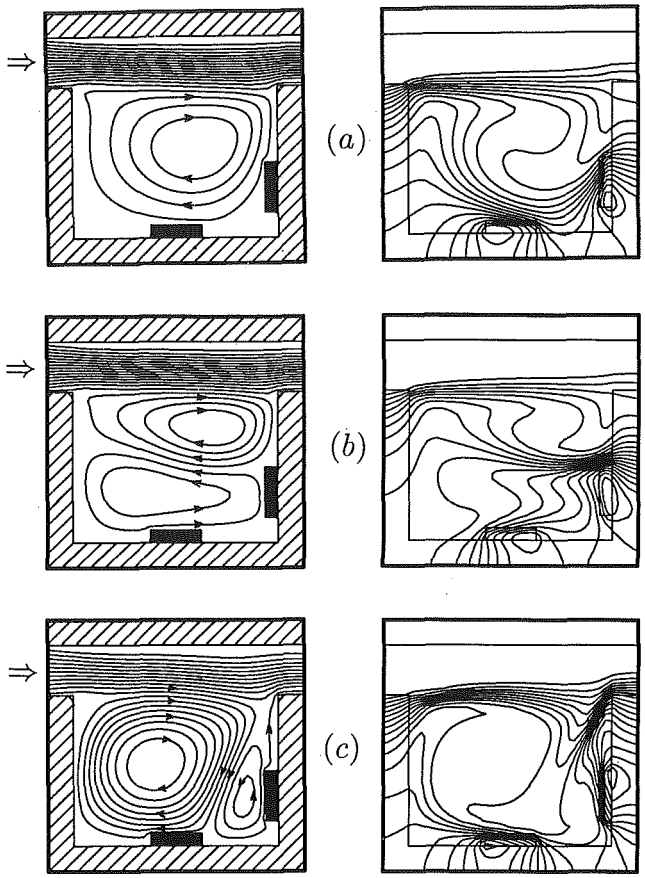

Fig. 6 Calculated streamlines and isotherms for the steady solutions obtained in the BR configuration, for Re = 100 and: (*a*) $Gr/Re^2 = 0.1$, $\Psi_{max} = 1.284$, $\theta_{max} = 0.540$; (*b*) $Gr/Re^2 = 1.0$, $\Psi_{max} = 1.287$, $\theta_{max} = 0.630$; (*c*) $Gr/Re^2 = 10.0$, $\Psi_{max} = 1.730$, $\theta_{max} = 0.273$

characteristics of a natural convection boundary layer and a plumelike pattern of isotherms at all values of Gr/Re^2 chosen, while for source **R**, such a pattern makes its appearance for $Gr/Re^2 = 10$. Source **R** is shown to be subject to an opposing recirculating flow. At $Gr/Re^2 = 50$, the solution was still steady for the **LR** configuration, while the solution was periodic for the other configurations, as will be discussed later.

For the same values of Re and Gr/Re^2 as before, the corresponding results for the **LB** configuration are shown in Fig. 5. The buoyancy-induced flows due to both the sources are now in the same direction, aiding the recirculating flow. Therefore a unicellular flow pattern is observed at all values of Gr/Re^2, with the recirculation gradually increasing with an increase in Gr/Re^2. Thermal boundary layers are clearly observed over both sources. The **BR** configuration gives rise to a variety of flow patterns, as seen in Fig. 6. At $Gr/Re^2 = 0.1$, the external flow dominates over the buoyancy effects and the flow field resembles the one generated in a driven cavity, i.e., a cavity whose top wall is moving horizontally. At $Gr/Re^2 = 1$ the buoyancy effects from both sources generate a secondary cell, which is counterrotating with respect to the original cell. However, at a higher buoyancy level, $Gr/Re^2 = 10$, the buoyancy effects from source **B** again add to the recirculation of the original cell, while the secondary cell is now due to the buoyancy effects from source **R** only and is restricted to a region adjacent to the right vertical wall. This change in the flow patterns and the direction of the buoyancy-induced flow from source **B** can be seen in the isotherm plots. The origin of the thermal boundary layer alternates between the left and right edges of the source as Gr/Re^2 increases from 0.1 to 10. A stratified layer of fluid can always be observed between the two cells, where the heat transfer takes place by diffusion.

The streamlines and isotherms for solutions obtained considering all three heat sources simultaneously are shown in Fig. 7, for Re = 100 and values of Gr/Re^2 equal to 0.1, 1, and 10. Only at $Gr/Re^2 = 10$, does a secondary cell appear near the bottom of the right sidewall.

Periodic Solutions. As already mentioned, for the **LB** and **BR** configurations, the solutions become periodic at Re = 100 and $Gr/Re^2 = 50$, while they are still steady in the **LR** configuration. This periodic behavior of selected quantities such as the maximum stream function, average Nusselt number, and maximum temperature at the sources, is shown in Fig. 8. Regular oscillations of gradually decreasing amplitudes were observed for all quantities, which persisted even after the end of the transient, which occurred at $\tau \simeq 400$. For $\tau \geq 400$, a steady-periodic state results for the **LB** and **BR** configurations, as characterized by regular, almost sinusoidal variation with time, and this final state is shown in Fig. 8. When this steady-periodic state is attained, the instantaneous flow and thermal fields have the form shown in Fig. 9. The **LR** configuration is the only stable one, with the secondary cell increasing in size and two thin thermal boundary layers arising along the two sources. The **LR** and **BR** configurations show basically the same flow patterns as for $Gr/Re^2 = 10$, with the intensity of the recirculation increasing and the development of large thermal gradients near the bottom of the cavity.

These periodic results have been shown to be of physical, and not of numerical, origin in a detailed study by the authors (Papanicolaou and Jaluria, 1992). Numerical tests using different initial conditions, time steps, and grid sizes for an enclosure with a single, flush source on the left vertical wall (let it be called **L** configuration), verified the presence of the os-

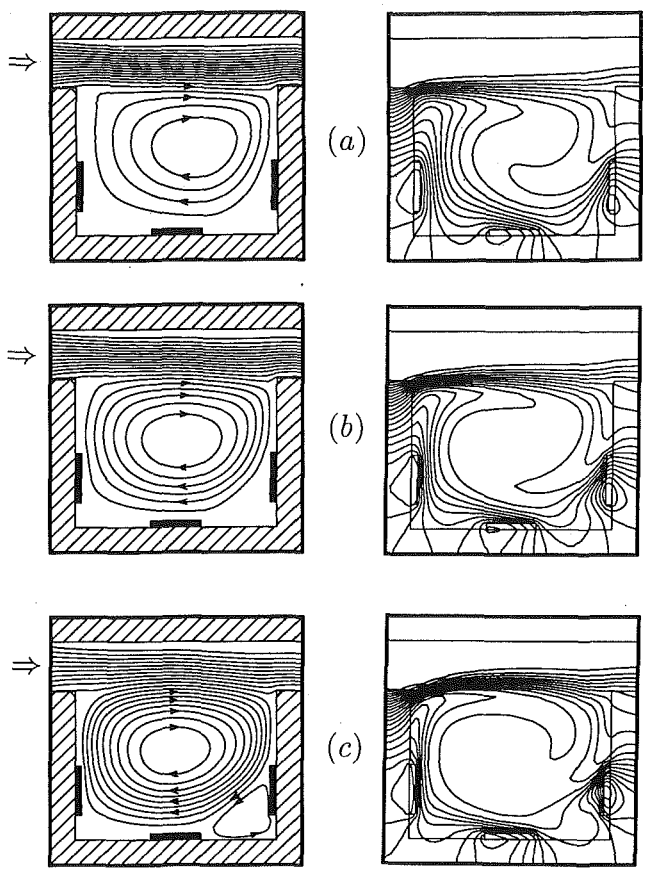

Fig. 7 Calculated streamlines and isotherms in the LBR configuration, for Re = 100 and: (*a*) $Gr/Re^2 = 0.1$, $\Psi_{max} = 1.300$, $\theta_{max} = 0.718$; (*b*) $Gr/Re^2 = 1.0$, $\Psi_{max} = 1.500$, $\theta_{max} = 0.540$; (*c*) $Gr/Re^2 = 10.0$, $\Psi_{max} = 1.976$, $\theta_{max} = 0.389$

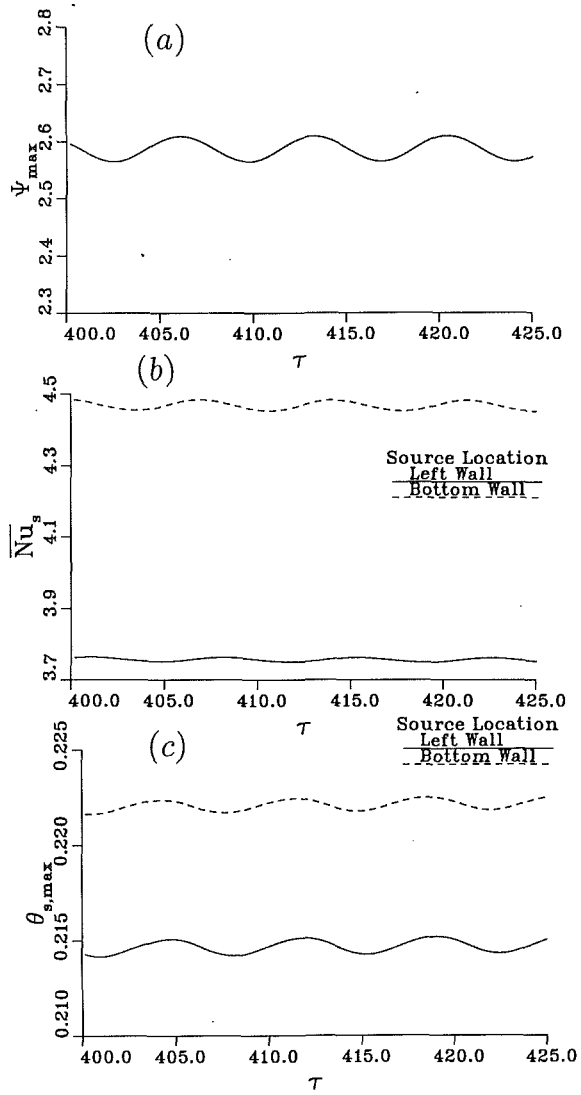

Fig. 8 Periodic behavior of the maximum stream function, average Nusselt number and maximum temperature at the sources, in the LB configuration, for Re = 100, $Gr/Re^2 = 50$, and $\tau \geq 400$

cillations, characterized by distinct frequencies. The observed frequencies near the critical point were found to be functions of both the Grashof and the Reynolds number. For the value of the Reynolds number under consideration here, Re = 100, the critical value of Gr/Re^2 in the **L** configuration was found to be $Gr/Re^2 \simeq 33$. In previous numerical and experimental investigations on natural convection in closed cavities, a similar periodic behavior has been observed and has been shown to be the first transition on the route to turbulence, occurring in the form of Hopf bifurcation (Winters, 1987). For mixed convection in enclosures, periodic oscillations, although eventually damped, were also observed by Simoneau et al. (1988) for opposing forced flows. Interestingly enough, in the **LR** configuration the flow is found to be steady even at $Gr/Re^2 = 50$. Table 1 compares the frequencies and amplitudes A_Ψ of the maximum stream function[2] for three different configurations, the **L** configuration with a single source and two configurations of the present work that consider two heat sources, namely **LB** and **BR**. It appears that the **BR** configuration is the most unstable of the three and it can be observed that the presence of a second source at the bottom makes the single source configuration more stable (lower amplitudes), at least at $Gr/Re^2 = 50$. The frequencies when two sources are present are lower than that for a single source.

Heat Source Temperatures. One of the most important results here is certainly the magnitude of the maximum temperatures that develop over the heat sources $\theta_{s,max}$. In the configuration studied, the temperature obtained is the "case" temperature, i.e., the temperature at the outside surface of the component case. If the internal resistance of the component and the amount of heat that is lost to the fluid are known, the chip temperature can be determined from the case temperature. The results are here presented for varying locations and varying heat inputs, the latter expressed in terms of the corresponding Grashof numbers. The variation of $\theta_{s,max}$ with Gr/Re^2 for each configuration where the source appears is shown in Fig. 10. For the configurations **LB** and **BR**, the solution changes from steady to periodic between $Gr/Re^2 = 10$ and $Gr/Re^2 = 50$. Therefore, at $Gr/Re^2 = 50$, the mean values of $\theta_{s,max}$ are shown in Fig. 10. One may conclude that as the heat inputs from the sources increase, the left wall location maintains lower temperatures in the **LB** configuration rather than the **LR** configuration, the bottom location does so in the **BR** configuration and the right wall location in the **BR** configuration.

The effect of Gr on the actual maximum temperature $T_{s,max}$ can not be observed in Fig. 10, because θ is nondimensionalized by ΔT, which itself varies with Gr. Therefore, one can only compare values of θ at the same Grashof number. In order to study the effect of the Grashof number, a more suitable quantity would be the product $\theta \times Gr$ because this is found to be $\theta \times Gr \propto (T - T_i)$, i.e., proportional to the physical tempera-

[2] $A_\Psi = \Psi_{max,max} - \Psi_{max,mean}$, where the first subscript in Ψ refers to space and the second one refers to time.

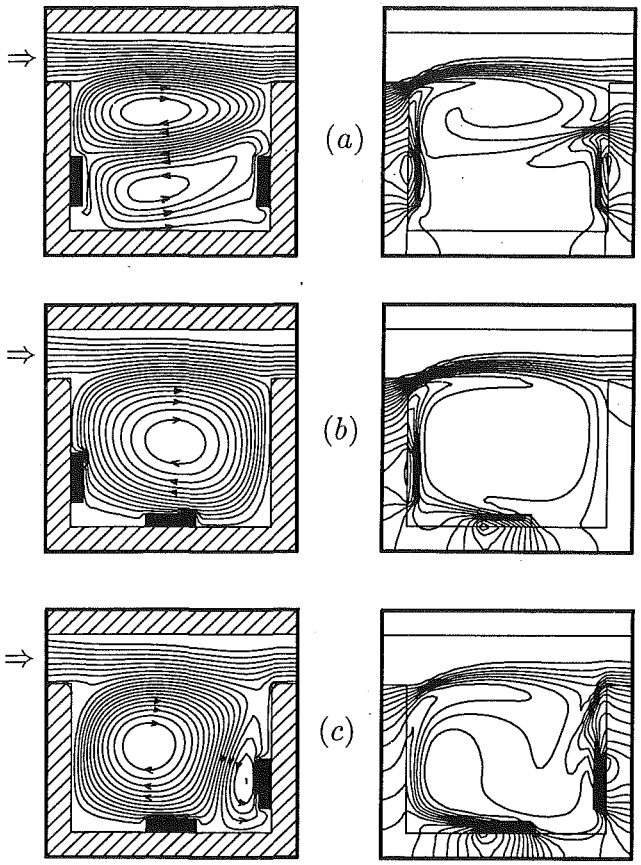

Fig. 9 Calculated streamlines and isotherms for steady and periodic solutions obtained for Re = 100 and Gr/Re^2 = 50: (*a*) LR configuration (steady), $\Psi_{max} = 2.718$, $\theta_{max} = 0.248$; (*b*) LB configuration (periodic), $\Psi_{max} = 2.587$, $\theta_{max} = 0.222$; (*c*) BR configuration (periodic), $\Psi_{max} = 2.410$, $\theta_{max} = 0.168$

Table 1 Comparison of the dimensionless frequencies and amplitudes of the periodic variation of the maximum stream function for various configurations at Re = 100 and Gr/Re^2 = 50

Configuration	Frequency	A_Ψ/Ψ_{max}
L (1 flush source)	0.2542	1.857
LB	0.1398	0.966
BR	0.1525	14.087

Table 2 Fraction of the heat input from each source transferred to the fluid directly for the LR configuration at Re = 100

Source Location	*Gr/Re²*			
	0.1	1.0	10	50
Left Wall	0.704	0.752	0.730	0.709
Right Wall	0.736	0.702	0.768	0.789

tures. A logarithmic plot of the variation of the product $\theta \times Gr$ with Gr/Re^2 was also made and showed clearly that the maximum physical temperatures at the sources increase as the heat inputs increase, as expected, and the variation is almost linear over the range considered.

Heat Transfer From the Sources. The heat transfer from the sources can be studied through the average Nusselt number over the perimeter of the sources. A local heat transfer coefficient $h(s)$ is first defined in terms of the heat flux input q_s''

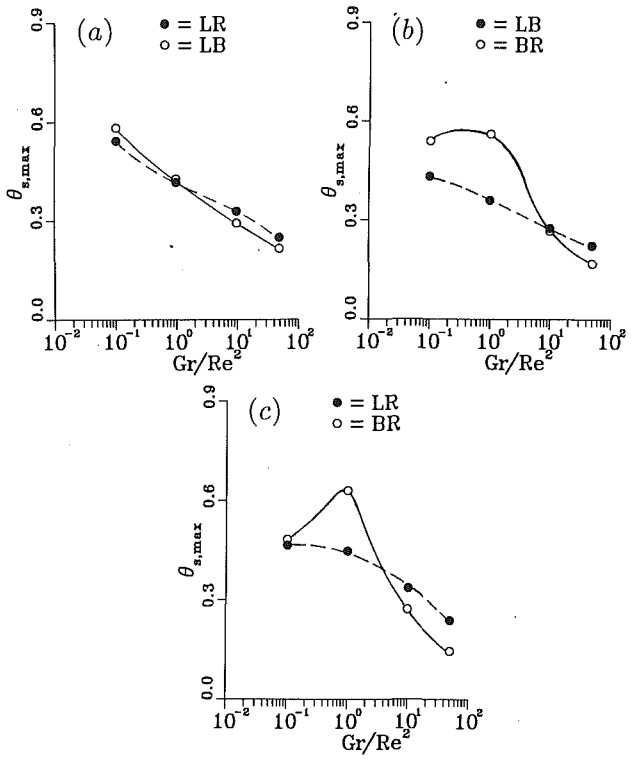

Fig. 10 Comparison of the maximum temperature for each source location in the configurations considered, at various values of Gr/Re^2, for: (*a*) left wall location; (*b*) bottom wall location; (*c*) right wall location

per unit area of the surface of the source. The mean heat transfer coefficient then is:

$$\bar{h} = \frac{q_s''}{\bar{T}_s - T_i} = \frac{q_s''}{\left(\frac{1}{\Pi_s}\int_{\Pi_s} T(s)ds\right) - T_i} \tag{11}$$

Using this result and after nondimensionalizing, the following expression is obtained for $\overline{Nu}$ at the source:

$$\overline{Nu}_s = \frac{\bar{k} H_i}{k_f} = \frac{1}{\frac{1}{\Pi_s^*}\int_{\Pi_s^*} \theta(s^*)ds^*} = \frac{1}{\bar{\theta}_s} \tag{12}$$

It is clear from the definition above that $\overline{Nu}_s$ expresses the total heat transfer rate from the source, both through the fluid directly and through the solid walls. If interest lies in the amount of heat q''_{s_f} transferred to the fluid directly at the heat source surface, q_s'' in Eq. (11) should be replaced by $q''_{s_f} = -k_f(\partial T/\partial n)_f$, where n is the direction normal to the source surface. If the corresponding Nusselt number is computed and compared to the total Nusselt number $\overline{Nu}_s$, the fraction of the surface heat flux of the source that is transferred directly to the fluid can be found. This quantity for the **LR** configuration at different values of Gr/Re^2 and for each source is shown in Table 2. For the particular values of the thermal properties chosen, 70–80 percent of the heat flux of each source is directly transferred to the fluid, while the rest is first transferred to the walls of the enclosure and then to the fluid. Such a result answers a fundamental question that very often arises in electronic packaging, because there is usually a need to have an estimate of the amount of the dissipated power that flows through the leads and the solder joints of an electronic module to the printed circuit card. When good estimates of the thermal conductivities of the various materials along the path of heat flow and the associated thermal resistances have been obtained, lead, joint, and card temperatures can be predicted. For more

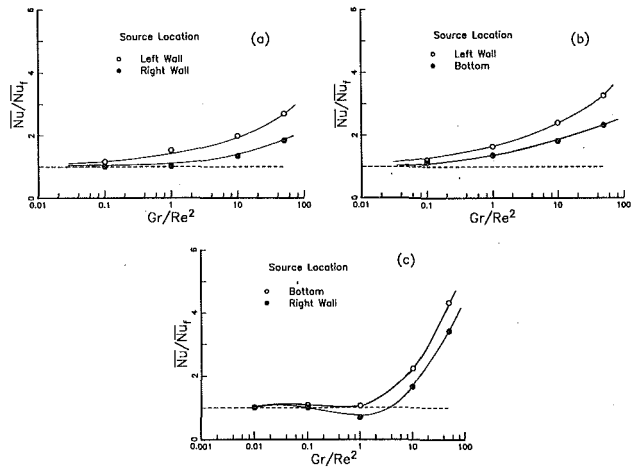

Fig. 11 Ratio of the average Nusselt number at the source in mixed convection $\overline{Nu}$ to the forced convection value Nu_n at various values of Gr/Re^2, for $Re = 100$: (*a*) LR; (*b*) LB; (*b*) BR

detailed results, a conduction model for the card can be developed, using the heat input $q''_{s,s}$ as a boundary condition.

For most values of Gr/Re^2, source **R** is found to have a higher $\overline{Nu}_s$, with the value $Gr/Re^2 = 1$ being the only exception. Based on Figs. 4 and 6, it appears that the recirculating flow interacts with source **R** at lower temperatures than either one of the other two sources, since, at the point of interaction, it has already been precooled by exchanging heat with the external flow. Source **L** seems to have the lowest heat transfer rate for each applicable configuration. Contrary to source **R**, source **L** always interacts with a recirculating flow already preheated by another source upstream. Therefore, the left wall location is found to be the most ineffective in terms of heat removal and the right wall location is the most effective.

With the forced convection results known, the relative magnitude of the average Nusselt number $\overline{Nu}_s$ at the sources for mixed convection (with the subscript s omitted for brevity) over the corresponding value for forced convection $\overline{Nu}_f$, at different values of Gr/Re^2, can be plotted, as shown in Fig. 11. Generally, the ratio $\overline{Nu}/\overline{Nu}_f$ increases with Gr/Re^2, except in the **BR** configuration at low Gr/Re^2. In that case, the opposing effects of the external flow are stronger and $\overline{Nu}/\overline{Nu}_f$ decreases first with Gr/Re^2, before buoyancy dominates and an increasing trend is observed. This behavior was also found in the opposing-forced-flow results of Simoneau et al. (1988), where the Nusselt number curves crossed the forced convection asymptote as Gr/Re^2 decreases before approaching the asymptotic value. The results do not seem to correlate very well over the entire range of Gr/Re^2 studied and for all configurations. Only as buoyancy dominates and the natural convection limit is approached, an almost linear behavior is observed in the logarithmic values of the data as Gr/Re^2 increases, with the slope of the line again varying for each configuration. Unfortunately, for the present problem the natural convection limit of the Nusselt number Nu_n is not known, unlike the problem studied by Simoneau et al. (1988). In that particular case, Nu_n was taken from the corresponding value for the benchmark problem of natural convection in a square, closed cavity (de Vahl Davis and Jones, 1982). Here, in the natural convection dominated range ($Gr/Re^2 \geq 1$), and for $Re = 100$ the results can be described by a correlation of the following form:

$$\frac{\overline{Nu}}{\overline{Nu}_f} \propto \left(\frac{Gr}{Re^2}\right)^C \tag{13}$$

where C depends on the configuration and the source location and has the computed values shown in Table 3. The correlation

Table 3 Exponent values in Eq. (13)

Configuration	Source Location	C	C_T
LR	L	0.143	0.167
LR	R	0.149	0.175
LB	L	0.174	0.211
LB	B	0.135	0.156
BR	B	0.357	0.555
BR	R	0.404	0.678

Table 4 Exponent of Gr or Ra found in previous studies

Reference	Fluid	Exponent	Orientation
1. Turner and Flack (1980)	Air	0.320	Vertical
2. Keyhani et al. (1988b)	Pr = 1, 25, 166	0.205-0.207	Vertical
3. Shen et al. (1989)	Pr = 1	0.118, 0.177, 0.203	Vertical
4. Joshi et al. (1991)	Fluorinert	0.210	Vertical
5. Kang and Jaluria (1990)	Air	0.170	Vertical
6. " " " (1990)	"	0.217	Horizontal
7. Mahaney et al. (1991)	Water	0.222	Horizontal

Note: Gr in study 1 and Ra in 2 were based on the cavity height and width respectively. Values in 3 are for each source (bottom to top). Only 7 included mixed convection effects.

was also modified to include the dependence on the conventional Grashof number, which is based on a characteristic temperature difference rather than a characteristic heat flux. This Grashof number is here denoted by Gr_T and is obtained by substituting ΔT of our nomenclature list by $\overline{T}_s - T_i$. Sparrow and Gregg (1956) demonstrated that there is a relationship of the form $Gr = \overline{Nu}\, Gr_T$, using our notation. The corresponding exponent in the correlation, denoted by C_T, is also listed in Table 3.

All these have correlation coefficients close to 0.99. It can be observed in Table 3 that in the **BR** configuration the variation of the Grashof number has a much larger effect on the heat transfer compared to the other two configurations. Clearly, the effect of the Reynolds number alone on the heat transfer is not included in this correlation and more data is needed. A wide range of Reynolds number was covered only for mixed convection from a single source in a cavity with adiabatic walls (Papanicolaou and Jaluria, 1990).

Several experimental heat transfer correlations exist, although obtained in configurations and parameter ranges with minor to significant differences from the present ones. The most relevant were those derived in the experimental studies by Turner and Flack (1980), Keyhani et al. (1988a, 1988b), Chen et al. (1991), and Joshi et al. (1991) for sources mounted on vertical surfaces, Kang et al. (1990) and Mahaney et al. (1991) for sources on horizontal surfaces, and Kang et al. (1990) for both orientations. Very relevant are also the correlations obtained in the numerical study of Shen et al. (1989). Most of these works studied natural convection and the correlations demonstrated the effect of the Grashof or Rayleigh number on the heat transfer from the sources or blocks. However, the length scale in the definition of Gr or Ra was not in all cases the length of the source, as in the present study, but one of the overall dimensions of the cavity (height or width). Table 4 summarizes the exponent values found in the aforementioned references, in the most appropriate correlations for comparisons with Eq. (13) of the present study. The results of Kang et al. (1990) are not presented here, since their objective was to show the effect of varying Re, while Gr was kept fixed.

Comparing the results in Table 3 and Table 4, despite the differences in the configurations, one can observe that the **LB** configuration of this work and the result for source **L** agrees well with the results of Shen et al. (1989) for the middle source and those of Kang et al. (1990) for the vertical configuration.

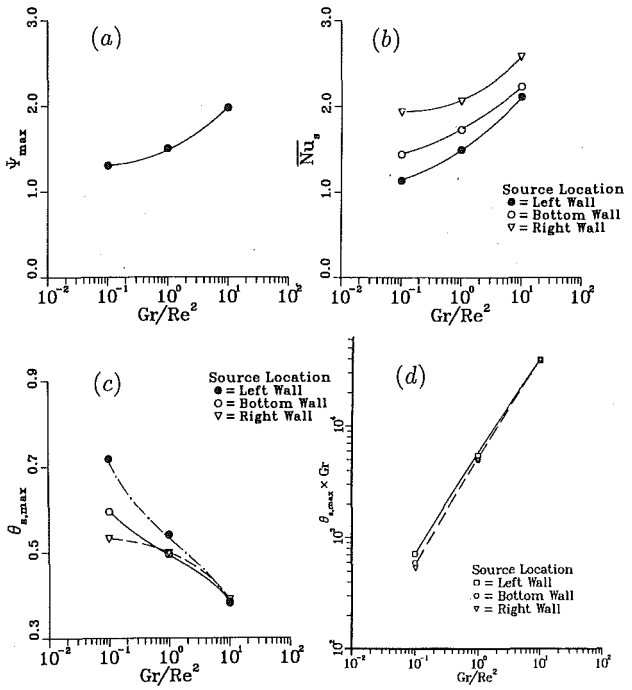

Fig. 12 Effect of Gr/Re^2 in the LBR configuration at $Re = 100$ on: (*a*) maximum stream function; (*b*) average Nusselt number at the sources; (*c*) maximum source temperatures (dimensionless); (*d*) maximum source temperatures (physical)

The **L** source in the **LB** configuration does bear some similarities with the middle source of Shen et al. (1989), since both are subject to upstream effects by one other source. In this work, this effect can be realized by observing the flow patterns of Fig. 5. Heat transfer from source **B** in the **LB** configuration is characterized by an exponent that is between the results of Shen et al. (1989) for sources 1 and 2. The same can be said for both sources in the **LR** configuration where, as shown in Figs. 4 and 9, the heat removal by the recirculating flow from each source is greatly obstructed by the presence of the other source. Therefore, deviations from the case where no such obstructions are present are expected. The **BR** configuration is characterized by exponents that are much larger than all other cases. In this case too, the interaction between the sources is very strong and the flow patterns so diverse that deviations are justified. It is interesting to observe, however, that the exponent for source **B** is close to 1/3, which is a well-established value for natural convection in air layers heated from below at large Ra (see Hollands et al., 1975).

The fact that all other exponents in Table 4 seem to be around 0.21 indicates similarities to the $Gr^{1/5}$ law, which is also an established result for the laminar natural convection boundary layer from a heat source on a vertical plate, as discussed by Kang et al. (1990). The result of Turner and Flack (1980) seems to deviate somewhat from other correlations, but it may have to do with the isothermal conditions at the sources maintained in their experiment, unlike all other references, where constant flux heaters were used. As can be seen in Table 3, when the Grashof number is based on a characteristic temperature difference (as for an isothermal source), higher exponents are obtained.

Finally, the present results were compared against the criterion for the definition of the forced convection regime, introduced by Sparrow and Gregg (1959), according to which the Nusselt numbers should differ by less than 5 percent from the asymptotic forced convection value. The forced convection regime here is found to be given by $Gr/Re^2 \leq 0.01$, for all configurations studied and for all heat sources, as can be seen in Fig. 11. It should be noted that in the **LR** and **LB** configurations the value of $\overline{Nu}_s$ monotonically decreases to the forced convection value for all source locations, while in the **BR** configuration a nonmonotonic behavior was observed at low Gr/Re^2, due to buoyancy-opposing recirculation, as explained in a previous section.

Results for Three Heat Sources (LBR Configuration). The effect of varying Gr/Re^2, obtained by varying Gr, on the various results of interest is shown in Fig. 12. The maxiumum stream function is higher at the same Gr/Re^2 in the LBR configuration as expected, compared to the three configurations with two sources. Besides, the Nusselt numbers are lower and the maximum source temperatures are higher in most cases. For source **L**, this is true at all values of Gr/Re^2 and both the **LR** and **LB** configurations, while for source **B** this happens at all cases except for $Gr/Re^2 = 10$ in the **BR** configuration, where higher $\overline{Nu}_s$ and lower $\theta_{s,max}$ are found. This shows that the existence of a unicellular flow pattern (Fig. 7*b*), rather than a flow pattern with two cells (Fig. 6*b*), leads to more favorable heat transfer results. The right wall location always exhibits higher temperatures in the **LBR** configuration than in the **LR** and **BR** configurations, but not always a lower $\overline{Nu}_s$. However, again for $Gr/Re^2 = 10$, comparing the **LBR** with the **BR** case, the temperature is lower in the **LBR** configuration and $\overline{Nu}_s$ is higher. The physical maximum temperatures at the sources increase with Gr/Re^2 as shown in Fig. 12(*d*), though the dimensionless temperatures decrease. From the logarithmic plot, a dependence of the form $T_{s,max} - T_i \propto Gr^{0.9}$ was found in the **LBR** configuration.

Conclusions

A numerical procedure was developed to simulate the laminar mixed convective cooling of electronic components located in an enclosure. Results are presented for the flow field and the temperature distribution both in the fluid and the solid walls (conjugate problem). The numerical method presented is very robust and capable of treating different numbers, locations, and thicknesses of heat sources. In general, it appears that the location of the source on the right vertical wall is the most favorable in terms of cooling. Laminar results are predicted up for up to $Gr = 10^5$ for all configurations studied, but at $Gr = 5 \times 10^5$ in some cases, periodic oscillatory solutions were found. This result indicates that at a certain amount of heat input by the components, oscillatory flow and thermal fields may develop in the cavity. The two-dimensional model studied here applies to two or three long rows of electronic modules mounted on either one of two vertical printed circuit boards or on a horizontal board and extending in the direction normal to the plane under consideration. The results from the various cases studied are extremely helpful in understanding the flow patterns that develop in an air-cooled electronic enclosure and the thermal interactions between the components. This allows for an evaluation of the various alternative placements of the components and selection of the one that leads to the best thermal performance. Quantitative heat transfer results were also obtained and compared to previously existing data for configurations of relevance to the present ones.

Acknowledgments

The authors acknowledge the partial support from NSF, under grant No. CBT-88-03049, and from the Department of Mechanical and Aerospace Engineering, Rutgers University, for this work.

References

Afrid, M., and Zebib, A., 1989, "Natural Convection Air Cooling of Heated

Components Mounted on a Vertical Wall," *Num. Heat Transfer*, Vol. 15, pp. 243–259.

Braaten, M. E., and Patankar, S. V., 1984, "Analysis of Laminar Mixed Convection in Shrouded Arrays of Heated Rectangular Blocks," in: *Fundamentals of Natural Convection/Electronic Equipment Cooling*, ASME HTD-Vol. 32, pp. 77–84.

Chen, L., Keyhani, M., and Pitts, D. R., 1991, "Convection Heat Transfer Due to Protruded Heat Sources in an Enclosure," *AIAA J. of Thermophysics*, Vol. 5, No. 2, pp. 217–223.

Davalath, J., and Bayazitoglu, Y., 1987, "Forced Convection Cooling Across Rectangular Blocks," ASME JOURNAL OF HEAT TRANSFER, Vol. 109, pp. 321–328.

de Vahl Davis, G., and Jones, I. P., 1982, "Natural Convection in a Square Cavity: a Comparison Exercise," Univ. of New South Wales, School of Mech. and Indust. Eng., Report 1982/FMT/3.

Elpidorou, D., Prasad, V., and Modi, V., 1991, "Convection in a Vertical Channel With a Finite Wall Heat Source," *Int. J. Heat Mass Transfer*, Vol. 34, No. 2, pp. 573–578.

Habchi, S., and Acharya, S., 1986, "Laminar Mixed Convection in a Partially Blocked, Vertical Channel," *Int. J. Heat Mass Transfer*, Vol. 29, No. 11, pp. 1711–1722.

Hollands, K. G. T., Raithby, G. D., and Konicek, L., 1975, "Correlation Equations for Free Convection Heat Transfer in Horizontal Layers of Air and Water," *Int. J. Heat Mass Transfer*, Vol. 18, pp. 879–884.

Incropera, F. P., 1988, "Convection Heat Transfer in Electronic Equipment Cooling," ASME JOURNAL OF HEAT TRANSFER, Vol. 110, pp. 1097–1111.

Jaluria, Y., and Torrance, K. E., 1986, *Computational Heat Transfer*, Hemisphere, Washington, DC.

Joshi, Y., Kelleher, M. D., Powell, M., and Torres, E. I., 1991, "Natural Convection Heat Transfer From an Array of Rectangular Protrusions in an Enclosure Filled With Dielectric Liquid," in: *Heat Transfer Enhancement in Electronics Cooling*, S. H. Bhavnani and M. Greiner, eds., ASME HTD-Vol. 183, pp. 9–18.

Kang, B., Jaluria, Y., and Tewari, S. S., 1990, "Mixed Convection Cooling of an Isolated Heat Dissipating Module on a Horizontal Plate," ASME JOURNAL OF HEAT TRANSFER, Vol. 112, pp. 653–661.

Keyhani, M., Prasad, V., and Cox, R., 1988a, "An Experimental Study of Natural Convection in Vertical Cavity With Discrete Heat Sources," ASME JOURNAL OF HEAT TRANSFER, Vol. 110, pp. 616–624.

Keyhani, M., Prasad, V., Shen, R., and Wong, T.-T., 1988b, "Free Convection Heat Transfer From Discrete Heat Sources in a Vertical Cavity," in: *Natural and Mixed Convection in Electronic Equipment Cooling*, R. A. Wirtz, ed., ASME HTD-Vol. 100, pp. 13–24.

Khalilollahi, A., and Sammakia, B. G., 1989, "Transient Mixed Convection in Air Adjacent to Discrete Uniform Flux Heat Sources," in: *Numerical Simulation of Convection in Electronic Equipment Cooling*, ASME HTD-Vol. 121, pp. 55–60.

Kim, W. T., and Boehm, R. F., 1990, "Combined Free and Forced Convective Heat Transfer From Multiple Rectangular Wall Blocks in Vertical Channels," in: *Mixed Convection and Environmental Flows*, R. L. Mahajan et al., eds., ASME HTD-Vol. 152, pp. 1–8.

Mahaney, H. V., Incropera, F. P., and Ramadhyani, S., 1990, "Comparison of Predicted and Measured Mixed Convection Heat Transfer From an Array of Discrete Sources in a Horizontal Rectangular Channel," *Int. J. Heat Mass Transfer*, Vol. 33, No. 6, pp. 1233–1245.

Papanicolaou, E., and Jaluria, Y., 1990, "Mixed Convection From Isolated Heat Sources in a Rectangular Enclosure," *Num. Heat Transfer*, Part A, Vol. 18, pp. 427–461.

Papanicolaou, E., 1991, "Mixed Convection From Isolated Heat Sources in a Cavity—a Study of Various Regimes and Configurations," Ph.D. Thesis, Rutgers University, New Brunswick, NJ.

Papanicolaou, E., and Jaluria, Y., 1992, "Transition to a Periodic Regime in Mixed Convection in a Square Cavity," *J. Fluid Mech.*, Vol. 239, pp. 489–509.

Papanicolaou, E., and Jaluria, Y., 1993, "Mixed Convection From a Localized Heat Source in a Cavity With Conducting Walls," *Num. Heat Transfer*, Part A, Vol. 23, pp. 463–484.

Patankar, S. V., 1980, *Numerical Heat Transfer and Fluid Flow*, Hemisphere, Washington, DC.

Rizk, T. A., and Kleinstreuer, C., 1989, "Forced Convection Cooling of a Linear Array of Blocks in Open and Porous Matrix Channels," in: *Heat Transfer in Electronics*, R. K. Shah, ed., ASME HTD-Vol. 111, pp. 155–159.

Said, S. A. M., and Muhanna, A., 1990, "Investigation of Natural Convection in a Vertical Parallel-Walled Channel With a Single Square Obstruction," in: *Simulation and Numerical Methods in Heat Transfer*, A. F. Emery, ed., ASME HTD-Vol. 157, pp. 73–80.

Sathe, S. B., and Joshi, Y., 1990, "Natural Convection Liquid Cooling of a Substrate-Mounted Protrusion in a Square Enclosure: Effects of Thermophysical Properties, Geometric Dimensions and Boundary Conditions," in: *Thermal Modeling and Design of Electronic Systems and Devices*, R. A. Wirtz and G. L. Lehmann, eds., ASME HTD-Vol. 153, pp. 73–80.

Schmidt, R. R., 1991, "Convection Cooling of Electronic Equipment," IBM Tech. Report, TR 00.3620.

Shen, R., Prasad, V., and Keyhani, M., 1989, "Effect of Aspect Ratio and Size of Heat Source on Free Convection in a Discretely Heated Vertical Cavity," in: *Numerical Simulation of Convection in Electronic Equipment Cooling*, ASME HTD-Vol. 121, pp. 45–54.

Simoneau, J. P., Inard, C., and Allard, F., 1988, "Numerical Approach to Interaction Between an Injection and Laminar Natural Convection in a Thermally Driven Cavity," in: *Natural Convection in Enclosures*, R. S. Figliola and P. G. Simpkins, eds., ASME HTD-Vol. 99, pp. 45–51.

Sparrow, E. M., and Gregg, J. L., 1956, "Laminar Free Convection From a Vertical Plate With Uniform Surface Heat Flux," *Trans. ASME*, Vol. 78, pp. 435–440.

Sparrow, E. M., and Gregg, J. L., 1959, "Buoyancy Effects in Forced-Convection Flow and Heat Transfer," ASME *Journal of Applied Mechanics*, Vol. 26, pp. 133–134.

Turner, B. L., and Flack, R. D., 1980, "The Experimental Measurement of Natural Convective Heat Transfer in Rectangular Enclosures With Concentrated Energy Sources," ASME JOURNAL OF HEAT TRANSFER, Vopl. 102, pp. 236–241.

Winters, K. H., 1987, "Hopf Bifurcation in the Double-Glazing Problem With Conducting Boundaries," ASME JOURNAL OF HEAT TRANSFER, Vol. 109, pp. 894–898.

Zebib, A., and Wo, Y. K., 1985, "A Two-Dimensional Conjugate Heat Transfer Model for Forced Air Cooling of an Electronic Device," *Proc. of the International Electronic Packaging Conference*, Orlando, FL.

Optical Properties of Soot in Buoyant Laminar Diffusion Flames

Ü. Ö. Köylü
Research Fellow.

G. M. Faeth
Professor.
Fellow ASME

Department of Aerospace Engineering,
The University of Michigan,
Ann Arbor, MI 48109-2118

The structure and optical properties of soot were studied in the fuel-rich (underfire) region of buoyant laminar diffusion flames of ethylene and acetylene burning in coflowing air. The objective was to evaluate scattering predictions based on the Rayleigh–Debye–Gans (RDG) approximation for polydisperse fractal aggregates of spherical primary soot particles having constant diameters, for conditions where the Guinier (small angle) regime, and the transition between the Guinier and the power-law (large-angle) regimes, were dominant, in order to supplement earlier work for conditions where the power-law regime was dominant. Soot structure was measured using thermophoretic sampling and analysis by transmission electron microscopy (TEM) to yield primary particle diameters, distributions of the number of primary particles per aggregate, and the aggregate mass fractal dimensions. Soot optical property measurements included vv, hh, hv, and vh differential scattering cross sections, total scattering cross sections, and the albedo at 514.5 nm, as well as several soot structure parameters inferred from these measurements using the approximate theory. The approximate RDG theory generally provided an acceptable basis to treat the optical properties of the present soot aggregates over a range of conditions spanning the Guinier and power-law regimes. Other scattering approximations were less satisfactory with performance progressively becoming less satisfactory in the order: RDG polydisperse fractal aggregate scattering using a single mean squared radius of gyration (from the Guinier regime), Mie scattering for an equivalent sphere, and Rayleigh scattering—the last underestimating differential scattering levels by a factor of roughly 100 for the present test conditions.

Introduction

Both predictions of continuum radiation from flames, and nonintrusive laser-based measurements of soot structure and concentrations, require an understanding of the optical properties of soot. Soot optical properties are a challenging problem, however, due to the complexities of soot structure. In particular, soot consists of small spherical primary particles that collect into open structured aggregates having a broad distribution of sizes; see Jullien and Botet (1987) and references cited therein. Thus, although the individual primary particles generally are small enough to satisfy the Rayleigh scattering approximation, even early work showed that soot aggregates usually exhibited neither simple Rayleigh nor Mie scattering behavior (Erickson et al., 1964; Dalzell et al., 1970; Wersborg et al., 1972; Magnussen, 1974). As a result, improved methods have been sought based on the Rayleigh–Debye–Gans (RDG) scattering approximation while treating the aggregates as polydisperse collections of mass fractal objects (denoted the RDG-PFA scattering approximation in the following); see Jullien and Botet (1987), Martin and Hurd (1987), Dobbins and Megaridis (1991), and Köylü and Faeth (1994). The objective of the present investigation was to conduct an evaluation of RDG-PFA theory by measuring both the structure and scattering properties of soot found in the fuel-rich (underfire) region of buoyant laminar jet diffusion flames.

Although RDG-PFA theories have been available for some time, and have been used to interpret soot scattering properties and to infer soot aggregate structure properties from scattering measurements (Dobbins et al., 1990; Puri et al., 1993; Sorensen et al., 1992), evaluation of the method has only just begun. Köylü and Faeth (1993) discuss recent attempts to evaluate various approximations of soot scattering properties using more exact solutions for simulated aggregates. Unfortunately, computational limitations have prevented definitive results for the relatively large soot aggregates often encountered in practice. An alternative approach involves direct experimental evaluation by measuring the soot structure properties needed for RDG-PFA scattering predictions and comparing these predictions with measured scattering properties for the same soot population. Köylü and Faeth (1994) recently carried out a study along these lines for the large soot aggregates found in the overfire region of buoyant turbulent diffusion flames at long characteristic flame residence times. It was found that the RDG-PFA predictions were in reasonably good agreement with measurements of scattering and extinction properties over the wavelength range 514.5–1152 nm. However, these overfire soot aggregates were too large for practical scattering measurements in the small-angle (Guinier) regime where use of the RDG scattering approximation is least reliable (Nelson, 1989; Köylü and Faeth, 1993), in order to complete a thorough evaluation of the approximate theory. Thus, the specific objective of the present investigation was to extend the work of Köylü and Faeth (1994) in order to consider soot aggregates in the fuel-rich (underfire) region of buoyant laminar diffusion flames, where smaller aggregate sizes provide greater access to the Guinier regime as well as the transition regime between the Guinier and the power-law (large-angle) regimes.

Present measurements were carried out in ethylene and acetylene/air flames, which are representative of lightly and heavily sooting materials (Köylü and Faeth, 1992). Soot structure was measured using thermophoretic sampling and analysis by transmission electron microscopy (TEM), to find primary particle diameters, distributions of the number of primary particles per aggregate, and aggregate mass fractal dimensions. Soot optical property measurements included differential scattering cross sections for various polarizations of incident and scattered light (vv,

Contributed by the Heat Transfer Division and presented at the ASME Winter Annual Meeting, New Orleans, Louisiana, November 28–December 3, 1993. Manuscript received by the Heat Transfer Division May 1993; revision received December 1993. Keywords: Combustion, Fire/Flames, Radiation. Associate Technical Editor: W. L. Grosshandler.

hh, *vh*, and *hv*), total scattering cross sections, and the albedo at 514.5 nm. Predictions of scattering properties were based on the measured structure properties, considering several scattering approximations, as follows: Rayleigh scattering, Mie scattering for an equivalent sphere, RDG-PFA scattering following Dobbins and Megaridis (1991), and RDG-PFA scattering following Köylü and Faeth (1994).

The paper begins with descriptions of experimental and theoretical methods. Results are then considered, treating soot structure properties and evaluation of soot scattering approximations in turn.

Experimental Methods

Apparatus. The test apparatus consisted of a round coflowing laminar jet diffusion flame burner, directed vertically upward, having nearly the same port dimensions as the arrangement used by Santoro et al. (1983) and Dobbins and Megaridis (1987). The burner involved fuel flowing from a center tube, having an inside diameter of 14.3 mm and a wall thickness of 0.9 mm, with air flowing from a concentric outer tube, having an inside diameter of 102 mm. Both flows passed through a 50 mm deep bed of 2-mm-dia stainless steel balls, a 10 mm gap, and a 25 mm long honeycomb (1 mm hexagonal cells). The downstream end of the honeycomb was flush with the exit of the fuel and air tubes. The burner could be traversed in three directions (5 μm positioning accuracy in the two horizontal directions and 0.5 mm positioning accuracy in the vertical direction) in order to accommodate rigidly mounted instrumentation.

Fuel gases were stored in commercial cylinders under pressure. Air was obtained by filtering the laboratory air supply. Both gas flows were controlled by metering valves and measured using rotameters. The rotameters were calibrated using a wet test meter.

The flames were shielded because they were easily disturbed by drafts. The primary shield was a screen (0.3 mm wire diameter, 200 wires/m, square mesh) wrapped around the outside of the air tube and extending 300 mm from the burner exit. Slits in the screen provided access for sampling and scattering measurements. Additional flow shielding, as well as reduced background light levels, was provided by a black cloth enclosure having a diameter of 1 m that surrounded the entire apparatus.

Soot Structure Measurements. The structure of soot was measured by thermophoretic sampling and analysis using TEM,

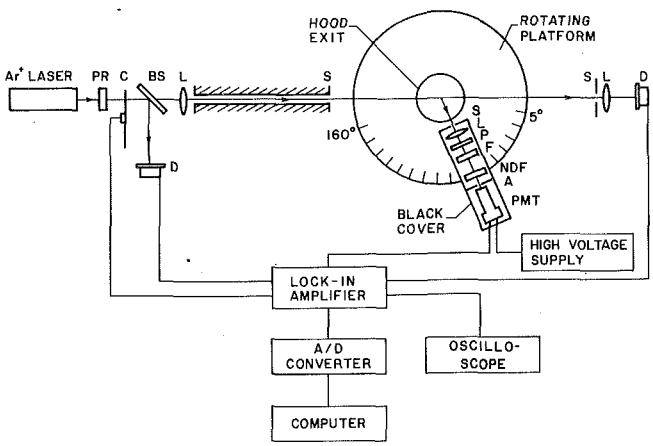

Fig. 1 Sketch of the light scattering apparatus: A = detector aperture, BS = beam splitter, C = chopper, D = laser power detector, F = laser-line filter, L = lens, NDF = neutral-density filter, P = polarizer, PMT = photomultiplier detector, PR = polarization rotator, and S = variable aperture

similar to Dobbins and Megaridis (1987) and Köylü and Faeth (1992). The sampling surfaces were the carbon-supported copper grids used to hold TEM specimens (3 mm diameter, 200 mesh copper grids supported by a 20 nm thick elemental carbon film, SPI Supplies, Philadelphia, part No. 3520C). The grids were aligned in the vertical direction, parallel to the mean flow direction at the axis. The grids were mounted on a 1 × 4 × 15 mm metal strip using double-backed adhesive which was mounted in turn on a retractable probe. The probe was stored in a cylinder located outside the screen shield, with roughly a 50 mm stroke to reach the flame axis. A double-acting pneumatic cylinder rapidly drove the probe out of the storage cylinder to the sampling position and returned it again to the cylinder when sampling was complete. Sampling times were measured using a pair of light-interrupting sensors. Sampling times were controlled so that soot aggregates covered no more than 10 percent of the surface of the TEM grid in order to avoid overlapping aggregates on the grid. This required 18–30 ms sampling times with 2–3 ms traveling times of the grid through the flame to the axis where measurements were made. Thus, residence times of the grid in

Nomenclature

A = albedo
C = optical cross section
d = diameter of fuel port
d_p = primary particle diameter
D_f = mass fractal dimension
D_{30} = aggregate volume mean diameter, Eq. (14)
$E(m)$ = refractive index function $= \mathrm{Im}((m^2-1)/(m^2+2))$
$f(qR_g)$ = aggregate form factor, Eq. (2)
$F(m)$ = refractive index function $= |(m^2-1)/(m^2+2)|^2$
$g(\lambda, R_g, D_f)$ = aggregate total scattering factor, Eq. (5)
i = $(-1)^{1/2}$
k_f = fractal prefactor, Eq. (1)
m = refractive index of soot $= n + i\kappa$
n = real part of refractive index of soot
n_a = mean number of aggregates per unit volume
n_p = mean number of primary particles per unit volume
N = number of primary particles per aggregate
N_c = aggregate size for onset of power-law regime, Eq. (7)
$p(N)$ = probability density function of aggregate size
q = modulus of scattering vector = $(4\pi/\lambda)\sin(\theta/2)$
Q = volumetric optical cross section
R_g = radius of gyration of an aggregate
$\bar{R}^2_{gG}$ = mean square radius of gyration for the Guinier regime, Eq. (10)
$\bar{R}^2_{gL}$ = mean square radius of gyration for the power-law regime, Eq. (11)
x_p = primary particle optical size parameter = $\pi d_p/\lambda$
θ = angle of scattering from forward direction
κ = imaginary part of refractive index of soot
λ = wavelength of radiation
ρ_v = depolarization ratio
σ_N = standard deviation of N
σ_p = standard deviation of d_p

Subscripts

a = absorption
h = horizontal polarization
ij = incident (i) and scattered (j) polarization direction
s = total scattering
v = vertical polarization

Superscripts

a = aggregate property
p = primary particle property
$\bar{(\ )}$ = mean value over a polydisperse aggregate population

the soot layer were only 3–5 percent of residence times at desired conditions along the flame axis so that contamination of the samples from the soot layer was small.

The principles of thermophoretic sampling are discussed elsewhere (Dobbins and Megaridis, 1987; Köylü and Faeth, 1992; Rosner et al., 1991). For present conditions, primary particle diameters are smaller than the mean free path so that the thermophoretic velocities of individual particles are the same. In addition, Rosner et al. (1991) have shown that the thermophoretic velocities of aggregates are the same as individual primary particles, even when the aggregates are larger than mean free path lengths. Thus, there is no intrinsic bias with respect to aggregate size for the thermophoretic sampling technique.

The samples were observed using a JEOL 2000 FX analytical electron microscope system with a 1 nm edge-to-edge resolution. Latex spheres having a diameter of 91 nm (with a standard deviation of 5.8 nm) were used to calibrate the TEM measurements. The details of the TEM measurements, and the software used to analyze the images, are discussed by Köylü and Faeth (1992). Experimental uncertainties of soot structure parameters are considered when these measurements are discussed. All measurements were repeatable within the stated uncertainties.

Soot Scattering Measurements. The arrangement for soot scattering measurements was similar to Köylü and Faeth (1994), except for changes in optics to improve the spatial resolution so that underfire conditions could be treated. A sketch of the arrangement appears in Fig. 1. An argon-ion laser having an optical power of 1700 mW at 514.5 nm was used for the scattering measurements. The incident laser beam was passed through a polarization rotator and a mechanical chopper (operating at 1250 Hz) before being focused at the axis of the flame using a 350 mm focal length lens. This yielded a waist diameter of 150 μm and a confocal length of roughly 140 mm. The collecting optics were mounted on a turntable surrounding the burner so that scattering angles, θ = 20–160 deg, could be considered. The collecting optics consisted of an 85 mm focal length lens, a dichroic sheet polarizer, a laser line filter (1 nm bandwidth) and a cooled photomultiplier. The lens aperture defined a solid collection angle of 0.7 msr with a 0.4 mm long sampling volume at θ = 90 deg, which increased to roughly 1.2 mm at θ = 20 and 160 deg. Neutral-density filters were used in the optical path to control the dynamic range of detection. The detector output passed through a lock-in amplifier and was stored on a computer, sampling at 500 Hz for 10 s and averaging five sampling intervals to achieve a repeatability within 10 percent.

The angular light scattering system was calibrated by measuring Rayleigh scattering from nitrogen gas. After correction for the reciprocal sin θ dependence of the scattering volume, the *vv* and *hh* differential cross sections were within 5 percent of Rayleigh scattering predictions for θ of 20–160 deg. Absolute volumetric differential scattering cross sections of soot were found from ratios of the detector signal for soot and nitrogen, after accounting for signal attenuation in the optical path, based on the nitrogen optical properties of Rudder and Bach (1968). Total volumetric scattering cross sections were found by integrating the volumetric differential scattering cross sections over the whole spherical surface. This required extrapolation of the measurements to reach θ = 0 and 180 deg; however, uncertainties caused by the extrapolations were small due to the relatively slow variation of scattering properties near the forward and backward directions and the relatively small solid angles involved.

The laser power was monitored continuously and did not fluctuate. The dark current of the photomultiplier also did not vary with time and was small, e.g., roughly 1 percent of the *vh* and *hv* scattering signals. Effects of fluorescence from the reactive soot-containing mixture at fuel-rich conditions in the test flame are more difficult to evaluate but are not thought to be large. In particular, fluorescence contributions are the same for all scattering signals; therefore, they can be no larger than the *vh* and *hv* scattering signals, which are only on the order of 10^{-2} of the main scattering signals of interest, e.g., $\bar{C}^a_{vv}(\theta)$. Additionally, values of $\bar{\rho}^a_v$ for the present underfire soot were comparable to values measured by Köylü and Faeth (1994) for overfire soot, where fuel-lean conditions and substantial dilution imply negligible effects of fluorescence. Thus, it is suspected that effects of fluorescence were small even for *vh* and *hv* scattering measurements, although quantitative evaluation of effects of fluorescence on optical measurements of soot properties at fuel-rich conditions clearly merits further attention. Based on these considerations, the overall experimental uncertainties (95 percent confidence) of the angular (excluding depolarization ratios and $\bar{C}^a_{hh}(\theta)$ near 90 deg) and the total light scattering measurements were comparable and were estimated to be less than 20 percent, dominated by finite sampling times, the finite aperture of the detector, and the angular uncertainty of the collecting optics.

Test Conditions. Measurements were limited to soot found along the axis of the fuel-rich region of the ethylene and acetylene/air flames summarized in Table 1. The ethylene/air flame was nonsooting while the acetylene/air flame was soot emitting. Two heights above the burner exit were considered for each of the flames: 50 and 70 mm for the ethylene/air flame and 30 and 45 mm for the acetylene/air flame. These conditions provide access to both the Guinier and power-law regimes while involving a reasonable range of soot aggregate structure properties.

Theoretical Methods

Present RDG-PFA Scattering Theory. Predictions of soot optical properties were based on methods described by Jullien and Botet (1987), Martin and Hurd (1987), and Dobbins and Megaridis (1991) for a single aggregate. However, attention was focused on the treatment of Köylü and Faeth (1994) for polydisperse aggregate populations. This involves use of the RDG scattering approximation so that effects of multiple- and self-scattering are ignored, the electric field of each particle is assumed to be the same as the incident field, and differences of the phase shift of scattered light from various points within a particular primary particle are neglected. The RDG scattering approximation requires that both $|m - 1| \ll 1$ and $2x_p|m - 1| \ll 1$ (Kerker, 1969; van de Hulst, 1957; Bohren and Huffman, 1983), which is questionable due to the relatively large refractive indices of soot (Köylü and Faeth, 1993). Recent computational studies also suggest significant effects of multiple scattering for soot aggregates, see Köylü and Faeth (1993) and references cited therein. Thus, use of RDG theory only can be justified by its capabilities to treat measured soot properties, which is considered during the present investigation.

The major assumptions with respect to aggregate structure are as follows (Köylü and Faeth, 1994): spherical primary particles having constant diameters, primary particles do not overlap but just touch one another, uniform refractive indices, and the aggregates are mass fractal-like objects. The mass fractal approximation implies the following relationship between the number of particles in an aggregate and its radius of gyration (Jullien and Botet, 1987):

Table 1 Summary of test flames[a]

Fuel	Ethylene/Air	Acetylene/Air
Fuel mass flow rate (mg/s)	5.0	4.0
Air mass flow rate (mg/s)	400	400
Condition	nonsooting	sooting
Flame height (mm)	83	55

[a]Coflowing buoyant laminar jet burner with fuel and air port diameters of 14.3 and 102 mm at atmospheric pressure, 99 ± 0.5 kPa.

$$N = k_f(R_f/d_p)^{D_f} \quad (1)$$

Based on past measurements for both overfire and underfire soot, $k_f = 8.1$ was used during present work (Köylü and Faeth, 1994; Puri et al., 1993). The assumptions of nearly constant diameter primary particles and mass fractal-like behavior are justified by the present soot structure measurements, as discussed later, while the remaining assumptions are typical of past work; see Köylü and Faeth (1993) and references cited therein. One change from the approach of Köylü and Faeth (1994), however, was that the measured aggregate size distribution was used directly in the computations, to avoid potential errors due to empirical fits of the distribution.

Only the main results of the RDG-PFA scattering theory will be summarized in the following; see Köylü and Faeth (1994) for the complete formulation. The treatment begins with the scattering cross sections for a single fractal aggregate under the RDG approximation:

$$C^a_{vv}(\theta) = C^a_{hh}(\theta)/\cos^2\theta = N^2 C^p_{vv} f(qR_g) \quad (2)$$

where C^p_{vv} is the scattering cross section of a primary particle under the Rayleigh scattering approximation. The form factor, $f(qR_g)$, in Eq. (2) is expressed as follows (Freltoft et al., 1986; Jullien and Botet, 1987; Lin et al., 1989; Martin and Hurd, 1987):

$$f(qR_g) = \exp(-(qR_g)^2/3), \quad \text{Guinier regime} \quad (3)$$

$$f(qR_g) = (q^2R_g^2)^{-D_f/2}, \quad \text{power-law regime} \quad (4)$$

where the boundary between the small q (Guinier) regime and the power-law regime is $(qR_g)^2 = 3D_f/2$, chosen to match the value and derivative of $f(qR_g)$ where the regimes meet, following Dobbins and Megaridis (1991). The total scattering cross section then becomes:

$$C^a_s = N^2 C^p_s g(\lambda, R_g, D_f) \quad (5)$$

where $g(\lambda, R_g, D_f)$ takes on different forms according to whether the power-law regime is reached for $\theta \leq 180$ deg; see Köylü and Faeth (1994) for these expressions.

The mean optical cross sections of populations of randomly oriented polydisperse aggregates (polydisperse aggregates) are found by integrating over all aggregate sizes, as follows:

$$\bar{C}^a_j = \int_{N=1}^{\infty} C^a_j(n)p(N)dN; \quad j = pp, s, a \quad (6)$$

where $p(N)$ is the measured size distribution of the aggregate population. In general, Eq. (6) must be integrated numerically when scattering extends over both the Guinier and power-law regimes. However, simple closed-form expressions are possible when all the aggregates are either in the Guinier ($p(N) \ll 1$ for $N \geq N_c$) or power-law ($p(N) \ll 1$ for $N \leq N_c$) regimes, where

$$N_c = k_f(3D_f/(2q^2d_p^2))^{D_f/2} \quad (7)$$

This yields (Köylü and Faeth, 1993b):

$$\bar{C}^a_{vv}(\theta) = \bar{N}^2 C^p_{vv} \exp(-q^2\bar{R}^2_{gG}/3), \quad \text{Guinier regime} \quad (8)$$

$$\bar{C}^a_{vv}(\theta) = \bar{N}^2 C^p_{vv}(q^2\bar{R}^2_{gL})^{-D_f/2}, \quad \text{power-law regime} \quad (9)$$

The mean-squared radius of gyration in the limiting expressions of Eqs. (8) and (9) is found as a N^2-weighted average in the Guinier regime, and as fractal dimension-weighted average in the power-law regime, as follows:

$$\bar{R}^2_{gG} = \int_{N=1}^{\infty} R_g(N)^2 N^2 p(N)dN \Big/ \int_{N=1}^{\infty} N^2 p(N)dN,$$

Guinier regime (10)

$$\bar{R}^2_{gL} = \left[\int_{N=1}^{\infty} R_g(N)^{2D_f} p(N)dN \Big/ \int_{N=1}^{\infty} R_g(N)^{D_f} p(N)dN\right]^{2/D_f},$$

power-law regime (11)

The general expression for the total scattering cross section of the polydisperse aggregate population is

$$\bar{C}^a_s = C^p_s \int_{N=1}^{\infty} N^2 g(\lambda, R_g, D_f)p(N)dN \quad (12)$$

which must be numerically integrated in both scattering regimes. The absorption cross section of the polydisperse aggregate population is evaluated quite simply for RDG-PFA scattering, as follows:

$$\bar{C}^a_a = \bar{N} C^p_a \quad (13)$$

Notably, Köylü and Faeth (1994) determined absorption cross sections for overfire soot aggregates by direct measurements of scattering and extinction cross sections, finding good agreement with Eq. (13). Finally, the albedo is defined in the usual manner, $\bar{A}^a = \bar{C}^a_s/(\bar{C}^a_s + \bar{C}^a_a)$.

Other Scattering Theories. Other approximate scattering theories that were evaluated using the present measurements included Rayleigh scattering, Mie scattering for an equivalent sphere, and the RDG-PFA approach of Dobbins and Megaridis (1991). The Rayleigh and Mie scattering theories are well known; see Bohren and Huffman (1983) for the complete formulations. The equivalent diameter for the Mie scattering computations was taken to be the volume mean diameter of the aggregate population, in the usual manner (Köylü and Faeth, 1993):

$$D_{30} = \bar{N}^{1/3} d_p \quad (14)$$

The RDG-PFA approach of Dobbins and Megaridis (1991) is identical to the present formulation when all the aggregates are in the Guinier regime. Scattering in the power-law regime is found, however, by using the limiting expression of Eq. (9) with $\bar{R}^2_{gL}$ replaced by $\bar{R}^2_{gG}$. The two regimes are connected by requiring continuity of $\bar{C}^a_{vv}(\theta)$ through the first derivative with respect to $q^2\bar{R}^2_{gG}$, analogous to Eqs. (3) and (4) for an individual aggregate. Thus, the weighting of the scattering properties by the aggregate size distribution function is somewhat distorted in the transition and power-law regimes. This tends to underestimate both the extent of the transition regime in terms of $q^2\bar{R}^2_{gG}$, as well as scattering cross sections in the transition and power-law regimes; see Freltoft et al. (1986), Köylü and Faeth (1994), and Sorensen et al. (1992).

Results and Discussion

Soot Structure Measurements. The general appearance of the soot aggregates in the ethylene and acetylene/air flames is illustrated in the TEM photographs appearing in Figs. 2 and 3. The soot aggregates had smaller primary particle diameters, and larger numbers of primary particles per aggregate, in the ethylene/air flame than the acetylene/air flame. However, the variation of aggregate properties within each flame was modest over the range of streamwise conditions that were considered. The present results are qualitatively similar to other TEM observations of soot at fuel-rich conditions in laminar diffusion flames (Dobbins and Megaridis, 1987). In particular, the soot consists of open (rather than compact) structures of aggregated primary particles that have nearly constant diameters. The aggregates exhibit a broad range of sizes, with the largest aggregates having maximum dimensions on the order of 1 μm. This yields aggregate optical size parameters, based on the maximum aggregate dimension, greater than 5, which implies significant potential for departure from Rayleigh scattering behavior. Such behavior was

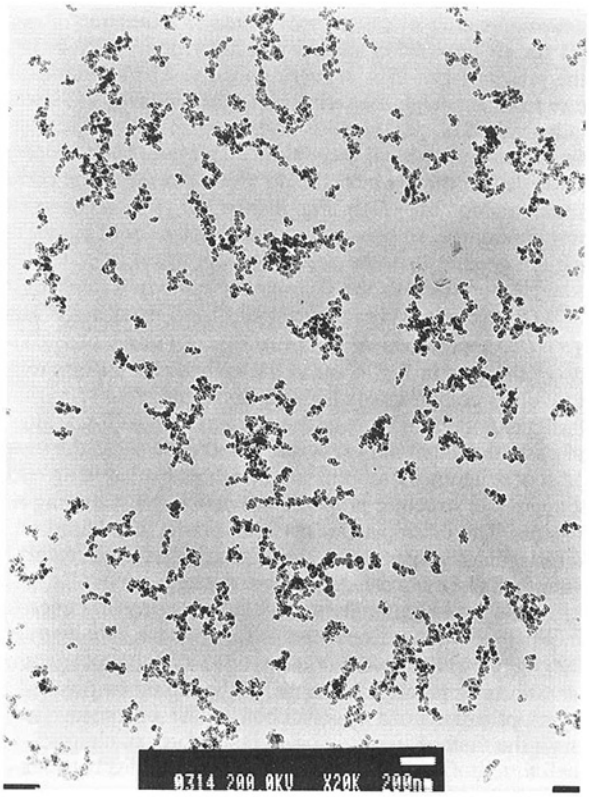

Fig. 2 Typical TEM photograph of soot in the ethylene/air flame: x/d = 3.50

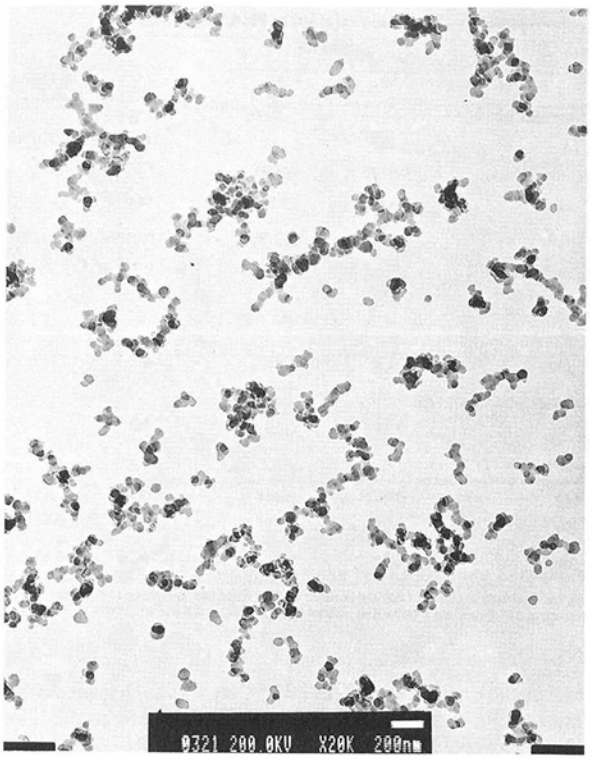

Fig. 3 Typical TEM photograph of soot in the acetylene/air flame: x/d = 3.15

confirmed by aggregate scattering measurements to be discussed later.

The TEM measurements of soot structure properties are summarized in Table 2 for the four test conditions that were considered. Primary particle diameters were obtained by measuring roughly 200–300 primary particles within a sample of 20 aggregates, to yield uncertainties (95 percent confidence) of $\bar{d}_p$ less than 2 percent. The standard deviations of the diameters about $\bar{d}_p$ are relatively small, less than 18 percent, which supports the constant primary particle diameter assumption of the RDG-PFA scattering theory.

Aggregate properties in Table 2 were found using a sample of 200 aggregates at each condition. This yielded uncertainties of $\bar{N}$ (95 percent confidence) less than 20 percent. The standard deviations of $\bar{N}$ are comparable to $\bar{N}$ itself, which is characteristic of the broad size distributions of typical soot aggregate populations (Dobbins and Megaridis, 1987; Köylü and Faeth, 1992). The log-normal size distribution function provided a reasonable fit of the present measurements, similar to overfire soot aggregates (Köylü and Faeth, 1992), although the measurements were used directly to predict scattering properties, as noted earlier. The moment, $\bar{N}^2$, plays a crucial role in the scattering properties of soot aggregates (this is particularly evident from Eqs. (8) and (9) for limiting conditions). Unfortunately, it is not practical to obtain a very accurate determination of this moment by sampling due to the broad size distribution of soot aggregates. Thus, uncertainties of $\bar{N}^2$ (95 percent confidence) were only less than 40 percent. Aggregate fractal dimensions were found as described by Köylü and Faeth (1992) to yield uncertainties (95 percent confidence) less than 0.06. The present values of D_f were in the range 1.73–1.77, which is comparable to earlier sampling measurements at both under- and overfire conditions for a wide variety of fuels; see Megaridis and Dobbins (1990), Köylü and Faeth (1992), and references cited therein. This suggests that D_f might have a universal value for soot aggregates in diffusion flames, which would vastly simplify measurements needed to define aggregate scattering properties. Values of D_{30} were computed from Eq. (14), yielding values of roughly 90 and 180 nm for ethylene and acetylene soot, respectively. Thus, the aggregate optical size parameters based on this dimension are in the range 0.5–1.2, so that Rayleigh scattering from aggregates is questionable, as noted earlier.

Evaluation of Scattering Theories. Soot optical properties were computed using the refractive indices of Dalzell and Sarofim (1969), i.e., $m = 1.57 + 0.56i$ at a wavelength of 514.5 nm, in order to be consistent with earlier work (Köylü and Faeth, 1992, 1993, 1994). However, this choice also is justified by the soot scattering observations of Köylü and Faeth (1994), where it was found that the refractive indices of Dalzell and Sarofim (1969) yielded values of $F(m)/E(m)$ that were in better agreement with measurements than other values in the literature.

In order to evaluate the scattering theories, measured volumetric optical cross sections must be related to predicted optical cross sections from a knowledge of the number of aggregates per unit volume, as follows:

$$\bar{Q}_j^a = n_a \bar{C}_j^a; \quad j = pp, s, a \tag{15}$$

Table 2 Summary of soot structure properties from TEM measurements[a]

x/d (-)	$\bar{d}_p(\sigma_p)$ (nm)	$\bar{N}(\sigma_N)$ (-)	$\bar{N}^2/\bar{N}$ (-)	D_f (-)	D_{30} (nm)
Ethylene/air flames:					
3.50	24(3.9)	50(46)	91	1.73	88
4.90	21(3.7)	83(76)	154	1.73	92
Acetylene/air flames:					
2.10	53(6.4)	31(35)	70	1.77	166
3.15	54(6.4)	43(48)	97	1.74	189

[a]For the fuel-rich region of buoyant laminar diffusion flames at normal temperature and pressure.

Table 3 Summary of soot scattering properties[a]

Flame	Ethylene/Air		Acetylene/Air	
x/d	3.50	4.90	2.10	3.15
Primary particles:				
x_p (-)	0.147	0.128	0.324	0.330
$\bar{C}^p_{vv}$ (nm²/sr)	0.0144	0.0065	1.67	1.87
$\bar{C}^p_s$ (nm²)	0.121	0.054	14.0	15.7
A^p (-)	0.0012	0.0018	0.0196	0.0185
n_p (cm^{-3}) × 10^{-10}	32	40	9.7	9.3
Aggregates:				
$\bar{C}^a_{vv}(90°)$ (nm²/sr)	24.1	25.2	478	719
$\bar{C}^a_s$ (nm²) × 10^{-3}	0.23	0.26	5.7	9.6
$\bar{A}^a$ (-)	0.062	0.063	0.20	0.22
$\bar{\rho}^a_v(90°)$	0.012	0.011	0.026	0.025
n_a (cm^{-3}) × 10^{-9}	6.30	4.80	3.13	2.17

[a]For the fuel-rich region of buoyant laminar diffusion flames at normal temperature and pressure at 514.5 nm. Soot refractive indices from Dalzell and Sarofim (1969).

while $n_p = \bar{N} n_a$. During the earlier study of overfire soot aggregates (Köylü and Faeth, 1994), the value of n_a was found from direct laser absorption measurements of $\bar{Q}^a_a$, with $\bar{C}^a_a$ computed from Eq. (13) given $\bar{N}$ from the structure measurements. An alternative procedure was used during the present investigation, however, in order to avoid the relatively large uncertainties of volumetric absorption coefficient measurements in the present flame environments. In particular, variable soot concentrations imply that laser extinction measurements for chord-like paths through the flames must be deconvoluted, which yields large experimental uncertainties near the axis where present measurements were made (Santoro et al., 1983). Thus, scattering measurements were used instead, based on predicted values of $\bar{C}^a_{vv}(\theta)$ from Eq. (9) in the power-law regime. This was reasonable because scattering at present test conditions exhibited power-law regimes that could be correlated according to Eq. (9). Additionally, the present RDG-PFA scattering theory yielded good predictions in the power-law regime for the large soot aggregates found in the overfire region of buoyant turbulent diffusion flames (Köylü and Faeth, 1994). Finally, use of the RDG scattering approximation is better justified in the power-law regime than the Guinier regime, based on both theoretical and computational considerations (Nelson, 1989).

Reference soot optical properties for the four test conditions, along with n_a and n_p, are summarized in Table 3. Values of x_p are in the range 0.128–0.330, which marginally places the individual primary particles in the Rayleigh scattering regime (Kerker, 1969). The values of $\bar{A}^a$ are 10–100 times larger than A^p, highlighting the much larger scattering from aggregates than from individual primary particles. The albedo is a measure of the error incurred when soot volume fractions are computed from laser extinction measurements using the Rayleigh scattering approximation. Thus, such errors would be in the range 7–28 percent for present conditions, with the higher values being comparable to the properties of soot aggregates in the overfire region (Köylü and Faeth, 1994). However, corrections of this magnitude still are rather small in comparison to effects of current uncertainties concerning soot refractive indices. Present values of n_p in the range 10^{11}–10^{12} primary particles per cubic centimeter are comparable to earlier measurements of Dobbins et al. (1990) and Megaridis and Dobbins (1990) for similar flame conditions, helping to justify the present determinations of n_p and n_a from scattering measurements.

Measured values of $\bar{Q}^a_{vv}(\theta)$ are plotted as a function of qd_p in Fig. 4 for all four test conditions, along with predictions based on the present RDG-PFA scattering theory. The substantial departure from Rayleigh scattering behavior, where $\bar{Q}^a_{vv}(\theta)$ would be independent of qd_p, is quite evident, with forward scattering being roughly an order of magnitude larger than back scattering. A power-law regime, which should yield a straight line correlation with a slope of $-D_f$ in Fig. 4 (see Eq. (9)) is observed at all test conditions. However, only the ethylene soot aggregates, which are smaller than the acetylene soot aggregates, exhibit a reasonable approach to the Guinier regime where both $\bar{Q}^a_{vv}(\theta)$ and $\bar{C}^a_{vv}(\theta)$ are relatively independent of qd_p from Eq. (8), and $\bar{Q}^a_{vv}(\theta)/Q^p_{vv}$ approaches $\bar{N}^2/\bar{N}$ from Eqs. (8) and (15). Thus, many of the data in Fig. 4 are in the extended transition regime that involves complex polydisperse aggregate effects.

Two predictions based on the present RDG-PFA scattering theory are illustrated in Fig. 4, one based entirely on the present TEM soot structure measurements, and the other based on refitted soot aggregate structure properties to match the scattering measurements. The discrepancies between predictions based on the structure measurements and the scattering measurements are smaller than those observed for large soot aggregates (Köylü and Faeth, 1994), and generally are within experimental uncertainties. In particular, the discrepancies for ethylene soot aggregates are negligible while those for the larger acetylene soot aggregates are less than 37 percent. Nevertheless, it should be recalled that the present predictions are matched in the power-law regime through the method used to find n_a; therefore, an alternative approach to find n_a would increase the discrepancies between predictions and measurements.

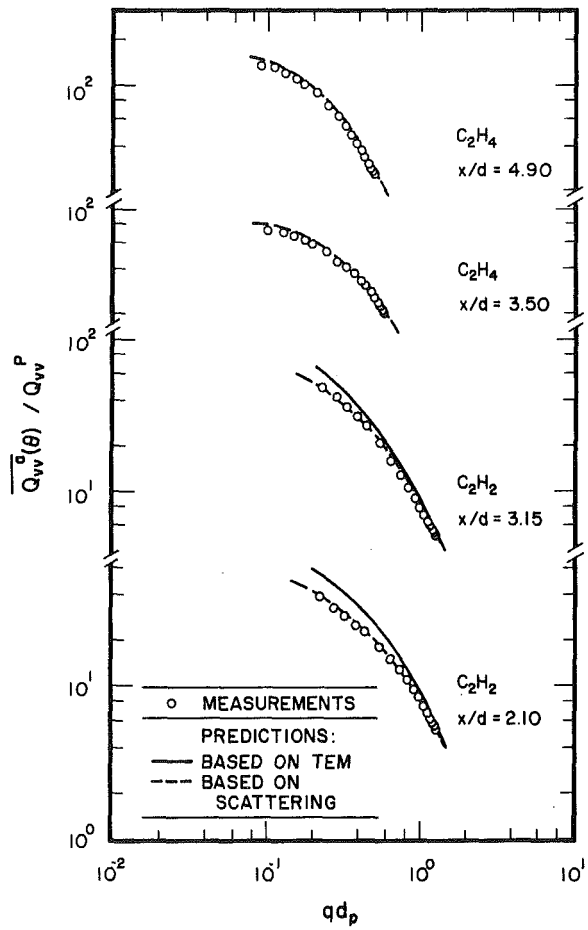

Fig. 4 Measured and predicted volumetric *vv* soot scattering cross sections in the ethylene and acetylene/air flames as a function of the modulus of the scattering vector

Table 4 Soot structure and optical properties from thermophoretic sampling (TS) and light scattering (LS) measurements[a]

x/d	$(\bar{R}^2_{gL})^{1/2}$ (nm)		$\bar{R}(^2_{gG})^{1/2}$ (nm)		D_f		$\bar{A}^a$	
	TS	LS	TS	LS	TS	LS	TS	LS
Ethylene/air flames:								
3.50	97	90	121	117	1.73	1.72	0.061	0.062
4.90	115	111	144	140	1.73	1.74	0.060	0.063
Acetylene/air flames:								
2.10	179	137	241	185	1.77	1.77	0.21	0.20
3.15	224	163	297	200	1.74	1.76	0.23	0.22

[a]For the fuel-rich region of buoyant laminar diffusion flames at normal temperature and pressure for a wavelength of 514.5 nm. Soot refractive indices from Dalzell and Sarofim (1969).

Based on past experience, it was felt that the sampling limitations of the soot structure measurements, particularly the higher moments of the aggregate size distribution, were primarily responsible for the discrepancies between the scattering predictions and measurements seen in Fig. 4 (Köylü and Faeth, 1994). Thus, the higher moments and the aggregate fractal dimensions were refitted to yield the predictions based on scattering measurements illustrated in Fig. 4. This involved keeping d_p and the lower moment $\bar{N}$ the same as before, while adjusting the higher moments. These adjustments will be represented by $\bar{R}^2_{gG}$ and $\bar{R}^2_{gL}$ in the following. The results illustrated in Fig. 4 indicate that the present RDG-PFA scattering theory provides a reasonable basis to fit the higher moments of soot structure properties based on measured scattering properties in this manner. The resulting values of the adjusted parameters from the light scattering measurements, along with the values found directly from the TEM sampling measurements, are summarized in Table 4. Differences between the TEM sampling and light scattering determinations of the moments for ethylene soot, and the fractal dimensions of both ethylene and acetylene soot, are small in comparison to experimental uncertainties. The differences between the two determinations of higher moments are larger for acetylene soot but still are comparable to anticipated experimental uncertainties. Values of the soot albedo predicted assuming RDG behavior for absorption through Eq. (13) and using the two sets of structure properties, also are listed in Table 4. The results are nearly the same, which is helpful because estimates of the soot albedo are required to evaluate potential errors of laser extinction measurements of soot concentrations. Nevertheless, a more definitive assessment of albedo predictions would be desirable, based on direct measurement of absorption.

Measured and predicted angular scattering patterns of ethylene and acetylene soot are illustrated in Figs. 5 and 6, respectively. These results are for the lowest position in the ethylene flame and the highest position in the acetylene flame, which spans the range of soot aggregate sizes (in terms of D_{30}). The predictions are based on the refitted soot structure properties from the light scattering measurements, which are in excellent agreement with measured values of $\bar{C}^a_{vv}(\theta)$, as discussed in connection with Fig. 4. Similar to Köylü and Faeth (1994), the formulation for $\bar{C}^a_{hh}(\theta)$ was modified from the approach based on Eq. (2) in order to account for observed depolarization phenomena. This was done analogous to Rayleigh scattering theory as follows (Rudder and Bach, 1968):

$$\bar{C}^a_{hh}(\theta) = \bar{C}^a_{vv}(\theta)[(1 - \bar{\rho}^a_v)\cos^2\theta + \bar{\rho}^a_v] \qquad (16)$$

The corresponding estimates of hv and vh scattering cross sections are:

$$\bar{C}^a_{hv} = \bar{C}^a_{vh} = \bar{C}^a_{vv}(90°)\bar{\rho}^a_v \qquad (17)$$

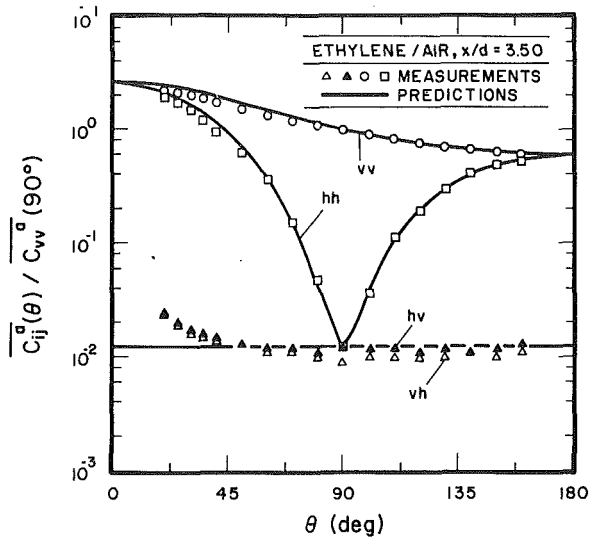

Fig. 5 Measured and predicted angular soot scattering patterns in the ethylene/air flame: $x/d = 3.50$

The measured values of $\bar{\rho}^a_v(\theta)$ at $\theta = 90°$ are summarized in Table 3; as noted earlier, their magnitudes are similar to the values observed by Köylü and Faeth (1994) for overfire soot. The present results for $\bar{C}^a_{hh}(\theta)$, $\bar{C}^a_{hv}(\theta)$ and $\bar{C}^a_{vh}(\theta)$ also are in qualitative agreement with earlier findings for the much larger overfire soot aggregates (Köylü and Faeth, 1994): Eq. (16) is in excellent agreement with measured values of $\bar{C}^a_{hh}(\theta)$ while Eq. (17) is effective except for the forward-scattering direction where the measured values show a steady increase as the forward scattering direction is approached. It is not known at this point whether the increase of hv and vh scattering as forward scattering is approached follows from the strong forward scattering of soot aggregates or whether it is caused by experimental difficulties. In particular, experimental uncertainties for the vh and hv scattering components increase in the forward scattering direction due to effects of polarization vector misalignment when scattering is strong (Köylü and Faeth, 1994). Clearly, additional consideration of the depolarization ratios of soot aggregates would be useful; however, vh and hv scattering levels are small and have little

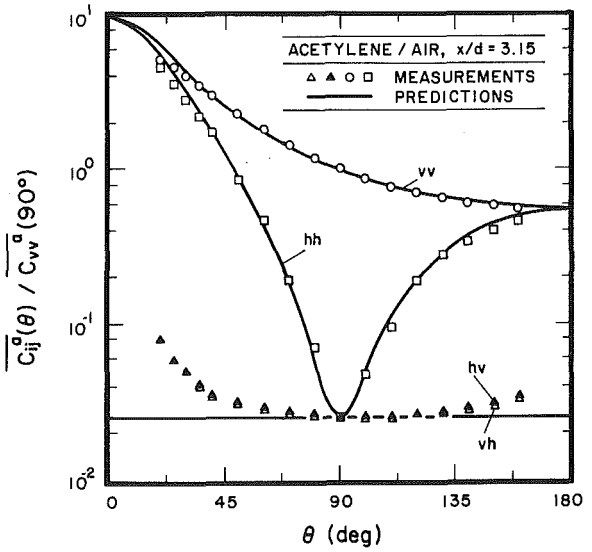

Fig. 6 Measured and predicted angular soot scattering patterns in the acetylene/air flame: $x/d = 3.15$

effect on total scattering estimates for most conditions of interest. Thus, uncertainties about the evaluation of Eq. (17) in the forward-scattering direction are not very important.

Finally, measured values of $\bar{Q}^a_{vv}(\theta)$ along with the predictions from the various approximate theories are plotted as a function of qd_p in Fig. 7. Results for the ethylene/air flame at $x/d = 4.90$ are illustrated. These conditions correspond to the largest $\bar{N}$ over the present test range, although findings at other conditions were similar. Predictions shown on the plot include Mie scattering for an equivalent sphere, RDG-PFA scattering using the formulation of Dobbins and Megaridis (1991) and RDG-PFA scattering using the formulation of Köylü and Faeth (1994). The Mie scattering predictions are based on D_{30} from Table 2. The RDG-PFA predictions are based on the structure properties from the TEM measurements.

Rayleigh scattering predictions are not illustrated in Fig. 7 because they are totally unsuitable, yielding $\bar{Q}^a_{vv}(\theta)/\bar{Q}^a_{vv} = 1$, which is off the scale of the figure. Typical of past evaluations of the Mie scattering approximation for an equivalent sphere (Köylü and Faeth, 1993), this approximation is not very satisfactory for large soot aggregates. In particular, although Mie scattering theory yields the correct order of magnitude of the scattering level for the present conditions, the angular variation of $\bar{Q}^a_{vv}(\theta)$ is substantially underestimated. Naturally, both RDG-PFA theories yield the same results at small qd_p in the Guinier regime where their formulations are identical. However, the approach of Dobbins and Megaridis (1991) underestimates both the extent of the transition regime and the magnitude of $\bar{Q}^a_{vv}(\theta)$ in the transition and power-law regimes. This occurs because the averaging procedure used by Dobbins and Megaridis (1991) does not account for different weightings of optical properties in the Guinier and power-law regimes. This difficulty in the power-law regime is significant because this regime tends to dominate total scattering computations, and comprises the most accessible angle range for scattering measurements used to find soot structure, for typical soot aggregates.

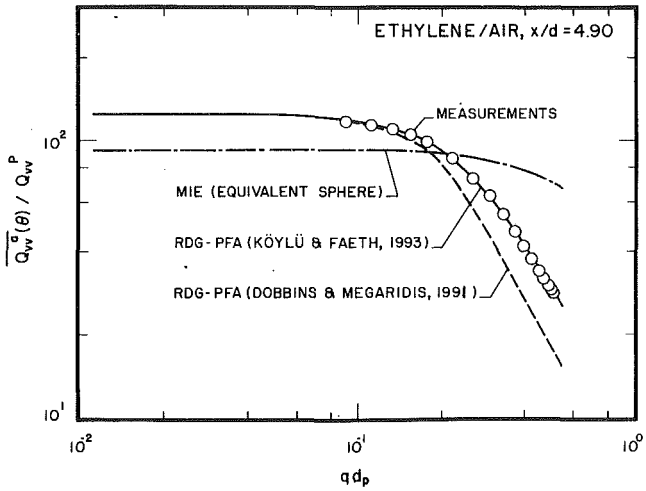

Fig. 7 Various predictions and measurements of volumetric *vv* soot scattering cross sections in the ethylene/air flame: $x/d = 4.90$

Conclusions

The optical properties of underfire soot were studied in order to extend an earlier evaluation of approximate soot scattering theories in the power-law (large-angle) regime to the Guinier (small-angle) regime. Test conditions included laminar ethylene/air and acetylene/air diffusion flames, which provided a range of soot aggregate optical properties spanning both the Guinier and power-law scattering regimes. The main conclusions of the study are as follows:

1 The approximate RDG-PFA scattering theory of Köylü and Faeth (1994) yielded predictions that agreed with present measurements within experimental uncertainties. Combined with earlier findings for large overfire soot aggregates, reasonably good performance of this approach has been established for soot from a variety of fuels over the following ranges: x_p of 0.128–0.330, $\bar{N}$ of 31–467, $\bar{N}^2/\bar{N}$ of 70–1330, $\bar{C}^a_{vv}(0°)/\bar{C}^a_{vv}(180°)$ of 10–1000 and $\bar{A}^a$ of 0.06–0.29 (with soot structure properties based on TEM measurements).

2 The main limitation of the approach involves accurate determination of higher order moments, such as $\bar{N}^2$, of the aggregate size distribution function from sampling measurements; thus, it is recommended that these parameters be determined from scattering measurements whenever possible. The performance of other approximate soot aggregate scattering theories generally was not satisfactory over the same range of conditions: Rayleigh scattering substantially underestimated scattering levels, Mie scattering for an equivalent sphere yielded poor estimates of the angular variation of differential scattering cross sections, and RDG-PFA scattering using the approach of Dobbins and Megaridis (1991) underestimated both the extent of the transition regime and scattering levels in the power-law regime.

3 The fractal dimensions of soot aggregates appear to be nearly universal over the same range of conditions; for example, combined results for both TEM and light scattering measurements yielded $D_f = 1.77$ with a standard deviation of 0.04. The TEM and light scattering measurements of D_f also were in good agreement, within 1 percent.

4 Past proposals for the use of light scattering measurements to infer soot structure properties, e.g., Dobbins et al. (1990) and Puri et al. (1993), should be re-examined in view of present findings. In particular, scattering from typical soot aggregates in the underfire region is dominated by the transition regime. Unfortunately, optical properties within the transition regime are unusually complex so that approximations of solely Guinier or power-law scattering, which simplify the determination of structure properties, generally are not appropriate for interpreting scattering measurements.

Acknowledgments

This research was supported by the Building and Fire Research Laboratory of the National Institute of Standards and Technology, Grant No. 60NANB1D1175, with H. R. Baum serving as Scientific Officer; and by NASA, Grant No. NAG3-1245, under the technical management of D. L. Urban of the Lewis Research Center. The authors also wish to acknowledge the help of the staff of the Electron Microbeam Analysis Laboratory at the University of Michigan.

References

Bohren, C. F., and Huffman, D. R., 1983, *Absorption and Scattering of Light by Small Particles,* Wiley, New York, pp. 477–482.

Dalzell, W. H., and Sarofim, A. F., 1969, "Optical Constants of Soot and Their Application to Heat Flux Calculations," ASME JOURNAL OF HEAT TRANSFER, Vol. 91, pp. 100–104.

Dalzell, W. H., Williams, G. C., and Hottel, H. C., 1970, "A Light Scattering Method for Soot Concentration Measurements," *Combust. Flame,* Vol. 14, pp. 161–170.

Dobbins, R. A., and Megaridis, C. M., 1987, "Morphology of Flame-Generated Soot as Determined by Thermophoretic Sampling," *Langmuir,* Vol. 3, pp. 254–259.

Dobbins, R. A., Santoro, R. J., and Semerjian, H. G., 1990, "Analysis of Light Scattering From Soot Using Optical Cross Sections for Aggregates," *Twenty-Third Symposium (International) on Combustion,* The Combustion Institute, Pittsburgh, PA, pp. 1525–1532.

Dobbins, R. A., and Megaridis, C. M., 1991, "Absorption and Scattering of Light by Polydisperse Aggregates," *Appl. Optics,* Vol. 30, pp. 4747–4754.

Erickson, W. D., Williams, G. C., and Hottel, H. C., 1964, "Light Scattering Measurements on Soot in a Benzene–Air Flame," *Combust. Flame,* Vol. 8, pp. 127–132.

Freltoft, T., Kjems, J. K., and Sinha, S. K., 1986, "Power-Law Correlations and Finite Size Effects in Silica Particle Aggregates Studied by Small-Angle Neutron Scattering," *Physical Review B,* Vol. 33, pp. 269–275.

Jullien, R., and Botet, R., 1987, *Aggregation and Fractal Aggregates,* World Scientific Publishing Co., Singapore, pp. 45–60.

Kerker, M., 1969, *The Scattering of Light,* Academic Press, New York, pp. 414–486.

Köylü, Ü. Ö., and Faeth, G. M., 1992, "Structure of Overfire Soot in Buoyant Turbulent Diffusion Flames at Long Residence Times," *Combust. Flame,* Vol. 89, pp. 140–156.

Köylü, Ü. Ö., and Faeth, G. M., 1993, "Radiation Properties of Flame-Generated Soot," ASME JOURNAL OF HEAT TRANSFER, Vol. 115, pp. 409–417.

Köylü, Ü. Ö., and Faeth, G. M., 1994, "Optical Properties of Overfire Soot in Buoyant Turbulent Diffusion Flames at Long Residence Times," ASME JOURNAL OF HEAT TRANSFER, Vol. 116, pp. 152–159.

Lin, M. Y., Lindsay, H. M., Weitz, D. A., Ball, R. C., Klein, R., and Meakin, P., 1989, "Universality of Fractal Aggregates as Probed by Light Scattering," *Proc. Roy. Soc. London A,* Vol. 423, pp. 71–87.

Magnussen, B. F., 1974, "An Investigation Into the Behavior of Soot in a Turbulent Free Jet C_2H_2-Flame," *Fifteenth Symposium (International) on Combustion,* The Combustion Institute, Pittsburgh, PA, pp. 1415–1425.

Martin, J. E., and Hurd, A. J., 1987, "Scattering from Fractals," *J. Appl. Cryst.,* Vol. 20, pp. 61–78.

Megaridis, C. M., and Dobbins, R. A., 1990, "Morphological Description of Flame-Generated Materials," *Combust. Sci. Tech.,* Vol. 77, pp. 95–109.

Nelson, J., 1989, "Test of a Mean Field Theory for the Optics of Fractal Clusters," *J. Modern Optics,* Vol. 36, pp. 1031–1057.

Puri, R., Richardson, T. F., Santoro, R. J., and Dobbins, R. A., 1993, "Aerosol Dynamic Processes of Soot Aggregates in a Laminar Ethene Diffusion Flame," *Combust. Flame,* Vol. 92, pp. 320–333.

Rosner, D. E., Mackowski, D. W., and Garcia-Ybarra, P., 1991, "Size- and Structure-Insensitivity of the Thermophoretic Transport of Aggregated Soot Particles," *Combust. Sci. Tech.,* Vol. 80, pp. 87–101.

Rudder, R. R., and Bach, D. R., 1968, "Rayleigh Scattering of Ruby-Laser Light by Neutral Gases," *J. Opt. Soc. Amer.,* Vol. 58, pp. 1260–1266.

Santoro, R. J., Semerjian, H. B., and Dobbins, R. A., 1983, "Soot Particle Measurements in Diffusion Flames," *Combust. Flame,* Vol. 51, pp. 203–218.

Sorensen, C. M., Cai, J., and Lee, N., 1992, "Test of Static Structure Factors for Describing Light Scattering From Fractal Soot Aggregates," *Langmuir,* Vol. 8, pp. 2064–2069.

van de Hulst, H. C., 1957, *Light Scattering by Small Particles,* Dover Publications, New York.

Wersborg, B. L., Howard, J. B., and Williams, G. C., 1972, "Physical Mechanisms in Carbon Formation in Flames," *Fourteenth Symposium (International) on Combustion,* The Combustion Institute, Pittsburgh, PA, pp. 929–940.

K-Distribution Analysis of Gas Radiation With Nongray, Emitting, Absorbing, and Anisotropic Scattering Particles

K. C. Tang
Graduate Research Assistant.
Student Mem. ASME

M. Q. Brewster
Professor.
Mem. ASME

Department of Mechanical and Industrial Engineering,
University of Illinois at Urbana–Champaign,
Urbana, IL 61801

The K-distribution technique is presented for predicting nongray gas radiation in the presence of particle scattering. This technique transforms the otherwise formidable spectral integration problem from the frequency domain to the K or gas absorption coefficient domain. This transformation is made possible by the negligible variation of blackbody intensity and particle radiative properties with frequency within a gas band. Application of the K-distribution technique to an isothermal emission problem is made. Results are compared with those from the Monte-Carlo method. These results show that, with the K-distribution technique, the detailed absorption line structure within a gas band as well as the scattering effect due to particles can be simulated with great numerical accuracy and computational efficiency. Essentially, line-by-line accuracy is achieved without line-by-line spectral integration.

Introduction

In modeling the radiation absorption and emission behavior of gases, models that describe the spectrally averaged characteristics of a vibration-rotation band are often used (Brewster, 1992; Edwards et al., 1987; Goody and Yung, 1989). In general, these band models are difficult to implement in the analysis of a mixture consisting of nongray gases and scattering particles (Goody and Yung, 1989). Most analyses invoke simplified assumptions such as gray, nonemitting, nonscattering, or isotropic scattering media. Therefore, these analyses are restricted to special conditions.

Recent studies of radiative heat transfer have been devoted to developing new solution techniques for combined particle and nongray gas media. One approach, developed by Walters and Buckius (1990, 1992), is to define several characteristic lengths for an absorbing, emitting, and scattering medium by using the photon pathlength method. Application of this method makes it possible to examine rigorously the interaction between the nongray absorption and emission of gases and the scattering properties of particles. However, in their formulation the optically thin gas limit was used. As an example of a more conventional approach, Fiveland and Jamaluddin (1989) studied the radiative heat transfer of a nonhomogeneous, nongray, absorbing, emitting, anisotropic scattering medium including gas contributions by using the discrete-ordinate method. In the frequency integration process, the range of wavelengths was subdivided into a finite number of bands within which the radiative properties were assumed uniform. The total contribution was obtained by summing the solutions for each band. With some attention paid to the grid mismatching problem, this method can be coupled with flow field computational codes relatively easily. Application of this method to highly nongray media, however, usually incurs a substantial computational cost increase. Another approach that can be taken to combined gas–particle media is that of Grosshandler and Modak (1981). In this approach, the gas and particle radiation are determined separately and then added together with an allowance for spectral overlap. This approach is best suited for low albedos and becomes more questionable as the importance of scattering increases.

Another approach for solving nongray gas radiation with particles is the *K*-distribution method. This method has been used extensively in the atmospheric science area (Arking and Grossman, 1972; Domoto, 1974; Goody and Yung, 1989). In most cases, the main focus of these studies has been the transmission function of atmospheres with pure gas mixtures without scattering particles. This paper extends the application of the *K*-distribution method to the radiative heat transfer problem of a mixture with highly nongray gases in the presence of nongray emitting, absorbing, and scattering particles, which can be found in many engineering systems. While the total flux for a gas band is calculated by integrating the spectral intensity using the *K*-distribution method, the spectral intensity is obtained by solving the radiative transfer equation using the discrete-ordinate method.

K-Distribution Analysis

By considering the propagation of radiation in a one-dimensional, nongray, emitting, absorbing, and scattering medium, the radiative transfer equation for a multicomponent medium can be written as follows:

$$\mu \frac{dI_\nu(\mu)}{dx} = -\sum_i (K_{s\nu_i} + K_{a\nu_i}) I_\nu(\mu) + \sum_i K_{em\nu_i} I_{b\nu}(T_i) + \sum_i \frac{K_{s\nu_i}}{2} \int_{-1}^{1} I_\nu(\mu') p_i(\mu, \mu') d\mu', \quad (1)$$

where I_ν is the spectral radiation intensity, ν is the wave number, T_i is the local temperature of species i, $I_{b\nu}$ is the spectral intensity of blackbody emission at T_i, $K_{a\nu_i}$, $K_{s\nu_i}$, and $K_{em\nu_i}$ are the nongray absorption, scattering, and emission coefficients of species i, μ is the direction cosine of the polar angle measured from the x axis, $p_i(\mu, \mu')$ is the phase function of species i, which is a representation of intensity scattered from the incident radiation (direction μ') into the direction under consideration μ. The subscript i represents the species considered in radiative transfer analysis, which are gas and particles for this case. The spectral intensity can be obtained by solving the radiative transfer equation and the associated specific boundary conditions for different cases. Then, the spectral radiative heat flux can be obtained by

$$q_\nu = 2\pi \int_{-1}^{1} I_\nu(\mu') \mu' d\mu'. \quad (2)$$

Contributed by the Heat Transfer Division for publication in the JOURNAL OF HEAT TRANSFER. Manuscript received by the Heat Transfer Division May 1993; revision received January 1994. Keywords: Radiation. Associate Technical Editor: M. F. Modest.

Based on the frequency-dependent properties of the medium, the radiative transfer equation is solved on a spectral basis by substituting the corresponding radiative properties of the medium at specific frequencies to get the spectral intensity I_ν. The total radiative heat flux over the entire spectral region can then be determined by integrating I_ν with respect to frequency as follows:

$$q = \int_0^\infty q_\nu d\nu = 2\pi \int_0^\infty \int_{-1}^{1} I_\nu(\mu')\mu' d\mu' d\nu. \quad (3)$$

The most direct method to perform the frequency integration is to divide the frequency domain into a finite number of frequency subintervals. The radiative properties inside each frequency subinterval can be treated as constants if the frequency subinterval is small enough. The total radiative heat flux is obtained by summing the spectral radiant flux of all the frequency subintervals. This method can be easily applied to study the effect of nongray properties of solid and liquid particles that have slow variation with frequency. However, this method is not feasible when applied to gas absorption bands due to the very rapid spectral variation of absorption coefficient in an absorption band. This requires very small wave number increments in the integration with respect to the wave number. Under this circumstance, a very large amount of computer time is needed in order to reach desirable accuracy. Therefore an alternative method is called for that recognizes the widely different spectral characteristics of gas and particle radiative properties.

The key to the K-distribution method is in the nature of the spectral variation of the various properties and functions that appear in the radiative transfer equation, such as absorption coefficients, scattering coefficients, and blackbody function. Within a gas absorption band, the variation of blackbody intensity and particle radiative properties with frequency is very slow (Goody and Yung, 1989) while the gas absorption coefficient varies rapidly. Therefore, the former quantities can be treated as constants within the gas absorption band. With this simplification applied to the spectral radiative transfer equation, the spectral intensity within a gas absorption band will be a function of the absorption coefficient of the gas only. Therefore, Eq. (3) for a gas absorption band with band width $\Delta\nu$ can be written as:

$$q_{\Delta\nu} = \frac{1}{\Delta\nu} \int_{\Delta\nu} Q[K_{a_g}(\nu)] d\nu, \quad (4)$$

where

$$Q[K_{a_g}(\nu)] = 2\pi\Delta\nu \int_{-1}^{1} I_\nu[K_{a_g}(\nu), \mu']\mu' d\mu'. \quad (5)$$

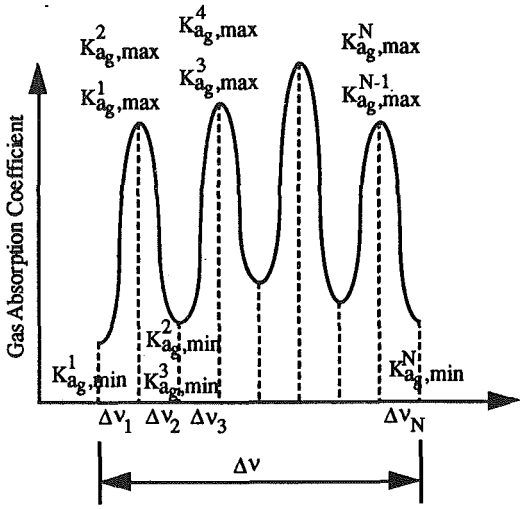

Fig. 1 Schematic diagram of gas absorption band

Consider a band $\Delta\nu$ in which the absorption coefficient $K_{a_g} = K_{a_g}(\nu)$ has a finite number of maxima and minima as shown in Fig. 1. The $\Delta\nu$ can be broken at the maxima ($K^j_{a_g,\max}$) and minima ($K^j_{a_g,\min}$) into subintervals $\Delta\nu_j$, $j = 1, 2, \ldots, N$. Within these subintervals, the gas absorption coefficient is a monotonically increasing or decreasing function of wave number. The integration with respect to ν in Eq. (4) can be transformed into an integration over absorption coefficient K_{a_g} which is the so-called K-distribution method (Domoto, 1974; Goody and Yung, 1989) as follows:

$$\frac{1}{\Delta\nu}\int_{\Delta\nu} Q[K_{a_g}(\nu)]d\nu = \frac{1}{\Delta\nu}\sum_{j=1}^{N}\int_{\Delta\nu_j} Q[K_{a_g}(\nu)]d\nu$$

$$= \sum_{j=1}^{N}\int_{(K^j_{a_g,\min})}^{(K^j_{a_g,\max})} Q[K_{a_g}(\nu)]\frac{1}{\Delta\nu}\left|\frac{d\nu_j}{dK_{a_g}}\right| dK_{a_g}. \quad (6)$$

Rearranging Eq. (6) with the introduction of the step function yields

$$\frac{1}{\Delta\nu}\int_{\Delta\nu} Q[K_{a_g}(\nu)]d\nu = \int_0^\infty Q(K_{a_g})f(K_{a_g})dK_{a_g}, \quad (7)$$

Nomenclature

f = coefficient for delta-Eddington phase function (Eq. (12)), $f = 0.111$ or function defined by Eq. (8)
g = coefficient for delta-Eddington phase function, $g = 0.215$
h = step function
I = intensity
K_a = absorption coefficient
K_e = extinction coefficient
K_{em} = emission coefficient
K_s = scattering coefficient
N = particle number density
p = scattering phase function
p' = modified phase function defined by Eq. (13)
P = pressure
Q = function defined by Eq. (5)
q = radiative heat flux
Q_s = scattering efficiency
Q'_s = modified scattering efficiency defined by Eq. (14)
S_c = mean line intensity
T = temperature
W = slab width
x = spatial coordinate
α = integrated band intensity
β = line width parameter
δ = line spacing or delta function
θ = slab polar angle
Θ = single-scattering polar angle
μ = direction cosine of considered polar angle θ ($\mu = \cos\theta$)
μ' = direction cosine of irradiation polar angle θ' or dummy argument
ρ = density
ω = band width parameter

Subscripts

a = absorption
b = blackbody
c = center
e = extinction
em = emission
g = gas
i = species (gas, particles)
j, k = dummy index
max = maximum
min = minimum
p = particle
s = scattering
ν = wave number

where

$$f(K_{a_g}) = \sum_{j=1}^{N} \frac{1}{\Delta\nu} \left| \frac{d\nu_j}{dK_{a_g}} \right| [h(K_{a_g} - K^j_{a_g,\min}) - h(K_{a_g} - K^j_{a_g,\max})], \quad (8)$$

and h is the step function.

From Eq. (8), it can be seen that $f(K_{a_g})$ is actually the absorption coefficient distribution function and $f(K_{a_g})dK_{a_g}$ is the probability density function of the absorption coefficient, which is between K_{a_g} and $K_{a_g} + dK_{a_g}$. This probability density function is obtained by *standard* statistical analysis based on the gas absorption spectra. This frequency integration K-distribution method can be combined with the "direct" method to calculate the total radiative heat flux by

$$q = \sum_{\text{all } \Delta\nu} q_{\Delta\nu}. \quad (9)$$

It is clear that the wave number integration is replaced by an integration over the K_{a_g} space after the K-distribution function $f(K_{a_g})$ is introduced. In short, the total flux for a gas absorption band is no longer dependent on the ordering of the highly nongray gas absorption coefficient with respect to wave number. The advantage of the K-distribution method is, therefore, that the number of radiative heat flux calculations is greatly reduced compared with the line-by-line calculation. The number of flux calculations depends on the maximum absorption coefficient of a gas band, regardless of the spectral variation in gas absorption coefficient. Thus, this technique provides significant computational advantage especially in studying the effect of the detailed line structure within gas bands in the presence of particle scattering. Since the frequency integration is performed in a way "independent" of the method used to solve the radiative transfer equation, the calculation of the radiation from a gas and particle mixture is easily implemented by choosing an appropriate transfer equation solution method. In this study, the spectral intensity is obtained by solving the multicomponent radiative transfer equation (Eq. (1)) by using the discrete-ordinate method, which calculates the spectral intensity resulting from the nongray gas and the emitting, absorbing, and anisotropic scattering particles.

Results and Discussion

Problem Description. A one-dimensional sample problem is used to demonstrate the K-distribution method. The geometry considered in this paper is an infinite parallel slab with cold and black boundaries, which contains a uniform mixture of carbon particles, CO_2, and N_2. The width of the slab considered is 5 m. The mixture temperature is 1000 K and the total mixture pressure is 1 atm. The CO_2 mole fraction of 0.21 and the carbon particle size of 30 μm is considered. The carbon particle concentrations N of interest are 2.0×10^7, 2.0×10^8, and 2.0×10^9 particle/m^3. This problem was selected to match the specifications of a round-robin test problem considered as part of a Symposium on Solution Methods for Radiative Heat Transfer in Participating Media (Tong et al., 1992).

Gas Absorption Coefficient. The gas absorption coefficient for CO_2 is determined by the Elsasser narrow-band model (Goody and Yung, 1989) in this study:

$$K_{a_g}(\nu) = \rho \frac{S_c}{\delta} \frac{\sinh(2\beta)}{\cosh(2\beta) - \cosh(2\pi(\nu - \nu_c)/\delta)}, \quad (10)$$

Table 1 Maximum absorption coefficient for CO_2 bands (P = 1 atm, CO_2 mole fraction = 0.21, T = 1000 K)

CO_2 band	2.0 μm	2.7μm	4.3μm	9.4 μm	10.4 μm	15 μm
$K_{a_g,\max}$ (cm^{-1})	9.6×10^{-4}	1.0×10^{-1}	4.0×10^{0}	4.8×10^{-3}	9.1×10^{-3}	1.6×10^{0}

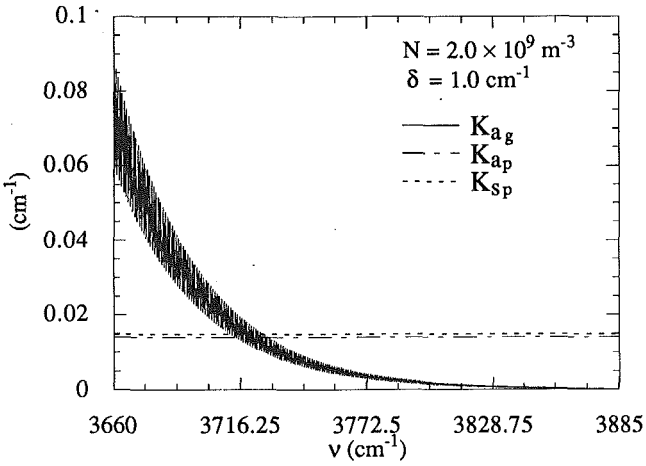

Fig. 2 Gas absorption coefficient, particle scattering, and absorption coefficients for 2.7 μm CO_2 band (δ = 1.0 cm^{-1}, N = 2.0 × 10^9 m^{-3})

where ν is wave number, the subscript c represents the band center, ρ is absorbing species partial density, β is line width parameter, δ is line spacing, and S_c/δ is mean-line-intensity-to-spacing ratio or spectrally smoothed mass absorption coefficient. The value of S_c/δ is given by the Edwards' exponential wide-band model (Edwards and Balakrishnan, 1973) as:

$$\frac{S_c}{\delta} = \frac{\alpha}{\omega} e^{-a|\nu - \nu_c|/\omega}, \quad (11)$$

where α is integrated band intensity, ω is band width parameter, and $a = 1$ for head-forming bands (i.e., 4.3 μm band) and 2 for non-head-forming bands. The correlations for α, β, ω can be obtained from Edwards and Balakrishnan's paper (1973). The value of δ is a function of wave number, pressure, and temperature (Ludwig et al., 1973). For practical purpose, the value of δ is assumed to be 1.0 cm^{-1} in this study in order to account for the highly nongray nature of the gas absorption coefficient.

Radiative Properties of Carbon Particles. The absorption and scattering efficiencies of 30-μm-dia spherical carbon particles have been computed (Foster and Howarth, 1968; Tong et al., 1992) using Mie theory and the optical constants for carbon specimen number 2 in Foster and Howarth (1968). The scattering phase function is represented by the gray delta-Eddington function (Menguc and Viskanta, 1985; Tong et al., 1992) as

$$p(\Theta) = 2f\delta(1 - \cos\Theta) + (1 - f)(1 + 3g\cos\Theta), \quad (12)$$

where $f = 0.111$ and $g = 0.215$. However, the first term on the right-hand side of the delta-Eddington function is the radiation scattered into the forward direction, which means that this portion of radiation is actually not attenuated due to scattering by the

Table 2 Band-by-band radiative heat flux (W/cm^2) at boundary (P = 1 atm, CO_2 mole fraction = 0.21, T = 1000 K, δ = 1.0 cm^{-1})

CO_2 band	N=2.0×10^{7}m^{-3}		N=2.0×10^{8}m^{-3}		N=2.0×10^{9}m^{-3}	
	DO	MC	DO	MC	DO	MC
2.0 μm	1.902×10^{-2}	1.871×10^{-2}	3.354×10^{-2}	3.336×10^{-2}	3.916×10^{-2}	3.899×10^{-2}
2.7 μm	3.298×10^{-1}	3.307×10^{-1}	3.845×10^{-1}	3.827×10^{-1}	3.916×10^{-1}	3.903×10^{-1}
4.3 μm	5.218×10^{-1}	5.549×10^{-1}	5.670×10^{-1}	5.811×10^{-1}	5.729×10^{-1}	5.687×10^{-1}
9.4 μm	6.113×10^{-2}	6.050×10^{-2}	9.065×10^{-2}	9.005×10^{-2}	9.846×10^{-2}	9.810×10^{-2}
10.4 μm	4.987×10^{-2}	4.919×10^{-2}	8.003×10^{-2}	7.949×10^{-2}	8.826×10^{-2}	8.780×10^{-2}
15.0 μm	1.846×10^{-1}	1.817×10^{-1}	2.108×10^{-1}	2.086×10^{-1}	2.119×10^{-1}	2.101×10^{-1}

DO calculated by the K-distribution method associated with discrete-ordinate method
MC calculated by the Monte-Carlo method

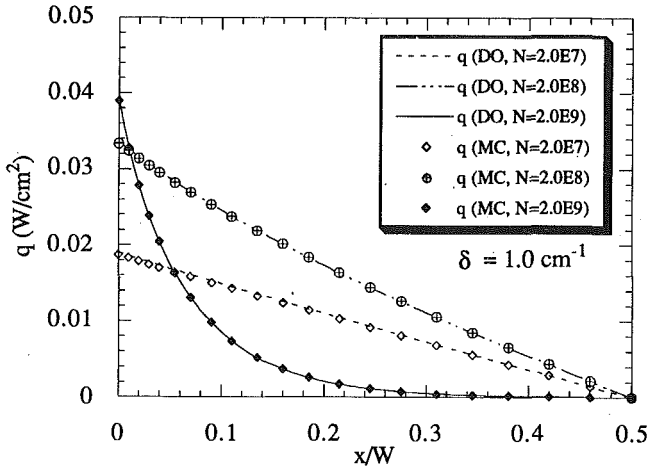

Fig. 3 Radiative heat flux for 2.0 μm CO_2 band (δ = 1.0 cm^{-1})

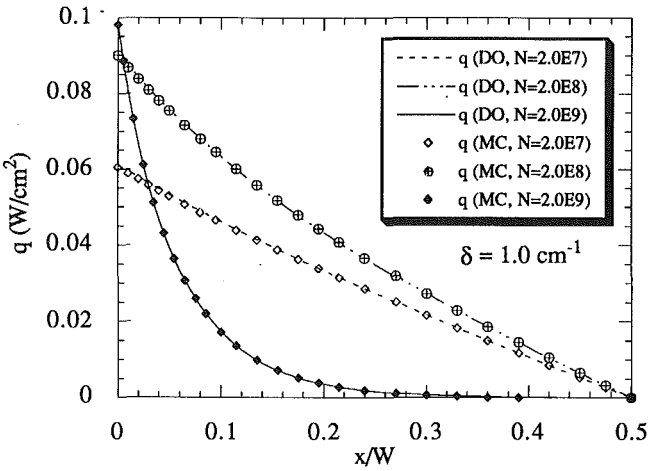

Fig. 5 Radiative heat flux for 9.4 μm CO_2 band (δ = 1.0 cm^{-1})

particle. Therefore, the delta-Eddington phase function can be modified by removing the forward-scattering spike to

$$p'(\Theta) = 1 + 3g \cos \Theta \tag{13}$$

and the scattering efficiency Q_s is reduced by the fraction of "unscattered" or forward-scattered radiation

$$Q_s' = (1 - f)Q_s. \tag{14}$$

With these modifications, the resulting modified radiative system is identical to the original radiative system (Joseph and Wiscombe, 1976) and the difficulty in dealing with the delta function can be avoided.

Band-by-Band Flux. Six CO_2 bands are considered in this study, including the 2.0 μm, 2.7 μm, 4.3 μm, 9.4 μm, 10.4 μm, and 15 μm bands. The maximum absorption coefficients for these bands (P = 1 atm, CO_2 mole fraction = 0.21, T = 1000 K) are presented in Table 1. It is clear that the maximum absorption coefficient for different bands varies over a very wide range with relatively large values appearing in the fundamental (4.3 μm and 15 μm) bands and relatively small values in the overtone and combination-difference bands. Figure 2 shows the gas absorption coefficient, particle absorption coefficient, and particle scattering coefficient for the 2.7 μm band with δ = 1.0 cm^{-1} and $N = 2.0 \times 10^9$ m^{-3}. It is obvious from Fig. 2 that the gas absorption coefficient changes rapidly for the case of δ = 1.0 cm^{-1}. Figure 2 indicates that the gas radiation for the 2.7 μm band dominates the radiative heat transfer near the band center while the particles become important only at the edge of the band. For the stronger bands such as 4.3 μm and 15 μm bands, the gas radiation may dominate the radiative heat transfer within the band. On the other hand, the particles may dominate the radiation for the 2.0 μm, 9.4 μm, and 10.4 μm bands.

The total radiative heat flux for the CO_2 bands is calculated by the K-distribution method associated with the discrete-ordinate method. In order to examine the accuracy of the K-distribution method, the Monte-Carlo simulation is also performed. Table 2 presents the numerical results of the total radiative heat flux at the boundary (i.e., x = 0) for each CO_2 gas band for δ = 1.0 cm^{-1}. From Table 2, it can be seen that the radiative heat fluxes at the boundary obtained from the K-distribution method are in good agreement with the Monte-Carlo results. For the strong bands, such as 4.3 μm and 15.0 μm bands, an increase in particle number density (N) does not increase the heat flux at the boundary significantly. This is due to the fact that the gas absorption coefficient is much larger than the particle absorption and scattering coefficients. For the weaker bands, the flux at the boundary increases as the particle number density increases.

The heat flux distribution within the gas and particle mixture for the 2.0 μm, 2.7 μm, and 9.4 μm bands are plotted in Figs. 3–5. The symbol "DO" in these figures denotes that the radiative heat flux is calculated by the K-distribution method associated

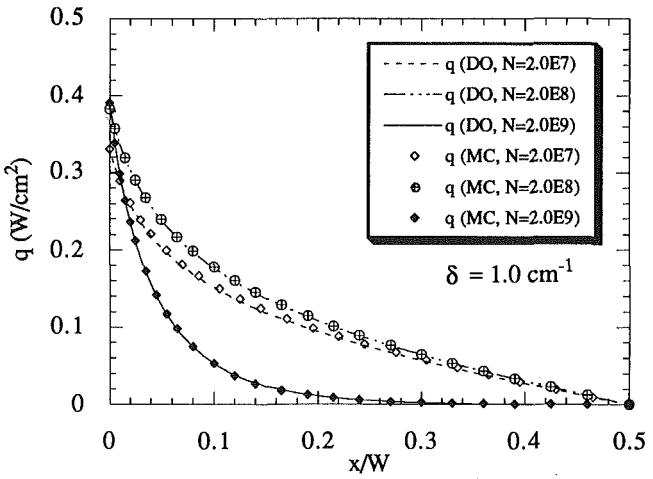

Fig. 4 Radiative heat flux for 2.7 μm CO_2 band (δ = 1.0 cm^{-1})

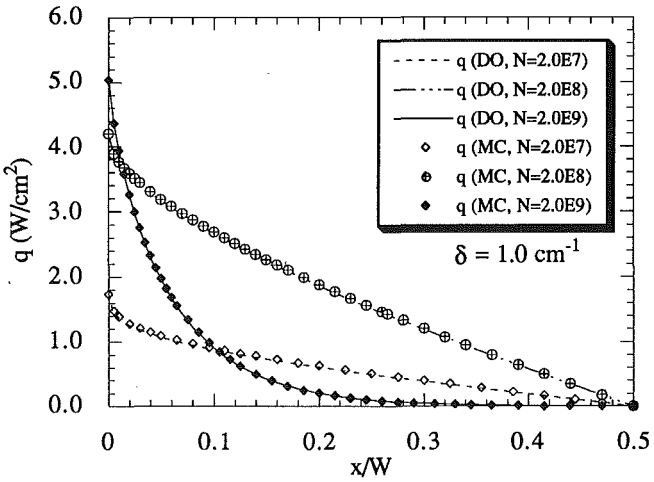

Fig. 6 Total radiative heat flux (δ = 1.0 cm^{-1})

Table 3 Total radiative heat flux (W/cm^2) (P = 1 atm, CO_2 mole fraction = 0.21, T = 1000 K, δ = 1.0 cm^{-1}, W = 5.0 m)

N (m^{-3})	N=2.0×10^7		N=2.0×10^8		N=2.0×10^9	
x	DO	MC	DO	MC	DO	MC
0	1.717×10^0	1.737×10^0	4.211×10^0	4.204×10^0	5.068×10^0	5.040×10^0
W/8	8.044×10^{-1}	8.242×10^{-1}	2.447×10^0	2.467×10^0	6.220×10^{-1}	6.253×10^{-1}
W/4	4.994×10^{-1}	5.197×10^{-1}	1.516×10^0	1.531×10^0	1.025×10^{-1}	9.762×10^{-2}
3W/8	2.422×10^{-1}	2.487×10^{-1}	7.295×10^{-1}	7.380×10^{-1}	1.728×10^{-2}	2.047×10^{-2}
W/2	0.000×10^0	0.000×10^0	0.000×10^0	0.000×10^0	0.000×10^0	0.000×10^0

DO calculated by the K-distribution method associated with discrete-ordinate method
MC calculated by the Monte-Carlo method

with the discrete-ordinate method while "MC" represents the flux obtained by the Monte-Carlo method. Figure 3 is the heat flux distribution for 2.0 μm band with δ = 1.0 cm^{-1}. This figure indicates that the particle radiation dominates throughout the whole band width. Therefore, the increase in particle concentration significantly affects the radiative heat flux for this gas band. Figure 4 is the result for the 2.7 μm band where the gas absorption coefficient is much greater than the scattering and absorption coefficients of the particles. In addition, the gas absorption coefficient and path length are large enough that the mixture is optically thick. Therefore, the variation in the number density of particles does not influence the boundary flux significantly. The results for the 9.4 μm band are presented in Fig. 5. This band has gas absorption coefficient comparable with the particle absorption and scattering coefficients. The heat flux distribution depends on the magnitudes of both the gas and particle radiative properties.

Total Flux. The total flux for the entire spectral region is shown in Fig. 6. Figure 6 is the radiative heat flux distribution for three different particle number densities ($N = 2.0 \times 10^7$, 2.0×10^8, and 2.0×10^9 m^{-3}) with line spacing δ = 1.0 cm^{-1}. The radiative heat fluxes at x = 0, $W/8$, $W/4$, $3W/8$, and $W/2$ m are listed in Table 3 for δ = 1.0 cm^{-1}. From Fig. 6 and Table 3, it can be seen that the comparison between the K-distribution solutions and the Monte-Carlo solutions is again very good.

The radiative heat flux at x = 0 increases when the particle number density (N) increases as would be expected. However, it should be noted that the total flux at locations away from the boundary does not necessarily increase monotonically as the particle number density increases. The small magnitude in total flux near the center of the slab for the high particle loading case is due to the fact that the radiative heat flux is asymptotic to a function of dI_b/dx, which is 0 for an isothermal medium, as the optical thickness increases. The value of δ has only a minor influence on the total flux for the entire spectral region because the magnitude of radiation from CO_2 gas is much smaller than the radiation from particles for the particular parameters selected for this round-robin problem. Other parameters, particularly higher effective albedos, would show a greater importance of line structure and greater usefulness for the K-distribution method when the gas absorption coefficient is comparable with the extinction coefficient of particles. This is especially important when the gas absorption coefficient is comparable with particle extinction coefficient within a gas absorption band where the band models are unable to reflect the nature of the rapidly changing optical thickness from very optically thin to extremely optically thick and so forth over a very small range of wave numbers.

Table 4 Divergence of total radiative heat flux (W/cm^3) calculated by the K-distribution method (P = 1 atm, CO_2 mole fraction = 0.21, T = 1000 K, W = 5.0 m)

N (m^{-3})	N=2.0×10^7	N=2.0×10^8	N=2.0×10^9
0	3.067×10^{-1}	3.262×10^{-1}	5.014×10^{-1}
W/8	5.713×10^{-3}	1.698×10^{-2}	1.836×10^{-2}
W/4	4.353×10^{-3}	1.340×10^{-2}	2.895×10^{-3}
3W/8	3.946×10^{-3}	1.195×10^{-2}	5.095×10^{-4}
W/2	3.842×10^{-3}	1.153×10^{-2}	1.753×10^{-4}

Table 5 Comparison of CRAY Y-MP cpu time (s) used by the K-distribution method and Monte-Carlo method for calculating total radiative flux with line spacing: δ = 1.0 cm^{-1}

N (m^{-3})	N=2.0×10^7		N=2.0×10^8		N=2.0×10^9	
Method	DO	MC	DO	MC	DO	MC
CPU time (sec)	190.	5460.	275.	6725.	250.	7790.

DO calculated by the K-distribution method associated with discrete-ordinate method
MC calculated by the Monte-Carlo method

Table 4 tabulates the divergence of total radiative heat fluxes for different particle number densities ($N = 2.0 \times 10^7$, 2.0×10^8, and 2.0×10^9 m^{-3}) with δ = 1.0 cm^{-1} at x = 0, $W/8$, $W/4$, $3W/8$, and $W/2$ m. The maximum divergence of total flux occurs at x = 0 and attenuates rapidly as x increases. Again the divergence of total radiative heat flux at x = 0 increases as the particle number density (N) increases while the divergence of total flux at locations away from the boundary does not necessarily increase monotonically as the particle number density increases.

The CPU time required for calculating the total radiative flux with line spacing δ = 1.0 cm^{-1} for the K-distribution method and the Monte-Carlo method on the CRAY Y-MP is summarized in Table 5. It is clear from this table that the CPU time required by the K-distribution method is much smaller than the CPU time required by the Monte-Carlo method. This computational advantage is achieved with essentially no loss in accuracy. Hence the K-distribution method is capable of examining the influence of detailed line structure of gas band radiation in the presence of scattering without line-by-line spectral integration.

Finally it should be noted that the K-distribution method is inefficient when the particle loading, medium temperature, and/or gas concentration are not homogeneous. In this case, the K-distribution analysis needs to be performed at every spatial nodal point so that the K-distribution becomes inefficient. For the case of inhomogeneous mixtures, the correlated K-distribution method (Goody and Yung, 1989), which expresses the function $f(K_{a_g})$ in terms of cumulative probability, can be used. This problem is addressed elsewhere (Goody et al., 1989).

Summary

The K-distribution method provides great computational efficiency and is easy to implement in calculating the radiation from highly nongray gas bands in the presence of emitting, absorbing, and anisotropic scattering particles. In addition, the K-distribution solutions are in good agreement with the Monte-Carlo solutions. The solution method for the radiative transfer equation can be arbitrarily chosen provided that the K-distribution method is used to handle the spectral integration. It gives effectively line-by-line accuracy without the infeasible line-by-line spectral integration.

Acknowledgments

Support for this work from the University of Illinois Research Board and computer time provided by the National Center for Supercomputing Applications at the University of Illinois at Urbana–Champaign is gratefully acknowledged.

References

Arking, A., and Grossman, K., 1972, "The Influence of Line Shape and Band Structure on Temperatures in Planetary Atmospheres," *Journal of Atmospheric Science*, Vol. 29, No. 5, pp. 937–949.

Brewster, M. Q., 1992, *Thermal Radiative Transfer and Properties*, Wiley, New York.

Domoto, G. A., 1974, "Frequency Integration for Radiative Transfer Problems Involving Homogeneous Non-gray Gases: The Inverse Transmission Function," *J. Quant. Spectrosc. Radiat. Transfer,* Vol. 14, pp. 935–942.

Edwards, D. K., and Balakrishnan, A., 1973, "Thermal Radiation by Combustion Gases," *Int. J. Heat Mass Transfer,* Vol. 16, pp. 25–40.

Edwards, D. K., Sakurai, Y., and Babikian, D. S., 1987, "A Two-Particle Model for Rocket Plume Radiation," *Journal of Thermophysics,* Vol. 1, No. 1, pp. 13–20.

Fiveland, W. A., and Jamaluddin, A. S., 1989, "Three-Dimensional Spectral Radiative Heat Transfer Solutions by the Discrete-Ordinates Method," *Proceedings of 1989 National Heat Transfer Conference, Heat Transfer Phenomena in Radiation, Combustion and Fires,* ASME HTD-Vol. 106, pp. 43–48.

Foster, P. J., and Howarth, C. R., 1968, "Optical Constants of Carbons and Coals in the Infrared," *Carbon,* Vol. 6, pp. 719–729.

Goody, R. M., and Yung, Y. L., 1989, *Atmospheric Radiation Theoretical Basis,* 2nd ed., Oxford University Press, Inc., New York.

Goody, R., West, R., Chen, L., and Crisp, D., 1989, "The Correlated-*K* Method for Radiation Calculations in Nonhomogeneous Atmospheres," *J. Quant. Spectrosc. Radiat. Transfer,* Vol. 42, No. 6, pp. 539–550.

Grosshandler, W. L., and Modak, A. T., 1981, "Radiation From Nonhomogeneous Combustion Products," *Eighteenth Symposium (International) on Combustion,* The Combustion Institute, pp. 601–609.

Joseph, J. H., and Wiscombe, W. J., 1976, "The Delta-Eddington Approximation for Radiative Flux Transfer," *Journal of Atmospheric Science,* Vol. 33, pp. 2452–2459.

Ludwig, C. B., Malkums, W., Reardon, J. E., and Thomson, J. A. L., 1973, *Handbook of Infrared Radiation From Combustion Gases,* NASA SP-3080, National Technical Information Service, Springfield, VA.

Menguc, M. P., and Viskanta, R., 1985, "Radiative Transfer in Three-Dimensional Rectangular Enclosures Containing Inhomogeneous, Anisotropically Scattering Media," *J. Quant. Spectrosc. Radiat. Transfer,* Vol. 33, No. 6, pp. 533–549.

Tong, T. W., Yuen, W. W., Skocypec, R. D., and Fiveland, W. A., 1992, "Problem Statement," presented at the Symposium on Solution Methods for Radiative Heat Transfer in Participating Media, 1992 National Heat Transfer Conference, San Diego, CA.

Walters, D. V., and Buckius, R. O., 1990, "On the Characteristic Lengths for Absorbing, Emitting, and Scattering Media," *Int. J. Heat Mass Transfer,* Vol. 33, pp. 805–813.

Walters, D. V., and Buckius, R. O., 1992, "Mean Emission Length Approach to Multidimensional Radiative Transfer Including Scattering and Real Gas Absorption," *Int. J. Heat Mass Transfer,* Vol. 35, pp. 131–140.

The Cylindrical Electrostatic Liquid Film Radiator for Heat Rejection in Space

H. Kim

S. G. Bankoff

Department of Chemical Engineering.

M. J. Miksis

Department of Engineering Sciences and Applied Mathematics.

Northwestern University, Evanston, IL 60208

A new space radiator concept has been proposed (Kim et al., 1991, 1992a, b, 1993) in which a thin film of hot liquid, flowing along the inside of a closed membrane, rejects waste heat by radiation to the surroundings. In previous versions, the radiator rotates, supplying most of the driving force for the liquid flow. In the present design, the cylinder is stationary, and the liquid flows circumferentially under its initial momentum. Moderately large Reynolds numbers are required to overcome viscous drag, and prevent excessive thickening of the film. The major design consideration involves the application of an internal electrostatic field to pull the liquid away from the site of a membrane puncture due to micrometeorite impact. Calculations are presented that show that leaks can be stopped with a safety factor of two or more, while the surface wave thus produced is washed harmlessly out of the system. Some preliminary heat transfer performance characteristics are presented. The advantages of this concept include the absence of moving parts and the ease of deployment, compared to rotating units, and a factor of at least three for the reduction of the weight per unit surface area compared to heat pipes.

1 Introduction

Current designs for space radiators for an orbiting space station, or for a lunar base, make use of heat pipes, because of their ruggedness and simplicity. However, their specific weight relative to power is a serious consideration, because of their internal wick structure, relatively thick walls and/or bumpers to withstand micrometeorite impacts, and the consequent need for redundancy as large as 20 percent. Furthermore, their large internal pressure, compared to the surroundings, presents the possibility that a jet of frozen particles will result from even a small puncture. These particles may require considerable time to sublime at space temperatures, and may coat sensitive optics and instrumentation. Hence, it is better to design for zero coolant loss.

The weight problem is particularly important if large amounts of power are required. However, it can also be significant for smaller electrical loads, such as air-conditioning and cooling of electronic cooling equipment, because of the low radiator temperatures. To overcome these problems, droplet and membrane radiators, among others, have been proposed. However, the droplet sprays may suffer from excessive coolant loss, and the membrane radiators are vulnerable to puncture by space debris or micrometeorites. These may not lead to leaks if the membrane is not wetted by the coolant, in view of the large capillary pressures across the meniscus. This is because a meniscus must be formed at the mouth of a hole before leakage can begin, and the minimum radius of the meniscus will be equal to the radius of the hole if the contact angle is 90 deg. However, this cannot be relied upon for practical use. Hence, a backup system is required to stop a leak once it occurs. Kim et al. (1991) proposed the use of internal electrostatic fields to stop a leak of a dielectric fluid from a membrane radiator. The concept was termed the electrostatic liquid film radiator (ELFR). For nuclear power a liquid metal (lithium) is used for radiator temperatures between 500 K and 800 K; for lower temperature applications, organic liquids are suggested. For temperatures above about 800 K, tin or a molten salt may be employed.

The nonrotating cylindrical radiator described herein consists of two concentric thin membranes, closed at both ends to prevent escape of vapor. The coolant liquid is injected circumferentially along a line parallel to the axis, forming a thin film flowing along the outer wall of the annular space between the inner and outer membranes. The liquid flows under its initial momentum around the circumference, and is picked up by deflector vanes at the exit point. It then is returned to the circulating secondary system for heat exchange with the primary coolant. In this respect, the design is similar to the heat-pipe pumped-loop system. However, it may eventually be feasible to dispense with the secondary liquid loop altogether by using the primary coolant in the radiator in some applications, resulting in a further dramatic increase in power–weight ratio. The membranes may be very thin (less than 100 μm) because of the low vapor pressure of the inlet liquid (0.03 Pa for lithium at 700 K). Outgassing is accomplished through small holes at the ends. Because of the low vapor pressure, evaporation losses are negligible. The inner membrane is covered by an array of segmented electrodes formed on its surface by metallizing, with corresponding segments placed oppositely on the outer surface of the radiator. These membranes may be flexible, so that the radiator can be rolled up for launch, and unfurled once in space. The conductive outer segments are of carbon in order to give a high emissivity, and also a high contact angle with the coolant liquid. A small van de Graaf generator (about 1 kg in weight) within the space vehicle is connected by isolated wires to each inner electrode. When a leak is detected by the change in resistance of one of the outer conductive segments, the electrostatic field is locally switched on by charging the opposite inner metallized foil. The electrostatic field exerts a normal tensile stress on the liquid, tending to stop the leak. The carbon segments can also be used to melt frozen coolant for startup in space.

The principal design question is to determine the specific parameter regimes where it will be possible to stop a leak, i.e., where the pressure over the puncture is sufficiently below the sum of the hydrostatic pressure within the liquid film and the vapor pressure. Since the capillary pressure for a static liquid metal hemisphere standing at the mouth of a 1 μm puncture is very large (~0.5 MPa), the use of the electrostatic field will be needed only for large punctures. Even for small contact angles, capillary forces will be sufficient to prevent leakage, in view of the vapor pressure of 0.03 Pa. However, once a leak starts, the

Contributed by the Heat Transfer Division for publication in the JOURNAL OF HEAT TRANSFER. Manuscript received by the Heat Transfer Division January 1993; revision received January 1994. Keywords: Space Power Systems, Thin Film Flow. Associate Technical Editor: Y. Bayazitoglu.

capillary contribution to the pressure balance at the puncture disappears. A careful analysis is therefore needed to establish the feasible working ranges of the ELFR. In this paper, this is done by solving, both analytically and numerically, models for the film motion in the presence of an electric field. Several different limits of the equations of motion are considered, and the implications of each limiting case are discussed.

Two related kinds of electrostatic liquid film radiator (ELFR) concepts have already been explored. These are the plane-flow radiator (Kim et al., 1992a) as a local approximation for a radiator with small radial curvature, and the rotating conical or tapered-disk radiator (Kim et al., 1992b, 1993; Bankoff et al., 1993). The latter designs give freedom to optimize the effective driving force and hydrostatic pressure for film stability and weight minimization, but are complicated by rotating return pumps and piping, and are hence more subject to mechanical failure. On the other hand, the nonrotating cylindrical radiator is very simple and mechanically rugged, but is limited by the fact that the centrifugal force component is due only to the inlet fluid velocity in the circumferential direction. The momentum will decrease due to viscous drag, and hence the film thickness will increase in the direction of flow. To prevent excessive film thickening, a relatively large inlet Reynolds number must be used. Also, the fluid path length can be reduced by using symmetrically placed multiple inlets and outlets. This precludes using lubrication theory to model the dynamics of the film because the inertial effects appear at lowest order. Hence the Karman–Pohlhausen integral method is used to derive an evolution equation for the film thickness and the pressure.

In this paper, therefore, the effect is investigated of an electrostatic field on a thin liquid film flowing circumferentially within the inner wall of a nonrotating hollow circular cylinder. It is shown that a leak can be stopped with a safety factor of about two from a puncture as large as several millimeters in diameter, which is statistically of very low probability. Redundancy can be further provided by dividing the radiator into segments by internal circumferential ribs. Any one segment can be shut off without affecting the other segments.

The heat transfer aspects and design results for similar radiators are discussed by Bankoff et al. (1993). The lower limit of the Reynolds number in those cases are determined by film rupture and appearance of dry spots which reduce the heat transfer efficiency. This is not expected to be a problem here.

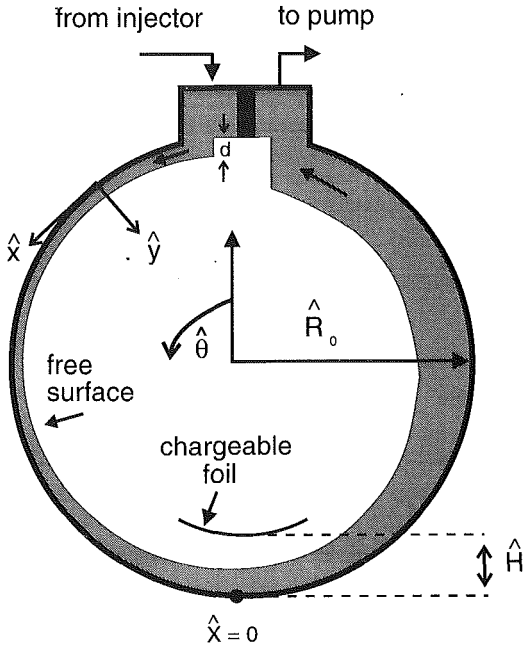

Fig. 1 Diagram of cylindrical tangential-flow radiator

2 Formulation of the Problem

The liquid is injected into the radiator at a specified flow velocity U_0 through a small gap of height d at the entrance of the radiator (Fig. 1). The liquid flows as a viscous film circumferentially around the cylinder. A polar coordinate system $(\hat{r}, \hat{\theta})$ can be introduced with $-\pi \le \hat{\theta} < \pi$. The entrance is located at $\hat{\theta} = -\pi$.

For convenience a coordinate system $(\hat{x}, \hat{y})$ is introduced, as shown in Fig. 1. This new coordinate system is defined by

$$\hat{x} = \hat{R}_0\hat{\theta}, \quad \hat{y} = \hat{R}_0 - \hat{r}, \tag{1}$$

where $\hat{R}_0$ is the inner radius of the hollow cylindrical radiator. The polar velocity components $(\hat{V}_r, \hat{V}_0)$ are set to $(-\hat{V}_y, \hat{V}_x)$,

Nomenclature

$Ca = 2\mu U_0/\sigma$ = capillary number
d = characteristic film thickness
$\hat{\mathbf{E}}^v$ = electric field vector in vacuum
$\hat{E}_n^v$ = normal component of electric field
$\hat{E}_t^v$ = tangential component of electric field
$\mathbf{E} = (\zeta(\partial\phi/\partial x), H(\partial\phi/\partial y))$
F = characteristic unit of electric field
$h = \bar{h}/\xi\hat{R}_0$
$\hat{h}$ = fluid interface in $(\hat{r}, \hat{\theta})$ coordinates
$\bar{h}$ = film thickness in transformed rectangular coordinate system
$\hat{H}$ = distance from wall to electrode
h_c = critical height
$H = \hat{H}/d$
$K = \epsilon_0 dF^2/16\pi\mu U_0$
$\bar{K} = K\xi$
l = length of charged foil
$p = (\hat{p} + (\sigma/\hat{R}_0))/\rho U_0^2$
$\hat{p}$ = pressure
$\bar{p} = p/\xi$
p_{vap} = vapor pressure at inlet temperature
q = local flow rate
$\hat{r}$ = radial distance from center of cylinder
$R = \xi$ Re
$\hat{R}_0$ = radius of circular cylinder
Re $= \rho U_0 d/\mu$ = Reynolds number
$t = \hat{t}U_0/\hat{R}_0$
$\hat{t}$ = time
U_0 = characteristic unit of velocity in the $\hat{x}$ direction
V_f = fluid region
V_v = vacuum region
$V_x = \hat{V}_x/U_0$
$V_y = \hat{V}_y/\xi U_0$
$\hat{V}_r, \hat{V}_x, \hat{V}_y, \hat{V}_0$ = velocity component in the $\hat{r}, \hat{x}, \hat{y}, \hat{\theta}$ directions
$\hat{\mathbf{V}}$ = fluid velocity vector
$x = \hat{x}/\hat{R}_0$
$\hat{x}$ = azimuthal distance along the cylinder
$y = \hat{y}/\xi\hat{R}_0$
$\hat{y}$ = distance coordinate normal to the wall
ϵ_0 = dielectric constant of vacuum
ϵ_f = dielectric constant of fluid
$\zeta = \hat{H}/\hat{R}_0$
$\hat{\theta}$ = polar coordinate measured from inlet, $-\pi \le \hat{\theta} < \pi$
μ = fluid viscosity
$\xi = d/\hat{R}_0$
ρ = fluid density
σ = surface tension
$\phi = \hat{\phi}/F\hat{H}$
$\hat{\phi}$ = electric potential
$\hat{\phi}_v$ = electric potential in vacuum
$\hat{\phi}_f$ = electric potential in fluid
Φ = dimensionless electric potential along $\hat{y} = \hat{H}$

respectively. The free surface of the film $\hat{r} = \hat{h}(\hat{t}, \hat{\theta})$ is changed to

$$\hat{h}(\hat{t}, \hat{\theta}) = \hat{R}_0 - \bar{h}(\hat{t}, \hat{x}), \tag{2}$$

where $\bar{h}(\hat{t}, \hat{x})$ is the film thickness in the new coordinate system, with the liquid domain defined by $-\pi\hat{R}_0 \le \hat{x} < \pi\hat{R}_0$ and $0 \le \hat{y} \le \bar{h}(\hat{t}, \hat{x})$.

The inner membrane wall, at a distance $\hat{H}$ from the outer wall, is covered with conductive segments, one of which is charged with a high voltage. This charged foil (electrode) of arc length l, is centered over a puncture at $\hat{x} = 0$. Define d as the inlet thickness of the film and

$$\xi = \frac{d}{\hat{R}_0}. \tag{3}$$

It is assumed that $\xi \ll 1$, so that the film is thin relative to the expected length scale of the disturbances in the circumferential direction. If $d/\hat{H} \ll 1$ then the charged foil is very far from the wall relative to the thickness of the film. Therefore, to leading order in the ratio of $d/\hat{H}$, one can assume that the charged foil does not see the film, and the electrostatic problem for the electric field decouples from the fluid dynamics problem. The ratio $\zeta = \hat{H}/\hat{R}_0$ is assumed to be order one.

It is also assumed that the charged foil is far from the fluid inlet and outlet points. Together with the thin-film limit, $\xi \ll 1$, this allows the approximation of the electric field due to the foil by that resulting from a two-dimensional charged foil about a cylinder with a large circumference. Thus, it is assumed that the field decays to zero as the magnitude of $\hat{x}$ gets large, and the geometry is similar to the plane flow case. The electric field is determined by solving the Laplace equation

$$\nabla^2\hat{\phi} = 0, \tag{4}$$

for the electric potential $\hat{\phi}(\hat{x}, \hat{y})$ in the fluid, $\hat{\phi}_f$, and for the electric potential, $\hat{\phi}_v$, in the region above the fluid, but below the charged foil. The fluid region, V_f, is defined by $0 \le \hat{y} \le \bar{h}(\hat{x}, \hat{t})$ and $-\pi\hat{R}_0 \le \hat{x} < \pi\hat{R}_0$ (later it is assumed that $\pi\hat{R}_0$ tends to infinity), where $\hat{y} = \bar{h}(\hat{x}, \hat{t})$ is the height of the film above the cylinder wall, and the vacuum region, V_v, is defined by the strip $-\pi\hat{R}_0 \le \hat{x} < \pi\hat{R}_0$ and $\bar{h}(\hat{x}, \hat{t}) \le \hat{y} \le \hat{H}$. The subscript or superscript f denotes quantities in V_f, and the subscript or superscript v quantities in V_v, unless no confusion can occur. The boundary conditions are:

$$\hat{\phi}(\hat{x}, \hat{H}) = F\hat{H}\Phi(\hat{x}), \quad \text{for} \quad \hat{y} = \hat{H},$$
$$\hat{\phi} = 0, \quad \text{for} \quad \hat{y} = 0. \tag{5}$$

The function $\Phi(\hat{x})$ is a given dimensionless function of $\hat{x}$, and the product $F\hat{H}$ is a constant with units of electric potential. Along $\hat{y} = \bar{h}(\hat{x}, \hat{t})$ the boundary conditions are continuity of electric potential and continuity of the normal displacement field:

$$\hat{\phi}^f(\hat{x}, \bar{h}, \hat{t}) = \hat{\phi}^v(\hat{x}, \bar{h}, \hat{t}), \quad \epsilon_f \frac{\partial\hat{\phi}^f}{\partial n} = \epsilon_0 \frac{\partial\hat{\phi}^v}{\partial n}. \tag{6}$$

Here the partial derivative is in the direction of the outward unit normal, $\mathbf{n}$, to the interface. The interface, $\hat{y} = \bar{h}(\hat{x}, \hat{t})$, is unknown, so that the solution of this electrostatic problem is coupled to the dynamics of the film. However, since $\xi \ll 1$, this decouples the electric field problem from the motion of the fluid (see Kim et al., 1992a, for a discussion of this decoupling). To solve for the electric field the two-dimensional unbounded result is therefore used (Kim et al., 1992a).

The liquid film is governed by the incompressible Navier–Stokes equations. Letting d be the unit of length in the $\hat{y}$ direction, $\hat{R}_0$ the unit of length in the $\hat{x}$ direction, U_0 the unit of velocity in the $\hat{x}$ direction (this will be chosen later), ξU_0 the unit of velocity in the $\hat{y}$ direction, $\hat{R}_0/U_0$ the unit of time, ρU_0^2 the unit of pressure, F the unit of electric field, ϵ_0 the unit of electrical permittivity, $H = \hat{H}/d$ the dimensionless foil height, and $x = \hat{x}/\hat{R}_0$, $y = \hat{y}/\xi\hat{R}_0$, $h = \bar{h}/\xi\hat{R}_0$, $t = \hat{t}U_0/\hat{R}_0$, $p = (\hat{p} + (\sigma/\hat{R}_0))/\rho U_0^2$, $V_x = \hat{V}_x/U_0$, $V_y = \hat{V}_y/\xi U_0$, $\zeta = \hat{H}/\hat{R}_0$, $\phi = \hat{\phi}/F\hat{H}$ the dimensionless electric potential and $E = \hat{E}/F$ the dimensionless electric field, the dimensionless equations of motion can be determined. Note that an augmented dimensionless pressure has been introduced, combining the normal stresses due to the liquid pressure and the base-state capillary pressure. The continuity equation becomes

$$\frac{\partial V_x}{\partial x} + (1 - \xi y)\frac{\partial V_y}{\partial y} - \xi V_y = 0, \tag{7}$$

while the x and y components of the momentum equation are

$$\frac{\partial V_x}{\partial t} + \frac{V_x}{1-\xi y}\frac{\partial V_x}{\partial x} + V_y\frac{\partial V_x}{\partial y} - \frac{\xi}{1-\xi y}V_xV_y$$
$$= -\frac{1}{1-\xi y}\frac{\partial p}{\partial x} + \frac{\xi}{\mathrm{Re}}\left[-\frac{V_x^2}{(1-\xi y)^2} - \frac{1}{(1-\xi y)}\frac{1}{\xi}\frac{\partial V_x}{\partial y} + \frac{1}{\xi^2}\frac{\partial^2 V_x}{\partial y^2} + \frac{1}{(1-\xi y)^2}\frac{\partial^2 V_x}{\partial x^2} - \frac{2\xi}{(1-\xi y)^2}\frac{\partial V_y}{\partial x}\right], \tag{8}$$

and

$$\xi\frac{\partial V_y}{\partial t} + \xi V_y\frac{\partial V_y}{\partial y} + \frac{\xi}{1-\xi y}V_x\frac{\partial V_y}{\partial x} + \frac{V_x^2}{1-\xi y}$$
$$= -\frac{1}{\xi}\frac{\partial p}{\partial y} - \frac{\xi}{\mathrm{Re}}\left[\frac{\xi V_y}{(1-\xi y)^2} + \frac{1}{1-\xi y}\frac{\partial V_y}{\partial y} - \frac{1}{\xi}\frac{\partial^2 V_y}{\partial y^2} - \frac{\xi}{(1-\xi y)^2}\frac{\partial^2 V_y}{\partial x^2} - \frac{2}{(1-\xi y)^2}\frac{\partial V_x}{\partial x}\right]. \tag{9}$$

The characteristic Reynolds number is given by

$$\mathrm{Re} = \frac{\rho U_0 d}{\mu}. \tag{10}$$

Along the solid wall, $y = 0$, the no-slip boundary condition is:

$$V_x = V_y = 0. \tag{11}$$

On the fluid interface, $y = h(x, t)$, one has the kinematic condition,

$$\frac{\partial h}{\partial t} + \frac{V_x}{1-\xi h}\frac{\partial h}{\partial x} = V_y, \tag{12}$$

the continuity of tangential stress,

$$\left[(1-\xi h)^2 - \xi^2\left(\frac{\partial h}{\partial x}\right)^2\right]\left(\frac{\xi}{1-\xi h}\frac{\partial V_y}{\partial x} + \frac{1}{\xi}\frac{\partial V_x}{\partial y} + \frac{V_x}{1-\xi h}\right)$$
$$+ 2\xi(1-\xi h)\frac{\partial h}{\partial x}\left(\frac{\partial V_y}{\partial y} - \frac{1}{1-\xi h}\frac{\partial V_x}{\partial x} + \xi\frac{V_y}{1-\xi h}\right) = 0, \tag{13}$$

and the continuity of normal stress,

$$\frac{\xi}{Ca}\left\{\left(1 + \frac{\xi}{1-\xi h}\frac{\partial^2 h}{\partial x^2}\right)\left[(1-\xi h)^2 + \xi^2\left(\frac{\partial h}{\partial x}\right)^2\right]^{-1/2} - 1 + \xi^2\left(\frac{\partial h}{\partial x}\right)^2\left(1 - \frac{\xi}{1-\xi h}\frac{\partial^2 h}{\partial x^2}\right)\left[(1-\xi h)^2 + \xi^2\left(\frac{\partial h}{\partial x}\right)^2\right]^{-3/2}\right\}$$
$$= -\frac{\mathrm{Re}}{2}p + K\left[\frac{1}{\epsilon_f} - 1\right][(E_n^v)^2 + \epsilon_f(E_t^v)^2]$$
$$+ \xi\left[(1-\xi h)^2\frac{\partial V_y}{\partial y} + \xi^2\left(\frac{\partial h}{\partial x}\right)^2\left(\frac{1}{1-\xi h}\frac{\partial V_x}{\partial x} - \frac{\xi}{1-\xi h}V_y\right) - \xi(1-\xi h)\frac{\partial h}{\partial x}\left(\frac{\xi}{1-\xi h}\frac{\partial V_y}{\partial x} + \frac{1}{\xi}\frac{\partial V_x}{\partial y} + \frac{V_x}{1-\xi h}\right)\right]$$
$$\times\left[(1-\xi h)^2 + \xi^2\left(\frac{\partial h}{\partial x}\right)^2\right]^{-1}. \tag{14}$$

Here the capillary number

$$Ca = \frac{2\mu U_0}{\sigma}, \tag{15}$$

and the dimensionless constant of the electrostatic field

$$K = \frac{\epsilon_0 dF^2}{16\pi\mu U_0}, \tag{16}$$

have been introduced and the pressure above the liquid film has been set to zero. Also, the dimensionless electric field is defined as

$$\mathbf{E} = \left(\zeta \frac{\partial\phi}{\partial x}, H \frac{\partial\phi}{\partial y}\right), \tag{17}$$

with the normal component $E_n = \mathbf{E}\cdot\mathbf{n}$ and the tangential component $E_t = \mathbf{E}\cdot\tau$ where τ is the unit tangent to the interface. It is seen from Eq. (14) that the charged foil suspended above the liquid film influences the fluid motion only via the inhomogeneous term in the normal stress equation.

The dimensionless constants, Re, Ca, and K all have to be specified, since these are three independent parameters in the description of the free surface flow. If a specific fluid in a given experimental situation is considered, the only free parameter is the characteristic velocity U_0. Then as U_0 is varied, one finds that Re and Ca vary linearly with U_0, while K is inversely proportional to U_0. The results will be presented from this point of view, taking the physical parameters for lithium at 700 K ($\mu = 0.0038p$ and $\rho = 493$ kg/m^3). Hence for fixed electric field strength F we will have K changing as the Reynolds number changes.

Equations (7)–(14) determine the motion of the liquid film. Initial conditions are still required to solve for the evolution of the liquid. Since our primary concern is the effect of the electric field on this film flow, the entrance length is assumed to be very short, so that the flow quickly exhibits a parabolic velocity profile.

3 Thin Film Limit

Taking the thin film limit, $\xi \ll 1$, in Eqs. (4)–(14) one can derive a nonlinear evolution equation for the height, $h(x, t)$ of the film. The flow of the entering liquid is assumed to be uniform. Thus, the film thickness can be set to $h = 1$ at $x = -\pi$ for the inlet boundary condition. This inlet boundary condition is reasonable for the long wavelength model, since the primary concern is the effect of the electric field on the stability of the film.

One finds from the dimensionless versions of Eqs. (4)–(6) that, at leading order in ξ, the electric potential is a linear function of y, with coefficients which depend on x and t. Equations (5) and (6) then imply that

$$\phi_0^f = \Phi(x)\frac{y}{\epsilon_f}\left\{h(x,t)\left\{\frac{1}{\epsilon_f} - 1\right\} + H\right\}^{-1} \quad \text{for} \quad 0 < y < h(x,t) \tag{18}$$

and

$$\phi_0^v = \Phi(x)\left\{1 + (y-H)\left[h(x,t)\left\{\frac{1}{\epsilon_f} - 1\right\} + H\right]^{-1}\right\} \quad \text{for} \quad h(x,t) < y < H. \tag{19}$$

Additional corrections to the electric potential require the next-order correction in $h(x, t)$.

Depending on the diameter of the hollow cylinder, a larger Reynolds number than 0(1) may be necessary for film stability. Hence the thin film limit is considered with Re $= O(1/\xi)$ and U_0 as the mean velocity of flow at the entrance of the radiator. Two ranges of dimensionless electrostatic field K are considered, i.e., $K = O(1)$ and $K = O(1/\xi)$. In order to consider the effect of the electrostatic field on the leading-order pressure, the pressure p is assumed to be of order ξ when $K = O(1)$, and order one when $K = O(1/\xi)$. Under these conditions a nonlinear system of equations valid at leading order in ξ can be derived from Eqs. (7)–(14). However, it is not possible to solve these nonlinear equations using lubrication theory. In order to obtain a simple evolution equation we use the Karman–Pohlhausen approximation. This has recently been applied to other thin film problems with considerable success (Kim et al., 1992a, 1992b, 1993; Prokopiou et al., 1991; Rahman et al., 1989). Thus $R = \xi$ Re $= O(1)$ is assumed, while all the other variables are of order one.

3.1 Order One Electrostatic Constant: $K = O(1)$. Let $\bar{p} = p/\xi = O(1)$. We can then obtain the leading order in ξ equations of motion from Eqs. (7)–(9). Here we will assume that the fluid has perfect conductivity ($\epsilon_f \to \infty$). Integrating these equations is clearly difficult even though they represent only the leading order behavior of the thin film. In order to simplify the analysis the Karman–Pohlhausen quadratic-velocity-profile approximation is introduced:

$$V_x = \frac{3q}{h}\left[\frac{y}{h} - \frac{1}{2}\left(\frac{y}{h}\right)^2\right], \tag{20}$$

where q is the local flow rate defined by

$$q = \int_0^h V_x dy. \tag{21}$$

To derive the nonlinear evolution equation, one first integrates the leading order equations, then substitutes Eq. (20) into the leading order horizontal momentum equation and integrates in y from 0 to h. Prokopiou et al. (1991) give additional details. The result of these calculations is a coupled set of equations for the height h and the flow rate q:

$$\frac{\partial h}{\partial t} + \frac{\partial q}{\partial x} = 0, \tag{22}$$

and

$$\frac{\partial q}{\partial t} + \frac{\partial}{\partial x}\left(\frac{6}{5}\frac{q^2}{h}\right) = -\frac{3}{R}\frac{q}{h^2}. \tag{23}$$

This is a nonlinear hyperbolic system of equations, in which the film thickness h is not affected by the electrostatic field. The leading order pressure is

$$\bar{p} = -3\frac{q^2}{h^2}\left(\frac{y^3}{h^2} - \frac{3}{4}\frac{y^4}{h^3} + \frac{3}{20}\frac{y^5}{h^4}\right) + \frac{6}{5}\frac{q^2}{h} - \frac{2K}{R}(E_n^v)^2. \tag{24}$$

The design requires a negative pressure in the liquid under the charged foil in order to stop a leak out of a puncture. In particular we need $p < -p_{\text{vap}}$. For this requirement one can calculate a critical film height h_c from Eq. (24) for the pressure to equal $-p_{\text{vap}}$ on the wall at $y = 0$,

$$h_c = \frac{6}{5}q^2\frac{R}{2K(E_n^v)^2 - Rp_{\text{vap}}}. \tag{25}$$

It is of interest to consider the steady-state solutions of Eqs. (22) and (23). From Eq. (22) we see that q is constant at steady state and with the inlet boundary condition $h = 1$ at $x = -\pi$ we can get the following leading order film thickness at steady state:

$$h_s = 1 + \frac{5}{2}\frac{1}{q}\frac{(x+\pi)}{R}, \tag{26}$$

so that the film thickness h increases linearly as x increases. With the limits $K = O(1)$ and $\bar{p} = O(1)$, note that the leading order pressure depends on h and q due to the effects of a centrifugal force produced from V_x in the y-momentum equation.

3.2 Order $1/\xi$ Electrostatic Constant: $K = O(1/\xi)$. When $K = O(1)$ the leading order film height is not affected by the electrostatic field, as seen from the previous section. Hence, to introduce the electrostatic field into Eq. (23), assume that $K = \bar{K}/\xi = O(1/\xi)$ and $p = O(1)$. Using these assumptions in Eqs. (7)–(9) the leading order terms in ξ can be determined. We note that the leading order continuity of the normal stress along the interface $y = h(x, t)$ is ($Ca \to \infty$, $\epsilon_f \to \infty$) leads to

$$p = -\frac{2\bar{K}}{R}(E_n^v)^2. \tag{27}$$

With the same procedures as in the $K = O(1)$ case, and again using the Karman–Pohlhausen approximation, the following evolution equations result:

$$\frac{\partial h}{\partial t} + \frac{\partial q}{\partial x} = 0, \tag{28}$$

and

$$\frac{\partial q}{\partial t} + \frac{\partial}{\partial x}\left(\frac{6}{5}\frac{q^2}{h}\right) = -\frac{3}{R}\frac{q}{h^2} + \frac{2\bar{K}}{R}h\frac{\partial (E_n^v)^2}{\partial x}. \tag{29}$$

The leading-order pressure is given by Eq. (27), and is always negative in this analysis.

The steady-state solution, determined from Eq. (29) with $q =$ const, is

$$\frac{dh}{dx} = -\frac{5}{3}\frac{\bar{K}}{R}\frac{h^3}{q^2}\frac{\partial (E_n^v)^2}{\partial x} + \frac{5}{2}\frac{1}{R}\frac{1}{q}. \tag{30}$$

This steady-state solution of the Karman–Pohlhausen approximation is plotted in Fig. 2. In order to simulate a slowly varying potential, let $\Phi = \exp(-10x^2)$ in Eq. (19). This potential has the slowly varying form of the assumptions. For boundary conditions, let $h = 1$ and $q = 1$ at $x = -\pi$ where the effect of the electric field is very small. In order to simulate an experimental situation, set $\hat{R}_0 = 0.2$ m, $d = 2$ mm, $\hat{H} = 0.02$ m, $\xi = 0.01$, and $F = 2$ KV/mm at $U_0 = 0.138$, 0.275, 0.55 m/s with the other physical parameters for lithium at 700 K. These chosen velocities vary Re and K. In Fig. 2, results are plotted for Re = 356.8, 713.6, 1427.1, which correspond to the above-mentioned values of U_0, and the values of $K = 27.2$, 13.6, 6.8, respectively. Note that the film thins with increasing Re and the effect of the electric field is to cause a sudden decrease, then an increase in the steady-state profiles.

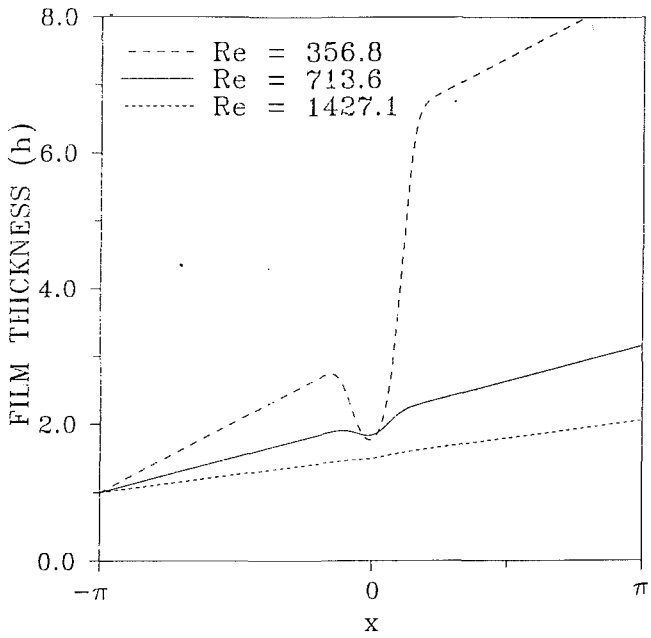

Fig. 2 Steady-state solutions in the Karman–Pohlhausen model Eq. (45) with $F = 2$ KV/mm, $\hat{R}_0 = 0.2$ m, $d = 0.002$ m, and $\hat{H} = 0.02$ m (Re = 356.8, 713.6, 1427.1)

4 Numerical Solutions

The approximate model given by Eqs. (28) and (29) for $K = O(1/\xi)$ is now solved numerically, using a two-step Lax–Wendroff method with diffusion and antidiffusion (Sod, 1985). Numerical convergence checks were done. When $K = O(1)$ the evolution equation is not affected by the electric field. The limit where $H \gg 1$ is taken, so that the charged foil is far away from the wall of the flowing film. As noted before, this decouples the electrostatic problem from the fluid problem.

Suppose that the fluid is a perfect conductor and that Φ at $y = H$ is given by

$$\Phi(x) = \begin{cases} 1 & \text{for } -\dfrac{l}{2} \le x \le \dfrac{l}{2} \\ 0 & \text{otherwise.} \end{cases} \tag{31}$$

Here again, it is assumed that $\pm\pi$ tends to $\pm\infty$, so the electrostatic problem is two dimensional and defined on an infinite interval. In the limit where the thin film is not seen at leading order in ξ by the charged foil, the solution of this electrostatic problem can be found in Morse and Feshbach (1953). In terms of the normal component of the electric field along the plane $y = 0$ we have

$$E_n^v = -1 + \frac{1}{1 + e^{-(\pi/\xi H)(l/2 - x)}} + \frac{1}{1 + e^{-(\pi/\xi H)(l/2 + x)}}. \tag{32}$$

Equation (32) can now be used in Eq. (29) and the resulting system can be solved numerically. The normal electric field as given by Eq. (32) is used. This clearly violates the slowly varying assumptions of the derivation of the approximate models, but it will illustrate the usefulness of these models. In Kim et al. (1992a) it has been shown that even though the slowly varying assumption is violated by Eq. (31), good results can be expected from Eqs. (28) and (29).

As an illustrative set of calculations, take $F = 2$ KV/mm, $\hat{H} = 0.02$ m, $d = 0.002$ m, $\hat{R}_0 = 0.2$ m, $\xi = 0.01$, and $U_0 = 0.275$ m/s and all physical properties for lithium at 700 K. This will give Re = 713.6 and $K = 13.6$. Also, select $H = 0.2$ m and $l = 0.005$ m. Initial conditions are given by the steady-state shapes of the Karman–Pohlhausen method, Eq. (30), without the electric field. At $t = 0$ the electric field is turned on and a disturbance is generated. Figure 3 shows the dimensionless film thickness h as a function of x for $t_n = n(0.125)$, $n = 1, \ldots, 16$. As time increases a disturbance begins along the precursor trough, and develops into a shock. This is harmless to the operation of the ELFR, since it occurs downstream of the foil and has a small amplitude. Hence it will be washed away.

To make the shock profile weaker, the inlet velocity U_0 is doubled from that in Fig. 3, i.e., $U_0 = 0.55$ m/s, while the other parameters are unchanged. This raises the Reynolds number and decreases K, to Re = 1427.1 and $K = 6.8$. Figure 4 shows the height h for $t_n = n(0.1)$, $n = 1, \ldots, 16$. As in Fig. 3, the height of the film under the foil at first decreases with increasing x, and then increases.

From Eq. (27) and the fact that at leading order p is independent of y, the augmented pressure at the wall is negative, and must be greater in magnitude than the vapor pressure of the fluid at the inlet temperature in order to stop a leak. Note that this capillary pressure considered here is due to the curvature of the cylinder. This is relatively small, but for liquid metals, which have high surface tension, this capillary effect is of the order of 2 Pa for a 0.1 m radius cylinder, which is considerably larger than the electrostatic contribution, which depends on the mag-

nitude of the electric field. This contribution is thus very important, allowing an increase of the inlet lithium temperature from 700 K (p_{vap} = 0.03 Pa) to 800 K (p_{vap} = 0.98 Pa), with a safety factor of two for leak stoppage. Furthermore, the capillary pressure opposing leakage from a small puncture is much larger, amounting to several atmospheres for liquid lithium. On the other hand, for radiator temperatures less than 400 K an organic liquid must be used as the coolant. The base-state capillary-pressure contribution is then an order of magnitude lower, and the electrostatic-field contribution to leak stoppage, once a leak has been established, is needed. The present analysis applies to this case equally well. For radiator temperatures above about 800 K, molten salts may be used, again requiring a backup system because of their relatively low surface tension.

5 Design Considerations

Figures of merit for space radiators are power per unit area, and weight per area. The outer membrane is a composite, consisting of a metal (niobium) liner to resist corrosion by the lithium, an insulating nonconductive layer, and an outer thin coat of graphite segments, which are wired to serve as leak detectors, or, if need be, heaters to melt frozen coolant. In contrast to heat pipes, the pressure difference across the radiator walls is virtually zero, so that a very thin membrane (100 μm) can be used. The weight of the liquid is neglected, since a secondary coolant is needed for all radiator systems. With heat pipes, this liquid is separate from the liquid sealed within, but with this radiator, the secondary liquid is used directly in the radiator. Hence, for inner and outer membrane radii of 0.18 m and 0.2 m, and a mean density of 2×10^3 kg/m^3 the weight per unit external surface area is of the order of 0.5 kg/m^2. This contrasts with a recent figure of 6–7 kg/m^2 for carbon–carbon heat pipes. Even allowing for the (small) van de Graaf generator and the piping, there seems to be a large weight advantage for this type of radiator. Additional discussion is given by Bankoff et al. (1993).

Assuming an emissivity of 0.9 and a mean radiator temperature of 700 K, this gives a radiator power of about 10 kW/m. Hence a 1000 kW (thermal) power plant would require an array of cylinders totaling 100 m in length with a view factor close to unity. If the radiator temperature is raised to 800 K, the required area is reduced by more than 40 percent. If oppositely spaced inlet and outlet ports are used, the cylinder diameter can be increased by a factor of four, with a corresponding decrease in the total length. With these modifications, the total cylinder length is about 15 m, with an outer diameter of 0.8 m. This would appear to be a feasible configuration.

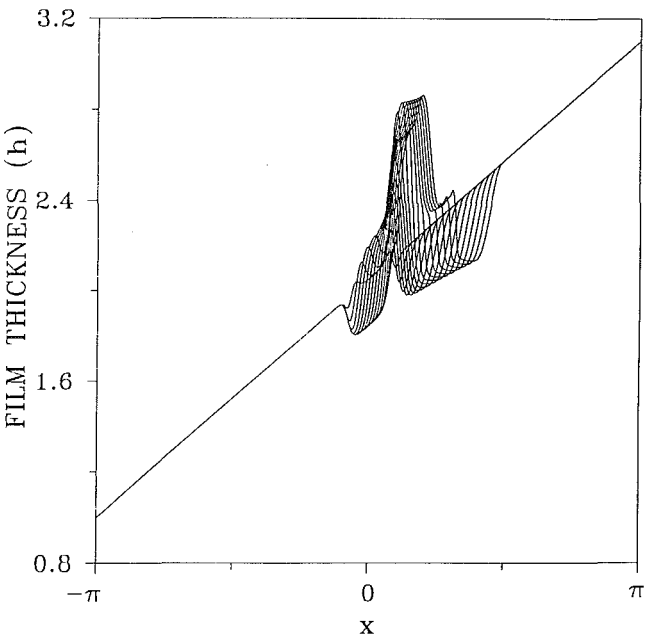

Fig. 3 Free surface h versus x as determined by Eqs. (43) and (44) for $t = n(0.125)$, $n = 1, \ldots, 16$ with F = 2 KV/mm, $\hat{R}_0$ = 0.2 m, d = 0.002 m, $\hat{H}$ = 0.02 m, Re = 713.6, K = 13.6 and the other parameter for lithium at 700 K

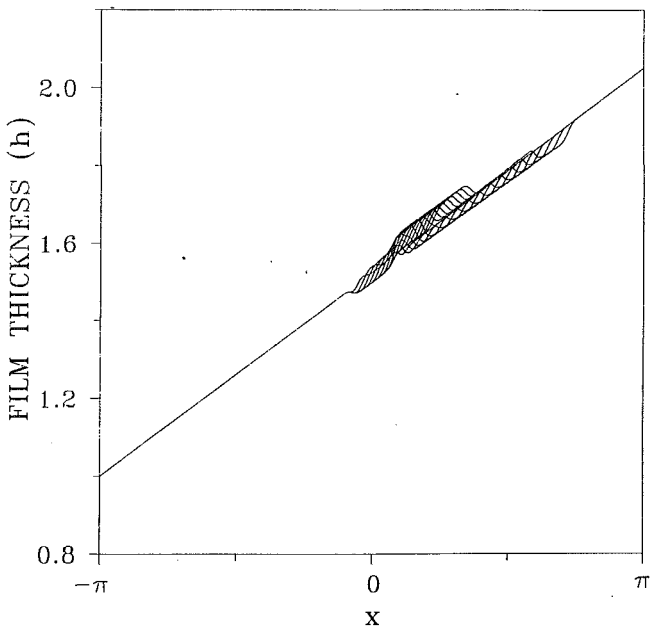

Fig. 4 Free surface h versus x as determined by Eqs. (43) and (44) for $t = n(0.1)$, $n = 1, \ldots, 16$ with F = 2 KV/mm, $\hat{R}_0$ = 0.2 m, d = 0.002 m, $\hat{H}$ = 0.02 m, Re = 1427.1, K = 6.8 and the other parameter for lithium at 700 K

6 Conclusions

A novel type of space radiator, consisting of a stationary thin-membrane cylinder, with coolant flowing circumferentially along the inner wall, is examined herein. The advantages of this radiator over heat pipes is the large difference in weight per unit effective surface area. The advantage of this radiator over rotating ELFR designs is the absence of moving parts. Furthermore, the cylindrical curvature results in a capillary restraining pressure, which adds to the electrostatic-field pressure, and may make the electrostatic system unnecessary for liquid metals. For organic coolants, however, the capillary pressure effect probably needs to be supplemented by the electrostatic-field pressure. The nonlinear coupled evolution equations for the film thickness as a function of space and time have been solved for typical parameter values. These show that the surface waves produced by the electrostatic field are convected out of the puncture region, and are washed harmlessly away. It would appear, therefore, that this type of radiator would possess significant advantages over heat-pipe radiators.

Acknowledgments

This work was partially supported by Department of Energy grant No. DE-FG07-89FR12894. HK was also supported in part by the Korea Gas Company.

References

Bankoff, S. G., Miksis, M. J., Kim, H., and Gwinner, R., 1993, "Design Considerations for the Rotating Electrostatic Liquid-Film Radiator," *Proc. of the 6th Int. Topical Meeting on Nuclear Reactor Thermalhydraulics*, Grenoble, France, Oct. 5–8; also in *Nucl. Eng. and Design*, Vol. 149, 1994, pp. 441–447.

Kim, H., Bankoff, S. G., and Miksis, M. J., 1991, "Lightweight Space Radiator With Leakage Control by Internal Electrostatic Fields," *Proc. Eighth*

Symp. on Space Nuclear Power Systems, Albuquerque, NM, CONF-910116, pp. 1280–1285.

Kim, H., Bankoff, S. G., and Miksis, M. J., 1992a, "The Effect of an Electrostatic Field on Film Flow Down an Inclined Plane," *Phys. Fluids,* Vol. 4, pp. 2117–2130.

Kim, H., Bankoff, S. G., and Miksis, M. J., 1992b, "The Electrostatic Liquid-Film Radiator for Heat Rejection in Space," presented at the 1992 National Heat Transfer Conference, ASME/AIChE, Anaheim, CA.

Kim, H., Bankoff, S. G., and Miksis, M. J., 1993, "Interaction of an Electrostatic Field With a Liquid Film Flow Within a Rotating Conical Space Radiator," *AIAA J. Propulsion and Power,* Vol. 9, pp. 245–254.

Landau, L. D., Lifshitz, E. M., and Pitaevskii, L. P., 1984, *Electrodynamics of Continuous Media,* Pergamon Press, Oxford, United Kingdom.

Morse, P. M., and Feshbach, H., 1953, *Methods of Theoretical Physics,* McGraw-Hill, New York.

Prokopiou, T. H., Cheng, M., and Chang, H.-C., 1991, "Long Waves on Inclined Films at High Reynolds Number," *J. Fluid Mech.,* Vol. 222, pp. 665–692.

Rahman, M. M., Faghri, A., Hankey, W. L., and Swanson, T. D., 1989, "Heat Transfer to a Thin Liquid Film With a Free Surface," *Proceedings of the National Heat Transfer Conference,* Vol. 110, pp. 161–168.

Sod, G. A., 1985, *Numerical Methods in Fluid Dynamics: Initial and Initial Boundary-Value Problems,* Cambridge University Press, New York.

Z. M. Zhang

R. U. Datla

S. R. Lorentz

Radiometric Physics Division,
National Institute of Standards
and Technology,
Gaithersburg, MD 20899

H. C. Tang

Scientific Computing Environments Division,
National Institute of Standards
and Technology,
Gaithersburg, MD 20899

Thermal Modeling of Absolute Cryogenic Radiometers

This work consists of a detailed thermal modeling of two different radiometers operated at cryogenic temperatures. Both employ a temperature sensor and an electrical-substitution technique to determine the absolute radiant power entering the aperture of a receiver. Their sensing elements are different: One is a germanium resistance thermometer, and the other is a superconducting kinetic-inductance thermometer. The finite element method is used to predict the transient and steady-state temperature distribution in the receiver. The nonequivalence between the radiant power and the electrical power due to the temperature gradient in the receiver is shown to be small and is minimized by placing the thermometer near the thermal impedance. In the radiometer with a germanium resistance thermometer, the random noise dominates the uncertainty for small incident powers and limits the ultimate sensitivity. At high power levels, the measurement accuracy is limited by the uncertainty of the absorptance of the cavity. Recommendations are given based on the modeling for future improvement of the dynamic response of both radiometers.

Introduction

Optical radiometers measure radiant power or irradiance in the spectral region from ultraviolet to far-infrared. These devices play an important role in the measurements of the solar constant and solar irradiance (Fröhlich, 1991; Zhang et al., 1987), the evaluation of the earth radiation budget (Mahan et al., 1989), and the determination of the Stefan–Boltzmann constant and thermodynamic temperatures (Quinn and Martin, 1985). Thermal modeling and design are crucial for the construction of high-accuracy absolute radiometers.

Figure 1 shows a schematic of the receiving portion of an absolute cryogenic radiometer (hereafter ACR) made by Cambridge Research and Instrumentation, Inc. [1]. A conical receiver, made of oxygen-free high-conductivity (OFHC) copper and Aeroglaze (formerly Chemglaze) Z302 specular black paint [2], is thermally isolated from a heat sink by a thin AISI 304 stainless steel tube. Two germanium resistance thermometers (GRTs) are attached to the receiver, and two electrical heaters are wrapped around the receiver. The electrical leads of the heaters and GRTs are niobium-titanium wire that is superconducting at temperatures below 9 K. The heat sink is linked to a liquid-helium bath, and its temperature is stabilized by a temperature controller using the heater and a GRT on the heat sink. The aperture is made of Invar, and its area is determined with an uncertainty of 0.05 percent (Datla et al., 1992).

Absolute radiometers can be operated in either a passive mode (open loop) or an active mode (closed loop). In the passive mode, radiation enters the receiver and causes its temperature to rise relative to the heat sink. When the receiver reaches steady state, a shutter in front of it (not shown in Fig. 1) is closed and the electrical heater is turned on. The electrical power is increased until the receiver reaches the same temperature as that with radiative heating. The radiant power absorbed by the receiver is determined by measuring the electrical power supplied to the heater. In the active mode, electrical power is supplied to the heater before the shutter is opened. When the shutter is opened, the electrical power is reduced to maintain the same temperature. The reduction in the electrical power is equal to the radiant power. Both the passive and active modes are based on the principle of electrical substitution. The error caused by the nonequality between the electrical and radiant powers is known as nonequivalence.

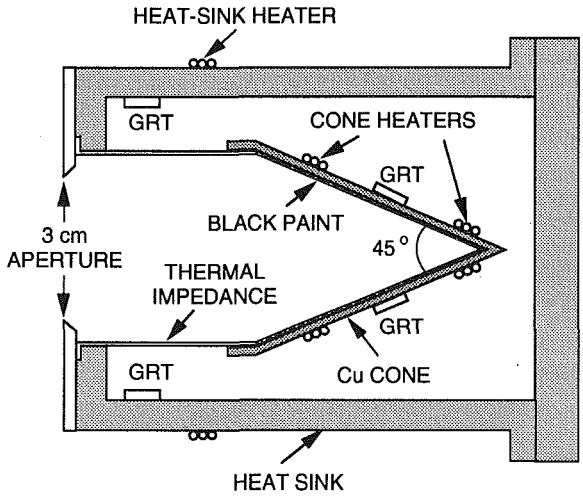

Fig. 1 Schematic of an absolute cryogenic radiometer, where GRT refers to germanium resistance thermometer

The ACR shown in Fig. 1 is installed in a low-temperature chamber at the Low-Background Infrared (LBIR) facility at NIST, for testing and calibrating blackbody sources, infrared detectors, and other optical components (Ebner et al., 1989). The inner wall of the LBIR chamber is cooled to 20 K by a closed-cycle helium refrigerator. The radiometer operates between 2 and 4 K with an overall uncertainty of less than 1 percent for radiant powers between 20 nW and 100 μW. Datla et al. (1992) performed a detailed characterization of this radiometer based on experiments and a lumped-parameter model. The lumped-parameter model, however, cannot predict the nonequivalence due to the temperature gradient in the receiving cone.

Recently, Sauvageau et al. (1991) developed a new temperature sensor, a superconducting kinetic-inductance thermometer, for radiometer applications. A prototype detector using the superconducting kinetic-inductance device demonstrated that a noise equivalent power (NEP) of 0.7 pW can be achieved over a 100 s integration time, which is about 150 times more sensitive than the ACR based on GRTs. A new radiometer, using the superconducting kinetic-inductance thermometer

Contributed by the Heat Transfer Division and presented at the National Heat Transfer Conference, Atlanta, Georgia, August 8–11, 1993. Manuscript received by the Heat Transfer Division May 1993; revision received October 1993. Keywords: Cryogenics, Measurement Techniques, Radiation. Associate Technical Editor: M. F. Modest.

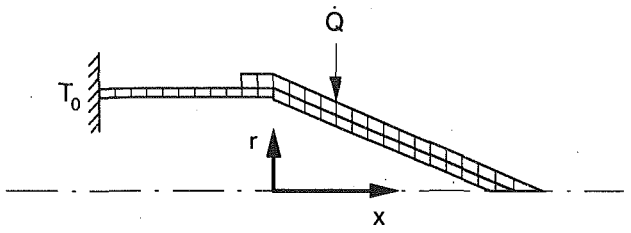

Fig. 2 Illustration of the thermal model for the finite element analysis, where power $\dot{Q}$ is introduced only at specific locations (axial symmetry about x axis)

(hereafter SKACR), will be located at the exit port of a cryogenic monochromator, which will be installed in the LBIR chamber for high-accuracy spectral measurements. Thermal analysis and modeling are required to predict the accuracy and sensitivity of the SKACR.

Mahan et al. (1987) used a finite element method to analyze the steady-state temperature field and dynamic response of infrared radiometers. In that study, the radiant power was at the milliwatt level. The radiometers employed in the present study measure radiant powers in the range from subnanowatt to submilliwatt. A commercial finite-element-analysis program, ANSYS [3], is employed to model the temperature distribution in the two cryogenic radiometers. With the knowledge of the radiometer geometry and the thermophysical properties of the materials at cryogenic temperatures, the present study predicts the responsivity, the temperature distribution along the receiver cone, the nonequivalence between radiative and electrical heating, and the dynamic temperature response. The results from the numerical modeling are compared with experimental data. Different error components of the absolute cryogenic radiometers are assessed. The effect of the specular and diffuse reflectance of the black coating on the total absorptance of the cone is also analyzed. This study will facilitate the future improvement of the design of absolute cryogenic radiometers.

Thermal Modeling

The thermal conduction in the receiver of the ACR is simplified as a three-component axially symmetric system as illustrated in Fig. 2, where the thicknesses of the materials are exaggerated. The temperature at the end of the stainless steel tube is assumed to be constant and equal to the heat sink temperature T_0. Since the radiometers operate at ultra-high vacuum and very low temperatures, convective and radiative heat losses from the cone to the heat sink are negligible. The heat flow is mainly through the stainless steel since the thermal conductance of the leads for the GRTs and heaters is also negligible. Quantitative justifications are given in the following section. Both the radiative heating and the electrical heating are treated as surface load with a total power Q. Hence, a uniform heat flux is applied only at certain locations, either from the inner surface or from the outer surface of the cone, while adiabatic boundary conditions are assumed elsewhere.

A general-purpose finite-element-analysis package, ANSYS Revision 5.0, is employed to model the thermal conduction. For transient thermal analysis, the governing equation is

$$[\mathbf{C}]\{\dot{\mathbf{T}}\} + [\mathbf{K}]\{\mathbf{T}\} = \{\dot{\mathbf{Q}}\} \tag{1}$$

where $\mathbf{T}$ and $\dot{\mathbf{T}}$ are the vectors of the nodal temperature and its time derivative, and $\mathbf{C}$ and $\mathbf{K}$ are the heat capacity and thermal conductance matrices, respectively. The heating power vector $\dot{\mathbf{Q}}$ accounts for the heat flow across the boundary since there is no internal heat generation. In the computation, the Crank–Nicolson scheme (Shih, 1984) is selected to integrate the governing equation with respect to time, and Newton–Raphson iteration (Reddy, 1984) is used to solve the nonlinear matrix equation due to the temperature dependence of the thermal conductivity and specific heat.

A SPARC workstation [4] runs the thermal modeling program. A typical steady-state analysis takes less than one minute CPU time. The transient analysis for 100 s takes 2 to 20 hours of CPU time depending on the size of the integration time step.

The discussion above is applicable to the modeling of the SKACR, which has a more complicated geometry.

Absolute Cryogenic Radiometer Using a Germanium Resistance Thermometer

The physical dimensions of the ACR were described by Datla et al. (1992). The diameter of the aperture is 3 cm and the outer diameter of the stainless steel tube is approximately 3.81 cm. The thickness of the stainless steel tube is 50 μm and that of the Cu cone is 127 μm. The height of the cone is 4.6 cm, and the length of the stainless steel tube is 3.2 cm with 0.2 cm overlap with the copper. The stainless steel tube is modeled using line elements since the heat flow through it is along the x direction.

The specific heats of the stainless steel and copper are obtained from Touloukian and Buyco (1970). The thermal conductivity of the stainless steel is obtained from Touloukian et al. (1970), and that of the OFHC copper is extrapolated linearly to 2.2 K from the data available at higher temperatures (Jensen et al., 1980). The densities of the stainless steel and Cu from 2 to 4 K are 1 to 2 percent higher than those at room temperature (Jensen et al., 1980). The density of the paint is assumed to be equal to the value at room temperature provided by the Lord Corp. [2]. The low-temperature data of the specific heat of the Aeroglaze Z302 are provided by the Cambridge Research and Instrumentation, Inc. [1]. Since no data are available for the thermal conductivity of the paint, its influence is investigated using different values.

The thermal conductance of the stainless steel tube is of the order of 10^{-5} W K^{-1}. The maximum thermal conductance due to thermal radiation is estimated to be less than 10^{-7} W K^{-1}. The Nb-Ti leads of the GRTs and heaters from the cone to the heat sink are approximately 5 cm long with a diameter of 50 μm. The thermal conductance of the leads from the cone to the heat sink calculated using the thermal conductivity meas-

Nomenclature

B = electronic bandwidth, Hz
$\mathbf{C}$ = heat capacity matrix, J K^{-1}
c = specific heat, J K^{-1} g^{-1}
d = thickness, m
G = thermal conductance, W K^{-1}
$\mathbf{K}$ = thermal conductance matrix, W K^{-1}
k = thermal conductivity, W m^{-1} K^{-1}
k_B = Boltzmann constant $= 1.381 \times 10^{-23}$ J K^{-1}
I_b = bias current, A
NEP = noise equivalent power, W
$\dot{\mathbf{Q}}$ = heating power vector, W
$\dot{Q}$ = heating power, W
R = electrical resistance, Ω
r = coordinate, m
$\mathbf{T}$ = nodal temperature vector, K
$\dot{\mathbf{T}}$ = vector of the time derivative of nodal temperature, K s^{-1}
T = temperature of the receiver, K
T_0 = temperature of the heat sink, K
t = time, s
x = coordinate, m
λ = wavelength in vacuum, m
ρ = density, kg m^{-3}
τ = $1/e$ time constant, s

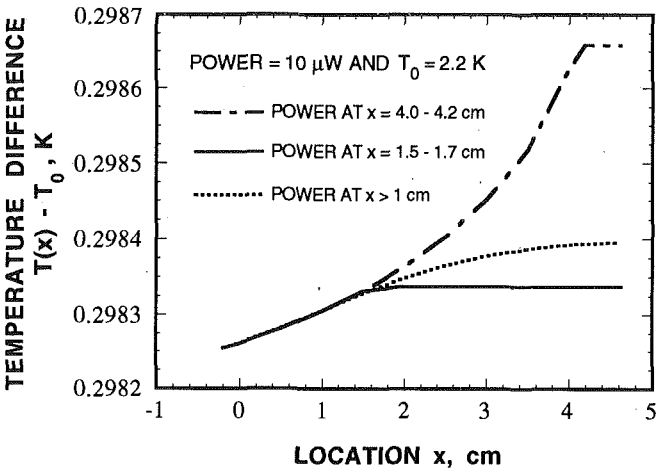

Fig. 3 Predicted temperature distribution along the receiver

ured by Flachbart et al. (1978) is less than 10^{-7} W K^{-1} at temperatures from 2 to 4 K. The radiometer operates in an ultrahigh vacuum system at a pressure less than 10^{-12} bar. The heat loss due to free-molecule thermal conduction of the residual gas, as calculated from Kennard's formula (Kennard, 1938) is less than 10^{-8} W K^{-1}. Hence, the heat transfer from the receiver to the heat sink is dominated by the thermal conduction along the stainless steel tube. This justifies the assumption of adiabatic boundary conditions.

The total mass of the GRTs, the heater wires, and the epoxy used to attach the GRTs and the wires is less than 10 percent of that of the copper cone, while the stainless steel tube possesses a heat capacity more than 10 times larger than that of the copper cone. Hence, the heat capacity of the system is dominated by the stainless steel tube and the heat capacities of the GRTs and peripheral items are negligible. It will be seen later that the time constant of the ACR is limited by the large heat capacity of the stainless steel tube.

Nonequivalence. A total of 382 nodes and 273 elements are used for the analysis of the ACR, with the largest dimension of the elements equal to 0.05 cm. For the steady-state case, the nodal temperatures are converged to within 0.5 μK between two consecutive iterations after six or seven iterations. The difference of the temperature solution from that obtained when the number of the elements is doubled is less than 1 μK. Since the heat transfer from the cone to the heat sink is through the stainless steel tube only, the temperature at the joint of the stainless steel and the copper can be calculated using the temperature-dependent thermal conductivity of the stainless steel. The agreement between the analytical solution and the finite element method is within 1 μK for a power of 10 μW and a heat sink temperature of 2.2 K.

Figure 3 shows the predicted temperature distribution along the cone for 10 μW input power when the heat sink temperature is 2.2 K. Three heating patterns are considered. Two cases account for the electrical heating from the outside of the Cu cone at locations x = 1.5–1.7 cm or x = 4.0–4.2 cm, respectively, by applying constant heating power at the nodes outside the Cu cone. In the third case, a uniform heat flux is applied on the inner surface of the black paint at $x > 1$ cm, corresponding to $r < 1.5$ cm, to simulate radiative heating. The nonuniform distribution of the absorbed radiant power on the cone is not considered because the three cases discussed here should provide an estimate of the largest nonequivalence. The temperature gradient across the cone is negligible, even though the thermal conductivity of the paint is assumed to be three orders of magnitude smaller than that of the copper. The responsivity of 30 K mW^{-1} calculated for 10 μW power and T_0 = 2.2 K agrees with the experimental value of 29.7 ($\pm$0.1) K mW^{-1} at approximately 2 K (Datla et al., 1992). The largest temperature difference for different heating patterns occurs near the apex of the cone, with a maximum of approximately 0.3 mK. If the GRT were mounted at the apex of the cone, a maximum nonequivalence of 0.1 percent would exist for different heating patterns. For the GRT at the middle, taking x = 2.5 cm, the nonequivalence between the two electrical heaters is 64 μK, which is comparable with the value of 100 ($\pm$50) μK measured by Datla et al. (1992). The nonequivalent power based on the present calculation is 0.02 percent. If the thermometer is placed near the base of the cone, nonequivalence due to the temperature gradient can essentially be eliminated. In the high-accuracy radiometer developed by Martin et al. (1985), a GRT was located close to the thermal impedance in order to reduce the nonequivalence.

Both the nonequivalent temperature and the temperature response increase with larger heating powers, but their ratio, i.e., the power nonequivalence, changes little. Hence, nonequivalence depends only slightly on the power level.

The effect of the thermal conductivity and boundary resistance between the black paint and the copper cone is investigated by changing the thermal conductivity of the paint. If k_{paint} is changed from 10^{-3} k_{Cu} to 10^{-5} k_{Cu}, the calculated temperature of the inner surface of paint will be higher than that of the copper cone by a maximum of 0.15 mK for 10 μW total heating power. Yet, the temperature along the copper cone does not vary with the change of thermal conductivity of the paint since the heat flux from the paint to the copper stays the same everywhere. Hence, nonequivalence caused by the temperature gradient across the paint is negligibly small.

In the analysis above, the boundary resistance between the copper and the stainless steel is neglected. The thermal contact resistance between two nominally flat surfaces could be significant due to surface roughness (Cooper et al., 1969). In the present radiometer, the cylindrical portion of the copper cone and the stainless steel tube are brazed in vacuum using a special silver-copper alloy. This process yields almost ideal surface contacts. The thickness of the solder is approximately 50 μm, and the overlapping width is 2 mm. The thermal boundary resistance between the copper and the stainless steel due to the surface roughness and the thermal resistance of the solder is negligibly small compared with the large thermal resistance along the thin stainless steel tube. Since the contact resistance has little impact on the total thermal impedance and the temperature gradient of the copper cone, the predictions of the responsivity and nonequivalence are valid even though a finite thermal resistance exists between the copper and the stainless steel.

As discussed by Foukal et al. (1990), Martin et al. (1985), and Mahan et al. (1987), one of the advantages of a cryogenic radiometer is the dramatic increase of the thermal diffusivity of the conducting material, such as copper, from room temperature to cryogenic temperatures. Another advantage is that an almost adiabatic boundary condition can be achieved on the surface of the receiver since convective and radiative heat losses are negligibly small. This reduces substantially the nonequivalence between radiative and electrical heating. The use of superconducting wires eliminates the error caused by Joule heating of the leads. The instrumental correction analyzed by Hengstberger (1989) for absolute radiometers operating at room temperature will be drastically reduced for cryogenic radiometers if the thermometer is mounted close to the thermal impedance.

The absorptance of the receiver directly affects the accuracy of absolute radiometers. The absorptance of the receiving cone is determined by its geometry and the radiative properties of the paint. The specular reflectance of the Aeroglaze Z302 paint, measured at room temperature, is less than 10.5 percent for 0.3 μm $< \lambda <$ 40 μm (Datla et al., 1992) and the diffuse reflectance is less than 1 percent in the visible spectral region

(Martin et al., 1985). The effective absorptance of the ACR receiving cone measured at $\lambda = 632.8$ nm using an integrating sphere is 99.87 percent with an uncertainty of 0.1 percent (Ebner et al., 1989).

One can estimate the absorptance of the cone if the specular and diffuse reflectances are assumed to be independent of the angles of incidence. For radiation nearly parallel to the axis of the cone, if the specular reflectance of the paint is 10 percent, only 0.01 percent of the incident radiant power will leave the cone after the fourth reflection. If the diffuse reflectance is 1 percent, approximately 0.25 percent of the incident radiant power will be directly reflected back through the opening of the cone. To achieve an effective absorptance of 99.9 percent with the present geometry, the diffuse reflectance of the paint must be less than 0.4 percent. It is important to determine the directional-spectral reflectance of the paint at cryogenic temperatures in order to predict the spectral absorptance of the cone accurately at operating temperatures.

Dynamic Response and Noise Analysis. In the transient modeling of the ACR, a convergence criterion of 10 μK is used. Different integration time steps are compared, and the temperature solutions agree within 1 percent between a time step of 0.05 s and 0.02 s. Since the temperature changes almost exponentially with time, the time step is taken to be 0.05 s for the first 20 s after the input power is changed and 0.25 s for later times. A 50 percent rise-time of 18 s is obtained using a 10 μW step input. This agrees with the experimental value of 18.4 ($\pm$0.1) s obtained using a pulse of 10 μW heater power (Datla et al., 1992). The calculated $1/e$ time constant by assuming an exponential increase is $\tau = 26$ s. The heat capacity of the cone is relatively small compared with that of the stainless steel tube. If the product of the density and specific heat, ρc, of the material used for the thermal impedance is assumed to be 1000 times smaller than the value of stainless steel, the time constant τ would be as small as 5 s. Another way to improve the dynamic response of the ACR would be to modify the geometry of the thermal impedance. For example, the stainless steel tube could be replaced by several narrow strips, as suggested by Mahan et al. (1987). If both the cross-sectional area and the length of the stainless steel tube could be reduced to one-third of their present values, the heat capacity of the stainless steel would be reduced by a factor of nine, while the thermal conductance would be the same.

Since the ACR is a thermal detector that utilizes the change of electrical resistance to determine a temperature variation, the inherent noises are the phonon noise and the Johnson noise (Low, 1961). Taking the heat sink temperature $T_0 = 2.2$ K, the resistance of the germanium thermometer $R = 12000\ \Omega$, $dR/dT = -12{,}000\ \Omega\ \mathrm{K}^{-1}$, the bias current $I_b = 1\ \mu$A, the thermal conductance $G = 3.3 \times 10^{-5}\ \mathrm{W\,K}^{-1}$, and the electronic bandwidth $B = 1$ Hz, the noise equivalent power of the phonon noise is

$$\mathrm{NEP}_{\mathrm{phonon}} = (4k_B G T_0^2 B)^{1/2} = 9.4 \times 10^{-14}\ \mathrm{W} \qquad (2)$$

and that of the Johnson noise is

$$\mathrm{NEP}_{\mathrm{Johnson}} = \frac{(4k_B R T_0 B)^{1/2}}{I_b |dR/dT| (1/G)} = 3.3 \times 10^{-12}\ \mathrm{W} \qquad (3)$$

The background noise associated with a 20 K blackbody is negligibly small. The ACR works in the active mode. The temperature of the heat sink is stabilized by a controller through the heater on the heat sink. A digital servo system actively controls the temperature of the receiver by adjusting the power of the receiver heater. The peak-to-peak temperature variation of both the receiver and the heat sink is approximately 5 μK. The root-mean-square fluctuation of the electrical power of the receiver heater is approximately 0.2 nW. This NEP of 0.2 nW is much larger than the phonon noise or the Johnson noise. Hence, the sensitivity of the ACR is limited by the thermal instability of the receiver and the noise associated with the electronic control system.

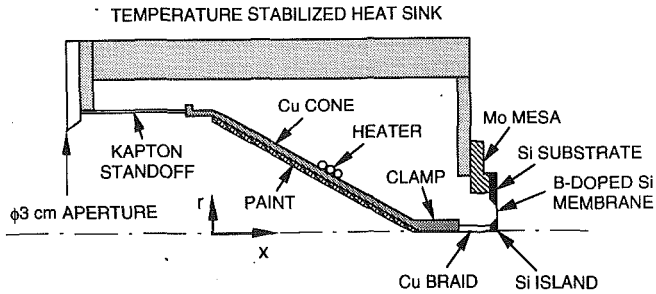

Fig. 4 Superconducting kinetic-inductance absolute cryogenic radiometer (not to scale)

At a radiant power of 20 nW, the 0.2 nW NEP of the ACR yields a random component to the uncertainty of 1 percent. When the power exceeds 200 nW, the uncertainty of 0.1 percent due to the random noise is comparable with the combined systematic uncertainty of 0.12 percent (Datla et al., 1992), and the uncertainty of the receiver absorptance of 0.1 percent becomes the largest error source.

The dynamic range of the ACR is limited by the critical temperature of the superconducting Nb–Ti leads, which is approximately 9 K. Both the temperature responsivity of the cone (dT/dQ) and the resistance responsivity of the GRT (dR/dT) decrease with increasing temperature. The receiver will be at approximately 4.5 K for a heating power of 100 μW. This power is chosen in practice as the upper bound of the ACR for the measurement of radiant power.

Superconducting Kinetic-Inductance Absolute Cryogenic Radiometer (SKACR)

Figure 4 shows half of the cross section of the SKACR to be installed in the LBIR facility (Sauvageau et al., 1991). The heat flow from the cone to the heat sink is mainly through a 9-μm-thick boron-doped-silicon membrane. The width of the membrane from the Si island to the Si substrate is 400 μm. The temperature sensing element is a bridge device consisting of four niobium microstripline inductors on a 1 cm^2 Si chip, two on the Si island and the other two on the Si substrate. The silicon island is thermally linked to the cone by a Cu wire braid and a clamp. The inductance of the superconducting microstripline is a function of temperature. The temperature difference between the island and the substrate yields an imbalance current in the bridge, which is determined by using a DC SQUID galvanometer. Details of the device fabrication and mechanism were discussed by Sauvageau et al. (1991) and McDonald (1987).

The Kapton standoff is a thin tube, 3.8 cm in diameter, 3 cm long, and 25 μm thick. The height of the 50-μm-thick copper cone is approximately 4.6 cm. The apex angle of the cone is 45 deg. The Cu braid from the apex of the cone to the Si island is 1 cm long with an effective cross-sectional area of 1.4×10^{-3} cm^2. In the present model, the clamp at the apex of the cone is taken to be cylindrical for simplicity. The thickness of the Si chip is approximately 200 μm. The Si island and substrate are modeled as axially symmetric, while they are actually concentric squares in the SKACR. The diameter of the silicon chip is assumed to be 1 cm and the diameter of the Si island is taken to be 0.24 cm on the side with membrane and 0.20 cm on the other side of the chip. The Kapton standoff and the Cu braid are modeled with axially symmetric line elements. The Mo mesa is essentially at the same temperature as that of the heat sink. As with the ACR, the thickness of the black paint has almost no effect on the steady-state analysis since most of the

Table 1 Temperature (in K) distribution at the receiver of the superconducting kinetic-inductance radiometer with 10 μW heating power loaded at different positions, where the heat sink temperature T_0 is 4 K

	Cu CONE $x = 0$	Cu CONE $x = 2.3$ cm	Cu CONE $x = 4.0$ cm	Si ISLAND
HEATING POWER AT $x = 1.5 - 1.7$ cm	4.196452	4.196380	4.195976	4.193204
HEATING POWER AT $x = 4.0 - 4.2$ cm	4.195918	4.195919	4.195923	4.193209
TEMPERATURE DIFFERENCE	0.000534	0.000461	0.000053	- 0.000005

heat is conducted along the Cu layer. The dynamic response of the SKACR is modeled for different paint thicknesses. The heat conduction by the Nb–Ti leads is negligible as discussed in the previous section. The boundary resistance between the Cu braid and the Si island is estimated to be 10^{-3} W K^{-1} (Sauvageau et al., 1991), which is taken into account by using an effective cross-sectional area of the Cu braid.

The thermophysical properties of Mo and crystalline Si are from Touloukian and Buyco (1970), Touloukian et al. (1970), and Jensen et al. (1980). The thermophysical properties of Kapton are from Schramm et al. (1973), where the data of thermal conductivity for temperatures up to 4.5 K are extrapolated linearly, viz., $k_{\text{Kapton}}(T) = 1.3 \times 10^{-3} \times T$ W m^{-1} K^{-1}. Sauvageau et al. (1991) determined that the effective thermal conductivity of the Si membrane is given by $k_{\text{membrane}}(T) = 1.54 \times 10^{-2} \times T^2$ W m^{-1} K^{-1}. The specific heat and density of the Si membrane are assumed to be the same as those of Si crystal.

A total of 278 elements and 410 nodes are used for the computation of the steady-state temperature distribution, and an initial time step of 0.05 s is used for the dynamic analysis. The maximum error in the temperature distribution due to the element size is less than 1 μK, and that due to the time step is less than 1 percent.

Table 1 lists the computed temperatures of the Cu cone and the Si island for a 10 μW heating power at x = 1.5–1.7 cm and x = 4.0–4.2 cm, respectively, where the heat sink is at 4 K. The calculated temperature responsivity is approximately 20 K mW^{-1}. The temperature difference between the two cases is also listed in Table 1. The difference at the base of the cone is as large as 0.5 mK, while that at the Si island is only 5 μK. Hence, the power nonequivalence is less than 0.003 percent. The 5 μK temperature difference at the Si island is due to the fact that the Kapton standoff is not a perfect insulator. About 1 percent of the heat is conducted through the Kapton standoff.

Figure 5 shows the dynamic temperature response of the SKACR to a 10 μW step power at T_0 = 4 K for paint thicknesses, d_{paint}, of 0, 50, and 100 μm. The position of the power input does not affect the calculated temperatures at the Si island since the convergence criterion of 10 μK used for the transient analysis is larger than the temperature difference caused by different heating positions. The corresponding $1/e$ time constants are computed to be 5.3, 7.7, and 10.1 s. These are in agreement with those calculated from the ratio of the total heat capacity of the receiver to the thermal conductance of the Si membrane. The time constant resulting from experiments is 11 ($\pm$0.5) s at 4 K, indicating that the thickness of the paint is close to 100 μm. The total thermal mass of the heater wire is less than 1 percent of that of the Cu cone. Therefore, neglecting the heat capacity of the heater wire does not introduce a significant error in the predicted time constant. The epoxy used to attach the heater wire and leads to the Cu cone may increase the total heat capacity by several percent. The time

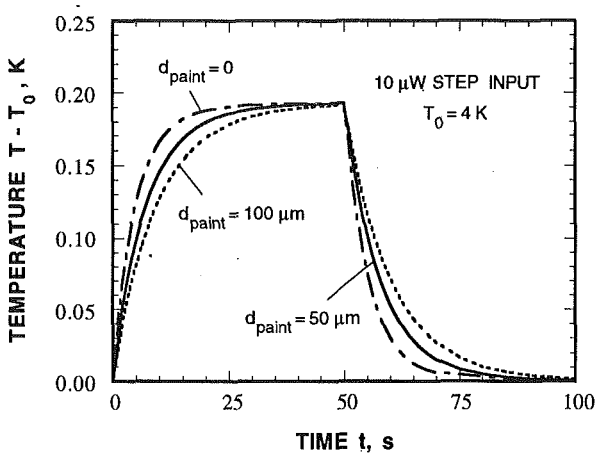

Fig. 5 Dynamic response of the SKACR to a step power input

constant of the SKACR can be reduced by decreasing the thickness of the paint. The thickness of the paint, however, must be much larger than the radiation penetration depth in order to achieve near-unity absorptance of the cone. The penetration depth of the paint could be determined from the transmittance of the paint on a transparent substrate, such as silicon in the infrared or quartz in the visible.

Summary and Conclusions

This work, for the first time, performs a comprehensive thermal analysis of two highly sensitive cryogenic radiometers with the aid of a finite-element-analysis program. It helps the future development of absolute cryogenic radiometers and the realization of spectral irradiance standards in the mid-infrared. The conclusions and recommendations based on this study are given as follows:

The nonequivalence due to different heating patterns is shown to be 0.02 percent in the GRT-based ACR and can be reduced if the temperature sensor is placed closer to the thermal impedance. The power nonequivalence of the SKACR is less than 0.003 percent.

In order to reduce the time constant of the GRT-based ACR, the thermal impedance should be implemented with a different geometry or material of smaller heat capacity. The dynamic response of the SKACR could be improved by reducing the thickness of the black paint.

It is random noise that limits the ultimate sensitivity of the absolute cryogenic radiometers. For large incident powers, the uncertainty in the determination of the absorptance of the receiver cone becomes the dominant error source. The diffuse reflectance of the paint strongly affects the absorptance of the cone. For the present receiver geometry, a diffuse reflectance of less than 0.4 percent is required to achieve an effective absorptance of 99.9 percent.

The directional-spectral reflectance of the black paint should be measured at cryogenic temperatures in order to predict the absorptance of the cone. The wavelength-dependent absorptance of the receiver should be characterized for the high-accuracy spectral calibration equipment to be installed in the LBIR facility. Methods to reduce the noise associated with the electronic feedback system and that due to the thermal instability should be further investigated.

Acknowledgments

The authors are grateful to Dr. D. G. McDonald of NIST/Boulder and C. C. Hoyt of the Cambridge Research and Instrumentation, Inc., for providing information related to the radiometers. We would like to thank Prof. J. R. Mahan of the Virginia Polytechnic Institute and State University for mak-

ing several unpublished theses of his students available to us. Helpful discussions with Dr. C. L. Cromer, Dr. B. C. Johnson, Dr. J. E. Hardis, Dr. M. L. Reilly, and Dr. V. I. Sapritsky of NIST, Prof. H. D. Drew of the University of Maryland, and Prof. B. B. Mikic and Prof. J. L. Smith of MIT are also acknowledged. The official reviewers' comments are much appreciated.

References

Note: References made in this paper to particular brand names or specific suppliers are for the ease of understanding by the reader and do not constitute an endorsement of products or services by the National Institute of Standards and Technology over other competitive suppliers of similar products or services, which may be equally or better suited for the purpose.

1 Cambridge Research and Instrumentation, Inc., 21 Erie Street, Cambridge, MA 02139.

2 Lord Corporation, Industrial Coatings Division, 2000 W. Grandview Blvd., Erie, PA 16514.

3 Swanson Analysis Systems, Inc., Johnson Road, P.O. Box 65, Houston, PA 15342.

4 Sun Microsystems, Inc., 2550 Garcia Avenue, Mountain View, CA 94043.

Cooper, M. G., Mikic, B. B., and Yovanovich, M. M., 1969, "Thermal Contact Conductance," *Int. J. Heat Mass Transfer*, Vol. 12, pp. 279–300.

Datla, R. U., Stock, K., Parr, A. C., Hoyt, C. C., Miller, P. J., and Foukal, P. V., 1992, "Characterization of an Absolute Cryogenic Radiometer (ACR) as a Standard Detector for Radiant Power Measurements," *Appl. Opt.*, Vol. 31, pp. 7219–7225.

Ebner, S. C., Parr, A. C., and Hoyt, C. C., 1989, "Update on the Low Background IR Calibration Facility at the National Institute of Standards and Technology," in: *Imaging Infrared: Scene Simulations, Modeling, and Real Image Tracking*, A. J. Huber, M. J. Triplett, and J. R. Wolverton, eds., Proc. SPIE-Vol. 1110, pp. 49–60.

Flachbart, K., Feher, A., Janos, S., Malek, Z., and Ryska, A., 1978, "Thermal Conductivity of Nb–Ti Alloy in the Low-Temperature Range," *Phys. Stat. Sol. B*, Vol. 85, pp. 545–551.

Foukal, P. V., Hoyt, C., Kochling, H., and Miller, P., 1990, "Cryogenic Absolute Radiometers as Laboratory Irradiance Standards, Remote Sensing Detectors, and Pyroheliometers," *Appl. Opt.*, Vol. 29, pp. 988–993.

Frölich, C., 1991, "History of Solar Radiometry and the World Radiometric Reference," *Metrologia*, Vol. 28, pp. 111–115.

Hengstberger, F., 1989, "Instrumental Corrections in Absolute Radiometers," in: *Absolute Radiometry: Electrical Calibrated Thermal Detectors of Optical Radiation*, F. Hengstberger, ed., Academic Press, Boston, MA, Chap. 6, pp. 193–233.

Jensen, J. E., Tuttle, W. A., Stewart, R. B., Brechna, H., and Prodell, A. G., eds., 1980, *Brookhaven National Laboratory Selected Cryogenic Data Notebook*, Vols. 1 and 2, Brookhaven National Lab., Upton, NY, Sections 7, 8, and 14.

Kennard, E. H., 1938, *Kinetic Theory of Gases*, McGraw-Hill, New York, Chap. 8.

Low, F. J., 1961, "Low-Temperature Germanium Bolometer," *J. Opt. Soc. Am.*, Vol. 51, pp. 1300–1304.

McDonald, D. G., 1987, "Novel Superconducting Thermometer for Bolometric Applications," *Appl. Phys. Lett.*, Vol. 50, pp. 775–777.

Mahan, J. R., Kowsary, F., Tira, N., and Gardiner, B. D., 1987, "Transient Conduction-Radiation Analysis of an Absolute Active Cavity Radiometer Using Finite Elements," in: *International Symposium on Thermal Problems in Space-Based Systems*, F. Dobran and M. Imber, eds., ASME HTD-Vol. 83, New York, pp. 39–47.

Mahan, J. R., Tira, N. E., Lee, R. B., and Keynton, R. J., 1989, "Comparison of the Measured and Predicted Response of the Earth Radiation Budget Experiment Active Cavity Radiometer During Solar Observations," *Appl. Opt.*, Vol. 28, pp. 1327–1337.

Martin, J. E., Fox, N. P., and Key, P. J., 1985, "A Cryogenic Radiometer for Absolute Radiometric Measurements," *Metrologia*, Vol. 21, pp. 147–155.

Quinn, T. J., and Martin, J. E., 1985, "A Radiometric Determination of the Stefan–Boltzmann Constant and Thermodynamic Temperatures Between −40°C and +100°C," *Phil. Trans. R. Soc. Lond. A*, Vol. 316, pp. 85–189.

Reddy, J. N., 1984, *An Introduction to Finite Element Method*, McGraw-Hill, New York, Chaps. 2, 3, and 4.

Sauvageau, J. E., McDonald, D. G., and Grossman, E. N., 1991, "Superconducting Kinetic Inductance Radiometer," *IEEE Trans. Magn.*, Vol. 27, pp. 2757–2760.

Schramm, R. E., Clark, A. F., and Reed, R. P., 1973, *A Compilation and Evaluation of Mechanical, Thermal, and Electrical Properties of Selected Polymers*, NBS Monograph, No. 132, U.S. Department of Commerce, pp. 643–692.

Shih, T. M., 1984, *Numerical Heat Transfer*, Hemisphere, Washington, DC, Chap. 5.

Touloukian, Y. S., Powell, R. W., Ho, C. Y., and Klemens, P. G., 1970, "Thermal Conductivity: Metallic Elements and Alloys," in: *Thermophysical Properties of Matter*, Y. S. Touloukian and C. Y. Ho, eds., Vol. 1, IFI/Plenum, New York.

Touloukian, Y. S., and Buyco, E. H., 1970, "Specific Heat: Metallic Elements and Alloys," in: *Thermophysical Properties of Matter*, Y. S. Touloukian and C. Y. Ho, eds., Vol. 4, IFI/Plenum, New York.

Zhang, Z. M., Ge, X. S., and Wang, Y. F., 1987, "A Novel Pyrheliometer of High Accuracy," *Solar Energy*, Vol. 39, pp. 371–377.

Leidenfrost Evaporation of Liquid Nitrogen Droplets

S. Chandra
Assistant Professor.

S. D. Aziz
Research Assistant.

Department of Mechanical Engineering,
University of Toronto,
Toronto, Ontario M5S 1A4 Canada

The evaporation of a single droplet of liquid nitrogen, levitated during film boiling above a solid, impervious surface, was studied experimentally. The droplet initial diameter (1.9 mm), surface temperature (~20°C), ambient temperature (~20°C), and ambient pressure (~0.1 MPa) were held constant. The principal parameters varied were the surface material (copper or glass), and roughness (0.35 to 50 μm). Measurements were made of the droplet diameter evolution and the surface temperature variation during droplet impact. Predictions from existing models of droplets in Leidenfrost evaporation agree well with measurements of the droplet evaporation rate. The droplet lifetime was found to be slightly longer on the glass surface than it was on the copper surface, corresponding to the greater cooling of the glass surface during droplet impact. The droplet evaporation rate was unchanged by small increases in surface roughness. However, ridges on the surface with a height of the same magnitude as the thickness of the vapor film under the drop caused vapor bubble nucleation in the droplet, and significantly reduced the droplet evaporation time.

Introduction

When a drop of liquid comes in contact with a solid surface that is at a temperature higher than the boiling point of the liquid, it begins to evaporate rapidly. If the temperature of the surface is sufficiently high (i.e., above the so-called "Leidenfrost temperature") the pressure of vapor escaping from below the drop is enough to levitate the drop. It then floats above the surface on a thin film of its own vapor, in a state of film boiling known as Leidenfrost evaporation (Gottfried et al., 1966). Heat transfer to the drop from the surface occurs by conduction across this insulating vapor layer, and is much less than it would be in the case of direct liquid–solid contact.

A surface at room temperature is sufficiently hot to support the film boiling of a droplet of a cryogenic liquid such as liquid nitrogen, which has a Leidenfrost temperature of about 90 K (Keshock, 1968). Consequently, a study of film boiling is of relevance to the production, storage, and handling of cryogenic liquids, during which liquid–solid contact may occur. Gaseous fuels such as hydrogen and natural gas are frequently stored in the form of a cryogenic liquid. In the event of a spill, extended liquid masses break up into smaller droplets, which go into film boiling. To estimate the fire hazard posed it is necessary to know the concentration of fuel in the air, which is governed by the evaporation rate of the droplets. A study of droplet-wall heat transfer is also important to applications such as: the design of cryogenic heat exchangers and pipelines, through which a mist of droplets is carried along by a stream of gas; the cooling of surfaces using a liquid nitrogen spray; and the direct injection of liquefied fuel sprays into a combustor.

Previous investigators have measured the total evaporation time of extended masses (initial volume 0.161 ml to 10.55 ml) of liquid nitrogen on a smooth metal surface (Keshock, 1968; Keshock and Bell, 1970). Experimentally measured evaporation times were much shorter than those predicted by theory (Baumeister et al., 1971); the discrepancy was attributed to contamination by ice crystals formed by condensation of atmospheric moisture. Empirical corrections had to be made to the observed evaporation times to account for the presence of ice (Schoessow et al., 1978). Awonorin and Lamb (1990) studied the evaporation of liquid nitrogen droplets placed on a gelatin slab, and developed an empirical correlation to predict the droplet lifetime. The evaporation rate of smaller droplets (initial volume 7.8 μl to 14.2 μl) of liquid nitrogen on a copper surface was measured by Mikhaylov et al. (1975). The measured evaporation times in both cases were less than those predicted by analytical models.

This work was undertaken to study experimentally the evaporation of a single droplet of liquid nitrogen placed on a solid surface. Of interest were small diameter droplets, representative of sizes found in liquid nitrogen sprays. The information to be obtained was: the rate of droplet evaporation, from which droplet-wall heat transfer coefficients can be calculated; the effect of surface thermal properties, which may influence the evaporation rate; and the effect of surface roughness, which can disrupt film boiling. In contrast to previous experiments, where ice contamination may have occurred, the atmosphere surrounding the droplets was strictly controlled so as to eliminate any moisture. No empirical corrections were therefore required in comparing the results with theory.

Measurements were made of the droplet diameter evolution during evaporation. The variation in surface temperature was recorded during the impact and evaporation of a droplet on the surface. Surfaces of two different materials were used: glass, which has a low thermal conductivity, and copper, with a high conductivity. Copper surfaces with several different surface roughness values were used, ranging from 0.35 μm to 50 μm. The following parameters were held constant during the experiments: initial droplet diameter (1.9±0.1 mm, corresponding to a volume of 4.2 μl); ambient temperature (~20°C); initial surface temperature (equal to the ambient temperature ~20°C); and ambient pressure (~0.10 MPa).

Experimental

Figure 1 shows a schematic of the apparatus used to form a droplet of liquid nitrogen, deposit it on the test surface, and record the evaporation. An acrylic desiccator, 0.3 m × 0.3 m × 0.3 m in size, was used as an enclosure in which a moisture-free atmosphere could be maintained. The desiccator was evacuated using a vacuum pump at the start of the experiment,

Contributed by the Heat Transfer Division for publication in the JOURNAL OF HEAT TRANSFER. Manuscript received by the Heat Transfer Division April 1993; revision received October 1993. Keywords: Cryogenics, Phase-Change Phenomena, Sprays/Droplets. Associate Technical Editor: L. C. Witte.

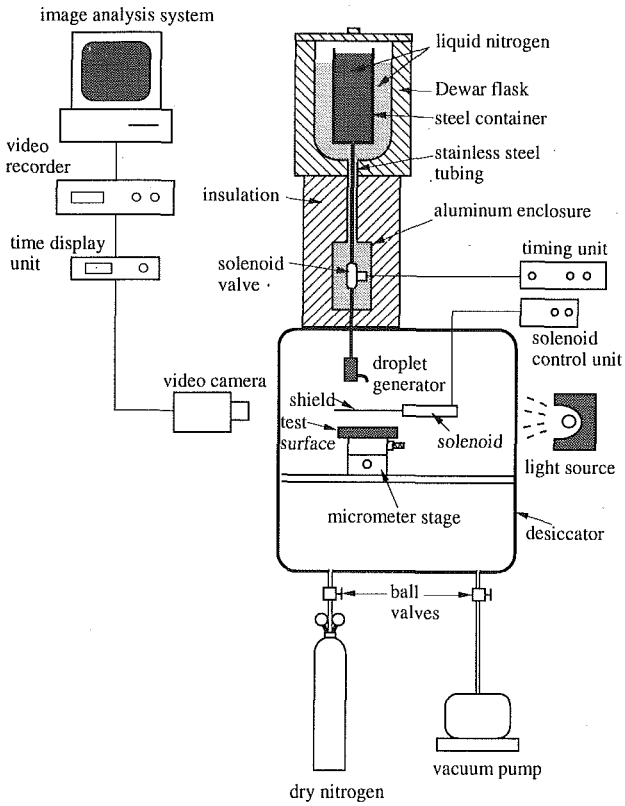

Fig. 1 Schematic of the apparatus

and then filled with dry nitrogen (Matheson Gas Products) from a cylinder. A slight flow of gas was maintained during the experiment to sustain a small positive pressure in the desiccator, preventing any leakage of atmospheric moisture into it.

Conventional methods of forming a droplet by forcing liquid through a hypodermic needle and letting it detach under its own weight have proved unsuccessful with liquid nitrogen (Keshock, 1968). Nitrogen has a low latent heat of vaporization: The liquid boils as soon as it contacts the exposed tip of the needle and is expelled. The droplet generator used in our experiments is shown in Fig. 1. Liquid nitrogen was stored in a cylindrical steel container, and supplied by gravity feed through a stainless steel tube attached to the bottom of the container. A solenoid valve (Asco 8263A240LT) regulated the flow of liquid, with the opening of the valve controlled by a timing unit. The container, tubing, and solenoid valve were all immersed in liquid nitrogen, preventing any boiling inside the tube that would result in liquid being ejected. Silicone rubber insulation was wrapped around the entire assembly. A cylindrical teflon container was attached to the end of the tube, after it entered the test enclosure (Fig. 2). A short length of stainless steel tubing, bent at right angles, was inserted into an opening in the side of the container. The end of this tube was blocked with solder, and a hole drilled through the tube wall at the bend. To generate a droplet, the solenoid valve was opened so that liquid nitrogen filled the teflon container and the side tube. Once the tubes walls cooled, the liquid overflowed through the hole onto the outer surface of the tube, accumulated at the soldered tip, and detached under its own weight so that droplets started to fall at a steady rate. The shield covering the test surface was then moved aside for a time long enough to permit a single drop to fall onto the surface. Using this method, droplets with a diameter of 1.9 ± 0.1 mm were formed. The droplets were released from a height of 27 mm above the surface, so that the impact Weber number ($We = \rho_l U^2 d/\sigma$) was 90, low enough that the droplets did not shatter upon impact.

The test surface was made slightly concave, to prevent droplets rolling off the edges. For the glass surface, a 50.8-mm-dia plano-concave lens was used, with a thickness of 3.5 mm at the edge and 2.5 mm at the center. The copper surface was 50.8 mm in diameter and 6.35 mm thick at the edges, with a 1.5 deg incline machined from the edge to the center. The surface was polished with 600 grit emery cloth, giving a surface with average roughness (R_a, defined as the arithmetic average deviation of surface irregularities from a hypothetical perfect surface (Baumeister et al., 1978)) of 0.35 μm. To examine the effect of surface finish on droplet evaporation, the roughness of the copper surface was increased by polishing it with either 220 or 80 grit emery cloth, producing surface roughnesses of 0.8 μm and 1.7 μm, respectively. To obtain test surfaces with even greater roughness, concentric ridges, spaced 0.25 mm apart, were machined on the copper surface. Two such serrated surfaces were made, with ridges with heights of 25 μm and 50 μm, respectively.

The evaporation of a droplet placed on a surface was recorded using a Pulnix TM745 video camera, equipped with a Nikon 105 mm macro lens. A slide projector was used as a light source to provide direct back lighting, so that the droplet appeared as a black silhouette with sharply defined edges. The

Nomenclature

A = area for heat transfer from surface to droplet
a = horizontal droplet axis
A_f = frontal cross-sectional area of the droplet
B = transfer number
b = vertical droplet axis
C = specific heat
d = equivalent droplet diameter
g = acceleration due to gravity
h = coefficient of heat transfer from surface to droplet
k = thermal conductivity
P = pressure
q_{cond} = conduction heat flux into droplet
q_{rad} = radiation heat flux into droplet
q_{surf} = heat flux from surface to droplet
r = radial coordinate
r_0 = radius of the flattened bottom of the droplet
r_{max} = maximum radius of the bottom of the droplet
R_a = average surface roughness
S = Stefan–Boltzmann constant
t = time
T = temperature
ΔT = $T_s - T_l$
U = droplet impact velocity
V = droplet volume
w = velocity of the vapor leaving the bottom of the droplet
We = Weber number $= \rho_l U^2 d/\sigma$
α = thermal diffusivity
β = $(k\rho C)^{1/2}$
δ = vapor film thickness
ϵ = emissivity
λ = latent heat of vaporization
λ' = defined in Eq. (9)
μ = viscosity
ρ = density
σ = surface tension

Subscripts

i = initial
l = liquid
s = surface
v = vapor
∞ = ambient

Superscripts

$*$ = dimensionless variable

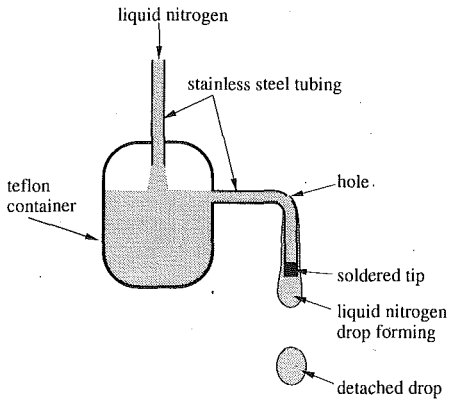

Fig. 2 Detail of droplet generator

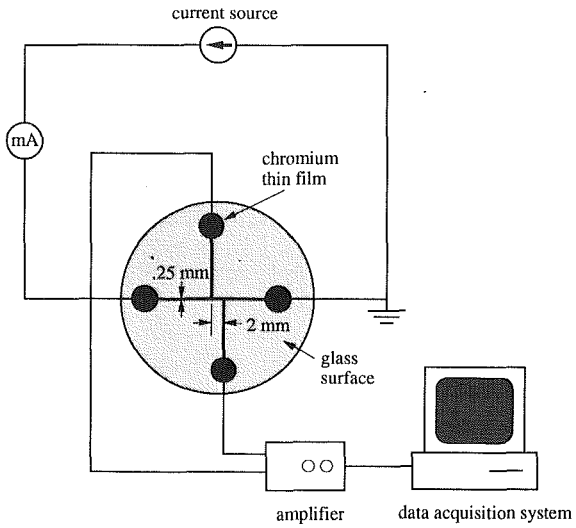

Fig. 3 Thin film temperature sensor

video camera had an electronic shutter, which allowed the exposure time of each frame to be reduced to 0.1 ms, sufficient to prevent any blurring of the image due to droplet motion. A For.A VTG-33 video timer unit was used to add a time display with a resolution of 0.01 s to the video image before it was recorded on a Mitsubishi HSU80 video recorder.

Droplet evaporation was also photographed using a 35 mm camera (Nikon F3) driven by a motor drive (Nikon MD4) at a rate of up to 6 frames per second. A slide projector was used to provide back lighting. To eliminate light reflections within the drop, and allow phenomena such as bubble formation in the liquid to be seen, an opal glass diffuser (Ealing 26-6528) was placed 25 mm behind the droplet. Kodak TMAX 400 ASA film was used to photograph droplets on a glass surface. The rough copper surfaces had a very low reflectivity, reducing the light available for photography: TMAX 3200 ASA film was therefore used instead.

Droplet dimensions were measured from video images using a computer-based image analysis system. Each video image was transferred to a Macintosh IIci computer through a Data Translation Quick Capture video board. The droplets were not perfectly spherical, but exhibited a slight flattening under their own weight as they rested on the surface. An equivalent diameter (d) was therefore defined as (Avedisian and Fatehi, 1988):

$$d = 2(A_f/\pi)^{1/2} \tag{1}$$

in which A_f was the frontal cross-sectional area of the droplet, measured using the Image Analyst software package (Automatix Inc.); a scale factor was obtained from an image of a 3-mm-dia. stainless steel ball-bearing. The uncertainty in the diameter measurement, corresponding to the size of one pixel of the video image, was ± 0.04 mm. Alternate definitions of the equivalent diameter, such as $d = (a^2b)^{1/3}$ where a and b were the horizontal and vertical droplet axes (Chandra and Avedisian, 1988), yielded values that differed from Eq. (1) by less than 3 percent.

The change in surface temperature was measured for both glass and copper surfaces during the impact of a liquid nitrogen droplet. The temperature of a flat glass surface was measured using a thin film sensor (Fig. 3), fabricated by sputtering a 0.5-μm-thick layer of chromium through a stainless steel mask. Chromium adhered strongly to glass; a stable film was made by sputtering approximately 0.01 μm of chromium oxide on the glass and then depositing pure chromium over that. A constant 1 mA current was passed through the thin film, and the voltage drop across the center 2 mm length amplified and recorded using a MacAdios II data acquisition board (GW Instruments). Details of the current source and amplifier have been given earlier (Chandra, 1990). To calibrate the temperature sensor the test surface was placed on an ice block, the two separated by layers of insulating cloth; the surface temperature was varied by changing the insulation thickness. The voltage drop was recorded at different temperatures, as measured by two chromel-alumel thermocouples taped to the surface on either side of the thin film sensor.

The temperature of a copper surface was measured using a chromel–alumel thermocouple made from 0.127-mm-dia teflon insulated wire, which was inserted into a small hole drilled vertically through the center of the surface. The hole was filled with solder, and the surface polished with emery cloth so as to leave the bare thermocouple bead exposed. The thermocouple reference junction was kept in an ice bath, with the output amplified with a gain of 1000 and recorded using the data acquisition system. The measured temperatures were estimated to be accurate to within ±0.5°C. Surface temperature changes as small as 0.05°C could be resolved, however, using the 12 bit data acquisition board. Temperature measurements were done for both flat and concave surfaces. The droplet rolled off the flat surface after impact, whereas it remained at the center of the concave surface and evaporated, so that the surface temperature variation during the entire droplet lifetime could be measured.

Results and Discussion

The evaporation of a single droplet on a glass surface is shown in a sequence of photographs in Fig. 4. The first photograph (labeled $t = 0$ s) was taken approximately 0.5 s after impact, once the droplet was in a state of stable film boiling and no longer rolling on the surface; subsequent photographs were taken at 2 s intervals. The shape of the droplet initially alternated between being spherical ($t = 0$ s) and flattened ($t = 20$ s), as the droplet oscillated. Eventually, as the droplet grew smaller, it became almost perfectly spherical ($t \geq 6$ s).

The variation in shape presents a problem in formulating models of droplets in Leidenfrost evaporation, since some assumption has to be made as to the shape of the droplet. Two approaches have been used: either the droplet is assumed to have a flat bottom (Gottfried and Bell, 1966; Baumeister et al., 1966; Wachters et al., 1966), with the vapor flow between the droplet and the surface represented by flow between two parallel plates, or else the droplet is be assumed to be perfectly spherical (Nguyen and Avedisian, 1987; Zhang and Gogos, 1991). The choice of geometry has significant consequences: flat plate models predict that as the droplet evaporates the thickness of the vapor film (δ) between the droplet and surface decreases; models based on a spherical droplet predict that δ *increases* as the droplet grows smaller.

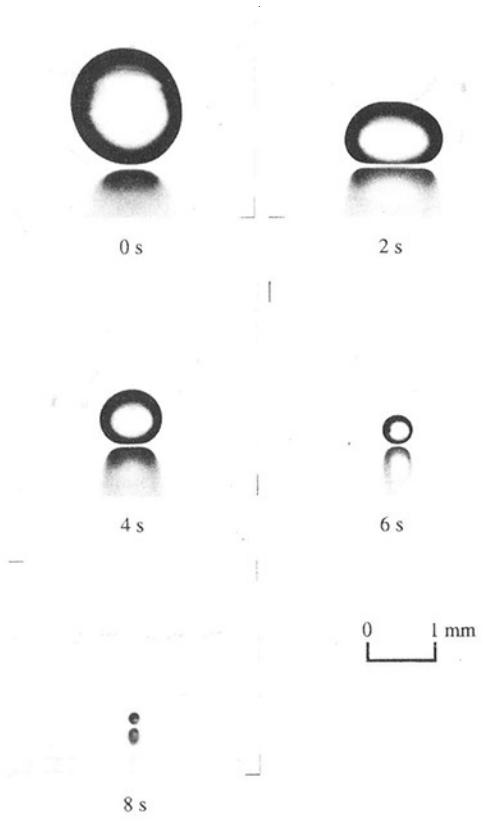

Fig. 4 Leidenfrost evaporation of a liquid nitrogen droplet on a glass surface

The vapor gap between the droplet and the surface can be seen clearly in Fig. 4. The gap thickness was measured at the closest spacing between the droplet and surface from enlarged video images: the results are shown in Fig. 5 for a droplet evaporating on a glass surface. The error bars represent the resolution of the measurement. This measurement, though crude, does show that δ decreases as the droplet grows smaller. A simple analytical expression for the magnitude of the vapor gap thickness (based on a flat plate model) is given by Gottfried and Bell (1966):

$$\delta = \left(\frac{9\ \mu_v\ k_v\ \Delta T}{8\ \rho_v\ \rho_l\ \lambda\ g}\right)^{1/4} \left(\frac{3\ V}{4\ \pi}\right)^{1/12} \tag{2}$$

The variation of δ calculated form Eq. (2) is shown by the solid line in Fig. 5. The evolution of droplet volume used for the calculation was measured from video images. The predictions appear to be qualitatively similar to the experimental measurements, insofar as δ decreases with time. Values of δ calculated from alternate flat plate models (e.g., Baumeister et al., 1966) are similar to those obtained from Eq. (2).

Results from models of spherical droplets with small initial diameter ($d < 150$ μm) (Nguyen and Avedisian, 1987; Zhang and Gogos, 1991) predict a sharp increase in δ during the last few milliseconds of the droplet lifetime. We were unable to observe whether this occurred, since the time resolution of our video record was too low, with an interval between successive frames of 33 ms. Previous observations (Chandra, 1990) of droplets of water or liquid hydrocarbons in Leidenfrost evaporation have, however, found oscillation in the levitation height of the droplet as the droplet became smaller, with the droplet alternately rising and falling back to the surface. These oscillations, though, may have been simply due to natural convection currents in the air surrounding the droplet. In these

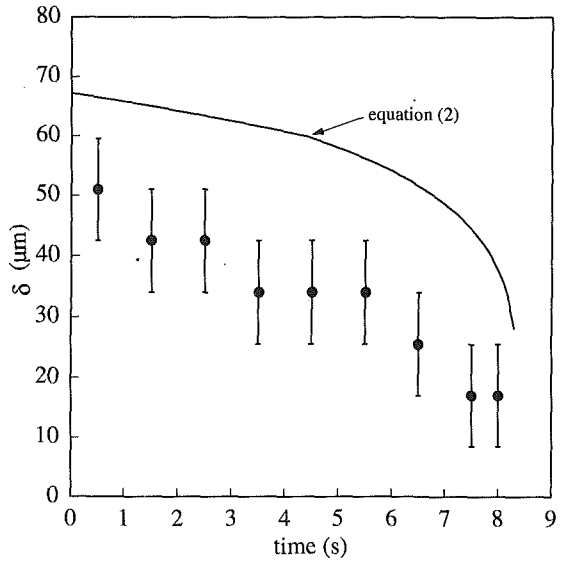

Fig. 5 Measured vapor gap thickness under a liquid nitrogen drop evaporating on a glass surface, compared with the theoretical predictions

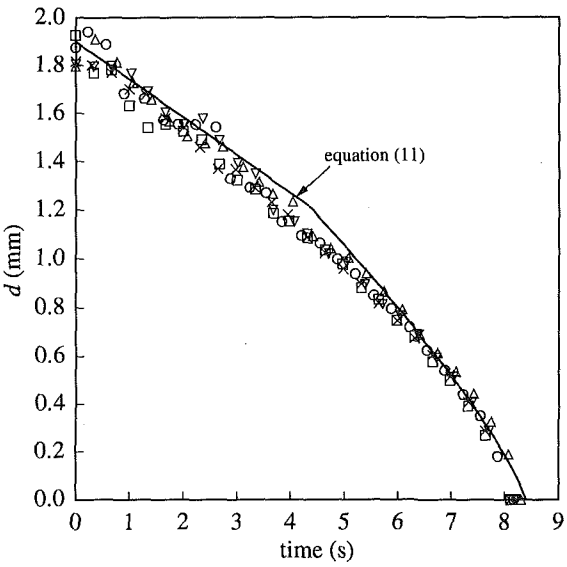

Fig. 6 Diameter evolution of five liquid nitrogen droplets on a copper surface, compared with the theoretical prediction

earlier experiments the surface was heated to a temperature greater than that of the ambient air. Heating a horizontal surface creates buoyancy-driven air currents with recirculating eddies, which could carry along the droplet as it grew smaller. In the present experiments the surface and surrounding atmosphere were at the same temperature. Any convective currents created because of the temperature difference between the cold droplet and warmer ambient air would flow downward, acting to hold the droplet at the surface.

Figure 6 shows diameter measurements made from video records of the evaporation of five different droplets of liquid nitrogen placed on a copper surface. $t = 0$ corresponds to the instant of droplet impact on the surface. Distortions in the droplet shape immediately after impact caused some scatter in the data during the early stages of evaporation ($t < 1$ s). As the droplets grew smaller, and more spherical, the repeatability of the measurements increased. The average droplet evaporation time was 8.2 ± 0.1 s.

The droplet evaporation rate may be calculated by assuming

that heat transfer to the droplet occurs principally by conduction through the vapor film separating the liquid and the glass surface. An energy balance gives:

$$\lambda \rho_l \frac{dV}{dt} = hA\ \Delta T \tag{3}$$

Evaluating Eq. (3) requires values for the heat transfer coefficient (h) and the surface area of heat transfer (A). Baumeister et al. (1966) derived theoretical expressions for these, based on a model that assumed the droplet to be in the shape of a flattened disk resting on a vapor film of uniform thickness. They obtained the velocity and pressure distribution in the vapor gap by solving the continuing, momentum, and energy equations, assuming creeping flow. Radiation and mass diffusion were neglected. Droplet shapes were calculated from a solution of the Laplace equation. The shape was found to depend on droplet volume: Large droplets were flattened under their own weight and small droplets were almost spherical. Small droplets were defined as those having $V^* < 0.8$, where V^* was a nondimensional volume defined by:

$$V^* = \frac{V}{(\sigma/\rho_l\, g)^{3/2}} \tag{4}$$

In our experiments $V^* = 0.8$ corresponded to a droplet diameter $d = 1.2$ mm, reached after approximately $t = 4.5$ s (Fig. 6). Observations confirmed that droplets with a diameter smaller than this were spherical (see Fig. 4, $t = 6$ s and 8 s), and larger diameter droplets were flattened on the bottom (Fig. 4, $t = 2$ s and 4 s).

The calculated surface area and heat transfer coefficient for a small droplet ($V^* < 0.8$) were:

$$A = 1.81\ V^{2/3} \tag{5}$$

$$h = 1.1 \left(\frac{k_v^3 \lambda' g\, \rho_l\, \rho_v}{\Delta T\, \mu_v\, V^{1/3}} \right)^{1/4} \tag{6}$$

and for a large droplet ($V^* \geq 0.8$):

$$A = 1.25\ (\rho_l g/\sigma)^{1/4}\ V^{5/6} \tag{7}$$

$$h = 1.075 \left(\frac{k_v^3 \lambda' g^{1/2}\, \rho_l^{1/2}\, \rho_v\, \sigma^{1/2}}{\Delta T\, \mu_v\, V^{2/3}} \right]^{1/4} \tag{8}$$

in which λ' was defined as:

$$\lambda' = \lambda \left(1 + \frac{7}{20} \frac{C_v\, \Delta T}{\lambda} \right)^{-3} \tag{9}$$

Defining a nondimensional time:

$$t^* = \frac{t}{\left(\frac{\rho_l^{1/2}\, \mu_v\, \lambda^4 \sigma^{5/2}}{k_v^3 g^{7/2}\, \lambda' \rho_v\, \Delta T^3} \right)^{1/4}} \tag{10}$$

and integrating Eq. (3) after substitution of Eqs. (4)–(10) gives the variation of droplet volume during evaporation:

$$V^{*1/3} = V_i^{*1/3} - 0.448 t^* \qquad \text{for } (V^* \geq 0.8) \tag{11a}$$

$$V^{*5/12} = V_i^{*5/12} - 0.832 t^* - 0.813 \quad \text{for } (V^* < 0.8) \tag{11b}$$

The droplet diameter evolution calculation from Eq. (11), with $d = (6V/\pi)^{1/3}$, is shown by the solid line in Fig. 6. The droplet was assumed to be at the saturation temperature ($T_l = 77$ K); liquid properties were evaluated at this temperature. Vapor properties were evaluated at the film temperature, $(T_l + T_s)/2$. The surface temperature was set at $T_s = 290$ K, based on surface temperature measurements described below.

The theoretical predictions are in good agreement with experiment, in spite of neglecting diffusive mass transfer from the droplet, and heat transfer from the surrounding gas. The atmosphere surrounding the droplet was pure nitrogen; no concentration gradients existed, and diffusion would have been negligible. The heat fluxes due to radiation (q_{rad}) and conduction (q_{cond}) from the surrounding atmosphere to an isolated droplet are (Kuo, 1986):

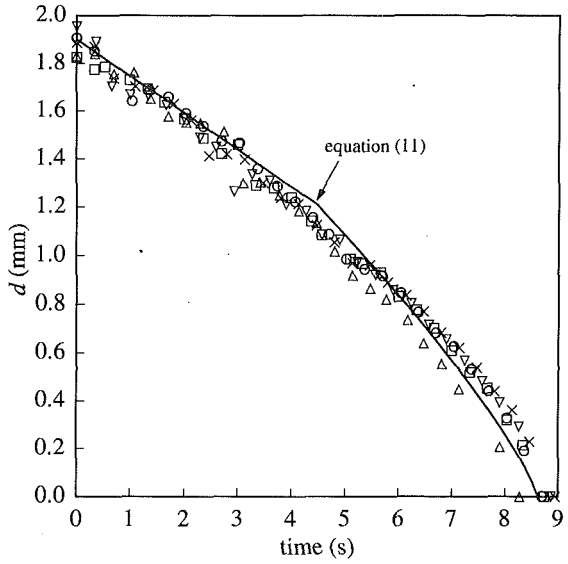

Fig. 7 Diameter evolution of five liquid nitrogen droplets on a glass surface, compared with the theoretical prediction

$$q_{rad} = \epsilon S\ (T_\infty^4 - T_l^4) \tag{12}$$

$$q_{cond} = \frac{2}{d} \frac{k_v}{C_v} \lambda \ln(1 + B) \tag{13}$$

Estimating the heat flux from the surface ($q_{surf} = h\Delta T$) from Eq. (6) and assuming $\epsilon = 1$ in Eq. (12), we find $q_{rad}/q_{surf} \sim 1$ percent, and $q_{cond}/q_{surf} \sim 6$ percent. The error introduced by neglecting heat transfer from the surroundings would therefore be expected to be small.

The thermal properties of the test surface can influence droplet evaporation, due to cooling of the surface during droplet impact. A copper surface would be expected to show little change in temperature; conversely, a low-conductivity glass surface would show significant undercooling during the impact of a liquid nitrogen droplet (Baumeister and Simon, 1973). T_s would be reduced by surface cooling, increasing the droplet evaporation time. Figure 7 shows the droplet diameter variation during the evaporation of five different droplets on a glass surface. The average droplet lifetime was 8.7 s, an increase of 6 percent compared to evaporation on a copper surface.

The variation of surface temperature (T_s), measured at a single point on a flat test surface directly under an impacting drop is shown for both a copper surface (Fig. 8) and a glass surface (Fig. 9). The time $t = 0$ corresponds to the moment of droplet impact, when the surface temperature was T_i (~ 20°C). The droplet rebounded after impact on the test surface and rolled off, after which the surface temperature recovered its original value. The temperature of a copper surface decreased by only about 1°C–3°C during droplet impact. For a glass surface the change was larger, approximately 13°C.

The diameter evolution of a droplet evaporating on a copper surface was calculated from Eq. (11) by assuming $T_s = 290$ K. The calculation was repeated for a glass surface assuming $T_s = 280$ K: the result is shown by the solid line in Fig. 7. The droplet lifetime was predicted to increase by 3 percent as a consequence of the 10 K reduction in surface temperature.

An analytical solution for surface temperature variation during droplet impact can be found by modeling the surface as a semi-infinite body, initially at uniform temperature T_i. The droplet, at temperature T_l, is brought in proximity to the surface at time $t = 0$, the liquid and solid being separated by a vapor film of uniform thickness δ. If the only mechanism for

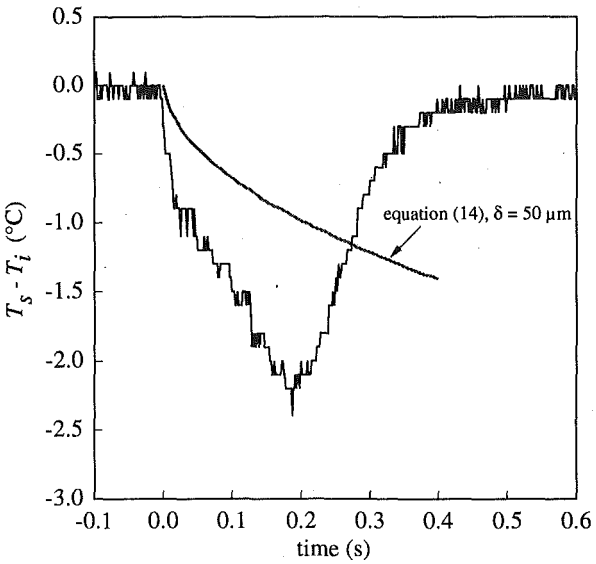

Fig. 8 Temperature variation of a copper surface during the impact of a liquid nitrogen droplet, compared with the theoretical prediction

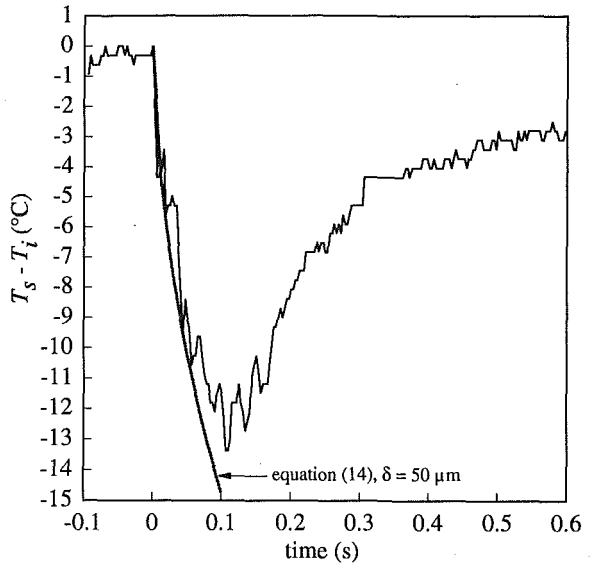

Fig. 9 Temperature variation of a glass surface during the impact of a liquid nitrogen droplet, compared with the theoretical prediction

heat transfer from the surface to the droplet is one-dimensional conduction through the vapor layer, the variation in T_s is given by (Carslaw and Jaeger, 1959):

$$\frac{T_s - T_i}{T_l - T_i} = \frac{2}{1+\beta_s/\beta_v} \sum_{n=0}^{\infty} \left(\frac{\beta_s - \beta_v}{\beta_s + \beta_v}\right)^n \text{erfc}\left(\frac{(2n+1)\delta}{2\sqrt{\alpha_v t}}\right) \quad (14)$$

where $\beta = (k\rho C)^{1/2}$.

No measurements were made of δ during droplet impact. We may, however, estimate its magnitude from a simple force balance, in which the impacting droplet is assumed to be supported by the pressure of the vapor film below it. An estimate of the pressure in the liquid (P_l) during impact is given by the stagnation pressure

$$P_l \sim \rho_l U^2/2 \quad (15)$$

If the bottom of the droplet is assumed to be flattened during impact into a circle of radius r_0, the vapor flow can be modeled as radial flow between parallel plates, giving the pressure distribution in the vapor (Gottfried and Bell, 1966):

$$P_v(r) \sim 3\mu_v\, w(r_0^2 - r^2)/\delta^3 \quad (16)$$

w is the velocity of the vapor leaving the bottom of the droplet, whose magnitude is calculated from an energy balance at the droplet surface:

$$\lambda\rho_v\, w \sim k_v\, \Delta T/\delta \quad (17)$$

A force balance at the liquid–vapor interface gives that

$$P_l \pi r_o^2 = 2\pi \int_0^{r_o} P_v\, r dr \quad (18)$$

Combining Eqs. (15)–(18) yields an expression for δ

$$\delta \sim \left(\frac{3\,\mu_v\, r_o^2\, k_v\, \Delta T}{U^2 \rho_v\, \rho_l \lambda}\right)^{1/4} \quad (19)$$

r_o varies during droplet impact, starting from a value of 0 and increasing to a maximum radius (Chandra and Avedisian, 1991)

$$r_{\max} \sim (d_i/2)(\text{We}/6 + 2)^{1/2} \quad (20)$$

For large We (as in our experiments, where We ~ 90), Eq. (20) reduces to $r_{\max} \sim d_i(\text{We}/24)^{1/2}$. Substituting an average value of $r_o = r_{\max}/2$ into Eq. (19), and assuming that the surface temperature variation is small, so that $\Delta T \approx T_i - T_l$, we obtained an estimate for the magnitude of δ:

$$\delta \sim \left(\frac{3\,\mu_v\, k_v\, (T_i - T_l)\, d_i^2}{96\,\sigma\lambda\rho_v}\right)^{1/4} \quad (21)$$

δ is independent of the impact velocity, and depends only on the surface temperature and droplet diameter. Substituting the values used in our experiment into Eq. (21), we obtain $\delta \sim 50\ \mu$m.

The temperature variation, calculated from Eq. (14) with $\delta = 50\ \mu$m, is compared in Figs. 8 and 9 with experimental temperature measurements for both copper and glass surfaces. Good agreement is seen between the prediction and the measurement for the glass surface (Fig. 9). The agreement was not as good for the copper surface (Fig. 8); note, however, that the temperature change was so small for the copper surface that the difference between theory and experiment (~1°C) was of the same magnitude as the variation in the measured surface temperature from drop to drop.

Increasing the surface roughness of the copper surface from $R_a = 0.35\ \mu$m to $R_a = 0.8\ \mu$m or $R_a = 1.7\ \mu$m had no measurable effect on the evaporation rate of the droplet. The evaporation time was reduced significantly, however, when ridges with a height of the same magnitude as the thickness of the vapor film under the droplet were machined on the surface. Figure 10 shows the diameter variation during the evaporation of droplets placed on copper surfaces with ridges of height 25 μm and 50 μm, respectively, compared with evaporation on a smooth surface ($R_a = 0.35\ \mu$m). Figure 11 is a sequence of photographs of the evaporation of a droplet placed on a surface with 25 μm ridges. The evaporation was similar on all the surfaces during the early part of the evaporation ($0 \le t \le 5$ s). However, after $t \approx 5$ s, bubbles started forming inside droplets placed on the rough surfaces (see Fig. 11, $t = 5.2$ s). The bubbles grew until they occupied a large portion of the droplet volume (Fig. 11, $t = 5.8$ s), and then exploded, shattering the droplet. The data point at $d = 0$ in Fig. 10 corresponded to the last video frame in which the droplet could be seen.

Surface roughness can influence droplet evaporation if the projections are large enough to penetrate the vapor film and contact the liquid, providing nucleation sites for bubbles to form. The observed bubble formation indicates that liquid–solid contact may occur with the grooved surfaces. No bubbles were formed as long as the surface roughness remained much

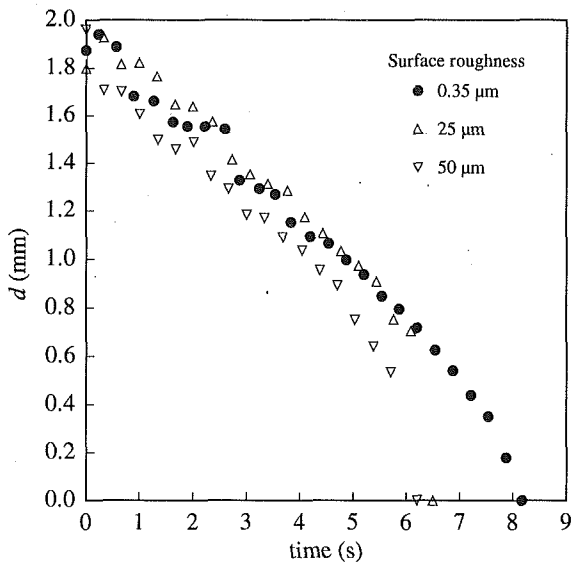

Fig. 10 Diameter evolution of liquid nitrogen drops on copper surfaces of different roughness

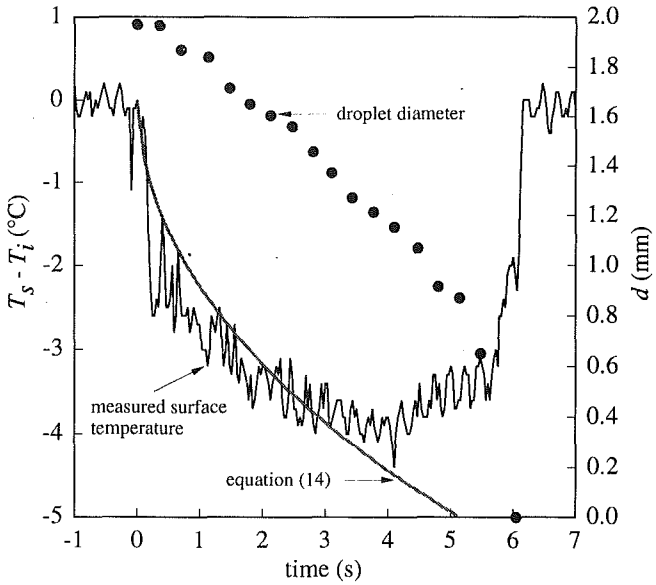

Fig. 12 Measured temperature variation of a copper surface with 25 μm ridges under an evaporation liquid nitrogen droplet, compared with theory; the droplet diameter evolution is plotted on the same axes

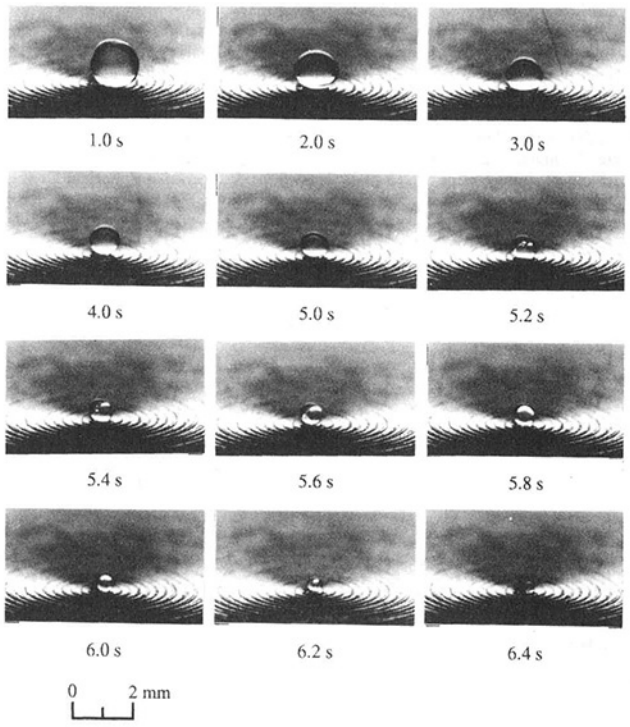

Fig. 11 The evaporation of a liquid nitrogen droplet on a copper surface with 25 μm ridges

smaller than the thickness of the vapor film between the liquid and the solid. Also, bubbles were formed only toward the end of the droplet lifetime, typically starting at $t \approx 5$ s after droplet deposition. This suggests that as the droplet evaporates δ becomes smaller (see Fig. 5), until the peaks of the ridges break through the vapor layer and touch the liquid.

Bubble nucleation in droplets has previously been observed by Hall (1987) when water droplets were placed on a smooth quartz surface, initially at a temperature (~500°C) well above the Leidenfrost point. As the surface under the drop cooled its temperature became sufficiently low to allow liquid-solid contact, initiating the growth of bubbles, which ruptured the drop. Tevepaugh and Keshock (1979) and Benton and Keshock (1982) studied the film boiling of droplets of several different liquids placed on heated surfaces, which had grooves or pins machined on them. The heat transfer from the surface to the droplet was found to be enhanced due to intermittent contact between the liquid drops and the surface projections. Bubble formation was observed in the liquid, but since the droplets were considerably larger ($V^* > 30$) than those used in our experiments they were not shattered by the vapor breakthrough.

Surface roughness had no significant effect on the evaporation rate of the droplets as long as there was no liquid–solid contact and bubbles did not nucleate (see Fig. 10, $t < 5$ s). The measured temperature drop during droplet impact on a copper surface was also independent of surface roughness, lying in the range 1°C–3°C for roughness varying from 0.35 μm to 50 μm.

Figure 12 shows the surface temperature variation directly under an evaporating liquid nitrogen droplet, over the entire droplet lifetime. A concave copper surface with 25 μm ridges was used, so that the droplet remained at the center of the surface after deposition. The evolution of droplet diameter is plotted on the same axes, as is the predicted surface temperature variation from Eq. (14) assuming a value of $\delta = 50$ μm. Bubbles were first observed in the droplet at $t = 4.9$ s. The bubbles grew larger, breaking through the droplet surface at $t = 5.8$ s, and all the liquid had evaporated by $t = 6.2$ s. The agreement between the predicted and measured surface temperature is good over most of the droplet lifetime (Fig. 12, $t < 4$ s). However, once the droplet becomes small and spherical the one-dimensional conduction model is no longer valid, and the theory and measurement diverge.

Conclusions

Measurements of the evaporation rate of droplets of liquid nitrogen placed on a solid surface were found to be in good agreement with predictions from a model of droplets in Leidenfrost evaporation. Copper surfaces showed very small temperature variations (1°C – 3°C) during the impact of a liquid nitrogen; glass surfaces were cooled by a larger amount (~13°C). Because of this cooling the droplet lifetime was longer on a glass surface than on a copper surface. Small increases in surface roughness had no effect on droplet evap-

oration. However, when the surfaces roughness was of the same magnitude as the thickness of the vapor film under the droplet (25–50 μm), bubbles formed inside the droplet and the droplet lifetime was reduced. Changes in surface roughness appeared to have little effect on the cooling of the surface during droplet impact.

Acknowledgments

Funding for this project was provided by Energy, Mines and Resources (EM&R), Canada, through the Center for Hydrogen and Electrochemical Studies (CHES). Additional support was obtained from a grant from the Natural Sciences and Engineering Research Council (NSERC) of Canada.

References

Avedisian, C. T., and Fatehi, M., 1988, "An Experimental Study of the Leidenfrost Evaporation Characteristics of Emulsified Liquid Droplets," *International Journal of Heat and Mass Transfer*, Vol. 31, pp. 1587–1603.

Awonorin, S. O., and Lamb, J., 1990, "The Leidenfrost Phenomenon: Experimental Investigation of the Vaporization of Nitrogen Droplets on a Food Surface," *Journal of Food Science*, Vol. 55, pp. 808–816.

Baumeister, K. J., Hamill, T. D., and Schoessow, G. J., 1966, "A Generalized Correlation of Vaporization Times of Drops in Film Boiling on a Flat Surface," *Proceedings of the Third International Heat Transfer Conference*, Vol. 6, pp. 66–73.

Baumeister, K. J., Keshock, E. G., and Pucci, D. A., 1971, "Anomalous Behavior of Liquid Nitrogen Drops in Film Boiling," *Advances in Cryogenic Engineering*, Vol. 16, pp. 445–454.

Baumeister, K. J., and Simon, F. F., 1973, "Leidenfrost Temperature–Its Correlation for Liquid Metals, Cryogens, Hydrocarbons and Water," ASME JOURNAL OF HEAT TRANSFER, Vol. 95, pp. 166–173.

Baumeister, T. Avallone, E. A., and Baumeister, T., III, 1978, *Marks' Standard Handbook for Mechanical Engineers*, 8th ed., McGraw-Hill, New York, pp. 13–76.

Benton, D. J., and Keshock, E. G., 1982, "Liquid-Solid Contact and Its Relationship to Improved Film Boiling Heat Transfer Rates," *Proceedings of the 7th International Heat Transfer Conference*, Vol. 4, pp. 125–130.

Carslaw, H. S., and Jaeger, J. C., 1959, *Conduction of Heat in Solids*, 2nd ed., Oxford University Press, London, United Kingdom, pp. 319–323.

Chandra, S., and Avedisian, C. T., 1988, "The Evaporation and Combustion of Levitated Arrays of Two, Three, and Five Droplets at a Hot Surface," *Proceedings of the Royal Society of London*, Vol. A418, pp. 365–382.

Chandra, S., 1990, "Droplet Evaporation and Combustion Near a Surface," Ph.D. Thesis, Cornell University, Ithaca, NY.

Chandra, S., and Avedisian, C. T., 1991, "On the Collision of a Droplet With a Solid Surface," *Proceedings of the Royal Society of London*, Vol. A432, pp. 13–41.

Gottfried, B. S., and Bell, K. J., 1966, "Film Boiling of Spheroidal Droplets," *I&EC Fundamentals*, Vol. 5, pp. 561–568.

Gottfried, B. S., Lee, C. J., and Bell, K. J., 1966, "The Leidenfrost Phenomenon: Film Boiling of Liquid Droplets on a Flat Plate," *International Journal of Heat and Mass Transfer*, Vol. 9, pp. 1167–1187.

Hall, C. M., 1987, "Secondary Nucleation in Superheated Water Drops on a Heated Quartz Surface," *Nuclear Energy*, Vol. 26, pp. 247–252.

Keshock, E. G., 1968, "Leidenfrost Film Boiling of Intermediate and Extended Bubbly Masses of Liquid Nitrogen," Ph.D. Thesis, Oklahoma State University.

Keshock, E. G., and Bell, K. J., 1970, "Heat Transfer Coefficient Measurements of Liquid Nitrogen Drops Undergoing Film Boiling," *Advances in Cryogenic Engineering*, Vol. 15, pp. 271–282.

Kuo, K. K., 1986, *Principles of Combustion*, Wiley, New York.

Mikhaylov, I. F., Glazunov, G. P., and Kosik, N. A., 1975, "Evaporation of Liquid Nitrogen Droplets on Metal Surfaces," *Heat Transfer—Soviet Research*, Vol. 7, pp. 35–36.

Nguyen, T. K., and Avedisian, C. T., 1987, "Numerical Solution for Film Evaporation of a Spherical Liquid Droplet on an Isothermal and Adiabatic Surface," *International Journal of Heat and Mass Transfer*, Vol. 30, pp. 1497–1509.

Schoessow, G. J., Chmielewski, C. E., and Baumeister, K. J., 1978, "Effect of Ice Contamination on Liquid Nitrogen Drops in Film Boiling," *Advances in Cryogenic Engineering*, Vol. 23, pp. 295–300.

Tevepaugh, J. A., and Keshock, E. G., 1979, "Influence of Artificial Surface Projections on Film Boiling Heat Transfer," *Advances in Enhanced Heat Transfer*, ASME, New York, pp. 133–140.

Wachters, L. H. J., Bonne, H., and van Nouhuis, H. J., 1966, "The Heat Transfer From a Hot Horizontal Plate to Sessile Water Drops in the Spheroidal State," *Chemical Engineering Science*, Vol. 21, pp. 923–936.

Zhang, S., and Gogos, G., 1991, "Film Evaporation of a Spherical Droplet Over a Hot Surface: Fluid Mechanics and Heat/Mass Transfer," *Journal of Fluid Mechanics*, Vol. 222, pp. 543–563.

S. DasGupta

I. Y. Kim

P. C. Wayner, Jr.

The Isermann Department of Chemical Engineering, Rensselaer Polytechnic Institute, Troy, NY 12180-3590

Use of the Kelvin–Clapeyron Equation to Model an Evaporating Curved Microfilm

A Kelvin–Clapeyron change-of-phase heat transfer model is used to evaluate experimental data for an evaporating meniscus. The details of the evaporating process near the contact line are obtained. The heat flux and the heat transfer coefficient are a function of the film thickness profile, which is a measure of both the intermolecular stress field in the contact line region and the resistance to conduction. The results indicate that a stationary meniscus with a high evaporative flux is possible. At equilibrium, the augmented Young–Laplace equation accurately predicts the meniscus slope. The interfacial slope is a function of the heat flux.

Introduction

The diverse technological importance of the process of fluid flow and heat transfer in the contact line region of an extended liquid meniscus have initiated extensive theoretical and experimental research over the years. The mechanism whereby the leading edge of an evaporating thin film can stay in contact with the substrate is discussed herein along with a detailed description of heat transfer characteristics. It is of interest to many heat transfer processes such as the evaporating meniscus in capillary cooling devices (heat pipes, grooved evaporators, etc.), the rewetting of a hot surface, microlayer evaporation in boiling, and the spreading of an apparently isothermal film. Fluid flow and change-of-phase heat transfer in very thin liquid films are intrinsically connected because of their common dependence on the intermolecular force field, system geometry, and gravity. Large stresses are present in this region, which includes the varying force fields associated with both the liquid–vapor and the liquid–solid interfaces. Due to the interfacial forces, the liquid–solid system can either be completely wetting (zero apparent isothermal contact angle, θ), partially wetting ($0 < \theta < 90$ deg), or nonwetting ($\theta > 90$ deg). The modifier apparent is used to emphasize the fact that we cannot see the real contact angle, which is at the molecular level. Figure 1 is a schematic drawing of the contact line region for a thin film of liquid on a solid substrate. Completely and partially wetting contact line regions are presented for both evaporating and nonevaporating conditions. Herein completely wetting systems are emphasized.

For both the completely and partially wetting cases, the concept of an interline thickness, δ_0, which is the thickness at the junction of the evaporating and the nonevaporating segments of the liquid film, has been used (Potash and Wayner, 1972; Wayner et al., 1976; Renk et al., 1978; Wayner, 1982). The equilibrium vapor pressure of a liquid is a function of the temperature and the intermolecular force field in the liquid. Therefore, the Kelvin equation has been used to describe the effect of the pressure jump at the liquid–vapor interface on the change in vapor pressure of a small drop of liquid. Similarly the Clausius–Clapeyron equation has been used to describe the effect of a temperature change on the vapor pressure. Although these two effects are of fundamental importance to heat transfer, their use at the leading edge of an evaporating curved liquid film is still more intriguing. In this region, the near presence of a solid changes the intermolecular stress field, and therefore, the vapor pressure of the liquid film.

The foundation for the study of the mechanics and thermodynamics of ultrathin films was established by Derjaguin and his co-workers. The important point about their research was that the stress field change due to the near presence of the solid could be represented by a change in the effective pressure in the liquid, the disjoining pressure. It is due to the presence of an excess chemical potential in a thin film as a result of the solid–liquid–vapor intermolecular force field (Derjaguin and Zorin, 1957; Derjaguin and Churaev, 1976). The predominant contribution to the disjoining pressure is the van der Waals dispersion forces. The introduction of the concept of disjoining pressure allows the interfacial effects to be easily incorporated within conventional thermodynamics (Wayner et al., 1976; de Feijter, 1988; Wayner, 1991). The result was the development of the augmented Young–Laplace equation for the pressure jump at the liquid–vapor interface (Derjaguin and Zorin, 1957; Wayner, 1980, 1982). A large amount of literature for the isothermal case, which is beyond the scope of this paper, has been developed in connection with this concept (e.g., Bascom et al., 1964; Derjaguin et al., 1965; Ingram, 1974; Kayser et al., 1985; Teletzke et al., 1987; Truong and Wayner, 1987; Gee et al., 1989; Beaglehole and Christenson, 1992). Similarly for the nonequilibrium case, important contributions were made by many researchers, e.g., Renk et al. (1978), Holm and Goplen (1979), Moosman and Homsy (1980), Cook et al. (1981), Tan et al. (1990), Burelbach et al. (1990), Bankoff (1990), and Wayner (1991). We have found these concepts to be extremely useful in the development of models of the evaporating meniscus (Wayner et al., 1991). Recently, Swanson and Peterson (1993), and Khrustalev and Faghri (1993) have used this type of model to analyze a micro heat pipe. Wu and Peterson (1991) studied a wickless heat pipe using the classical equation of capillarity to describe the fluid dynamics. Xu and Carey (1990) used a completely wetting fluid to study film evaporation from a microgrooved surface with classical capillary equation in the thicker part of the liquid film and the disjoining pressure equation for the thin film meniscus region on the side walls. The model by Wayner and his co-workers incorporates the augmented Young–Laplace equation, kinetic theory, and the extended Clapeyron equation. The analytical procedures allow the critical interfacial properties of the system to be initially evaluated in situ and then be used to obtain additional details concerning the evaporation process. In addition we have developed experimental techniques to evaluate these models (DasGupta et al., 1991; DasGupta and Wayner, 1993). The generally excellent match between the experimental results and the numerical solutions of the theoretical model equations enabled us to obtain consistent and justifiable values of the modified Hamaker constant (DasGupta et al., 1993a).

Contributed by the Heat Transfer Division and presented at the ASME Winter Annual Meeting, New Orleans, Louisiana, November 28–December 3, 1993. Manuscript received by the Heat Transfer Division August 1993; revision received December 1993. Keywords: Evaporation, Phase-Change Phenomena, Thin Film Flow. Associate Technical Editor: A. Faghri.

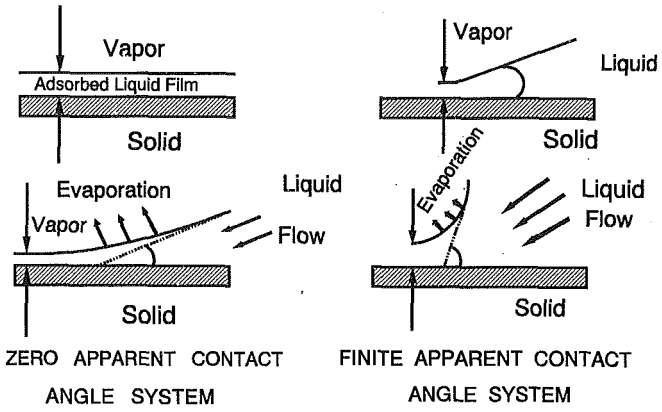

Fig. 1 Conceptual (not to scale) view of contact line represented by adsorbed film thickness, δ_0. The second subscript *e* denotes equilibrium.

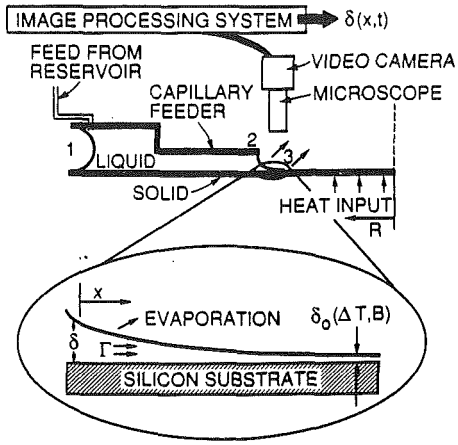

Fig. 2 Schematic view of the circular capillary feeder

In the present paper, we discuss some important aspects and utility of these models in light of recent experimental results. The slopes of the experimentally obtained equilibrium meniscus profiles will be compared with the predictions from the augmented Young–Laplace equation. For pure fluids at relatively low levels of evaporation, the evaporative heat fluxes and the heat transfer coefficients of the thin evaporating film will be determined using improved experimental techniques and theoretical modeling. The significance of the numerical values and the trends in these quantities will be addressed. A theoretical modeling and simulation of a high heat flux evaporating meniscus in a micro heat pipe will be discussed.

Experimental

Only a very brief description of the experiments is given herein. The experimental details are given by DasGupta et al. (1991, 1993b) and Wayner et al. (1991). A cross-sectional diagram of the circular capillary feeder system is shown in Fig. 2. The experimental substrate was a single crystal silicon with a native oxide of about 3 nm. Liquid flowed from a reservoir (maintained at the same height as in the capillary feeder) as a result of a difference in capillary and disjoining pressure (caused by intermolecular forces) and formed a meniscus at the edge of the thinner gap at position 2. The contact line region, area 3, governed the critical initial condition for the stability and behavior of the evaporating meniscus and hence the performance of the capillary feeder system. In the thinnest portion of the meniscus represented by δ_0, evaporation did not occur. The details of the liquid film thickness profile in the contact line region were measured as a function of the evaporation rate using ellipsometry and microcomputer-enhanced video microscopy based on interferometry. The errors in these measurement techniques were described by DasGupta et al. (1993b). The final estimate was an error of about ±4 Å for the adsorbed thin film region. The max-

Nomenclature

A = $6\pi\bar{A}$ = Hamaker constant, J
a = coefficient defined by Eq. (5), kg/m^2 s K
b = coefficient defined by Eq. (5), s/m
C = accommodation coefficient
h_{lv} = convective heat transfer coefficient, W/m^2 K
Δh_m = heat of vaporization per unit mass, J/kg
K = curvature, m^{-1}
k = thermal conductivity of the liquid film, W/m K
l = characteristic length, Eq. (15), m
$\dot{m}$ = evaporative mass flux, kg/m^2 s
m^{id} = ideal evaporative mass flux, kg/m^2 s
M = molecular weight, kg/kg mole
P_v = reference vapor pressure, N/m^2
P_l = liquid pressure, N/m^2
P_{lv} = vapor pressure at liquid–vapor interface, N/m^2
q = evaporative heat flux, W/m^2
q^{id} = ideal evaporative heat flux, W/m^2
$q^{\max}$ = maximum evaporative heat flux, W/m^2
Q = power input setting, W
$\bar{Q}$ = dimensionless interfacial heat flux
R = universal gas constant, J/mol K
ΔT = characteristic temperature difference between solid and vapor, K
T_{lv} = temperature of the liquid–vapor interface, K
T_s = substrate temperature, constant, K
T_v = temperature of the vapor, constant, K
U = overall heat transfer coefficient, W/m^2 K, Eq. (30)
V_l = molar volume of the liquid, m^3/kg mole
x = coordinate distance along the substrate, m
Z = distance, defined by Eq. (21)
α = dimensionless parameter, Eq. (23)
γ = evaporation coefficient
Γ = mass flow rate per unit width of the film, kg/m s
δ = thickness of the liquid film, m
Δ = difference
δ_0 = reference film thickness, m
ΔQ = small uncontrolled source or sink, W
ϵ = dimensionless parameter
η = dimensionless film thickness $= \delta/\delta_0$
θ_a = apparent contact angle, deg
κ = dimensionless parameter
ν = kinematic viscosity, m^2/s
ξ = dimensionless distance
Π = disjoining pressure, N/m^2
Π_0 = characteristic pressure, N/m^2
σ = surface tension, N/m
ϕ = dimensionless pressure difference

Subscripts

e = equilibrium
l = liquid
lv = liquid–vapor
s = solid
v = vapor

Superscripts

id = ideal, based on kinetic theory
$'$ = derivatives

imum error in the capillary meniscus region was less than 0.01 μm based on repeated measurements and the absolute value of the error decreased (always within 5 percent) as the thin film was approached. The data presented in this paper are for relatively low heat fluxes, but recent studies indicate that the capillary feeder successfully replenishes the evaporated liquid even at high rates of evaporation. Figure 3 is an example of experimental data for propanol menisci at two different situations—very near equilibrium with very small evaporation (Q = 0.0 W) and evaporation with controlled rate of heat inputs. In an isothermal horizontal system of spreading liquid on a solid substrate at the exit of a capillary, the curvature should remain constant in the region where dispersion forces can be neglected. So the film profile in this range approximates a parabola and a plot of $\delta^{1/2}$ versus x is a straight line. If the curvature is constant, it is related to the slope of this line as $K_c = 2(d\delta^{1/2}/dx)^2$. The experimental values of $\delta^{1/2}$ are given in Fig. 3. For the case where Q = 0.0 W, $\delta^{1/2}$ versus x is nearly a straight line, which means the system was very close to isothermality, but for the cases involving evaporation the lines bend downward, showing the presence of a curvature gradient. Plotting $\delta^{1/2}$ versus x, therefore, clearly demonstrates that the film thickness profile and curvature are definitely functions of the heat flux. This is not obvious from a plot of δ versus x. Note that the data are for completely wetting systems. However, because of the method of presentation in Fig. 3, it appears as if there is a finite contact angle. Herein we address the significance of the film thickness profile measurements.

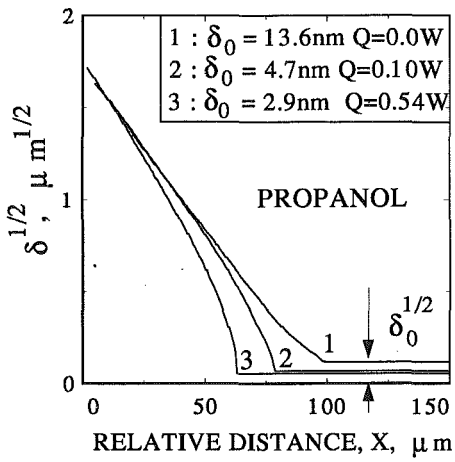

Fig. 3 Film thickness profiles of propanol menisci at different levels of evaporation. The data are essentially continuous for the capillary region since each pixel measures a region with a diameter of 0.625 μm.

Theoretical

At steady state, liquid flows in the film because of evaporation, which is a function of local superheat and pressure. The local superheat is the temperature difference between the liquid–vapor interface, T_{lv}, and the vapor phase, T_v, which is presumed to be isothermal and pure. The tendency of the liquid to evaporate is reduced by adsorption and a negative capillary pressure. In this study the adsorption forces are restricted to the London–van der Waals dispersion force and the film is assumed to be fairly flat so that lubrication approximation holds. Marangoni flow is expected to be relatively small because of the purity of the fluid and the small temperature variation along the substrate for the low heat flux cases studied herein. It has been experimentally observed that the average temperature change along the substrate in the region where evaporation occurs is of the order of 10^{-2} °C, whereas the average temperature difference across the liquid film and interface, ΔT, is of the order of 10^{-4} °C. Therefore, we feel that the constant substrate temperature assumption is justified. These small temperature gradients also indicate that the Marangoni effects are relatively small. Since the film has a resistance to heat conduction, the thicker portions of the film will be less superheated at the liquid–vapor interface than the thinner portions. If the film is sufficiently thin, the liquid–solid intermolecular force field will keep the spreading (zero contact angle) film from evaporating even though it is superheated. Therefore we expect the evaporation rate to be highest where the film thickness is moderate.

The literature provides relationships that are the basis for the following model for liquid flow and heat transfer in the evaporating thin films (Potash and Wayner, 1972; Moosman and Homsy, 1980; Teletzke et al., 1987; Wayner, 1991). The development of the model, boundary conditions, and numerical solution scheme have been discussed in great detail in a recent publication by DasGupta et al. (1993a). Herein we will only introduce the basic model equations so that newer data and applications of the model, e.g., the estimation of the heat transfer coefficients, etc., can be emphasized.

The liquid pressure, P_l, is related to the vapor phase pressure, P_v, by the modified form of the augmented Young–Laplace equation. This model accounts for both the disjoining and capillary pressures present in a curved evaporating thin liquid film (Wayner et al., 1976).

$$P_l - P_v = \frac{\bar{A}}{\delta^3} - \sigma \frac{d^2\delta}{dx^2} \tag{1}$$

where $6\pi\bar{A}$ is the Hamaker constant (negative for a spreading liquid), $\delta(x)$ is the film thickness, and σ is the surface tension. The first term on the right-hand side of Eq. (1) is called the disjoining pressure, Π, and it represents the body force on the liquid due to dispersion phenomena. The limitations of the expression for disjoining pressure are discussed by Truong and Wayner (1987). The complete expression for curvature (K) is given by the following expression:

$$K = \frac{\dfrac{d^2\delta}{dx^2}}{\left[1 + \left(\dfrac{d\delta}{dx}\right)^2\right]^{3/2}} \tag{2}$$

Therefore, the simplified expression for the curvature is valid only if the square of the slope is small compared to one. The maximum slope of the film thickness profiles in our experiments is 0.12 and hence we feel that the use of the simplified form of curvature is justified.

The mass flow rate per unit width of the film, $\Gamma(x)$, in a slightly tapered thin film is related to the pressure gradient in the flow direction by lubrication theory:

$$\Gamma(x) = \frac{-1}{3\nu}\delta^3 \frac{d}{dx}[P_l] \tag{3}$$

ν is the kinematic viscosity. Equations (1) and (3) demonstrate that the mass flow rate is a function of the thin film shape, $\delta(x)$.

Wayner et al. (1976) used a Kelvin–Clapeyron equation for the variation of equilibrium vapor pressure with temperature and disjoining pressure in a horizontal thin film. The following quasi-thermodynamic solution for the evaporative flux as a function of the temperature and pressure jumps at the interface is a model based on the Kelvin–Clapeyron equation (Wayner, 1991):

$$\dot{m} = a(T_{lv} - T_v) + b(P_l - P_v) \tag{4}$$

where $\dot{m}$ is the evaporative flux, defined as the amount of liquid evaporating from the liquid film per unit area per unit time, T_{lv} is the temperature of the liquid–vapor interface, and T_v is the temperature of the vapor. According to Eq. (4) evaporation is promoted by superheat and hindered by low liquid film pressure. The coefficients, a and b, are defined as

$$a = C\left(\frac{M}{2\pi RT_{lv}}\right)^{1/2}\left(\frac{P_v M\Delta h_m}{RT_v T_{lv}}\right), \quad b = a\frac{V_l T_v}{M\Delta h_m} \tag{5}$$

C is the accommodation coefficient, defined as equal to $2\gamma/(2-\gamma)$, where γ is the evaporation coefficient. For this analysis, γ has been taken to be equal to 1.0 and therefore C has a value of 2.0. M is the molecular weight, P_v is the vapor pressure at temperature T_v, V_l is the molar volume of the liquid. Δh_m is the enthalpy of vaporization per unit mass, at temperature T_{lv}. In practice T_{lv} is unknown. However, if the temperature differences are small compared to the absolute temperature, the known substrate temperature, T_s, may be substituted for the unknown T_{lv} in Eq. (5) to calculate a and b. Following Moosman and Homsy (1980), the one-dimensional heat conduction heat transfer solution for the film is used to eliminate T_{lv} in favor of T_s in Eq. (4) and is further simplified using Eq. (1):

$$\dot{m} = \frac{1}{1+\dfrac{a\Delta h_m}{k}\delta}\left[a(T_s - T_v) + b(P_l - P_v)\right]$$

$$= \frac{1}{1+\dfrac{a\Delta h_m}{k}\delta}\left[a(T_s - T_v) + b\left(\frac{\bar{A}}{\delta^3} - \sigma\frac{d^2\delta}{dx^2}\right)\right] \tag{6}$$

where k is the thermal conductivity of the liquid. This equation clearly demonstrates the direct effect of film thickness and intermolecular forces on the evaporation rate. The evaporative flux is linked to the flow rate in the film through a material balance:

$$\frac{d\Gamma}{dx} = -\dot{m} \tag{7}$$

The coupled differential equations are thus Eq. (1) and

$$\frac{1}{3\nu}\frac{d}{dx}\left(\delta^3\frac{dP_l}{dx}\right) = \frac{1}{1+\dfrac{a\Delta h_m}{k}\delta}\left[a\Delta T + b(P_l - P_v)\right] \tag{8}$$

where

$$\Delta T = T_s - T_v \tag{9}$$

The variables are nondimensionalized in the following way. For a strictly flat film, $\delta(x, t) = \delta_0$. Since there is no pressure gradient in such a film, the right-hand side of Eq. (8) must be zero. Hence,

$$b(P_l - P_v) = -a\Delta T; \quad \frac{\bar{A}}{\delta_0^3} = -\frac{a}{b}\Delta T \tag{10}$$

If δ_0 is so chosen, the flat film is a solution to the governing Eqs. (1) and (8). The reference thickness is thus fixed and the reference pressure is the magnitude of the disjoining pressure of such a film. This pressure is obtained from Eq. (10) as

$$\Pi_0 = \left(\frac{a}{b}\right)\Delta T \tag{11}$$

The dimensionless pressure difference is defined in the following way

$$\phi = (P_l - P_v)/\Pi_0 \tag{12}$$

As described by DasGupta et al. (1993a), the governing Eqs. (1) and (8) are nondimensionalized to obtain

$$\phi = -\frac{1}{\eta^3} - \epsilon\frac{d^2\eta}{d\xi^2} \tag{13}$$

$$\frac{1}{3}\frac{d}{d\xi}\left(\eta^3\frac{d\phi}{d\xi}\right) = \frac{1}{1+\kappa\eta}(1+\phi) \tag{14}$$

where ξ is the dimensionless position, defined as

$$\xi = \frac{x}{l} \quad \text{where} \quad l = \sqrt{\frac{-\bar{A}}{\nu a\Delta T}}; \quad \bar{A} < 0 \tag{15}$$

The dimensionless thickness is $\eta = \delta/\delta_0$. The dimensionless groups κ and ϵ are

$$\kappa = \frac{a\Delta h_m\delta_0}{k}; \quad \epsilon = \frac{\sigma\delta_0 b\nu}{-\bar{A}} \tag{16}$$

The parameter κ is a measure of the importance of the resistance of the film to thermal conduction. The parameter ϵ is a measure of the importance of capillary pressure effects relative to disjoining pressure effects. We impose two far-field conditions. The first condition is

$$\text{For} \quad \xi \to \infty: \quad \eta \to 1; \quad \phi \to -1 \tag{17}$$

The film thickness is assumed to asymptotically approach the nonevaporating adsorbed film thickness. The second condition is

$$\text{For} \quad \xi \to -\infty: \quad \eta \to \infty; \quad \phi \to -\phi_m \tag{18}$$

The liquid pressure difference is assumed to approach a constant value, ϕ_m, in the thicker portion of the meniscus, which can be experimentally varied by varying the base pressure in the meniscus.

The left-hand side of Eq. (14) is also the dimensionless mass or heat flux, where the scaling factors, m^{id} and q^{id}, are obtained using

$$m^{id} = a\Delta T; \quad q^{id} = a\Delta T\Delta h_m \tag{19}$$

Discussion

The governing equations were solved numerically and compared with the experimental data for an extended meniscus (DasGupta et al., 1993a), which gave consistent and justifiable values of the modified Hamaker constant. A Taylor series expansion of the fourth-order nonlinear transport model was used to evaluate the extremely sensitive initial conditions at the interline. In a related paper (DasGupta et al., 1993b), the pressure field was evaluated and the coupling between the disjoining and capillary pressure was demonstrated. In the present work we used the same methodology to estimate the values of the modified Hamaker constants and the interfacial temperature differences for our experiments and to determine the slopes of the meniscus profiles. Since the solution scheme and subsequent analysis have already been presented in great detail in those two publications, they are not repeated herein. The recent experiments and the analysis presented in this paper will demonstrate the validity of the augmented Young–Laplace equation, by comparing the equilibrium meniscus slope from the experiments and from the solution of the equation. The present study and the discussion of the results from another study will confirm the potentials of high heat flux evaporation from an extended meniscus.

Meniscus Slope. The slopes, $d\delta/dx$, are calculated by analyzing the experimental data using the proposed model (Eqs. (13) and (14)) and are presented as functions of film thickness in Fig. 4 for propanol at different levels of evaporation. It must be mentioned that for our reference frame, the slope is always negative (film thickness decreases as distance increases). In the subsequent discussion about the magnitudes and trends in the slope profiles under different conditions we refer to their absolute values.

As can be seen from Fig. 4, the slope and hence the magnitude of the apparent contact angle increase with increase in heat input (evaporation). This is an important experimental confirmation of the effect of heat flux on the slope and curvature of a meniscus. These figures clearly demonstrate that the profiles essentially start from a flat film region (zero slope and curvature), pass

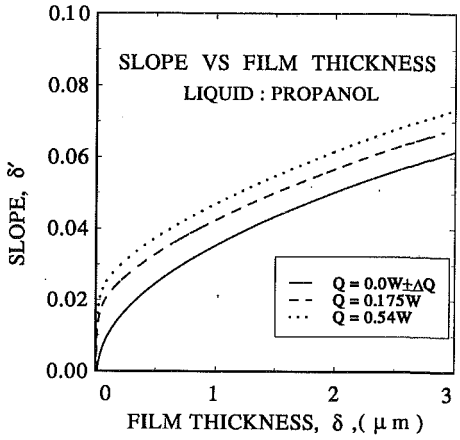

Fig. 4 Slope versus film thickness of propanol menisci at different levels of evaporation

through a region where the slope ($d\delta/dx$) increases rapidly (specially for the cases involving evaporation), and then the slopes of the slope ($d\delta/dx$) versus distance (or film thickness) curves stabilize to become weak functions of distance or film thickness. In the legend of Fig. 4, a very small heat flux, $\pm\Delta Q$, has been added to the $Q = 0.0$ W case to indicate that small disturbances were present due to uncontrolled environment. This will be apparent in the next subsections where the reference temperature difference and the heat fluxes will be discussed.

Next the slope profiles from the data analysis are compared with the slope profiles obtained from the solution of the augmented Young–Laplace equation. The augmented Young–Laplace equation can be written for a point in the thicker portion of the meniscus, where the disjoining pressure effects are negligible, and for another point where both effects are present. The curvature at the thicker portion of the meniscus (K_∞) is nearly constant (DasGupta et al., 1993b):

$$\sigma K - \frac{\bar{A}}{\delta^3} = \sigma K_\infty, \quad Q = 0 \tag{20}$$

The following variables are introduced next to obtain Eq. (22) from Eq. (20):

$$\eta = \frac{\delta}{\delta_0} \quad Z = x\left(\frac{K_\infty}{\delta_0}\right)^{1/2} \tag{21}$$

$$\frac{d^2\eta}{dZ^2} + \left(\frac{-\bar{A}}{\sigma K_\infty \delta_0^3}\right)\frac{1}{\eta^3} = 1 \tag{22}$$

Equations (20)–(22) are valid for an *equilibrium situation* where no evaporation or condensation is taking place. In the development of Eq. (20), a simplified expression for curvature is used, which is valid if the square of the slope is very small compared to one. For our experiments, $d\delta/dx$ is small (the value of the maximum slope is 0.12) and hence using the simplified form of curvature is justified. A dimensionless variable, α, is defined next:

$$\alpha^3 = \frac{-\bar{A}}{\sigma K_\infty \delta_0^3} \tag{23}$$

Equation (22) can now be written as

$$\frac{d^2\eta}{dZ^2} = 1 - \frac{\alpha^3}{\eta^3} \tag{24}$$

We note that the value of α can be calculated from experimental measurement (δ_0) and subsequent analysis of the data (to obtain $\bar{A}$ and K_∞). For the equilibrium case, $Q = 0$ and $\alpha = 1$. Any values of α other than unity will signify the deviation of a meniscus from the equilibrium situation. The following discussion of two experimental cases, which were very close to equilibrium, will demonstrate the utility of the model and the evaluation of the values of α. After multiplying both sides of this equation by $2d\eta/dZ$, it can be integrated (C_1 is the constant of integration):

$$\left(\frac{d\eta}{dZ}\right)^2 = 2\eta + \frac{\alpha^3}{\eta^2} + C_1 \tag{25}$$

The boundary condition used for the completely wetting case is

$$\text{For} \quad \eta = \alpha \quad \frac{d^2\eta}{dZ^2} = 0 = \frac{d\eta}{dZ} \tag{26}$$

We note that this can be viewed as an artificial boundary condition for a nonequilibrium system for which $\alpha > 1$. The utility of the extended model is demonstrated below.

Using the boundary condition, the slope of the meniscus can be expressed as

$$\frac{d\delta}{dx} = -(K_\infty \delta_0)^{1/2}\sqrt{2\eta + \frac{\alpha^3}{\eta^2} - 3\alpha} \tag{27}$$

Hence if the curvature at the thicker end of the meniscus, K_∞, along with $\bar{A}$, δ_0, and σ are known, the slope of the meniscus can be directly calculated as a function of the film thickness, using only the augmented Young–Laplace equation. The minus sign in Eq. (27) is indicative of the fact that for the reference frame selected, the meniscus slope should always be negative (film thickness decreases as distance increases).

Table 1 summarizes two experimental cases with Q (power input) = 0.0 W $\pm$ ΔQ. $\pm\Delta Q$ represents a very small uncontrolled source or sink due to the surroundings. The values of δ_0 are obtained experimentally, σ is from the literature, and the values of $\bar{A}$ and K_∞ are obtained by the match between the actual experimental profile and the numerically solved theoretical profiles. The values of α obtained using Eq. (23) in Table 1 clearly indicate that both the propanol and octane menisci were very close to equilibrium (when $Q = 0.0$ W). The interfacial temperature differences, obtained by the match between the data and the numerical solution of the model, show that the values of ΔT ($=T_s - T_v$), the reference temperature difference at $\delta = \delta_0$, are very small. Hence it is expected that if Eq. (27) is used to calculate the slope as a function of film thickness for these two cases using the values from Table 1, the results will be close to that obtained from the experimental data analysis.

Figures 5 and 6 are plots of the slope as functions of film thickness. The solid lines are obtained from data analysis, the triangles in the figures are obtained using Eq. (27) with the values of α given in Table 1. It is evident from these figures that the experimental results are very close to the points (the triangles in the graph) obtained using Eq. (27). These results clearly demonstrate the validity of the augmented Young-Laplace equation to predict the equilibrium meniscus shape.

Calculation of Evaporative Heat Flux Profile. The dimensionless interfacial evaporative heat flux, $\dot{Q}$, profiles are presented in Fig. 7 for propanol. The ideal heat flux, $q^{id} = a\Delta T\Delta h_m$,

Table 1 Selected characteristics of ethanol and octane menisci at Q = 0.0 W $\pm$ ΔQ

Liquid	δ_0 (nm)	$\bar{A}$ (J)	K_∞ (1/m)	$\sigma \times 10^2$ (N/m)	α	ΔT (K)
Propanol	13.6±0.4	3.81×10^{-23}	637	2.34	1.005	7.06×10^{-6}
Octane	19.1±0.4	7.55×10^{-23}	422	2.09	1.071	1.20×10^{-5}

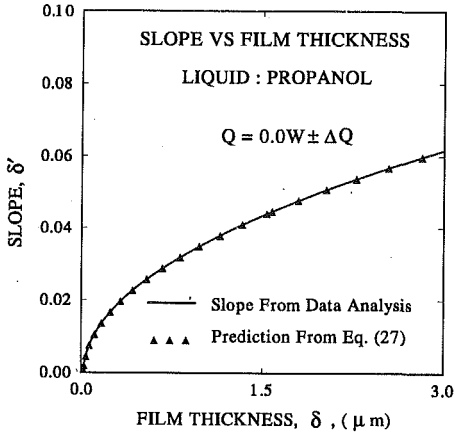

Fig. 5 Comparison of actual meniscus slope with that predicted from the augmented Young–Laplace equation for propanol for a situation very close to equilibrium (Q = 0.0 W ± ΔQ)

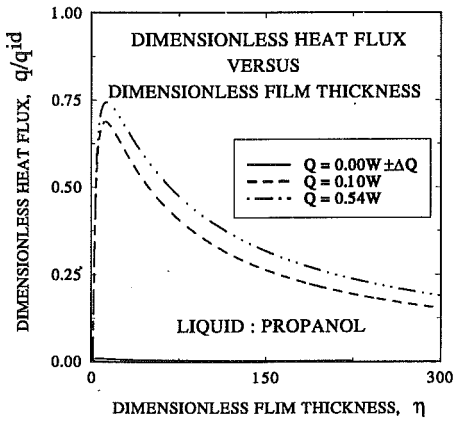

Fig. 7 Dimensionless heat flux versus dimensionless film thickness. Propanol: Q = 0.0 W ± ΔQ, q^{id} = 3.84 × 10^0 W/m², Q = 0.1 W, q^{id} = 3.8 × 10^1 W/m², Q = 0.54 W, q^{id} = 1.86 × 10^2 W/m².

based on kinetic theory, is given in the caption. The left-hand side of Eq. (14), which is equal to $\dot{Q} = q/q^{id}$, can be used to describe the characteristics of the profile. Note the presence of a very small evaporation for the Q = 0.0 W case (almost obscured by the horizontal axis). At the interline, δ_0, the dimensionless pressure, ϕ, is given by $\phi = -1$. Therefore, the flux is equal to zero. The absolute value of ϕ decreases as the thickness increases. Therefore, the interfacial flux increases because the effect of interfacial forces decreases. This increase does not continue indefinitely because of conductive resistance in the liquid film, which is represented by $\kappa\eta$ in Eq. (14). Therefore, we obtain a maximum in the flux profile and note that the resistances are substantial. A recent numerical study by Stephan and Busse (1992) also predicted substantial resistances in the contact line region. We note that the actual increase in heat flux as the heat input to the system increases is somewhat eclipsed by the considerably different values (included in the caption of Fig. 7) of the scaling factors for the heat flux, q^{id}, for the three cases.

The maximum flux, $q^{\max}$, can be obtained by multiplying the maximum value of the dimensionless interfacial evaporative heat flux (Fig. 7), by the reference ideal heat flux, q^{id}. The maxima occurred at thickness values of approximately 5 to 15 times δ_0 in these studies. The ideal heat flux was obtained using Eq. (19). The experimental results of the variation of $q^{\max}$ with ΔT ($\Delta T = T_s - T_v$) for several liquids at different levels of evaporation are presented in Fig. 8. A few of the experiments at relatively higher heat fluxes (e.g., the two R113 data points at the higher end of ΔT in Fig. 8) were performed with a smaller gap of the capillary feeder to provide stability to the evaporating menisci at high heat fluxes. For the small region ΔT is assumed to be a constant. The values of $q^{\max}$ for different liquids depend on various parameters, e.g., the liquid–solid interactions, the gap width of the capillary device, the thermophysical properties of the liquid, etc. The exact nature of the functional relationship between these quantities and the heat flux is quite complex and yet to be understood. More experimental data on a wide range of ΔT are needed to develop any correlation. Presently experiments at higher heat fluxes (higher ΔT) are restricted by limitations of the experimental setup (magnification, resolution, etc.) as well as the varying nature of the working liquids. The figure shows that $q^{\max}$ is a strong function of ΔT and it increases with increase in ΔT. This is due to both the increase in ΔT and the increase in the vapor pressure. Note the close to linear relationship between $q^{\max}$ and ΔT, on a logarithmic plot, even for different fluids. The two data points in the lower ΔT range, which show deviation from linearity, were distinctively different from the other data points due to their close proximity to equilibrium with very small evaporation. We believe that the nature of the $q^{\max}$ versus ΔT plot is due to stable evaporation of the liquid meniscus, sustained by continuous liquid flow from the capillary feeder toward the contact line region for the evaporation levels studied herein. We note that further experiments with high heat fluxes are needed to understand this complex phenomenon completely.

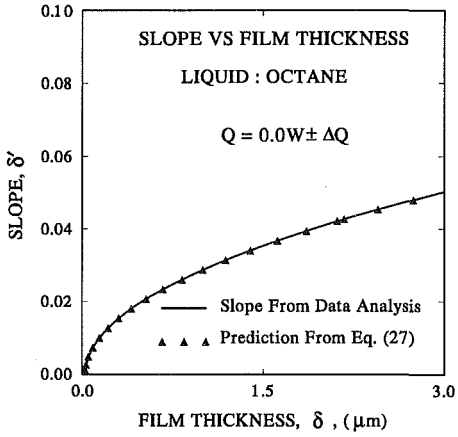

Fig. 6 Comparison of actual meniscus slope with that predicted from the augmented Young–Laplace equation for octane for a situation very close to equilibrium (Q = 0.0 W ± ΔQ)

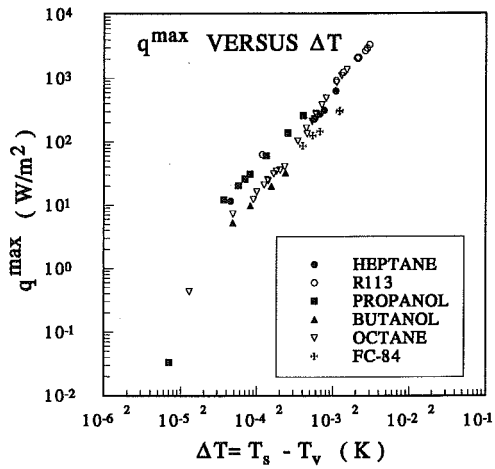

Fig. 8 Maximum heat flux (q^{max}) versus ΔT for different liquids

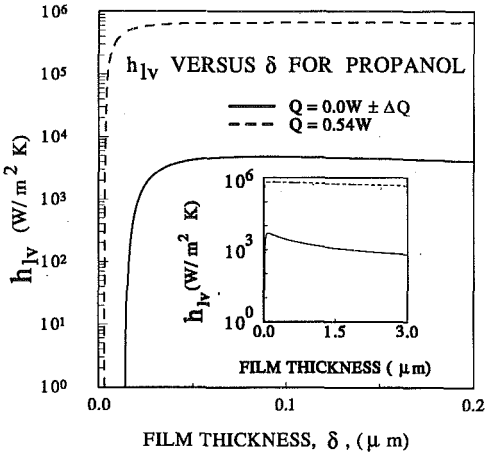

Fig. 9 Convective heat transfer coefficient at the interface versus film thickness. Propanol: Q = 0.0 W ± ΔQ, $\Delta T = 7.06 \times 10^{-6}$ K and Q = 0.54 W, $\Delta T = 2.55 \times 10^{-4}$ K.

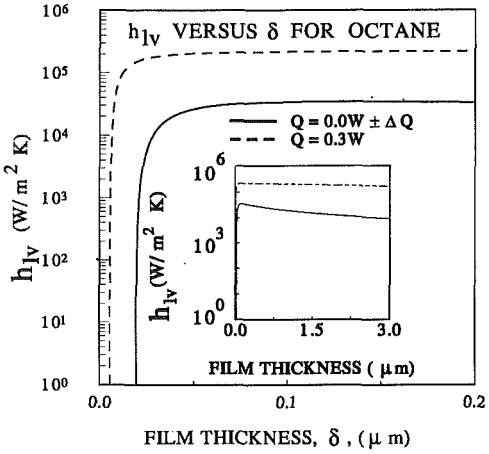

Fig. 10 Convective heat transfer coefficient at the interface versus film thickness. Octane: Q = 0.0 W ± ΔQ, $\Delta T = 1.29 \times 10^{-5}$ K and Q = 0.3 W, $\Delta T = 4.53 \times 10^{-4}$ K.

For example, the maximum possible stable heat flux, which is a function of the liquid–solid system and the size of the capillary feeder, is an important unknown.

Heat Transfer Coefficient. The convective heat transfer coefficient, h_{lv}, corresponding to the change-of-phase heat transfer at the liquid–vapor interface, has been defined as

$$q = h_{lv}(T_{lv} - T_v) \tag{28}$$

where q is the heat flux leaving the interface and $(T_{lv} - T_v)$ is the interfacial temperature difference. Combining Eqs. (4) and (28), h_{lv} can be expressed as

$$h_{lv} = \frac{q}{(T_{lv} - T_v)} = \frac{a\dot{m}\Delta h_m}{\dot{m} - b(P_l - P_v)} \tag{29}$$

This expression for h_{lv} does not require the knowledge of T_{lv} as a function of the distance along the substrate, which is impossible to measure experimentally. Whereas, the experimentally obtained film thickness profile, which is a measure of the pressure field, can be analyzed, using the proposed model, to obtain the pressure drop, $(P_l - P_v)$, across the liquid–vapor interface and the mass flux, $\dot{m}$, as functions of film thickness or distance (DasGupta et al., 1993b). These, combined with the thermophysical properties of the liquid (to calculate a, b, and Δh_m), are used to evaluate the numerical values of the heat transfer coefficients. It is noted that though the heat transfer coefficient is for the interface, it is connected to the liquid–solid interactions by its dependence on the pressure field.

Figures 9 and 10 are plots of the heat transfer coefficients as functions of film thickness. It is clear from the figures that the values of the heat transfer coefficients depend on the operating temperature (or heat input) level. The heat transfer coefficient starts from a value equal to zero in the adsorbed thin film region but increases rapidly and reaches a nearly constant value in the thicker portion of the meniscus for a specific heat input level. The value increases with increase in heat input. For clarity purposes, the large variation of h_{lv} at small film thicknesses are presented in the large figures, whereas the variation over the whole experimental range of film thickness is displayed at the inset. It is apparent from Fig. 9 that the Q = 0.0 W case for propanol was indeed very close to equilibrium, as shown by the small value of the heat transfer coefficient. We note that even though the heater was off for the isothermal cases, a very small amount of conducted heat from the uncontrolled environment could have caused the phase change as shown in Fig. 7. For a heat input case, these figures demonstrate that high evaporation rates (an h close to 10^6 W/m^2 K for propanol for a relatively small heat input of 0.54 W) are possible in a cooling device using an evaporating extended meniscus. The present study is therefore a valuable precursor to future high heat flux experiments and analysis that are needed to explore fully the heat sink potential of the contact line region of a stationary curved thin film in which the profile and fluid flow responds to the heat flux.

In Fig. 11, the conduction heat transfer resistances in the thin film and the convection resistance at the liquid–vapor interface are plotted. The figure shows that in the thinner portion of the film the conduction resistance is small compared to the resistance to evaporative heat transfer. But with the increase in the film thickness, the conduction resistance increases and can become the predominant resistance to heat transfer present in the system, as was observed by Stephan and Busse (1992).

A plot of the overall heat transfer coefficient, U, based on heat transfer from the liquid–solid interface to the vapor versus the film thickness for propanol meniscus at 0.54 W is presented in Fig. 12. U is related to the heat transfer resistances in the liquid film and at the liquid–vapor interface by the following relation:

$$\frac{1}{U} = \frac{\delta}{k} + \frac{1}{h_{lv}} \tag{30}$$

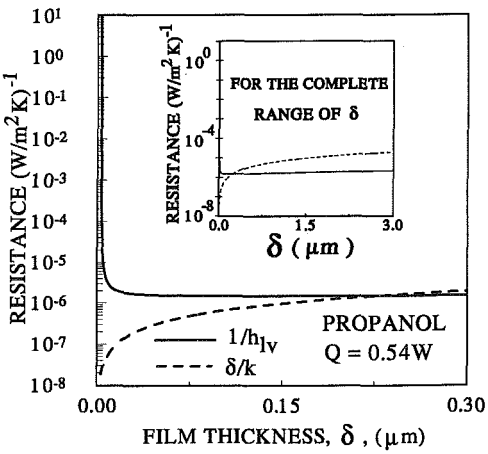

Fig. 11 Heat transfer resistances versus film thickness for propanol meniscus at Q = 0.54 W

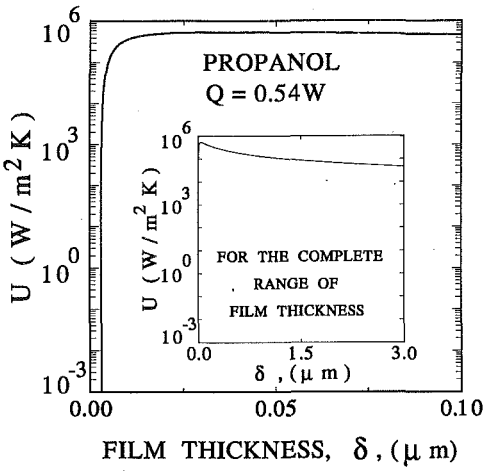

Fig. 12 Overall heat transfer coefficient versus film thickness for propanol meniscus at Q = 0.54 W

As expected, the overall heat transfer coefficient quickly reaches a maximum in the thinner portions of the film and starts to decrease thereafter due to the increase in the film conduction resistance.

In a recent theoretical study Schonberg et al. (1993) used these equations to evaluate the microscopic part of a steady meniscus in a small (2 μm) channel at high heat fluxes. Conduction in the liquid phase in the macroscopic region was calculated using finite element analysis. They found that the heat flux is a function of the long-range van der Waals dispersion forces, which represent the interfacial conditions. Their results predict that, even though the real contact angle is 0 deg (completely wetting system), the apparent contact angle can have a substantial value. This is probably due to large viscous stresses in the contact line region and can have a substantial effect on the capillary suction of the devices. Their work shows that a very high heat flux ($1.2 - 1.5 \times 10^6$ W/m^2, based on a 2 μm microchannel) is theoretically possible in a stable evaporating meniscus. However, it must be emphasized that unknowns like stability at high heat fluxes in extremely small systems have not been studied experimentally. In some preliminary experiments oscillations of the meniscus have been observed. It has also been noted that the pressure drop associated with the vapor removal from a rapidly evaporating meniscus can be substantial. Both of these phenomena are functions of the design, the working fluid, the solid substrate, the temperature level of operation, etc., and are extremely complex.

Conclusions

1 The utility of a Kelvin–Clapeyron change-of-phase heat transfer model based on interfacial thermodynamics, kinetic theory, and the augmented Young–Laplace equation is demonstrated.
2 At equilibrium, the augmented Young–Laplace equation accurately predicts the meniscus slope. The interfacial slope is a function of the heat flux.
3 The heat flux and heat transfer coefficient of an evaporating thin liquid film are strong functions of the film thickness profile, curvature, and ΔT.
4 The results from the experiments and a related theoretical study suggest that a stable evaporating meniscus with a high heat flux is possible.

Acknowledgments

This material is based on work partially supported by the National Science Foundation under grant #CTS-9123006. Any opinions, findings, and conclusions or recommendations expressed in this publication are those of the authors and do not necessarily reflect the view of the NSF.

References

Bankoff, S. G., 1990, "Dynamics and Stability of Thin Heated Films," ASME JOURNAL OF HEAT TRANSFER, Vol. 112, pp. 538–546.

Bascom, W. D., Cottington, R. L., and Singleterry, C. R., 1964, "Dynamic Surface Phenomena in the Spontaneous Spreading of Oils on Solids," *Contact Angle, Wettability and Adhesion,* R. E. Gould, ed., Adv. Chem. Ser. Vol. 43, Am. Chem. Soc., Washington, DC, pp. 355–379.

Beaglehole, D., and Christenson, H. K., 1992, "Vapor Adsorption on Mica and Silicon: Entropy Effects, Layering and Surface Forces," *J. Phys. Chem.,* Vol. 96, pp. 3395–3403.

Burelbach, J. P., Bankoff, S. G., and Davis, S. H., 1990, "Steady Thermocapillary Flows of Thin Liquid Layers. II. Experiment," *Physics of Fluids A,* Vol. 2, pp. 322–333.

Cook, R., Tung, C. Y., and Wayner, P. C., Jr., 1981, "Use of Scanning Microphotometer to Determine the Evaporative Heat Transfer Characteristics of the Contact Line Region," ASME JOURNAL OF HEAT TRANSFER, Vol. 103, pp. 325–330.

DasGupta, S., Sujanani, M., and Wayner, P. C., Jr., 1991, "Microcomputer Enhanced Optical Investigation of an Evaporating Liquid Film Controlled by a Capillary Feeder," *Proceedings of the Second World Conference on Experimental Heat Transfer, Fluid Mechanics and Thermodynamics,* J. F. Keffer et al., eds., Elsevier Science Publishing Co. Inc., New York, pp. 361–368.

DasGupta, S., and Wayner, P. C., Jr., 1993, "Use of Image Processing to Study an Evaporating Extended R113 Meniscus," *Imaging in Transport Processes,* S. Sideman and K. Hijikata, eds., Begell House Inc. Publishers, New York, Chap. 31, pp. 367–377.

DasGupta, S., Schonberg, J. A., Kim, I. Y., and Wayner, P. C., Jr., 1993a, "Use of the Augmented Young–Laplace Equation to Model Equilibrium and Evaporating Extended Menisci," *J. Colloid Interface Sci.,* Vol. 157, pp. 332–342.

DasGupta, S., Schonberg, J. A., and Wayner, P. C., Jr., 1993b, "Investigation of an Evaporating Extended Meniscus Based on the Augmented Young-Laplace Equation," ASME JOURNAL OF HEAT TRANSFER, Vol. 115, pp. 201–208.

de Feijter, J. A., 1988, "Thermodynamics of Thin Liquid Films," *Thin Liquid Films,* I. B. Ivanov, ed., Marcel Dekker, Inc., New York, pp. 1–47.

Derjaguin, B. V., and Zorin, Z. M., 1957, "Optical Study of the Adsorption and Surface Condensation of Vapors in the Vicinity of Saturation on a Smooth Surface," *Proc. 2nd Int. Conf. Surface Activity,* J. H. Schulman, ed., Butterworths, London, Vol. 2, pp. 145–152.

Derjaguin, B. V., Nerpin, S. V., and Churaev, N. V., 1965, "Effect of Film Transfer Upon Evaporation of Liquids From Capillaries," *Bull. Rilem,* Vol. 29, pp. 93–98.

Derjaguin, B. V., and Churaev, N. V., 1976, "The Definition of Disjoining Pressure and Its Importance in the Equilibrium and Flow of Thin Films," *Colloid J. USSR,* Vol. 38, pp. 438–448.

Gee, M. L., Healy, T. W., and White, L. R., 1989, "Ellipsometric Studies of Alkane Adsorption on Quartz," *J. Colloid Interface Sci.,* Vol. 131, No. 1, pp. 18–23.

Holm, F. W., and Goplen, S. P., 1979, "Heat Transfer in the Meniscus Thin Film Region," ASME JOURNAL OF HEAT TRANSFER, Vol. 101, pp. 543–547.

Ingram, B. J., 1974, "Wetting of Silica by *n*-Alkanes," *J. Chem. Soc., Faraday Trans. I.,* Vol. 70, pp. 868–876.

Kayser, R. F., Schmidt, J. W., and Moldover, M. R., 1985, "Wetting Layers and Dispersion Forces for a Fluid in Contact With a Vertical Wall," *Phys. Rev. Lett.,* Vol. 54, pp. 707–710.

Khrustalev, D., and Faghri, A., 1993, "Thermal Analysis of a Micro Heat Pipe," *Proceedings of National Heat Transfer Conference,* Atlanta, GA.

Moosman, S., and Homsy, G. M., 1980, "Evaporating Menisci of Wetting Fluids," *J. Colloid Interface Sci.,* Vol. 73, pp. 212–223,

Potash, M., Jr., and Wayner, P. C., Jr., 1972, "Evaporation From a Two-Dimensional Extended Meniscus," *Int. J. Heat Mass Transfer,* Vol. 15, pp. 1851–1863.

Renk, F., Wayner, P. C., Jr., and Homsy, G. M., 1978, "On the Transition Between a Wetting Film and a Capillary Meniscus," *J. Colloid Interface Sci.,* Vol. 67, pp. 408–414.

Schonberg, J. A., DasGupta, S., and Wayner, P. C., 1993, "An Augmented Young–Laplace Model of an Evaporating Meniscus in a Micro-channel With High Heat Flux," *Aerospace Heat Exchanger Technology 1993,* R. K. Shah and A. Hashemi, eds., Elsevier Science Publishers B. V., pp. 239–254.

Stephan, P. C., and Busse, C. A., 1992, "Analysis of the Heat Transfer Coefficient of Grooved Heat Pipe Evaporator Walls," *Int. J. Heat Mass Transfer,* Vol. 35, pp. 383–391.

Swanson, L. W., and Peterson, G. P., 1993, "The Interfacial Thermodynamics of the Capillary Structures in Micro Heat Pipes," presented at 1993 National Heat Transfer Conference, Aug. 8–11, Atlanta, GA.

Tan, M. J., Bankoff, S. G., and Davis, S. H., 1990, "Steady Thermocapillary Flows of Thin Liquid Layers. I. Theory," *Phys. Fluids A,* Vol. 2, pp. 313–321.

Teletzke, G. F., Scriven, L. E., and Davis, H. T., 1987, "How Liquids Spread on Solids," *Chem. Eng. Comm.,* Vol. 55, pp. 41–81.

Truong, J. G., and Wayner, P. C., Jr., 1987, "Effect of Capillary and Van der Waals Dispersion Forces on the Equilibrium Profile of a Wetting Liquid: Theory and Experiment," *J. Chem. Phys.,* Vol. 87, pp. 4180–4188.

Wayner, P. C., Jr., Kao, Y. K., and LaCroix, L. V., 1976, "The Interline Heat Transfer Coefficient of an Evaporating Wetting Film," *Int. J. Heat Mass Transfer,* Vol. 19, pp. 487–492.

Wayner, P. C., Jr., 1980, "Interfacial Profile in the Contact Line Region of a Finite Contact Angle System," *J. Colloid Interface Sci.,* Vol. 77, pp. 495–499.

Wayner, P. C., Jr., 1982, "Adsorption and Capillary Condensation at the Contact Line in Change of Phase Heat Transfer," *Int. J. Heat Mass Transfer,* Vol. 25, No. 5, pp. 707–713.

Wayner, P. C., Jr., 1991, "The Effect of Interfacial Mass Transport on Flow in Thin Liquid Films," *Colloids and Surfaces,* Vol. 52, pp. 71–84.

Wayner, P. C., Jr., DasGupta, S., and Schonberg, J. A., 1991, "Effect of Interfacial Forces on Evaporative Heat Transfer in a Meniscus," *U.S. Air Force Report,* No. WL-TR-91-2061.

Wu, D., and Peterson, G. P., 1991, "Investigation of the Transient Characteristics of a Micro Heat Pipe," *J. Thermophysics,* Vol. 5, pp. 129–134.

Xu, X., and Carey, V. P., 1990, "Evaporation From a Micro-grooved Surface—An Approximate Heat Transfer Model and Its Comparison With Experimental Data," *J. Thermophysics,* Vol. 4, pp. 512–520.

An Experimental and Analytical Investigation of Ice Formation From a Circular Water Jet Impinging on a Horizontal Cold Surface

M. K. Moallemi

M. N. Naraghi

Department of Mechanical and Industrial Engineering,
Polytechnic University,
Six Metrotech Center,
Brooklyn, NY 11201

The transient freezing of water impinging vertically on a subzero disk through a circular jet is studied experimentally to determine the interaction of the fluid flow and the solidification process. Experiments are performed over a range of the jet Reynolds number ($1600 < Re_i < 3500$) based on the average velocity and radius of the falling jet at the impingement point. For this range of Reynolds numbers, that corresponds to tube Reynolds numbers less than 1100, and in the absence of solidification, the thin liquid film is characterized by a smooth circular hydraulic jump whose diameter is measured and correlated with the jet Reynolds number. The solidification process is initiated away from the jet (i.e., outside of the hydraulic jump) and moves inward toward the jet. The formation and growth of ice on the cold surface affect the flow field over the surface. This effect manifests itself in the form of a rapid reduction of the hydraulic jump diameter accompanied by instability in its position until its complete disappearance. The effect of fluid flow on the solidification process is found to be a small reduction in the nucleation temperature. The ice layer profiles at different times for different values of jet Reynolds number, and Stefan numbers of the surface and jet are also measured and reported. An approximate model is developed for the calculation of the transient crust growth by neglecting the interaction between the flow and solidification. The predicted solid crust profiles are compared with the measured ones, and the extent of the flow-freezing interactions is discussed. The approximate model is also used for a parametric study of the problem for a constant temperature surface.

1 Introduction

Solidification problems in which forced convection is occurring in the melt are encountered in nature and many technologically important processes. The formation of an ice cover on a river, the freezing of water pipes, solidification of a lava stream flowing over rocks or soil, and solidification of a metal ingot are a few applications that have motivated research in this area. In some industrial processes, such as the impingement of the molten metal on a spinning disk, or coating of layers on moving sheets or tubes, and ice-making refrigerators, the impinging liquid jet solidifies on the surface. In these applications, the interaction between the growth of the frozen layer and the warm liquid flowing over it may bring forth complications in addition to the basic nonlinearity of the transient phase-change problem. Previous investigations have sought to characterize the interplay between melt flow and the solidification process from both theoretical and experimental perspectives in a variety of geometric configurations and boundary conditions. Cheung and Epstein (1984) presented a general review of the subject, and recent developments related to the materials processing are reviewed by Smith and Hoadley (1987).

Depending on the flow and surface configurations and their temperatures, there are three major aspects of flow-freezing interaction that may arise to influence the heat transfer and solidification rates. First, the motion of the interface and volumetric change due to phase change may influence the velocity field near the heat transfer surface, which may in turn affect the heat transfer rate at the interface. Second, the shape of the solidified layer may distort the flow field adjacent to it, causing a change in the convective heat transfer characteristics. Third, the variation of the heat transfer rate in the flow direction, if present, may cause a nonuniform crust growth over the cold surface. This may result in two-dimensional heat conduction in the crust, which may alter the streamwise variation of the heat transfer coefficient over the interface. There is another form of flow-freezing interaction that only arises in transient solidification under the condition that no solid nucleus is initially present on the cold surface. The fluid flow may suppress the freezing process by preventing solid nucleation beyond the limits observed in conduction controlled solidification. The freezing of supercooled liquid after the inception of solidification is known to be very rapid, and this may change the flow field near the moving interface, and as a result, the heat transfer and freezing rates. This aspect of flow-freezing interaction has received less attention compared to the other ones. The important findings of previous investigations on flow-freezing interactions in external flow geometries are briefly reviewed here, since an extensive review of melting and freezing in internal and external flows is already available (Cheung and Epstein, 1984).

Boundary layer flows over growing surfaces have been studied both experimentally (Savino and Siegel, 1967; Hirata et al., 1979; Gilpin et al., 1980) and theoretically (Lapadula and Mueller, 1966; Beauboeuf and Chapman, 1967; Savino and Siegel, 1969; Epstein, 1976; Hirata et al., 1979). The theoretical studies, with the exception of Hirata et al. (1979), are based on two important simplifying assumptions, i.e., streamwise heat

Contributed by the Heat Transfer Division and presented at the National Heat Transfer Conference, San Diego, California, August 9–12, 1992. Manuscript received by the Heat Transfer Division October 1992; revision received October 1993. Keywords: Forced Convection, Jets, Phase-Change Phenomena. Associate Technical Editor: F. P. Incropera.

conduction in the crust layer is neglected, and effects of the motion and the shape of the solid–liquid interface on the flow are assumed to be negligible. With these assumptions, the convective heat transfer coefficient (without phase change) may be used at the interface to calculate the transient growth of the crust. The extent of validity of these assumptions is examined experimentally and theoretically by Hirata et al. (1979) who studied the shape of the steady-state ice layer formed by a boundary layer flow over a constant temperature horizontal flat plate. From these works, it can be concluded that the effect of phase change on the flow field is generally insignificant for both transient and steady-state conditions, mainly because the crust formation does not cause flow constriction, the interface velocity is usually much smaller than the free-stream velocity, and the volumetric change due to phase change for most materials is too small to distort the flow field. The streamwise conduction in the crust is reported (Hirata et al., 1979) to be important only for thick crusts, deposited in flows with large cooling temperature ratios, $(T_f - T_s)/(T_\infty - T_f)$.

The interaction of fluid flow and solid nucleation is addressed in the experimental study presented by Savino and Siegel (1967) for a boundary layer flow over a flat horizontal plate. In the absence of an initial ice patch on the cold surface, the surface needs to be cooled extensively (to as low as −11°C in some cases) before ice nucleation. The temperature of the flowing water near the surface is reported to be as low as −7°C before initiation of freezing. This level of supercooling is well within the required range for inception and growth of ice crystals in the absence of water flow, i.e., 1 to 20°C supercooling depending on water quality, surface characteristics, etc. (Hallett, 1964). Therefore, no conclusions on the influence of flow on ice nucleation are drawn in this study. The formation of ice is reported to be very sudden and covering the entire surface instantaneously. This so-called *flash-freezing* is accompanied by a sudden increase in the surface and water temperatures. The abrupt crust formation over the plate and flow of latent heat in two directions away from the interface has an obvious impact on the thermal boundary layer and heat transfer over the plate, at least for a short period following the flash-freezing. The effect of flash-freezing on the boundary layer flow is not reported. This is not expected to be significant, since the ice layer is initially uniform and thin (compared to the height of the channel), and the flow adjusts to the interface shape without any significant change in the radial pressure gradient.

Phase-change heat transfer in stagnation flow has also received considerable attention. Most of the investigations are, however, focused on the jet impingement melting problem in connection with the use of hot liquid jets for drilling into ice or frozen soil, and ablation of heat shields for space-craft (cf. Cheung and Epstein, 1984). Solidification of a liquid discharged from a jet onto a chilled surface has not been examined adequately in spite of important applications in materials processing (e.g., rapid solidification, and planar continuous casting; Smith and Hoadley, 1987), ice making (ASHRAE, 1990) and nuclear technology (cf. Epstein, 1976; Cheung and Epstein, 1984). Savino et al. (1970) examined the crust formation in the stagnation region of a submerged liquid jet experimentally. Their measurements of the temporal variation of the interface position at the stagnation point are in good agreement with the predictions of a heat conduction model with a moving boundary by using a forced convection heat transfer coefficient in the interface energy balance equation. They concluded that the phase-change process does not alter the heat transfer characteristics of the impinged surface. This may be attributed to the fact that the crust growth is not extensive enough to cause flow constriction, nor is it nonuniform enough to distort the velocity field.

The main objective of this work is to develop a fundamental understanding about different aspects of flow-freezing interactions. The work is motivated by its applications in the manufacturing of ice for consumption or cold-storage via *belt-ice* method and *inverted-mold* method (ASHRAE, 1988), in which water strikes and flows over a chilled surface while forming ice on it. In view of these applications, the transient freezing of a liquid film flow, generated by an unsubmerged jet issuing vertically from a long circular pipe and impinged onto a horizontal chilled disk, is considered. For the configuration examined, the various forms of interactions between the fluid flow and its solidification mentioned above are present at a considerably more extensive level than those examined by previous investigators, i.e., crust

Nomenclature

A = coefficient in Eq. (6)
B = coefficient in Eq. (6)
c = specific heat, J/kgK
d = tube diameter, m
Fo = Fourier number = $t\alpha_s/r_i^2$
Fr_δ = Froude number = $\bar{u}/\sqrt{g\delta}$
g = gravitational acceleration, kg/m^2
h_f = latent heat, J/kg
k = thermal conductivity, W/mK
Nu = local Nusselt number based on liquid film thickness = $q_l\delta/k_l(T_b - T_f)$
p = pressure, Pa
Pr = liquid Prandtl number = ν/α
q_l = heat flux at solid/liquid interface, W/m^2
Q = volume flow rate, m^3/s
r = radial coordinate, m
r_h = radial position of hydraulic jump, m
r_i = radius of impinging jet, m
R = dimensionless radial position = r/r_i
Re_i = impingement point Reynolds number = $Q/\nu r_i$
Re_d = pipe Reynolds number = $4Q/\pi d\nu$
s = thickness of solidified layer, m
S = dimensionless thickness of solidified layer = s/r_i
Ste_j = Stefan number of jet = $c_j(T_j - T_f)/h_f$
Ste_l = local Stefan number of liquid = $c_l(T_b - T_f)/h_f$
Ste_c = Stefan number of ice/solid based on coolant temperature = $c_s(T_f - T_c)/h_f$
Ste_s = Stefan number of the solid crust = $c_s(T_f - T_s)/h_f$
t = time, s
T = temperature, K
u_r, u_z = velocity components, m/s
$\bar{u}$ = mean radial velocity = $Q/2\pi r\delta$, m/s
z = coordinate normal to surface, m
Z = dimensionless coordinate normal to surface = z/r_i
α = thermal diffusivity, m^2/s
δ = thickness of liquid film, m
Δ = dimensionless thickness of liquid film = δ/r_i
η = dimensionless coordinate for liquid film = $(z - s)/\delta$
θ = dimensionless solid (ice) temperature = $(T - T_f)/(T_f - T_s)$
θ_b = dimensionless film bulk temperature = $(T_b - T_f)/(T_j - T_f)$
θ_l = dimensionless liquid temperature = $(T_l - T_f)/(T_j - T_f)$
θ_s = dimensionless surface temperature = $(T_s - T_f)/(T_f - T_c)$
κ = ratio of phase properties = $(c_s k_l)/(c_l k_s)$
ν = kinematic viscosity, m^2/s
ρ = density, kg/m^3

Subscripts

b = bulk
c = coolant (ethylene glycol)
f = fusion/interface
h = hydraulic jump
i = impingement point
j = jet
l = liquid film
s = solid (ice) or surface
∞ = free stream/surface

Superscripts

init = nucleation initiation

formations in plane stagnation or boundary layer flows. This is mainly due to the presence of a free surface in the case of spreading film flow that makes it more sensitive to the crust formation. The strong streamwise dependency of the flow and heat transfer is also likely to give rise to nonuniform crust growth over the surface, which may in turn influence the film flow and heat transfer over the surface. Moreover, since transient solidification is considered, with no ice patch present on the surface initially, the interplay of flow and solid nucleation is also examined. These features make the situation examined conducive to a phenomenological study of different forms of interaction between the liquid flow and its solidification.

Experiments are performed over a range of Reynolds number, $1600 < \mathrm{Re}_i < 3500$ or $270 < \mathrm{Re}_d < 1100$, for which the radial spread of the impinging jet is characterized by a thin fast-moving laminar film that goes through a smooth circular *hydraulic jump* (a rather rapid increase of depth and reduction of mean velocity) at a certain radial distance. For different Stefan numbers of jet and surface, the temporal and spatial variations of the surface and the liquid temperatures are measured and reported to illustrate the flow-freezing interactions. The ice layer profiles at different times for different values of Reynolds number, and Stefan numbers of the surface and jet, are also measured and reported. Based on the experimental findings, two approximate models are developed, one for the calculation of the heat transfer by a radially spreading flow, and one for the calculation of solidification with forced convection heat transfer at the interface, after neglecting the interaction between the two processes. The predicted solid crust profiles are compared with the experimental data to quantify further the flow-freezing interactions.

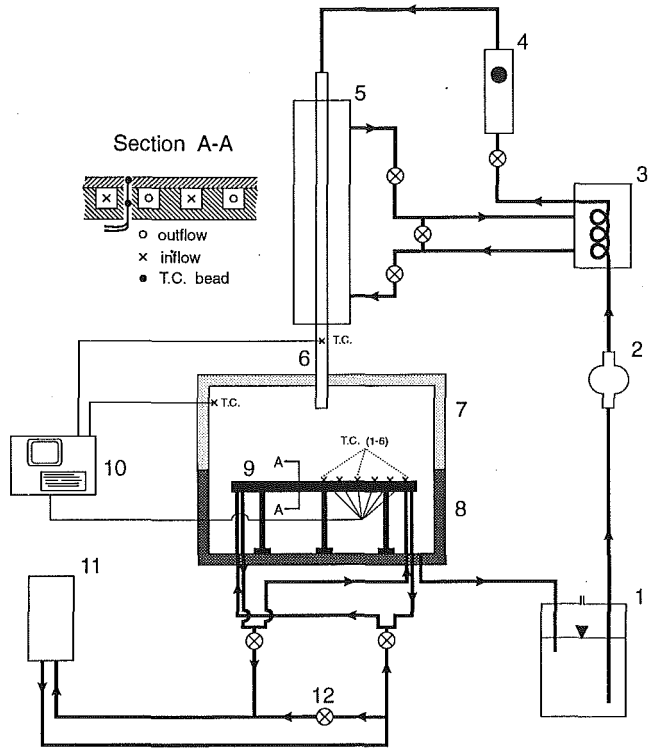

Fig. 1 Schematic diagram of the setup: (1) liquid reservoir, (2) pump, (3) constant-temperature bath, (4) rotameter flowmeter, (5) jet heat exchanger, (6) jet pipe, (7) and (8) test enclosure, (9) disk plate, (10) data acquisition system, (11) constant temperature bath for plate, (12) plate valves. Thermocouples #1 to #6, on the disk surface, are positioned at r = 0.0, 2.0, 5.0, 8.5, 11.5, and 14.0 cm, respectively.

2 Experimental Setup and Procedure

The experiments are carried out using a closed-loop water jet system, shown schematically in Fig. 1. Deionized water is pumped from a cylindrical reservoir of 2.7 liters volume, through a helical coil made of thin-walled copper tubing (6.4 mm ID) that is placed in a constant-temperature bath (Neslab model RTE-210). This is connected via a rotameter flowmeter to a long circular tube (6.3 mm ID, and 100 diameters long) from which the vertical jet issued. This long tube is chosen to provide fully developed laminar velocity profiles at its exit (i.e., Re_d ranged from 270 to 1100). Flows with higher tube Reynolds numbers are not examined to preclude the propagation of the tube and jet flow fluctuations into the spreading film flow. All tests are conducted for a tube to surface spacing of 9.0 cm, for which the falling jet is free of interfacial instabilities.

The thermostated liquid from the constant-temperature bath is circulated in a heat exchanger jacket that covered two thirds of the jet tube, and fine adjustment of the liquid jet temperature is achieved through an appropriate valve setting. The jet strikes a circular horizontal surface of 30.5 cm diameter consisting of two copper disks of 11.2 and 5.6 mm thickness, of which the thicker one is machined to provide a double-loop, multipass, countercurrent passage for the coolant when covered by the thinner disk. The two disks are furnace-brazed together for good thermal contact, and the top surface is ground, lapped, and polished to better than ± 5 μm flatness across the disk diameter, with final disk heat exchanger thickness 17.2 mm. The disk is provided with three adjustable legs for accurate leveling. A second constant-temperature bath (Neslab model RTE-220) is connected through a valve system to the double-loop coolant passage in the disk. The disk is placed in a plexiglass cubical box with 35 cm long sides and 12 mm thick walls in which the liquid dripping from the disk is collected. The jet is attached to the enclosure box vertically with its axis exactly aligned with the axis of the disk, with provisions for orientation adjustment and height variation. A ribbon of cotton gauze (with 0.5 mm × 0.5 mm mesh) is wrapped flush around the disk to reduce surface tension on the edge of the disk and facilitate radial spread of the jet with a smooth and stable hydraulic jump. With this downstream flow condition, the measurements indicate that the film thickness is essentially constant far from the hydraulic jump; and from this, it is inferred that the disk diameter is not a defining parameter of the problem, for the flow conditions examined. The tubings and valves, the liquid reservoir, and the test enclosure box (with the exception of the observation side during the data runs) are insulated using styrofoam and polyurethane foam to reduce the heat gain from the environment.

A total of 16 copper-constantan thermocouples (wire diameter 0.127 mm) are installed on the disk: four to measure coolant temperatures at the inlets and outlets on the disk heat exchanger, and 12 to measure the disk temperatures. These are installed at six radial positions: at the center of the disk (i.e., the jet impingement point), and at radii 0.0, 2.0, 5.0, 8.5, 11.5, and 14.0 cm. The thermocouple wires are inserted from the back through 2.0-mm-diam holes drilled in the copper disks, and the tips are either flush-mounted on the surface or glued to the copper 8.0 mm below the surface using a high thermal conductivity epoxy. Two fine thermocouples (wire diameter 0.01 mm) are installed on an $x-y$ traversing system for measuring the liquid film temperature at different radial positions on the disk. Besides these, the liquid bulk temperatures before the jet discharge and after dripping from the disk, and the air temperatures at two points in the test enclosure are also measured. The thermocouples are connected to an HP-3497 data acquisition system interfaced with a computer that controlled data collection and storage at preselected time intervals. All the thermocouples are calibrated with accuracies of ± 0.15°C for the regular ones, and ± 0.07°C for the fine ones used for liquid temperature measurements (all with 95 percent confidence).

The jet flow rate is measured using a rotameter that is calibrated with an accuracy of ± 7 percent. The diameter of the jet

at the impingement point, the profile of the overriding liquid film (before any solidification run), and thickness of the crust are measured using a needle attached to an $x-y$ traversing system. The traversing system is fixed to the enclosure box and has a resolution and repeatability of 0.01 mm in either direction. The needle is connected to a multimeter where it shows sensitivity to any contact of the needle with water, ice, and the disk surface.

The preparation for a typical experiment begins by setting the jet flow rate and temperature at preselected values, and the constant-temperature bath connected to the disk heat exchanger at about 0.5°C below the desired coolant temperature at the inlet of the heat exchanger to compensate for the heat gain in the valves and tubings. With the jet at its preselected temperature impinging onto the disk, the valves on the surface coolant line are opened slightly and adjusted as required until the surface attained an average constant temperature close to 0°C. Meanwhile, jet diameter and height of the liquid film over the surface are measured with the traversing system. The test enclosure is then closed and covered with insulating foam. Final adjustments of jet and surface temperatures are made while waiting for the air in the enclosure to drop below 5°C to start the data run. An analytical sensitivity study (Naraghi, 1994) indicates that this condition is adequate to keep the heat gain through the free surface to less than 5 percent of the heat transferred to the disk heat exchanger by the liquid film during any experiment. The enclosure is cooled passively by the disk and cold liquid film flow for over one hour for its temperature to stabilize.

A data run begins by closing the coolant bypass and fully opening the intake and return valves of the disk heat exchanger. Throughout a typical run, the temperatures of the plate, coolant, and liquid are measured at preselected time intervals, ranging from 2 to 10 seconds depending on the duration of the run. A video camera that is installed at a 45 deg angle from the jet axis is used to record the hydraulic jump and any interaction between solidification and fluid flow during the run. The thickness of ice crust on the surface cannot be measured during the run without interfering with the thin film flow. Therefore, a run is terminated at an appointed time to measure the solid thickness over the disk; and for other solidification times, new runs have to be started from the beginning with the same initial flow and temperature conditions. The flow field and crust thickness did not reach a steady-state condition for any of the cases examined due to the flow instabilities generated by the growing solid. Therefore, it was decided to stop any given run soon after the flow lost its radial characteristics. The termination sequence is started by diverting the water jet away from the disk, and tilting the disk to remove all the remaining water from the surface. An absorbent paper is then used to collect any left-over droplets. This sequence of operations requires about 15 seconds. The thickness of the ice layer is then determined by first measuring the height of the ice covered surface and subtracting the measured height of the surface after the ice is melted by a heat gun. In both measurements, the needle and traversing system with electric contact indicator are used. The estimated uncertainty for the ice thickness measurement is ±0.05 mm.

3 Analysis

In this section, an approximate solution is developed for the modeling of the transient growth of ice crusts over a horizontal disk in the presence of a radially spreading water flow. The intent is to use the prediction of this model along with the experimental data to infer the effects of flow on the crust growth, and the influence of the crust growth on the convective heat transfer at the solid–liquid interface. Therefore, the experimental conditions are modeled closely. Specifically, the temporal and radial variations of the disk temperature are accounted for in the model formulation. The effect of solid nucleation, however, is not included by starting the modeling at a time t_0 when the disk is covered with a known layer of ice, $s(r, t_0)$, and the liquid is not supercooled.

Two approximate models, one for the crust growth calculation and one for the heat transfer from the radially spreading flow, are developed by assuming that the interactions between the two are negligible. The schematic of the problem and the coordinates are shown in Fig. 2. Using the experimental data as inputs for these two models, the transient crust profiles are calculated and compared with the experimental data at the equivalent solidification times to quantify the flow-freezing interaction. The development of the two models and the associated calculation procedure are presented next, and the results of the calculations and the parametric studies are presented in the results and discussion section.

3.1 Transient Crust Growth. The solidification of a liquid confined to a wall (disk) with time-varying surface temperature, and a convective heat transfer condition at the solid–liquid interface, is considered. The radial heat conduction in the solid is assumed to be negligible. This is well justified where the crust thickness is thin compared to the radial position. The model is applied to the region downstream of the impingement point, where the convective heat transfer at the interface does not vary significantly in the flow direction, and thus, one-dimensional conduction in the solid is valid. The thermophysical properties are taken to be independent of temperature, and solidification of a pure substance is modeled with a definite freezing temperature, T_f, characterized by a sharp liquid–solid interface.

With these assumptions, the conservation of energy in the solid and at the interface (at any radial position r) can be written as:

$$\frac{\partial T}{\partial t} = \alpha_s \frac{\partial^2 T}{\partial z^2} \quad \text{for} \quad 0 \le z \le s(t), \quad t \ge t_0, \tag{1}$$

$$k_s \left.\frac{dT}{dz}\right|_{z=s} - q_l = \rho h_f \frac{ds}{dt} \quad \text{at} \quad z = s(t), \tag{2}$$

where q_l is the convective heat transfer at the interface, which is treated as an unknown function of radial position on the disk that will be calculated from the model presented in the next part. The initial and boundary conditions of the problem are as follows:

$$\begin{aligned} &\text{at } t = t_0 \quad T = T_s \quad \text{for} \quad 0 \le z \le s_0 = s(t_0), \\ &\text{at } z = 0 \quad T = T_s \quad \text{for} \quad t \ge t_0, \\ &\text{at } z = s(t) \quad T = T_f \quad \text{for} \quad t \ge t_0. \end{aligned} \tag{3}$$

In these equations, the surface temperature T_s and the ice thickness s are functions of time and also the radial position.

At any radial position, the one-dimensional transient phase-change problem formulated above is solved by an integral method (Ozisik, 1980), after rendering the governing equations dimensionless using the following dimensionless variables:

$$\text{Fo} = \frac{t\alpha_s}{r_i^2}, \quad Z = \frac{z}{r_i}, \quad S = \frac{s}{r_i}, \quad \text{and} \quad \theta = \frac{T - T_f}{T_f - T_s}. \tag{4}$$

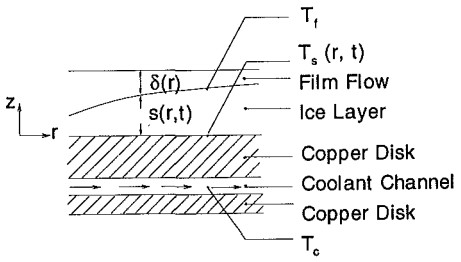

Fig. 2 Schematic of the physical problem and coordinates

Equation (1) is integrated over the crust thickness, and the result upon applying Leibnitz's rule and the boundary condition at the interface reduces to

$$\left.\frac{\partial\theta}{\partial Z}\right|_{Z=S} - \left.\frac{\partial\theta}{\partial Z}\right|_{Z=0} = \frac{1}{\mathrm{Ste}_s}\frac{d}{d\mathrm{Fo}}\left[\mathrm{Ste}_s\int_0^{S(\mathrm{Fo})}\theta dZ\right] \quad (5)$$

To simplify the solution of Eq. (5), the temperature profile is approximated by a quadratic polynomial in z,

$$\theta = -A[1 - (Z/S)] + B[1 - (Z/S)^2] \quad (6)$$

The temperature boundary condition at the disk surface and the energy balance at the interface, Eq. (2), are enforced to determine the coefficients A and B (Ozisik, 1980, p. 418),

$$A = \frac{1}{\mathrm{Ste}_s}\left[\frac{c_s k_l}{c_l k_s}\frac{S}{2\Delta}\mathrm{Ste}_l\mathrm{Nu} - 1 + \sqrt{\left(\frac{c_s k_l}{c_l k_s}\frac{S}{2\Delta} - 1\right)^2 + 2\mathrm{Ste}_s}\right], \quad (7a)$$

$$B = \frac{1}{\mathrm{Ste}_s}\left[\frac{c_s k_l}{c_l k_s}\frac{S}{2\Delta}\mathrm{Ste}_l\mathrm{Nu} - 1 - \mathrm{Ste}_s + \sqrt{\left(\frac{c_s k_l}{c_l k_s}\frac{S}{2\Delta}\mathrm{Ste}_l\mathrm{Nu} - 1\right)^2 + 2\mathrm{Ste}_s}\right]. \quad (7b)$$

The dimensionless variables introduced in Eq. (7) are the local Stefan number of liquid film $\mathrm{Ste}_l = c_l(T_b - T_f)/h_f$, which depends on radial position through $T_b(r)$, the temporal radial Stefan number of the solidified crust $c_s(T_f - T_s)/h_f$ with $T_s(r, t)$, and the local Nusselt number of the over-riding liquid film $\mathrm{Nu} = q_l\delta/k_l(T_b - T_f)$, which is also a function of the radial position on the disk. Substituting Eqs. (2) and (6) into Eq. (5) results in

$$\frac{S}{6}\frac{d}{d\mathrm{Fo}}\left[S\left(5 + 2\mathrm{Ste}_s + \frac{\kappa S}{2\Delta}\mathrm{Ste}_l\mathrm{Nu} - \sqrt{\left(\frac{\kappa S}{2\Delta}\mathrm{Ste}_l\mathrm{Nu} - 1\right)^2 + 2\mathrm{Ste}_s}\right)\right] = 1 + 2\mathrm{Ste}_s - \frac{3\kappa S}{2\Delta}\mathrm{Ste}_l\mathrm{Nu} - \sqrt{\left(\frac{\kappa S}{2\Delta}\mathrm{Ste}_l\mathrm{Nu} - 1\right)^2 + 2\mathrm{Ste}_s}, \quad (8)$$

where κ is the ratio of the properties of the two phases defined in the nomenclature, and is equal to the ratio of thermal diffusivity of liquid to that of solid where the densities of the two phases are the same.

For situations where convective heat transfer q_l is negligible (i.e., $\mathrm{Ste}_l\mathrm{Nu} = 0$) and surface temperature T_s is constant (i.e., $\mathrm{Ste}_s = \mathrm{const}$), Eq. (8) renders a closed-form solution for $S(t)$ (Ozisik, 1980). For the general conditions considered here, Eq. (8) is integrated over time using a fourth-order Runge–Kutta scheme (Press et al., 1989). The marching integration is performed starting at a time Fo_0 at which the crust profile is measured, and at radial positions at which the transient disk temperature measurements are available. In the modeling of experiments for which jet temperature is close to the fusion temperature ($T_j \leq 0.3$°C), the convective heat transfer at the interface q_l is taken to be negligible at radial positions beyond the hydraulic jump. For higher T_j, q_l is evaluated from the model presented in the next section for heat transfer by a radially spreading thin film flow.

3.2 Heat Transfer by a Radially Spreading Film Flow. The intent of the present analysis is to evaluate the convective heat transfer rate q_l at the solid liquid interface. For this purpose, the effect of solidification on the flow is assumed to be negligible. The integral boundary layer method is employed to predict the heat transfer rate to a constant temperature horizontal surface from a radially spreading thin film flow. The film flow model and calculation is similar to that of Rahman et al. (1991), and is used for the region beyond the hydraulic jump and includes the gravity effects. The heat transfer model is developed for the same region, and the bulk film temperature at the jump, which is an independent parameter of this model, is calculated in terms of jet temperature and flow conditions using the analytical relations for heat transfer inside the jump (Liu et al., 1991).

To formulate the model equations, steady-state, two-dimensional (r, z), laminar flow of a Newtonian fluid over a horizontal, constant temperature surface is considered. In other words, the effects of crust formation and the variation of its thickness on the film flow are assumed negligible. The boundary layer assumptions are taken to be valid, and surface tension effects are negligible. The thermophysical properties of the fluid are assumed to be constant. After applying these assumptions, the governing equations of the problem, the conservation equations for mass, momentum, and energy, take the following forms:

$$\frac{\partial u_z}{\partial z} + \frac{1}{r}\frac{\partial}{\partial r}(ru_r) = 0, \quad (9)$$

$$u_r\frac{\partial u_r}{\partial r} + u_z\frac{\partial u_r}{\partial r} = \frac{-1}{\rho}\frac{\partial p}{\partial r} + \nu\frac{\partial^2 u_r}{\partial z^2}, \quad (10)$$

$$\frac{\partial p}{\partial z} + \rho g = 0, \quad (11)$$

$$u_r\frac{\partial T_l}{\partial r} + u_z\frac{\partial T_l}{\partial z} = \alpha_l\frac{\partial^2 T_l}{\partial z^2}. \quad (12)$$

These equations are applied for $s \leq z \leq s + \delta(r)$, where $\delta(r)$ is the local film thickness. On the surface, $z = 0$, the boundary conditions are

$$u_r = u_z = 0, \quad \text{and} \quad T_l = T_f. \quad (13)$$

The boundary conditions at the free surface, $z = s + \delta(r)$, are:

$$\frac{\partial u_r}{\partial z} = 0, \quad p = p_a, \quad \text{and} \quad \frac{\partial T_l}{\partial z} = 0. \quad (14)$$

At the jump, $r = r_h$,

$$u_z = 0, \quad \text{and} \quad \delta(r_h) = \delta_h, \quad (15)$$

The pressure and its radial gradient may be expressed in terms of the film thickness by integrating Eq. (11) over the film thickness, using the pressure boundary condition of Eq. (14), to yield

$$p = p_a + \rho g(s + \delta - z), \quad \text{and} \quad \frac{\partial p}{\partial r} = \rho g\frac{d\delta}{dr}. \quad (16)$$

Since the crust thickness is assumed constant in the flow calculations, the radial variation of the liquid film thickness and the heat transfer at the solid surface is calculated by first integrating Eqs. (9)–(11) over the film thickness. Integrating Eq. (9) yields

$$u_z|_\delta = \frac{-1}{r}\frac{\partial}{\partial r}\int_s^{s+\delta} ru_r dz + \frac{d\delta}{dr}u_r|_{s+\delta} \quad (17)$$

The integral on the right is related to the flow rate Q of the film via

$$Q = 2\pi r\delta\bar{u} = 2\pi r\int_s^{s+\delta} u_r dz. \quad (18)$$

With the assumption that Q is constant, Eq. (17) is simplified as

$$u_z|_{s+\delta} = \frac{d\delta}{dr}u_r|_{s+\delta}. \quad (19)$$

Substituting Eq. (16) into Eq. (10) and integrating with respect to z, with the velocity boundary conditions (13) and (14), and after applying Eq. (19), the result is

$$\frac{1}{r}\frac{d}{dr}\left[\int_s^{s+\delta} ru_r^2 dz\right] = -g\delta\frac{d\delta}{dr} - \nu\left.\frac{\partial u_r}{\partial z}\right|_{z=s}. \tag{20}$$

The energy equation is integrated over the film thickness after first combining it with the continuity equation. The result upon applying the boundary conditions (13) and (14) reduces to

$$\frac{1}{r}\frac{d}{dr}\left[\int_s^{s+\delta} ru_r T_l dz\right] = -\alpha_l\left.\frac{\partial T_l}{\partial z}\right|_{z=s}. \tag{21}$$

To simplify the solutions of Eqs. (19) and (20), the velocity and temperature profiles are approximated by quadratic polynomials in $\eta = (z - s)/\delta$. The boundary conditions, Eqs. (13) and (14), are satisfied by

$$\frac{u_r}{\bar{u}} = 3\eta\left(1 - \frac{\eta}{2}\right), \quad \text{and}$$

$$\theta_l = \frac{T_l - T_f}{T_j - T_f} = \frac{5\theta_b}{2}\eta\left(1 - \frac{\eta}{2}\right), \tag{22}$$

where $\bar{u}$ is the mean radial velocity defined by Eq. (18), and θ_b is the dimensionless liquid bulk temperature defined as

$$\bar{u}\theta_b = \int_0^1 u_r\theta_l d\eta. \tag{23}$$

The assumed velocity and temperature profiles are best suited, and used, in the region behind the hydraulic jump where equality of the hydrodynamic and thermal boundary layers is a valid assumption for water with $\mathrm{Pr} = O(5)$.

Substituting the velocity and temperature profiles into Eqs. (20) and (21), integrating, and using Eq. (18) to eliminate $\bar{u}$ results in the following nonlinear ordinary differential equations:

$$\left(1 - \frac{5\Delta}{6\Delta_h \mathrm{Fr}_{\delta h}^2}\right)\frac{d\Delta}{dR} = \frac{5\pi R}{\mathrm{Re}_i} - \frac{\Delta}{R}, \tag{24}$$

$$\frac{d\theta_b}{dR} = \frac{-5\pi R\theta_b}{\mathrm{Pr}\,\mathrm{Re}_i\Delta}. \tag{25}$$

where Re_i is the impingement point Reynolds number defined as $Q/\nu r_i$, and $\mathrm{Fr}_{\delta h}$ is the local Froude number calculated at the hydraulic jump.

The liquid film thickness Δ is calculated by numerical integration of Eq. (24), starting from the hydraulic jump $R = R_h$ at which the film thickness Δ_h (and via these $\mathrm{Fr}_{\delta h}$) is known from experimental measurements. Knowing $\Delta(R)$, the bulk temperature of the liquid film is evaluated via marching integration of Eq. (25). This requires the knowledge of dimensionless bulk temperature θ_b at the jump position that could not be measured accurately and without affecting the flow. The analytical correlations of Liu et al. (1991) is used to calculate the variation of the liquid bulk temperature from the impingement point to the hydraulic jump, in terms of jet Reynolds number. The heat transfer at the surface, required for the crust growth model, is then calculated from

$$q_l = k_l\left.\frac{\partial T_l}{\partial z}\right|_{z=s} = \frac{k_l(T_j - T_f)}{\delta}\left.\frac{\partial\theta_l}{\partial\eta}\right|_{\eta=0}. \tag{26}$$

Using the temperature profile of Eq. (22) to cast q_l in the form appearing in Eq. (8) results

$$\mathrm{Ste}_l\mathrm{Nu} = 2.5\theta_b\mathrm{Ste}_j \tag{27}$$

where Ste_j is the liquid Stefan number based on the jet temperature.

4 Results and Discussion

4.1 General Observations. The disk heat exchanger is designed to provide a constant surface temperature. This is not, however, achieved under all jet and surface conditions due to extensive radial variation of the heat transfer rate over the surface. Since the jet is cooled by the surface, the high heat transfer rate in the vicinity of the impingement point causes the surface temperature in this region to rise above the set value. In the region beyond the hydraulic jump, however, the heat transfer from the slow-moving and thicker liquid film is relatively lower and considerably more uniform, resulting in surface temperatures that are lower and closer to the coolant temperature. (Throughout this work, coolant is referred to the thermostated liquid, water–ethylene–glycol mixture, which is passed through the multipass disk heat exchanger; and is not to be mistaken for the liquid water jet whose spread and solidification over the disk are studied.) Examination of the temperature measurements indicates that although there is a considerable temperature nonuniformity over the entire disk, the surface temperature variation in the two zones (i.e., preceding the jump, and beyond the jump) is relatively much lower. The results presented here are limited to the experimental conditions for which the maximum temperature deviation among thermocouples 3 to 6 (positioned from $r = 5.0$ to 14.0 cm, Fig. 1) is less than 0.5°C at any instant during an experimental run. Due to the strong transient nature of the problem, however, the temporal variation of the disk surface temperature is quite extensive during the early stages of the solidification. The disk surface usually attains a steady-state temperature only after the disk is covered by a layer of ice, which has already affected the film flow. Therefore, the cases examined are described according to the average of coolant temperatures at the inlet and the outlet of the disk heat exchanger, T_c, which remains essentially constant throughout any experimental run. For a general characterization of the surface, a Stefan number Ste_c is defined based on T_c, which the disk temperature approaches at long solidification times. For the solid/ice layer, a Stefan number Ste_s is defined based on the local and temporal surface temperature, as revealed by the approximate analysis. Similarly, two Stefan numbers are defined for the liquid: Ste_j based on the jet temperature is used to describe the experiments, and Ste_l based on the local bulk temperature of the liquid is used to characterize the liquid film in the analysis. Therefore, where Ste_c and Ste_j are used as the independent parameter, the results are dependent on the disk material, and the effectiveness of the disk heat exchanger.

As explained in the experimental procedure, a data run is started by closing the bypass valve and opening the inlet and outlet valves to the disk heat exchanger at a time when the jet is at its preselected temperature and the disk surface temperature is close to 0°C (±0.2°C). The temperature histories of the liquid jet and film, as well as temperatures at three points on the disk surface, are presented in Figs. 3(*a*) and 3(*b*), for two different run times but for the same flow, coolant, and surface conditions. The temperature magnitudes and gradients for the two runs are in excellent agreement, indicating that the tests are quite reproducible. This is an important characteristic of the experimental setup and procedure, and permits comparing the crust profiles of successive runs, in the discussion on the transient growth of the crust. Moreover, this justifies the use of solid thickness measurements at an early time as an input to the approximate model for calculation of the crust profiles at later times. The difference in the liquid temperature measurements for the two runs is due to the slight change in the position of the corresponding thermocouple between the runs (closer to the free surface for the run of Fig. 3(*a*) compared to the run of Fig. 3(*b*)). The location of maximum surface temperature is at the impingement point since the liquid is cooled by the surface; therefore, it is likely that the liquid temperature at some time before the initiation of solidification at some downstream point (at $r = 11.5$ cm in Fig. 3) drops below the surface temperature at the impingement point.

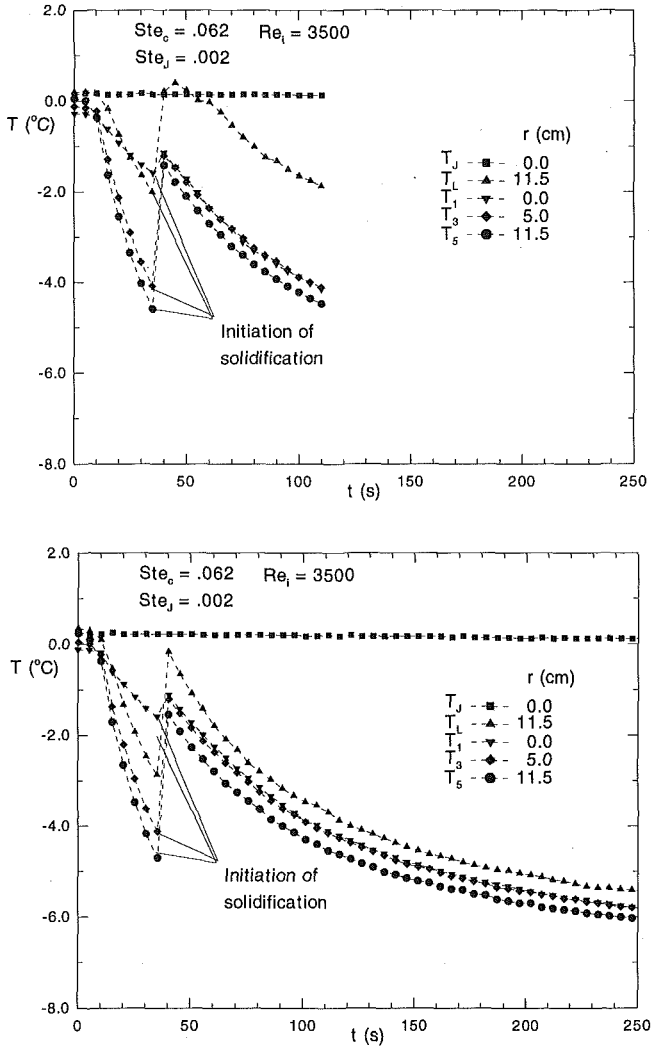

Fig. 3 Temporal variations of surface, liquid jet, and film temperatures for Re_i = 3500, Ste_c = 0.062, and Ste_j = 0.002 for total run times: (*a*) t = 110 s, and (*b*) t = 250 s

The transient temperatures of the surface and liquid in Fig. 3 show that cooling of the surface is accompanied by supercooling of the water film prior to ice nucleation. Nucleation of ice, a sudden appearance of a ring, takes place in the outer region of the disk (near the fifth and sixth thermocouples), and is followed by its rapid propagation toward the impingement point. The rapid solidification of supercooled liquids is a known phenomenon, referred to as *flash-freezing* (Savino and Siegel, 1967), and has been observed for water (Hallett, 1964; Savino and Siegel, 1967) and liquid metals (Smith and Hoadley, 1987). Comparisons of the temperature histories and video records of the experiments reveal that the instantaneous increase in the liquid and surface temperatures coincides with the sudden appearance and rapid propagation and growth of the ice crust. The temperature histories of the surface and the liquid indicate that during the rapid solidification period, the latent heat released at the interface is transferred in two directions, i.e., into the crust and the disk, and also into the liquid flowing over the crust. These results are particularly in quantitative agreement with Savino and Siegel (1967), who had reported the presence of a supercooled liquid layer over a chilled plane and subsequent temperature inversion after inception of solidification. For the data run of Fig. 3(*a*), the liquid thermocouple is close to the free surface, and measures liquid temperatures above the jet temperature soon after the nucleation of ice. This is followed by a gradual decrease in the liquid temperature until the thermocouple is covered with ice. For the data run of Fig. 3(*b*), the liquid thermocouple is very close to the surface, and is covered with ice during the short flash freezing period.

4.2 Effects of Water Flow on Ice Nucleation. Solid nucleation is a complex phenomenon governed by a host of parameters; including liquid composition (purity), surface roughness and morphology, and cooling rate, to name a few (Hallett, 1964; Savino and Siegel, 1967; Smith and Hoadley, 1987). To investigate the influence of the flow on nucleation, in addition to the solidification experiments with the jet flow, a series of experiments is conducted with the same setup and following the same procedure, but without the impinging jet. Instead of the jet flow, the disk is covered with a 5-mm-thick film of stagnant water, to simulate the limiting no-flow condition (i.e., $Re_i = 0$). The measured time histories of liquid and surface temperatures are very much like those with the jet running (e.g., Fig. 3), and demonstrate a period of liquid supercooling followed by nucleation and rapid growth of the ice layer. The average surface temperature at the initiation of solidification T_s^{init} and the corresponding initiation time t_s^{init} for these measurements are summarized in Table 1. Similar data from the experiments with the jet running, and for different values of Re_i, Ste_j, and Ste_c are also included in the table for comparison. In the presence of the jet flow, T_s^{init} is calculated by averaging the readings of the fourth, fifth, and sixth thermocouples over which ice formation starts. Results of successive and repeated runs are shown in a single row. The comparison reveals that fluid flow causes a drop of order 1°C in the nucleation temperature (from −4.1°C for stagnant fluid to −4.9°C for jet impingement flow). The change in nucleation temperature appears to be independent of the jet Reynolds number (as long as there is a flow). However, the range of Re_i examined is too small to draw any firm conclusions.

The results presented in Table 1 indicate a large variation in the solid nucleation time for the experiments in which the coolant temperature is close to (but still lower than) the solid nucleation temperature. An example of this observation is shown in Figs. 4(*a*) and 4(*b*) where the temporal variations of the liquid and surface temperatures are presented for the same set of experimental conditions, Re_i = 2250, Ste_j = 0.009 (T_j = 0.7°C), and Ste_c = 0.035 (T_c = −5.6°C). The figures illustrate similar initial conditions and cooling rates before and after solid nucleation, and the only difference noticed is in the times of solid nucleation. From these figures and the results presented in Table 1, it is inferred that if the surface and liquid are cooled very slowly when the nucleation temperature is reached, the solid nucleation becomes a random phenomenon that may occur at any time, and even the nucleation temperature may be passed slightly without initiation of solidification. The temporal variations of the disk surface temperatures before the initiation of solidification, such as those shown in Figs. 3 and 4, are approximated by an exponentially decaying function of time,

Table 1 Variation of the solid nucleation time and temperature with jet Reynolds number, and liquid and coolant temperatures

Re_i	Ste_j / T_j(°C)	Ste_c / T_c(°C)	t_s^{init} (s)	T_s^{init}(°C)	τ (s)
*	*	$T_c \geq -4.0$	≥ 600	no solidif.	—
*	*	0.026 / −4.2	150 to 300	−4.0 to −4.2	100 to 130
*	*	0.028 / −4.5	44 to 66	−4.0 to −4.1	73 to 85
*	*	0.035 / −5.6	28 to 50	−4.0 to −4.1	35 to 40
≥ 1600	0.004 / 0.3	$T_c \geq -5.2$	≥ 600	no solidif.	—
1600	0.004 / 0.3	0.035 / −5.6	90 to 170	−4.8 to −5.0	50 to 55
1720	0.039 / 3.1	0.035 / −5.6	150 to 240	−4.8 to −5.1	51 to 110
2250	0.009 / 0.7	0.035 / −5.6	100 to 275	−4.6 to −5.0	53 to 145
1720	0.039 / 3.1	0.062 / −10.0	30 to 38	−4.7 to −4.9	39 to 41
2950	0.005 / 0.4	0.062 / −10.0	36 to 40	−4.7 to −4.9	43 to 45
3500	0.002 / 0.2	0.062 / −10.0	35 to 45	−4.7 to −4.8	44 to 46

* No jet flow

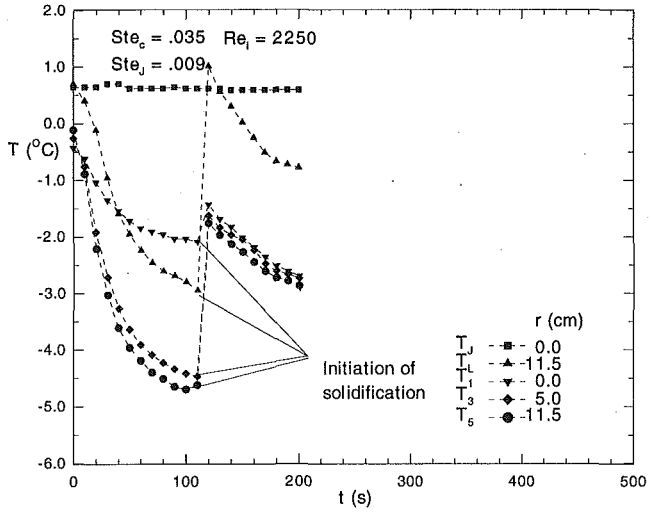

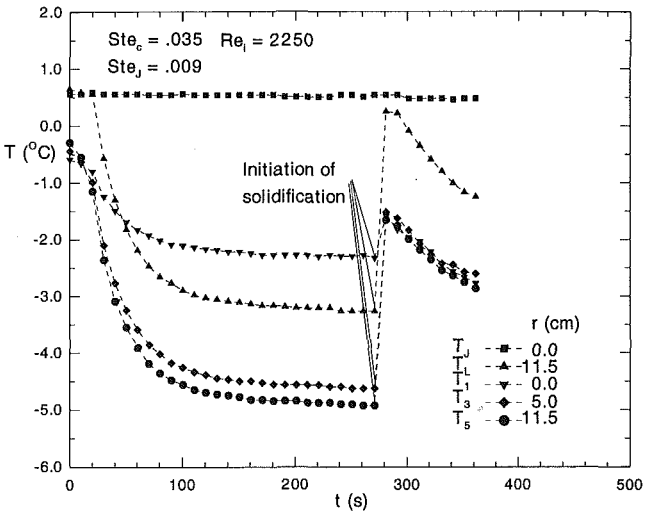

Fig. 4 Temporal variations of surface, liquid jet, and film temperatures for Re$_i$ = 2250, Ste$_c$ = 0.035, and Ste$_J$ = 0.009 for total run times: (*a*) t = 200 s, and (*b*) t = 360 s

$$\frac{T - T_c}{T_f - T_c} = C \exp\left(\frac{-t}{\tau}\right). \tag{28}$$

The least-squares method is used to determine the coefficient C and the time constant τ for different data runs, and the results are presented in Table 1. The results indicate that the time constant is small and remains almost constant in repeat and successive runs in experiments for which the coolant temperature is well below the nucleation temperature. On the other hand, in experiments for which the coolant temperature is close to the nucleation temperature, τ has relatively larger values and changes significantly in repeat and successive runs. This again indicates that when the surface cooling rate is slow, the solid nucleation becomes a random phenomenon. This observation is common to experiments with and without the jet flow. The effects of jet Reynolds number and temperature on the randomness of solid nucleation time appears to be insignificant.

4.3 Effects of Solidification on Flow. In the absence of solidification, liquid film thickness over the disk is measured for several values of Reynolds number, and the radial variations of film thickness preceding the jump are compared with those of Ishigai et al. (1977) in Fig. 5. The analytical solution of Watson (1964) for laminar film spreading is also shown in the figure for comparison. The figure indicates good agreement between present results and previous work. The radial position of the jump is also measured for different values of Reynolds number both with the needle-traversing system and from the video records. These results are also in good agreement with the published data, and establish confidence in the experimental setup and measurement technique using video records.

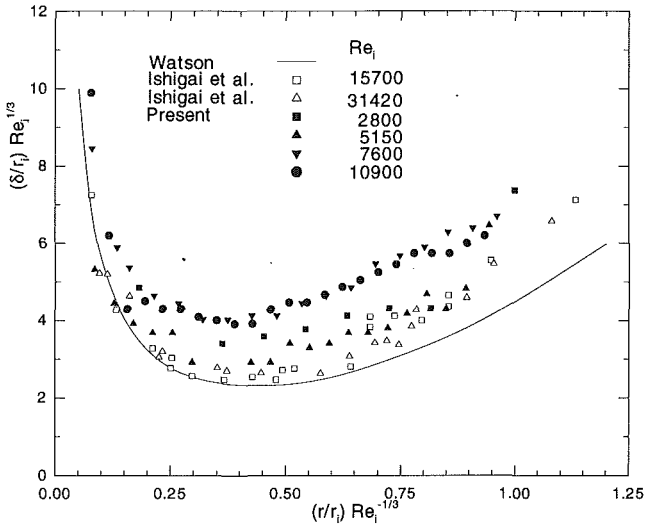

Fig. 5 Radial variation of liquid film thickness inside the hydraulic jump

As an indicator of the influence of transient crust growth on the film flow, temporal variation of jump radius is presented in Figs. 6 and 7. These figures show that the jump radius remains constant during the early stage of solidification (the flash-freezing period and some time after it) when the crust growth is rapid but uniform. The jump radius then starts to decrease until complete disappearance of the jump. The drop in the jump radius is usually accompanied by flow instabilities in the form of an oscillatory radial motion of the jump. Examination of radial variation of the crust, which will be presented next, indicates that the reduction of the jump radius and its eventual closing is due to the nonuniform growth of the crust over the disk. This is in agreement with observations of Craik et al. (1981), who studied transient behavior of a circular jump produced on the bottom horizontal surface of an initially empty tank. They reported that with

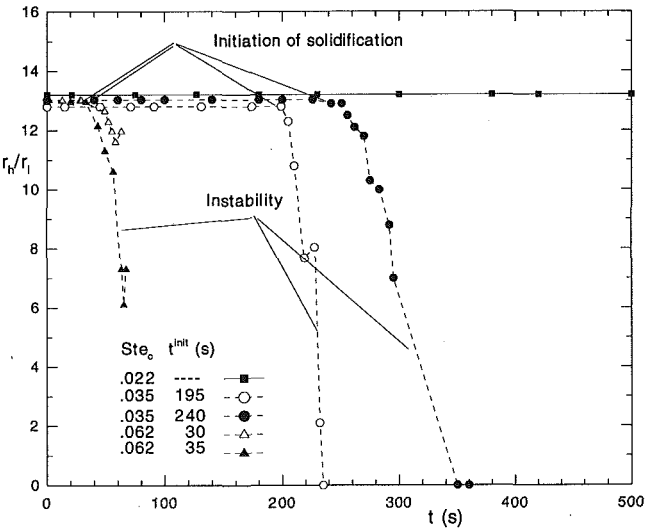

Fig. 6 Effect of Ste$_c$ on temporal variation of jump radius due to crust formation, for Re$_i$ = 1720 and Ste$_J$ = 0.039 (T_J = 3.1°C)

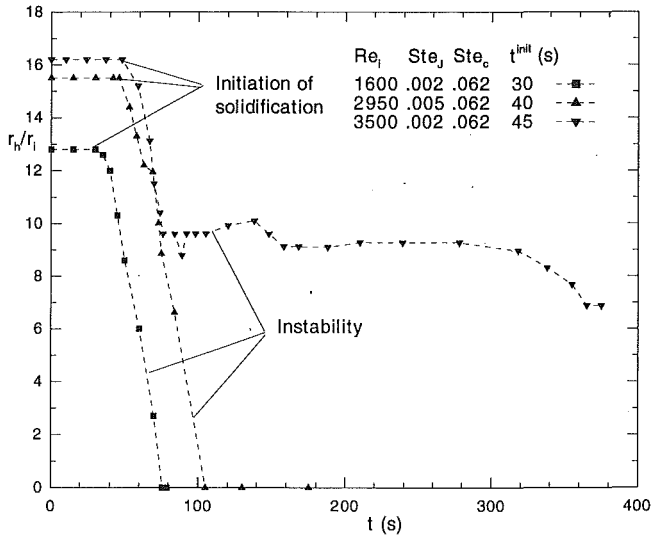

Fig. 7 Effect of Re_i on temporal variation of jump radius due to crust formation, for $Ste_c = 0.062$ ($T_c = -10.0$°C)

the increase in the outer film thickness, due to the filling of the tank with time (increasing the weir), the jump became unstable and its radius decreased until its disappearance.

For $Re_i = 1720$ and $Ste_j = 0.009$, the temporal variations of the jump radius for two different coolant temperatures are shown in Fig. 6. This figure indicates that the decrease in the jump radius occurs sooner and at a faster rate after solidification starts for runs with lower coolant temperatures. The lower coolant temperature (higher Ste_c) runs are noted to have higher crust growth rates and, as will be shown later, are characterized by more radially nonuniform crusts. The jump instability is also noticed to be more violent for higher growth rate cases. Figure 6 also shows that the random nature of nucleation promoted by slow cooling rates for $Ste_c = 0.035$ ($T_c = -5.6$°C) does not change the rate of change of jump radius after initiation of solidification. Slower crust growth rates, however, have been noticed in some cases to prolong the period of jump instability.

For constant coolant temperature ($T_c = -10.0$°C, $Ste_c = 0.062$), Fig. 7 illustrates that a decrease in Re_i results in the close-up of the jump to start sooner and at a faster rate. This is also attributed to the increase in the nonuniformity and growth rate of the crust with the decrease of Re_i. The small change in the jet temperature in these runs, from $T_j = 0.2$ to 0.4°C ($Ste_j = 0.002$ to 0.005) is not expected to have any effect, as is also revealed by the parametric study. For the case with $Re_i = 3500$, the hydraulic jump does not close, as may be noticed in Fig. 7, but is converted to an almost vertical standing wave at the bottom of a hill of ice formed at the stagnation point. This case will be discussed again later when crust profiles are presented.

4.4 Effects of Flow on Crust Growth. Figure 8 presents the crust thickness profiles of three successive runs for the same jet and surface conditions. The profiles are designated by their solidification time, taken to be the time interval between the nucleation time (i.e., the time of rapid temperature rise in the surface and liquid) and the termination time of a run. The locations of the jump on the disk at the corresponding times are also shown in the figure. Over the outer region of the jump, the crust thickness increases slowly with r, due to the radial decrease of heat transfer coefficient and the film bulk temperature. The profiles have wavy fluctuations of small amplitude and long wavelength that may be attributed to the presence of a low-intensity flow instability. In the inner jump region, and early into the solidification process, the crust thickness is nonuniform due to the extensive variation in the heat transfer coefficient in this region. When the jet temperature is close to solidification temperature T_f, the interplay of flow and freezing influences impingement point heat transfer characteristics in a way that the rate of crust growth at the impingement point exceeds the growth rate in its neighborhood, and the crust takes the shape of a hill at this point. This phenomenon (i.e., growth of an ice valley into an ice hill) is also observed in a run with $Re_i = 2950$, $Ste_c = 0.062$, and $Ste_j = 0.002$, and can be explained in terms of mutual interaction of flow instabilities and heat transfer. For a liquid jet at or close to its freezing temperature, any small radial change in heat transfer rate (induced by a flow instability) in the jet impingement region yields a small relative maximum crust thickness in the vicinity of the impingement point. The flow adjusts itself to the new crust shape, and this in turn amplifies the initial instability in the flow and heat transfer. The crust will eventually divert the flow to accommodate the proper form of heat transfer rate compatible with the crust shape.

The predictions of the analytical solution are also shown in Fig. 8. As explained in detail in the analysis, the calculations of the crust growth are performed behind the hydraulic jump, at the points where the surface temperatures are measured (i.e., at thermocouples number two to six). The ice crust profile measured 65 seconds after initiation of solidification and the transient surface temperature measurements are used as input for the solution procedure to calculate the crust thicknesses at the later times. The predictions of the approximate solution are in good agreement with the experimental data, and reveal insignificant flow-freezing interaction (that is neglected in the model) after the initial period of solidification and beyond the hydraulic jump.

The ice crust profiles over the disk at three different times after nucleation are presented in Fig. 9 for $Re_i = 2250$, $Ste_j = 0.012$ ($T_j = 1.0$°C), and $Ste_c = 0.035$. The ice crust profile measured 35 seconds after initiation of solidification and the transient surface temperature measurements are used as input for the solution procedure to calculate the crust thicknesses at the later times. The disagreement between the predicted and measured crust thickness is less than 10 percent, which is of the order of amplitude of the crust profile wave, and does not show a consistent trend (i.e., the predicted crust thicknesses are not always higher or always lower then the measured values). It may be inferred that the crust waviness is due to flow instability and its influence on the convective heat transfer, which was neglected in the analysis. Compared with the crust profiles of Fig. 8, the profiles of Fig. 9 are steeper near the impingement point, and have a higher level of waviness. This is attributed to the higher convective heat trans-

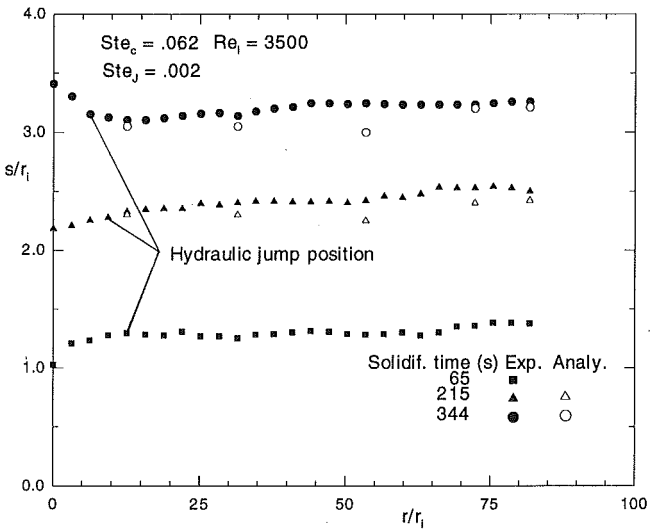

Fig. 8 Radial variation of ice crust thickness at different times from nucleation, for $Ste_c = 0.062$, $Ste_j = 0.002$, and $Re_i = 3500$ ($r_i = 1.80$ mm)

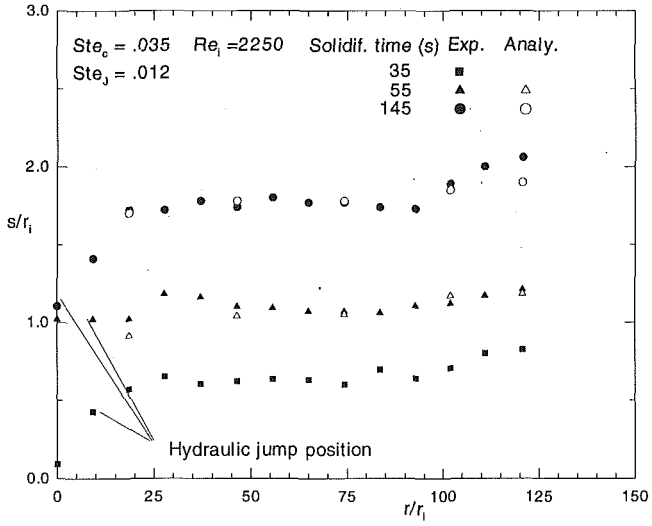

Fig. 9 Radial variation of ice crust thickness at different times from nucleation, for Ste$_c$ = 0.035, Ste$_j$ = 0.012, and Re$_i$ = 2250 (r_i = 1.1 mm)

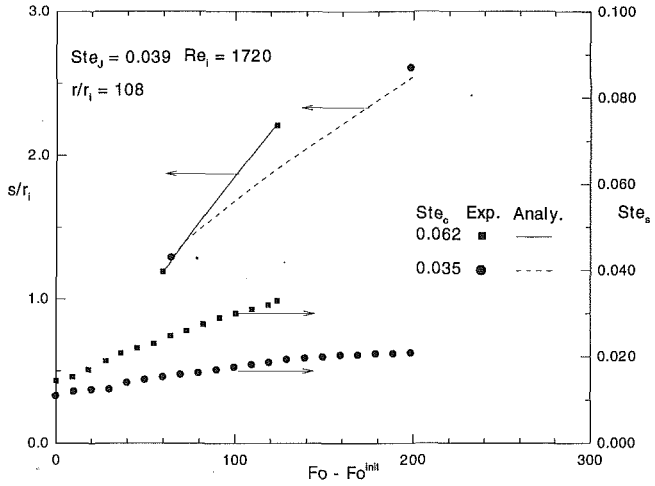

Fig. 10 Comparison of the measured and predicted transient crust thickness (left axis) and the temporal variation of surface Stefan number (right axis) at r/r_i = 108 (r_i = 0.8 mm) for Ste$_j$ = 0.039, and Re$_i$ = 1720

fer for the runs of Fig. 9 due to the relatively higher liquid jet temperature. High heat transfer rate in the impingement region also prevents formation of ice hills at the stagnation point in Fig. 9.

Figure 10 presents the temporal variations of crust thickness at r = 8.5 cm (r/r_i = 108) for Re$_i$ = 1720, Ste$_j$ = 0.039 (T_j = 3.1°C) for two values of coolant Stefan number. This radial position corresponds to the location of thermocouple number 4, measurements of which are also presented in dimensionless form Ste$_s$ in Fig. 10. Using the transient surface Stefan number Ste$_s$ and the early time crust thickness, the approximate model is employed to calculate the crust thicknesses at the later time at which the crust profile is measured. The results of this calculation are in very good agreement with the measurements, as may be seen in Fig. 10. The figure indicates that the crust growth is faster for the higher coolant Stefan number, which is expected. The early part of the transient crust thickness lines may appear to be contradicting the general trend, as the crust thickness for the case with the smaller Ste$_c$ (the dashed line) is higher than the crust thickness for the run with the larger Ste$_c$ (the solid line). This apparent discrepancy is due to the difference in the crust thickness growths during the flash-freezing period, which is not accounted for in the analysis.

It needs to be emphasized here that a parametric experimental study of the problem is not meant in presenting Figs. 8–10. A parametric experimental study is prohibited by the multiplicity of the governing parameters, and the fact that each experiment has to be conducted several times to collect transient crust growth data. Figures 8–10 are presented with the intention to validate the theoretical model for the range of independent parameters considered, and through this, assess the significance of the flow-freezing interactions.

4.5 Parametric Results. The theoretical model indicates that the governing parameters of the problem are jet Reynolds number Re$_i$, the fluid Prandtl number Pr, and the jet and surface Stefan numbers. Moreover, since the film flow beyond the hydraulic jump is modeled, the radial position of the hydraulic jump R_h, and the liquid film thickness Δ_h and bulk temperature θ_{bh} at this point are the other input parameters of the model. The values of R_h and Δ_h are measured in the absence of solidification for a range of Re$_i$ (Naraghi, 1994), and are used in the calculations. The bulk film temperature at the jump is calculated in terms of the jet parameters (i.e., Re$_i$ and Ste$_j$) using the analytical relations for heat transfer inside the jump reported by Liu et al. (1991). The results presented in this section are calculated for a disk with uniform surface temperature (i.e., constant Ste$_s$), whereas the model predictions of the crust thickness presented earlier are calculated with the measured transient surface temperature in order to be able to compare them with the measured crust profiles. To account for the solid nucleation and the subsequent flash-freezing, the marching integration in time is started at Fo$_1$, at which the disk is assumed to be covered with a uniform S = 1, thick layer of ice. The results are produced for water, with its thermophysical properties evaluated at 0.0°C.

The effects of jet Reynolds number and temperature on the transient growth of the ice crust at a fixed point on the disk (R = $3R_h$) are shown in Fig. 11. The figure indicates that the crust growth is independent of Re$_i$ if the jet is issued at the fusion temperature of the liquid, i.e., Ste$_j$ = 0. This is expected, since in the absence of a temperature gradient in the over-riding liquid film, the convective heat flux vanishes at the interface (q_l = 0 in Eq. (2) or Ste$_l$Nu = 0 in Eq. (8)), and the solidification rate becomes independent of the liquid film flow, as well as radial position on the constant surface temperature disk. This is consistent with the theoretical model that neglects any mechanical in-

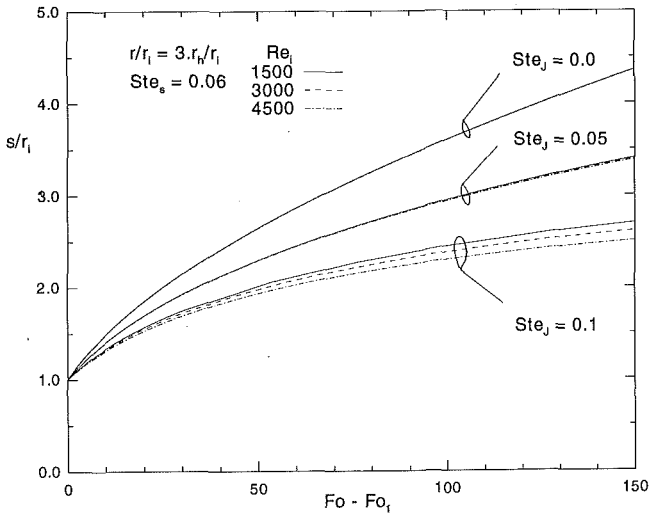

Fig. 11 Effects of Re$_i$ and jet Stefan number on the transient thickness of the crust at a point on disk at constant surface temperature

fluence from the film flow on solidification, and does not allow liquid supercooling. For a fixed Ste_s, an increase in Re_i results in a thinner crust if Ste_j is greater than zero. The crust growth is also slower for higher Ste_j at a fixed Re_i, and its sensitivity to a change in jet temperature is much greater than a change in the jet Reynolds number.

The effects of surface temperature and the jet flow on the transient crust thickness at a radial position on the disk are presented in Fig. 12. The figure shows that for a fixed Ste_j and at any Re_i, the crust grows faster if Ste_s is increased (i.e., surface temperature is reduced). A decrease in the jet Reynolds number also results in a thicker crust at a constant Ste_s, but this effect is more pronounced for lower surface temperatures. For $Ste_j = 0.05$ and $Re_i = 3000$, the effect of surface temperature on the transient thickness of the crust at three radial positions on the disk is shown in Fig. 13. The figure indicates that the solidified crust is generally thicker at larger radial distances, for fixed surface and jet conditions. This is essentially due to the radial decrease of the convective heat transfer at the interface. When the convective heat flux vanishes at the interface ($Ste_j = 0$), as mentioned earlier, the crust thickness becomes independent of the radial position as well as the jet Reynolds number.

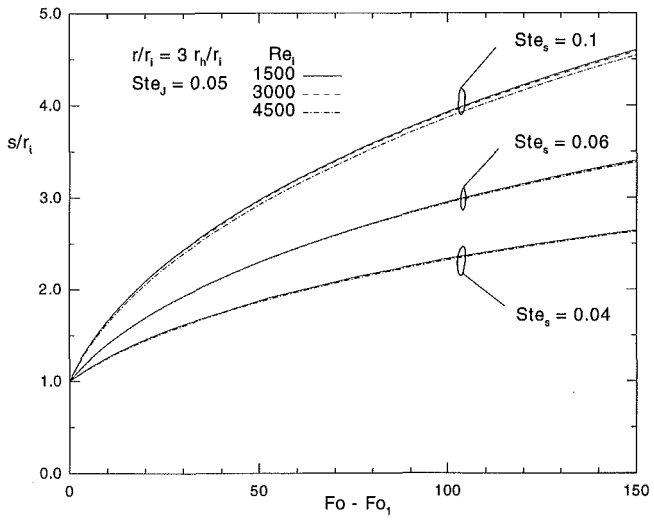

Fig. 12 Effects of Re_i and surface Stefan number on the transient thickness of the crust at a point on disk for a constant jet temperature

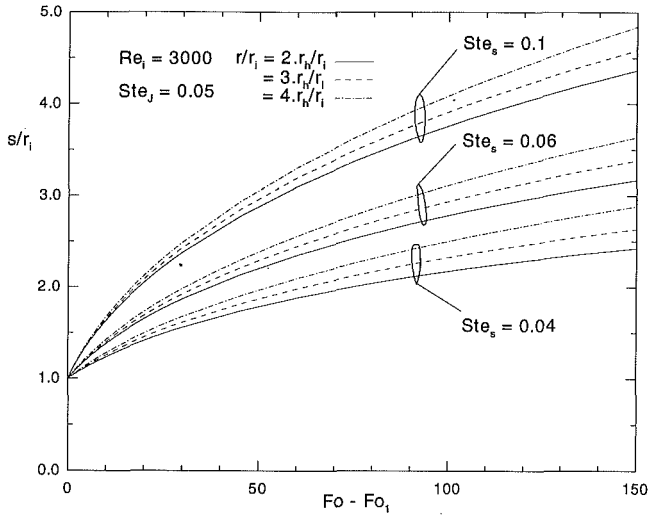

Fig. 13 Effects of the surface Stefan number on the transient thickness of the crust at different points on disk for a constant jet temperature and flow rate

Conclusions

The transient freezing of water impinging on a subzero disk through a circular jet is studied experimentally. Different aspects of flow-freezing interaction are investigated for a range of jet Reynolds number and Stefan numbers based on the jet and the coolant temperatures. After a period of liquid subcooling, the solidification process is initiated in the form of flash-freezing in the outer region of the hydraulic jump, and moves inward toward the impingement point. The effect of fluid flow on the solidification process is a small reduction in the nucleation temperature. The formation and growth of ice on the cold surface affects the flow field over the surface. This effect manifests itself in the form of a rapid reduction of the hydraulic jump radius accompanied by instability in its position until its complete disappearance.

The temporal and spatial variations of the ice crust are used to explain the interplay of water flow and heat transfer in defining the transient thickness of the crust, and the flow and heat transfer instabilities produced by the nonuniform growth of the crust. A theoretical model is developed assuming that the effect of the crust growth on the over-riding film flow is negligible. With this assumption, the problem of film flow and heat transferred from it to the interface is solved independent of the solidification problem. The ice crust profile predictions of the approximate model are in good agreement with the experimental measurements, validating the model assumptions and the corresponding solution procedure for the range of parameters examined. Most importantly, this indicates that the effect of solidification and crust growth on the heat transfer characteristics of the over-riding liquid film is in fact negligible. The theoretical model is used for a parametric study of the problem. The results indicate that the crust growth is slower for larger Re_i, and more significantly so for higher jet temperatures. The model predictions also show that the radial nonuniformity of the crust is due to the radial variation of the convective heat transfer, which also intensifies with an increase in the jet Reynolds number and temperature.

References

ASHRAE, 1988, *Equipment,* American Society of Heating, Refrigerating and Air-Conditioning Engineers, Inc., Atlanta, GA.

ASHRAE, 1990, *Refrigeration,* American Society of Heating, Refrigerating and Air-Conditioning Engineers, Inc., Atlanta, GA.

Beauboeuf, R. T., and Chapman, A. J., 1967, "Freezing of Fluids in Forced Flow," *International Journal of Heat and Mass Transfer,* Vol. 10, pp. 1581–1587.

Cheung, F. B., and Epstein, M., 1984, "Solidification and Melting in Fluid Flow," in: *Advances in Transport Processes,* Vol. 3, A. S. Majumdar and R. A. Mashelkar, eds., Wiley Eastern Ltd., New Delhi, pp. 35–117.

Craik, A. D. D., Latham, R. C., Fawkes, M. J., and Gribbon, P. W. F., 1981, "The Circular Hydraulic Jump," *Journal of Fluid Mechanics,* Vol. 112, pp. 347–362.

Epstein, M., 1976, "The Growth and Decay of a Frozen Layer in Forced Flow," *International Journal of Heat and Mass Transfer,* Vol. 19, pp. 1281–1288.

Gilpin, R. R., Hirata, T., and Cheng, K. C., 1980, "Wave Formation and Heat Transfer at an Ice–Water Interface in the Presence of a Turbulent Flow," *Journal of Fluid Mechanics,* Vol. 99, Part 3, pp. 619–640.

Hallett, J., 1964, "Experimental Studies of the Crystalization of Supercooled Water," *Journal of Atmospheric Science,* Vol. 21, No. 6, pp. 671–682.

Hirata, T., Gilpin, R. R., Cheng, K. C., and Gates, E. M., 1979, "The Steady State Ice Layer Profile on a Constant Temperature Plate in a Forced Convection Flow—I. Laminar Regime," *International Journal of Heat and Mass Transfer,* Vol. 22, pp. 1425–1433.

Ishigai, S., Nakanishi, S., Mizuno, M., and Imamura, T., 1977, "Heat Transfer of the Impinging Round Water Jet in the Interference Zone of Film Flow Along the Wall," *Bulletin of the JSME,* Vol. 20, No. 139, pp. 85–92.

Lapadula, C. L., and Mueller, W. K., 1966, "Heat Conduction With Solidification and a Convective Boundary Condition at the Freezing Front," *International Journal of Heat and Mass Transfer,* Vol. 9, pp. 702–704.

Liu, X., Lienhard, J. H. V., and Lombara, J. S., 1991, "Convective Heat Transfer by Impingement of Circular Liquid Jets," ASME JOURNAL OF HEAT TRANSFER, Vol. 113, pp. 571–582.

Naraghi, M. N., 1994, "An Experimental and Analytical Investigation of Fluid Flow and Heat Transfer Interactions With Solidification of a Liquid Jet Impinging Onto a Horizontal Surface," Polytechnic University, New York.

Özişik, M. N., 1980, *Heat Conduction,* Wiley, New York.

Press, W. H., Flannery, B. P., Teukolsky, S. A., and Vetterling, W. T., 1989, *Numerical Recipes,* Cambridge University Press, Cambridge, United Kingdom, p. 554.

Rahman, M. M., Hankey, W. L., and Faghri, A., 1991, "Analysis of the Fluid Flow and Heat Transfer in a Thin Liquid Film in the Presence and Absence of Gravity," *International Journal of Heat and Mass Transfer,* Vol. 34, No. 1, pp. 103–114.

Savino, J. M., and Siegel, R., 1967, "Experimental and Analytical Study of the Transient Solidification of a Warm Liquid Flowing Over a Chilled Flat Plate," NASA TN D-4015.

Savino, J. M., and Siegel, R., 1969, "An Analytical Solution for Solidification of a Moving Warm Liquid Onto an Isothermal Cold Wall," *International Journal of Heat and Mass Transfer,* Vol. 12, pp. 803–809.

Savino, J. M., Zumdieck, J. F., and Siegel, R., 1970, "Experimental Study of Freezing and Melting of Flowing Warm Water at a Stagnation Point of a Cold Plate," *Proceedings of the 4th International Heat Transfer Conference,* Paper Cu 2.10.

Smith, T. J., and Hoadley, A. F. A., 1987, "Recent Developments in Modeling Metal Flow and Solidification," in: *Modeling of Flow and Solidification of Metals,* T. J. Smith, ed., Martinus Nijhoff Publishers, Dodrecht–Boston–Lancaster, pp. 277–302.

Watson, E. J., 1964, "The Radial Spread of a Liquid Jet Over a Horizontal Plane," *Journal of Fluid Mechanics,* Vol. 20, Part 3, pp. 481–499.

S. A. Fomin[1]
Visiting Research Associate Professor.

P. S. Wei
Professor.
Mem. ASME

Institute of Mechanical Engineering,
National Sun Yat-Sen University,
Kaohsiung, Taiwan

V. A. Chugunov
Professor,
Applied Mathematics Department,
Kazan State University,
Russian Federation

Melting Solid Plug Between Two Coaxial Pipes by a Moving Heat Source in the Inner Pipe

Melting of a solid plug in the gap between two coaxial pipes by inserting a moving heat source in the inner pipe is investigated. Using a scale analysis, closed-form solutions for temperatures of liquid in the inner pipe, solid plug and liquid in the annular gap, and the surrounding medium around the outer pipe are determined. It is shown that eight independent dimensionless parameters are required to specify the entire process. The effects of independent parameters on the shapes of the molten region in the gap are found. The analysis and results provided are useful for the design of oil pipes.

Introduction

Over the exploitation of various types of coaxial pipelines and heat exchangers in industry, plugs are sometimes formed either in the inner pipe or in the annulus between pipes. This problem can readily occur at a low surrounding temperature in cold regions in the world. In the oil industry a steel casing pipe is run in the borehole to protect walls of the well from contaminations, erosion, or cracking. The other smaller tubing is inserted inside and used for boring, pumping, or cleaning the well. Coaxial pipes are occasionally plugged by solid paraffin setting on the walls, especially at low surrounding temperature. Aside from a common paraffin plug in the tubing, the plug in the annulus also forms in the case of pumping oil through the gap between the tubing and casing. This method has been used to separate oil from different oil strata. The oil from the lower stratum with a higher pressure goes through the tubing while that of the upper stratum with a low pressure flows through the annulus. Another example of paraffin plugging the annulus is in ordinary rod-pumping wells. In rod-pump wells a rod-pump is provided to "suck" the oil from an oil bearing formation under low pressure. In such wells, paraffin plugging sometimes occurs in the annulus.

Paraffin plugging in the tubing can be solved by using special cutters, or resistive heating or thermopenetrators. Since surface temperatures of the thermoelectrical penetrator are higher than the melting point of paraffin, a close contact between them induces melting. The contact melting process has been studied in detail by Moallemi and Viskanta (1986) and Fomin and Cheng (1991). These studies deal with fundamental features of contact melting rather than a specific technique.

In order to remove the solid plug from the annulus, a heat source can be inserted in the inner tube. Different kinds of heat sources used for this purpose were discussed by Sadykov et al. (1976). The most effective and least expensive source of energy results from a chemical reaction of thermite (Ivanov and Sadykov, 1986). One example is $Fe_2O_3 + 2Al = Al_2O_3 + 2Fe$ (e.g., Gaskell, 1981). Thermite is a substance that can burn in any medium without supplying oxygen. Thermite is made in cylindrical-shaped units with the same diameter as the tubing and a length of around 2 m so that they can be readily placed in series in a cartridge. The cartridge suspended by a cable then is sunk into the bore hole at an approximate level of plugs. When the lower end of one thermite unit is burned, the cartridge moves up or down the bore hole by the cable to enhance melting of solid paraffin. As the combustion front of thermite moves upward the molten region of paraffin grows in the same direction.

In the present work, melting solid paraffin in the gap between two coaxial pipes by inserting a moving heat source in the inner pipe is studied. Although the present model is mainly proposed for oil pipes, a similar method and result can be applied for different annular piping systems or heat exchangers involving phase change. Using a scale analysis, the mathematical model is constructed and justified, and control dimensionless parameters are determined. A relevant design and quantitative evaluation for velocities of the cartridge and combustion front, selections and arrangements of different heat sources, and materials of pipes therefore are expected.

System Model and Analysis

Consider coaxial pipes in an oil well, as illustrated in Fig. 1(a). The outer pipe (or casing) is surrounded by rock. Since oil went through the annular gap between pipes, paraffin solidifies and blocks the flow of oil. Hence thermite is required to burn in the inner pipe (or the production tubing). Energy released by combustion is convected downward and melts the solid paraffin through the inner pipe. The absolute velocity of the cartridge within which the thermite is burned is V_0. The combustion front in the thermite sustains an upward relative velocity V_c. The resulting absolute velocity V of the heat source therefore is $V_0 + V_c$. By attaching a cylindrical coordinate system at the combustion front, as illustrated in Fig. 1(b), the burned thermite and solid paraffin (and rock) move downward at relative speeds $-V_c$ and $-V$, respectively. In order to simplify the analysis the major assumptions made are the following:

1 Heat transfer is in a quasi-steady state observed form the combustion front.
2 The ratio of the gap between coaxial pipes to the interior radius of the inner pipe is small. In reality, its range is between 0.1 and 0.7. Choosing this ratio as a small perturbation parameter, the present work can be considered as a zeroth-order approximation. The main features of the process can be simply revealed.
3 Free convection between coaxial pipes is ignored due to the narrow gap. In oil pipes the relevance also results from a highly viscous paraffin.
4 The Peclet numbers in thermite, rock, and paraffin are around 100 or higher. They were estimated by choosing an interior radius of the inner pipe of 3×10^{-2} m, a gap of 10^{-2} m, speeds of combustion of around 3–5 mm/s (Malt-

[1] On sabbatical leave from Applied Mathematics Department, Kazan State University, Russian Federation.

Contributed by the Heat Transfer Division for publication in the JOURNAL OF HEAT TRANSFER. Manuscript received by the Heat Transfer Division June 1993; revision received February 1994. Keywords: Modeling and Scaling, Moving Boundaries, Phase-Change Phenomena. Associate Technical Editor: Y. Bayazitoglu.

cev et al., 1977; Ivanov and Sadykov, 1986; Arhipov, 1992), and thermal diffusivities of 10^{-6}, 0.8×10^{-6}, and 1.5×10^{-7} m^2/s for burned thermite, rock, and paraffin, respectively (Maltcev et al., 1977).

5 Temperature at the combustion front T_c is above 1000 K (Maltcev et al., 1977; Arhipov, 1992), which is estimated by choosing the specific heat $c_5 \approx 1000$ J/kg-K and energy released for combustion 10^6 J/kg provided by Sadykov et al. (1976) and Arhipov (1992). The melting temperature of paraffin is around 310 K. Hence, the ratio of temperature differences $\psi = (T_m - T_\infty)/(T_c - T_m) \sim 0.1$.

6 Physical and thermal properties are chosen to be mean values within the temperature range considered.

Governing Equations and Boundary Conditions. With the above-mentioned assumptions, energy equations of paraffin, rock, and thermite reduce to

$$-V_i \frac{\partial T_i}{\partial y} = \alpha_i \left[\frac{\partial^2 T_i}{\partial y^2} + \frac{1}{r} \frac{\partial}{\partial r} \left(r \frac{\partial T_i}{\partial r} \right) \right] \tag{1}$$

where the velocity $V_i = V$ for the subscript $i = 1, 2, 3$ indicting regions of rock, molten, and solid paraffin, respectively, while the velocity $V_i = V_c$ for the subscript $i = 4, 5$ represents regions of the burned and unburned thermite, respectively. Energy balance between latent heat and conduction at the interface of solid and molten paraffin $f(y) \equiv r_m(y) - r_1$ is

$$\rho_3 V L \frac{df}{dy} = -k_3 \frac{\partial T_3}{\partial r} + k_2 \frac{\partial T_2}{\partial r} + \left(k_3 \frac{\partial T_3}{\partial y} - k_2 \frac{\partial T_2}{\partial y} \right) \frac{df}{dy} \tag{2}$$

Energy transport across inner and outer pipes yields, respectively (Incropera and DeWitt, 1990)

$$T_{i_{r=r_1}} - T_{j_{r=r_t}} = \hat{R}_1 k_i \frac{\partial T_i}{\partial r_{r=r_1}} = \hat{R}_1 k_j \frac{\partial T_j}{\partial r_{r=r_t}} \tag{3}$$

$$T_{1_{r=r_w}} - T_{i_{r=r_2}} = \hat{R}_2 k_1 \frac{\partial T_1}{\partial r_{r=r_w}} = \hat{R}_2 k_i \frac{\partial T_i}{\partial r_{r=r_2}} \tag{4}$$

where the subscripts $i = 2, 3$ and $j = 4, 5$; thermal resistances $\hat{R}_1$ and $\hat{R}_2$ are functions of the conductivity and thickness of pipes. Boundary conditions are $T_1 \to T_\infty$ for $r, y \to \infty$, $T_3, T_4, T_5 \to T_\infty$ for $y \to \pm\infty$. Introducing a heat transfer coefficient, h_j, heat transfer rates at the interior wall of the inner pipe can be calculated by

$$k_j \frac{\partial T_j}{\partial r_{r=r_t}} = h_j (T_{j_{r=r_t}} - \bar{T}_j) \quad j = 4, 5 \tag{5}$$

where the local mean temperature of thermite $\bar{T}_j$ is defined as

$$\bar{T}_j = \frac{2}{r_t^2} \int_0^{r_t} r T_j dr \tag{6}$$

Energy Eq. (1) in the thermite can be simplified to a one-dimensional form by integrating over the cross section and substituting boundary condition (5). This gives

$$-V_c \frac{d\bar{T}_j}{dy} = \alpha_j \frac{d^2 \bar{T}_j}{dy^2} + \frac{2\alpha_j h_j}{r_t k_j} (T_{j_{r=r_t}} - \bar{T}_j) \quad j = 4, 5 \tag{7}$$

where the last term on the right-hand side represents radial energy transfer from the thermite across the inner pipe. Determination of the heat transfer coefficient h_j requires an experimental measurement. However, it can be roughly obtained

Nomenclature

$B = (r_w/k_1)/[(x_0/k_3)(1 - F) + \hat{R}_2]$
$\mathrm{Bi}_2 = (x_0/k_2)/(1/h_4 + \hat{R}_1)$
$\mathrm{Bi}_3 = (r_w/k_1)/[1/h_4 + \hat{R}_1 + \hat{R}_2 + (x_0/k_2)]$
$B_0 = (r_w/k_1)/[(x_0/k_3) + \hat{R}_2]$
c = constant pressure specific heat
$D = (r_w/r_t)^2 (V/V_c)\alpha_4/\alpha_1$
$D_2 = \rho_1 c_1 k_1/(\rho_2 c_2 k_2)$
$D_3 = \rho_1 c_1 k_1/(\rho_3 c_3 k_3)$
f, F = coordinate of solid paraffin-oil interface, $f = r_m - r_1$, $F = f/x_0$
h_j = heat transfer coefficient
J_0, J_1 = Bessel function of the first kind of order 0 and 1
k = conductivity
k_1^T, k_2^T = conductivity of inner and outer pipe
L = latent heat
l_5 = axial length scale in region 5 = r_t/Pe_5
l_4 = axial length scale in region 4 = $r_t\,\mathrm{Pe}_4$
l' = axial length scale in regions 1 and 2 in area IV = $x_0\,\mathrm{Pe}_3/\mathrm{Ste}_3$
l^* = axial length scale in region 2 in area II = $\psi x_0\,\mathrm{Pe}_2/\mathrm{Ste}_2$
Pe_1 = Peclet number = Vr_w/α_1
$\mathrm{Pe}_2 = Vx_0/\alpha_2$
$\mathrm{Pe}_3 = Vx_0/\alpha_3$
$\mathrm{Pe}_4 = V_c r_t/\alpha_4$
$\mathrm{Pe}_5 = V_c r_t/\alpha_5$
r = radial coordinate, as shown in Fig. 1(*b*)
R = dimensionless radial coordinate = r/r_w
r_m = radius of interface
$R_{p2} = x_0 k_4/k_2 r_t$
$R_{p3} = x_0 k_4/k_3 r_t$
r_t = interior radius of inner pipe
$R_t = k_4/h_4 r_t$
r_w = external radius of outer pipe
$R_w = r_w k_4/r_t k_1$
r_1, r_2 = external and interior radius of inner and outer pipes, respectively
$R_1 = \hat{R}_1 k_4/r_t$
$R_2 = \hat{R}_2 k_4/r_t$
$\hat{R}_1, \hat{R}_2$ = conduction resistance of inner and outer pipes, $\hat{R}_1 = \delta_1/k_1^T$; $\hat{R}_2 = \delta_2/k_2^T$
$\mathrm{Ste}_2 = c_2(T_m - T_\infty)/L$
$\mathrm{Ste}_3 = c_3(T_m - T_\infty)/L$
T = temperature
T_c = temperature at combustion front
$\bar{T}$ = mean temperature, as defined in Eq. (6)
t = dimensionless variable = $-(Y - Y_0)/D$
t' = $-(Y - Y_1)/D$
V = absolute velocity of combustion front
V_c = combustion speed
V_0 = absolute velocity of cartridge = $V - V_c$
X = dimensionless coordinate = $(r - r_1)/x_0$
$x_0 = r_2 - r_1$
y, Y = dimensional and dimensionless axial coordinate, $Y = y/l_5$ or y/l_4, as shown in Fig. 1(*b*)
Y_0, Y_1 = Bessel function of the second kind and order 0 and 1, or displacement as shown in Fig. 1(*b*)
$Y^* = y/l^*$
$Y' = y/l'$
α = thermal diffusivity
δ_1, δ_2 = thickness of inner and outer pipe
θ^* = solution of Eq. (17) subject to Eq. (18) having $\theta_4/\psi + 1 = 1$
$\theta_1 = (T_1 - T_\infty)/(T_m - T_\infty)$
$\theta_2 = (T_2 - T_m)/(T_c - T_m)$
$\theta_3 = (T_3 - T_m)/(T_\infty - T_m)$
$\theta_4 = (\bar{T}_4 - T_m)/(T_c - T_m)$
$\theta_5 = (\bar{T}_5 - T_\infty)/(T_c - T_\infty)$
ρ = density
$\psi = (T_m - T_\infty)/(T_c - T_m)$
φ = quantity defined by Eq. (31)
φ_0 = quantity defined by Eq. (31) where Bi_3 is replaced by B_0

Subscripts

i = rock ($i = 1$), molten ($i = 2$), and solid ($i = 3$) paraffin
j = unburned ($j = 5$) and burned thermite ($j = 4$)
m = melting
∞ = ambient

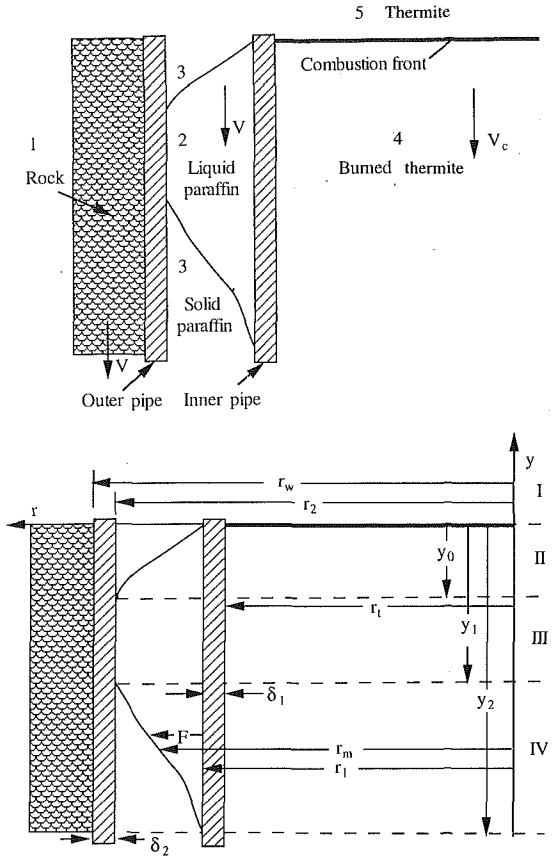

Fig. 1 Physical model for analysis: (*a*) different regions, and (*b*) different areas and coordinate systems

provided that a parabolic distribution of temperature $T_j = T_{j_{r=r_t}} + C(r^2 - r_t^2)$ is assumed, where C is a function of y. Introducing this distribution into Eqs. (6) and (5) the heat transfer coefficient yields $h_j = 4k_j/r_t$. As a consequence, the heat transfer coefficient is of the order of several thousands in SI unit system. Substituting Eq. (5) into Eq. (3) to eliminate the temperature gradient, the temperature at the interior wall of the inner pipe in Eq. (7) yields

$$T_{j_{r=r_t}} = \frac{T_{l_{r=r_t}} + h_j \hat{R}_1 \bar{T}_j}{1 + h_j \hat{R}_1} \tag{8}$$

This work applies a scale analysis (Bejan, 1984) for a further simplification.

Scale Analysis and Dimensionless Equations. Thermal boundary layer ahead of the combustion front in the unburned thermite or region 5 ($y > 0$ and $r < r_t$) is determined by equating axial convection and conduction. Hence Eq. (1) leads to the axial length scale $l_5 = r_t/\mathrm{Pe}_5$. Ignoring radial convection, which is of the order of $1/\mathrm{Pe}_5^2$, energy Eq. (7) reduces to

$$-\frac{d\theta_5}{dY} = \frac{d^2\theta_5}{dY^2} \tag{9}$$

The solution of Eq. (9) yields $\theta_5 = \exp(-Y)$, which is satisfied by $\theta_5 = 1$ and 0 at $Y = 0$ and ∞, respectively.

In region 4 ($y_2 < y < 0$ and $r < r_t$) temperature is determined by equating axial convection and radial conduction across the inner pipe. Equation (7) then leads to the axial length scale $l_4 = r_t\,\mathrm{Pe}_4$, which is much larger than the thickness of the thermal boundary layer in the unburned thermite. Energy Eq. (7) in region 4, by ignoring axial conduction, which is of the order of $1/(\mathrm{Pe}_4)^2$, and substituting Eq. (8) reduces to

$$-\frac{d\theta_4}{dY} = \frac{2}{R_t + R_1}(\theta_{2_{r=r_t}} - \theta_4) \tag{10}$$

In view of different characteristic quantities, the physical domain can be divided into five regions (see Fig. 1a) and four areas (see Fig. 1b). In the annulus all paraffin in area I is solid; paraffin is partially melted in area II. In area III paraffin is completely liquid state, and solidification occurs in area IV. The existence of the region where all paraffin is liquid can be verified by estimating the maximum thickness of the molten zone. Using the Stefan condition (2) the maximum thickness of the molten zone is found to be $x_m \sim [k_2(T_c - T_m)l_4/\rho_3 LV]^{1/2}$ or $x_m/x_0 \sim (\mathrm{Ste}_2\,\mathrm{Pe}_4 r_t/\psi\,\mathrm{Pe}_2 x_0)^{1/2}$, which is greater than unity for the Stefan number Ste_2/ψ of around 10 and $x_0/r_t \sim 0.1$. Scale analyses in paraffin and rock are described as follows.

Area I ($y > 0$). Temperature in most of the region in area I is a constant and equal to the ambient temperature. This is because of an extremely thin thermal boundary layer, whose thickness is usually around 0.1 mm for a combustion speed $V_c \sim 3$ mm/s.

Area II ($y_0 < y < 0$). Radial heat transfer from the burned thermite is responsible for melting solid paraffin in the annulus. By equating latent heat for melting and radial heat conduction, Eq. (2) gives the axial length scale $l^* = \psi x_0\,\mathrm{Pe}_2/\mathrm{Ste}_2$. Since the Peclet number $\mathrm{Pe}_2 \sim 100$ and the Stefan number $\mathrm{Ste}_2/\psi \sim 10$, the axial conduction, which is of the order of $(\mathrm{Ste}_2/\psi\,\mathrm{Pe}_2)^2$, is small. The dimensionless forms of Eqs. (1) and (2) therefore reduce to

$$-\frac{\mathrm{Ste}_2}{\psi}\frac{\partial\theta_2}{\partial Y^*} = \frac{\partial^2\theta_2}{\partial X^2} \quad \text{for} \quad Y^* < 0, X > 0 \tag{11}$$

$$\frac{dF}{dY^*} = \frac{\partial\theta_2}{\partial X_F} \quad \text{at} \quad X = F(Y^*) \tag{12}$$

Other boundary conditions at the solid–liquid interface are

$$\theta_2 = 0 \quad \text{at} \quad X = F(Y^*) \tag{13}$$

The molten region can be assumed to start at the same level of the combustion front because of an extremely thin thermal boundary layer near the combustion front in area I. This gives

$$F = 0 \quad \text{at} \quad Y^* = 0 \tag{14}$$

A boundary condition at the external wall of the inner pipe by substituting Eq. (8) into Eq. (3) yields

$$\frac{\partial\theta_2}{\partial X_{r=r_1}} = \mathrm{Bi}_2(\theta_{2_{r=r_1}} - \theta_4) \tag{15}$$

where the dimensionless temperature in the burned thermite, θ_4, is approximately equal to 1. This is attributed to the fact that the ratio of length scales between the thermit and molten region in area II is $l^*/l_4 \sim (x_0/r_t)^2 \sim 0.01$.

Area III ($y_1 < y < y_0$). The axial length scale is the same as that in region 4, $l_4 \sim r_t\,\mathrm{Pe}_4$. For a small gap between pipes and high Peclet number Eq. (1) for the molten paraffin yields

$$\frac{\partial^2\theta_2}{\partial X^2} = 0 \tag{16}$$

Since a high Peclet number and the resulting $(r_w/l_4)^2 \ll 1$, Eq. (1) in rock reduces to

$$-D\frac{\partial\theta_1}{\partial Y} = \frac{1}{R}\frac{\partial}{\partial R}\left(R\frac{\partial\theta_1}{\partial R}\right) \tag{17}$$

Substituting the solution of Eq. (16) into boundary conditions (4) and Eqs. (10), respectively, yield

$$\frac{\partial\theta_1}{\partial R_{r=r_w}} = \mathrm{Bi}_3\left(\theta_{1_{r=r_w}} - 1 - \frac{\theta_4}{\psi}\right) \tag{18}$$

$$\frac{d\theta_4}{dY} = -\frac{2\,\mathrm{Bi}_3\psi}{R_w}\left(\theta_{1_{r=r_w}} - 1 - \frac{\theta_4}{\psi}\right) \tag{19}$$

Other boundary conditions are

$$\theta_1 = 0 \quad \text{as} \quad R \to \infty \tag{20}$$

$$\theta_1 = 0,\ \theta_4 = 1 \quad \text{at} \quad Y = Y_0 \tag{21}$$

where the location of the point $Y = Y_0$ is found from the solution in area II.

Area IV ($y_2 < y < y_1$). Using the same analysis as that of area III, the energy equation in region 1 is found to be similar to Eq. (17). The temperature in the solid paraffin is governed by an equation similar to Eq. (16). Substituting the solution of θ_3 into Eq. (4) leads to

$$\frac{\partial\theta_1}{\partial R_{r=r_w}} = \frac{R_w}{R_2 + R_{p3}(1-F)}\left(\theta_{1_{r=r_w}} - 1\right) \tag{22}$$

The axial length scale of the molten region in area IV can be obtained by satisfying the energy balance between energy released due to solidification and radial conduction. The Stefan boundary condition (2) then gives $l' = x_0\,\mathrm{Pe}_3/\mathrm{Ste}_3$. It is noted that radial conduction from molten paraffin to the interface can be neglected by comparison with that from the interface to the outer pipe. This is because the scale for temperature in liquid paraffin is smaller than that of solid paraffin. Otherwise, solidification is unable to start. Substituting the linear profile of temperature in the solid paraffin θ_3 and utilizing boundary condition (4), Eq. (2) reduces to

$$\frac{dF}{dY'} = \frac{R_{p3}}{R_2 + R_{p3}(1-F)}\left(1 - \theta_{1_{r=r_w}}\right) \tag{23}$$

Other boundary conditions are

$$F = 1,\ \theta_1 = \theta_1(Y_1, R) \quad \text{at} \quad Y = Y_1 \tag{24}$$

where the locations Y_1 and θ_1 at this point are obtained from the solution in area III.

Closed-Form Solutions. Solutions of areas II, III, and IV are found as follows.

Area II. Governing equations and boundary conditions (11)–(15) represent a one-phase Stefan problem. An integral method developed by Goodman (1958) and improved by Volkov et al. (1988) is used. Convergence of this method was proved by Grigoriev et al. (1984). Multiplying by $X + 1/\mathrm{Bi}_2$, integrating with respect to X and Y^* between 0 and F and 0 and Y^*, respectively, and substituting boundary conditions (12)–(15), energy Eq. (11) becomes

$$\frac{\mathrm{Ste}_2}{\psi}\int_0^F \theta_2\left(X + \frac{1}{\mathrm{Bi}_2}\right)dX = -\left(\frac{F^2}{2} + \frac{F}{\mathrm{Bi}_2}\right) - Y^* \tag{25}$$

A first approximation to the temperature profile is chosen to be

$$\theta_2 = \frac{\mathrm{Bi}_2}{1 + \mathrm{Bi}_2 F}(F - X) \tag{26}$$

which is satisfied by boundary conditions (13) and (15). Substituting Eq. (26) and integrating Eq. (25) lead to an equation for the shape of the solid–liquid interface

$$Y = -\frac{D}{D_2}\left(\frac{R_{p2}}{R_w}\right)^2\left[\frac{\mathrm{Bi}_2}{1 + \mathrm{Bi}_2 F}\left(\frac{F^2}{2\,\mathrm{Bi}_2} + \frac{F^3}{6}\right) + \frac{\psi}{\mathrm{Ste}_2}\left(\frac{F^2}{2} + \frac{F}{\mathrm{Bi}_2}\right)\right] \tag{27}$$

Setting $F = 1$, Eq. (27) determines the location at which the solid–liquid interface contacts the interior wall of the outer pipe. A second approximation to temperature is chosen as

$$\theta_2 = 1 + a_1\left(X + \frac{1}{\mathrm{Bi}_2}\right) + a_2\left(\frac{X^3}{6} + \frac{X^2}{2\,\mathrm{Bi}_2} + X + \frac{1}{\mathrm{Bi}_2}\right) \tag{28}$$

where a_1 and a_2 are considered as functions of the depthwise coordinate. Substituting Eq. (28) into Eq. (25) and utilizing Eqs. (12) and (13), the unknown a_1, a_2 and F are obtained. A comparison of numerical results between the first and second-order approximations shows that the difference does not exceed 2–3 percent. The first-order approximation, Eqs. (26) and (27) therefore is used for an investigation.

Area III. Equations (17), (18), (20), and (21) allow an application of Duhamel's theorem (Carslaw and Jaeger, 1959). Hence, temperature in this region is governed by

$$\theta_1 = \frac{\partial}{\partial t}\int_0^t \left[1 + \frac{\theta_4(\tau)}{\psi}\right]\theta^*(R, t-\tau)d\tau \tag{29}$$

where $t \equiv -(Y - Y_0)/D$ and temperature θ^* is the solution of Eq. (17) subject to boundary condition (18) having $\theta_4/\psi + 1 = 1$ (Carslaw and Jaeger, 1959). Combining Eqs. (18) and (19) and introducing Eq. (29) give

$$\theta_4 = 1 - \frac{2\psi D\,\mathrm{Bi}_3}{R_w}\int_0^t \left(1 + \frac{\theta_4}{\psi}\right)\varphi(t-\tau)d\tau \tag{30}$$

where the function $\varphi \equiv -(\partial\theta^*/\partial R)_{r=r_w}/\mathrm{Bi}_3$ and

$$\varphi(t-\tau) = \frac{4\,\mathrm{Bi}_3}{\pi^2}\int_0^\infty e^{-s^2(t-\tau)} \times \frac{ds}{s\{[sJ_1(s) + \mathrm{Bi}_3 J_0(s)]^2 + [sY_1(s) + \mathrm{Bi}_3 Y_0(s)]^2\}} \tag{31}$$

Area IV. Solidification of molten paraffin starts at the location $Y = Y_1$ which corresponds to a dimensionless variable $t = t_1$. Temperature $\theta_1 = \theta_{1,\mathrm{IV}}(t', R)$ is decomposed into

$$\theta_{1,\mathrm{IV}}(t', R) = \theta_1(t_1 + t', R) + u(t', R) \tag{32}$$

where the new variable $t' \equiv t - t_1 = (Y_1 - Y)/D$. The first term on the right-hand side of Eq. (32) is referred to the solution in area III. Substituting Eq. (32) into Eqs. (17), (22)–(24), a supplementary problem for $u(t', R)$ is obtained. After a bit of manipulations by using the Duhamel's theorem an integral equation for $u(t', 1)$ can be obtained

$$u(t', 1) = 1 - \left(1 + \frac{\theta_4}{\psi}\right)\frac{\mathrm{Bi}_3}{B} - \left(1 - \frac{\mathrm{Bi}_3}{B}\right)\theta_1 - \frac{B_0}{B}\frac{\partial}{\partial t'}\int_0^{t'}\left\{\frac{B}{B_0} - \left(\frac{B}{B_0} - 1\right)u - \frac{B}{B_0}\left[\left(1 - \frac{\mathrm{Bi}_3}{B}\right)\theta_1 + \left(1 + \frac{\theta_4}{\psi}\right)\frac{\mathrm{Bi}_3}{B}\right]\right\} \times \varphi_0(t' - \tau)d\tau \tag{33}$$

where the quantities B_0 and B are

$$B_0 \equiv \left(\frac{R_w}{R_{p3}}\right)\left(1 + \frac{R_2}{R_{p3}}\right)^{-1}$$

$$B \equiv \left(\frac{R_w}{R_{p3}}\right)\left(1 - F + \frac{R_2}{R_{p3}}\right)^{-1} \tag{34}$$

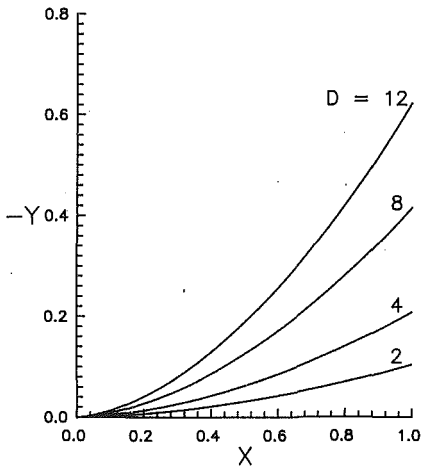

Fig. 2 Shape of interface between solid and liquid paraffin in area II as a function of the dimensionless parameter D ($Bi_2 = 5$, $Bi_3 = 1$, $R_w = 2$, $\psi = 0.1$, $R_2/R_{p2} = 0.1$)

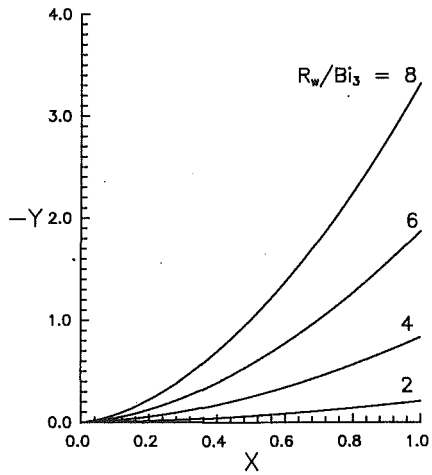

Fig. 3 Shape of interface between solid and liquid paraffin in area II as a function of the dimensionless parameter R_w/Bi_3($Bi_2 = 5$, $D = 16$, $R_w = 4$, $\psi = 0.1$, $R_2/R_{p2} = 0.1$).

Substituting Eqs. (32) and (33) into Eq. (23) and integrating with respect to Y' lead to

$$F = 1 - \frac{R_w}{R_{p3}} D_3\,\mathrm{Ste}_3\left\{\mathrm{Bi}_3\int_0^{t'}\left(1+\frac{\theta_4}{\psi}-\theta_1\right)d\tau + B_0\int_0^{t'}\left\{\frac{B}{B_0}-\left(\frac{B}{B_0}-1\right)u-\frac{B}{B_0}\left[\left(1-\frac{\mathrm{Bi}_3}{B}\right)\theta_1 + \left(1+\frac{\theta_4}{\psi}\right)\frac{\mathrm{Bi}_3}{B}\right]\right\}\varphi_0(t'-\tau)d\tau\right\} \quad \text{at} \quad r = r_w \qquad (35)$$

Results and Discussion

In this study, independent dimensionless parameters required to determine melting solid paraffin in the gap between coaxial pipes are found to be $D(R_{p2}/R_w)^2/D_2$, Bi_2, Ste_2/ψ in area II, ψ, Bi_3, D/R_w in area III, and R_w/R_{p3}, R_2/R_{p3}, ψ, Bi_3 and D_3 Ste_3 in area IV, respectively. Without loss of generality, properties of solid and liquid paraffin are assumed to be identical. Hence, the parameter R_w/R_{p3} becomes a function of Bi_3, Bi_2, and R_2/R_{p2}. The number of independent parameters reduces to eight. They are selected to be $Bi_2(\equiv(x_0/k_2)/(1/h_4 + \hat{R}_1))$, $Bi_3(\equiv(r_w/k_1)/[1/h_4 + \hat{R}_1 + \hat{R}_2 + (x_0/k_2)])$, R_w $(\equiv r_w k_4/r_t k_1)$, R_2/R_{p2} $(\equiv \hat{R}_2 k_2/x_0)$, D $(\equiv(r_w/r_t)^2(V/V_c)\alpha_4/\alpha_1)$, ψ $(\equiv(T_m - T_\infty)/(T_c - T_m))$, D_2 $(\equiv\rho_1 c_1 k_1/\rho_2 c_2 k_2)$, and $Ste_2(\equiv c_2(T_m - T_\infty)/L)$. To evaluate dimensionless parameters, pipes are chosen to be steels. Properties of paraffin and rock were, for example, presented by Moallemi and Viskanta (1985, 1986) and Incropera and DeWitt (1990).

Melting solid paraffin starts from area II as a result of high temperatures in the thermite burned. The effects of the dimensionless parameter D on shapes of the interface between solid and liquid paraffin are shown in Fig. 2. Aside from the ratio of velocities between rock and the combustion front, the parameter D can also be represented by $D = (r_w/r_t)\,\mathrm{Pe}_1/\mathrm{Pe}_4 = l_1/l_4$ which indicates a ratio of the axial length scale of rock to that of the burned thermite. Choosing dimensionless parameters $Bi_2 = 5$, $Bi_3 = 1$, $R_w = 2$, $\psi = 0.1$, $R_2/R_{p2} = 0.1$, the length of area II is found to increase with the parameter D. This is because an increase in the velocity or the axial length of rock (and paraffin) increases axial energy transport resulting from the depthwise convection and reduces energy required for melting. Since the velocity ratio $V/V_c = 1 + (V_0/V_c)$ the velocity of the cartridge should be smaller than that of the combustion front to enhance melting in area II.

As shown in Fig. 3, the region of the solid paraffin in area II decreases with the parameter $R_w/Bi_3(\equiv(1/h_4 + \hat{R}_1 + \hat{R}_2 + x_0/k_2)/(r_t/k_4))$, which represents the ratio of the total resistance of convection resistance and conduction resistances of pipes and paraffin to conduction resistance in the burned thermit. A decrease in R_w/Bi_3 indicates a reduction of the total resistance. Hence, radial energy transport becomes comparatively easy. Melting rates therefore increase. The maximum length in area II is significantly reduced.

The efficiency of removing the paraffin plug depends on the length of area III. The effects of different parameters on the length of area III (i.e., $Y_1 - Y_0$) are listed in Table 1. Case 1 is referred to dimensionless parameters $Bi_2 = 5$, $Bi_3 = 1$, $R_w = 2$, $\psi = 0.1$, $D = 2$, $R_2/R_{p2} = 0.1$. The length of area III is found to be 4.4, which is approximately 40 times longer than that in area II (see Fig. 2) under the same conditions. Comparing cases 1 and 2 indicates that the length is decreased by increasing the parameter D. This is attributed to a decrease in energy transport for melting, as mentioned previously.

A decrease of Bi_3 results in an increase of the length in this area by comparing cases 2 and 3. This is because energy dissipated to rock becomes small for a high total resistance between the burned thermite and paraffin. Therefore, more energy is used for melting solid paraffin. It can be seen that the total resistance has opposite effects on melting paraffin in areas II and III. In other words, lengths of areas II and III are both increased with the total resistance. Comparing cases 2 and 4 indicates that an increase in R_w increases significantly the length of area III. The effects of the temperature at the combustion front, which is governed by the parameter ψ, are found from cases 2 and 5. It is seen that a high temperature at the combustion front significantly increases the length of area III. Computations also found that the effects of parameters Bi_2 and Ste_2 on shapes of the interface within reasonable working conditions were insignificant.

The occurrence of area IV is a result of solidification. This is because temperatures in the thermite decrease and eventually become as low as those in liquid paraffin. As shown in Fig. 4 an increase in the parameter D increases the length of area IV. The

Table 1 Length of completely molten paraffin (area III) as a function of independent parameters

Cases	Bi_2	Bi_3	R_w	ψ	D	R_2/R_{p2}	$Y_0 - Y_1$
1	5	1	2	0.1	2	0.1	4.4
2	5	1	2	0.1	4	0.1	4
3	5	0.5	2	0.1	4	0.1	5.2
4	5	1	3	0.1	4	0.1	6.4
5	5	1	2	0.05	4	0.1	7.2

slow solidification is attributed to a large axial length scale associated with higher temperatures in rock. Energy dissipated to rock thus is reduced. The length of area IV can be approximately four times larger than that of area II. In Fig. 5, a decrease of the parameter R_w/Bi_3 reduces the length of liquid paraffin. This is because the total resistance between the burned thermite and paraffin decreases and molten paraffin solidifies rapidly.

Conclusions

The conclusions drawn are the following:

1 The present study provides an understanding of melting solid plug between coaxial pipes by inserting a moving heat source in the inner pipe. The physical process therefore involves energy transport between combustion, convection, and conduction, and phase changes of melting and solidification in different domains. Provided that properties between solid and liquid are identical, the entire process is determined by eight independent parameters. In this study, they are chosen to be Bi_2, Bi_3, R_w, R_2/R_{p2} (or R_w/R_{p2}), D, ψ, D_2, and Ste_2.

2 The closed-form solutions are found. For an application to oil pipes the dimensional results showed that the length of completely molten paraffin (i.e., area III) can be as large as 50 m. The length in area IV for solidification of liquid paraffin can be around 15 m, which is approximately four times longer than that for melting solid paraffin in area II. In all cases, area II has the least length.

3 The length of area III determines the efficiency of removing paraffin plug. An increase in dimensionless parameter R_w, and a decrease in D, Bi_3, ψ, enhance the melting of solid paraffin and increase the length of this area. The parameter R_w represents the ratio of conduction resistance of rock to that of the burned thermite, D the ratio of axial length scales between rock and the burned thermite, Bi_3 the ratio of conduction resistance of rock to a sum of convection resistance between the thermite and inner pipe and conduction resistances of pipes and paraffin, ψ the ratio of temperature differences between the melting and ambient temperatures and the combustion and melting temperatures. The effects of the parameter Bi_2 indicating the ratio of conduction resistance of paraffin to a sum of convection resistance and conduction resistance of the inner pipe, and the Stefan number Ste_2 representing the ratio of sensible heat of paraffin from the ambient temperature to the melting point to latent heat for melting, however, are insignificant.

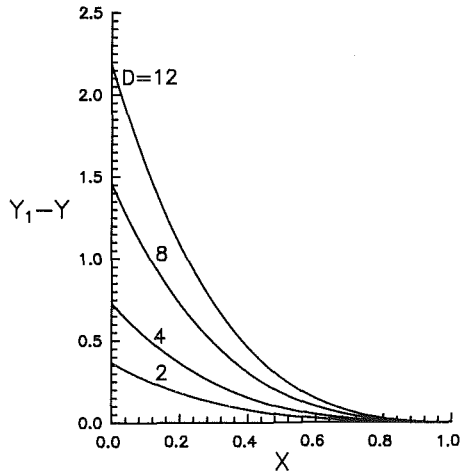

Fig. 4 Shape of interface between solid and liquid paraffin in area IV as a function of the dimensionless parameter D ($\mathrm{Bi}_2 = 5$, $\mathrm{Bi}_3 = 1$, $R_w = 2$, $\psi = 0.1$, $R_2/R_{p2} = 0.1$)

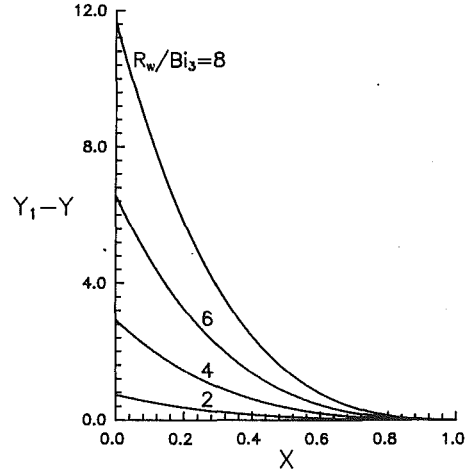

Fig. 5 Shape of interface between solid and liquid paraffin in area IV as a function of the dimensionless parameter R_w/Bi_3($\mathrm{Bi}_2 = 5$, $D = 16$, $R_w = 4$, $\psi = 0.1$, $R_2/R_{p2} = 0.1$)

4 Lengths of areas II and IV are reduced by decreasing the total resistance between the burned thermite and paraffin. Increasing the speed ratio between the combustion front and the cartridge increases lengths of areas II and IV while the length of area III is reduced.

5 The analysis and results provided by the present work can be used for designing oil pipes and selecting heat sources so that paraffin plugging the gap between two coaxial pipes can be effectively and economically removed.

Acknowledgments

This work was sponsored by the Kazan Institute of Chemical Technology. The authors acknowledge Professor I. F. Sadykov, Dr. V. G. Ivanov, and Dr. V. G. Arhipov, for providing empirical data and suggestions. The work was carried out by Convex 3840 mini-supercomputer in the National Sun Yat-Sen University.

References

Arhipov, V. G., 1992, Kazan Institute of Chemical Technology, private communication.

Bejan, A., 1984, *Convection Heat Transfer,* Wiley, New York, pp. 17–21.

Carslaw, H. C., and Jaeger, J. C., 1959, *Conduction of Heat in Solids,* Clarendon Press, Oxford, United Kingdom, pp. 336–337.

Fomin, S. A., and Cheng, S., 1991, "Optimization of the Heating Surface Shape in the Contact Melting Problem," *Third International Conference on Inverse Design Concepts and Optimization in Engineering Sciences,* G. S. Dulikravich, ed., Washington, DC, Oct. 23–25, pp. 253–262.

Gaskell, D. R., 1981, *Introduction to Metallurgical Thermodynamics,* 2nd ed., Hemisphere Publ., New York, pp. 148–150.

Goodman, T. R., 1958, "The Heat Balance Integral and Its Application to Problems Involving a Change of Phase," ASME JOURNAL OF HEAT TRANSFER, Vol. 80, pp. 335–342.

Grigoriev, S. G., Lapin, A. V., and Chugunov, V. A., 1984, "Investigation of Galerkin Method for One-Phase Stefan's Problems," Transactions of the Academy of Science of USSR, Siberian Branch: *Numerical Methods in Mechanics of Continuous Medium,* Vol. 15, pp. 17–26 [in Russian].

Incropera, F. P., and DeWitt, D. P., 1990, *Introduction to Heat Transfer,* Wiley, New York, pp. 96–103; A14.

Ivanov, V. G., and Sadykov, I. F., 1986, "Equipment for the Decay of the Hydration Plug," Auther Invention Certificate No. 140122 (USSR) [in Russian].

Maltcev, V. M., Maltcev, V. I., and Kashparov, I. Ya., 1977, *The Characteristics of Combustion,* Nauka, Moscow, Chaps. 1–3 [in Russian].

Moallemi, M. K., and Viskanta, R., 1985, "Melting Around Migrating Heat Source," ASME JOURNAL OF HEAT TRANSFER, Vol. 107, pp. 451–458.

Moallemi, M. K., and Viskanta, R., 1986, "Analysis of Close Contact Melting Heat Transfer," *International Journal of Heat and Mass Transfer,* Vol. 29, pp. 855–867.

Sadykov, I. F., Ivanov, V. G., and Fatkullin, A. H., 1976, "Chemical Heater for Oil Stratum," *Neftepromyslovoe delo,* Vol. 12, pp. 31–37 [in Russian].

Volkov, I. K., Chugunov, V. A., and Salamatin, A. N., 1988, "Generalization of the Method of Integral Relations and Its Application to Some Heat Flow Problems," *Journal of Soviet Mathematics,* Vol. 41, pp. 1013–1025.

Journal of Heat Transfer

Technical Notes

This section contains shorter technical papers. These shorter papers will be subjected to the same review process as that for full papers.

The Lattice Temperature in the Microscopic Two-Step Model

D. Y. Tzou,[1] M. N. Özişik,[2] and R. J. Chiffelle[1]

Nomenclature

C_e = volumetric heat capacity of electrons, J/m^3 K
C_l = volumetric heat capacity, J/m^3 K
C_T = equivalent thermal wave speed in the two-step model, m/s
G = electron–phonon coupling factor, W/m^3 K
h = Planck's constant, Js
k = Boltzmann constant, J/K
K = thermal conductivity, W/m K
n = volumetric number density, 1/m^3
N = number of terms in truncation
p = Laplace transform parameter
t = time, s
T = absolute temperature, K
T_D = Debye temperature, K
v_s = speed of sound, m/s
x = space variable, m
α_T = equivalent thermal diffusivity in the two-step model, m^2/s
β = dimensionless time
γ = transformation variable
δ = dimensionless distance
θ = dimensionless temperature
τ = relaxation time, s
ω = frequency in the Fourier transform

Subscripts and Superscripts

0 = initial value
a = atom
e = electron
l = lattice
W = quantity at the wall

[1] Department of Mechanical Engineering, University of New Mexico, Albuquerque, NM 87131.
[2] Department of Mechanical and Aerospace Engineering, North Carolina State University, Raleigh, NC 27695.

Contributed by the Heat Transfer Division of THE AMERICAN SOCIETY OF MECHANICAL ENGINEERS. Manuscript received by the Heat Transfer Division September 1993; revision received February 1994. Keywords: Conduction, Laser Processing, Transient and Unsteady Heat Transfer. Associate Technical Editor: Y. Bayazitoglu.

Introduction

The microscopic two-step model pioneered by Anisimov et al. (1974) and advanced later by Fujimoto et al. (1984), Brorson et al. (1987), Elsayed-Ali et al. (1987), and Elsayed-Ali (1991) addresses the phonon–electron interactions in the short-time transient of metal films. Especially for the high-rate heating induced by a short-pulse laser (Qiu and Tien, 1992, 1993), the typical response time is on the order of picoseconds, which is comparable to the phonon–electron thermal relaxation time. Thermodynamic equilibrium between phonons and electrons, consequently, cannot be assumed and heat transfer in the electron gas and the metal lattice has to be considered separately. When applied to the prediction of the surface reflectivity of a gold film, an indication for arrival of the hot electron gas, the two-step model (Qiu and Tien, 1992, 1993) yields excellent results in comparison with experimental data. The diffusion theory assuming an instantaneous thermodynamic equilibrium between the electron gas and the metal lattice, on the other hand, predicts a *reversed trend* for the reflectivity at the back surface of the film. When the transient time becomes so short, in other words, the nonequilibrium thermodynamic transition is an important issue to be addressed in the model of high-rate heat transfer.

The two-step model involves two coupled energy equations governing the heat transfer in the electron gas and the metal lattice. It assumes *diffusion* for heat transport in the electron gas, namely an instantaneous thermodynamic equilibrium with the metal lattice, and neglects the ballistic electron component in the short-time transient. Since the temperature of the metal lattice is a major concern to practical engineers, we focus our attention on it in this work. For this purpose the temperature of the electron gas shall be eliminated from the two coupled energy equations to give a *single* equation governing the temperature of the metal lattice. At the initial stage of exploration, we impose a strong condition that all the thermal properties, including the volumetric heat capacity of the electron gas, remain constant during the two-step process. The real behavior with temperature-dependent properties is thus a combination of a series of such states at which the thermal properties are adjusted according to the corresponding temperature. Also, the volumetric heat source is neglected for the time being to have a better focus on the way in which temperature "waves" evolve. Because heat diffusion is assumed in the electron gas, the wavelike behavior in this work results from the thermal relaxation in the metal lattice.

The Microscopic Two-Step Model

The two-step model assumes *diffusion* in the electron gas while a heat balance in a lumped sense is assumed for the metal lattice:

$$C_e \frac{\partial T_e}{\partial t} = \nabla \cdot (K \nabla T_e) - G(T_e - T_l) \qquad (1)$$

$$C_l \frac{\partial T_l}{\partial t} = G(T_e - T_l), \tag{2}$$

where K is the thermal conductivity of the electron gas at temperature T_e. The energy exchange between the electron gas and the metal lattice is dominated by the electron–phonon coupling factor G. Within the limits of the Wiedemann–Franz law, as shown by Qiu and Tien (1992, 1993), G can be approximated by

$$G = \frac{\pi^4 (n_e v_s k)^2}{K} \tag{3}$$

with v_s being the speed of sound,

$$v_s = \frac{k}{2\pi h} (6\pi^2 n_a)^{-1/3} T_D. \tag{4}$$

A single equation governing the temperature of the metal lattice can be obtained by eliminating the temperature of the electron gas (T_e) from Eqs. (1) and (2). Assuming constant thermal properties,[3] it is found

$$\frac{\partial^2 T}{\partial x^2} + \frac{\alpha_e}{C_T^2} \frac{\partial^3 T}{\partial x^2 \partial t} = \frac{1}{\alpha_T} \frac{\partial T}{\partial t} + \frac{1}{C_T^2} \frac{\partial^2 T}{\partial t^2}, \tag{5}$$

where T is the lattice temperature with the subscript l omitted from here on for convenience. The thermal diffusivity of the electron gas, α_e, is defined by K/C_e. The *equivalent* thermal diffusivity (α_T) and thermal wave speed (C_T) in such a phonon–electron system, respectively, are defined as

$$\alpha_T = \frac{K}{C_e + C_l}, \quad C_T = \sqrt{\frac{KG}{C_e C_l}}. \tag{6}$$

At room temperature, since heat capacity of the metal lattice (C_l) is approximately two orders of magnitude larger than that of the electron gas (C_e), the value of α_T is approximately the same as the macroscopic value (K/C_l) of the metal lattice. When heat capacity of the electron gas increases with temperature, however, the value of α_T decreases from the macroscopic value. The expression for the equivalent thermal wave speed in Eq. (6) is new in the thermal wave theory. From a microscopic point of view, the thermal wave speed relates to the number densities of free electrons and atoms in the metal lattice.

Equation (5) governing the lattice temperature is a new type of differential equation in the field of heat conduction. The mixed-derivative term, second order in space and first order in time, results from the short-time interaction between phonons and electrons. For the case of the number density of free electrons approaching infinity, i.e., $n_e \to \infty$, the coupling factor G approaches infinity according to Eq. (3). The thermal wave speed (C_T), according to Eq. (6), approaches infinity and Eq. (5) is reduced to the classical diffusion equation in this case. From a mathematical point of view, the effect of phonon–electron interactions induces a mixed-derivative term and a *wave* term. Comparing to the classical thermal wave equation without the mixed-derivative term, Eq. (5) is expected to display a stronger dispersive behavior due to involvement of the additional first-order time-derivative in the mixed-derivative term. This is a similar behavior to that in fluids with the Jeffery type constitutive equation depicting a stronger rate-dependency in the stress versus strain-rate response (Joseph and Preziosi, 1989). The metal lattice is the only source for the possible relaxation behavior reflected by the presence of the wave term in Eq. (5). The strong dispersion thus results from the diffusion assumed for heat transport in the electron gas.

The Wave Structure

From a mathematical point of view, the effect of phonon–electron interactions dominates over the wave behavior and diffusion because it appears as the *highest order differential* in Eq. (5). The thermal wave emanating from the end in a semi-infinite, one-dimensional medium is probably the simplest system for examining the nonequilibrium temperature represented by Eq. (5). Due to presence of the wave effect, we need *two* initial conditions at $t = 0$:

$$T(x, 0) = T_0 \quad \text{and} \quad \frac{\partial T}{\partial t}(x, 0) = 0 \quad \text{for} \quad x \in [0, \infty]. \tag{7}$$

The thermal disturbance in the medium is induced by a suddenly imposed temperature at $x = 0$:

$$T(0, t) = T_W \quad \text{for} \quad t > 0. \tag{8}$$

The thermal disturbance, lastly, vanishes at a distance far away from the end:

$$T(x, t) \to T_0 \quad \text{as} \quad x \to \infty. \tag{9}$$

Equations (5) and (7)–(9) can be made dimensionless by introducing the following variables:

$$\theta(x, t) = \frac{T(x, t) - T_0}{T_w - T_0}, \quad \beta = \frac{C_T^2 t}{2\alpha}, \quad \delta = \frac{C_T x}{2\alpha}. \tag{10}$$

The results are

$$\frac{\partial^2 \theta}{\partial \delta^2} + B \frac{\partial^3 \theta}{\partial \delta^2 \partial \beta} = \frac{\partial^2 \theta}{\partial \beta^2} + 2 \frac{\partial \theta}{\partial \beta} \quad \text{with } B = \frac{1}{2}\left(1 + \frac{C_l}{C_e}\right) \tag{11}$$

$$\theta(\delta, 0) = 0 \quad \text{and} \quad \frac{\partial \theta}{\partial \beta}(\delta, 0) = 0 \quad \text{for} \quad \delta \in [0, \infty) \tag{12}$$

$$\theta(0, \beta) = 1 \quad \text{and} \quad \theta(\delta, \beta) \to 0 \quad \text{as} \quad \delta \to \infty. \tag{13}$$

The Laplace transformed solution satisfying Eqs. (11)–(13) can be readily obtained:

$$\bar{\theta} = \frac{e^{-\sqrt{(p(p+2))/(1+Bp)}\,\delta}}{p}. \tag{14}$$

where

$$\theta(\delta, \beta) = \frac{1}{2\pi i} \int_{\gamma - i\infty}^{\gamma + i\infty} \bar{\theta}(\delta; p) e^{p\beta} dp. \tag{15}$$

Three branch points at $p = 0$, $-1/B$, and -2 exist in Eq. (14). The contour integration of Eq. (15) with appropriate branch cuts, for the most part, results in an improper integral. A numerical evaluation for the improper integral is still unavoidable, which motivates the use of a direct numerical scheme for the Laplace inversion.

Introducing the variable transformation

$$p = \gamma + i\omega, \tag{16}$$

with γ being a real constant in the straight cut of Bromwich contour and ω a real variable, first of all, Eq. (15) becomes

$$\theta(\delta, \beta) = \frac{e^{\gamma\beta}}{2\pi} \int_{-\infty}^{\infty} \bar{\theta}(\delta; p = \gamma + i\omega) e^{i\omega\beta} d\omega. \tag{17}$$

The *Fourier* integral thus obtained can then be approximated by its Riemann sum. Denoting ω as the wave frequency and τ the half-period of its oscillations, i.e., $\omega = n\pi/\tau$ for the nth wave mode and $\Delta\omega_n = \pi/\tau$ for all modes,

[3] In reality, heat capacity (C_e) of the electron gas increases linearly with the temperature. For a better focus on the nonequilibrium evolution of the lattice temperature, however, we assume a constant value to approximate its average in the process.

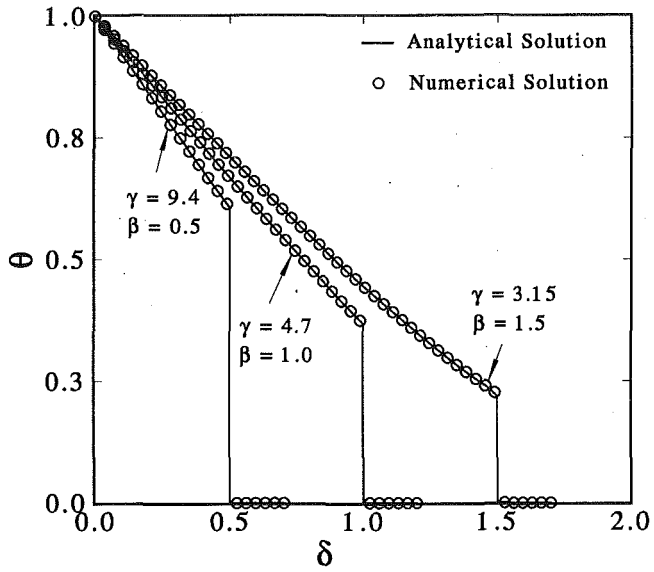

Fig. 1 Comparison of the numerical and analytical solutions, for the thermal wave model with $\beta = 0.5$, 1, and 1.5. The relation $\beta\gamma = 4.7$ is satisfied for all cases.

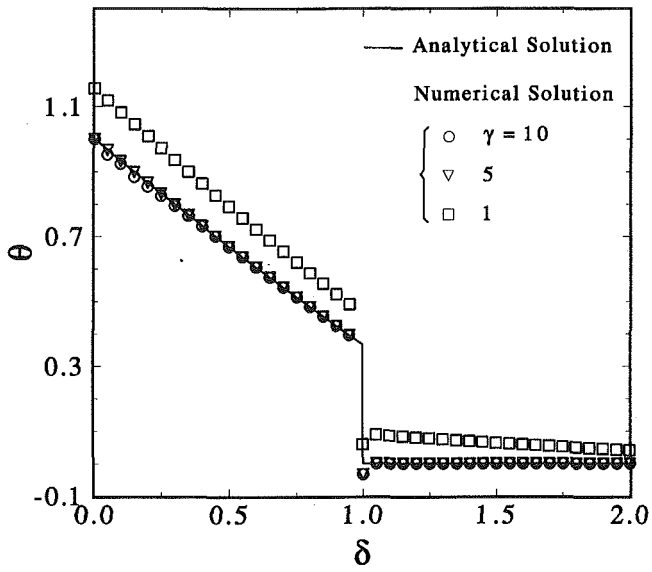

Fig. 2 Convergence of the temperature distributions at various values of γ; $\beta = 1$

$$\theta(\delta, \beta) = \frac{e^{\gamma\beta}}{2\tau} \sum_{n=-\infty}^{\infty} \bar{\theta}\left(\delta, p = \gamma + \frac{in\pi}{\tau}\right) e^{i(n\beta\pi/\tau)}. \quad (18)$$

Noticing further that the wave modes with positive and negative n values appear in pairs and

$$\bar{\theta}\left(\delta, \gamma + \frac{in\pi}{\tau}\right) e^{i(n\beta\pi/\tau)} + \bar{\theta}\left(\delta, \gamma - \frac{in\pi}{\tau}\right) e^{-i(n\beta\pi/\tau)} = 2Re\left[\bar{\theta}(\delta, \gamma + \frac{in\pi}{\tau}) e^{i(n\beta\pi/\tau)}\right], \quad (19)$$

Eq. (17) can be expressed as

$$\theta(\delta, \beta) = \frac{e^{\gamma\beta}}{\tau}\left[\frac{1}{2}\bar{\theta}(\delta, \gamma) + Re \sum_{n=1}^{\infty} \bar{\theta}\left(\delta, \gamma + \frac{in\pi}{\tau}\right) e^{i(n\beta\pi/\tau)}\right] \quad (20)$$

where Re represents the real part of a complex function. Since the function $e^{i(n\beta\pi/\tau)}$ has a fundamental period of 2π, the physical domain of β in Eq. (20) is $0 \leq \beta \leq 2\tau$. At $\beta = \tau$, more precisely, Eq. (20) yields

$$\theta(\delta, \beta) \cong \frac{e^{\gamma\beta}}{\beta}\left[\frac{1}{2}\bar{\theta}(\delta, \gamma) + Re \sum_{n=1}^{N} \bar{\theta}\left(\delta, \gamma + \frac{in\pi}{\beta}\right)(-1)^n\right] \quad (21)$$

which is the inverse solution for θ (temperature) at any values of δ (space) and β (time). Accuracy of the Riemann-sum approximation depends on the value of γ and the truncation error dictated by N. Since the kernel function contains a branch point at zero, the value of γ must be selected greater than zero to include all the branch points. At a selected value of γ, the value of N must be increased until a prescribed threshold of summation is achieved.

For $B = 0$, the combination of Eq. (14) with Eq. (21) gives the classical wave solution. Figure 1 compares the numerical solutions obtained by the present algorithm with the analytical solutions obtained by Baumeister and Hamill (1969). At typical instants of time ($\beta = 0.5$, 1.0, and 1.5), the values of γ satisfying the relation of $\beta\gamma \equiv 4.7$ yield satisfactory and rapidly convergent solutions. Under the prescribed threshold for convergence, 10^{-7} for the Euler norm between two successive approximations, dramatic changes of temperature across the thermal wavefront are successfully captured by using $N = 30{,}000$ in the series of Eq. (21). The numerical inversion for temperature, despite the fact that the value of γ explicitly appears in Eq. (21), is *independent of* the value of γ selected in the analysis. The value of γ, however, affects the numerical characteristics of convergence. Figure 2 demonstrates this behavior by using $\gamma = 1$, 5, and 10 in the numerical convergence for $\beta = 1$. Under the same number of terms used in Eq. (21), $N = 30{,}000$, the curves with $\gamma = 5$ and 10 have already approached the analytical solution while the one with $\gamma = 1$ has not. It is until $N \cong 45{,}000$ that the curve of $\gamma = 1$ can achieve the same convergence. The finer-tuned value of $\gamma = 4.7$ removes the overrelaxed behavior of temperature at the thermal wavefront, $\delta = \beta = 1$.

Figure 3 shows *diminution* of the sharp wavefront due to strong dispersion in the phonon–electron interaction ($B \neq 0$). When the value of B deviates from zero, numerically, absence of

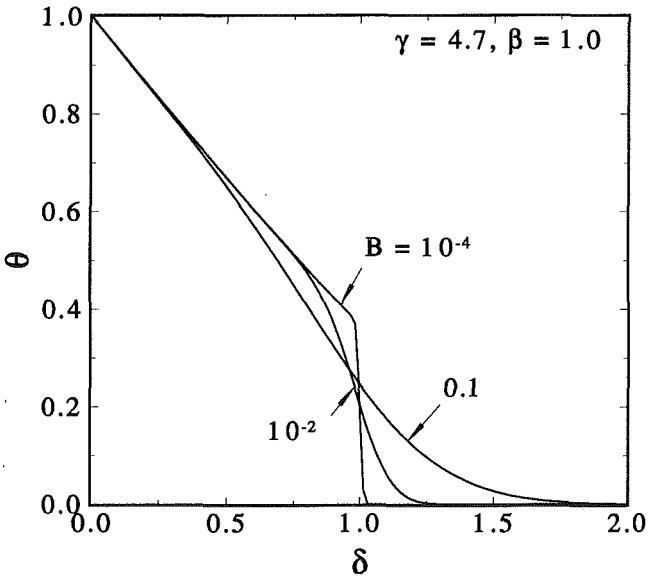

Fig. 3 Diminution of a sharp wavefront in the two-step model; $B = 10^{-4}$, 10^{-2}, and 10^{-1}

the sharp wavefront actually fastens the convergence. The results shown in Fig. 3 for $B = 0.01$ and 0.1 were obtained by using about 30 terms in the series to achieve the convergence. Though difficult to show analytically, the relation $\beta\gamma \equiv 4.7$ for γ again yields rapidly convergent solutions. The wavefront becomes blunt when the value of B deviates from zero (0). The practical value of B, depending on the heat capacity of the electron gas, ranges from 0.5 to 100. The temperature curves, as shown in Fig. 4 for $B = 1$, 10, and 50, decay monotonically and the heat-affected zone extends to a large distance from the wall. Diminution of the sharp wavefront and the large heat-affected zone resembles the diffusion behavior.

The Rate Effect

Although the sharp wavefront is destroyed by the effect of phonon–electron interactions and the heat-affected zone becomes large, the monotonically decaying behavior shown in Fig. 4 should not be confused with that of pure diffusion. For further illustrations, we introduce an initial rate of temperature, $\dot{\theta}_0$, in the initial conditions:

$$\theta(\delta, 0) = 0 \quad \text{and} \quad \frac{\partial\theta}{\partial\beta} = \dot{\theta}_0 \quad \text{for} \quad \delta \in [0, \infty) \qquad (22)$$

where $\dot{\theta}_0 = 2\alpha\dot{T}_0/C^2(T_w - T_0)$. The transformed solution satisfying Eqs. (11), (13), and (22) is

$$\bar{\theta} = \left[\frac{p + 2 - \dot{\theta}_0}{p(p+2)}\right] e^{-\sqrt{(p(p+2))/(1+B\beta)}\,\delta} + \frac{\dot{\theta}_0}{p(p+2)} \qquad (23)$$

which is readily invertible by Eq. (21). When $\dot{\theta}_0 = 0$, Eq. (23) reduces to Eq. (14). For $B = 10$, $\beta = 3$, and $\gamma = 1.61$ ($\beta\gamma \equiv 4.8$), Fig. 5 shows the temperature distributions at various values of $\dot{\theta}_0$. The temperature level, as expected, increases with the initial rate of temperature ($\dot{\theta}_0$). When the value of $\dot{\theta}_0$ increases to 3, the field temperature *exceeds* the boundary temperature at the wall ($\theta = 1$ at $\delta = 0$). The lattice temperature in the two-step model is sensitive to the temperature rate whereas the diffusion model is not.

Actually, the time rate of change of temperature is the main cause for the temperature overshooting discussed by Taitel (1972). When two sharp wavefronts meet at a point in the solid, it produces a large time rate of change of temperature, $\partial T/\partial t$. Since the *initial time* of the point starts from the instant that the two wavefronts meet, the local temperature rate brought about by the impingement of two wavefronts serves as the *initial* heating provided to the point. The local temperature, as a result, becomes larger than the boundary temperature due to the rate effect. This phenomenon also exists in the lattice temperature of the microscopic two-step model. The amount of temperature overshooting, however, is not as pronounced (compared to that in the classical thermal wave theory) due to stronger dispersion in the phonon–electron interaction. Including that in the case of classical waves, however, the temperature overshoot may not have a practical engineering sense. A slight change in the boundary conditions may totally destroy the overshoot phenomenon (Bai and Lavine, 1991). The real physical scale (x) corresponding to the values of δ in Fig. 5, in addition, is on the order of 10^{-2} Å. The ballistic electron component and the quantum mechanical behavior in heat transport, which are not incorporated in the two-step model, become equally important on this scale.

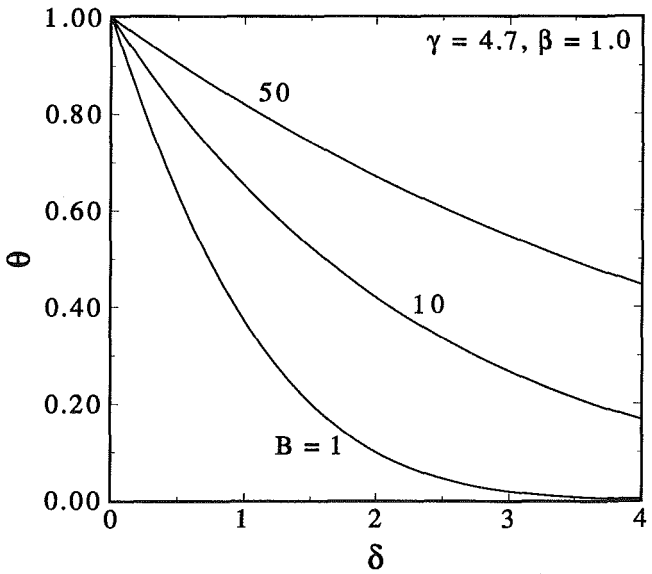

Fig. 4 Temperature distributions in the two-step model; B = 1, 10, and 50

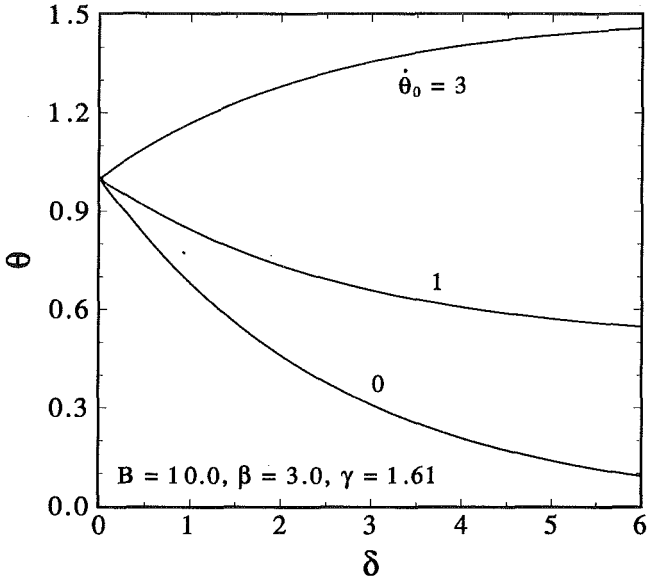

Fig. 5 The effect of initial temperature rate on the distributions of the lattice temperature: two-step model with B = 10.0, β = 3.0, and γ = 1.61 ($\beta\gamma$ = 4.83)

Conclusion

The nonequilibrium temperature of the metal lattice in the microscopic two-step model has been studied in this work. While a wave term is present in the energy equation governing the metal lattice, the sharp wavefront is destroyed by the strong dispersion in the phonon–electron interaction. For practical values of B in the two-step model, as shown in Fig. 4, the temperature curve behaves like diffusion. The transitional behavior shown in Fig. 3 is thus a mathematical illustration for the effect of the mixed-derivative term when compared to the classical thermal wave equation. This behavior, to be reiterated, will not be observed in the two-step heat transport process because the value of B is larger than 0.5 in reality.

The presence of the wave term in the two-step energy equation, in spite of the similarity of the temperature distributions to diffusion in Fig. 4, allows a specification of the time-rate of change of temperature ($\partial T/\partial t$) in the initial conditions. As a result, the value of $\partial T/\partial t$ at $t = 0$ participates in the determination of the *time history* of temperature. In comparison with diffusion where a specification of the initial temperature rate is impossible, the two-step model provides more detailed information for the way in which temperature evolves with time. This is an extremely important information for the heat transport process occurred in short times, like the present one. We also note that the *immediate*

response of the lattice temperature shown in Figs. 3 to 5 is a direct result of the initial condition, $T(x, 0) = T_0$. This condition assumes that the initial temperature of the solid rises to T_0 *immediately,* which eliminates all the possible relaxation behavior in the metal lattice. Should a more realistic simulation be attempted, the heat flux vector should be specified in the initial condition rather than temperature. The physical time at which the field temperature becomes sensible is then calculated to reveal the phase lag in thermal relaxation. This may be the reason that Qiu and Tien (1992) shift the initial time to a negative value in their analysis. Including the temperature-dependent heat capacity of the electron gas, the relaxation behavior of the metal lattice in the short-time transient is an important subject to be further studied.

Although the classical thermal wave model has led to many interesting phenomena (Tzou, 1992) and the relaxation behavior has been shown admissible within the framework of the second law of the extended irreversible thermodynamics (Tzou, 1993), the wave concept does not capture the microscale response in space (Bayazitoglu and Peterson, 1992). With regard to the lattice equation, Eq. (5), where the microscopic effect in heat transport is absorbed, an effort has recently been made (Tzou, 1994) to capture the *microscopic* effect in another phase lag of the temperature gradient. While the wave behavior is preserved by the traditional phase lag of the heat flux vector, the new phase lag of the temperature gradient gives the same mixed-derivative term in Eq. (5). Mathematical analogy between the two approaches is thus established. We shall leave the more detailed discussion to a future communication.

Acknowledgments

DYT and RJC gratefully acknowledge the research support by the National Science Foundation under Grant No. MSS-9220993 with the University of New Mexico.

References

Anisimov, S. I., Kapeliovich, B. L., and Perel'man, T. L., 1974, "Electron Emission From Metal Surfaces Exposed to Ultra-short Laser Pulses," *Soviet Physics JETP,* Vol. 39, pp. 375–377.

Bai, C., and Lavine, A. S., 1991, "Thermal Boundary Conditions for Hyperbolic Heat Conduction," ASME HTD-Vol. 253, pp. 37–44.

Baumeister, K. J., and Hamill, T. D., 1969, "Hyperbolic Heat Conduction Equation—A Solution for the Semi-infinite Body Problem," ASME JOURNAL OF HEAT TRANSFER, Vol. 91, pp. 543–548.

Bayazitoglu, Y., and Peterson, G. P., eds., 1992, *Fundamental Issues in Small Scale Heat Transfer,* ASME HTD-Vol. 227.

Brorson, S. D., Fujimoto, J. G., and Ippen, E. P., 1987, "Femtosecond Electron Heat-Transport Dynamics in Thin Gold Film," *Physical Review Letters,* Vol. 59, pp. 1962–1965.

Elsayed-Ali, H. E., Norris, T. B., Pessot, M. A., and Mourou, G. A., 1987, "Time-Resolved Observation of Electron–Phonon Relaxation in Copper," *Physical Review Letters,* Vol. 58, pp. 1212–1215.

Elsayed-Ali, H. E., 1991, "Femtosecond Thermoreflectivity and Thermotransmissivity of Polycrystalline and Single-Crystalline Gold Films," *Physical Review B,* Vol. 43, pp. 4488–4491.

Fujimoto, J. G., Liu, J. M., and Ippen, E. P., 1984, "Femtosecond Laser Interaction With Metallic Tungsten and Non-equilibrium Electron and Lattice Temperature," *Physical Review Letters,* Vol. 53, pp. 1837–1840.

Joseph, D. D., and Preziosi, L., 1989, "Heat Waves," *Reviews of Modern Physics,* Vol. 61, pp. 41–73.

Qiu, T. Q., and Tien, C. L., 1992, "Short-Pulse Laser Heating on Metals," *International Journal of Heat and Mass Transfer,* Vol. 35, pp. 719–726.

Qiu, T. Q., and Tien, C. L., 1993, "Heat Transfer Mechanisms During Short-Pulse Laser Heating of Metals," ASME JOURNAL OF HEAT TRANSFER, Vol. 115, pp. 835–841.

Taitel, Y., 1972, "On the Parabolic, Hyperbolic and Discrete Formulations of the Heat Conduction Equation," *International Journal of Heat and Mass Transfer,* Vol. 15, pp. 369–371.

Tzou, D. Y., 1992, "Thermal Shock Phenomena Under High-Rate Response in Solids," in: *Annual Review of Heat Transfer,* Chang-Lin Tien, ed., Hemisphere Publishing Inc., Washington, DC, Chap. 3, pp. 111–185.

Tzou, D. Y., 1993, "An Engineering Assessment to the Relaxation Time in Thermal Waves," *International Journal of Heat and Mass Transfer,* Vol. 36, pp. 1845–1851.

Tzou, D. Y., 1994, "A Universal Model for Heat Conduction From Macroscopic to Microscopic Scales," ASME JOURNAL OF HEAT TRANSFER, accepted for publication.

Film/Substrate Thermal Boundary Resistance for an Er–Ba–Cu–O High-T_c Thin Film

P. E. Phelan,[1] Y. Song,[2] O. Nakabeppu,[3] K. Ito,[3] K. Hijikata,[3] T. Ohmori,[4] and K. Torikoshi[5]

Nomenclature

c = film specific heat, J kg^{-1} K^{-1}
d = film thickness, nm
I = bias current, mA
q = heat flux from strip 1 to the substrate, W cm^{-2}
R = electrical resistance, kΩ
R_b = film/substrate thermal boundary resistance, K cm^2 W^{-1}
T = temperature, K
T_C = critical temperature, below which the electrical resistance is zero, K
V = voltage, mV
ρ = film density, kg m^{-3}
τ = time constant for exponential decay of the film voltage, ns

Subscripts and Superscripts

s = substrate
1 = wide strip (heater)
2 = narrow strip (sensor)
+ = inlet
− = outlet

Introduction

The thermal design and operation of thin-film electronics at low temperatures depends crucially on the thermal resistance at the boundary between the film and the substrate (R_b). Optimal design of such systems made from high-temperature superconductors (HTS), including passive microwave devices, digital devices based on Josephson junctions, optical switches, and infrared radiation detectors (bolometers), is also dependent on accurate knowledge of R_b. Furthermore, the mechanism of the observed voltage response of thin-film HTS to pulsed and chopped irradiation cannot be unambiguously determined unless a firm estimate of R_b is in hand (Flik et al., 1990). Direct experimental measurement of R_b, however, over the temperature range of most practical interest, which includes the boiling point of nitrogen (77 K) and below, has not been reported.

Thermal contact resistance at cryogenic temperatures between a metal and a dielectric, or between two dielectrics, can be several orders of magnitude higher than that at room temperature. This

[1] Department of Mechanical Engineering, University of Hawaii at Manoa, 2540 Dole Street, Holmes 302, Honolulu, HI 96822.

[2] Department of Physics and Astronomy, University of Hawaii at Manoa, 2505 Correa Road, Watanabe Hall, Honolulu, HI 96822.

[3] Department of Mechanical Engineering Science, Tokyo Institute of Technology, 2-12-1 Ohokayama, Meguro-ku, Tokyo 152 Japan.

[4] Exploratory Technology Department II, Ishikawajima-Harima Heavy Industries Co., 1 Shin-Nakahara-cho, Isogo-ku, Yokohama 235 Japan.

[5] Mechanical Engineering Laboratory, Daikin Industrial Corporation, 1304 Kaneoka, Sakai-shi, Osaka 591 Japan.

Contributed by the Heat Transfer Division and presented at the ASME Winter Annual Meeting, Anaheim, California, November 8–13, 1992. Manuscript received by the Heat Transfer Division June 1992; revision received February 1994. Keywords: Conduction, Cryogenics, Direct-Contact Heat Transfer. Associate Technical Editor: L. S. Fletcher.

response of the lattice temperature shown in Figs. 3 to 5 is a direct result of the initial condition, $T(x, 0) = T_0$. This condition assumes that the initial temperature of the solid rises to T_0 *immediately,* which eliminates all the possible relaxation behavior in the metal lattice. Should a more realistic simulation be attempted, the heat flux vector should be specified in the initial condition rather than temperature. The physical time at which the field temperature becomes sensible is then calculated to reveal the phase lag in thermal relaxation. This may be the reason that Qiu and Tien (1992) shift the initial time to a negative value in their analysis. Including the temperature-dependent heat capacity of the electron gas, the relaxation behavior of the metal lattice in the short-time transient is an important subject to be further studied.

Although the classical thermal wave model has led to many interesting phenomena (Tzou, 1992) and the relaxation behavior has been shown admissible within the framework of the second law of the extended irreversible thermodynamics (Tzou, 1993), the wave concept does not capture the microscale response in space (Bayazitoglu and Peterson, 1992). With regard to the lattice equation, Eq. (5), where the microscopic effect in heat transport is absorbed, an effort has recently been made (Tzou, 1994) to capture the *microscopic* effect in another phase lag of the temperature gradient. While the wave behavior is preserved by the traditional phase lag of the heat flux vector, the new phase lag of the temperature gradient gives the same mixed-derivative term in Eq. (5). Mathematical analogy between the two approaches is thus established. We shall leave the more detailed discussion to a future communication.

Acknowledgments

DYT and RJC gratefully acknowledge the research support by the National Science Foundation under Grant No. MSS-9220993 with the University of New Mexico.

References

Anisimov, S. I., Kapeliovich, B. L., and Perel'man, T. L., 1974, "Electron Emission From Metal Surfaces Exposed to Ultra-short Laser Pulses," *Soviet Physics JETP,* Vol. 39, pp. 375–377.

Bai, C., and Lavine, A. S., 1991, "Thermal Boundary Conditions for Hyperbolic Heat Conduction," ASME HTD-Vol. 253, pp. 37–44.

Baumeister, K. J., and Hamill, T. D., 1969, "Hyperbolic Heat Conduction Equation—A Solution for the Semi-infinite Body Problem," ASME JOURNAL OF HEAT TRANSFER, Vol. 91, pp. 543–548.

Bayazitoglu, Y., and Peterson, G. P., eds., 1992, *Fundamental Issues in Small Scale Heat Transfer,* ASME HTD-Vol. 227.

Brorson, S. D., Fujimoto, J. G., and Ippen, E. P., 1987, "Femtosecond Electron Heat-Transport Dynamics in Thin Gold Film," *Physical Review Letters,* Vol. 59, pp. 1962–1965.

Elsayed-Ali, H. E., Norris, T. B., Pessot, M. A., and Mourou, G. A., 1987, "Time-Resolved Observation of Electron–Phonon Relaxation in Copper," *Physical Review Letters,* Vol. 58, pp. 1212–1215.

Elsayed-Ali, H. E., 1991, "Femtosecond Thermoreflectivity and Thermotransmissivity of Polycrystalline and Single-Crystalline Gold Films," *Physical Review B,* Vol. 43, pp. 4488–4491.

Fujimoto, J. G., Liu, J. M., and Ippen, E. P., 1984, "Femtosecond Laser Interaction With Metallic Tungsten and Non-equilibrium Electron and Lattice Temperature," *Physical Review Letters,* Vol. 53, pp. 1837–1840.

Joseph, D. D., and Preziosi, L., 1989, "Heat Waves," *Reviews of Modern Physics,* Vol. 61, pp. 41–73.

Qiu, T. Q., and Tien, C. L., 1992, "Short-Pulse Laser Heating on Metals," *International Journal of Heat and Mass Transfer,* Vol. 35, pp. 719–726.

Qiu, T. Q., and Tien, C. L., 1993, "Heat Transfer Mechanisms During Short-Pulse Laser Heating of Metals," ASME JOURNAL OF HEAT TRANSFER, Vol. 115, pp. 835–841.

Taitel, Y., 1972, "On the Parabolic, Hyperbolic and Discrete Formulations of the Heat Conduction Equation," *International Journal of Heat and Mass Transfer,* Vol. 15, pp. 369–371.

Tzou, D. Y., 1992, "Thermal Shock Phenomena Under High-Rate Response in Solids," in: *Annual Review of Heat Transfer,* Chang-Lin Tien, ed., Hemisphere Publishing Inc., Washington, DC, Chap. 3, pp. 111–185.

Tzou, D. Y., 1993, "An Engineering Assessment to the Relaxation Time in Thermal Waves," *International Journal of Heat and Mass Transfer,* Vol. 36, pp. 1845–1851.

Tzou, D. Y., 1994, "A Universal Model for Heat Conduction From Macroscopic to Microscopic Scales," ASME JOURNAL OF HEAT TRANSFER, accepted for publication.

Film/Substrate Thermal Boundary Resistance for an Er–Ba–Cu–O High-T_c Thin Film

P. E. Phelan,[1] Y. Song,[2] O. Nakabeppu,[3] K. Ito,[3] K. Hijikata,[3] T. Ohmori,[4] and K. Torikoshi[5]

Nomenclature

c = film specific heat, J kg^{-1} K^{-1}
d = film thickness, nm
I = bias current, mA
q = heat flux from strip 1 to the substrate, W cm^{-2}
R = electrical resistance, kΩ
R_b = film/substrate thermal boundary resistance, K cm^2 W^{-1}
T = temperature, K
T_C = critical temperature, below which the electrical resistance is zero, K
V = voltage, mV
ρ = film density, kg m^{-3}
τ = time constant for exponential decay of the film voltage, ns

Subscripts and Superscripts

s = substrate
1 = wide strip (heater)
2 = narrow strip (sensor)
+ = inlet
− = outlet

Introduction

The thermal design and operation of thin-film electronics at low temperatures depends crucially on the thermal resistance at the boundary between the film and the substrate (R_b). Optimal design of such systems made from high-temperature superconductors (HTS), including passive microwave devices, digital devices based on Josephson junctions, optical switches, and infrared radiation detectors (bolometers), is also dependent on accurate knowledge of R_b. Furthermore, the mechanism of the observed voltage response of thin-film HTS to pulsed and chopped irradiation cannot be unambiguously determined unless a firm estimate of R_b is in hand (Flik et al., 1990). Direct experimental measurement of R_b, however, over the temperature range of most practical interest, which includes the boiling point of nitrogen (77 K) and below, has not been reported.

Thermal contact resistance at cryogenic temperatures between a metal and a dielectric, or between two dielectrics, can be several orders of magnitude higher than that at room temperature. This

[1] Department of Mechanical Engineering, University of Hawaii at Manoa, 2540 Dole Street, Holmes 302, Honolulu, HI 96822.

[2] Department of Physics and Astronomy, University of Hawaii at Manoa, 2505 Correa Road, Watanabe Hall, Honolulu, HI 96822.

[3] Department of Mechanical Engineering Science, Tokyo Institute of Technology, 2-12-1 Ohokayama, Meguro-ku, Tokyo 152 Japan.

[4] Exploratory Technology Department II, Ishikawajima-Harima Heavy Industries Co., 1 Shin-Nakahara-cho, Isogo-ku, Yokohama 235 Japan.

[5] Mechanical Engineering Laboratory, Daikin Industrial Corporation, 1304 Kaneoka, Sakai-shi, Osaka 591 Japan.

Contributed by the Heat Transfer Division and presented at the ASME Winter Annual Meeting, Anaheim, California, November 8–13, 1992. Manuscript received by the Heat Transfer Division June 1992; revision received February 1994. Keywords: Conduction, Cryogenics, Direct-Contact Heat Transfer. Associate Technical Editor: L. S. Fletcher.

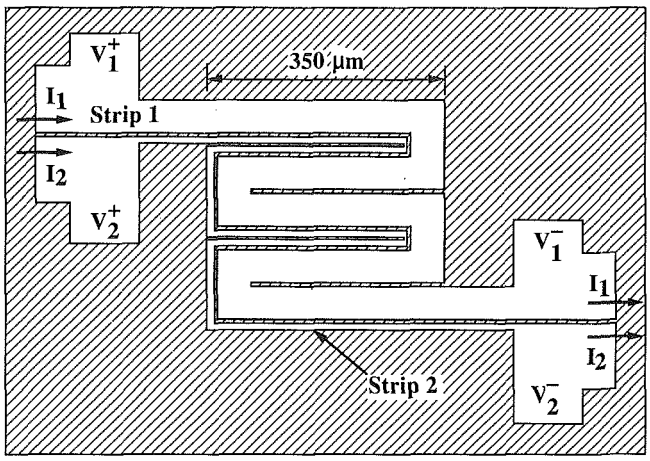

Fig. 1 Two-strip etching pattern for measuring the thermal boundary resistance between strip 1 and the substrate. The width of strip 1 is 50 μm, that of strip 2 is 10 μm, and the distance separating the strips is 5 μm.

phenomenon, for temperatures less than about 30 K, can be satisfactorily explained by *acoustic mismatch theory* (AMT) (Little, 1959; Swartz and Pohl, 1989). In brief, AMT assumes that the transmission of phonons at an interface is governed by continuum wave theory, such that phonons can be reflected or transmitted at an interface in the same manner as photons are described by electromagnetic wave theory. Acoustic mismatch theory predicts that R_b is proportional to the inverse of the third power of the temperature, and therefore increases significantly with decreasing temperature (Swartz and Pohl, 1989).

At temperatures higher than about 30 K, R_b predicted from AMT can be much lower than measured values at solid–solid interfaces (Swartz and Pohl, 1989). Phonon heat transport across the interface appears to become very sensitive to surface and subsurface structure at these temperatures. The dominant phonon wavelength for heat flow at 86 K, the minimum temperature measured in this study, is only ~0.5 nm, where the dominant phonon frequency is calculated as described by Swartz and Pohl (1989). Considering this very short length scale, the film probably does not appear continuous to the heat-transporting phonons, and thus AMT is not generally applicable at the temperatures encountered in this study.

To date, only one study has been reported in which R_b was directly measured for high-T_c thin films. Nahum et al. (1991) measured R_b over the temperature range 97 K $\leq T \leq$ 177 K for Y–Ba–Cu–O (YBCO) films deposited on sapphire with or without various intervening buffer layers. Their results indicate that $R_b \approx 10^{-3}$ K cm^2 W^{-1}, and is relatively independent of temperature.

The thermal contact resistance can also be indirectly estimated from the measured time constant of the transient voltage response to a heat or optical input. The values of R_b from four such studies (Carr et al., 1990; Marshall et al., 1991; Levey et al., 1992; Zeuner et al., 1992) lie between 8×10^{-4} and 3×10^{-3} K cm^2 W^{-1} for temperatures ranging between 30 K and room temperature. Two of these measurements concerned YBCO films deposited on MgO substrates (Carr et al., 1990; Marshall et al., 1991), another was for a YBCO film on a $LaAlO_3$ substrate (Levey et al., 1992), and the other was for Tl–Ba–Ca–Cu–O (TBCCO) films on MgO substrates (Zeuner et al., 1992). Still lacking after all these investigations, however, is a direct measurement of R_b for temperatures below 97 K.

The present study is an experimental investigation of R_b for a normal-state Er–Ba–Cu–O (EBCO) film deposited on an MgO substrate. The thermal contact resistance is directly measured using the method of Swartz and Pohl (1989). The minimum substrate temperature is 86 K. The results suggest that R_b for this film is comparable to the previously reported values.

Experiment

Apparatus. The experimental sample was a 70-nm-thick Er–Ba–Cu–O film on an MgO (100) substrate, and was prepared by ionized cluster beam codeposition. Details of the deposition procedure are given elsewhere (Yamanashi et al., 1989). The film was chemically etched in the double meander pattern shown in Fig. 1 by a 1 percent H_3PO_4 solution, resulting in two electrically insulated Er–Ba–Cu–O strips. Strip 1 is 50 μm wide, and strip 2 is 10 μm wide. They are separated by a distance of 5 μm, and each has a total length of 1.970 mm. Electrical contacts were made to the eight sputtered Au pads with Ag paste.

The mounted sample was cooled to cryogenic temperatures in a closed-cycle refrigeration system. Thermal contact between the mounted sample and the cold finger of the refrigerator was achieved with Apiezon thermal grease. During the course of the experiments, the sample was maintained in a vacuum environment, with two layers of shielding between the sample and the room-temperature vacuum shroud. The sample temperature, for isothermal conditions, was measured with a Si diode temperature sensor (accurate to within ±0.1 K) mounted next to the sample on the cold finger. The output voltages were recorded with a computerized data acquisition system.

Procedure. The experimental method is similar to that presented by Swartz and Pohl (1989). Referring to Fig. 1, the wide strip (strip 1) is used as the heater, and the narrow strip (strip 2) is used as the temperature sensor. Due to degradation from the etching process, the critical temperature (T_C) of strip 2 is slightly less than that of strip 1: 67 K and 69 K, respectively. Four electrical contacts, including the voltage taps V_i^+ and V_i^-, are made to each strip, allowing for independent four-point measurement of the resistance of each strip for various bias currents. Initially, the sample was cooled to well below T_C, and then calibration curves for the electrical resistance of the two strips were determined with a small bias current ($\leq$5 μA) while the sample slowly heated up to room temperature. The results of the calibration are given in Fig. 2. The curves were fitted with a third-order polynomial function for 80 K $< T \leq$ 91 K, by a second-order polynomial function for 91 K $< T \leq$ 116 K, and by a linear function for 116 K $< T <$ 240 K. In the subsequent measurements, the temperature of each strip, T_1 and T_2, respectively, is determined from the measured electrical resistances and the fitted curves.

In order to measure the thermal boundary resistance between strip 1 and the substrate, a relatively large DC current is passed through strip 1, while a much smaller sensing current ($I_2 \leq 5$ μA) is passed through strip 2. The Joule heating in strip 1 in-

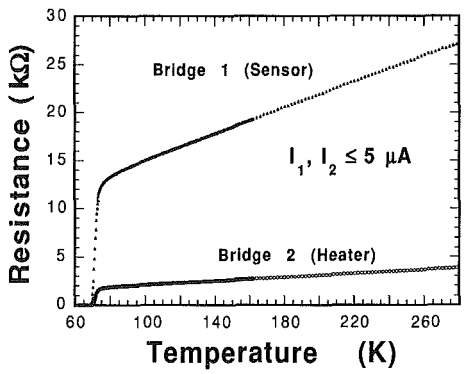

Fig. 2 Calibration curves, taken under isothermal conditions and with small bias currents, for the electrical resistances of both strips

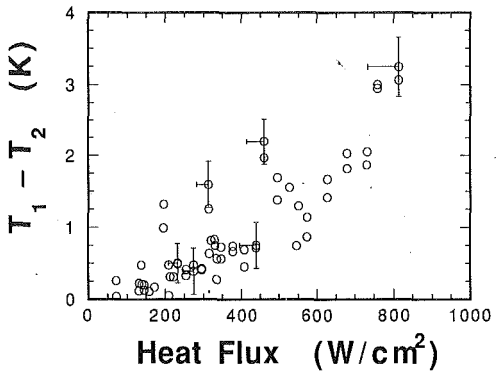

Fig. 3 Film/substrate temperature drop versus heat flux, for all values of substrate temperature

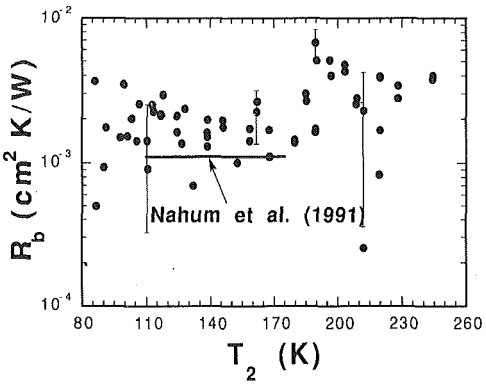

Fig. 4 Thermal boundary resistance between strip 1 and the substrate, as a function of the approximate substrate temperature

creases its temperature and the nearby substrate temperature, and thus causes the temperature of strip 2 to increase. Under steady-state conditions, R_b can be easily determined from the definition of the thermal boundary resistance:

$$R_b = \frac{T_1 - T_S}{q} \tag{1}$$

where T_S is the substrate temperature directly underneath strip 1, and q is the heat flux from strip 1 caused by the Joule heating, provided both temperatures and the heat flux are known. In the present experiment, q is accurately calculated from the known voltage and current of strip 1, along with its contact area (9.85×10^{-4} cm^2). The substrate temperature T_S is nearly equal to T_2, since the two strips are separated by only 5 μm and are intertwined, and the small heat flux from strip 2 does not result in a significant temperature difference between the substrate and strip 2. Both T_1 and T_2 are determined from the steady-state values of their electrical resistances, which are considered to attain steady state after subsequent data points change by less than 0.1 percent, after which the remaining points are averaged. Note that since the resistance of a superconductor can be a function of the bias current in its transition region between the normal and superconducting states, the R_b measurements are performed at temperatures well above the transition temperature, which is less than 80 K for both strips.

Uncertainty. There are four possible causes of uncertainty: (a) the general determination of the temperatures T_1 and T_2 from R_1 and R_2; (b) the temperature drop in the substrate between strip 1 and strip 2; (c) the temperature drop across the film thickness; and (d) the heat leak out through the electrical leads. Error (a) is estimated as the standard deviation of the difference between the curves fitted through the calibration data points, and the data points themselves. This process yields the uncertainty in the temperature difference, $T_1 - T_2$, of about 0.3 K. The resulting median uncertainty in R_b is about 10^{-3} cm^2 K/W, and varies depending on the value of T_2. For error (b), the relatively high thermal conductivity of the MgO substrate (230 W m^{-1} K^{-1} at 100 K) renders this error negligible except where the highest temperatures and heat fluxes are encountered. For example, at 250 K and for a heat flux of 800 W cm^{-2}, which corresponds approximately to the highest temperature and heat flux in the experiment, the estimated temperature drop between the strips is about 0.4 K. At 100 K and for a heat flux of 400 W cm^{-2}, however, the temperature drop is only about 0.06 K. Error (b), then, is negligible for the majority of the reported data, but may be significant for the highest temperatures and heat fluxes. Error (c) is considered negligible, since the film thickness is only 70 nm. Finally, error (d) is determined to result in an error in the measured heat flux from strip 1 to the substrate of about 10 percent. The error bars drawn in Figs. 3 and 4, which are for representative data points, only consider errors (a) and (d).

Results and Discussion

The dependence of the temperature drop between the two strips, that is, between the film and the substrate, on the heat flux, is given in Fig. 3. This figure includes all the measured data, which span a substrate temperature range of 86 K $\leq T_2 \leq$ 244 K. Neglecting the scatter in the data, $T_1 - T_2$ tends to increase with increasing q. Because of the varying substrate temperature, it is difficult to make any conclusions regarding the linearity of the relationship. The increased error (b) at large q also adds uncertainty. In general, however, the data follow the expected pattern.

Figure 4 shows how the measured values of R_b vary with substrate temperature. Some data from Nahum et al. (1991) (their Fig. 2, sample a) are also shown for comparison. The present data, for the most part, are clustered in the range $1 \sim 5 \times 10^{-3}$ cm^2 K W^{-1}, which is slightly higher than the measurements of Nahum et al. (1991). The values of R_b tend to increase with increasing substrate temperature, but there may be some effect of the heat flux, along with the increased error (b) at high temperatures.

Table 1 presents a direct comparison of the various results that have been reported for R_b for high-T_C films. Nahum et al. (1991) reported that R_b was independent of the heat flux, and concluded that within their measured temperature range, the electrical resistance did not vary with bias current. In the "time constant" method, the exponential time constant (τ) for the voltage of the high-T_C film to decay after an optical pulse is measured, and then R_b can be estimated from

Table 1 Reported values of R_b for high-T_c films

Study	Film/Substrate	Substrate Temperature (K)	Method	R_b (cm^2 K W^{-1})
Carr et al., 1990	YBCO/MgO	81	time constant	8×10^{-4}
Marshall et al., 1991	YBCO/MgO	300	optical transient grating	9×10^{-4}
Nahum et al., 1991	YBCO/sapphire + buffer layers	97 ≤ T ≤ 177	direct measurement	$\sim 1 \times 10^{-3}$
Levey et al., 1992	YBCO/$LaAlO_3$	90	time constant	3×10^{-3}
Zeuner et al., 1992	TBCCO/MgO	30 ≤ T ≤ 150	optical response	$\sim 1 \times 10^{-3}$
present	EBCO/MgO	86 ≤ T ≤ 244	direct measurement	$1 \sim 5 \times 10^{-3}$

$$R_b = \frac{\tau}{d\rho c} \quad (2)$$

where d is the film thickness, ρ is the film density, and c is the film specific heat. This expression can be derived from the analytic expression for the temperature rise of a film subjected to a step heat input (Flik et al., 1990). Equation (2) can only be considered an estimate, however, since it implicitly assumes that the resistance of the film, and hence its voltage for constant bias current, depends linearly on the temperature. The three values of R_b obtained in this manner are 8×10^{-4} K cm^2 W^{-1} (Carr et al., 1990), 3×10^{-3} K cm^2 W^{-1} (Levey et al., 1992), and 1×10^{-3} K cm^2 W^{-1} (Zeuner et al., 1992). Finally, from the "optical transient grating" technique, in which two low-power simultaneous laser pulses are used to excite acoustic waves in the high-T_C film (Marshall et al., 1991), a time constant is also determined, which is inserted into Eq. (2) to give R_b. The value of R_b measured in this way is about 9×10^{-4} K cm^2 W^{-1}.

All reported values of R_b for high-T_c films are relatively large. The acoustic mismatch theory, which assumes a perfectly smooth interface on the order of the phonon wavelength, predicts $R_b \sim 10^{-5}$ K cm^2 W^{-1} at 100 K (Little, 1959), which is about two orders of magnitude below our lowest values of R_b. The large thermal boundary resistance may be due to imperfect unit cell orientation, or to a preponderance of dislocations or defects, near the film/substrate interface.

Conclusions

The thermal boundary resistance between an Er–Ba–Cu–O film and an MgO substrate was directly measured for substrate temperatures as low as 86 K. In general, the present values of R_b range from $1 \sim 5 \times 10^{-3}$ K cm^2 W^{-1}, which are comparable with those reported earlier, both from direct and indirect measurements.

Acknowledgments

This material is based upon work supported by the National Science Foundation under Grant No. CTS93-07753. The authors also owe their gratitude to H. Ito and colleagues at Mitsubishi Electric Co., who furnished the high-T_C sample; Dr. Y. Kozono and colleagues at Hitachi Co., who patterned the sample; and Professor J. R. Gaines of the University of Hawaii at Manoa, who allowed us the use of his cryogenic laboratory facilities. One of the authors (P.E.P.) also wishes to thank the Japan Society for the Promotion of Science and the Japan Ministry of Education for their generous financial support during the initiation of this project.

References

Carr, G. L., Quijada, M., Tanner, D. B., Hirschmugl, C. J., Williams, G. P., Etemad, S., Dutta, B., DeRosa, F., Inam, A., Venkatesan, T., and Xi, X., 1990, "Fast Bolometric Response of High T_C Detectors Measured With Subnanosecond Synchrotron Radiation," *Applied Physics Letters,* Vol. 57, pp. 2725–2727.

Flik, M. I., Phelan, P. E., and Tien, C. L., 1990, "Thermal Model for the Bolometric Response of High T_C Superconducting Films to Optical Pulses," *Cryogenics,* Vol. 30, pp. 1118–1128.

Frenkel, A., Chang, C. C., Clausen, E., Venkatesan, T., Lin, P. S. D., Wu, X. D., Inam, A., and Lalevic, B., 1990, "SEM and Electrical Studies of Current Induced Superconducting-Resistive Transitions in $Y_1Ba_2Cu_3O_{7-x}$ Thin Films," *Journal of Materials Research,* Vol. 5, pp. 691–703.

Levey, C. G., Etemad, S., and Inam, A., 1992, "Optically Detected Transient Thermal Response of High T_C Epitaxial Films," *Applied Physics Letters,* Vol. 60, pp. 126–128.

Little, W. A., 1959, "The Transport of Heat Between Dissimilar Solids at Low Temperatures," *Canadian Journal of Physics,* Vol. 37, pp. 334–349.

Marshall, C. D., Fishman, I. M., and Fayer, M. D., 1991, "Ultrasonic Wave Propagation and Barrier-Limited Heat Flow in Thin Films of $YBa_2Cu_3O_{7-x}$," *Physical Review B,* Vol. 43, pp. 2696–2699.

Nahum, M., Verghese, S., Richards, P. L., and Char, K., 1991, "Thermal Boundary Resistance for $YBa_2Cu_3O_{7-\delta}$ Films," *Applied Physics Letters,* Vol. 59, pp. 2034–2036.

Swartz, E. T., and Pohl, R. O., 1989, "Thermal Boundary Resistance," *Reviews of Modern Physics,* Vol. 61, pp. 605–668.

Yamanashi, K., Yasunaga, S., Kawagoe, Y., Sato, K., and Imada, K., 1989, "Synthesis of Superconducting Y–Ba–Cu–O Thin Films by Ionized Cluster Beam Codeposition," *Nuclear Instruments and Methods in Physics Research,* Vol. B37/38, pp. 930–934.

Zeuner, S., Lengfellner, H., Betz, J., Renk, K. F., and Prettl, W., 1992, "Heat Propagation in High-T_C Films Investigated by Optical Response Measurements," *Applied Physics Letters,* Vol. 61, pp. 973–975.

Determination of the Reaction Function in a Reaction-Diffusion Parabolic Problem

H. R. B. Orlande[1] and M. N. Özişik[1]

Introduction

The study of reaction-diffusion problems has several applications, including, among others, nonlinear heat conduction (Joseph and Sparrow, 1970), chemical reactor analysis, and combustion (Kamenetskii, 1969).

A vast amount of literature exists on the analysis and solution of linear inverse diffusion problems. In the case of nonlinear inverse diffusion, the available works are mostly concerned with the estimation of temperature-dependent properties, such as thermal conductivity and heat capacity (Artyukhin and Nenarokomov, 1987; Jarny et al., 1986). In such cases, a functional form, e.g., B-Splines, was used to approximate the dependence of the unknown quantity on temperature and the inverse analysis was reduced to a parameter estimation problem.

In this work we apply a function estimation approach based on the *conjugate gradient method* of inverse analysis with *adjoint equation* to estimate the unknown reaction function in a reaction-diffusion parabolic problem. It is assumed that no prior information is available on the functional form of the unknown quantity.

Inverse Analysis for Estimating Reaction Function

The inverse analysis of function estimation approach, utilizing the conjugate gradient method with adjoint equation, consists of the basic steps described below (Jarny et al., 1991).

The Direct Problem. For the present study, the direct problem is taken as the one-dimensional reaction-diffusion system given by:

$$C(T)\frac{\partial T}{\partial t} - \frac{\partial}{\partial x}\left[k(T)\frac{\partial T}{\partial x}\right] - g(T) = 0 \quad \text{in } 0 < x < L;\ \text{for } t > 0 \quad (1a)$$

$$\frac{\partial T}{\partial x} = 0 \quad \text{at } x = 0;\ \text{for } T > 0 \quad (1b)$$

$$k(T)\frac{\partial T}{\partial x} = \phi_L(t) \quad \text{at } x = L;\ \text{for } t > 0 \quad (1c)$$

$$T(x, 0) = F(x) \quad \text{for } t = 0;\ \text{in } 0 < x < L \quad (1d)$$

[1] Mechanical and Aerospace Engineering Department, North Carolina State University, Raleigh, NC 27695-7910.

Contributed by the Heat Transfer Division of THE AMERICAN SOCIETY OF MECHANICAL ENGINEERS. Manuscript received by the Heat Transfer Division May 1993; revision received October 1993. Keywords: Conduction, Numerical Methods, Transient and Unsteady Heat Transfer. Associate Technical Editor: Y. Bayazitoglu.

$$R_b = \frac{\tau}{d\rho c} \quad (2)$$

where d is the film thickness, ρ is the film density, and c is the film specific heat. This expression can be derived from the analytic expression for the temperature rise of a film subjected to a step heat input (Flik et al., 1990). Equation (2) can only be considered an estimate, however, since it implicitly assumes that the resistance of the film, and hence its voltage for constant bias current, depends linearly on the temperature. The three values of R_b obtained in this manner are 8×10^{-4} K cm^2 W^{-1} (Carr et al., 1990), 3×10^{-3} K cm^2 W^{-1} (Levey et al., 1992), and 1×10^{-3} K cm^2 W^{-1} (Zeuner et al., 1992). Finally, from the "optical transient grating" technique, in which two low-power simultaneous laser pulses are used to excite acoustic waves in the high-T_C film (Marshall et al., 1991), a time constant is also determined, which is inserted into Eq. (2) to give R_b. The value of R_b measured in this way is about 9×10^{-4} K cm^2 W^{-1}.

All reported values of R_b for high-T_c films are relatively large. The acoustic mismatch theory, which assumes a perfectly smooth interface on the order of the phonon wavelength, predicts $R_b \sim 10^{-5}$ K cm^2 W^{-1} at 100 K (Little, 1959), which is about two orders of magnitude below our lowest values of R_b. The large thermal boundary resistance may be due to imperfect unit cell orientation, or to a preponderance of dislocations or defects, near the film/substrate interface.

Conclusions

The thermal boundary resistance between an Er–Ba–Cu–O film and an MgO substrate was directly measured for substrate temperatures as low as 86 K. In general, the present values of R_b range from $1 \sim 5 \times 10^{-3}$ K cm^2 W^{-1}, which are comparable with those reported earlier, both from direct and indirect measurements.

Acknowledgments

This material is based upon work supported by the National Science Foundation under Grant No. CTS93-07753. The authors also owe their gratitude to H. Ito and colleagues at Mitsubishi Electric Co., who furnished the high-T_C sample; Dr. Y. Kozono and colleagues at Hitachi Co., who patterned the sample; and Professor J. R. Gaines of the University of Hawaii at Manoa, who allowed us the use of his cryogenic laboratory facilities. One of the authors (P.E.P.) also wishes to thank the Japan Society for the Promotion of Science and the Japan Ministry of Education for their generous financial support during the initiation of this project.

References

Carr, G. L., Quijada, M., Tanner, D. B., Hirschmugl, C. J., Williams, G. P., Etemad, S., Dutta, B., DeRosa, F., Inam, A., Venkatesan, T., and Xi, X., 1990, "Fast Bolometric Response of High T_C Detectors Measured With Subnanosecond Synchrotron Radiation," *Applied Physics Letters,* Vol. 57, pp. 2725–2727.

Flik, M. I., Phelan, P. E., and Tien, C. L., 1990, "Thermal Model for the Bolometric Response of High T_C Superconducting Films to Optical Pulses," *Cryogenics,* Vol. 30, pp. 1118–1128.

Frenkel, A., Chang, C. C., Clausen, E., Venkatesan, T., Lin, P. S. D., Wu, X. D., Inam, A., and Lalevic, B., 1990, "SEM and Electrical Studies of Current Induced Superconducting-Resistive Transitions in $Y_1Ba_2Cu_3O_{7-x}$ Thin Films," *Journal of Materials Research,* Vol. 5, pp. 691–703.

Levey, C. G., Etemad, S., and Inam, A., 1992, "Optically Detected Transient Thermal Response of High T_C Epitaxial Films," *Applied Physics Letters,* Vol. 60, pp. 126–128.

Little, W. A., 1959, "The Transport of Heat Between Dissimilar Solids at Low Temperatures," *Canadian Journal of Physics,* Vol. 37, pp. 334–349.

Marshall, C. D., Fishman, I. M., and Fayer, M. D., 1991, "Ultrasonic Wave Propagation and Barrier-Limited Heat Flow in Thin Films of $YBa_2Cu_3O_{7-x}$," *Physical Review B,* Vol. 43, pp. 2696–2699.

Nahum, M., Verghese, S., Richards, P. L., and Char, K., 1991, "Thermal Boundary Resistance for $YBa_2Cu_3O_{7-\delta}$ Films," *Applied Physics Letters,* Vol. 59, pp. 2034–2036.

Swartz, E. T., and Pohl, R. O., 1989, "Thermal Boundary Resistance," *Reviews of Modern Physics,* Vol. 61, pp. 605–668.

Yamanashi, K., Yasunaga, S., Kawagoe, Y., Sato, K., and Imada, K., 1989, "Synthesis of Superconducting Y–Ba–Cu–O Thin Films by Ionized Cluster Beam Codeposition," *Nuclear Instruments and Methods in Physics Research,* Vol. B37/38, pp. 930–934.

Zeuner, S., Lengfellner, H., Betz, J., Renk, K. F., and Prettl, W., 1992, "Heat Propagation in High-T_C Films Investigated by Optical Response Measurements," *Applied Physics Letters,* Vol. 61, pp. 973–975.

Determination of the Reaction Function in a Reaction-Diffusion Parabolic Problem

H. R. B. Orlande[1] and M. N. Özişik[1]

Introduction

The study of reaction-diffusion problems has several applications, including, among others, nonlinear heat conduction (Joseph and Sparrow, 1970), chemical reactor analysis, and combustion (Kamenetskii, 1969).

A vast amount of literature exists on the analysis and solution of linear inverse diffusion problems. In the case of nonlinear inverse diffusion, the available works are mostly concerned with the estimation of temperature-dependent properties, such as thermal conductivity and heat capacity (Artyukhin and Nenarokomov, 1987; Jarny et al., 1986). In such cases, a functional form, e.g., B-Splines, was used to approximate the dependence of the unknown quantity on temperature and the inverse analysis was reduced to a parameter estimation problem.

In this work we apply a function estimation approach based on the *conjugate gradient method* of inverse analysis with *adjoint equation* to estimate the unknown reaction function in a reaction-diffusion parabolic problem. It is assumed that no prior information is available on the functional form of the unknown quantity.

Inverse Analysis for Estimating Reaction Function

The inverse analysis of function estimation approach, utilizing the conjugate gradient method with adjoint equation, consists of the basic steps described below (Jarny et al., 1991).

The Direct Problem. For the present study, the direct problem is taken as the one-dimensional reaction-diffusion system given by:

$$C(T)\frac{\partial T}{\partial t} - \frac{\partial}{\partial x}\left[k(T)\frac{\partial T}{\partial x}\right] - g(T) = 0 \quad \text{in } 0 < x < L; \text{ for } t > 0 \quad (1a)$$

$$\frac{\partial T}{\partial x} = 0 \quad \text{at } x = 0; \text{ for } T > 0 \quad (1b)$$

$$k(T)\frac{\partial T}{\partial x} = \phi_L(t) \quad \text{at } x = L; \text{ for } t > 0 \quad (1c)$$

$$T(x, 0) = F(x) \quad \text{for } t = 0; \text{ in } 0 < x < L \quad (1d)$$

[1] Mechanical and Aerospace Engineering Department, North Carolina State University, Raleigh, NC 27695-7910.

Contributed by the Heat Transfer Division of THE AMERICAN SOCIETY OF MECHANICAL ENGINEERS. Manuscript received by the Heat Transfer Division May 1993; revision received October 1993. Keywords: Conduction, Numerical Methods, Transient and Unsteady Heat Transfer. Associate Technical Editor: Y. Bayazitoglu.

Such a problem is encountered in the mathematical modeling of several physical processes, involving different forms of the reaction function $g(T)$.

The *direct problem* defined above by Eqs. (1) is concerned with the determination of the temperature distribution $T(x, t)$ in the medium, when the volumetric heat capacity $C(T)$, the thermal conductivity $k(T)$, the boundary and initial conditions, and the reaction function $g(T)$ are known.

The Inverse Problem. For the *inverse problem*, the reaction function $g(T)$ is regarded as unknown but everything else in Eqs. (1) is known. In addition, temperature data are considered available at some appropriate locations within the medium at various time steps.

The inverse analysis utilizing the conjugate gradient method requires the solution of the direct, sensitivity, and adjoint problems, together with the gradient equation. The development of sensitivity and adjoint problems are discussed next.

The Sensitivity Problem. The solution of the direct problem (1) with reaction function $g(T)$ unknown, can be recast as a problem of optimum control, that is, choose the control function $g(T)$ such that the following functional is minimized:

$$J[g(T)] \equiv \frac{1}{2}\int_{t=0}^{t_f}\sum_{m=1}^{M}\{T[x_m, t; g(T)] - Y_m(t)\}^2 dt \qquad (2)$$

where $Y_m(t)$ and $T[x_m, t; g(T)]$ are the measured and estimated temperatures, respectively, at a location x_m in the medium. If an estimate is available for $g(T)$, the temperature $T[x_m, t; g(T)]$ can be computed from the solution of the direct problem given by Eqs. (1).

In order to develop the sensitivity problem, we assume that the reaction function $g(T)$ is perturbed by an amount $\varepsilon\Delta g(T)$. Then, the temperature $T(x, t)$ undergoes a variation $\varepsilon\Delta T(x, t)$ and due to the nonlinear character of the problem, this perturbation on temperature causes variations on the temperature-dependent physical properties, as well as on the reaction function. The sensitivity problem is obtained by applying the following limiting process (Jarny et al., 1991):

$$\lim_{\varepsilon\to 0}\frac{\mathscr{L}_\varepsilon(T_\varepsilon) - \mathscr{L}(T)}{\varepsilon} = 0 \qquad (3)$$

where $\mathscr{L}_\varepsilon(T_\varepsilon)$ and $\mathscr{L}(T)$ are the operator forms of the direct problem given by Eqs. (1), for the perturbed and unperturbed quantities, respectively. After some manipulations, the following sensitivity problem results for the determination of the sensitivity function $\Delta T(x, t)$ (Orlande and Özişik, 1993):

$$\frac{\partial(C\Delta T)}{\partial t} - \frac{\partial^2(k\Delta T)}{\partial x^2} - \frac{dg}{dT}\Delta T - \Delta g = 0$$

$$\text{in } 0 < x < L; \text{ for } t > 0 \qquad (4a)$$

$$\frac{\partial(k\Delta T)}{\partial x} = 0 \quad \text{at } x = 0; \text{ for } t > 0 \qquad (4b)$$

$$\frac{\partial(k\Delta T)}{\partial x} = 0 \quad \text{at } x = L; \text{ for } t > 0 \qquad (4c)$$

$$\Delta T(x, 0) = 0 \quad \text{for } t = 0; \text{ in } 0 < x < L \qquad (4d)$$

where $C \equiv C(T)$, $k \equiv k(T)$, $\Delta T \equiv \Delta T(x, t)$, $g \equiv g(T)$, and $\Delta g \equiv \Delta g(T)$.

The Adjoint Problem and the Gradient Equation. To derive the adjoint problem and the gradient equation, we multiply Eq. (1*a*) by the Lagrange multiplier $\lambda(x, t)$ and integrate over the time and space domains. The resulting expression is then added to the functional given by Eq. (2) to obtain

$$J[g(T)] = \frac{1}{2}\int_{x=0}^{L}\int_{t=0}^{t_f}\sum_{m=1}^{M}(T - Y)^2\delta(x - x_m)dtdx + \int_{x=0}^{L}\int_{t=0}^{t_f}\left\{C(T)\frac{\partial T}{\partial t} - \frac{\partial}{\partial x}\left[k(T)\frac{\partial T}{\partial x}\right] - g(T)\right\} \times \lambda(x, t)dtdx \qquad (5)$$

where $\delta(\bullet)$ is the Dirac delta function.

By allowing the directional derivative of the functional given by Eq. (5) to go to zero, the following adjoint problem:

$$-C\frac{\partial\lambda}{\partial t} - k\frac{\partial^2\lambda}{\partial x^2} - \frac{dg}{dT}\lambda + \sum_{m=1}^{M}(T - Y)\delta(x - x_m) = 0$$

$$\text{in } 0 < x < L; \text{ for } t > 0 \qquad (6a)$$

$$\frac{\partial\lambda}{\partial x} = 0 \quad \text{at } x = 0; \text{ for } t > 0 \qquad (6b)$$

$$\frac{\partial\lambda}{\partial x} = 0 \quad \text{at } x = L; \text{ for } t > 0 \qquad (6c)$$

$$\lambda(x, t_f) = 0 \quad \text{for } t = t_f; \text{ in } 0 < x < L \qquad (6d)$$

and the following gradient equation:

$$J'[T, g(T)] = -\lambda(x, t) \qquad (7)$$

are obtained (Orlande and Özişik, 1993).

The Conjugate Gradient Method of Minimization. The iterative procedure for the determination of the reaction function is taken as (Jarny et al., 1991):

$$g^{p+1}(T) = g^p(T) - \beta^p d^p(T) \qquad (8)$$

and the direction of descent $d^p(T)$ is given by:

$$d^p(T) = J'[T, g^p(T)] + \gamma^p d^{p-1}(T) \qquad (9)$$

where the superscript p denotes the number of iterations and the conjugation coefficient γ^p is determined from (Lasdon et al., 1967):

$$\gamma^p = \frac{\int_{x=0}^{L}\int_{t=0}^{t_f}\{J'[T; g^p(T)]\}^2 dtdx}{\int_{x=0}^{L}\int_{t=0}^{t_f}\{J'[T; g^{p-1}(T)]\}^2 dtdx}$$

$$\text{for } p = 1, 2, \ldots \quad \text{with } \gamma^0 = 0 \qquad (10)$$

The coefficient β^p, which determines the step size in going from iteration p to $p + 1$ in Eq. (8), is obtained by minimizing $J[g^{p+1}(T)]$ given by Eq. (2) with respect to β^p. The following expression results:

$$\beta^p = \frac{\int_{t=0}^{t_f}\sum_{m=1}^{M}[T(x_m, t; g^p) - Y_m(t)]\Delta T(x_m, t; d^p)dt}{\int_{t=0}^{t_f}\sum_{m=1}^{M}[\Delta T(x_m, t; d^p)]^2 dt} \qquad (11)$$

where $\Delta T(x_m, t; d^p)$ is the solution of the sensitivity problem at position x_m and time t, which is obtained from Eqs. (4) by setting $\Delta g(T) = d^p(T)$.

Once $d^p(T)$ is computed from Eq. (9) and β^p from Eq. (11), the iterative process defined by Eq. (8) can be applied to determine $g^{p+1}(T)$, until a specified stopping criterion based on the discrepancy principle is satisfied (Orlande and Özişik, 1993).

The Computational Algorithm. The algorithm for the iterative scheme given by the conjugate gradient method is summarized below.

Suppose $g^p(T)$ is available at iteration p, then:

Step 1. Solve the direct problem given by Eqs. (1) to obtain $T(x, t)$;
Step 2. Check the stopping criterion. Continue if not satisfied;
Step 3. Solve the adjoint problem given by Eqs. (6) to obtain $\lambda(x, t)$;
Step 4. Compute the gradient of the functional from Eq. (7);
Step 5. Knowing $J'[T, g^p(T)]$, compute first the conjugation coefficient from Eq. (10) and then the direction of descent from Eq. (9);
Step 6. Solve the sensitivity problem given by Eqs. (4) by setting $\Delta g(T) = d^p(T)$, to determine $\Delta T(x, t)$;
Step 7. Compute the search step size β^p from Eq. (11);
Step 8. Knowing β^p and $d^p(T)$, compute the new estimate $g^{p+1}(T)$ from Eq. (8) and go to step 1.

Results and Discussion

In order to examine the accuracy of the function estimation approach using the conjugate gradient method as applied to the analysis of the inverse problem previously described, we studied test cases by using simulated measured temperatures as the input data for the inverse analysis. The simulated temperature data were generated by solving the direct problem for a specified reaction function. The temperatures calculated in this manner were considered exact measurements, T_{ex}, and the simulated measured temperature data, Y, containing measurement errors, were determined as

$$Y = T_{ex} + \alpha\sigma \tag{12}$$

where $\alpha\sigma$ is the error term and σ is the standard deviation of the measurements. For normally distributed errors, with zero mean and a 99 percent confidence level, α lies within the range

$$-2.576 < \alpha < 2.576 \tag{13}$$

The values of α were randomly determined with the subroutine DRNNOR from the IMSL (1987).

To generate the simulated measurements, the direct problem given by Eqs. (1) was expressed in dimensionless form by taking the coefficients $k(T)$ and $C(T)$ as

$$k(T) = k_0(1 + k_1T); \tag{14a}$$

$$C(T) = C_0(1 + C_1T) \tag{14b}$$

and by introducing the following dimensionless variables:

$$\theta = \frac{T - T_0}{\left(\frac{\phi_L}{k_0}\right)L}; \tag{15a}$$

$$\Gamma = \frac{g(T)L}{\phi_L}; \tag{15b}$$

$$\tau = \frac{k_0 t}{L^2 C_0}; \tag{15c}$$

$$\eta = \frac{x}{L}; \tag{15d}$$

$$\Phi = \frac{q}{\phi_L} \tag{15e}$$

where k_0, k_1, C_0, and C_1 are constants, T_0 is the initial temperature in the medium, which is assumed to be uniform, and ϕ_L is the heat flux applied at the boundary $x = L$, which is assumed to be constant.

The direct, sensitivity, and adjoint problems were solved by using the combined method of finite differences with 51 mesh points, 100 time steps, and $\theta = 2/3$. These values were chosen by comparing the numerical solution of the direct problem with a known analytic solution. The agreement between the two solutions was better than 1 percent.

The accuracy of the present method of inverse analysis was verified under strict conditions by using a single sensor in the region and by considering reaction functions with exponential behavior, sharp corners, and discontinuities.

Numerical experiments were made in order to estimate the optimum sensor position, which corresponds to the smallest rms error. The rms error is defined here as

$$e_{\text{rms}} = \sqrt{\frac{1}{P}\sum_{i=1}^{P}[g_{ex}(T_i) - g_{est}(T_i)]^2} \tag{16}$$

where the subscripts *ex* and *est* denote "exact" and "estimated" quantities, respectively, and $P = 100$ denotes the number of temperature measurements used in the inverse analysis. Generally, the optimum sensor position was in the left half of the medium (i.e., $0 < \eta < 0.5$) and the results obtained with sensors located at $\eta > 0.5$ were not in good agreement with the exact solution.

For all test cases analyzed here, we considered $k_1 = C_1 = 0$, $\sigma = 0$ (errorless measurements) and $\sigma = 0.01\theta_{\max}$, where $\theta_{\max}$ is the maximum temperature measured by the sensor. The duration of the simulated experiments was taken as $\tau = 1$. The initial guess used was the exact value of the reaction function at the final temperature measured by the sensor, so that the instabilities inherent in the conjugated gradient method at the final temperature could be avoided.

Figure 1 shows the results for an exponential variation of the dimensionless reaction function. The agreement between estimated and exact reaction functions is excellent, for both situations of errorless and inexact measurements, and such was the case for other smooth functional forms tested. The optimum sensor position for this case was at $\eta = 0.2$ and the rms error for $\sigma = 0.01\theta_{\max}$ was 0.1047.

Figure 2 shows similar results for a reaction function with a triangular variation. A comparison of the exact reaction function with the one estimated by using errorless measurements ($\sigma = 0$) indicates that the present function estimation approach can resolve sharp corners, although some smoothing is noticed at the corner at $\theta = 1$. The agreement between the exact solution and the results obtained by using measurements with random errors is good. The optimum sensor position for this case was at $\eta = 0.2$ and the rms error for $\sigma = 0.01\theta_{\max}$ was 0.0885.

Figure 3 presents the results obtained for a step variation of the reaction function. The curve obtained with errorless measurements ($\sigma = 0$) is in good agreement with the exact solution, although some oscillations are observed near the discontinuities. The results obtained by using measurements with random errors are also in good agreement with the exact functional form of the reaction function. The optimum sensor position for this case was at $\eta = 0.3$ and the rms error for $\sigma = 0.01\theta_{\max}$ was 0.2097.

Acknowledgments

The CPU time for this work has been provided by the North Carolina Supercomputing Center. One of the authors (H.R.B.O.) would like to acknowledge the support provided by CNPQ, an agency of the Brazilian government.

References

Artyukhin, E. A., and Nenarokomov, A. V., 1987, "Coefficient Inverse Heat-Conduction Problem," *J. Engr. Phys.*, Vol. 53, pp. 1085–1090.

IMSL Library Edition 10.0, 1987, *User's Manual Math Library*, Houston, TX.

Jarny, Y., Delaunay, D., and Bransier, J., 1986, "Identification of Nonlinear Thermal Properties by an Output Least Square Method," *Proceedings, 8th International Heat Transfer Conference*, pp. 1811–1816.

Jarny, Y., Özişik, M. N., and Bardon, J. P., 1991, "A General Optimization Method Using Adjoint Equation for Solving Multidimensional Inverse Heat Conduction," *Int. J. Heat Mass Transfer*, Vol. 34, pp. 2911–2929.

Joseph, D. D., and Sparrow, E. M., 1970, "Nonlinear Diffusion Induced by Nonlinear Sources," *Quart. Appl. Math*, pp. 327–342.

Kamenetskii, D. A. F., 1969, *Diffusion and Heat Transfer in Chemical Kinetics*, Plenum Press, New York.

Lasdon, L. S., Mitter, S. K., and Warren, A. D., 1967, "The Conjugate Gradient Method for Optimal Control Problem," *IEEE Trans. Automatic Control*, Vol. 12, pp. 123–138.

Orlande, H. R. B., and Özişik, M. N., 1993, "Determination of the Reaction Function in a Reaction-Diffusion Parabolic Problem," *Proceedings, 1st International Conference on Inverse Problems in Engineering: Theory and Practice*, in press.

Convection in Heat-Generating Porous Media With Permeable Boundaries—Natural Ventilation of Grain Storage Bins

W. E. Stewart, Jr.,[1,3] L. Cai,[2,3] and L. A. Stickler[4]

Introduction

Several studies have centered around the cooling of stored agricultural crops, including Burton et al. (1955) for potatoes, Holman and Carter (1952) for soybeans, Schmidt (1955) for wheat, and Thompson et al. (1971) for corn. The similarities between the storage of grain and other agricultural products to heat-generating porous media has been recognized by several investigators. Beukema and Bruin (1982), Stewart and Dona (1988), and Dona and Stewart (1989) studied the effects of natural convection flows in heat-generating porous media as they relate to agricultural product storage. Stewart and Dona (1988) showed that multicellular flows occur within grain storage bins near the top of cylindrical bins as evidenced in experiments.

It is reasonable to expect that heat-generating porous media (bed of grain) in an upright cylinder with permeable boundaries may experience lower maximum and average temperatures due to buoyant, convective flows across the permeable boundaries, in comparison to a nonvented, totally enclosed, grain storage bin. Since a heat-generating porous medium generates natural convection flows, the addition of permeable boundaries on a grain storage bin may reduce media temperatures to near the values occurring in a forced flow, aerated storage bin (Stewart and Burns, 1992).

Numerical Model

Several previous studies have shown the effects of Brinkman's extension and Forschheimer's formulation of Darcy's equations for flow in porous media. The effects of inertia and variable fluid thermophysical properties on maximum and average bed temperatures were shown by Stewart and Dona (1988) and Dona and Stewart (1989) for an upright cylinder. This study employs the modified Darcy's equation using Forchheimer's formulation (Irmay, 1958).

For the physical situation of an upright, short circular cylinder the dimensionless governing energy equation for two-dimensional flow in the r and z directions using Forchheimer's formulation of the momentum equations for porous media (also see Stewart and Dona, 1988, for nomenclature), for

$$\sigma \frac{\partial \theta}{\partial t} + \frac{1}{r}\frac{\partial \psi}{\partial z}\frac{\partial \theta}{\partial r} - \frac{1}{r}\frac{\partial \psi}{\partial r}\frac{\partial \theta}{\partial z} = \frac{1}{r}\frac{\partial}{\partial r}\left(r\frac{\partial \theta}{\partial r}\right) + \frac{\partial^2 \theta}{\partial z^2} + \frac{R}{H} \quad (1)$$

for constant properties, except for the temperature-dependent variables of c_p and μ, where θ and ψ are the dimensionless temperature and stream function, respectively. The continuity equation is satisfied by using the stream function. Taking cross derivatives of the momentum equations and substituting the stream function results in the single dimensionless momentum equation

$$\left(1 + \frac{n}{m}\frac{\alpha}{R}V_T\right)\left(\frac{1}{r^2}\frac{\partial \psi}{\partial r} - \frac{1}{r}\frac{\partial^2 \psi}{\partial r^2} - \frac{1}{r}\frac{\partial^2 \psi}{\partial z^2}\right) - \frac{n}{m}\frac{\alpha}{R}\frac{1}{V_T} \times \left(\frac{1}{r}\frac{\partial \psi}{\partial r}\right)\left[\left(\frac{1}{r}\frac{\partial \psi}{\partial z}\right)\left(\frac{1}{r}\frac{\partial^2 \psi}{\partial z \partial r} - \frac{1}{r^2}\frac{\partial \psi}{\partial z}\right) - \left(\frac{\partial \psi}{r^2 \partial r} - \frac{1}{r}\frac{\partial^2 \psi}{\partial r^2}\right)\frac{1}{r}\frac{\partial \psi}{\partial r}\right] - \frac{n}{m}\frac{\alpha}{R}\frac{1}{V_T}\frac{1}{r}\frac{\partial \psi}{\partial z} \times \left(\frac{1}{r}\frac{\partial \psi}{\partial z}\frac{1}{r}\frac{\partial^2 \psi}{\partial z^2} + \frac{1}{r}\frac{\partial \psi}{\partial r}\frac{1}{r}\frac{\partial^2 \psi}{\partial z \partial r}\right) = \mathrm{Ra}\frac{\partial \theta}{\partial r} \quad (2)$$

where Ra is a modified Rayleigh number, which varies with temperature. Equations (1) and (2) were used to solve for streamline and isotherm distributions for several sets of boundary conditions, as described below for Models 1–5. The equations were solved using an upwinding explicit transient finite differencing scheme.

The size of the uniform finite difference mesh was determined by increasing the grid refinement until there were no significant changes, less than 1 percent, in the results for ψ and θ. The resultant mesh was 31 by 61 in the r and z directions, respectively. The time step was gradually decreased until the results did not change significantly, less than 1 percent. The dimensionless time step used was 0.001, which corresponds to a real time step of approximately 30 seconds.

The amount of heat generated was compared to the amount of heat lost by conduction at the impermeable boundaries and the net convective flux at the permeable boundaries. The heat loss calculated was within 1 percent of the heat generated, at steady-state conditions. The steady-state convergence criterion was set as a change of 10^{-8} or less for both θ and ψ in succeeding time steps. The use of Darcy's formulation instead of Forchheimer's formulation of the momentum equations resulted in heat balance differences greater than 2 percent.

Physical Models

The simulations were performed for a shelled corn and air porous media system, with a porosity of 0.43. A single wall boundary temperature and inlet air temperature of 15.5°C was considered. Uniform heat-generating rates of 10 W/m^3 and 20.3 W/m^3, approximating 10 and 20 percent moisture corn, respectively, were modeled. A single grain bin size of outside radius of 2 m and height of 4 m was modeled.

Model 1 is a cylinder totally enclosed, with isothermal cylinder wall and top surface at T_∞, and an adiabatic bottom surface. Model 2 is similar to Model 1 except for forced ventilation, with permeable upper (as ventilated or partially filled bin) and lower surfaces, as with bins with forced convection fan equipment, using two different specified air velocities. Model 3 is for both upper and lower permeable boundaries, as in Model 2, but without forced flow. Model 4 is as Model 3 except upper boundary is impermeable as to simulate a full grain bin, permeable inner cylinder (allowing ambient air to enter the lower boundary and exit through the permeable inner cylinder), inner cylinder radius R_0 of 0.05 R, 0.1 R, 0.15 R, and 0.2 R. Model 5 is as Model 4 except with an upper permeable boundary.

[1] Professor.

[2] Graduate Research Assistant.

[3] Energy Research Laboratory, 105 Engineering Building, University of Missouri—Kansas City, 5605 Troost, Kansas City, MO 64110.

[4] InterMountain Research, Olathe, KS 66062.

Contributed by the Heat Transfer Division of THE AMERICAN SOCIETY OF MECHANICAL ENGINEERS. Manuscript received by the Heat Transfer Division July 1992; revision received May 1994. Keywords: Natural Convection, Packed and Fluidized Beds, Porous Media. Associate Technical Editor: C. E. Hickox, Jr.

Kamenetskii, D. A. F., 1969, *Diffusion and Heat Transfer in Chemical Kinetics*, Plenum Press, New York.

Lasdon, L. S., Mitter, S. K., and Warren, A. D., 1967, "The Conjugate Gradient Method for Optimal Control Problem," *IEEE Trans. Automatic Control*, Vol. 12, pp. 123–138.

Orlande, H. R. B., and Özişik, M. N., 1993, "Determination of the Reaction Function in a Reaction-Diffusion Parabolic Problem," *Proceedings, 1st International Conference on Inverse Problems in Engineering: Theory and Practice*, in press.

Convection in Heat-Generating Porous Media With Permeable Boundaries—Natural Ventilation of Grain Storage Bins

W. E. Stewart, Jr.,[1,3] L. Cai,[2,3] and L. A. Stickler[4]

Introduction

Several studies have centered around the cooling of stored agricultural crops, including Burton et al. (1955) for potatoes, Holman and Carter (1952) for soybeans, Schmidt (1955) for wheat, and Thompson et al. (1971) for corn. The similarities between the storage of grain and other agricultural products to heat-generating porous media has been recognized by several investigators. Beukema and Bruin (1982), Stewart and Dona (1988), and Dona and Stewart (1989) studied the effects of natural convection flows in heat-generating porous media as they relate to agricultural product storage. Stewart and Dona (1988) showed that multicellular flows occur within grain storage bins near the top of cylindrical bins as evidenced in experiments.

It is reasonable to expect that heat-generating porous media (bed of grain) in an upright cylinder with permeable boundaries may experience lower maximum and average temperatures due to buoyant, convective flows across the permeable boundaries, in comparison to a nonvented, totally enclosed, grain storage bin. Since a heat-generating porous medium generates natural convection flows, the addition of permeable boundaries on a grain storage bin may reduce media temperatures to near the values occurring in a forced flow, aerated storage bin (Stewart and Burns, 1992).

Numerical Model

Several previous studies have shown the effects of Brinkman's extension and Forschheimer's formulation of Darcy's equations for flow in porous media. The effects of inertia and variable fluid thermophysical properties on maximum and average bed temperatures were shown by Stewart and Dona (1988) and Dona and Stewart (1989) for an upright cylinder. This study employs the modified Darcy's equation using Forchheimer's formulation (Irmay, 1958).

For the physical situation of an upright, short circular cylinder the dimensionless governing energy equation for two-dimensional flow in the r and z directions using Forchheimer's formulation of the momentum equations for porous media (also see Stewart and Dona, 1988, for nomenclature), for

$$\sigma \frac{\partial \theta}{\partial t} + \frac{1}{r}\frac{\partial \psi}{\partial z}\frac{\partial \theta}{\partial r} - \frac{1}{r}\frac{\partial \psi}{\partial r}\frac{\partial \theta}{\partial z} = \frac{1}{r}\frac{\partial}{\partial r}\left(r\frac{\partial \theta}{\partial r}\right) + \frac{\partial^2 \theta}{\partial z^2} + \frac{R}{H} \quad (1)$$

for constant properties, except for the temperature-dependent variables of c_p and μ, where θ and ψ are the dimensionless temperature and stream function, respectively. The continuity equation is satisfied by using the stream function. Taking cross derivatives of the momentum equations and substituting the stream function results in the single dimensionless momentum equation

$$\left(1 + \frac{n}{m}\frac{\alpha}{R}V_T\right)\left(\frac{1}{r^2}\frac{\partial \psi}{\partial r} - \frac{1}{r}\frac{\partial^2 \psi}{\partial r^2} - \frac{1}{r}\frac{\partial^2 \psi}{\partial z^2}\right) - \frac{n}{m}\frac{\alpha}{R}\frac{1}{V_T} \times \left(\frac{1}{r}\frac{\partial \psi}{\partial r}\right)\left[\left(\frac{1}{r}\frac{\partial \psi}{\partial z}\right)\left(\frac{1}{r}\frac{\partial^2 \psi}{\partial z \partial r} - \frac{1}{r^2}\frac{\partial \psi}{\partial z}\right) - \left(\frac{\partial \psi}{r^2 \partial r} - \frac{1}{r}\frac{\partial^2 \psi}{\partial r^2}\right)\frac{1}{r}\frac{\partial \psi}{\partial r}\right] - \frac{n}{m}\frac{\alpha}{R}\frac{1}{V_T}\frac{1}{r}\frac{\partial \psi}{\partial z} \times \left(\frac{1}{r}\frac{\partial \psi}{\partial z}\frac{1}{r}\frac{\partial^2 \psi}{\partial z^2} + \frac{1}{r}\frac{\partial \psi}{\partial r}\frac{1}{r}\frac{\partial^2 \psi}{\partial z \partial r}\right) = \mathrm{Ra}\frac{\partial \theta}{\partial r} \quad (2)$$

where Ra is a modified Rayleigh number, which varies with temperature. Equations (1) and (2) were used to solve for streamline and isotherm distributions for several sets of boundary conditions, as described below for Models 1–5. The equations were solved using an upwinding explicit transient finite differencing scheme.

The size of the uniform finite difference mesh was determined by increasing the grid refinement until there were no significant changes, less than 1 percent, in the results for ψ and θ. The resultant mesh was 31 by 61 in the r and z directions, respectively. The time step was gradually decreased until the results did not change significantly, less than 1 percent. The dimensionless time step used was 0.001, which corresponds to a real time step of approximately 30 seconds.

The amount of heat generated was compared to the amount of heat lost by conduction at the impermeable boundaries and the net convective flux at the permeable boundaries. The heat loss calculated was within 1 percent of the heat generated, at steady-state conditions. The steady-state convergence criterion was set as a change of 10^{-8} or less for both θ and ψ in succeeding time steps. The use of Darcy's formulation instead of Forchheimer's formulation of the momentum equations resulted in heat balance differences greater than 2 percent.

Physical Models

The simulations were performed for a shelled corn and air porous media system, with a porosity of 0.43. A single wall boundary temperature and inlet air temperature of 15.5°C was considered. Uniform heat-generating rates of 10 W/m^3 and 20.3 W/m^3, approximating 10 and 20 percent moisture corn, respectively, were modeled. A single grain bin size of outside radius of 2 m and height of 4 m was modeled.

Model 1 is a cylinder totally enclosed, with isothermal cylinder wall and top surface at T_∞, and an adiabatic bottom surface. Model 2 is similar to Model 1 except for forced ventilation, with permeable upper (as ventilated or partially filled bin) and lower surfaces, as with bins with forced convection fan equipment, using two different specified air velocities. Model 3 is for both upper and lower permeable boundaries, as in Model 2, but without forced flow. Model 4 is as Model 3 except upper boundary is impermeable as to simulate a full grain bin, permeable inner cylinder (allowing ambient air to enter the lower boundary and exit through the permeable inner cylinder), inner cylinder radius R_0 of 0.05 R, 0.1 R, 0.15 R, and 0.2 R. Model 5 is as Model 4 except with an upper permeable boundary.

[1] Professor.

[2] Graduate Research Assistant.

[3] Energy Research Laboratory, 105 Engineering Building, University of Missouri—Kansas City, 5605 Troost, Kansas City, MO 64110.

[4] InterMountain Research, Olathe, KS 66062.

Contributed by the Heat Transfer Division of THE AMERICAN SOCIETY OF MECHANICAL ENGINEERS. Manuscript received by the Heat Transfer Division July 1992; revision received May 1994. Keywords: Natural Convection, Packed and Fluidized Beds, Porous Media. Associate Technical Editor: C. E. Hickox, Jr.

Results and Discussion

The transient solution was used to determine the total dimensional time to reach steady state. The stream function solution tended to converge much more slowly than the temperature. The temperature results for Model 1 are similar to the previous results of Stewart and Dona (1988), revealing a relatively high maximum bed temperature, since the cylinder containing the heat-generating porous media is entirely enclosed with impermeable boundaries. The maximum and average temperature results of 323 K and 363 K at 20.3 W/m^3 and 307.5 K and 330 K at 10 W/m^3, respectively, for Model 1 form the basis of comparison to all the other models, which have at least one permeable boundary.

The simulations performed for Model 2 represent the situation of a typical grain storage bin with a permeable lower deck and top surface, with fan equipment used for forced ventilation. The isotherm and stream function results for Model 2 for a heat generation rate of 10 W/m^3 for uniform inflow velocity of 0.1 m/s on the lower boundary show a straight, vertical stream function as expected. The inflow of air at 15.5°C represents a uniform ventilating flow, which produces a horizontally stratified temperature distribution except near the wall where the wall temperature is at a cooler isothermal temperature (15.5°C). The maximum and average temperatures are only one to two degrees higher than the inflow air temperature for the higher air velocity (0.1 m/s) and the lower heat generation rate (10 W/m^3) modeled. At the highest heat generation rate and lowest inflow air velocity, the maximum temperature for Model 2 exceeds the ambient temperature by more than 5°C, although the average grain bed temperature is less than 2°C greater than the inflow air temperature.

Model 3 simulates a naturally ventilated version of Models 1 and 2. For the lowest heat generation rate, the air flow patterns (stream function results), shown in Fig. 1, are a result of the buoyancy-driven convection due to the internal heat generation. The streamline results in Fig. 1 show that the cooler, ambient air enters from both the upper and lower permeable surfaces. Near the outer cylinder wall ($r \sim 1$), the ambient air enters from the top permeable surface, moves downward along the cylinder wall, and continues this path by exiting through the lower permeable surface (ψ = 0.8 and 0.9). For ψ of 0.7 or less, the cooler air enters then from the top of the cylinder near r of 0.8. As the air flows through the grain bed, it is heated and reverses in direction, exiting through the permeable upper surface between r of about 0.3 and 0.75. For ψ of 0.8 and greater, the cooling air enters through the bottom permeable surface and exits through the upper permeable surface.

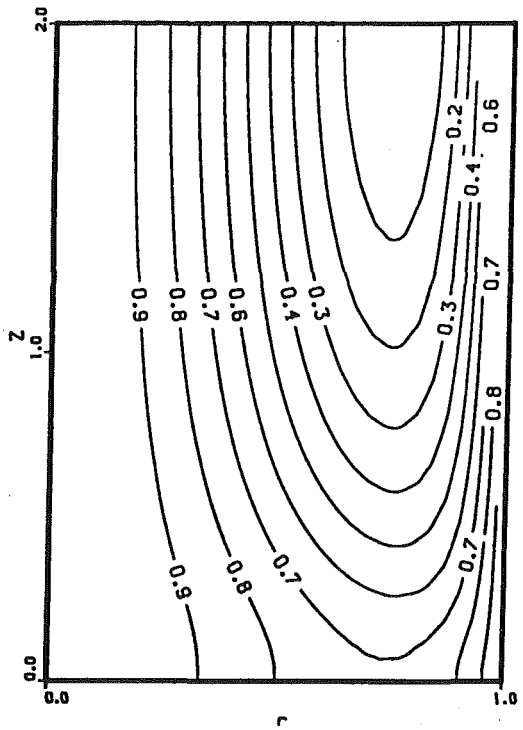

Fig. 1 Steady-state streamline results for Model 3 with $\dot{q}'''$ of 10 W/m^3

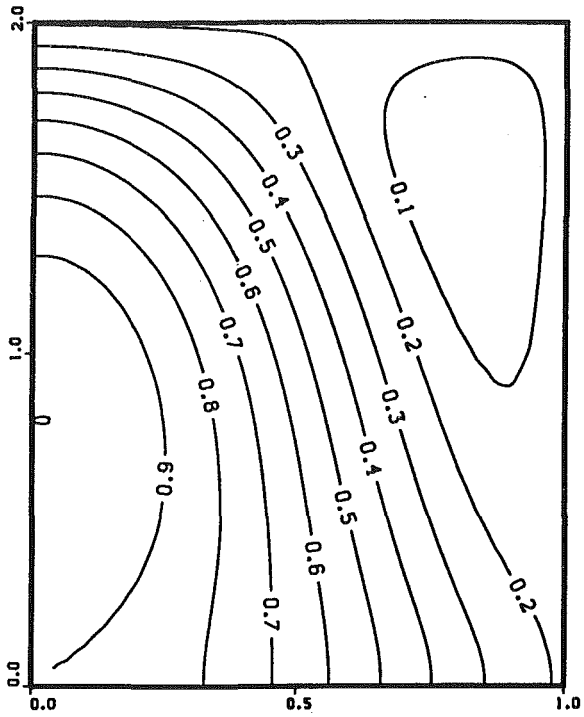

Fig. 2 Steady-state streamline results for Model 4 with $\dot{q}'''$ of 10 W/m^3 and R_0/R of 0.2

The maximum and average temperatures for Model 3 increase significantly over the forced ventilation case and are only slightly less than the completely enclosed bin of Model 1. At steady-state conditions the maximum temperature is 40°C greater than the ambient temperature, T_∞, for the lower heat generation rate of 10 W/m^3.

Model 4 simulates a bin that is completely full with a permeable annulus of radius R_0. The dimensionless stream function results are shown in Fig. 2 for $\dot{q}'''$ of 10 W/m^3 and R_0/R of 0.2, which yields the lowest maximum and average temperatures, 306 K and 297 K, respectively. The reduction in storage bin volume is only 4 percent with the annulus, but the reduction in maximum temperature compared to Model 3 is almost 23°C, from 329 K to 306 K.

Decreasing the inner radius to r_0 of 0.1 (R_0/R = 0.1) for Model 5, with an annulus and permeable upper boundary, increases the maximum temperature about 3.7°C and the average temperature about 1.2°C above the temperature results for r_0 of 0.2 in Model 4. The inner radius ratio of 0.1 only decreases the total storage volume by 1 percent. The stream function results are shown in Fig. 3 for the conditions $\dot{q}'''$ of 10 W/m^3 and R_0/R of 0.2. The maximum temperature for Model 5 is less than 17°C above ambient, about 1°C less than for Model 4. The average temperature is less than 8°C above the ambient temperature, just slightly less than for Model 4, showing the greater effect of the permeable annulus than the permeable upper boundary. Even though the recirculation zone of Model 4 is eliminated in Model 5, the maximum bed temperature is not reduced significantly. The maximum temperature within the grain bed for Model 5 of 17°C above ambient, compared to 1°C or less for Model 2 for forced ventilation, may be acceptable in practice.

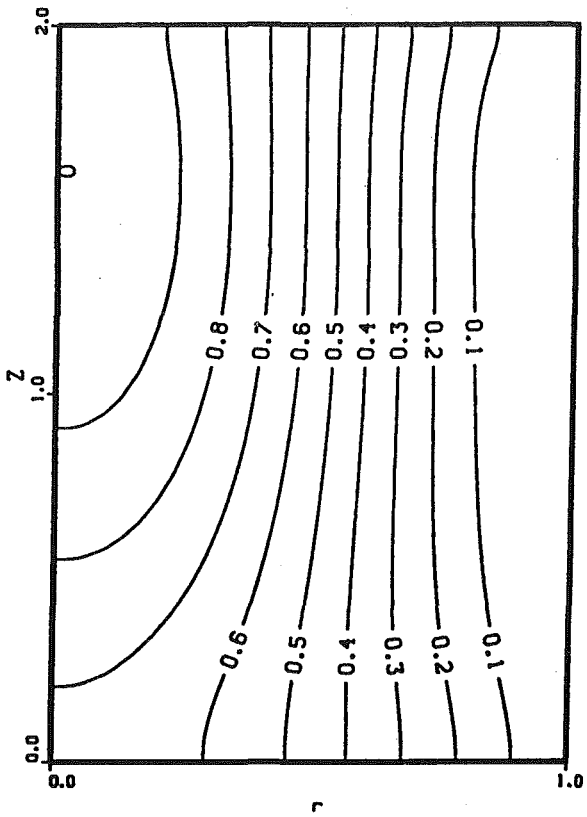

Fig. 3 Steady-state streamline results for Model 5 with $\dot{q}'''$ of 10 W/m^3 and R_0/R of 0.2

Conclusions

Two new storage bin designs using a permeable annulus along the centerline of the bin were modeled. Maximum and average bed temperatures can approach within 8°C of the ambient air temperature for a heat generation rate of 10 W/m^3 and ambient air temperatures of 15.5°C. The new design could eliminate the need for forced ventilation equipment and the associated equipment and energy use costs. Multiple permeable annuli may provide for additional bed temperature reduction.

References

Beukema, K. J., and Bruin, S., 1982, "Heat and Mass Transfer During Cooling and Storage of Agricultural Products," *Chemical Engineering Science,* Vol. 37, No. 2, pp. 291–298.

Burton, W. G., Mann, G., and Wager, H. G., 1955, "The Storage of Ware Potatoes in Permanent Buildings. II. The Temperature of Unventilated Stacks of Potatoes," *Journal of Agricultural Science,* Vol. 46, pp. 150–163.

Dona, C. L. G., and Stewart, W. E., Jr., 1989, "Density and Viscosity Effects in a Heat-Generating Porous Medium," ASME JOURNAL OF HEAT TRANSFER, Vol. III, pp. 1100–1102.

Holman, L. E., and Carter, D. G., 1952, "Soybean Storage in Farm Type Bins," *Illinois Agricultural Experiment Station Bulletin 553,* pp. 451–495.

Irmay, S., 1958, "On the Theoretical Derivation of Darcy and Forchheimer Formulae," *Transactions of the American Geophysical Union,* Vol. 39, pp. 702–706.

Patterson, R. J., Bakker-Arkema, F. W., and Bickert, W. G., 1971, "Static Pressure Airflow Relationships in Packed Beds of Granular Biological Materials Such as Grain—II," *Transactions of the American Society of Agricultural Engineering,* Vol. 14, pp. 172–174, 178.

Schmidt, J. L., 1955, "Wheat Storage Research at Hutchinson, Kansas and Jamestown, North Dakota," USDA Technical Bulletin 1113, p. 98.

Stewart, W. E., Jr., and Dona, C. L. G., 1987, "Free Convection in a Heat Generating Porous Medium in a Finite Vertical Cylinder," *Proceedings ASME/JSME Thermal Engineering Joint Conference,* Honolulu, HI, Vol. II, pp. 353–358.

Stewart, W. E., Jr., and Dona, C. L. G., 1988, "Numerical Analysis of Natural Analysis of Natural Convection Heat Transfer in Stored High Moisture Corn," *Journal Agricultural Engineering Research,* Vol. 40, pp. 275–284.

Stewart, W. E., Jr., and Burns, A. S., 1992, "Convection in Heat Generating Porous Media in a Concentric Annulus With a Permeable Outer Boundary," *Int. Comm. Heat Mass Transfer,* Vol. 19, pp. 127–136.

Thompson, T. L., Villa, L. G., and Cross, O. E., 1971, "Simulated and Experimental Performance of Temperature Control System for Chilled High Moisture Grain Storage," *Transactions of the American Society of Agricultural Engineering,* pp. 554–559.

Laminar Film Condensation on a Horizontal Elliptical Tube With Variable Wall Temperature

Sheng-An Yang[1] and Cha'o-Kuang Chen[2]

Nomenclature

A = amplitude of the wall temperature variation
a, b = semimajor, semiminor axis of ellipse
C_p = specific heat of condensate at constant pressure
g = acceleration due to gravity
$h, \bar{h}$ = local, mean condensing heat transfer coefficient
h_{fg} = latent heat of condensation
h'_{fg} = modified latent heat of condensation described by Rohsenow (1956)
Ja = Jakob number = $C_p \overline{\Delta T}/h'_{fg}$
k = thermal conductivity of condensate
Nu, $\overline{\text{Nu}}$ = local, mean Nusselt number
Pr = Prandtl number
Ra = Rayleigh number = $\rho(\rho - \rho_v)g\text{Pr}\, D_e^3/\mu^2$
x = coordinate measuring length along circumference from top of tube
y = coordinate normal to the elliptical surface
δ^*, δ = nondimensional, local thickness of condensate film
θ = angle measured from top of tube
μ = absolute viscosity of condensate
ρ, ρ_v = density of condensate, vapor
ϕ = the angle between the tangent to tube surface and the normal to direction of gravity

1 Introduction

The problem of laminar-film condensation of pure vapors on surfaces of various forms, such as flat plates, spheres, circular and noncircular cylinders, and axisymmetric bodies, has been extensively studied since Nusselt (1916). Among these studies, Karimi (1977) used the Nusselt-Rohsenow (1956) model to analyze laminar film condensation on isothermal helical cylinders and related configurations, like circular cylinders, spheres, and elliptical cylinders, and obtained numerical solutions by using finite difference methods. Later, Wang et al. (1988) showed theoretically and experimentally that an elliptical tube did possess some advantages over a cylindrical one. However, they studied laminar film condensation on a horizontal elliptical tube with uniform wall temperature, and they miscalculated the mean condensation coefficient $\bar{h}$ for an ellipse using $\bar{h} = (1/\pi)\int_0^\pi h d\theta$ instead of taking an averaged value over the entire perimeter. For an elliptical tube, the radius

[1]Associate Professor, Department of Tool & Mold Engineering, National Kaohsiung Institute of Technology, Kaohsiung, Taiwan.

[2]Professor, Department of Mechanical Engineering, National Cheng-Kung University, Tainan, Taiwan.

Contributed by the Heat Transfer Division of THE AMERICAN SOCIETY OF MECHANICAL ENGINEERS. Manuscript received by the Heat Transfer Division March 1992; revision received May 1993. Keywords: Condensation, Natural Convection. Associate Technical Editor: L. C. Witte.

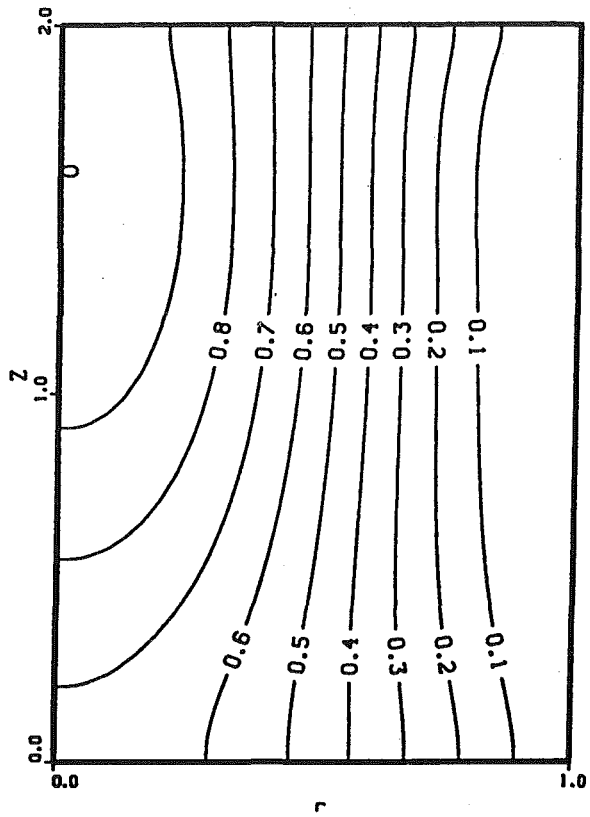

Fig. 3 Steady-state streamline results for Model 5 with $\dot{q}'''$ of 10 W/m^3 and R_0/R of 0.2

Conclusions

Two new storage bin designs using a permeable annulus along the centerline of the bin were modeled. Maximum and average bed temperatures can approach within 8°C of the ambient air temperature for a heat generation rate of 10 W/m^3 and ambient air temperatures of 15.5°C. The new design could eliminate the need for forced ventilation equipment and the associated equipment and energy use costs. Multiple permeable annuli may provide for additional bed temperature reduction.

References

Beukema, K. J., and Bruin, S., 1982, "Heat and Mass Transfer During Cooling and Storage of Agricultural Products," *Chemical Engineering Science,* Vol. 37, No. 2, pp. 291–298.

Burton, W. G., Mann, G., and Wager, H. G., 1955, "The Storage of Ware Potatoes in Permanent Buildings. II. The Temperature of Unventilated Stacks of Potatoes," *Journal of Agricultural Science,* Vol. 46, pp. 150–163.

Dona, C. L. G., and Stewart, W. E., Jr., 1989, "Density and Viscosity Effects in a Heat-Generating Porous Medium," ASME JOURNAL OF HEAT TRANSFER, Vol. III, pp. 1100–1102.

Holman, L. E., and Carter, D. G., 1952, "Soybean Storage in Farm Type Bins," *Illinois Agricultural Experiment Station Bulletin 553,* pp. 451–495.

Irmay, S., 1958, "On the Theoretical Derivation of Darcy and Forchheimer Formulae," *Transactions of the American Geophysical Union,* Vol. 39, pp. 702–706.

Patterson, R. J., Bakker-Arkema, F. W., and Bickert, W. G., 1971, "Static Pressure Airflow Relationships in Packed Beds of Granular Biological Materials Such as Grain—II," *Transactions of the American Society of Agricultural Engineering,* Vol. 14, pp. 172–174, 178.

Schmidt, J. L., 1955, "Wheat Storage Research at Hutchinson, Kansas and Jamestown, North Dakota," USDA Technical Bulletin 1113, p. 98.

Stewart, W. E., Jr., and Dona, C. L. G., 1987, "Free Convection in a Heat Generating Porous Medium in a Finite Vertical Cylinder," *Proceedings ASME/JSME Thermal Engineering Joint Conference,* Honolulu, HI, Vol. II, pp. 353–358.

Stewart, W. E., Jr., and Dona, C. L. G., 1988, "Numerical Analysis of Natural Analysis of Natural Convection Heat Transfer in Stored High Moisture Corn," *Journal Agricultural Engineering Research,* Vol. 40, pp. 275–284.

Stewart, W. E., Jr., and Burns, A. S., 1992, "Convection in Heat Generating Porous Media in a Concentric Annulus With a Permeable Outer Boundary," *Int. Comm. Heat Mass Transfer,* Vol. 19, pp. 127–136.

Thompson, T. L., Villa, L. G., and Cross, O. E., 1971, "Simulated and Experimental Performance of Temperature Control System for Chilled High Moisture Grain Storage," *Transactions of the American Society of Agricultural Engineering,* pp. 554–559.

Laminar Film Condensation on a Horizontal Elliptical Tube With Variable Wall Temperature

Sheng-An Yang[1] and Cha'o-Kuang Chen[2]

Nomenclature

A = amplitude of the wall temperature variation
a, b = semimajor, semiminor axis of ellipse
C_p = specific heat of condensate at constant pressure
g = acceleration due to gravity
$h, \bar{h}$ = local, mean condensing heat transfer coefficient
h_{fg} = latent heat of condensation
h'_{fg} = modified latent heat of condensation described by Rohsenow (1956)
Ja = Jakob number = $C_p \overline{\Delta T}/h'_{fg}$
k = thermal conductivity of condensate
Nu, $\overline{\text{Nu}}$ = local, mean Nusselt number
Pr = Prandtl number
Ra = Rayleigh number = $\rho(\rho - \rho_v)g\text{Pr}\, D_e^3/\mu^2$
x = coordinate measuring length along circumference from top of tube
y = coordinate normal to the elliptical surface
δ^*, δ = nondimensional, local thickness of condensate film
θ = angle measured from top of tube
μ = absolute viscosity of condensate
ρ, ρ_v = density of condensate, vapor
ϕ = the angle between the tangent to tube surface and the normal to direction of gravity

1 Introduction

The problem of laminar-film condensation of pure vapors on surfaces of various forms, such as flat plates, spheres, circular and noncircular cylinders, and axisymmetric bodies, has been extensively studied since Nusselt (1916). Among these studies, Karimi (1977) used the Nusselt-Rohsenow (1956) model to analyze laminar film condensation on isothermal helical cylinders and related configurations, like circular cylinders, spheres, and elliptical cylinders, and obtained numerical solutions by using finite difference methods. Later, Wang et al. (1988) showed theoretically and experimentally that an elliptical tube did possess some advantages over a cylindrical one. However, they studied laminar film condensation on a horizontal elliptical tube with uniform wall temperature, and they miscalculated the mean condensation coefficient $\bar{h}$ for an ellipse using $\bar{h} = (1/\pi)\int_0^\pi h d\theta$ instead of taking an averaged value over the entire perimeter. For an elliptical tube, the radius

[1]Associate Professor, Department of Tool & Mold Engineering, National Kaohsiung Institute of Technology, Kaohsiung, Taiwan.

[2]Professor, Department of Mechanical Engineering, National Cheng-Kung University, Tainan, Taiwan.

Contributed by the Heat Transfer Division of THE AMERICAN SOCIETY OF MECHANICAL ENGINEERS. Manuscript received by the Heat Transfer Division March 1992; revision received May 1993. Keywords: Condensation, Natural Convection. Associate Technical Editor: L. C. Witte.

of surface curvature is not a constant and cannot be omitted in evaluating $\bar{h}$.

The wall temperature T_w may often vary significantly over the circumferential length of the tube (Fujii et al., 1972), even if the coolant temperature inside the tube is constant. For film condensation on a circular tube with a variable wall temperature (a cosine distribution), Memory and Rose (1991) found that the local condensate film thickness and heat flux depend markedly on the amplitude of the surface temperature variation; however, the mean heat transfer coefficient is virtually unaffected by surface temperature variation. A circular tube is an elliptical tube of zero ellipticity, and a flat plate is an elliptical tube with ellipticity to one. Hence, the general case for an elliptical tube of any ellipticity under nonuniform wall temperature conditions is of major interest.

2 Analysis

Consider a horizontal elliptical tube, with major axis $2a$ in the direction of gravity and minor axis $2b$, situated in a quiescent, pure vapor, which is at its saturation temperature T_{sat}. The wall temperature T_w is nonuniform and below the saturation temperature. Thus, condensation occurs on the wall and a continuous film of the liquid runs downward over the tube under the influence of gravity.

The physical model under consideration is shown in Fig. 1, where the curvilinear coordinates (x, y) are aligned along the elliptical wall surface and its normal. For a laminar, steady-state condensate film with constant fluid properties, Nusselt's local mass flow rate is expressible in terms of the film thickness $\delta(x)$ without reference to the history of the film up to this location, as

$$\dot{m}=\frac{\rho(\rho-\rho_v)g\delta^3}{3\mu}\sin\phi \tag{1}$$

Since the temperature distribution in the condensate layer may be assumed linear in the Nusselt-Rohsenow condensation theory, one has

$$h'_{fg}\frac{d\dot{m}}{dx}=k\frac{T_{sat}-T_w}{\delta}=k\Delta T/\delta \tag{2}$$

where $h'_{fg}=h_{fg}+3C_p\Delta T/8$. In order to derive the local film thickness δ at the circumferential arc length x (or angle θ) in terms of ϕ, one can substitute Eq. (1) into Eq. (2) and obtain

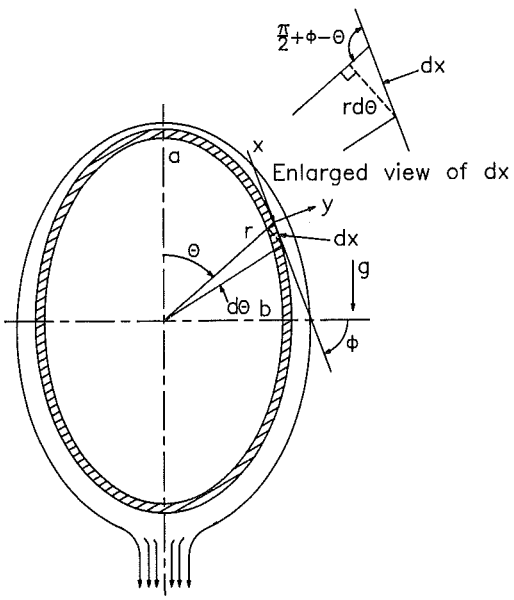

Fig. 1 Schematic and coordinate system for the condensate film flow on the elliptical surface

$$\frac{\rho(\rho-\rho_v)gh'_{fg}}{3\mu}\frac{d(\delta^3\sin\phi)}{dx}=\frac{k}{\delta}\Delta T \tag{3}$$

By using the properties of an ellipse, one may obtain the radial distance from the centroid of ellipse

$$r=a[(1-e^2)/(1-e^2\cos^2\theta)]^{0.5} \tag{4}$$

where $e=\sqrt{a^2-b^2}/a$ is the ellipticity. The differential arc length is

$$dx=\pi D_e ds/2 \tag{5}$$

where $s=\int_0^\phi(1-e^2\sin^2\phi)^{-3/2}d\phi/\int_0^\pi(1-e^2\sin^2\phi)^{-3/2}d\phi$ is the dimensionless streamwise length, and an equivalent diameter D_e is

$$D_e=2\frac{a}{\pi}\int_0^\pi\left[(1-e^2)/\sqrt{(1-e^2\sin^2\phi)^3}\right]d\phi. \tag{6}$$

Once the wall temperature distribution is specified or fitted by experimental data, one may calculate the mean wall temperature as

$$\overline{T_w}=\frac{2}{\pi}\frac{a}{D_e}\int_0^\pi T_w(\phi)\left[(1-e^2)/\sqrt{(1-e^2\sin^2\phi)^3}\right]d\phi \tag{7}$$

and express the temperature difference across the film as

$$T_{sat}-T_w=(T_{sat}-\overline{T_w})F_t(\phi)=\overline{\Delta T}F_t(\phi) \tag{8}$$

$F_t(\phi)$, the nonisothermality function, is the dimensionless temperature profile in the circumferential direction.

Substituting Eqs. (5)–(8) into Eq. (3), and introducing a transformation of variable from x to ϕ, one obtains the local dimensionless film thickness at ϕ as follows:

$$\delta^*=\delta\left[\frac{D_e k\mu\overline{\Delta T}}{h'_{fg}\rho(\rho-\rho_v)g}\right]^{-1/4}$$

$$=F(\phi)\left\{\frac{1}{\pi}\int_0^\pi\left[(1-e^2/\sqrt{(1-e^2\sin^2\phi)^3}\right]d\phi\right\}^{-1/4} \tag{9}$$

where

$$F(\phi)=(\sin\phi)^{-1/3}$$

$$\times\left\{2(1-e^2)\int_0^\phi F_t(\phi)(\sin\phi)^{1/3}(1-e^2\sin^2\phi)^{-3/2}d\phi\right\}^{1/4}.$$

The local heat flux q is given by

$$q=k\frac{\Delta T}{\delta} \tag{10}$$

then, with Eqs. (9) and (10), the dimensionless heat flux

$$q^*=q\left[\frac{\overline{\Delta T}^{-3}D_e}{\rho(\rho-\rho_v)g\,h'_{fg}}\frac{\mu}{k^3}\right]^{1/4} \tag{11}$$

is given by

$$q^*=F_t(\phi)/\delta^* \tag{12}$$

From Eqs. (10) and (12), the local heat transfer coefficient can be shown to be:

$$\mathrm{Nu}=\frac{hD_e}{k}=[\mathrm{Ra}/\mathrm{Ja}]^{1/4}/\delta^* \tag{13}$$

Next, we are interested in an expression for the mean heat transfer coefficient. Substituting Eq. (1) into Eq. (2) by canceling δ, and integrating gives

$$\dot{m}=\frac{1}{3}\left[\frac{64\,k^3a^3\overline{\Delta T}^3}{\mu(h'_{fg})^3}\rho(\rho-\rho_v)g\right]^{1/4}$$

$$\times\left\{(1-e^2)\int_0^\pi\frac{F_t(\phi)(\sin\phi)^{1/3}}{(1-e^2\sin^2\phi)^{3/2}}d\phi\right\}^{3/4} \tag{14}$$

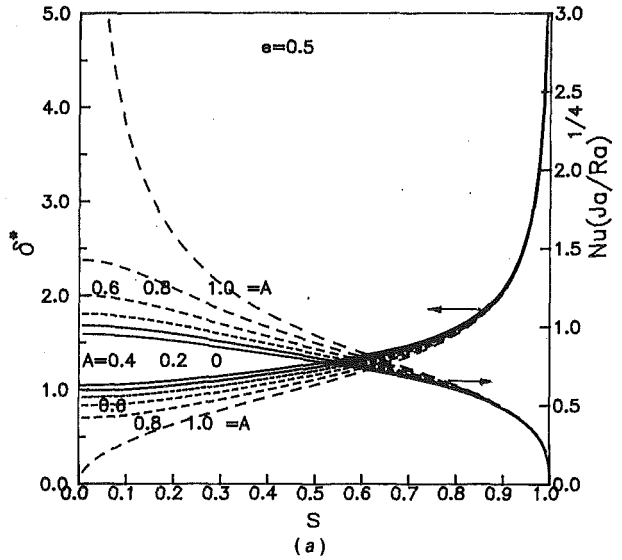

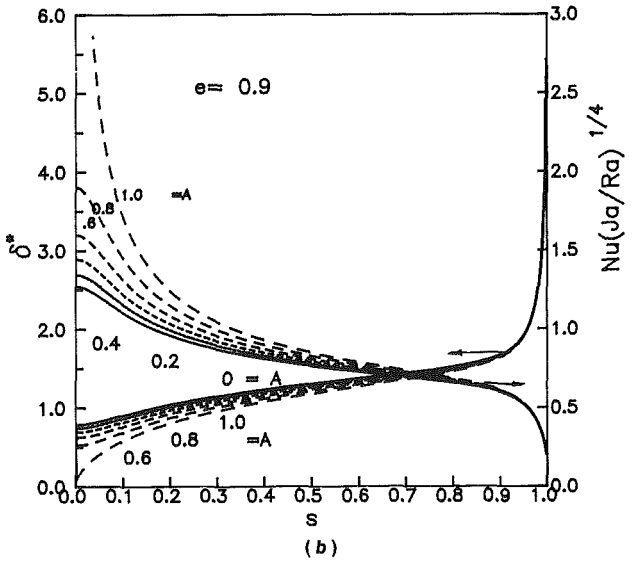

Fig. 2 *(a)* $e = 0.5$ and *(b)* $e = 0.9$; variation of dimensionless local film thickness and heat transfer coefficient with streamwise length

Noting that the relation above gives only half of the condensate mass flow from the tube, one finds that an energy balance within the condensate film over an entire elliptical perimeter per unit tube length yields

$$2\dot{m}\, h'_{fg} = \bar{h}\,(\pi D_e)\,\overline{\Delta T} \tag{15}$$

Inserting Eq. (14) into Eq. (15), one may obtain the mean Nusselt number as follows:

$$\overline{\mathrm{Nu}} = \frac{\bar{h} D_e}{k} = \left(\frac{128}{81\pi}\right)^{1/4} [\mathrm{Ra/Ja}]^{1/4} S_f(e) \tag{16}$$

where

$$S_f(e) = \left\{ \int_0^{\pi} \frac{F_t(\phi)(\sin\phi)^{1/3}}{(1-e^2\sin^2\phi)^{3/2}}\, d\phi \Big/ \int_0^{\pi} (1-e^2\sin^2\phi)^{-3/2} d\phi \right\}^{3/4}$$

For the limiting case, $e = 1$, it is noted that an elliptical tube becomes a vertical plate with both sides experiencing condensation. At the same time, its equivalent diameter D_e is equal to 2 (l/π), where l is the length of the vertical plate. Therefore, for the flat plate one should use l instead of D_e for Ra and $\overline{\mathrm{Nu}}$ in Eq. (16) and express the temperature difference across the film in terms of the x coordinate instead of the angular coordinate ϕ. If the nonisothermality function $F_t(x)$ reflects a power-law variation of wall temperature, there exist similarity solutions. When $F_t(x) = 1$, the present solution reduces to Nusselt's solution for a vertical flat plate with the isothermal surface.

3 Results and Discussion

It is noted that these analytical expressions of mean Nusselt numbers for horizontal elliptical tubes/circular tube are available once the wall temperature profiles are given. Representative numerical results for the common axisymmetric case that involves the cosine distribution of nonisothermal wall temperature variation

$$F_t(\phi) = 1 - A\cos(\phi) \tag{17}$$

will be illustrated and discussed later. It is noted that $0 \le A \le 1$, where the amplitude A depends largely on the ratio of

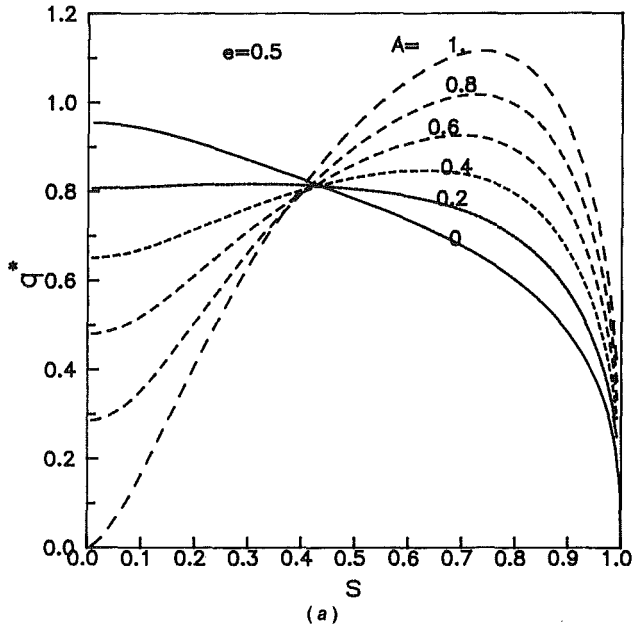

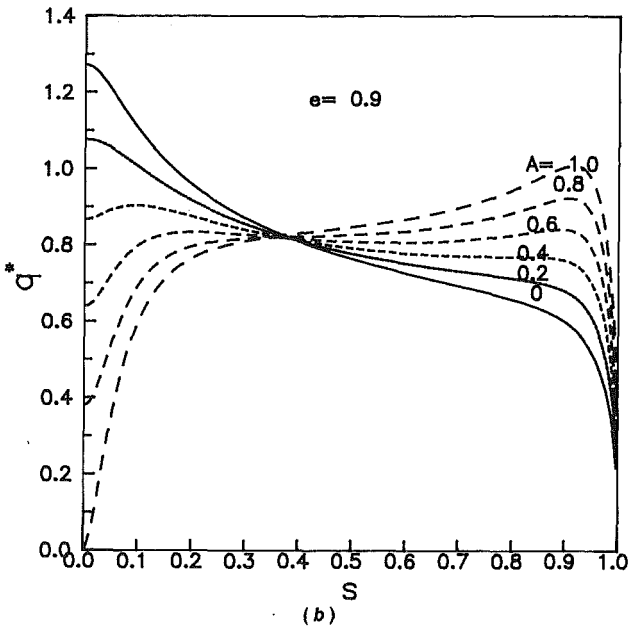

Fig. 3 *(a)* $e = 0.5$ and *(b)* $e = 0.9$; variation of dimensionless local heat flux with dimensionless film streamwise length

the outside-to-inside heat transfer coefficients. When $A = 0$, the wall temperature is uniform. In fact, the nonisothermality function coincides with the experiment of Lee et al. (1984) for circular tube.

Equations (9) and (13) have been evaluated numerically for different values of ellipticity and the nonisothermality function at particular angular position ϕ, or its corresponding dimensionless circumferential position s. These results are shown in Fig. 2(a) and 2(b). It is seen that δ^* decreases as A increases; the local heat transfer coefficient, Nu, increases as A increases. Note that as e approaches one, δ^* at the top ($s = 0$) approaches zero, which is the same as for a vertical plate. The local heat transfer coefficients increase significantly with increasing ellipticity near both the top and bottom of tube. When $e = 0$ (circular tube), the dependence of dimensionless film thickness on dimensionless circumferential position (or angle) coincides with the solution of Memory and Rose (1991).

In Figs. 3(a) and 3(b), the results from Eq. (12) show that, for the isothermal wall ($A = 0$), the heat flux decreases continuously around the elliptic tube. As A increases, the heat flux first rises where the effect of the increasing ΔT outweighs that of the increasing film thickness. Subsequently, the heat flux reaches a maximum at a location on the lower half of the elliptic tube before decreasing to zero as the film thickness becomes infinite. As ellipticity e increases for a particular amplitude A, the maximum heat flux shifts to the lower location near the bottom of tube, and decreases in magnitude.

The mean heat transfer coefficient increases less than 0.1 percent as A goes from 0 to 1, and generally speaking, the mean heat transfer coefficient is virtually unaffected by the wall temperature cosine distribution for any elliptic tube of a particular e. For a cylinder ($e = 0$) despite the wide variation of δ and q with the circumferential (or angular) position, the mean heat transfer coefficient for the condensate film, based on a mean value of ΔT, is extremely accurate.

In Fig. 4, the mean heat transfer coefficient for an ellipse with its major axis oriented in the direction of gravity is compared with that for an ellipse with its minor axis oriented in the direction of gravity. In the former case, $\overline{Nu}$ increases with increasing e very slowly at small e, and at a much greater pace at large e. For isothermal cases, $A = 0$, the reduced results agree well with Karimi's (1977) solution using the finite difference method.

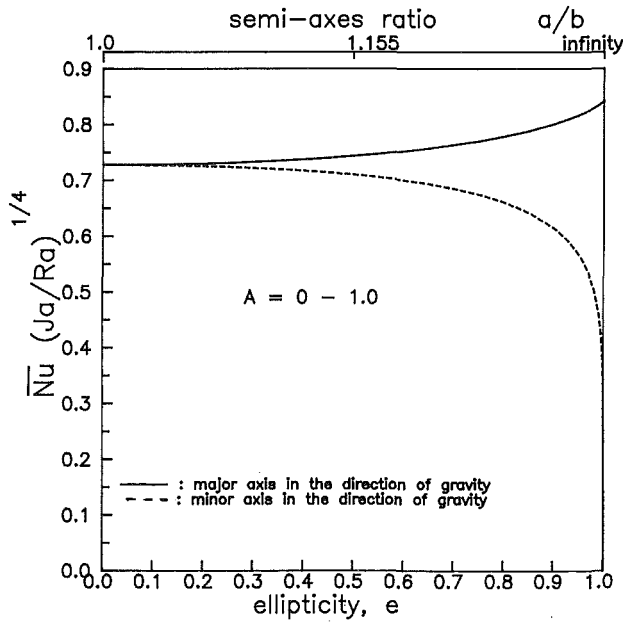

Fig. 4 Dependence of dimensionless mean heat transfer coefficient on ellipticity or semi-axis ratio

4 Concluding Remarks

1 Prior finite difference solutions for condensation on elliptical tubes can be replaced with a simple Nusselt-Rohsenow calculation in almost all cases of practical importance.

2 The mean heat transfer coefficient is also nearly unaffected by the wall temperature variation with a cosine distribution, although the local heat transfer coefficient and film flow characteristics are appreciably influenced.

3 The present solutions are very accurate for large Prandtl numbers, but for small Prandtl numbers, are restricted to small values of Jakob number, as similar to the Nusselt-Rohsenow type.

References

Fujii, T., Uehare,H., and Oda, K., 1972, "Filmwise Condensation on a Surface With Uniform Heat Flux and Body Force Convection," *Heat Transf. Jpn. Res.*, No. 4, pp. 76–83.

Karimi, A., 1977, "Laminar Film Condensation on Helical Reflux Condensers and Related Configurations," *Int. J. Heat Mass Transfer*, Vol. 20, pp. 1137–1144.

Lee, W. C., Rahbar, S., and Rose, J. W., 1984, "Film Condensation of Refrigerant 113 and Ethanediol on a Horizontal Tube—Effect of Vapor Velocity," ASME JOURNAL OF HEAT TRANSFER, Vol. 106, pp. 524–530.

Memory, S. B., and Rose, J. W., 1991, "Free Convection Laminar Film Condensation on a Horizontal Tube With Variable Wall Temperature," *Int. J. Heat Mass Transfer*, Vol. 34, No. 11, pp. 2775–2778.

Nusselt, W., 1916, "Die oberflachen Kondensation des Wasserdampes," *Zeitschrift des Vereines Deutscher Ingenieure*, Vol. 60, pp. 541–546, 569–575.

Rohsenow, W. M., 1956, "Heat Transfer and Temperature Distribution in Laminar-Film Condensation," *Trans. ASME*, Vol. 78, pp. 1645–2648.

Wang, C. Y., Joseph, Jiang, Z., and Feng, Yi, 1988, "Laminar Film Condensation of Pure Saturated Vapors on Horizontal Elliptical Tubes," *Proceedings of Int. Symp. on Phase Change Heat Transfer*, pp. 307–311, May 20–31.

Prediction of the Onset of Significant Void in Flow Boiling of Water

J. T. Rogers[1,2] and Jing-Hui Li[1]

Nomenclature

C_d = bubble drag coefficient
C_p = specific heat
C_s = empirical correction factor in equation for surface tension force (Rogers et al., 1987)
C_1, C_2 = functions of equilibrium contact angle (Rogers et al., 1987)
C_3 = function of equilibrium and advancing and retreating contact angles (Rogers et al., 1987)
d_e = equivalent diameter
F_R = empirical factor to allow for bubbly (rough) surface and other effects
g = acceleration of gravity
h_0 = heat transfer coefficient
p = pressure
q'' = heat flux at wall
Re = Reynolds number = $\rho_f \bar{u} d_e / \mu_f$
Re_b = bubble Reynolds number at departure = $\rho_f u_r (2r_b)/\mu_f$

[1] Department of Mechanical and Aerospace Engineering, Carleton University, Ottawa, Ontario, Canada.

[2] Mem. ASME.

Contributed by the Heat Transfer Division and presented at the Winter Annual Meeting, Anaheim, California, November 8–13, 1992. Manuscript received by the Heat Transfer Division March 1993; revision received January 1994. Keywords: Boiling, Multiphase Flows, Nonequilibrium Flows. Associate Technical Editor: R. A. Nelson, Jr.

the outside-to-inside heat transfer coefficients. When $A = 0$, the wall temperature is uniform. In fact, the nonisothermality function coincides with the experiment of Lee et al. (1984) for circular tube.

Equations (9) and (13) have been evaluated numerically for different values of ellipticity and the nonisothermality function at particular angular position ϕ, or its corresponding dimensionless circumferential position s. These results are shown in Fig. 2(a) and 2(b). It is seen that δ^* decreases as A increases; the local heat transfer coefficient, Nu, increases as A increases. Note that as e approaches one, δ^* at the top ($s = 0$) approaches zero, which is the same as for a vertical plate. The local heat transfer coefficients increase significantly with increasing ellipticity near both the top and bottom of tube. When $e = 0$ (circular tube), the dependence of dimensionless film thickness on dimensionless circumferential position (or angle) coincides with the solution of Memory and Rose (1991).

In Figs. 3(a) and 3(b), the results from Eq. (12) show that, for the isothermal wall ($A = 0$), the heat flux decreases continuously around the elliptic tube. As A increases, the heat flux first rises where the effect of the increasing ΔT outweighs that of the increasing film thickness. Subsequently, the heat flux reaches a maximum at a location on the lower half of the elliptic tube before decreasing to zero as the film thickness becomes infinite. As ellipticity e increases for a particular amplitude A, the maximum heat flux shifts to the lower location near the bottom of tube, and decreases in magnitude.

The mean heat transfer coefficient increases less than 0.1 percent as A goes from 0 to 1, and generally speaking, the mean heat transfer coefficient is virtually unaffected by the wall temperature cosine distribution for any elliptic tube of a particular e. For a cylinder ($e = 0$) despite the wide variation of δ and q with the circumferential (or angular) position, the mean heat transfer coefficient for the condensate film, based on a mean value of ΔT, is extremely accurate.

In Fig. 4, the mean heat transfer coefficient for an ellipse with its major axis oriented in the direction of gravity is compared with that for an ellipse with its minor axis oriented in the direction of gravity. In the former case, $\overline{Nu}$ increases with increasing e very slowly at small e, and at a much greater pace at large e. For isothermal cases, $A = 0$, the reduced results agree well with Karimi's (1977) solution using the finite difference method.

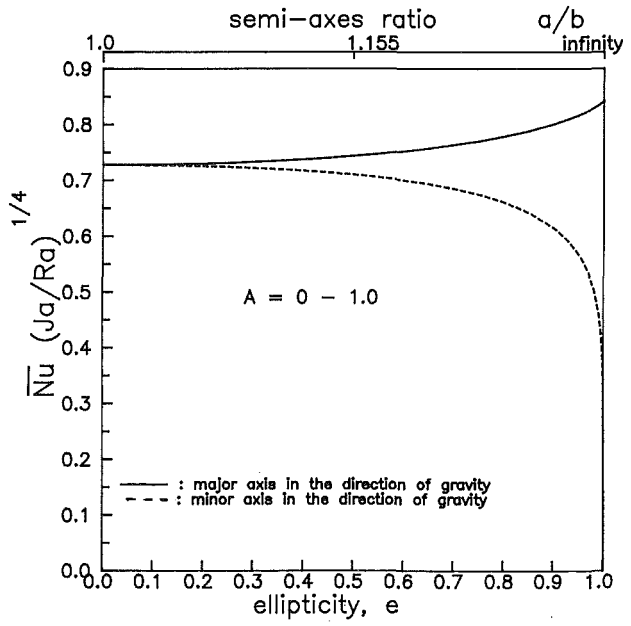

Fig. 4 Dependence of dimensionless mean heat transfer coefficient on ellipticity or semi-axis ratio

4 Concluding Remarks

1 Prior finite difference solutions for condensation on elliptical tubes can be replaced with a simple Nusselt-Rohsenow calculation in almost all cases of practical importance.

2 The mean heat transfer coefficient is also nearly unaffected by the wall temperature variation with a cosine distribution, although the local heat transfer coefficient and film flow characteristics are appreciably influenced.

3 The present solutions are very accurate for large Prandtl numbers, but for small Prandtl numbers, are restricted to small values of Jakob number, as similar to the Nusselt-Rohsenow type.

References

Fujii, T., Uehare,H., and Oda, K., 1972, "Filmwise Condensation on a Surface With Uniform Heat Flux and Body Force Convection," *Heat Transf. Jpn. Res.*, No. 4, pp. 76–83.

Karimi, A., 1977, "Laminar Film Condensation on Helical Reflux Condensers and Related Configurations," *Int. J. Heat Mass Transfer*, Vol. 20, pp. 1137–1144.

Lee, W. C., Rahbar, S., and Rose, J. W., 1984, "Film Condensation of Refrigerant 113 and Ethanediol on a Horizontal Tube—Effect of Vapor Velocity," ASME JOURNAL OF HEAT TRANSFER, Vol. 106, pp. 524–530.

Memory, S. B., and Rose, J. W., 1991, "Free Convection Laminar Film Condensation on a Horizontal Tube With Variable Wall Temperature," *Int. J. Heat Mass Transfer*, Vol. 34, No. 11, pp. 2775–2778.

Nusselt, W., 1916, "Die oberflachen Kondensation des Wasserdampes," *Zeitschrift des Vereines Deutscher Ingenieure*, Vol. 60, pp. 541–546, 569–575.

Rohsenow, W. M., 1956, "Heat Transfer and Temperature Distribution in Laminar-Film Condensation," *Trans. ASME*, Vol. 78, pp. 1645–2648.

Wang, C. Y., Joseph, Jiang, Z., and Feng, Yi, 1988, "Laminar Film Condensation of Pure Saturated Vapors on Horizontal Elliptical Tubes," *Proceedings of Int. Symp. on Phase Change Heat Transfer*, pp. 307–311, May 20–31.

Prediction of the Onset of Significant Void in Flow Boiling of Water

J. T. Rogers[1,2] and Jing-Hui Li[1]

Nomenclature

C_d = bubble drag coefficient
C_p = specific heat
C_s = empirical correction factor in equation for surface tension force (Rogers et al., 1987)
C_1, C_2 = functions of equilibrium contact angle (Rogers et al., 1987)
C_3 = function of equilibrium and advancing and retreating contact angles (Rogers et al., 1987)
d_e = equivalent diameter
F_R = empirical factor to allow for bubbly (rough) surface and other effects
g = acceleration of gravity
h_0 = heat transfer coefficient
p = pressure
q'' = heat flux at wall
Re = Reynolds number = $\rho_f \bar{u} d_e / \mu_f$
Re_b = bubble Reynolds number at departure = $\rho_f u_r (2r_b)/\mu_f$

[1] Department of Mechanical and Aerospace Engineering, Carleton University, Ottawa, Ontario, Canada.

[2] Mem. ASME.

Contributed by the Heat Transfer Division and presented at the Winter Annual Meeting, Anaheim, California, November 8–13, 1992. Manuscript received by the Heat Transfer Division March 1993; revision received January 1994. Keywords: Boiling, Multiphase Flows, Nonequilibrium Flows. Associate Technical Editor: R. A. Nelson, Jr.

r_b = bubble radius at departure
T_s = saturation temperature
T_b^+ = nondimensional temperature difference between the wall and the liquid at bubble tip = $(C_{pf}\rho_f u^*/q'')(T_w - T_s)$
ΔT_d = liquid subcooling at OSV (bubble departure point)
$\bar{u}$ = channel average liquid velocity
u_r = liquid velocity at y_r, from the universal velocity profile
u^* = shear stress velocity = $\sqrt{\tau_w/\rho_f}$
y_b = distance from wall to the tip of bubble at departure
y_r = one-half the distance from the wall to the tip of the bubble at departure
y_b^+ = nondimensional distance from the wall to the tip of bubble at departure = $\rho_f u^* y_b/\mu_f$
θ_0 = static or equilibrium contact angle
μ = dynamic viscosity
ρ = density
σ = surface tension
τ_w = shear stress at the wall

Subscripts

f = liquid
w = heated wall surface

Introduction

The prediction of the point of onset of significant void (OSV), also known as the initial point of net vapor generation (IPNVG), is very important in flow boiling systems. Knowledge of the void profile, which requires prediction of the OSV point, is vital for the prediction of two-phase friction and momentum pressure losses, flow stability limits, and reactivity effects in nuclear reactors.

A paper by Rogers et al. (1987) presents OSV results for low-pressure (~150 kPa), low-velocity (<1 m/s) conditions and describes an analytical model that predicts the observed behavior. The validity of the OSV model of Rogers et al. for use at low pressures and velocities has been confirmed by Chatoorgoon et al. (1990) in experiments at pressures in the range of 152 to 211 kPa and inlet velocities in the range of 0.32 to 0.47 m/s.

Since the mechanistic model of Rogers et al. predicts OSV behavior in annuli of small equivalent diameter at low pressure and inlet velocities quite well, it seemed desirable to determine whether this model could be extended to apply over wide ranges of pressure, inlet velocities, and geometries. Accordingly, a study was undertaken to examine this question using data on OSV from the literature. The results of this study are presented in this paper. A description of the work undertaken is given in the M.Eng. thesis of J. Li (1992) and some results have been presented by Rogers and Li (1992).

Outline of Analytical Model for OSV

The analytical model is described in detail by Rogers et al. (1987) and an outline of the model is given by Rogers and Li (1992), so that only a brief description is provided here. The model is a bubble-detachment type, as are those of Bowring (1962), Levy (1967), and Staub (1968), rather than an energy-balance type, such as those of Griffith et al. (1958), Rouhani (1968), and Rouhani and Axelson (1970). It utilizes the results of Al-Hayes and Winterton (1981) and Winterton (1984) for bubble departure from a wall. As in the models of Levy and Staub, it is assumed that bubble departure occurs when the forces tending to detach the bubble overcome those tending to hold it on the surface. The forces considered in the model for vertical upward flow are the buoyant force and the bubble drag force, tending to detach the bubble, and the surface tension force, tending to hold the bubble on the wall. Other forces are ignored (Rogers and Li, 1992). The model treats the bubble basically as a distorted truncated sphere with the contact angle varying from the equilibrium contact angle, θ_0, symmetrically around the periphery of the line of contact.

The model predicts that the bubble radius at departure is given by:

$$r_b = \frac{3}{4\pi}\frac{C_2}{C_1}C_d\frac{u_r^2}{g}\left[\left\{1+\frac{8\pi^2}{3}\frac{C_1C_3}{C_2^2}\frac{C_s}{C_d^2}\frac{g\sigma}{\rho_f u_r^4}\right\}^{1/2}-1\right] \quad (1)$$

As in the Levy and Staub models, it is postulated that a bubble can only grow and detach if it is entirely within the superheated layer, i.e., when the temperature at the bubble tip is no lower than the saturation temperature. From this condition, the definition of T_b^+ and the definition of the heat transfer coefficient, it can be shown that the subcooling at the bubble departure point is given by:

$$\Delta T_d = q''\left[\frac{1}{F_R h_0}-\frac{T_b^+}{C_{pf}\rho_f u^*}\right] \quad (2)$$

where h_0 is given by the heat transfer coefficient for fully developed single-phase turbulent flow over a smooth surface and the value of the friction factor needed to determine u^* is similarly given by the friction factor for fully developed single-phase turbulent flow over a smooth surface. The value of T_b^+, the nondimensional temperature difference between the wall and the liquid at the bubble tip, y_b^+, is determined from the Martinelli equations for the universal temperature profile on a smooth surface. As explained by Rogers et al. (1987) and Rogers and Li (1992), F_R is an empirical correction factor to allow for the bubble-covered "rough" surface before the OSV point and for other effects.

Experimental results obtained by McLeod (1986) were used to determine the value of the empirical factor F_R for low-pressure (<150 kPa) and low-velocity (<1 m/s) conditions, assuming a range of equilibrium contact angles from 30 to 80 deg, a range that might be expected for water on smooth metallic surfaces. The values obtained for F_R were 1.11 ± 0.036 and 1.06 ± 0.022 for θ_0 = 30 and 80 deg, respectively. The uncertainty represents one standard deviation.

Extension of Model to Other Conditions

Experimental data from the literature were analyzed so as to extend the applicable range of the model of Rogers et al. to other conditions, in particular to higher pressures and inlet velocities, but also to different geometries. The sources of the experimental data used are listed in Table 1. All the investigators listed in Table 1 used water as the working fluid except for Dix (1971), who used Freon-114. Because of the small amount of nonwater data, the work described here concentrated on the water data. Comments on the applicability of the model to the Freon data are given later in this paper.

The method used to assess the applicability of the model to the experimental results was to establish the subcooling at OSV from the experimental data, substitute it into Eq. (2), and solve for F_R for the given conditions. Properties were evaluated at the saturation temperature. This procedure was followed assuming equilibrium contact angles from 30 to 80 deg, judged to span the probable range of contact angles for water on metallic surfaces (Rogers et al., 1987).

Values of F_R from all the investigations with water listed in Table 1, i.e., all except that of Dix, were then plotted against various dimensional and nondimensional parameters in an attempt to establish a reliable correlation, as described in Rogers and Li (1992). Satisfactory correlations were obtained using the bubble Reynolds number, Re_b, for the range of θ_0 = 30 deg to θ_0 = 80 deg, for flow Reynolds numbers ≥10,000. Data at lower flow Reynolds numbers did not correlate well, which is not surprising since the model assumes turbulent flow conditions and ignores forces that may become significant at lower Reynolds numbers.

Values of F_R for all the water data for Re ≥ 10,000 are given by:

Table 1 Experimental OSV data[1]

Investigator	Geometry and Size mm	Pressure bar	Velocity m/s	Heat Flux W/m²*10⁻⁶	Number of Experimental Points[2]	
G.G. Bartolemei (1967)	Tube D=15.4, 24.0	15.0-45.0	1.00-1.14	0.38-0.80	11	(11)
G.G. Bartolemei (1982)	Tube D = 12.0	30.0-148	0.54-3.50	0.34-2.21	20	(20)
E.L. Bibeau (1990)	Annulus OD = 21.8 ID = 12.7	1.55	0.22-0.46	0.30-0.98	5	(2)
H. Christensen (1961)	Rectangular 44.4 x 11.1	27.6-68.9	0.77-1.15	0.21-0.50	4	(4)
J. Costa (1967)	Rectangular 38x2, 38x3.6 Tube, D=6.0	1.74-4.99	3.17-8.19	1.0-4.2	43	(43)
G.E. Dix (1971)	Annulus OD = 18.64 ID = 9.50	3.14-8.48	0.07-0.16	0.004-0.03	47	(0)
Z. Edelman (1981)	Tube D = 11.3	1.013	0.10-0.19	0.049-0.096	6	(0)
R.A. Egen (1957)	Rectangular 25.4 x 2.62	138	0.63-1.31	0.25-1.58	7	(7)
R. Evangelisti (1969)	Annulus OD = 13.0, ID = 7.0	1.128	0.64-1.48	0.437-0.885	3	(3)
P. Griffith (1958)	Rectangular 12.7 x 12.7	82.7-138	0.63-1.38	0.31-1.91	12	(12)
D.A. Labuntsov (1984)	Tube D = 12.1	20.0-70.0	1.00-4.00	0.58-1.16	3	(3)
R. Martin (1972)	Rectangular 50x2, 50x2.8	78.48	1.03-3.03	0.4-1.7	8	(8)
G.W. Maurer (1960)	Rectangular 25.4 x 2.21	85.5-143	0.79-7.66	0.306-3.79	15	(15)
R. McLeod (1986)	Annulus OD=22,25,30 ID = 13.1	1.55	0.07-0.48	0.6-1.19	41	(11)
S.Z. Rouhani (1965)	Annulus OD = 25.0 ID = 12.0	9.8-50.0	0.15-1.54	0.3-1.21	16	(16)
F.W Staub (1969)	Rectangular 76.2 x 7.62	1.12-3.08	0.34-2.93	0.308-0.792	11	(11)

[1] The fluid used by Dix is Freon-114, all others used water.

[2] The number in brackets is the number of experimental points with Re ≥ 10,000, i.e. those used in developing the correlation.

$$F_R = 1 + 17.58\ \mathrm{Re}_b^{-0.89} \quad \text{for} \quad \theta_0 = 30 \text{ deg} \tag{3}$$

$$F_R = 1 + 58.86\ \mathrm{Re}_b^{-1.03} \quad \text{for} \quad \theta_0 = 80 \text{ deg} \tag{4}$$

Comparison of Models and Experimental Results

All the OSV data from the investigations listed in Table 1 for water for Reynolds numbers of 10,000 or greater were compared to the predictions of the models of Bowring (1962), Levy (1967), and Saha and Zuber (1974) as well as to the predictions of the present model. A plot of the predicted values of $\Delta T_d/q''$ against the experimental values assuming $\theta_0 = 80$ deg is shown in Fig. 1; similar plots for the other models are given by Rogers and Li (1992). Table 2, which summarizes the results of the comparisons, shows that the correlations of the present model give significantly lower relative standard deviations from the data than do the other correlations.

Therefore, it is concluded that the present modification to the model of Rogers et al. (1987), using Eq. (2) with F_R given by Eqs. (3) or (4) gives the best prediction of all the OSV data for water with Re ≥ 10,000. The use of $\theta_0 = 80$ deg gives a slightly better correlation than the use of $\theta_0 = 30$ deg, but this difference is not very significant. This correlation is considered valid over the following ranges of parameters, subject to the overriding requirement that Re ≥ 10,000:

$$0.2 \le \bar{u} \le 8.2 \text{ m/s}$$

$$101 \le p \le 14{,}800 \text{ kPa}$$

$$0.0038 \le d_e \le 0.024 \text{ m}$$

$$210{,}000 \le q'' \le 4{,}200{,}000 \text{ W/m}^2$$

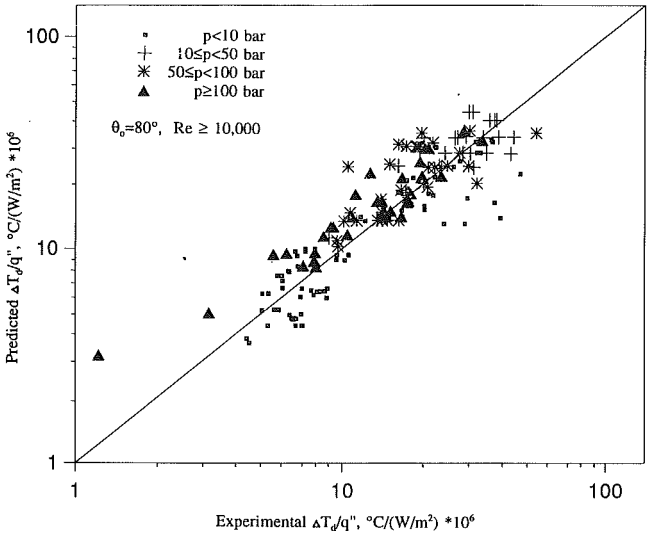

Fig. 1 Comparison between experimental values and present model predictions of $\Delta T_d/q''$ for $\theta_0 = 80$ deg

Effects of Various Parameters on OSV

Figure 2 shows the effect of velocity on $\Delta T_d/q''$ for various pressures for $\theta_0 = 80$ deg and $d_e = 0.01$ m. At high velocities, $\Delta T_d/q''$ increases slowly as pressure increases at pressures up to 50 bar and then decreases slowly as pressure increases above that value. This type of behavior with pressure is similar to that predicted by the Levy model under those conditions (Li, 1992). As velocity decreases, $\Delta T_d/q''$ for any pressure increases until a velocity around 0.5 m/s is reached. Below this velocity, the behavior of $\Delta T_d/q''$ becomes more complicated, with $\Delta T_d/q''$ continuing to increase at high pressures, but decreasing at low pressures. This reversed effect of velocity on $\Delta T_d/q''$ at low pressures was noted and explained in the original study of Rogers et al. (1987).

Very similar behavior is predicted for $\theta_0 = 30$ deg, with the same magnitudes and trends of $\Delta T_d/q''$ as exhibited for $\theta_0 = 80$ deg. Thus, the insensitivity of the predicted OSV point to θ_0 for low-pressure, low-velocity conditions, noted by Rogers et al. (1987), is seen to apply over the entire ranges of variables examined here. The insensitivity of the OSV point to contact angle results from the effects of two factors: the projected area of the bubble and the distance from the wall to the tip of the bubble, y_b. As θ_0 increases from 30 deg, the projected area increases, so that bubble detachment tends to occur earlier, i.e., at high ΔT_d. As θ_0 increases, y_b also increases, so that the tip of the bubble extends into a colder region, which tends to retard bubble detachment, so that it occurs at lower ΔT_d. The net effect is that OSV is almost independent of static contact angle over the entire effective range from 30 to 80 deg.

It has been shown (Rogers and Li, 1992) that $\Delta T_d/q''$ is predicted to increase as the channel equivalent diameter increases for a given velocity and pressure. This trend is similar to that predicted by the Levy model as well as by the Saha–Zuber model at low d_e values (Li, 1992) and has been explained by Rogers

Table 2 Deviations of model predictions of $\Delta T_d/q''$ from the data (data from all investigations listed in Table 1 for water, Re ≥ 10^4)

	Maximum deviation (°C/(W/m²)) x 10⁶	Relative Standard deviation
Bowring Model	81	0.717
Levy Model	24	0.578
Saha-Zuber Model	31	0.563
Present Model, $\theta_0 = 30°$	23	0.360
$\theta_0 = 80°$	26	0.338

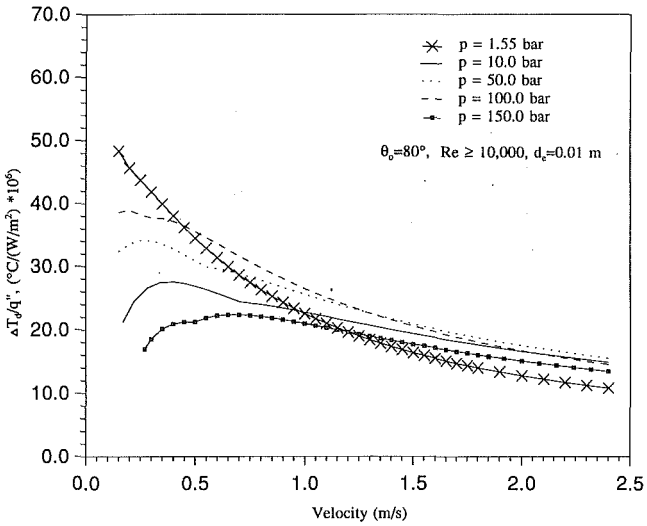

Fig. 2 Effect of velocity on $\Delta T_d/q''$ by the present model, θ_0 = 80 deg

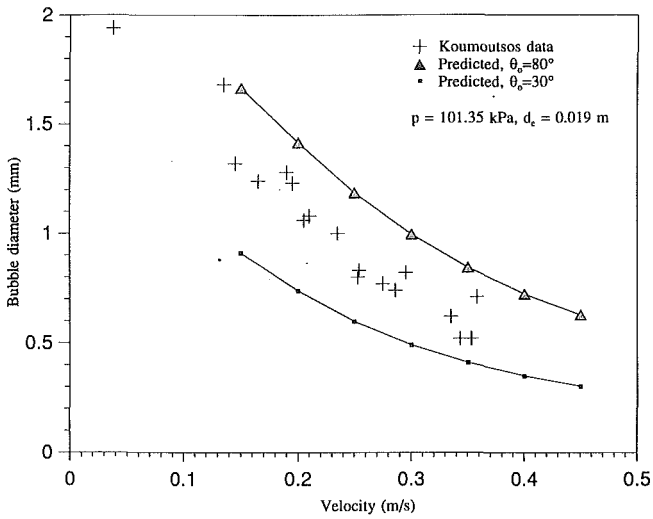

Fig. 3 Comparison of predicted bubble diameter at departure with data of Koumoutsos

and Li. As Table 1 shows, the OSV data considered in this study were generated in tubes, annuli, and rectangular slots. No effect of these different channel shapes on the OSV point could be established from the analysis of the data.

The results of Dix (1971) with Freon-114 were obtained at quite low Reynolds numbers (~9000 at the highest). Therefore these data are below the range of validity of the recommended model so that it would not be expected to, and indeed, did not, predict the Freon-114 results well.

Bubble Parameters at OSV

The recommended model can be used to investigate bubble parameters and characteristics at OSV. Certain conclusions can be drawn from these investigations about the applicability of the model to other conditions than those covered in the studies considered in this paper.

The model predicts that the radius of the departing bubble at OSV, r_b, increases as inlet velocity decreases and decreases as pressure increases, as would be expected in both cases. The magnitudes of bubble diameter at departure predicted by the model are compared to the measurements of Koumoutsos et al. (1968), as also reported by Winterton (1984), in water at atmospheric pressure in Fig. 3. Figure 3 shows that the predictions of r_b from the model are in reasonably good agreement with the measurements, with the predictions for θ_0 = 30 deg and θ_0 = 80 deg bracketing all the measured values.

Recently, experimental data on bubble diameter at departure in refrigerant R113 were reported by Klausner et al. (1993). Although these data were not taken at the OSV point, but under two-phase horizontal stratified flow conditions at thermodynamic qualities from 0.2 to 16.5 percent, and although the present model has not been validated for refrigerant R113, predictions of the bubble diameter at departure by Eq. (1) using the properties of R113 at a saturation temperature of 60°C, representative of the range reported by Klausner et al., were made. Although the static contact angle for R113 on smooth surfaces is quite low (<5 deg), the dynamic contact angle for such a highly wetting liquid can be much higher (Tong et al., 1990). Therefore, considering the velocities to which the departing bubble were exposed in the experiments of Klausner et al., the range of contact angles used in the predictions for their data was again 30 to 80 deg. The contact angle corrections to allow for advancing and retreating interfaces were again assumed to be ±10 deg, as for water (Rogers et al., 1987). The results in Fig. 4 show that the data are predicted quite well in magnitude and trend for θ_0 = 80 deg while they are underpredicted for θ_0 = 30 deg.

The effects of inlet velocity and pressure on the forces acting on the bubble at detachment have been shown by Rogers and Li (1992). As for the original low-pressure model of Rogers et al. (1987), the drag and surface tension forces are predominant over most of the velocity range. Only at velocities less than about 0.25 m/s does buoyant force exceed 10 percent of the drag and surface tension forces. The predominance of drag and surface tension forces is only slightly affected by pressure. As pointed out by Rogers (1987), this predicted behavior supports the empirical conclusion of Levy (1967) that buoyant force does not affect OSV under the conditions of his study, i.e., high velocities and pressure. Insights gained from this assessment of forces acting on a bubble at the OSV point can be used to conclude that the model can be applied with some confidence to vertical downward flows and to horizontal flows as well as to vertical upward flows (Rogers and Li, 1992).

Conclusions

The OSV model of Rogers et al. (1987), which was based on experimental data obtained at low pressure and relatively low velocities, has been extended to a wide range of pressures, velocities, and geometries using existing data from the literature.

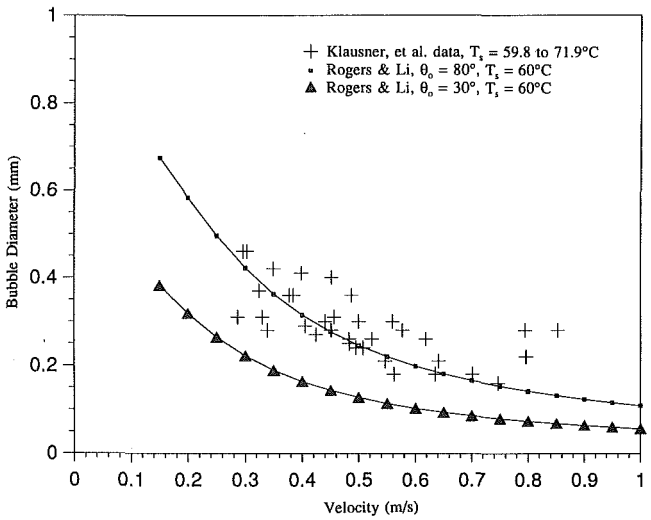

Fig. 4 Comparison of predicted bubble diameter at departure with data of Klausner et al. for R113

Using the model, the subcooling at OSV for water flows can be predicted using Eq. (2), as in the original model, but with F_R given by Eq. (3) or (4) for equilibrium bubble contact angles of 30 and 80 deg, respectively. The recommended model gives better predictions of all the OSV data considered than do other commonly used models. While predicted OSV points are not very sensitive to the choice of θ_0, slightly better correlation is obtained with $\theta_0 = 80$ deg. The model is valid for flow Reynolds numbers equal to or greater than 10,000.

The model predicts trends with various parameters that would be expected or can be explained and also predicts bubble diameter at departure that agree reasonably well with measured diameters of bubbles at detachment in water and refrigerant R113 flows near atmospheric pressure, considering the uncertainty in dynamic contact angles.

The model enables conclusions to be drawn as to the importance of the various forces at OSV, suggesting that drag and surface tension forces predominate over the range of the validity of the model with the buoyant force being less than 10 percent of the drag force even at the lowest velocities in the range of validity. This finding validates the use of the model for vertical downward flows and horizontal flows as well as for vertical upward flows under most conditions.

Further work is required to develop a model for Reynolds numbers less than 10,000, and to test the model against OSV data for fluids other than water.

Acknowledgments

Financial support for this work was provided by the Natural Sciences and Engineering Research Council of Canada under research grant No. A6342. The authors thank Marilyn Boreham and Christie Egbert for typing the paper and Jiri Slaby for preparing the final versions of the figures.

References

Al-Hayes, R. A. M., and Winterton, R. H. S., 1981, "Bubble Diameter on Detachment in Flowing Liquids," *Int. J. Heat Mass Transfer,* Vol. 24, pp. 223–230.

Bartolemei, G. G., and Chanturiya, V. M., 1967, "Experimental Study of True Void Fraction When Boiling Sub-cooled Water in Vertical Tubes," *Thermal Engineering,* Vol. 14, No. 2, pp. 123–128.

Bartolemei, G. G., Brantov, V. G., Molochnikov, Yu. S., and Kharitonov, Yu. V., 1982, "An Experimental Investigation of True Volumetric Vapour Content With Sub-cooled Boiling in Tubes," *Thermal Engineering,* Vol. 29, No. 3, pp. 132–135.

Bibeau, E. L., and Salcudean, M., 1990, "The Effect of Flow Direction on Void Growth at Low Velocity and Low Pressure," *Int. Comm. Heat Mass Transfer,* Vol. 17, pp. 19–25.

Bowring, R. W., 1962, "Physical Model Based on Bubble Detachment and Calculation of Steam Voidage in the Sub-cooled Region of a Heated Channel," HPR-10, Institutt for Atomenergi, Halden, Norway.

Chatoorgoon, V., Dimmick, G. R., Carver, M. B., Selander, W. N., and Shoukri, M., 1990, "Application of Void Generation and Condensation Models to Predict Sub-cooled Boiling Data at Low Pressures," *Third International Conference on Simulation Methods in Nuclear Engineering,* Canadian Nuclear Society, Montreal, Quebec, pp. 358–379.

Christensen, H., 1961, "Power-to-Void Transfer Functions," Argonne National Laboratory, ANL-6385.

Costa, J., 1967, "Measurement of the Acceleration Pressure Drop; Study of the Appearance of Vapour and Void Fraction in Sub-cooled Boiling at Low Pressure," Centre d'Etudes Nucleaires de Grenoble, European Two-Phase Group Meeting, Winfrith.

Dix, G. E., 1971, "Vapour Void Fraction for Forced Convection With Sub-cooled Boiling at Low Flow Rates," Ph.D. Thesis, University of California, Berkley.

Edelman, Z., and Elias, E., 1981, "Void Fraction Distribution in Low Flow Rate Sub-cooled Boiling," *Nuclear Engineering and Design,* Vol. 66, pp. 375–382.

Egen, R. A., Dingee, D., and Chastain, J., 1957, "Vapour Formation and Behaviour in Boiling Heat Transfer," Battelle Memorial Institute, BMI-1163.

Evangelisti, R., and Lupoli, P., 1969, "The Void Fraction in an Annular Channel at Atmospheric Pressure," *Int. J. Heat Mass Transfer,* Vol. 12, pp. 699–711.

Griffith, P., Clark, J. A., and Rohsenow, W. M., 1958, "Void Volumes in Sub-cooled Boiling," ASME Paper No. 58-HT-19.

Klausner, J. F., Mel, R., Bernhard, D. M., and Zeng, L. Z., 1993, "Vapor Bubble Departure in Forced Convection Boiling," *Int. J. Heat Mass Transfer,* Vol. 36, pp. 651–662.

Koumoutsos, N., Moissis, R., and Spyridonos, A., 1968, "A Study of Bubble Departure in Forced Convection Boiling," ASME JOURNAL OF HEAT TRANSFER, Vol. 90, pp. 223–230.

Labuntsov, D. A., Lobachev, A. G., Kol'chugin, B. A., and Zakharova, E. A., 1984, "The Main Principles of Variation in Vapour Content of Equilibrium and Non-equilibrium Two-Phase Flows in Channels of Different Geometry," *Thermal Engineering,* Vol. 31, No. 9, pp. 506–508.

Levy, S., 1967, "Forced Convection Sub-cooled Boiling: Prediction of Vapor Volumetric Fraction," *Int. J. Heat Mass Transfer,* Vol. 10, pp. 951–965.

Li, J., 1992, "The Onset of Significant Void in Boiling Flows Over a Wide Range of Operation Conditions," M. Eng. Thesis, Carleton University, Ottawa, Ontario, Canada.

Martin, R., 1972, "Measurement of the Local Void Fraction at High Pressure in a Heating Channel," *Nuclear Science and Engineering,* Vol. 48, pp. 125–138.

Maurer, G. W., 1960, "A Method of Predicting Steady-State Boiling Vapour Fractions in Reactor Coolant Channels," Westinghouse Electric Corp., Atomic Power Division, WAPD-BT-19.

McLeod, R. D., 1986, "Investigation of Sub-cooled Void Fraction Growth in Water Under Low Pressure and Low Flow Rate Conditions," M. Eng. Thesis, Carleton University, Ottawa, Ontario, Canada.

Rogers, J. T., Salcudean, M., Abdullah, Z., McLeod, D., and Poirier, D., 1987, "The Onset of Significant Void in Up-flow Boiling of Water at Low Pressure and Velocities," *Int. J. Heat Mass Transfer,* Vol. 30, pp. 2247–2260.

Rogers, J. T., and Li, J., 1992, "Prediction of the Onset of Significant Void in Flow Boiling of Water," *Fundamentals of Sub-cooled Flow Boiling,* R. D. Boyd, Sr., and S. G. Kandlikar, eds., ASME HTD-Vol. 217.

Rouhani, S. Z., 1965, "Void Measurement in the Region of Sub-cooled and Low Quality Boiling," Symposium on Two-Phase Flow, University of Exeter.

Rouhani, S. Z., 1968, "Calculation of Steam Volume Fraction in Sub-cooled Boiling," ASME JOURNAL OF HEAT TRANSFER, Vol. 90, pp. 158–164.

Rouhani, S. Z., and Axelson, E., 1970, "Calculation of Void Volume Fraction in the Sub-cooled and Quality Boiling Regions," *Int. J. Heat Mass Transfer,* Vol. 13, pp. 383–393.

Saha, P., and Zuber, N., 1974, "Point of Net Vapor Generation and Vapor Void Fraction in Sub-cooled Boiling," *Proc. Fifth International Heat Transfer Conference,* Tokyo, Vol. IV, pp. 175–179.

Staub, F. W., 1968, "The Void Fraction in Sub-cooled Boiling. Prediction of Initial Point of Net Vapor Generation," ASME JOURNAL OF HEAT TRANSFER, Vol. 90, pp. 151–157.

Staub, F. W., 1969, "Heat Transfer and Hydraulics: The Effects of Sub-cooled Voids," Final report, NYO-3679-8.

Tong, W., Bar-Cohen, A., Simon, T. W., and You, S. M., 1990, "Contact Angle Effects of Boiling Incipience of Highly Wetting Liquids," *Int. J. Heat Mass Transfer,* Vol. 33, pp. 91–104.

Winterton, R. H. S., 1984, "Flow Boiling: Prediction of Bubble Departure," *Int. J. Heat Mass Transfer,* Vol. 27, pp. 1422–1424.

A Technique for Establishing Inverted Annular Flow Through a Fast Power Transient

X. C. Huang[1] and G. Bartsch[2]

Introduction

During the quenching process of a hot metal tube, a sequence of different flow regimes and boiling modes may occur along the flow direction, e.g., the single-phase liquid flow, bubbly flow, inverted annular flow, agitated flow, dispersed flow, and single-phase vapor flow. Of the flow regimes ahead of the quench front, the inverted annular flow together with the axial heat conduction through the tube wall represents one of the important heat transfer mechanisms that directly influence the quenching velocity. Therefore, many experimental studies have been conducted for the inverted annular flow under steady-state conditions.

[1] Research Associate, Dept. of Mechanical Engineering, University of Ottawa, 770 King Edward, Ottawa, Ontario, Canada K1N 6N5.

[2] Institut fuer Energietechnik, TU Berlin, Marchstr. 18, 10587 Berlin, Federal Republic of Germany.

Contributed by the Heat Transfer Division of THE AMERICAN SOCIETY OF MECHANICAL ENGINEERS. Manuscript received by the Heat Transfer Division June 1993; revision received December 1993. Keywords: Boiling, Measurement Techniques, Transient and Unsteady Heat Transfer. Associate Technical Editor: R. Nelson, Jr.

Using the model, the subcooling at OSV for water flows can be predicted using Eq. (2), as in the original model, but with F_R given by Eq. (3) or (4) for equilibrium bubble contact angles of 30 and 80 deg, respectively. The recommended model gives better predictions of all the OSV data considered than do other commonly used models. While predicted OSV points are not very sensitive to the choice of θ_0, slightly better correlation is obtained with $\theta_0 = 80$ deg. The model is valid for flow Reynolds numbers equal to or greater than 10,000.

The model predicts trends with various parameters that would be expected or can be explained and also predicts bubble diameter at departure that agree reasonably well with measured diameters of bubbles at detachment in water and refrigerant R113 flows near atmospheric pressure, considering the uncertainty in dynamic contact angles.

The model enables conclusions to be drawn as to the importance of the various forces at OSV, suggesting that drag and surface tension forces predominate over the range of the validity of the model with the buoyant force being less than 10 percent of the drag force even at the lowest velocities in the range of validity. This finding validates the use of the model for vertical downward flows and horizontal flows as well as for vertical upward flows under most conditions.

Further work is required to develop a model for Reynolds numbers less than 10,000, and to test the model against OSV data for fluids other than water.

Acknowledgments

Financial support for this work was provided by the Natural Sciences and Engineering Research Council of Canada under research grant No. A6342. The authors thank Marilyn Boreham and Christie Egbert for typing the paper and Jiri Slaby for preparing the final versions of the figures.

References

Al-Hayes, R. A. M., and Winterton, R. H. S., 1981, "Bubble Diameter on Detachment in Flowing Liquids," *Int. J. Heat Mass Transfer,* Vol. 24, pp. 223–230.

Bartolemei, G. G., and Chanturiya, V. M., 1967, "Experimental Study of True Void Fraction When Boiling Sub-cooled Water in Vertical Tubes," *Thermal Engineering,* Vol. 14, No. 2, pp. 123–128.

Bartolemei, G. G., Brantov, V. G., Molochnikov, Yu. S., and Kharitonov, Yu. V., 1982, "An Experimental Investigation of True Volumetric Vapour Content With Sub-cooled Boiling in Tubes," *Thermal Engineering,* Vol. 29, No. 3, pp. 132–135.

Bibeau, E. L., and Salcudean, M., 1990, "The Effect of Flow Direction on Void Growth at Low Velocity and Low Pressure," *Int. Comm. Heat Mass Transfer,* Vol. 17, pp. 19–25.

Bowring, R. W., 1962, "Physical Model Based on Bubble Detachment and Calculation of Steam Voidage in the Sub-cooled Region of a Heated Channel," HPR-10, Institutt for Atomenergi, Halden, Norway.

Chatoorgoon, V., Dimmick, G. R., Carver, M. B., Selander, W. N., and Shoukri, M., 1990, "Application of Void Generation and Condensation Models to Predict Sub-cooled Boiling Data at Low Pressures," *Third International Conference on Simulation Methods in Nuclear Engineering,* Canadian Nuclear Society, Montreal, Quebec, pp. 358–379.

Christensen, H., 1961, "Power-to-Void Transfer Functions," Argonne National Laboratory, ANL-6385.

Costa, J., 1967, "Measurement of the Acceleration Pressure Drop; Study of the Appearance of Vapour and Void Fraction in Sub-cooled Boiling at Low Pressure," Centre d'Etudes Nucleaires de Grenoble, European Two-Phase Group Meeting, Winfrith.

Dix, G. E., 1971, "Vapour Void Fraction for Forced Convection With Sub-cooled Boiling at Low Flow Rates," Ph.D. Thesis, University of California, Berkley.

Edelman, Z., and Elias, E., 1981, "Void Fraction Distribution in Low Flow Rate Sub-cooled Boiling," *Nuclear Engineering and Design,* Vol. 66, pp. 375–382.

Egen, R. A., Dingee, D., and Chastain, J., 1957, "Vapour Formation and Behaviour in Boiling Heat Transfer," Battelle Memorial Institute, BMI-1163.

Evangelisti, R., and Lupoli, P., 1969, "The Void Fraction in an Annular Channel at Atmospheric Pressure," *Int. J. Heat Mass Transfer,* Vol. 12, pp. 699–711.

Griffith, P., Clark, J. A., and Rohsenow, W. M., 1958, "Void Volumes in Sub-cooled Boiling," ASME Paper No. 58-HT-19.

Klausner, J. F., Mel, R., Bernhard, D. M., and Zeng, L. Z., 1993, "Vapor Bubble Departure in Forced Convection Boiling," *Int. J. Heat Mass Transfer,* Vol. 36, pp. 651–662.

Koumoutsos, N., Moissis, R., and Spyridonos, A., 1968, "A Study of Bubble Departure in Forced Convection Boiling," ASME JOURNAL OF HEAT TRANSFER, Vol. 90, pp. 223–230.

Labuntsov, D. A., Lobachev, A. G., Kol'chugin, B. A., and Zakharova, E. A., 1984, "The Main Principles of Variation in Vapour Content of Equilibrium and Non-equilibrium Two-Phase Flows in Channels of Different Geometry," *Thermal Engineering,* Vol. 31, No. 9, pp. 506–508.

Levy, S., 1967, "Forced Convection Sub-cooled Boiling: Prediction of Vapor Volumetric Fraction," *Int. J. Heat Mass Transfer,* Vol. 10, pp. 951–965.

Li, J., 1992, "The Onset of Significant Void in Boiling Flows Over a Wide Range of Operation Conditions," M. Eng. Thesis, Carleton University, Ottawa, Ontario, Canada.

Martin, R., 1972, "Measurement of the Local Void Fraction at High Pressure in a Heating Channel," *Nuclear Science and Engineering,* Vol. 48, pp. 125–138.

Maurer, G. W., 1960, "A Method of Predicting Steady-State Boiling Vapour Fractions in Reactor Coolant Channels," Westinghouse Electric Corp., Atomic Power Division, WAPD-BT-19.

McLeod, R. D., 1986, "Investigation of Sub-cooled Void Fraction Growth in Water Under Low Pressure and Low Flow Rate Conditions," M. Eng. Thesis, Carleton University, Ottawa, Ontario, Canada.

Rogers, J. T., Salcudean, M., Abdullah, Z., McLeod, D., and Poirier, D., 1987, "The Onset of Significant Void in Up-flow Boiling of Water at Low Pressure and Velocities," *Int. J. Heat Mass Transfer,* Vol. 30, pp. 2247–2260.

Rogers, J. T., and Li, J., 1992, "Prediction of the Onset of Significant Void in Flow Boiling of Water," *Fundamentals of Sub-cooled Flow Boiling,* R. D. Boyd, Sr., and S. G. Kandlikar, eds., ASME HTD-Vol. 217.

Rouhani, S. Z., 1965, "Void Measurement in the Region of Sub-cooled and Low Quality Boiling," Symposium on Two-Phase Flow, University of Exeter.

Rouhani, S. Z., 1968, "Calculation of Steam Volume Fraction in Sub-cooled Boiling," ASME JOURNAL OF HEAT TRANSFER, Vol. 90, pp. 158–164.

Rouhani, S. Z., and Axelson, E., 1970, "Calculation of Void Volume Fraction in the Sub-cooled and Quality Boiling Regions," *Int. J. Heat Mass Transfer,* Vol. 13, pp. 383–393.

Saha, P., and Zuber, N., 1974, "Point of Net Vapor Generation and Vapor Void Fraction in Sub-cooled Boiling," *Proc. Fifth International Heat Transfer Conference,* Tokyo, Vol. IV, pp. 175–179.

Staub, F. W., 1968, "The Void Fraction in Sub-cooled Boiling. Prediction of Initial Point of Net Vapor Generation," ASME JOURNAL OF HEAT TRANSFER, Vol. 90, pp. 151–157.

Staub, F. W., 1969, "Heat Transfer and Hydraulics: The Effects of Sub-cooled Voids," Final report, NYO-3679-8.

Tong, W., Bar-Cohen, A., Simon, T. W., and You, S. M., 1990, "Contact Angle Effects of Boiling Incipience of Highly Wetting Liquids," *Int. J. Heat Mass Transfer,* Vol. 33, pp. 91–104.

Winterton, R. H. S., 1984, "Flow Boiling: Prediction of Bubble Departure," *Int. J. Heat Mass Transfer,* Vol. 27, pp. 1422–1424.

A Technique for Establishing Inverted Annular Flow Through a Fast Power Transient

X. C. Huang[1] and G. Bartsch[2]

Introduction

During the quenching process of a hot metal tube, a sequence of different flow regimes and boiling modes may occur along the flow direction, e.g., the single-phase liquid flow, bubbly flow, inverted annular flow, agitated flow, dispersed flow, and single-phase vapor flow. Of the flow regimes ahead of the quench front, the inverted annular flow together with the axial heat conduction through the tube wall represents one of the important heat transfer mechanisms that directly influence the quenching velocity. Therefore, many experimental studies have been conducted for the inverted annular flow under steady-state conditions.

[1] Research Associate, Dept. of Mechanical Engineering, University of Ottawa, 770 King Edward, Ottawa, Ontario, Canada K1N 6N5.

[2] Institut fuer Energietechnik, TU Berlin, Marchstr. 18, 10587 Berlin, Federal Republic of Germany.

Contributed by the Heat Transfer Division of THE AMERICAN SOCIETY OF MECHANICAL ENGINEERS. Manuscript received by the Heat Transfer Division June 1993; revision received December 1993. Keywords: Boiling, Measurement Techniques, Transient and Unsteady Heat Transfer. Associate Technical Editor: R. Nelson, Jr.

One frequently used technique for establishing the steady-state inverted annular flow is the hot-patch technique, which was first proposed by Groeneveld and Gardiner (1978). The hot patch may be indirectly heated with cartridge heaters or directly heated in the form of locally reduced wall thickness. To establish inverted annular flow with the hot-patch technique, the test section and the hot patch are heated to a high temperature with no liquid flow. Liquid flow is introduced into the test section subsequently. After some careful adjustment of the heating power to the test section, a vapor patch can be established over the entire heat transfer surface. One problem related to this technique is that the test section must be heated first under dry conditions that may change the surface condition after repeated heating and quenching processes, especially for liquids with high saturation temperatures. For cryogenic liquids with low saturation temperatures, the hot patch may be first heated without diverting the flow. The vapor patch can be made to spread out of the hot patch by increasing the heating power to the test section. However, for high flow rates and high inlet subcoolings, the spreading speed of the vapor patch can be very slow and the wall temperature in the upstream region may exceed the temperature limit of decomposition of the cryogenic liquid.

Another method is to use temperature-controlled test sections, which can be brought to the film boiling regime without dry heating of the test section (Cheng et al., 1978; Johannsen and Kleen, 1984). However, this type of test section is very complicated and expensive to construct and is furthermore restricted to short test sections with large wall thickness.

In the following we propose a transient technique for quickly establishing the inverted annular flow, which was tested for water using a directly heated thin-walled test section under low flow and low pressure conditions.

Principle

During a steady-state or slow power-transient experiment with a uniformly heated tube, the critical-heat-flux phenomenon usually occurs first at the outlet. Wall temperatures in this region rise quickly to a very high level, while the rest of the heat transfer surface remains in nucleate boiling. The cause of this axial nonuniformity is the change of the local thermodynamic condition or/and flow regime along the test section. The new technique uses a power transient. The potential nonuniform boiling heat transfer normally occurring along the inner surface of the tube will be dominated by the uniform heat source inside the wall, so that the axial wall temperature changes along the test section will be reduced. Therefore, there is the possibility that, if the power transient is fast enough, the whole test section wall may be brought to a high temperature level, i.e., into the film boiling regime, quite uniformly. Once the inverted annular flow has been reached, it can be maintained by quickly reducing the power input to the test section to an appropriate lower level, which corresponds to the steady-state film boiling heat transfer.

Experimental Setup

The test section used to test the above-mentioned principle is an Inconel-600 tube of 12 mm o.d., 1.5 mm wall thickness with a length of 399 mm. It is heated directly with a low-voltage DC power supply (15 V × 2500 A), which can be controlled manually or automatically using a function generator. Sixteen NiCr–Ni sheathed thermocouples of 0.5 mm diameter are fixed on the outer surface of the test section by clamps with an average axial distance of about 16 mm. Exact thermocouple locations are given in Fig. 1. The measurement of the wall temperature and loop signals is accomplished by a Keithley Series 500 Data Acquisition and Control System.

The water loop consists of a centrifugal pump, filters, demineralizer, turbine flow meters, pressurizer, condenser, and cooler. Double-distilled water is used to fill the loop and a high purity of water is maintained using the demineralizer. The present loop

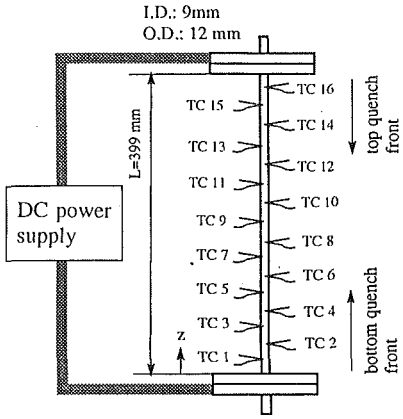

Thermocouple locations

TC No.	z (mm)	TC No.	z (mm)
1	16	9	197
2	42	10	219
3	64	11	242
4	85	12	266
5	105	13	295
6	123	14	316
7	145	15	348
8	168	16	370

Fig. 1 Sketch of the test section

allows the stabilization of the inlet condition for pressure from 0.1 to 1.0 MPa, mass flux from 50 to 500 kg/m^{2}s, and inlet subcooling from 5 to 50 K. Both upward and downward flow tests can be conducted with the loop by arranging the bypass.

Uncertainties of the directly measurable data are ±5 kPa for pressure, ±1.5 percent for mass flow rate, ±1 K for inlet subcooling, and ±1 K for wall temperatures.

Experimental Results

The above-described experimental technique was tested for mass flux less than 200 kg/m^{2}s and inlet subcooling lower than 30 K both at the atmospheric pressure and at the pressure of 0.4 MPa. The upper limits of the mass flux and the inlet subcooling are imposed by the limit of the present power supply. A fast rampwise power transient was applied at first for heating the test section, but it turned out to be more convenient simply to use a power surge.

Experimental results are shown in Fig. 2 for the inlet condition of 0.1 MPa pressure, 50 kg/m^{2}s mass flux, and 10 K inlet subcooling. The test section was first heated with a power of about 0.8 kW. Nucleate boiling occurred on the heat transfer surface at this condition. The heating power was then suddenly switched to a much higher level of about 13 kW. This could create a temperature transient as high as 100 K/s. As the wall temperatures at all measurement locations reached about 600°C after about 5 s, the power supply was switched back to the lower value of 0.8 kW. After this process, the inverted annular flow prevailed over the entire heat transfer surface, as is illustrated in Fig. 2 for both upward flow and downward flow. Because no hot patches were provided at the inlet and outlet of the present test section, quenching took place subsequently as expected. For the case of upward flow, there were two quench fronts originating from the outlet and inlet, which met each other at the middle of the test section. In contrast, there was only one quench front originating from the inlet for downflow. The quenching pattern (the number of quenching fronts and the wall temperature traces) depends on the inlet subcooling. This parametric effect may be due to the interaction between vapor bubbles produced behind the quenching front and the vapor film in the inverted annular flow regime.

The peak heating power of 13 kW has proved to be high enough for the parameter range studied. A higher heating power does not obviously influence the results except that the duration of the power pulse must be correspondingly reduced to keep the same wall temperature. However, if the selected peak heating power is not high enough, part of the boiling surface may not be brought to the film boiling regime and this can be regarded as the criterion for selecting the appropriate peak heating power. The lower value of the heating power must be chosen according to the inlet conditions and the required wall temperature in the inverted annular flow regime. Actually it is very convenient to

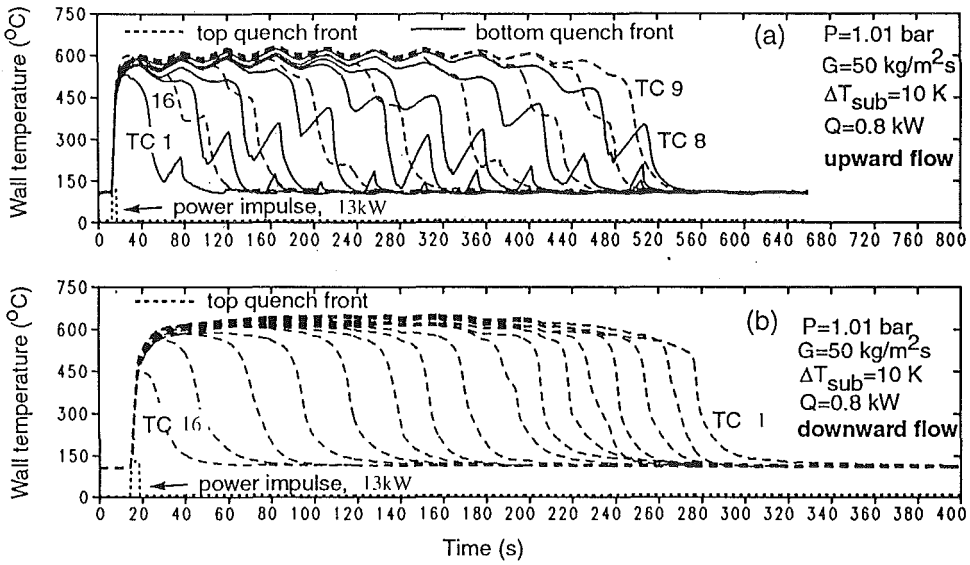

Fig. 2 Wall temperature traces for upward and downward flows

adjust the power settings because an experimental run can be repeated within several minutes.

The application of the present method requires that the power supply system be quickly switched between two or three different power levels. Electronically controllable power supplies usually have both manual and automatic control modes. Through different settings of these two modes, this requirement can be easily satisfied. Another possibility is to use two or three transformers with different settings that are connected to the test section via a multiswitch. To prevent the test section from being overheated, the wall temperature measurements should also be simultaneously used for burnout protection, which can trigger a complete shutdown of the heating power if one of the thermocouple readings exceeds the preset value. According to our experience, the timing of switching the power supply from the peak value to the lower value can be reliably determined according to thermocouple readings.

To study the steady-state inverted annular flow, the present technique must be combined with the existing hot-patch technique to anchor the quenching front.

Summary

An experimental technique for quickly establishing inverted annular flow via a fast power transient was proposed that does not require the fluid flow be first diverted into a bypass. This may help to reduce possible changes in the boiling surface conditions due to repeated heating of an empty tube, especially for fluids with high saturation temperatures. To achieve fully steady-state inverted annular flow, this method should be combined with the existing hot-patch technique to anchor the quenching front. The present technique was tested for water under low flow and low pressure conditions. Its applicability for other flow conditions and other fluids will be further explored in future studies.

References

Cheng, S. C., Ng, W. W. L., and Heng, K. T., 1978, "Measurement of Boiling Curves of Subcooled Water Under Forced Convective Conditions," *International Journal of Heat and Mass Transfer,* Vol. 21, pp. 1385–1392.

Groeneveld, D. C., and Gardiner, G., 1978, "A Method of Obtaining Flow Film Boiling Data for Subcooled Water," *International Journal of Heat and Mass Transfer,* Vol. 21, pp. 664–665.

Johannsen, K., and Kleen, U., 1984, "Steady-State Measurement of Forced Convective Surface Boiling of Subcooled Water at and Beyond Maximum Heat Flux via Indirect Joule Heating of a Test Section of High Thermal Conductance," *Multi-Phase Flow and Heat Transfer III, Part B: Applications,* T. N. Veziroglu and A. E. Bergles, eds., Elsevier Science Publisher B. V., Amsterdam, pp. 755–776.

Semi-analytical Design of a Falling Film Absorber

A. T. Conlisk[1]

Nomenclature

B = mass transfer driving parameter
c_p = specific heat
D_{AB} = mass diffusion coefficient
Fr = Froude number
g = acceleration due to gravity
h = h^*/h_0^*
h^* = dimensional film thickness
h_0^* = dimensional film thickness at the inlet
h_1 = $h = 1 + \delta^{1/2}Bh_1 + \ldots$
h_{abs} = heat of absorption
Ja = Jakob number = $c_p\Delta T/h_{abs}$
k = thermal conductivity
L = tube length
Le = Lewis number = Pr/Sc
$\dot{m}$ = dimensionless mass flux
$\dot{m}_{a0}$ = scaled absorbed mass flux
Pr = Prandtl number = $\mu c_p/k$
Re = Reynolds number = $U_0h_0^*/\nu$
Sc = Schmidt number = ν/D_{AB}
T_{Sin} = film surface temperature at the inlet

[1] Department of Mechanical Engineering, The Ohio State University, Columbus, OH 43210.

Contributed by the Heat Transfer Division and presented at the International Absorption Heat Pump Conference, New Orleans, Louisiana, January 18–21, 1994. Manuscript received by the Heat Transfer Division July 1993; revision received May 1994. Keywords: Condensation, Mass Transfer, Thin Film Flow. Associate Technical Editor: Y. Bayazitoglu.

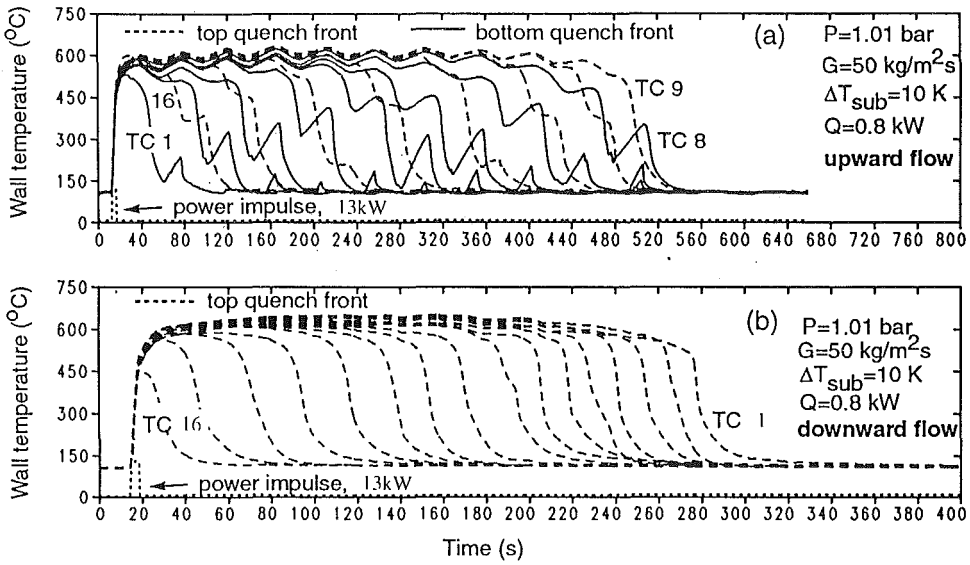

Fig. 2 Wall temperature traces for upward and downward flows

adjust the power settings because an experimental run can be repeated within several minutes.

The application of the present method requires that the power supply system be quickly switched between two or three different power levels. Electronically controllable power supplies usually have both manual and automatic control modes. Through different settings of these two modes, this requirement can be easily satisfied. Another possibility is to use two or three transformers with different settings that are connected to the test section via a multiswitch. To prevent the test section from being overheated, the wall temperature measurements should also be simultaneously used for burnout protection, which can trigger a complete shutdown of the heating power if one of the thermocouple readings exceeds the preset value. According to our experience, the timing of switching the power supply from the peak value to the lower value can be reliably determined according to thermocouple readings.

To study the steady-state inverted annular flow, the present technique must be combined with the existing hot-patch technique to anchor the quenching front.

Summary

An experimental technique for quickly establishing inverted annular flow via a fast power transient was proposed that does not require the fluid flow be first diverted into a bypass. This may help to reduce possible changes in the boiling surface conditions due to repeated heating of an empty tube, especially for fluids with high saturation temperatures. To achieve fully steady-state inverted annular flow, this method should be combined with the existing hot-patch technique to anchor the quenching front. The present technique was tested for water under low flow and low pressure conditions. Its applicability for other flow conditions and other fluids will be further explored in future studies.

References

Cheng, S. C., Ng, W. W. L., and Heng, K. T., 1978, "Measurement of Boiling Curves of Subcooled Water Under Forced Convective Conditions," *International Journal of Heat and Mass Transfer,* Vol. 21, pp. 1385–1392.

Groeneveld, D. C., and Gardiner, G., 1978, "A Method of Obtaining Flow Film Boiling Data for Subcooled Water," *International Journal of Heat and Mass Transfer,* Vol. 21, pp. 664–665.

Johannsen, K., and Kleen, U., 1984, "Steady-State Measurement of Forced Convective Surface Boiling of Subcooled Water at and Beyond Maximum Heat Flux via Indirect Joule Heating of a Test Section of High Thermal Conductance," *Multi-Phase Flow and Heat Transfer III, Part B: Applications,* T. N. Veziroglu and A. E. Bergles, eds., Elsevier Science Publisher B. V., Amsterdam, pp. 755–776.

Semi-analytical Design of a Falling Film Absorber

A. T. Conlisk[1]

Nomenclature

B = mass transfer driving parameter
c_p = specific heat
D_{AB} = mass diffusion coefficient
Fr = Froude number
g = acceleration due to gravity
h = h^*/h_0^*
h^* = dimensional film thickness
h_0^* = dimensional film thickness at the inlet
h_1 = $h = 1 + \delta^{1/2}Bh_1 + \ldots$
h_{abs} = heat of absorption
Ja = Jakob number = $c_p\Delta T/h_{abs}$
k = thermal conductivity
L = tube length
Le = Lewis number = Pr/Sc
$\dot{m}$ = dimensionless mass flux
$\dot{m}_{a0}$ = scaled absorbed mass flux
Pr = Prandtl number = $\mu c_p/k$
Re = Reynolds number = $U_0h_0^*/\nu$
Sc = Schmidt number = ν/D_{AB}
T_{Sin} = film surface temperature at the inlet

[1] Department of Mechanical Engineering, The Ohio State University, Columbus, OH 43210.

Contributed by the Heat Transfer Division and presented at the International Absorption Heat Pump Conference, New Orleans, Louisiana, January 18–21, 1994. Manuscript received by the Heat Transfer Division July 1993; revision received May 1994. Keywords: Condensation, Mass Transfer, Thin Film Flow. Associate Technical Editor: Y. Bayazitoglu.

T_{Win} = wall temperature at the inlet
ΔT = $T_{Sin} - T_{Win}$
ΔT_W = overall wall temperature difference
u = dimensionless fluid velocity in the y direction
u_0 = $u = \epsilon u_0 + \ldots$
U_0 = velocity scale
ω = dimensionless velocity in the z direction
y = dimensionless coordinate normal to wall
z = dimensionless coordinate along the wall
α = ρ_ω/ρ
δ = $1/\epsilon$ ReSc
ϵ = h_0^*/L
η = y/h
θ = $(T - T_{Win})/\Delta T$
θ_S = dimensionless film surface temperature
θ_W = dimensionless wall temperature
ν = mixture kinematic viscosity
ρ = mixture density
ρ_ω = density of water
ω_A = mass fraction of species A
ω_{ASin} = film surface mass fraction at the inlet
ω_{ABULK} = mass fraction in the bulk; constant
$\Delta\omega$ = $\omega_{ASin} - \omega_{ABULK}$
Ω = scaled mass fraction (Eq. (3))

Introduction

The design of an absorption heat pump usually begins with a thermodynamic analysis of the proposed cycle; the outputs of this analysis are inlet and outlet mass fractions and temperatures of each component of the heat pump, and the required mass fluxes. However, the thermodynamic analysis does not address how or whether the desired states can be reached. The present and also previous work (Conlisk, 1992, 1994; Patnaik et al., 1993; Perez-Blanco, 1988; Andberg and Vliet, 1983; Miller, 1991, 1992) addresses the question of how the desired states may be reached based on a nonequilibrium analysis of the heat and mass transfer processes that occur within a falling film absorber.

The purpose of the present paper is to present a design procedure, requiring a minimum of input data, to predict the performance of a vertical tube absorber. This work can be used to size absorbers without the need to build expensive test facilities. In what follows we show that, in fact, the solution for the mass fraction within the liquid film may be obtained analytically using the Laplace transform. Moreover, since the flow rates of interest are low, the fluid motion within the film may be calculated analytically. This means that only the temperature distribution within the liquid film must be calculated numerically. It is useful to note that the present numerical method is extremely robust and is able to resolve the discontinuity of the temperature and absorbed mass flux at the inlet of the tube without the numerical instabilities present in conventional finite difference techniques (Conlisk, 1992). The advantage of the present approach over conventional one or two-dimensional computational approaches is that heat transfer coefficients are not required for solution of the problem; there are no free parameters employed in the present work. In addition, the approach has been validated by comparison with recent experimental data (Conlisk, 1992); the comparison between theory and experiment is discussed in the next section. Additional references and an extensive discussion of past work in the area are given by Conlisk (1992, 1994).

The geometry of the present study is depicted in Fig. 1. The focus of this work is on the heat and mass transfer within the liquid film, which is assumed to be a lithium bromide–water mixture. Two aspects of the present work not considered by Conlisk (1992) are of interest here. First, the behavior of the total mass absorbed into the tube as a function of increasing flow rate and tube length is identified. Second, it is pointed out here that absorption solutions may be obtained only for a limited range of inlet mass fraction and temperature for a given vapor pressure.

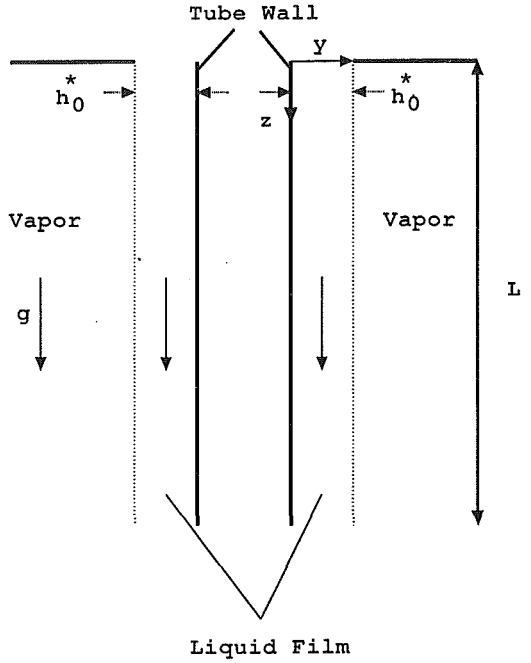

Fig. 1 Cross-sectional view of the vertical tube considered in the present work

The fully two-dimensional solutions presented here thus suggest inlet conditions that can lead to better performance of the absorber. This feature of the present work is impossible to predict using a one-dimensional approach.

Since the film thickness is much smaller than the tube radius, and the length of the tube, gradients in the direction normal to the wall are dominant and thus the terms in the Navier–Stokes equations involving curvature are negligible. Other assumptions are as in Grossman (1983), except for the assumption of constant film thickness, which will emerge from the analysis. In this case the solution of the Navier–Stokes equations for the velocity field in dimensionless form is given by the classical Nusselt solution (Nusselt, 1916)

$$u = -\epsilon\, \mathrm{ReFr} y^2 h_z/2, \quad \omega = \mathrm{Fr}\, \mathrm{Re}(yh - y^2/2), \tag{1}$$

where $\epsilon = h_0^*/L$, $\mathrm{Fr} = gh_0^*/U_0^2$ is a Froude number, and $h_z = dh/dz$. Here all distances normal to the wall have been normalized on the initial film thickness and the axial coordinate has been normalized on the length of the tube (L); velocities have been normalized on U_0. By a mass balance at the interface, the amount of fluid absorbed is given by

$$\dot{m}_a = -d\dot{m}/dz = u_0 - wdh/dz, \quad \text{at} \quad y = h. \tag{2}$$

Because the film is very thin, the continuity equation requires that $u = O(\epsilon)$ and so u_0 is defined by $u = \epsilon u_0 + \ldots$ where $\ldots$ denotes lower order terms. The negative sign in Eq. (2) indicates that the velocity of the fluid into the film is in a direction opposite to the outward unit normal to the liquid film surface. To determine the appropriate values of h_0^* and U_0 given the flow rate, the definition of the solution flow rate at the inlet specifies the product $U_0 h_0^*$; in addition, the average velocity is related to h_0^* through the Nusselt relation $U_0 = gh_0^{*2}/\nu$ where ν is the kinematic viscosity, thus determining each of the values of U_0 and h_0^*. In this case ReFr = 1; the parameters for which solutions are presented are given in Table 1.

The Heat and Mass Transfer Problems

Mass Transfer. The governing equation for mass transfer is the convection–diffusion equation and this equation may be

Table 1 Parameters and fit constants C_1 and C_2 considered in this work

Absorber length, m	0.5–2.0
Absorber tube radius, m	10^{-2}
Mass flux, kg/min	0.3–0.9
Solution temperature, K	327.00
Mass fraction of LiBr at inlet	0.6200
Absorber pressure, torr	9.83
Reynolds number	20–50
Prandtl number	21.12
Schmidt number	2421
Lewis number	0.0087
Froude number	0.03–0.05
Jakob number	0.0005
ϵ	$\sim 10^{-4}$
C_1	−0.00490
C_2	1.9891

solved numerically; however, using simple scaling arguments, the governing equation may be reduced to a simple heat equation. Define a scaled mass fraction (species A is water)

$$\Omega = \frac{\omega_A - \omega_{ABULK}}{\omega_{ASin} - \omega_{ABULK}}, \tag{3}$$

and near the interface defining, $\bar{\eta} = (1 - \eta)/\delta^{1/2}$; then in terms of Ω we have, to leading order in the small parameter δ,

$$\frac{\partial^2 \Omega}{\partial \bar{\eta}^2} = h^2 w \frac{\partial \Omega}{\partial z} - \frac{B}{\alpha} \frac{\partial \Omega}{\partial \bar{\eta}}\bigg|_{\bar{\eta}=0} \frac{\partial \Omega}{\partial \bar{\eta}}, \tag{4}$$

where B is an overall mass transfer driving parameter and is defined by $B = (\omega_{ASin} - \omega_{ABULK})/(1 - \omega_{ASin})$. In this problem B is small and often much less than δ; at the liquid–vapor interface,

$$\delta^{1/2} B \frac{\partial \Omega}{\partial \bar{\eta}} = \alpha h \dot{m}_a (1 + O(B)) \quad \text{at} \quad \bar{\eta} = 0. \tag{5}$$

Equation (4) balances for $B \to 0$; however the boundary condition at $\bar{\eta} = 0$ does not; the conclusion that must be reached is that since B and δ are both small, then $\dot{m}_a \sim \delta^{1/2} B$; that is, the lack of an $O(1)$ mass fraction difference and the fact that δ is small limits the amount of vapor that may be absorbed at the interface. Because of this, the film thickness variation is small and to leading order, we may take $h = 1$. Because δ is small, away from the interface, we expect the mass fraction to be constant.

The solution to this problem subject to the initial condition $\Omega = 0$ at $z = 0$ and $\Omega = 0$ as $\bar{\eta} \to \infty$ is given by

$$\Omega = -\{2/(\pi)\}^{1/2} \int_0^z \dot{m}_{a0} e^{-\bar{\eta}^2/8(z-t)} dt/(z - t)^{1/2}, \tag{6}$$

where $\dot{m}_{a0}$ is the leading order nonzero term in the absorbed flux. The leading order film thickness variation is defined by $\dot{m}_{a0} = -(dh_1/dz)$, where we have written $h = 1 + \delta^{1/2} B h_1 + \ldots$ in light of the discussion above. The average value of the mass fraction may be computed directly from the solution given above and the result is $\Omega_{AVE} = \delta^{1/2} \int_0^\infty \Omega d\bar{\eta} = 2\alpha\delta^{1/2} h_1$.

Heat Transfer. The energy equation in the present problem is also given by a heat equation (Conlisk, 1992) with boundary conditions $\theta = \theta_w$ at $\eta = 0$, and

$$\text{Ja} \frac{\partial \theta}{\partial \eta} = -\epsilon \, \text{RePr} \delta^{1/2} B \dot{m}_{a0} \quad \text{at} \quad \eta = 1. \tag{7}$$

The initial condition is $\theta = 0$ at $z = 0$. Note that the assumption of constant wall temperature has *not* been invoked.

The details of the numerical scheme used to solve the problem are discussed in detail by Conlisk (1992); those results indicate that the temperature distribution exhibits a boundary layer character in the regime near the inlet to the tube due to the discontinuity there. In addition, extensive comparisons with experiments conducted at Oak Ridge by Miller (1992) have been made and these are summarized on Tables 2 and 3. The wall temperature for data sets 1 and 2 is as described by Conlisk (1992). Note the good agreement with the data; it is important further to emphasize that no free parameters have been used to produce the results and so the results depicted on Table 3 are truly predictive.

Table 2 Selected parameters for two of the data sets provided by Miller (1992); from Conlisk (1992)

Data set	1	2
Mass flux, kg/min	0.5018	0.3590
Solution temperature, K	308.02	327.00
Mass fraction of LiBr at inlet	0.5633	0.6261
Absorber pressure, torr	10.86	9.83
Reynolds number	31.31	20.18
ϵ	0.00019	0.00017
C_1	−0.00560	−0.00490
C_2	2.2118	1.9891

Design Procedure

To close the problem for the calculation of the absorbed mass flux $\dot{m}_{a0}$ and initiate the design process, equilibrium will be assumed at the interface and the temperature and mass fraction are assumed to be related linearly. Using the definition of B, assuming the bulk properties are constant, the equation for ω_{ASin} is given by

$$\omega_{ASin}^2 - \left(1 + \omega_{ABULK} + \beta_0 - C_1 \frac{\text{Le}^{1/2} h_{abs}}{c_p}\right) \omega_{ASin} + \omega_{ABULK} + \beta_0 - C_1 \frac{\text{Le}^{1/2} h_{abs}}{c_p} \omega_{ABULK} = 0, \tag{8}$$

where $\beta_0 = \beta\Delta\omega$ and C_1 and C_2 are fixed constants defined by the equilibrium condition, $\Omega_S = (C_1 \Delta T/\Delta\omega)\theta_S + \beta$. The details of how Eq. (8) is derived are given by Conlisk (1992).

To specify the wall temperature we assume

$$\theta_\omega = \frac{\Delta T_W}{\Delta T} z^{1/2}. \tag{9}$$

In Eq. (9) ΔT_W is a parameter to be specified and is the overall temperature difference between the inlet and the outlet at the wall and is defined by $\Delta T_W = T_{Wout} - T_{Win}$. This parameter can be chosen to obtain a desired outlet temperature based on a cycle analysis. In a countercurrent design, which is of interest here, $\Delta T_W < 0$. All the results to be discussed here correspond to the absorber pressure of 9.83 torr, and inlet solution properties given in Table 1.

Figure 2 gives the results for the dimensionless mass flux parameter $M_{a0} = -\epsilon\delta^{1/2} B \dot{m}_{a0}$ as a function of the parameter ϵ; for fixed Reynolds number, increasing values of ϵ correspond to shorter tube lengths. Note that as ϵ increases, M_{a0} increases substantially. This result suggests that the use of long tubes to in-

Table 3 Comparisons between theory and experiment for the parameters of Table 1; from Conlisk (1992). No free constants are used in the comparisons.

Data set	1	2
Average mass fraction libr out		
Experiment	0.5404	0.6104
Theory	0.5359	0.6082
Average temperature out		
Experiment	308.13	322.94
Theory	301.64	320.82
Mass absorbed, kg/min		
Experiment	0.0213	0.0092
Theory	0.0257	0.0107

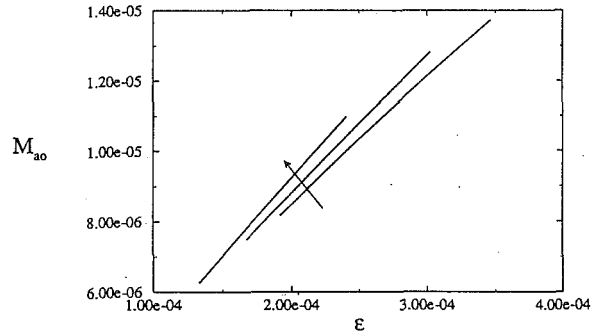

Fig. 2 Dimensionless mass absorption parameter M_{a0} as a function of ϵ for several solution Reynolds numbers, Re = 16.87, 33.74, 50.61, and $\Delta T_W = -5$ K. Arrow denotes decreasing Reynolds number.

crease heat and mass transfer area is not an efficient means to increase the absorption rate to the tube surface. For reference, the value of $\epsilon = 0.00024$ corresponds to a tube length of about one meter; a Reynolds number of 16.87 corresponds to a flow rate of 0.3 kg/min. On the other hand, M_{a0} decreases as the Reynolds number is increased. As noted above, this is because the region near the interface over which substantial mass transfer takes place is proportional to $\mathrm{Re}^{-1/2}$ by the definition of δ.

The outlet mass fraction of water as a function of ϵ is depicted on Fig. 3. Here we note that the mass fraction of water is higher at the lower Reynolds numbers and this is consistent with the result for the absorbed mass flux.

The present results are sensitive to the bulk mass fraction at the inlet. Table 4 depicts results for three values of the bulk inlet mass fraction. Note the rapid decrease in the value of $\Delta\omega$, which is the overall mass transfer driving potential as the mass fraction approaches 0.385. Additional results for this temperature and pressure show that for $\omega_{ABULK} \simeq 0.387$, $\Delta\omega$ actually becomes negative, indicating that mass transfer *toward* the film surface is taking place. This situation is clearly not desirable. Since the calculation of the inlet surface mass fraction depends only on thermodynamic properties (see Eq. (8)) and is independent of flow rate, this result is valid for the range of lengths and solution flow rates considered. This means that essentially no numerical work beyond evaluating Eq. (8) is required to determine whether the given inlet state (T, p, ω) will yield $\Delta\omega > 0$ as desired.

Discussion

In the present paper we have presented solutions for the heat and mass transfer problems for a falling film, which can be used to size absorbers. The main advantage of the present approach is that no free parameters have been used to calculate the solutions and thus the results presented here are truly predictive in character. This fact differentiates this paper from all previous work in this area.

A major result of the present calculations for the LiBr–water mixture is that increasing tube length to increase heat and mass transfer rates is of limited utility in increasing the absorption rate. Moreover, increasing flow rate is counterproductive as well, as noted by the decrease in dimensionless mass flux as the Reynolds number increases. The implication is that a bank of short tubes operating at lower individual Reynolds numbers will be most efficient for the absorption process.

It has often been stated that the effect of waves on the mass transfer process may act to enhance the mass transfer process (Javdani, 1974; see Conlisk, 1992, for additional references). It is well known that a laminar film may exhibit a wavy character for a Reynolds number, based on mass flow rate as low as about 30. A quantitative approach had been taken much earlier by Javdani (1974). He suggests that the enhancement effect, based on a significant increase in the Sherwood number, is a function of a single dimensionless variable. A detailed discussion of the application of the Javdani analysis to the present situation is described in Conlisk (1992) and suggests that the direct effect of waves on mass transfer within the film is negligible.

Table 4 Behavior of the solutions for several values of ω_{ABULK}. The specific data here are for $L = 1$ m, solution Reynolds number 33.74, $\Delta T_W = -5$ K. Note that the parameters $\Delta\omega$ and ΔT are independent of Reynolds number.

ω_{ABULK}	0.3750	0.3800	0.3850
$\Delta\omega$	0.0057	0.0033	0.0009
ΔT, K	1.2400	0.7160	0.1900
B	0.0092	0.0053	0.0014
Ja	0.0009	0.0005	0.0001
ω_{Aout}	0.3820	0.3858	0.3896
T_{Bout}	322.92	322.83	322.73
$\dot{m}_{abs}$, kg/min	0.0068	0.0057	0.0045

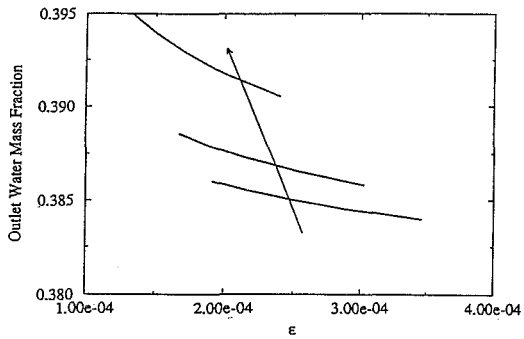

Fig. 3 Mass fraction of water at the outlet of the tube as a function of ϵ for several values of Re = 16.87, 33.74, 50.61, and $\Delta T_W = -5$ K. Arrow denotes decreasing Reynolds number.

Acknowledgments

The continuing cooperation of Mr. William A. Miller of Oak Ridge National Laboratory and Professor Horacio Perez-Blanco of Penn State is greatly appreciated. The author is grateful for many fruitful discussions with both. The LiBr–water properties were provided by Mr. Miller.

References

Andberg, J. W., and Vliet, G. C., 1983, "Design Guidelines for Water–Lithium Bromide Absorbers," *ASHRAE Trans.*, Vol. 89, Part 1B, pp. 220–232.

Conlisk, A. T., 1992, "Falling Film Absorption on a Cylindrical Tube," *AIChE J.*, Vol. 38, No. 11, pp. 1716–1728.

Conlisk, A. T., 1994, "The Use of Boundary Layer Techniques in Absorber Design," *Proceedings of the International Absorption Heat Pump Conference*, Jan., New Orleans, pp. 163–170.

Grossman, G., 1983, "Simultaneous Heat and Mass Transfer in Film Absorption Under Laminar Flow," *Int. J. Heat Mass Transfer*, Vol. 26, No. 3, pp. 357–371.

Javdani, K., 1974, "Mass Transfer in Wavy Liquid Films," *Chem. Eng. Sci.*, Vol. 29, pp. 61–69.

Miller, W. A., 1991, 1992, private communications.

Nusselt, W., 1916, "Die Oberflachenkondensation des Wasserdampfes," *Z. Vereines deutscher Ing.*, Vol. 60, p. 569.

Patnaik, V., Perez-Blanco, H., and Ryan, W. A., 1993, "A Simple Analytical Model for the Design of Vertical Tube Absorbers," to appear, *ASHRAE Trans.*

Perez-Blanco, H., 1988, "A Model of an Ammonia–Water Falling Film Absorber," *ASHRAE Trans.*, Vol. 94, Part 1, pp. 467–483.

Journal of Heat Transfer

Discussion

Measurement of Radiative Properties of Ash and Slag by FT-IR Emission and Reflection Spectroscopy[1]

S. P. Bhattacharya.[2] Markham et al. presented results on emittance measurements of ash and slag samples. As evident from the paper, the measurements were hemispherical, not normal. Therefore, all emittance figures in the paper should be interpreted as hemispherical emittance. Figure 7 of the paper shows three curves, one for the measured emittance of a fused slab and the remaining two predicted values, one at normal emergence (Eq. (7) of the paper), and the other considering an empirical void fraction of 0.15. Both the predicted values are about 10 percent different from the measured value. This difference is due to the fact that the predicted values are for normal emittance, which are compared against measured values that are hemispherical. For dielectric materials, the ratio of hemispherical and normal emittance is about 0.9 (Wall et al., 1994), and this is close to the ratio of the data in the top two curves in Fig. 7. The lead author (J. R. Markham) kindly supplied the spectral values of real (n) and absorption (k) indices of the fused sample material shown in Fig. 6 of the paper. Using these spectral n and k, spectral normal emittance and spectral hemispherical emittance of a smooth opaque slab (for which the authors calculated normal emittance, Eq. (7)) was calculated. Results are plotted in Fig. 1, which shows excellent agreement between the measured data and the predicted hemispherical emittance. In these calculations, the perpendicular and parallel components of the directional complex reflectivity are calculated first, then the arithmetic average of the two is taken considering unpolarized thermal radiation; the directional reflectivities are then integrated to get spectral hemispherical reflectivity (R_λ); and finally the spectral hemispherical emittance for an opaque slab is estimated using $\epsilon_\lambda = 1 - R_\lambda$. The procedure is after Özişik (1985) and details are available from Bhattacharya (1994). Thus it is not necessary to assume any arbitrary void fraction in order to get better agreement with the measured data. It is not clear from the paper as to the surface roughness of the fused slab, but clearly the excellent agreement between the measured and predicted hemispherical emittance values show negligible effect of the surface roughness.

Figure 8 of the paper shows the measured hemispherical emittance and predicted values for a pressed opaque wafer prepared from the ground sample. The emission characteristics clearly resembles that of powdery deposits (Wall et al., 1993). The predicted values in the paper were obtained using a simplified two-stream model and required an arbitrary choice of a constant value of 0.6 for the asymmetry factor (g). In fact, for the investigated wavelength range, 1.6–20 μm, fine particles ($\sim$2 μm) of the particular material may have asymmetry factors ranging between 0.1 and 0.8 (Bhattacharya, 1994). The albedo (ω) values in the paper were apparently taken to be spectral although it is not clear based on what particle size(s) these were calculated. However, it is known that two-stream model predictions are neither normal nor hemispherical (Brewster, 1992), because they assume an isotropic distribution of the emitted flux over the hemisphere. For powdery deposits in particular, the distribution of emitted flux is not isotropic. Although not shown here, two-stream calculations were performed using Eq. (8) of the paper with spectral values of both g (instead of a constant value of 0.6 assumed in the paper) and ω corresponding to the distributed sizes of mean diameters 1 and 2 μm. These results (Bhattacharya, 1994) are higher than the measured values reported by Markham et al. The reasonable agreement between the measured data and the predicted values in their paper using the two-stream model seems to be coincidental. It is not clear what particle size was considered in their predictions. In fact, particle size and distribution have a significant effect on any prediction. Figure 2 shows the measured emittance and several predicted hemispherical emittance values for two different mean particle sizes of 1 and 2 μm, having different distributions. While a monosize appears to match closely the measured data up to about 5 μm wavelength, the trend thereafter suggests the possible presence of a distribution of particle sizes. These calculations are based only on independent and multiple scatter in an opaque slab using a discrete ordinate method. Details of the calculation procedure are available in Bhattacharya (1994). However, for pressed slabs of fine particles, dependent effects are known to be significant, although difficult to quantify. Clearly, fundamental knowledge on dependent effects, effects of surface morphology, as well as an accurate knowledge of the size distribution are required before improved and meaningful predictions can be made.

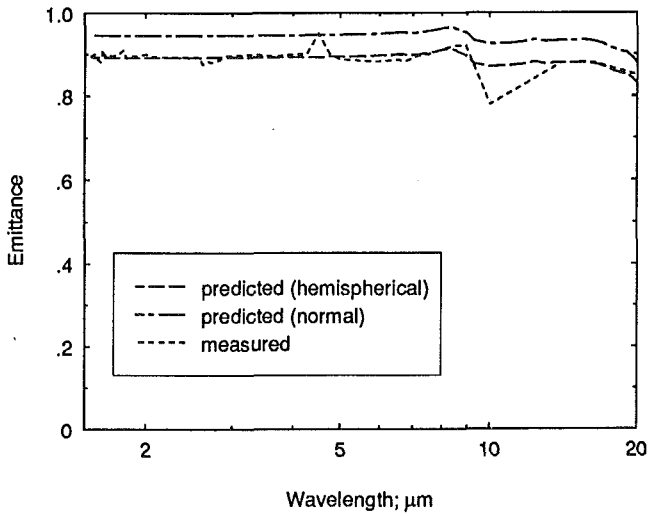

Fig. 1 Comparison of measured emittance and predicted normal and hemispherical emittance for a fused slab

[1] By J. R. Markham, P. E. Best, P. R. Solomon, and Z. Z. Yu, published in the May 1992 issue of the ASME JOURNAL OF HEAT TRANSFER, Vol. 114, pp. 458–464.

[2] Doctoral student, Department of Chemical Engineering, The University of Newcastle, Newcastle 2308, Australia.

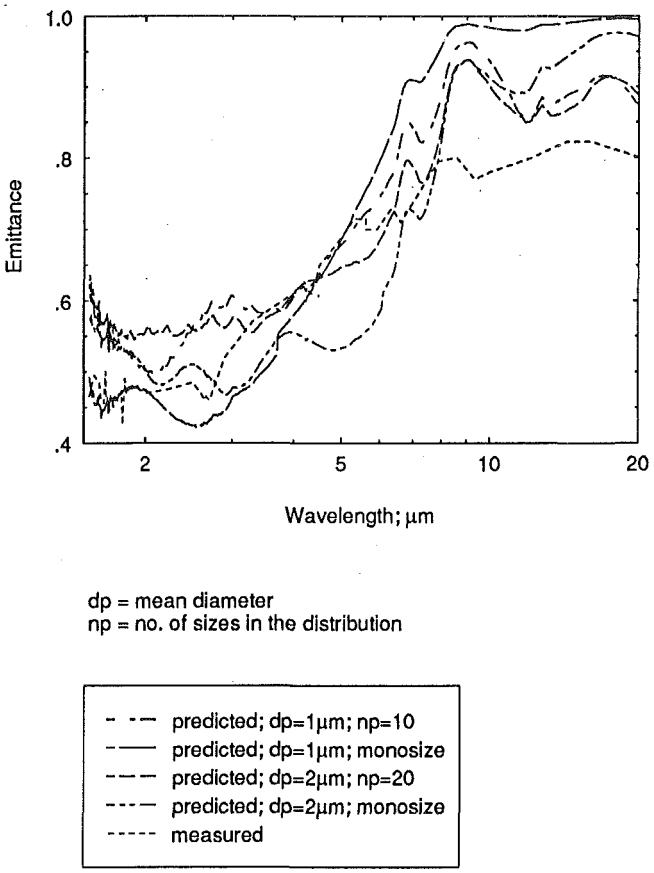

Fig. 2 Comparison of measured emittance and predicted values for the pressed wafer of ground sample, showing the effect of particle size and size distribution

There is a minor mistake in the paper, which needs to be corrected for convenience of future users of this excellent work. On page 460, first paragraph of the paper, "the incident radiation is attenuated by $1/e$" should actually be "$1/e$ of the incident radiation is transmitted in a distance of 0.8×10^{-2} mm."

References

Brewster, M. Q., 1992, *Thermal Radiation Transfer and Properties,* Wiley.

Bhattacharya, S. P., 1994, "Radiative Transfer Due to Fly Ash in Furnaces," PhD Thesis, The University of Newcastle, in preparation.

Markham, J. R., 1993, Advanced Fuel Research Inc., East Hartford, CT 06108, private communication.

Özişik, M. N., 1985, *Radiative Transfer and Its Interactions With Conduction and Convection,* Ection Werbel and Peck, New York.

Wall, T. F., Bhattacharya, S. P., Zhang, D. K., Gupta, R. P., and He, X., 1993, "The Properties and Thermal Effects of Ash Deposits in Coal Fired Furnaces," *Progress in Energy and Combustion Science,* Vol. 19, pp. 487–504.

Authors' Closure

Much of the discussion given by S. P. Bhattacharya results from a misunderstanding of terms used in our paper. In particular, he refers to our measurements being of hemispherical emissivity, when we reported them as directional. An explanation of our measurements should clarify the terms.

For samples that exhibit a Christiansen maximum in emissivity ($\epsilon = 1$), we measure spectral radiance for a small acceptance angle for near-normal take-off. Knowing (i.e., measuring) that $\epsilon = 1$ at the Christiansen wavenumber allows a determination of ϵ_ν over the whole spectrum. We refer to this determination of ϵ_ν as normal spectral emissivity. It is clearly a directional measurement.

The method of closure is also applied in our paper; for opaque samples $\epsilon_\nu = 1 - \rho_\nu$. It is relevant to ask which spectral reflectivity, ρ_ν, should be used in the equation to yield the directional ϵ_ν referred to above. In a thoughtful experiment the sample is placed in an isothermal environment, with a small opening for normal viewing of the surface. Radiation emerging from this opening is the cavity radiation for the isothermal temperature. Evidently, the sum of normal spectral emissivity and hemispherical-directional spectral reflectivity (Siegel and Howell, 1981, p. 45) is unity. For the conditions of our measurements, the hemispherical-directional spectral reflectivity is equal to the directional-hemispherical spectral reflectivity, as usual for this experiment (Siegel and Howell, 1981, p. 67).

The value of ϵ_ν that results from the application of the equation of closure is evidently the normal spectral emissivity; and it is gratifying that the spectral values so determined by closure agree well with values of the normal spectral emissivity directly measured (for examples: Fig. 2*c* in the paper under discussion; and Markham et al., 1990). S. P. Bhattacharya is incorrect in his interpretation of our measurements.

In his discussion, S. P. Bhattacharya also indicates his discontent with our modeling effort. While the two-stream model assumes hemispherical isotropy of scattering, real-life, nonisotropic scattering can be investigated by the model if the scattering is parameterized into two-stream form, as discussed by Bohren (1987). The agreement between experiment and model calculation is readily understood in these terms: It is not a coincidence.

We encourage S. P. Bhattacharya to continue to develop his modeling techniques in this area since improved models, especially of the deposition process, would significantly improve the ability to model the heat transfer in real coal-fired furnaces. We are pleased that our spectroscopic technique to measure the radiative properties of ash and slag can provide data that can be utilized for advancement of such models. We thank the author for indicating the mistake in our paper, which should read "the incident radiation is attenuated by $1 - 1/e$ in a distance of 0.8×10^{-2} mm."

References

Bohren, C. F., 1987, "Multiple Scattering of Light and Some of Its Observable Consequences," *Am. J. Phys.,* Vol. 55, pp. 524–533.

Markham, J. R., Solomon, P. R., and Best, P. E., 1990, "An FT-IR Based Instrument for Measuring Spectral Emittance of Material at High Temperature," *Rev. Sci. Instr.,* Vol. 61, pp. 3700–3708.

Siegel, R., and Howell, J. R., 1981, *Thermal Radiation Heat Transfer,* 2nd ed., Hemisphere, Washington, DC.

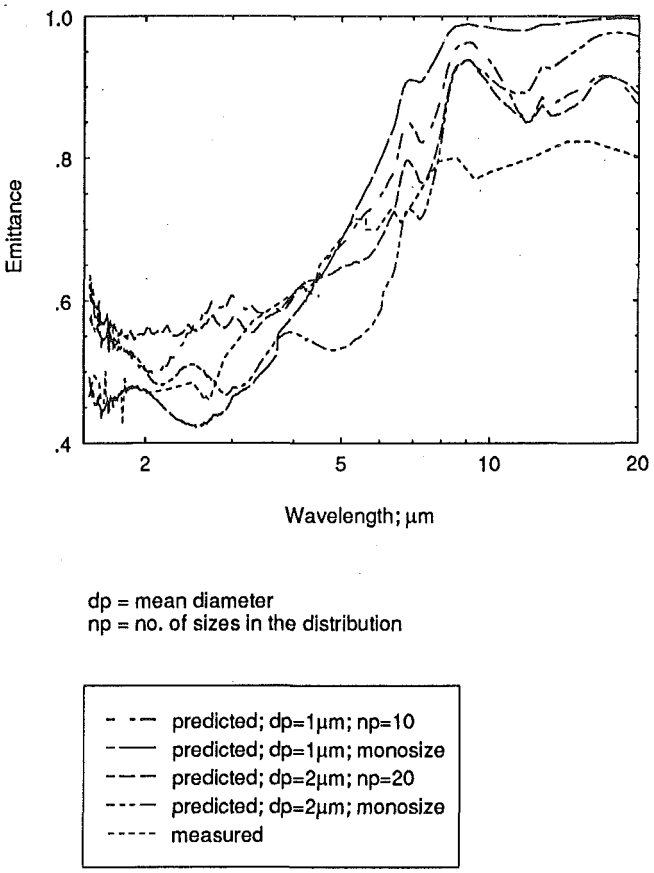

Fig. 2 Comparison of measured emittance and predicted values for the pressed wafer of ground sample, showing the effect of particle size and size distribution

There is a minor mistake in the paper, which needs to be corrected for convenience of future users of this excellent work. On page 460, first paragraph of the paper, "the incident radiation is attenuated by $1/e$" should actually be "$1/e$ of the incident radiation is transmitted in a distance of 0.8×10^{-2} mm."

References

Brewster, M. Q., 1992, *Thermal Radiation Transfer and Properties,* Wiley.

Bhattacharya, S. P., 1994, "Radiative Transfer Due to Fly Ash in Furnaces," PhD Thesis, The University of Newcastle, in preparation.

Markham, J. R., 1993, Advanced Fuel Research Inc., East Hartford, CT 06108, private communication.

Özişik, M. N., 1985, *Radiative Transfer and Its Interactions With Conduction and Convection,* Ection Werbel and Peck, New York.

Wall, T. F., Bhattacharya, S. P., Zhang, D. K., Gupta, R. P., and He, X., 1993, "The Properties and Thermal Effects of Ash Deposits in Coal Fired Furnaces," *Progress in Energy and Combustion Science,* Vol. 19, pp. 487–504.

Authors' Closure

Much of the discussion given by S. P. Bhattacharya results from a misunderstanding of terms used in our paper. In particular, he refers to our measurements being of hemispherical emissivity, when we reported them as directional. An explanation of our measurements should clarify the terms.

For samples that exhibit a Christiansen maximum in emissivity ($\epsilon = 1$), we measure spectral radiance for a small acceptance angle for near-normal take-off. Knowing (i.e., measuring) that $\epsilon = 1$ at the Christiansen wavenumber allows a determination of ϵ_ν over the whole spectrum. We refer to this determination of ϵ_ν as normal spectral emissivity. It is clearly a directional measurement.

The method of closure is also applied in our paper; for opaque samples $\epsilon_\nu = 1 - \rho_\nu$. It is relevant to ask which spectral reflectivity, ρ_ν, should be used in the equation to yield the directional ϵ_ν referred to above. In a thoughtful experiment the sample is placed in an isothermal environment, with a small opening for normal viewing of the surface. Radiation emerging from this opening is the cavity radiation for the isothermal temperature. Evidently, the sum of normal spectral emissivity and hemispherical-directional spectral reflectivity (Siegel and Howell, 1981, p. 45) is unity. For the conditions of our measurements, the hemispherical-directional spectral reflectivity is equal to the directional-hemispherical spectral reflectivity, as usual for this experiment (Siegel and Howell, 1981, p. 67).

The value of ϵ_ν that results from the application of the equation of closure is evidently the normal spectral emissivity; and it is gratifying that the spectral values so determined by closure agree well with values of the normal spectral emissivity directly measured (for examples: Fig. 2*c* in the paper under discussion; and Markham et al., 1990). S. P. Bhattacharya is incorrect in his interpretation of our measurements.

In his discussion, S. P. Bhattacharya also indicates his discontent with our modeling effort. While the two-stream model assumes hemispherical isotropy of scattering, real-life, nonisotropic scattering can be investigated by the model if the scattering is parameterized into two-stream form, as discussed by Bohren (1987). The agreement between experiment and model calculation is readily understood in these terms: It is not a coincidence.

We encourage S. P. Bhattacharya to continue to develop his modeling techniques in this area since improved models, especially of the deposition process, would significantly improve the ability to model the heat transfer in real coal-fired furnaces. We are pleased that our spectroscopic technique to measure the radiative properties of ash and slag can provide data that can be utilized for advancement of such models. We thank the author for indicating the mistake in our paper, which should read "the incident radiation is attenuated by $1 - 1/e$ in a distance of 0.8×10^{-2} mm."

References

Bohren, C. F., 1987, "Multiple Scattering of Light and Some of Its Observable Consequences," *Am. J. Phys.,* Vol. 55, pp. 524–533.

Markham, J. R., Solomon, P. R., and Best, P. E., 1990, "An FT-IR Based Instrument for Measuring Spectral Emittance of Material at High Temperature," *Rev. Sci. Instr.,* Vol. 61, pp. 3700–3708.

Siegel, R., and Howell, J. R., 1981, *Thermal Radiation Heat Transfer,* 2nd ed., Hemisphere, Washington, DC.